

AD-777 641

FRACTURE MECHANICS OF AIRCRAFT STRUCTURES

ADVISORY GROUP FOR AEROSPACE RESEARCH AND DEVELOPMENT

JANUARY 1974

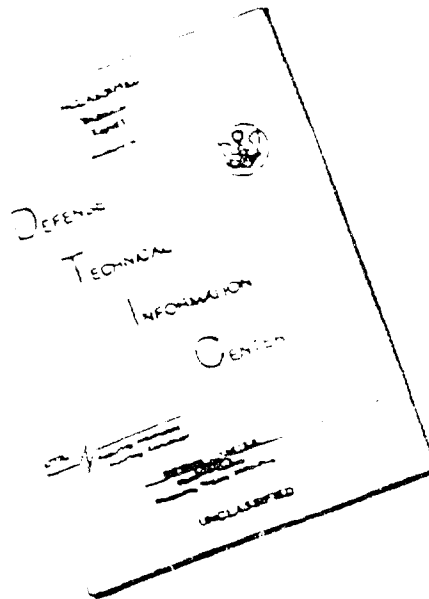
DISTRIBUTED BY:

**NTIS**

National Technical Information Service  
U. S. DEPARTMENT OF COMMERCE

BEST AVAILABLE COPY

# DISCLAIMER NOTICE



THIS DOCUMENT IS BEST  
QUALITY AVAILABLE. THE COPY  
FURNISHED TO DTIC CONTAINED  
A SIGNIFICANT NUMBER OF  
PAGES WHICH DO NOT  
REPRODUCE LEGIBLY.

REPRODUCED FROM  
BEST AVAILABLE COPY

THIS DOCUMENT CONTAINED  
BLANK PAGES THAT HAVE  
BEEN DELETED



AD777641  
AGARD-AG-176

AGARD-AG-176

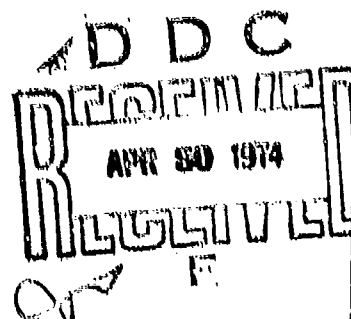


AGARDograph No. 176

on

# Fracture Mechanics of Aircraft Structures

Edited by  
H. Liebowitz



NORTH ATLANTIC TREATY ORGANIZATION

Republics of  
NATIONAL TECHNICAL  
INFORMATION SERVICE  
U. S. Department of Commerce  
Springfield, VA 22151



DISTRIBUTION AND AVAILABILITY  
ON BACK COVER

DISTRIBUTION STATEMENT A

NORTH ATLANTIC TREATY ORGANISATION  
ADVISORY GROUP FOR AEROSPACE RESEARCH AND DEVELOPMENT  
(ORGANISATION DU TRAITE DE L'ATLANTIQUE NORD)

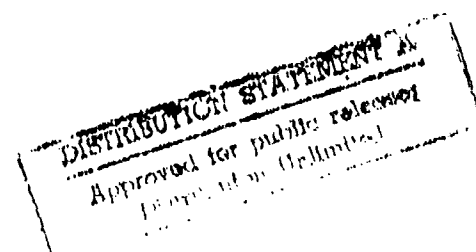
AGARDograph No.176

**FRACTURE MECHANICS OF AIRCRAFT STRUCTURES**

Edited by

Harold Liebowitz

Dean and Professor of Engineering and Applied Science  
School of Engineering and Applied Science  
George Washington University  
Washington D.C. 20006, USA



## THE MISSION OF AGARD

The mission of AGARD is to bring together the leading personalities of the NATO nations in the fields of science and technology relating to aerospace for the following purposes:

- Exchanging of scientific and technical information;
- Continuously stimulating advances in the aerospace sciences relevant to strengthening the common defence posture;
- Improving the co-operation among member nations in aerospace research and development;
- Providing scientific and technical advice and assistance to the North Atlantic Military Committee in the field of aerospace research and development;
- Rendering scientific and technical assistance, as requested, to other NATO bodies and to member nations in connection with research and development problems in the aerospace field;
- Providing assistance to member nations for the purpose of increasing their scientific and technical potential;
- Recommending effective ways for the member nations to use their research and development capabilities for the common benefit of the NATO community.

The highest authority within AGARD is the National Delegates Board consisting of officially appointed senior representatives from each member nation. The mission of AGARD is carried out through the Panels which are composed of experts appointed by the National Delegates, the Consultant and Exchange Program and the Aerospace Applications Studies Program. The results of AGARD work are reported to the member nations and the NATO Authorities through the AGARD series of publications of which this is one.

Participation in AGARD activities is by invitation only and is normally limited to citizens of the NATO nations.

The content of this publication has been produced directly from material supplied by AGARD or the authors.

Published January 1974

539.4:629.73.02



Printed by Technical Editing and Reproduction Ltd  
Harford House, 7-9 Charlotte St, London, W1P 1HD

## THE MISSION OF AGARD

The mission of AGARD is to bring together the leading personalities of the NATO nations in the fields of science and technology relating to aerospace for the following purposes:

- Exchanging of scientific and technical information;
- Continuously stimulating advances in the aerospace sciences relevant to strengthening the common defence posture;
- Improving the co-operation among member nations in aerospace research and development;
- Providing scientific and technical advice and assistance to the North Atlantic Military Committee in the field of aerospace research and development;
- Rendering scientific and technical assistance, as requested, to other NATO bodies and to member nations in connection with research and development problems in the aerospace field.
- Providing assistance to member nations for the purpose of increasing their scientific and technical potential;
- Recommending effective ways for the member nations to use their research and development capabilities for the common benefit of the NATO community.

The highest authority within AGARD is the National Delegates Board consisting of officially appointed senior representatives from each member nation. The mission of AGARD is carried out through the Panels which are composed of experts appointed by the National Delegates, the Consultant and Exchange Program and the Aerospace Applications Studies Program. The results of AGARD work are reported to the member nations and the NATO Authorities through the AGARD series of publications of which this is one.

Participation in AGARD activities is by invitation only and is normally limited to citizens of the NATO nations.

The content of this publication has been produced directly from material supplied by AGARD or the authors.

Published January 1974

539.4:629.73.02



Printed by Technical Editing and Reproduction Ltd  
Harford House, 7-9 Charlotte St, London. W1P 1HD

## PREFACE

The Structures and Materials Panel of the NATO Advisory Group for Aerospace Research and Development (AGARD) consists of engineers, scientists and technical administrators from industry, government and universities throughout the NATO nations, and is concerned with the advancement of aerospace research and development and the application of the results to the design and construction of, and the solution of problems arising during the operation of NATO military vehicles, systems and equipment. The biannual Panel Meetings provide forums for specialist multi-national discussions of problems and of research information and for initiating and monitoring cooperative studies and experimental programmes. The Panel also provides a mechanism for the planning, preparation and distribution of surveys and reports on the present state of knowledge in technical areas within the fields of Structures and Materials selected because of their importance and their relevance to current or future problems facing the NATO aerospace community.

Three years ago, the Panel, realizing that the many problems in the aerospace field experienced with new high-strength materials, flaw susceptibility, stress corrosion, non-destructive testing, fractographic material examination, crack propagation and residual strength aspects of the fatigue of aircraft structures, and brittle fracture all require that fracture mechanics concepts and related approaches be made available to the engineer and designer, set up a Fracture Mechanics Working Group to commission and monitor the preparation of a comprehensive survey of the pertinent information available on the applications of fracture mechanics to the fracture of metals. In addition this work was to cover stress concentration procedures, experimental-design approaches and other available methods of interest to the aerospace structures and materials engineer and the evaluation of the different techniques available for designing against brittle-type fracture of metals. It was recognized that fracture mechanics was an inter-disciplinary growth area of research of ever increasing importance to those people concerned with the design and operational management of aircraft especially in the light of the modern airframe fail-safe design philosophy and aircraft safety. It was therefore decided that the resulting critical survey report should be given a wide circulation within the NATO nations.

The Panel was very fortunate from the outset in securing the services as Coordinator and Editor of Professor H. Liebowitz, Dean of the School of Engineering and Applied Science, The George Washington University, Washington, D.C., a world renowned expert on the fracture of materials.

An essential feature of AGARD activities is the pooling of relevant knowledge within the NATO nations and the bringing together of specialists for informed discussions and debate on the subject concerned. This occurred in full measure within the Fracture Mechanics Working Group and the Panel is indebted not only to Professor H. Liebowitz, the Coordinator and Editor for his outstanding efforts and to all the members and participants of the Working Group for their valuable contributions, but especially to the many contributors to the monograph "Fracture Mechanics of Aircraft Structures" itself from the six nations: France, Germany, Italy, Netherlands, UK and USA and who are listed by name in the preliminary pages.

T. Gaymann  
Chairman  
AGARD Structures and Materials Panel  
Munich, Germany  
November 25, 1973

B.P. Mullins  
Chairman  
Fracture Mechanics Working Group  
AGARD Structures and Materials Panel  
Farnborough, Hants, England  
November 25, 1973

LIST OF CONTRIBUTORS

(Numbers in parentheses indicate the pages on which the authors' contributions begin.)

W. BARROIS (325; 346)  
Military Chief Engineer (Retired)  
Engineer at the Soci t  Nationale  
Industrielle A rospatiale  
Aircraft Division  
Paris, France

J.I. BLUHM (14; 74; 89; 95; 118)  
Acting Chief  
Theoretical and Applied Mechanics  
Research Laboratory  
Army Materials and Mechanics  
Research Center  
Watertown, Massachusetts 02172

Dr. ING. ENRICO BOLIS (413)  
Direttore Servizio Centrale  
Controllo Qualita  
AERITALIA  
Corso Marche, 41  
10146 Torino, Italy

Dr. DAVID BROEK (121; 167; 181; 195; 367)  
Technische Hogeschool Delft  
Tussenafdeling der Metaakkunde  
Delft 8, Rotterdamseweg 137  
The Netherlands

Dr. D.J. CARTWRIGHT (592)  
Mechanical Engineering  
University of Southampton  
Southampton, England

EBERHARD DICKHAUT (485)  
Chief of NDT Laboratory  
Motoren-Und Turbinen - Union  
M nchen GmbH, 8000 M nchen-Allach  
8 M nchen 50, Dachauer Str. 665  
M nchen, Germany

JOHN EFTIS (32)  
Associate Professor of Engineering  
and Applied Science  
School of Engineering and  
Applied Science  
George Washington University  
Washington, D.C. 20006

KLAUS GR NEWALD (494)  
Dornier System GmbH  
Research Department  
799 Friedrichshafen  
POB 648, W. Germany

Dr. ING. WOLFGANG HANSEN (475)  
Chief of Production Planning  
Motoren-Und Turbinen - Union  
M nchen GmbH, 8000 M nchen-Allach  
8 M nchen 50, Dachauer Str. 665  
M nchen, Germany

C.E. HARTBOWER (418)  
Aerojet Solid Propulsion Co.  
P.O. Box 13400  
Sacramento, California 95813

G.H. HASLAM (314)  
National Engineering Lab  
Glasgow, Scotland

Prof. H.H. JOHNSON (110)  
Chairman, Materials Science and  
Engineering  
College of Engineering  
Cornell University  
Ithaca, New York 14850

D.L. JONES (32)  
Assistant Research Professor of  
Engineering  
School of Engineering and Applied  
Science  
George Washington University  
Washington, D.C. 20006

W.T. KIRKBY (8; 288; 580)  
Structures Department  
Royal Aircraft Establishment  
Farnborough, Hampshire, England

Dr. EKKART KNORR (396)  
Industrieanlagen-Betriebsgesellschaft mbH  
8012 Ottobrunn  
Einsteinstrasse, Germany

HAROLD LIEBOWITZ (1; 32)  
Dean and Professor of Engineering  
and Applied Science  
School of Engineering and  
Applied Science  
George Washington University  
Washington, D.C. 20006

W.T. MATTHEWS (509)  
U.S. Army Materials and  
Mechanics Research Center  
Watertown, Massachusetts 02172

WOLFRAM OBERPARLEITER (370)  
Industrieanlagen-Betriebsgesellschaft mbH  
8012 Ottobrunn  
Einsteinstrasse, Germany

C.J. PEEL (503)  
Materials Department  
Royal Aircraft Establishment  
Farnborough, Hants, England

D.P. ROOKE (592)  
Royal Aircraft Establishment  
Farnborough, Hants,  
England

Dr. WALTER SCH TZ (370)  
Industrieanlagen-Betriebsgesellschaft mbH  
8012 Ottobrunn  
Einsteinstrasse, Germany

T. SWIFT (226)  
Senior Engineer Scientist  
Structural Mechanics Subdivision  
Douglas Aircraft Company  
McDonnell Douglas Corporation  
Long Beach, California 90801

C.F. TIFFANY (294)  
Engineering Advisor  
Aeronautical Systems Division  
United States Air Force  
Wright-Patterson Air Force Base  
Ohio 45433

H. VLIETGER (195)  
National Aerospace Laboratory  
Sloterweg 145, Amsterdam 17  
The Netherlands

HOWARD A. WOOD (3; 18)  
Aerospace Engineer  
Air Force Flight Dynamics Laboratory  
Air Force Systems Command  
Wright-Patterson Air Force Base  
Ohio 45433

## FOREWORD

The Structures and Materials Panel's Fracture Mechanics Working Group under the Chairmanship of Dr B.P.Mullins has been working, since its inception in 1971, to make available a requisite body of knowledge to facilitate an understanding of fracture and its implications for and applications to aircraft.

The survey on fracture mechanics has essentially been oriented to present practical aspects of aircraft. Theoretical discussions and presentations have been included, however, to afford the engineer, scientist, and aircraft designer an appreciation of the complexity of the problems involved.

The Editor, Professor H.Liebowitz, wishes to thank the Chairman, Dr Mullins, and the members of the Working Group, Mr W.Barrois, France; Dr T.Gaymann, Germany; and Col C.K.Grimes, USA, for their significant efforts and assistance in providing guidance and direction during the course of preparing the survey on fracture mechanics. Also, appreciation is given to the administrative and technical staff, especially to Dr P.K.Bamberg and Ms. Alice Guerillot, of the Structures and Materials Panel in Paris for the many helpful suggestions and assistance rendered. In addition, the Panel Coordinators from each NATO country participated in obtaining the data and surveys to make this effort a truly international cooperative project. Special thanks are due to Mr J.I.Blum who participated in the Working Group's study; also appreciation should be expressed to Drs T.E.Sullivan, A.J.Barrett, F.Niordson, J.W.Mar and W.Schütz, and Messrs N.E.Promisel, H.P.vanLeeuwen, T.F.Kearns, R.L.Ballard, and G.C.Deutsch and the other members and participants of the Structures and Materials Panel for their interest and participation in helping to achieve the objectives of this study.

Special thanks are also due to the many contributors indicated in the List of Contributors for their unfailing cooperation and untiring assistance in providing the material for the survey on Fracture Mechanics of Aircraft Structures.

H.Liebowitz  
Coordinator and Editor  
Washington, D.C.  
November 15, 1973

CONTENTS

PREFACE	111
LIST OF CONTRIBUTORS	iv
FOREWORD	v
I. INTRODUCTION (Liebowitz)	1
II. HISTORY OF LOADING OF AIRCRAFT AND EXAMPLES OF AIRCRAFT FAILURE	3
II.A Spectrum of Loading Aircraft (Wood)	3
II.B Examples of Aircraft Failure (Kirkby)	8
II.C Fracture Regimes (Bluhm)	14
III. THE USE OF FRACTURE MECHANICS PRINCIPLES IN THE DESIGN AND ANALYSIS OF DAMAGE TOLERANT AIRCRAFT STRUCTURES (Wood)	18
IV. BASIC CONCEPTS OF FRACTURE MECHANICS (Eftis, Jones, Liebowitz)	32
Appendices: Summary of Basic Test Methods and Limitations (Bluhm, Johnson)	74
V. FAIL-SAFE DESIGN PROCEDURES	120
V.A Basic Information (Broek)	121
V.B Fail-Safe Design Concepts and Fatigue Crack Propagation in Real Structures (Broek)	167
V.B.1 The Prediction of Crack Propagation (Broek)	167
V.B.2 Built-up Sheet Structures (Broek)	181
V.C Residual Strength	194
V.C.1 Built-up Sheet Structures, Wings (Vlieger, Broek)	195
V.C.2 The Application of Fracture Mechanics in the Development of the DC-10 Fuselage (Swift)	226
V.C.3 Heavy Sections (Kirkby)	288
V.C.4 Aerospace Pressure Vessels (Tiffany)	294
V.C.5 An Example of a Method for Predicting Failure (Haslam)	314
V.D Service Failures and Laboratory Tests (Barrois)	325
V.E Possibilities of Fatigue Life Assessment of Aircraft Structures Based on Random or Programmed Fatigue Tests (Barrois)	346
V.F Outlook, Future Developments (Broek)	367
VI. EXPERIMENTAL TECHNIQUES FOR DETERMINING FRACTURE TOUGHNESS VALUES (Schutz)	370
VII. FLAW DETECTION METHODS	395
VII.A Reliability of the Detection of Flaws and of the Determination of Flaw Size (Knorr)	396
VII.B Non-destructive Testing and Fracture Mechanics (Bolis)	413
VII.C Detection and Determination of Flaw Size by Acoustic Emission (Hartbower)	418
VII.D Surface Dye Penetrants (Hansen)	475
VII.E Magnetic Particle Testing (Dickhaut)	485
VII.F Flaw Detection by means of Holographic Interferometry (Grunewald)	494
VII.G An Analysis of a Test Fatigue Failure by Fractography and Fracture Mechanics (Peel)	503
Appendix 1. Typical Plane Strain Fracture Toughness of Aircraft Materials (Matthews)	509
2. Fracture Toughness Test Results (Kirkby)	580
3. Stress Intensity Factor Solutions (Rooke, Cartwright)	592
4. International System of Units	601
Subject Index	605
Author Index	614



## I. INTRODUCTION

by

Harold Liebowitz

The rising incidence in recent years of dangerous, costly, and sometimes lethal fractures of military and commercial aircraft has underscored the need for the widespread dissemination of available fracture mechanics information pertaining to aircraft. The results of fracture mechanics work in aircraft design, materials selection, nondestructive evaluation, and other important problem areas are usually not disseminated on a sufficiently broad scale nor always to the proper recipients.

The situation is made even more urgent because of the continuing development of larger, more complex, and more expensive structures which make it essential that development and application of design practices safeguarding against premature fracture be accelerated in an efficient and organized manner.

The fracture mechanics survey has been designed to fill this need. The survey makes available to aircraft designers, materials scientists, nondestructive evaluation engineers, and aeronautical and aerospace engineers a comprehensive and interdisciplinary examination of current fracture mechanics thought and practice with emphasis upon aircraft.

The chapters have been organized so that the reader may obtain an understanding of fracture mechanics concepts and their relationship and application to the unique problems of aircraft design. The importance of fail-safe design concepts in aircraft structural design is strongly emphasized with detailed discussions of the basic concepts and their applications to design, materials, and testing.

Efforts have been made in the survey to balance the information so that theoretical discussions are complemented by presentations of actual applications of these concepts. For those who must apply fracture mechanics principles to predict crack growth and critical crack lengths, many new approaches and tools are being developed which should prove invaluable. Descriptions are included on improved non-destructive testing methods, and the use of acoustic emissions, surface dye penetrants, magnetic particle testing, holography, and fractography to facilitate the determination of flaw sizes and cracks.

It has been found that a number of fracture problems develop because responsible persons are not sufficiently aware of information from other disciplines which would have made it possible to foresee the fracture. The regular dissemination of applicable information in the engineer's and scientist's own and related fields of interest could help increase the meaningful contributions which can be made to the problems of fracture prevention design to minimize the failure of structures.

The fracture mechanics survey provides an international medium for disseminating pertinent technical material, data, and information on an interdisciplinary basis. Also, this survey attempts to utilize much of the information generated by government sponsored studies and that obtained from industrial research into the factors pertaining to aircraft design, materials selection, and fracture mechanics.

Specifically, each chapter in the survey presents the following information:

Chapter II presents a summary of airframe service loadings particularly related to that portion of life following the initiation of a crack. Discussions are included on structural, operational, and internal airframe environments and the significance of airframe loadings. To enable the designer to anticipate areas of structure or components which will require particular attention in design, a series of photographs are included depicting failures that have stemmed from undetected fatigue damage. The chapter concludes with a discussion of fracture regimes to enable the designer to recognize the various specific fracture modes which might be operative under different conditions. If the relevant fracture mode governing an expected failure is recognized, then appropriately relevant design criteria can be used or developed for use in the design relationships.

Chapter III reviews current trends in the usage of high strength structural materials for aerospace applications and illustrates the manner in which fracture control procedures may be implemented to achieve a high degree of damage tolerance.

Chapter IV presents a concise and somewhat technical review of fracture mechanics, highlighting its strengths as well as current limitations, while at the same time establishing some perspective as to its relation to the general fracture process. In so doing, the importance of the role of nondestructive inspection as one of several potential safeguards against failure by fracture should become apparent. This information should enable designers to approach the problem of fracture-safe design in a more rational manner, comparatively speaking, than has been possible in the past. Since fracture in practical situations is usually initiated by existing flaws in processed and fabricated structural components, it seems quite reasonable to expect that those involved with nondestructive inspection of materials should have an awareness of the interrelation between flaw size and the fracture process.

Chapter IV is augmented by several appendixes which discuss the application of the following methods to the fracture process: J-integral; crack opening displacement (COD); resistance method; the Kuhn-Hardrath method; crack propagation laws; environmental effects in fracture; and a brief summary of the limitations of these methods.

Chapter V treats in detail the importance of fail-safe design and discusses the basic fail-safe design concepts. Following this theoretical discussion are numerous examples of the application of fracture mechanics concepts to the design of aircraft wings, the development of the DC-10 fuselage, the prediction of the residual strength of relatively thick structures, aerospace pressure vessels, and estimating the life to failure of a cylindrical pressure vessel subjected to repeated internal pressure. Before concluding with a discussion of the outlook for future developments in fail-safe design, attention is given to the relationship of service failures and laboratory tests and the possibilities of fatigue life assessment of aircraft structures based on random or programmed fatigue tests.

Chapter VI describes two standard methods, both published by ASTM, Test for Plane Strain Fracture Toughness of Metallic Materials and Sharp Notch Tension Testing of High Strength Sheet Materials, and the problems which have to be solved but are not covered by these standard procedures.

Chapter VII discusses the present reliability of crack detection methods and the means for determining crack size. The current and future possibilities of the applicability of nondestructive testing and flaw detecting methods are discussed in detail. These methods include: acoustic emission; surface dye penetrants; magnetic particle testing; holographic interferometry; and fractography.

The appendixes contain detailed information on typical plane strain fracture toughness of aircraft materials (steel, titanium and aluminum alloys); fracture toughness test results for the same materials; the titles and references of approximately 140 configurations for which stress intensity factors have been determined; and for the convenience of the reader, the international system of units has been included, as well as a list of selected references; an author and subject index complete the survey.

Since the survey represents a first step to provide the engineer and scientist with a current compilation of fracture mechanics concepts and applications, it is strongly suggested that an effort be made to update the fracture mechanics survey periodically and encourage by other means the widest possible dissemination of all applicable information.

II. HISTORY OF LOADING OF AIRCRAFT AND EXAMPLES OF AIRCRAFT FAILURE  
II.A SPECTRUM OF LOADING OF AIRCRAFT

Howard A. Wood

1.1 Introduction . . . . .	3
1.2 The Structural Environment . . . . .	3
1.3 Frequency of Occurrence and Significance of Airplane Loadings. . . . .	4
References . . . . .	7

1.1 Introduction

Primary aircraft structural components generally contain flaws, defects or anomalies of variable shape, orientation, and criticality, which are either inherent in the basic material or are introduced during the manufacturing and assembly processes. A large portion of service cracks found in aircraft structures are initiated from tool marks, manufacturing defects and the like<sup>14</sup>. Under the combined driving forces of environment and service loading, these flaws may grow to catastrophic proportions resulting in serious reduction of service life or complete loss of the aircraft. Thus, to a large degree, the integrity of the basic airframe is dependent upon the safe and controlled growth of cracks as well as the achievement of residual strength in their presence. Acceptance of this condition requires the designer and analyst to select basic materials, structural configurations and allowable stress in accordance with intelligent criteria and coupled with the likelihood of discovering service cracks in the field, well in advance of fracture.

There is an abundance of fracture evidence to support these observations<sup>3,10,13-15</sup> in which likely causes of cracking or failure have been documented. In coupling statistics of this nature, one becomes aware of the true nature of the aircraft environment.

In the following discussion, airframe service loadings and experience will be summarized, particularly if they are related to that portion of the life following the initiation of a crack. A comprehensive treatment of loads is beyond the scope of this paper. The reader is referred to the excellent manual prepared by Taylor<sup>1</sup>.

1.2 The structural environment

The operational behaviour of structures and materials is affected by the magnitude and cumulative effects of external loads coupled with the possible detrimental action of the internal airframe chemical, thermal and stress environment. Taylor<sup>1</sup> has described the environment in which the aircraft operates as "... the source of all the loads that are applied to it ... The environment is easy to define; it is the atmosphere up to some prescribed height and the prepared ground from which aircraft operate". The presence of moisture, chemicals, suspended contaminants and natural occurring influences such as rain, dust, and sea coast atmosphere can cause deterioration in structural strength both due to the premature cracking and acceleration of subcritical crack growth<sup>9,10</sup>. Anderson<sup>3</sup> has attempted to quantify the significant structural environment as ranges of temperature from at least  $-50^{\circ}\text{C}$  to  $+50^{\circ}\text{C}$ , and all possible ranges of humidity in a pressure spectrum from nearly  $15 \text{ lb/in}^2$  to about  $2-3 \text{ lb/in}^2$ .

While it is pertinent to discuss and summarize the external loadings experienced by the airframe, the significant concern is the response of materials in the structure to these accelerations in the presence of the internal environment. It has been the general practice to describe loads in terms of CG acceleration; however, the response of the airframe to these external influences depends upon the aero-elastic characteristics of the structure.

(a) The operational environment

The loadings experienced during operation depend to a large degree upon the type of aircraft (e.g. fighter, bomber, transport, etc.) and upon the particular mission being flown. Naturally induced loadings due to *atmospheric turbulence* result when the airframe penetrates air masses moving transversely to it. *Maneuver loads* result when the aircraft is accelerated around one or more of its axes by deflection of the control surfaces. Once per flight loads may include cabin pressurisation and the reversal of load on the wings, i.e. the 'ground-air-ground' cycle. Landing impact, ground roll during landing and take off, taxiing, turning, and braking constitute the source of *ground induced loadings*. Specific turbulence conditions exist in and near clouds and storms, in clear air, and in the wake of other aircraft. These are the subject of detailed studies<sup>1,16</sup>. Localized *buffeting turbulence* is initiated mainly by the shape of the aircraft and can occur in regions and cavities such as control surfaces, bomb bays, etc.<sup>1</sup>. *Wake turbulence* is particularly significant during air-to-air refuelling. *Sonic loads* occur in the vicinity of power plants and as pseudo noise in turbulent and separated airflow and can react in the presence of the structure causing localized oscillatory stresses associated with resonances of the surface structure<sup>1</sup>.

The contribution made by these separate loading actions will be dependent on the operational role of the aircraft - for example, maneuver loads may predominate with strike aircraft, whereas the cabin pressurization load and the ground-air-ground cycle may be the paramount considerations with a long range transport aircraft. In the case of aircraft intended to operate 'in the field' from semi-prepared runways the taxiing loads may be of major significance.

(b) Internal airframe environment

In their summary of airframe environmental influences<sup>8</sup>, Astley and Scott categorize the atmospheric environment in terms of conditions that apply in any space or on the ground and in the absence of air. An excellent discussion of the thermal and chemical environment is presented. *Humidity/water* constitutes the chief cause of concern in airframes because of its ability to carry dissolved or suspended contaminants and forms the basis of all good electrolytes. Water may be present in the residue of fuel tanks and its influence must be investigated. Perhaps most significant, however, is the manner in which the airframe reacts in the presence of the corrosive atmosphere present. This segment of the environment is concerned

with the form of stresses present, mainly, those residual stresses induced during part fabrication, materials processing and assembly. The latter can be caused by mismatch of parts, eccentricities, force fitting of members and in interference fit fasteners. To a somewhat lesser extent, body stresses which result from the static geometry and mass of the airframe are available to be coupled. Under adverse environment these conditions can result in stress corrosion cracking in some of the alloys commonly used. Their effects are additive to the operation stresses which result and significantly influence the sub-critical growth behaviour of flaws in the airframe structure.

### 1.3 Frequency of occurrence and significance of airframe loadings

As discussed previously, the true significance of the external loadings is the way in which individual elements of the structure respond. For example, a large variable sweep aircraft performing low altitude maneuvers may encounter severe turbulence of such frequency and duration that the cumulative effect for some time period may be particularly damaging to wing structure, whereas the structural members of the sweep mechanism during this time period may react differently and encounter a rather large sustained loading spectrum perhaps critical for sustained loading crack growth. Thus, in considering the fracture problem, cyclic as well as static or sustained, loads must be considered.

Repeated loads in themselves may vary in frequency of occurrence as shown in Fig.1<sup>2</sup>. Maneuver loads may vary significantly with the particular mission segment as shown by King<sup>11</sup>, Fig.2. Individual aircraft may assume rather broad mission requirements as illustrated in Fig.3<sup>12</sup>. Gusts and atmospheric turbulence may be less significant for fighter than for transports<sup>4,18</sup>. Fighters experience more frequent load excursions to design limit load factor than do transports as shown by Hardrath<sup>4</sup> in Fig.4. Gust loads can be quite different in severity and distribution in different regions of the world<sup>1</sup>. In general, gusts are less frequent at high altitude<sup>1,18</sup>, and increased speed of entry can intensify the experienced acceleration<sup>3</sup>. Fig.5 includes gust data variation with altitudes presented by Bryan<sup>18</sup>.

One (a) per flight	Many per flight
1g wing lift (air-ground-air cycle)	Wing loads from gusts
Tail balance loads	Wing loads from maneuvers
Flap loads	Fin loads from gusts and maneuvers
Cabin pressure loads	Fuselage loads from gusts and maneuvers
Landing gear impact	Landing-gear taxiing loads
Engine thrust/thrust reversal	Propeller, slip-stream or jet-stream loads
Etc.	Engine vibrations Etc.

(a) In some instances this denotes one group of loads per flight.

Fig.1 Some repeated loads on aircraft structures

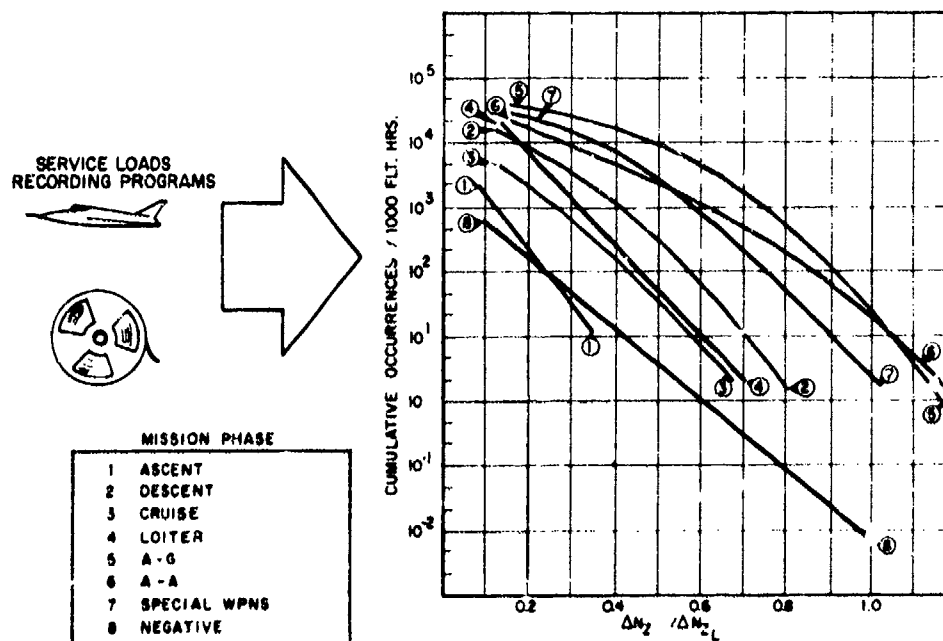


Fig. 2-Variation of maneuver load occurrences with mission phase (11)

MISSION DEFINITION, C-130 E

MISSION NUMBER	NAME	REMARKS
1	PROFICIENCY TRAINING	NORMAL ALTITUDE WITH S & G LANDING
2	BASIC TRAINING	NORMAL ALTITUDE WITH T & G LANDING
3	SHUTTLE	INCLUDES MULTIPLE SORTIES
4	SHORT RANGE LOGISTICS	11.5 HRS 14.5 HRS DURATION
5	LONG RANGE LOGISTICS	14.5 HRS DURATION
6	AIRDROP	ALL MISSIONS WITH AIRDROP
7	STORM RECONNAISSANCE	SPECIFIC BASE ASSIGNMENT 180 HRS DURATION
8	COMBAT TRAINING	LOW ALTITUDE WITH T & G OR S & G
9	LOW LEVEL	LOW ALTITUDE WITHOUT T & G OR S & G

S & G - STOP AND GO

T & G - TOUCH AND GO

Fig. 3-Example of broad range of mission requirements (12)

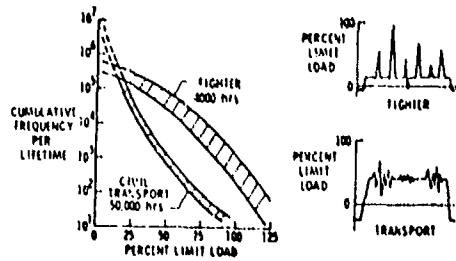


Fig. 4-Load experience in aircraft (7)

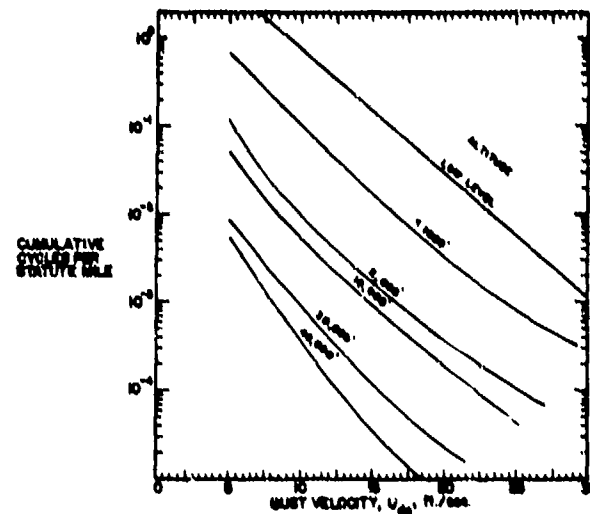


Fig. 5-Atmospheric gust load environment (From Bryan) (18)

Military aircraft in general fly a broader and more widely varied mission than commercial transports, and the effects of turbulence and ground conditions may be more or less severe depending upon the mission. For example, high speed and low altitude operations coupled with terrain following can result in frequent maneuver loadings and almost continuous, severe loadings associated with flight through the turbulence at low altitudes<sup>16</sup>.

Whereas it has been customary in the past to describe envelopes of speed and load factor and to accumulate experiences of repeated loadings independent of cyclic frequency and cyclic duration, it is becoming increasingly necessary to account for these factors, particularly where material-environmental influences may dictate the need. In addition, sustained loading-environmental spectra, as indicated in Fig. 6, may need to be described in particular instances<sup>6</sup>.

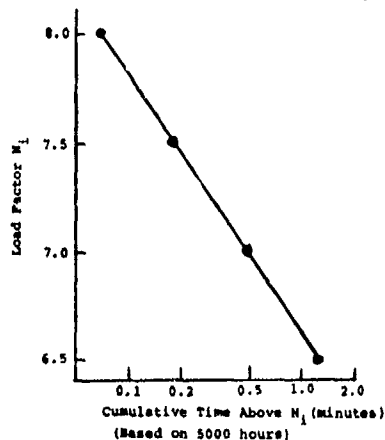


Fig. 6-Example of derived sustained load spectrum-fighter aircraft (6)

#### 1.4 Representation of airframe loads for fracture control considerations

In the assessment of structural integrity, it is essential that the most realistic representation of the loading-environment be constructed both for analytical predictions as well as for qualification testing. Mission description results in formation of a profile of key parameters including the most representative sequence of loads, cyclic frequencies, periods of sustained loading, environment, temperature and time. An example of such a flight profile is shown in Fig.7.

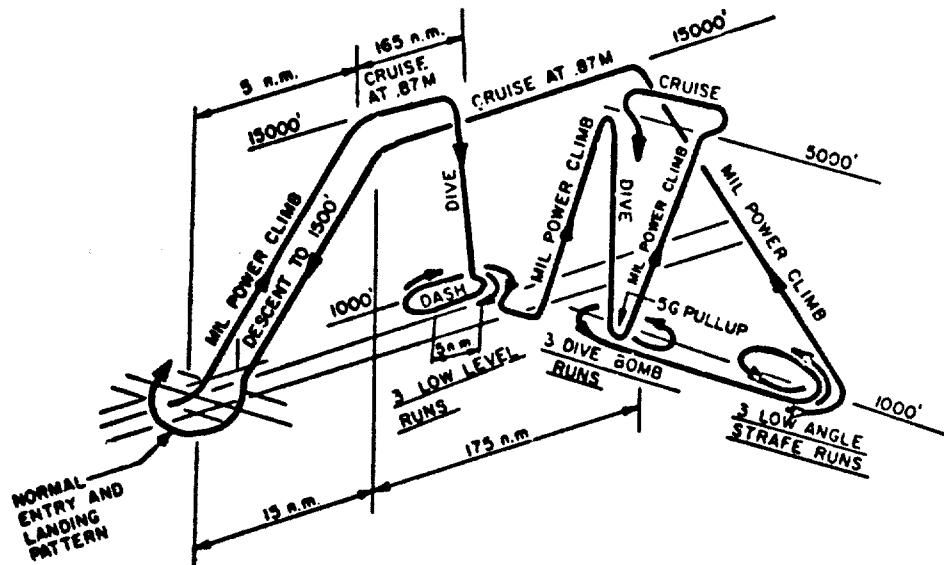


Fig. 7a-Typical profile for tactical aircraft conventional weapons delivery mission

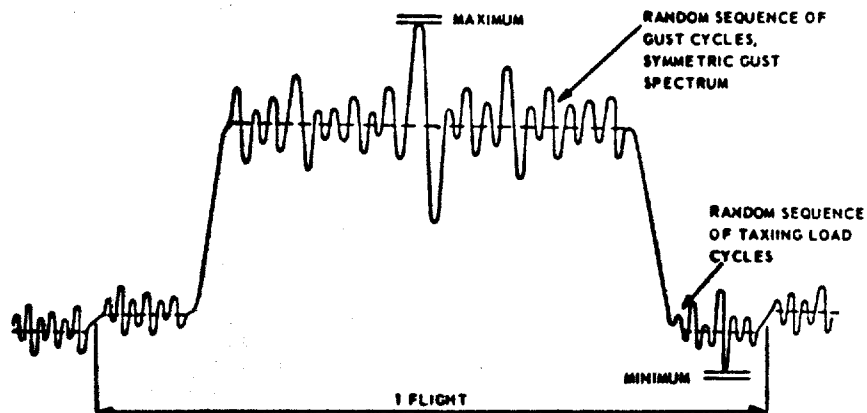


Fig. 7b-Simplified flight-load profile for transport wing root (5)

Load sequence and block size are particularly significant in flight load simulation. Important differences have been noted when test results are compared with randomized ordering. Data from Schijve<sup>5</sup> are presented in Fig.8, to illustrate this fact.

Development of the flight load profile presumes that sequences of loads is essentially deterministic. This is generally far from the truth for most missions since gusts and maneuvers generally occur in a random fashion. The portion of the profile most deterministic however, is the ground-to-air cycle (Fig.7), and its occurrence once per flight in programmed growth tests can be significant.

Fig.9 includes data from Ref.3 on the order of magnitude periods and number of loads occurring in the service life of several types of aircraft.

The question of how best to couple combined cyclic and sustained loading in the simulation of the flight environment remains open. To a large extent, for analysis and test, the importance of this endeavor depends upon the sensitivity of the particular material to the loading environment. At least two methods appear to be possible at the current time<sup>6</sup>; representing the time at high load in terms of peak load factor versus representative sinusoidal frequency in which case the appropriate material growth behavior at these frequencies must be evaluated; and representing the sustained load environment as shown in Fig.6 in which case, an incremental model of sustained and cyclic loading such as in Ref.22 would be used.

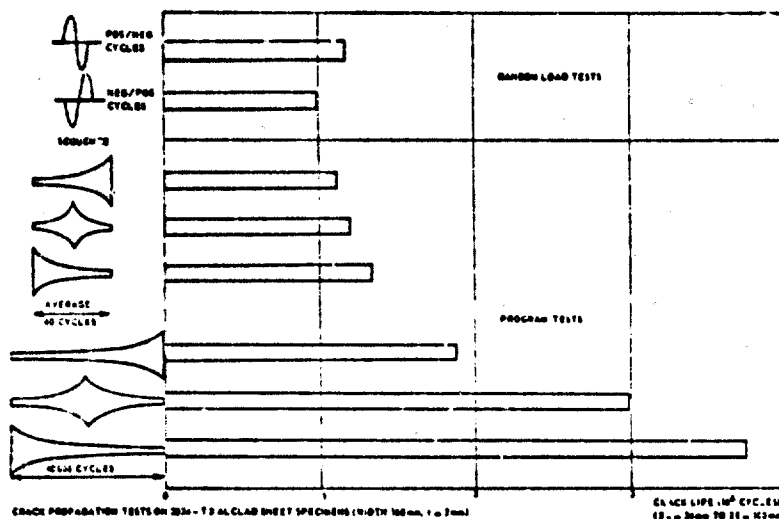
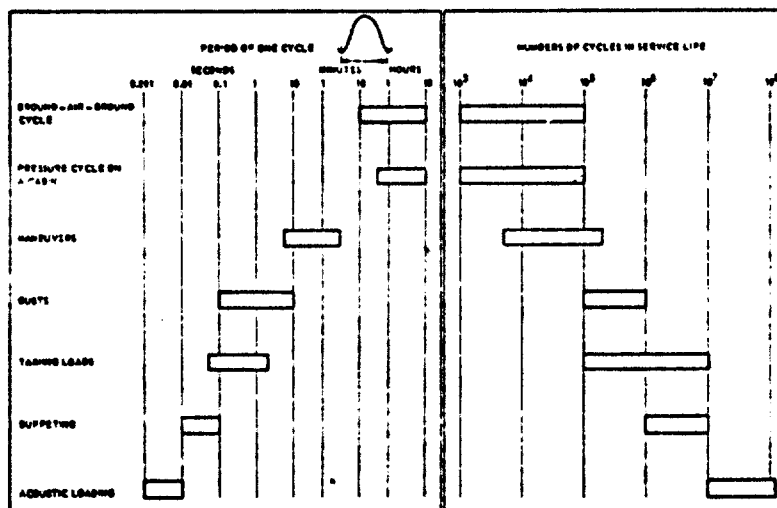


Fig. 8-Effects of load sequence and size of load period on program fatigue life. Comparison with random load test results (5)

Fig. 9-Periods and numbers of several types of aircraft fatigue loads-orders of magnitude (12)



#### REFERENCES

- 1 J. Taylor. Manual of aircraft loads. AGARDograph 83.
- 2 Navair, 01-1A-13. Fatigue of aircraft structures. Naval Air Systems Command, Dept. of the Navy, 1966.
- 3 W.E. Anderson. Fatigue of aircraft structures. Battelle Pacific Northwest Labs., Report BNWL-SA-4120 (submitted to Metallurgical Reviews), 1971.
- 4 H.F. Hardrath. Fatigue and fracture mechanics. AIAA Paper 70-512, 1970.
- 5 J. Schijve. The accumulation of fatigue damage in aircraft materials and structures. AGARDograph 157.
- 6 J.C. Ekvall. Lockheed Aircraft Co. Progress Reports on Contract F33615-71-C-1324, Air Force Flight Dynamics Lab., 1971.
- 7 WADD TR 60-398. Optimum fatigue spectra. March 1962, Air Force Systems Command, Air Force Flight Dynamics Lab.
- 8 AGARD Conference Proceedings No.53. Engineering practice to avoid stress corrosion cracking. (The environment encountered in aircraft service, W. Astley, J. Scott.)
- 9 AGARD Manual 8-70. Manual on fatigue of structures.
- 10 J.P. Gallagher. Corrosion fatigue crack growth rates above and below  $K_{ISCC}$  in steels. Proceedings of the 1971 Conference on Corrosion (ASTM), Vol. 0, 4, December 1971.
- 11 T.T. King. From TR-70-144.
- 12 A. Shevemaker, et al. From TR-70-144.
- 13 R.J. Gran, et al. Investigation and analysis development of early life structural failure. AFFDL-TR-70-149, March 1971.
- 14 D.R. Donaldson and W.F. Anderson. Crack propagation behavior of some airframe materials. Proceedings of the Crack Propagation Symposium, Vol. II, Cranfield, September 1961.
- 15 US Army, Trecom TR-64-36. Engineering survey of aircraft structural failures caused by corrosion, fatigue and abrasion. July 1964, Univ. of Oklahoma, Research Institute.
- 16 J. Jones. From TR-70-144.
- 17 Proposed Mil-Std-2000. The USAF Structural Integrity Program.
- 18 D. Bryan. From TR-70-144.
- 19 Fitch, et al. From TR-70-144.
- 20 Whitford and Dominic. From TR-70-144.
- 21 Wei-Landes. Correlation between sustained and fatigue crack growth in high strength steels. Materials Research and Standards (ASTM), July 1969.
- 22 J.P. Gallagher. Corrosion fatigue crack growth rates above and below  $K_{ISCC}$  in steels. Proceedings of the 1971 Conference on Corrosion (ASTM), Vol. 0, 4, December 1971.

structural development process for aircraft structural integrity under fatigue conditions. AFFDL-TR-70-144, Conference Proceedings, Air Force Conference - Miami Fl, 15-18 December 1969.

### 1. Introduction

For almost three decades fatigue has been recognised as a potential threat to the safety and reliability of aircraft. Failures have occurred ranging in importance from complete destruction to failures requiring unscheduled repair and replacement of parts. Correspondingly, over the same period, methods and procedures have been developed for use in design, testing, and operation of aircraft which are aimed at achieving freedom from significant fatigue troubles throughout the service life of the aircraft.

Notwithstanding the care taken, situations do arise in service in which cracks are found in primary structure of the airframe during routine inspections. When such a situation arises, two questions will be asked - "Is it safe to continue to operate the aircraft (with or without load/maneuver restriction) pending repair?" "If so, when must the next inspection of the damaged area be made?" The first question concerns the residual strength of the structure with a crack of known geometry and the second question concerns also the rate of growth of the crack.

The possibility that such a situation may arise is, of course, recognised in design and is reflected in the choice of materials having favourable crack propagation properties and residual strength (fracture toughness) for use in areas of the structure subject to fatigue loading. Indeed, in the case of 'fail-safe' aircraft, one of the design objectives is to ensure that any cracks that may occur in service can be found before the strength of the aircraft falls below an acceptable level. This objective is tackled in design by calculation and, as part of the airworthiness certification process, tests are normally made on a complete airframe, or major components, to demonstrate that such an objective may be achieved.

The development over recent years of an analytical approach to problems of crack growth and residual strength of structures and components, which is based on the use of linear elastic fracture mechanics has provided a valuable tool for use in design and for use in tackling problems of crack growth and residual strength as they arise in service.

### 2. Examples of failure

Before discussing in detail, in subsequent chapters of this Survey, the way in which fracture mechanics concepts may be applied in the design phase, or in dealing with problems arising from cracks in service, it would be of interest to look at a selection of failures that have stemmed from undetected fatigue damage. Knowledge of the situations in which fatigue damage has originated in the past will enable the designer to anticipate areas of structure, or components, which will require particular attention in design. The selection of photographs chosen (Figs.1-18) cover damage which has resulted in complete loss of an aircraft, serious damage on landing or, at the least, significant unserviceability problems: some failures in test are also included. It will be seen that the examples include failures in fabricated structures (Figs.1-4, 14-18) extrusions (Figs.4, 5, 15, 17-18) and forgings (Figs.6-11): the damage has originated from stress concentrations, such as cut-outs, bolt and rivet holes - often with evidence of fretting, from flaws in the material, and from imperfections in welding. Crack lengths at failure range from those measured in millimetres to those measured in tens of centimetres.

In the previous section an indication has been given of the nature and complexity of the various forms of loading which may be experienced by different parts of the structure. The examples of failure shown in this section serve to illustrate the geometrical complexity of the structure in which cracks may be growing. It is evident, then, that much is demanded from the structural analyst in applying fracture mechanics principles to predict crack growth behaviour and critical crack lengths in the foregoing circumstances.



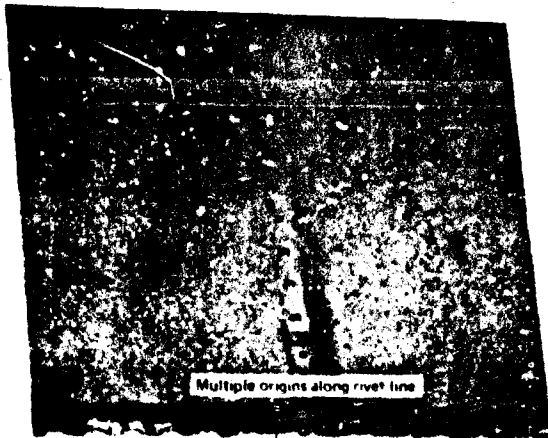


Fig. 1 In service failure - pressure cabin skin



Fig. 2 Pressure cabin skin failure - growth of damage along rivet line



Fig. 3 Pressure cabin failure - crack through underlying frame



Fig. 4 In service failure - mainplane spar boom



Fig. 5 In service failure - landing gear door up-lock operating lever



Fig. 6 In service failure - pivot bracket

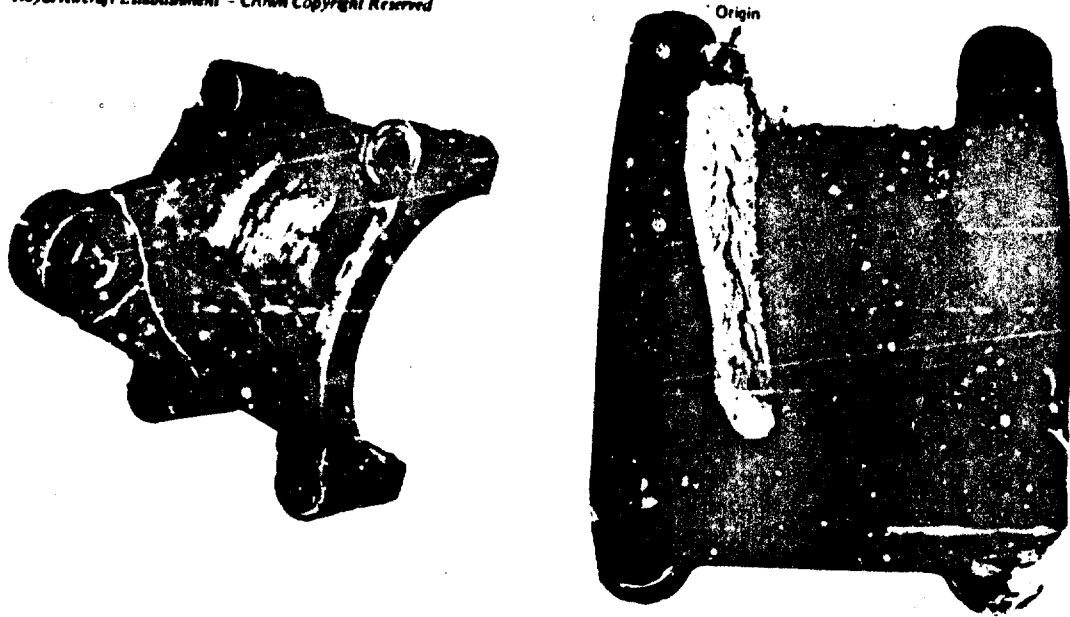


Fig. 7 In service failure - half axle clamp



Fig. 8 In service failure - undercarriage torque link



Fig. 9 In service failure - nose-wheeling casting

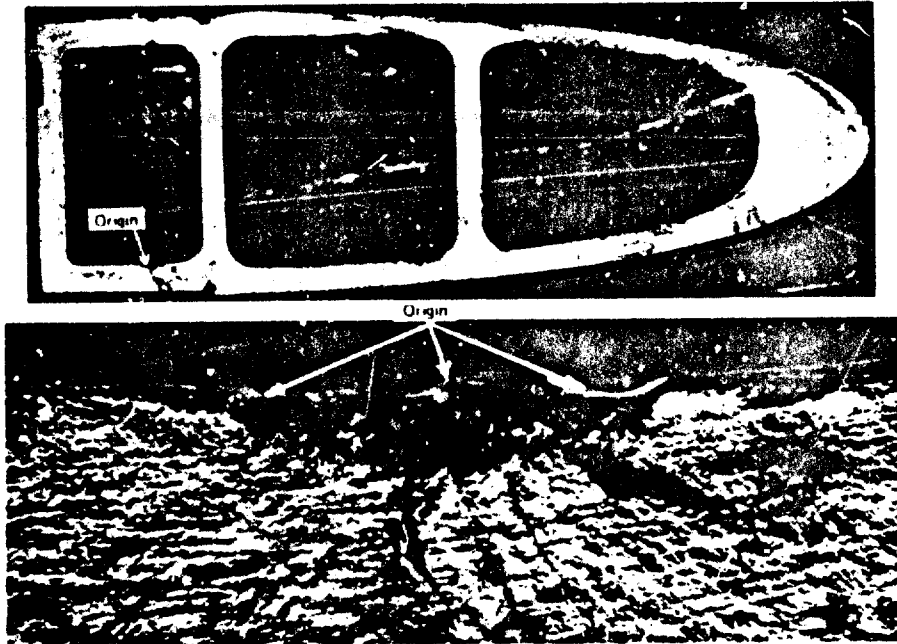


Fig. 10 In service failure - helicopter rotor blade extrusion



Fig. 11 In service failure - helicopter rotor drive yoke

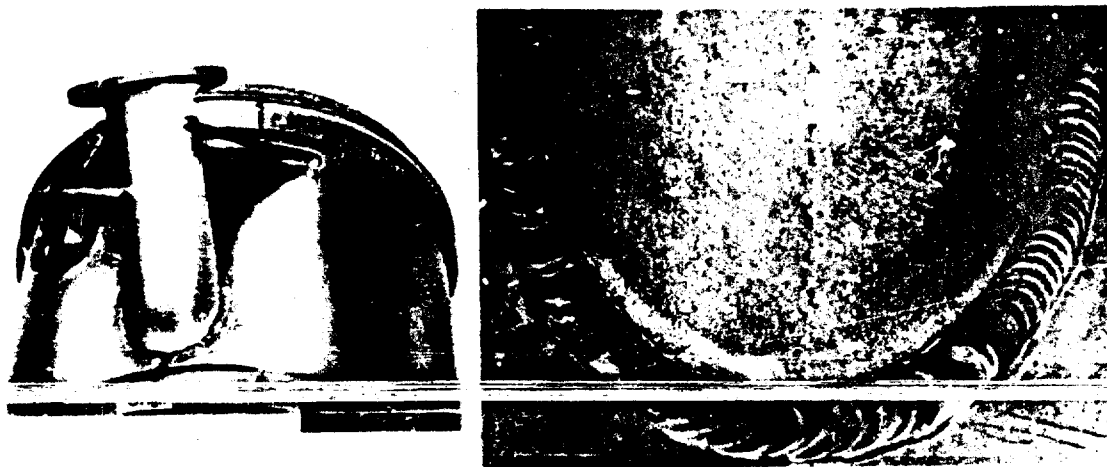


Fig. 12 In service failure - hydraulic reservoir

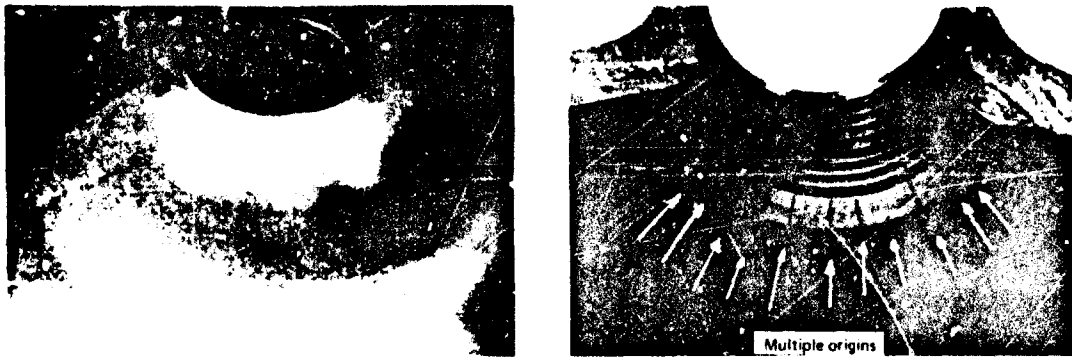


Fig. 13 In service failure - air bottle

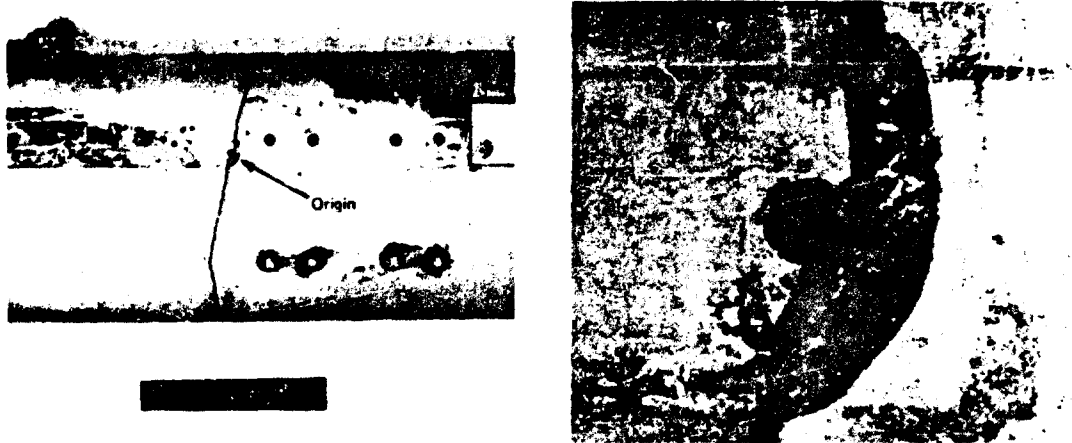


Fig. 14 In service failure - tubular lift strut

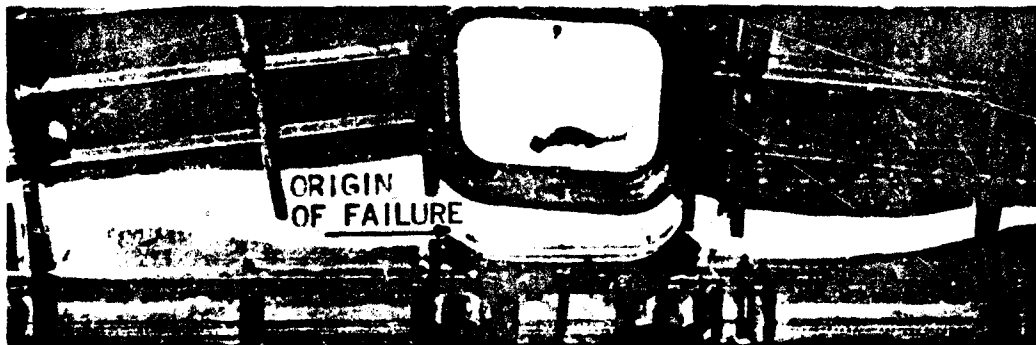


Fig. 15 Failure in test - aircraft pressure cabin

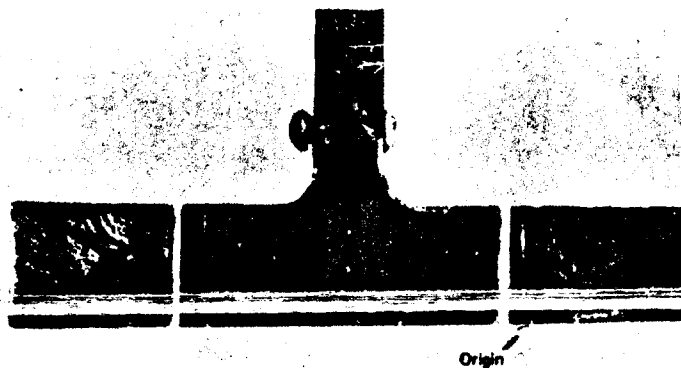


Fig. 16 Failure in test - spar boom

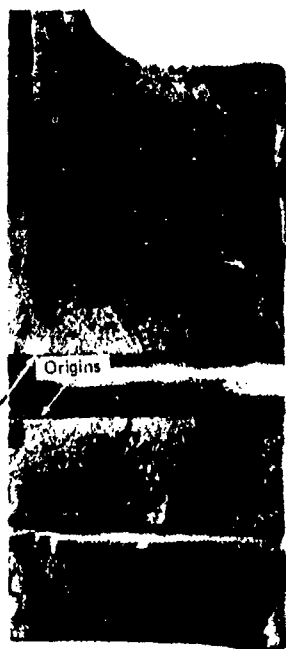
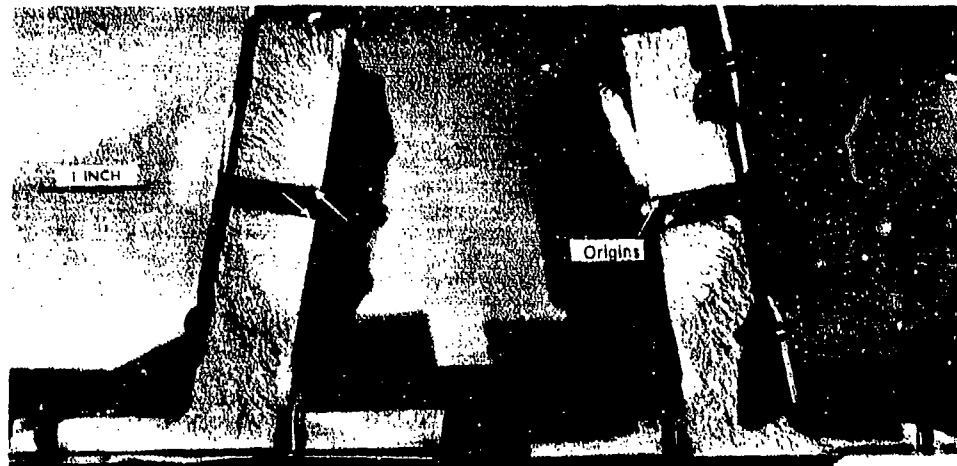


Fig. 17 Failures in test - spar booms



Fig. 18 Failure in test - tubular control rod

## II.C FRACTURE REGIMES

J. I. BLUHM

## 1. Introduction

It is quite obvious, in view of the foregoing, that the loading spectrum on aircraft is indeed a complex and ill-defined quantity which nevertheless must be a consideration of major proportions in any prediction of the types of failures discussed. Both deterministic and probabilistic considerations have a role in such predictions and much is yet to be learned as to how best to treat this "loading" problem. Some failures are the consequence of only a few or even a single isolated load application; others are associated with and characteristic of large numbers of repeated load applications; still others result from truly random spectrum types of loading.

Beyond the immediate problem of defining the loading, there exists the further need for recognition that prediction of failure under a set of prescribed loading conditions requires an acute awareness of the anticipated or possible failure modes. In an ordinary structural sense this entails, for example, the obvious recognition of potential elastic compression instability (buckling) in a column or of compression yielding or "compression" fracturing in a ductile or brittle column respectively. Predictive analyses for failure are useless if they fail to provide for treatment of the mode of failure which is most apt to limit the structural integrity of the components.

In a similar but more detailed vein, and as a basis of discussion for this immediate section, it is essential to recognize the various specific fracture modes which might be operative under different conditions. If we recognize the relevant fracture mode governing an expected failure, then appropriately relevant design criteria can be used or developed for use in the design relationships.

At the engineering level, the study of fracture can be simplified by recognizing, identifying and characterizing regimes wherein different fracture behavior are observed. Over a range of temperature, for example, the resistance to defects (toughness) is noted to vary widely, leading to an appreciable spread in real component strength. The fracture mode is not only associated frequently with temperature but also with component geometry. Again, wide variations of strength, ductility and toughness are observed to be associated with such fracture modes as cleavage or brittle fracture, flat ductile or dimple fracture and shear fracture. And, finally, the point to be made - and perhaps of most significance to the engineer - is that, depending on the fracture mode to be anticipated, one can utilize different applicable analytical design approaches to safeguard against unanticipated fracture in service. More specifically, if we consider the simple case of an aircraft component or "structure" constructed of an alloy steel, one might plot the static strength of that part as a function of temperature. Figure 1 suggests schematically, the nature of the response of such a typical "real" structure. This behavioral pattern lends itself to a first simple (and admittedly incomplete) illustration of several temperature based "fracture regimes."

## 2. LINEAR ELASTIC FRACTURE MECHANICS

In the low temperature region, the "structure" normally exhibits a very low strength and the fracture is characteristically brittle, i.e., little or no ductility is evident (particularly if the structure is notched or cracked). But these are precisely the prerequisite conditions for use of linear elastic fracture mechanics (LEFM), the offshoot of Griffith's original work on glass. In this regime, a useful fracture predictive tool is available with the large store of analytical techniques born of Inglis (1) and Griffith (2,3) and nurtured to maturity by Irwin (4,5), Orowan (6) and a host of more recent investigators. In essence, we can understand and apply with a good deal of confidence, the tools of LEFM - at least for those conditions and materials for which the basic assumption of "elastic" behavior is essentially valid. Inherent in the LEFM concept is the presence of a "crack" of known size and shape and knowledge of the "plane strain fracture toughness" of the material expressed either as  $G_{IC}$  or  $K_{IC}$ , the critical energy absorption rate and the critical stress intensity factor respectively.\* The effect of a crack at low temperature is always to reduce (as might be expected) the strength of the structure. This will be seen to be in contrast, under certain conditions, to the behavior in the high temperature regime.

## 3. LIMIT DESIGN

At the other end of the temperature scale, i.e., the high temperature region, it is recognized that materials generally tend to exhibit unusually large plastic flow prior to and during fracture. This observation is in direct contrast to the "zero" or limited ductility of structural materials in the low temperature region. Therefore, of course, the LEFM approach is not applicable in this high temperature regime. On the other hand, these high temperature conditions are precisely those associated with so-called "limit" design based upon plasticity theory. Like LEFM, limit design concepts have been developed to a high level of sophistication (see for example, Prager (7) and Hodge (8)), and a great number of useful analyses are available in the literature. Limit design techniques lead invariably to estimates of maximum allowable "loads," at which loads, the material merely continues to flow at constant or decreasing load and fracture per se does not occur as in the LEFM model.

The residual strength of a wide variety of notched or cracked configurations has been catalogued using results of plasticity theory. Though much of that work is based upon idealized plasticity theory which generally ignores strain hardening, appreciable practical insight is never the less provided, via this discipline, to the understanding and the prediction of the behavior of notched structures.

\*More recently the crack opening displacement COD has also been suggested as a parameter for defining this toughness. The relation between COD ( $\delta$ ) and  $G_{IC}$  is approximate  $\delta \approx G_{IC}/\sigma_{YS}$ .

STRENGTH

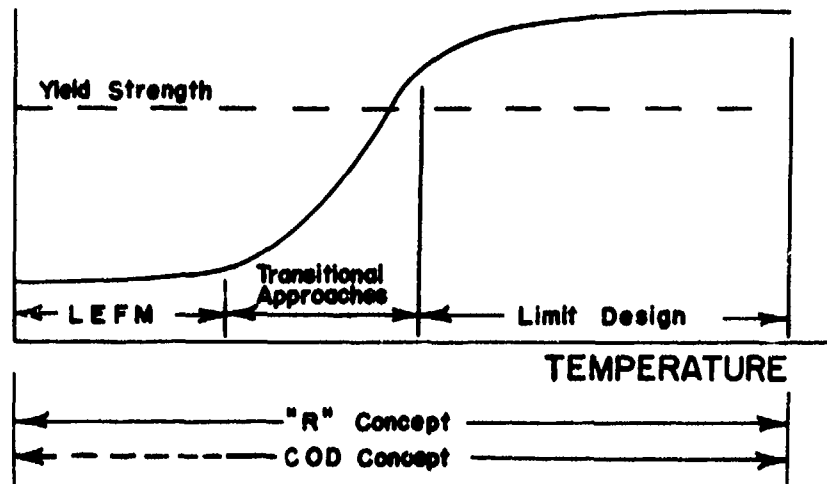


Figure 1. Schematic representation of range of applicable strength approaches.

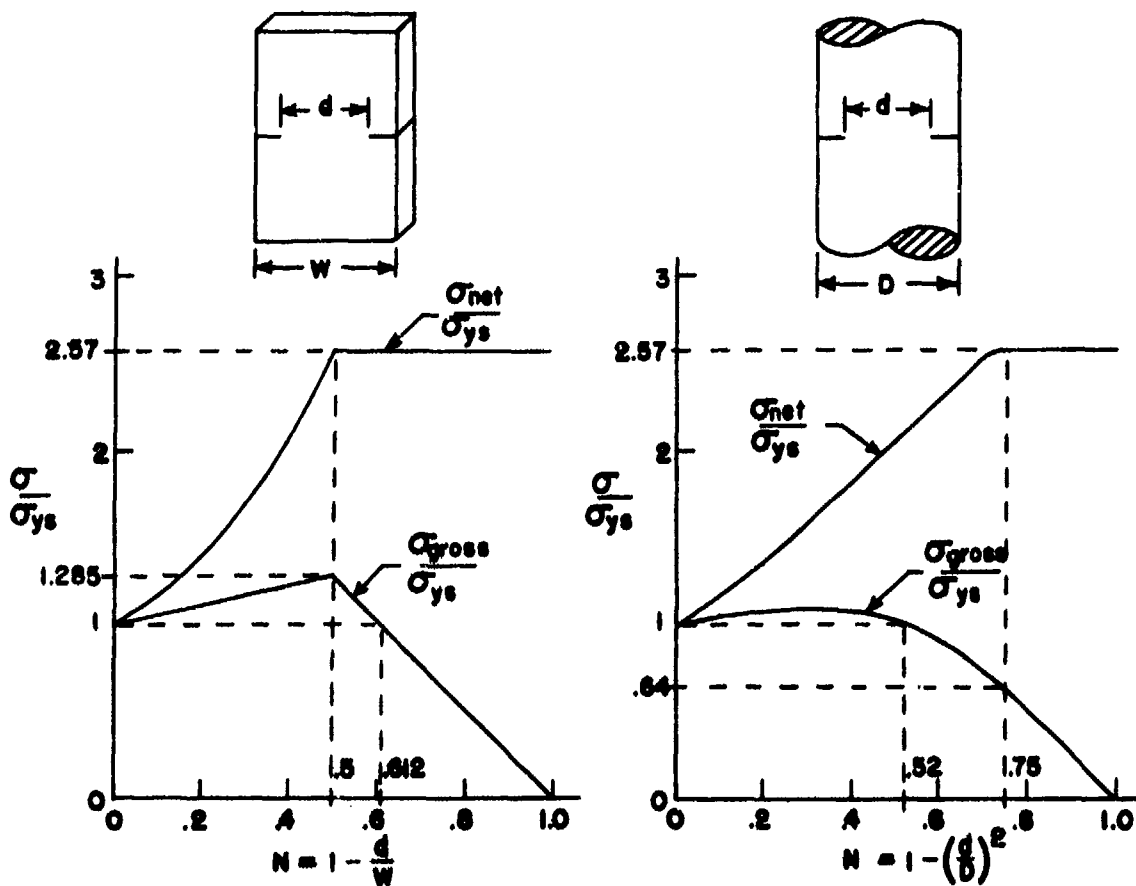


Figure 2. Limit stresses in notched plates and notched cylinders in tension.

In contrast to their effects in the LEFM regime, cracks at elevated temperatures do not necessarily weaken a structure. On the contrary, they may, as seen in Fig. 2, augment the strength by as much as 28 percent in load-carrying capacity is theoretically possible.

#### 4. Transition Approaches

Whereas then, as inferred in the foregoing, useful tools are available for design at the extremes of behavioral regimes exemplified by LEFM on one hand and limit design on the other, most real life problems unfortunately lie somewhere in between these extremes. Some advances have been made with respect to cases of restricted plastic flow, i.e. where departure from linear elasticity occurs in only a small region near the crack tip. For these situations, minor modifications are applied to LEFM techniques using plastic zone size corrections. For materials exhibiting more extensive plastic flow, such techniques are not appropriate and alternate rational approaches need to be developed. From a pragmatic point of view, the behavior in this "grey" regime has, in the interim, been most effectively treated by one of the "transition" considerations. These are generalized to include, for the purpose of this document, all approaches intermediate between and spanning the extremes of LEFM and limit design. Among the commonly used concepts are transition temperature, energy absorption or fracture appearance as reflected by Charpy type impact specimens, Drop Weight Tear Test (DWTT), Dynamic Tear Test (DTT), Nil Ductility Test (NDT), Crack Opening Displacement (COD), Crack Arrest Temperature (CAT), Resistance Method (R-G), and others.

#### 5. General Discussion

It is important to observe at the outset that there is no unique failure mode for each material, but rather a range of fracture modes governed by a number of variables. Normally "brittle" materials can frequently be "made" to appear ductile by (a) raising the temperature, (b) superimposing sufficient hydrostatic pressure, or (c) lowering the rate of loading. Conversely, normally ductile materials can frequently be "embrittled" by (a) lowering the temperature, (b) decreasing the magnitude of hydrostatic pressure, or alternatively, applying a hydrostatic tension component of stress, or (c) increasing the strain rate. These effects are shown schematically in Fig. 3. Certainly a unique unambiguous strain (or stress) criteria does not appear to be assignable for fracture considerations.

In addition to these overt environmental factors, the issue is complicated further by the fact that the fracture mode is conditioned in plate specimens upon such geometric factors as plate thickness, for example. This effect can probably be considered, however, as equivalent to modifying the hydrostatic stress component via its influence on the stress state in regions of geometric irregularities such as notches or naturally induced cracks.

Notches and cracks, intentional or otherwise, represent a geometry induced perturbation of the stress state which tends to enhance brittle fracture. The stress state at the base of a notch in a thick plate (Fig. 4) varies, for example, from uniaxial tension at the free lateral surface at (a), to biaxial tension at mid thickness at (b), to triaxial tension subsurface at (c). With a sharper notch a plane strain constraint is more nearly achieved, facilitating this latter triaxial tension condition. Additionally, if a small plastic zone develops, then Poisson's ratio approaches a value of 1/2 and idealized hydrostatic tension is fully developed locally. The importance and significance of notch specimens for evaluation of brittle behavior of materials undoubtedly stems from this characteristic peculiarity of inducing hydrostatic tension. In recent years the use of specimens artificially cracked by fatiguing has come to be more and more in favor since "cracks" represent the ultimate in notch severity. Of course, it should be appreciated that the strength of "cracked" specimens generally is significantly lower than those of more gently notched specimens. Design which presumes presence of cracks, though conservative, may therefore overly penalize structures where design, material selection, processing, and inspection procedures have significantly minimized the probability of encountering cracks beyond a given minimum size.

Nevertheless, the concept of a crack, in conjunction with low temperature and/or high strain rate does provide a basis for such conservative design approaches as the Linear Elastic Fracture Mechanics technique. Somewhat less conservative approaches utilize the LEFM but modify it by considering a small plastic zone at the crack tip.

#### REFERENCES

1. Inglis, C. E., "Stresses in a Plate Due to Presence of Cracks and Sharp Corners," Trans. INR, Vol 55, Part 1 1913, 219-230.
2. Griffith, A. A., "The Phenomenon of Rupture and Flow in Solids," Phil Trans Roy. Soc (London) Series A, Vol 222 1920, 163-198
3. Griffith, A. A., "The Theory of Rupture;" Proc First International Congress of Applied Mechanics, Delft 1924, 55-63.
4. Irwin, G. R., "Fracture," Encyclopedia of Physics, Vol 6, Berlin: Springer Verlag 1958, 551-589.
5. Irwin, G. R., "Fracture Mechanics," Proc. First Symposium on Naval Structural Mechanics, Stanford University, Stanford, California, August, 1958, 557-594.
6. Orowan, E., "Reports on Progress in Physics," Vol 12, 1949, 185.
7. Prager, W., "General Theory of Limit Design," Proceeds of 8th International Congress on Applied Mechanics, Istanbul, Vol 2, 1952, 65-72.
8. Hodge, P.G., Jr., Limit Analysis of Rotationally Symmetric Plates and Shells, Prentice Hall, International Series in Theoretical and Applied Mechanics, 1963.



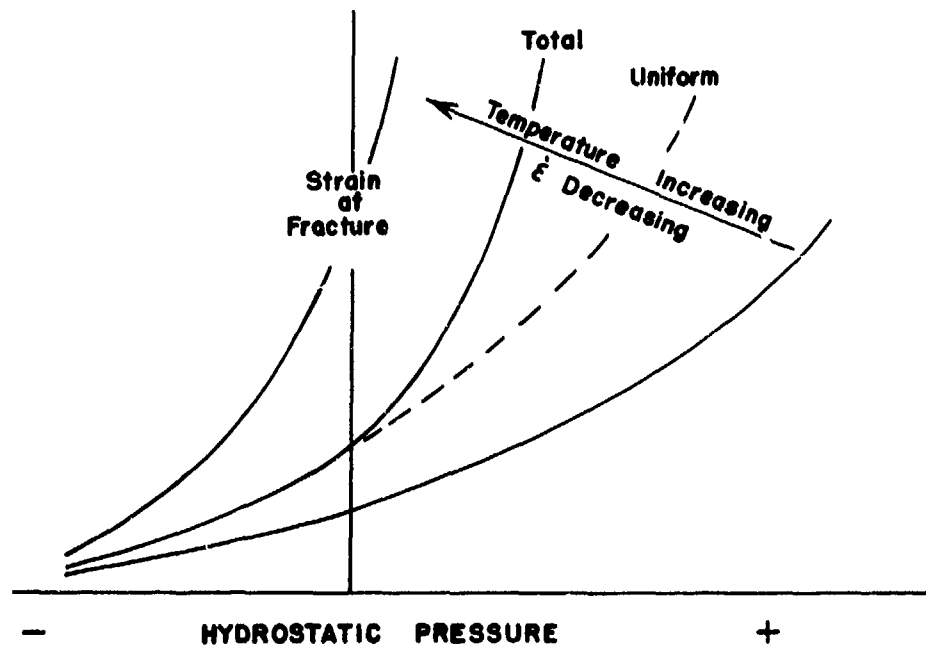


Figure 3. Schematic illustrating effect of superimposed hydrostatic pressure on strain to fracture and effects of temperature and/or strain rate.

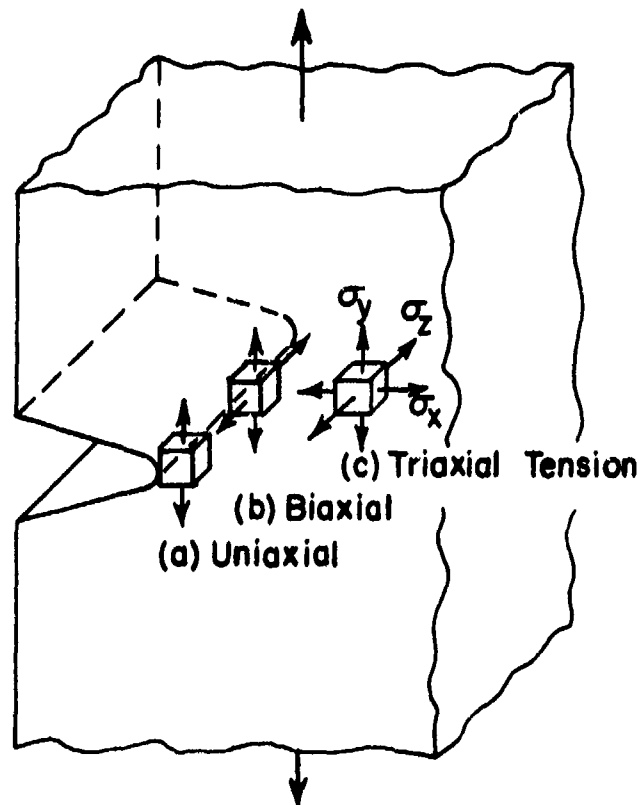


Figure 4. Sketch showing variation in stress state in vicinity of notch in thick plate.

III. THE USE OF FRACTURE MECHANICS PRINCIPLES IN THE DESIGN AND ANALYSIS OF  
DAMAGE TOLERANT AIRCRAFT STRUCTURES

Howard A. Wood

1. Introduction . . . . .	19
2. Materials Utilization - The Need for Fracture Control . . .	19
3. Fracture Control - Basic Objectives . . . . .	21
4. Fracture Control - Requirements . . . . .	25
5. Summary of New Requirements . . . . .	26
6. Conclusions - Some Problems and Concerns . . . . .	27
References . . . . .	31

This survey reviews current trends in the usage of high strength structural materials for aerospace applications and illustrates the manner in which fracture control procedures may be implemented to achieve a higher degree of damage tolerance. Experiences with the application of fracture requirements to two current designs are related. These experiences have contributed immensely to the formulation of specifications for use "across the board" on all new systems. Important aspects of the proposed USAF Damage Tolerance Criteria, including initial damage assumption and crack growth analyses, are discussed.

Howard A. Wood

## 1 Introduction

Recent cases of catastrophic failure of primary structure in first line USAF aircraft due in part to the presence of undetected flaws and cracks have emphasized the need for fracture control procedures to augment traditional static and fatigue design and qualification requirements. Such procedures, when effectively implemented, would insure the reduction in the probability of catastrophic failure due to undetected flaws and allow the safe operation of the air vehicle within the prescribed service period.

With regard to aircraft structural design, fracture control implies the intelligent selection, usage and control of structural materials, the design and usage of highly accessible, inspectable and damage tolerant structural configurations, and the control of safe operating stresses (Figure 1).

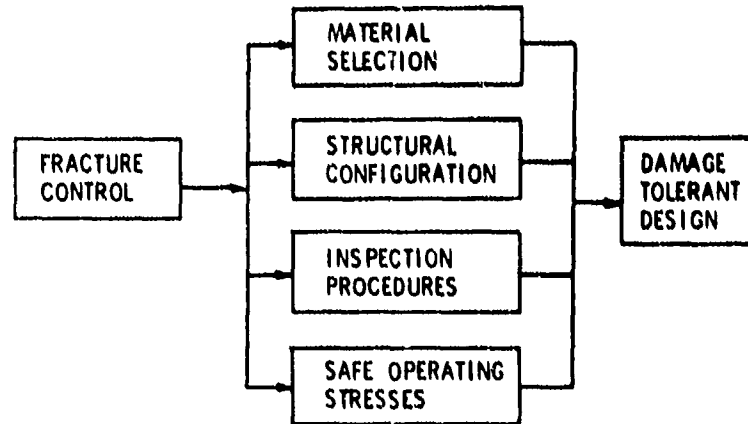


Fig.1 The objectives of fracture control procedures

In design, consideration is given to the likelihood that all new structure contains flaws, introduced during the processing of the basic material, during part forming or during the assembly process, with the size and character of initial flaws governed by the capability to detect during the manufacturing cycle. Analysis and tests are performed to verify that the assumed initial flaws will not grow to catastrophic proportions and cause failure in the prescribed service period.

The traditional USAF approach to insuring structural integrity is to design for a crack free service life through conventional fatigue analysis, careful attention to workmanship, surface finish and protection, detailed design, local stresses and ease of inspection. Demonstration is accomplished through a full scale airframe cycle test to simulated service conditions. The achievement of these goals of "fatigue quality" or "durability" are, of course, essential, and the implementation of fracture control procedures is in no way intended to replace fatigue requirements.

Naturally, there has been resistance among many to accept the pre-existent flaw philosophy in aircraft design, because of the weight penalties normally associated with supplemental strength and life requirements. There are those who cite aircraft performance degradation and the time and cost of implementing fracture requirements as deterrents.

Effective employment of fracture control procedures on new USAF designs has been hampered by the lack of an adequate material environmental data base for most materials, deficiencies in fracture analysis techniques, uncertainties with regard to production and in-service inspection capability, poorly prepared specifications, and inexperience with respect to requirements for full scale proof of compliance testing.

## 2 Materials Utilization - The Need for Fracture Control

The obvious desire for more efficient aircraft structures has resulted in the selection and use of high strength alloys in primary members with little regard for the general decrease in fracture toughness associated with increased yield strength (Figure 2). So, too, sophistication in design and analysis techniques and closely monitored weight saving programs have afforded some the opportunity to exploit conventional alloys such as 7075 aluminum far beyond the practical limits with the result being higher

allowable design stresses with each aircraft system. These general practices of course, have reduced the tolerance of the structure to both initial manufacturing defects and service produced cracks. Critical flaw sizes are often on the order of the part thickness and many times much less, making positive detection during normal field service inspections improbable. Higher design stresses, of course, increase the likelihood of early fatigue cracking in-service and may result in loss of fleet readiness and expensive maintenance and/or retrofit programs.

For a specific application, the designer must select a material of reasonably high strength in order to meet static strength requirements and still achieve minimum weight. A parameter for evaluating structural efficiency ( $\sigma_{ys}/\text{material density}$ ) will be mentioned later. In the selection process, however, fracture toughness must be a consideration. The achievement of maximum yield strength and maximum fracture toughness is often difficult as is illustrated in Figure 2. It is generally recognized that within certain material groups, toughness decreases with increasing yield strength. This trend is illustrated in Figure 2 for aluminum, titanium and several selected steels where material data from Table 1 have been plotted. Variations in  $K_{IC}$  can be expected for any given alloy and strength level and these variations are generally due to metallurgical aspects, impurities or manufacturing processing. This variability makes the selection of a "design allowable" extremely difficult.

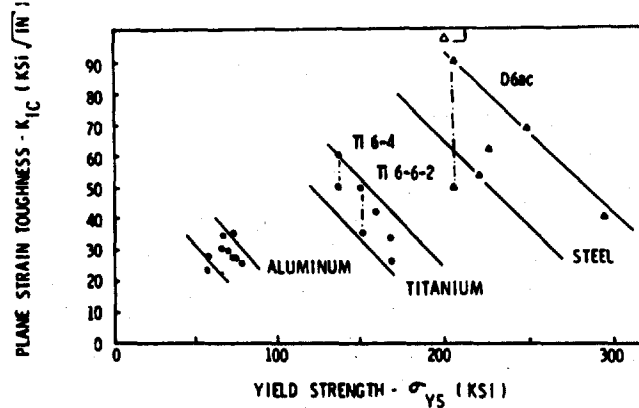


Fig.2 Trends in fracture toughness

TABLE 1  
Typical Material Properties

Material	(1) Yield Strength $\sigma_{ys}$ (Typical)	(2) Plane Strain Tough. $K_{IC}$	(3) $2 \left[ \frac{K_{IC}}{\sigma_{ys}} \right]^2$	(4) $\left[ \frac{K_{IC}}{\sigma_{ys}} \right]^2$	(5) $\frac{\sigma_{ys}}{\rho}$	(6) $\frac{K_{IC}}{\rho}$
<b>Steels</b>						
D6ac	200	50-90	.120 - .30	.06 - .15	724	177(316)
A360	220	53	.12	.06	777	182
2024	247	29	.16	.08	872	244
1008H	286	29	.20	.100	1007	314
H-11	294	40	.04	.02	1029	141
9H1 4Co 2C	180-190	110-170	1.22	.61	600	467
<b>Aluminum</b>						
7075-T73 (forging)	66	31	.44	.22	600	310
2024-T361 (plate)	50	23	.32	.16	500	230
2024-T361 (ext)	50	20	.46	.23	600	290
2014-T6	66	35	.56	.28	600	300
7075-T661 (plate)	70	26	.22	.11	700	290
7175-T73 (forging)	75	35	.44	.22	700	300

Material	(1) Yield Strength $\sigma_{ys}$ (Typical)	(2) Plane Strain Tough. $K_{IC}$	(3) $2 \left[ \frac{K_{IC}}{\sigma_{ys}} \right]^2$	(4) $\left[ \frac{K_{IC}}{\sigma_{ys}} \right]^2$	(5) $\frac{\sigma_{ys}}{\rho}$	(6) $\frac{K_{IC}}{\rho}$
<b>Aluminum (con'g)</b>						
7075-T6 (plate)	76	27	.26	.13	760	270
7075-T6 (forging)	75	27	.26	.13	780	270
7079-T6	69	30	.38	.19	690	300
<b>Titanium</b>						
Ti 6Al-4V(ann)	137	50-60	.26(.30)	.13(.15)	856	312(375)
Ti 6Al-4V(STA)	158	41	.16	.07	908	256
Ti 6Al-4V-2Sn(ann)	190	38-50	.10(.22)	.06(.11)	937	219(312)
Ti 6Al-4V-2Sn(STA)	163	34	.08	.04	1018	212
Ti-13V-11Cr-3Al(STA)	168	25	.04	.02	1050	156

\*\* ASTM Thickness Required for Plane Strain Fracture

\*\*\* Equivalent to  $\sigma_c$  for  $\sigma_{c,limit} = .6\sigma_{ys}$

In specifying a particular material and strength level (minimum acceptable  $\sigma_{ys}$ ), the designer usually would not be concerned about those quantities of material which possessed strength levels on the upper end of the normal range. However, because of the dramatic decrease in  $K_{IC}$ , he must in many cases limit the upper bound of acceptable range of yield strength. This is one procedure used to specify titanium alloys. In Figure 2,  $K_{IC}$  ranges for two common titanium alloys are noted. The data are shown at one yield strength value to illustrate the fallacy in specifying only  $\sigma_{ys}$  minimum.

The material selection process is therefore a tradeoff procedure wherein many concurrent requirements must be satisfied. For the case in point, the designer must establish a criteria for accepting either a reduced toughness or strength level. The choice might be dictated by overall flaw tolerance. This is illustrated in Figure 3 where the ordinate,  $(K_{IC}/\sigma_{ys})^2$ , a parameter indicative of crack size, is used. Since structures are designed to withstand (statically) a percentage of the yield strength, this parameter may be conveniently used to illustrate flaw tolerance sensitivity. Examination of Figure 3 indicates a more dramatic reduction in the crack length parameter, with increased yield strength.

The same trend is repeated in Figure 4; however, the yield strength has been normalized to the material density  $\rho$ . The parameter  $\sigma_{ys}/\rho$  is one form of structural efficiency used to select materials. Note that material ranking has changed with titanium being superior to steel. One exception illustrated is the 18% Ni maraging steel and 9Ni 4C which fall beyond the bounds illustrated. There are recognizable limits on both the values of  $(K_{IC}/\sigma_{ys})^2$  and  $(\sigma_{ys}/\rho)$  for materials in use today. The bounds are illustrated in Figure 4.

The data presented in Figure 4 clearly illustrate the relationship of non-destructive inspection (NDI) capability and material selection to resist brittle fracture. For example, a through the thickness crack will experience plane strain fracture when  $K = K_{IC} = \sigma \sqrt{\pi a_c}$ . If fracture is assumed to occur at the design limit stress, the value of critical crack length,  $a_c$ , can be computed. For many aircraft structures, design limit stress is of the order of  $\sigma_L = 0.6\sigma_{ys}$  and  $a_c = \left(\frac{K_{IC}}{0.6\sigma_{ys}}\right)^2 \frac{1}{\pi} \approx \left(\frac{K_{IC}}{\sigma_{ys}}\right)^2$ . Thus, each point on

Figure 4 might be considered the critical characteristic flaw dimension for plane strain fracture, and thus describe the sensitivity level required for fleet inspection. For this type of selection criteria, many materials may be prohibited because of the extremely small flaws which must be detected. Limits of NDI practice are not well defined.

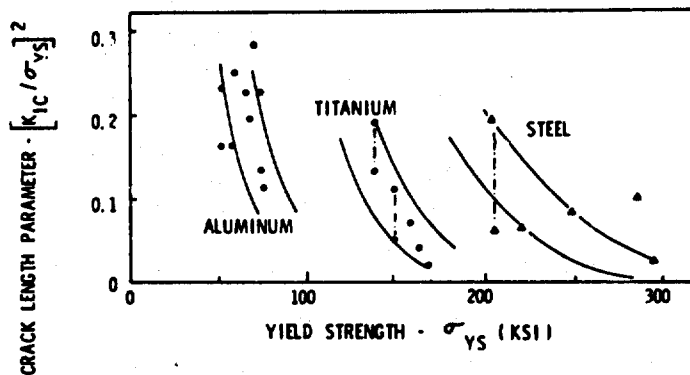


Fig.3 Variation of crack length parameter

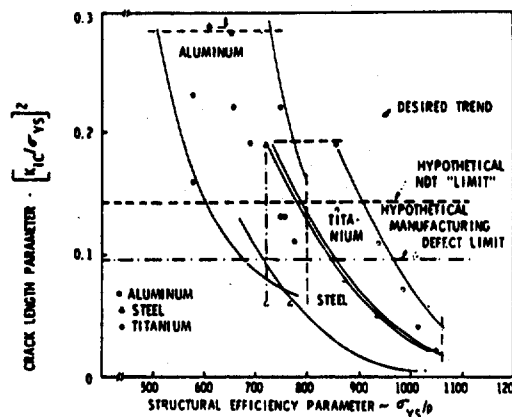


Fig.4 Variation of crack length parameter with structural efficiency parameter

With the technological trend in material utilization growing toward greater strength to weight ratios, it seems logical also to define more realistic limits on the material selection based on uncontrollable "human element" defects. Thus, the crack size definition of Figure 4 might indicate limits produced by normal tool marks, scratches or gouges produced during manufacture or maintenance. If these limits are recognized as sound, then more effective means of inspection may be required, such as proof of testing (Figure 5).

In the previous discussion it was assumed that plane strain fracture was the dominant consideration. Fortunately, this is not always the case for many engineering materials because of the effects of thickness, plasticity, geometry, etc. (Figure 6 and 7). The question does remain, however, as to what role  $K_{Ic}$  has in the material selection and analysis process. It is perhaps safe to conclude that the selection of candidate materials for a specific consideration can be made on the basis of superior  $K_{Ic}$ , as long as the materials are similar. The decision, however, rests upon the thickness required to fulfill the task. In Figure 7, the variation of critical stress intensity factor with thickness is illustrated for several alloys. (Ref. 1)

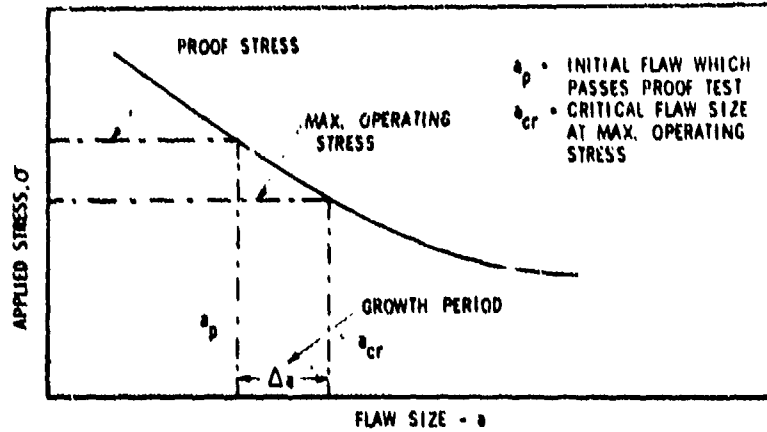


Fig.5 Proof test concept

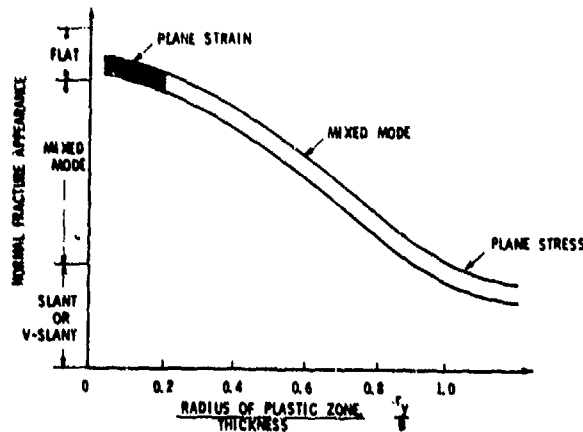


Fig.6 Trend in fracture mode appearance vs. crack tip plastic zone parameter

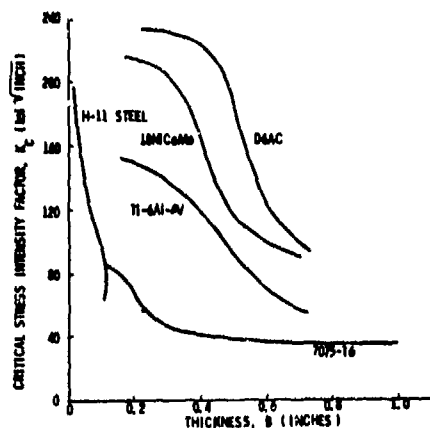


Fig.7 Nominal critical stress intensity for several materials

Material selection based on cyclic growth considerations is not as clearly defined, since observed trends in cyclic rate data, for a non-aggressive environment indicate that materials within a group or class generally fall within a narrow scatterband, with little, if any dependence on toughness. Average growth rate curves have been included in Figure 8 to illustrate the relative relationship between materials. Hahn (Ref. 2) has observed that the rate,  $da/dn$ , can be approximated for many materials as:

$$da/dn = 8 \left( \frac{\Delta K}{K} \right)^2$$

in the central or log linear portion of the growth rate curve. Several points are shown in Figure 8 using the Hahn expression. Because of the relationship of growth rate to modulus,  $E$ , the data can be normalized to the material density,  $\rho$ , as indicated in Figure 9 where rate curves are seen to converge. It is apparent then, that a material's advantage can only be assessed on an individual application basis. Growth under variable amplitude spectrum loading, for example, may produce different trends in growth retardation due to the interaction of loads. Generally speaking, however, the time to failure from an initial flaw is dependent upon the toughness  $K_{IC}$  as illustrated in Figure 10. The relative effect, however, may be dependent upon the shape and severity of the spectrum. The selection of materials for repeated load application in the presence of flaws may be seriously influenced by the chemical and thermal environments in which the structure must operate.

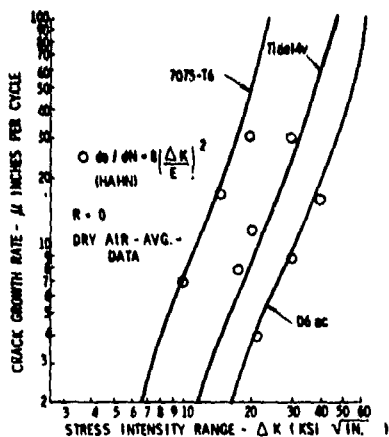


Fig.8 Fatigue crack growth data for typical aircraft structural materials

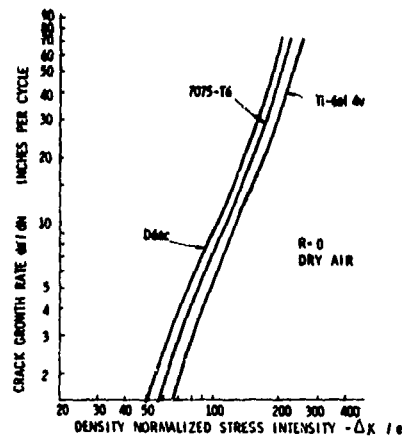


Fig.9 Comparative crack growth rate data

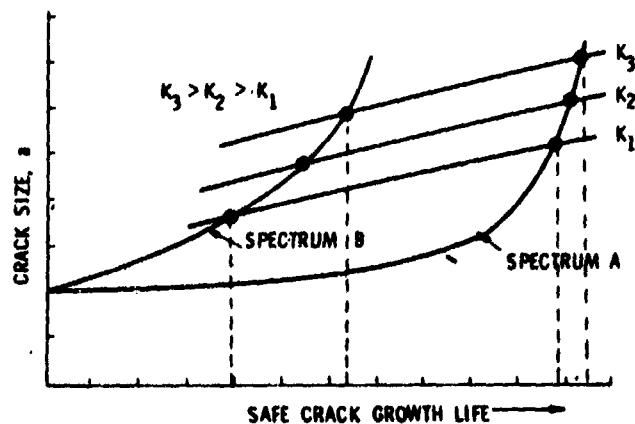


Fig.10 Effect of fracture toughness on life for various spectra

### 3 Fracture Control - Basic Objectives

Of the recent Air Force experiences with high strength materials, none is more dramatic or illustrative of the need for fracture control than that of D6ac steel used in major structural locations of the F-111, Reference 3. An accident in December 1969, which has been attributed to the presence of a critical defect in the steel wing pivot fitting, was the singular event which caused wide spread action and reaction within the Air Force and the contractor and resulted in the formation of a fleet recovery program and structural proof test effort.

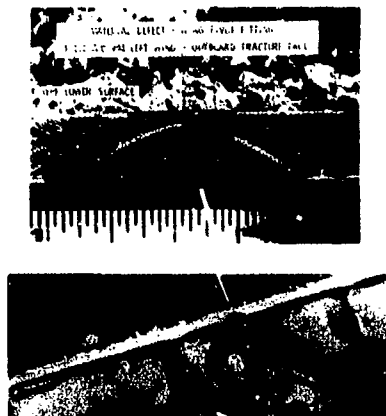


Fig.11 Wing pivot flaw

The flaw responsible for this incident is shown in Figure 11. Critical depth occurred in the structure at a point less than the thickness of the member. The dark region of the flaw is surmised to have originated during the manufacture of the basic forging. Subsequent analysis of this material (D6ac steel, strength level 220 ksi) during the fleet recovery program, revealed its sensitivity to quenching procedure during heat treatment with a greater than two to one variation in fracture toughness, K<sub>IC</sub>, resulting even though standard tensile properties fell within the acceptable range. The effect of this 2:1 variation of K<sub>IC</sub> is to reduce the critical crack size by a factor of four.

With somewhat "ideal" conditions existing in this instance (i.e., the flaw occurring in a region of high stress, and orientated normal to the principal stress direction) brittle fracture of this unexposed flaw was inevitable. The subsequent recovery program for the F-111 fleet and the proof test program are well documented. (Ref. 3) This incident resulted in the largest single investigation of a structural alloy ever to be undertaken (Ref. 4).

The wing pivot flaw is an excellent example to illustrate the need for fracture control considerations in design and will be used here to assist in identifying major goals which are to be achieved as the result of instituting fracture requirements.

In examining this failure, one could conclude that a higher toughness would have resulted in a larger critical crack size, possibly through-the-thickness and a much improved probability of detection. For some cases, fuel leakage might be expected. Thus, we can say that fracture considerations should encourage the intelligent selection of materials and control procurement and processing to insure consistent properties; assist in establishing inspection procedures including such requirements as positive detection and leak before break situation. In addition to material selection, growth of flaws can be lessened and critical crack sizes increased considerably by limiting or controlling design stress. This can have additional benefit from the point of view of fatigue resistance or durability and can significantly result in reduced maintenance cost and system down time.

The wing pivot fitting used in this example is essentially a single load path member. Failure of this element resulted in loss of the aircraft. A more damage tolerant structural arrangement, including possible multiple load paths or crack arrest members, if properly designed, could have improved the overall safety.

In Section II, materials data were presented to illustrate how strength-weight (efficiency) could result in the selection of material with an undesirable level of toughness. Likewise, the choice based on fatigue alone might lead to serious difficulty since many high strength materials (steels, for example) may have acceptable fatigue resistance but possess low resistance to brittle fracture and subcritical flaw growth (stress corrosion cracking, for example).

Structural configurations which possess multiple load paths, crack stoppers, etc., are necessary and desirable, however, their ability to function and meet specific preassigned goals must be demonstrated early in design.

Controlling design stress levels for common structural materials can have untold benefits from both the strength and fatigue points of view and can prevent costly field maintenance problems. For example, multiple load path, redundant and "fail safe" arrangements may effectively prevent the loss of aircraft, so long as adequate and frequent inspections are planned. The sole dependence of the fail safe approach to achieving fracture control without regard to limiting design stresses may result in frequent member failures, costly unscheduled maintenance and aircraft down time. This situation can be alleviated by requiring each member in the multiple or redundant set to be inherently resistant to flaw growth within prescribed bounds (i.e., must have a safe life with cracks.)



The ability to detect and quantify flaws and cracks, both in the raw product form and the final assembled structural article, remains as the most significant measure in deterring catastrophic fracture. Because we institute fracture control procedures is in fact a frank admittance that serious flaws can and often do go undetected. This fact was dramatically pointed out by Packman, et al (Ref. 5) in a study for the Air Force Materials Laboratory. The data in Figure 12 has been obtained from that report and depict the sensitivity and reliability of common NDI methods in controlled laboratory experiments. The results are quite surprising because relatively large flaws were not detected. This does not mean that all hope is lost of improving our methods and procedures. On the contrary, continued development of improved NDI techniques is mandatory.

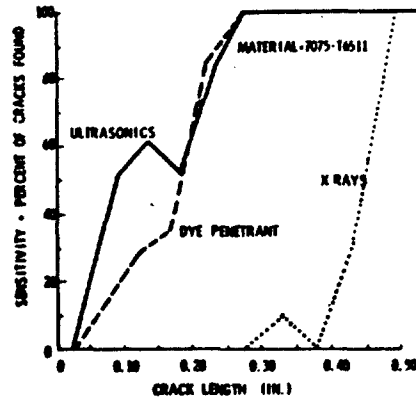


Fig.12 Demonstration of flaw detection capability

#### 4 Fracture Control - Requirements

Preparation of detailed step by step requirements for fracture control is a difficult task because of the numerous classes of aircraft (i.e., fighter bombers, trainers, etc.) in use today by the Air Force and because of the various types of structural arrangements which comprise these airframes. Aside from the selection, procurement and control of processes for engineering materials, implementation of fracture considerations consists of the formulation of safe crack life and strength goals which must be satisfied by primary structure. Compliance with these requirements is accomplished by analysis in all cases and often requires substantiation by element, component or full scale testing. The fracture analysis is completed in connection with the conventional analysis (e.g., static and fatigue) for which a flaw free structure is assumed.

In the fulfillment of these analyses, basic materials allowable, knowledge of operational environments and an analysis capability to perform complex flaw growth and strength analyses are among the items necessary. Supplemental tests may be required to establish or substantiate stress intensity relationships, verify real time and spectrum growth behavior, and demonstrate crack arrest capability.

Within the USAF, early attempts have been made to define and implement fracture control programs for systems currently in the design stages. Figure 13 includes a summary of the major elements for two of these systems.

	Bomber	Fighter
• MATERIAL SELECTION	YES	YES
• MATERIAL CONTROL	$K_{Ic}$ YES (MCS) EXTENSIVE	NUMBER (#) YES CRITICAL ITEMS
• FRACTURE TEST PROGRAM	EXTENSIVE (~ 2000 TESTS)	YES
• BASIC ALLOWABLES DATA ( $K_{Ic}$ @ $\sigma$ / $K_{ISCC}$ @ $\sigma$ )	YES	
• SPECTRUM LOADED TESTS (SMALL ELEMENTS & COMPONENTS)	YES (~ 300 TESTS)	(~ 100 TESTS)
• FULL SCALE TESTS	YES (1) YES (2)	YES (1)
• FAIL-SAFE DESIGN	YES (1) YES (2)	YES (WING ATTACH YES) YES
• QUALITY ASSURANCE	YES	YES
• NDI CAPABILITY DEMONSTRATION	YES	YES
• SPECIAL N.D.I. PROCEDURES (INCLUDING DWG. CONTROL)	YES	YES

Fig.13 Fracture control elements current systems

As an example of the strong wording of these directives, the following is extracted from early versions of the requirements for the bomber.

"...Primary structures which are not fail safe shall be designed so that initial flaws or cracks will not propagate to critical crack length during the lifetime of the aircraft. Through fracture data tests and analysis, the characteristics and dimensions of the smallest initial defect that could grow to critical size during the service life shall be determined. Once these initial flaws sizes have been identified, quality control procedures shall be developed such that parts containing initial flaws of these dimensions will not be accepted. In the event that the identified initial flaws sizes are smaller than the quality control detection capability, changes shall be made in the materials and/or stress levels so that initial flaws compatible with quality control capability can be tolerated."

The requirements were further modified to require that the service life analysis be made with specific initial crack size assumptions. In other words, the initial crack size is to be treated as a design allowable. For example:

"...These initial defect limits are as follows, (a) In the absence of special NDI procedures as indicated below, the minimum allowable defect size shall be 0.150" in its critical dimension, i.e., 0.150" deep for a surface flaw... (b) Defects smaller than 0.150" will be allowed if special NDI procedures are followed with a demonstrated ability to detect flaws of the required size with a 95% probability at a 50% confidence level..." (This was later amended to 95% confidence that at least 90% of flaws greater than critical size are found.)

The analysis of each part was to be performed as follows:

"...The analysis shall assume the presence of a crack like defect, placed in the most unfavorable orientation with respect to the applied stress and material properties and shall predict the growth behavior in the chemical, thermal and sustained and cyclic stress environment to which the component is subject."

With regard to material selection, usage and control, measures were to be instituted to insure adequate toughness in production. The early version of the requirements stated

"...Specifications shall be prepared to insure materials having minimum guaranteed  $K_{Ic}$  are used in manufacture."

While the intent was certainly sincere, the wording was revised to be more direct and more nearly definitive.

"...The materials from which the structures are to be fabricated shall be controlled by a system of procedures and/or specifications which are sufficient to preclude the utilization in fracture critical areas of materials possessing static fracture properties significantly inferior to those assumed in design."

To those familiar with aircraft structural design and analysis, these requirements seemed profound in nature, and when circulated among the major airframe manufacturers in 1970, certainly caused a mild furor. Nevertheless, the basic meaning of these requirements is still with us, both as contractual obligations on the bomber program and requirements for future systems.

Because of inexperience, several items of the early requirements needed strengthening, or at least clarification.

First, the early requirements lacked sufficient strength regarding the safe crack growth goals of multiple load path or fail safe structure.

The second point concerns the statement regarding the control and assurance of material property consistency. This simply means that properties must be guaranteed by the metal producers, or that screening of stock and segregation must be performed with the selection of only the superior material for production, a costly procedure in any case. The question of what properties to control is often asked.  $K_{Ic}$  is the logical choice since it is the only property for which standards exist. The rate of fatigue crack growth  $da/dn$  is perhaps more significant on life but does not appear to be as sensitive to basic material processing procedures as does the toughness,  $K_{Ic}$ .

The third item concerns the identification of fracture critical parts. Since the requirements stipulate that all primary members be designed for safe crack growth, a tremendous bookkeeping task is involved, to say nothing of the costs incurred in tracing materials, processes and parts through the manufacturing stage and the establishment of standards for field maintenance. What will most probably evolve in a specific design are sensitivity analyses for certain parts to examine effects on life due to material property variation, initial flaw size, etc.. Where applicable, parts will be further classified as to function, safety, etc., so as to lessen the stringent requirements for traceability and material property control on those parts where these controls are unwarranted.

##### 5 Summary of New Requirements

The lessons learned in applying fracture mechanics to these two systems have been beneficial in the formulation of general "across the board" damage tolerant or fracture requirements for future USAF aircraft. The overall scheme currently defining these requirements is shown in Figure 14 and includes as major documentation, Military Standard 1530, the description of the Air Force Aircraft Structural Program (ASIP), and the detailed requirements (Military Specifications) which provide the specific wording of the requirements.

The key elements of Mil Std 1530 are included in Figure 15.

Advisory Inputs		Responsible Organization	Approval Authority	Current Status
NONE	USAF REG 80-13 INSTRUCTS SPO's TO COMPLY WITH MIL-STD 1530	ASD	USAF HQS	MINOR REVISIONS REQUIRED
I.A.C. ATA	MIL-STD 1530 DESCRIBES ASIP	ASD/EN	USAF HQS	IN PREPARATION
ATA	MIL-A-8866 PROVIDES SPECIFIC DAMAGE TOLERANT REQ.	ASD/EN AFFDL	ASD	REQUIRES UPDATING
NONE	FRACTURE MECHANICS HANDBOOK	ASD/EN	ASD	BEING INITIATED
VOL I GUIDELINES FOR COMPLIANCE VOL II BASIC DATA		AFFDL AFPL	ASD/EN ASD/EN	

Fig.14 USAF specifications and control for design of damage tolerant aircraft

THE STANDARD REQUIRES:

- DAMAGE TOLERANT DESIGN OF ALL NEW USAF AIRCRAFT SYSTEMS
- "SAFETY OF FLIGHT" STRUCTURE BE DESIGNED ASSUMING THE PRESENCE OF PRE-EXISTING DAMAGE REGARDLESS OF DAMAGE TOLERANT DESIGN CONCEPT USED.
- A FRACTURE CONTROL PLAN BE ESTABLISHED AND IMPLEMENTED
- DAMAGE TOLERANCE ANALYSES & TEST
- AIR FORCE APPROVAL OF IMPORTANT FRACTURE TASKS
  - MATERIAL SELECTIONS
  - JOINT SELECTIONS
  - FRACTURE CRITICAL CRITERIA
  - ANALYSES & TESTS
  - INSPECTION, PROCESS CONTROL, & QUALITY CONTROL PROCEDURES

THE STANDARD ALLOWS:

- CONTRACTOR CHOICE OF DESIGN APPROACH
  - SLOW CRACK GROWTH STRUCTURE
  - CRACK ARREST STRUCTURE
  - MULTI-LOAD PATH STRUCTURE

Fig.15 Key elements of Mil. Std. 1530 as applied to damage tolerance

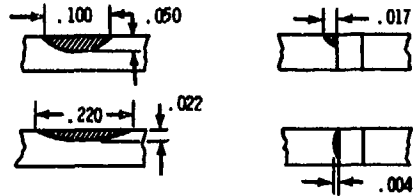
An initial draft of the currently proposed Damage Tolerance Requirements has been prepared and includes specific growth requirements for each classification of structure (i.e., slow crack growth and Fail Safe) based upon the planned degree of and frequency of inspection. This initial draft, summarized in Tables 2, 3 and 4 is currently being evaluated on several existing aircraft structures, to determine the relative sensitivity and impact of the various elements such as initial damage, inspection frequency, etc., on the design stresses.

The important variables which control the severity of the crack growth design requirements are the initial damage sizes,  $a_1$ ,  $a_2$ , and  $a_3$ , and the frequency of inspection. Initial damage size assumptions for intact structure ( $a_1$ ), reflect the production inspection capability of the contractor and must be demonstrated in an approved NDI program to prescribed levels of confidence. Flaw size,  $a/Q$ , treated as an allowable, reflects all possible types and shapes which have equal initial severity as shown in Figure 16. It is important to qualify NDI capability for flaws emanating from fastener holes so as to measure any possible increase in detection sensitivity due to the presence of the hole. Otherwise, it must be assumed that the crack sizes demonstrated are acting in conjunction with the open hole. In the analysis of parts for safe crack growth, this is the most severe case. If NDI is qualified to an  $(a/Q)$  value or range, rather than a fixed surface length, or depth, the analyst must assume the worst case, that of a shallow crack and examine the possibility of it becoming critical prior to becoming a semi-circular flaw (Figure 17) since experimental data has indicated that shallow flaws grow faster in the depth direction.

## 6 Conclusions - Some Problems and Concerns

With the initiation of firm requirements for damage tolerant design and analysis and the institution of an extensive applied research activity, the USAF has made impressive strides toward insuring structural safety in future aircraft. In applying these requirements, however, some problem areas and concerns still remain particularly with regard to the amount of success we can expect to achieve. For example, in examining the requirements for safe growth within the bounds of the initial and final crack sizes, Figure 18, we see that inspection, maximum stress and fracture toughness govern the end points (A) and (C). For a specified life goal, the designer must trade stress level, material type of construction, etc., to fit the growth curve within this envelope.  $K_{IC}$  may be relatively unimportant in this process, particularly if the shape of the growth curve starts out flat and curves sharply toward the end of life.

1. EQUIVALENT CRACKS BASED ON DETECTABLE  $A = 0.050$   
( $A/Q$ ) = 0.022



2. EQUIVALENT CRACKS BASED ON DETECTABLE  $A/Q = 0.50$

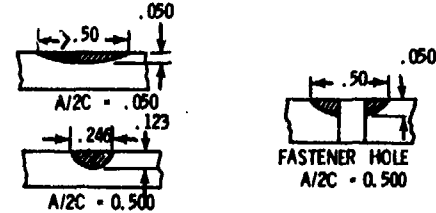


Fig.16 - Equivalent surface flaws based on detection capability

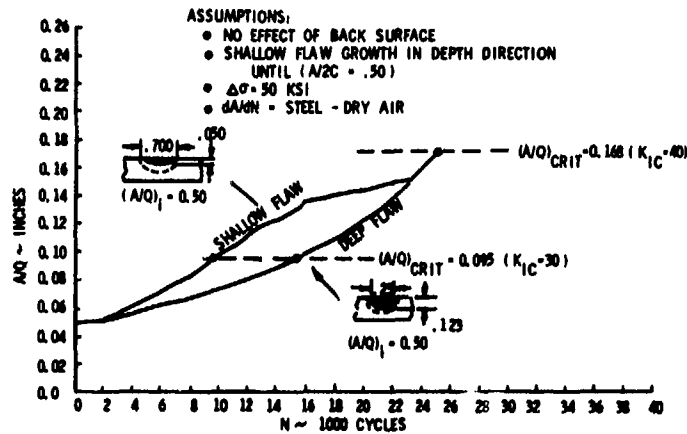


Fig.17 Growth of equivalent flaws under sinusoidal loading

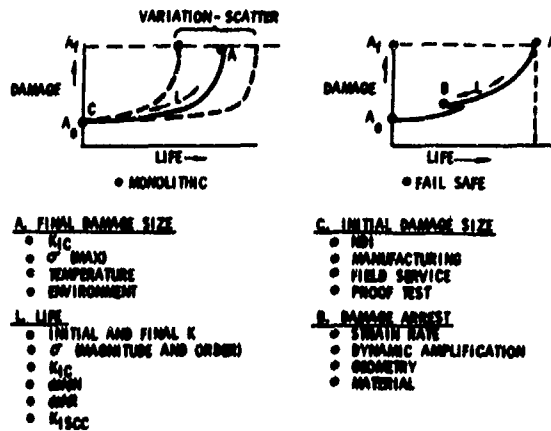


Fig.18 Factors which influence crack growth life

I don't want to convey the wrong impression, however, since  $K_{IC}$  can govern the size of final crack in-service and the larger  $K_{IC}$  of course is desired. Between the end points, however, much takes place with the shape of the growth curve dependent upon the many factors summarized in Figure 18, including the ratio of initial to final stress intensity. The shape is also dependent upon the type of mission flown, the number and relative magnitudes of the flight stress cycles and the amount of growth retardation which may occur due to the presence of overloads or proof cycles, the material and the environment, their inter-relationship and the sequence in which the loadings are applied. Sequence effects are among the least understood and constitute an area where a considerable amount of benefit can be gained through further

research. Whereas the initial and final crack sizes may be considered deterministic, ( $K_{IC}$  with a few percent, for example), growth rate behavior under variable amplitude and environment is extremely complex and difficult to predict even when loads and sequences are known. This coupled with the fact that flight load environment information in most cases is not deterministic make the problem at first glance untenable. Scatter in basic growth rate data can be as much as 2:1 for most materials, even in a controlled nonaggressive atmosphere. Thus, it appears that life predictions within this accuracy may be the best we can achieve. What adds to the difficulty is that many of the spectrum effects are often difficult to separate from normal scatter in basic growth rate.

Under certain conditions (i.e., small crack sizes and low stress amplitude), growth occurs at very low ranges of  $\Delta K$ , Figure 19, a region of the growth rate curve for which there is little data due mainly to the time and expense incurred in the generation. Likewise, until recently, there has been little call for low  $\Delta K$  growth rate data. The concept of threshold or lower limit of growth rate  $\Delta K_0$  is presented and data are available which show this to be related to the elastic modulus. Recent experiences indicate that basic growth rate data may be specimen dependent, that is, there are observed differences between compact tension and surface flow growth rates (Figure 20) attributable to maximum stress levels, for example (Ref. 5). Crack front stabilization, for example, is thought to affect growth results at low  $\Delta K$  values.

Thus, there are many as yet unanswered effects on basic growth rate data generation, which must be resolved if we are to use this basic data to predict complex loading cases. Figure 19 includes a summary of these factors.

The subject of scatter factor or confidence factor to be used in design with safe growth predictions remains undiscussed. Current recommended practice is to use upper bound growth rates with conservative accounting of factors such as variations in anticipated usage and amount of retardation.

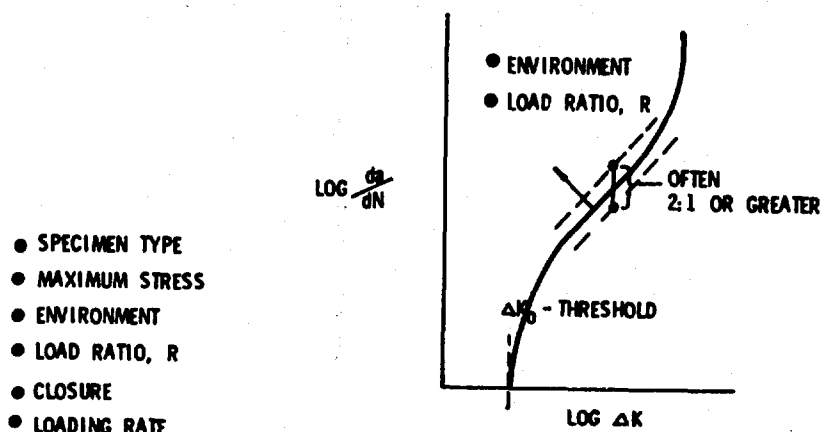


Fig.19 Factors which influence measured crack propagation data

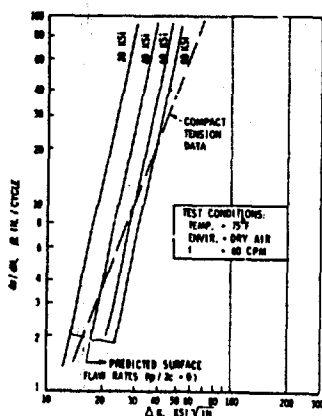


Fig.20 Surface flow data adjusted to  $a/2c = 0$  and compared with compact tension data

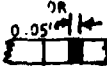
DEGREE OF INSPECTABILITY	FREQUENCY OF INSPECTION	MIN. PERIOD OF UNREPAIRED SERVICE USAGE (F <sub>XX</sub> )	MIN. REQ'D RESIDUAL STRENGTH (P <sub>XX</sub> )	MIN. ASSUMED INITIAL DAMAGE SIZES (a)	MIN. ASSUMED IN-SERVICE DAMAGE SIZES (I)	DAMAGE GROWTH LIMITS
IN FLIGHT EVIDENT	←----- N/A -----→					
GROUND EVIDENT	←----- N/A -----→					
WALK AROUND VISUAL	SPECIFIED IN CONTRACT DOCUMENTS (10 FLTS. TYPICAL)	5 X FREQ (F <sub>WV</sub> )	P <sub>WV</sub>	a/Q = 0.10	2" Open Thru Crack Unless Detection Of Smaller Size Demonstrated	1 Shall not grow to critical @ P <sub>WV</sub> in F <sub>WV</sub> a Shall not grow to critical @ P <sub>DM</sub> in F <sub>DM</sub>
SPECIAL VISUAL	SPECIFIED IN CONTRACT DOCUMENTS (1 YR. TYP)	2 X FREQ (F <sub>SV</sub> )	P <sub>SV</sub>	OR  OR SHALLER IF DEMONSTRATED		1 Shall not grow to critical @ P <sub>SV</sub> in F <sub>SV</sub> a Shall not grow to critical @ P <sub>DM</sub> in F <sub>DM</sub>
DEPOT OR BASE LEVEL	SPECIFIED IN CONTRACT DOCUMENTS (1/4 LIFE-TIME TYP.)	2 X FREQ (F <sub>DM</sub> )	P <sub>DM</sub>		(a/Q)DM	1 Shall not grow to critical @ P <sub>DM</sub> in F <sub>DM</sub> a Shall not grow to critical @ P <sub>DM</sub> in F <sub>DM</sub>
NON INSPECTABLE	N/A	2 LIFETIMES (F <sub>LT</sub> )	P <sub>LT</sub>		N/A	a Shall not grow to critical @ P <sub>LT</sub> in F <sub>LT</sub>

TABLE 2  
Requirements: Slow Crack Growth Structure

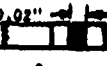
DEGREE OF INSPECTABILITY	FREQUENCY OF INSPECTION	MIN. PERIOD OF UNREPAIRED SERVICE USAGE (F <sub>XX</sub> )	MIN. REQUIRED RESIDUAL STRENGTH (P <sub>XX</sub> )	MIN ASSUMED INITIAL DAMAGE SIZE		MIN. ASSUMED IN-SERVICE DAMAGE SIZE (I)	DAMAGE GROWTH LIMITS
				INTACT NEW STRUCTURE a <sub>1</sub>	IN REMAINING STRUCTURE a <sub>2</sub>		
IN FLIGHT EVIDENT	N/A	RETURN TO BASE (F <sub>FE</sub> )	P <sub>FE</sub>	↑	↑	2 Cracked Skin Panels Plus Failed Central Stringer (Or Equivalent)	a <sub>1</sub> Shall not cause initial rapid propagation @ P <sub>DM</sub> in F <sub>DM</sub> 1 Shall not cause complete failure @ P <sub>FE</sub> in F <sub>FE</sub>
GROUND EVIDENT	EVERY FLIGHT	ONE FLIGHT (F <sub>GE</sub> )	P <sub>GE</sub>	a/Q = 0.03 	↑	2 Cracked Skin Panels Plus Failed Central stringer (or equivalent)	a <sub>1</sub> Shall not cause initial rapid propagation at DM in F <sub>DM</sub> 1 Shall not cause complete failure @ P <sub>GE</sub> in F <sub>GE</sub>
WALK AROUND VISUAL	SPECIFIED IN CONTRACT DOCUMENTS (10 FLIGHTS TYPICAL)	5 X FREQ (F <sub>WV</sub> )	P <sub>WV</sub>	Or Smaller IF Demonstrated	↓	a <sub>2</sub> OR 2" or Greater through crack in skin at failed stringer or whichever is applicable Smaller crack if demonstrated	a <sub>1</sub> Shall not cause initial rapid propagation @ P <sub>DM</sub> in F <sub>DM</sub> 1 Shall not cause complete failure @ P <sub>WV</sub> in F <sub>WV</sub>
SPECIAL VISUAL	SPECIFIED IN CONTRACT DOCUMENTS (ONE YEAR TYPICAL)	2 X FREQ (F <sub>SV</sub> )	P <sub>SV</sub>	↓	↓		a <sub>1</sub> Shall not cause initial rapid propagation @ P <sub>DM</sub> in F <sub>DM</sub> 1 Shall not cause complete failure @ P <sub>SV</sub> in F <sub>SV</sub>
DEPOT OR BASE LEVEL	SPECIFIED IN CONTRACT DOCUMENTS (1/4 LIFE-TIME TYPICAL)	2 X FREQ (F <sub>DM</sub> )	P <sub>DM</sub>	↓	↓	(a/Q)DM As specified in 2.3.5 or a <sub>2</sub>	a <sub>1</sub> Shall not cause initial rapid propagation @ P <sub>DM</sub> in F <sub>DM</sub> 1 Shall not cause complete failure @ P <sub>DM</sub> in F <sub>DM</sub>

TABLE 3  
Requirements: Crack Arrest Structure

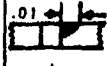
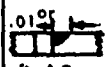
DEGREE OF INSPECTABILITY	FREQUENCY OF INSPECTION	MIN PERIOD OF UNREPAIRED SERVICE USAGE (F <sub>XX</sub> )	MIN REQ'D RESIDUAL STRENGTH (P <sub>XX</sub> )	MIN ASSUMED INITIAL DAMAGE SIZE			MIN ASSUMED IN-SERVICE DAMAGE SIZE	DAMAGE GROWTH LIMITS
				INTACT NEW STRUCTURE (a <sub>1</sub> )	REMAINING STRUCTURE			
					DEPENDENT LOAD PATH (a <sub>2</sub> )	INDEPENDENT LOAD PATH (a <sub>3</sub> )		
IN FLIGHT EVIDENT	N/A	RETURN TO BASE (F <sub>FE</sub> )	P <sub>FE</sub>		Failed Load Path Plus	Failed load path plus		a <sub>1</sub> Shall not grow to critical @ P <sub>DM</sub> in F <sub>DM</sub> a <sub>2</sub> or a <sub>3</sub> Shall not grow to critical @ P <sub>FE</sub> in F <sub>FE</sub>
GROUND EVIDENT	EVERY FLIGHT	ONE FLIGHT (F <sub>GE</sub> )	P <sub>GE</sub>	a/Q = .03	a <sub>1</sub> + Δ a in adjacent load paths	a/Q = .01 or .01 	a <sub>2</sub> or a <sub>3</sub>	a <sub>1</sub> Shall not grow to critical @ P <sub>DM</sub> in F <sub>DM</sub> a <sub>2</sub> or a <sub>3</sub> Shall not grow to critical @ P <sub>GE</sub> in F <sub>GE</sub>
WALK AROUND VISUAL	SPECIFIED IN CONTRACT DOCUMENTS (10 FLTS TYPICAL)	5 X FREQ (F <sub>WV</sub> )	P <sub>WV</sub>	or Smaller if Demonstrated	2" crack Plus	Δ a in adjacent load paths	a <sub>3</sub>	a <sub>1</sub> Shall not grow to critical @ P <sub>DM</sub> in F <sub>DM</sub> a <sub>2</sub> or a <sub>3</sub> Shall not grow to critical @ P <sub>WV</sub> in F <sub>WV</sub>
SPECIAL VISUAL	SPECIFIED IN CONTRACT DOCUMENTS (ONE YEAR TYPICAL)	2 X FREQ (F <sub>SV</sub> )	P <sub>SV</sub>		a <sub>1</sub> + Δ a in adjacent load paths	or 2" crack plus	(a/Q)DM	a <sub>1</sub> Shall not grow to critical @ P <sub>DM</sub> in F <sub>DM</sub> a <sub>2</sub> or a <sub>3</sub> Shall not grow to critical @ P <sub>SV</sub> in F <sub>SV</sub>
DEPOT OR BASE LEVEL	SPECIFIED IN CONTRACT DOCUMENTS (1/4 LIFE-TIME TYPICAL)	2 X FREQ (F <sub>DM</sub> )	P <sub>DM</sub>		adjacent load paths	a/Q = .01 	as specified in 2.3.5	a <sub>1</sub> Shall not grow to critical @ P <sub>DM</sub> in F <sub>DM</sub> a <sub>2</sub> Or a <sub>3</sub> Shall not grow to critical @ P <sub>DM</sub> in F <sub>DM</sub> (a/Q)DM Shall not grow to critical @ P <sub>DM</sub> in F <sub>DM</sub>
NON INSPECTABLE	N/A	ONE LIFETIME (F <sub>LT</sub> )	P <sub>LT</sub>			in adjacent load paths	N/A	a <sub>1</sub> Shall not grow to critical @ P <sub>LT</sub> in F <sub>LT</sub> a <sub>2</sub> or a <sub>3</sub> Shall not grow to critical @ P <sub>LT</sub> in F <sub>LT</sub>

TABLE 4  
Requirements: Fail-Safe Structure

REFERENCES

1. Wood, H.A. "Fracture Control Procedures for Aircraft Structural Integrity" AFFDL-TR-71-89 July 1971
2. AFFDL-TR-70-144 "Proceedings of the Air Force Conference on Fatigue and Fracture of Aircraft Structures and Materials" Dec. 1969
3. Hinders, U.A., "F-111 Design Experience - Use of High Strength Steel" AIAA 2nd Aircraft Design and Operations Meeting, July, 1970
4. MCIC-72-04, "Crack Behavior in D6ac Steel," Battelle Columbus Lab. Columbus, OH
5. Packman, P.L., Pearson, H.J., Owens, J.S., and Young, G., "The Applicability of a Fracture Mechanics - NDT Design Criterion for Aerospace Structures" WESTEC Conference, March 10, 1969, Los Angeles, CA.

IV. BASIC CONCEPTS IN FRACTURE MECHANICS<sup>1</sup>

by

John Eitis  
 Douglas L. Jones  
 Harold Liebowitz

1. Introduction . . . . .	.33
2. Macroscopic Classification of Fracture . . . . .	.34
3. Early Developments in Fracture Mechanics . . . . .	.35
4. Linear Elastic Fracture Mechanics . . . . .	.38
4.1 Stress Intensity Factor and Fracture Toughness . . . . .	.38
4.2 Relation between the Griffith and Irwin Approaches . . . . .	.41
4.3 Plasticity Correction . . . . .	.43
4.4 Thickness and Fracture Mode Transition, Plane Strain Size Requirements . . . . .	.45
4.5 Temperature and Fracture Mode Transition . . . . .	.47
4.6 Strain-rate Effects on Plane Strain Fracture Toughness . . . . .	.49
5. Fracture Toughness in Semibrittle Fracture . . . . .	.51
5.1 Crack Opening Displacement (COD). . . . .	.52
5.2 Crack Growth Resistance Curves (R-Curve) . . . . .	.54
5.3 J-Integral . . . . .	.55
5.4 Nonlinear Energy Characterization of Fracture Toughness . . . . .	.55
6. Applications of Fracture Mechanics Concepts . . . . .	.58
6.1 Damage Tolerant Structures . . . . .	.58
6.2 Critical Crack Size . . . . .	.58
6.3 Practical Applications . . . . .	.61
7. Fatigue Crack Growth . . . . .	.62
7.1 Constant Amplitude Fatigue Loading . . . . .	.62
7.2 Variable Amplitude Fatigue Loading . . . . .	.63
7.3 Practical Applications . . . . .	.66
8. Summary . . . . .	.68
9. References . . . . .	.69

<sup>1</sup>Manuscript was previously accepted for publication in the Journal of Engineering Fracture Mechanics.



## 1. INTRODUCTION

The processes involved in the fracture of solids are so complicated and varied that no single formula or criterion can be expected to realistically describe all of the observed fracture phenomena. Despite this rather pessimistic assessment, a sizeable body of useful knowledge concerning certain aspects of fracture does currently exist, having been obtained from extensive theoretical and experimental research efforts. This information enables designers to approach the problem of fracture-safe design in a more rational manner, comparatively speaking, than has been possible in the past. Since fracture in practical situations is usually initiated by existing flaws in processed and fabricated structural components, it seems quite reasonable to expect that those involved with nondestructive inspection of material should have an awareness of the interrelation between flaw size and the fracture process.

The objective of this chapter is to present a concise and somewhat technical review of fracture mechanics, highlighting its strengths as well as its current limitations, while at the same time establishing some perspective as to its relation to the general fracture process. In so doing, the importance of the role of nondestructive inspection as one of several potential safeguards against failure by fracture should become apparent.

The lack of a comprehensive understanding of the failure process in structural materials has resulted in the catastrophic failure, over the past fifty years, of a variety of engineering structures [1,2,3]. Analysis of the failed components of such structures as pressure vessels, storage tanks, welded ship structures, aircraft parts, bridges, pipelines, turbine blades and housings, rocket motor casings and various heavy machine parts, have shown that crack or flaw induced brittle fracture has often been responsible for the failures. If it is assumed that design and construction decisions were compatible in each of these cases with the appropriate conventional design code requirements and construction specifications, the need to establish supplementary design criteria, as well as fabrication and inspection techniques, to insure against fracture failure becomes abundantly clear. The problem in this respect is further intensified by current trends in materials technology and applications. The trend toward use of exceptionally high yield strength materials, such as is available in certain steel, aluminum and titanium alloys, presents the designer with an unfortunate dilemma. The advantages of higher strength materials that he now has at his disposal for structural applications are offset by a significant reduction in ductility, a factor that tends to enhance the possibility of failure by unstable fracture.

Theoretical and experimental considerations coupled with failure studies of fractured structures reveal many contributing factors and influences with regard to the susceptibility of a solid to fracture. Among the most significant are the existence of flaws (cracks) and notches in the structure, the service temperature, geometry and thickness of section, the state of stress in the immediate vicinity of the pre-existing crack or notch tip, and the rate of load application, in addition to the yield strength, ductility, metallurgical composition and grain structure of the material. Several of these factors will be discussed in some detail subsequently. They are mentioned here only to give some illustration of the inadequacy of conventional design practices relative to the question of fracture-safe design. Indeed, design standards currently in use in design of buildings, bridges and other civil engineering type structures are based entirely on the yield strength and some measure of ductility of the material. Although the designer has freedom in determining the distribution of applied loads, selecting nominal section sizes, and introducing designed stress concentrators such as threads, holes, openings and corners; a design approach which depends solely on yield strength presumes a high level of material integrity throughout the life of the structure. In other words, it does not acknowledge and deal with the possibility that severe stress concentrations may be introduced by material processing, structural fabrication and environmental changes. Stress concentrations can be introduced by welds, machine tool markings, stress corrosion and inherent material microstructural defects, which under a combination of unfavorable circumstances may lead to a catastrophic fracture. The yield-strength oriented design procedure also excludes the possibility of subcritical crack nucleation and growth under cyclic loadings at acceptable load levels, i.e., fatigue induced fracture. On the hypothesis that flaws or cracks of some kind are always present in processed and fabricated structural components, it is clear that design based only on maintaining nominal stresses below some predetermined percentage of the yield strength is inadequate to safeguard against the possibility of failure by fracture.

Designers of heavy machinery, pressure vessels, ship and aircraft structures often employ additional measures such as Charpy-V notch impact and notched-bar tensile tests as

qualitative aids in evaluating and selecting materials which are less likely to be fracture prone within a given set of design and operational circumstances. For example it is standard practice to select materials with a measured Charpy energy value greater than that which has previously been found in practice to successfully resist fracture in similar structures. While this practice is an improvement over a design method relying entirely on yield strength, it nevertheless has serious deficiencies. Difficulties arise when applying such an approach to new types of design, to the use of thicker sectioned structures and to newly developed materials, particularly to materials having higher yield strengths. A rational basis for extrapolation of past experience to new situations is an inherent requirement with this approach. Furthermore the design engineer is not provided with the kind of information that he can readily translate into design requirements, namely, allowable stress levels.

Although it is important to include fracture considerations in the design process, it should be emphasized that careful manufacturing and inspection techniques must also be considered as being complementary to effective fracture-safe design. The probability of introducing serious flaws into a structural component must be minimized during the processing and fabricating stages. Inspection techniques must be developed which can easily and economically identify and characterize potentially dangerous flaws. When combined with given allowable flaw size criteria, such techniques will then determine a rational basis for rejection of unsafe structural components.

The discussion of fracture mechanics which follows shall be confined, by and large, to discussion of the assessment of fracture resistance or fracture toughness in structural metals in situations where fracture is essentially brittle or semibrittle. Only under restrictions of this kind can the fracture problem be treated theoretically with any degree of realism and confidence at this stage in the development of a general theory. Other than the brief mention given in the discussion of different types of fracture, no account will be given of the microscopic and metallographic aspects of fracture, nor will fracture dynamics be discussed. The technically important problem of environmentally induced fracture, e.g., through stress corrosion cracking, hydrogen and irradiation embrittlement and creep fracture at elevated temperatures, must likewise, for lack of space, also be omitted.

## 2. MACROSCOPIC CLASSIFICATION OF FRACTURE

Fracture on the atomic scale, can occur in crystalline solids in one of two ways; by direct separation normal to specific crystallographic planes, so called cleavage or brittle fracture, and by extreme slip or glide plane decohesion, which is usually referred to as shear or plastic fracture [4]. From the metallurgical viewpoint, the ability to classify fracture into two or three distinct categories becomes more difficult. In real single and polycrystalline solids, the micro-mechanisms associated with crack nucleation and crack growth are quite numerous and complex, and are just beginning to be understood with the recent development of electron fractography [5]. Fracture surfaces in polycrystalline metals usually exhibit mixtures of cleavage, microvoid coalescence and slip type micromechanisms in the overall fracture process. Dominance of any one particular micromechanism generally requires special circumstances, such as low temperatures and high strain rates which are conducive to cleavage separation in body-centered cubic materials [6,7].

The engineering classification of fracture is based on macroscopic considerations of material separation, and employs designations such as brittle, semibrittle (or quasi-brittle) and ductile to categorize fracture. Broadly speaking, brittle fracture exhibits virtually no macroscopically observable plastic deformation on or near the fracture surface. The fracture surfaces are almost completely flat across the severed section, having a crystalline texture and a shiny appearance. The basic micromechanism involved in the separation process is cleavage. Once an existing crack or flaw starts to grow it tends rapidly to crack instability or sudden unstable fracture with relatively low energy absorption. Brittle fracture is most commonly observed in high yield strength metals and glassy solids subject to low temperature, high strain rates and a high degree of stress triaxiality in the vicinity of the edge or tip of a flaw (crack). At the other extreme, ductile fracture is accompanied by extensive plastic deformation. A conventional uniaxial tensile test performed on a low yield strength initially uncracked aluminum alloy or mild steel bar at room temperature provides a typical example of a ductile type fracture. Considerable localized reduction of cross-section takes place as a result of plastic slip processes before the bar fails by shear sliding across the remaining necked section. The essential micromechanism involves slip or glide plane decohesion. The fractured surface is usually inclined relative to the tensile direction, with a fibrous texture and a dull surface appearance. Extensive plastic deformation necessitates high energy expenditure so that ductile fracture is comparatively difficult to initiate and to maintain in the sense that applied loading must be maintained throughout the fracture process. Low yield strength, high temperature, low strain rates and a low degree of stress triaxiality are circumstances which promote ductile fractures.

Semibrittle fracture is by far the most common type of failure, occurring in a wide variety of metals, under widely varying conditions of loading rates, test temperatures and specimen sizes. Microvoid coalescence, cleavage, and slip have been identified as distinct micromechanisms active in the fracture process. The fracture surfaces possess features which are common to both brittle and ductile type fractures, that is, they are partially square and shiny and partially slanted and fibrous. The initial phase of semibrittle fracture is generally marked by slow, stable crack extension coupled with moderate plastic deformation at the root of the notch or crack. This phase continues

until some critical load level is reached, whereupon unstable crack propagation ensues, having mixed brittle and ductile surface features. The energy absorption required for semibrittle fracture naturally falls between the low and high extremes common to brittle and ductile fractures. The fracture surfaces of medium strength metals fractured at or near room temperature are characteristically semibrittle in appearance.

In crystalline solids such as structural metals, the essential distinguishing feature separating brittle, semibrittle and ductile fractures lies in the degree of plastic deformation which accompanies separation. Since it is not possible to establish precise quantitative measures in this respect, the limitations of the above classification scheme are quite apparent. It should also be remembered that these rather imprecise designations are not always consistent with microscopic observations. In polycrystalline metals X-ray diffraction and electron fractography often reveal small amounts of microplastic deformations on fracture surfaces which macroscopically appear brittle. Thus it must be emphasized that the engineering scheme for classifying fracture is to be understood only in a phenomenological sense, and that the terms brittle and ductile can have different meaning to different people, depending on the scale of observation.

### 3. EARLY DEVELOPMENTS IN FRACTURE MECHANICS

The effects of stress concentrations due to holes or cutouts in otherwise continuous structural members were first recognized during the latter part of the Nineteenth Century. Figures 3.1 and 3.2 illustrate the variation of the stress component parallel to the direction of the uniform tension applied to an infinite sheet containing a circular or elliptical hole, according to the theory of elasticity [8,9]. The presence of a circular hole raises the stress level at the edge of the hole to three times the applied stress level, while for the elliptic hole, the stress concentration at the edge with the smaller radius of curvature increases in proportion to the slenderness ratio of the ellipse, i.e., to the ratio of the major to minor axes. When the major axis is twice the minor axis the stress concentration is five. These results approximate quite accurately the situation for finite sheets with holes when similarly loaded, provided that the major dimension of the hole is very much smaller than the dimensions of the sheet. Hence their practical significance is immediately apparent.

A crack or flaw of finite proportions can be thought of as the limiting case of an elliptic hole as the ratio  $b/a$  approaches zero, as illustrated in Fig. 3.3. According to the theory of elasticity, the maximum stress parallel to the direction of the applied load at the edge of the crack increases in this case without limit. This behavior explains why cracks oriented transversely to the direction of applied tensile loads tend to grow or spread. However, the material at the edge of a sharp crack obviously cannot support infinitely large stresses. In real metals a state of plastic yield develops over a small region bordering the edge of the crack, Fig. 3.4. This point will be discussed in more detail subsequently. It suffices here merely to point out that the plastic enclaves which develop at the borders of a stationary crack, however small, tend to inhibit potential crack growth through blunting of the curvature of the crack tip. Hence, any set of circumstances which inhibits the free development of plastic yield at the crack borders, e.g., low temperature, fast rate of load application, high degree of stress triaxiality in the crack region, tends to promote easy crack expansion, or brittle fracture. For any given crack size, an increase in plastic enclave development generally requires greater net section stresses for initiating crack extension.

The first critical load-crack size relation appropriate to brittle fracture (actually ideal brittle fracture in the sense that all plasticity effects are ignored) was introduced by Griffith in 1921 [10,11]. Referring to Fig. 3.3, let  $U_0$  represent the total elastic strain energy in an uncracked infinite sheet of unit thickness loaded as shown. Suppose that a crack of length  $2a = c$  is introduced slowly enough such that all dynamic effects are negligibly small, while the loaded boundary is held fixed. Since the plane dimensions of the sheet are infinite while the crack size is finite, the applied stress will remain at the same level  $\sigma$  as the crack is inserted. Let  $U$  designate the strain energy of the cracked sheet. With the loaded boundary held fixed the applied load can do no work as the crack appears. Consequently the strain energy in the body can only decrease by virtue of the relaxation of the stresses over the surfaces which define the crack. Thus  $U < U_0$ . The creation of new surfaces which total area  $2c$ , assuming the crack to extend through the unit thickness of the sheet, requires an expenditure of energy which Griffith assumed to be linearly proportional to the crack surface area,  $\gamma_s \cdot 2c$ , where  $\gamma_s$  is a fracture surface energy density. The surface energy density is presumed to be determinable by experiment for any given solid at any given temperature. The quantity  $2\gamma_s c$  can be interpreted as the work done by the relaxing stress as the new internal surface (crack) is introduced. In other words,  $2\gamma_s c$  represents the energy expended in overcoming the inherent cohesion of the solid across the plane crack surface. Using the plane strain linear elastic solution for the elliptic hole of Fig. 3.2, [12], in the limit as  $2b$  approaches zero, Griffith deduced that insertion of a crack  $2a = c$ , subject to the given circumstances, changes the elastic strain energy by  $\pi\sigma^2 c^2 (1-\nu^2)/4E$ ,  $E$  being Young's modulus and  $\nu$  Poisson's ratio [13]. The strain energy of the cracked body with a stationary crack  $2a = c$  is thus

$$U = U_0 - \frac{\pi\sigma^2 c^2}{4E} (1-\nu^2), \quad (3.1)$$

while the total energy is

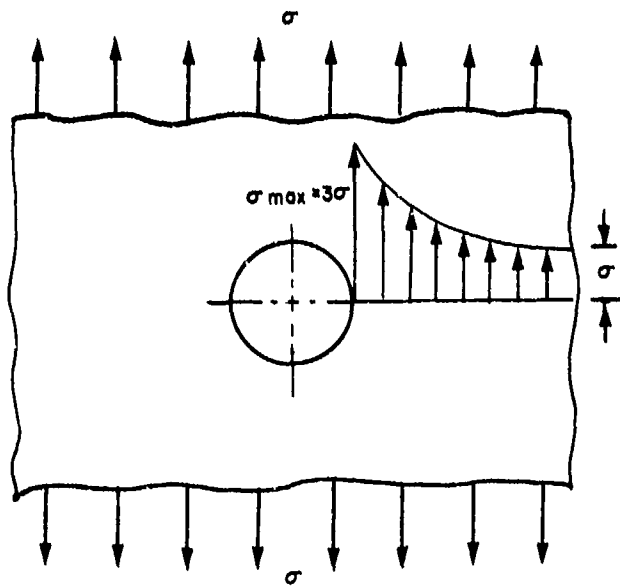


Figure 3.1

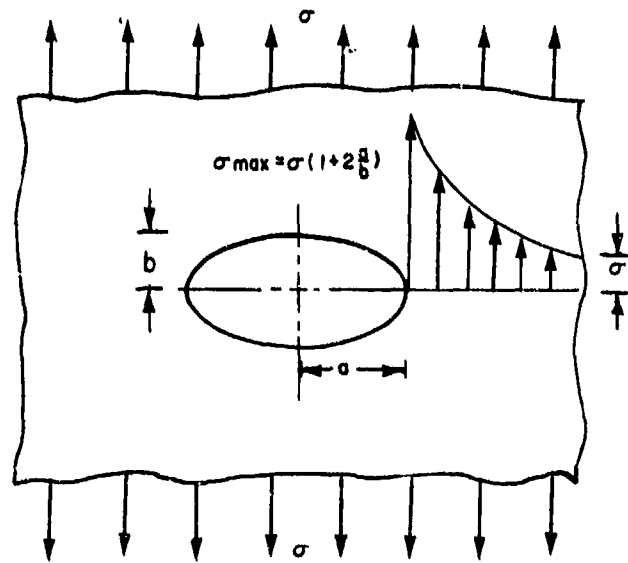


Figure 3.2

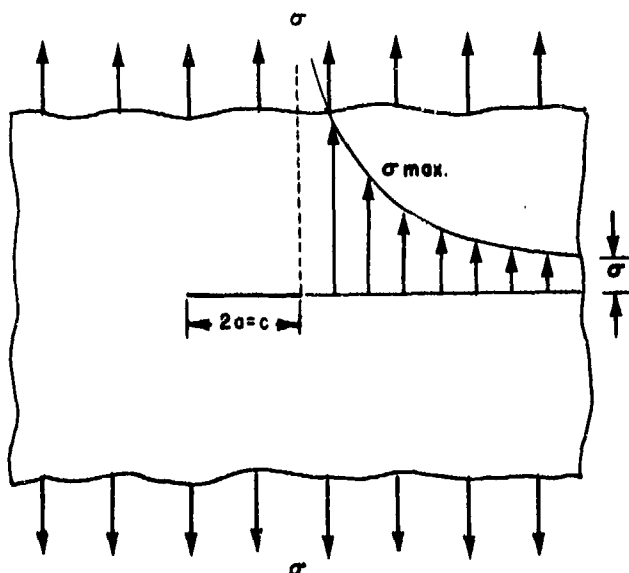


Figure 3.3

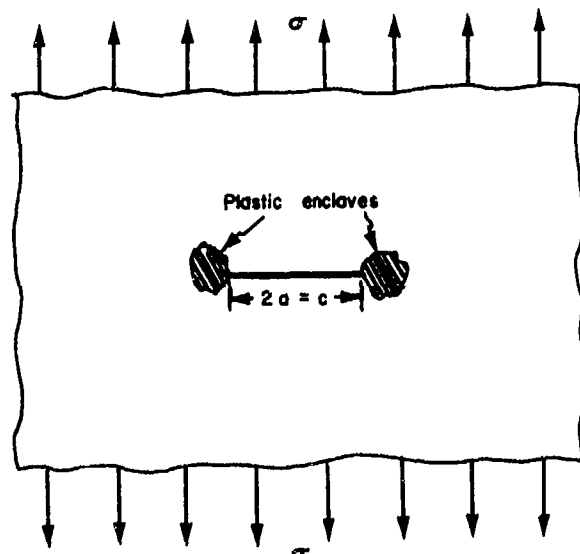


Figure 3.4

$$\Psi = U + 2\gamma_s c = U_0 - \frac{\pi\sigma^2 c^2}{4E} (1-\nu^2) + 2\gamma_s c. \quad (3.2)$$

$\Psi$ , which is actually the thermodynamic free energy of the cracked solid because isothermal conditions are here implied, varies only as the crack size since all the other quantities appearing on the right size of Eq. (3.2) are fixed under the assumed circumstances.

Griffith postulated that the crack is in a state of unstable or critical equilibrium, that is, at a point of incipient growth, when the free energy attains a stationary (in this case maximum) value. Analytically this means the parameters which determine the critical crack equilibrium state are obtained from the condition

$$\left. \frac{d\Psi}{dc} \right|_{\substack{\text{fixed} \\ \text{boundary}}} = 0 \quad (3.3)$$

which from Eq. (3.2) leads to the requirement that

$$- \frac{dU}{dc} = 2\gamma_s, \quad (3.4)$$

or

$$\sigma^2 c = \frac{4E\gamma_s}{\pi(1-\nu^2)}. \quad (3.5)$$

For a given applied load  $\sigma$  the critical equilibrium crack size is thus

$$c = 2a = \left[ \frac{4E\gamma_s}{\pi(1-\nu^2)} \right] \frac{1}{\sigma^2}. \quad (3.6)$$

Alternatively, for a given crack size  $2a = c$ , Eq. (3.5) can be viewed as determining the applied stress level which is necessary to bring on a state of incipient crack growth, or

$$\sigma = \sqrt{\frac{4E\gamma_s}{\pi c(1-\nu^2)}}. \quad (3.7)$$

This is Griffith's formula. It can be interpreted as a brittle fracture criterion for the plane infinite sheet described in Fig. 3.3 (for conditions of plane stress, the factor  $(1-\nu^2)$  is replaced by unity).

Despite the limited circumstances for which Eq. (3.7) is strictly valid, it nevertheless shows remarkably good experimental correlation with fracture tests performed on glassy solids. It does not, however, yield results compatible with experiment when applied to fracture in structural metals. One reason for this lies in the development of plastic deformation at the crack tip regions, mentioned previously, which the Griffith derivation ignores. In situations where the extent of plastic deformation in the crack tip region is substantially smaller than the crack size, the fracture stress is generally observed to be proportional to  $1/\sqrt{c}$ , in agreement with Eq. (3.7). However, the constant of proportionality necessary to correlate with experimental data for finite-sized specimens is found to be much greater than that appearing in the Griffith formula. In an attempt to rationalize this discrepancy, Irwin and Orowan [15,16] proposed independently that a plastic work term  $\gamma_p$  be added to the fracture surface energy  $\gamma_s$  in Eq. (3.7) in order to account for any plastic deformation associated with the separation process. Thus

$$\sigma = \sqrt{\frac{4E(\gamma_s + \gamma_p)}{\pi c(1-\nu^2)}}. \quad (3.8)$$

was proposed as a possible generalization of Griffith's formula to instances of semi-brittle fracture. For structural metals, experimental data requires that the plastic work factor  $\gamma_p$  be  $10^3$  to  $10^6$  times larger than the surface energy  $\gamma_s$  [14].

It should be pointed out that for Eq. (3.8) to be even approximately valid, it is necessary to assume that the plastic enclaves be confined to very narrow strip-like regions on each side of the crack plane as the crack extends. Recent experimental delineations of crack-tip plastic enclaves show numerous instances in which this condition is not even remotely satisfied [17,18,19]. Instead it is more common to find plastic regions which extend away from the crack plane, as in Fig. 3.4, requiring that the crack-front plastic work be volume dependent and not, therefore, a characteristic constant or property of the material as Eq. (3.8) implies. It thus appears that the Irwin-Orowan modification of the Griffith formula is inadequate to deal with fracture in circumstances in which front plasticity is readily observable.

Griffith's formula applies rigorously only to the artificial case of an elastic solution for a plane infinite body. Thus, apart from the error associated with the omission of possible plasticity effects, additional error will arise when the theory is applied to cracked bodies of finite size. In the next section linear elastic fracture

mechanics, which considers the effect of finite geometry in establishing a fracture criterion, is considered.

#### 4. LINEAR ELASTIC FRACTURE MECHANICS

The simplest possible continuum theory of fracture is founded upon the supposition that a cracked solid under load experiences small deformations which are everywhere elastic in character. This assumption is observed to be reasonably valid in strong solids such as structural metals, metallic and ionic crystals and glassy solids. When coupled with guidelines which define the limits of applicability of an essentially elastic treatment, a linear elastic theory of fracture has much practical utility because of its ability to relate fracture behavior in the laboratory to potential fracture of structural members in service. Since the theory is applied most successfully in those situations which can be treated analytically as problems of two-dimensions, most of the discussion which follows will be limited to the plane case.

##### 4.1 Stress Intensity Factor and Fracture Toughness

In Griffith's theory of brittle fracture a critical stress-crack size relation is derived from an energy postulate, while the treatment by Irwin leads to stress-crack size relations by focusing attention on the elastic stresses very close to the tip of the crack [20,21,22]. For analytical purposes imagine an existing flaw or opening in a body to be, ideally, a plane sharp-ended crack. The solid is assumed to be homogeneous and isotropic, with the crack extending through the thickness of the body. Referring to Fig. 4.1, a local coordinate system is chosen so that the z axis is collinear with the leading edge of the crack, assumed to have a straight front, the y direction is perpendicular to the plane of the crack while the x direction points in the direction of expected crack extension. Loadings on the boundaries of the solid are taken to be applied symmetrically with respect to either the x-y plane or the x-z plane. If the z dimension of the body is large a condition of plane strain will exist throughout the body. At the other extreme, if the z dimension of the solid is small relative to the x and y dimensions, as in a thin plate, a plane stress situation will exist. Both of these situations are idealized cases. More realistically, in all but very thin plate-like specimens a mixed plane stress, plane strain state will exist across the z dimension, varying from plane stress at and very near the x-y plane surfaces to plane strain over the central portion. Any plastic deformation which may occur at the crack borders is neglected in a first approximation. Plasticity effects, provided they are small, are subsequently treated as a minor correction to the elastic analysis.

Three basic modes of crack surface displacements which can lead to crack extension are shown in Fig. 4.2. In the opening mode the crack surfaces move apart symmetrically with respect to the x-z plane. Because of space limitations attention will be confined only to the opening mode of separation since this mode is used almost exclusively in fracture toughness testing. It should be realized, however, that the essential results and conclusions associated with opening mode displacements also apply to the other two modes shown in Fig. 4.2.

Corresponding to the opening mode conditions outlined above, the stresses and displacements at points close to the crack border can be shown to have the form [23]

$$\sigma_x = \frac{K}{\sqrt{2\pi r}} \cos \frac{\theta}{2} [1 - \sin \frac{\theta}{2} \sin \frac{3\theta}{2}] + \dots \quad (4.1)$$

$$\sigma_y = \frac{K}{\sqrt{2\pi r}} \cos \frac{\theta}{2} [1 + \sin \frac{\theta}{2} \sin \frac{3\theta}{2}] + \dots \quad (4.2)$$

$$\sigma_{xy} = \frac{K}{\sqrt{2\pi r}} \sin \frac{\theta}{2} \cos \frac{\theta}{2} \cos \frac{3\theta}{2} + \dots \quad (4.3)$$

$$\sigma_z = \begin{cases} \nu(\sigma_x + \sigma_y), & \text{(plane strain).} \\ 0, & \text{(plane stress).} \end{cases} \quad (4.4)$$

$$\sigma_{xz} = \sigma_{yz} = 0 \quad (4.5)$$

$$u_x = K \frac{2(1+\nu)}{E} \sqrt{\frac{r}{2\pi}} \cos \frac{\theta}{2} [1 - 2\nu + \sin^2 \frac{\theta}{2}] + \dots \quad (4.6)$$

$$u_y = K \frac{2(1+\nu)}{E} \sqrt{\frac{r}{2\pi}} \sin \frac{\theta}{2} [2 - 2\nu - \cos^2 \frac{\theta}{2}] + \dots \quad (4.7)$$

$$u_z = 0 \quad \text{(plane strain).} \quad (4.8)$$

In these expressions only the first term of a series expansion is shown. The omitted terms involve increasing half powers of the ratio of r divided by the crack length, and consequently, are important only at large distances from the crack tip [24]. Very near the crack tip the first term in each of these series dominates, especially for the stresses, since they are proportional to  $r^{-1/2}$ . Thus over a region for which r is very small compared to the plane dimensions of the body, e.g., the crack length or the

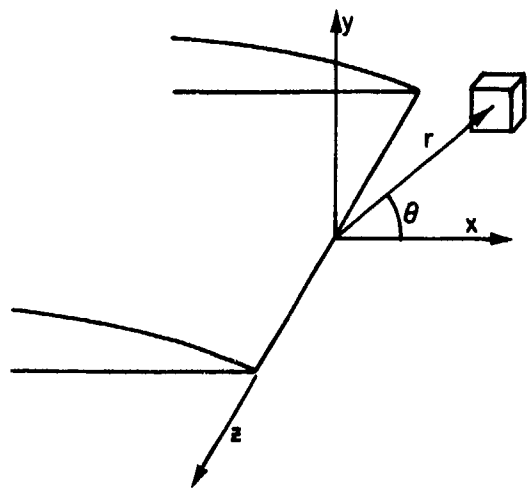
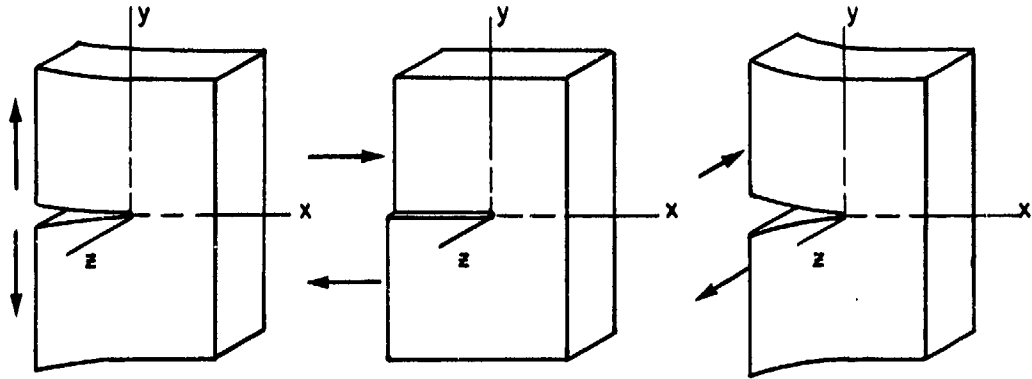
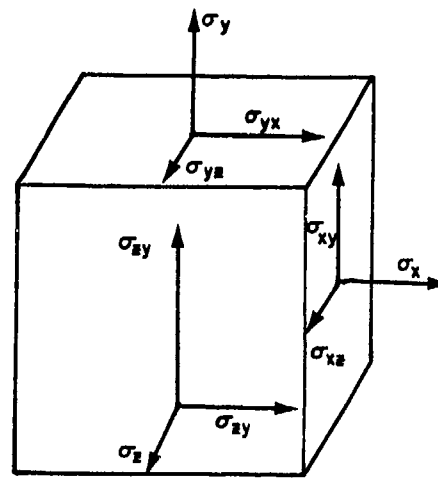


Figure 4.1



(a) OPENING-MODE I

(b) EDGE SLIDING-MODE II

(c) TEARING-MODE III

Figure 4.2

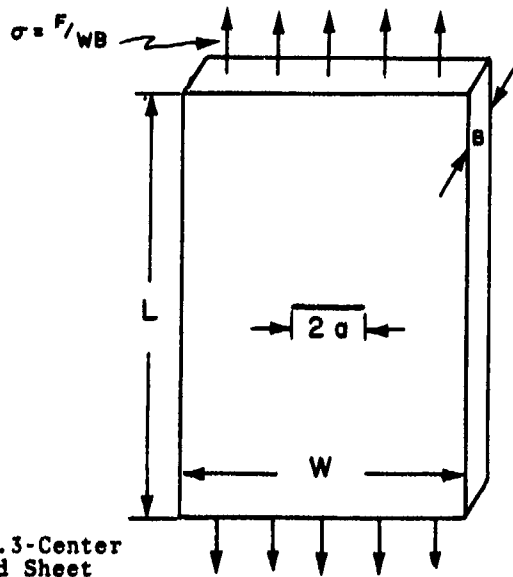


Fig. 4.3-Center Cracked Sheet

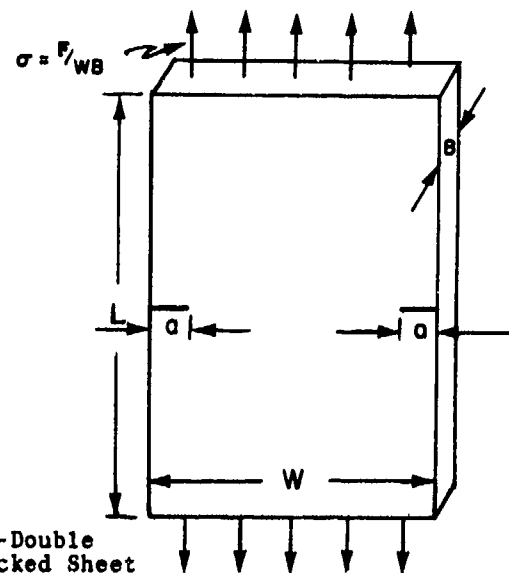


Fig. 4.4-Double Edge Cracked Sheet

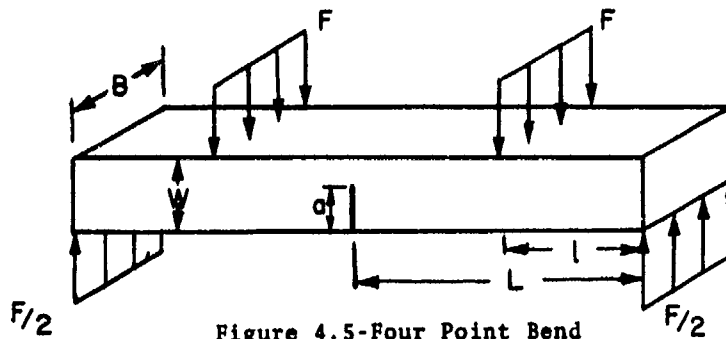


Figure 4.5-Four Point Bend

specimen width, the above expressions specify the tip region elastic stresses and displacements to an acceptable degree of accuracy. The K term in these equations is independent of r and  $\theta$ , and serves only as a positive multiplying factor which can be shown to depend on the applied boundary load and the crack size. Its explicit functional form in any given situation depends on the geometry of the cracked body and the location of the crack. In fracture mechanics terminology K is referred to as a "stress Intensity factor."

The significance of the above expressions is due to their generality, since they hold for all stationary plane cracks, regardless of the configuration of the body or the location of the crack. What changes in these equations, in going from one configuration to another, is only the functional form of K. Thus the state of elastic stress and displacement in the immediate region bordering a plane crack is, in effect, entirely characterized by the stress intensity factor K. Expressions similar in form to Eqs. (4.1) - (4.8) have been developed for the sliding and tearing modes of crack surface separation [23]. Determination of the explicit form of K for any given cracked body configuration requires an exact solution of the corresponding elasto-static boundary value problem, discussion of which is beyond the scope of this article. Interested readers can consult References [21, 22, 23, 25, 26] for details and for additional appropriate references.

The only exact opening mode solutions that are available thus far are for infinite regions. For the plane infinite sheet loaded as shown in Fig. 3.3, the stress intensity factor is

$$K = \sigma\sqrt{\pi a} \quad (4.9)$$

For a plane circular (penny-shaped) crack with diameter  $2a$  located in the interior of an infinite solid loaded in uniform tension directed perpendicularly to the plane of the crack, K has the form

$$K = 2\sigma\sqrt{\frac{a}{\pi}} \quad (4.10)$$

where  $\sigma$  is the applied tensile stress. For finite sized regions acceptable approximate expressions for K have been determined by a variety of techniques. A tabulation can be found in References [23, 25]. Stress intensity factors for inhomogeneous and anisotropic cracked bodies are discussed in References [23, 26].

Widely used opening mode stress intensity factors for specimen configurations designed specifically for laboratory fracture toughness testing are recorded below for subsequent reference. For the center cracked sheet, as illustrated in Fig. 4.3,

$$K = \sigma\left\{\pi a \sec\left(\frac{\pi a}{W}\right)\right\}^{1/2} \quad [25] \quad (4.11)$$

and for the double edge cracked sheet as shown in Fig. 4.4,

$$K = \sigma\sqrt{a} \left\{1.98 + 0.36\left(\frac{2a}{W}\right) - 2.12\left(\frac{2a}{W}\right)^2 + 3.42\left(\frac{2a}{W}\right)^3\right\} \quad (4.12)$$

where  $0 < \frac{2a}{W} \leq 0.7$ , [25], or alternatively

$$K = \sigma \left\{W \tan\left(\frac{\pi a}{W}\right) + 0.1 \sin\left(\frac{2\pi a}{W}\right)\right\}^{1/2}, \quad [27]. \quad (4.13)$$

For a single edge cracked sheet, Eq. (4.12) is replaced by

$$K = \sigma\sqrt{a} \left\{1.99 - 0.41\left(\frac{a}{W}\right) + 18.70\left(\frac{a}{W}\right)^2 - 38.48\left(\frac{a}{W}\right)^3 + 53.85\left(\frac{a}{W}\right)^4\right\} \quad (4.14)$$

for  $0 < \frac{a}{W} \leq 0.6$ , [25, 28]. For the four-point bend specimen-illustrated in Fig. 4.5,

$$K = \frac{6M}{B[W-a]^{3/2}} f\left(\frac{a}{W}\right), \quad M = F(L-l), \quad L = 4W, \quad (4.15)$$

a/W	0.05	0.1	0.2	0.3	0.4	0.5	0.6
f(a/W)	0.36	0.49	0.60	0.66	0.69	0.72	0.73

[23]

or alternatively

$$K = \frac{6M}{BW^2} \sqrt{a} \left\{1.99 - 2.47\left(\frac{a}{W}\right) + 12.97\left(\frac{a}{W}\right)^2 - 23.17\left(\frac{a}{W}\right)^3 + 24.80\left(\frac{a}{W}\right)^4\right\} \quad (4.16)$$



for  $0 < \frac{a}{W} \leq 0.6$ , [25, 29].

For the notched round specimen, Fig. 4.6,

$$K = 0.233 \left( \frac{4F}{\pi d^2} \right) \sqrt{\pi D}, \quad d = 0.707D, \quad [30] \quad (4.17)$$

or

$$K = FD^{-3/2} [1.72 \left( \frac{D}{d} \right) - 1.27], \quad [25, 31] \quad (4.18)$$

for

$$0.5 \leq d/D \leq 0.8 .$$

For the compact tension specimen shown in Fig. 4.7,

$$K = \frac{100F}{WR} \sqrt{a} \left\{ 0.296 - 1.855 \left( \frac{a}{W} \right) + 6.557 \left( \frac{a}{W} \right)^2 - 10.170 \left( \frac{a}{W} \right)^3 + 6.389 \left( \frac{a}{W} \right)^4 \right\} \quad (4.19)$$

for  $0.3 \leq \frac{a}{W} \leq 0.7$ ,  $\frac{H}{W} = 0.6$ , [25, 32].

The expressions for  $K$  given by Eqs. (4.11) - (4.19) although approximate are nevertheless of considerable value because they provide a simply determinable measure of the resistance of a material to brittle fracture. For example, if for any one of these specimens the applied load and crack size that is observed in a test to correspond to onset of crack propagation is substituted into the corresponding expression for  $K$ , a critical stress intensity fracture value is determined. When, furthermore, the specimen dimensions are chosen so as to ensure essentially plane strain conditions, then this critical plane strain stress intensity value, designated by  $K_{Ic}$ , may be taken as a definition of the plane strain fracture toughness of the material  $Ic$  tested. Experiments conducted on a variety of high strength structural metals indicate that each material has a characteristic  $K_{Ic}$  value which is basically the same regardless of the design of the specimens used for  $Ic$  tests. The choice of particular test geometry is thus largely a matter of test program economy and laboratory convenience. A decade of laboratory testing has shown, for the high yield strength metals at least, that a lower bound  $K_{Ic}$  value exists for each material. Consequently it is possible to interpret the  $K_{Ic}$  value as a fracture resistance material property which, under certain conditions, can be used to estimate the load that a structural member containing a crack of specified dimensions can be expected to sustain without fracture. Several examples which serve to illustrate this concept are presented in Section 6.

#### 4.2 Relation Between the Griffith and Irwin Approaches

Irwin has shown by use of Eqs. (4.2) and (4.7), for  $y$ -direction stress and displacement, that the work done per unit area by the stress field in slowly extending both ends of a crack in a sheet of unit thickness (in plane strain), while the outer boundary is held fixed, is simply  $2K^2(1-\nu^2)/E$  [21, 33]. As a result of Clapeyron's Theorem in linear elastostatics [34], it follows that this work represents twice the rate at which energy disappears from the elastic strain energy field as the crack extends, i.e., the elastic strain energy release rate, traditionally designated by the symbol  $G$ . Thus

$$G = - \frac{\partial U}{\partial c} \quad (4.20)$$

and for opening mode crack surface displacements

$$G_I = \frac{K_I^2 (1-\nu^2)}{E} \quad (4.21)$$

in plane strain. For plane stress a similar calculation yields

$$G = \frac{K^2}{E} . \quad (4.22)$$

The notation used in these expressions is compatible with that commonly found in fracture mechanics literature.  $K_I$  and  $G_I$  represent the stress intensity factor and the elastic strain energy release rate in plane strain, while  $K$  and  $G$  denote these same quantities for either plane stress or mixed plane stress-plane strain conditions. At the onset of fast crack propagation a subscript (c) is used to designate critical values. Thus  $K_{Ic}$  and  $G_{Ic}$  represent critical values in plane strain and  $K_c$  and  $G_c$  specify critical values for plane stress or for mixed plane stress-plane strain (mixed mode) conditions.

For the infinite sheet of Fig. 3.3 in plane strain it follows from Eq. (4.9) that at the onset of crack propagation

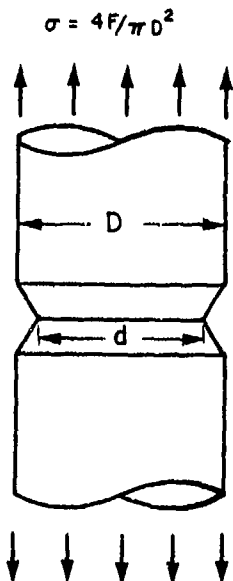


Figure 4.6-Notched Round

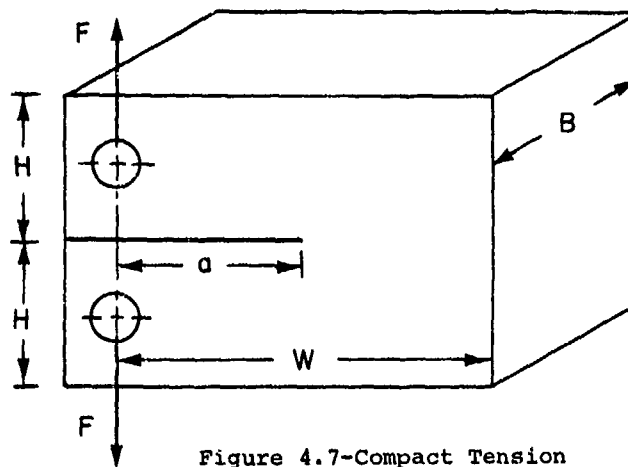


Figure 4.7-Compact Tension

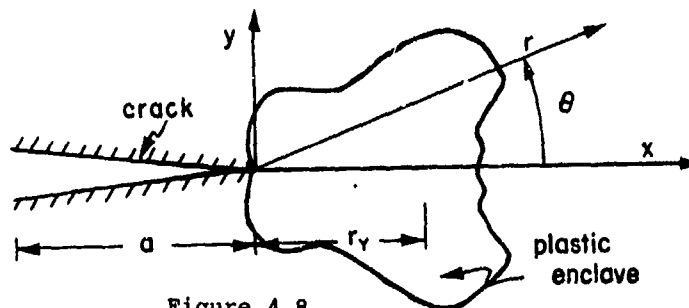


Figure 4.8

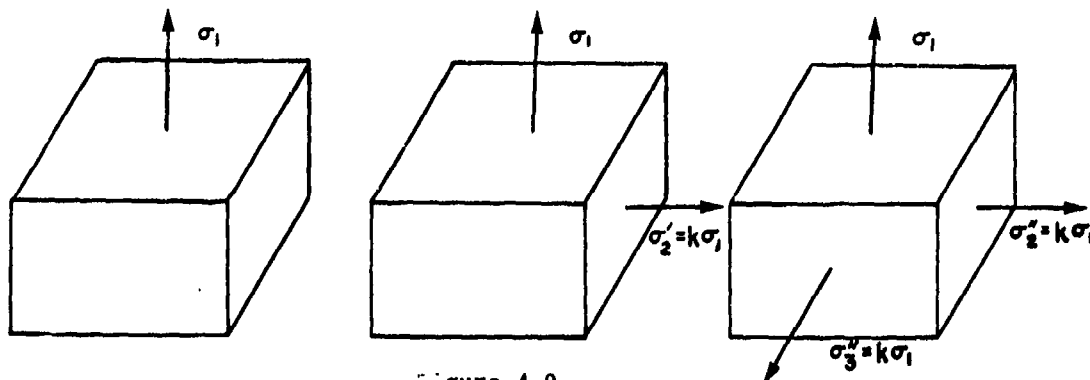


Figure 4.9

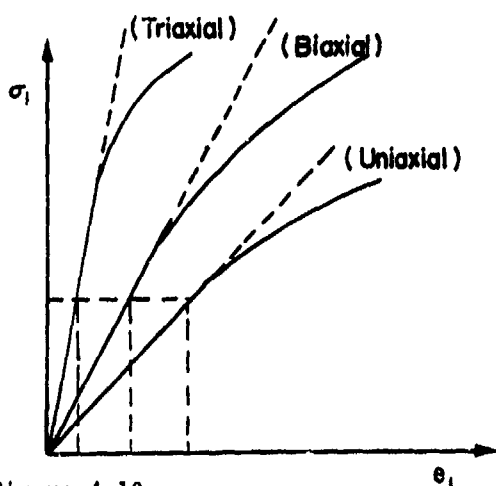


Figure 4.10

$$G_{IC} = \frac{K^2 I_C (1-\nu^2)}{E} = \frac{\pi \sigma^2 c (1-\nu^2)}{2E} \quad (4.23)$$

where it is understood that  $\sigma$  and  $c$  are the load and crack size which are observed at the critical condition.

In Griffith's theory the state of critical and unstable equilibrium is attained when Eq. (3.3) or (3.4) is satisfied. From Eqs. (3.1) and (3.4) this leads to the requirement that

$$\frac{\pi \sigma^2 c (1-\nu^2)}{2E} = 2\gamma_s \quad (4.24)$$

From Eqs. (4.23) and (4.24) it is seen that the onset of crack propagation in Irwin's theory corresponds to unstable equilibrium in Griffith's theory when the elastic strain-energy release rate has the critical value

$$G_{IC} = 2\gamma_s \quad (4.25)$$

or when

$$\sigma = \sqrt{\frac{2E\gamma_s}{\pi c (1-\nu^2)}} \quad (4.26)$$

The surface energy  $\gamma_s$  in the Griffith theory must be determined by experiment for any given material. Irwin's theory likewise must rely on experimental determination of the critical value of  $G_{IC}$  (or  $K_{IC}$ ) for a given material because a purely theoretical criterion for fracture in a continuous solid analogous, for example, to the onset of yield condition employed in the theory of plasticity, has yet to be formulated.

#### 4.3 Plasticity Correction

The inevitability of plastic deformation at the tip of a crack in structural metals, as well as the importance of such an occurrence from the viewpoint of fracture toughness, was discussed briefly in Sec. 3. However, the crack tip stress and displacement relations and the explicit formulas for  $K$  discussed in Section 4.1 are based entirely on elastic analysis. Valid application of such analysis to practical situations is therefore contingent upon the requirement that the extent and influence of any crack tip plastic yield on the surrounding elastic stresses and displacements, or on any quantity determined by them, be comparatively small. From Eqs. (4.20) - (4.22) it is seen that  $K$  is related to the rate of change with crack size of the total elastic strain energy in the body. If the crack tip region over which plastic deformation takes place is relatively small, then the contribution of such a region to the total elastic strain energy rate of the body will also be comparatively small [33]. Thus elastically calculated  $K$  formulas will be substantially correct, i.e., will be affected only to a minor degree by the existence of small crack front yield zones.

A somewhat rational, if not rigorous, method for correcting for small scale plastic yield effects at the crack border has been proposed by Irwin [35, 36], based on the following argument. The presence of a plastic zone at the crack front tends to elevate the elastic stress level in the elastic region between the boundary of the plastic enclave and the free edge of the cracked body as a consequence of the redistribution of stress caused by the plastic deformation. To compensate for this increase, the actual half crack length can be imagined to be increased by an amount  $r_y$ , which represents a measure of the plastic enclave dimension along the plane of the crack under conditions of small-scale yielding, as in Fig. 4.8. In other words, the actual stress in the elastic-plastic solid corresponding to a half crack length,  $a$ , is imagined to be equivalent to the stress that would arise from an "effective" half crack length

$$a_e = a + r_y \quad (4.27)$$

in a perfectly elastic material. A precise, realistic calculation of the shape (and therefore the size) of the crack-tip plastic enclave is currently not possible because of the mathematical difficulties associated with the required elastic-strain hardening plastic analysis. However, elastic-perfectly plastic analysis for the tearing mode problem (mode III of Fig. 4.2) indicates a circular plastic zone with radius proportional to  $K^2$  divided by the square of the yield stress in simple shear [37]. A result similar in form, mathematically, is obtained for the opening mode from Eq. (4.2) if, along the plane of the crack,  $\theta = 0$ , the  $y$ -direction stress is set equal to the uniaxial yield stress of the material  $\sigma_y$  at some distance  $r = r_y$  from the crack tip. These considerations prompted Irwin to propose as a rough measure of the plastic zone size

$$r_y = \frac{1}{2\pi} \left(\frac{K}{\sigma_y}\right)^2 \quad (\text{plane stress}) \quad (4.28)$$

and

$$r_{IY} = \frac{1}{6\pi} \left( \frac{K_I}{\sigma_Y} \right)^2 \quad (\text{plane strain}) \quad (4.29)$$

The plane-strain plastic zone size measure is reduced by a factor of one-third in order to account for the constraining effect of the lateral  $\sigma_z$  stress, which is zero in plane stress.

Near the crack tip along the plane of expected crack extension a state of triaxial tension exists for the plane strain case, which reduces to biaxial tension in plane stress. The effect that such a difference in the state of stress may have on the mechanical behavior of the material can be demonstrated qualitatively as follows. Consider a solid which is subjected to a series of tensile tests; the first uniaxial, the second biaxial and the third triaxial, as illustrated in Fig. 4.9.

For each case in increasing order of dimensionality

$$E_{(1)} = \frac{\sigma_1}{e_1}$$

$$E_{(2)} = \frac{\sigma_1}{e_1} = \frac{\sigma_1}{\frac{1}{E_{(1)}} [\sigma_1 - \nu\sigma_2']} = \frac{E_{(1)}}{1-\nu k}$$

$$E_{(3)} = \frac{\sigma_1}{e_1} = \frac{\sigma_1}{\frac{1}{E_{(1)}} [\sigma_1 - \nu(\sigma_2'' + \sigma_3'')]} = \frac{E_{(1)}}{1-2\nu k}$$

where  $E_{(1)}$ ,  $E_{(2)}$  and  $E_{(3)}$  are the effective elastic moduli in each case. The (1)-direction elastic stress-strain relations can then be expressed in the form

$$\sigma_1 = E_{(1)} e_1$$

$$\sigma_1 = \frac{E_{(1)}}{1-\nu k} e_1$$

$$\sigma_1 = \frac{E_{(1)}}{1-2\nu k} e_1$$

for the uniaxial, biaxial and triaxial situations respectively. Setting  $k = 1$  and choosing  $\nu = 1/3$ , for a given level of stress  $\sigma_1$  in the elastic range the corresponding strain  $e_1$  increases with decrease in the degree of dimensionality of the applied tensile stress system, Fig. 4.10. A triaxial tensile state of stress tends to, in effect, "embrittle" material behavior relative to biaxial and uniaxial states. Applying this result to the crack problem, the  $\sigma_z$  stress near the crack border, Fig. 4.1, (which is a principal stress since shear stresses vanish along the crack plane) in the plane strain state acts as an elastic constraint to plastic yielding in this region. As the crack opens in the tensile mode the material at the tip of the crack is pulled apart. When  $\sigma_z$  is very small compared to  $\sigma_x$  and  $\sigma_y$ , as in the plane stress case, a thickness reduction or "necking down," which is associated with relatively large plastic enclave development can be readily observed in front of the crack [38]. Thus it is seen that the degree of plastic yield which occurs at the front of a sharp crack is largely determined by the yield strength of the material, and by the degree of stress triaxiality which prevails near the tip of the crack.

If the K formulas are corrected for small scale plastic yield effects according to Eqs. (4.27) - (4.29), for center cracked sheets in plane stress, Eqs. (4.9) and (4.11) become

$$K^2 = \sigma^2 \left[ \nu a + \frac{1}{2} \left( \frac{K}{\sigma_Y} \right)^2 \right] \quad (4.30)$$

and

$$K^2 = \sigma^2 \left( \left[ \nu a + \frac{1}{2} \left( \frac{K}{\sigma_Y} \right)^2 \right] \cdot \sec \left[ \frac{1}{2} \left( \frac{K}{\sigma_Y} \right)^2 \right] \right) \quad (4.31)$$

for the notched round bar in plane strain, replacing the notch diameter  $d$  by  $d-2r_{IY}$  allows Eq. (4.17) to be modified to the form

$$K_I \left( 1 - \frac{\sqrt{2}}{3\sqrt{D}} \left( \frac{K_I}{\sigma_Y} \right)^2 \right)^2 = 0.233 \sigma_N \sqrt{\pi D} \quad (4.32)$$

where  $d = \sqrt{2} \cdot D$  and  $\sigma_N = 4F/wd^2$ . Critical fracture toughness values are obtained from

these expressions by "trial and error" calculations.

#### 4.4 Thickness and Fracture Mode Transition, Plane Strain Size Requirements

In view of the effect of stress triaxiality on the size of the plastic enclaves, a schematic representation of the crack-tip plastic zone might then appear as shown in Fig. 4.11, which illustrates qualitatively the change from plane stress conditions near the plate surfaces to plane strain conditions through the central portion. When the thickness  $B$  is large compared with the plastic enclave size factor  $(K/\sigma_y)^2$ , most of the plate is in a state of plane strain. If the thickness is reduced such that the bell-shaped ends of the plastic enclaves overlap, then a state of plane stress is attained. Actual experimental observation of plastic enclaves show a wide variation of shapes depending on the plastic properties of the different materials [38, 39]. Figure 4.11 is, therefore, shown for illustrative purposes only. Nevertheless, it is generally true that thick-sectioned bodies which approach plane strain conditions tend to suppress crack front plastic yield, compared to thinner sectioned structural members which yield more readily at the crack border owing to the reduced elastic constraint. One might then expect to find fracture toughness variation with thickness because of the plastic enclave size dependency on thickness. Experiments show this to be generally true for high yield strength metals. These same experiments also show a distinct correlation between fracture surface appearance and thickness. Figure 4.12 illustrates schematically data obtained for 7075-T6 aluminum alloy tested at room temperature [40, 41]. The principal features of Fig. 4.12 have also been observed for other high strength metals including steels, aluminum and titanium alloys [14, 42, 43]. Fracture toughness in general increases with reduction in specimen thickness at a rate which varies for different materials. Beyond a certain thickness, the fracture toughness approaches a lower bound value  $K_{IC}$  (or  $G_{IC}$ ), which remains independent of further increase in  $B$ . However, the variation of  $K_{IC}$  in the thin sheet or foil range has not as yet been well enough documented to warrant any general statements [44].

Fracture surface appearance also shows correlation with specimen thickness. Thick sections, essentially in a plane strain state, exhibit a wide portion of the thickness as a relatively flat smooth fracture surface (square fracture) coupled with thin oblique shear edges called "shear lips," Fig. 4.13a. The proportion of square fracture to oblique shear fracture increases with increase in thickness, Fig. 4.12. In thin specimens the fracture surface is entirely, or almost entirely, oblique shear (slant fracture), Fig. 4.13c. In the range of thicknesses over which  $K_{IC}$  attains its uppermost values, the fracture surfaces are generally observed to be 100 percent slant fracture. The portion of the fracture toughness versus thickness curve which changes rapidly corresponds roughly to a change in fracture surface appearance from slant to square. In other words a fracture mode transition occurs over the range of thicknesses intermediate between thickness values which give primarily plane stress and plane strain states at the crack tip.

Slant fracture is associated with a shear separation process whereas square fracture is better characterized by a cleavage-type separation. Since slant fracture occurs in thin sections with relatively extensive plastic yield compared to square fracture, which is typical of thick sections, the ratio of plastic zone size to sheet thickness is significant in determining the degree of elastic constraint at the crack tip, and thus the appearance of the fracture surface. This fact is clearly shown by means of the dimensionless parameter  $\beta$  introduced by Irwin [45, 46].

$$\beta_C = \frac{1}{B} \left( \frac{K_C}{\sigma_y} \right)^2 = \frac{2\pi r_y}{B} \quad (4.33)$$

$$\beta_{IC} = \frac{1}{B} \left( \frac{K_{IC}}{\sigma_y} \right)^2 = \frac{6\pi r_{IY}}{B} \quad (4.34)$$

Figure 4.14 illustrates the fracture appearance, in terms of percent of slant fracture  $S = 1 - P = (1 - A/B) \times 100$ , plotted against the relative plastic zone size parameter  $\beta$  for a large number of high strength steels and several titanium alloys tested at room temperature. Note that when  $\beta = \beta_C$  is greater than  $2\pi$  the transition to oblique shear fracture is almost complete, being greater than eighty percent. At  $\beta_C = 2\pi$ ,  $B = r_y$ . Thus when the plastic enclave size is equal to or greater than the sheet thickness, the fracture mode is one of plastic shear approaching plane stress conditions. For values of  $\beta = \beta_C$  less than about 0.5, the fracture appearance is more than ninety percent flat, approaching plane strain, with  $B \approx 40 r_y$ . Under these circumstances fracture toughness values approach a minimum value, independent of further increase in section thickness as indicated by Fig. 4.12. In other words, for all thickness values  $B \geq 40 r_y = 2.1 (K_{IC}/\sigma_y)^2$  a fracture toughness test performed on any one of the specimen designs shown in Figs. 4.3-7 will yield approximately the same lower bound  $K_{IC}$  value. Subsequent tests performed on high strength maraging steels using several different test specimen designs have confirmed this result [25]. These tests have also demonstrated that in the range of crack length to specimen width ratio  $0.3 < 2a/W < 0.5$  in sheet specimens, or  $0.3 < a/W < 0.5$  in bend specimens, (i) there is no significant variation in  $K_{IC}$  values with change in ligament length ( $W/2 - a$ ) in sheet specimens, or ( $W - a$ ) in bend specimens, (ii)  $K_{IC}$  is independent of initial crack size provided the crack length is approximately forty times  $r_{IY}$ .

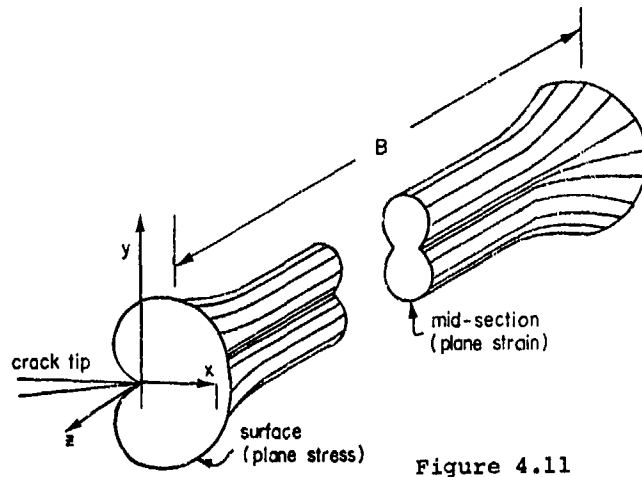


Figure 4.11

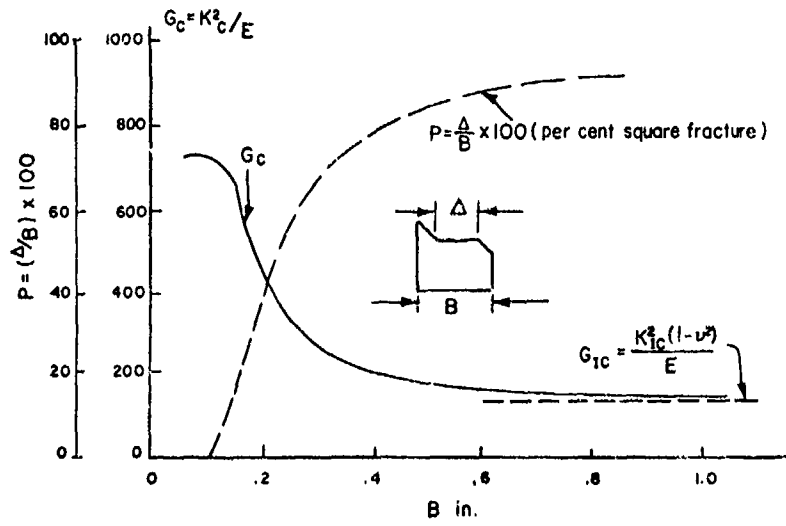


Figure 4.12

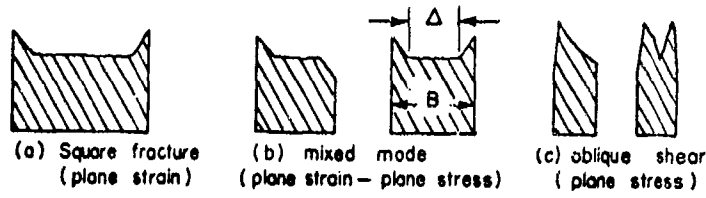


Figure 4.13

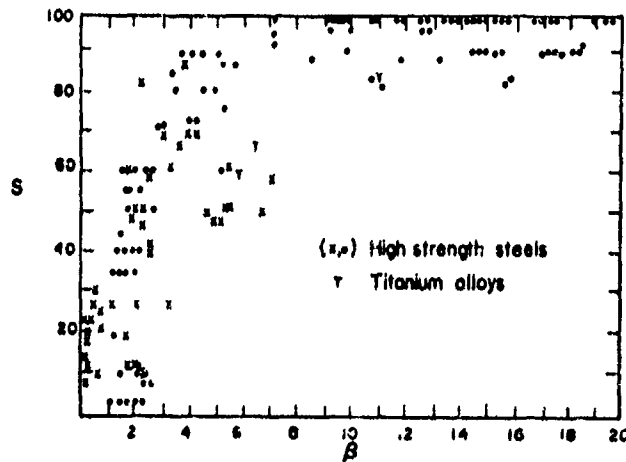


Figure 4.14

We have previously referred to the possibility of interpreting the  $K_{IC}$  value for a given material as a fracture resistance material property. Implied in this interpretation is the ability to ascribe any such value, obtained from small sized laboratory test specimens, to the full sized structural component. This of course means that a laboratory determined  $K_{IC}$  value must be independent of specimen dimensions and specimen configuration. On the basis of the experimental data discussed above these requirements will be satisfied when test specimen thickness and crack length are of sufficient magnitude relative to the plastic zone size measure. Accordingly, the most recent recommendations by the American Society for Testing and Materials for  $K_{IC}$  testing suggest that both test specimen thickness and crack length be no less than  $2.5 (K_{IC}/\sigma_y)^2$  in order to ensure valid  $K_{IC}$  values.

Mixed-mode and fully plane stress fracture toughness values exhibit significant section thickness dependency in all structural metals that have been tested. For this reason  $K_{IC}$  values cannot be considered in the same way as  $K_{IC}$  values for any given material as a material property independent of size and geometry. The thickness dependency of  $K_{IC}$  is, of course, related to the relatively greater degree of crack front plastic yield associated with non-plane strain conditions. In addition to thickness,  $K_{IC}$  values may also depend on specimen width and crack size, as illustrated by Figs. 4.15 and 4.16, [48], obtained from sheet specimens. With decrease in size, a significant lowering of  $K_{IC}$  occurs when the net section stress,  $\sigma_n$ , at onset of fracture increases beyond  $0.9 \sigma_y$ . Similar trends have also been observed for thin-sheet 7075-T6 aluminum alloy [49]. There is at present, however, insufficient experimental data available covering a wide range of structural metals to warrant general specimen size recommendations for minimizing the effects of these variables on  $K_{IC}$ . Furthermore, contrary to the plane strain situation, it is possible that each particular material or alloy system may require different size criteria [50 - 53].

The degree of sharpness of the crack-simulating notch or slot in a test specimen can affect the  $K_{IC}$  value through notch blunting, with its concomitant stress-relieving effects. Data obtained from tests performed on thin steel sheets is shown schematically in Fig. 4.17, indicating the variation of fracture toughness with notch root radius. Above a certain minimum root radius,  $K_{IC}$  increases in proportion to the square root of the notch radius. This minimum notch root radius varies with the material in question. Values ranging from as low as 0.0002 inches for H-11 steels (high yield strength levels) to as high as 0.010 inches for 7075-T6 aluminum alloy have been observed [54, 55]. After considerable study, [55, 56], it is now the general practice in fracture toughness testing to use a "natural" crack which has been initiated at the root of a notch or saw-cut slit in test specimens. Such sharp cracks may be produced by striking with a sharp wedge at low temperatures, or more usually by fatigue at low cyclic stresses.

Because of the thickness dependency of  $K_{IC}$  it should not be concluded that  $K_{IC}$  values are of little importance as compared with  $K_{IC}$  values. For structural uses of sheet material, as in the aerospace industry, design based on the lower bound plane strain fracture toughness would require unreasonably thick panels in normally thin-sectioned structural members. This would be particularly true for the tough low strength alloys. However the  $K_{IC}$  tests used to evaluate the fracture toughness in such circumstances should be carried out at the thickness of the intended structural application.

#### 4.5 Temperature and Fracture Mode Transition

Since the introduction of notched bar impact testing at the beginning of this century, e.g., the Charpy V-notch test, it has been apparent that low-to-medium yield strength steels exhibit a rather abrupt change in fracture energy over a relatively narrow range of temperature variation. Within this narrow temperature range a transition in mode of fracture takes place, from a tough fibrous (oblique shear) fracture requiring high energy absorption at higher temperatures, to a brittle cleavage (flat) fracture requiring low energy absorption at lower temperatures. Figure 4.18 illustrates schematically the typical behavior of a medium strength steel. The transition in fracture mode arises from basic differences in the micromechanisms by which the fracture is produced at different temperatures. The abruptness of the energy-temperature curve and the temperatures at which it occurs varies with different materials, and with the metallurgical processing of any given material, e.g., its heat treatment. Temperature transition phenomena are pronounced in materials with body-centered cubic and hexagonal close-packed lattice structures, for example, iron, molybdenum and zinc. It is much less significant in materials with face-centered cubic lattice structure such as copper, aluminum and nickel [57].

The increase in Charpy V-notch energy required for fracture with increasing temperature suggests that the same behavior would be expected for fracture toughness values. The same conclusions can also be inferred from other experimental information. Both the ultimate tensile strength and the yield strength of structural metals are known to vary inversely with temperature. Further, both  $K_{IC}$  and  $K_{IC}$  tend to decrease with increasing ultimate tensile strength and/or yield strength, as seen in Figs. 4.19 and 4.20, [58, 52]. From these experimental observations,  $K_{IC}$  and  $K_{IC}$  can be expected to show significant temperature dependence, with a tendency to increase as the temperature is raised.

Figure 4.21 shows the variation of  $K_{IC}$  with temperature for a medium strength steel alloy 0.073 inch thick, together with the corresponding change in the percentage of square fracture observed on the fracture surfaces [41]. The transition in fracture appearance is continuous and is illustrated schematically in Fig. 4.22. Practically all

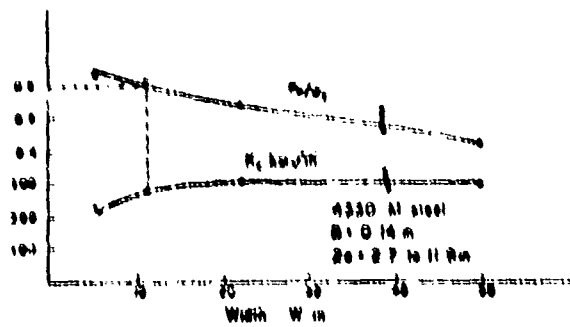


Figure 4.15

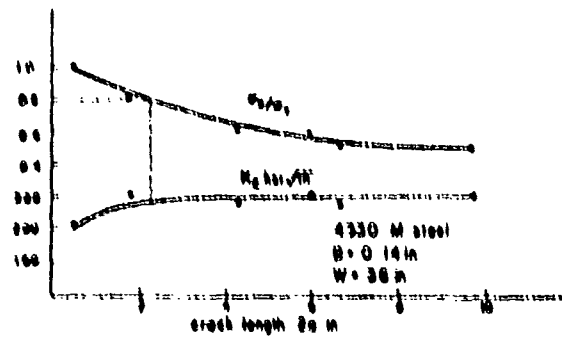


Figure 4.16

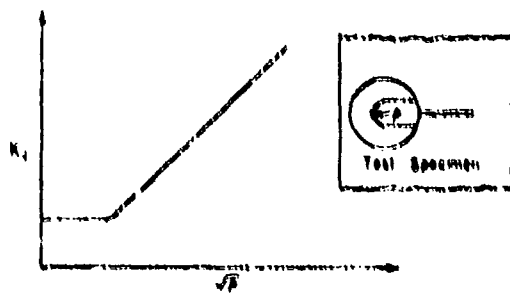


Figure 4.17

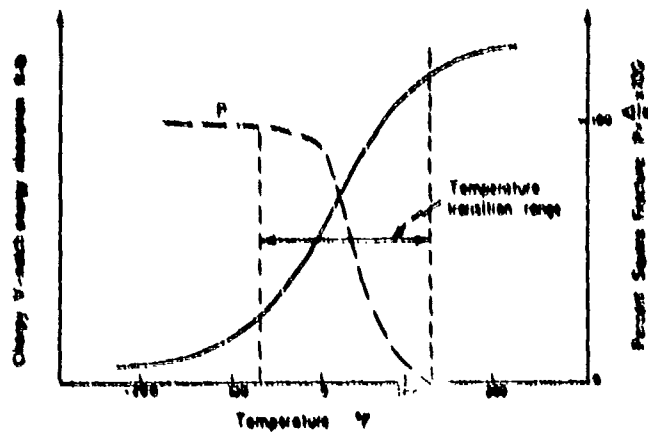


Figure 4.18

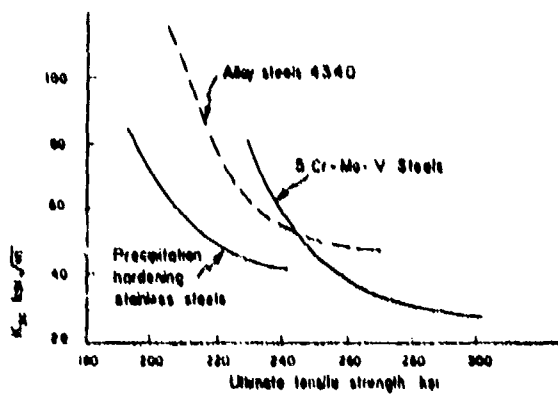


Figure 4.19

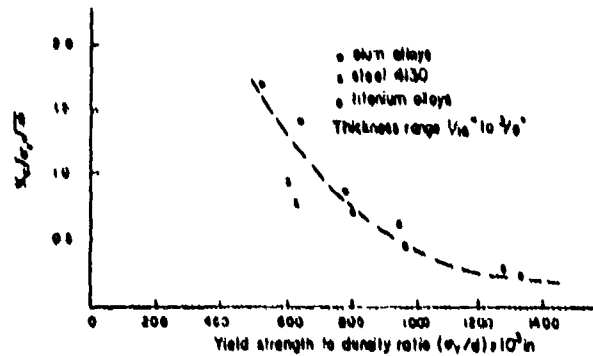


Figure 4.20

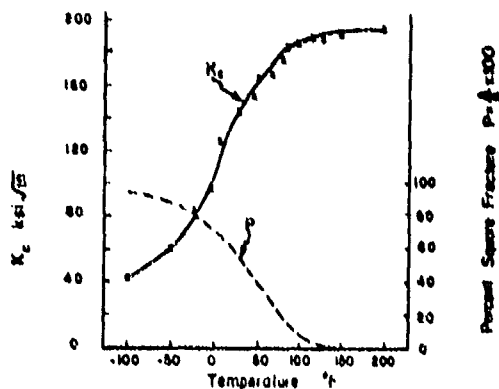


Figure 4.21

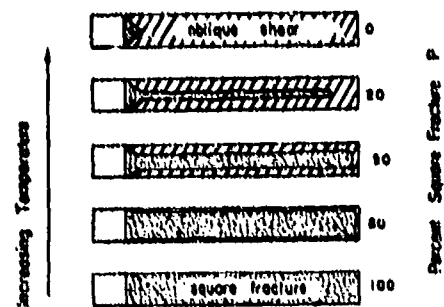


Figure 4.22



of the change in fracture surface appearance takes place within the range of temperature over which the fracture toughness transition occurs, exhibiting a behavior strikingly similar to the Charpy V-notch results. Thus for a certain class of structural metals, there is associated with  $K_{Ic}$  values a characteristic transition temperature range. It has also been observed that for a given material, the temperature transition range is smaller, i.e., the variation in fracture toughness with temperature is more abrupt, for thinner sections and lower yield strengths. This represents the added effect of a section thickness or geometry induced transition in fracture toughness and fracture mode. The physical bases of both transition effects, one due to the reduction of lateral stress constraint with reduction in section thickness and the other due to elevation in temperature, are similar in that both tend to promote crack front plastic yield, and thus shear type micro-mechanisms of separation. This in turn increases fracture toughness.

The character of the temperature dependence of plane strain fracture toughness  $K_{Ic}$  is more difficult to establish because with rise in temperature (with corresponding increase in the crack front plastic enclave size), specimen dimensions must be progressively enlarged so as to meet the ASTM recommended size criteria,  $B, a < 2.5 (K_{Ic}/\sigma_Y)^2$ . For example, for a test performed on a low strength A 533 Grade B steel using a compact tension test specimen design, Fig. 4.7, at room temperature 75°F with a yield stress of 70 ksi and a  $K_{Ic}$  value of about 150 ksi√in, it is necessary to use a specimen which is 30 inches wide and 12 inches thick [59]. At elevated temperatures the required specimen dimensions become prohibitively large. On the other hand, at low temperatures, say at -250°F, a plane strain fracture of this same material can be obtained on a specimen only 2 1/2 inches wide and 1 inch thick. Data obtained from this series of tests, Fig. 4.23, [59, 60], as well as from another series performed on a medium strength A 517-F alloy steel [61], clearly indicate a temperature transition phenomenon for plane strain fracture toughness.

Prior to the time that these tests were performed, it was generally felt that the relatively abrupt transition in absorbed energy to fracture observed in the Charpy V-notch impact test was due mainly to the transition in the state of stress, i.e., from plane strain below the temperature transition range to plane stress above this range [62]. Since a single sized specimen is used over the entire range of temperatures in the Charpy test, the observed transition effect was thought to be due simply to the impossibility of maintaining sufficient crack front stress triaxiality in small specimens because of the increasing plastic zone size with increasing temperature. Thus, it was reasoned that if the specimen size could be progressively increased in a series of temperature-plane strain fracture toughness tests, only a gradual rise in plane strain toughness with temperature might be anticipated [63]. The experimental results shown in Fig. 4.23 clearly demonstrate otherwise. Electron fractographic studies of the fractured surfaces in the steep 0 - 50°F temperature range in these tests revealed no significant differences in fracture surface appearance. Fracture surfaces were predominantly square fracture with little evidence of shear lips. The pronounced increase in  $K_{Ic}$  over a relatively narrow temperature range is thus a strictly temperature induced effect, independent of thickness. A higher rate of increase in fracture toughness would be expected if a section-thickness induced transition effect from plane strain conditions to mixed-mode or plane stress conditions were superimposed on the increase in plane strain toughness. This is borne out by the test results shown in Fig. 4.24, [61]. Since some materials exhibit a sharp decrease in fracture toughness with a relatively small drop in temperature, it is imperative that the designer have fracture toughness information at, and preferably lower than, the lowest service temperature. Ideally, it would be even more desirable to have information on the toughness variation over the whole range of possible service temperatures.

#### 4.6 Strain-Rate Effects on Plane Strain Fracture Toughness

In certain strain-rate sensitive materials, notably low-to-medium strength structural steels and soft titanium, a pronounced increase of yield strength occurs in a change from static to dynamic load application which leads to a loss of fracture toughness. In high strength aluminum, titanium and steel alloys this effect is not significant.

There is now sufficient evidence to justify the conclusion that in rate sensitive materials, fracture toughness is a rate dependent property where, furthermore, this dependence is also a function of temperature [64, 65, 66]. Figure 4.25 is illustrative of data obtained from static and dynamically loaded 3-point bend specimens of a medium strength A 517-F steel [67]. A more comprehensive and revealing picture of the fracture toughness variation over a wide spectrum of strain rates for a low strength steel is shown schematically in Fig. 4.26, [68, 69, 70, 71]. The curve to the right of the figure was obtained from wide plate crack propagation tests at -12°F. The curves to the left represent plane strain fracture toughness values over a range of strain rates of five orders of magnitude. A gap of three orders of magnitude separates the results from the fastest of the dynamically loaded tests and those from the slowest propagating cracks. The dotted horizontal line represents a hypothetical minimum  $K_{Ic}$  value for the -12°F temperature, suggested by the data points at both ends.

These limited test results appear to suggest that there is a minimum  $K_{Ic}$  for plane strain fracture toughness level at a given temperature in rate-sensitive materials. The location of this minimum along the strain-rate spectrum depends on temperature. The practical significance of such effects is manifest. If not properly anticipated, brittleness induced by high rates of loading, particularly at low temperatures, can lead to significant reduction in fracture toughness, and thus to unexpected service failures

Figure 4.23

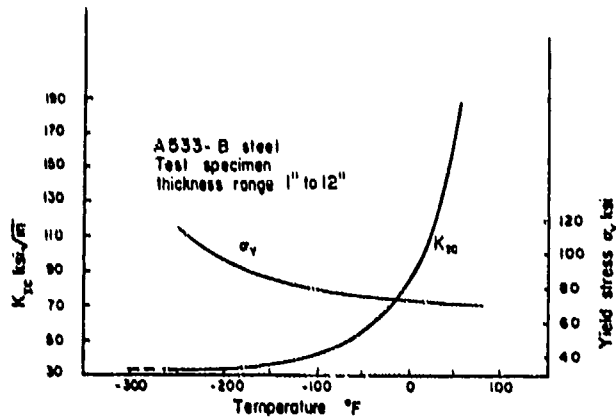


Figure 4.24

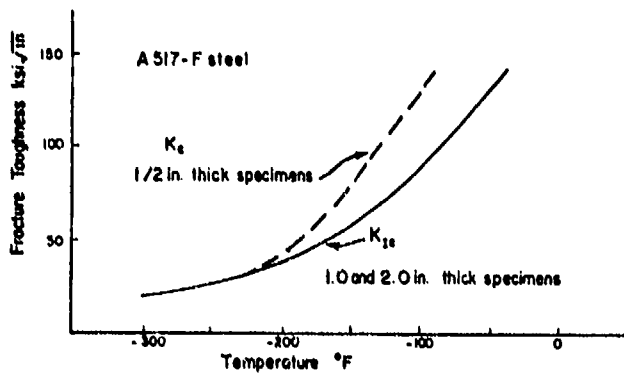


Figure 4.25

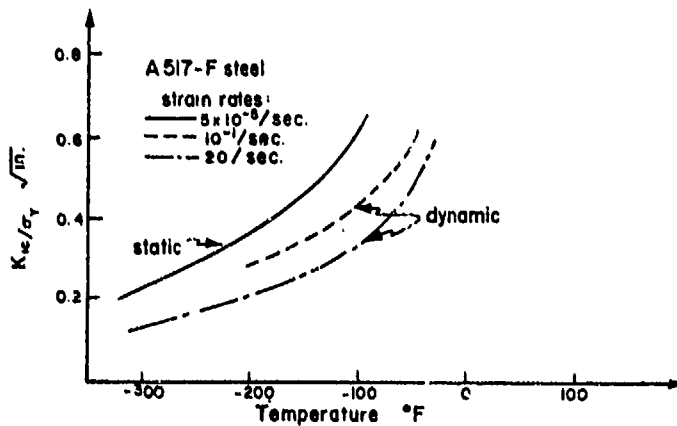
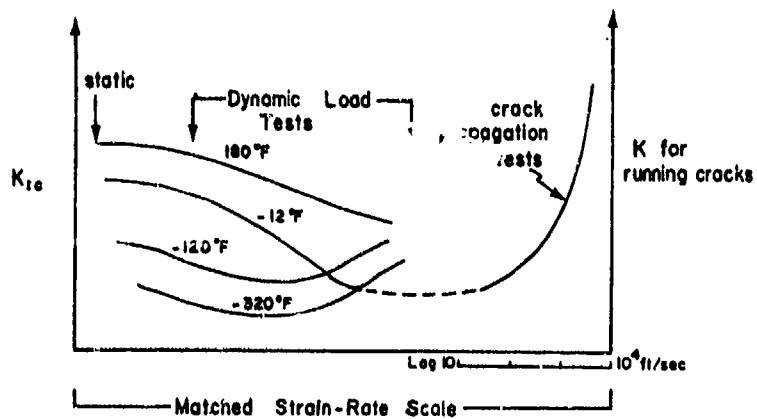


Figure 4.26



as temperatures drop and load rates increase. Unfortunately the experimental difficulties inherent in establishing the complete rate dependence of fracture toughness over a range of temperatures are formidable.

#### 5. FRACTURE TOUGHNESS IN SEMIBRITTLE FRACTURE

While there is no theoretical justification for limiting linear elastic fracture mechanics to high yield strength materials, difficulties of a practical nature arise when considerable crack-tip plasticity is observed prior to fracture. Unduly large and unwieldy specimen sizes become necessary in order to maintain validity of the linear elastic K characterization of the crack tip stress field.

It has previously been shown that to obtain the plane strain fracture toughness for a low strength A 533 steel,  $\sigma_Y = 70$  ksi and  $K_{IC} \approx 150$  ksi  $\sqrt{\text{in}}$  at room temperature, using a compact tension specimen, Fig. 4.7, it is necessary to use a specimen which is 30 in. wide and 12 in. thick. At higher temperatures for this same material, or for a ductile steel at the same temperature, still larger specimen dimensions will be required. This is clearly impractical because of limited laboratory capabilities, not to mention the high costs of performing such tests.

A similar situation prevails for  $K_{IC}$  testing of low-strength thin sheet specimens. This can be shown in several ways. Consider a center-cracked sheet specimen, Fig. 4.3, for which the stress intensity factor is given by Eq. (4.11). For a unit thickness the formula for K can be expressed in terms of the net section stress  $\sigma_N = F/(W-2a)$  as

$$K = \sigma_N \left(1 - \frac{2a}{W}\right) \left(\pi a \sec \left(\frac{\pi a}{W}\right)\right)^{1/2} \quad (5.1)$$

Choosing a crack-size to specimen-width ratio of one-half, i.e.,  $a = W/4$ , Eq. (5.1) can be modified and solved for W in the form

$$W = \frac{8\sqrt{2}}{\pi} \left(\frac{\sigma_Y}{\sigma_N}\right)^2 \left(\frac{K}{\sigma_Y}\right)^2 \quad (5.2)$$

When  $\sigma_N = \sigma_Y$  the entire ligament length  $(W-2a)$  approaches a state of plastic yield, a situation which clearly invalidates use of an elastic analysis. Suppose it is assumed that for  $\sigma_N/\sigma_Y < 0.5$ , the crack front plastic enclave size is sufficiently small to justify retention of the elastic analysis. Then in place of Eq. (5.2) we have

$$W = 14.4 \left(\frac{K}{\sigma_Y}\right)^2, \quad \sigma_N = 0.5\sigma_Y \quad (5.3)$$

For a low strength 2024-T3 aluminum alloy with  $\sigma_Y = 50$  ksi and  $K_{IC} = 87$  ksi  $\sqrt{\text{in}}$  at thickness  $B = 1/16$  in., application of Eq. (5.3) indicates that a specimen width of  $W \approx 44$  in. is necessary for valid application of linear elastic fracture mechanics. Again we are approaching the limits of practicability with specimens of this size.

A more revealing approach to the same problem can be seen in another way. The elastic stress components for the plane stationary crack problem with opening mode crack surface displacements can be expressed as a series expansion and written as [24, 72, 73]

$$\sigma_{jk} = \frac{K}{\sqrt{2\pi r}} f_{jk}^1(\theta) + \sum_{n=2}^{\infty} C_n \left(\frac{r}{a}\right)^{\frac{n}{2}-1} \cdot f_{jk}^n(\theta), \quad j, k = 1, 2 \quad (5.4)$$

where, corresponding to Eqs. (4.1)-(4.3),  $\sigma_{11} = \sigma$ ,  $\sigma_{22} = \sigma_y$ ,  $\sigma_{12} = \sigma_{xy}$  and  $f_{jk}^n(\theta)$  represent functions of the angle  $\theta$ . Referring to Fig. 5.1, for values of  $r/a \ll 1$ , all terms appearing under the summation sign in Eq. (5.4) can be ignored in comparison to the first term, so that for all points close to the crack front

$$\sigma_{jk} \approx \frac{K}{\sqrt{2\pi r}} f_{jk}^1(\theta) \quad (5.5)$$

which is a compact representation of equations (4.1) - (4.3). It is clear that the degree of accuracy represented by the retention of only the first term of Eq. (5.4) depends on the extent to which  $r/a \ll 1$ . In Fig. 5.1,  $r_b$  represents the radius of a circular region enclosing the crack tip within which Eq. (5.5) gives acceptable values of the elastic stresses. In metals, crack front plastic yield invariably occurs, so that a plastic enclave whose size along the plane of the crack is roughly  $r_y$ , is embedded within  $r_b$ . If  $r_y$  is very much smaller than  $r_b$ , then the elevation of elastic stresses within  $r_b$  caused by the plastic deformation within  $r_y$  is negligible. Hence Eq. (5.5) is a valid approximation for the crack-tip stresses for all points exterior to the plastic enclave but within the circle of radius  $r_b$ , provided that  $r_y/a < r/a < r_b/a \ll 1$ . (For purposes of discussion, it is sufficient to consider the plastic enclave to be circular and centered at the crack tip). Studies designed to determine the variation in accuracy of Eq. (5.5) with change in  $r/a$ , for several different test specimen configurations indicate that, for  $r/a = 0.05$ , an error of the order of 10 percent can be expected. (See Ref. [25], pgs. 75, 76 for details). In other words, with  $r/a = 0.05$ , for all

points lying outside the plastic enclave but interior to the radius  $r_b = 0.05a$  the elastic crack tip stresses given by (5.5), or equivalently by (4.1) - (4.3), can be expected to be about 90 percent or more accurate. Accepting this as a tolerable level of accuracy, we consider once again the 2024-T3 aluminum alloy sheet discussed previously. For the indicated  $K$  and  $\sigma_y$  values  $r \approx 0.5$  in. For this value of  $r$ , the above inequalities require that  $0.5/a < r/a \leq 0.05$ , or, equivalently, that the crack length  $2a > 20$  in. For a crack size to width ratio of  $(2a/W) = 0.5$ , it is necessary to have a specimen width  $2a/W = 0.5 > 20/W$ , or  $W > 40$  in., which corresponds to the result of the previous analysis. Thus, for tough low-strength ductile materials which develop large plastic enclave sizes in plane stress, retention of a linear elastic approach to the assessment of fracture toughness requires the use of very wide test specimens.

In order to circumvent these limitations several different proposed methods of determining fracture toughness in situations where crack front plastic yield is appreciable (semibrittle fracture) are currently under investigation. At this time, however, none of these proposed methods has obtained sufficient acceptance to be recognized as an international or national standard.

Accordingly, a brief outline of the better-known of these methods is presented below.

### 5.1 Crack-Opening Displacement (COD)

For situations in which significant crack-tip plastic yielding occurs prior to unstable fracture, a certain amount of opening displacement (blunting) of the crack or notch tip is often observed. This crack opening displacement (COD) has been proposed as a measure of fracture resistance in situations where crack-tip yielding is greater than allowable limits for the elastic  $K$  characterization of fracture toughness [74, 75].

In situations of small crack-tip yielding, an approximate relationship has been established between the COD concept and the linear elastic  $G$  or  $K$  quantities. This relation is obtained by considering the crack tip yield region to be represented by a circle of diameter  $2r_y$ . The actual crack and plastic zone combination is then replaced for analysis purposes by an effective elastic crack,  $a_e = a + r_y$ , as shown in Fig. 5.2a. The crack-opening displacement,  $\delta$ , is defined as the separation of the faces of the effective elastic crack at the position corresponding to the tip of the real crack, and represents the actual crack-tip opening due to plastic yield, as seen in Fig. 5.2b.

The COD or  $\delta$  can be calculated by first substituting  $\theta = \pi$  and  $r = r_y$  in Eq. (4.7) for the plane strain  $y$ -direction displacement, giving

$$u_y(r_y, \pi) = \frac{2K}{\pi E} (1-\nu^2) \sqrt{2\pi r_y} \quad (5.6)$$

Then with  $\delta = 2u_y(r_y, \pi)$  and  $r_y = 1/6\pi (K/\sigma_y)^2$ , Eq. (4.21) becomes

$$\delta = \frac{4}{\pi\sqrt{3}} \frac{G}{\sigma_y}$$

A similar analysis in the case of plane stress gives

$$\delta = \frac{4}{\pi} \frac{G}{\sigma_y}$$

In keeping with the approximate nature of the entire calculation, a value of unity is assumed for the coefficient multiplying  $G/\sigma_y$ , so that

$$\delta \approx \frac{G}{\sigma_y} \quad (5.7)$$

Within the limitation of small plastic enclave size, Eq. (5.7) merely recharacterizes  $G$ , the elastic energy release rate of the entire body, in terms of the deformation of the material at the tip of the crack.

Regardless of the relative size of the yield zone at the crack tip, however, crack extension can be expected to take place at some critical COD value. This critical value designated by  $\delta_c$  (at a given temperature, section thickness and strain rate) has been proposed and is currently being investigated as a measure of resistance to fracture. If, as is often the case with ductile materials, crack growth initiation is followed by slow stable crack growth prior to crack propagation, the observed value of  $\delta$  at the onset of catastrophic crack propagation should be taken as the critical COD.

Another example of an elastic analysis with simulated plasticity can be seen in Dugdale's "strip-yield" model [76]. In situations where such a model may be reasonably applied, the "strip-yield" model permits consideration of plastic zones more extensive than can be tolerated by the Irwin  $r_y$  correction discussed previously. The Dugdale model consists of a crack of length  $2a$  in a thin infinite sheet (in plane stress) which is loaded uniformly in tension normal to the plane of the crack. The plastic yield at the ends of the crack is assumed to be confined to a very narrow band of length  $s$ ,

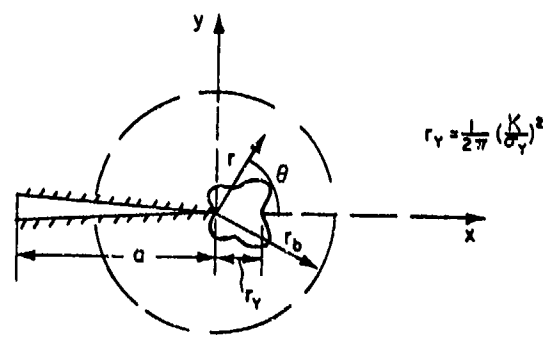


Figure 5.1

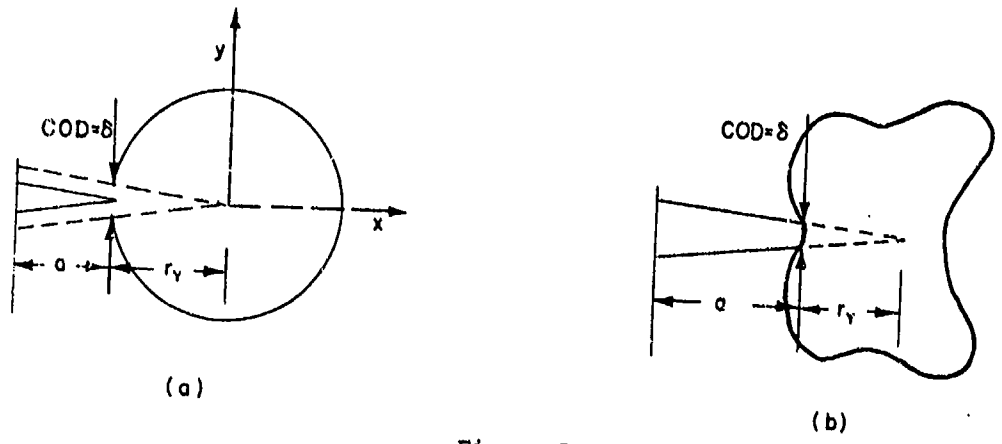


Figure 5.2

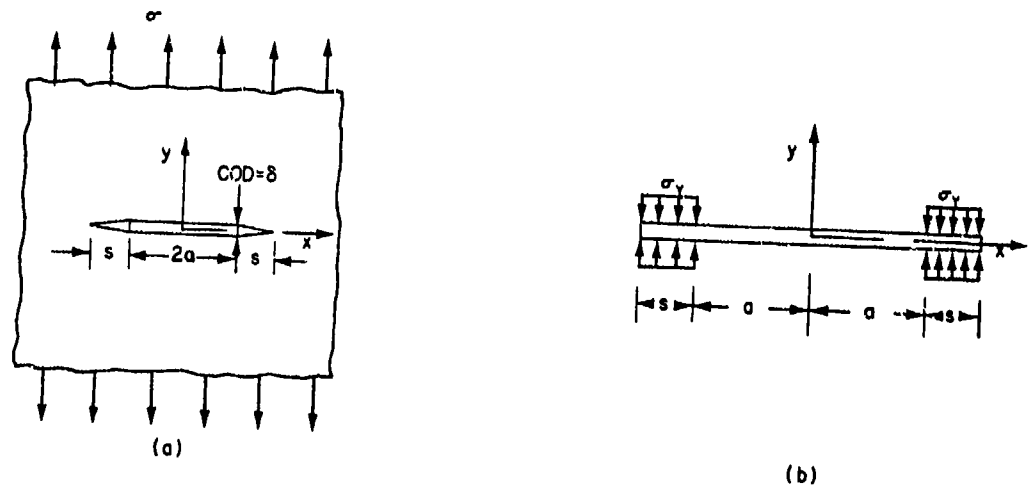


Figure 5.3

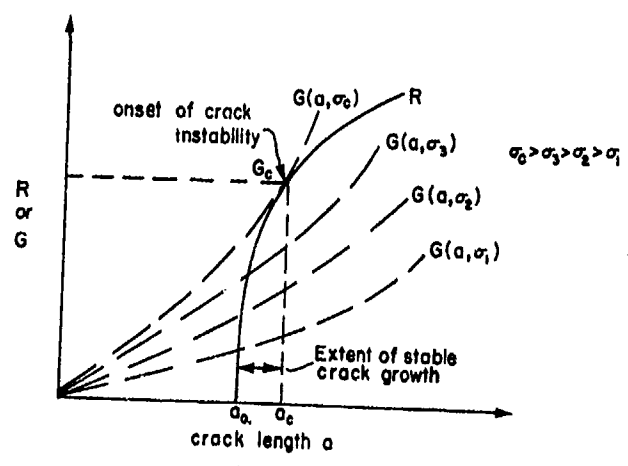


Figure 5.4

oriented along the length of the crack, Fig. 5.3a. Plastic zones having this shape have been observed in thin sheet specimens of mild strain-hardening materials [77]. The crack shown in Fig. 5.3a is replaced by an extended crack  $a+s$ , loaded over the length  $s$  by a compressive stress of constant magnitude equal to the yield stress of the materials, Fig. 5.3b. This model was developed to simulate the constraining effect of the actual strip-like plastic zones for ideal elastic-plastic material response, and permits elastic analysis of the sheet having the geometry of Fig. 5.3b. The characteristic singularity of the stresses at the tip of a crack in the elastic analysis of Sec. (4.1) is replaced in the Dugdale model by finite stresses at the tip of the extended crack. The opening of the crack walls at distance  $x = \pm a$  of Fig. 5.3b corresponds to the crack opening displacement at the ends of the crack of Fig. 5.3a, and can be shown to be [78]

$$\delta = \frac{8\sigma_y a}{\pi E} \ln \sec \left( \frac{\pi \sigma}{2 \sigma_y} \right) \quad (5.8)$$

In terms of a series expansion of the log sec function

$$\delta = \frac{8\sigma_y a}{\pi E} \left( \frac{1}{2} \left( \frac{\pi \sigma}{2 \sigma_y} \right)^2 + \frac{1}{12} \left( \frac{\pi \sigma}{2 \sigma_y} \right)^4 + \frac{1}{45} \left( \frac{\pi \sigma}{2 \sigma_y} \right)^6 + \dots \right) \quad (5.9)$$

For small values of the ratio of applied stress to yield stress, say  $(\sigma/\sigma_y) < 0.1$ , only the first term of the series expansion is significant. Use of Eqs. (4.9) and (4.22) for the center-cracked infinite sheet in plane stress, reduces the first term of Eq. (5.9) to Eq. (5.7). Since no restriction is placed on the length of the plastic zone dimension  $s$  in the "strip-yield" model, it has been suggested on the basis of some experimental results and numerical elastic-plastic solutions of notched bar configurations, that the "strip-yield" model gives a good estimate of the relationship between COD, crack length and applied stress in the presence of extensive plasticity, under a wide range of conditions including plane strain [79, 80, 81].

The initial apparatus for measuring the COD consisted of a paddle gage which was inserted into the crack tip, with the magnitude of the crack opening indicated by a rotation of the paddle. Measurements with the paddle gage were initially rather successful, but subsequent attempts at duplicating the results at other laboratories led to the conclusion that the technique was too tedious to give satisfactory results. In current application, the COD is not measured directly; instead, a standard clip gage is employed to measure center-crack displacements or edge displacements in edge-notched specimens. The clip gage results are then correlated with COD values by use of experimental calibration curves.

## 5.2 Crack Growth Resistance Curves (R-Curves)

Considerable slow, stable crack growth prior to unstable fracture is often observed in fracture toughness testing, especially as the ductility of the material increases or the thickness decreases. It is also known that  $K_{IC}$  (or  $G_C$ ) values demonstrate sizable variations with specimen width and initial crack size. The lack of a unique  $K_{IC}$  value for a given material, together with stable crack growth which is characteristic of  $K_{IC}$  testing, has led to the development of the crack growth resistance curve (R-curve) [82, 83, 50].

The basic concept of the R-curve can be stated as follows: As the rate of energy available for crack extension,  $G$ , is increased during specimen loading, it is opposed by an increasing resistance to crack extension,  $R$ , such that  $G$  and  $R$  remain in equilibrium up to the point of crack instability. The R-curve represents the rate of energy absorption in the creation of new surfaces and in plastic deformation throughout the border region of the crack.

For illustrative purposes consider the center-cracked sheet with an initial crack length  $2a_0$ , for which Eqs. (4.11) and (4.22) give

$$G = \frac{\sigma^2 \pi a}{E} \sec \left( \frac{\pi a}{W} \right) \quad (5.10)$$

Although the values of  $G$  and  $R$  are equal up to the point of instability, they represent distinctly different physical quantities. The rate of energy absorption required by the stable, continuous growth of a crack into plastically deformed regions increases with crack extension, so that the R-curve has the form shown in Fig. 5.4. The G-curves in Fig. 5.4 are plotted as a function of the crack length using Eq. (5.10), with each curve representing a particular value of the applied stress as a parameter. As the crack extends slowly, equality of  $G$  with  $R$  requires increasing value of the applied stress  $\sigma$ , thus raising the  $G(a, \sigma)$  curve. Points of intersection of the  $G$  and  $R$  curves represent stable crack lengths for a given value of applied stress. When the  $G(a, \sigma)$  curve is raised sufficiently to become tangent to  $R$ , unstable crack extension occurs at the critical applied stress  $\sigma_c$ . Analytically the condition for crack instability requires that

$$G(a, \sigma_c) = R(a, \sigma_c) \text{ and } \left( \frac{\partial G}{\partial a} \right)_{\sigma_c} = \left( \frac{\partial R}{\partial a} \right)_{\sigma_c} \quad (5.11)$$

which determines the fracture toughness  $G_c$  (or  $K_{Ic}$ ) and the critical crack length,  $a_c$ .

The degree of dependence of  $G_c$  on both initial crack length and specimen width depends on the shape of the R-curve for the material, thickness and temperature under investigation. The R-curve is generally considered to be a material property, independent of specimen size, configuration and initial crack size. This proposition, however, has not been definitively established since results which both agree and disagree with this hypothesis have been reported [84, 85, 54]. Nevertheless, acceptance of this assumption allows the  $G_c$  dependency on specimen width and initial crack size to be illustrated qualitatively as shown in Figures 5.5 and 5.6 [50]. In Fig. 5.5 the initial crack size is held constant while the specimen width is varied, and in Fig. 5.6 the width is fixed while the initial crack size is changed.

An R-curve can be constructed, for example for the center-cracked sheet specimen, by substituting into Eq. (5.10) observed test values for load and associated crack size. This gives a corresponding value of elastic energy rate which is equal to R at the observed crack length. The locus of all such values (points of the R vs. a plot) constitutes the R-curve. A discussion of various testing techniques which have been developed for R-curve determinations can be found in Reference [86]. Attempts have been made to construct R-curves through use of observed shear-lip dimensions [83], and by plastic enclave strain measurements [19], in order to estimate the plastic deformation rate contribution to R.

### 5.3 J Integral

The nonelastic behavior of semibrittle materials which encouraged the development of the COD and R-curve concepts, has also led to the definition of the J integral by Rice [87] and its subsequent development as a fracture criterion in fracture mechanics testing. The J integral is a two-dimensional, energy line integral defined by the relation

$$J = \int_{\Gamma} (W dy - \vec{T} \cdot \frac{\partial \vec{u}}{\partial x} ds) \quad (5.12)$$

where W is the strain energy density,  $\vec{T}$  is the traction vector determined by  $\vec{T} = \vec{\sigma} \cdot \vec{n}$  over the contour  $\Gamma$ , and  $\vec{u}$  is the displacement vector, Fig. 5.7. The line integral of Eq. 5.12 can be shown to be path independent when taken about any closed path, [87]. Therefore, the value of J obtained from a closed contour close to the tip of a crack, as in Fig. 5.7, involving the near-tip stress and displacement fields can be equivalently evaluated by a closed contour which comprises the outer specimen boundary. Under normal conditions this procedure allows a much more simplified evaluation process. The J integral is thought to be applicable to elastic materials or elastic-plastic materials which can be treated by a deformation theory of plasticity, provided that there is no unloading of stresses in the plastically deformed regions.

Because of the path independent nature of the J integral, it is possible to show that

$$J = - \frac{\partial P}{\partial a} \quad (5.13)$$

which represents the rate of change of potential energy with respect to crack size. Thus in the linear elastic case and, also for small scale crack-tip yielding the J integral represents the same quantity as G. For a nonlinear elastic body, J may be interpreted as the energy available for crack extension but, for the general elastic-plastic behavior, this interpretation is no longer valid.

The J integral has also been examined as to its validity as a fracture criterion under plane strain conditions by evaluating the integral at the critical conditions of impending crack growth. The fracture parameter in plane strain,  $J_{Ic}$ , has been evaluated by several researchers [88, 89, 90] using an involved experimental technique requiring a number of identical specimens with a specified variation in original crack size. It is significant that a relatively constant value for  $J_{Ic}$  was obtained for the various specimens from these tests which would tend to confirm its usefulness as a plane strain fracture criterion. However, other researchers using different experimental techniques have found considerable variations in  $J_{Ic}$  values. Thus it seems that, apart from questions of its validity for general elastic-plastic behavior, further research efforts are essential if the significance of  $J_{Ic}$  as a fracture criterion is to be satisfactorily understood.

### 5.4 Nonlinear Energy Characterization of Fracture Toughness

For many situations in fracture toughness testing, the strain energy stored under the linear portion of the load-displacement curve is a small portion of the total strain energy absorbed up to the onset of unstable fracture. This is especially true for thin specimens of low-to-medium yield strength materials. In such circumstances, sizable crack tip plastic deformation makes application of the linear elastic K characterization of fracture toughness invalid when conventional sized specimens are used. Consequently, an empirical method which characterizes fracture toughness in terms of the total strain energy rate at crack instability has recently been proposed by Liebowitz and Eftis [91, 92].

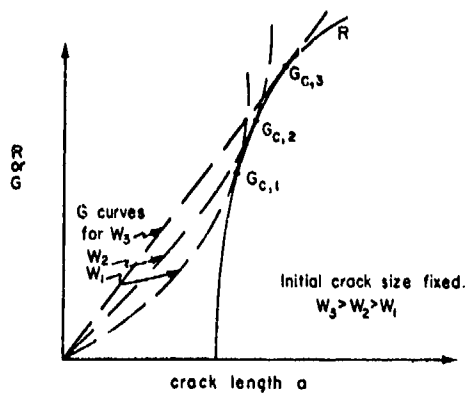


Figure 5.5

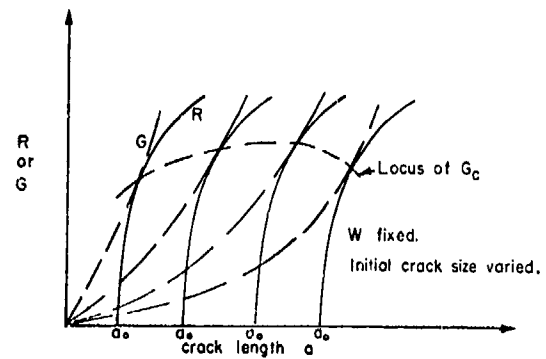


Figure 5.6

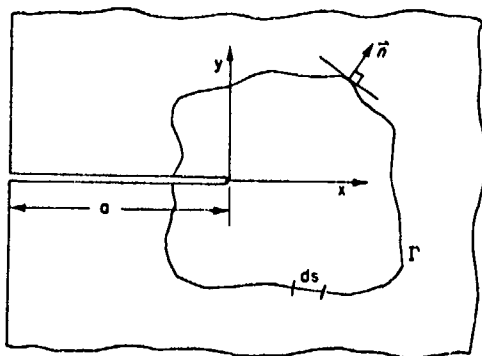


Figure 5.7

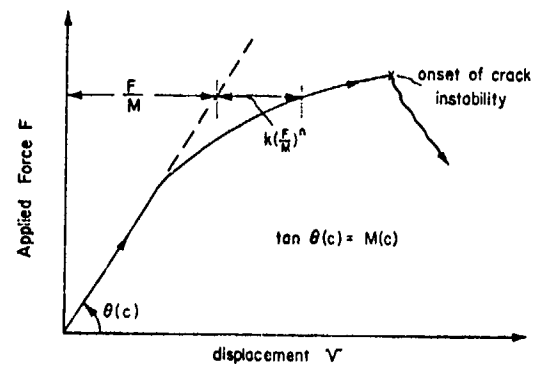


Figure 5.8

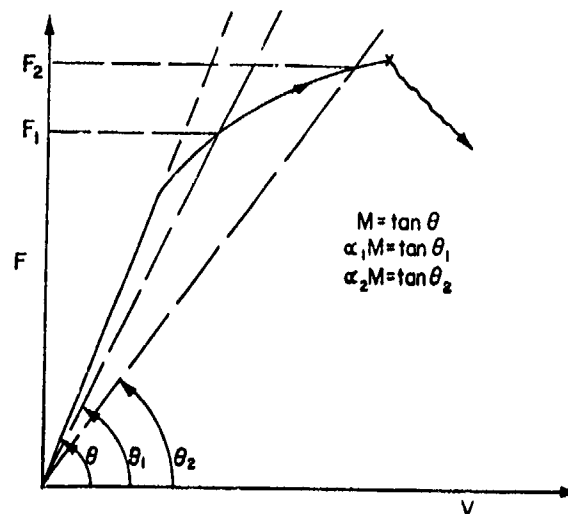


Figure 5.9



Although this method can be applied to any specimen geometry, it will be discussed for the center-cracked sheet, where for convenience the thickness dimension is taken as unity. Let  $v$  designate the displacement of a gage point located at the point of application of a slowly applied load,  $F$ , which increases monotonically until fracture instability occurs. A load-displacement record for a fracture toughness test in which there is significant crack-tip plastic yield, and possibly slow, stable crack growth prior to crack instability, appears typically as shown in Fig. 5.8. The actual load-displacement record can be represented quite adequately by the simple three-parameter relation

$$v = \frac{F}{M} + k \left( \frac{F}{M} \right)^n, \quad (5.14)$$

where  $M(c)$  is the crack size dependent elastic compliance (per unit thickness) of the cracked specimen. The nonlinear part of the load-displacement curve is characterized by the parameters  $k \geq 0$  and  $n \geq 1$ , and is a measure of the degree of crack front plastic yield and stable crack growth present in the test situation.

The total strain energy in the specimen for any displacement  $v$  in the nonlinear range consists of a linear elastic part,  $U_L$ , and a nonlinear part,  $U_{NL}$ , and is represented by the total area under the load-displacement curve. It can be calculated from Eq. 5.14 as

$$\begin{aligned} U &= U_L + U_{NL} = F \cdot v - \int_0^F v dF \\ &= \frac{1}{2M} F^2 + k \left( \frac{n}{n+1} \right) \left( \frac{1}{M} \right)^n F^{n+1}. \end{aligned} \quad (5.15)$$

The rate of change of  $U$  with slow crack extension, under fixed-grip conditions, can be shown to be

$$\begin{aligned} \left[ \frac{\partial U}{\partial c} \right]_v &= \left[ \frac{\partial U_L}{\partial c} \right]_v + \left[ \frac{\partial U_{NL}}{\partial c} \right]_v \\ &= \left[ 1 + \frac{2nk}{n+1} \left( \frac{F}{M} \right)^{n-1} \right] \frac{1}{2} F^2 \left[ \frac{d}{dc} \left( \frac{1}{M} \right) \right]_v. \end{aligned} \quad (5.16)$$

Since the first term on the right side of (5.16) is the elastic strain energy rate contribution, i.e.,

$$- \left[ \frac{\partial U_L}{\partial c} \right]_v = \frac{1}{2} F^2 \left[ \frac{d}{dc} \left( \frac{1}{M} \right) \right]_v = G, \quad (5.17)$$

it is logical to define

$$\tilde{G} = - \left[ \frac{\partial U}{\partial c} \right]_v = \tilde{C} G \quad (5.18)$$

$$\text{where } \tilde{C} = \left[ 1 + \frac{2nk}{n+1} \left( \frac{F}{M} \right)^{n-1} \right] \geq 1. \quad (5.19)$$

When  $\tilde{G}$  is evaluated at the load corresponding to the onset of crack instability, it represents a nonlinear fracture toughness measure,  $G_c$ . The quantity  $\tilde{C}$  represents the degree of nonlinearity which exists primarily as a consequence of crack-tip plastic yield and stable crack growth. When the value of  $\tilde{C}$  is very close to unity, the load-displacement record is essentially linear. This situation corresponds to a fracture toughness test under plane strain conditions in which there is no significant crack-tip plastic yield and no significant stable crack growth prior to crack instability [25], so that, when  $\tilde{C} \rightarrow 1.0$ ,  $G_c \rightarrow G_{Lc}$ . On the other hand,  $\tilde{C}$  can have values considerably greater than unity for more ductile materials in thin sheet specimens. This method is therefore a generalization of the linear elastic characterization of fracture toughness which is based only on the linear portion of the load-displacement curve.

The three parameters  $M$ ,  $n$  and  $k$  are determined directly from the test record.  $M$  represents the slope of the linear portion of the curve. In order to evaluate  $n$  and  $k$ , two secant lines are drawn to the load-displacement curve as shown in Fig. 5.9. The secant moduli are obtained as  $\alpha_1 M$  and  $\alpha_2 M$ , where  $0 < \alpha_2 < \alpha_1 < 1$ . The values of  $\alpha_1$  and  $\alpha_2$  are somewhat arbitrary except that the secant line represented by  $\alpha_2 M$  should intersect the curve near the point of crack instability. In this case  $F_2 = F_c$  and Eq. (5.19) reduces to

$$\tilde{C} = 1 + \frac{2n}{n+1} \left( \frac{1-\alpha_1}{\alpha_1} \right) \quad (5.20)$$

which is independent of the elastic compliance M as expected, and where

$$n = 1 + \frac{\ln\left[\frac{\alpha_2(1-\alpha_1)}{\alpha_1(1-\alpha_2)}\right]}{\ln(F_1/F_2)} \quad (5.21)$$

Since G, as given by (5.17), can be evaluated by the usual elastic compliance methods and C can be calculated by means of Equations (5.20) and (5.21), G is completely known for any given test situation.

## 6. APPLICATIONS OF FRACTURE MECHANICS CONCEPTS

### 6.1 Damage Tolerant Structures

The application of fracture mechanics concepts introduced in the previous sections of this chapter has led to the evolution of a general class of structures known as damage tolerant structures. These structures are developed with the knowledge that it is possible to maintain structural integrity even though certain flaws are known to exist in the material. Proper use of fracture mechanics allows the prediction of maximum flaw sizes allowable for the safe use of these structures. The procedure of employing damage tolerant structures has also been referred to as a fail safe or fracture safe philosophy as discussed, for example in Ref. [42].

The fail safe philosophy assumes that during the service life of a structural component, fatigue cracks or other damage will not progress to a catastrophic condition between specified inspection intervals. This concept covers all of the primary structure in aircraft so that the loss of one component does not permit catastrophic failure of the entire structure. The deployment of redundant components or materials which exhibit slower fatigue crack growth rates can be used to implement such a fail safe concept. In addition, stringers are often used as crack arrest elements which are then incorporated into the evaluation of critical stresses for the structural design procedure.

Proceeding from a metallurgical orientation, Pellini [93] developed the concept of fracture safe design (FSD). This work was initiated around 1950 and has evolved through several phases of development in the succeeding years. The first phase involved the identification of a Nil Ductility Transition (NDT) temperature for steel below which there is effectively no permanent deformation prior to fracture. The method is designed to protect against fracture initiation due to the presence of small flaws in low or intermediate strength steels when used in the transition temperature range. Protection is obtained by restricting the lowest service temperature to a specified increment above the NDT. The second phase of FSD restricts the lowest service temperature to a small increment above the Crack Arrest Temperature (CAT) which assures that brittle crack propagation cannot occur, regardless of flaw size, and is therefore called a nonprovisional design.

The third phase of fracture safe design involves the development of a Fracture Analysis Diagram (FAD) which identifies limiting values of applied stress as a function of service temperature. The curves that comprise the FAD are a function of the initial flaw sizes and define the conditions of stress and temperature at which brittle fracture would be expected to occur. Depending on the choice of initial flaw size, the FAD can represent provisional or nonprovisional FSD methods. A simplified FAD for a steel exhibiting the typical brittle-to-ductile transition is shown in Fig. 6.1. For design considerations, reference is made to two critical design points. Designs which are based on a small temperature increment above the NDT temperature are provisional, since protection against fracture is a function of initial flaw size. Designs based on a small temperature increment above the CAT are nonprovisional because brittle fracture will not occur, regardless of initial flaw size.

The fourth phase introduces fracture mechanics concepts into FSD and leads to the development of the Ratio Analysis Diagram (RAD). The principal difference between the FAD and RAD developments is that the brittle-to-ductile transition is analyzed in the RAD as a function of yield strength rather than temperature. A Ratio Analysis Diagram as developed by Goode and Judy [94] for aluminum alloys is seen in Fig. 6.2 where lines of constant ratio,  $\frac{K_{Ic}}{\sigma_y}$ , have been determined from the elliptical surface crack geometry. The principal value of the RAD is in determining the expected type of failure. For example, the 1 in. thick specimens, the elastic-plastic region lies between the 1.0 and 0.63 ratio lines, the plastic region lies above the 1.0 line and the brittle region below the 0.63 line (where fracture mechanics concepts must be employed).

### 6.2 Critical Crack Size

An important application of fracture mechanics to the nondestructive inspection process is the identification of a critical crack size for a particular structural application where it is assumed that the material properties and applied stresses are known. Problems of brittle fracture resulting from embedded flaws and part-through surface cracks are particularly important to aerospace applications. Hence, the discussion of critical crack sizes in this section will emphasize flaws of this type.

Consider first the penny-shaped (circular disk) crack of radius,  $a$ , in an infinite solid subjected to uniform tensile stress,  $\sigma$ , normal to the crack plane. The stress intensity factor for this geometry was previously given in Section 4 as

$$K = 2\sigma\sqrt{\frac{\pi}{a}} \quad (6.1)$$

For given service load and fracture toughness values, it is then possible to solve Eq. (6.1) for the critical crack size,  $a_c$ , in the form

$$a_c = \frac{\pi}{4} \left( \frac{K_{IC}}{\sigma} \right)^2 \quad (6.2)$$

A structure is determined to be safe only when flaws of this type having diameters smaller than  $2a_c$  exist in this configuration.

A more general treatment of the problem of embedded flaws involves consideration of an embedded flat elliptical crack. A crack of this type in an infinite solid subjected to uniform normal tensile stress has been obtained in the form [26]

$$K = \frac{\sigma}{E(k)} \left( \frac{b}{a} \right)^{1/2} (a^2 \sin^2 \theta + b^2 \cos^2 \theta)^{1/4} \quad (6.3)$$

where  $E(k)$  is the complete elliptic integral of the second kind,  $2a$  is the major axis,  $2b$  is the minor axis and  $\theta$  is the angle from a major axis measured in the plane of the crack. Equation (6.3) gives the stress intensity factor at all points around the periphery of the crack as a function of the angle  $\theta$ . The most critical point occurs at the minor axis, i.e., at  $\theta = \frac{\pi}{2}$ , at which

$$K = \frac{\sigma b^{1/2}}{E(k)} \quad (6.4)$$

where  $E(k)$  is now a function only of the ratio  $a/b$ . It should be mentioned that Eqs. (6.2-4) apply only for the case of completely brittle fracture. A considerable amount of effort has been directed toward inclusion of the effects of small-scale plastic deformation into these expressions but the results have not obtained wide acceptance and so are not included here.

As with the case of the embedded elliptical flaw, considerable effort has been directed toward obtaining stress intensity functions for the elliptical surface crack, Fig. 6.3a. For an elliptical surface crack of depth,  $a$ , and length,  $2c$ , subjected to tension normal to the plane of the crack, the elastic stress intensity has been given in the form [95]

$$K = \frac{\sigma\sqrt{\pi a}}{E(k)} (1-k^2 \cos^2 \theta)^{1/4} \quad (6.5)$$

where  $k^2 = (1 - \frac{c^2}{a^2})^2$ , and the other terms have the same meaning as in Eq. (6.3). The stress intensity factor assumes its maximum value at  $\theta = \frac{\pi}{2}$  and has the form proposed by Irwin [95]

$$K = \frac{1.1 \sigma\sqrt{\pi a}}{(E(k)^2 - 0.212(\sigma/\sigma_Y)^2)^{1/2}} \quad (6.6)$$

when corrected for small scale crack-front plastic yield by the addition of the term  $0.212(\frac{\sigma}{\sigma_Y})^2$ . An additional modification of Eq. (6.5) has been developed in the form [42, 96]

$$K = \frac{1.1 M_k \sigma\sqrt{\pi a}}{(E(k)^2 - 0.212(\frac{\sigma}{\sigma_Y})^2)^{1/2}} \quad (6.7)$$

where  $M_k$  is called the backface correction factor, values of which are given in Fig. 6.3b. The use of  $M_k$  has permitted some lessening of the initial restrictions on crack depth-to-thickness ratio and the limited amount of allowable plastic deformation. Shaw and Kobayashi [97] also have presented stress intensity factors for embedded and surface flaw geometries.

All of the results for elliptic embedded and surface flaws can be solved for critical crack size in the same manner as was demonstrated for Eq. (6.1). However, because of the nature of Eqs. (6.3-7) it is necessary to solve for  $a_c$  by an iterative process rather than obtaining a direct solution similar to Eq. (6.2). Nevertheless, the same basic procedure applies so that once the crack dimensions are identified it will be a straightforward matter to verify whether unstable propagation would be predicted. Further, for situations approaching the geometry of the standard test specimens,

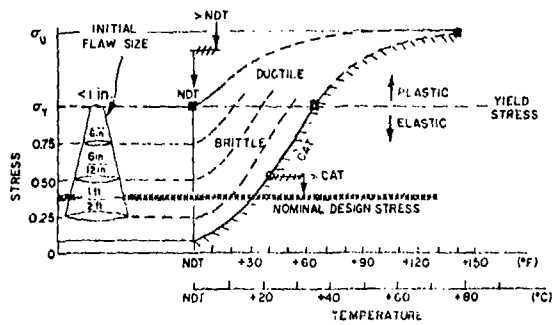


Figure 6.1

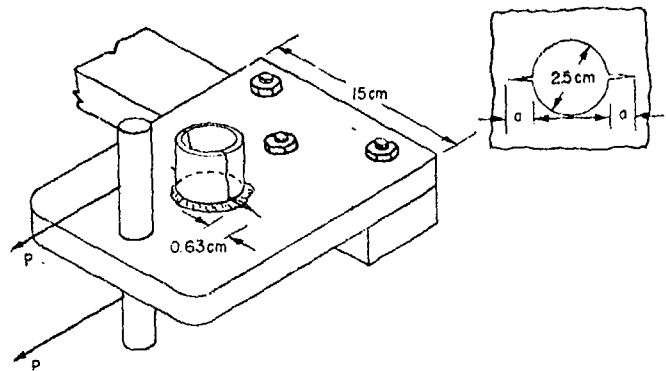


Figure 6.4

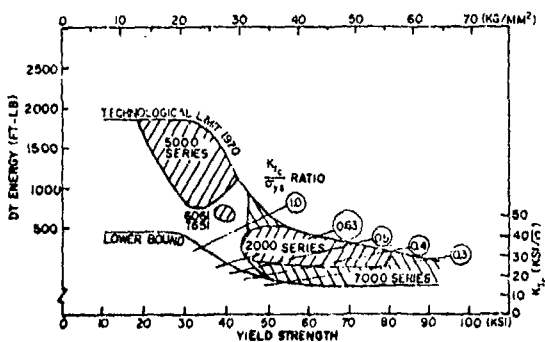


Figure 6.2

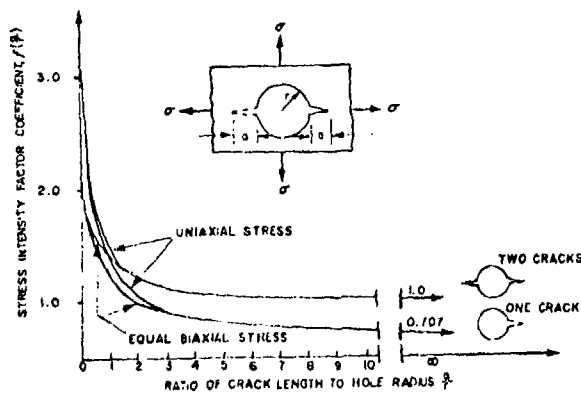


Figure 6.5

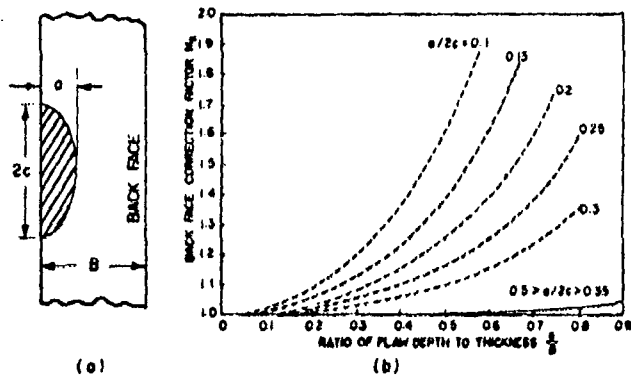


Figure 6.3

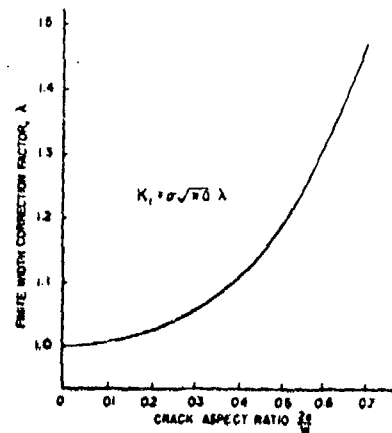


Figure 6.6

Eqs. (4.11-19) can also be employed for the determination of critical crack sizes. Two example applications of this technique will be discussed next.

### 6.3 Practical Applications

In order to obtain a reasonable insight into the method of applying fracture mechanics techniques, two examples will be discussed. The geometry of the first example will be that of a standard fracture mechanics test while the second will deal more directly with an aerospace application.

Example 1. Consider a center-cracked panel of 7075-T6 aluminum alloy which has the following characteristics (see Fig. 4.3):

$$\begin{aligned}2a &= 10.0 \text{ cm} \\ W &= 50 \text{ cm} \\ B &= 0.31 \text{ cm}^2 \\ \sigma_Y &= 518 \text{ MN/m}^2 \\ \sigma_U &= 573 \text{ MN/m}^2 \\ K_C &= 60.2 \text{ MN/m}^{3/2}\end{aligned}$$

where the  $K_C$  value is selected to be compatible with the actual service conditions. Determine whether the sheet will sustain a stress of  $138 \text{ MN/m}^2$  if a crack of length  $a = 10.0 \text{ cm}$  has been discovered during periodic inspection. Also determine the critical crack size for this applied stress and the factor of safety if the stress is sustained.

Solution. The governing stress intensity factor for this geometry has been given in Sec. 4 as

$$K = \sigma \left( \pi a \sec \left( \frac{\pi a}{W} \right) \right)^{1/2} .$$

for the given geometry and loading, the stress intensity factor becomes

$$\begin{aligned}K &= 138 \left( 3.14 \times 0.05 \sec \frac{3.14 \times 0.05}{0.50} \right)^{1/2} \\ &= 56.1 \text{ MN/m}^{3/2} .\end{aligned}$$

Since this value is less than the fracture toughness, the panel will sustain the applied stress with a factor of safety of

$$\text{S.F.} = \frac{60.2}{56.1} = 1.07 .$$

The critical crack size is determined from the same equation by substituting the values

$$K_C = 60.2 \text{ MN/m}^{3/2} \quad \text{and} \quad \sigma = 138 \text{ MN/m}^2$$

and solving for  $a_c$  from

$$\pi a_c \sec \left( \frac{\pi a_c}{W} \right) = \left( \frac{60.2}{138} \right)^2 = 0.1903 .$$

When this equation is solved by iteration, it is found that the critical crack size is  $a = 5.67 \text{ cm}$ , so that flaws less than this size can be permitted without unstable fracture.

The second example is a modification of an example developed by Wilhem [42].

#### Example 2.

A feed-through arm has developed through the thickness cracks, due to fatigue loading, as shown in Fig. 6.4. The arm material is 2219-T87 aluminum alloy, 1.88 cm thick, with  $\sigma_Y = 386 \text{ MN/m}^2$  and  $K_{Ic} = 29.7 \text{ MN/m}^{3/2}$ . The hole is 2.5 cm in diameter, as shown, and it is desired to determine whether the arm will sustain a stress of  $103 \text{ MN/m}^2$  with a safety factor of 25 when the crack has been determined to be,  $a = 0.63 \text{ cm}$ .

Solution. The center cracked plate formula can also be used for this problem when a modification factor  $f(\frac{a}{F})$ , as shown in Fig. 6.5, and a finite width correction factor are included. The equation for this geometry thus has the form

$$K_I = \sigma \sqrt{\pi a} \lambda f \left( \frac{a}{F} \right) .$$

For use in the equation above, it is seen that  $\frac{a}{F} = \frac{0.25}{0.5} = 0.5 + f \left( \frac{a}{F} \right) = 1.8$ . It is also necessary to determine whether plane strain conditions apply to this problem which are considered to apply when the thickness,

$\sigma = 2.5 \left( \frac{K_{tU}}{Y} \right)^2$ . Thus  $2.5 \left( \frac{1.4}{1.0} \right)^2 = 1.4 \text{ cm} = B$  so that failure would be anticipated

under conditions of plane strain. The finite width correction factor is determined from Fig. 6.6 to be  $\gamma = 1.04$  for a crack aspect ratio,  $\frac{a}{W} = 0.25$ . It is then possible to solve for the critical stress by solving

$$\sigma_c = \frac{K_{tU}}{\sqrt{\pi a} \cdot f\left(\frac{a}{W}\right)} = \frac{K_{tU}}{\sqrt{\pi a} \cdot 1.04} = 111 \text{ MN/m}^2$$

Therefore, it is seen that the stress of  $101 \text{ MN/m}^2$  will be supported but the factor of safety is only  $\text{F.S.} = \frac{111}{101} = 1.10$  or 10 percent rather than 25 percent, as required, and the part should be replaced.

## 7. FATIGUE CRACK GROWTH

### 7.1 Constant Amplitude Fatigue Loading

When a structural element, which contains irregular geometry such as sharp internal corners, welding flaws, or holes, is loaded in a cyclic manner, the appearance of fatigue cracks is a common occurrence. The fatigue life is considered to be comprised of three distinct portions: (a) crack nucleation, (b) crack growth and (c) unstable final failure. Crack nucleation under cyclic loading is characterized by localized plasticity, usually on well-identified slip planes, resulting from dislocation motion in certain preferred regions and directions. The percentage of total specimen life expended in crack nucleation is a function of the irregularities of component design (stress concentration factor) although other factors may also be significant. It is generally accepted that the portion of specimen life expended in crack nucleation is proportional to the stress concentration factor whereas the time expended in crack growth is relatively constant. Since quantitative relationships between stress concentration factors and crack nucleation periods have not been widely presented in the literature, primary emphasis in this section will be directed toward the crack growth phase of fatigue failures.

Crack growth laws for constant amplitude fatigue tests have evolved from both theoretical and semi-empirical considerations. Crack growth laws which are based on theoretical considerations usually involve constants which are related to basic material properties such as yield strength, work hardening coefficient, etc. However, these laws are usually more complex than the semiempirical laws and usually do not fit experimental data as well. Since the semiempirical laws provide simplicity and a better fit to experimental data, only semiempirical laws will be discussed in this section.

Semiempirical laws are based mostly on the observation that many theoretical laws contain the factor  $\sqrt{a}$  which is the proper functional form of the variable  $a$  and  $a$  for the geometry upon which the theoretical models are based [98]. The various models were examined by Paris and Erdogan [99] who then recommended a growth law of the form

$$\frac{da}{dN} = C_0 K^4 \quad (7.1)$$

where  $C_0$  is an empirical constant and  $K$  is the stress intensity factor at maximum load. A modification of Eq. (7.1) given by

$$\frac{da}{dN} = C_1 (\Delta K)^n, \quad (7.2)$$

where  $\Delta K = K_{\max} - K_{\min}$ ,  $C_1$  and  $n$  are material constants, has been developed which fits experimental data for a wide range of materials and loading conditions. For example, Fig. 7.1 demonstrates the good correlation represented by Eq. (7.2) for 7075-T6 and 2024-T3 aluminum alloys [100].

Although the instances of successful correlation of Eq. (7.2) with experiments are quite numerous, there exist many situations in which it does not accurately predict crack growth rates. For example, it has been found that a two slope representation of Eq. (7.2) can often improve the accuracy of the model, as is seen for three aluminum alloys in Fig. 7.2, [101]. The two slopes are  $n = 13$  for very slow growth rates and  $n = 3$  for growth rates greater than approximately  $10^{-5}$  inches/cycle. Furthermore, a threshold value of  $\Delta K$  exists below which the crack growth rate is zero. Near this threshold value, the growth rates appear to be significantly dependent upon the load ratio  $R = K_{\min}/K_{\max}$  [102]. Further it has been seen that, at high growth rates, the rate appears to be sensitive to material properties, load ratio and stress state.

Several improvements to Eq. (7.2) have been advanced which can remedy some of the problems discussed above. A proposed modification of Eq. (7.2) to include the effects of stress ratio and very high and low growth rates has the following form [103]

$$\frac{d(2a)}{dN} = \frac{C_2 (\Delta K)^n}{(1-R)K_c - \Delta K} \quad (7.3)$$

where the value of  $K_0$  should be determined for the particular specimen geometry. This result provides considerably better correlation with experimental data and, consequently, has gained rather widespread usage. Still another proposed growth law asserts that the mean stress can be expected to contribute significantly to crack growth rates and therefore takes the form [104]

$$\frac{d(2a)}{dN} = C_3 e^{-C_4 R} \sigma_{\max}^3 \sqrt{2a} \left[ 1 + 10 \left( \frac{2a}{w} \right)^2 \right] \quad (7.4)$$

where  $R = \frac{\sigma_{\min}}{\sigma_{\max}}$ ,  $\sigma_{\min} = \sigma_{\text{mean}} - \sigma_{\text{amp}}$ ,  $\sigma_{\max} = \sigma_{\text{mean}} + \sigma_{\text{amp}}$

and  $C_3$ ,  $C_4$  are empirical constants.

In relation to NDI applications, it is usually less important to know the crack growth rate at any point than it is to know the total number of cycles until unstable failure occurs. Thus any of the crack growth equations can be integrated numerically over any desired crack size increment to obtain the expected remaining life. For example, Eq. (7.3) can be integrated directly under the conditions of uniform sinusoidal loading on an infinite plate, for  $n = 3$ , which gives

$$N_c - N_0 = \frac{2}{\pi C_2 (1-R)^2 \sigma^2} \left[ \frac{K_c}{K_0} - 1 - \ln \frac{K_c}{K_0} \right] \quad (7.5)$$

where  $N_c$  is the critical number of cycles at instability,  $N_0$  is the initial value, and  $K_0$  is the initial value of the stress intensity factor. An example of the application of these growth laws will be discussed in Sec. 7.3.

## 7.2 Variable Amplitude Fatigue Loading

Because the loads applied to aerospace structures are not represented well by constant amplitude fatigue tests, many researchers utilize more complex loading programs for the purpose of determining relative rates of growth. The most common types of variable amplitude programs are block or programmed loading, [105], which includes flight simulation programs, [106, 107], and random loading programs. Programmed loading is usually obtained by varying certain parameters such as maximum or minimum loads in the conventional fatigue test. Random loading programs are usually categorized into two types: (a) narrow band spectra in which a random amplitude is imposed on a constant frequency fatigue test, and (b) wide band spectra in which both the amplitude and frequency are varied in a random manner. A thorough treatment of the random loading problem has been given by Hilberry [108].

Contrary to the situation for constant amplitude fatigue loading, current procedures for analyzing variable amplitude fatigue tests do not usually lead to laws describing the increment of crack growth per cycle. Instead these theories, usually referred to as fatigue damage accumulation theories, often employ graphical procedures in their solution. The Palmgren-Miner rule is the most widely known of the fatigue damage accumulation or incremental damage theories, [109, 110]. Palmgren first assumed that  $n_i$  load cycles having the same mean load and load amplitude will consume a portion of fatigue life equal to  $n_i/N_i$ , where  $N_i$  is the failure life in a constant amplitude fatigue test having the same mean value and amplitude. Secondly, he assumed that failure will occur when the sum of the consumed life portions equals 100 percent or

$$\sum_i n_i/N_i = 1. \quad (7.6)$$

Equation (7.6) was subsequently refined by dividing the life into a crack nucleation period and a crack propagation period [111],

$$\sum_i n_i^1/N_i^1 = 1 \quad \text{and} \quad \sum_i n_i^2/N_i^2 = 1, \quad (7.7)$$

where  $n_i^1$  and  $n_i^2$  are numbers of cycles spent in the crack nucleation and crack propagation periods respectively, while  $N_i^1$  and  $N_i^2$  represent the corresponding crack nucleation and crack propagation lives. The values of  $N_i^1$ ,  $N_i^2$  and  $N_i$  are obtained from S-N diagrams of standard constant-amplitude fatigue tests.

The Palmgren-Miner rule is also referred to as the linear cumulative damage rule since it is assumed that the damage in a constant amplitude test is a linear function of the number of cycles. However, it has since been shown that linearity was not required for  $\sum n/N = 1$  to hold, although it is necessary that the material be insensitive to load cycle sequences which means that interaction effects must be insignificant. In general, interaction effects are significant as will be discussed below.

The Palmgren-Miner rule has been extended to random loading by assuming that the damage caused by each stress peak is equal to the damage caused by one cycle in a standard fatigue test with the same stress amplitude. If  $N_0$  is the total number of peaks to failure, the expected probability value of the damage is

$$E(D) = N_p \int_{-\infty}^{\infty} \frac{w(\sigma)}{N(\sigma)} d\sigma \quad (7.8)$$

where  $w(\sigma)$  is the peak-probability density function. Approximating the constant amplitude S-N curve as a straight line on a log-log plot gives

$$N(\sigma) = B/\sigma^b \quad (7.9)$$

where  $b$  is the inverse of the slope and  $B$  is a constant. Substituting this distribution into Eq. (7.8) yields

$$E(D) = \frac{N_p B}{B} \int_{-\infty}^{\infty} \sigma^b w(\sigma) d\sigma \quad (7.10)$$

If a Gaussian distribution function is used for  $w$  in terms of a normalized variable  $z$  (zero mean and unit variance), Eq. (7.10) can be rewritten as

$$E(D) = \frac{N_p \sigma^b}{B} \int_{-\infty}^{\infty} z^b w(z) dz \quad (7.11)$$

If no damage is caused by stress peaks occurring below zero (in compression) and the new positive peak probability density function is renormalized, the expected value of the damage becomes

$$E(D) = \frac{N_p \sigma^b}{B} \int_0^{\infty} z^b w(z) dz \quad (7.12)$$

According to the Palmgren-Miner rule, failure should occur when  $E(D) = 1$ .

Several objections have been raised to the Palmgren-Miner rule based on interaction effects, sequence effects, damage due to cycles below the fatigue limit, favorable effects of positive peak loads, etc., all of which can lead to  $\sum n_i/N \neq 1$ . The favorable effects of positive peak loads result from the creation of a zone of residual compressive stress at the crack tip. Several theories have been advanced which preserve the concept of incremental damage accumulation while characterizing stress interaction effects by some kind of adjusted S-N curves. Freudenthal and Heller [112] started from the concept that damage increments in a random load test are altered by stress interaction effects. This leads to a failure criterion

$$\sum_i \frac{n_i}{N_i \omega_i} = 1 \quad (7.13)$$

called a "quasi-linear rule of cumulative damage" where  $\omega_i$  is either constant or a simple function of stress amplitude as determined from standard fatigue tests. This criterion implies the application of the Palmgren-Miner rule to adjusted S-N curves and, since it was assumed that  $\omega_i > 1$ , the curves are reduced life curves.

Corten and Dolan [113] include interaction effects by postulating that the maximum load cycle in a programmed test will be decisive for the initial damage, since it will determine the number of points at which crack growth will start. After this number has been established, crack growth is again assumed to be a cumulative process without interaction. For a program test they obtain the relation

$$N_g = \frac{N_1}{\sum_i \alpha_i (\sigma_{ai}/\sigma_{a1})^d} \quad (7.14)$$

where  $N_g$  is the program fatigue life,  $\sigma_{a1}$  is the maximum stress amplitude with corresponding constant amplitude fatigue life  $N_1$ ,  $\alpha_i$  is the percentage of cycles applied at  $\sigma_{ai}$  and  $d$  is an experimental constant. Since  $\alpha_i N_g = n_i$ , Eq. (7.14) can be rewritten

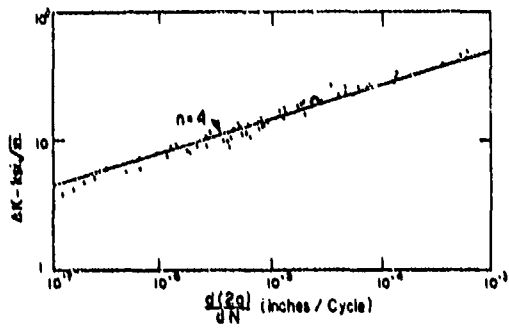
$$\sum_i \frac{n_i}{N_1} \left( \frac{N_1}{N_1} \left( \frac{\sigma_{ai}}{\sigma_{a1}} \right)^d \right) = 1 \quad (7.15)$$

which is similar in form to Eq. (7.13). Expanding this to random loading in the same manner as before gives

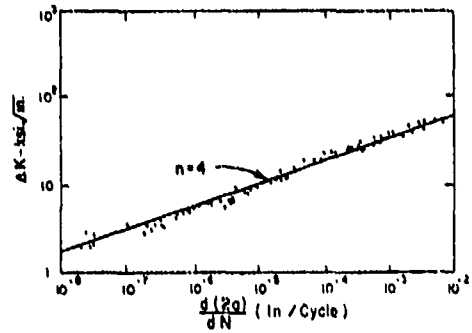
$$E(D) = \frac{N_p}{A} \sigma_{rms}^d \int_0^{\infty} z^d w(z) dz \quad (7.16)$$

where again it is assumed that no damage is caused by the peaks below zero.





(a)



(b)

Figure 7.1

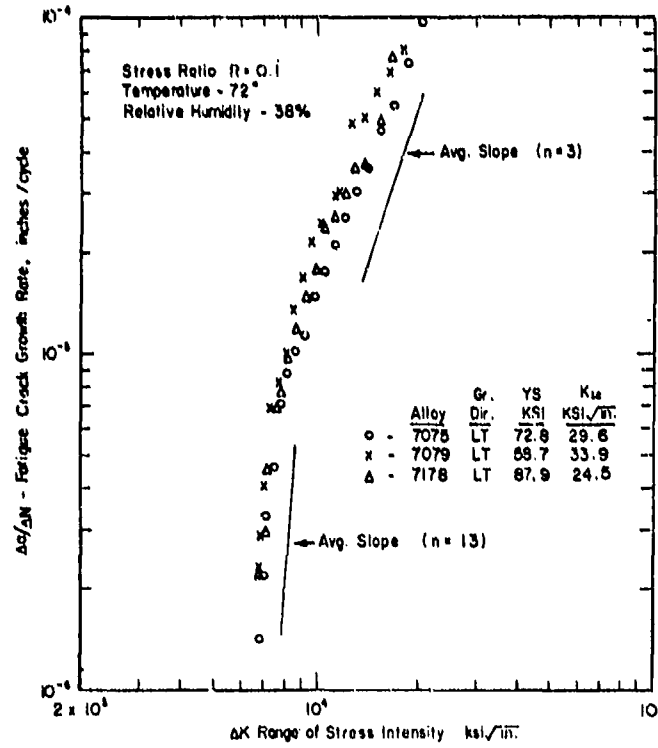


Figure 7.2

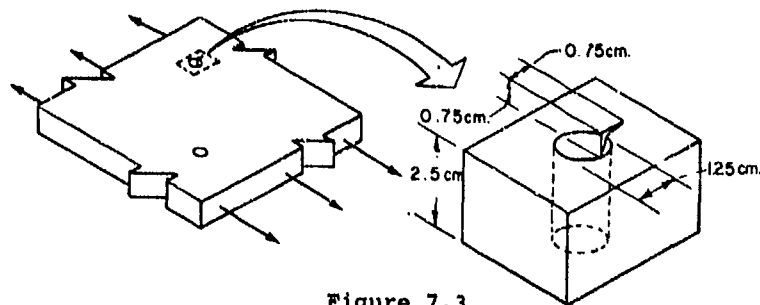
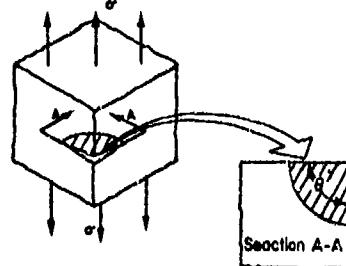


Figure 7.3

Uniform Tensile Stress - Corner Crack



$\frac{b}{90^\circ}$	$M_k$
0	0.705
0.2	0.650
0.4	0.625
0.5	0.620
0.6	0.625
0.8	0.650
1.0	0.705

Figure 7.4

As in Sec. 6, two examples will be discussed, the first of which will be a standard fracture mechanics specimen and the second will represent a more typical aerospace component.

**Example 3.** Suppose that the sheet in Example 1 is subjected to a constant amplitude fatigue stress with  $\sigma_{\max} = 138 \text{ MN/m}^2$ ,  $\sigma_{\min} = 27.6 \text{ MN/m}^2$  and a through-the-thickness crack of length  $2a = 2.25 \text{ cm}$  has been discovered. Predict what will be the remaining life of the sheet by use of the laws

$$(a) \quad \frac{d(2a)}{dN} = C_1 (\Delta K)^4$$

$$(b) \quad \frac{d(2a)}{dN} = \frac{C_2 (\Delta K)^2}{(1-R)K_{Ic} - \Delta K}$$

at three different intermediate crack lengths for the evaluation of growth rates. The constants for these equations are  $C_1 = 2.40 \times 10^{-10}$ ,  $C_2 = 0.0303 \times 10^{-8}$ ,  $n = 3.2$  for 7075-T6 with  $R = 0.2$ . Then use the integrated form of Eq. (b)

$$N_c - N_o = \frac{2}{\pi C_2 (1-R)^2 \sigma^2} \left( \frac{K_{Ic}}{K_{Io}} - 1 - \ln \frac{K_{Ic}}{K_{Io}} \right)$$

to determine the remaining life. Assume that each crack tip is growing at the same rate and recall from Example 1 that the critical crack size for this problem is  $2a_c = 11.35 \text{ cm}$ .

**Solution.** Select for the three crack growth intervals 2.25-5.28, 5.28-8.32, and 8.32-11.35 cm. For Eqs. (a) and (b) it is necessary to determine the number of cycles expended in growing the crack for each of the three intervals, and then sum to obtain the estimated total life.

$$\text{Equation (a).} \quad 2.25 \leq 2a \leq 5.28, \quad \bar{a} = 0.0188\text{m}$$

$$\begin{aligned} \Delta K &= \Delta \sigma \left( \pi \bar{a} \sec \frac{\pi \bar{a}}{w} \right)^{1/2} = 110 \left( 0.0188 \pi \sec \frac{0.0188 \pi}{0.5} \right)^{1/2} \\ &= 26.8 \text{ MN/m}^{3/2} \end{aligned}$$

$$\begin{aligned} \frac{d(2a)}{dN} &= C_1 (\Delta K)^4 = 2.40 \times 10^{-10} (26.8)^4 \\ &= 1.238 \times 10^{-4} \text{ m/cyc} \end{aligned}$$

$$N_1 = \frac{0.0303}{1.238 \times 10^{-4}} = 245 \text{ cycles.}$$

$$5.28 \leq 2a \leq 8.32 \quad \bar{a} = 0.034\text{m}$$

$$\Delta K = 110 \left( 0.034 \pi \sec \frac{0.034 \pi}{0.5} \right)^{1/2} = 36.4 \text{ MN/m}^{3/2}$$

$$\frac{d(2a)}{dN} = C_1 (\Delta K)^4 = 2.40 \times 10^{-10} (36.4)^4 = 4.21 \times 10^{-4} \text{ m/cyc}$$

$$N_2 = \frac{0.0303}{4.21 \times 10^{-4}} = 72$$

$$8.32 \leq 2a \leq 11.35 \quad \bar{a} = 0.0492\text{m}$$

$$\Delta K = 110 \left( 0.0492 \pi \sec \frac{0.0492 \pi}{0.5} \right)^{1/2} = 44.2 \text{ MN/m}^{3/2}$$

$$\frac{d(2a)}{dN} = C_1 (\Delta K)^4 = 2.40 \times 10^{-10} (44.2)^4 = 9.16 \times 10^{-4} \text{ m/cyc}$$

$$N_3 = \frac{0.0303}{9.16 \times 10^{-4}} = 33$$

$$N_{TOTAL} = 245 + 72 + 33 = 350 \text{ cycles.}$$

$$\text{Equation (b). } 2.25 \leq 2a \leq 5.28, \bar{a} = 0.0188\text{m}$$

$$\Delta K = 26.8 \text{ MN/m}^{3/2}$$

$$\frac{d(2a)}{dN} = \frac{C_2 (\Delta K)^n}{(1-R)K_{Ic} - R} = \frac{3.61 \times 10^{-8} (26.8)^{3.2}}{(0.8 \times 60.2) - 26.8}$$

$$= 6.27 \times 10^{-5} \text{ m/cyc}$$

$$N_1 = \frac{0.0303}{6.27 \times 10^{-5}} = 483 \text{ cycles}$$

$$5.28 \leq 2a \leq 8.32, \bar{a} = 0.034\text{m}$$

$$\Delta K = 36.4 \text{ MN/m}^{3/2}$$

$$\frac{d(2a)}{dN} = \frac{3.61 \times 10^{-8} (36.4)^{3.2}}{(0.8 \times 60.2) - 36.4} = 3.03 \times 10^{-4} \text{ m/cyc}$$

$$N_2 = \frac{0.0304}{3.03 \times 10^{-4}} = 100$$

$$8.32 \leq 2a \leq 11.35, \bar{a} = 0.0492$$

$$\Delta K = 44.2 \text{ MN/m}^{3/2}$$

$$\frac{d(2a)}{dN} = \frac{3.61 \times 10^{-8} (44.2)^{3.2}}{(0.8 \times 60.2) - 44.2} = 1.66 \times 10^{-3} \text{ m/cyc}$$

$$N_3 = \frac{0.0303}{1.66 \times 10^{-3}} = 18$$

$$N_{TOTAL} = 483 + 100 + 18 = 601 \text{ cycles.}$$

Now the integrated form of the equation will be used where

$$N_0 = 0, a_0 = 0.0113\text{m}$$

$$K_{I0} = 138 \left( 0.0113\pi \sec \frac{0.0113\pi}{0.5} \right)^{1/2} = 26.0 \text{ MN/m}^{3/2}$$

$$N_c = \frac{2}{\pi \times 3.61 \times 10^{-8} (1-0.2)^2 (138)^2} \left( \frac{60.2}{26.0} - 1 - \ln \frac{60.2}{26.0} \right)$$

$$N_c = 690 \text{ cycles.}$$

It is quite apparent that a wide range of estimates for remaining cycles to failure are obtained from these equations. However, since both Eqs. (a) and (b) have been shown to fit experimental results quite well, it is necessary that the constants  $C_1$ ,  $C_2$ , and  $n$  be selected very carefully for the specific material and component geometry of interest. However, Eq. (a) should not be used for crack sizes near the region of final instability since the assumptions made in its derivation do not hold there. The integrated form of Eq. (b) is expected to predict a different number of cycles to failure since it is based on the infinite sheet model and uses  $n = 3$  for the exponent of the  $\Delta K$  term. In addition, the constant  $C_2$  and the value selected for  $K_{Ic}$  also affect the predicted number of cycles to failure and should be carefully selected for the particular application of interest.

**Example 4.** This example is a modification of an example problem given by Wilhelm [42] and analyzes a corner crack which has developed at the top surface of a bolt hole as shown in Fig. 7.3. The plate thickness is 2.5 cm and the material is an alloy steel with  $\sigma_y = 689 \text{ MN/m}^2$  and  $K_{Ic} = 143 \text{ MN/m}^{3/2}$ . There exists a cyclic tensile stress as shown with  $\sigma_{max} = 483 \text{ MN/m}^2$  and  $\sigma_{min} = 9.6 \text{ MN/m}^2$ . A semicircular crack has developed to a depth of 0.75 cm and it is desired to know how many cycles will be required for the crack to grow through the back thickness. Also determine how many cycles will be expended before the critical crack size is reached, assuming that the crack changes from a semicircular to a straight through-the-thickness crack after it reaches the back surface.

**Solution.** The first part of the problem is solved by determining the stress intensity factor when the crack has just penetrated through the plate. The crack length for this condition is  $a = 2.5 \text{ cm}$ , and the stress intensity factor is given by

$$K_I = M_k \sigma \sqrt{\pi a}$$

where  $M_k$  has the value 0.705 for  $\frac{0}{50} = 1$  from Fig. 7.4. The stress intensity factor then is

$$\begin{aligned} K_I &= 0.705 \times 483 \sqrt{0.025\pi} \\ &= 95.4 \text{ MN/m}^{3/2} \end{aligned}$$

Eq. (7.5) is used to estimate the number of cycles where it will be assumed that the crack grows under plane strain conditions and  $C_2 \approx 2.1 \times 10^{-9}$ . The initial value of stress intensity factor  $K_{I0}$  is

$$\begin{aligned} K_{I0} &= 0.705 \times 483 \sqrt{0.0075\pi} \\ &= 52.3 \text{ MN/m}^{3/2} \end{aligned}$$

so that

$$\begin{aligned} N_c &= \frac{2}{\pi C_2 (1-R)^2 \sigma^2} \left[ \frac{K_I}{K_{I0}} - 1 - \ln \frac{K_I}{K_{I0}} \right] \\ &= \frac{2}{\pi \times 2.1 \times 10^{-9} (1-0.02)^2 (483)^2} \left[ \frac{95.4}{52.3} - 1 - \ln \frac{95.4}{52.3} \right] \\ &= 302 \text{ cycles.} \end{aligned}$$

The stress intensity factor for the second part of the problem can be obtained from Fig. 6.4 for a through crack at a hole where  $a = 2.5$  cm and  $r = 0.63$  cm. The stress intensity factor  $K_{I0}$  is, for  $f\left(\frac{a}{r}\right) = 0.75$ ,

$$\begin{aligned} K_{I0} &= \sigma \sqrt{\pi a} f\left(\frac{a}{r}\right) \\ &= 483 \times 0.75 \sqrt{0.025\pi} \\ &= 102 \text{ MN/m}^{3/2} \end{aligned}$$

so that

$$\begin{aligned} N_c &= \frac{2}{\pi \times 2.1 \times 10^{-9} (1-0.02)^2 (483)^2} \left[ \frac{143}{102} - 1 - \ln \frac{143}{102} \right] \\ &= 87 \text{ cycles.} \end{aligned}$$

Thus the total expected life would be about 390 cycles with only 87 cycles remaining after the crack progressed through to the back side of the component. Note also that no finite width correction was utilized in the second part of the problem so this result assumes a very large cross section for the component.

## 8. SUMMARY

The linear elastic fracture mechanics approach to design against fracture of structural components is basically a stress intensity approach which establishes criteria for fracture instability in the presence of a crack. A basic assumption of this approach is the assumed presence of a crack or crack-like defect in the structure. The method essentially relates the stress field in the vicinity of the crack tip to the applied stress on the structure, the material properties, and the defect size necessary to cause unstable fracture.

The elastic stress field near a crack tip can be adequately described by a single parameter, the stress intensity factor  $K$ . The analytical form of the stress intensity factor depends upon the geometry of the structure and the location of the crack, while the magnitude of  $K$ , determined from this form, depends on the size of the flaw and the external loads on the body. Once the stress intensity factor for a given structural geometry is known, the stress conditions in the region of the crack tip can be established from knowledge of the applied stress and the crack size. Fracture failure in the presence of a crack-like defect is normally defined as rapid defect growth (crack propagation) which occurs whenever the crack tip stresses exceed some critical value. Since the crack-tip stress field can be described in terms of the stress intensity factor, a critical value of  $K$  can be used to define the critical conditions for failure, that is, either  $K_{Ic}$  or  $K_{oc}$ , depending on the existing stress conditions.

Because of the limited applicability of plane isothermal linear elastic stress analysis to any real cracked-body situation, fracture mechanics has relied heavily on experimental results in developing information about the effects of geometry (size), temperature, and strain-rate on fracture toughness values. As a consequence of these efforts, it is recognized that fracture toughness under conditions of plane strain, i.e.,  $K_{Ic}$ , remains independent of size considerations and can accordingly be interpreted as a fracture resistance material property.

When the critical stress intensity factor or fracture toughness value appropriate to a given set of service conditions (which include material type and yield strength, section thickness, temperature and possibly load rate) has been established, it is then possible to compute either the maximum allowable stress or flaw size which can be sustained by the structure. Crack growth rates under cyclic loading conditions can also be expressed in terms of the stress intensity factor, and are now used to describe the growth of defects from sub-critical to critical sizes. Information of this kind then can be used to establish realistic maximum operating conditions, quantitative material requirements and meaningful inspection and acceptance criteria.

Since the time of Griffith's research into the fracture properties of glass, fracture has been the subject of considerable investigation, both microscopic as well as macroscopic. However it was not until the post World War II period that a mechanics of fracture evolved, providing with the help of experiment, a basis for its application as an engineering methodology. Although currently limited in its range of applications, fracture mechanics offers materials engineers and designers, and especially those involved with NDI techniques, a useful and effective tool for the prevention of brittle fracture in structures utilizing high strength materials. While methods for effective assessment of fracture resistance of the more ductile structural materials are not firmly established, there appears to be no significant reason why this area of fracture mechanics cannot also be developed into a successful engineering methodology.

#### 9. REFERENCES

- [1] W. B. Biggs, *Brittle Fracture of Steel*, MacDonald and Evans, London, 1960.
- [2] C. F. Tipper, *The Brittle Fracture Story*, Cambridge Univ. Press, 1962.
- [3] E. Parker, *Brittle Behavior of Engineering Structures*, J. Wiley, New York, 1957.
- [4] T. Yokobori, *An Interdisciplinary Approach to Fracture and Strength of Solids*.
- [5] C. D. Beachem, *Microscopic Fracture Processes*. Fracture, Vol. 1, ed. by H. Liebowitz, Academic Press, New York, 1968.
- [6] J. R. Low, *The Fracture of Metals*, Prog. Mater. Sci. Vol. 12, 1, 1963.
- [7] N. J. Petch, *Metallographic Aspects of Fracture*. Fracture, Vol. 1, ed. by H. Liebowitz, Academic Press, New York, 1968.
- [8] S. P. Timoshenko and J. N. Goodier, *Theory of Elasticity*, McGraw Hill, New York, 1970.
- [9] G. N. Savin, *Stress Concentration Near Holes*, Pergamon Press, New York, 1961.
- [10] A. A. Griffith, *The Phenomena of Rupture and Flow in Solids*, Phil. Trans. R. Soc. Vol. A 221, 1921.
- [11] A. A. Griffith, *The Theory of Rupture*, Proc. 1st Int. Congr. Appl. Mech., Delft, 1924.
- [12] C. E. Inglis, *Stresses in a Plate Due to the Presence of Cracks and Sharp Corners*, Trans. Inst. Nav. Archit. Vol. 60, 1913.
- [13] G. C. Sih and H. Liebowitz, *On the Griffith Energy Criteria for Brittle Fracture*, Int. J. Solid Struct. Vol. 3, 1967.
- [14] V. Weiss and S. Yukawa, *Critical Approach of Fracture Mechanics*, ASTM STP No. 381, Am. Soc. Test. Mater., 1965.
- [15] G. R. Irwin, *Fracture Dynamics*, Fracturing of Metals, Am. Soc. Metals, Cleveland, 1948.
- [16] E. Gowan, *Energy Criteria of Fracture*, Weld. Res. Suppl. Vol. 20, 1955.
- [17] G. T. Hahn and A. R. Rosenfield, *Plastic Zones Generated by Cracks Growing Under Load*, Int. J. Fracture Mech., Vol. 4, 2, 1968.
- [18] G. T. Hahn, A. K. Mukherjee and A. R. Rosenfield, *Plastic Zone Formation and Stable Crack Growth in High Strength Alloy Sheets*, Engrg Fracture Mech., Vol. 2, 1971.
- [19] D. P. Rooke and P. J. Bradshaw, *A Study of Crack Tip Deformation and a Derivation of Fracture Energy*, Proc. 2nd Int. Conf. Fracture, Brighton, United Kingdom, 1969.

- [20] G. R. Irwin, Analysis of Stresses and Strains Near the End of a Crack Traversing a Plate, *Trans. Am. Soc. Mech. Engrs, J. Appl. Mech.*, 1957.
- [21] G. R. Irwin, *Fracture, Handbuch der Physik, Vol. VI, Springer, Berlin, 1958.*
- [22] G. R. Irwin, *Fracture Mechanics. Structural Mechanics*, ed. by Goodier and Hoff, Pergamon Press, New York, 1960.
- [23] P. C. Paris and G. C. Sih, *Stress Analysis of Cracks, ASTM STP No. 381, Am. Soc. Test. Mater.*, 1965.
- [24] M. L. Williams, On the stress Distribution at the Base of a Stationary Crack, *Trans. Am. Soc. Mech. Engrs, J. Appl. Mech.*, 1957.
- [25] W. F. Brown, Jr., and J. E. Srawley, Plane Strain Crack Toughness Testing of High Strength Metallic Materials, *ASTM STP No. 410, Am. Soc. Test. Mater.*, 1969.
- [26] G. C. Sih and H. Liebowitz, *Mathematical Theories of Brittle Fracture. Fracture, Vol. 2*, ed. by H. Liebowitz, Academic Press, New York, 1968.
- [27] R. W. Boyle, A. M. Sullivan and J. M. Krafft, Determination of Plane Strain Fracture Toughness with Sharply Notched Sheets, *Weld. J. Res. Suppl.*, Vol. 41, 1962.
- [28] B. Gross, J. E. Srawley and W. F. Brown, Stress Intensity Factors for a Single Edged Notch Tension Specimen by Boundary Collocation of a Stress Function, *Tech. Note D-2395, NASA, 1964.*
- [29] B. Gross and J. E. Srawley, Stress Intensity Factors for Single Edge Notch Specimens in Bending or Combined Bending and Tension by Boundary Collocation of a Stress Function, *Tech. Note D-2603, NASA, 1965.*
- [30] G. R. Irwin, J. A. Kies, and H. L. Smith, Fracture Strength Relative to Onset and Arrest of Crack Propagations, *Proc. Am. Soc. Test. Mater.*, Vol. 58, 1958.
- [31] H. F. Bueckner, Coefficients for Computation of the Stress Intensity Factor  $K_I$  for a Notched Round Bar. *Fracture Toughness Testing and its Applications, ASTM, STP 381, Am. Soc. Test. Mater.*, 1965.
- [32] E. T. Wessel, State of the Art of the WOL Specimen for  $K_{Ic}$  Fracture Toughness Testing, *Engrg Fracture Mech.*, Vol. 1, 1968.
- [33] G. R. Irwin, Relation of Stresses Near a Crack to the Crack Extension Force, *IXth Int. Congr. Appl. Mech.*, Brussels, 1956.
- [34] I. Sokolnikoff, *Mathematical Theory of Elasticity, McGraw-Hill, New York, 1956.*
- [35] G. R. Irwin, Plastic Zone Near a Crack and Fracture Toughness, *Proc. Seventh Sagamore Conf.*, Syracuse Univ., 1960.
- [36] G. R. Irwin, Fracture Testing of High Strength Sheet Materials Under Conditions Appropriate for Stress Analysis, *NRL Report 5486, Washington, D. C.*, 1960.
- [37] F. A. McClintock and G. R. Irwin, Elasticity Aspects of Fracture Mechanics. *Fracture Toughness Testing and its Applications, ASTM STP 381, Am. Soc. Test. Mater.*, 1965.
- [38] G. T. Hahn, A. K. Mukherjee and A. R. Rosenfield, Plastic Zone Formation and Stable Crack Growth in High Strength Alloy Sheets, *Engrg Fracture Mech.*, Vol. 2, 1971.
- [39] G. T. Hahn and A. R. Rosenfield, Sources of Fracture Toughness; The Relation Between  $K_{Ic}$  and the Ordinary Tensile Properties of Metals. *Applications Related Phenomena in Titanium Alloys, ASTM STP 432, Am. Soc. Test. Mater.*, 1968.
- [40] J. F. Knott, Mechanics and Mechanisms of Large-Scale Brittle Fracture in Structural Metals, *J. Mater. Sci. Eng.*, Vol. 7, 1, 1971.
- [41] Fracture Testing of High-Strength Sheet Materials, Report of a Special ASTM Committee, *Bull. Am. Soc. Test. Mater.*, 1960.
- [42] D. P. Wilhem, *Fracture Mechanics Guidelines for Aircraft Structural Applications, TR AFFDL-TR-69-111, 1970, National Tech. Inform. Service, Springfield, Va., USA.*
- [43] G. R. Irwin, *Fracture Mechanics. Structural Mechanics*, ed. by Goodier and Hoff, Pergamon Press, New York, 1960.
- [44] A. M. Sullivan, J. Stoop and C.N. Freed, The Influence of Sheet Thickness Upon the Fracture Resistance of Structural Aluminum Alloy, *Sixth Nat. Symp. Fracture Mech.*, Am. Soc. Test. Mater., 1972.

- [45] G. R. Irwin, *Fracturing and Fracture Mechanics*, T. A. and M: Report No. 202, Univ. Illinois, 1961.
- [46] *Progress in Measuring Fracture Toughness and Using Fracture Mechanics*, Mater. Res. Stand., Vol. 2, 1962.
- [47] J. Marin, *Mechanical Behavior of Engineering Materials*, Prentice Hall, Englewood Cliffs, N.J., 1962.
- [48] *Progress in Measuring Fracture Toughness and Using Fracture Mechanics*, Mater. Res. and Stand., Vol. 4, 1964.
- [49] G. R. Irwin, *Relation of Crack Toughness Measurements to Practical Applications*, Weld. J. Res. Suppl., 1962.
- [50] J. E. Srawley and W. F. Brown, *Fracture Toughness Test Methods. Fracture Toughness Testing and Its Applications*, ASTM STP 381, Am. Soc. Test. Mater., 1965.
- [51] A. M. Sullivan and C. N. Freed, *The Influence of Geometric Variables on  $K_{Ic}$  Values for Two Thin Sheet Alum. Alloys*, NRL Report 7270, U. S. Naval Research Lab., Wash., D. C., 1971.
- [52] A. M. Sullivan and C. N. Freed, *Plane Stress Fracture Resistance of One Steel Sheet and Two Titanium Sheet Alloys*, NRL Report 7332, U. S. Naval Research Lab., Wash., D. C., 1971.
- [53] C. N. Freed, A. M. Sullivan and J. Stoop, *Comparison of Plane Stress Fracture Toughness for Three Alum. Sheet Alloys*, NRL Report 7299, U. S. Naval Research Lab., Wash., D. C., 1972.
- [54] C. M. Carman, D. F. Armiento and H. Marcus, *Crack Resistance Properties of High Strength Aluminum Alloys*, Proc. First Int. Conf. Fracture, Sendai, Japan, 1966.
- [55] J. E. Srawley, *Small Fatigue Cracks as Fracture Origins in Tests of High Strength Steel Sheet*, Proc. Am. Soc. Test. Mater., Vol. 62, 1962.
- [56] *Screening Tests for High Strength Alloys using Sharply Notched Cylindrical Specimens*, Mater. Res. and Stand., Vol. 4, 1964.
- [57] V. F. Zackay, W. W. Gerberich and E. R. Parker, *Structural Modes of Fracture. Fracture*, Vol. 1, ed. by H. Liebowitz, Academic Press, New York, 1968.
- [58] E. A. Steigewald, *Plane Strain Fracture Toughness of High Strength Materials*, Engrg Fracture Mech., Vol. 1, 1969.
- [59] E. T. Wessel, *Linear Elastic Fracture Mechanics for Thick Walled Welded Steel Pressure Vessels: Material Property Considerations. Practical Fracture Mechanics for Structural Steel*, Chapman and Hall/UKAEA, 1969.
- [60] A. W. Clark and E. T. Wessel, *Application of Fracture Mechanics to Medium Strength Steels*, ASTM STP 463, Am. Soc. Test. Mater., 1969.
- [61] J. M. Barsom and S. T. Rolfe,  *$K_{Ic}$  Transition-Temperature Behavior of A 517-F Steel*, Engrg Fracture Mech., Vol. 2, 1971.
- [62] G. R. Irwin, *Linear Fracture Mechanics, Fracture Transition and Fracture Control*, Engrg Fracture Mech., Vol. 1, 1968.
- [63] F. J. Loss and W. F. Pellini, *Coupling of Fracture Mechanics and Temperature Transition Approaches to Fracture-Safe Design. Practical Fracture Mechanics for Structural Steel*, Chapman and Hall/UKAEA, 1969.
- [64] G. R. Irwin, *Crack Toughness Testing of Strain-Rate Sensitive Materials*, ASME Paper No. 63-WA-217, 1963.
- [65] G. R. Irwin and A. A. Wells, *A Continuum-Mechanics View of Crack Propagation*, Metall. Rev., Vol. 10, 38, 1965.
- [66] J. M. Krafft and G. R. Irwin, *Crack Velocity Considerations. Fracture Toughness Testing and its Applications*, ASTM STP 381, Am. Soc. Test. Mater., 1965.
- [67] L. K. Shoemaker and S. T. Rolfe, *The Static and Dynamic Low Temperature Crack Toughness Performance of Seven Structural Steels*, Engrg Fracture Mech., Vol. 2, 1971.
- [68] J. M. Krafft and A. M. Sullivan, *Effects of Speed and Temperature on Crack Toughness and Yield Strength in Mild Steel*, Trans. Amer. Soc. Metals, Vol. 58, 1965.
- [69] J. M. Krafft, *Correlation of Plane Strain Crack Toughness With Strain Hardening*

- Characteristics of a Low, Medium and a High Strength Steel, Appl. Mater. Res., Vol. 3, 1964.
- [70] J. Eftis and J. M. Krafft, A Comparison of the Initiation With the Rapid Propagation of a Crack in a Mild Steel Plate, Trans. Am. Soc. Mech. Engrg., J. Bas. Engrg, Vol. 87, 1965.
- [71] C. E. Turner and J. C. Randon, Fracture Toughness Measurements on Low Strength Structural Steels, Proc. Second Int. Conf. on Fracture, Brighton, U.K., 1969.
- [72] B. Cotterell, Notes on the Path and Stability of Cracks, Int. J. Fracture Mech., Vol. 2, 1966.
- [73] J. E. Srawley, Linear Elastic Fracture Mechanics - A Review of Principals and Methods. Practical Fracture Mechanics for Structural Steel, Chapman and Hall/UKAEA, 1969.
- [74] A. A. Wells, Notched Bar Tests, Fracture Mechanics and Strength of Welded Structures, Br. Weld. J., Vol. 12, 1, 1965.
- [75] F. M. Burdekin and D. E. Stone, The Crack Opening Displacement Approach to Fracture in Yielding Materials, J. Strain Analy. Vol. 1, 2, 1966.
- [76] D. S. Dugdale, Yielding of Steel Sheets Containing Slits, J. Mech. Phys. Solids, Vol. 8, 1960.
- [77] A. R. Rosenfield, P. K. Dai and G. T. Hahn, Crack Extension and Propagation Under Plane Stress, Proc. First Int. Conf. Fracture, Sendai, Japan, 1965.
- [78] J. N. Goodier and F. A. Field, Plastic Energy Dissipation in Crack Propagation. Fracture of Solids, J. Wiley, New York, 1963.
- [79] F. M. Burdekin, Crack Opening Displacements, A Review of Principles and Methods. Practical Fracture Mechanics for Structural Steel, Chapman and Hall/UKAEA, 1969.
- [80] A. A. Wells, Crack Opening Displacements from Elastic-Plastic Analyses of Externally Notched Tension Bars, Engrg Fracture Mech., Vol. 1, 1969.
- [81] A. Cowan and N. Kirby, The Application of COD Measurements to Large Scale Test Behavior. Practical Fracture Mechanics for Structural Steel, Chapman and Hall/UKAEA, 1969.
- [82] G. R. Irwin, Fracture Testing of High Strength Sheet Materials Under Conditions Appropriate for Stress Analysis, NRL Report 5486, U. S. Naval Research Lab., Wash., D. C., 1960.
- [83] J. M. Krafft, A. M. Sullivan and R. W. Boyle, Effect of Dimensions on Fast Fracture Instability of Notched Sheets, Proc. Crack Propagation Symp., Vol. I, Cranfield, The College of Aeronautics, 1962.
- [84] C. N. Freed, A. M. Sullivan and J. Stoop, Crack Growth Resistance Characteristics of High-Strength Sheet Alloys, NRL Report 7374, U. S. Naval Research Lab., Wash., D. C., 1972.
- [85] R. H. Heyer and D. E. McCabe, Plane Stress Fracture Toughness Testing Using a Crack-Line Loaded Specimen, Engrg Fracture Mech., Vol. 4, 1972.
- [86] Fracture Toughness Evaluation by R-Curve Methods, ASTM STP 527, Am. Soc. Test. Mater., 1973.
- [87] J. R. Rice, Mathematical Analysis in the Mechanics of Fracture. Fracture, Vol. 2, ed. by H. Liebowitz, Academic Press, New York, 1968.
- [88] Begley, J. A. and Landis, J. D., The J Integral as a Fracture Criterion. Fracture Toughness, Proceedings of the 1971 National Symposium on Fracture Mechanics, Part II, ASTM STP 514, Am. Soc. Test. Mater., 1972.
- [89] Landis, J. D. and Begley, J. A., The Effect of Specimen Geometry on  $J_{IC}$ . Fracture Toughness, Proceedings of the 1971 National Symposium on Fracture Mechanics, Part II, ASTM STP 514, Am. Soc. Test. Mater., 1972.
- [90] R. J. Bucci, P. C. Paris, J. D. Landis, and J. R. Rice, J Integral Estimation Procedures. Fracture Toughness, Proceedings of the 1971 National Symposium on Fracture Mechanics, Part II, ASTM STP 514, Am. Soc. Test. Mater., 1972.
- [91] Liebowitz, H. and Eftis, J. M., On Nonlinear Effects in Fracture Mechanics, Engrg Fracture Mech., vol. 3, 1971.
- [92] H. Liebowitz and J. Eftis, Correcting for Nonlinear Effects in Fracture Toughness Testing, Nucl. Engrg, Des., Vol. 8, 4, 1972.



- [93] W. S. Pellini, Integration of Analytical Procedures for Fracture-Safe Design of Metal Structures, U. S. Naval Research Lab. Report 7251, 1971.
- [94] R. J. Goode and R. W. Judy, Jr., Fracture-Safe Design of Aluminum and Titanium Alloy Structures, U. S. Naval Research Lab. Report 7281, 1972.
- [95] G. R. Irwin, Characteristics of Part-Through Cracks in Tension. The Surface Crack: Physical Problems and Computation Solutions, Am. Soc. Mech. Engrs., 1972.
- [96] C. D. Little and P. M. Bunting, The Surface Flaw in Aircraft Structures and Related Fracture Mechanics Analysis Problems. The Surface Crack: Physical Problems and Computational Solutions, Am. Soc. Mech. Engrs, 1972.
- [97] R. C. Shaw and A. S. Kobayashi, On the Surface Flaw Problem. The Surface Crack: Physical Problems and Computational Solutions, Am. Soc. Mech. Engrs, 1972.
- [98] P. C. Paris, The Growth of Cracks Due to Variations in Loads, Ph.D. Dissertation, Lehigh University, 1962.
- [99] P. C. Paris and F. Erdogan, A Critical Analysis of Crack Propagation Laws, J. Bas. Engrg. Trans. Am. Soc. Mech. Engrs, Series D, Vol. 85, 1963.
- [100] H. H. Johnson and P. C. Paris, Sub-Critical Flaw Growth, Engrg Fracture Mech., Vol. 1, 1, 1968.
- [101] R. E. Zinkham, H. Liebowitz and D. L. Jones, Fracture Toughness - Strength Relationships in Al-Zn-Mg-Cu Alloys. Int. Conf. on Mech. Behavior of Mater., Kyoto, Japan, 1971.
- [102] R. J. Cooke and C. J. Beevers, The Effect of Load Ratio on the Threshold Stresses for Fatigue Crack Growth in Medium Carbon Steels. To appear in Engrg Fracture Mech.
- [103] R. G. Forman, N. E. Kearney and R. M. Engel, Numerical Analysis of Crack Propagation in Cyclic Loaded Structures, J. Bas. Engrg, Trans. Am. Soc. Mech. Engrs, Vol. 89, 3, 1967.
- [104] D. Brock and J. Schijve, The Influence of the Mean Stress on the Propagation of Fatigue Cracks in Aluminum Alloy Sheet. Nat. Aero. Res. Inst. Report NLR-TM-M2111, Amsterdam, 1963.
- [105] J. C. McMillan and R. M. N. Pelloux, Fatigue Crack Propagation Under Program and Random Loads. Fatigue Crack Propagation, ASTM STP 415, Am. Soc. Test. Mater., 1967.
- [106] J. Schijve, The Accumulation of Fatigue Damage in Aircraft Materials and Structures, Symposium on Random Load Fatigue, AGARD CP-118, 1972.
- [107] J. Schijve, Effects of Test Frequency on Fatigue Crack Propagation Under Flight-Simulation Loading, Symposium on Random Load Fatigue, AGARD-118, 1972.
- [108] B. M. Hillberry, Fatigue Life of 2024-T3 Aluminum Alloy Under Narrow- and Broad-Band Random Loading. Effects of Environment and Complex Load History on Fatigue Life, ASTM STP 462, Am. Soc. Test. Mater., 1970.
- [109] Palmgren, A., Die Lebensdauer von Kugellager, Z.V.D.I., Vol. 68, 1924.
- [110] Miner, M. A., Cumulative Damage in Fatigue, J. Appl. Mech., Vol. 12, 1945.
- [111] Langer, B. F. Fatigue Failure from Stress Cycles of Varying Amplitude, J. Appl. Mech., Vol. 4, 1937.
- [112] A. M. Freudenthal and R. A. Heller, On Stress Interaction in Fatigue and a Cumulative Damage Rule, J. Aerospace Sc., Vol. 26, 1959.
- [113] H. J. Corten and T. J. Dolan, Cumulative Fatigue Damage. Int'l. Conf. on Fatigue of Metals. Inst. Mech. Engrg, London, 1956.

## APPENDICES TO CHAPTER IV

The following appendices are included to provide additional information on several testing methods of particular interest in the aircraft field.

Appendix IV-1	Resistance Method (J. I. Bluhm) . . . . .	74
IV-2	The Kuhn-Hardrath Method (J. I. Bluhm) . . . . .	99
IV-3	Crack Propagation Laws (J. I. Bluhm) . . . . .	95
IV-4	Environmental Effects in Fracture (H. H. Johnson) . . . . .	110
IV-5	Summary of Limitations (J. I. Bluhm) . . . . .	118

Appendix IV-1  
RESISTANCE METHOD  
J. I. Bluhm

If a moderately thin plate with a through fatigue induced crack, either edge cracked or center cracked, is loaded so to extend the crack, the fracture surface will in general develop with a continuously varying appearance starting as a macroscopically flat fracture and gradually shifting to a gross shear mode. For thicker plates, the ultimate fracture will in general consist of a mixed flat "valley" or "shelf" sandwiched between two shear surfaces. This fracture pattern depends also on the specific material and temperature of the test.

Figure 1 schematically displays the range of typical fracture growth patterns one might obtain for a given material over a range of temperatures. Characteristically, the onset of propagation starts in the mid-thickness region and is generally a flat fracture mode; as propagation progresses this may or may not, depending upon the test temperature, gradually shift either partially or wholly to shear fracture. If the fracture path is long enough (wide plate) a steady state pattern is eventually achieved and the crack progresses with no further changes in proportions of flat to shear fracture. The flat mode of fracture absorbs less energy per unit area than the shear mode so there is a gradual increase in the resistance to fracture as the crack progresses, eventually achieving a steady state distribution.

The variation of this resistance with crack length is now generally called the "Resistance Curve," and fracture prediction techniques based upon this resistance curve have been characterized as Resistance Methods.

Attempts to determine the shape of the resistance curves frequently result, at some critical load for a given crack size, in premature unstable or catastrophic fracture and data beyond this point cannot therefore be obtained. In the historical development of fracture mechanics, however, it was precisely these instability points which were identified as characterizing the material, see e.g., Irwin and Kies (1). In one instance, common to thick plates, the plane strain fracture toughness was closely identified with the acoustic emission known as "pop-in" which occurred when the initial starter crack advanced spontaneously. It is not so certain today that pop-in assures a valid plain strain fracture toughness value. However, it is generally appreciated that a valid plane strain fracture toughness value is in fact a material constant. In another instance, more commonly noted in thin sheet, the instability was identified with the plane stress fracture toughness. This value, labeled  $G_c$ , is a function of thickness and, in fact, of plate width as well and cannot be construed as a material characteristic.

In any event, these "critical" values  $G_{Ic}$  and  $G_c$  are merely specific instability points on the more general R curve and could be noted as  $R_{Ic}$  and  $R_c$ . Again note that the instability associated with  $G_{Ic}$  is generally uniquely located on the G - a plane, whereas that associated with  $G_c$  is not.

In the early years of fracture mechanics, emphasis was principally directed toward low toughness, high strength, bulky materials and the interest lay principally in determining and understanding plane strain fracture criteria. Continued growth of interest has developed with respect to the plane stress situation corresponding to the phenomenon generally encountered in thin sheet such as aircraft skins, etc. Additionally, the advent of large thick wall vessels of intermediate and high toughness for reactor components has led to a thrust toward a more in-depth understanding of fracture mechanics, no longer limited by the analytical method of linear elastic fracture mechanics.

The resistance method provides some of the basic material characterization necessary for this vital task. The role of strain-rate on the resistance curve still remains a gap to be filled as does the problem of translation from plate type specimens (from which all R curves are obtained) to other configurations. Nevertheless, in conjunction with appropriate structural analysis it promises to provide a universal tool for assuring structural integrity of critical elements and for implementing adequate fail-safe design criteria.

Curve R of Fig. 2, originating at the initial dimensionless crack length  $a_0/w$ , schematically portrays this changing unit resistance to fracture (i.e., in terms of energy per unit fracture area) as a function of crack extension normalized with respect to plate width W. This R curve characterizes the material for the given thickness and temperature of test. However, the behavior of a cracked specimen under load depends not only on this resistance curve but also upon the rate, with respect to crack length, at which stored elastic strain energy is released during crack propagation. These are the "G" (elastic strain energy release rate) curves in Fig. 2 which characterize the structures as distinct from the material. The problem of the designer is to integrate these material characteristics and the structural characteristics as reflected by these R and G curves and assure a fail-safe structure.

These G curves can be determined either experimentally or analytically. Stable or catastrophic fracture depends, as we will see, upon the relative shapes of these R and G curves. The level of the energy release rate is a function of the load. When the load is raised to a level such that the release rate (energy available for propagation) just exceeds, for the given crack size, the resistance rate (energy required for propagation), then, according to linear elastic fracture mechanics criteria, propagation can proceed spontaneously; the various G curves (Fig. 2) are particular members of a family of G curves for specific values of applied load. It is apparent that propagation does not take place until the load in the specimen reaches a value, such that the corresponding G curve goes through the point O, corresponding to the initial crack length  $a_0$ . As this load is exceeded, the available energy,  $G$ , becomes greater than that required for propagation, R, and the crack extends. In the particular case illustrated in Fig. 2 the growth which occurs at point O will be spontaneous and rapid and often even accompanied by an audible "pop"; subsequently the crack will come to rest at the point A. This pop or pop-in behavior is attributable to the peculiar shape of the R curve shown, particularly its low slope at the onset of fracture,

corresponding to the "thumbnail" flat fracture visible in Fig. 1. This pop-in phenomena, in conjunction with the appropriate relations between load, crack length and energy release rate functions, has been used as a means of determining the minimum possible value of propagation resistance toughness, even in a thin specimen where the shear fracture mode predominates and tends to obscure this minimum value. This minimum toughness has been called the plane strain fracture toughness,  $G_{Ic}$ , and, as stated earlier, is considered to be characteristic of the material (and temperature) and independent of specimen geometry.

The extent of pop-in instability and its significance is dependent on the relative shapes of the resistance,  $R$ , and energy release rate,  $G$ , curves. The pop-in may, in fact, be completely suppressed - intentionally - by control of (a) the nature of the loading after the critical load is reached and/or (b) the specimen configuration.

Two extremes of loading conditions are frequently considered; one corresponding to a very "soft" system equivalent to constant loading; the other, corresponding to a "hard" system equivalent to constant deflection "loading." The existence of unstable growth, such as pop-in phenomena or, contrariwise, the slow steady growth of a crack, is highly dependent on which of these types of loading condition prevails. Weiss, Grewal, Rosenberg, and Lin (2) have discussed this in some detail. This effect will be discussed further in this section.

Figures 3 and 4 illustrate an important difference in behavior for the single edge notch and the three point notch bend specimens. In both cases the constant load curve behaves in the same fashion as the tension sheet, i.e., with a monotonically rising  $G$  vs  $a$  curve, but the constant deflection curves show display negative slopes in all instances except for the shorter critical cracks of the single edge notch specimens. This negative slope facilitates controlled stable growth even in those materials which would otherwise tend to fracture spontaneously (Bluhm 3) and permits multiple fracture toughness measurements to be made on a single specimen even in rate sensitive materials. Such procedures have indeed been exploited by Bluhm, Gordon, and Morrissey (4) in double cantilevered specimens which can be designed to exaggerate this negative slope.

Clausing (5) has analyzed, in detail, the criteria for stable crack growth for a variety of specimens for both load controlled and/or displacement controlled systems. He relates the stability in a displacement controlled specimen to the relation

$$\frac{da}{d\Delta} = \frac{f_1 (MEWG_A)^{1/2}}{\frac{dG_A}{d(a/w)} - (f_2 - f_3)G_A}$$

where

$$f_1 = \frac{2Y(a/w)^{1/2}}{EBA} \text{ (dimensionless parameter)}$$

$$f_2 = \frac{2}{Y} \frac{dY}{d(a/w)} + \frac{1}{(a/w)} \text{ (dimensionless parameter)}$$

$$f_3 = \frac{4MY^2(a/w)}{EBA} \text{ (dimensionless parameter)}$$

and

$G_A$  = the elastic energy release rate (available energy)

$Y$  = a dimensionless geometrical parameter after e.g. Srawley and Gross (6)

$E$  = Young's modulus

$B$  = the thickness of the specimen

$W$  = the width of the specimen

$A$  = the compliance

$a$  = the crack length

$\Delta$  = the displacement

$M$  = the factor 1,  $(1 - \nu^2)$  or  $(1 + \nu^2)$  depending upon the fracture mode and stress state.

Clausing attributes the stability of the crack growth to negative values of  $(f_2 - f_3)$ . Figure 5 shows the relative shapes of the  $(f_2 - f_3)$  vs  $a/w$  curves for various types of high compliance specimens. The effect of low compliance is also shown for the straight double cantilever beam specimen.

It is to be noted that Clausing has presented a rate insensitive behavior for the purposes of his analysis. Rate sensitivity would require more severe constraints to assure stable growth. Bluhm et al (4) have attempted to account for this by providing specimen configurations with a relatively high negative  $dG_A/da$ .

Depending upon the material and thickness, etc., the initial flat "thumbnail" fracture may be sufficiently suppressed so that a well defined pop-in is not observed even in otherwise well behaved tensile sheet specimens. Nevertheless, considering again the type of resistance,  $R$ , and energy release rate,  $G$ , curves shown in Fig. 2, note that the spontaneous "Pop-in" extends the crack from "0" to "A". Note further that as the load is continuously increased beyond this so-called pop-in load, the crack continues to grow, now more slowly, along the path "AB" until finally, at a load corresponding to the uppermost curve where the  $G_A$  and  $G_R$  curves are tangent to each other, the crack again propagates spontaneously without further arrest.

With this specimen, load configuration and material resistance ( $R$ ) curve illustrated, one obviously, could not actually determine the resistance curve; since the system does exhibit the instability points at 0 and B. Such a test could, however, provide the unique and characteristic plane-strain fracture toughness,  $G_{Ic}$ , corresponding to the point 0 and a non-unique, non-characteristic "mixed mode" toughness,  $G_c$ , corresponding to the point B.

This mixed mode fracture plane strain value,  $G_{Ic}$ , is the width and the thickness though the  $R$  curve is in tangent point common to toughness,  $G_c^*$ , should predicted effect of width relationship for the

ness,  $G_c$ , determined by the instability condition in contrast to the material characteristic. It is recognized as being dependent upon both specimen. This width dependence is readily rationalized as follows: width (for rate insensitive materials) the  $G$  curve is not and the the instability point corresponding to the apparent fracture predicted to vary with width. Figure 6, after Bluhm (7), shows the present  $G_c$  based upon a simple approximate but reasonable analytical curve defined as follows:

$$R = G_c \left[ 1 - e \left( - \frac{a-a_0}{k} \right) \right] \quad (1)^*$$

where  $a_0$  and  $a$  are the initial and instantaneous half crack lengths and  $k$  is a constant dictating the crack extension required for the steady state fracture mode to become essentially established.

It is noted that we have defined  $R$  in terms of energy absorption rate, as has been the custom generally. More recently some investigators, Clausing (5) and Meyer and McCabe (8), have chosen to define  $R$  in terms of paralleling stress intensity, i.e., ksi $\sqrt{in}$ . Conversion is achieved via relations of the form

$$GE = K^2 \quad (\text{plane stress})$$

$$GE = (1-\nu^2)k^2 \quad (\text{plane strain})$$

In this form  $K$  exhibits some ambiguity because of its dependence on the stress state whereas if conventional energy/unit area is used, as for  $R$ , this value is independent (analytically) of which stress state is presumed to exist. Meyer and McCabe (8) have reported Irwin's suggestion of an integrated set of nomenclature to distinguish regions of the "R" curve as follows:

$G_{Ic}$  (or  $K_{Ic}$ ) - Plane Strain Fracture Toughness - Associated with an instability point, i.e., point 0 in Fig. 2.

$G_c$  (or  $K_c$ ) - Plane Stress (Mixed Mode) Fracture Toughness - Associated with an instability point, i.e., point B in Fig. 2.

$G_R$  (or  $K_R$ ) - General Resistance - Associated with any point on the resistance curve - not necessarily an instability point.

Since the resistance curves for a plate do in general tend to approach a stable level, independent of crack growth, provided the plate is adequately wide, it is suggested that the symbol  $G_c$  (or  $K_c$ ) should be reserved for this steady state level which is in fact characteristic of the material (for a given thickness) and that the instability point should be associated with  $G_c^*$  (or  $K_c^*$ ). These various regions (points) are shown in Fig. 2. This notation is that used in Fig. 6.

The significance of the distinction of these terms will be expanded upon in the remaining text.

Clausing (5) has used the notation  $G_A$  for the applied (or available) Elastic Energy Release Rate. Thus, adding this to the list we have

$G_A$  (or  $K_A$ ) - General Elastic Energy Release Rate associated with any point of the curve formerly identified as the  $G$  curve.

\*We have here ascribed to the symbol  $G_c$  the actual value of the fracture toughness corresponding to steady state shear lip development consistent with the thickness.

It is suggested that the following consistent notation be adopted:

Available Energy Curve

$G_A$  (or  $K_A$ ) Elastic Energy Release Rate - formerly the  $G$  curve

Required Energy Curve

$G_R$  (or  $K_R$ ) General Resistance Associated with any point on R curve

$G_c$  (or  $K_c$ ) Resistance Associated with Steady State Level of Shear Development

$G_c^*$  (or  $K_c^*$ ) Resistance Associated with Mixed or Plane Stress Fracture Mode and Instability Point

$G_{Ic}$  (or  $K_{Ic}$ ) Resistance Associated with Plane Strain Fracture and Instability Point.

Recall how we describe the resistance curve by Eq. 1. The general shape of that curve was described by Irwin and Kies (9) and Kraft, Sullivan and Royle (10) and is shown in Fig. 7 with several  $G_A$  curves to illustrate the transition from slow to rapid crack growth.

A more general representation of the resistance curve, taking into account, at least qualitatively, both the initial flat fracture and the ultimate shear or mixed fracture (per Fig. 1) is suggested as follows:

$$R = G_R = G_{Ic} \left[ e^{-\rho \left( \frac{a-a_0}{k} \right)} \cos \left( \frac{a-a_0}{k} \right) \right] + G_c \left[ 1 - e^{-\left( \frac{a-a_0}{k} \right)} \right] \text{ for } a \geq a_0 \quad (2)$$

It can readily be verified that this permits the smooth transition from  $G_{Ic}$  (flat fracture) to the steady state (mixed) mode  $G_c$  and qualitatively suggests the R curve shown in Fig. 2.

It is further noted that this form for the resistance curve leads to prediction of the observed pop-in phenomena and of the width effect in unstable crack growth corresponding to  $G_c^*$ .

Clausing (5) has proposed a simple alternate form given by

$$G_R = G_{RC} \left[ 1 - \rho \left[ \exp - \left( \frac{\lambda - A_0}{3t} \right) \right] \right] \quad (3)$$

where  $t$  is the thickness and  $G_{RC}$  is the volume of  $G_R$  at which the crack starts to propagate. The shape of the curve is also shown in Fig. 7. Note the nonzero intercept at  $A = A_0$ . It is now clear that this latter form can reasonably predict the occurrence of pop-in.

Goode and Judy (11) have suggested that "unstable fracture in the brittle mode is not possible for rising  $G_R$  curves." However, it should be evident from the present discussion that stability or instability is the result of the interplay between the R curve and the G curve. Figure 3, for example, shows schematically such an interplay which does indeed suggest a potential instability - even for rising  $G_R$  curves.

The interplay between the curves of energy rate required for propagation,  $G_R$  and the energy rate available for propagation,  $G$ , leads to a variety of possible responses ranging from slow crack extension to unstable catastrophic propagation. Intermediate phenomena include combinations of slow growth, pop-in, and catastrophic growth. The particular behavior which actually takes place is highly dependent upon the overall system flexibility which dictates propagation under constant load on one extreme, and propagation under constant deflection on the other extreme. The discussion immediately following is taken from Bluhm (12).

Consider the curves initially proposed by Irwin and Kies (9) and Kraft, et al (10) and shown in Fig. 7. Two points are worth noting. First, as the load is gradually increased, thus increasing the elevation of the  $G_A$  curve, propagation of the crack takes place under slow equilibrium conditions. This propagation begins upon the application of an infinitesimal load, as long as the resistance curve,  $G_R$ , originates at a zero level and is not vertical at the initial crack length,  $a_0$ , since, even for infinitesimal load under these conditions, the energy release rate,  $G_A$ , is greater than the resistance,  $G_R$ . This prediction of crack extension under infinitesimal load is contrary to observation. Pursuing the Irwin-Kraft model of Fig. 7 further, note that as the load is increased, the crack continues to spread under equilibrium conditions until the load is such that the  $G_A$  curve corresponding to the increased load is just tangent to the  $G_R$  curve, at point F. At this point, the crack becomes unstable and grows rapidly. This "typical"  $G_R$  curve does not reflect the frequent observation where the initial cracking is the plane strain "thumbnail pop-in," mentioned earlier.

Taking these discrepancies into account, Bluhm (13) has suggested the  $G_R$  curve as shown in Fig. 8. (See also Eq. 2.) Here the horizontal (or near horizontal) segment of the  $G_R$  curve, at small values of crack length or tension, is associated with the thumbnail plane strain fracture and (except for possible rate effects) is insensitive to crack length. When the load is raised to the point where the corresponding  $G_A$  curve [identified as  $G_A$  (pop-in)] intercepts the origin of the  $G_R$  curve as P, then the crack advances under constant load in a burst and comes to rest at point A. Subsequently, on continued loading,

slow growth takes place from point A to point F where rapid rupture finally occurs at a load corresponding to the  $G_A$  (pop-thru) curve. This instability is usually associated with the  $G_C$  value. At larger values of crack extension, one would expect the  $G_R$  curve to level off at a  $G_C$  value representative of the material (and the thickness) tested. The transition from the  $G_{IC}$  level to the  $G_C$  level is thought to be associated with the transient growth of the shear lips in accordance with the sketch of Fig. 9.

A pre-machined but inadequately sharp "crack" may first extend through a minute region of restricted local plastic flow before it forms into a crack sharp enough to initiate the flat plane strain fracture normally observed and customarily identified as the "thumbnail" fracture.\* This eventual plane strain fracture front progresses most rapidly in the plane of the machined crack and in a direction normal to the initially straight front at the thickness centerline and tends to lag behind near the free lateral surfaces. As the flat fracture approaches these stress-free lateral surfaces, the failure transforms to a shear mode of failure forming the normal shear lips. As the crack extends, the incremental growth process stabilizes to a steady state situation where the relative shear lip and flat fracture proportions of the fracture surfaces remain essentially constant. This latter process is the one illustrated in Fig. 9. In the special case of a minute plastic zone at the crack tip the corresponding resistance curve might be visualized in a general manner as shown in Figure 10. Here the short ductile initiation region is followed by the usual flat fracture (thumbnail), the transition range where the shear lips start to form, and, finally, the steady state propagation region.

It is worth noting that though the shape of the  $G_R$  curve of Fig. 10 could readily lead, in conjunction with a  $G_A$  curve shown, to a well defined "pop-in", the resulting toughness value calculated using the pop-in load would be a fictitiously high one corresponding to the level "O" rather than the level "L". Figure 11 shows an alternate  $G_R$  curve which would, in principle, also lead to erroneous values of  $G_{IC}$  if based upon the usual instability criteria.

For the situation sketched in Fig. 10, a valid determination of  $G_{IC}$ , particularly if the material being tested is not rate sensitive, can, nevertheless, be obtained by use of modified specimens having a highly negative  $G_A$  vs  $a$  slope. Such a configured specimen leads to a highly stable crack growth condition, at least after the initial pop-in. The subsequent propagation energy rate can then be identified as  $G_{IC}$  corresponding to the level L (in Fig. 10 or 11).

One additional comment on the  $G_A$  curve is in order. It has been presumed that the  $G_A$  curve is independent of fracture modes, i.e. flat fracture vs shear fracture. This is probably not so - on an exact basis. We have noted that the propagation mode actually changes as shown in Fig. 9; the  $G_A$  curve might be modified to reflect this change, though the correction is not expected to be significant. Figure 12 shows schematically two such curves, one for flat fracture (corresponding to  $G_{IC}$ ) and one for mixed fracture, i.e., flat center region plus shear lip corresponding to  $G_C^{**}$ . The transitional behavior associated with the change from flat to mixed fracture is suggested by the dotted line.

In the foregoing discussion it has been assumed that in the course of crack propagation, the gross stress or load remained constant. For very long specimens, or "soft" testing machines, such a condition may be approached. However, in most instances it is highly unlikely that such an extreme degree of "softness" will be encountered; furthermore, with the economic motivation to cut specimen size to a minimum, specimens are not apt to be very long or "soft". In the following analysis [see also Weiss et al 2] therefore, we have considered, as the alternative extreme condition, the situation in which crack propagation occurs under a constant deflection boundary condition. In any real test, the load conditions will probably be intermediate between the constant load and the constant deflection condition.

Defining the compliance,  $c$ , in terms of the deflection,  $\delta$ , load,  $p$ , and thickness,  $t$ , as follows

$$\bar{c} = \frac{\delta}{p/t} \quad (4)$$

one can write immediately, for the elastic energy release rate  $G$ , the relation

$$G = \frac{1}{2} (p/t)^2 \frac{d\bar{c}}{da} \quad (5)$$

\* A related observation has been reported by Blum (14) in Aluminum 5086 H14 sheet. The toughness curve (resistance curve) shows an extremely high peak near the end of the energy range of interest normal for this material. In this case the failure is by plane stress rather than plane strain fracture.

\*\*  $G_C$  is commonly identified with fractures which are not 100% flat, i.e., they contain contributions of both flat and shear fracture.

where  $a$  is the crack length. From this relation one can express the critical load,  $P_0$ , at which, for a given fracture toughness,  $G_0$ , the crack starts to propagate\*; thus we obtain

$$P_0 = 2G_0 t^2 / (d\bar{c}/da)_{a=a_0} \quad (6)$$

where  $a_0$  is the crack length at initiation.

If now, after propagation has started, one assumes a quasi-static quasi-equilibrium condition with fixed end deflection, one can obtain the following relation between the instantaneous load,  $p$ , and the compliance

$$p\bar{c} = P_0 \bar{c}_0 \quad (7)$$

which merely imposes the initial assumption that the deflection,  $\delta$ , is a constant during the fracturing process (and hence equal to the deflection at the onset of fracturing). Substituting this and Eq. 6 into Eq. 5, we obtain

$$G_A(\text{const defl}) = G_0 \frac{\bar{c}_0}{\bar{c}} \frac{d\bar{c}/da}{(d\bar{c}/da)_{a=a_0}} \quad (8)$$

Figures 3 and 4 show the relative shapes of the Energy Release Rate curve  $G$  for both constant load deflection conditions.

It is obvious that, if instabilities occur in a test aimed at determining the  $G_R$  curve, the test effort is frustrated. The  $G_R$  curve would be determinable only to crack lengths up to the instability point. Negative slopes of the  $G_A$  vs  $a$  curve tend to suppress this instability. Bluhm (3,4) has suggested that, by special specimen design,  $G_A$  curves of the type shown in Fig. 13, tending to exaggerate this negative slope, can be achieved.

Both the specimen contour and the loading configuration (const load - vs. const deflection) can be controlled to achieve this goal. Clausen (5) has analyzed crack line loaded specimens and showed conditions under which they are stable. He concludes that, for a "hard test" system, stability of crack growth in such specimens is insured over the entire range of crack extension.

Systems used successfully in this and/or similar ways, even for brittle materials, have been described by Bluhm et al (4), and Heyer and McCabe (8,15).

Heyer and McCabe have championed the use of R curve determinations for characterization of materials, and pointing out that such a representation would be applicable across the spectrum of brittle and tough materials.

From the prior discussion it is apparent that, since the resistance curve reflects to a great extent the transition from flat to shear mode of fracture (and the relative properties of these modes), the thickness may have an important role in shaping this resistance curve.

There is considerable evidence in the literature which shows that the tendency toward brittle behavior in plates is exaggerated as the thickness increases. Thin specimens tend to fail in a ductile mode and at net stresses generally above the yield strength, whereas thick specimens show marked tendencies toward brittleness and low stress failure. In terms of crack propagation resistance or fracture toughness, typical results are given in Fig. 14. Note that in the thin section the fracture is exclusively shear, and has been identified with "plane stress" fracture. Beyond a critical value of thickness, the fracture takes on a dual appearance - part shear and part flat. For very thick plates, the fracture toughness approaches a value dictated by a plane strain state near the crack tip. This value is the plane strain fracture toughness,  $G_{Ic}$ , frequently associated with "pop-in" and is the controlling toughness parameter in low stress failure.

It appears that the shear lips which constitute final shear failure tend toward a maximum size independent of the specimen size and depend only on material and temperature. This concept of a constant shear lip size is consistent with a plastic zone size governed by yield strength and fracture toughness.

\* Here  $G_0$  is the fracture toughness corresponding to the initial mode of crack propagation; generally, it will be equivalent to the plane strain toughness,  $G_{Ic}$ .

From fracture mechanics relationships (24), the dimensionless plastic zone size  $r_p/t$  is given by the equation, Irwin (16),

$$r_p/t = \frac{1}{2\pi} \left( \frac{K_c}{\sigma_{ys}} \right)^2$$

where

$$K_c^2 = G_c H$$

Now, letting

$$\frac{1}{\pi} \left( \frac{K_c}{\sigma_{ys}} \right)^2 = \beta$$

this dimensionless plastic zone size can be expressed in the form

$$r_p/t = \beta/2\pi$$

There is a considerable body of data which supports the contention that the transition from flat to full shear fracture is closely related to this plastic zone size. Figure 15 shows a collection of data based upon a variety of heat treatments and thicknesses of high strength steels and titanium alloys. Based upon these data, it is reasonable to conclude that fracture is predominantly of a shear mode, provided  $\beta \geq 2\pi$ , i.e., if the plastic zone is at least as great as the thickness of the plate. On the other hand, in a thicker plate (smaller ratio of plastic zone size to thickness) flat fracture error starts to appear.

The concept of a characteristic shear lip thickness dependent, for a given material, essentially only upon temperature of test, leads to a simple model which predicts, at least qualitatively, thickness effects and observed transitional behavior. Figure 16, after Blum (17) shows schematically the consequence of the critical thickness concept on a series of notched specimens of different thicknesses tested at various temperatures. Keeping in mind the fact that the shear lip mode of fracture is volume controlled and reflects a higher toughness level than the flat fracture mode, it is evident that the variation in toughness shown in Fig. 16, at a given temperature, is consistent with Fig. 14. Furthermore, for a given thickness, this model anticipates the transitional behavior normally observed with changes in temperature and sketched in Fig. 17.

The general critical shear lip concept, in conjunction with characteristic toughness values identified with each mode of fracture, permits a simple correlation of different size specimens, such as the Charpy V-notch ( $C_V$ ) and Drop Weight Tear Test (DWTT) test specimens, for example. In particular, in Fig. 18, a comparison is shown of the total energy absorbed in these two specimens when tested at temperatures such that fracture in both was by full development of the shear lip. In the Resistance curve concept this would correspond to the upper shelf value of the  $G_R$  value is  $G_C$ . The predicted result in the case of 100% shear fracture is based on the relation.

$$\frac{E_{C_V}}{E_{DWTT}} = \frac{L_{C_V} t_{C_V}^2}{L_{DWTT} t_{DWTT}^2}$$

where  $E$ ,  $L$ , and  $t$  correspond to the total energy, length of the fracture path, and thickness of the specimen. The excellent correlation between practice and theory is evident in Fig. 18 where the data of Pellini (18) is plotted against the prediction provided by the above relation.

More generally, one can - at least semi-quantitatively - correlate the energy absorbed between any two specimens tested at the same temperature, by using the simple hypothesis that the shear lip thickness tends toward a constant value determined by the temperature, and by weighing the various modes of fracture in proportion to their relative toughness and areas. A more exacting correlation can be effected by recognizing the characteristic variations of the  $G_R$  curve with crack extension. It is this potential for providing predictive failure criterion, even in the plane strain region, that makes the resistance method of such interest to the engineering community.



#### REFERENCES

1. Irwin, G. R. and Kies, J. A., "Critical Energy Release Rate Analysis of Fracture Strength," Welding Research Supplement, Vol. 19, April 1954, pp. 193-198.
2. Weiss, V., Grewal, K., Rosenberg, W. and Lin, H., "The Effect of Testing System Stiffness on Fracture Behavior of Sheet Specimen," AFML-TR-67-37, Aug., 1967.
3. Bluhm, J. I., "Fracture Arrest," In "Fracture", Edited by H. Liebowitz, Academic Press Inc., N.Y., Vol. 5, 1969, pp. 1-63.
4. Bluhm, J. I., Gordon, Jr., B. E., and Morrissey, R. J., "Exploitation of Contoured Double Cantilever Beam Specimen in Crack Growth and Arrest Studies," Presented at the 1970 Army Science Conference, West Point, N.Y., 16-19 June 1970.
5. Clausing, D. P., "Crack Stability in Linear Elastic Fracture Mechanics," Int. J. of Fract. Mechs., Vol. 5, Sept. 1969, pp. 211-227.
6. Srawley, J. E. and Gross, B., NASA Tn D-3820, Feb. 1967.
7. Bluhm, J. I., "Failure Analysis - Theory and Practice" Presented at the William Hunt Eisenman Conference on Failure Analysis, Sponsored by ASM Waldorf Astoria Hotel, N.Y., N.Y., 12-14 July 1966 and the Conrad Hilton Hotel, Chicago, Ill., 30 Jan. - 1 Feb. 1968.
8. Heyer, R. H. and McCabe, D. E., "Crack Growth Resistance in Plane Stress Fracture Testing" Presented at the 4th National Symposium on Fracture Mechanics, Carnegie-Mellon Institute, 24-26 Aug. 1970.
9. Irwin, G. R. and Kies, J. A., "Fracture Theory as Applied to High Strength Steels for Pressure Vessels" Presented at the Golden Gate Metals Conference, San Francisco, Cal., 4-6 Feb. 1960.
10. Kraft, J. M., Sullivan, A. M. and Boyle, R. W., "Effects of Dimensions on Fast Fracture Instability of Notched Sheets" Unpublished report of the Naval Research Laboratory, Wash., D.C.
11. Goode, R. J. and Judy, R. W. Jr., "Fracture Extension Resistance (R-Curve) Fracture of Nonfrangible Aluminum Alloys", NRL Report 7262, 11 June 1971.
12. Bluhm, J. I., "To Pop or Not to Pop," Presented to ASTM Subcommittee for Fracture Testing of Medium Strength Metals, 12 Jan. 1965.
13. Bluhm, J. I., "Fracture Mechanics," SAE Paper No. 655C, Presented at the Meeting of Automotive Engineering Congress, Detroit, Mich., 14-18 Jan. 1963.
14. Bluhm, J. I., Discussion to paper by E. P. Klier et al entitled "Sheet Metal", Proceedings of ASTM, Vol. 64, 1964, pp. 665-668.
15. Heyer, R. H. and McCabe, D. E., "Plane Stress Fracture Toughness Testing Using a Crack Line Loaded Specimen," Presented at the National Symposium in Fracture Mechanics, Lehigh Univ., 25 Aug. 1969. To be published in J. of Engrg. Fract. Mechs.
16. Irwin, G. R., "Fracturing and Fracture Mechanics" Univ. of Ill. TAM Report No. 202, Oct. 1961.
17. Bluhm, J. I., "Geometry Effects on Shear Lip and Fracture Toughness Transition Temperature for Bimodal Fracture," Proc. ASTM, Vol. 62, 1962, p 1.
18. Pellini, W. S., "Advances in Fracture Toughness Characterization Procedures and in Quantitative Interpretation to Fracture-Safe Design for Structural Steel," NRL Report No 6713, April 1968.

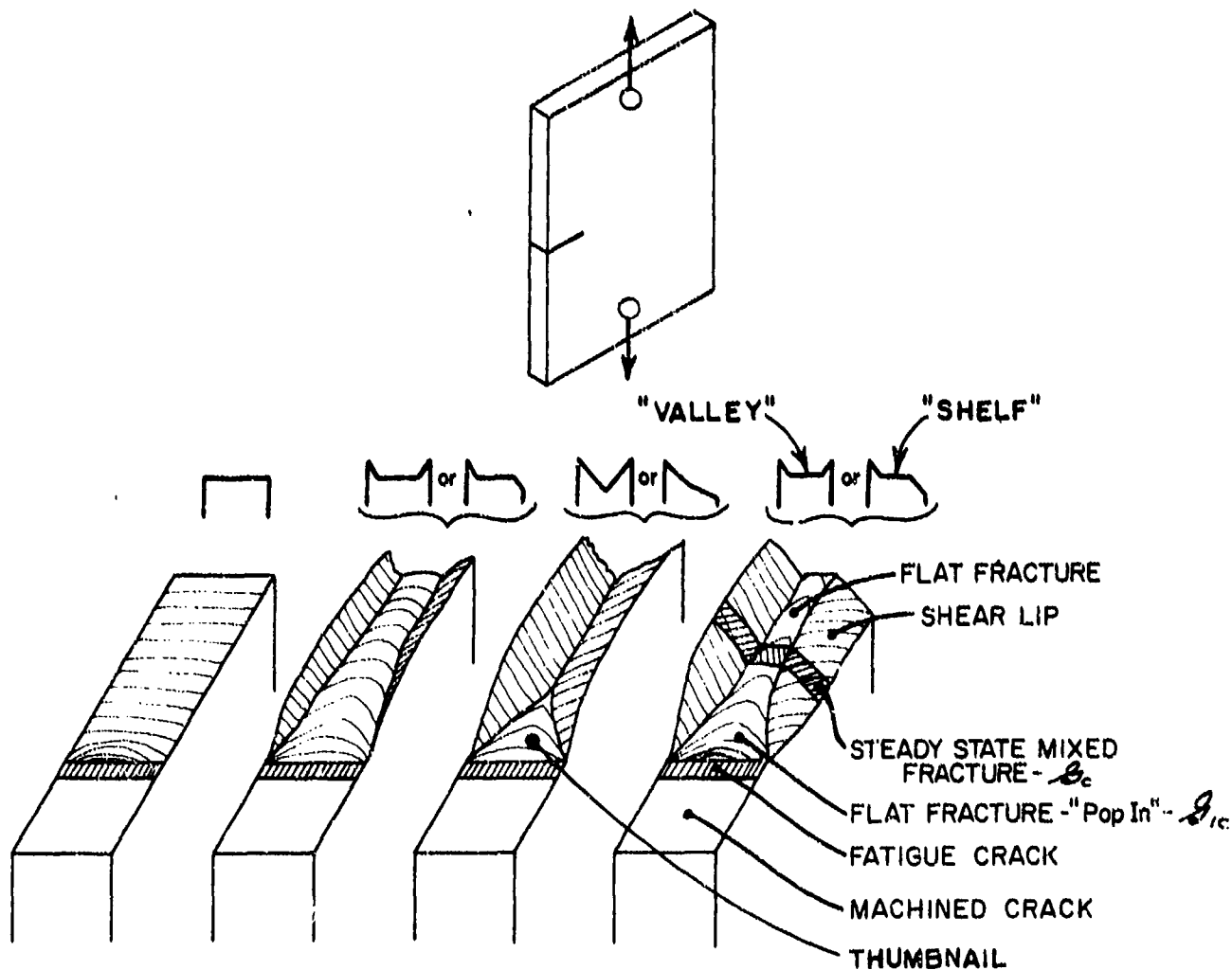


Fig.1 Schematic of crack growth patterns in single edge notched plates.

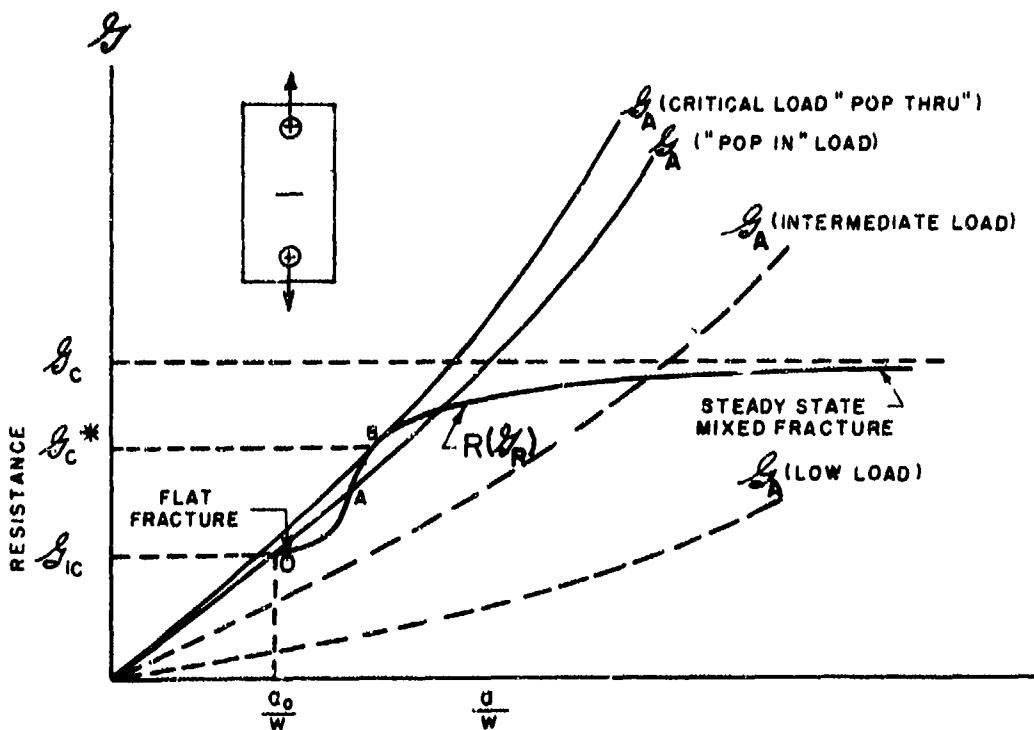


Fig.2 Schematic resistance/energy release rate changes in crack length

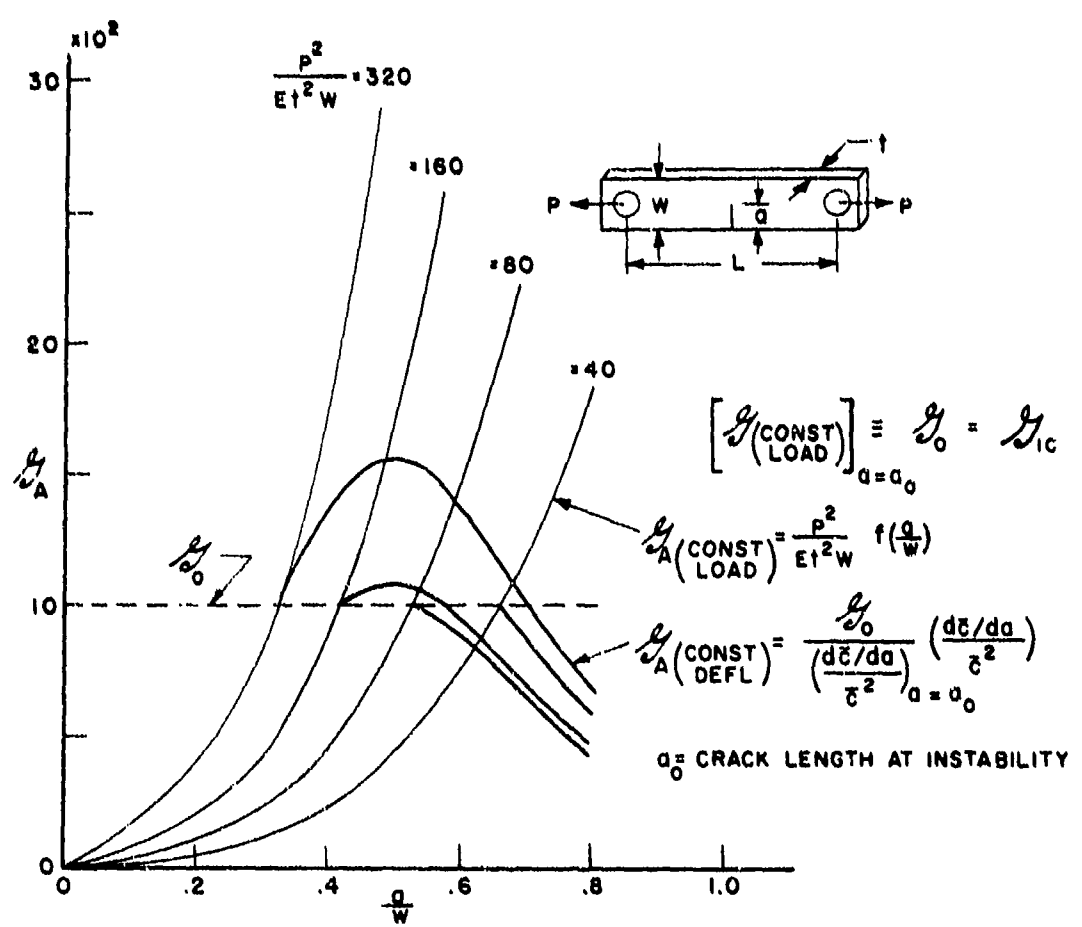


Fig.3 Constant load/constant deflection energy release rate curves – tension specimen

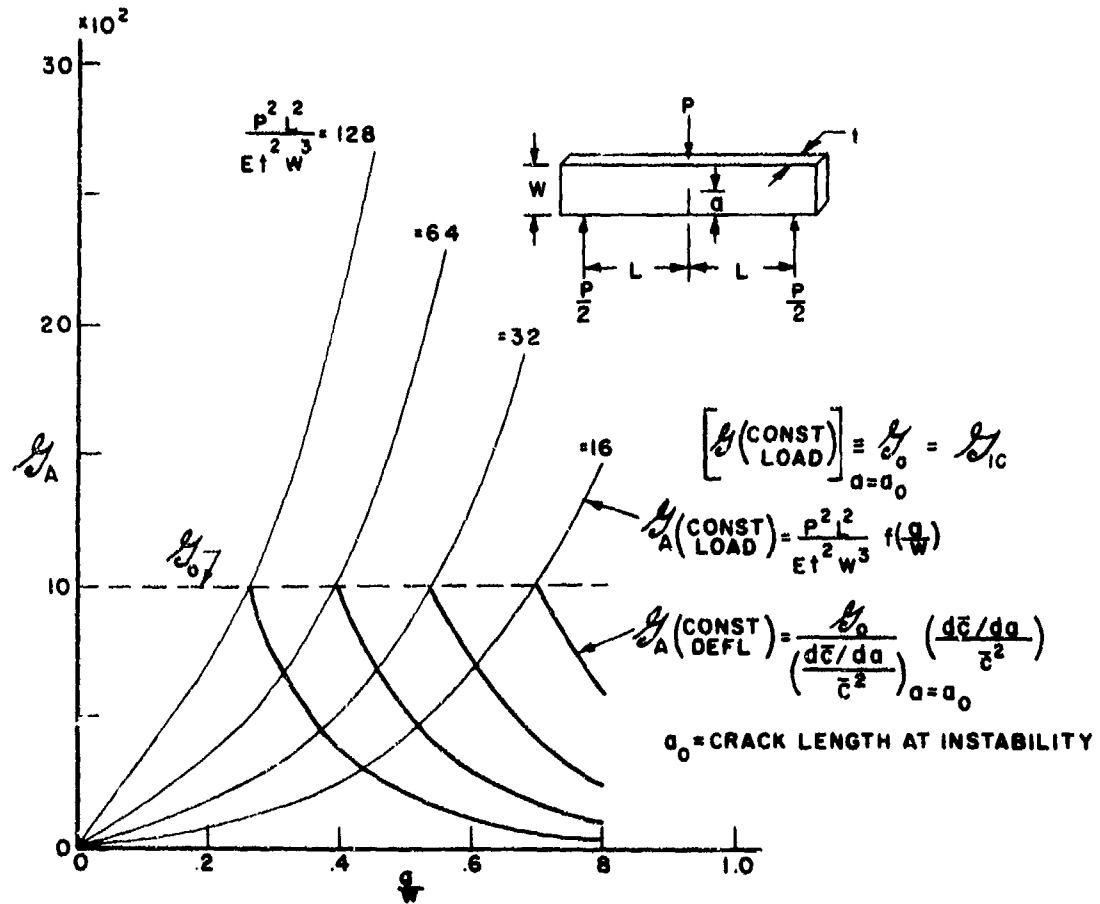
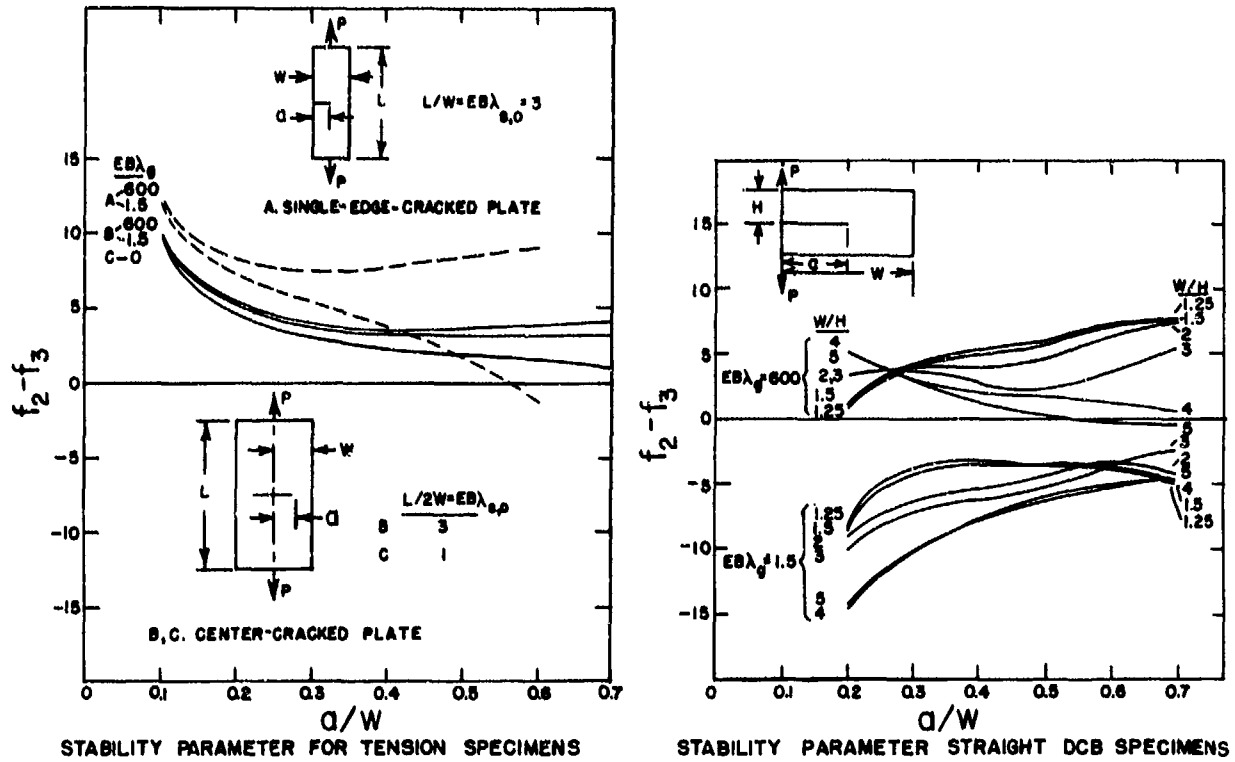
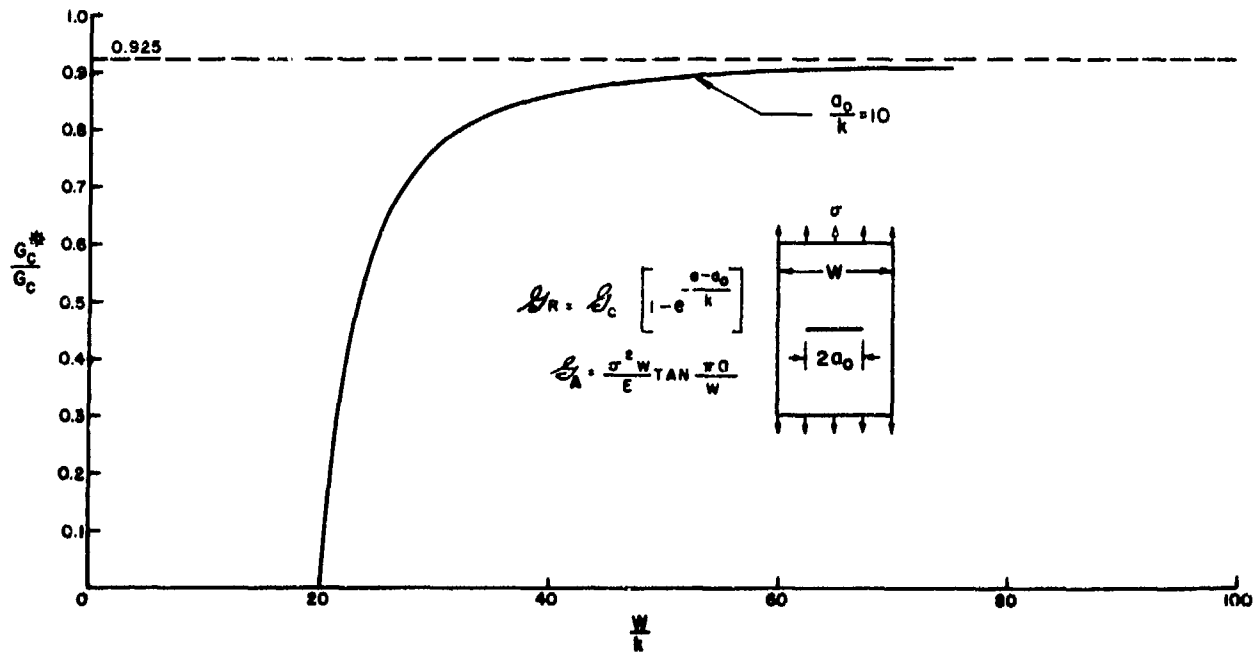


Fig.4 Constant load/constant deflection energy release rate curves – bending specimen

Fig.5 Stability parameters (after Clausen<sup>5</sup>)Fig.6 Effect of plate width on apparent fracture toughness,  $G_c^*$

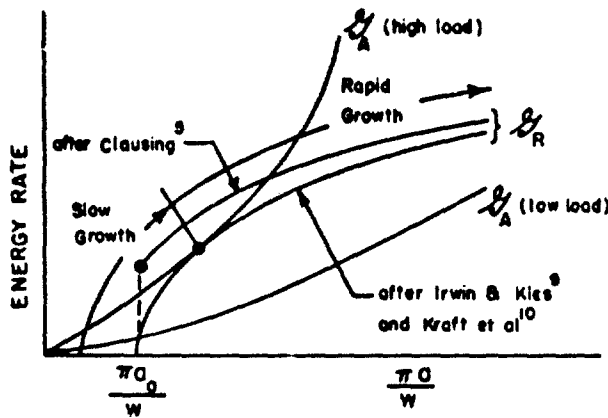


Fig. 7 Schematic  $G_A$ ,  $G_R$  curves

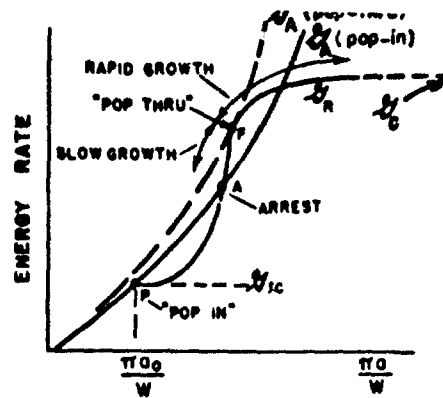


Fig. 8 Modification of "R" curve to show "pop in" - after Bluhm<sup>13</sup>

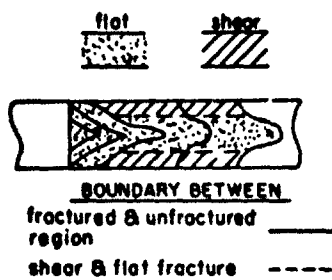


Fig. 9 Incremental fracture process (schematic)

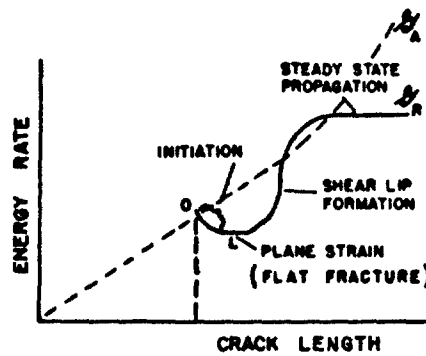


Fig. 10 Generalized stages of "resistance" curve

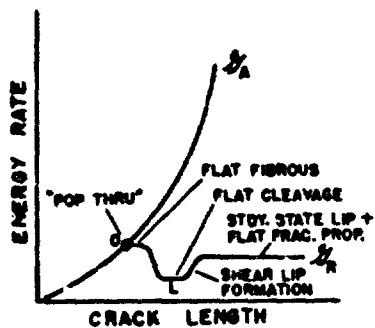


Fig. 11 "Pop thru" not indication of  $G_{IC}$

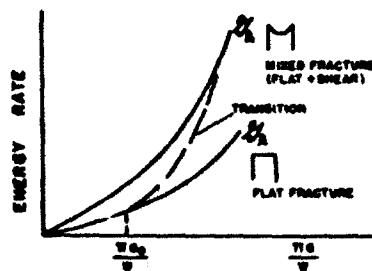


Fig. 12 Influence of fracture mode shape on elastic energy release rate

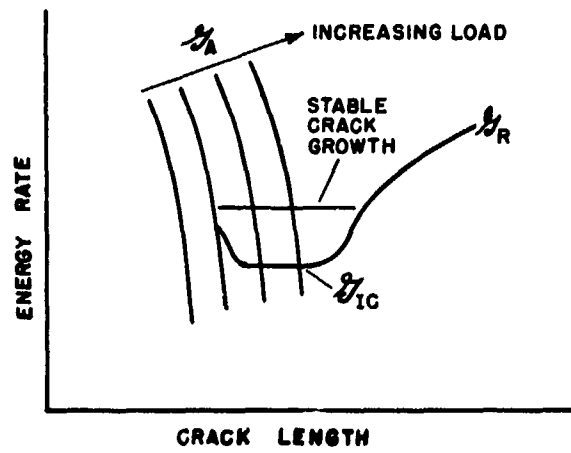


Fig.13 Evaluation of  $G_{IC}$  using negative  $G - a$  slope

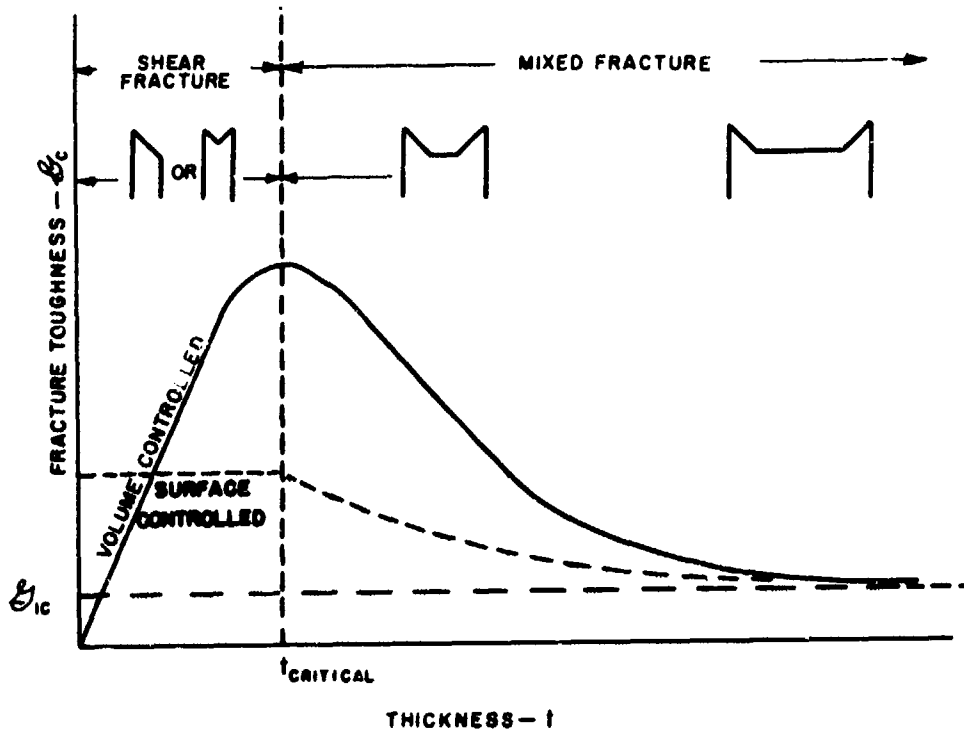


Fig.14 Thickness effect on fracture toughness

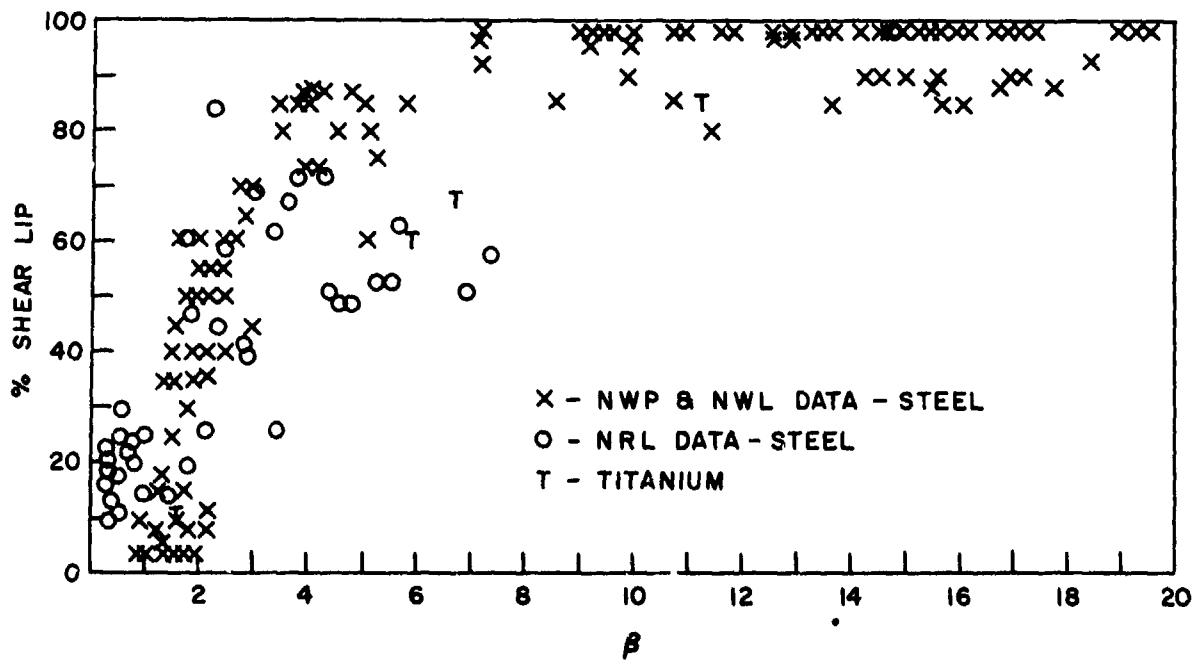


Fig.15 Effect of plastic zone size on percent shear (after Irwin<sup>16</sup>)

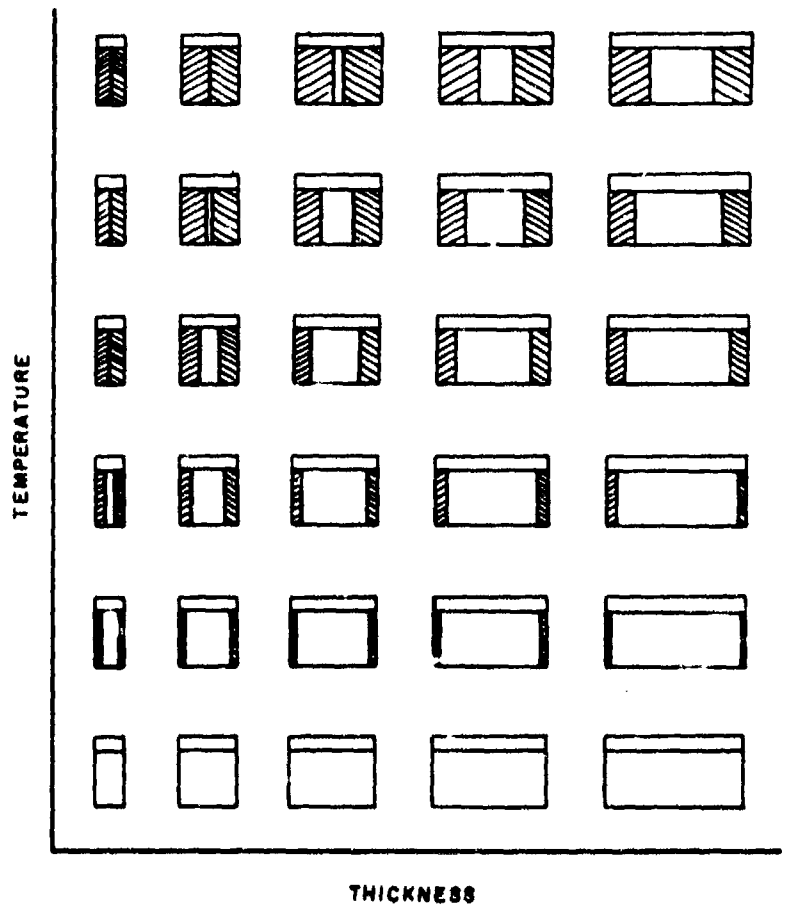


Fig.16 Schematic showing effect of temperature and thickness on fracture mode in notched plates (after Bluhm<sup>17</sup>)

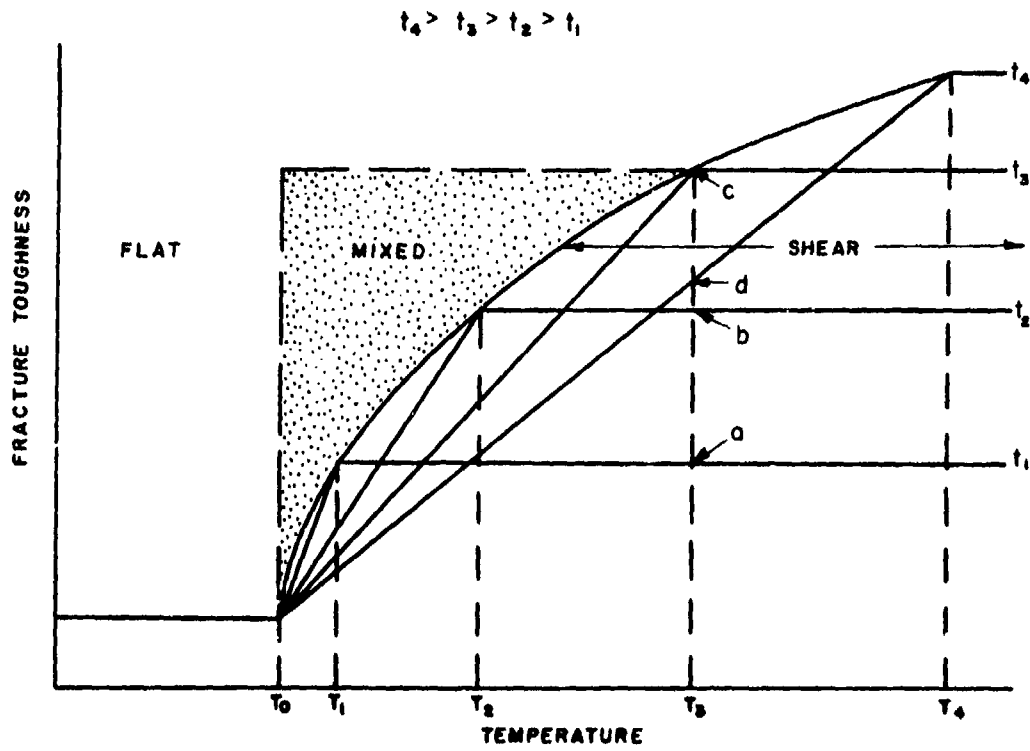


Fig.17 Schematic diagram of transition behavior as a function of thickness (after Bluhm<sup>17</sup>)

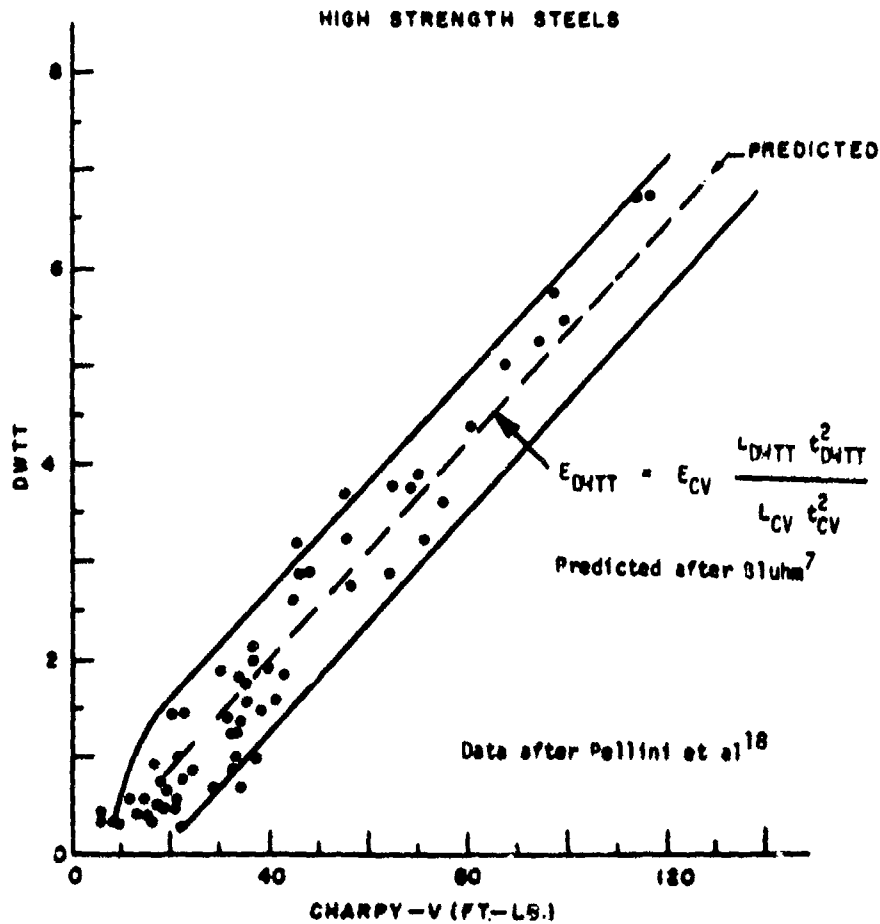


Fig.18 Correlation between drop weight tear test and the Charpy V-notch specimen



Appendix IV-2  
THE KUHN-HARDRATH METHOD  
J. I. Bluhm

The exploitation of the Griffith approach to the fracture problem has been directed, for the most part, to the prediction of fracture - particularly brittle fracture in relatively large parts, i.e., where plane strain fracture was the mode of failure usually noted. It was and is recognized, of course, that regimes of structural configurations exist and are in common usage where such a constraint is not applicable. Thin sheet construction, as utilized in modern aircraft and missile technology, represents glaring examples of such applications. Concurrent with the early Irwinian development of linear elastic fracture mechanics, of the NACA group (1-7) approached the failure problem for a somewhat more pragmatic point of view, which encompassed the regime of thin sheet failure, i.e., the plane stress mode. An excellent resume of this approach, which we identify as the Kuhn-Hardrath (K-H) approach, is provided by Kuhn (1); the immediately following discussion highlights details of that paper.

As in the Irwin approach, but more explicitly, the posed problem is to determine the residual strength of a structural element which contains a "damaged" region. The "damage" in the K-H approach covers the spectrum from a notch (or fillet, etc.) to its degenerate and generally most severe configuration - a crack. In essence, then, the K-H approach is aimed at providing a practical technique for predicting the residual strength of structural elements, particularly in sheet form, containing notches and/or cracks.

As pointed out by Kuhn (1), the most severe defect is the crack; one might therefore start by discussing cracks directly without reference to notches. It is desirable however to introduce notch discussions first for two reasons: "(a)...the crack strength analysis method is derived by considering the crack as the limiting case of a notch...as the notch radius approaches zero, i.e.,  $\rho \rightarrow 0$ , and hence all the basic assumptions and considerations involved in the notch strength analysis are pertinent; and (b)...the literature contains test results on notched specimens representing an investment of millions of dollars; if this investment is to bear full fruit, it is necessary to establish and maintain contact between 'notch strength' and 'crack strength'."

There is, however, an additional reason why notches should be considered first. Fatigue cracks most generally initiate at sites of local stress concentrations such as holes or notches, and though it is conservative to presume the eventual presence of a crack and design around its presence, in many applications one may be paying an exorbitant penalty weightwise and/or performancewise. The early stages of crack development, if they are to be reliably predicted, must be based upon a rational analysis of the behavior of the notched rather than the cracked body; secondly, there are many critical applications where cyclic damage (and subsequent crack initiation) are not significant design considerations - rather, failure occurs under essentially monotonic loading. Under these conditions the desired information is the strength of a notched body - not one which is necessarily cracked.

Basically the K-H approach starts with an expression for the elastic stress concentration factor,  $K_T$ , (determined either theoretically or experimentally). It recognizes, however, that the maximum effective stress from a fracture point of view is not merely the nominal stress,  $S_N$ , multiplied by this stress concentration factor. Instead, the Neuber concept is introduced to attempt to account for the microscopic heterogeneity of the material.

Neuber (8) recognized that with sharp notches even brittle materials did not fracture when the maximum stress,  $\sigma_{max}$ , at the notch tip (determined as  $K_T \times S_N$ ) reached a fixed critical value independent of notch configuration. He recognized that one could not use the ordinary theory of elasticity with its implied permissive use of infinitesimal elements. Grain size inhibits this approach; hence new concepts had to be introduced if one wished to use classical elasticity results for sharp notches and particularly cracks. Neuber visualized, therefore, that the material was composed of numerous small but finite particles and that an effective (or Neuber) stress concentration factor,  $K_N$ , should be defined on the basis of the average stress over one such particle of depth,  $\epsilon$ , at the tip of the notch, i.e., Fig. 1. Neuber letting  $\rho'$  be the effective radius of that particle (i.e.,  $\rho' = \epsilon/2$ ) considered it a new material constant and observed that its value was approximately 0.5mm for the steel he was examining. He concluded that in the limiting process of going from a gentle notch to a sharp or pointed notch, the effective stress concentration factor is, in fact, a function of the material.

For gentle notches the effective stress concentration factor,  $K_N$ , is indeed the same as the theoretical stress concentration factor,  $K_T$ . Furthermore, for the hypothetical case of an idealized material having Neuber particles of zero size (equivalent to a homogeneous material)  $K_N$  should also reduce to  $K_T$ . The transition from a gentle notch to the sharp notch should conform with these conditions.

Neuber proposed the following relation in attempting to meet these conditions:

$$K_N = 1 + \frac{K_T - 1}{1 + (\rho'/\rho)^{1/2}} \quad (1)$$

where  $\rho$  is the notch tip radius (see Fig. 2) and  $K_{T_0}$  is the theoretical stress concentration factor for zero flank angle; the other quantities have already been defined. As implied, this relation is valid over the entire range of notch radii including, of course, the limiting value of  $\rho = 0$  in the pointed or sharp notch or crack. However, if the sides of the notch are not parallel a further correction was recognized as necessary since the resulting angle, for sharp notches at least, could seriously influence the theoretical stress concentration factor or defined by Neuber for a parallel sided notch. Accordingly, Neuber modified Eq. (1) to include this flank angle,  $\omega$ , (Fig. 2) correction as follows:

$$K_N = 1 + \frac{K_{T_0} - 1}{1 + \frac{\pi}{\pi - \omega} (\rho'/\rho)^{1/2}} \quad (2)$$

Whereas Neuber's results for  $K_{T_0}$  were developed for infinite sheets, in the K-H approach the  $K_{T_0}$  determination implies corrections for finite width sheets. Such corrections are exploited for example in McEvily and Illg (6), and Kuhn (1,3). These corrections stem both from theoretical work as well as experimental investigations. Specifically, Kuhn (1), using Dixon's results (9) for a crack, used the relation:

$$K_{T_0} = 1 + 2k_w (\alpha/\rho)^{1/2} \quad (3)$$

with

$$k_w = \left[ \frac{1 - \frac{2\alpha}{w}}{1 + \frac{2\alpha}{w}} \right]^{1/2} \quad (\text{for central cracks})$$

$$k_w = 1 - \frac{2\alpha}{w} \quad (\text{for edge cracks})$$

Here  $w$  is the plate width and  $2a$  and  $a$  are the crack length for the center cracked and edge cracked specimen respectively.

More recently Bowie (10) has provided detailed and accurate analytical solutions for cracks in finite width plates and has suggested a rather general and simple method for determining the stress state in such bodies; these results can appropriately be utilized in the K-H approach.

An additional consideration introduced in the K-H approach is the stress alleviating influence associated with the plastic deformation which takes place at the tip of the notch. The plasticity correction is of the form:

$$K_p = 1 + (K_N - 1) \frac{E_1}{E_2} \quad (4)$$

where  $E_1$  and  $E_2$  are secant moduli corresponding to  $\sigma_{max}$  and to the average stress remote from the notch respectively.

Letting the maximum stress  $\sigma_{max}$  be redefined as the ultimate strength,  $\sigma_u$ , then  $E_1$  can be identified as  $E_u$ . If attention is further confined to cases where the net section stress at failure,  $S_N$ , is less than the yield strength,  $\sigma_y$ , i.e.,  $S_N < \sigma_y$ , then the average stress remote from the notch is in the elastic region and  $E_2 = E$ . Eq. (4) then can be written as an ultimate strength factor,  $K_u$ :

$$K_u = 1 + (K_N - 1) \frac{E_u}{E} \quad (5)$$

Subject to the constraint  $S_N < \sigma_y$ . On the other hand if  $S_N > \sigma_y$  the K-H approach implies Eq.(5) should be written as follows:

$$K_u = 1 + (K_N - 1) \frac{E_u}{(E E_N)^{1/2}} \quad (6)$$

when  $E_N$  is the secant modulus corresponding to the net stress,  $S_N$ .

Summarizing then for the notch specimen, the ultimate strength,  $\sigma_u$ , is given by:

$$\sigma_u = K_u \times S_N \quad (7a)$$

$$K_u = 1 + (K_N - 1) \frac{E_u}{E} \quad (7b)$$

and

$$K_N = 1 + \frac{K_{T_0} - 1}{1 + \frac{\pi}{\pi - w} (\rho'/\rho)^{1/2}} \quad (7c)$$

and

$$K_{T_0} = 1 + 2k_w (a/\rho)^{1/2} \quad (7d)$$

These relations represent the K-H approach and provide the predictive tools for determining the residual strength of a notched body starting from its original geometry and related theoretical stress concentration factor. The latter can be determined using either analytical or experimental approaches, feeding a size factor consideration into the consideration via the Neuber particle concept and finally incorporating a plasticity correction.

When these relationships are combined for a finite width plate and are interpreted in terms of a crack instead of a notch, i.e.,  $\rho \rightarrow 0$ , then the final ultimate strength factor,  $K_u$ , appears in the form:

$$K_u = \left[ 2k_w (a/\rho')^{1/2} \right] \frac{E_u}{E} \quad (8)$$

and the strength in the form

$$\sigma_u = K_u S_N \quad (9)$$

Note that  $\rho'$ , presumably a material constant, must be experimentally determined and  $k_w$ , defined by Equation 3 accounts for the width effects and must be determined either experimentally or analytically.

Hudson (11) applied this approach to a specific stainless steel and by taking care to minimize the buckling influence found it had satisfactory predictive capability. For the material investigated he found that the Neuber particle parameter was approximately 0.18 inch. This is undoubtedly large relative to microstructural elements and confirms the feeling (as has been suggested by others including Kuhn) that the quantity  $\rho'$  should indeed be considered only as a parameter in Equation 1 and not necessarily a material related constant. Hudson showed quite effectively that the results of residual strength tests were significantly influenced by buckling and that the K-H method applied in the present form only if buckling were inhibited.

Broek (12) observed that cracked sheets frequently exhibited slow crack growth under increasing loading prior to final rapid fracture. He noted that the initiation of this slow crack growth appeared to be governed by the relation:

$$\sigma_1 (a_0)^{1/2} = K_{IC} \quad (10)$$

when  $\sigma_1$  is the nominal (gross) stress at the instant of initiation of slow crack extension,  $a_0$  is the initial crack length, and  $K_{IC}$  is plane strain fracture toughness. Broek, however, had some reservations as to the physical acceptability of this criteria since it had also been observed that sheet specimens with cracks initially induced at  $45^\circ$  to the surface continued to extend slowly under static loading in a shear mode. This appeared to be incompatible with the  $K_{IC}$  quantity in Eq. 10. He noted, nevertheless, that initiation of slow crack growth appeared to occur at a value of  $\sigma_1 (a_0)^{1/2}$  which was relatively independent of the thickness, thus tending to confirm Eq. 10 (since  $K_{IC}$  is generally presumed to be a material property and hence independent of thickness).

Broek attempted to predict residual strength of sheet panels by incorporating this slow growth consideration. Using as a starting point resistance curves of Chapter I as shown in Fig. 3 (see also Section E-8) he notes the crack is stable and does not extend if  $\sigma < \sigma_1$ , but at  $\sigma = \sigma_1$  the crack slowly extends under the influence of increasing stress following the curved path shown. At a value of gross stress where  $\sigma = \sigma_c$  (point F in Fig. 3), the crack becomes unstable and extends catastrophically. It is clear from Fig. 3 that analytically this instability governing unstable growth, hence residual strength of the panel, is given by the simultaneous condition that the two curves (i.e., the resistance rate R curve and the energy release rate G curve corresponding to the initial stress T) must have a common amplitude

$$\frac{\partial V}{\partial a} + \frac{\partial W}{\partial a} = 0 \quad (11a)$$

$$\frac{\partial^2 V}{\partial a^2} + \frac{\partial^2 W}{\partial a^2} = 0 \quad (11b)$$

when V and W are related to the R and G curves as follows:

$$R = \frac{dW}{da}$$

and

$$G = - \frac{\partial V}{\partial a}$$

This latter condition was first developed by Gowan (13). It should be noted that whereas Eqs. 11 are applicable to crack instability whether it be ductile or brittle crack extension, Eq. 11b is superfluous if only the brittle mode of extension is involved; thus reducing to the single commonly recognized Griffith relation, Eq. 11a.

When Eqs. 11 were applied to a series of large panels, the following relationship was developed as a reasonable criteria for residual strength:

$$\sigma_c a_c^p = \text{constant} \quad (12)$$

where p depends upon material. Broek suggests on the basis of admittedly limited data that the critical crack length,  $a_c$ , is proportional to the initial crack length,  $a_0$ , in the form:

$$a_c = \alpha a_0$$

so that Eq. 12 can be rewritten in the more useful form for design:

$$\sigma_c a_0^p = \text{constant} \quad (13)$$

Thus, for a given material, two tests should be adequate to determine the constants. Eq. 13 is in effect, then, a relation for prediction of residual strength in terms of gross stress,  $\sigma$ , and initial crack length,  $a_0$ . Limited data in support of this type of relation are provided in Broek's paper; this data relates to thin cylindrical pressure vessels and stiffened panels as well as unstiffened flat panels. Extensions to incorporate finite width effects were not entirely satisfactory.

An attempt to provide a finite width correction for flat panels is discussed by Broek (14). He essentially used the scheme similar to that suggested by Bluhm (15). Broek assumes an "R" curve which is independent of width but introduces for the "G" curve a relation which takes into account the finite width of the panel. These are then introduced into Eq. 11 leading to the relation between  $a_0$  and  $a_c$  as follows:

$$a_0 = a_c - \frac{w}{\pi} \frac{\alpha-1}{\alpha} \sin \frac{\pi a_c}{w}$$

For the special case when  $a_0/w$  is kept constant, Broek shows that this approach leads to the prediction:

$$\sigma_c w^{1/2\alpha} = \text{constant} \quad (14)$$

Figure 4 taken from Broek (14) tends to support the reasonableness of this approach. Buckling of cracked thin skin specimens introduces further difficulties into the interpretation of the results which Broek (14) also discusses briefly.

In a later paper, Broek (16) suggests that, at least for the two materials investigated: 2024-T3 and 7075-T6, the criteria (Eq. 13) appeared to be appropriately independent of the sharpness of the crack. This conclusion was based upon a comparison of the behavior of specimens containing a saw cut in contrasted to ones with a fatigue crack generated at two levels of alternating stress. Broek (17) also investigated rate of loading effects and showed that over a range of loading rates such that the test duration varied from approximately 0.4 sec. to 30 minutes, tests on 2024-T3 exhibited no influence on the above criteria for residual strength.

## REFERENCES

1. Kuhn, P., "Residual Strength in the Presence of Fatigue Cracks," presented in sections to the Structures and Materials Panel, AGARD in Torino Italy, Apr 17, 1967 and Ottawa, Canada, Sept 25, 1967.
2. Kuhn, P., "Notch Effects on Fatigue and Static Strength," presented at the Symposium on Aeronautical Fatigue, sponsored by the International Committee on Aeronautical Fatigue and the Structure and Materials Panel of AGARD, Rome, Italy, Apr 1963.
3. Kuhn, P., "The Prediction of Notch and Crack Strength under Static or Fatigue Loading," Paper No. 843C presented at the Air Transport and Space meeting sponsored by the Society of Automotive Engineers Inc. and the American Society of Mechanical Engineers, New York, New York, Apr 27-30, 1964.
4. Kuhn, P. and Figge, I.E., "Unified Notch-Strength Analysis for Wrought Aluminum Alloys," NASA TN D-1259, 1962.
5. Peters, R.W. and Kuhn, P., "Bursting Strength of Unstiffened Pressure Cylinders with Slits," NASA TN 3993, Apr 1957.
6. McEvily, A. J. Jr., Illg, W., and Hardrath, H.F., "Static Strength of Aluminum Alloy Specimens Containing Fatigue Cracks," NACA TN 3816, 1956.
7. Kuhn, P. and Hardrath, H.F., "An Engineering Method for Estimating Notch-Size Effect in Fatigue Tests on Steel," NACA TN 2805, 1952.
8. Neuber, H. "Theory of Notch Stresses: Principles for Exact Stress Calculation," J.W. Edwards, Ann Arbor, Michigan, 1946.
9. Dixon, J.R., "Stress Distribution Around a Central Crack in a Plate Loaded in Tension; Effect of Finite Width of Plate," J. Roy. Aeron. Soc., 1960.
10. Bowie, O.L., "Solution of Plane Crack Problems by Mapping Techniques," to be published in a book edited by G.C. Sih.
11. Hudson, "Fatigue Crack Propagation and Residual Static Strength of PH 15-7 Mo (TH 1050) Stainless Steel," NASA Technical Note TN D-3151, Dec 1965.
12. Broek, D., "The Residual Strength of Cracked Sheet and Structures," National Aero and Astronautical Res Inst Report NLR-TM M.2135, Aug 1964.
13. Orowan, E., "Conditions of High Velocity Ductile Fracture," J. Appl. Phys. Vol 26, No. 7, July 1955.
14. Broek, D., "The Effect of Finite Specimen Width on the Residual Strength of Light Alloy Sheet," Nat'l Aerospace Lab (NLR), the Netherland Report NLR-TR M.2152, Sept 1965.
15. Bluhm, J.I., "Fracture Mechanics," Paper No. 655C presented to the Automotive Engineering Congress, Detroit, Mich, Jan 14-18, 1963, sponsored by the Society of Automotive Engineers, also in "Fracture of Structural Metals," Army Materials Research Agency, Watertown, Mass., Report No. WAL MS-48, 1962.
16. Broek, D., "The Residual Strength of Aluminum Alloys Sheet Specimens Containing Fatigue Cracks or Saw Cuts," Nat'l Aerospace Lab Rept NLR-TR M.2143, Mar 1966.
17. Broek, D., "The Influence of the Loading Rate on the Residual Strength of Aluminum Alloy Sheet Specimens," Nat'l Aerospace Laboratory (NLR) The Netherland Report NLR-TR M2154 Oct 1965.

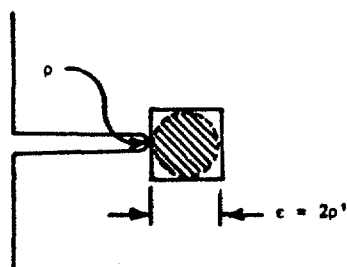


Figure 1. Representation of Neuber "particle" at notch/crack tip

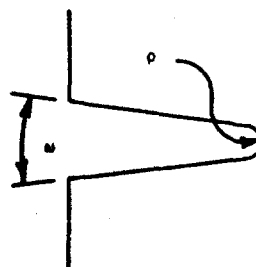


Figure 2. Identification of flank angle,  $\omega$ , and notch radius,  $\rho$

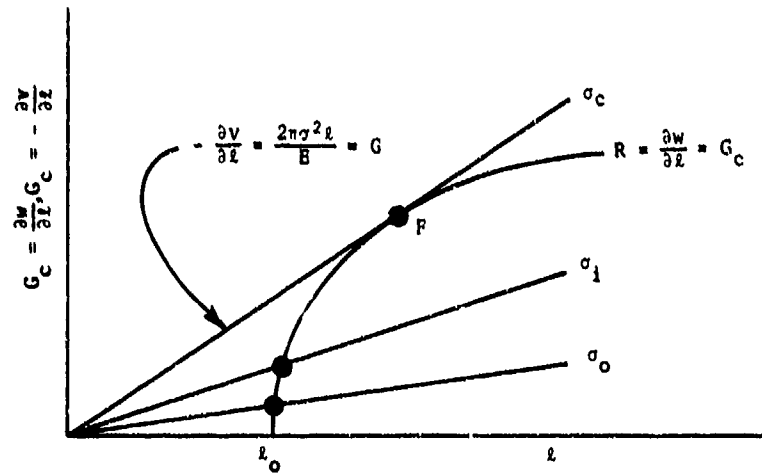


Fig.3 Energy relations for slow and fast crack growth

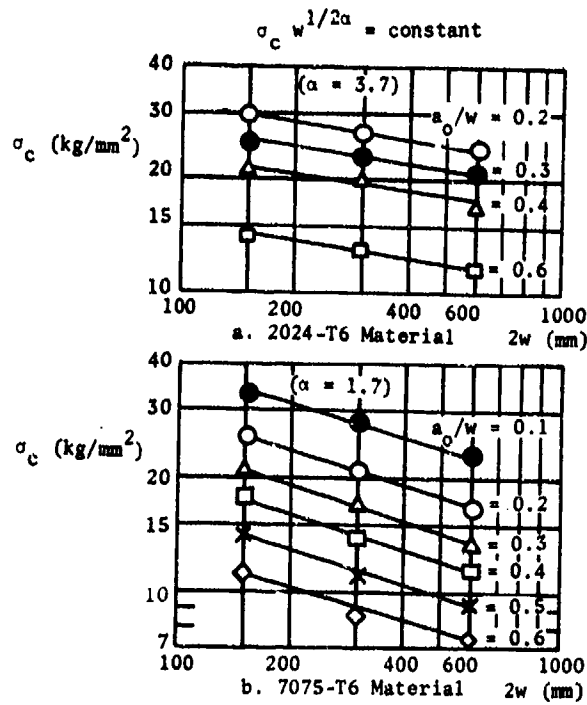


Fig.4 Relation between sheet width and residual strength (after Break)

Appendix IV-3  
CRACK PROPAGATION LAWS

J. I. Bluhm

a. Introduction

Fatigue has generally been characterized by several stages; nucleation (at "defects") of cracks, microcrack propagation and coalescence, macrocrack propagation and, finally, catastrophic fracture. Nucleation appears to occur very early in the fatigue life of a body and is considered to be the consequence of repeated cyclic slip. It is also clear that nucleation of microcracks is not restricted to a single site in a given body; generally a number of such microcracks will develop at various sites. These microcracks will then grow at different and not necessarily continuous rates; eventually one such microcrack will dominate in the growth process and become the macrocrack which leads ultimately to final failure.

Since the gross stresses at a point are amplified by the presence of a geometric notch, it is not surprising that nucleation, initial microcrack growth and even early macrocrack growth is usually associated with such regions. In the vicinity of a notch, microscopic regions containing defects are subjected to stresses representing the product of the stress concentration factors of the notch and the microdefect.

If we consider for illustration a simple case of a plate with a relatively blunt notch per Fig. 1, then one may identify certain of these regions of fatigue more readily. In Fig. 1a we observe the grossly expanded region of the base of a notch showing representative grains, each having its own anisotropic characterization, its own subgrain boundaries and otherwise generally loaded with other defects such as dislocations, inclusions, voids, etc. As a result of the external cyclic loading, damage occurs at some of these sites and eventually at a number of these sites microcracks as shown are formed. These are discrete disconnected cracks with random orientation depending upon both the stress state and the given orientation. With repeated cyclic loading more sites may contribute to microcrack formation and some of the existing ones will grow and coalesce with others; eventually the growth will be restricted to one or two such cracks and a single "dominant" crack will prevail. Figure 1b suggests the appearance of such a dominant crack. It has been observed that generally the initial dominant crack tends to be of at an inclined angle to the tensile loading whereas at later growth stages it tends to follow a path perpendicular to the load direction; these have been identified in the literature on Stage I and Stage II crack propagation. It is noted that since the "length" of this dominant crack is of the order of the radius of the notch that the stress state at its crack tip is a function of both the applied load and the initial notch geometry; at this stage of growth the notch geometry cannot be ignored in determining the levels of stresses at the crack tip. The crack is undergoing a transient stage of growth "feeling" initially predominately the effect of the initial notch. When the crack has extended further as in Fig. 1c, such that the crack is relatively long compared to the notch tip radius, then the effects of initial notch configuration may be ignored; only the crack configuration becomes significant, we identify this regime as the "steady state" regime. "Steady state" growth continues to take place until the crack reaches a critical size at which time catastrophic fracture or ductile collapse as in Fig. 1d takes place. This presumes that the plate is large enough so that critical crack size is achieved before the influence of the free edge of the plate starts to affect the crack tip stresses.

In the present, we shall confine our attention to this "steady state" regime of macrocrack propagation. For the reader who is interested in details relative to the earlier stages of fracture including pertinent design approach and/or discussion relating to the breakout of fatigue regimes, one may see typically references 1-18.

b. Representative Crack Propagation Laws

A brief glance at Table 1 taken from reference 19 would suggest that, at least as of that writing (1967), there appeared to be no generally accepted predictive relation for crack growth. More recent surveys by Barrois (20) or Pelloux (21) tend to confirm that status even as late as 1970. In view of the transient and developing state of knowledge in this specific area, we will not attempt to identify the appropriate propagation law but rather we will describe several laws of current and/or historic interest and describe where possible some of their limitations. Christensen and Harmon (19) has noted that most of the various relationships proposed in the literature are reasonably valid for the restricted ranges of applicability for which they were developed, but that generally they did not provide sufficient generality to account, explicitly, for many of the loading parameters known to be significant. Only a limited number of available "laws" explicitly take into account even the more obviously pertinent material properties as such; they are instead generally incorporated in experimentally determined "constants".

(1) One load parameter laws

Most early crack propagation studies attempted to correlate the cyclic crack growth rates,  $da/dn$ , to various functions of the instantaneous crack length,  $a$ , and the alternating stress,  $\sigma_a$ . Many of those relationships can be expressed approximately in the following functional form\*

$$\frac{da}{dn} = f(\sigma_a, a, C_1) \quad (1)$$

\*The following discussion is largely borrowed from the paper by Paris and Erdogan (23).

where the  $C_1$ 's are (hopefully) constants selected to fit the experimented data. Note that in this form only one load defining parameter,  $\sigma$ , enters explicitly into the relations. In this form, then, generalization to cover load variables is limited. Nevertheless, it is useful to examine a number of such relations which have been proposed. Head (22) suggested a model exploiting rigid plastic work hardening elements and developed the form:

$$\frac{da}{dn} = 1/2 \frac{C_1 \sigma^3 a^{3/2}}{(C_2 - \sigma) \omega_0} \quad (2)$$

Where  $C_1$  reflects a combination of material properties slightly dependent however on mean stress,  $C_2$  is the yield strength and  $\omega_0$ , the size of the plastic zone at the crack tip. As pointed out by Paris and Erdogan (23), Head (22) assumed  $\omega_0$  to be a constant where as Frost and Dugdale (24) observed it to increase with crack length; Irwin (25) had shown that  $\omega_0 \approx \sigma^2 a$ . When this was introduced into Eq 2 Paris and Erdogan obtained Head's "corrected" law 4:

$$\frac{da}{dn} = \frac{C_1 \sigma^2 a}{C_2 - \sigma} \quad (3a)$$

This may be reduced assuming  $K^2 = \sigma^2 a$  (for an infinite plate) to the form:

$$\frac{da}{dn} = \frac{C_3 K_{\max}^2 a^{1/2}}{C_2 a^{1/2} - K_{\max}} \quad (3b)$$

Note that whereas Eqs. 3 do in fact reflect the situation where the plastic zone may indeed increase with crack length as observed by Frost and Dugdale (24) and as might be expected in constant load tests, this is not necessarily a valid generalization. For tests in which  $\sigma^2 a$  is maintained constant then according to Irwin (25) the plastic zone would be constant. Frost and Dugdale proposed another such one parameter relation:

$$\frac{da}{dn} = \frac{\sigma^3 a}{C_4} \quad (4a)$$

where  $C_4$  is a constant depending both on material and mean stress. In normalized form\* this can be expressed as:

$$\frac{da}{dn} = \frac{C K_{\max}^3}{a^{1/2}} \quad (4b)$$

Paris and Erdogan (23) suggested the relation:

$$\frac{da}{dn} = C(\Delta K)^4 \quad (5)$$

where  $\Delta K$  is the stress intensity factor range of  $K$ . They plotted limited crack propagation data for both 2024-T3 and 7075-T6 aluminum alloys; this data from several sources and covering some six decades of  $\frac{da}{dn}$  are shown reproduced in Figs. 1a and 1b. It is suggested by the authors that this data appears to substantiate the exponent 4 in Eq. 5 as a good engineering approximation.

Barsom (26), examining the crack propagation rates at the higher range of energy release rates (or  $K$ 's), quotes work of others to suggest that observed accelerated growth rates at a higher  $\Delta K$ 's are associated with a superposition of ductile fracture on the fatigue striation mechanisms. This ductile fracture mode intuitively would be expected to increase the apparent fracture toughness; hence a fatigue dilemma crops up; the toughness increases, but nevertheless the crack propagation also increases. The transition behavior discussion by Wilhem (27) is more consistent with the overriding influence of increased toughness. Barsom basically suggests a relation equivalent to:

$$\frac{da}{dn} = C\Delta K^2 \quad (6)$$

but points out that a transition occurs (see Fig. 3) when the range of the crack opening displacement,  $\Delta\delta$ , is approximately  $1.6 \times 10^{-3}$  inches. The crack opening displacement,  $\delta$ , is defined by the relation  $\delta = \frac{G}{\sigma_y}$ , where  $G$  is the elastic energy release rate and  $\sigma_y$  is the 0.2% offset yield strength.

\*For purposes of this review we shall express all crack growth rate, not only in the original form (with minor editorial changes) but also in a form expressed in stress intensity notation; i.e.,  $K_{\max}$ , or  $\Delta K$  and  $R$ , the max stress intensity factor and the stress or load ratio  $R = \frac{\sigma_{\min}}{\sigma_{\max}} = \frac{P_{\min}}{P_{\max}}$ . We shall further attempt to reduce all results to the infinite plate case to provide a common base for evaluation. Such forms will be called the "normalized" or "reduced" form.



Beuwkes (28) has proposed a similar form that explicitly accounts for the yield strength, Young's modulus, and Poisson's Ratio in a constant C. This constant, furthermore, takes on distinct values for plane strain and plane stress. Beuwkes provides impressive evidence that the large bulk of valid data (excluding only data for which buckling was not inhibited in thin sheet specimens) fits this predictive relation closely:

Frost and Dixon (29) suggested the relation:

$$\frac{da}{dn} = C \sigma^3 a \quad (7a)$$

or in reduced form:

$$\frac{da}{dn} = \frac{C_1 K_{\max}^3}{a^{1/2}} \quad (7b)$$

which is identical to that of Frost and Dugdale (Eq. 4).

Pelloux (21) has suggested a direct relation between crack growth rates and the Crack Tip Opening Displacement (CTOD) in the form:

$$\frac{da}{dn} = 1/2 \text{ CTOD} = \frac{1}{8\pi} \frac{(\Delta K)^2}{\sigma_y E} \quad (8)$$

where  $\sigma_y$  & E are the yield strength and elastic modulus respectively.

Most of the crack propagation studies reported in the literature relate to unidirectional loading. Using quasi elliptical flat plates with thru thickness cracks, Joshi and Shewchuk (30) were able to study the effects of biaxial loading on crack propagation rates in 2024-T351 aluminum alloy. Their limited results are shown in Fig. 4a and 4b. They were able to account for biaxial stresses by using an effective stress intensity factor based upon the maximum strain energy theory for failure. They defined the equivalent stress intensity factor as  $K_e = \sigma_e a^{1/2}$  where  $\sigma_e^2 = \sigma_1^2 + \sigma_2^2 - \nu \sigma_1 \sigma_2$  and as shown in Fig. 4b obtained excellent nominalization.

## (2) Two load parameter laws

In order to include effects of mean stress, a number of "two load parameter" equations have been proposed. Paris and Gomez (31) suggested the functional form:

$$\frac{da}{dn} = f \left[ K_{\max}, \frac{K_{\max}}{K_{\min}} \right] \quad (9)$$

but provided no explicit suggestion for the functional form.

Broek and Schijve (32) recognized the need for unambiguously defining the load parameter (at least for simple loading) and suggested the form:

$$\frac{da}{dn} = C_1 e^{-C_2 R} (\sigma a^{1/2})^3 [1 + 10 (a/b)^2] \quad (10a)$$

or in reduced form

$$\frac{da}{dn} = C_3 e^{-C_2 R} K_{\max}^3 \quad (10b)$$

where:  $C_1, C_2$  are constants  
 $R$  is the stress ratio  $\sigma_{\min} / \sigma_{\max}$   
 $a$  is the half crack length  
 $b$  is the half plate width

This form leads to a linear relation when  $\log \frac{da}{dn}$  is plotted against  $\log K$  with slope equal to 1/3. Data from Broek and Schijve (32) shown in Fig. 5, shows marked deviation from such linearity thus casting some doubts on the global validity of this form of relation. It is worth noting that this "raw" data does however highlight several features: (a) curves for different R's are distinct, (b) a tendency for a "threshold" level of  $K_{\max}$  exists below which  $\frac{da}{dn}$  approaches zero, and (c) at high value of  $K_{\max}$  there is evidence of exaggerated crack growth. Broek & Schijve did not attempt to build these latter behavioral characteristics into crack growth laws.

Forman, Kearney, and Engle (33) suggested the following alternative form which explicitly predicts the exaggerated growth at high  $\Delta K$ :

$$\frac{da}{dn} = \frac{C \Delta K^n}{(1-R) K_c - \Delta K} \quad (11a)$$

or recognizing  $\Delta K = (1-R) K_{\max}$

$$\frac{da}{dn} = \frac{C_1 (1-R)^{n-1} K_{\max}}{K_c - K_{\max}} \quad (11b)$$

Here C and n are material and numerical constants respectively, and  $K_c$  is the critical stress intensity factor for fracture. Representative results taken from Forman, et. al. (33) are shown in Fig. 6.

Tomkins (34) starting from a simple shear flow model derived the following relation:

$$\frac{da}{dn} = C \Delta \sigma^3 \sigma_m a \quad (12a)$$

or

$$\frac{da}{dn} = C_1 (1-R)^3 (1+R) K^4 \times \frac{1}{a} \quad (12b)$$

Figure 7 shows some of his results.

Hudson and Scardina (35) evaluated wide sheet crack propagation rates with R values from 0 to -0.8 and compared the results with the prediction relations of Paris and Erdogan, Eq. 5, Broek and Schijve, Eq. 10 and Forman, et. al., Eq. 11. They concluded that the Forman relation represented the best fit. Figure 8 shows those three relations superposed on data for different R values. Agreement with the Broek and Schijve data, though fairly good at low  $\Delta K$ 's, is poor at the higher level. Comparing the Paris and Forman relations, the latter appears to be in better agreement with this data; additionally it incorporates the load ratio parameter R in explicit form whereas the Paris relation requires experimental determination of a constant for each value of R.

It is noted also that the Forman relation, Eq. 11, predicts the "S" shaped response curve; i.e., "accelerated" growth rates at the higher K's and decelerated growth rates at the lower K's. It predicts, in fact, a catastrophic rate as K approaches  $K_c$  which is intuitively satisfying though the infinite rate actually predicted is not compatible with observed behavior of relatively tough materials. This relation, furthermore, does not predict threshold behavior (value of  $\Delta K$  below which crack propagation does not occur), except for the limiting case of  $\Delta K = 0$ . Recent papers by Bucci, et al (38,39) discuss this threshold phenomena. Bluhm, et al (40) and Johnson (41) have proposed semi-empirical relations which, not only show a form which can account for the high  $\Delta K$  acceleration, but which also address the threshold behavior at other than zero stress states. The Bluhm relation follows:

$$\frac{da}{dn} = C \frac{\left[ \frac{\Delta K}{\Delta K_t} - 1 \right]^m}{\left[ 1 - \frac{K_{\max}}{K_c^*} \right]^n} \quad (13a)$$

or in reduced form,

$$\frac{da}{dn} = C \frac{\left[ (1-R) \frac{K_{\max}}{\Delta K_t} - 1 \right]^m}{\left[ 1 - \frac{K_{\max}}{K_c^*} \right]^n} \quad (13b)$$

where:

$\Delta K_t$  is the threshold level of  $\Delta K$

$K_c^*$  is the effective fracture toughness at the fatigue stress level and includes terms explicitly to account for thickness and stress level

C, m, n are constants

Johnson (41) proposed a similar relation essentially as follows:

$$\frac{da}{dn} = C \log \left[ \frac{K_{Ic} - \Delta K_t}{K_{Ic} - \Delta K} \right]^{1/n} \quad (14a)$$

or in reduced form

$$\frac{da}{dn} = C \log \left[ \frac{K_{IC} - \Delta K_t}{K_{IC} - (1-R) K_{max}} \right]^{1/n} \quad (14b)$$

Where  $\Delta K_t$  represents the threshold level of the range of K.

These relations predict the trends observed at the extreme of applied  $\Delta K$ 's. Pearson (42,43) has used the following modified Forman relation to correlate data on several aluminum alloys using half-inch thick specimens:

$$\frac{da}{dn} = 1/2 \frac{C \Delta K^m}{[(1-R) K_{IC} - \Delta K]} \quad (15)$$

This yields fair correlation over much of the intermediate range of test conditions, but crack rates are underestimated at low rates and at high mean stresses.

Mukherjee and Burns (44), recently investigated effects of loading frequency, mean stress, and the range of stress intensity factors on crack growth rates in polymethylmethacrylate and suggested the form:

$$\frac{da}{dn} = \gamma f^a K_{mean}^b (K)^c \quad (16a)$$

or (in reduced form)

$$\frac{da}{dn} = \gamma f^a K_{max}^b \left[ \frac{1+R}{2} \right]^b (1-R)^c \quad (16b)$$

where  $\gamma$ ,  $a$ ,  $b$ , and  $c$  are material constants determined by a multiple regression analysis and  $f$  is the frequency of loading.

Correlation with experimental results is shown in Figs. 9a and 9b from their paper. They claim a discrepancy of less than 15 percent between the experimental and predicted number of cycles over the limited range of frequencies and crack lengths investigated.

#### c. Programmed and Random Loading

In many structural applications, particularly for aircraft, the loading is neither simple harmonic nor is it maintained at a fixed amplitude. It is therefore of major interest to designers to have design formula for treating such cases. One may consider two major classes of such complex loading histories: programmed or block loading as shown in Fig. 10 and random loading which is defined generally in terms of the spectral power distribution.

Consider first the load history such as shown in Fig. 10. Here a simple cyclic load is maintained at constant peak and constant mean stress for a large number of cycles and then these two load parameters are changed to a new set of arbitrary values and again maintained constant for a significant number of cycles. These changes may be effected a number of times in the life of the component in question.

An obvious and simple approach to design is merely to use a selected one or two load parameter equations for crack growth rates and apply it repeatedly for each block of uniform loading. A number of investigators have examined the behavior of cracks growing under such conditions. McMillan, et al (45) concentrated on measurement of fatigue striations noting the changes in striation appearance and spacing at different load levels. He reported computed rates which are unconservative though not in error by more than a factor of two. Studies by McMillan and Pelloux (45) of single overloads show, furthermore, that such overloads generally tend to cause crack growth retardation. Matthews, et al (46) have observed (for cyclic loading) that step increases in the stress intensity factor led to a significant transient exaggeration of the crack propagation rate before it settled down to the anticipated "steady state" rate. In neither of these last studies, however, were crack propagation laws suggested to account for this phenomenon. Though a number of investigative and/or exploratory studies are underway covering various aspects of programmed loading and even random loading, little has been crystallized with respect to practical design laws.

In the area of random load fatigue testing, an excellent review of the state-of-the-art is provided by Swanson (47); that review also provides an extensive bibliography pertaining to crack propagation under random loading. Although a number of the investigators referenced therein have experimentally determined crack propagation rates under various random input, no explicit "laws" were proposed. Examination of papers presented at the recent Symposium of the International Committee on Aeronautical Fatigue (48,49) tends to reinforce the thought that emphasis in fatigue is being directed more and more toward the random

load approach. A number of models for behavior under random load were presented; no definite laws have been generally acceptable. The papers by Diamond, et al (48) and Wood (49) reflect current direction toward developing rational laws for "life" in lieu of crack propagation rates. Bussa, et al (50) proposed a detailed and sophisticated "life prediction model" for random loading based upon the relation:

$$\text{Life} = C K_t^a (\sigma)^b (P)^c (E)^d \quad (17)$$

where:

- C, a, b, c, and d are material constants
- $K_t$  is the stress concentration factor
- $\sigma$  is the maximum nominal stress
- P is the probability of maximum load occurrence
- E is a low load elimination factor.

Example application to the simple constant amplitude condition led to prediction of  $10 \times 10^5$  cycle whereas actual life was  $3.5 \times 10^5$  cycle, somewhat on the unconservative direction.

Another rather general approach to the life prediction approach to the random loading process is suggested by Erisman (51) in which he basically adopts Miner's rule but assumes

$$\sum_i \frac{n_i}{N_i} \neq 1$$

is permissible. Then defining four parameters which form the basis of his "M.I.S.S." method he proposes the relation:

$$\Sigma = f(\rho_m, \rho_j, \rho_p, \rho_q) \quad (18)$$

where:

- $\rho_m$  is the parameter defining the Mean stress effect
- $\rho_j$  is the parameter defining the Interaction effect (between mean and oscillating stress)
- $\rho_p$  is the parameter defining the Spectral effect and
- $\rho_q$  is the parameter defining the Sequene effect

No results are discussed in the paper.

#### d. Geometry and/or Structural Considerations

Most of the discussion thus far has related to homogeneous monolithic, isotropic materials, and, in fact, most of the fundamental understanding of fatigue to date has stemmed from studies on such materials. However, it is important practically from the aeronautical or structural engineer's point of view to be aware of the effects of other considerations such as thickness effects, or structural stiffening effects, etc. on propagation laws. In fact there is a major critical gap in our knowledge of crack propagation as related to whole classes of advanced materials such as composites.

It would appear straightforward to presume that inasmuch as geometry, thickness effects and stiffener effects cause perturbation of either the stress state at the crack tip or of the effective fracture toughness (hence the pertinent material constants) that many of the formulations already expressed earlier would be appropriate as long as one takes the perturbation into account.

Thickness, for example, is well known to influence fracture toughness (52-56) and as such would certainly be a significant factor to be routinely incorporated into such crack propagation laws as Forman Eqs. 11a, 11b, etc. where the toughness parameter is explicitly visible or in other relations such as that of Mukherjee Eqs. 16 for example in which the toughness is undoubtedly expressed implicitly in some of the material constants.

Geometry effects which influence the stress distribution (or the stress intensity) would similarly be expected to have significant effects; they can be routinely taken care of, provided the stress perturbation is suitably incorporated. One example has already been mentioned upon width effects in plates in order to compensate for the practical recognition that structures are not infinite in breadth but rather finite. There are appreciable results of stress distribution and/or stress

intensity factor studies in the literature for isotropic, monolithic structure. The recent review by Paris and Sih (57) is a good source of such data. Bowie (58), more recently, summarized development of a modified mapping-collocation technique which has been applied to finite orthotropic as well as isotropic media and has wide applicability. Structurally significant detail such as stiffened panels, rivet effect cylinders, etc. have also been studied, (59-63) and stress intensity factors, or their equivalent, determined for such varied configuration. These various analytical and/or experimental results of stress distribution near crack tips will undoubtedly be a principal input to the crack propagation relationships, independent of which form(s) is eventually proven to be most useful for design.

TABLE 1 - Fatigue-crack growth equations

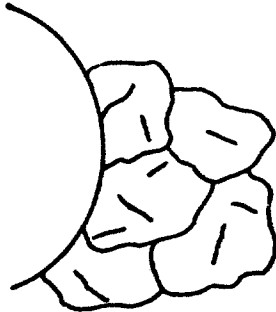
Date	Investigators	Equation
1935 to 1936	DeForest and Magnuson	No equation, but one of earliest experiments designed to measure fatigue-crack growth.
1938	Langer and Peterson	No equation, but first suggestions concerning the inclusion of crack propagation data into cumulative damage rules.
1953	Head	$dl/dn = \beta^{3/2}$
1956	McClintock	$[d(1/h)]/[d(\theta h)] = 1/4 \gamma_f [\ln h/2\rho - 1/2(1 - 4\rho^2/h^2)] \dots$ in torsion
1957 to 1958	Frost and Dugdale	$dl/dn = \text{constant} \dots$ constant stress $dl/dn = A\sigma^3 \dots$ constant load
1958	McEvily and Illg	$dl/dn = 2\alpha l^{3/2}$ , where $\alpha = 1/\epsilon(1)^{-3/2}$
1961	Hardrath and McEvily	$\log_{10}^{-1}(0.0051 K_n \sigma_{net} - 5.472 - 34/K_n \sigma_{net} - 34)$
1960	Schijve	$dl/dn = A \sigma_a^\beta$
1954		
1956	Weibull	$dl/dn = K W \sigma_i^\beta \dots$ constant cyclic $\sigma$
1960		$[d(1/w)]/dn = K(\sigma_0^\beta)/[(1 - 1/w)^\beta] \dots$ constant cyclic load
1961	Valluri	$dl/dn = K1/[(1 - 1/W)_4] \sigma_{crk}^4 (1 - \sigma_i/\sigma_{crk})^2 (1 - R)^2$
1961	Denke and Christensen	$dl/dn = \bar{u}(1/l_c)/[(1 - 1/l_c)^4]$
1961	Paris, Gomez, and Anderson	$dl/dn = K_a = \sigma \sqrt{1/2\alpha}$
1963	Liu	$dl/dn = c\sigma^2 l$
1965	Manson	$dl/dn = c(\Delta\sigma \sqrt{l})^8$

## REFERENCES

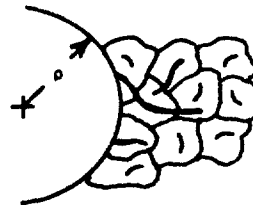
1. Dolan, T. J., "'Models' of the Fatigue Process," Fatigue - An Interdisciplinary Approach, Proceedings of the 10th Sagamore Army Materials Research Conference, Editors J. J. Burke, N. L. Reed, V. Weiss, Syracuse Univ Press, Syracuse, N. Y., 1964.
2. Manson, S. S., "Fatigue: A Complex Subject - Some Simple Approximations," Exp. Mech., July 1965.
3. Hardrath, H. F., "Cumulative Damage," Fatigue - An Interdisciplinary Approach, Proceedings of the 10th Sagamore Army Materials Research Conference, Editors J. J. Burke, N. L. Reed, V. Weiss, Syracuse Univ. Press, Syracuse, N. Y., 1964.
4. Grover, H. J., "An Observation Concerning the Cycle Ratio in Cumulative Damage," Symposium on Fatigue of Aircraft Structures, Special Tech. Pub. No. 274 published by the ASTM, 1959.
5. Head, A. K., "The Mechanisms of Fatigue of Metals," Jl of the Mech and Physics of Solids, Vol 1, 1953, pp. 134-141.
6. Wood, W. A. and Reimann, W. H., "Some Direct Observations of Cumulative Damage in Metals," Inst. for Study of Fatigue and Reliability, Columbia Univ., Tech Rpt No. 11, Oct 1964.
7. Wood, W. A., "Exp Approach to Basic Study of Fatigue," Inst. of Study of Fatigue & Reliability, Columbia Univ., Tech Rpt No. 24, Aug 1965.
8. Valluri, S. R., "A Theory of Cumulative Damage in Fatigue," ARL Report No. 182, Aeronautical Research Laboratory, Office of Aerospace Research, USAF, Dec 1961.
9. Valluri, S. R., "A Unified Engineering Theory of High Stress Level Fatigue," Presented at National IAS/ARD Joint Summer Mtg, Los Angeles, California, June 13-15, 1961
10. Barrois, W. G., Manual on Fatigue of Structures - Fundamental and Physical Aspect, AGARD-MAN-8-70.
11. Laird, C. and Smith, G. C., "Initial Stages of Damage in High Stress Fatigue in Some Pure Metals," Phil. Mag., Nov 1963, pp. 1945-1963.
12. Schijve, J., "Analysis of Fatigue Phenomenon in Aluminum Alloys," National Aero and Astronautical Research Institute, Amsterdam, Tech Rpt M 2122, 1964.
13. Rotvel, F., "Biaxial Fatigue Tests with Zero Mean Stresses Using Tubular Specimens," Int. J of Mech Sci., Pergamon Press, Vol 12, 1970, pp. 597-613.
14. Laird, C., "The Influence of Metallurgical Structures on the Mechanism of Fatigue Crack Propagation," Presented at 69th Annual Mtg of ASTM, June 27 - July 1, 1966.
15. Impellizzeri, L. F., "Cumulative Damage Analyses in Structural Fatigue," Effect of Environment and Complex Load History on Fatigue Life, ASTM STP 462, 1970.
16. Jacoby, G. H., "Comparison of Fatigue Lives Under Conventional Program Loading and Digital Random Loading," Effect of Environment and Complex Load History on Fatigue Life, ASTM STP 462, 1970.
17. Schijve, J., "Significance of Fatigue Cracks in Micro and Macro Range," Fatigue Crack Propagation, ASTM STP 415, 1967.
18. Grosskreutz, J. C., "Fatigue Mechanism in the Sub-Creep Range," Report prepared as part of a Fatigue Damage Survey undertaken by the Gas Turbine Panel of the Joint Committee on the Effect of Temperature on the Properties of Metals. To be published as an ASTM STP, 1970.
19. Christensen, R. H. and Harmon, M. B., "Limitations of Fatigue-Crack Research in the Design of Flight Vehicle Structures," Fatigue Crack Propagation, ASTM STP 415, 1967.
20. Barrois, W. G., "Manual on Fatigue of Structures - Fundamental and Physical Aspects," Advisory Group for Aerospace Research and Development, AGARD-MAN-8-70.
21. Pelloux, R. M., "Review of Theories and Laws of Fatigue Crack Propagation," Proceedings of the Air Force Conference on the Fatigue and Fracture of Aircraft Structures and Materials held at Miami Beach, Fla., Dec 1969, Rpt AFFDL TR 70-144, Sept 1970.
22. Head, A. K., "The Growth of Fatigue Cracks," Phil. Mag., Vol 44, Series 7, 1953, p 925.
23. Paris P. C. and Erdogan, F., "A Critical Analysis of Crack Propagation Laws," Trans. ASME, J of Basic Eng, Dec 1963, pp. 528-534.
24. Frost, N. and Dugdale, D. S., "The Propagation of Fatigue Cracks in Sheet Specimens," J of the Mech and Physics of Solids, Vol 6, No. 2, 1958, p 92.
25. Irwin, G., "Fracture Mode Transition for A Crack Traversing a Plate," J of Basic Eng, Trans ASME, Series D, Vol 82, No. 2, June 1960, p 417.

26. Barsom, J. M., "The Dependence of Fatigue Crack Propagation on Strain Energy Release Rate and Crack Opening Displacement," Damage Tolerance in Aircraft Structures, ASTM STP 486, 1970.
27. Wilhem, D. P., "Investigation of Cyclic Crack Growth Transitional Behavior Fatigue Crack Propagation," ASTM STP 415, p 363.
28. Beeuwkes, R., Analysis of Failure - Proc. 3rd Sagamore Ordnance Materials Research Conf. on "Materials Evaluation in Relation to Component Behavior," held at Duke Univ., Durham, N. C., cosponsored by OMRO and OOR of the U. S. Army, December 5-7 1956.
29. Frost, N. E., and Dixon, J. R., "A Theory of Fatigue Crack Growth," Int. J. Fract. Mech., Vol 3, No. 4, 1967, p 301.
30. Joshi, S. R. and Shewchuck, J., "Fatigue Crack Propagation in a Biaxial Stress Field," Exp. Mech., Dec 1970, p 529.
31. Paris, P. C. and Gomez, Andersen, A Rational Analytic Theory of Fatigue, The Trend in Eng., Vol 13 Not, Univ. of Washington, June 1971.
32. Broek, D. and Schijve, J., "The Influence of Mean Stress on the Propagation of Fatigue Cracks in Aluminum Alloy Sheet," Nat'l Aero Res Inst., Amsterdam, the Netherlands, Rpt NLR-TR M.2111, Jan 1963.
33. Forman, R. G., Kearney, V. E., and Engle, R. M., "Numerical Analysis of Crack Propagation in Cyclic Loaded Structures," J. of Basic Eng., Trans. ASME, Sept 1967, p 459.
34. Tonkins, B., "Fatigue Crack Propagation - An Analysis," Phil. Mag., Vol 18, No. 155, Nov 1968, pp. 1041 ff.
35. Hudson, C. M. and Scardina, J. T., "Effects of Stress Rates on Fatigue Crack Growth in 7075 T6 Aluminum Alloy Sheet," Eng. Frac. Mech., Vol 1, No. 3, April 1969, p 429.
36. Bucci, R. J., Clark, W. G., Jr., and Paris, P. C., "Fatigue Crack Propagation Rates Under a Wide Variation of  $\Delta K$  for a ASTM A517 Grade F (T-1) Steel," Paper presented at 5th Nat. Symp. on Fract. Mech., Univ. of Ill., Aug 31 - Sept 2, 1971.
37. Bucci, R. J., Paris, P. C., Hertzberg, R. W., Schmidt, R. A., and Anderson, A. F., "Very Low Fatigue Crack Growth Rates in Air and Dry Argon for a Titanium 6Al-4V Alloy," Paper presented at 5th Nat. Symp on Fract. Mech., Univ. of Ill., Aug 31 - Sept 2, 1971.
38. Paris, P. C., Weiss, W., and Wessel, E. T., "On the Threshold for Fatigue Crack Growth," Paper Presented at 5th Nat. Symp. on Fract. Mech., Univ. of Ill., Aug 31 - Sept 2, 1971.
39. Paris, P. C., Bucci, R. J., Wessel, E. T., Clark, W. G. Jr., and Mayer, T. R., "Very Low Fatigue Crack Growth Rates in A533 Steels," Paper Presented at 5th Nat. Symp. on Fract. Mech., Univ. of Ill., Aug 31 - Sept. 2, 1971.
40. Bluhm, J. I., Baratta, F., Driscoll, G. and Matthews, W., "Crack Propagation Rates at Extremes of Stress Intensity Factor," Unpublished report AMRC, Nov 1969.
41. Johnson, R. E., "Design Criterion for Residual Cyclic Life," General Electric Co. Technical Information Series Report No. R68AEG468, 1 Nov 1968.
42. Pearson, S., "The Effect of Mean Stress on Fatigue Crack Propagation in Half Inch (12.7 mm) Thick Specimen of Aluminum Alloy DTO 5050 and DTO 5090," RAE - TR 69195, Sept 1969.
43. Pearson, S., "The Effect of Mean Stress on Fatigue Crack Propagation in Half Inch Thick Specimen of Aluminum Alloy of High and Low Fracture Toughness," RAE TR 68297, Dec 1968.
44. Mukherjee, B., and Burns, D. J., "Fatigue Crack Growth in Polymethylmethacrylate," Exp. Mech., Oct 1971, p 433.
45. McMillan, J. C. and Pelloux, R. M. N., "Fatigue Crack Propagation Under Program and Random Loading," Fatigue Crack Propagation, ASTM STP 415, p 505.
46. Matthews, W. T., Baratta, F. I. and Driscoll, G. W., "Experimental Observations of a Stress Intensity History Effect Upon Fatigue Crack Growth Rate," Int. J. of Fract. Mech. 7, 1971, pp. 224-228.
47. Swanson, S. R., "Random Load Fatigue Testing: A State of the Art Survey," Materials Research and Standards, Vol 8, No. 4, ASTM, April 1968, p 10.
48. Diamond, Patruce, and Payne, A. E., "Reliability Analysis Applied to Structural Tests," presented at Sixth Symp. of the International Committee on Aeronautical Fatigue held in Miami Beach, Florida, U.S.A., May 12-14, 1971.
49. Mood, Howard A., "Fracture Control Procedures for Aircraft Structural Integrity," presented at Sixth Symp. of the International Committee on Aeronautical Fatigue held in Miami Beach, Florida, U.S.A., May 12-14 1971.
50. Bussa, S. L., Sheth, N. J., and Swanson, S. R., "Development of a Random Load Life Prediction Model," paper presented at the 73rd Annual Meeting of the ASTM, Toronto, Can., June 21-26, 1970.

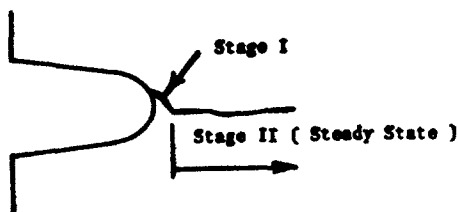
51. Erisman, T. H., "Fatigue Life Prediction Under Irregular Stress Conditions," J. of Strain Analysis, Vol. 5, No. 3, 1970.
52. Allen, F. C., "Effect of Thickness on the Fracture Toughness of 7075 Aluminum in the T-6 and T73 Condition," Damage Tolerance in Aircraft Structures, ASTM STP 486, p 16.
53. Bluhm, J. I., "A Model for the Effect of Thickness on Fracture Toughness," Proc. ASTM, Vol 61, 1961, p 1324.
54. Lui, H. W., "Size Effects on Fatigue Crack Propagation," Aerospace Res. Lab, Office Aerospace Research USAF, Wright-Patterson Air Force Base, ARL Rpt 64-68, April 1964.
55. Broek, D., "The Effect of the Sheet Thickness on the Fracture Toughness of Cracked Sheet," Nat. Aerospace Lab. NLL, Amsterdam, Rpt NLR-TR-M.2160, Jan 1966.
56. Frost, N. E., and Denton, K., "Effect of Sheet Thickness on Rate of Growth of Fatigue Cracks in Mild Steel," J. Mech. Eng. Sci., Vol 3, No. 4, 1961, p 295.
57. Paris, P. C. and Sih, G. C., "Stress Analysis of Cracks," Fracture Toughness Testing and its Application, ASTM STP 381, 1964, p 30.
58. Bowie, O. L., "Solution of Plane Crack Problems by Mapping Technique," to appear as chapter in book edited by G. C. Sih.
59. Crichlow, W. J., and Wells, R. H., "Crack Propagation and Residual State Strength of Fatigue Cracked Titanium and Steel Cylinders," paper presented at 69th Annual Meeting of ASTM held at Atlantic City, June 27 - July 1, 1966.
60. Bluhm, J. I. and Mardirosoian, M. M., "Fracture Arrest Capabilities of Annularly Reinforced Cylindrical Pressure Vessels," Exp. Mech. 3, No. 3, 1963, p 57 and Exp. Mech. 3, No. 12, 1963, p 1.
61. Poe, C. C. Jr., "Fatigue Crack Propagation in Stiffened Panels," Damage Tolerance in Aircraft Structures, ASTM STP 486, 1970, p 79.
62. Figge, I. E., and Newman, J. C., Jr., "Fatigue Crack Propagation in Structures with Simulated Rivet Force," Fatigue Crack Propagation, ASTM STP 418, 1966, p 71.
63. Lakshimikantham, C., "Analysis of Transverse Cracks in Stiffened Fiber-Reinforced Composite Strip under Tension," Army Materials and Mechanics Research Center, Watertown, Mass., Rpt No. AMMRC TR 71-1, Jan 1971.



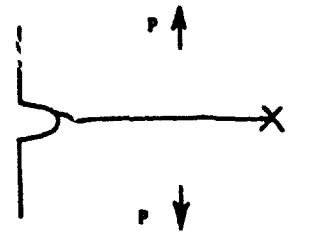
(a) Damaged sites showing nucleation of microcracks and some coalescence (microgrowth)



(b) Further microgrowth and appearance of dominant crack



(c) Steady state extension of dominant crack



(d) Final fracture imminent

Fig.1 Sequence of events from microcrack nucleation to final fracture



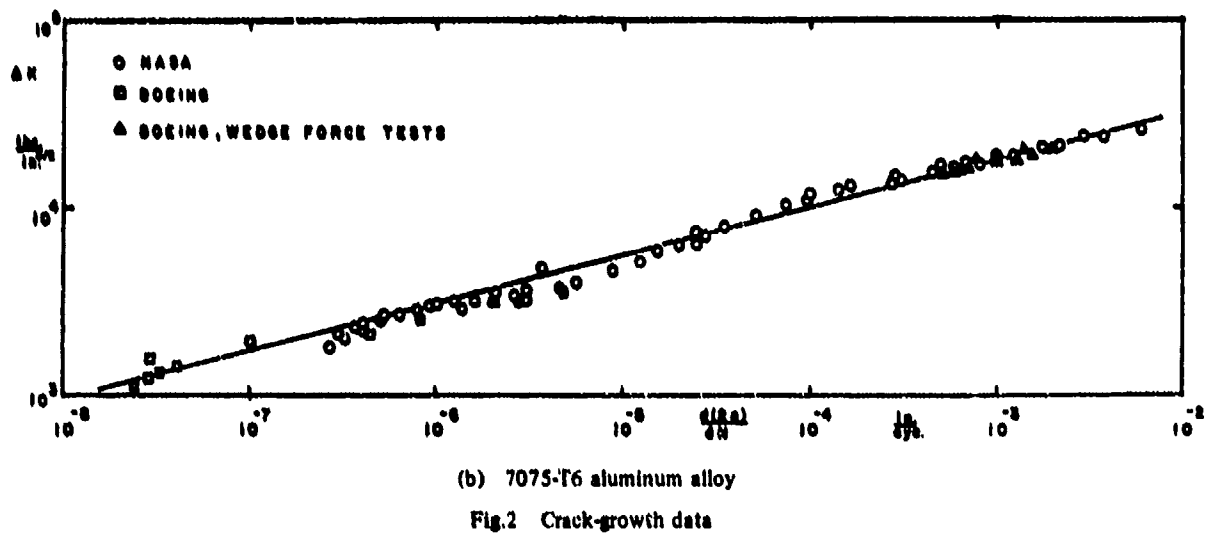
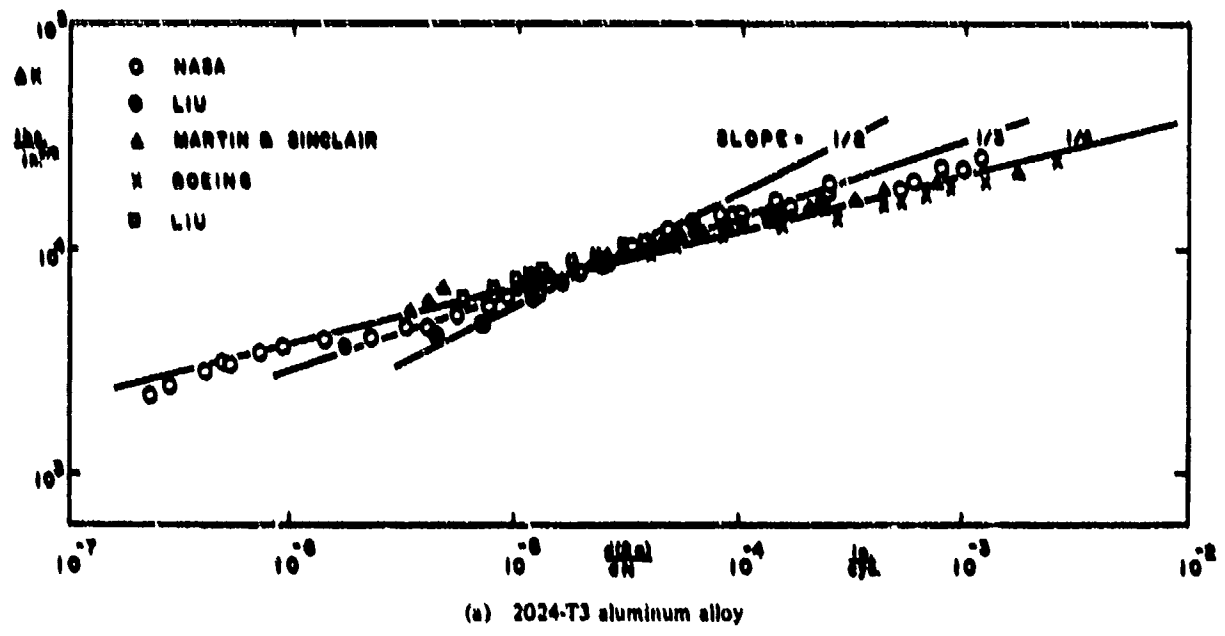


Fig.2 Crack-growth data

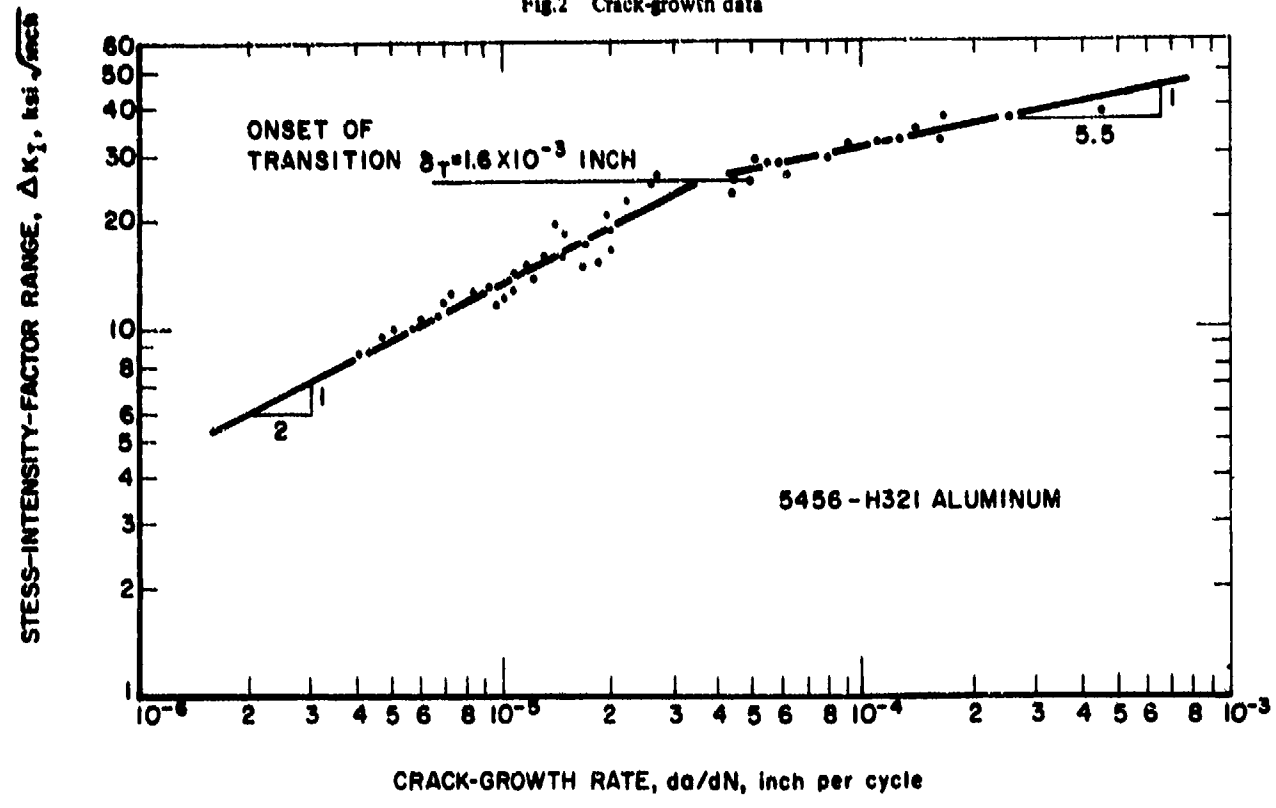


Fig.3 Fatigue crack growth rate as a function of stress intensity

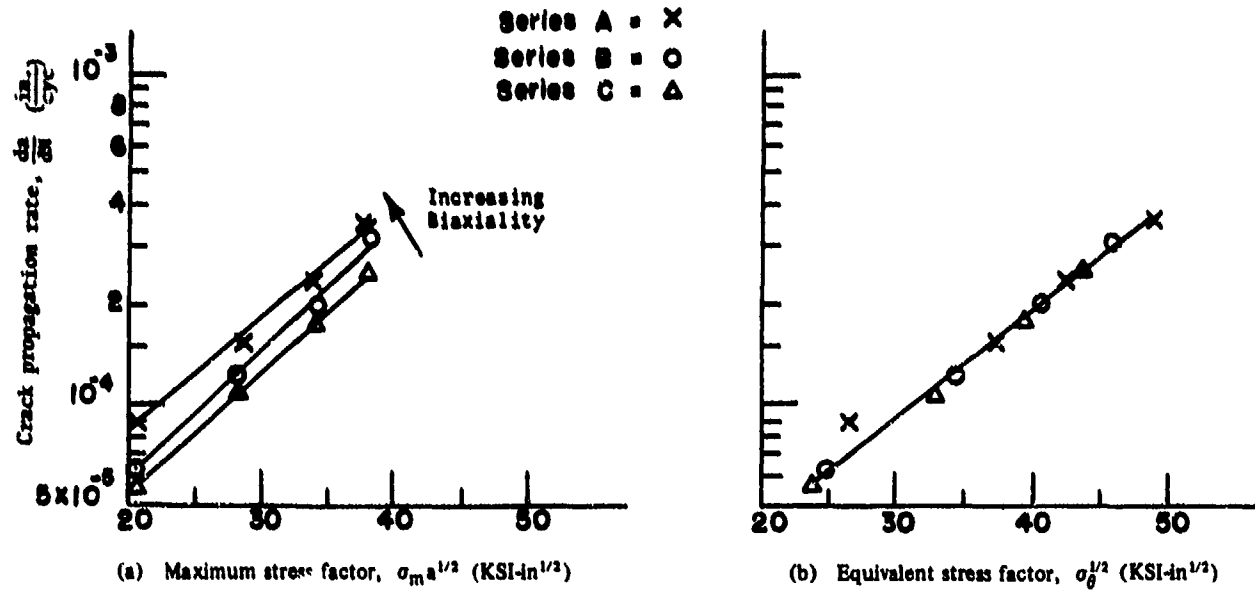


Fig.4 Stress factors under biaxial loading

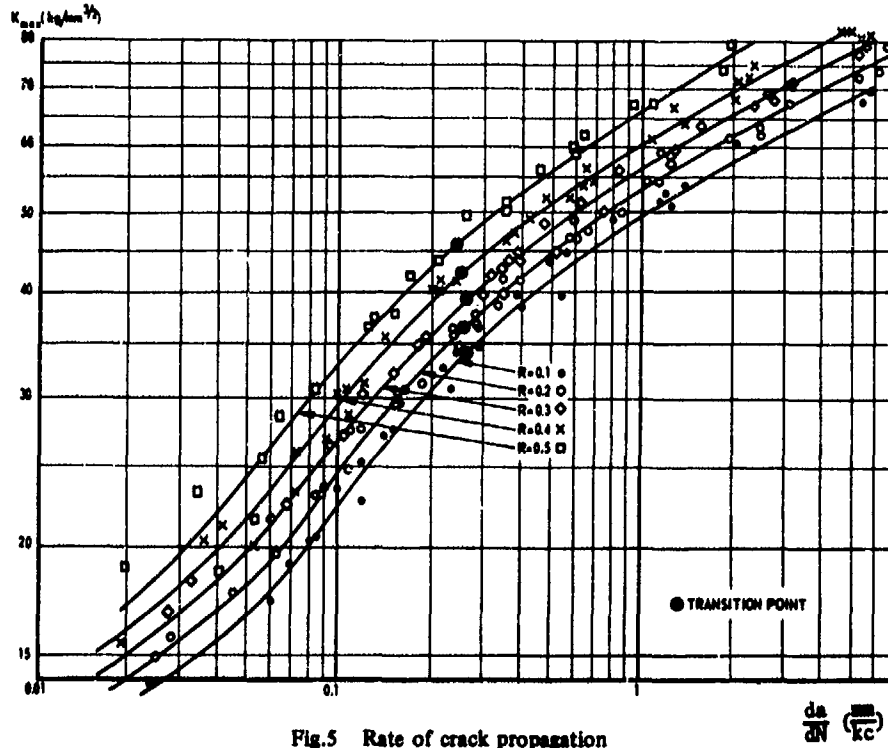


Fig.5 Rate of crack propagation

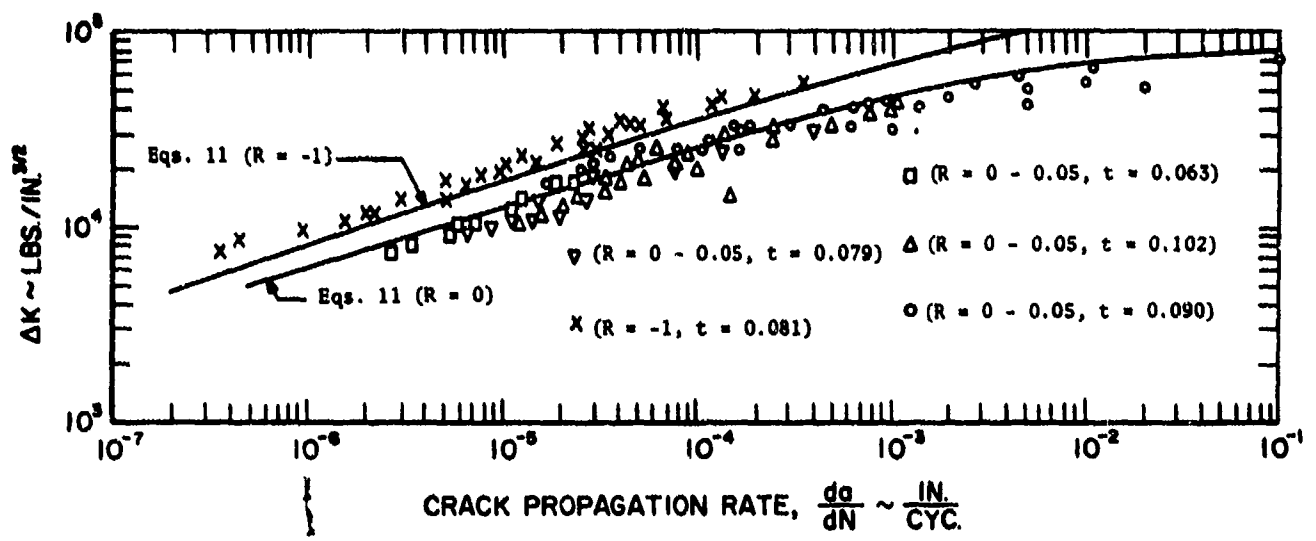


Fig.6 Comparison of experimental and theoretical crack-propagation rates in 2024-T3 aluminum plate for  $R = 1$  and  $R = 0$

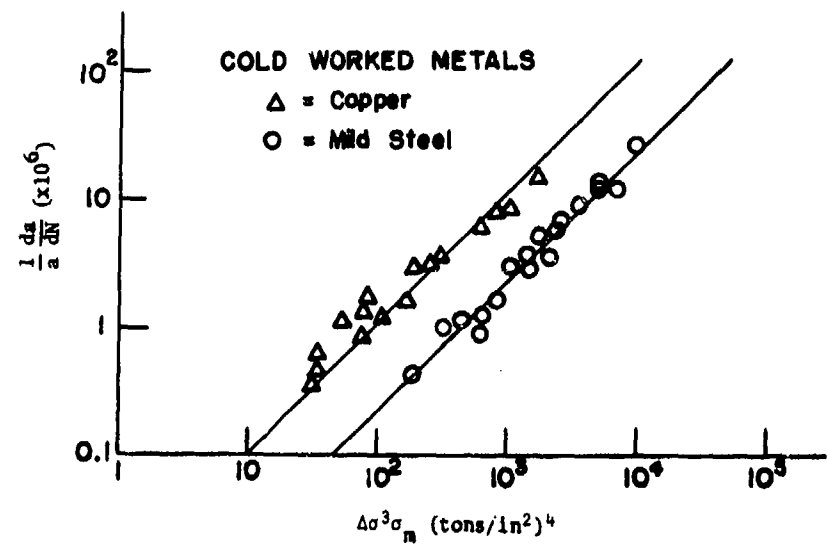


Fig.7 Crack propagation rate

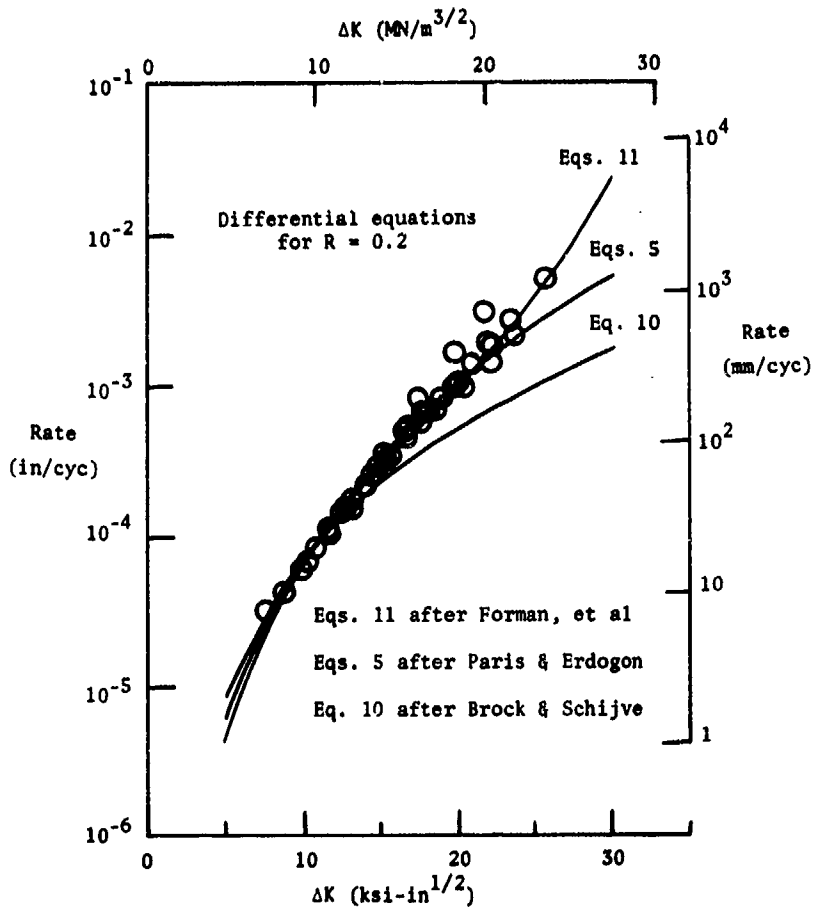


Fig.8 Correlation of experimental fatigue crack growth rates

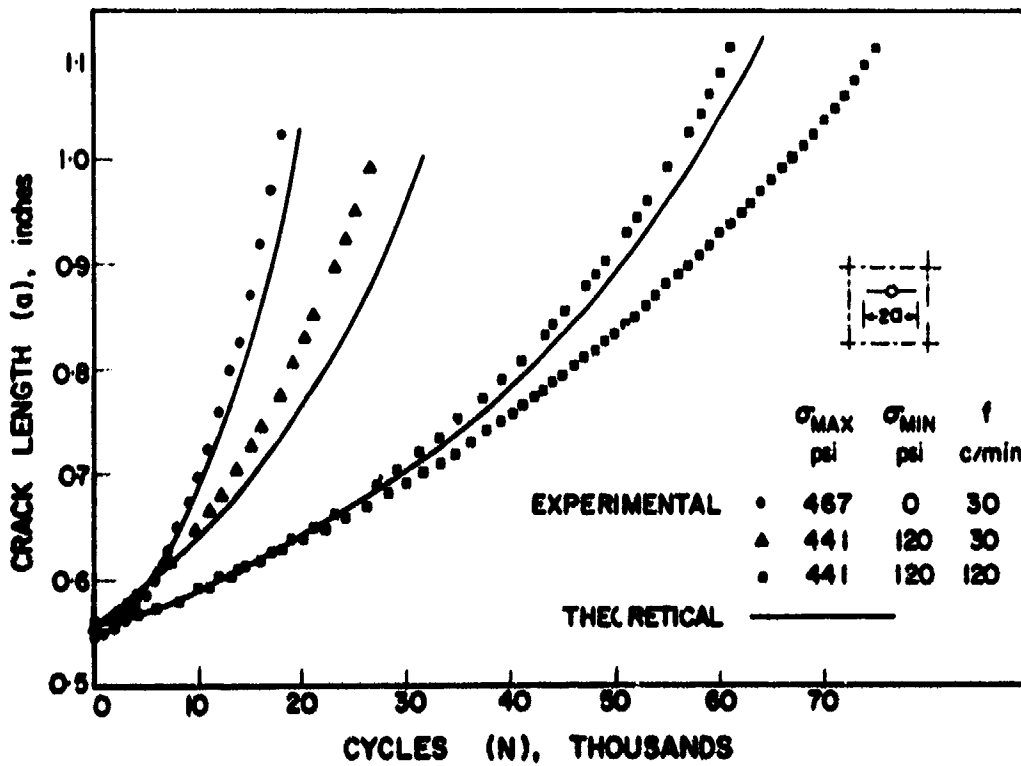


Fig.9 Through-thickness fatigue-crack growth from constant-load-amplitude tests

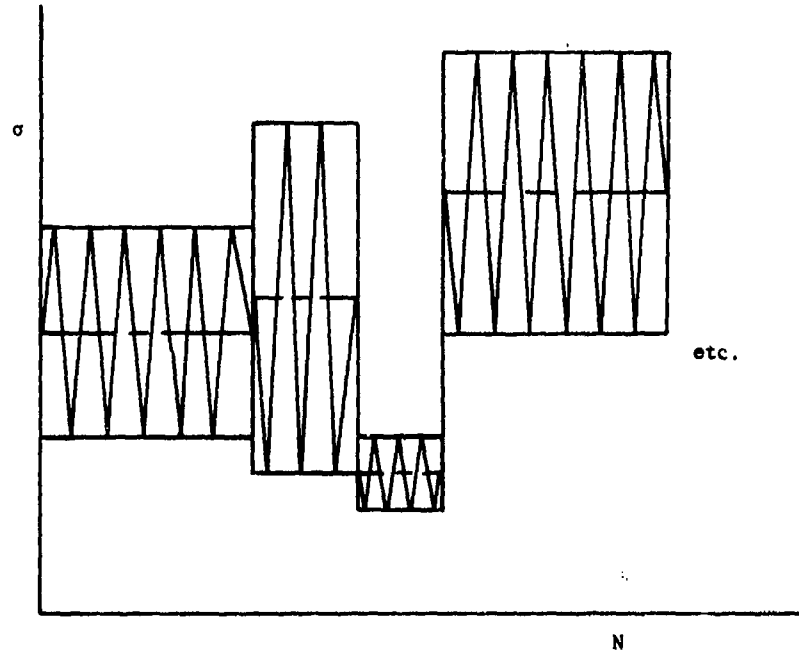


Fig.10 Illustration of programmed loading spectrum

Appendix IV-4  
ENVIRONMENTAL EFFECTS IN FRACTURE

H. H. Johnson

a. Introduction

Failures in aircraft structures and components are often adversely influenced by environmental factors. Since environmental cracking is more frequently encountered with the higher strength materials used in advanced structural systems, the area has received much attention in recent years.

Some important characteristics of environmental cracking are:

- environment-influenced cracks in service structures often emanate from prior flaws or metallurgical heterogeneities.
- it often commences at stress levels well below the normal non-environmentally influenced net section yield strength or fracture stress.
- the crack grows slowly in the opening mode under the combined influence of the stress state and the environment.
- rapid fracture will occur if the crack grows to a length such that the remaining section is overloaded.
- environmental cracking is more prominent with higher strength materials; the stress to initiate the crack growth process may be much lower due to the adverse effect of increasing strength level.
- the environment chemistry to cause cracking is much less specific or unique for higher strength materials, with aqueous media of most interest.
- the environment may catalyze crack initiation and growth under both static and dynamic loading.

The inclusion of environmental effects in fracture phenomena necessarily leads to a complex situation, in which the description of fracture must be largely phenomenological. This is evident from a schematic representation of the essential components of the environmental cracking event, Fig. 1. Metallurgy, chemistry, and mechanics are involved and are not easily separated.

The locus of the environmental cracking event is the crack tip region, where the essential interaction occurs between the environment and the stressed and plastically deforming material. Since characterization of the plastic zone is as yet primitive and the chemical interactions in the crack tip region are not easily studied, it is not surprising that quantitative understanding of environmental cracking remains largely at the macroscopic level.

b. Testing Methodology

The classical method for evaluating susceptibility to environmental cracking is to immerse a stressed specimen, usually with a smooth test section, in the suspect environment and record the time to failure. The environmental cracking characteristics are then concisely summarized by a plot of nominal stress vs time to failure. This allows a good characterization of the metallurgical and bulk environment factors, but the mechanics are poorly described by the nominal stress, especially since multiple cracking is often observed. Quantitative correlation of laboratory test data and service performance is therefore not feasible.

A further characteristic of this procedure is that it is largely a test for crack initiation. An identifiable crack usually appears rather late in the test life, often well after 50%, and the crack then propagates rather rapidly. Failure times are controlled mainly by the material-environment interaction at the smooth surface.

As with other fracture phenomena, it is useful to consider environmental cracking as composed of two phases, crack initiation and crack propagation. Initiation refers primarily to the formation of a crack at a smooth surface, and propagation to the growth of a crack, either subsequent to the initiation phase or from a preexistent crack-like flaw.

The classical procedure is primarily an initiation test; it is often useful as a screening device, particularly for lower strength materials. However, it has on occasion been dangerously misleading in the sense that it has indicated immunity in environments where service experience has demonstrated otherwise. For example, examination of service failures in high strength steels shows that environment-influenced fracture cracks almost invariably grow from prior flaws, and this circumstance is just not evaluated by the classical testing procedure, and a testing procedure which focuses upon crack propagation characteristics is essential.

Titanium alloys in aqueous media offer a second example of the separate importance of the initiation and propagation phases. Few service failures have been experienced with titanium alloys in aqueous media, yet laboratory tests with pre-cracked specimens suggest that these alloys have a substantial susceptibility to such media. The key factor is apparently the tenacious and rapidly forming film which is characteristic of titanium. In smooth section tests this film is protective; in pre-cracked tests where the stress is applied subsequent to the environment, the broken film is apparently unable to reform and be protective. The former case is in better accord with service experience, where it appears that film reformation often

occurs at the tips of flaws or crevices prior to exposure to the environment, and this limits the susceptibility to environmental cracking. As a result, titanium alloys have a better record in service than in the laboratory, with respect to cracking in aqueous media.

### c. Fracture Mechanics Approach

It has now been demonstrated that test procedures based upon linear elastic fracture mechanics are adequate to predict and interpret environmental cracking phenomena when crack propagation is the controlling feature (1, 2). This approach is at present most useful for materials of intermediate and high strength, where conditions are such that the size of the plastic zone around the crack tip is a small fraction of the specimen or structure dimensions, i.e., the material is in plane strain.

Within the fracture mechanics framework, the stress intensity factor (a quantitative measure of the locally elevated stress field surrounding the flaw and the associated plastic zone) is taken as the driving force for crack extension. It is appropriate, then, to consider on an experimental basis whether or not the stress intensity factor can correlate data from different specimen geometries and from structural failures.

The available experimental evidence does, in fact, strongly indicate that the stress intensity does correlate such data (1, 2) and is more suitable for that purpose than any other measure of the stress state. The evidence (1, 2) may be summarized in the following categories:

(1) Threshold stress intensities ( $K_{ISCC}$ ) are identical when measured by both crack initiation and crack arrest techniques (1-3). With end loading and crack-line wedge loading of center-cracked specimens of Ti-8Al-1Mo-1V alloys in 3-1/2% aqueous solutions of NaCl, good agreement between crack initiation and crack arrest stress intensities was obtained within the stress intensity range of 20-25 ksi-in<sup>1/2</sup> for initiation in end loading and within 20-22 ksi-in<sup>1/2</sup> for arrest in wedge loading. The net section stress increases with crack length with both loading configurations; however, concomitantly, the stress intensity decreases with wedge loading and increases with end loading. The existence of crack arrest with wedge loading, therefore, illustrates the importance of the stress intensity factor, as opposed to the net section stress.

(2) The invariance of the threshold stress intensity with specimen geometry has also been demonstrated with high strength steels (4), Fig. 2. Identical threshold stress intensities are observed for the three geometries, but systematic differences in failure time, and therefore crack growth rate, are noted. These distinctions reflect the different functional dependences of stress intensity on crack length for the three specimens and suggest that environmental cracks grow faster at higher stress intensities.

(3) Turning to crack propagation experiments, several lines of evidence suggest a unique relation exists between crack growth rate and stress intensity for a given material-environment system. Fig. 3 presents results of a constant stress intensity propagation experiment for high strength steel in water (1). These results show that constant stress intensity is clearly associated with a constant growth rate; over the same interval of crack extension the net section stress varies.

(4) For the Ti-8Al-1Mo-1V alloy in 3-1/2% aqueous solutions of NaCl, crack growth rates (3) from both end loaded and crack-line loaded specimens fall on a single curve, Fig. 4, when correlated in terms of the stress intensity factor.

Although more experimental data would be desirable, that available strongly suggests that the stress intensity factor is the appropriate parameter for characterizing the stress state in environmental cracking phenomena. Tiffany and Masters (5) tested wet and dry surface-flawed specimens to illustrate the detrimental effect of moisture and to compare the wet specimen results with a hydraulic actuator which had failed in the presence of moisture. Fig. 5 shows their results and the good correlation which they obtained on a stress intensity basis.

The threshold stress intensity is perhaps the single most important parameter descriptive of environmental cracking. Although occasionally there is some question as to whether or not it is an absolute limit, it always indicates a very sharp change in environmental cracking characteristics, with virtual immunity at the lower stress intensity levels and dangerous susceptibility at the higher levels. Therefore, it is the single most important design parameter to characterize the cracking phenomenon.

Crack growth rate measurements in many systems have shown a general correlation of these rates with stress intensities, as shown in Fig. 6. V-k curves of this characteristic shape have been observed for a wide variety of material-environment systems, including steels, titanium and aluminum alloys, and glass. Not all material-environment systems necessarily show all three regimes.

Environmental parameters, e.g., temperature and solution chemistry, are often observed to have different effects on the three regimes, suggesting that different mechanisms may operate in different regimes. In some instances regime II is associated with crack branching; this may represent a quasi steady state in which the environmental reaction occurs at a rate just sufficient to keep up with the propagating crack.

For some systems, notably steels and titanium alloys, regime I becomes vertical at a sufficiently low stress intensity, demonstrating the existence of a true threshold for environmental crack extension. Further, for both systems it is generally not possible to manipulate crack growth rates over orders of magnitude by variations in condition or heat treatment or by variations in environmental parameters such as temperature, imposed potential, etc. Therefore, the threshold stress intensity as a more important parameter.

For aluminum alloys the existing data do not indicate a true threshold stress intensity; rather, regime I becomes steeper at low stress intensities but does not appear to approach a true vertical asymptote. However, growth rates may be varied over many orders of magnitude for aluminum alloys by appropriate variations in composition, processing, and heat treatment schedules. Safe performance in quite long, but finite, life applications may be assured by this approach, even though stresses may exceed the threshold stress intensity.

It is generally observed for steels and titanium alloys that crack growth rates are short, ranging from a few minutes to a few hours, for a wide variety of processing and thermal treatments. Threshold stress intensities are usually unaffected by procedures which do effect changes in the crack growth rate. There has been very limited success in improving the threshold stress intensity by methods which do not simultaneously lower the yield strength. This is evident from studies (7, 8) of the environmental cracking behavior of maraging steels in aqueous media after a substantial variety of thermal treatments, and of 4340 steel with different prior austenite grain sizes.

For high strength quenched and tempered steels the threshold stress intensity is quite sensitive to strength level (6), Fig. 7. The rapid drop in  $K_{ISCC}$  at strength levels in the range of 180,000-200,000 psi is fairly general, and consistent with the much higher incidence of service failures with high strength steels.

A major limitation of the critical threshold stress intensity concept for environmental cracking is that it is essentially a static loading concept. Available evidence suggests that the static  $K_{ISCC}$  is of little relevance in situations involving dynamic or cyclic loading. Environment-accelerated fatigue crack growth has been observed at stress intensities well below  $K_{ISCC}$ . Environmental crack growth under cyclic loading is strongly load-frequency sensitive, as would be expected from a process involving interaction with the environment. At sufficiently high frequencies the crack growth rate is unaffected by environmental factors; the effect becomes more pronounced as the frequency is decreased.

It appears that in some structures, particularly in aerospace and military applications, environment-accelerated fatigue crack growth may well be the life-limiting process for the structure. More experimental attention to this area might be desirable.

In many experimental and practical situations, the crack grows at a controlled rate under stress state circumstances that require an increase in stress intensity. It has been observed (1) that when the stress intensity increases to the level corresponding to the fracture toughness of the material, e.g.,  $K_{IC}$ , an abrupt transition to rapid and unstable crack growth occurs. In other words, the basic fracture toughness is unaffected by the environmental interaction, which apparently can be described in mechanical terms as a local instability at the crack tip. There is no bulk degradation of material properties, and the effect of the environment is localized to the surface or near surface regions.

#### d. Mechanistic Considerations

It is evident that the micro-mechanism of environmental cracking involves aspects of chemistry, mechanics, and metallurgy in a complicated fashion. Not surprisingly, there is little agreement among investigators on the mechanisms operating in different material-environment systems. Most suggested mechanisms are built around one or more of the following concepts:

(1) Anodic dissolution - the crack tip area is considered anodic with respect to more remote regions, usually for metallurgical reasons, and therefore metal dissolution into aqueous media is concentrated at the crack tip.

(2) Weakening by adsorption - it is suggested that adsorption of specific species in the crack tip region results in a loss of cohesion of the matrix atoms. The exact physical mechanism to accomplish this is obscure, but presumably results from an alteration in the local electronic structure. The question as to whether the adsorption process is strain activated is open.

(3) Films - surface films play an important part in several mechanistic concepts. Rupture of protective films by plastic strain may be invoked to explain concentration of dissolution or embrittling mechanisms at crack tips. Also, the continual formation, rupture, and re-formation of brittle films has been suggested as a complete mechanism. Finally, passive films are protective and may explain immunity, as suggested earlier in the discussion of titanium alloys.

(4) Hydrogen - it is well known that hydrogen can embrittle many, but not all, of the alloys that are susceptible to environmental cracking. It has been suggested, and currently it is a very live issue, that hydrogen generated by corrosion reactions between the material and environment may be the actual embrittling agent in many environmental cracking phenomena.

Some aspects of these complicated questions have been clarified by recent investigations of crack tip chemistry. These investigations demonstrate that the electro-chemical nature of the media at the crack tip during steady state propagation may differ greatly from the bulk chemistry. These results suggest the availability of hydrogen at crack tips even when the bulk electrochemistry would suggest that this was not thermodynamically possible.

Barth, Steigerwald, and Troiano (9) used a permeation technique to ascertain the conditions under which hydrogen is discharged into steel from an aqueous environment. Even under bulk anodic potentials, they found hydrogen permeation through the steel when pitting was evident on the input surface. Hydrogen was not observed in the absence of pitting, except under cathodic potentials. For anodic potentials this suggests a close connection between pitting and the availability of hydrogen at the crack tip.



electrochemistry of aqueous solution in cracks. From measurements of local pH and potential in the crack tip region he concludes, Fig. 8, that the crack tip solution chemistry may differ greatly from that of the bulk solution.

The solution chemistry in the crack tip always becomes sufficiently acid so that the breakdown of water and the reduction of hydrogen ions is thermodynamically favored. This is observed for a variety of materials, even for solutions of highly alkaline bulk chemistry, or when the specimen was anodically polarized (2). This acidification of the crack tip solution presumably results from hydrolysis of dissolving metal ions. Therefore environmental cracks frequently occur under conditions where the crack tip chemistry is thermodynamically favorable to the discharge of hydrogen upon the crack tip surface. This is good circumstantial evidence for the involvement of hydrogen in the mechanism of the cracking process.

#### REFERENCES

1. Johnson, H.H. and Paris, P.C., J. Eng. Fract. Mech., 1, 1968, p 1.
2. Brown, B.F., "Coupling Program on Stress Corrosion Cracking," Final Technical Report Second Edition, ARPA, October 22, 1971.
3. Smith, H.R., Piper, D.E. and Downey, F.K., J. Eng. Fract. Mech., 1, 1968, p 1.
4. Beachem, C.D. and Brown, B.F., ASTM STP 425, 1967, pp. 31-40.
5. Tiffany C.F. and Masters, J.N., ASTM STP 381, 1965, pp. 249-277.
6. Peterson, M.H., Brown, B.F., Newbegin, R.L. and Groover, R.E., Corrosion 23, 1967, p 142.
7. Proctor, R.P.M. and Paxton, H.W., ASM Trans. Quart. 62, 1969, p 989.
8. Stavros, A.J. and Paxton, H.W., Met Trans. 1, 1970, p 3049.
9. Barth, C.F., Steigerwald, E.A. and Troiano, A.R., Corrosion 25, 1969, p 355.

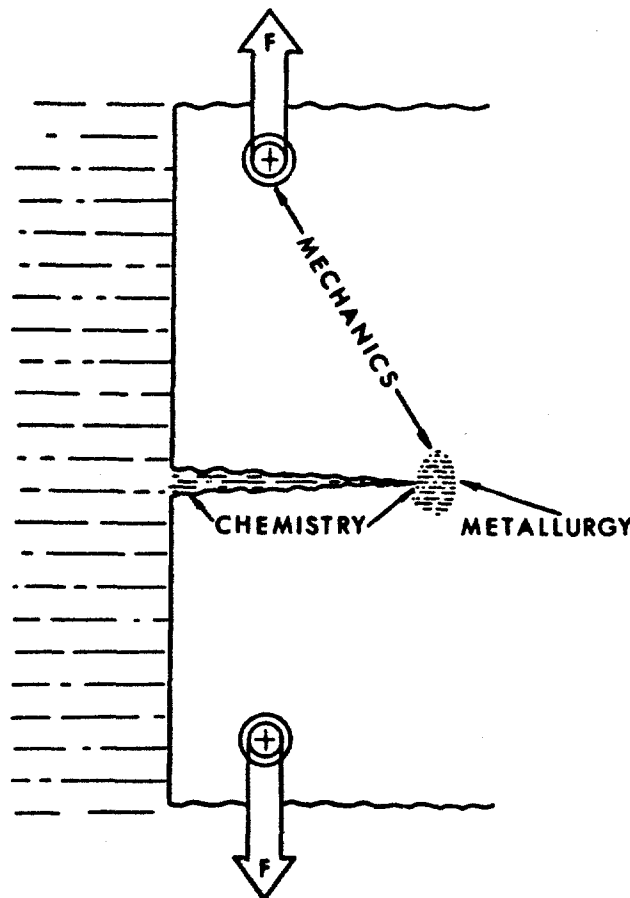


Fig. 1 Schematic representation of environmental cracking as a complex interaction involving metallurgy, mechanics, and chemistry (4)

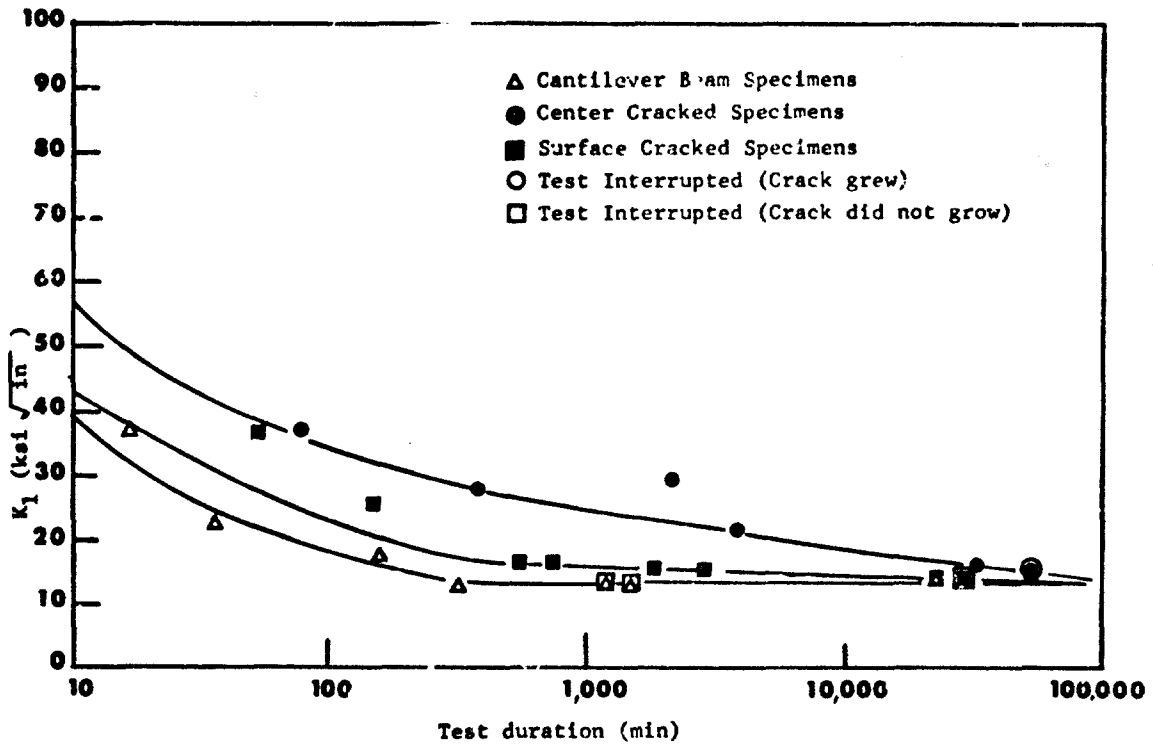


Fig.2 Comparison of threshold stress intensities ( $K_{Isc}$ ) for three specimen configurations (4)

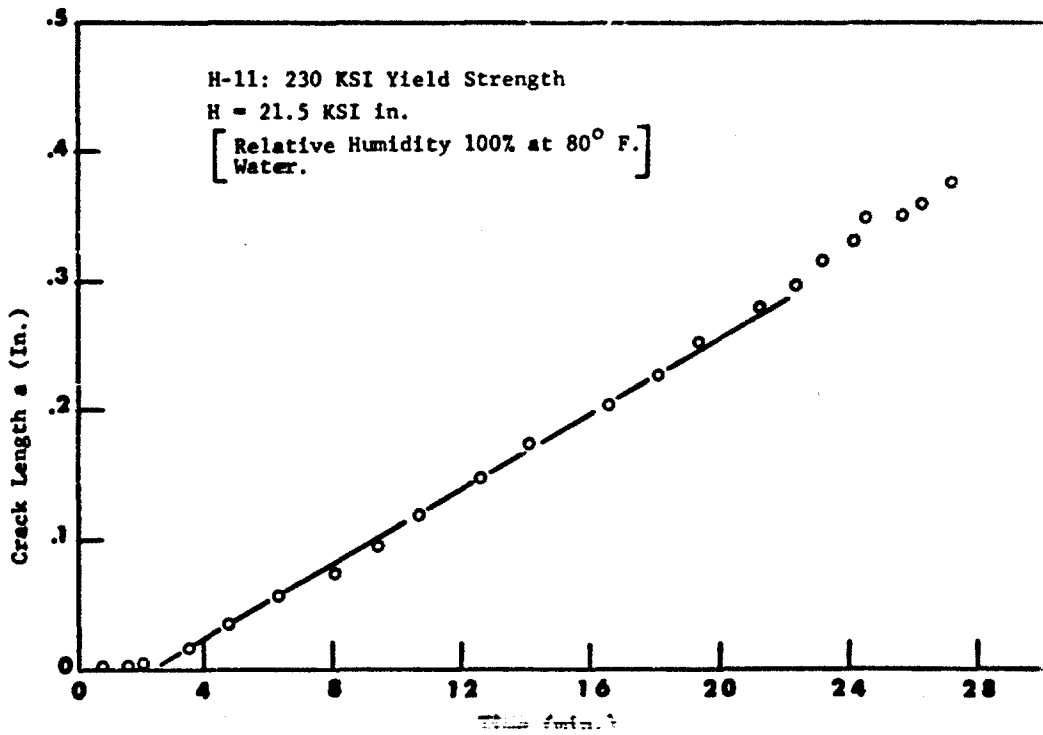


Fig.3 Constant crack growth rate in a constant stress intensity test, H-11 steel in water (1)

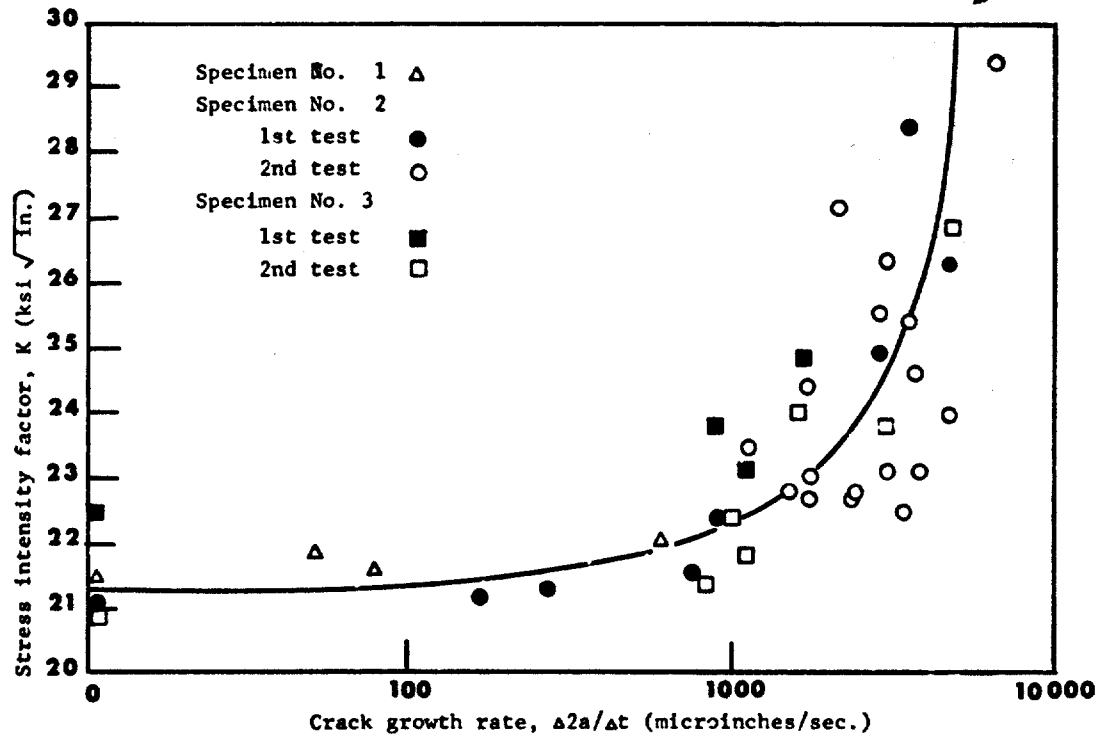


Fig.4 Crack growth rate versus stress field intensity, Ti-8Al-1Mo-1V in 3½% aqueous NaCl (3)

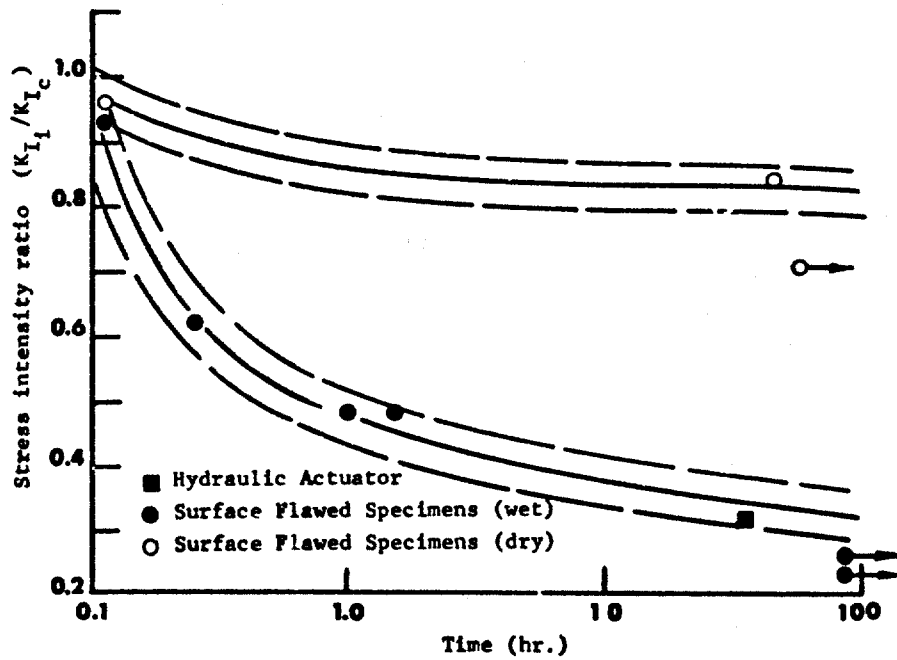


Fig.5 Correlation of hydraulic activator and surface flawed specimen results, 433C M steel (5)

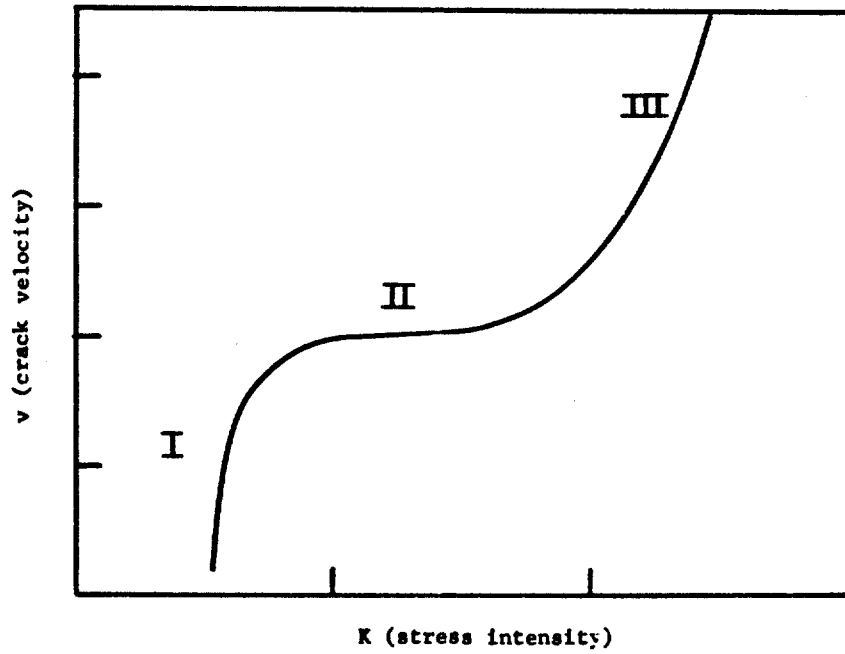
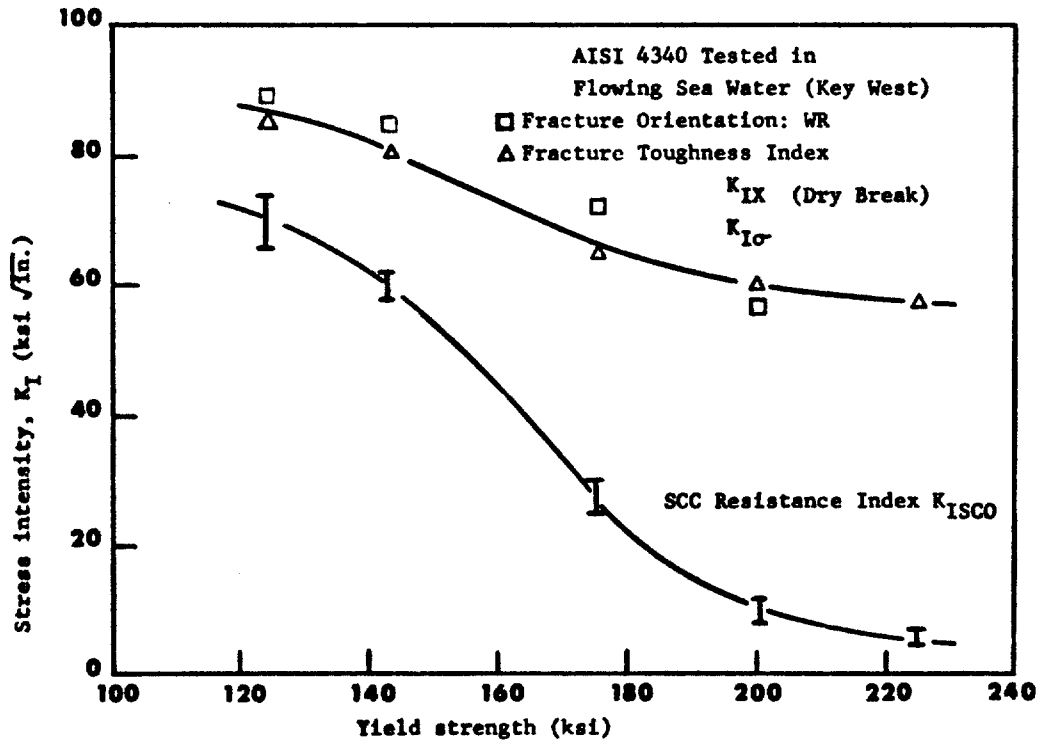


Fig.6 Schematic representation of typical crack velocity-stress intensity relation



4340 steel in water (6)

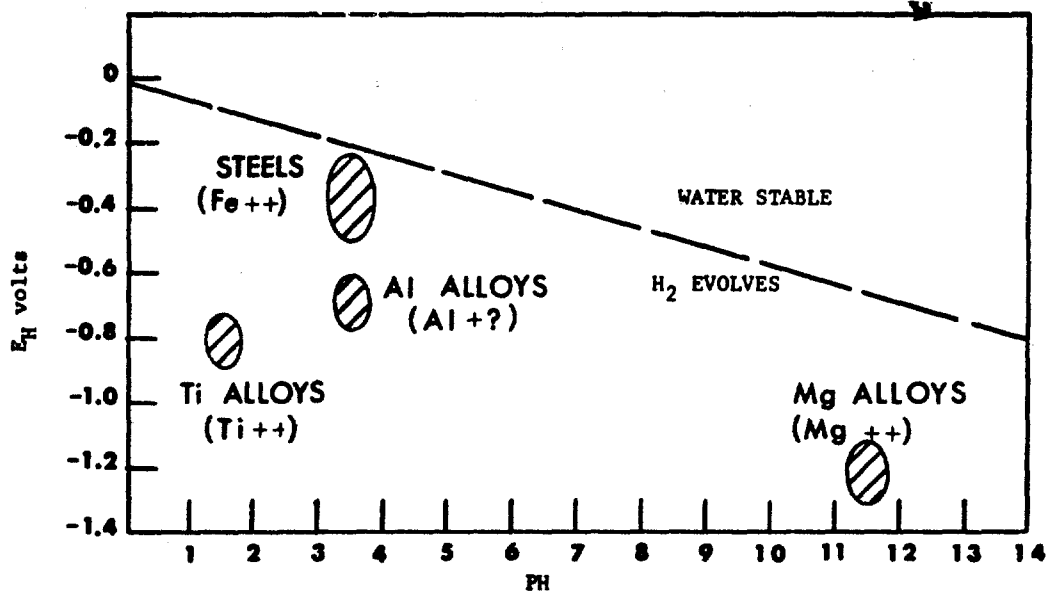


Fig.8 Potential vs. pH, demonstration of acidity at crack tips (2)

Appendix IV-5  
SUMMARY OF LIMITATIONS

Preliminary Comments:

J. I. Bluhm

In a broad sense, limitations to the applicability of mechanics to the fracture process entail difficulties associated with several areas as follows:

- a. Loading history, particularly when considered as a stochastic problem
- b. Material variability
- c. Environmental influences
- d. Nondestructive testing inspection techniques for flaw detection and characterization
- e. Stress analysis covering both the two and three-dimensional static and dynamic regimes
- f. Quantitative description of an adequate failure criteria

It is principally with respect to the latter two, i.e., analysis and description of a valid failure criteria, that this brief enumeration of limitations is addressed.

The J Integral\*

(a) The Rice energy line integral (Eq. 1 of Section E-6) applies only to two-dimensional problems; therefore, the J approach, as currently developed, is limited to problems of plane strain or generalized plane stress.

(b) Since the deformation theory of plasticity was used to substantiate the constancy of the J integral, it would appear that unloading is not permissible (i.e., fracture would have to proceed under constant or increasing loading). This would rule out applicability to materials which exhibit significant sub-critical crack growth prior to fracture since such extension implies local unloading near the crack tip. Additionally, as a consequence of the inadmissibility of the unloading and/or slow crack growth, the J<sub>c</sub> criteria appears to refer to crack initiation rather than propagation (this, however, is no more a restriction than the K<sub>1c</sub> criteria).

(c) Since material failing in plane stress generally exhibits slow crack growth, the J integral approach appears to be applicable only to plane strain (implied by the notation J<sub>1c</sub>).

(d) The J<sub>1c</sub> approach appears to be limited to configurations of contained plasticity

(e) Suitable J integral calibration must be developed for materials possessing plastic flow properties similar to those of the material one expects to test and for the particular specimen configurations which are to be used (1). This should include a study of the effect of root radius.

Crack Opening Displacement

(a) Considerable controversy persists in the scientific/engineering community as to the fundamental nature of the crack opening displacement (COD) measurement. This controversy stems from, among other factors, ambiguity as to what is being measured, where "it" should be measured, and how "it" should be measured. These uncertainties are gradually being displaced, however, with further developments of the concept.

(b) Currently the commonly recommended position for measurement of the COD is the elastic-plastic boundary. Pragmatically speaking, there are few existing acceptable general solutions appropriate for this purpose. Furthermore, this elastic-plastic boundary will be dependent upon the strain hardening characteristics of the material. (It has been suggested, however, by Wells (2) that this effect can be incorporated into the interpretation of results in the form of a small negative crack length correction.)

(c) The COD is dependent upon stress state and this, in turn, upon specimen configuration

(d) The COD does not appear to be a very sensitive measure for use in connection with high strength materials

(e) The COD, as normally determined, contains components of displacement which are not directly relevant to the fracturing process (3)

(f) No direct connection between the COD and an actual fracture mechanism has yet been established

Resistance Method

(a) Does not directly provide a characteristic which is unique to the material; geometry, particularly thickness, is known to be critical (This is also true of other measurements, i.e., K<sub>1c</sub> or COD).

\*This discussion follows that in the paper by J. A. Begley and J. D. Landes: "The J Integral as a Failure Criterion," Westinghouse Scientific Paper 71-1E7-MFPWR-P3, June 8, 1971; also presented at the 5th National Symposium on Fracture Mechanics held at the University of Illinois, Aug. 31 - Sept. 2, 1971.

(b) In the application of the resistance method, it is presumed that the elastic energy release rate is independent of the fracture mode; this still remains to be substantiated. Ambiguity of commonly measured parameters arise from distinguishable fracture modes which are specimen configuration sensitive; steady state tearing, transient unstable crack growth, i.e., pop-in, and catastrophic unstable crack growth provide potential measure of crack initiation resistance, crack propagation resistance and crack arrest resistance.

(c) The results of the R method are sensitive to the test system flexibility (or stiffness) as well, of course, as to the fracture mode.

#### The Kuhn-Hardrath Method

As originally developed, the particle size,  $\delta$ , carried over from the Neuber formulation to the Kuhn-Hardrath (K-H) technique, represented a physically acceptable concept of a critically stressed region near the notch tip. However, in subsequent studies, it appeared that in order to have the data match the predictions, the "particle size" was occasionally of the same order of size as the specimen itself, thus negating a physical significance to the particle size interpretation of  $\delta$ . It is noted also that this "particle size," which was hoped to be a material characteristic, is also geometry dependent, particularly thicknesswise. The general conclusion is that the particle size is merely a parameter in Eq. 1 of Section B-9 and should not be considered a material property.

The predictive capability of this approach is markedly effected by the presence of buckling. Since, in effect, the K-H approach was aimed at fracture prediction in thin sheet applications, this sensitivity to buckling is a serious consideration.

#### Crack Propagation Laws

No universally acceptable "law" exists even for simple tension-tension loading; few, if any, take into account the distinctions between various failure modes, i.e., plane stress or plane strain. History effects, though shown to be significant, have not generally been accounted for. Behavior of crack growth rate at low (threshold) levels is only recently receiving increased interest; factors governing this threshold level are yet to be specified. At the other end of the crack growth rate spectrum, i.e., at high stress intensity levels (greater than  $K_{Ic}$ ), the behavior is essentially unstudied.

Other areas relating to crack growth in which more information is needed and which limit confident use of existing propagation laws include:

- (a) Effects of environment
- (b) Applicability to composite materials
- (c) Effects of combined stress
- (d) Transient behavior associated with changing crack front
- (e) Tractable treatment of random loading
- (f) Stochastic treatment of data and incorporation of reliability/probabilistic considerations
- (g) Structural arrestors
- (h) Role of joints in crack propagation

#### REFERENCES

1. Irwin, G. R., "Plasticity Characterization of Progressive Crack Extension," Presentation to ASTM E-24 Committee, Sept. 8, 1971.
2. Wells, A. A., "Fracture Control of Thick Steels for Pressure Vessels," British Welding J., May 1968, p 221 ff.
3. Konazawa, T., Michida, S., Momota, S., and Hagiwara, Y., "A Study of the GOD Concept for Brittle Fracture," Proc. 2nd Int. Conf. on Fracture, Brighton, 1969, Chapman and Hall, p1.

## V. FAIL-SAFE DESIGN PROCEDURES

V.A	BASIC INFORMATION . . . . .	121
V.B	FAIL-SAFE DESIGN CONCEPTS AND FATIGUE CRACK PROPAGATION IN REAL STRUCTURES . . . . .	167

## D. Broek

V.A.1	The Fail-Safe Design Concepts . . . . .	121
A.2	Plane Strain Problems in Heavy Members with Surface Flaws, Corner Cracks at Holes, and other Natural Cracks . . . . .	125
A.2.1	Scope . . . . .	125
A.2.2	Basic Fracture Toughness Data . . . . .	125
A.2.3	Natural Cracks, Surface Flaws . . . . .	129
A.2.4	Summary . . . . .	133
A.3	Plane Stress and Transitional Modes; Sheets . . . . .	133
A.3.1	Introduction . . . . .	133
A.3.2	An Engineering Concept of Plane Stress . . . . .	133
A.3.3	The Effect of Sheet Thickness . . . . .	137
A.3.4	Other Methods of Analysis . . . . .	139
A.3.5	Determination of Residual Strength . . . . .	141
A.3.6	The Necessity of Confirmatory Testing . . . . .	145
A.4	Fatigue Crack Propagation . . . . .	149
A.4.1	Introduction . . . . .	149
A.4.2	Crack Growth Rate . . . . .	149
A.4.3	Variable Amplitude Service Loading . . . . .	157
A.4.4	Factors Affecting Crack Propagation . . . . .	159
A.4.5	Prediction of Crack Propagation in Fail-Safe Design . . . . .	161
	References . . . . .	162

V.B.1	The Prediction of Crack Propagation . . . . .	167
B.1.1	Introduction . . . . .	167
B.1.2	Load-time History . . . . .	167
B.1.3	Prediction Methods . . . . .	170
B.1.4	Confirmatory Testing . . . . .	179
B.2.	Built-up Sheet Structures . . . . .	181
B.2.1	Introduction . . . . .	181
B.2.2	The Stiffened Panel . . . . .	181
B.2.3	The Sandwich Panel . . . . .	185
B.2.4	Crack Propagation in Aircraft Structures . . . . .	187
B.2.5	Crack Arrest . . . . .	187
	References . . . . .	191



## V. FAIL-SAFE DESIGN PROCEDURES

### V.A BASIC INFORMATION

D. Broek

#### V.A.1 THE FAIL-SAFE DESIGN CONCEPTS

Operations economy demands a light aircraft structure. Such a light structure will have a limited life, not much longer than the economical service life of the aircraft. As a result of uncertainties in design loads and stress analysis and the possible occurrence of minor damage to the structure it has to be expected that cracks or partial failures occur long before the aircraft life is expended. Safety then requires a structural design, that can still withstand an appreciable load under the presence of cracks or failed parts. It also requires that the damage can be detected before it has extended to a dangerous size. The structure that meets these requirements is considered fail safe [1,2,3,4].

The damage that can occur to an aircraft structure can consist of fatigue cracks or fatigue failures, stress corrosion cracks or failures, and of foreign object damage (bird impact, sabotage bombs, battle damage of military aircraft). Fail-safety can be achieved in various ways. Four methods for fail-safe design are depicted in figure IIA 1. Two of these (a and c) are relatively well known; the other two (d and e) find very limited application, since they will only be used if the other two cannot be applied.

Figure VA 1a shows the case where the structure is made fail-safe by selecting materials with low growth rates and high residual strength and by adopting a design with inherent crack stopping capabilities. This method is particularly suitable in case of built-up sheet structures. (This method is sometimes referred to as the damage tolerance method). After some service period a crack may be initiated (point A' in top diagram). This crack is still so small that it would not be revealed by any of the existing inspection techniques. After A hours (lower diagram) it has grown to a size that allows detection. While the crack further increases in length the remaining strength of the structure will gradually deteriorate until after B hours it will drop below the acceptable fail-safe strength.

The period from A to B is available for crack detection. For a safe operation there should be at least two or three inspections in this period, since a crack of the minimum detectable length may just escape attention during a given inspection. Although the crack may have an appreciable length at the end of the safe period, it will be much smaller during the greater part of the time, since the high growth rates occur at a longer crack. This implies that relatively small cracks will have to be detected even if the maximum tolerable crack is relatively large. It also implies that a small increase of the tolerable crack length is not significant, since the last crack propagation will take the least time.

It should be noted that it is not strictly necessary to select a material with a low crack propagation rate. In principle the structure can be made fail-safe also if cracks propagate fast, if only the inspection interval is made short enough. Short inspection periods are not economical and therefore the aircraft may sell better if designed in crack resistant materials. Some remarks on the length of the inspection interval will follow later in this section.

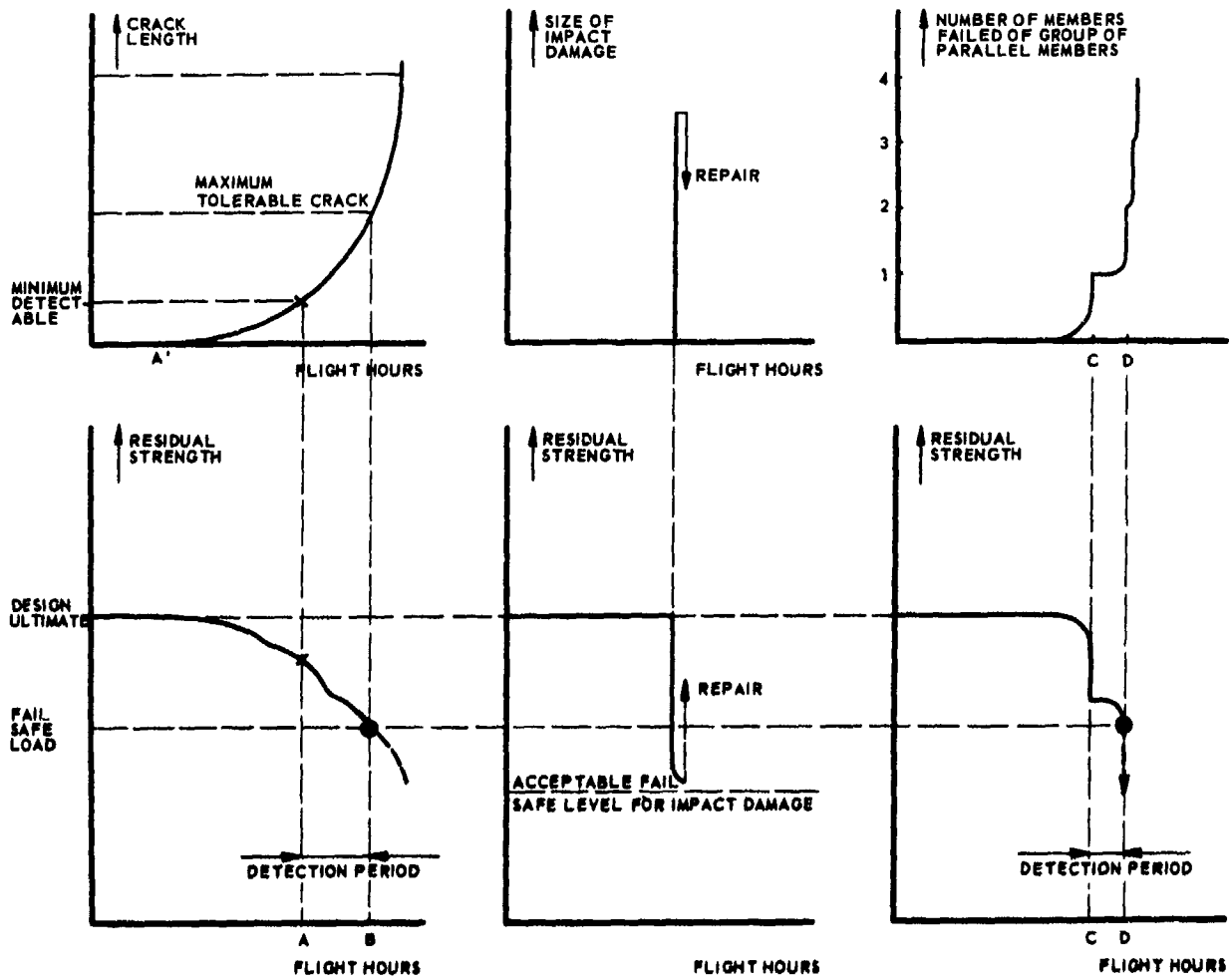
A special case of this fail-safe concept is the occurrence of impact or sabotage damage depicted in figure VA 1b. This damage is so obvious that the rest of the flight in which it occurred will be short and the pilot will be carefully maneuvering and terminate the flight at the nearest airport. It is unlikely that a high load will occur in this period and therefore the acceptable residual strength level may be lower than in other cases. Since the damage is obvious it will be repaired immediately.

A structure can also be fail-safe if the design allows for a multiple load path (Fig. VA 1c), i.e. if the load is transmitted by a number of parallel elements. When one of these elements has failed, neighbouring elements can take over its task, the penalty being a higher load in the remaining elements. The top graph shows how one member fails after C hours of service and the bottom graph indicates how this failure affects the residual strength. All other members of the group have experienced more or less the same load history and therefore more of them may be close to failure. Besides their load is increased due to failure of the first element. This implies that a second element may soon fail at D and then the strength will drop below the required safety level.

The time from C to D will be available for detection of the failure. If the failure of the first element was a premature failure induced by a minor damage the period CD can be fairly long. If the failure was not caused by special circumstances the period CD will fully depend upon the scatter in fatigue lives, since all elements experienced the same load history.

The two methods discussed in the previous paragraphs are the normal concepts for fail-safe design. It appears that crack detection is vitally important for fail-safety. Therefore chapter VII of this manual will be completely devoted to inspection techniques. A structure that is never inspected cannot normally be fail-safe. This implies that the structure cannot be fail-safe if the critical crack is so small that it cannot be detected. However, such structures can yet be made fail-safe by means of periodic proof testing or by means of periodic stripping, the two other fail-safe concepts depicted in figure VA 1d,e.

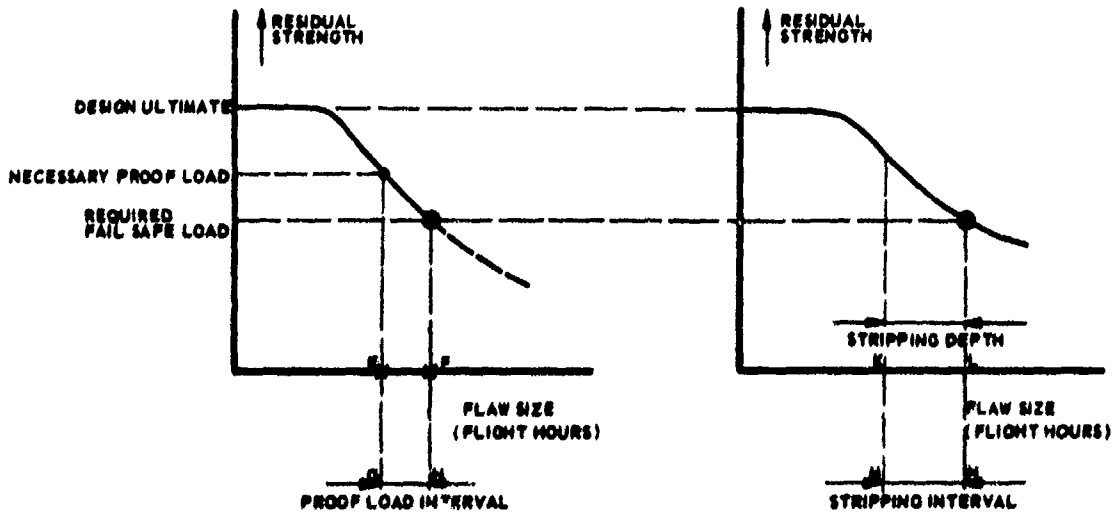
In case of periodic proof testing the structure is periodically subjected to a high proof load. If failure does not occur during proof loading, flaws of this size were not present. At the required fail-safe load the critical crack size is at F. An incidental crack of size E is not allowed to grow to F in the period between two proof loads. The time required from crack propagation from E to F is the proof load period.



A. FAIL SAFETY BASED ON MATERIAL AND STRUCTURAL PROPERTIES (DAMAGE TOLERANCE).

B. SPECIAL CASE OF IMPACT DAMAGE.

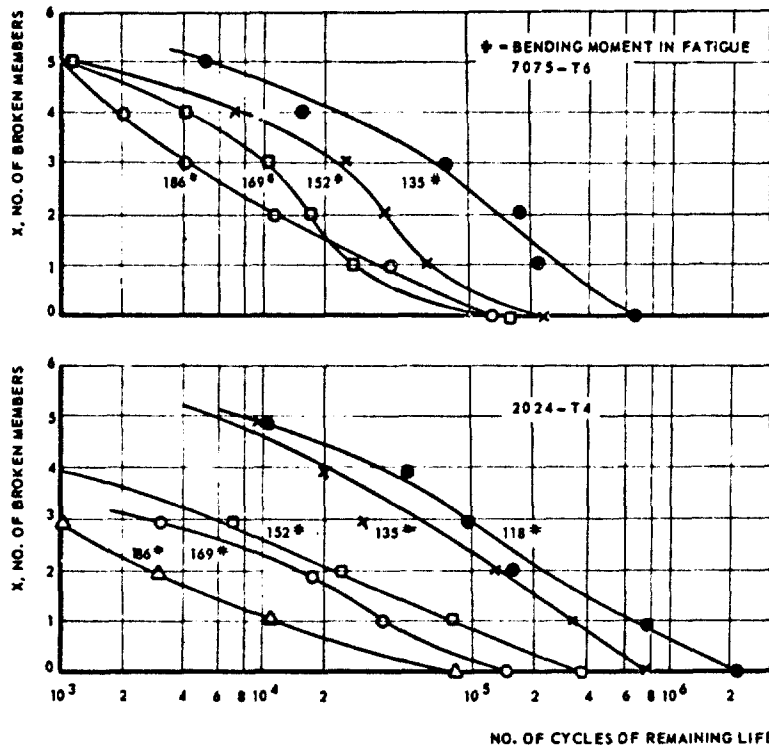
C. FAIL SAFETY BASED ON MULTIPLE LOAD PATH



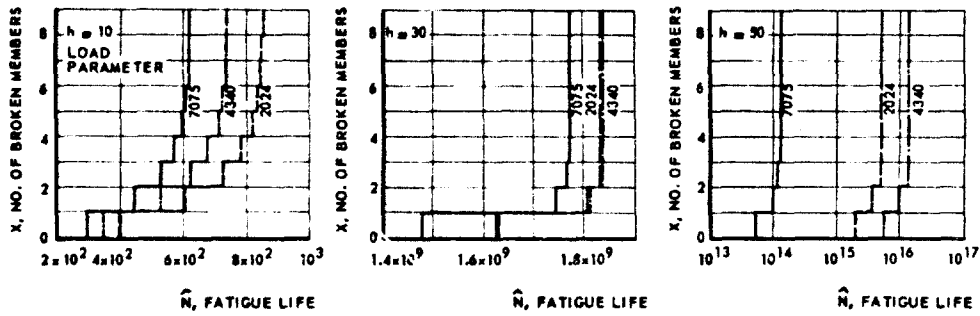
D. FAIL SAFETY BASED ON PERIODIC PROOF LOADS.

E. FAIL SAFETY BASED ON PERIODIC STRIPPING.

FIG. VA 1 DIFFERENT POSSIBILITIES FOR FAIL SAFE DESIGN.



a. EXPERIMENTAL RESULTS [5] SHOWING REMAINING LIFE OF A TEN MEMBER STRUCTURE IN CYCLE BENDING.



b. PREDICTED PROGRESSIVE BREAKDOWN OF TEN MEMBER STRUCTURE [6].

FIG. VA-2 FAIL - SAFETY OF MULTIPLE - LOAD - PATH REDUNDANT STRUCTURE.

During proof loading residual compressive stresses will be built up at the crack tip. This will slow down subsequent crack propagation. Parts of the structure may be under compression during proof loading. If cracks are present there, residual tensile stresses may occur at their tips, which may accelerate subsequent growth of the cracks in these regions.

Periodic proof testing has only found little application so far. The proof loading has to occur under controlled conditions. Clearly, this is complicated and very expensive. The method may work for structural parts that can be dismounted and tested in a simple rig, but proof testing of a complete airframe cannot easily be accomplished.

In case of periodic stripping the surface layer of the structure is machined away periodically at locations liable to develop cracks. Of course, this needs to be done only at places where cracks are likely to appear. If a flaw is almost of the critical size  $L$  (Fig. IIA 1e) it will be reduced to size  $K$  if a surface layer  $LK$  is removed. The time required for crack propagation from  $K$  to  $L$  (through a stripping layer thickness) will be the stripping interval. The stripping can be followed by shot peening to introduce favourable compressive stresses. Periodic stripping can be a solution for expensive thick-section structures, if the critical flaw is extremely small as is often the case for landing gears. It requires a good knowledge of the locations liable to cracking to select the areas to be stripped.

It follows from the foregoing that the essential part of the fail-safe analysis is the establishment of the inspection interval or in rare cases the proof test interval or the stripping interval. The procedure has to start out with the establishment of the required fail-safe load. This will usually be taken between 80 % and 100 % of the limit load. Then the critical flaw size at this fail-safe load is determined and the residual strength of the structure is determined for a range of crack sizes or flaw sizes. This provides the residual strength diagram. Finally, it has to be determined how long it will take the crack to grow from the minimum detectable size to the critical size. This information will allow establishment of the inspection period.

A structure might be made fail-safe irrespective of the material properties, if the inspection period is sufficiently short. This may prove possible for a few items where inspection is extremely easy, but economically, there will be a demand for a fixed and long inspection period. The inspection period is usually not determined by the fail-safe requirements but by operational requirements. For airliners large inspections are considered acceptable once every two years. In this period of time the aircraft may accumulate up to 10,000 hrs and up to 15,000 landings. It is obvious that a proof test interval or a stripping interval should not be much shorter.

Arguments will often be raised between the airworthiness authorities and the aircraft manufacturers regarding the critical crack length and the inspection period. It should be pointed out that improvement of the inspection technique is a much better guarantee for safety than an increase of the critical crack length. From figure VA 1a it appears that doubling the critical crack length does not even give a 50 % gain in detection period. But, reducing the minimum detectable crack length by 50 % almost doubles the detection period. Similarly, a lower crack propagation rate is of more importance than a higher residual strength or fracture toughness.

Of course, a long crack has a better chance to be detected than a small crack, but a crack is small during the greater part of its existence giving more than one chance for detection. It has to be pointed out that an aircraft cannot be argued fail-safe on the basis that large cracks will be found during a daily superficial inspection. Such a detection would prevent a catastrophe, but it has nothing to do with the rational fail-safe concept. High probability for crack detection exists when the inspector looks for cracks and knows where to look. So, even for the so-called obvious cracks the aircraft manufacturer should prescribe an inspection interval, which can then be much shorter than the two years interval for a major overhaul.

The question now arises of what use fracture mechanics can be in the solution of fail-safe problems. In order to prescribe a safe inspection interval, or to check whether safety is ensured throughout a given inspection interval, one needs information about residual strength and crack propagation. This information can be obtained from tests, but predictions can also be made by means of fracture mechanics. The latter is especially useful in the design stage.

Fracture mechanics cannot be of much use in case of the multiple-load-path structure. The time to failure of the second member has to be predicted by statistical means. This problem is beyond the scope of a fracture mechanics survey. The experimental work of Heller and Donat [5] and the theoretical work of Heller, Heller and Freudenthal [6] gives some ideas on this subject. Some of their results are presented here in figure VA.2. It may be expected that the method reasonably works for a redundant structure with many parallel members and an establishment of a safe inspection period seems possible. Sometimes however, it is thought that dual members can provide fail-safety. In that case it is virtually impossible to predict the time to failure of the second member, nor can this period be derived satisfactorily from tests; it depends completely on scatter in fatigue lives. This also means that inspection periods cannot be predicted, which implies that it is more or less a matter of luck if failure of the first member is timely detected. Therefore fail-safety can only be obtained with a simple dual-load path structure, if a failed element would be revealed at any routine inspection.

fully used under application of a scatter factor. (In the case of a multiple load path fail-safety is based on the scatter). Our increasing knowledge will make these methods more and more rational. A multiple load path may then be applied to provide additional safety to a structure which is made fail-safe by more predictable means. The fail-safe analysis will probably have to be supported by tests. The necessity of test and the requirements for useful tests will be given attention too in this volume.

For thick section aircraft parts, the critical crack length is often so small that fail-safety cannot be obtained on the basis of inspection. For these members it may be necessary to provide fail-safety by means of periodic stripping or periodic proof testing. In order to establish the re-

quired proof load or the required stripping depth, information is required about the residual strength diagram and the amount of crack propagation during the interval. In this case one has to completely rely on fracture mechanics, since useful tests are not feasible.

The major part of most aircraft structures consists of stiffened sheet structures. In these structures the critical crack length and the crack propagation rate are usually of a magnitude that allows timely detection of cracks. This means that the greater part of the aircraft structure can be made fail-safe on the basis of the easiest concept. It will be shown that calculation methods are presently available for a reliable calculation of the residual strength and a reasonable estimate of crack propagation. These methods have been recently developed and have seen only limited application so far, but they are promising for applications in future designs. The basic requirements for the fail-safe analysis (residual strength and crack propagation) will be discussed in this chapter (VA), the analysis methods for real structures will be dealt with in chapter VB (crack growth) and chapter VC (residual strength).

Finally some attention has to be given to the case of impact damage. This kind of damage will have an irregular shape and can occur at a variety of places. Fracture mechanics do not yet provide sophisticated means for the calculation of the residual strength. However, knowledge of the maximum allowable damage could be of some use for the saboteur or the enemy, but it is of less use for the aircraft operator. An exception could be made for bird impact and for parts where likelihood of (predictable) impact damage exists. The solution of the latter problem has to be provided by sound engineering judgement. Some information on this problem can be obtained from chapter VA.3.

#### V.A.2 PLANE STRAIN PROBLEMS IN HEAVY MEMBERS WITH SURFACE FLAWS, CORNER-CRACKS AT HOLES AND OTHER NATURAL CRACKS

##### V.A.2.1 SCORES

Application of any fail-safe concept requires the determination of the residual strength under the presence of cracks. The residual strength of heavy members, where a condition of plane-strain prevails at the crack tip, can be calculated from the plane-strain fracture-toughness. The various aspects of fracture toughness have been outlined in chapter VI, whereas chapter VII presents detailed information on fracture toughness testing and data generation. In this chapter the application of fracture toughness data in fail-safe problems will be considered; Section V.C.3 will treat the residual strength of heavy sections and this section will be concerned with the technical applicability of fracture toughness data. It will be tried to answer the following questions:

- a) How useful is a single  $K_{Ic}$  value and to what accuracy should it be known?
- b) Should valid  $K_{Ic}$  data be employed or are invalid data as useful?
- c) May the plane-strain fracture toughness be the basis for material selection?
- d) What are the limitations to the use of  $K_{Ic}$ ?
- e) How does  $K_{Ic}$  apply for natural cracks, such as surface flaws, corner cracks at holes and how should natural cracks be treated?

The latter question will be dealt with separately; the other questions are related and they will receive attention in connection with each other.

##### V.A.2.2 Basic fracture toughness data

As outlined in chapter VII there exist strict requirements for the execution of fracture toughness tests and for the generation of valid  $K_{Ic}$  data. Severe screening criteria set requirements to crack length and specimen dimensions. Specimens smaller than the required size show toughness values which depend upon the size of the specimen. Specimens of the required size or larger will yield valid toughness values which do not depend upon specimen size. This toughness value is called  $K_{Ic}$  and it is considered a material property at a given temperature in the same way as the tensile strength. Invalid toughness data are usually higher than  $K_{Ic}$ .

It is important to have an invariant material parameter to rank materials according to their toughness or as a basis for the control of material production. It can also be important if one wants to select a material for a structure, the dimensions of which are not limited by other criteria, but will depend only upon the strength of the material.

When dealing with a particular material in a particular application it is questionable whether a valid  $K_{Ic}$  should be used. What is needed then is a toughness value ( $K_{Ic}$  or  $K_{Ic}$ ) for the particular thickness of the structure under consideration and it is immaterial whether this value is formally valid or not. (The notation  $K_{Ic}$  is used here to indicate a toughness value for the opening mode, where plane strain requirements are not fulfilled). In fact the designer needs toughness values for a range of thicknesses of the materials he considers for application. Invalid toughness values  $K_{Ic}$  are generally larger than  $K_{Ic}$ . Therefore  $K_{Ic}$  is usually a safe and conservative value if pertinent toughness data are not available; however, this may not be so in the case of elliptical cracks.

For the high strength steels and most of the titanium alloys that find application in aircraft structures a valid  $K_{Ic}$  value will generally be required. These materials exhibit such a low toughness that plane strain will occur already at relatively low thickness. In aluminium alloys this will only occur in real heavy sections of thick plate, forgings or castings. Some of the aluminium alloys are so ductile, that a real  $K_{Ic}$  seems not to exist. Of course, some materials are so ductile that the use of any toughness value is meaningless as in the case of mild steel, but this is not yet the case for the toughness of the aircraft structural materials. Consequently, in general an applicable  $K_{Ic}$  value is required for all heavy members in aircraft structures and in many cases this has to be a valid  $K_{Ic}$ .

$K_{Ic}$  (kg/mm<sup>3/2</sup>)

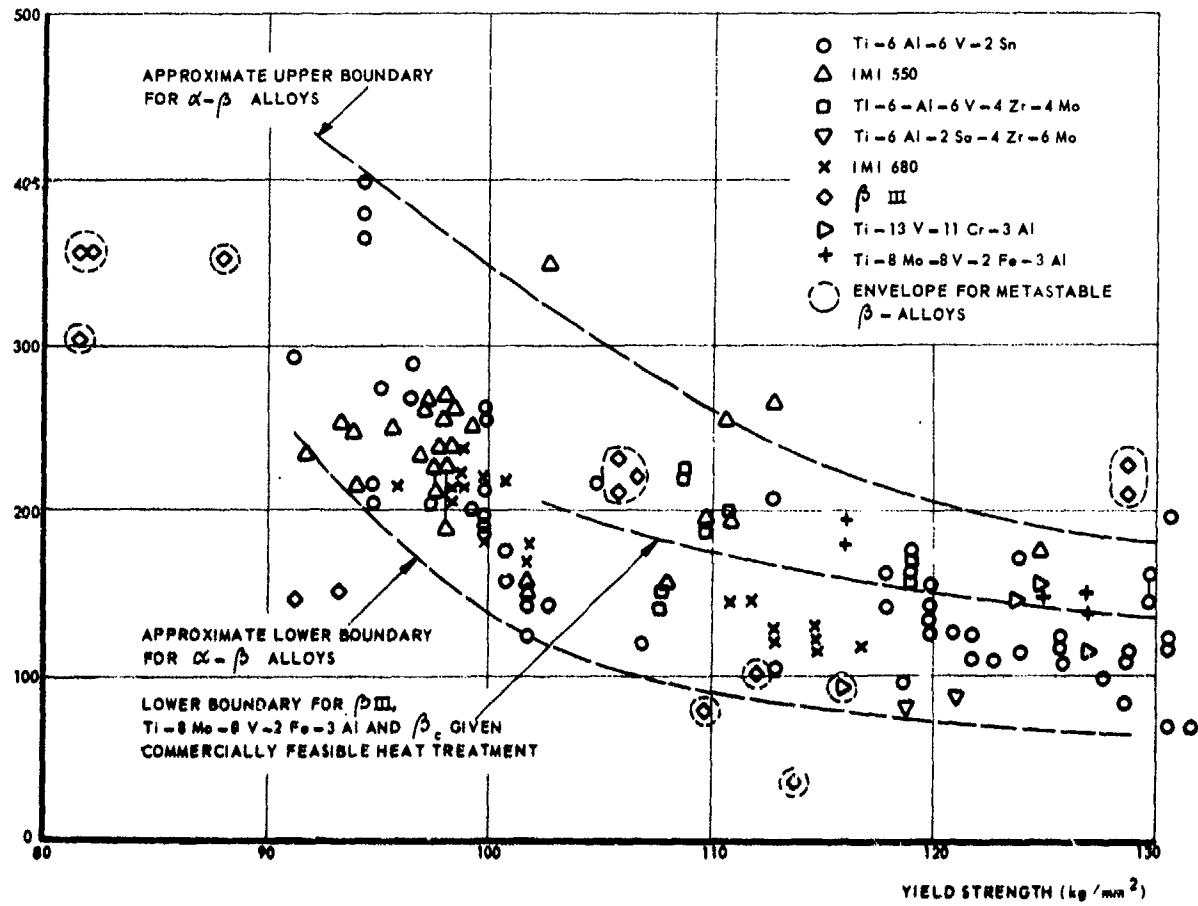


FIG. VA 3 FRACTURE TOUGHNESS OF TITANIUM ALLOYS AS A FUNCTION OF YIELD STRENGTH. DATA COMPILED BY WANHILL [7].

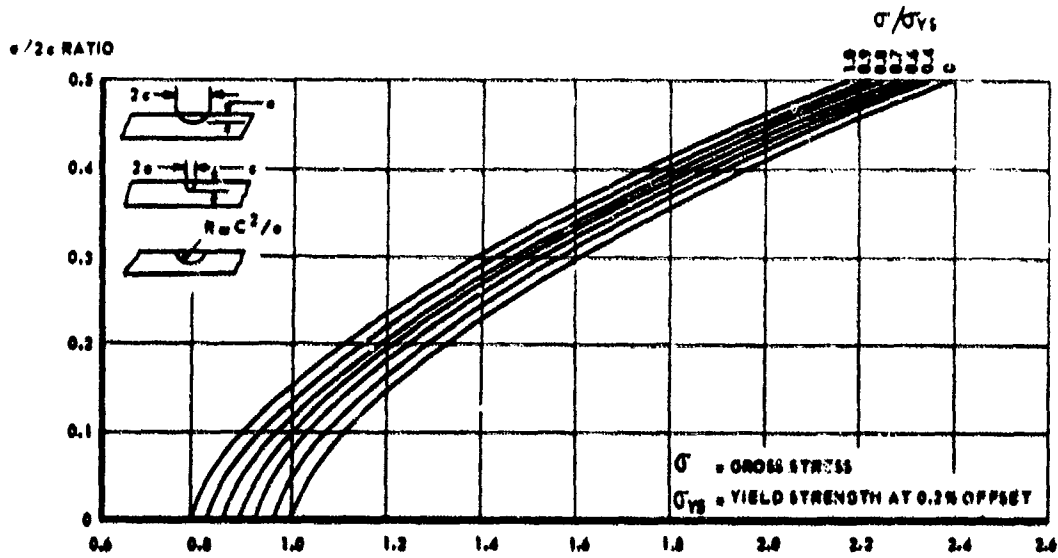


FIG. VA 4a FLAW PARAMETER, Q.

Heavy section aircraft parts are not designed on the basis of a crack criterion. These members often carry such high loads that super high strength materials are needed to keep the parts to a reasonable size and weight; the criterion is strength. A disadvantage of these high strength materials is their low toughness. This means that only very small cracks can be tolerated. Assuming that the fail-safe load is taken at limit load and that the undamaged part has a reserve strength of 10% with regard to the ultimate load condition it follows that

$$\sigma_{\text{fail safe}} = \frac{0.9}{1.5} \text{ UTS} = 0.6 \text{ UTS}$$

and since

$$K_{Ic} = \sigma_{\text{fail safe}} (\pi a)^{1/2}$$

it turns out that

$$(2a)_c = \frac{2}{\pi} (K_{Ic}/0.6 \text{ UTS})^2$$

where  $(2a)_c$  is the critical crack length. This critical crack length is given for a number of aircraft materials in the table below.

TABLE V.A.1 Tolerable flaw size

Material	UTS		TYS		$K_{Ic}$		$(2a)_c$	
	kg/mm <sup>2</sup>	ksi	kg/mm <sup>2</sup>	ksi	kg/mm <sup>3/2</sup>	ksi√in	mm	inch
7075-T6 aluminium	56	80	50	72	104	30	6.1	0.24
2014-T6 aluminium	47	67	59	41	105	30	8.8	0.35
D6 AC steel	203	290	175	250	157	45	1.05	0.04
4340 steel	182	260	147	210	150	42	1.02	0.05
Maraging (300) steel	185	264	173	248	290	82	4.4	0.17
6 Al-4V titanium	122	175	112	160	122	35	1.8	0.07
4 Al-4Mo-2Sn-0.5 Si titanium	107	153	98	140	250	71	9.6	0.38

For several materials the critical crack length is extremely small. If the fail-safe design is to be based on crack detection then cracks much smaller than the critical size must be revealed by the inspection procedure. In most materials quoted in the table the critical crack is not likely to be detected, let alone a sub-critical crack. Therefore, fail-safety can only be obtained by means of periodic stripping or periodic proof testing (see sec. V.A.1). Again, it appears that improvement of fatigue-crack propagation properties and stress-corrosion crack-propagation properties is more likely to be beneficial than an improvement of the fracture toughness. Also the rate of crack propagation will generally be a more important criterion for materials selection than toughness.

When the critical crack length is so small that fail-safety on the basis of crack detection cannot be realized, there is a good chance that the part will not be built fail-safe because periodic stripping or proof testing will be too expensive. In that case extreme precautions will be taken to ensure an extremely long crack-free service life, such that the likelihood of cracks occurring during the economic life is extremely remote. This can be achieved by shot peening or coining areas of stress concentration and the plastic expansion of holes, measures to introduce residual compressive stresses. Additional safety (not fail-safety in the real sense) can then be obtained by means of dual elements combined with frequent inspections.

If an aircraft part is being designed fail-safe in the real sense according to one of the concepts discussed in section V.A.1, information on fracture toughness is required to establish the residual strength properties. Then attention has to be paid to the limitations of a  $K_{Ic}$  value and to the limitations of the use of  $K_{Ic}$  and the usual large scatter in toughness values should not be disregarded.

The fracture toughness of a certain material depends strongly upon the yield strength. This is illustrated in figure VA 3 by data for titanium alloys as compiled by Washill [7]. Apparently, it is of importance to use  $K_{Ic}$  data for the material with the relevant heat treatment.

Still larger variations in toughness occur as a result of anisotropy. In thick sections there are usually appreciable differences in crack propagation properties and toughness in the three directions of the metal. The properties in the short transverse (thickness) direction are often by far inferior to the properties in the longitudinal and long transverse (width) direction. For aluminium alloy forgings of DFE 5024, Peel and Forayth [8] found fracture toughness values of 35.9 ksi√in, 19.3 ksi√in and 14.8 ksi√in for the longitudinal, transverse and short transverse direction respectively (125, 67 and 52 kg/mm<sup>3/2</sup>). For a maraging steel Payne [9] quotes  $K_{Ic}$  values in the short transverse direction of only 50% of those in longitudinal direction (see also chapter VII). These toughness variations arise from chemical banding and orientation of the grains as caused by the mechanical processing.

The inconsistency of fracture toughness due to heat treatment and anisotropy sets limitations to the usefulness of a single  $K_{Ic}$  value. The location of the expected crack has to be known and also the direction of the principal tensile stress to determine in which direction the crack will grow. But even then there will be limitations, since cracks occurring in service are often of a complicated geometry and occur at locations with a complicated stress distribution due to the presence of holes and joints. The applicability

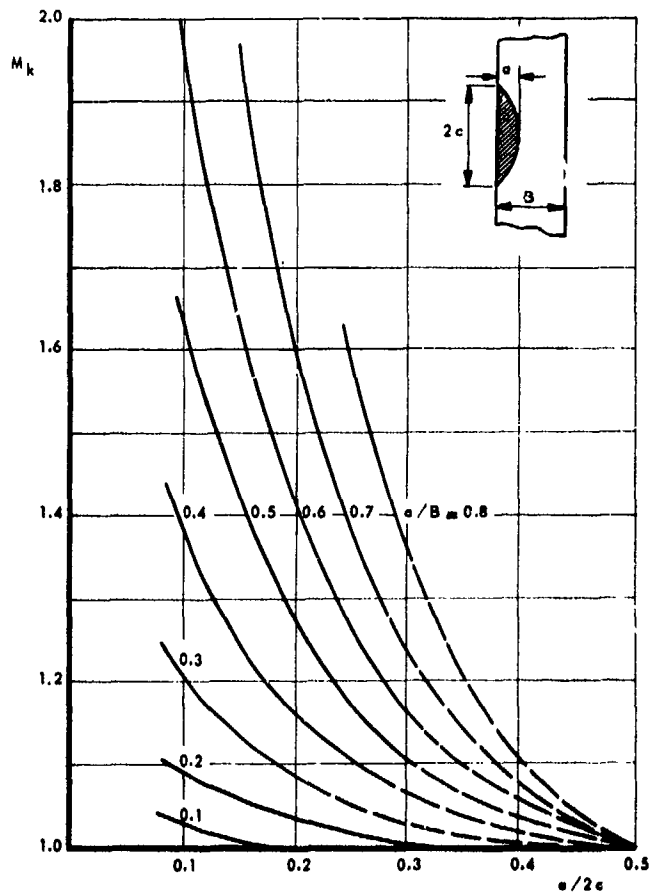


FIG. VA 4b KOBAYASHI CORRECTION ( $M_k$ ) FOR PROXIMITY OF FRONT FREE SURFACE

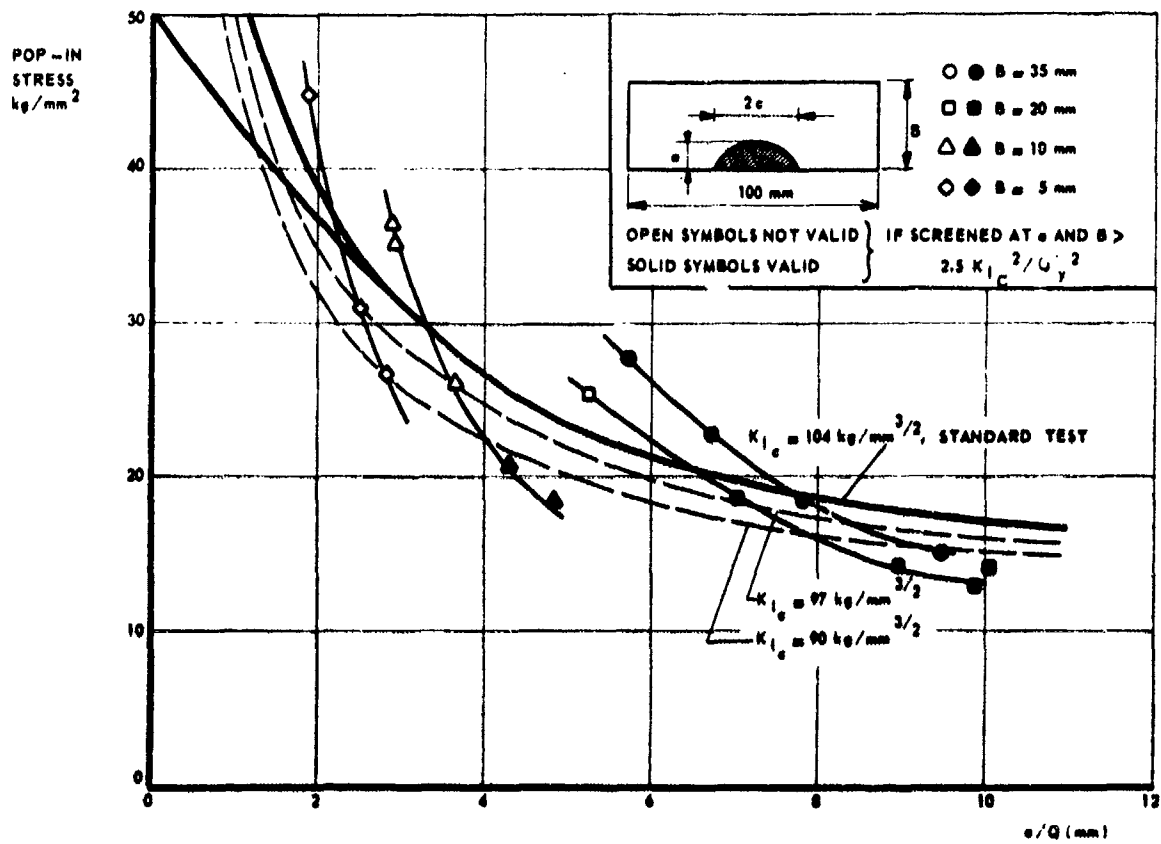


FIG. VA 5 TEST RESULTS OF SURFACE FLAW SPECIMENS [17] OF 7075-T6 PLATE



of  $K_{IC}$  data to natural cracks in areas of stress concentration will be discussed in the next section.

### V.A.2.3 Natural cracks, surface flaws, corner cracks at holes

In a real heavy-section-structure cracks will often be initiated in areas of stress concentration at fillets, holes etc. Besides, cracks in heavy members will not be through cracks but semi-elliptical surface flaws or quarter-elliptical corner cracks. Yet, the  $K_{IC}$  fracture toughness values to be used were determined from an edge cracked specimen with a through-the-thickness crack. The applicability of these standard  $K_{IC}$  data to natural cracks is often limited. In this section consideration will be given to surface flaws, corner cracks, and to corner cracks at loaded and unloaded holes.

There exists a fairly-well-established method to treat surface flaws as semi-elliptical cracks [10,11,12]. This method has been developed by Irwin [3] and it is based on the Green-Sneddon [14] solution for an elliptical crack with a sharp front embedded in an infinite body. The stress intensity varies along the crack front; it is given by:

$$K = \frac{\sigma}{\phi} \sqrt{\pi a} \left( \frac{a^2}{c^2} \cos^2 \theta + \sin^2 \theta \right)^{1/4} \quad (1)$$

with

$$\phi = \int_0^{\pi/2} (1 - k^2 \sin^2 \beta)^{1/2} d\beta \quad \text{with } k^2 = 1 - a^2/c^2 \quad (2)$$

In these equations  $a$  is the semi minor axis of the ellipse,  $c$  is the semi-major axis of the ellipse and  $\theta$  is the angular coordinate.

The stress intensity will be a maximum at the end of the minor axis where  $\theta = \pi/2$ . This maximum is:

$$K = \frac{\sigma}{\phi} \sqrt{\pi a} \quad (3)$$

In case of a semi-elliptical surface flaw the major axis will usually be along the surface and the minor axis will be pointing inward. Hence the maximum stress intensity will occur in the deepest point of the flaw. The crack is open at the surface which makes a correction to  $K$  necessary. This front free surface correction factor is taken [15] at 1.12. If the crack protrudes deeply inward, the proximity of the back free surface will also require a correction factor. This back free surface correction factor  $M_k$  has been determined by Kobayashi et al [16]. The factor depends upon the ratio between crack depth and thickness. Consequently the maximum stress intensity for a surface flaw will be:

$$K = 1.12 M_k \frac{\sigma}{\phi} \sqrt{\pi a} \quad (4)$$

Finally, a plastic zone correction is often applied. This means that  $a$  is replaced by a fictitious crack depth  $a + r$  where  $r$  is the plastic zone size. The plastic zone size can always be given as the ratio  $K^2/\sigma_{ys}^2$  multiplied by some constant, where  $\sigma_{ys}$  is the yield stress. This leads to

$$\left. \begin{aligned} K &= 1.12 M_k \sqrt{\pi a/Q} \\ Q &= \phi^2 - 0.212 \sigma^2 / \sigma_{ys}^2 \end{aligned} \right\} \quad (5)$$

$a/c$  is called the flaw parameter; it is a measure for crack depth and geometry. Values for  $M_k$  and  $Q$  can be obtained from figures VA 4a and b.

For rare cases that the minor axis of the surface flaw is along the surface and the major axis (c) points inward:

$$\begin{aligned} K_{\text{surface}} &= 1.12 \sigma \sqrt{a/Q} \\ K_{\text{body}} &= 1.12 M_k \sigma \sqrt{\pi c/Q} \cdot \sqrt{c/a} \end{aligned}$$

$K_{\text{body}}$  (the stress intensity at the end of the major axis) will be the larger if  $M_k > a/c$ .

Analysis of a surface flaw requires an important assumption. This assumption is that fracture will occur when somewhere along the periphery of the crack the stress intensity factor exceeds the critical value, i.e. when the maximum stress intensity is equal to  $K_{IC}$ . In general the maximum stress intensity will be at the deepest point of the crack and  $K_{IC}$  will then be given by eqs (5). It should be noted that the stress intensity along the rest of the crack front is still below  $K_{IC}$ .

In a test on a surface flaw specimen the fracture toughness would follow from eqs (5). As in the case of standard fracture tests screening criteria may be set to check the validity of the results. Generally accepted screening criteria for surface flaws do not exist, but they would probably amount to the conviction that crack size and specimen thickness are such that the plastic zone size is small compared to the plastic zone size. However, there is no strong demand for screening criteria for surface flaw specimens, since  $K_{IC}$  values have to be determined by means of standard tests and not on surface flaw specimens. Surface flaw specimens will be tested for their relevance in a certain application; then the specimen will also be given a relevant thickness and the toughness value obtained is the piece of data needed, whether valid or not.

Reversely, the residual strength of a surface flaw specimen can be determined from a given  $K_{IC}$  value determined from a standard test. The flaw shape has to be estimated and the flaw parameter  $a/c$  is determined for the case  $\sigma/\sigma_{ys} = 0$ . A first estimate of the residual strength is then obtained from

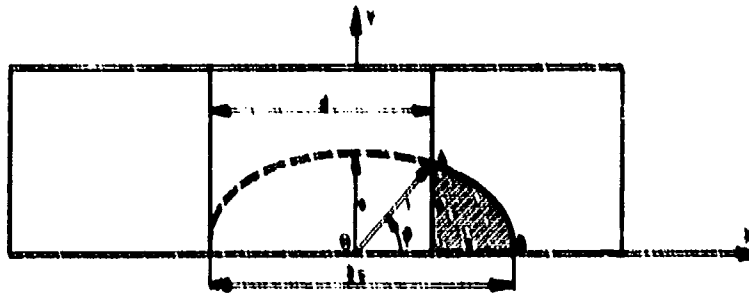


FIG. VA 6 EVALUATION OF CORNER CRACKS AT HOLES

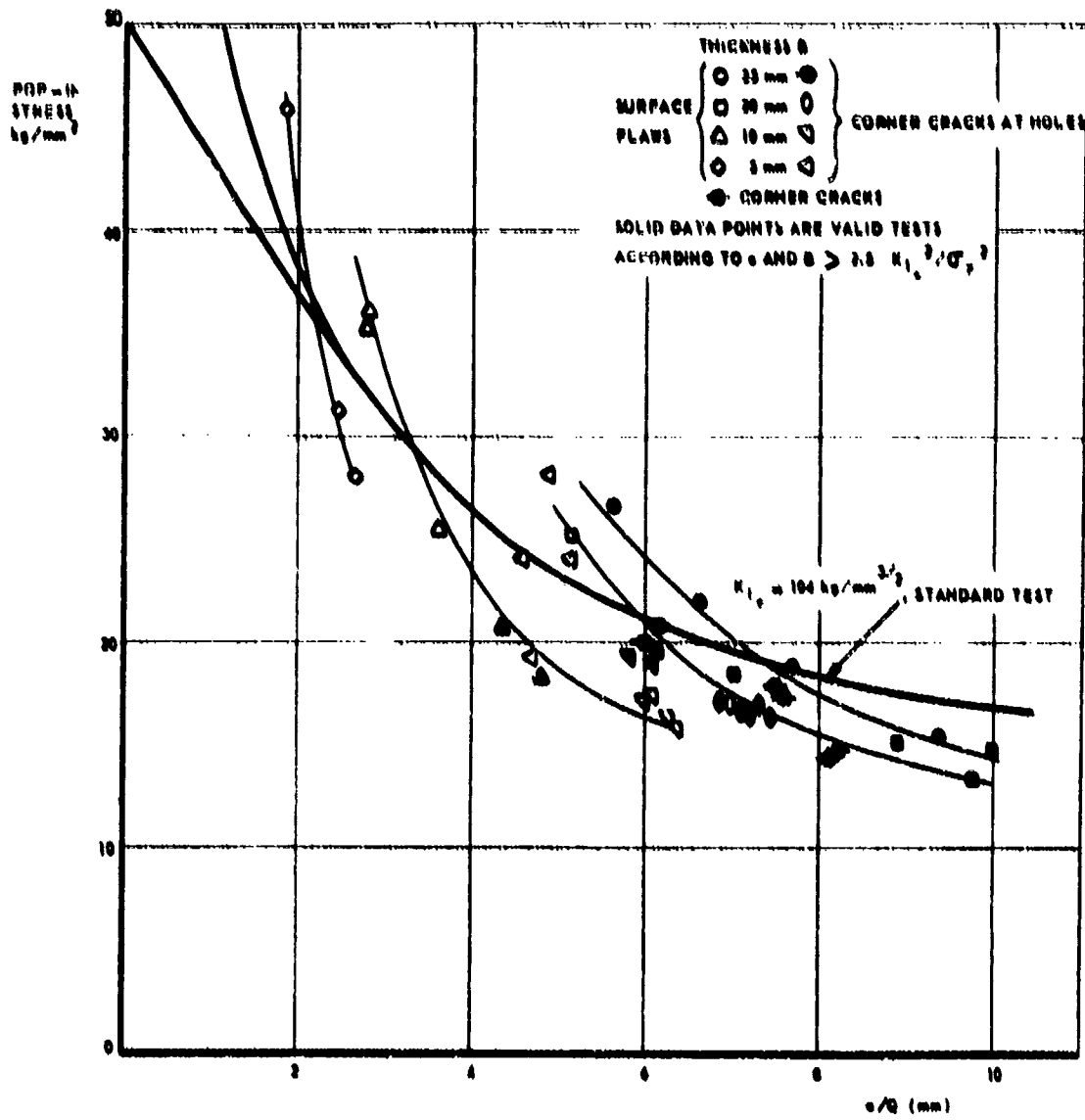


FIG. VA 7 COMPARISON OF SURFACE FLAWS, CORNER CRACKS AND CORNER CRACKS AT HOLES [17] IN 7075-T6 PLATE.

eqs (5). This allows calculation of  $\sigma/\sigma_{ys}$  and a more accurate determination of  $a/c$ , etc. The iteration need not be carried through if the plastic zone correction is neglected (i.e. only the case  $\sigma/\sigma_{ys} = 0$  is considered), which is usually satisfactory because of the inaccuracies in the estimated flaw shape.

The question arises whether standard  $K_{Ic}$  values can indeed be used to calculate the residual strength in the case of surface flaws and other crack geometries. The problem was studied by Broek et al [17] in an experimental investigation. The results for surface flaw specimens are shown in figure IIA 5. Analysis of the data of Randall [10] and Smith et al [18] reveals similar trends, although these data are too limited for an appraisal of this particular problem. The solid line drawn in figure IIA 5 represents the predicted residual strength for various values of  $a/c$  on the basis of  $K_{Ic} = 104 \text{ kg/mm}^{3/2}$  (30 ksi  $\sqrt{\text{in}}$ ) determined in a standard test. The dashed curves are based on two other values of  $K_{Ic}$ . Actual test results of surface flaw specimens are also shown and it is indicated whether these results would have complied with an arbitrary screening criterion for validity. It appears that the residual strength data of the surface flaw specimens fall on four separate lines. These curves intersect the three constant- $K_{Ic}$  curves. This indicates that surface flaw specimens, even if all are of the same thickness, do not show a constant  $K_{Ic}$ , since constant  $K_{Ic}$  curves do not intersect (see fig. VA 5). It means that  $K_{Ic}$  of a surface flaw specimen depends upon flaw shape and it is not a universal residual strength parameter for this kind of crack.

Yet, the residual strength values of the surface flaw specimens are not excessively far off the standard  $K_{Ic}$  value. Therefore a prediction on the basis of a standard  $K_{Ic}$  will be satisfactory for engineering purposes, particularly in view of:

- 1 The fact that the flaw shape parameter for a certain thickness is usually limited to a fairly small range (cf. fig. VA 5).
- 2 The scatter in standard  $K_{Ic}$  values.
- 3 The inaccurate knowledge of the flaw geometry.

In the following it will appear that  $K_{Ic}$  can be used also for more complicated natural-crack geometries. In order to present some insight into the limitations it will first be explained why a constant  $K_{Ic}$  for surface flaws does not exist basically.

The stress intensity varies along the contour of an elliptical crack. It is assumed that fracture will occur when the stress intensity at the end of the minor axis equals  $K_{Ic}$ , while the stress intensity at other locations is still below  $K_{Ic}$ . The larger the differences in  $K$  along the crack front (small  $a/c$ ) the more fracture will be delayed until  $K_{Ic}$  is exceeded over some distance along the crack front. Then the maximum  $K$  will be already larger than  $K_{Ic}$  to an amount depending upon crack shape.

As discussed earlier there is a strong anisotropy in fracture toughness. At the end of the minor axis the crack usually grows in thickness direction. At the end of the major axis the crack has to grow in width direction where  $K_{Ic}$  is substantially larger (and the stress intensity lower). Consequently, when crack extension is prone at the end of the minor axis it is still remote at the end of the major axis. This effect will be small when  $a/c$  is small since crack growth will then be mainly in thickness direction. Consequently the fracture toughness in case of surface flaws will depend upon flaw shape and it will be higher than  $K_{Ic}$  in thickness direction and lower than  $K_{Ic}$  in width direction. The more elongated the ellipse, the closer the toughness will be to  $K_{Ic}$  in thickness direction. This effect has to be accounted for in leak before break criteria for pressure vessels.

A quarter elliptical corner crack bears great resemblance to a semi-elliptical crack and it can be treated in exactly the same way [17]. In practice cracks often occur as a result of stress concentrations in fillets or at holes. When the cracks are extremely small, the best procedure is to use the actual stress (nominal stress times stress concentration factor) in the expressions for the stress intensity factor [17]. When the cracks have grown out of the area of stress concentration nominal stresses can be used again in case of very mild notches (e.g. at fillets).

In case of sharper notches the notch can become part of the crack, i.e. the part will act as if containing a fictitious crack of a length equal to the sum of the physical crack and the size of a notch. For the special case of cracks at holes it has been demonstrated by Bowie [19] that the hole acts as part of the crack when the crack length is in the order of magnitude of the hole radius. In case of a through the thickness crack of length  $a$  growing at one side of a hole of diameter  $d$ , there will be an effective total length of crack of  $2a_{\text{eff}} = a + d$ . This case will receive ample attention in section VA 3.

Cracks at holes in heavy sections will usually be corner cracks. When small, these cracks can be treated as corner cracks under stresses magnified by a stress concentration. When the cracks are larger the hole can be satisfactorily considered as part of the crack in the way [17] as shown in figure VA 6. The maximum stress intensity factor at the physical part of this fictitious crack will be at point A. The stress intensity factor follows from:

$$K = 1.2 \sigma \sqrt{\pi p/q}$$

with

$$\left. \left. \left. \frac{p^2(d+q)^2 (d-q)^2 (d-q)^{-1} + 4p^2 (d+q)^2}{4dq [4p^2 + (d-q)^2]} \right)^{1/4} \right\} \quad (6)$$

$d$ ,  $p$  and  $q$  are defined in figure IIA 6 and  $Q$  follows from figure IIA 4 with  $a/2c = p/2\sqrt{dq}$ . The front free surface correction has been taken at 1.2 in order to account for the greater compliance of the hole in comparison with a real crack.

Broek et al [17] tested specimens with corner cracks at loaded and unloaded holes. Figure VA 7 shows how these results compare with those of the surface flaws, which were presented earlier in figure VA 5. It turns out that the procedure described above is a good engineering method to predict the

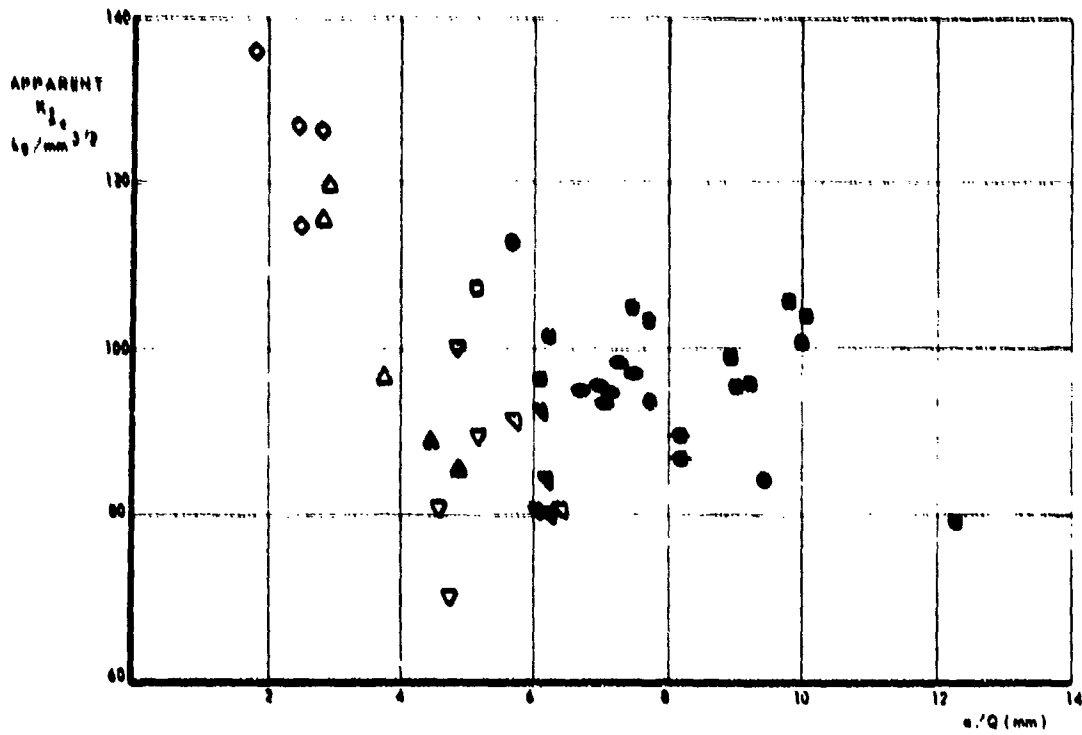


FIG. V A 8 VARIATION IN FRACTURE TOUGHNESS OF NATURAL CRACKS [17] (SPECIMEN WIDTH 100 mm OR 60 mm, 7075-T6).

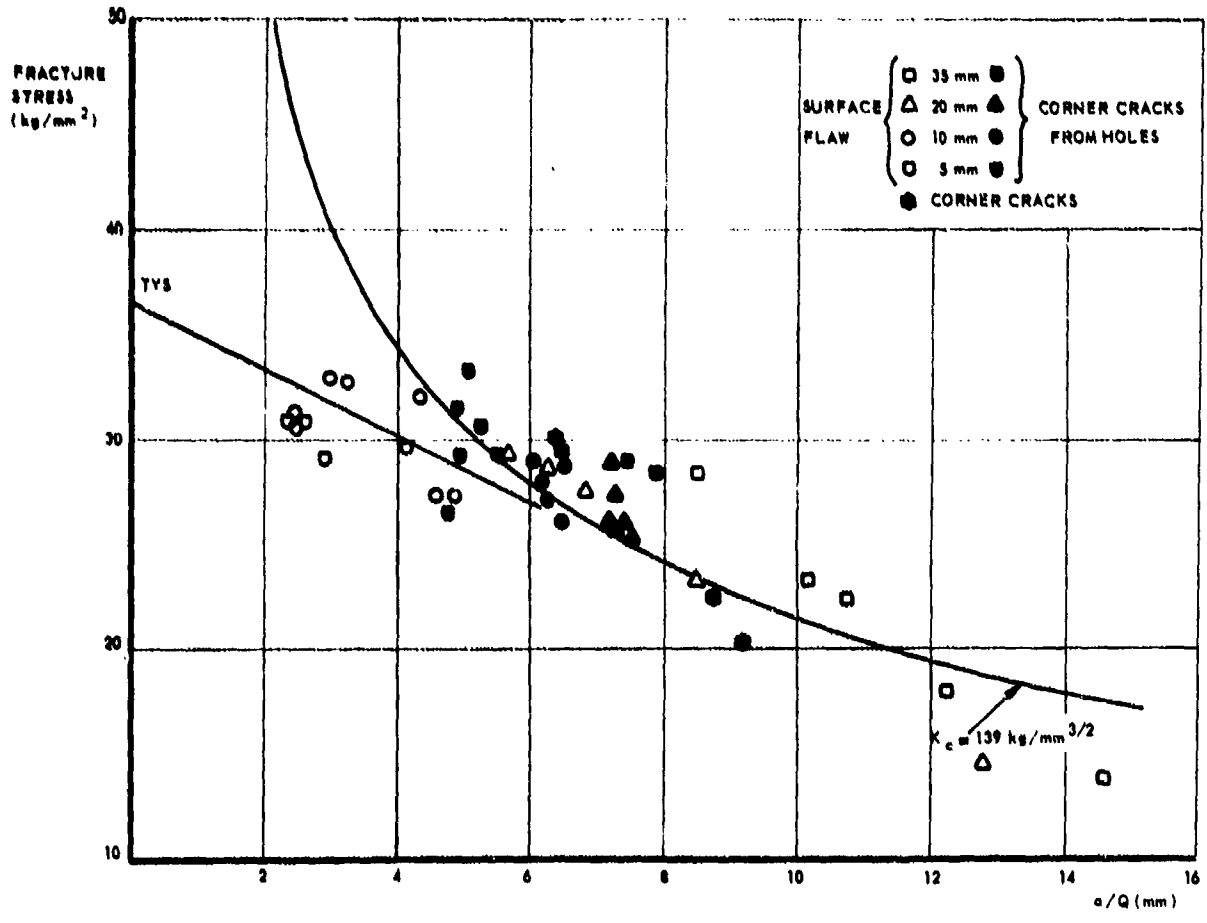


FIG. V A 9 RESIDUAL STRENGTH IN CASE OF NON-VALID TESTS [17] 2024-T3 PLATE

static strength of corner cracks at holes on the basis of standard fracture toughness data.

The variation of fracture toughness as observed in the tests on specimens with natural cracks, referenced in the preceding paragraphs, can be appreciated from figure IIA 8. It should be emphasized that the variation depends upon the material, since it is closely related to the anisotropy in fracture toughness.

In very ductile materials some slow crack growth may occur before fracture. This means that no real plane stress fracture toughness is applicable. In that case one can determine a fracture toughness from the 5% secant off-set of the crack opening displacement curve (see chapter V). Application of this fracture toughness value may be very conservative, since the specimens can bear more load before fracture occurs. In that case one may use a  $K_{10}$  value based on the real fracture stress, instead of  $K_{1c}$ . Figure VA 9 shows that application of such a  $K_{10}$  value for thick sections may work very well for natural cracks in a ductile aluminium alloy.

#### V.A.24 Summary

A choice of a material in a certain application requires knowledge of valid  $K_{10}$  data, which allows a fair comparison of materials. Use of valid  $K_{1c}$  data of parts of sub-critical thickness will generally give a safe estimate of the residual strength or the critical crack length. For parts of sub-critical thickness designed in high toughness materials, the use of  $K_{1c}$  may be too conservative and an invalid  $K_{1c}$  or  $K_{10}$  may be more adequate to the situation.

Heavy-sections of forgings or plate usually show a very large anisotropy in fracture toughness. Only those  $K_{10}$  data should be used which are relevant for the expected direction of crack growth.

Surface flaws, corner cracks and other natural cracks at holes or notches can be treated reasonably well with  $K_{10}$  data obtained from standard tests. From an engineering point of view the inaccuracies of this procedure are not large, particularly because the inconsistency of  $K_{1c}$  due to material variations and anisotropy introduces much larger uncertainties.

### V.A.3 PLANE STRESS AND TRANSITIONAL MODES; SHEETS

D. Broek.

#### V.A.3.1 Introduction

A generally accepted method for plane stress toughness testing and presentation of results does not exist. This is due to our difficulties in understanding the observed phenomena. By far the greatest part of aircraft structures consist of sheet and sheet structures and consequently the plane stress problem is of paramount importance for aircraft fail-safety. Fortunately, a useful engineering solution for the plane stress problem is readily available: the residual strength of a built-up sheet structure with a crack can be accurately predicted (c.f. chapter V, C.1) on the basis of the residual strength of the comparable unstiffened panel. There remain some problems in the presentation of unstiffened panel data, but as pointed out in this chapter, these can be treated satisfactorily in an engineering way, although further developments are necessary.

The various possible approaches to the plane stress problem and the residual strength of cracked sheets were discussed extensively in chapter V.A. They will not be repeated in detail here. Rather, this chapter will deal with the most rational engineering approach, particularly with respect to its applicability to the problem of built-up sheet structures. In principle, it is immaterial to the technical problem of a built-up structure (chapter V.C.1), by which method the unstiffened panel is treated, but presentation in terms of  $K_{10}$  appears to have advantages. Therefore, this chapter is concerned particularly with this approach. Note:  $K_{10}$  will be used here for the opening mode (mode I) plane stress fracture toughness in analogy with  $K_{1c}$  for mode I plane strain fracture toughness.

After a brief phenomenological description of the plane stress fracture process, the  $K_{10}$  approach is evaluated; brief consideration is given to other methods. The final part of the chapter deals with technical plane stress problems such as cracks emanating from holes, the effectivity of stop holes and the implications of intermittent slow crack growth.

#### V.A.3.2 An engineering concept of plane stress

Consider a sheet with a central transverse crack  $2a$ , loaded in tension at a nominal stress  $\sigma$  (Fig. VA 10). The stress can be raised to a value  $\sigma_c$  at which the crack will start to extend slowly [20]. This slow crack growth is stable; it stops immediately when the load is kept constant. Although the crack is longer now, a higher stress is required to maintain its propagation. Finally, at a certain critical stress  $\sigma_c$  a critical crack length  $2a_c$  is reached, where crack growth becomes unstable and sudden total fracture of the sheet results. When the initial crack is longer, crack growth starts at a lower stress and also the fracture stress (residual strength) is lower, but there is more slow crack growth (fig. VA 10).

As a first approximation it can be assumed that all events in crack propagation and fracture in plane stress are dictated by the stress intensity factor. One may label each event described with a pertinent value of the stress intensity factor by means of one of the following expressions:

$$K_{11} = \alpha \sigma_1 \sqrt{\pi a_0}, \quad K_{1c} = \alpha \sigma_c \sqrt{\pi a_c}, \quad K_{10} = \alpha \sigma_0 \sqrt{\pi a_0} \quad (7)$$

In these equations  $\alpha$  is a factor that depends upon panel geometry and size. Instead of using the natural crack size  $a$  the effective crack size  $a + r_p$  could be used in the equations,  $r_p$  being the plastic zone size, but it will appear in the course of this section that the plastic zone correction is not

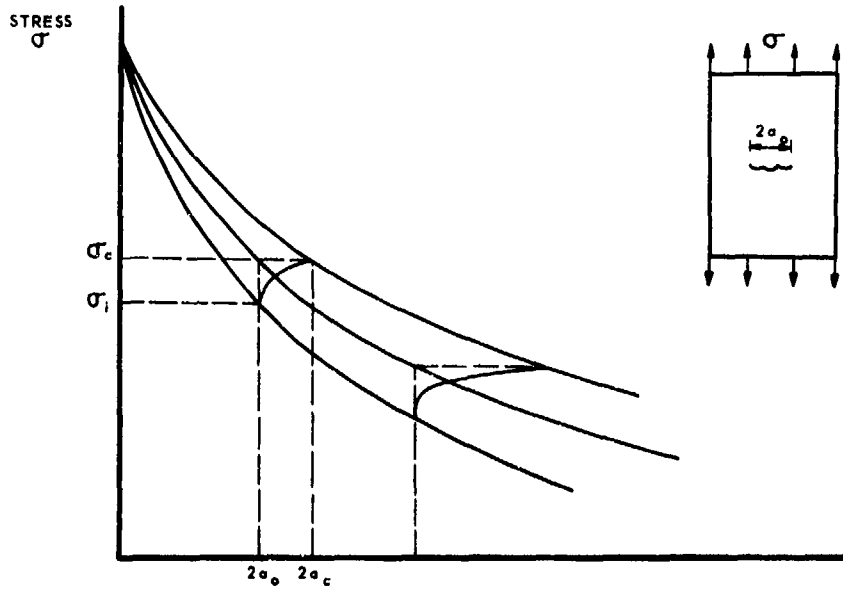


FIG. VA 10 RESIDUAL STRENGTH CHARACTERISTICS IN PLANE STRESS

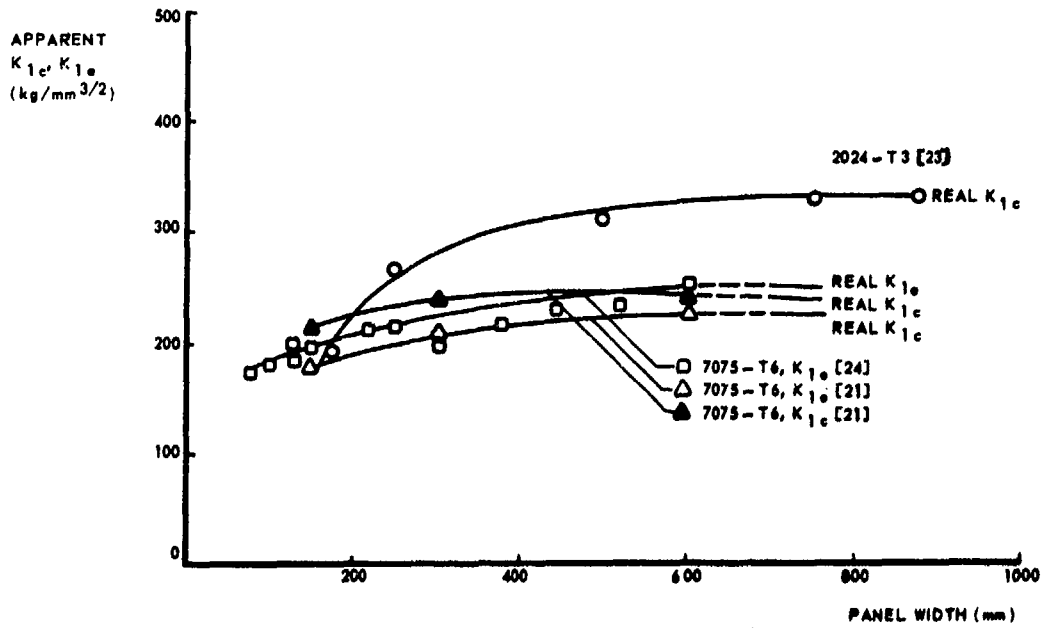


FIG. VA 11 APPARENT  $K_{Ic}$  AS A FUNCTION OF PANEL SIZE

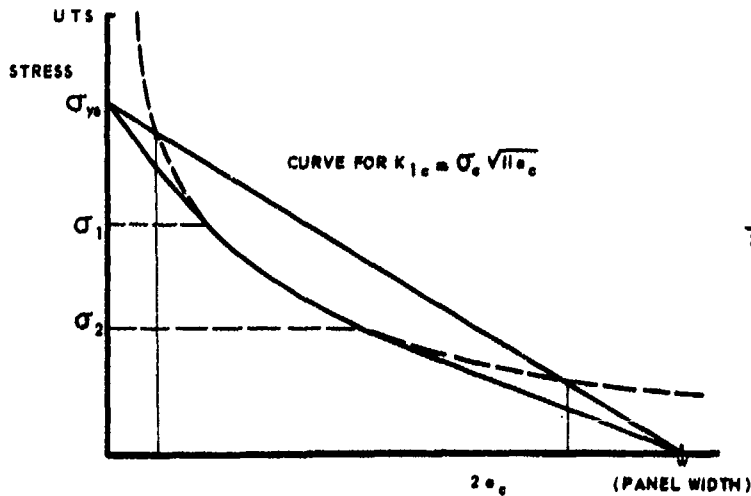


FIG. VA 12 ANALYSIS OF FEDDERSEN [25].

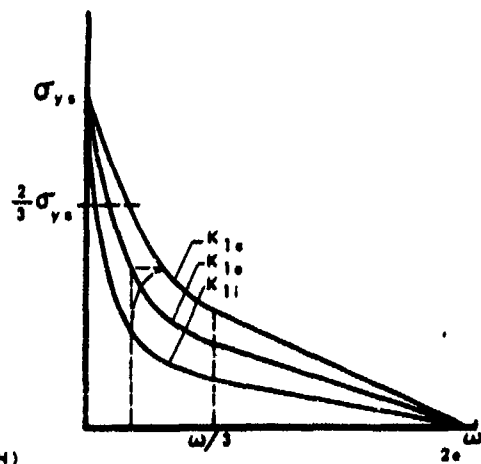


FIG. II A 13 METHOD OF FEDDERSEN [25].

necessary in the engineering approach.

Tests [11,20,21,22] have shown that  $K_{11}$ ,  $K_{10}$  and  $K_{10}$  are not constants with general validity like  $K_{10}$ . To a first approximation, however, they are constant for a given thickness, for a limited range of crack lengths and for a given panel size.  $K_{10}$  appears to depend on panel size as is shown in figure VA 11. It turns out that  $K_{10}$  is lower for narrow panels and gradually increases to a constant value beyond a certain panel size. This constant value for large panels is considered here to be the real  $K_{10}$  of the material at a given thickness. The reason why smaller panels exhibit lower  $K_{10}$  values will be explained later in this chapter.

For the design of a sheet structure of a given size, one needs access to  $K_{10}$  data for a variety of thicknesses. Feddersen [25] has proposed a method for data analysis and presentation, which is particularly rational and useful for engineers and designers [26]. For panels wide enough to produce the real  $K_{10}$  the relation between the residual strength and the crack length can be represented by the curve shown in figure VA 12. Also shown in figure VA 12 is a straight line representing the line for net section yielding; at all points of this line the net stresses on the uncracked ligament of the specimen are above yield. The shaded areas indicate the regions of crack sizes at which net section stresses above yield would be required to cause fracture at the given  $K_{10}$ . Since stresses above yield cannot occur, fracture in these regions will occur at stresses lower than those predicted by  $K_{10}$ ; i.e. the specimens will exhibit an apparent toughness lower than  $K_{10}$ .

Many theoretical analyses have been developed to account for this discrepancy, but these have failed to consolidate the data into a meaningful form over the full range of cracks. Thus, there remains to reduce the data to a simple general form for engineering applications. Feddersen [25] argues that the two linear tangents to the idealized K curve (fig. VA 12) can be used to establish a smooth and continuous curve for the residual strength, which he supports by extensive test data [27]. One tangent to the K-curve is drawn from the point  $\sigma = \sigma_{ys}$  where  $\sigma_{ys}$  is the yield strength, the other tangent is drawn from the point  $2a - w$ , the specimen width.

A tangent to the K curve at any point is:

$$\frac{d\sigma}{d(2a)} = \frac{d}{d(2a)} \left( \frac{K}{\sqrt{\pi a}} \right) = - \frac{\sigma}{4a} \quad (8)$$

For the tangent through  $(\sigma_{ys}, 0)$  this yields (see fig. IIA 12):

$$- \frac{\sigma_1}{4a_1} = - \frac{\sigma_{ys} - \sigma_1}{2a_1} \quad \text{or} \quad \sigma_1 = \frac{2}{3} \sigma_{ys} \quad (9)$$

This implies that the left-hand tangency point always is at two thirds of the yield stress, independent of K. For the tangent through  $(0, w)$  it follows that

$$- \frac{\sigma_2}{4a_2} = - \frac{\sigma_2}{w - 2a_2} \quad \text{or} \quad 2a_2 = w/3 \quad (10)$$

which indicates that the right hand point of tangency is always at a total crack length of one third of the specimen width. These procedures can be applied to all events in the process of plane stress cracking, i.e. to  $K_{10}$  as well as to  $K_{11}$  and  $K_{12}$  as amplified in figure VA 13.

It appears that this method of analysis is very useful as can be appreciated from the test data in figure VA 14. Evidently,  $K_{11}$ ,  $K_{10}$  or  $K_{12}$  have to be determined from those test results for which  $\sigma < 2/3 \sigma_{ys}$  and  $2a < w/3$ , otherwise irrelevant  $K_{10}$  values would be obtained. The two tangents to the curve have no sound physical basis, but they are simple and useful in an engineering analysis.  $K_{11}$  and  $K_{12}$  appear to be approximately constant for a limited range of crack lengths. However, it is exactly this range of crack lengths that is of practical importance. Cracks for which  $\sigma > 2/3 \sigma_{ys}$  are very small cracks for a sheet structure and often below the detection limit (because they are still hidden by other parts of the built-up structure). Cracks longer than  $w/3$  will never be allowed in large built-up structures. In the useful range of crack lengths the plastic zone correction to the crack length does not really improve the situation of constant  $K_{10}$  [25] and it unnecessarily complicates the simple engineering method. Since there are no sound arguments in favour of the application of the plastic zone correction it should rather be omitted.

The versatility of Feddersen's method is in the fact that it allows very simple presentation of plane stress fracture toughness data, which has long seemed impossible. The mere presentation of values for  $K_{11}$ ,  $K_{10}$  and  $K_{12}$  allows the user to establish the complete residual strength diagram for any given panel size. This is outlined in figure VA 15. The residual strength for various crack sizes can be determined from the  $K_{10}$  or  $K_{12}$  value. A tangent to the curve can be drawn from  $\sigma_{ys}$  to  $2/3 \sigma_{ys}$  and for any given panel width tangents can be drawn from  $w$  to  $w/3$ .

There exists a certain minimum panel size  $w_{min}$  where the two points of tangency coincide. Below that panel size the residual strength is determined by the net section yield criterion. Panels should have a certain minimum size in order to provide useful  $K_{11}$  and  $K_{10}$  data. The minimum size can be determined. From  $K = \sigma \sqrt{\pi a}$  it follows that the left point of tangency is given by:

$$K = 2/3 \sigma_{ys} \sqrt{\pi a_1} \quad \text{or} \quad 2a_1 = \frac{9}{2\pi} \frac{K^2}{\sigma_{ys}^2} \quad (11)$$

For the two points of tangency to coincide:  $1/3 w_{min} = 2a_1$  or with (11)

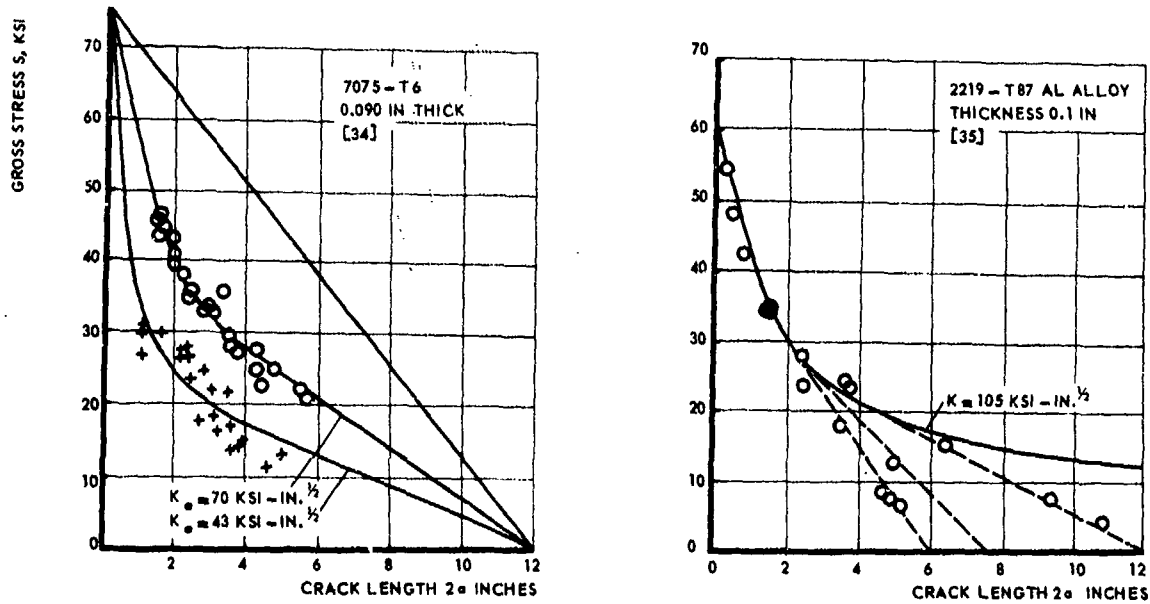


FIG. V A 14 USEFULNESS OF FEDDERSEN ANALYSIS [25] CONFIRMED BY TEST DATA [34, 35].

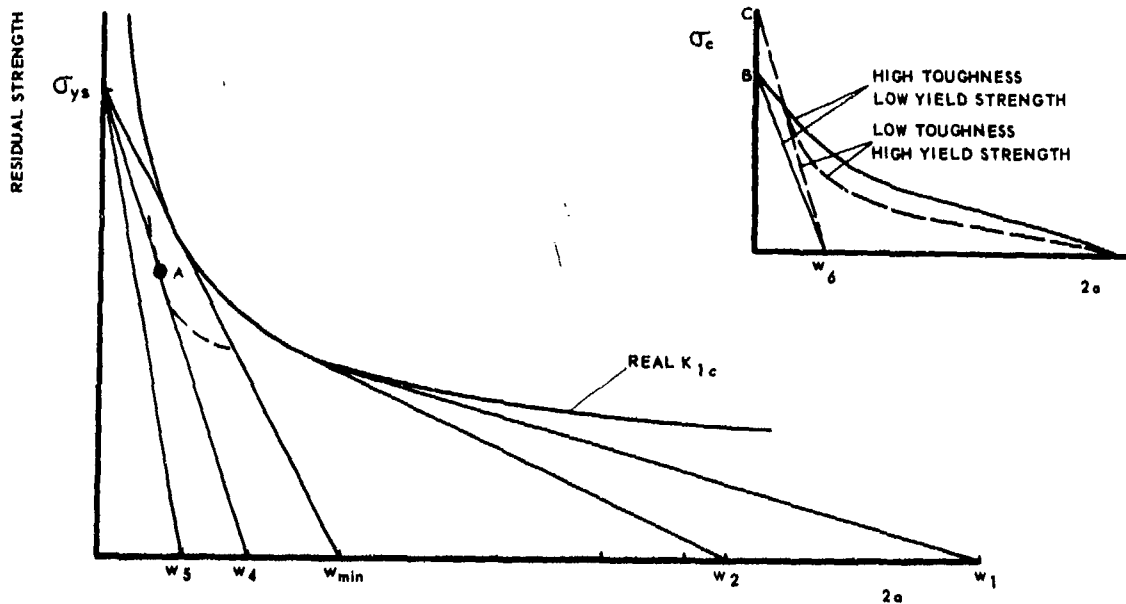


FIG. V A 15 RESIDUAL STRENGTH FOR VARIOUS PANEL SIZES.

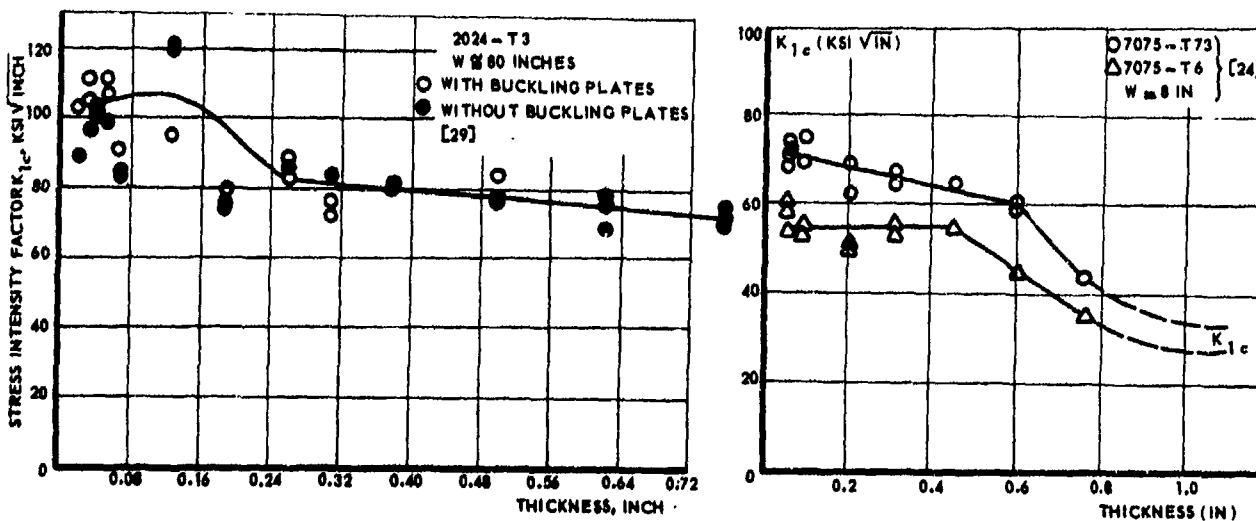


FIG. V A 16 THE EFFECT OF THICKNESS ON PLANE STRESS FRACTURE TOUGHNESS.



$$w_{\min} = \frac{27}{2\pi} \frac{K_{10}^2}{\sigma_{ys}^2} \quad (12)$$

The screening requirements for valid plane stress fracture toughness testing follow from these considerations. In fact, the only screening requirements are on crack length and stress, namely:

$$\sigma_0 < 2/3\sigma_{ys} \text{ and } 2a < w/3 \quad (13)$$

The latter of the two can be satisfied fairly easily by an appropriate choice of  $a/w$ . If the test yields a fracture stress below  $2/3\sigma_{ys}$  the test is valid and a useful  $K_{10}$  value can be calculated. If for cracks as large as  $2a = w/3$  still  $\sigma_{ys} = 2/3\sigma_{ys}$  the panel was too small. When a  $K$  value for such a test is calculated this apparent  $K_{10}$  will be smaller than the real  $K_{10}$  (dashed line through point A in fig. IIA 15), which explains the trend in apparent  $K_{10}$ -data as given by figure VA 11. (WARNING: If this too low  $K_{10}$  value were substituted in eq (12) a too small  $w_{\min}$  would be found and the test result might erroneously be considered valid. The size requirement is implied in eq (13) and therefore eq (13) is a sufficient screening criterion.

With eq (12) minimum panel sizes can be calculated from valid  $K_{10}$  values for the three alloys dealt with in figure IIA 11. These minimum sizes are approximately 520 mm for the 2024 alloy and 135 mm and 110 mm respectively for the two 7075 alloys. The curves in figure VA 11 indicate that a panel size of 110 mm for the 7075 material is still too small. This is due to the fact that there is a problem in accurately determining  $K_{10}$ , since measurement of the critical length is difficult. As the critical fracture condition is approached, crack growth gradually accelerates from a low rate to a high rate. Consequently, a unique designation of the critical crack length is difficult and measurements of the critical crack length are subjective and liable to have very low accuracy. Therefore  $K_{10}$  is usually a less reliable quantity than  $K_{1s}$ .

This may seem somewhat alarming, but it is not really of great importance in practice. For an unstiffened panel the residual strength should be calculated on the basis of  $K_{1s}$ , because it is the initial crack length that is given by the fatigue crack and that is detectable at an inspection. It is immaterial that this crack grows slowly to  $2a_c$  before fracture. The only thing that matters is which load or stress causes the panel to fail under the presence of the given fatigue cracks. For the calculation of the residual strength of a stiffened panel, use has to be made also of  $K_{1s}$  and  $K_{10}$  as will appear in chapter V.C.1. It turns out, however, that in case of stiffened panels some uncertainty in  $K_{10}$  usually does not affect the result too much, since stringer failure appears often to be the critical event (chapter V.C.1).

An important observation to be made from this analysis is that high toughness material can appear more crack sensitive than low toughness materials, in case the panels are smaller than  $w_{\min}$ . This is depicted in the insert of figure VA 15. The material with yield strength at B has a higher toughness than the material with yield strength C and hence it will have superior crack resistance in case of large panels. However, for panel sizes  $w_c$  and smaller this material is inferior, since the residual strength is determined by net section yield (dashed line B-w<sub>c</sub> is below solid line C-w<sub>c</sub>). This is a well-known effect [28] and it is also reflected by the intersection of the apparent  $K_{10}$  curves for the 2024 and 7075 alloys in figure VA 11. Hence, for the application in small panels or sheet structures (e.g. stringers) a low toughness, high yield strength material may exhibit a higher residual strength than a high toughness, low yield strength material. The latter, however, will probably show lower fatigue crack propagation rates and may still be preferable in a fail-safe design.

In conclusion it can be stated that the availability of valid  $K_{10}$  and  $K_{1s}$  values allows the user to establish the residual strength for any panel size including panels smaller than  $w_{\min}$  since the latter will fail at net section yield.

#### V.A.3.3 The effect of sheet thickness

It turns out that the values of  $K_{10}$  and  $K_{1s}$  depend upon thickness. This has been amply discussed in chapter IV. It will be insufficient to present a single set of  $K_{10}$ ,  $K_{1s}$ , and  $K_{1c}$  values for a particular sheet material. Rather a graph should be given on how these toughness parameters vary with thickness in the way shown in figure VA 16. Thicker plates lead to lower values of  $K_{10}$  and  $K_{1s}$  and the two curves merge at large thicknesses to the plane strain fracture toughness  $K_{1c}$ .  $K_{1c}$  is often considered independent of thickness.

It is generally assumed that there is an optimum sheet thickness, giving a maximum toughness. Such a maximum is depicted in figure VA 16a at the optimum thickness of 0.08 in, but not in figure VA 16b. Most results reported in the literature [20,23,29,30,31] show a maximum or suggest there is one [23,32]. The occurrence of a maximum can be made plausible in the following way.

First note that the stresses in the plastic zone at the very crack tip are always in the order of  $1.15\sigma_{ys}$  in plane stress and in the order of  $3\sigma_{ys}$  in plane strain, where  $\sigma_{ys}$  is the uni-axial yield stress. These stresses at the crack tip are in fact independent of the external stress and the crack length. Then the criterion for fracture is the exceedance of a critical strain at the crack tip. Consider four panels of thicknesses  $B_1, B_2, B_3, B_4$ . All panels have the same length of crack and are loaded to the same stress  $\sigma_1$ ; all panels are at the same stress intensity. Consequently, the size of the plastic zone is the same in all panels. This is depicted in the lower line of figure VA 17, which shows through the thickness sections of the four specimens; the height of the plastic zones at the stress  $\sigma_1$  is indicated by the dashed area.

In panels B2, B3, B4 the height of the plastic zone is still smaller than the thickness. This implies that yielding in thickness direction cannot take place freely, but is restrained by the surrounding

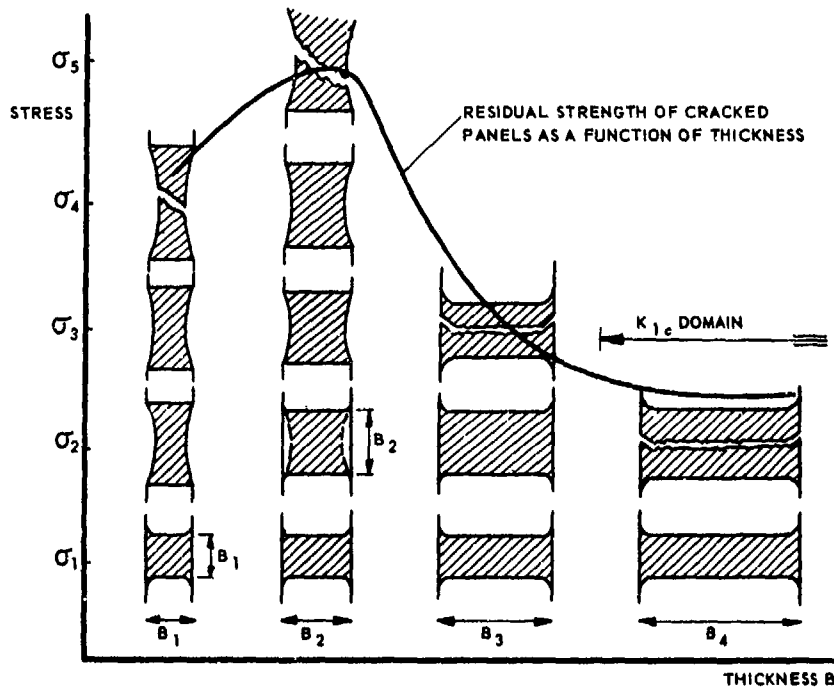


FIG. V A 17 RESIDUAL STRENGTH AS A FUNCTION OF THICKNESS

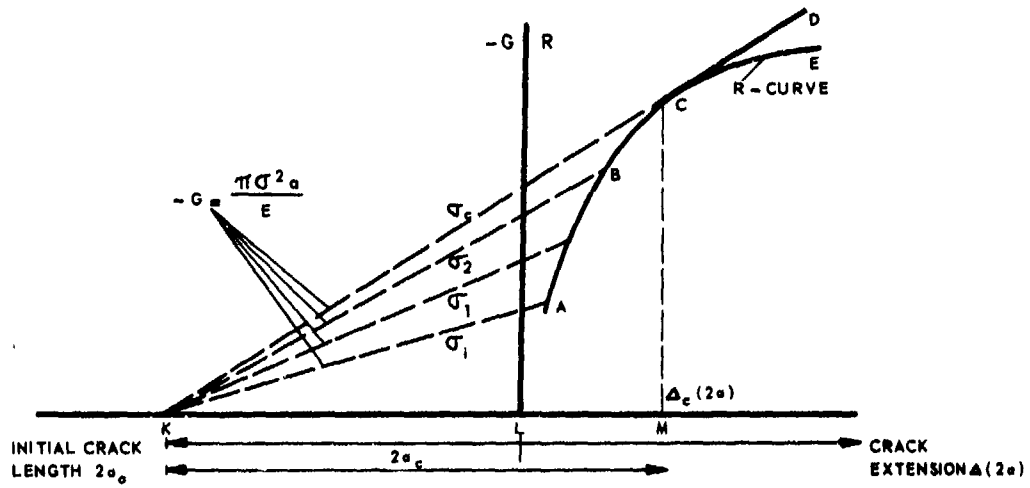


FIG. VA 18 THE ENERGY CONCEPT FOR PLANE STRESS FRACTURE

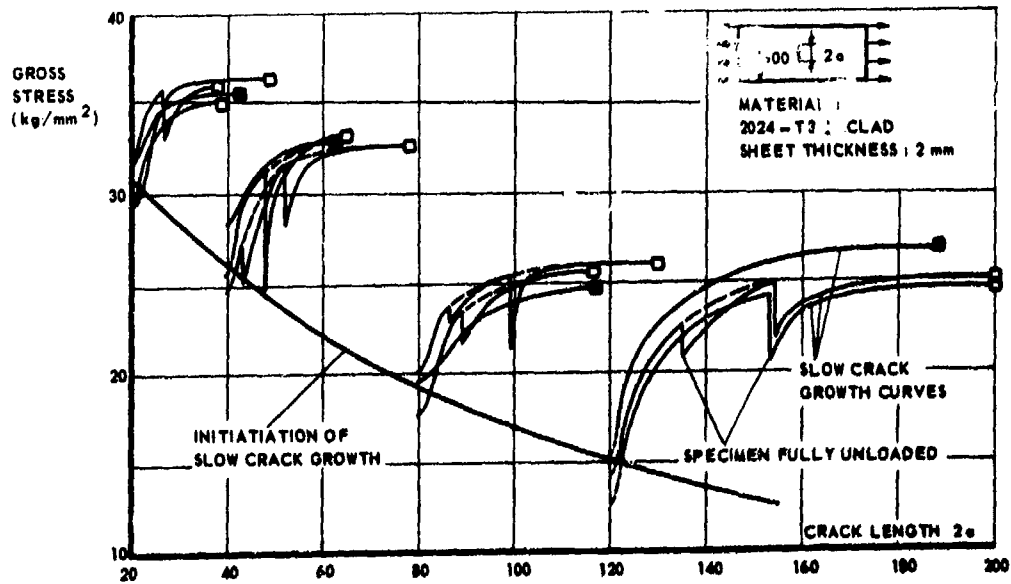


FIG. VA 19 INFLUENCE OF COMPLETE UNLOADING ON SUBSEQUENT STABLE CRACK GROWTH

elastic material; i.e. there exists a state of plane strain. In panel B1 the plastic zone is equal to the thickness and yielding in thickness direction experiences no restriction. That means that a state of plane stress can fully develop in panel B1 and the plastic zone in B1 will from now on be larger than in the other panels.

Increase of the stress to  $\sigma_3$  will cause failure in panel B4, because strains and stresses are large enough. Panel B3 is in the same situation as panel B4 and it is likely that some crack propagation will occur in the interior of panel B3. Yet this panel does not fail due to the effect of the regions of plane stress which exist near the specimen surface (since a stress perpendicular to the surface cannot exist) and which are relatively influential in this thinner panel. Also panel B2 is in the same situation, but this panel has a thickness just equal to the size of the presently existing plastic zone, which implies that plane stress will now develop in panel B2.

Further increase of the stress will cause failure in panel B3 at a stress  $\sigma_4$ . At  $\sigma_4$  the strains at the crack tip in panel B1 will be so large that failure occurs. The strains in panel B1 have been larger than those in panel B2 from the stress  $\sigma_3$  onwards. Therefore the strains in panel B2 will still be insufficient for fracture although the stresses will be approximately the same as in B1. Failure of B2 requires a further increase of the stress to  $\sigma_5$ .

Panels of a thickness larger than B4 will behave similarly as B4 and fail at the stress  $\sigma_1$ . This is the domain of plane strain fractures where valid  $K_{Ic}$  data can be obtained. The maximum residual strength will be reached by the panel that develops full plane stress just at the stress at which plane strain panels fail, i.e.  $B = r_{Ic}$ . Thinner panels will always have higher strains and will fail at lower stress. The maximum may not always show up in practice, since very thin sheets may have somewhat different properties than thicker sheet due to processing or cold work, whereas it has been assumed in the discussion that the microstructural properties would be identical for all thicknesses.

As shown in figure VA 17 the shape of the residual strength curve is associated with a transition of fracture mode. This fracture mode transition can be explained [30,33] on the basis of a change of planes of maximum shear stress.

#### V.A.3.4 Other methods of analysis

Various other methods for the analysis of plane stress data were discussed already in chapter IV. Some of these methods were designed as engineering concepts, such as the notch-strength analysis of Kuhn and Figge [36], the crack strength analysis developed by Kuhn [37] and the effective width concepts proposed by Crichlow [38] and Christensen [39] and Christensen and Denke [23]. The engineering method of Feddersen is preferable, because the use of  $K$  gives it a direct relation to well-established fracture mechanics concepts of plane strain fracture and fatigue crack propagation, but the use of  $K$  gives the method a great versatility since the results can easily be transferred to other panel geometries, even to such complicated things as built-up stiffened structures and sandwich panels, and none of the other methods gives consistently better results [40,41].

Still two other analyses methods are the energy balance concept and the critical-crack-opening-displacement concept. These two methods will be outlined very briefly here, because of their latest possibilities to be applied to stiffened panels [26,42] and because the energy concept can explain some typical phenomena to be discussed in the last two sections of this chapter V.A.3. For a detailed discussion of all plane stress analysis methods the reader is referred to chapter VI and to reviewing papers [40,41].

According to the energy concept there is a continuous balance between released and consumed energy during slow stable crack growth: if there were no balance, then either crack growth would stop or become unstable. Consequently, the energy release rate  $G$  ( $= -\partial P/\partial a$ ) equals the energy consumption rate  $R$  ( $= \partial W/\partial a$ ), i.e.

$$G + R = 0 \quad (14)$$

where  $G$  is released elastic energy and  $R$  is plastic energy consumed in the plastic zone ahead of the advancing crack.  $G$  can be measured during crack growth and an increasing  $G$  appears to be required to maintain slow growth. Apparently, the energy consumption  $R$  increases as the crack proceeds. According to eq (14) the instantaneous values of  $G$  during crack growth will indicate how  $R$  depends upon crack size.  $R$  appears to increase during slow crack growth as depicted diagrammatically in figure VA 18. Also shown in figure VA 18 are lines indicating how  $G$  depends upon crack size and applied stress.

During slow crack growth both  $G$  and  $R$  follow the line ABC, according to eq (14). After a crack extension  $\Delta(2a)$  the crack has reached a length  $2a$ . This point of fracture instability is given by C, because from this point  $G$  follows the line CD and remains larger than  $R$  (CE). Apparently the fracture condition is the point of tangency:

$$\frac{dG}{da} = \frac{dR}{da} \quad (15)$$

Eq (15) would be a useful fracture criterion if apart from the relation  $G = \pi \sigma^2 a / E$  also an analytic relation for  $R$  were available, otherwise the equation cannot be evaluated. Raju [43] has tried to derive such an expression on the basis of plasticity theory by calculating the rate of plastic energy consumption in the plastic zone ahead of the crack.

Krafft et al [44] have proposed  $R$  to be a function of  $\Delta a$  only and independent of  $a$ , i.e. the  $R$ -curve is invariant and is the same for any initial crack length. This suggestion has been used by Broek [20,21,45] to derive an engineering solution to eq (15). He observed that the critical crack length was approximately proportional to the initial crack length in many tests, i.e.

$$a_c = \alpha a_0 \quad (16)$$

This implies a certain relation between KM and LM in figure VA 18, which is the same for all tangents; it requires a distinct function for  $R$  given by

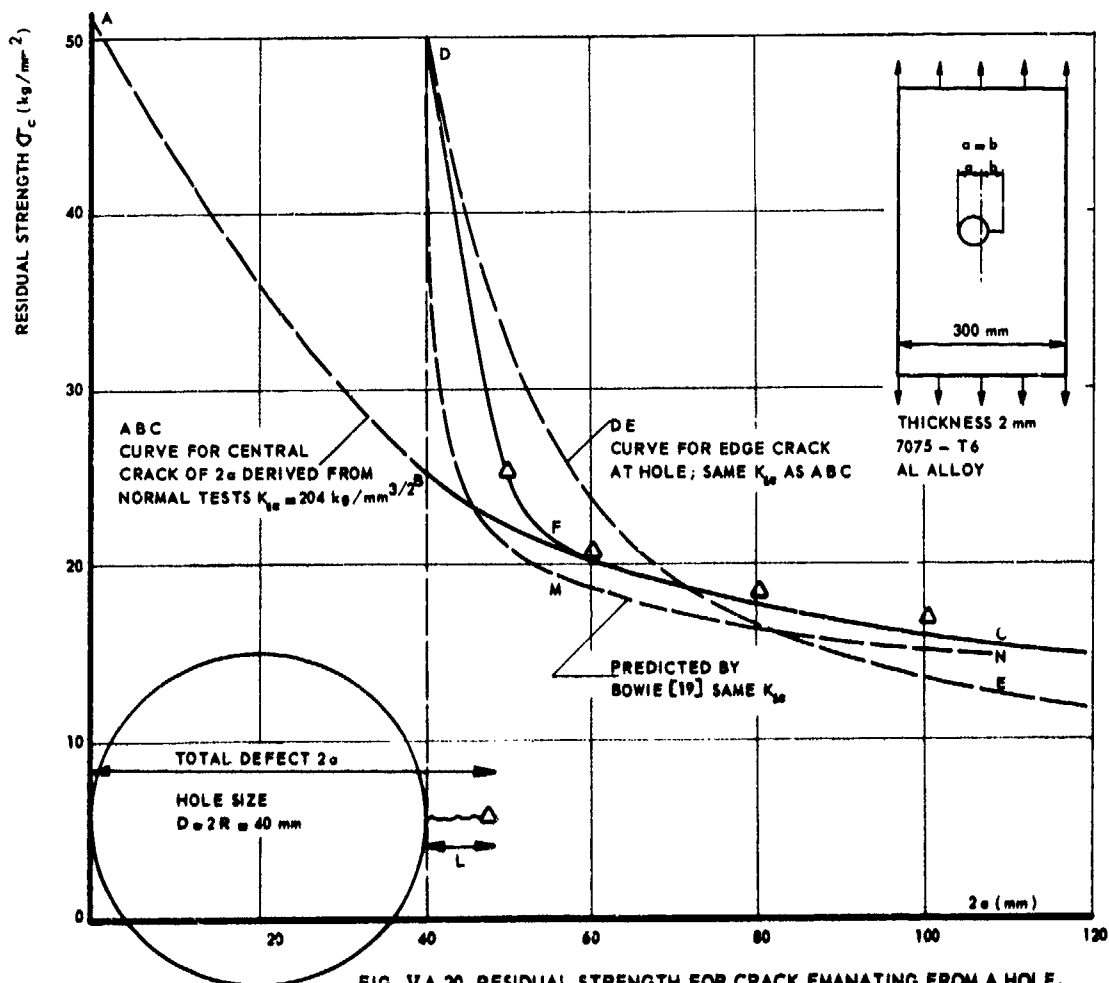


FIG. VA 20 RESIDUAL STRENGTH FOR CRACK EMANATING FROM A HOLE.

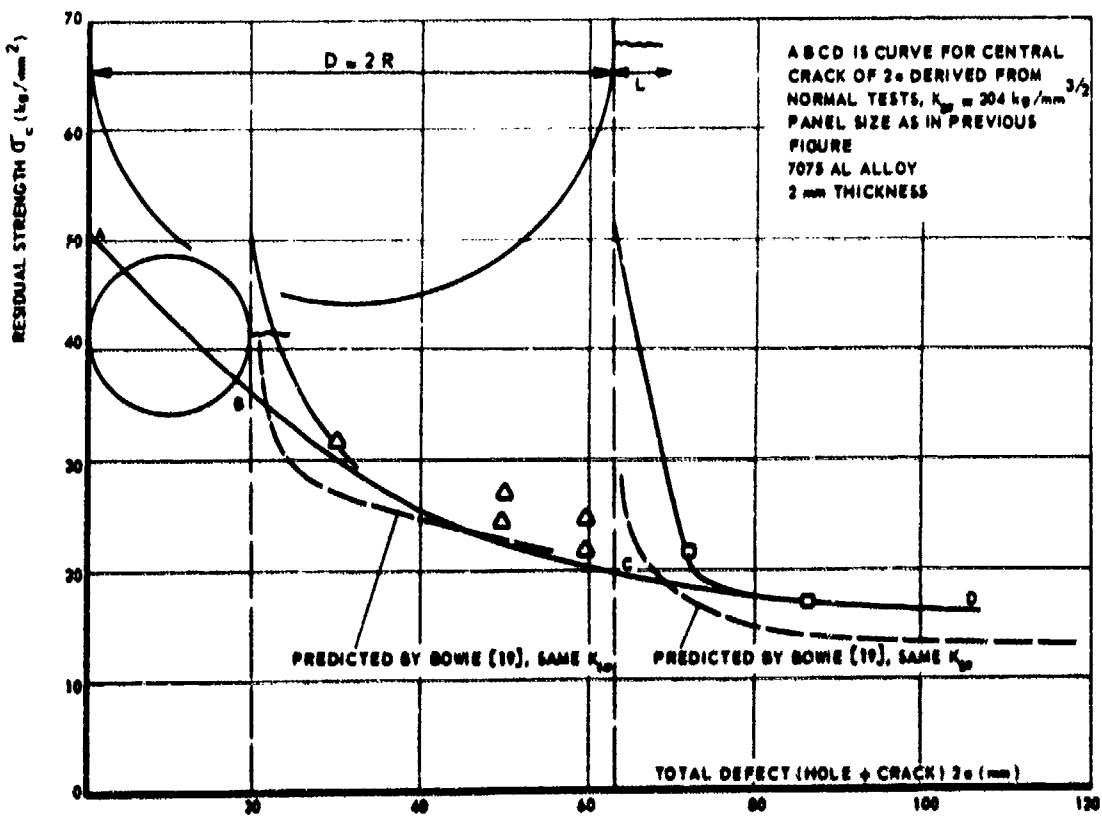


FIG. VA 21 RESIDUAL STRENGTH FOR CRACK EMANATING FROM HOLES.

$$R = \beta(a - a_0)^{(\alpha-1)/\alpha} \quad (17)$$

Eq (17) together with  $G = \pi\sigma^2 a/E$  allow evaluation of eq (15) to give

$$\left. \begin{aligned} \sigma_0 a_0^{1/2\alpha} &= \text{constant} \\ \sigma_0 a_0^{1/2\alpha} &= \text{constant} \end{aligned} \right\} \quad (18)$$

which reduce to  $K_{Ic} = \text{constant}$  and  $K_{IIc} = \text{constant}$  (Feddersen) if  $\alpha$  equals unity.

An evaluation of eq (15) is not essential for the use that will be made of the energy concept in the two following sections, nor for a qualitative outline of its use for complicated sheet structures and sandwich panels.

In the critical crack opening displacement concept it is hypothesized that fracture occurs when the crack tip opening  $b$  exceeds a critical value. It has been shown [46,47] that for small scale yielding  $b = 4G/\pi\sigma_y$ , but this is not essential, because the concept should be applicable also at large scale yielding. The critical crack opening displacement can be measured in a test and be used to predict the residual strength for other crack sizes. The latter is possible only if an analytical relation between  $b$  and the applied stress is available. For application of the concept to stiffened panels such a relation is not strictly necessary (o.f. chapter V.C.1).

#### V.A.3.5 Determination of the residual strength for practical fail-safe problems in case of unattiffened panels.

This section will be concerned with the following practical problems:

- a) The residual strength of unreinforced panels.
- b) Interrupted slow crack growth.
- c) Cracks emanating from cut outs and holes.
- d) Stop holes and other crack stoppers.
- e) Residual strength under combined tension and shear.
- f) Impact damage.

These subjects will be treated in the given order.

##### a) The residual strength of unreinforced panels.

For the prediction of the residual strength of a cracked panel an applicable plane stress fracture toughness value should be available; the toughness value should apply for the thickness of the panel under consideration. The residual strength has to be predicted for the case a fatigue crack of a certain length will develop in the structure. Hence, the residual strength has to be based on the size of the fatigue crack per se and it is not of interest that the crack will show some slow growth before the catastrophe. This means that residual strength of cracked unreinforced panels should be based on  $K_{Ic}$ , rather than  $K_{IIc}$  (Note that the problem is a different one for reinforced panels, chapter V.C.1).

When a useful figure for  $K_{Ic}$  is available, obtained from a sufficiently large panel, the residual strength can be determined for any size of panel and any length of crack with Feddersen's method discussed in section V.A.3.2. In case of small panels it is permissible to work with an apparent  $K_{Ic}$  value for the pertinent size of panel, but it is preferable to use real  $K_{Ic}$  values and net section<sup>10</sup> yield criterion for very small panels.

The residual strength can be calculated from  $\sigma_r = K_{Ic}/\sqrt{wa}$ , provided  $2a < w/3$  and  $\sigma_r < 2/3\sigma_{fs}$  otherwise use has to be made of the tangents. For a certain prescribed fail-safe stress  $\sigma_{fs}$  one can determine the permissible length of the fatigue crack from  $2a_0 = 2K_{Ic}^2/\sigma_{fs}^2$ . Note that it would be unrealistic to determine the permissible crack length from  $2a_0 = 2K_{Ic}^2/\sigma_{fs}^2$ , since it is the fail-safe load itself that makes the crack growing to  $2a_0$ . Again if  $2a_0 < w/3$  the tangent has to be used and also if  $\sigma_{fs} > 2/3\sigma_{ys}$ . In the latter case it might be considered too conservative to use the tangent, but since it will concern very small cracks which are difficult to detect it is advisable to perform confirmatory tests if higher stresses are allowed than the tangent would suggest permissible. When dealing with edge cracks  $K_{IIc}$  values from central cracks can be used, but the stress intensity factor should be calculated from the relevant expression for edge cracks given elsewhere in this volume.

##### b) Interrupted slow crack growth

A high load in service just insufficient to cause failure, may induce slow stable growth of an existing crack. A longer crack then remains, having possibly a lower residual strength. Tests on large 2024-T3 and 7075-T6 sheets [20,48,49] have indicated that this needs not to be feared. In these tests the specimens were loaded until the cracks had shown a certain amount of slow crack growth. Crack growth was then interrupted by fully unloading, after which the specimens were fractured at reloading. Some tests were interrupted twice.

Results of the tests on 2024-T3 panels are presented in figure VA 19 in comparison with continuous tests. The figure shows that after an interruption, re-initiation of crack growth is not in

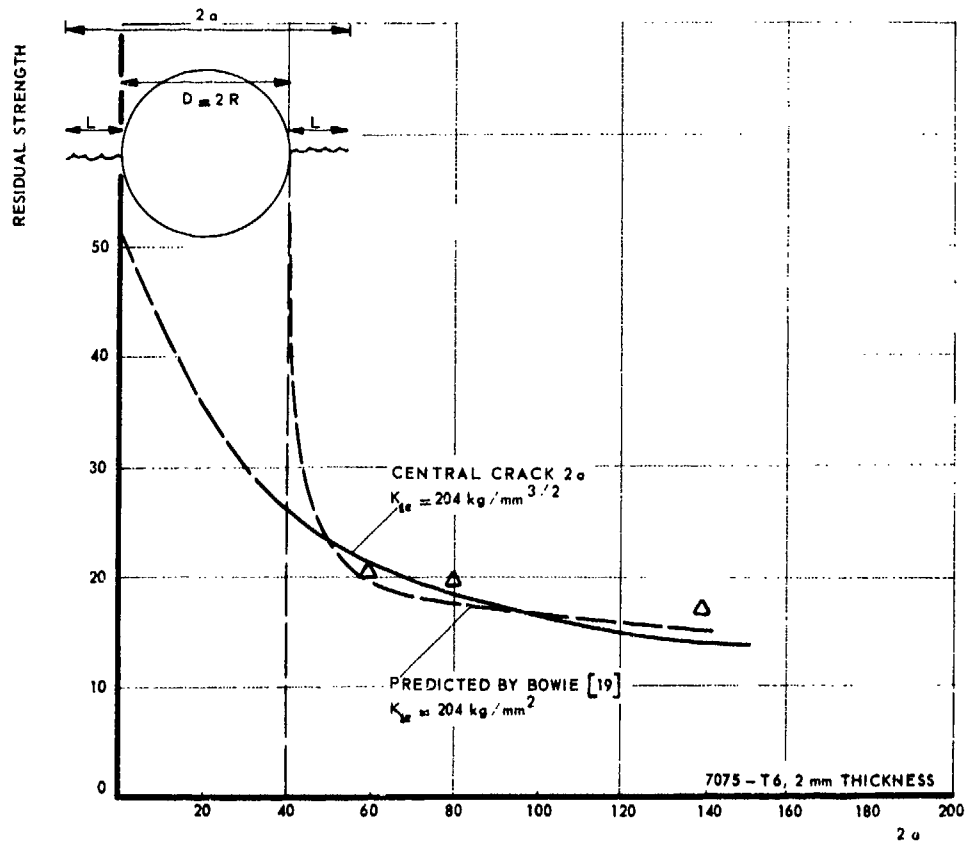


FIG. V A 22 RESIDUAL STRENGTH FOR CRACKS EMANATING FROM HOLE, SYMMETRIC CASE.

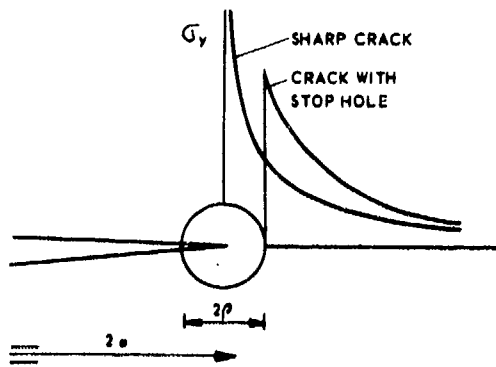


FIG. V A 23 CRACK WITH STOP HOLE

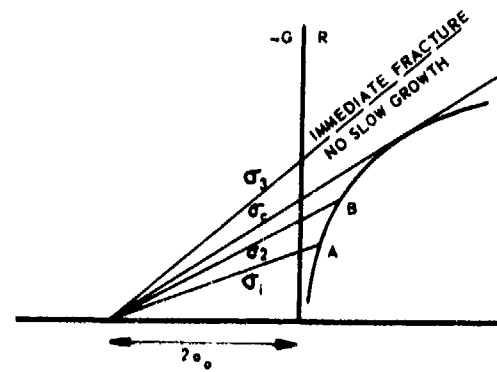


FIG. V A 24 BEHAVIOUR OF A CRACK WITH STOP HOLES.

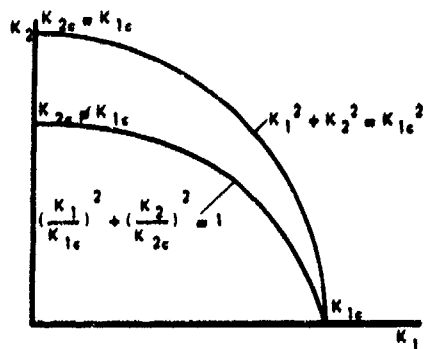


FIG. V A 25 COMBINED MODE FRACTURE

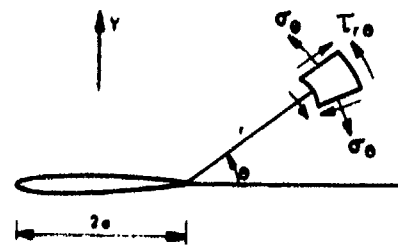


FIG. V A 26 STRESSES AT CRACK TIP

accordance with the curve for the onset of slow crack growth, but it takes place at stresses only slightly below those at which the tests were interrupted. Soon after re-initiation of crack growth, the original slow growth curve is followed again. The specimen apparently remembers its load history and ignores the unloading.

When a crack of the largest permissible size is actually present in service, it may show some slow growth if a high load, lower than the fail-safe load is met. Though the ultimate crack length is exceeded then, the structure can still bear the fail-safe load. The flight in which the high load occurred, most likely encountered extremely rough weather and therefore it is not inconceivable that more high loads, if not the fail-safe load, will be experienced soon after. It is reassuring that the residual strength is not impaired by the first high load and by the slow crack growth it caused.

The high load that induced the crack growth has introduced residual compressive stresses at the crack tip, which are known to slow down the rate of crack propagation under subsequent fatigue loading. Therefore it may be expected that the structure can safely reach the next inspection.

#### c) Cracks emanating from cutouts and holes

In practice cracks often occur in areas of stress concentrations at holes or at the edge of a cutout. Bowie [19] has analysed the case of cracks at the edge of a circular hole and he showed that the stress intensity factor can be expressed as:

$$K = \sigma \sqrt{\pi L} f(L/R) \quad (19)$$

where  $K$  is the radius of the hole and  $L$  is the length of a radial crack, measured from the edge of the hole. Values for  $f(L/R)$  are presented in the two upper lines of table IIA 2, for the case of a crack at one edge of the hole only and for the symmetric case of two cracks of equal size at either side of the hole.

As a first engineering approach one might assume that the combination of a hole and a crack would behave as a crack of length equal to the total defect size. For a crack at one side of the hole this would mean that the effective crack length  $2a_{\text{eff}}$  would be considered equal to  $2a_{\text{eff}} = 2R + L$  (-  $D + L$ ).

Hence:

$$K = \sigma \sqrt{\pi a_{\text{eff}}} = \sigma \sqrt{\pi L} \left( \frac{R}{L} + \frac{1}{2} \right)^{1/2} \quad (20)$$

For the symmetric case:  $2a_{\text{eff}} = 2R + 2L$  (-  $D + 2L$ ) and hence

$$K = \sigma \sqrt{\pi a_{\text{eff}}} = \sigma \sqrt{\pi L} \left( \frac{R}{L} + 1 \right)^{1/2} \quad (21)$$

Values of the approximate functions  $f(L/R)$  of eqs (20) and (21) are compared with the actual functions  $f(L/R)$  as derived by Bowie in table VA 2.

Table VA 2. Cracks at the edge of a hole. Values for  $f(L/R)$  in eqs (19), (20), (21).

L/R →	0.1	0.2	0.3	0.5	0.8	1	1.5	2	3	5
Bowie, 1 crack	2.73	2.30	2.04	1.73	1.47	1.37	1.18	1.06	0.94	0.80
Bowie, 2 cracks	2.73	2.41	2.15	1.83	1.58	1.45	1.29	1.21	1.14	1.07
1 crack eq (20)	3.21	2.35	1.95	1.58	1.32	1.22	1.08	1	0.94	0.84
2 cracks eq (21)	3.32	2.45	2.08	1.73	1.50	1.41	1.29	1.22	1.15	1.09

This table shows that the differences between the approximate method and Bowie's analysis are small for cracks larger than 0.1R. Bowie's method would predict a slightly lower residual strength than the approximate method over practically the whole range of crack sizes considered.

Brook and Vlieger [50] carried out tests to check the validity of the two methods. The results for cracks at one side of the hole are presented in figures VA 20 and VA 21; the symmetric case of two cracks is given in figure VA 22. The  $K_{\text{res}}$  value for the material was determined first from normal residual strength tests with the same size of panels. On the basis of this  $K_{\text{res}}$  (- 204 kg/mm<sup>3/2</sup>) the residual strength of the cracks at holes were predicted by using Bowie's analysis (dashed lines in all figures) and also by using the approximate method of eqs (20) and (21) (solid lines in all figures). The curves show that indeed Bowie's analysis predicts a somewhat lower residual strength. The test results do confirm the predicted lines very well.

It can be concluded that Bowie's analysis will give a safe conservative estimate of the residual strength of cracks emanating from holes and that the engineering method that considers the hole part of the crack gives very useful results for rough estimates.

In case of a reinforced hole - where measures have been taken to reduce or to eliminate the stress concentration - it is conceivable that a single crack has to be considered as an edge crack, such that the presence of the hole can be ignored as long as the reinforcement is intact. No information is available on this subject.

#### d) Stop holes and other crack stoppers

Sometimes small fatigue cracks in sheets may have to be temporarily prevented from growing

in a provisional way, pending a more elaborate repair at the earliest convenience. Such provisional measures can consist of drilling stop holes at the crack tips. The edges of the holes can be slightly cold worked in order to introduce residual compressive stresses. These measures can be quite satisfactory to stop fatigue crack growth for a while, but it should be emphasized that they do not improve the residual strength in general.

The problem of a blunt crack tip with tip radius  $\rho$  has been treated by several investigators [51,52,53]. It turns out that the stress intensity factor of a blunt crack tip is somewhat higher than that of a comparative sharp crack. The expressions derived take their simplest form when the center of the hole is located at the tip of the natural crack as in figure VA 23. According to Bowie and Neal [52] the stress intensity factor can then be approximated by

$$K = \sqrt{\pi a + 1.18\rho} \quad (22)$$

and the stresses  $\sigma_y$  at the crack tip according to Paris and Creager [53] as:

$$\sigma_y = \frac{K\sqrt{\pi a}}{\sqrt{2\pi r}} \left(1 + \frac{\rho}{2r}\right) - \frac{K_{crack}}{\sqrt{2\pi r}} \left(1 + \frac{\rho}{2r}\right) \quad (23)$$

The stress distribution according to eq (23) is depicted diagrammatically in figure VA 23. This shows that the stresses at the blunt crack tip are lower than at the sharp crack tip, whereas the stress intensity is higher. Apparently, this is a case where the condition for fracture cannot be determined by the stress intensity factor (in general, it is confusing to use stress intensity factors for other than natural cracks when dealing with fracture problems).

Consequently, the residual strength of the crack with stop holes cannot be determined on the basis of a stress intensity factor as in eq (22). From eq (23) and figure VA 23 it may appear that the initiation of slow stable crack growth from the stop holes will be postponed to a higher nominal stress. This has been demonstrated in tests reported by Broek [54]. However, once slow crack growth has started, the crack tip is a real sharp crack tip again and will behave as such: the residual strength is the same as in case of a crack without stop holes.

This behaviour can be explained on the basis of the energy balance concept as in figure VA 24. A sharp crack starts slow growth at  $\sigma_1$  and gives failure at the stress  $\sigma_c$ . When there are small stop holes the stress for crack initiation can be raised to  $\sigma_2$ . The energy balances will now be reached at B and fracture will occur at  $\sigma_2$  all the same. Stop holes can be made so large that crack initiation does not occur until at a stress  $\sigma_3$  larger than  $\sigma_c$ . In that case no energy balance can be reached and immediate fracture instability occurs, not preceded by slow growth. The latter will occur when the stop holes have a certain minimum size, which will depend upon the material properties. There is some evidence from tests [54] that this minimum size is in the order of 2 mm for 7075-T6 aluminium alloy sheet. It is certainly greater for 2024-T3 sheet, but it may be much smaller for materials of low toughness: for H-11 steel an increase of residual strength was observed already [55] at root radii in the order of 20 microns. Its size has to be determined from experiments and cannot be calculated on the basis of a stress intensity factor, as explained above.

When dealing with crack stoppers one has to consider not only prevention of crack initiation, but also arrest of crack propagation. The latter may occur when a propagating crack runs into a hole. In general, arrest of a running crack will occur when the crack runs into a region with a higher fracture toughness or in a region with lower stress intensity. The stress intensity may decrease when the crack enters a region affected by the presence of reinforcements, a problem which will receive ample attention in the chapter on stiffened panels (V.C.1). In an unstiffened panel cracks may run into rivet holes. It is very much a matter of available energy whether the crack will be arrested in such a case. Calculations of Kobayashi and Harden [56] indicate that there is little chance that cracks in unstiffened sheets may be arrested in rivet holes. Therefore the problem of crack arrest will not be discussed any further here; it will be dealt with in sections on stiffened panels. For a thorough treatment of the basic crack arrest theory the reader is referred to the work of Bluhm [57].

#### e) Residual strength under combined tension and shear

As pointed out elsewhere in this volume three modes of cracking can be distinguished: the opening mode, the sliding mode and the tear mode, denoted as modes I, II and III respectively. Wing box beams and aircraft fuselages are subjected mainly to normal loading, but they also experience torsional loading. Cracks that develop in these structures may therefore be exposed to tension and shear, which leads to mixed mode cracking. The combination of tension and shear gives a mixture of modes I and II. Several investigators have considered the mixed mode fracture problem [58,59,60,61,62], but a generally accepted analysis has not yet been developed. The references treat mixed modes of both I, II and III. For the problem considered here, the discussion can be limited to the I,II mixed mode.

Mode II loading under an in-plane shear stress  $\tau$  can be characterized by a stress intensity factor  $K_2 = \tau\sqrt{\pi a}$  analogous to mode I loading (e.g. 4Q). (Consistent with the previously used notations expressions  $K_1$  and  $K_2$  will be used here to emphasize plane stress). Under these conditions fracture will occur when  $K_2$  reaches a critical value  $K_{2c}$ .

When a certain combination of the two reaches a critical value. It is not easy to develop this fracture criterion. When using an energy balance criterion it can be stated that the total energy release rate  $G_t$  is given by:

$$G_t = G_1 + G_2 + G_3 \quad (24)$$

Fracture occurs when  $G_t$  is larger than the energy consumption rate and hence the fracture condition is given by  $G_t > R_t$  (assumed a constant here for simplicity). For I,II mixed mode loading  $G_3 = 0$ ,



$G_1 = K_1^2/E$  and  $G_2 = K_2^2/E$ , hence the fracture condition would be:

$$K_1^2 + K_2^2 = \text{constant} = K_0^2 \quad (25)$$

For mode I cracking  $K_2 = 0$  or  $K_1^2 = K_{1c}^2$  and for mode II cracking  $K_1 = 0$  or  $K_2^2 = K_{2c}^2$ . Consequently eq (25) predicts that the locus for combined mode cracking is a circle with radius  $K_0$ . This is depicted in figure VA 25. In reality  $K_{1c} \neq K_{2c}$  and the fracture condition is more likely to be:

$$\left(\frac{K_1}{K_{1c}}\right)^2 + \left(\frac{K_2}{K_{2c}}\right)^2 = 1 \quad (26)$$

The locus of fracture being an ellipse (Fig. VA 25). Fracture occurs when  $K_1$  and  $K_2$  reach values sufficient to satisfy eq (26).

An alternative fracture criterion has been proposed by Erdogan and Sih [58]. They make use of the observation that under combined loading crack extension takes place in the plane perpendicular to the direction of greatest tension. Under conditions of combined loading the stresses (see figure VA 26) are given by:

$$\left. \begin{aligned} \sigma_\theta &= \frac{1}{\sqrt{2\pi r}} \cos \frac{\theta}{2} \left[ K_1 \cos^2 \frac{\theta}{2} - \frac{3}{2} K_2 \sin \theta \right] \\ \tau_{r\theta} &= \frac{1}{\sqrt{2\pi r}} \cos \frac{\theta}{2} \left[ K_1 \sin \theta + K_2 (3 \cos \theta - 1) \right] \end{aligned} \right\} \quad (27)$$

The greatest tension will occur at  $\theta$  where  $\tau_{r\theta} = 0$ . Then Erdogan and Sih assume fracture to take place when  $\sigma_\theta$  is equal to that stress that leads to mode I fracture, which is  $\sigma_y = K_{1c}/\sqrt{2\pi r}$  (since  $\sigma_y$  is the largest tensile stress at the crack tip in mode I loading). Then the fracture condition is:

$$K_1 \cos^2 \frac{\theta}{2} - \frac{3}{2} K_2 \sin \theta = \frac{K_{1c}}{\cos \frac{\theta}{2}} \quad (28)$$

with

$$K_1 \sin \theta + K_2 (3 \cos \theta - 1) = 0 \quad (\text{from } \tau_{r\theta} = 0)$$

Results of tests on plexiglass specimens [58] appeared to show reasonable agreement with eq (28), however, they show a better agreement with eq (26) as is shown in figure VA 27.

Combined mode I and II tests are usually carried out on tension panels with oblique cracks [59,60,61]. For that case (figure VA 28) it follows that  $K_1 = \sigma \sin^2 \beta \sqrt{\pi a}$  and  $K_2 = \sigma \cos^2 \beta \sqrt{\pi a}$ . Results of such tests on aluminium alloy sheet specimens generally show good agreement with eq (26), as can be seen from figure VA 29. Therefore eq (26) is preferable for practical problems, since it allows more easily the reverse calculation from a given toughness value to critical crack length or residual strength. It can be observed from figures VA 27 and 29 that usually  $K_{2c} \approx 0.75 K_{1c}$ . With this knowledge eq (26) can be reduced to the useful engineering criterion of

$$\left. \begin{aligned} K_1^2 + 1.78 K_2^2 &= K_{1c}^2 \\ K_1 &= \sigma \sqrt{\pi a}, \quad K_2 = \tau \sqrt{\pi a} \end{aligned} \right\} \quad (29)$$

Eq (29) implies that fracture can be predicted from mode I plane stress fracture toughness values. For a material with known  $K_{1c}$  the critical crack length for a certain required fail-safe loading case or the fracture strength under the presence of a critical crack can easily be calculated for conditions of combined tension and shear.

#### f) Impact damage.

It is unlikely that fracture mechanics will ever be able to treat impact damage and ballistic damage in a reliable way, since this kind of damage is so irregular in nature. It can only be tried to derive rules of thumb from extensive and systematic investigations.

The work carried out by Jensen [63] and Campbell et al [64] has shown that the damage and residual strength of 7075-T6 aluminium panels exposed to gunfire varies with impact angle, projectile velocity and panel thickness. The damage of thick panels usually consisted of fairly smooth round holes with or without a surrounding spall; the residual strength in such cases can usually well be approximated by assuming that the maximum stress was the maximum stress exceeds the ultimate tensile stress of the material. Thin panels were more likely to develop crack-like damage and therefore the residual strength could very roughly be based on a fracture mechanics concept, by using an apparent fracture toughness value based on an effective crack length or defect size equal to the lateral dimension of the damage. It seems that the introduction of structural crack stoppers, such as reinforcements and splices are the best means to provide some degree of safety against impact damage.

#### V.A.3.6 The necessity of confirmatory testing

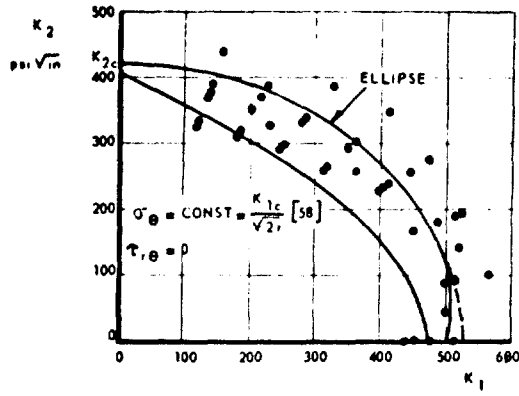


FIG. VA 27 COMBINED MODE FRACTURE OF PLEXIGLASS [58].

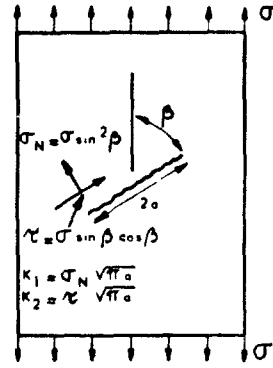


FIG. VA 28 COMBINED MODE FRACTURE TEST.

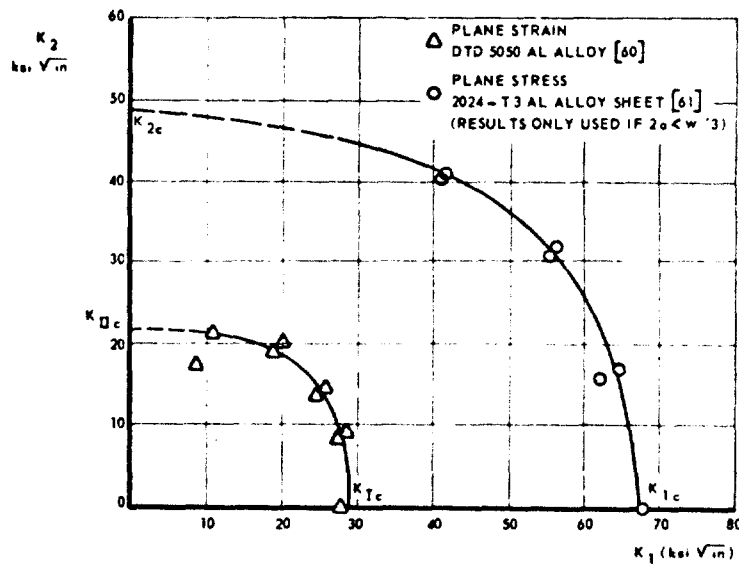


FIG. VA 29 COMBINED MODE FRACTURE IN AL-ALLOYS

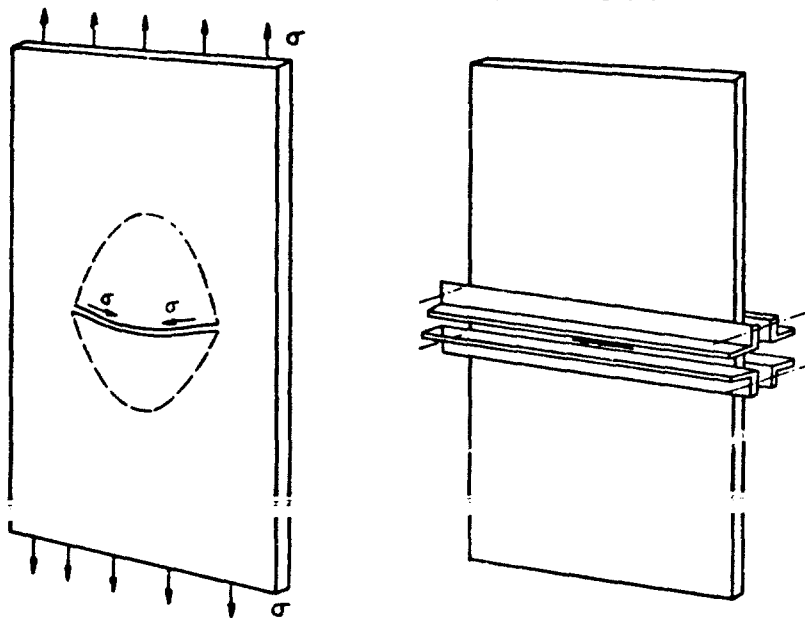


FIG. VA 30 CRACK BUCKLING AND ANTI-BUCKLING GUIDES.

If applicable plane stress fracture toughness data are not available, tests will have to be performed. Tests on material of the relevant thickness will have to be performed in confirmation with the criteria presented in this chapter:  $2a < w/3$  and  $\sigma_0 < 2/3 \sigma_{ys}$ .

Unlike plane strain specimens, the plane stress specimens need not always be fatigue cracked; when the toughness is high enough for the cracks to show significant amounts of slow growth, the crack can be simulated by a sharp saw cut. A saw cut will slightly increase the stress for onset of crack growth, but once crack growth has started the saw cut has changed into a real crack and the residual strength will be the same as for a fatigue crack of the same initial length. This has been demonstrated by tests [54].

When fracture of sheets with saw cuts is not preceded by slow crack growth, the simulation of the crack by means of a saw cut is not permissible. In that case the bluntness of the tip of the saw cut may be sufficient to raise the stress  $\sigma_1$  for crack initiation above the fracture stress  $\sigma_0$ , similarly as in the case of stop holes discussed in the previous section (Fig. VA 24).

The stress field equations for a cracked plate indicate that the stress  $\sigma_x$  along the edges of the crack is compressive and of the order of the applied longitudinal tensile stress. Especially in thin sheets this compressive stress can cause buckling of the plate segment adjacent to the crack. One can easily demonstrate this buckling by manually pulling a sheet of paper with a central transverse tear. Since buckling may affect slow crack growth and residual strength, it has been the subject of several investigations [22,65,66,67,68].

Carlson et al [67] have treated buckling formally as a plate stability problem. Usually however, a simple column buckling formula is used [22,65,66]. Since the transverse compressive stress along the crack edge is equal to the nominal uniform stress  $\sigma$ , buckling will commence when  $\sigma = \sigma_b$  defined by

$$\sigma_b = \frac{\pi^2 EB^2}{48 l_0^2} \quad (30)$$

Eq (30) is the Euler formula for buckling of a column of thickness B, modulus E and effective length  $l_0$  with hinged ends. The length of the column  $l_0$  will be related to the crack length a by

$$l_0 = \alpha a \quad (31)$$

There is difference of opinion as to the most realistic value of  $\alpha$ , which is in the order of 0.5 [65], but most probably depends upon sheet thickness [22,67].

For cracks of some length buckling occurs long before the specimen is ready to fail and therefore it may affect the residual strength. For this reason buckling is usually prevented in a residual strength tests by the application of rigid bars (Fig. VA 30), known as anti-buckling guides. Photo-elastic studies of Dixon and Strannigan [65] have shown that the maximum stress at the tip of a slit in an unrestrained model was about 30 percent greater than under the application of anti-buckling guides. This will of course affect the residual strength. Reductions in residual strength of about 10 percent were reported by Walker [22] and Trotman [68] and up to 40 percent by Forman [66]. Of course, the reduction must depend upon crack length. Some of the many data of Walker [22] are presented here in figure VA 31 to illustrate the effect of buckling on slow stable crack growth and residual strength.

Although buckling guides are usually considered a pre-requisite for a useful residual strength test, it is questionable whether they are always necessary. In practical sheet structures, buckling will often not be fully restrained. Even in stiffened structures buckling can sometimes be restrained only by the in-plane bending stiffness of the stringers; only when there is a stringer across the crack, buckling is fully prevented by the out-of-plane bending stiffness of the stringer. A calculation of the residual strength of a sheet structure in which buckling is not restrained should, of course, be based on tests without buckling guides, since  $K_{10}$  is lower for that case.

Airworthiness requirements [69] used to allow fail-safe testing by severing single elements such as stringers or spar caps while the structure is under load. The question sometimes arises whether it is similarly permissible to demonstrate fail-safety by cutting a slit while the structure is under load. Tests have shown [70] that this would provide false information. The specimens containing an initial central slit were loaded to the point that slow growth initiation was about to occur. From then on the load was kept constant and the two ends of the crack were propagated simultaneously by means of two jeweller fret saws until fracture occurred. Some test results are presented in figure VA 32.

At first glance one would expect failure during sawing to occur when the critical crack length, associated with the applied stress, is reached; i.e. at the passage of the upper curve in figure VA 32. Yet, sawing could be continued far beyond this point. It might be argued that the discrepancy could be due to the bluntness of the saw cut as compared to a fatigue crack, since the upper curve in figure VA 32 is valid for a slowly-growing actual crack. Vertically however, the data points are so far off the curve that the bluntness of the saw cut cannot be the sole cause of the discrepancy.

When the results are considered in liaison with the R-curve concept, they appear to be more rational. This is outlined in figure VA 33. The lower part of this figure shows the residual strength diagram. A crack of initial length  $a_0$  can be loaded to a stress  $\sigma_1$  (point A,) where slow crack growth commences. When the stress is raised to  $\sigma_2$  the crack will have propagated to  $a_2$  where fracture instability occurs. The upper part of figure VA 33 shows the corresponding energy-balance diagram in terms of the energy release rate G and the crack growth resistance R. Slow growth begins when the stress is raised to  $\sigma_1$ . Then  $G = \pi \sigma_1^2 a_0 / E$ , represented by point A. During further increase of the stress the R-curve is followed. Finally, when the stress has reached  $\sigma_2$  and the crack has grown to  $a_2$  (point C), the crack can propagate under constant stress; G will increase along C-G<sup>2</sup> and remain larger than R and fracture instability occurs.

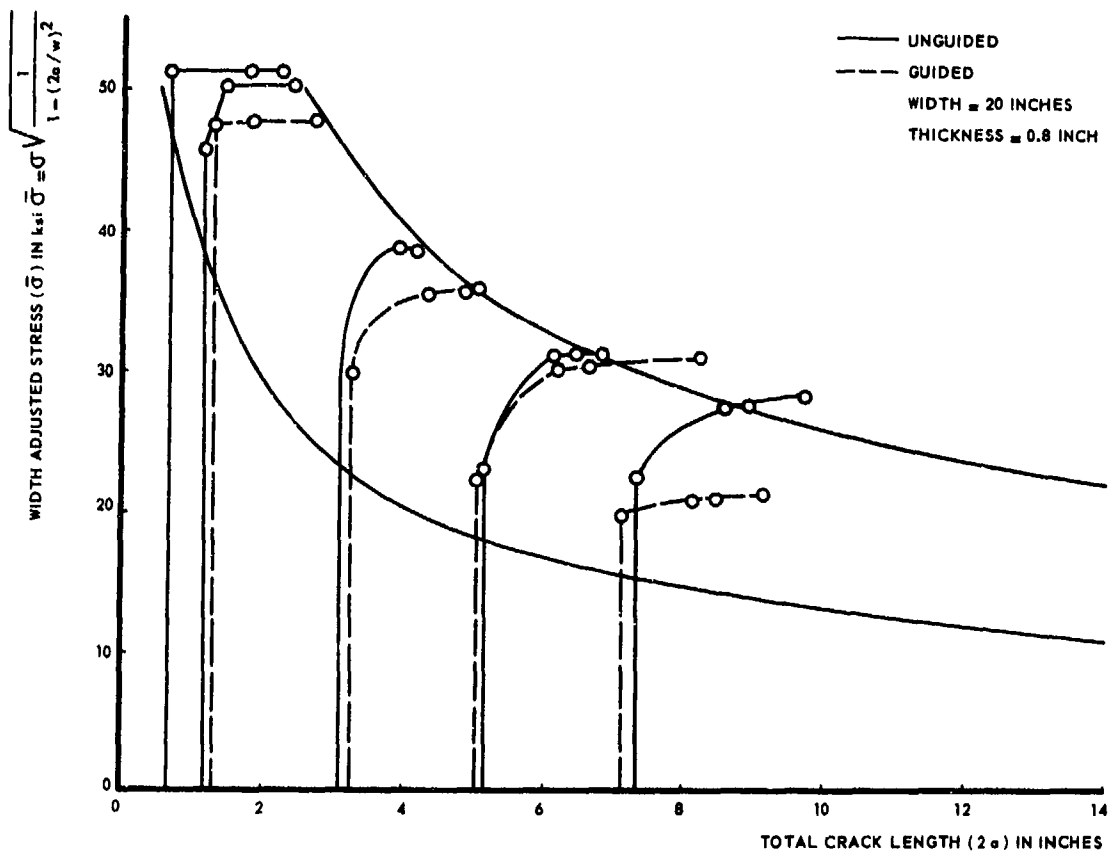


FIG. V A 31 EFFECT OF BUCKLING ON SLOW CRACK GROWTH AND RESIDUAL STRENGTH [22].

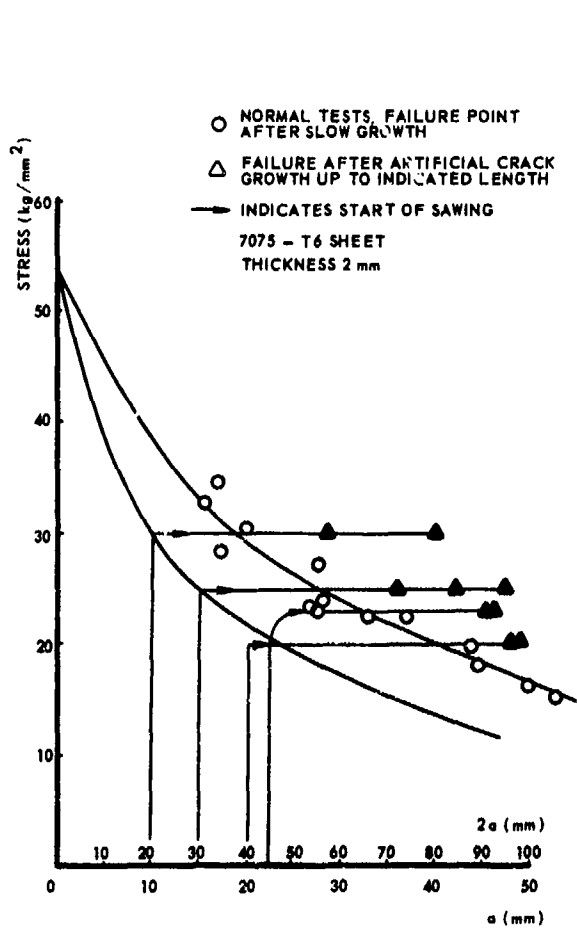


FIG. V A 32 ARTIFICIAL CRACK GROWTH UNDER CONSTANT STRESS [70].

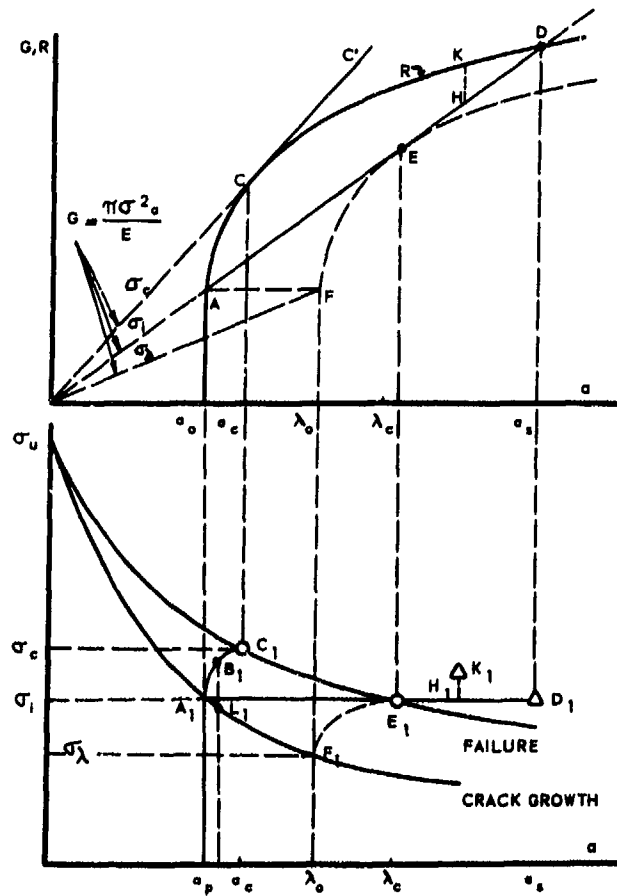


FIG. V A 33 EXPLANATION OF DATA IN PREVIOUS FIGURE [70].

Consider now a crack of initial length  $a_0$  loaded to  $\sigma_1$ . The crack is extended artificially by sawing, while the stress is kept constant at  $\sigma_1$ . The energy release rate  $G$  will increase proportionally to  $a$  according to  $G = \pi \sigma_1^2 a/E$  and it will follow the straight line A-D. Finally at D, the condition  $G > R$  is fulfilled and fracture instability occurs (point D, in the lower part of figure IIA 33). If fracture were to occur at E, as assumed in the first paragraph of this chapter, the R curve should shift during sawing to the position of the dashed curve in figure IIA 33, where fracture would occur at E. A shift of the R-curve during the test is unlikely [70].

When in the test described, sawing is stopped at H, followed by continuous loading, failure should occur at K. Equivalent points in the lower diagram are  $H_1$  and  $K_1$ . The latter was confirmed by tests also [70].

In conclusion it can be stated that the execution of a fail-safe test by means of extending the crack by sawing under load leads to an overestimation of the critical crack length.

#### V.A.4 FATIGUE CRACK PROPAGATION

##### V.A.4.1 Introduction

The determination of the fatigue crack propagation curve is an essential part of the fail-safe design procedure. It is the basis for the establishment of the inspection interval or the interval for stripping or proof testing (o.f. chapter V.A.1). Although residual strength calculation procedures have obvious shortcomings, the prediction of the fatigue crack propagation characteristic is still the least accurate part of the fail-safe design procedure, despite the vast amount of research that has been done on this subject. Yet, the developments achieved during the last decade justify a moderate optimism about the possibilities of prediction techniques.

This chapter deals with the technical problems of fatigue crack propagation. The use of fracture mechanics in fatigue as expressed by the relation between the crack propagation rate and the stress intensity factor, is briefly considered. This relation is especially useful when dealing with structures. However, the discussion is based on a very practical standpoint and is limited to an evaluation of the shortcomings of the relation and its applicability to technical problems. A detailed analysis of its physical aspects is beyond the scope of this chapter and the reader is referred to the pertinent literature [71,72,73,74].

If fatigue cracks would never develop in aircraft structures, the fail-safe problem would probably hardly exist. Fatigue crack propagation is therefore only part of the fatigue problem in aircraft structures. Yet, the question of fatigue endurance, safe-life prediction and crack-free life will not be considered here. They have received ample attention elsewhere [40,75] and the present volume deals with fail-safety alone. It is very troublesome to an aircraft operator if premature fatigue cracks occur, but it is immaterial to the fail-safe problem per se whether cracks occur late or early.

The interaction effects of cycles of different amplitudes and the retardation effect of overloads on crack growth during subsequent cycling, is considered, but that discussion is also limited to its practical engineering implications.

The discussion may seem to devote relatively much space to sheets. This is a consequence of the fact that the majority of fatigue crack propagation research has been performed on sheets.

##### V.A.4.2 Crack growth rate and stress intensity factor (constant amplitude loading)

The discussion of this section will cover the following items:

- a) Crack growth and  $\Delta K$  at zero cycle ratio.
- b) Effect of cycle ratio.
- c) Versatility of the concept, cracks emanating from holes.
- d) Shortcomings, practical standpoint.

##### a) Crack growth and $\Delta K$ at zero cycle ratio.

In the elastic case the stress intensity factor is a sufficient parameter to describe the whole stress field at the tip of a crack. When the size of the plastic zone at the crack tip is small compared to the crack length the stress intensity factor may still give a good indication of the stress environment of the crack tip. If two different cracks have the same stress environment, i.e. the same stress intensity factor, they may be expected to behave in the same manner and show the same rate of propagation. Hence, it may be expected that the rate of fatigue crack propagation per cycle  $da/dn$  is a function of the stress intensity factor range  $\Delta K$ :

$$\frac{da}{dn} = f(\Delta K) = f\left[(S_{\max} - S_{\min})\sqrt{\pi a}\right] = f\left[2S_a\sqrt{\pi a}\right] \quad (32)$$

where  $S_{\max}$  and  $S_{\min}$  are the maximum and minimum stress in a cycle, and  $S_a$  is the stress amplitude. Paris [76] and Paris, Gomez and Anderson [77] were first to recognize this and check it with test data. Of course, eq (30) will always be satisfied by data of specimens tested at the same stress levels. Data obtained from specimens tested at various stress levels should all fall on a single curve if eq (32) were applicable. Figure VA 34 shows a plot of data [78] obtained at three different stress levels, but the minimum stress in a cycle was always virtually zero (the cycle ratio  $R = S_{\min}/S_{\max} = 0.05$ ). The data in this figure, indeed, obey eq (32).

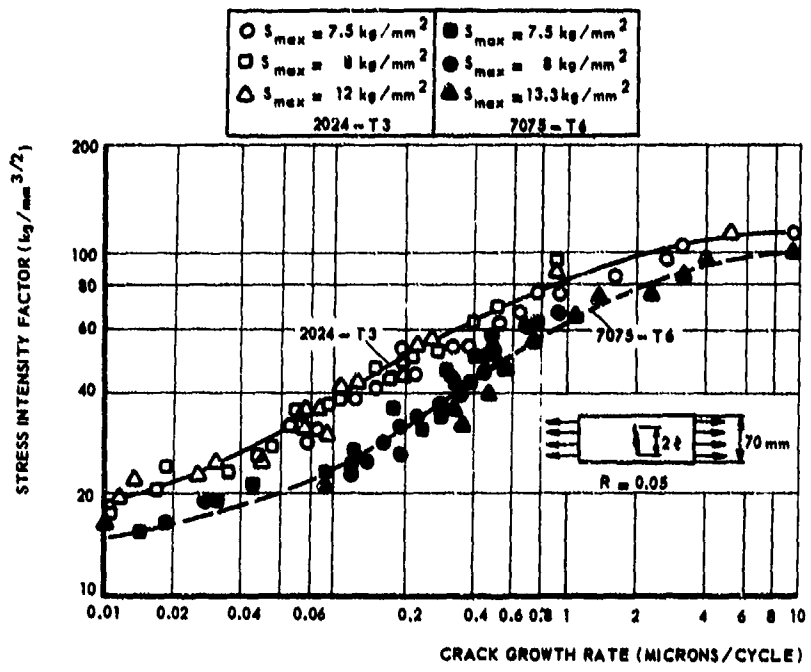


FIG. V A 34 RELATION BETWEEN INTENSITY FACTOR AND CRACK PROPAGATION RATE [75]

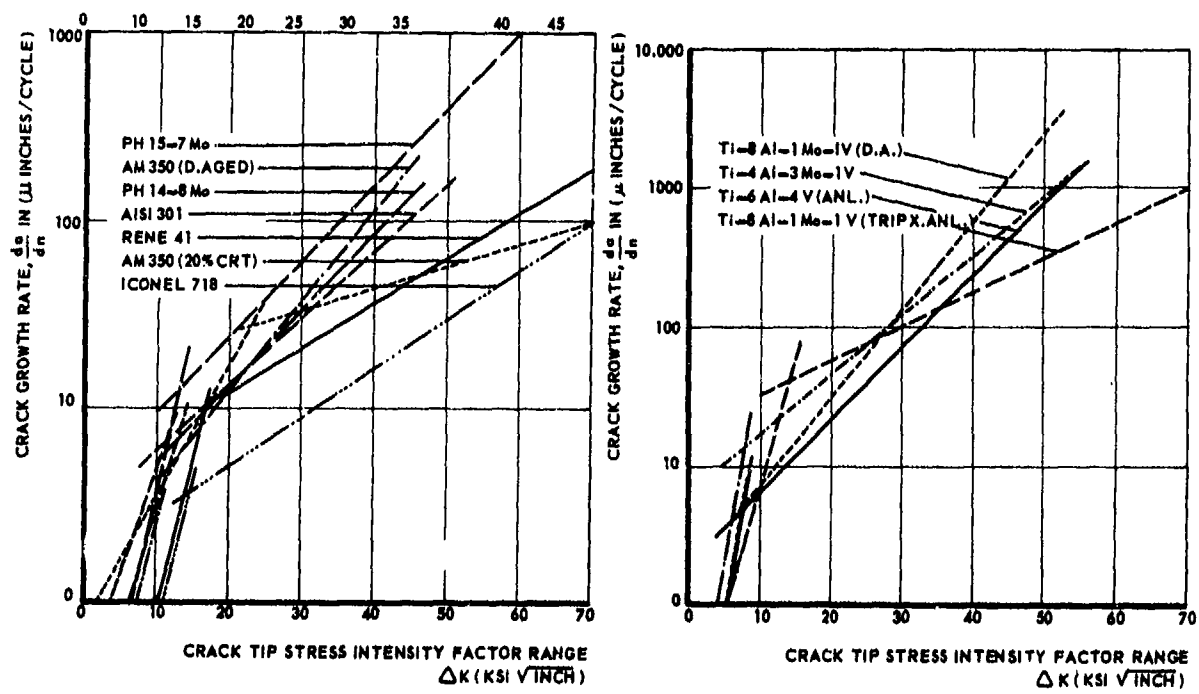


FIG. V A 35 CRACK GROWTH RATE VERSUS STRESS INTENSITY FACTOR [79, 80, 81]

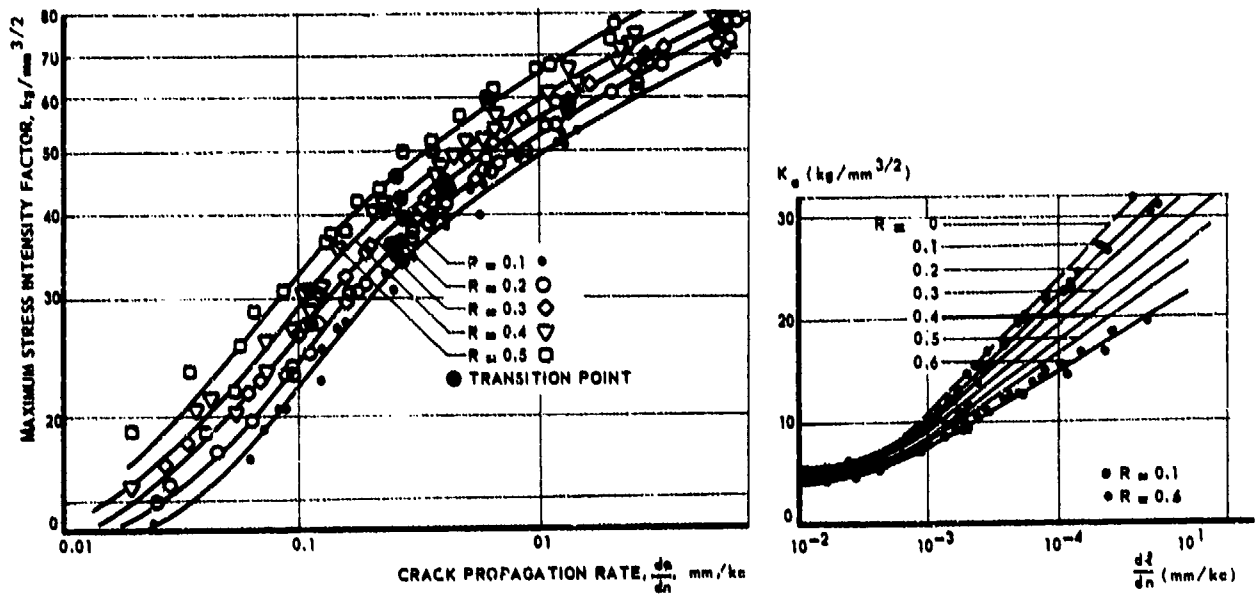


FIG. VA 36 EFFECT OF CYCLE RATIO ON THE RELATION BETWEEN CRACK GROWTH RATE AND STRESS INTENSITY FACTOR [89, 90], 2024 - T3 AL - ALLOY.

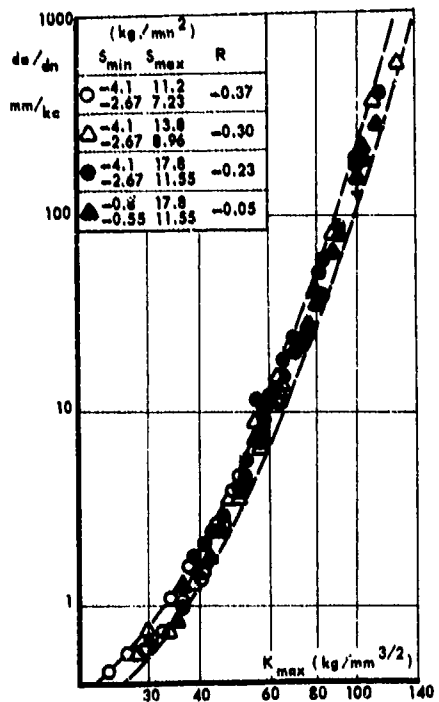


FIG. VA 37 CRACK PROPAGATION RATE AT NEGATIVE CYCLE RATIOS [96] 7075 - T6 AL - ALLOY.

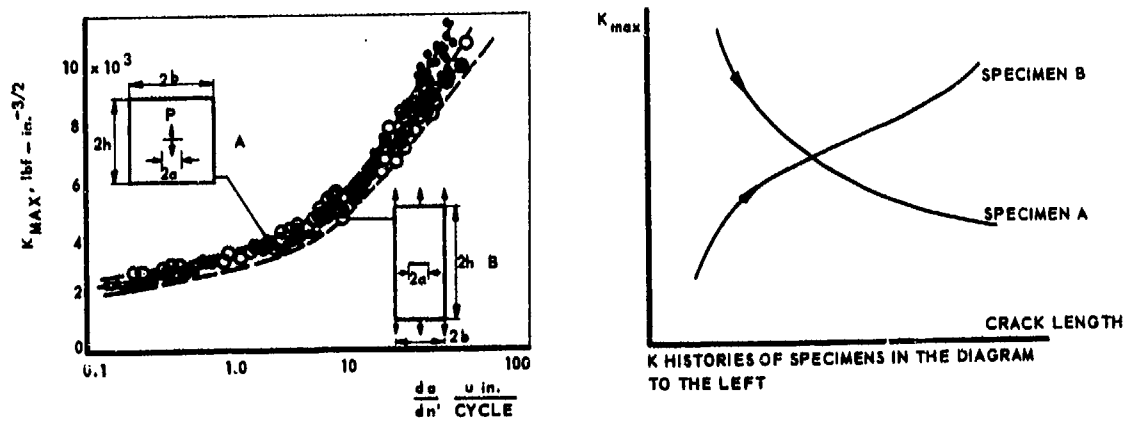


FIG. VA 38 CRACK GROWTH RATE FOR WEDGE OPENING LOADED AND UNIFORMLY LOADED SPECIMENS [98]

In a double-logarithmic plot the  $da/dn$  versus  $\Delta K$  data often fall on a straight line. Therefore it has been suggested many times that the relation of eq (32) should read

$$\frac{da}{dn} = C(\Delta K)^n \quad (33)$$

in which  $C$  and  $n$  are constants. There have been a lot of arguments as to the value of  $n$ . Values usually vary between 2 and 4. It turns out, however, that eq (33) does not really represent the test data. In reality the plot of  $da/dn$  versus  $\Delta K$  is an S-shaped curve, or at least consists of parts with different slopes [79,80,81] (figures VA 34 and VA 35). Only if the tests concern a limited range of  $\Delta K$  values the exponential relationship of eq (33) is found and then, of course, the value found for  $n$  depends upon the position of the  $\Delta K$  range (high, low or intermediate  $\Delta K$  values). When the  $\Delta K$ -values cover a sufficiently wide range, they show eq (33) to be incorrect. A deviation at the upper end of the  $\Delta K$  range may be expected when assuming that the crack is reaching a critical size at which  $da/dn$  must become infinite. Several other explanations for the deviations from linearity have been given; analysis of these is beyond the scope of the present discussion.

Recently, it has been tried to correlate the crack propagation rate with the crack opening displacement [82,83]. This usually leads to relations of the form:

$$\text{either } \frac{da}{dn} = C \frac{(\Delta K)^2}{E\sigma_{yc}} \quad \text{or} \quad \frac{da}{dn} = C \left(\frac{\Delta K}{E}\right)^2 \quad (34)$$

in which  $E$  is Young's modulus and  $\sigma_{yc}$  is the cyclic yield stress. These equations are interesting, because crack propagation can be considered a geometric consequence of crack tip opening [84,85,86]. It has been shown [e.g. 87] that data of a large variety of materials fall within one large scatterband when plotted on the basis of  $\Delta K/E$  versus  $da/dn$  as suggested by the second eq (34). However, a mere glance at figures VA 34 and VA 35 shows how materials with virtually the same Young's modulus can have widely different crack propagation properties. It is felt that this is due to the fact that many more parameters are involved than accounted for in eq (34).

Many other equations that have been proposed are analysed in a concise paper by Pelloux [88]. Further work to derive an equation with a sound physical basis is certainly needed; it can be predicted that this final equation will be a complicated one, if it has a general validity. For the technical problem of fatigue crack propagation the simple knowledge that  $da/dn$  is a function of the stress intensity factor will often be sufficient as will appear in this chapter.

#### b) Effect of cycle ratio

A fatigue cycle is determined by (a frequency and) two stress parameters. These can be the mean stress  $S_m$  and the stress amplitude  $S_a$ , the minimum stress in a cycle  $S_{min} = S_m - S_a$  and the maximum stress  $S_{max} = S_m + S_a$  or other combinations of two of these four parameters. As long as the cycle ratio  $R = S_{min}/S_{max}$  equals zero ones can speak unambiguously about the stress intensity factor of the fatigue cycle, since  $S_m = 0$  and  $S_{min} = -S_a$ . The hypothesis that the rate of crack propagation is a function of the stress intensity factor, presents no difficulties. When  $R \neq 0$  the range of the stress intensity  $\Delta K = 2S_a\sqrt{\pi a}$  is an insufficient description of the stress environment of the crack tip. The question arises whether  $da/dn$  will now be a function of  $\Delta K$  or of the maximum stress intensity in a cycle;  $K_{max} = S_{max}\sqrt{\pi a}$  or of  $\Delta K$  and  $K_{max}$ .

It appears [89,90,91] that the rate of crack propagation is a function of both  $\Delta K$  and  $K_{max}$ . This can be appreciated from figure VA 36, which shows two plots of the same load of data [89,90] one as a function of  $K_{max}$  and one as a function of  $\Delta K$ . From figures VA 36 it can be concluded that

$$\frac{da}{dn} = f(\Delta K, R) = f_2(K_{max}, R) = f_3(\Delta K, K_{max}) \quad (35)$$

Several investigators have tried to establish empirical relations which attempt to incorporate the effect of the cycle ratio, such that all data could be condensed to a single curve. Broek and Schijve [89] proposed a complicated relation, but also the following more simple ones:

$$\frac{da}{dn} = C K_{max}^2 \Delta K \quad (36)$$

A similar equation was given by Erdogan [91]. Walker [92,93] used the more general equation

$$\frac{da}{dn} = C K_{max}^m \Delta K^n \quad (37)$$

which he modified by introducing an effective  $\overline{\Delta K}$ , yielding

$$\frac{da}{dn} = C \overline{\Delta K}^n \quad \text{with } \overline{\Delta K} = S_{max} (1-R)^m \sqrt{\pi a} \quad (38)$$

Forman et al [94,95] proposed that  $da/dn$  should become infinite when the crack reaches a critical size, i.e. when  $K_{max}$  reaches  $K_{1c}$  (see chapter VA 3). They arrived at

$$\frac{da}{dn} = \frac{C \Delta K^n}{(1-R)K_{1c} - \Delta K} = \frac{C \Delta K^n}{(1-R)(K_{1c} - K_{max})} \quad (39)$$

which can be rearranged to give:



$$\frac{da}{dn} = \frac{C \Delta K^n K_{max}}{K_0 - K_{max}}, \quad n = n - 1 \quad (40)$$

The differences among these expressions are not large, and none of them has a general applicability, but each one may be found reasonably applicable in a limited region or for limited sets of data.

The question arises whether eq (35) still holds for  $R < 0$ , i.e. when the stresses go into compression. A crack is not much of a stress raiser in compression and the expressions for  $K$  lose their meaning. This suggests that

$$\frac{da}{dn} = f(K_{max}) \text{ for } R < 0 \quad (41)$$

There have been many arguments about the validity of eq (41). The data [96] plotted in figure IIA 37 seem to support the equations. Of course, a crack will not always close exactly at the moment the stress reverses from tension into compression. The moment of closure will depend upon the magnitude of the crack tip opening attained in the tension part of the cycle and upon the plastic deformation properties of the material [97]. Therefore, eq (41) should probably be modified into:

$$\begin{aligned} \frac{da}{dn} &= f_1(\Delta K, K_{max}) + f_2(K_{max}, R) \text{ for } R > 0 \\ \frac{da}{dn} &= f_3(K_{max}) \text{ for } R < 0 \\ b &= f_4(\text{material properties}) \approx 0 \end{aligned} \quad (42)$$

#### c) Versatility of the concept: cracks emanating from holes

A relation of the fatigue crack propagation rate with the stress intensity factor is very useful, because the stress intensity factor can be calculated for many different design configurations. Once a plot of the type of figures IIA 34 through 37 is obtained for a particular configuration it is principally possible to predict fatigue crack propagation in any other configuration for which the stress intensity factor is known. This can be proved by showing that crack propagation data obtained from specimens of different configurations fall on a single curve.

Figure VA 38 shows data presented by Figge and Newman [98] for two practical cases: the first is the uniformly loaded panel, the other the wedge force loaded panel. The latter has a certain similarity to a bolt or rivet force. The stress intensity factor for the wedge force loading decreases with crack length, for the uniformly loaded panel it increases with crack length (see figure VA 38b). This implies that the rate of crack growth in the wedge force loaded panel is high at the start of the test, but it gradually decreases as the crack proceeds, whereas the reverse occurs in the uniformly loaded panel. In the plot of  $da/dn$  versus  $\Delta K$  the data of one test run from lower left to upper right, the data of the other test run from upper right to lower left. Yet, a single curve can be drawn through the data points.

Another practical case is a crack emanating from a hole or cut out. Some data for this configuration were presented by Figge and Newman [98]. Data obtained recently by Broek [99] are given in figure VA 39. The stress intensity for a through crack emanating from a circular hole was determined by Bowie [19] and was presented here in chapter V.A.3, eq (19). Isida's [100] correction for crack eccentricity can be applied.

According to figure VA 39 there seems to be a large discrepancy between normal crack growth data and those for cracks at holes. This is partly due to the fact that cracks at holes experience only a very limited range of  $\Delta K$  values. In this range relatively many crack growth records are made and the relative error is large in measurements of small  $\Delta a$ , which may have led to a larger scatter. Bowles' solution implies (chapter VA 3) that the hole may be considered part of the crack as soon as the ratio between crack length and hole radius is in the order of 0.2. Then the crack plus the hole can be considered as a crack of effective length  $L + D$  (see figure VA 40). When this is done, it seems that the crack propagation curves for the cracks at holes agree very well with the curve obtained from a normal test (fig. VA 40). It should be noted, however, that figure VA 40 gives the propagation curve of a crack with 2 tips, which grows at a rate  $2 da/dn$  ( $da/dn$  at each tip). The cracks at holes, having only one tip, appear to increase in total length ( $L + D$ ) as if they had two tips.

An extrapolation of crack growth data to other configurations is principally possible, but it appears that it has to be done with care. Extrapolation to complicated structural geometries such as built-up sheet structures and sandwich panels will be discussed in chapter V.B.1.

#### d) Shortcomings, practical standpoint

Fatigue crack propagation is affected by many factors. The conspicuous influence of the environment on the rate of crack growth has been the subject of many investigations on a variety of materials [101 through 105]. Aircraft structures will be fatigued in an environment of engine fuel (integral wing tanks) or air, which may contain varying effects of water vapour. Only little is known about the influence of engine fuel. It has been shown that the rate of fatigue crack propagation in normal wet air can be an order of magnitude higher than in vacuum [102,106]. According to Hartman [101] the rate of growth in wet argon and wet oxygen was the same, rather than the oxygen. He observed the same rate of growth in wet argon and wet oxygen and again the same in dry argon and dry oxygen. This concerns an aluminium alloy. In a review of the effect of environment Achter [107] concluded that for other materials the reverse may be true.

There is no concurrence of opinion [e.g. 102,108,109] as to the explanation of the influence

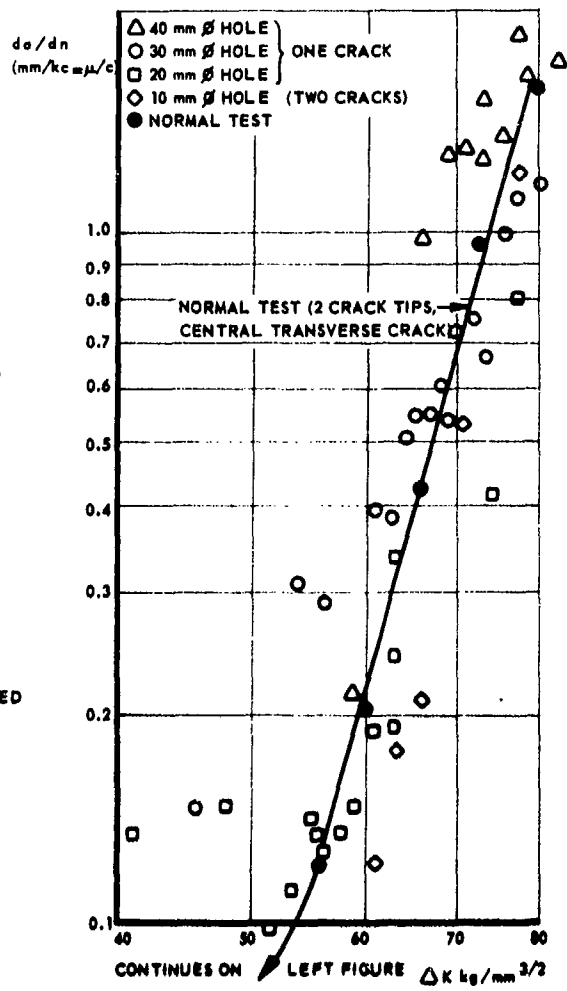
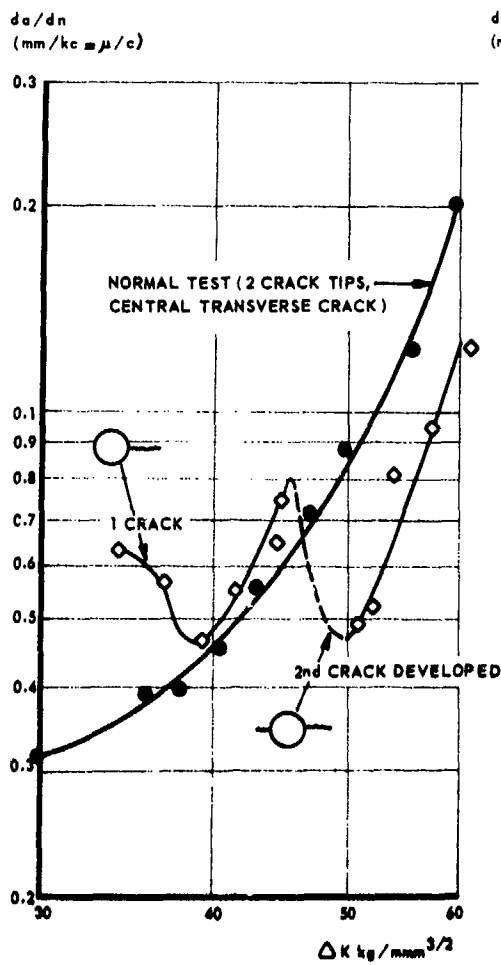


FIG. VA 39 GROWTH RATES OF CRACKS EMANATING FROM HOLES [99].

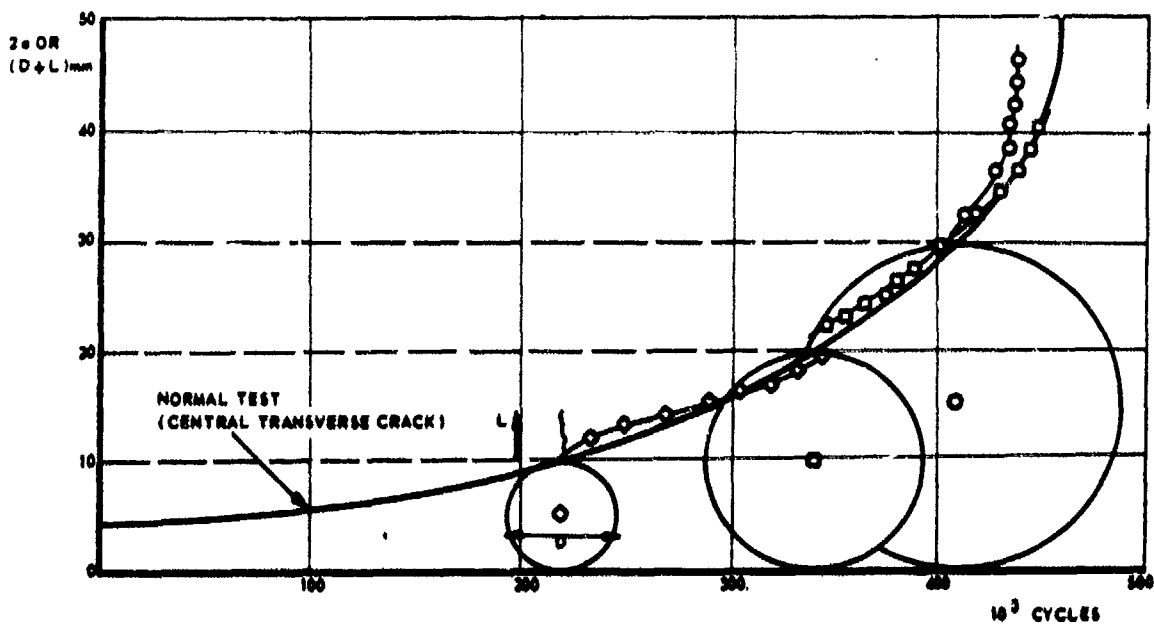


FIG. VA 40 PROPAGATION OF CRACKS EMANATING FROM HOLES [99].

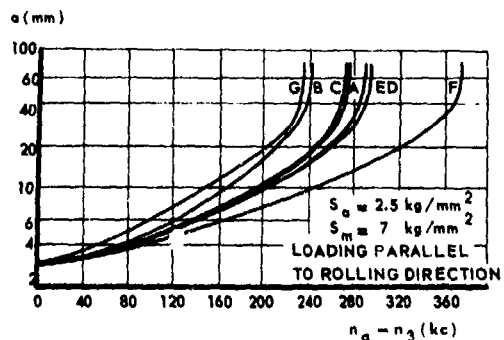
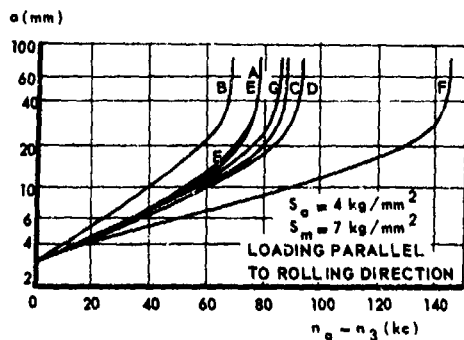


FIG. VA 41 FATIGUE CRACK PROPAGATION IN 2014-T3 ALUMINIUM ALLOY SHEET OBTAINED FROM SEVEN DIFFERENT (A - G) MANUFACTURERS [112].

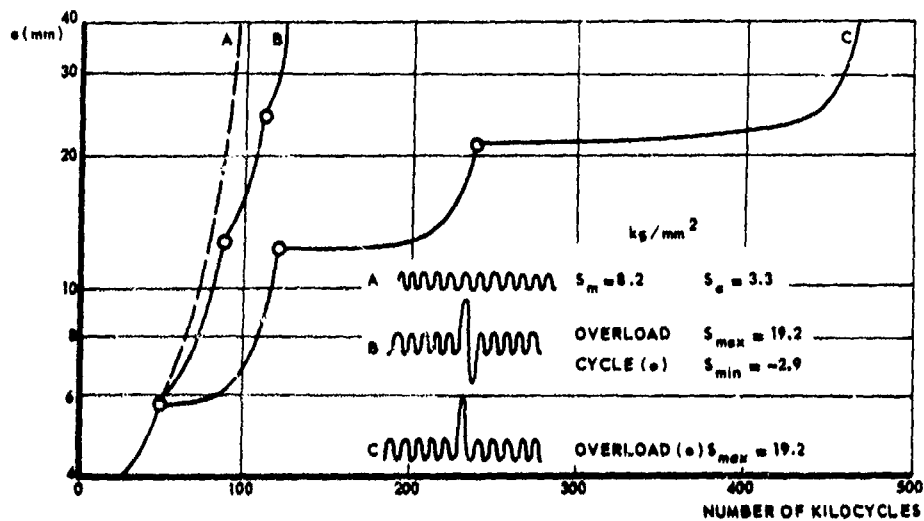


FIG. VA 42 THE DELAYING EFFECT OF OVERLOADS ON CRACK PROPAGATION AT CONSTANT AMPLITUDE 2024-T3 AL. ALLOY SHEET SPECIMENS [113, 114].

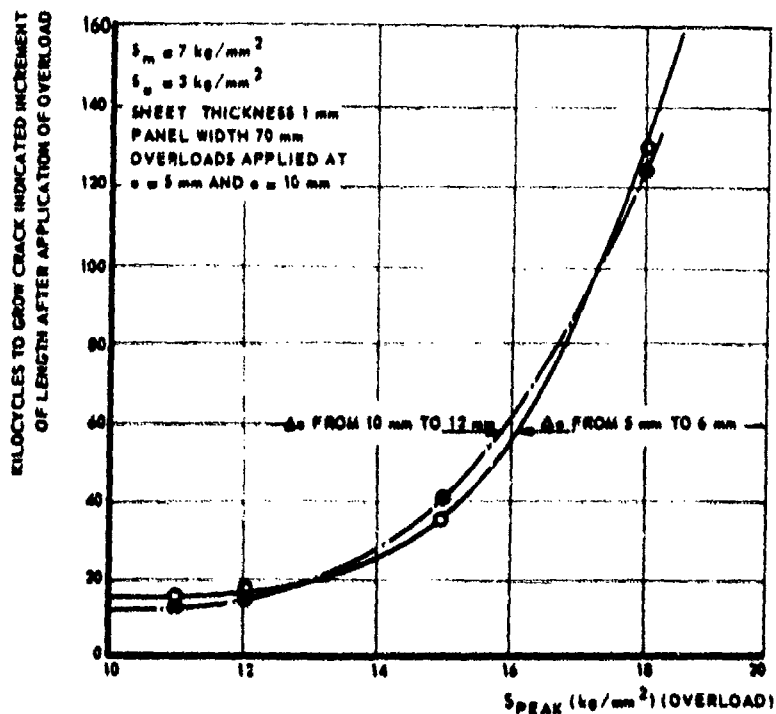
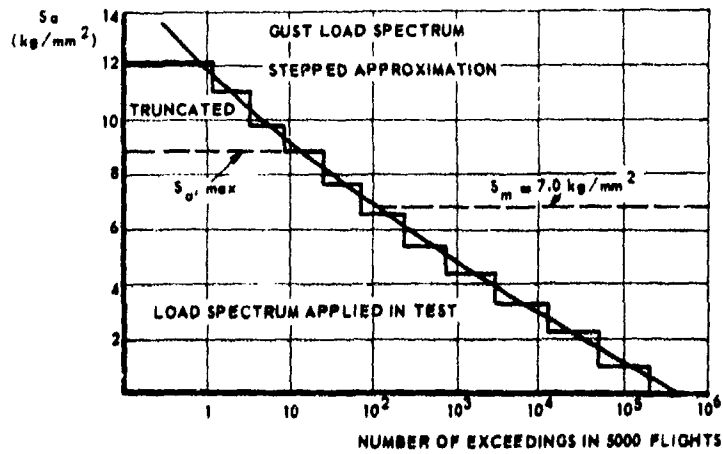


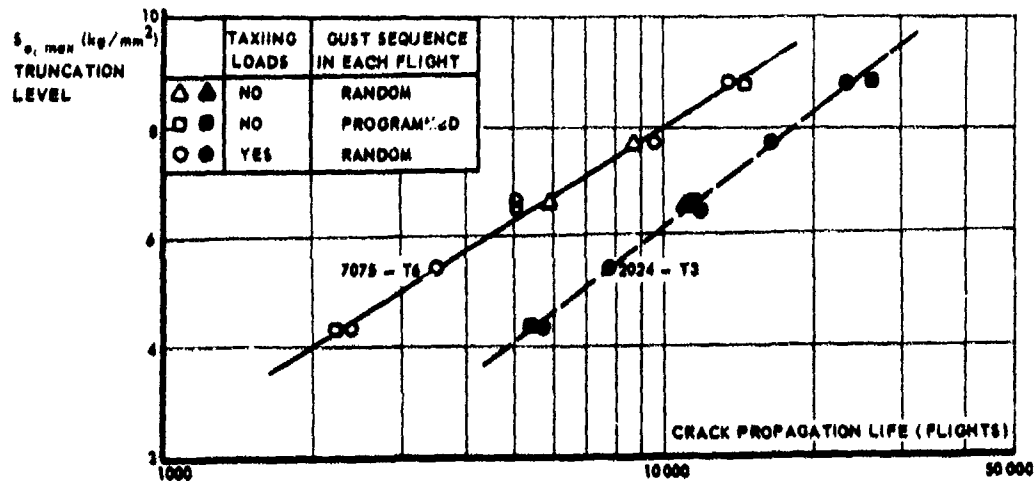
FIG. VA 43 DELAY OF CRACK PROPAGATION AS A FUNCTION OF OVERLOAD MAGNITUDE [119]

	LOAD SEQUENCE (ONLY SEVEREST FLIGHT SHOWN; EACH TEST CONSISTS OF MANY DIFFERENT FLIGHTS)	REMARKS	CRACK PROPAGATION LIFE			
			FLIGHTS		RATIO	
			2024-T3	7075-T6	2024-T3	7075-T6
A		RANDOM FLIGHT SIMULATION	10876	5889	0.92	1.16
B		TAXIING LOADS OMITTED	11781	5062	1	1
C		GUST CYCLES IN REVERSED SEQUENCE 	11184	4851	0.95	0.96
D		SMALL GUST CYCLES OMITTED ( $S_0 = 1.1 \text{ kg/mm}^2$ )	13924	7006	1.18	1.38
E		ONE GUST LOAD PER FLIGHT ONLY (THE LARGEST ONE)	36583	14556	3.11	2.88

a. LOAD SEQUENCES IN VARIOUS TEST SERIES AND TEST RESULTS



b. GUST SPECTRUM AND TRUNCATION LEVEL.



c. TEST RESULTS.

FIG. V A 44 FLIGHT SIMULATION TESTS OF SCHIJVE [123, 124, 125].

of the environment on the rate of propagation of fatigue cracks. It is likely that different explanations will apply to different materials. The effect is certainly a result of corrosive action and as such it is time-dependent. Therefore it is usually assumed that the environmental effect is associated with the small, but systematic effect of cycling frequency [102,109,110,111].

It is clear that slight variations in environmental circumstances may be the cause of considerable differences in the observed crack propagation properties of a given alloy. As reported by Schijve and De Rijk [112] an alloy of nominally the same composition but made by different manufacturers may have largely different crack propagation properties, which is illustrated in figure VA 41. Similar variations may occur for different batches of material as produced by one and the same manufacturer [112].

Apparently the rate of fatigue crack propagation is not such a consistent material property as the tensile strength and the yield stress. Fatigue crack growth is influenced by so many uncontrollable factors that it seems an even less consistent property than the fracture toughness. This implies that a large scatter has to be expected in practice, which is reflected already in the wide scatterbands in the data plots of  $da/dn$  versus  $\Delta K$ .

Then it must be concluded that there is little basis for arguments about the usefulness of the various expressions for the relation  $da/dn-\Delta K$  discussed in this chapter. The development of such an expression based on sound physical arguments should be encouraged; it may show which basic parameters are involved. The development of new empirical expressions to condense the data should not be discouraged, but their publication certainly should. The large scatter in actual data implies that any empirical expression may have certain merits (particularly when applied to limited amounts of data and alloys).

When predictions of crack growth have to be made, it will always be necessary to apply a large safety factor, in view of the effects discussed above. Therefore no particular expression for  $da/dn$  will have large advantages above another that gives a reasonable data fit. The use of a particular expression will be very much a matter of taste and therefore a best polynomial fit may be the most suitable in view of computer application. This conclusion is the more true because of the complicating factor of variable amplitude loading as will be discussed in the following section.

#### V.A.4.3 Variable-amplitude service-loading

So far the discussion has been limited to constant amplitude cycling. Since the service-load experience of an aircraft is by no means of constant amplitude, the ultimate goal of this chapter is to summarize the available means to predict fatigue crack propagation under random loading. Although a vast amount of publications exist on variable amplitude fatigue tests, the literature on crack propagation under variable amplitude loading is not abundant.

The interaction effects of cycles of different amplitudes is large in case of crack propagation. This can be demonstrated (Schijve and Broek [113,114], Hudson and Hardrath [115]) by applying overloads in a constant amplitude test. If an overload is applied in a constant-amplitude crack-propagation test, crack growth during subsequent constant-amplitude cycling will be extremely slow. Figure VA 42 [113,114] illustrates the retardation effect of overloads on crack propagation. The peak load has introduced a large plastic zone at the crack tip. This zone is stretched, but after unloading it still has to fit in the surrounding elastic material. Consequently, the surrounding material will exert compressive stresses [113,114] on the plastically deformed material at the crack tip. As soon as the crack has grown through the area of residual stresses, the original crack propagation curve will be resumed again.

Short range interaction effects can be studied fractographically [116,117,118], but the interaction effect can extend over thousands of cycles. The delay in crack propagation depends upon the magnitude of the overload [119] as is demonstrated by figure VA 43. The figure shows that small overloads cause a ready a small delay and that moderate overloads may cause delays expressed in many thousands of cycles. A very high overload may prevent any crack propagation at subsequent low amplitude cycling.

Negative loads are not liable to build up residual stresses, because a crack is not much of a stress raiser in compression. Frequently applied periodic negative loads in a constant amplitude crack propagation test caused practically no interaction effects [120] and the crack propagation was in good agreement with predictions based on a linear damage rule. Consequently, the so called ground-air-ground cycle will not be very damaging by itself (apart from contributing one large fatigue cycle), but it is detrimental in an indirect way, because it annihilates partly the residual stresses built up by positive overloads [113,114] and it therefore reduces the latter's beneficial effect (see figure VA 42).

Similar interaction effects occur during variable amplitude cycling [113,114,115,121] and random loading [122]. Therefore fatigue crack propagation during actual service loading is an important subject of research. In this respect the advanced work of Schijve [111,121,123,124,125] on flight simulation loading deserves ample attention. Figures VA 44 and VA 45 present a survey of his results. Truncation of the applied gust spectrum gives the best impression of the interaction effects. Truncation means that the magnitude of the highest gust cycles (only a small number of cycles of the total spectrum) is reduced to the next highest level (i.e. no loads are omitted). Further truncation reduces all largest cycles and all cycles of the second highest level to the magnitude of the third highest level, etc. According to figure VA 44, truncation of the two highest levels already reduced the crack propagation rate by more than 50%. The omission of thousands of the lowest amplitude cycles had only a small effect. It appears that crack propagation is influenced more by the magnitude of the aircraft encounters less severe service loading than was foreseen.

The large retardation effect of a single overload in a constant amplitude test cannot yet be accounted for in the relation between  $da/dn$  and  $\Delta K$ . This shows that there must be an effect of stress history on this relation, although such an effect did not appear in constant amplitude tests (c.f. figure VA 38 for largely different  $\Delta K$  histories). In case of random load tests and flight simulation tests some effective  $\Delta K$  could be defined, e.g.

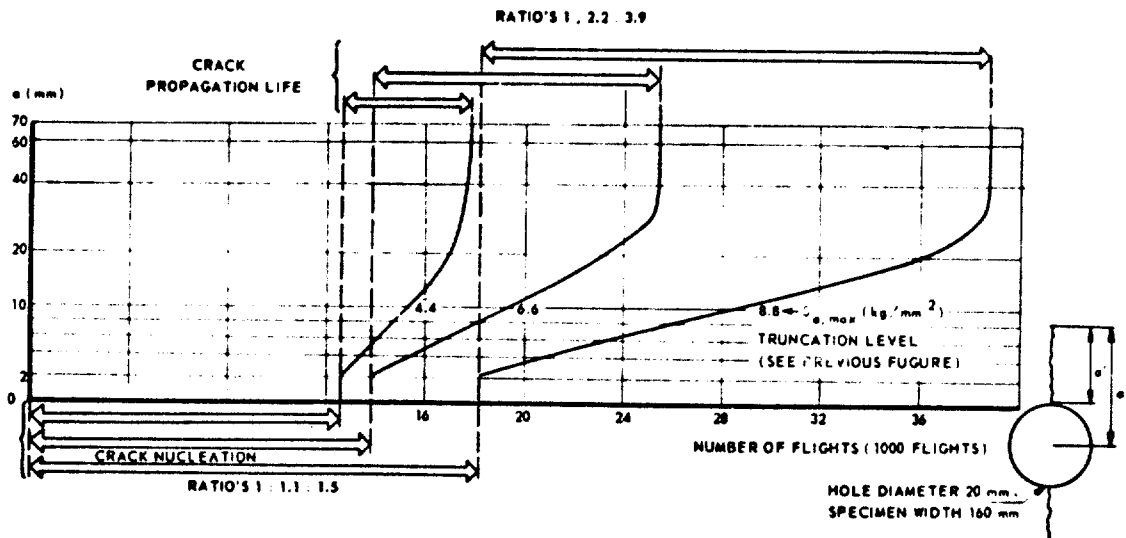


FIG. V A 45 CRACK PROPAGATION CURVES IN FLIGHT SIMULATION TESTS OF SCHIJVE [123, 124, 125]. SEE ALSO PREVIOUS FIGURE.

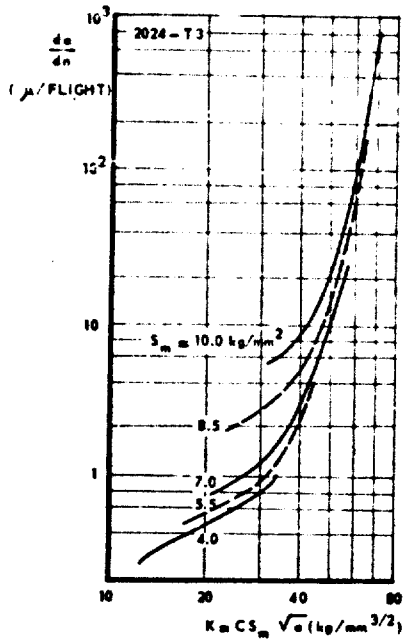


FIG. V A 46 CRACK PROPAGATION AND STRESS INTENSITY FACTOR IN FLIGHT SIMULATION TESTS OF SCHIJVE [111].

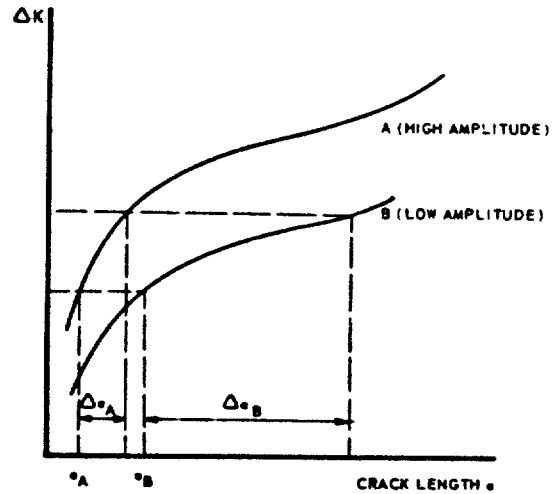


FIG. V A 47 DIFFERENT K HISTORY IN CONSTANT AMPLITUDE TESTING.

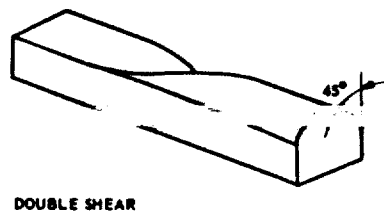
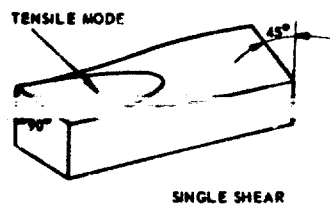


FIG. V A 48 THE TRANSITION OF A FATIGUE CRACK IN SHEET.

$$\overline{\Delta K} = \overline{S_{rms}} \sqrt{\pi a} \text{ or } \overline{\Delta K} = \overline{S_m} \sqrt{\pi a} \quad (43)$$

In these expressions  $\overline{S_{rms}}$  is the root-mean-square value of the random load and  $\overline{S_m}$  is some measure of the amplitude in flight simulation tests under the condition that differences between test will consist of proportional increase or reduction of all stresses in the sequence. Paris [76] has suggested already that

$$da/dn = f(\overline{\Delta K}) \quad (44)$$

Eq (44) was checked by Schijve [111] with data from flight simulation tests. Some results are shown in figure VA 46, which shows data of five flight simulation tests with exactly the same cycling sequence, but all stresses in one test were reduced proportionally with respect to those in another test (same R). The data certainly do not fit a single curve. This has to be attributed to interaction effects.

Actually, the relation between  $da/dn$  and  $K$  has to be supplemented by the parameter  $dK/da$  [111]. Consider the variation of  $\Delta K$  in two constant amplitude tests in figure VA 47. At a crack length  $a_A$  in specimen A and a crack length  $a_B$  in specimen B the same  $\Delta K$ -values apply and the crack propagation rates may be expected to be equal. Hence, both cracks extend the same amount  $\Delta a$  to  $a_A + \Delta a$  and  $a_B + \Delta a$  and then have a different  $\Delta K$  and a different propagation rate. At a crack length  $a_A + \Delta a_A$  and  $a_B + \Delta a_B$  the  $K$  values are also the same. However, since  $\Delta a_A \neq \Delta a_B$ , the cyclic strain histories of the crack tips will be different. Larger differences in cyclic strain histories occur in the case of figure VA 38 and of course, in a flight simulation test.

According to Schijve [111] equal crack rates may be expected if both  $K$  and  $dK/da$  are equal:

$$da/dn = f(\Delta K, K_{max}, dK/da) \quad (45)$$

Apparently, the effect of the  $K$ -history is negligible if the load amplitude is not abruptly varied, but if there are significant amplitude changes the  $K$ -history is important [111].

#### V.A.4.4 Factors affecting crack propagation

When predictions of crack propagation have to be made, data should be available relevant to the conditions prevailing in service. These data may be hard to get, since fatigue crack propagation is affected by an endless number of parameters. The influence of the environment and of the cycling frequency in relation to the environment have been discussed already in section V.A.4.2. Tests are usually not performed under controlled environmental conditions and part of the scatter in fatigue data may be attributed to this fact. For this reason the effect of environment was already considered in a previous section. Besides, the environmental conditions in service usually are not well known either.

Among the many factors that affect crack propagation, the following should be taken into consideration for crack growth predictions:

- a) Thickness
- b) Type of product
- c) Heat treatment
- d) Combined loading
- e) Cold deformation
- f) Temperature
- (g) (Manufacturer)
- (h) (Batch-to-batch variation)
- (j) (Environment)

For the factors lower in this list it is less likely that they can be properly accounted for. No attempt will be made to illustrate the effects of all these factors with data, particularly because some factors will have largely different effects on different materials. Nor, will it be tried to give a list of all the existing literature on these subjects. Rather, some general trends will be briefly mentioned, merely to indicate the existence of the effect of a particular parameter; a few entries to the literature may facilitate the search for more data.

The effect of material thickness can rather well be accounted for, because the thickness of the component under consideration will be readily known. In sheets there is a small, but systematic effect of thickness on crack propagation [126,127,128,129]. The effect appears to exist primarily before the fracture mode transition [126,127]. Fatigue cracks in sheets always start as a tensile-mode crack perpendicular to the sheet surface. When the crack grows in length the size of the plastic zone increases and plane stress can finally develop. This causes the fatigue crack to change to single or double shear [79,130] as depicted in figure VA 48. Plane stress develops when the size of the plastic zone is in the order of the sheet thickness. Therefore it is conceivable that the thickness effect is related with the fracture mode transition. Some data [126,127] are presented in figure VA 49, showing that growth rates are slightly higher in thicker sheets. In the latter the transition will require a larger plastic zone and hence at a greater length of crack.

Crack propagation in very thick sections encompasses some more problems. The cracks will develop as quarter elliptical corner cracks or semi-elliptical surface flaws. The stress intensity varies along the front of the flaw and its maximum value depends upon flaw shape. This has been outlined in chapter V.A.2. Assuming that the rate of crack propagation is a unique function of the crack growth rate, it follows that the crack growth rate will vary along the front of the flaw. The latter implies that the flaw shape will gradually change to semi-circular where  $K$  and  $da/dn$  are constant along the periphery.

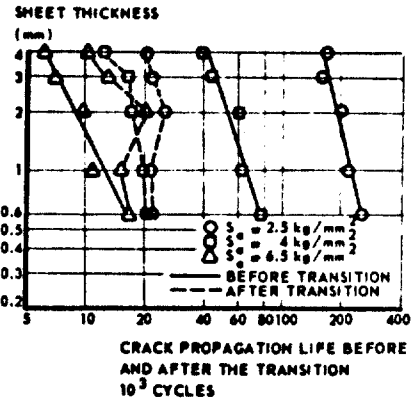
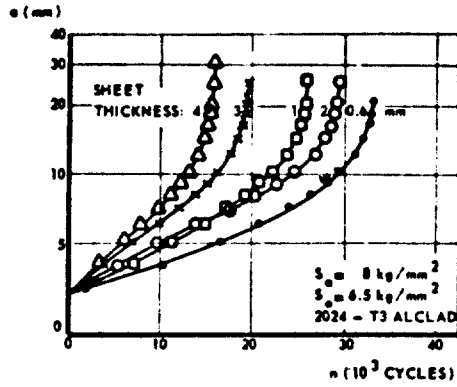


FIG. VA 49 THE INFLUENCE OF SHEET THICKNESS ON CRACK PROPAGATION.

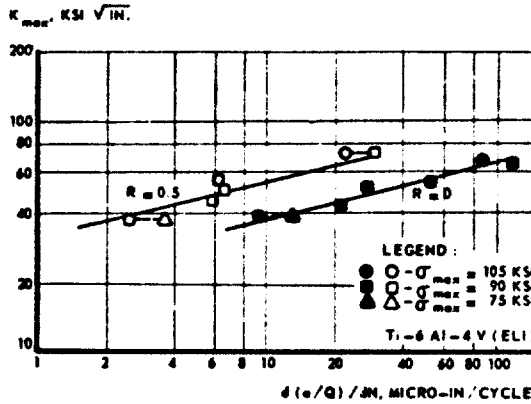


FIG. VA 50 SURFACE FLAW GROWTH CURVES [134].

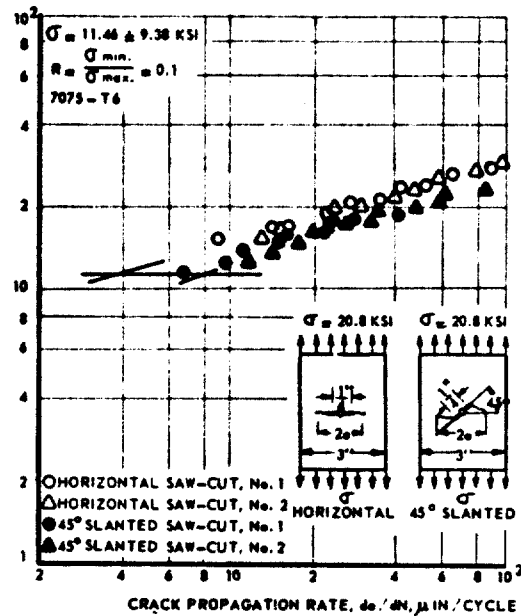


FIG. VA 51 COMBINED STRESS CRACK GROWTH [138].

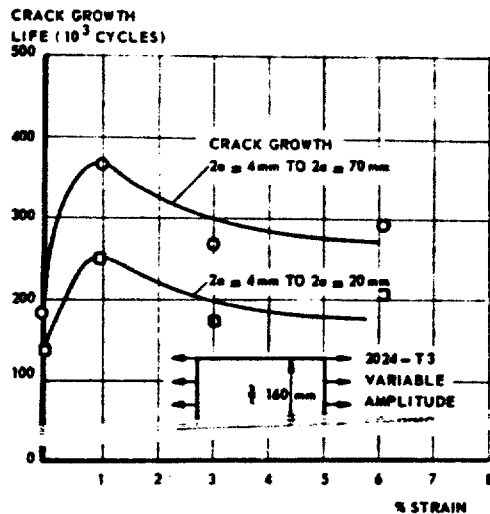


FIG. VA 52 INFLUENCE OF STRAINING BEFORE AGEING ON CRACK GROWTH [139, 140].

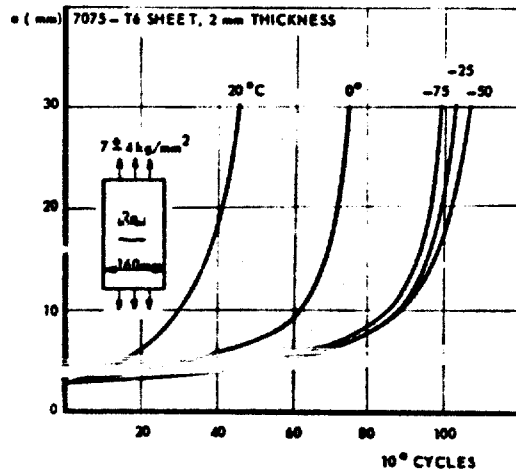


FIG. VA 53 EFFECT OF TEMPERATURE ON CRACK GROWTH [144].



The anisotropy of thick sections (chapter V.A.2) may cause a different behaviour.

The propagation of surface flaws has been investigated by Francis [131] and Hall [132,133,134]. It was noted that the cyclic life is primarily a function of the ratio  $K_1/K_0$  in which  $K_1$  is the maximum initial stress intensity in the first cycle and  $K_0$  is the fracture toughness. In chapter V.A.2 it was shown that an elliptical flaw can be described by  $a/Q$  in which  $a$  is the semi-minor axis of the ellipse and  $Q$  is a flaw shape parameter. The experiments of Hall [132,133,134] indicate that there is a relation between  $d(a/Q)/dn$  and the stress intensity factor in analogy with the case of sheets:

$$\frac{d(a/Q)}{dn} = f(\Delta K, K_{max}) \quad (46)$$

Figure VA 50 shows the validity of eq (46).

By mentioning anisotropy, the foregoing discussion has already touched the effect of type of product. The crack propagation characteristics for a particular alloy will differ for plate, extrusions and forgings, while especially the latter may exhibit a rather large anisotropy. Fatigue crack propagation in forged material has been studied by Van Leeuwen [135,136]. Closely related to this are the other processing variables and particularly the heat treatment. The heat treatment can have a large influence on fatigue crack growth and the effect may be different for different alloys [18,129,135,136,137]. A heat treatment designed to improve e.g. stress corrosion resistance may not always be beneficial for fatigue [135,136] and therefore it is worthwhile to check also fatigue crack growth rate when changing the heat treatment to suit other purposes.

The parameters discussed so far are fairly well defined and their effects could be accounted for in crack growth predictions if pertinent data are available. The conditions of combined loading, cold deformation and temperature are usually less well defined. In case of combined tension and shear loading, it is the position of the crack that is not known exactly. The problem of mixed mode loading has been discussed in chapter V.A.3. It is determined by the stress intensity factors  $K_1$ ,  $K_2$  and  $K_3$  for the different fracture modes. In case of aircraft wings and fuselages which are subjected to bending and torsion there exists a combination of  $K_1$  and  $K_2$ .

Crack propagation under conditions of combined loading have been studied by Walker [93] who considered the case of biaxial tension and by Iida and Kobayashi [138] who considered  $K_1$ ,  $K_2$  combined loading. Some data of the latter investigation are presented here in figure VA 51. It turned out that the crack tries to persist to the direction of maximum  $K_1$  value, with the  $K_2$  value reducing to its minimum (insert in figure VA 51). Iida and Kobayashi concluded that the existence of even a small  $K_2$  increases the crack propagation rate significantly. (It should be noted that  $da/dn$  in figure VA 51 is based on projected crack length in  $K_1$  direction. Since the crack has initially a steep inclination the actual growth rate is much larger than the one based on projected length). This is further illustrated by the following results:

da/dN at K = 11.5 ksi		
Crack orientation	$K_2/K_1$	da/dn ( $\mu$ in/cycle)
$\alpha = 0$ deg	0	3.8
$\alpha = 45$ deg	0.217	8.0
$\alpha = 60$ deg	0.110	6.6

In general, aluminium alloys are stretched between quenching and ageing. Also many material applications in aircraft structures require deformation by bending or stretching (curvature of skin panels, joggling, flanging). This deformation affects the ductility due to work hardening and due to its influence on subsequent ageing. Consequently, it may be expected to affect also the rate of fatigue crack propagation. Fatigue crack propagation of 2024 sheets are beneficially influenced by strains of 1 to 3 per cent [139,140], but larger strains introduce too much work hardening and the properties decrease again. This is illustrated in figure VA 52. It is self-evident that the effects can be different for other alloys.

Almost all material properties depend upon temperature and one of these is the rate of fatigue crack propagation [141,142,143,144,145]. Modern aircraft fly at high altitudes, where low temperatures prevail. Due to the large heat capacity of the fuel the structure may still be cold during descent when gusts are encountered and maneuvering loads occur. Low temperatures tend to have a beneficial effect on crack propagation properties [144] as depicted in figure VA 53. This is a result of the low moisture content of cold air.

The most difficult factors to account for in the prediction of crack growth are the manufacturer-to-manufacturer variation, the batch-to-batch variation and the effect of environment. Schijve [112] has proposed to keep close record of crack propagation properties of all material in stock, by performing a standard crack propagation test on each new delivery. If this is not feasible the variation of crack propagation properties can only be accounted for in a safety factor. The same will usually be the case for the environmental effect and also for the effect of many factors discussed above. To determine a rational safety factor, it is a prerequisite for the designer to have a fair knowledge of factors that affect crack growth and to have some insight into the nature of these effects.

#### V.A.4.3 Prediction of crack propagation in Callus's Anisotropy

From the foregoing discussions it may appear that it is virtually impossible to arrive at an accurate prediction of the rate of fatigue crack propagation in an actual aircraft structure. For the case of constant amplitude there are already so many complicating factors that reliable estimates of a crack propagation curve does not seem feasible. In case of an aircraft structure there is the additional difficulty of a complex geometry. Then there is the tremendous problem to predict the crack propagation

under random loading in this complex aircraft structure. In chapter V.B this problem will be analysed and it will be tried to develop the means to predict the crack propagation as accurately as is possible in the present stage of development.

A prediction of crack propagation will have to be based on test data which are applicable to the case under consideration, as for the type of material, environmental conditions, etc. Such data may be available in a plot of  $da/dn$  versus the stress intensity factor. When the loading conditions are known, predictions can be made by an integration procedure:

$$n = \int_{a_d}^{a_c} \frac{da}{F(\Delta K, K_{max})} \quad (46)$$

in which  $a_d$  is the minimum detectable crack size and  $a_c$  is the critical crack length. Such an integration will probably be carried out by an electronic computer and therefore it need not necessarily be based on an analytical relation between  $da/dn$  and the stress intensity factor. As discussed in section V.A.4.2 a best fit polynomial may be more suitable.

The integration for real aircraft service loading will receive ample attention in chapter V.B, together with other means to predict crack propagation under such circumstances. The problems involved in the treatment of complex structures will also be discussed in that chapter.

#### REFERENCES TO CHAPTER V.A

1. Lambert, J.A.B. The importance of service inspection in aircraft fatigue. *Aircraft Engineering* **32**, 10 (1967) pp 14 - 32.
- Troughton, A.J.
2. Hardrath, H.F. Fatigue crack propagation and final failure. *Mat.Res.and Stand.* **3** (1963) pp 116 - 121.
3. Schijve, J. Fatigue of aircraft structures. 4th Theodore von Karman memorial lecture, *Israel J. Techn.* **8** (1970) pp 1 - 20.
4. Cassner, E. Fatigue design procedures. Pergamon (1969).
- Schütz, W.
5. Heller, H.A. Experiments on the fatigue failure of a redundant structure. Columbia University TR No. 26 (1965).
- Donat, R.C.
6. Heller, A.S. Random fatigue failure of a multiple-load-path redundant structure.
- Heller, R.A.
- Freudenthal, A.M. Fatigue, an interdisciplinary approach pp 187-202. Burke et al ed. Syracuse Un. Press (1964).
7. Washill, H.J.H. Some considerations for the applications of titanium alloys in commercial aircraft. NLR report to be published. (1972)
8. Peel, C.J. Fracture toughness of Al-Zn-Mg-Cu alloys to DTD 5024. R.A.E. TR 69011 (1969).
- Forayth, P.J.E.
9. Payne, W.F. Incorporation of fracture toughness information in specifications. ASTM STP-381 (1965) pp 357-372.
10. Randall, P.W. Tests on surface flaw specimens. ASRM STP 410 (1967) pp 88 - 125.
11. Wilhem, D.P. Fracture mechanics guide lines for aircraft structures applications. AFFDL-TR-69-111 (1969).
12. Tiffany, C.F. Applied fracture mechanics. ASTM STP-381 (1965) pp 249-278.
13. Irwin, G.H. Crack extension force for a part-through crack in a plate. *J. Applied Mechanics*, Dec. 1962, pp. 651-654.
14. Green, A.E. The distribution of stress in the neighbourhood of a flat elliptical crack in an elastic solid. *Proc.Cambridge Phil.Soc.* **46** (1950) pp 159-164.
- Sneddon, I.N.
15. Paris, P.C. Stress analysis of cracks. ASTM STP-381 (1965) pp 30 - 81.
- Sih, G.C.
16. Kobayashi, A.S. Approximate stress intensity factor for an embedded elliptical crack near to parallel free surfaces. *Int.J.Fracture Mechanics* **1** (1965) pp 81 - 95.
- Zii, N.
- Hall, L.R.
17. Broek, D. Applicability of fracture toughness data to surface flaws and to corner cracks at holes. NLR TR 71033 (1971).
- Mederveen, A.
- Meulman, A.
18. Smith, S.H. Fatigue crack propagation and fracture toughness characteristics of 7079 aluminium-alloy sheets and plates in three aged conditions. NASA CR-996 (1968).
- Porter, T.K.
- Sump, W.D.
19. Bowie, O.L. Analysis of an infinite plate containing radial cracks originating from the boundary of an internal circular hole. *J. Math. and Phys.* **35** (1966).
20. Broek, D. The residual strength of light alloy sheets containing fatigue cracks. *Aerospace Proceedings* 1966, pp 811-835, McMillan, London 1966.
21. Broek, D. The effect of finite specimen width on the residual strength of light alloy sheet. NLR TR-M-2152 (1965).
22. Walker, E.K. A study of the influence of geometry on the strength of fatigue cracked panels. AFFDL-TR-66-92 (1966).
23. Christensen, R.H. Crack strength and crack propagation characteristics of high strength materials. ASD-TR-61-207 (1962).
- Denke, F.H.
24. Allen, F.C. Effect of thickness on the fracture toughness of 2025 aluminium in the ... (1971) pp 10-30.
25. Peddersen, C.E. Evaluation and prediction of the residual strength of center cracked tension panels. ASTM STP 486 (1971) pp 50 - 78.
26. Broek, D. Concepts in fail safe design of aircraft structures. DMIC memorandum 252 (1971).

27. Peddersen , C.E. Fracture and fatigue-crack propagation characteristics of 7075-T 7351  
Hyer , W.S. aluminium alloy sheet and plate. Battelle Mem.Inst.Report (1970).  
28. Broek , D. The static strength of aluminium alloy sheet containing blunt  
Jacobs , F.A. notches. NLR TR-M-2149 (1965)  
29. Peddersen , C.E. An experimental and theoretical investigation of plane stress  
Simonsen , F.A. fracture of 2024-T351 aluminium alloy.  
Hulbert , L.E. Battelle Mem.Inst.Rep. (1970).  
Hyer , W.S.  
30. Broek , D. The effect of sheet thickness on the fracture toughness of cracked  
sheet. NLR-TR-M-2160 (1966).  
31. Irwin , G.R. Fracture mode transition of a crack traversing a plate.  
ASME Trans.J.Basic Eng. 82 (1960) pp 417-425.  
32. Harpur , N.F. Crack propagation and residual strength of some aircraft structural  
materials. Cranfield symposium (1961) Vol.II pp 442-466.  
33. Broek , D. A study on ductile fracture. NLR TR 71021 (1971).  
34. Hudson , C.M. Effect of stress ratio on fatigue crack growth in 7075-T6 and  
2024-T3 Al-alloy specimens. NASA TN-D-5390 (1969).  
35. Eichenberger , T.W. Fracture resistance data summary. Boeing Rept.D2-20947 (1962).  
36. Kuhn , P. Unified notch-strength analysis for wrought Al-alloys.  
Figge , I.E. NASA-TN-D-1259 (1962).  
37. Kuhn , P. Residual strength in the presence of fatigue cracks.  
Presentation to Agard S and M panel, Turin (1967).  
38. Crichlow , W.J. The ultimate strength of damaged structures. Full Scale Fatigue  
testing of Aircraft Structures, pp 149 - 209.  
Ed. by Plantema and Schijve, Pergamon (1961).  
39. Christensen , R.H. Cracking and fracture in metals and structures.  
Cranfield Symposium (1961) Vol. II, pp 326 - 374.  
40. Barrois , W. Manual on fatigue of structures. Agard-Man-8-70 (1971).  
41. Broek , D. The residual strength of cracked sheet and structures.  
NLR-TN-M-2135 (1964).  
42. Liu , A.F. Material toughness and residual strength of damage tolerant aircraft  
Ekvall , J.C. structures. ASTM STP 486 (1971) pp 98 - 121.  
43. Raju , K.N. On the calculation of plastic energy dissipation during stable crack  
growth. Int.J.Fract.Mechanics 5 (1969) pp 101 - 112.  
44. Krafft , J.M. Effect of dimensions on fast fracture instability of notched sheets.  
Sullivan , A.M. Cranfield Symposium (1961) Vol. I, pp 8 - 28.  
Boyle , R.W.  
45. Broek , D. The energy criterion for fracture of sheets.  
Applied Materials Research (1965) pp 188 - 189.  
46. Wells , A.A. Application of fracture mechanics at and beyond general yielding.  
Brit.Welding J. 10 (1963) p 563.  
47. Burdekin , F.M. The crack opening displacement approach to fracture mechanics in  
Stone , D.E.W. yielding materials. J.of Strain Analysis 1 (1966) p. 145.  
48. Broek , D. The residual strength of cracked sheet-Tests interrupted after  
intermediate slow crack growth. NLR TR-M-2145 (1965).  
49. Broek , D. Some considerations on slow crack growth.  
Int.Journal of fracture Mechanics 4 (1968) pp 19 - 34.  
50. Broek , D. Residual strength for cracks emanating from holes in plane stress.  
Vlieger , H. To be published. In Int.J.Fracture Mech., September 1972.  
51. Srawley , J.E. Experimental determination of the dependence of crack extension force  
Jones , M.H. on crack length for a single-edge-notch tension specimen.  
NASA-TN-D-2396 (1964).  
52. Bowie , D.L. The effective crack length of an edge slot in a semi-infinite sheet  
Neal , D.M. under tension. Int.J. Fracture Mech. 3, 2 (1967) pp 111 - 119.  
53. Creager , M. Elastic field equations for blunt cracks with reference to stress  
Paris , P.C. corrosion cracking. Int.J.Fracture Mech.4 (1968) pp. 247-252.  
54. Broek , D. The residual strength of aluminium alloy sheet containing fatigue  
cracks or saw cuts. NLR TR-M-2143 (1965).  
55. ASTM Committee Fracture testing of high strength sheet materials. 3rd committee  
report. Mat.Res. and Standards 1, 11 (1961) pp 877 - 885.  
56. Kobayashi , A.S. Stress intensity factor for a straight crack approaching a circular  
Maiden , D.E. hole. Air Force Conf. on Fatigue and Fracture pp 217-223.  
AFFDL TR 70-144 (1970).  
57. Eluhs , J.I. Fracture arrest. Fracture; An advanced treatise, Vol.V, pp 1 - 63.  
Liebowitz, Ed. Academic Press (1969).  
58. Erdogan , F. On the crack extension in plates under plane loading and transverse  
Sih , G.C. shear. ASME Trans.J. Basis Eng 85 (1963) pp 519 - 527.  
59. Wilson , W.K. Fracture mechanics for combined loading and low to intermediate  
Clark , W.G. strength levels. Westinghouse Res.Lab.Rept. No. 10276 (1968).  
Wessel , E.T.  
60. Pook , L.P. The effect of crack angle on fracture toughness. NEL Rept.449 (1970).  
61. Hoakin , B.C. Fracture of tension panels with oblique cracks.  
Graff , D.G. ARL SM 305, Melbourne (1965).  
Foden , P.J.  
62. Tuba , L.S. Safety factors for mixed mode linear fracture mechanics.  
Wilson , W.K. Int.J. Fracture Mech. 6 (1970) pp 101 - 103.  
63. Jensen , J.E. The ballistic damage characteristics and damage tolerance of wing  
structural elements.  
ASTM STP 486 (1971) pp 215 - 229.  
64. Campbell , M.D. Correlation of residual strength of ballistically damaged panels  
Haskins , J.F. with fracture toughness theory. Air Force Conf. on Fatigue and  
Jensen , J.E. Fracture. AFFDL-TR-70-144 (1970) pp 539 - 555.

65. Dixon , J.R. Stress distribution and buckling in thin sheets with central slits. Fracture 1969, pp 105 - 108. Chapman and Hall (1969).
66. Forman , J.S. Experimental program to determine the effect of crack buckling and specimen dimensions on fracture toughness of thin sheet materials. AFFDL-TR-65-146 (1966).
67. Carlson , E.L. Buckling in thin cracked sheets. Air Force Conf. on Fatigue and Fracture. Zielesdorff , G.F. AFFDL-TR-70-144 (1970). pp 193 - 205. Harrison , J.G. Discussion. Cranfield Symposium (1961) Vol. II pp 539
68. Trotman , C.K. Appendix H to old Civil Air Regulations. Airworthiness requirements of Federal Aviation Agency, F.A.A.
69. Anon
70. Broek , D. Artificial slow crack growth under constant stress - The R-curve concept in plane stress - NLR TR 71088 (1971). Accepted for publication in Eng. Fracture Mechanics.
71. Schijve , J. Significance of fatigue cracks in micro-range and macro-range. ASTM STP 415 (1967) pp 415 - 459.
72. Liu , H.W. A mechanical model for fatigue crack propagation. Fracture (1969) pp 812-824, Chapman and Hall (1969).
73. McClintock , N. On the plasticity of the growth of fatigue cracks. Fracture of solids, pp 65 - 102. John Wiley (1963).
74. Weertman , F.A. Rate of growth of fatigue cracks calculated from the theory of infinitesimal dislocations distributed in a plane. Proc. 1st Fract. Conf., Sendai (1966) Vol. I, pp 153 - 164.
75. Schijve , J. The accumulation of fatigue damage in aircraft materials and structures. AGARDograph No. 157 (1972).
76. Paris , P.C. The growth of fatigue cracks due to variations in load. Ph.D. Thesis, Lehigh University (1962).
77. Paris , P.C. A rational analytic theory of fatigue. Gomes , M.P. The trend in Engineering 13 (1961) pp 9 - 14. Anderson , W.E.
78. Broek , D. The effect of intermetallic particles on fatigue crack propagation in aluminium alloys. Fracture (1969) pp 754-764, Chapman and Hall (1969).
79. Wilhem , D.P. Investigation of cyclic crack growth transitional behavior. ASTM STP 415 (1967) pp 363-383.
80. Hudson , C.H. Fatigue crack propagation in several titanium and stainless steel alloys and one super alloy. NASA TN-D-2331 (1964).
81. Hudson , C.H. Studies of fatigue crack growth in alloys suitable for elevated-temperature applications. NASA TN-D-2743 (1965).
82. McClintock , F.A. Discussion. ASTM STP 415 (1967) pp 170 - 174.
83. Hahn , G.T. The nature of the fatigue crack plastic zone. Air Force Conf. on Fatigue and Fracture (1969). Sarvat , H. AFFDL TR-70-144 (1970) pp 425-450. Rosenfield , A.R.
84. Schijve , J. Analysis of the fatigue phenomenon in aluminium alloys. NLR TR-M-2122 (1964).
85. Pelloux , R.M.N. Mechanism of formation of ductile striations. ASM Trans 62 (1969) pp 281 - 285.
86. Bowles , C.C. On the formation of fatigue striations. Int. J. Fract. Mechanics 8 (1972) pp 75 - 85. Broek , D.
87. Bates , R.C. Fractography and fracture mechanics. ASM Trans. 62 (1969) pp 380-388. Clark , W.Q.
88. Pelloux , R.M.N. Review of theories and laws of fatigue crack propagation. Air Force Conf. on Fatigue and Fracture (1969). AFFDL-TR-70-144 (1970) pp. 409-416.
89. Broek , D. The influence of the mean stress on the propagation of fatigue cracks in aluminium alloy sheets. NLR-TR-M-2111 (1963).
90. Schijve , J. The influence of the mean stress on the propagation of fatigue cracks in light alloy sheet. Aircraft Engineering 39, 3 (1967) pp 10-13.
91. Erdogan , F. Crack propagation theories. NASA-CR-901 (1967).
92. Walker , E.K. Effects of environments and complex load history on fatigue life. ASTM STP 462 (1970) pp 1 - 14.
93. Walker , E.K. An effective strain concept for crack propagation and fatigue with specific application to biaxial stress fatigue. Air Force Conf. on Fracture and Fatigue (1969). AFFDL-TR 70-144 (1970) pp 225-233.
94. Forman , R.G. Numerical analysis of crack propagation in a cyclic-loaded structure. ASME Trans J. Basic Eng. 89D (1967) p 459. Kearney , V.E.
95. Forman , R.G. Numerical analysis of crack propagation in cyclic-loaded structures. Engle , R.M. Paper No. WA/Net 66, ASTM Annual Meeting (1966).
96. Schijve , J. NLR data. To be published.
97. Elber , W. The significance of fatigue crack closure. ASTM STP 486 (1971) pp 230 - 242.
98. Figge , I.E. Fatigue crack propagation in structures with simulated rivet forces. Newman , J.G. ASTM STP 415 (1967) pp 71-93.
99. Broek , D. The propagation of fatigue cracks emanating from holes. NLR report to be published.
100. Isida , M. Crack tip stress intensity factors for the tension of an eccentrically cracked strip. ASME Trans, J. Appl. Mech. 33 E (1966) pp 674 - 676.
101. Hartman , A. On the effect of oxygen and water vapour on the propagation of fatigue cracks in an Al alloy. Int. J. Fracture Mech. 1 (1965) pp 167 - 188.
102. Bradshaw , F.J. Effect of environment and frequency on fatigue cracks in Al alloys. Wheeler , C. Int. J. Fract. Mech. 5 (1969) pp 255 - 268.
103. Dahlberg , E.P. Fatigue crack propagation in high strength 4340 steel in humid air. ASM Trans 58 (1965) pp 46 - 53.

- 105
104. Frost , N.E. The effect of environment on the propagation of fatigue cracks in mild steel. Appl.Mat.Res. 1 (1964) p 131.
105. Meyn , D.A. Frequency and amplitude effects on corrosion fatigue cracks in a titanium alloy. Met.Trans.2 (1971) pp 853-863.
106. Meyn , D.A. The nature of fatigue crack propagation in air and vacuum for 2024 aluminium. ASM Trans 61 (1968) pp 52 - 61.
107. Achter , M.R. Effect of environment on fatigue cracks. ASTM STP 415 (1967) pp 181-204.
108. Wei , R.P. Some aspects of environment enhanced fatigue crack growth. Eng .Fract.Mech. 1 (1970) pp 633 - 651.
109. Hartman , A. The effects of environment and load frequency on the crack propagation law for macro fatigue cracks. Eng .Fract.Mechanics 1 (1970) pp 615-631.
- Schijve , J.
110. Schijve , J. The effect of the frequency of an alternating load on the propagation of fatigue cracks. NLR TR-M-2092 (1961).
- Broek , D.
111. Schijve et al , J. Fatigue crack growth in aluminium alloy sheet under flight simulation loading. Effects of design stress level and loading frequency. NLR TR-72018 (1972).
112. Schijve , J. The fatigue crack propagation in 2024-T3 alclad sheet materials of seven different manufacturers. NLR TR-M-2162 (1966).
- De Rijk , P.
113. Schijve , J. Crack-propagation tests based on a gust spectrum with variable amplitude loading. Aircraft Engineering 34 (1962) pp 314 - 316.
- Broek , D.
114. Schijve , J. Fatigue crack propagation under variable amplitude loading. NLR-TR-M-2094 (1961).
- Broek , D.
- De Rijk , P.
115. Hudson , C.M. Investigation of the effects of variable amplitude loadings on fatigue crack propagation patterns. NASA-TN-D-1803 (1963).
- Hardrath , H.F.
116. McMillan , J.C. Fatigue crack propagation under program and random loads. ASTM STP 415 (1967) pp 505 - 535.
- Pelloux , R.M.N.
117. Hertsberg , R.W. Fatigue fracture surface appearance. ASTM STP 415 (1967) pp 205 - 225.
118. McMillan , J.C. The application of electron fractography to fatigue studies. ASTM STP 436 (1968) pp 89 - 123.
- Hersberg , R.W.
119. Broek , D. Interaction effects in fatigue crack propagation. To be published.
120. Schijve , J. The effect of ground-to-air cycles on the fatigue crack propagation in 2024-T3 alclad sheet material. NLR TR-M-2148 (1965).
- De Rijk , P.
121. Schijve , J. The crack propagation in two aluminium alloys in an indoor and an outdoor environment under random and programmed load sequences. NLR TR-M-2156 (1965).
- De Rijk , P.
122. Smith , S.H. Random-loading fatigue crack growth behaviour of some aluminium and titanium alloys. ASTM STP 404 (1966) p 76.
123. Schijve et al , J. Crack propagation in aluminium alloy sheet materials under flight simulation loading. NLR TR 68117 (1968).
124. Schijve , J. Cumulative damage problems in aircraft structures and materials. The Aeronautical Journal 74 (1970) pp 517 - 532.
125. Schijve et al , J. Crack propagation under flight simulation loading. Effect of truncating high gust loads. NLR TR 69050 (1969).
126. Broek , D. The effect of sheet thickness on the fatigue crack propagation in 2024-T3 sheet. NLR-TR-M 2129 (1963).
127. Broek , D. Fatigue crack growth; effect of sheet thickness. Aircraft Engineering 38, 11 (1966) pp 31 - 33.
- Schijve , J.
128. Ralithby , R.D. Propagation of fatigue cracks in wide unstiffened aluminium alloy sheet. RAE TN Structures 305 (1961).
- Bebb , M.E.
129. Donaldsen , D.R. Crack propagation behaviour of some airframe materials. Cranfield Symposium (1960) Vol.II pp 375 - 441.
- Anderson , W.E.
130. Broek et al , D. The transition of fatigue cracks in sheet. NLR-TR-M-2100 (1962).
131. Francis , P.H. The growth of surface microcracks in fatigue of 4340 steel. ASME Trans.J.Basic Eng (1969) pp 770-779.
132. Hall , L.R. Plane strain cyclic flaw growth in 2014-T62 and 6Al-4V (ELI) Titanium. NASA CR 72396 (1968).
133. Hall , L.R. On plane-strain cyclic flaw growth rates. Engineering Fracture Mech 3 (1971) pp 169 - 189.
134. Hall , L.R. Fracture and fatigue growth of partially embedded flaws. Air Force Conf. on Fracture and Fatigue (1969). AFFDL TR 70-114 (1970) pp 235 - 262.
- Finger , R.W.
135. Schra , L. Heat treatment studies of Al alloy 7079 forgings. NLR TR 69058 (1969).
- Van Leeuwen , H.P.
136. Van Leeuwen et al , H.P. Heat treatment studies of Al-Zn-Mg alloy forgings of the DTD 5024 type. NLR TR 72032 (1972).
137. Broek , D. The effect of heat treatment on the propagation of fatigue cracks in light alloy sheet material. NLR-TR-M-2134 (1963).
- Schijve , J.
- Nederveen , A.
138. Iida , S. Crack propagation rate in 7075-T6 plates under cyclic tensile and transverse shear loading. ASME Trans, J.Basic eng.(1969) pp 764-769.
- Kobayashi , A.S.
139. Broek , D. The effect of cold deformation and ageing on fatigue crack propagation and residual strength of 2024 sheet material. NLR-TR 69048 (1969).
- Bowles , G.Q.
140. Broek , D. The effect of precipitate size on crack propagation and fracture of an Al-Cu-Mg alloy. J.Inst.Metals 99 (1971) pp 255 - 257.
- Bowles , G.Q.
141. Schijve , J. The effect of temperature and frequency on the fatigue crack propagation in 2024-T3 sheet. NLR-TR-M-2138 (1963).
- De Rijk , P.
142. Lachenaud , R. Fatigue strength and crack propagation in AU 2 GN alloy as a function of temperature and frequency. In Current Aeronautical Fatigue Problems., pp 77 - 102, Schijve et al ed., Pergamon (1965).

143. James , C.A. Fatigue crack growth in 304 stainless steel at elevated temperature.  
Schwark , E.B. Met.Trans 2 (1971) pp 491 - 503.
144. Broek , D. Residual strength and fatigue crack growth in two aluminium alloy  
sheets at temperatures down to - 75° C.  
NLR report to be published.
145. Pierce , W.B. Factors influencing low-cycle crack growth in 2014-T6 aluminium sheet  
Sullivan , T.L. at - 320° F. NASA TN-5140 (1969).

## V.B.1 THE PREDICTION OF CRACK PROPAGATION

D. Broek

V.B.1.1 Introduction

In order to apply the fail-safe concept, it is necessary to make a reliable estimate of the number of flight hours it takes to propagate fatigue cracks from the minimum detectable size to the critical size. Inspection intervals will have to be based on this estimate, or rather fatigue crack propagation should take so much time that it covers two or three inspection periods. The prediction of fatigue crack propagation rates and crack propagation time for the real structure should occur on the basis of relevant data as for fatigue loads, crack propagation data and structural geometry.

Fatigue crack propagation is affected by a large number of parameters, which were described in the previous chapter. It will often be difficult to obtain the raw crack propagation data, directly applicable as a basis for prediction of fatigue crack propagation in service. The available data may be valid for slightly different circumstances, material thickness or heat treatment. In that case safety margins will have to be taken. The information given in the previous chapter may be of help in making this judgement.

Information about the fatigue loading may be available in the form of a load spectrum. The use of this information for the prediction of crack propagation involves some specific problems. This chapter starts with a discussion of these problems. Thereafter an analysis is made of the possible means for a prediction of crack propagation. Finally, particular problems are discussed, regarding built-up sheet structures, heavy sections and pressure vessels.

V.B.1.2 Load-time history

Load-time histories are described by statistical means. The various aspects of the load time history of an aircraft are dealt with in chapter V.B.1. Usually, the load data will be available in the form of a load spectrum or a power spectral density function. The latter can be translated into a load spectrum if the load is a Gaussian phenomenon. Load spectra are different for different types of aircraft. Large civil aircraft usually have a load spectrum that is determined primarily by gust loads, whereas the load spectrum of a fighter aircraft will be determined by maneuver loads. These two basic types of spectra are depicted in figure VB 1. It is usually assumed that the spectra for positive and negative gusts are symmetric, which allows presentation by a single curve. Maneuver spectra are asymmetric, since heavy positive maneuvers are more frequent than their negative counterparts.

It is worthwhile to be aware of the fact that load spectra are the result of counting procedures applied to actual load-time histories such as shown in figure VB 2. All counting methods have the tendency to neglect certain small load reversals. For an appraisal of the different counting techniques reference is made to a recent review by Schijve [1,2] and to the work of De Jonge [2] and Van Dijk [4]. The usefulness of the various counting methods may depend upon the purpose of the data. When the data have to be used for future aircraft design the usefulness may be judged on how well the counting method has described the actual load data. For fatigue calculations the usefulness depends on how well the method describes those loads which are the most relevant to the fatigue process.

It should be pointed out that resulting load spectra do not give any information about load sequence. This brings about one of the major problems, namely the definition of a load cycle. The counting procedure also has to cope with this problem in order to analyse the load time history. The question arises: what is important the load maxima and minima, or the load ranges. As is illustrated in figure VB 3 a certain load sequence can be described in various ways. The analysis of the various counting methods [1,4,5] pays ample attention to this problem. When the spectrum has to be applied for fatigue evaluation a similar problem arises.

The usual procedure for the fatigue calculation is to combine upward peak loads with downward peak loads of the same frequency of occurrence in order to generate a complete load cycle. This is illustrated for a single cycle in figure VB 1. Actual load records (fig. VB 2) do not justify this procedure, but it is considered conservative since it generates the largest possible cycles.

By using the load spectrum a flight-load profile has to be established. This requires an analysis of the various missions to be performed by the aircraft [6]. Two simplified flight profiles [1] concerning the wing bending moment are shown in figure VB 4. The following comments apply:

- a) Gust, maneuvers and taxiing loads were assumed to occur as one cycle.
- b) The sequence of loads was assumed random, without any correlation.
- c) Flight profiles may differ from flight to flight, especially with respect to the large cycles and the number of cycles.

Flight-load profiles of other aircraft parts can be largely different from those shown in figure VB 4 [7]. The flight profile of a fuselage structure will basically consist of one or two pressurization cycles and some bending and torsion due to tail loads during maneuvering, whereas aerodynamic loads can rather be neglected. The flight profiles of some aircraft members may be relatively easy to determine, because the loading is more deterministic than probabilistic.

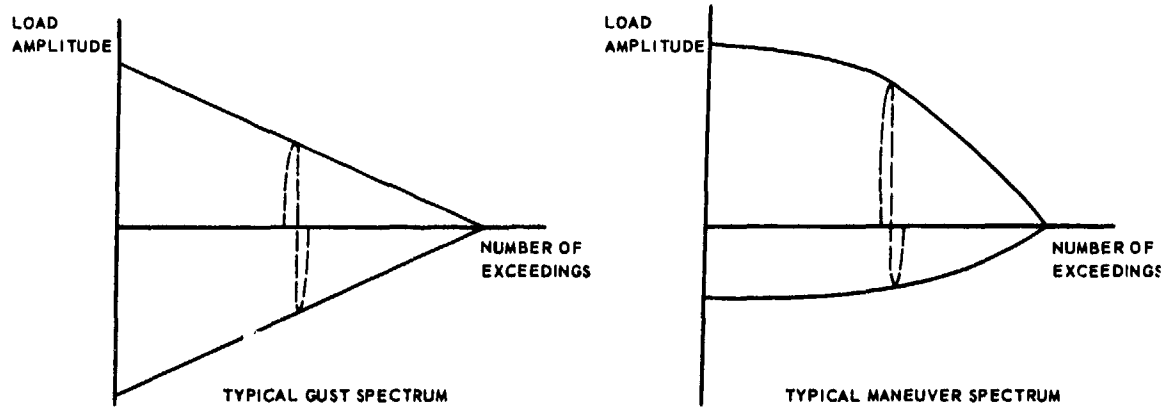


FIG. VB 1 OVERCRAFT LOAD SPECTRA.

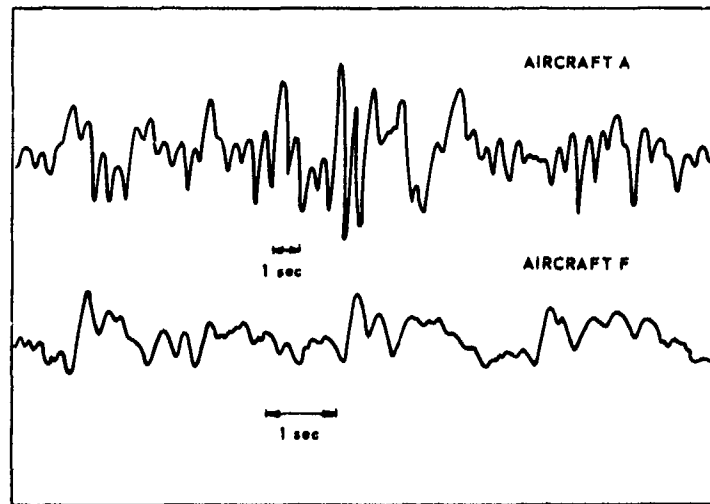


FIG. VB 2 STRAIN GAGE RECORDS OF THE WING BENDING MOMENT OF 2 AIRCRAFT FLYING IN TURBULENT AIR [2]

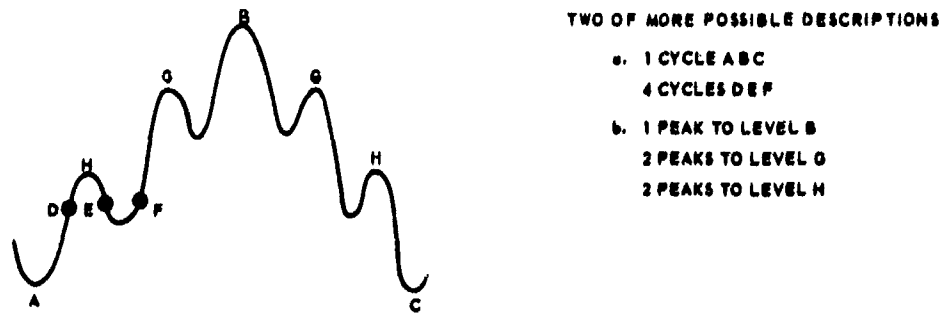
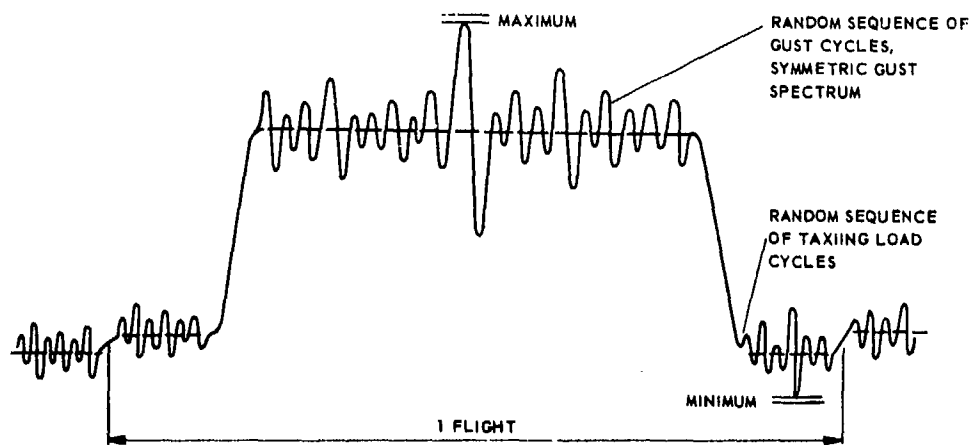
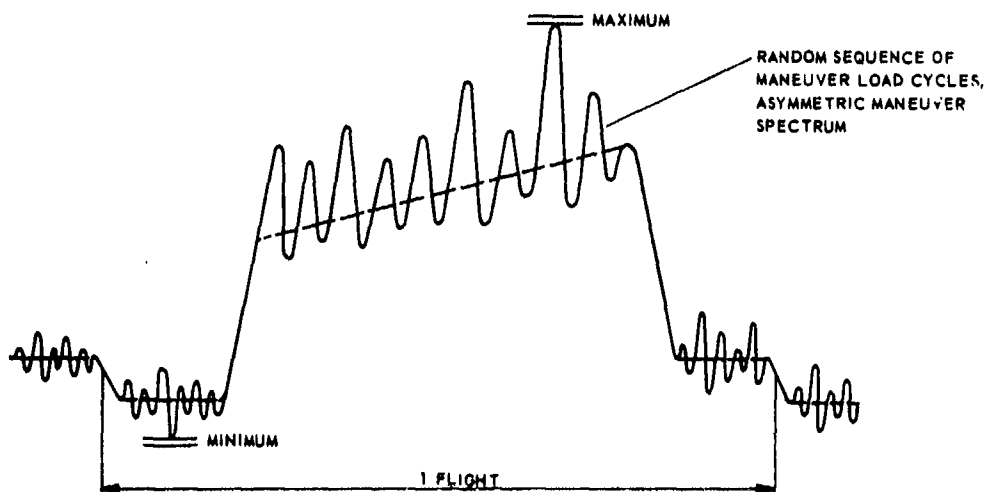


FIG. VB 3 DIFFICULTIES IN THE DEFINITION OF LOAD CYCLES.





a. TRANSPORT AIRCRAFT.



b. FIGHTER AIRCRAFT.

FIG. VB 4 TWO SIMPLIFIED EXAMPLES OF ESTIMATED FLIGHT-LOAD PROFILES FOR THE AIRCRAFT WING ROOT STRUCTURE [1].

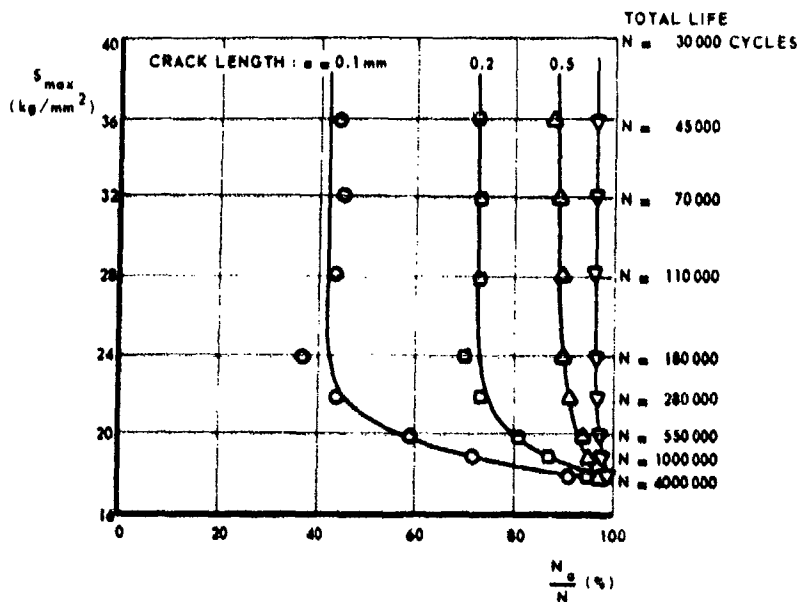


FIG. VB 5 PERCENTAGE OF FATIGUE LIFE COVERED BY CRACK PROPAGATION IN 2024-T3 SPECIMENS UNTIL A CRACK LENGTH HAS BEEN REACHED [15]. TESTS AT R = 0.

### V.B.1.3 Prediction methods

Estimates of fatigue crack propagation in service can be arrived at along three different ways. The three approaches are:

- a) Integration of constant amplitude data and making use of a linear cumulative damage rule.
- b) Integration of constant amplitude data and using a semi-empirical cumulative damage concept.
- c) Interpolation between flight simulation data, directly or via integration.

The merits of these methods are discussed in this chapter. It turns out that method a gives conservative results, method b requires further development and method c may become very reliable, once sufficient flight-simulation test data will have been generated.

#### a. Integration of constant amplitude data using a linear damage rule

In order to predict crack propagation under variable amplitude loading by using constant amplitude data, it is necessary to make use of a cumulative-damage rule. Several cumulative-damage rules for fatigue have been put forward in the literature. An excellent analysis of these rules has recently been given by Schijve [2]. He concluded that with respect to life estimates a theory distinctly superior to the Palmgren-Miner [8,9] is not available. Of course, a life prediction made with the Palmgren-Miner rule is a rough estimate only. The Palmgren-Miner rule has the inherent shortcoming that it does not account for interaction effects of high and low load cycles. However, the procedure contains many more uncertainties, which may be just as detrimental to the final results, as are the shortcomings of the Palmgren-Miner rule. These uncertainties concern:

- (1) The magnitude of the local stresses.
- (2) The scatter in constant amplitude fatigue data.
- (3) Applicability of the constant amplitude data to the pertinent circumstances.
- (4) Insufficient knowledge of expected load-time history.

In case of crack propagation the shortcomings (1) through (4) apply equally. However, the intrinsic shortcoming of the Palmgren-Miner rule will generally yield results, which are on the safe side. As pointed out in chapter V.A.4 the interaction effect of overloads during fatigue crack growth is always a retardation. Negative peak loads appeared to have no effect in itself, but could reduce the retardation in growth caused by high positive loads, the remainder still being a slight retardation. Apparently, the net interaction effects tend to be a deceleration of crack growth. Consequently, the neglect of interaction effects by the Palmgren-Miner rule will generally be on the safe side. Some attempts [10,11,12,13,14,19,43,44] have been made to account for the effect of overloads and the residual stresses introduced by them, but a quantitative evaluation for complex load histories is still difficult and contains many uncertainties. It must be concluded that the Palmgren-Miner rule at this moment is still a reasonable engineering damage rule, especially for crack propagation where interaction effects will exclude unsafe estimates. Shortcomings in the prediction will be largely due to other uncertainties not related to the damage rule.

For a prediction of crack propagation with the Palmgren-Miner rule the crack length is considered a measure for the amount of damage. In itself, Miner's rule can be fairly accurate for crack propagation, if crack length is taken as a measure for the damage. Miner's rule states that

$$\frac{n_1}{N_1} + \frac{n_2}{N_2} + \frac{n_3}{N_3} + \dots + \frac{n_i}{N_i} = 1 \quad (1)$$

for failure. It is a linear summation of the damage that occurs at various stress levels  $S_1, S_2 \dots S_i$ , irrespective of their individual values. Now if the damage criterion were a given length of crack, Miner's hypothesis would hold if, regardless of crack length and test stress, the same fraction of total lifetime,  $n/N$  was necessary to propagate the crack over a given interval. Figure VB 5 derived from [15], shows for a given crack length (ca 0.1, 0.2, 0.5, or 1.0 mm), and for all test stresses somewhat greater than the fatigue limit, that the fraction of total lifetime,  $n/N$ , to reach that crack length is essentially constant. Thus, Miner's rule appears to be a reasonable approximation for fatigue-crack propagation, except in accounting for interaction effects as discussed before.

Various ways can be followed for the prediction of the crack propagation life. The most simple approach is to use some sort of S-N curve for crack propagation. This curve gives the number of cycles required for the considered amount of crack propagation for various values of the constant cyclic stress (fig. VB 6). The Palmgren-Miner rule can be directly applied to the given load spectrum. It can be used to predict the results of the flight simulation tests presented in figure VA 44 of chapter V.A.4. The result is shown in table VB.1; the taxiing loads have been ignored since they appeared to have little effect; the crack propagation life in constant amplitude tests of purely ground air ground cycles has been estimated at 26000 cycles and 60000 cycles for the 7075 and the 2024 material respectively.

Table VB.1

S <sub>a</sub> (kg/mm <sup>2</sup> )	n in 5000 flights	R (fig. VA 4)		N/N	
		2024	7075	2024	7075
12.1	1	1800	1400	0.0006	0.0007
11.0	2	2100	1600	0.0010	0.0013
9.9	5	2600	1800	0.0019	0.0028
8.8	15	3300	2100	0.0045	0.0071
7.7	43	4500	2600	0.0095	0.0165
6.6	139	7300	3400	0.0191	0.0308
5.5	495	12000	5000	0.0412	0.0990
4.4	1903	21000	7500	0.0920	0.2540
3.3	8000	44000	13000	0.1816	0.6150
2.2	39250	260,000	31000	0.0150	1.2610
1.1	149902	1,000,000	200,000	0.1499	0.7460
0.1 S.	5000	60,000	26000	0.0832	0.1925
Total				0.5995	3.2367
Crack propagation life for 2024:				$\frac{1}{0.5995} \times 5000 = 8350$ flights	
				for 7075: $\frac{1}{3.2367} \times 5000 = 1550$ flights	

The crack propagation life of 2024 compares with the flight simulation data (fig. VA 44) for the case of a truncated spectrum to S<sub>a</sub> = 6 kg/mm<sup>2</sup>. This means that prediction would be valid for an aircraft not meeting excessively high gusts. The prediction for 7075 is at the low side. If the contribution of the ground-air-ground cycles would be omitted in the calculator (in order to compensate a little for the ignored retardation effects) the results would be 9700 flights and 1750 flights for the two materials respectively.

An alternative method would be to consider each flight as one load cycle, with the maximum given by the highest gust load in that flight and the minimum by the lowest (negative) gust load in the flight or the ground condition, whichever is the lower (see figure VA 44 flight type E). This calculation leads to crack propagation lives of 6400 flights and 2700 flights respectively for the two materials. Again the estimate is at the safe side. This procedure ignores the occurrence of many load cycles and it must be expected that it can easily lead to unsafe estimates.

In general it will be more useful to predict the crack propagation behaviour by integration from a plot of da/dn versus ΔK (figure VA 34). The advantage of this procedure is that it allows prediction of crack propagation for any geometry for which the stress intensity factor is known. As shown in chapter V.B.2 the stress intensity factor can be determined for built-up sheet structures and sandwich panels. Consequently, it is principally possible to predict the crack propagation of a panel of complicated geometry on the basis of a da/dn versus ΔK plot obtained from simple laboratory specimens.

Assuming that the load spectrum is known, the integration procedure can be carried out in many different ways, most of which are current procedures in aircraft design [17].

- a. Integrate, cycle by cycle, in random order starting with the minimum detectable crack length a<sub>1</sub>, subjected to a stress range, ΔS<sub>1</sub>. The stress-intensity range will be K<sub>1</sub> = αS<sub>1</sub>√πa<sub>1</sub>. Find (da/dn)<sub>1</sub> from a plot such as figure VA 34. The crack will extend over a length Δa = (da/dn)<sub>1</sub> × 1 and the new crack length will be a<sub>1</sub> + Δa, which will meet the next stress range, S<sub>2</sub>, etc.

This is an extremely laborious procedure, since it requires an integration over thousands of cycles. The calculation will have to be performed by computer. A problem is the sequence of loads; the choice will be a particular random order. A high load applied at a short length of crack will give a relatively low ΔK and consequently a low da/dn. If the same load were applied at a large crack its ΔK would have been much higher and its contribution to crack growth much larger. Hence the result of the calculation must be expected to depend upon load sequence.

- b. Integrate blocks of cycles of the same amplitude. For simplicity, the growth rate may be considered a constant during growth of a small increment of crack length. Application of this procedure to the flight simulation tests on 2024 material of figure VA 44, yields crack propagation lives varying from 9000 to 20,000 flights, depending upon integration step size.
- c. Integrate flights of one peak-to-peak (minimum to maximum) load cycle per flight. This procedure assumes that in one flight, crack growth is reasonably well approximated for the flight by considering the flight as one stress cycle representing the maximum and minimum stresses observed in each flight. According to the test data presented in figure VA 44 a test of this kind yields 36000 flights and 14500 flights for 2024 and 7075 respectively. Since interaction effects are small in such a test, the integration procedure will fairly well predict these test results. This means that the prediction will be dangerously unconservative. Apparently, the contribution of all the disregarded load excursions is still appreciable, despite interaction effects. Neglect of these load excursions in the integration procedure will therefore not be permitted.

- d. Smear out the total life spectrum in a number of occurrences per flight. (This implies that high loads may occur at the rate of only a fractional number per flight). (According to table VB.1, the maximum excursion S<sub>a</sub> occurs 0.0002 times per flight). Then sum this once per flight spectrum to obtain a

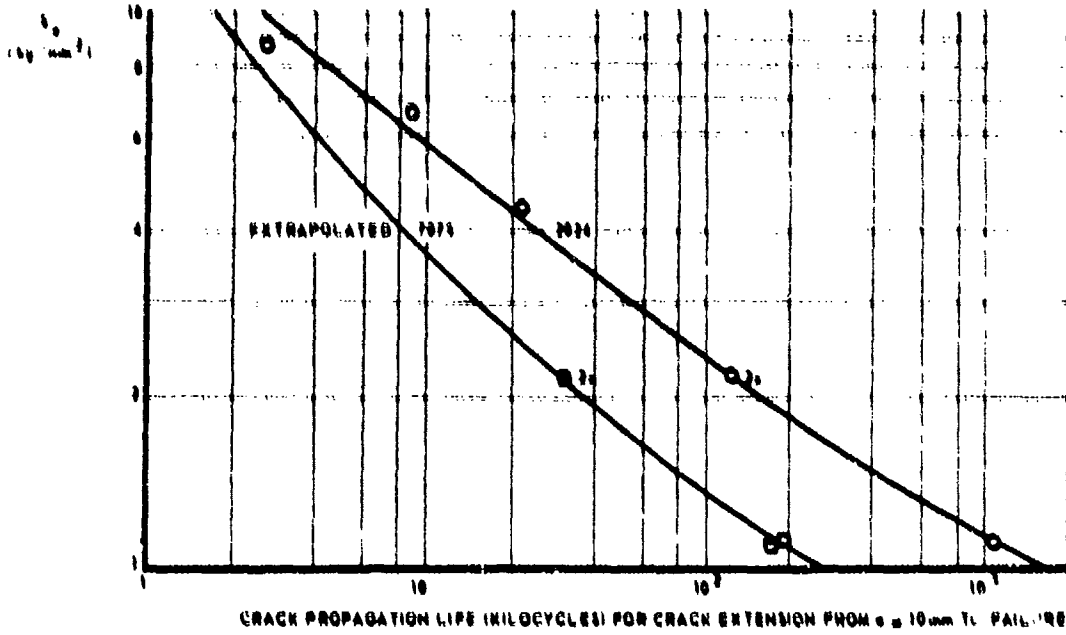


FIG. VB 6 CONSTANT AMPLITUDE TEST DATA PLOTTED AS S-N CURVES [16].

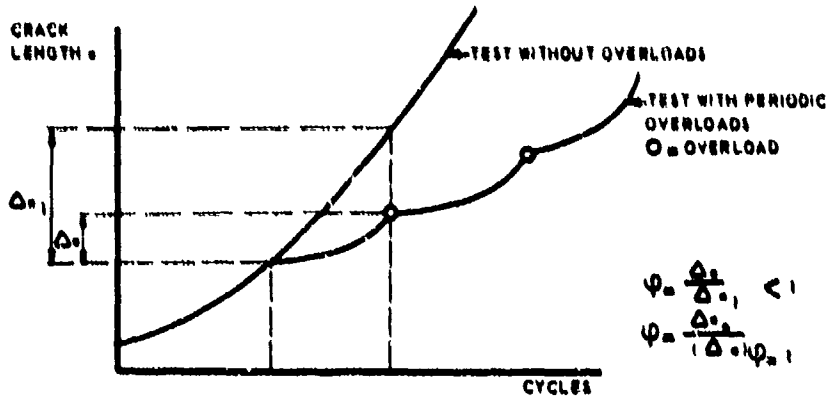


FIG. VB 7 DEFINITION OF RETARDATION FACTOR OF HABIBIE [19].

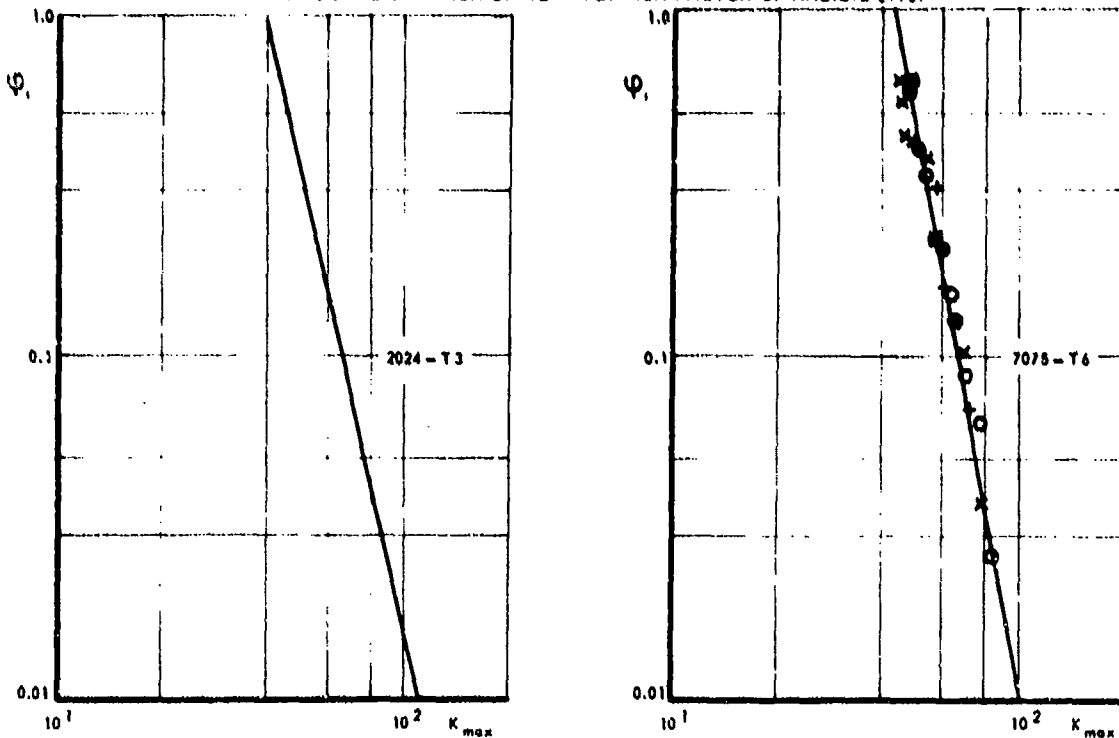


FIG. VB 8 RETARDATION FACTOR  $\phi$  IN FLIGHT SIMULATION TESTS [19].

crack-propagation rate per flight,  $da/dF$ . For simplicity, the flight growth rate may be assumed constant for a small increment of crack extension.

Obviously, all these methods will have serious shortcomings, which can be listed as follows:

- a) The outcome of the integration will depend upon the sequence used; a high load occurring only occasionally, will induce a higher  $\Delta K$  and, consequently, a higher  $da/dn$  when occurring at a large crack than at a short crack.
- b) The effects of loading frequency and environment can be accounted for only with an arbitrary safety factor.
- c) There is a large scatter in the raw data as a result of manufacturing procedures, batch-to-batch variations, metallurgical effects, and testing techniques.
- d) There is a lack of raw data. Usually, data for the right thickness, panel width, and machining conditions are not available.
- e) The average flight experience is used. Some aircraft of the fleet may meet more severe loading spectra (short flights, few beneficial high loads).
- f) The procedure assumes fair knowledge of the load spectrum.

The integration procedure assumes Miner's rule valid for crack propagation and ignores interaction effects. The results of the calculation may be better in case of a maneuver spectrum. The occurrence of high loads in a maneuver spectrum is relatively high. This means that the crack propagation resulting from the high loads themselves may be much larger than the contribution to crack propagation by low amplitudes. Retardation in crack propagation at low loads therefore become relatively less important with respect to the overall growth rate. The same reasoning applies to many aircraft members with more simple load spectra than the aircraft wing. Fuselages, undercarriages and many other parts have more deterministic load spectra and interaction effects may be less important. This has to be judged for all cases separately. The case of the aircraft wing receives relatively much attention, because it encounters the most complex problems.

It is emphasized once more that the use of a particular analytical relation for the  $da/dn$  versus  $\Delta K$  plot is neither much helpful for the integration procedure, nor will it yield predictably better results. The  $da/dn$  versus  $\Delta K$  data input can be based on a best fit plot and specific demands of the computer.

### 3. Integration by using semi-empirical cumulative damage concepts

The obvious shortcoming of the prediction procedures discussed so far is the neglect of interaction effects, although it turned out that this usually leads to conservative results for crack growth. Interaction effects have been almost exclusively attributed to the introduction of favourable residual compressive stresses at the crack tip [2,17,18]. This was discussed in chapter V.A.4. A theory predicting sequence effects should include the evaluation of the residual stresses and crack closure. A few attempts have been made to achieve this for life calculations [13,14]. This work still needs further development and it cannot as yet be applied to crack propagation.

Semi-empirical integration methods trying to account for interaction effects in crack propagation were proposed recently by Habibie [19], Wheeler [43] and Willenborg, Engle and Wood [44]. Habibie carries out an integration based on the relation of Forman, Kearney and Engle [20], which was discussed in chapter V.A.4, but the use of this relation is not essential. Habibie introduces a retardation factor  $\varphi$ . In the absence of any overloads;  $\varphi = 1$ . In case of periodic overloads the value of  $\varphi$  is determined by the ratio between the crack extension in the interval between two overloads and the crack extension in the same number of cycles in the absence of overloads. This is depicted in figure VB 7:

$$\varphi = \frac{\Delta a}{\Delta a_1} < 1 \quad (2)$$

The notation  $\Delta a_1$  is used here to indicate crack extension without retardation effects for which  $\varphi = 1$ .

Habibie recognizes that  $\varphi$  will depend upon the magnitude of the overload (see figure VA 43) and upon the ductility of the material and he postulates:

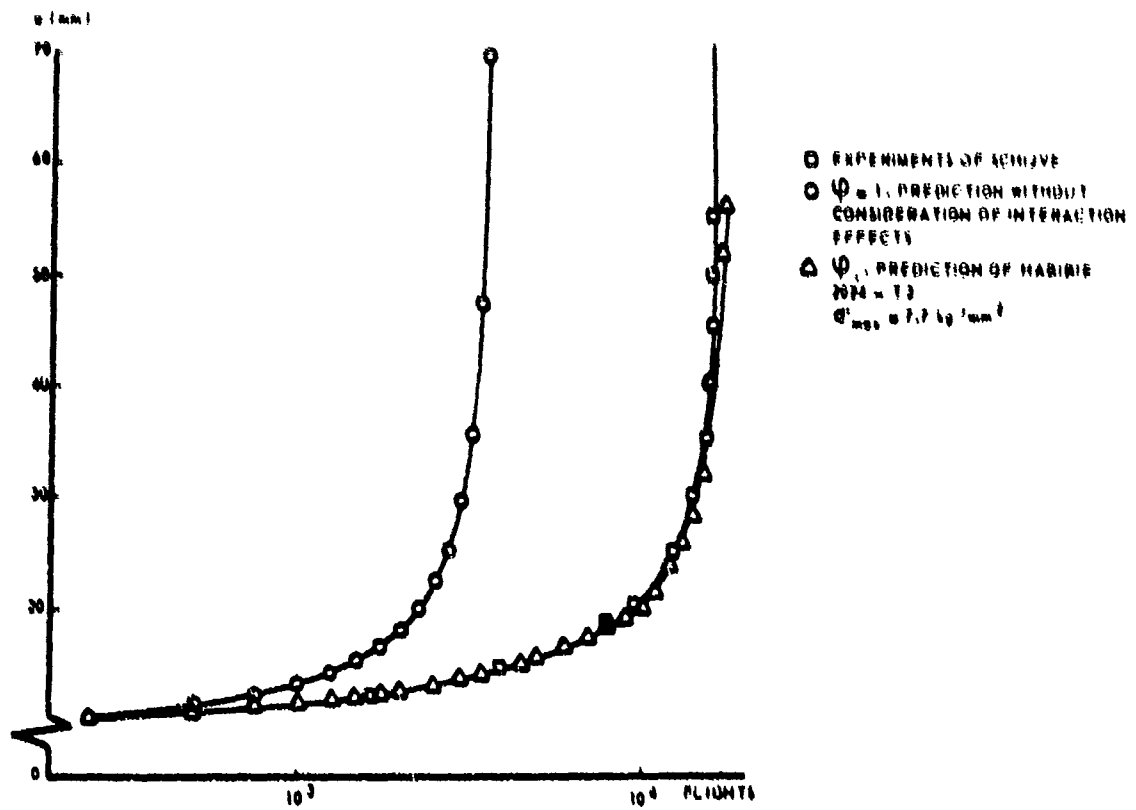
$$\varphi_1 = a \bar{K}_1^{-\gamma} \quad (3)$$

in which  $\bar{K}_1$  is the normalized (dimensionless) stress intensity factor at the overload and  $a$  and  $\gamma$  are material constants. Then he arrives at the following basic formula for his integration procedure:

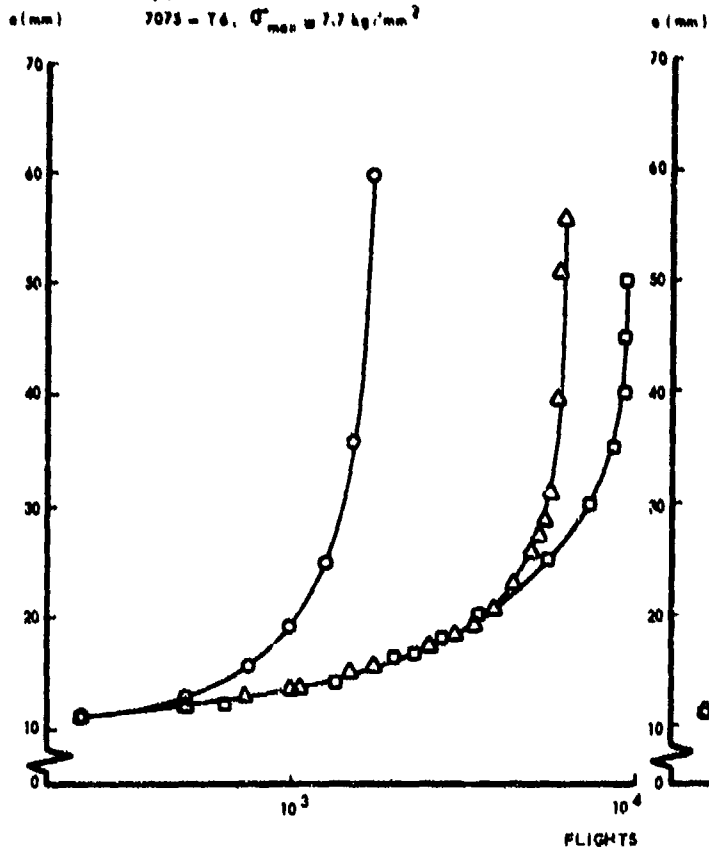
$$\left. \begin{aligned} a_{i+1} &= a_i + \Delta a_i \\ \Delta a_i &= \varphi \frac{c(1-R)^{D-1} K_{\max}^m}{K_0 - K_{\max}} \end{aligned} \right\} \quad (4)$$

where  $\Delta a_i$  is the crack extension in the  $i$ th cycle.

Habibie used the flight simulation tests of Schijve [16] to evaluate and check eq (4). (A summary of Schijve's data were presented in chapter V.A.4). He calculated crack extension for the flight simulation tests with  $\varphi = 1$  (ignoring interaction effects) and compared the result with the actual test



□ EXPERIMENTS OF SCHIJVE  
 ○  $\Psi = 1$  (NO INTERACTION CONSIDERED)  
 △  $\Psi_1$  (HABIBE)  
 $7075 - T6$ ,  $\sigma_{max} = 7.7 \text{ kg/mm}^2$



□ EXPERIMENTS OF SCHIJVE  
 ○  $\Psi = 1$  (NO INTERACTION CONSIDERED)  
 △  $\Psi_1$  (METHOD OF HABIBE)  
 $7075 - T6$ ,  $\sigma_{max} = 6.6 \text{ kg/mm}^2$

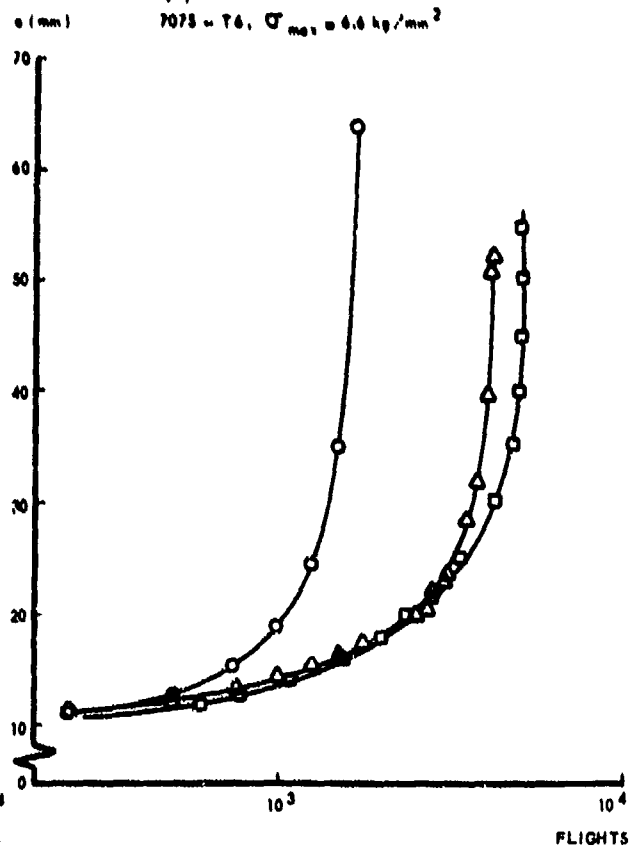


FIG. VB 9 COMPARISON OF SCHIJVE'S DATA [16] AND PREDICTIONS BY HABIBE [19].

data to determine  $\varphi$ . The procedure starts at the occurrence of maximum load and continues until the next occurrence. This yields one value of  $\varphi$ . The interval to the subsequent occurrence of the overload yields another value, etc. The maximum load in the flight simulation tests was not always the same, due to the truncation (see fig. VA 44) and hence the procedure could be repeated for other magnitudes of the highest load in the sequence. Each calculation ever yields one value for  $\varphi$  and these can be plotted versus the magnitude of  $K_I$  at which the procedure was started. The result is shown in figure VA 8.

The straight line in figure VB 8 supports the usefulness of eq (3) and it allows determination of  $\alpha$  and  $\gamma$ . Then it is possible to use eq (4) as an integration procedure for the purpose of predicting crack propagation, but there is one additional difficulty. In case of small cracks it may be expected [19] that the retardation effect of the highest cycle will be dominant and remain so until its next occurrence. When the crack is longer, also cycles of a somewhat lower magnitude will have an effect, until at large crack sizes every cycle causes a retardation which is effective only during one subsequent cycle. A continuous transition where  $\varphi$  accounts only for the highest overload in the first stage of crack growth and later gradually takes into account also cycles of lower magnitude is not yet feasible [19]. Habibie solved this problem by using three stages. In the first stage  $\varphi$  relates to the highest overload only, in the second stage the next three highest cycles are taken into account and in the third stage all cycles are considered. Habibie determined the extent of the three stages more or less by trial and error. He predicted the crack propagation curve for one of Schijve's flight simulation tests by using eqs (4) and the result of figure VB 8, and he started out with stage I, accounting for the retardation of the highest cycle only. He compared this result with the actual test result and when the discrepancy became too large, he changed to the next stage. It appeared necessary to change to stage II at  $2a/w \approx 0,25$  and to stage III at  $2a/w \approx 0,38$  where  $w$  is the sheet width.

On this basis Habibie made a prediction of crack propagation for a large series of flight simulation tests as performed by Schijve. Computertimes for the integration varied from 12 to 150 minutes per test. Some of the predicted crack propagation curves are presented here in figure VB 9 in comparison with the actual test results. Also shown are predictions for  $\varphi = 1$  (retardation effects disregarded). The latter curves result from the direct Miner integration as discussed in the previous section and they are at the safe side as might be expected.

The accuracy of Habibie's predictions is not too surprising, since they were made for the same test data that yielded the values for  $\varphi$ . More checks would have to be made by predicting crack propagation for other test series with the presently available  $\varphi$ -data.

The procedure proposed by Wheeler [43] is very similar to the method of Habibie, but it is better formulated in terms of the crack tip plastic zone. Wheeler also introduces a retardation parameter  $\varphi$ . It is based on the ratio of the current plastic zone size to the size of the plastic enclave formed at an overload (figure VB 10a). An overload occurring at a crack size  $a_o$  will cause crack tip plastic zone of a size

$$r_{po} = C_1 \frac{\sigma_o^2 a_o}{\sigma_{ys}^2} = C \frac{K_o^2}{\sigma_{ys}^2} \quad (5)$$

where  $\sigma_o$  is the overload stress and  $\sigma_{ys}$  the yield stress. When the crack has propagated further to a length  $a_1$  the current plastic zone size will be

$$r_{p1} = C_1 \frac{\sigma_1^2 a_1}{\sigma_{ys}^2} = C \frac{K_1^2}{\sigma_{ys}^2} \quad (6)$$

This current plastic zone is still embedded in the plastic enclave of the overload; the latter still proceeds over a distance  $\lambda$  in front of the current crack  $a_1$ . Wheeler (43) assumes that the retardation factor  $\varphi$  will be a power function of  $r_{p1}/\lambda$ . Since  $\lambda = a_o + r_{po} - a_1$  the assumption amounts to:

$$\varphi = \left( \frac{r_{p1}}{a_o + r_{po} - a_1} \right)^m \text{ as long as } a_1 + r_{p1} < a_o + r_{po} \quad (7)$$

If  $a_1 + r_{p1} \geq a_o + r_{po}$  the retardation factor becomes  $\varphi = 1$  by definition. The power  $m$  in equation (7) has to be determined empirically and Wheeler finds  $m = 1.43$  for 16ac steel and  $m = 3.4$  for Ti-6Al-4V. In order to show the similarity with the method of Habibie equations (5) and (6) must be substituted into equation (7), which leads to:

$$\varphi = \left( \frac{CK_1^2 / \sigma_{ys}^2}{a_o - a_1 + CK_o^2 / \sigma_{ys}^2} \right)^m \quad (8)$$

As the plastic zone is embedded in the plastic enclave the retardation factor is still defined as  $\varphi = 1$  and hence

$$\varphi = \left( \frac{K_1}{K_o} \right)^{2m} \quad (9)$$

With  $\nu = 2m$  equation (9) is almost identical to equation (3). According to figure VB 8 Habibie finds  $\nu \approx 5$  for the aluminum alloys and hence  $m = 2.5$  which is in the same order of magnitude as the values quoted above from the paper by Wheeler for a steel and titanium alloy.

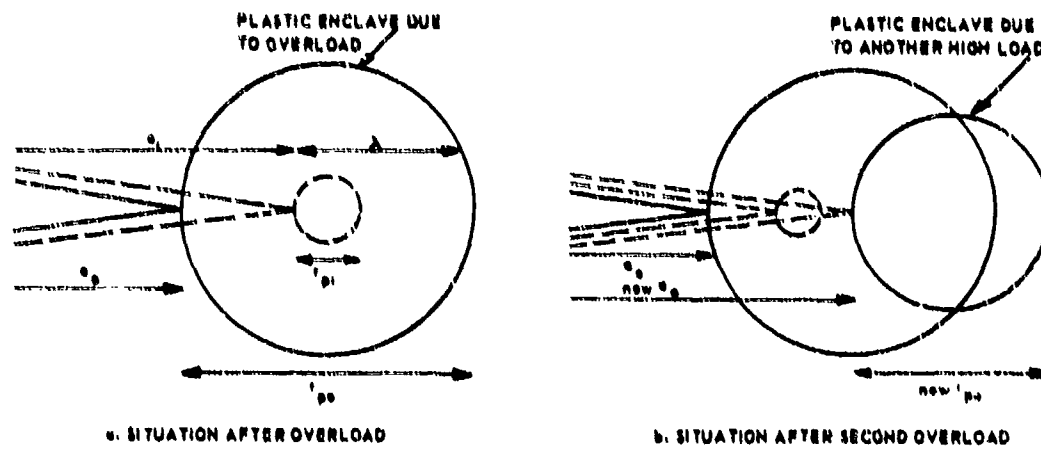


FIG. VB 10 THE MODEL OF WHEELER [43].

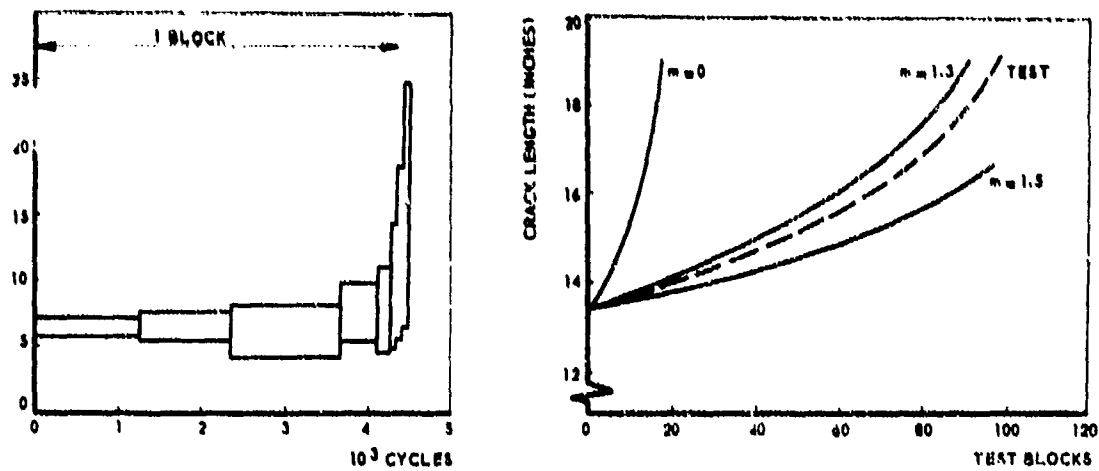


FIG. VB 11 PREDICTION OF CRACK GROWTH MADE BY WHEELER.

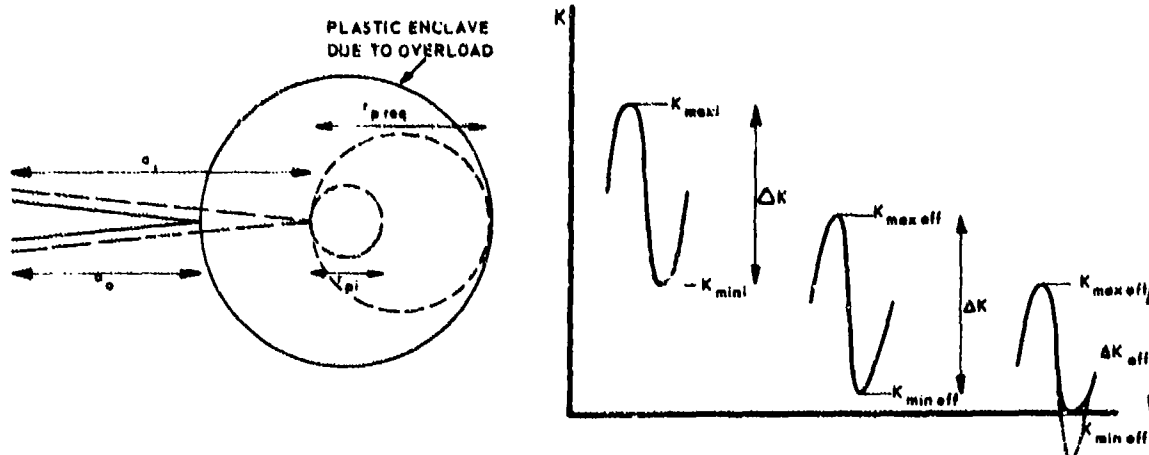


FIG. VB 12 THE MODEL OF WILLENBORG, ENGLE AND WOOD [44].



With the model of Wheeler the crack propagation curve can be predicted from a cycle by cycle integration. In case of a single overload in a constant amplitude test the retardation factor gradually decreases to unity while the crack progresses through the plastic envelope. If a second high load occurs which produces a plastic zone extending beyond the border of the plastic envelope the border of this new plastic zone will have to be used in the equations (Fig. VB 10b) and the momentaneous crack length will then be the new  $a_0$ .

Predictions made by Wheeler by using his integration method led to fairly good predictions of block-programme crack propagation tests. Some of his results are shown in figure VB 11. The advantage of Wheeler's model above the one of Habibe is that it yields a new value for  $\phi$  in every cycle without any further assumptions. This makes Wheeler's model more versatile in its application. Its validity for random load sequences and for different materials has still to be demonstrated.

Still another method was proposed by Willenborg, Engle and Wood (44). They also make use of the plastic envelope formed at the overload (Fig. VB 12). The plastic envelope extends to

$$a_p = a_0 + r_{p0} = a_0 + C \frac{K_0^2}{\sigma_{ys}^2} \quad (10)$$

where  $a_p$  is the distance from the centre of the crack to the boundary of the plastic envelope and the other symbols have the same meaning as in equation (5). Willenborg et al then consider the stress intensity that would be required to produce a plastic zone at the tip of the current crack  $a_1$  that would extend to the border of the plastic envelope (Fig. VB 12). This means they want to determine the  $K_{max}$  required to give:

$$a_1 + r_{p,req} = a_0 + r_{p0} \text{ or } r_{p,req} = a_p - a_1 \quad (11)$$

where  $r_{p,req}$  is the required plastic zone to give the wanted result. The  $K_{max,req}$  for this is given by

$$C \frac{K_{max,req}^2}{\sigma_{ys}^2} = a_p - a_1 = a_0 + r_{p0} - a_1 \quad (12)$$

In the first cycle subsequent to the overload  $a_1$  is still equal to  $a_0$ , hence  $K_{max,req}$  would be equal to  $K_0$ , the stress intensity of the overload.

Now Willensdorf et al make the rather queer assumption that the actual  $K_{max,i}$  occurring at the current crack length  $a_i$  will be effectively reduced by an amount:

$$K_{red} = K_{max,req} - K_{max,i} \quad (13)$$

This implies that they expect the action of residual compressive stresses of a magnitude:

$$\sigma_{res} = \frac{K_{max,req}}{\sqrt{y a_i}} - \frac{K_{max,i}}{\sqrt{y a_i}} \quad (14)$$

It means that both  $K_{max,i}$  and  $K_{min,i}$  in cycle  $i$  are reduced by an amount  $K_{red}$ . This gives:

$$\left. \begin{aligned} K_{max,eff,i} &= K_{max,i} - K_{red} = 2K_{max,i} - K_{max,req} \\ K_{min,eff,i} &= K_{min,i} - K_{red} = K_{min,i} + K_{max,i} - K_{max,req} \end{aligned} \right\} \quad (15)$$

If either  $K_{min,eff}$  or both  $K_{max,eff}$  and  $K_{min,eff}$  would be smaller than zero they are set at zero. If the latter occurs  $\Delta K_{eff,i}$  will be smaller than  $\Delta K_i$ , if not  $\Delta K_{eff,i} = \Delta K$  as can be seen from figure VB 12. The cycle ratio  $R_{eff}$  becomes

$$R_{eff} = \frac{K_{min,i} - K_{red}}{K_{max,i} - K_{red}} = \frac{2K_{min,i} + K_{max,i} - K_{max,req}}{2K_{max,i} - K_{max,req}} \quad (16)$$

Both  $\Delta K_{eff}$  and  $R_{eff}$  can be calculated and then  $da/dn$  can be calculated from

$$\frac{da}{dn} = \frac{C \Delta K_{eff}^n}{(1-R_{eff})K_c - \Delta K_{eff}} \quad (17)$$

Consider the special case that both  $K_{min,eff}$  and  $K_{max,eff}$  remain larger than zero (Fig. VB 12). Then  $\Delta K_{eff} = \Delta K$ . The reduction in crack propagation rate will only be caused by a reduction in  $R$ . Hence,

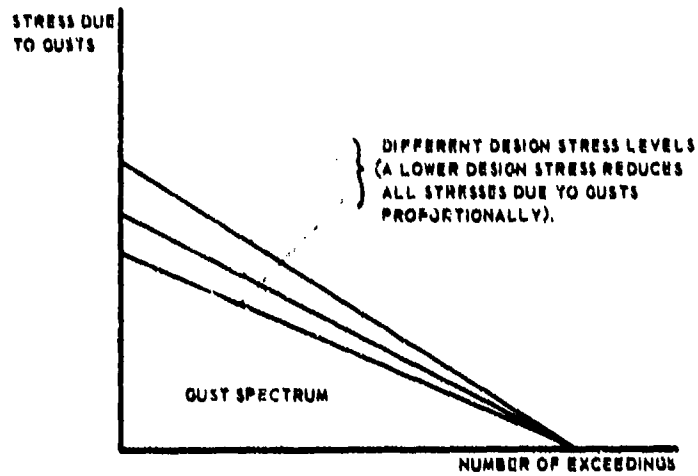
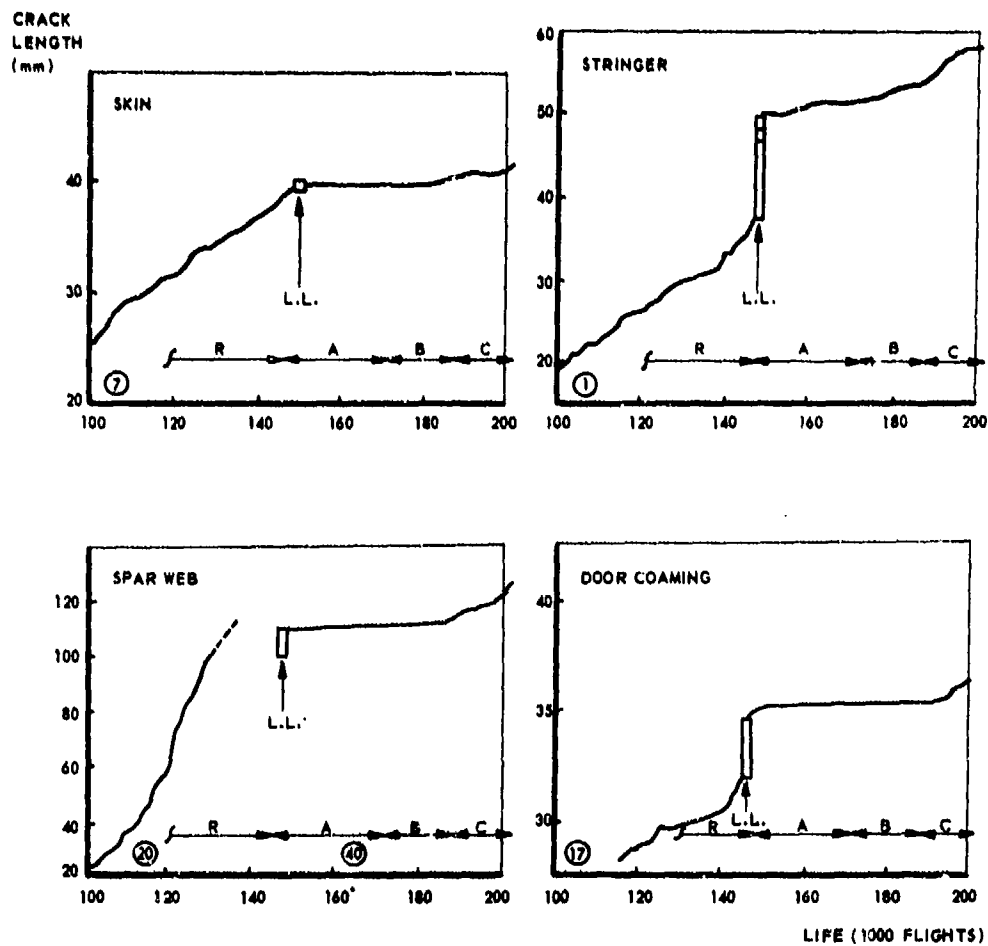


FIG. VB 13 THE EFFECT OF DESIGN STRESS LEVEL ON LOAD SPECTRUM.



- R : CERTIFICATION TESTS  
 L.L. : CRACK EXTENSION DUE TO LIMIT APPLICATION AT END OF CERTIFICATION TESTS  
 A, B, C : PERIODS OF SUBSEQUENT RESEARCH PROGRAM  
 A : LOW-AMPLITUDE GUST CYCLES OMITTED  
 B : LOWER TRUNCATION LEVEL  
 C : LOAD LEVELS INCREASED 25 PERCENT

FIG. VB 14 THE EFFECT OF LIMIT LOAD APPLICATION ON CRACK PROPAGATION [2].

$$\psi = \frac{1-R_i}{1-R_{eff}} = \frac{1 - \frac{K_{max,i} - \Delta K}{K_{max,i}}}{1 - \frac{K_{max,eff} - \Delta K}{K_{max,eff}}} = \frac{K_{max,eff}}{K_{max,i}} \quad (18)$$

Equation (18) gives some idea how this model compares with those of Habibie (Eq.3) and Wheeler (Eqs 8,9).

Also Willensdorf et al show integration results of block-programme crack propagation in good agreement with test results. An objection against their model is that the assumption regarding the residual compressive stresses (Eqs 13,14) is at least doubtful.

The methods considered are interesting attempts to account for load interaction effects in crack propagation estimates and further development should certainly be encouraged. For the time being neither method can be generalized. It is conceivable that flight simulation tests with gust and maneuver spectra would yield largely different values for  $\psi$ ; the maneuver spectrum contains relatively many high loads, which may be of influence for the retardation effects. The same can be said about other types of load histories.

#### c. Flight simulation test basis.

In 1965 Hardrath [21] presented a review on cumulative damage in which he concluded that new breakthroughs of our comprehension of the problem should not be expected in the near future. In 1972 Schijve [2] was only slightly more optimistic. Our phenomenological knowledge will steadily increase and especially for the case of crack propagation (rather than for fatigue life predictions) new prediction methods may be developed. These methods should account for interaction effects in a proper way and therefore they will have to be based on the crack tip residual stress field or crack tip closure or on both. Recalculations of the crack-tip stress-field will probably be required for each load reversal in a random-load sequence. This may involve considerable computer time. Therefore it deserves consideration to perform the crack growth prediction on an analog computer. The best analog computer available, one that has knowledge of the universal fatigue law, is a specimen in a closed loop electro-hydraulic fatigue machine. This analog computer can calculate about 20 cycles of crack propagation per second, which is probably much faster than an advanced digital computer can perform if it has to recalculate the stress field each cycle.

Particularly for the complicated load history of an aircraft wing it has considerable advantages to predict crack propagation on the basis of flight simulation test data as proposed by Schijve [2] and Broek [17]. Schijve [2] has advocated the compilation of flight simulation data. A handbook with this type of data would be useful for estimating fatigue properties. It would allow application of the flight-simulation interpolation method as proposed by Schijve.

In order to avoid extrapolation, extensive data obtained in flight simulation tests should be compiled. The data should cover the main variables of the load spectrum. For a certain structural material it should include the following variables

- a) Some typical shapes of gust and maneuver spectra.
- b) Design stress level. A change in design stress level would reduce or increase the load spectrum proportionally as depicted in figure VB 13.
- c) The magnitude of the ground-air-ground cycle and its frequency of occurrence.

If these data were available crack propagation for a particular flight profile, flight length (frequency of the ground-air-ground cycle) and design stress level could be predicted by interpolation. The requirements for adequate flight simulation testing are rather complex. It is beyond the scope of this survey to give a thorough discussion of these requirements, but they are given ample attention by Schijve [2].

Of course, the flight simulation interpolation method has also its shortcomings. The main problem involved, is in the fact that crack growth data cannot simply be given as a function of the stress intensity factor as has been outlined in chapter V.A.4. This implies that application of the data to stiffened sheet structures may be hardly possible. (It is shown in chapter V.B.2 that the prediction of crack propagation in built-up sheet structures has to be based on the stress intensity factor). Other shortcomings are that the flight simulation test does not properly account for frequency effects, environmental effects and many of the other parameters affecting crack growth, as discussed in chapter V.A.3. Therefore safety factors will still have to be applied.

#### V.B.1.4 Confirmatory testing

It will always be necessary to obtain a fair judgement on the reliability of crack growth estimates. The predictions may be compared with service experience from previous designs. A new design may have similarity to a previous design or it may be a further development of a previous one. This information can be used in a general way [2] by the choice of a stress level that yielded satisfactory results in previous structures. Of course, reconsideration of all relevant parameters will be necessary. The advantage of using service experience is, that the data were obtained under realistic circumstances from a large number of aircraft.

The crack propagation prediction may still have a low accuracy. The prediction may be useful in the early design stage when choices have to be made regarding the type of material and the type of structure, but when the aircraft reaches completion and all details have become definitive, a realistic test will often be necessary. Both the specimen and the load sequence should be representative for service conditions. This means that the test should be carried out on the actual component or a complete part of the structure.

With respect to the fatigue load, a flight simulation test representative for service loading is required. An exact simulation of the load-time history in service would be the preferable solution. In general, a load-time history will have to be designed on the basis of mission analysis and load statistics obtained with other aircraft. A good knowledge of the empirical trends is essential for the purpose. A major problem is the assessment of the highest load level to be applied in the flight-simulation test. As discussed before, this level may have a predominant effect on the life and the crack propagation. If the load level that will be reached (or exceeded) once in the target life of the aircraft is applied in a test, it may have a favourable effect on the fatigue life and crack growth. It should be realized that this load level is subject to statistical variation and that some aircraft will meet this load more than once, whereas other aircraft will never be subjected to it. In view of this Schijve [2] proposed that the load spectrum should be truncated at the load level exceeded ten times in the target life, in order to prevent that the test give too optimistic results.

Sometimes fail-safe loads are applied at regular intervals during a full-scale fatigue test to demonstrate that the aircraft is still capable of carrying the fail-safe load. The result may cause a crack growth delay. In other words, this procedure could give false information. The crack growth delay in a full-scale structure was recently shown [22,28] in tests on the F-28 wing. The certification test was completed after simulating 150000 flights. Then fail-safe loads (limit load) were applied. In a subsequent research program it turned out that several cracks did not grow any further as shown in figure VB 14.

The significance of low-amplitude cycles has been discussed in chapter V.A.4. Omission of these cycles from a flight-simulation test will considerably reduce the testing time. However, since such cycles may contribute to crack nucleation (fretting) and crack growth, the cycles can hardly be omitted during the certification tests. Taxiing load cycles can be omitted under certain conditions. In fact it appears admissible only if the cycles occur in compression for the components being tested [2]. Care should be taken that the ground-air-ground cycle reaches the most extreme minimum load occurring on the ground, including dynamic loads.

A full-scale test on a new aircraft design is an expensive test. In view of this there is every reason to require that the test gives realistic and relevant information. As said before, a full-scale fatigue test should be carried out with a carefully planned realistic representation of the service load-time history.

Several aspects can be mentioned that make full-scale testing of a new aircraft structure desirable:

- 1) Indication of fatigue critical elements and design deficiencies.
- 2) Determination of fatigue lives until visible cracking occurs.
- 3) Study of crack propagation, inspection and repair methods.
- 4) Measurements on residual strength (fail-safe tests, not to be carried out until end of fatigue test).
- 5) Economic aspects.
- 6) Determination of inspection methods.

(All these aspects have been amply discussed by Schijve [2]).

With respect to the latter aspect some remarks seem appropriate here, since it is so important for fail-safety. The full-scale test is also a training experiment for inspection techniques. It can be used to evaluate the most suitable inspection techniques for the various locations and the conditions under which the inspections should be carried out. It is the purpose of the fail-safe analysis to establish safe inspection intervals. The aircraft operator should also be provided with all the necessary information to make such an inspection successful. He should be informed about the most suitable inspection techniques, and the most effectual settings of inspection apparatus, all this information can be obtained during a fatigue test on full scale components or structures.

The uncertainties in the prediction of crack growth provide both economic and moral reasons to supply the aircraft user with every possible information that may be of aid to make aircraft fail-safety a reality.

V.B.2.1 Introduction

The major part of the aircraft structure consists of built-up panels of sheet and stringers. Therefore it is a little surprising that the literature on fail-safety pays relatively little attention to the propagation of fatigue cracks in built-up sheet structures as compared to unreinforced laboratory specimens. Fortunately some very useful work has become available during recent years. It appears that the complication of stiffening elements in a cracked structure can be solved in a rational way. In fact the additional problem of the stiffening elements is far less difficult than the other problems involved in fatigue crack propagation.

For built-up sheet structures containing cracks it is usually possible to establish a fairly accurate value for the stress intensity factor. If it is assumed that the rate of fatigue crack propagation is fully determined by the stress intensity factor, the crack propagation rate of the built-up structure will be equal to the growth rate in an unstiffened panel with the same stress intensity. This implies that the presence of stiffening elements would only add a problem of stress analysis to the complex procedure of predicting fatigue crack propagation. Since fatigue crack rates appear to be a function also of stress history there are additional difficulties involved, for which there does not yet exist a rational solution. However, these additional difficulties are pertinent to the fatigue problem, rather than to the effect of stiffening.

The determination of the stress intensity factor is also a requirement for the prediction of the residual strength of a built-up structure with cracks. The problem of residual strength of sheet structures is discussed in chapter V.C.1. Procedures to arrive at the stress intensity of such structures are amply discussed in chapter V.C.1 and are not repeated here. Only a brief outline of the basic assumptions will be given in the following sections on fatigue crack growth.

V.B.2.2 The stiffened panel

The stress intensity of a flat stiffened panel is affected by the presence of the stringers. For the case of simple flat stiffeners (figure VB 15) the effect of eccentricity can be neglected; the stress intensity factor can then be readily calculated [24,25,26,27,28] both analytically and by finite element methods.

The procedure to calculate the stress-intensity factor of a reinforced panel is illustrated in figure VB 16 (The uniformly loaded stiffened panel with crack 2a is a summation of four components, namely, (1) a uniformly loaded unstiffened panel with crack 2a, (2) a panel of the same dimensions with crack 2a loaded by a number of point loads exerted by the fasteners, (3) a uniformly loaded stringer, and (4) a stringer with the point loads. Compatibility requires the deformations of the stringers and underlying skin material to be the same, which gives equations to determine the fastener loads,  $P_j$ . The presence of the stiff reinforcement does not allow the skin to undergo the same large deformations as the unstiffened panel. The stringers will take over some load from the skin, such that the stress-intensity factor in the stiffened panel is lower than in the unstiffened panel with the same length of crack. On the other hand, the presence of the crack will locally enforce a higher load in the stringers and in the fasteners. The higher load in the stringers is determined by the so-called load concentration factor  $L$ , which follows from the calculations.

The stress-intensity factor in the stiffened panel will be

$$K = \alpha C_R \sigma \sqrt{\pi a} \quad \text{with } C_R < 1, \quad (19)$$

where  $C_R$  is the skin stress reduction factor.

The local stress in the stringer will be

$$\sigma_{\text{stringer}} = L \sigma, \quad \text{with } L > 1. \quad (20)$$

The fastener loads are given by

$$P_1 + P_2 \dots + P_j = (L - 1) \cdot \sigma \cdot A_{st} \quad (21)$$

where  $A_{st}$  is the stringer cross-sectional area.

Both  $L$  and  $C_R$  are functions of the ratio  $s/a$  ( $s$  = stringer pitch), the stringer cross section, the modulus of the stringer material, and the rivet pitch. The variations of  $L$  and  $C_R$  are given schematically in figure VB 16, as a function of crack length for the particular panel configuration of figure VB 15.

A heavy stringer can take more load from the skin and give a larger reduction of the stress intensity factor. Since the stringer is heavy, the load it takes from the sheet will be relatively small in comparison with the load it already carries and therefore the load concentration factor will be lower than for a light stringer.

As long as the crack tip is far from the stiffener, the reduction of the stress intensity is low. When the crack tip approaches the stringer the reduction becomes larger and it is at a maximum when the crack has just passed the stringer center line. The effect of the stringer decreases again when the crack grows longer. There remains a reduction, because the stringer tends to close the crack; this reduction is larger if the stringer has a higher stiffness and if the rivet pitch is smaller. When the crack tip approaches the next stringer there is again a larger reduction in stress intensity. This is illustrated by figure VB 17, derived from the work of Poe [27,28].

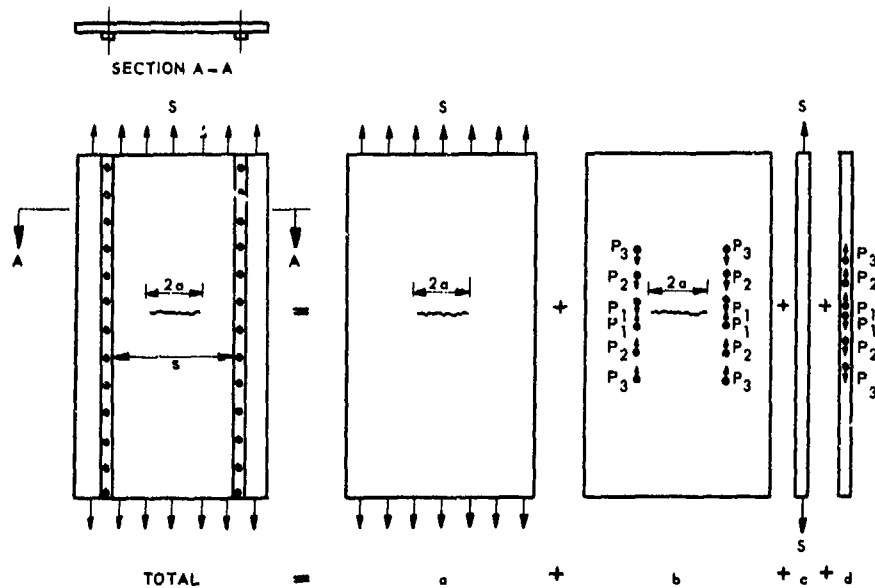


FIG. VB 15 DETERMINATION OF STRESS INTENSITY FACTOR IN STIFFENED PANELS.

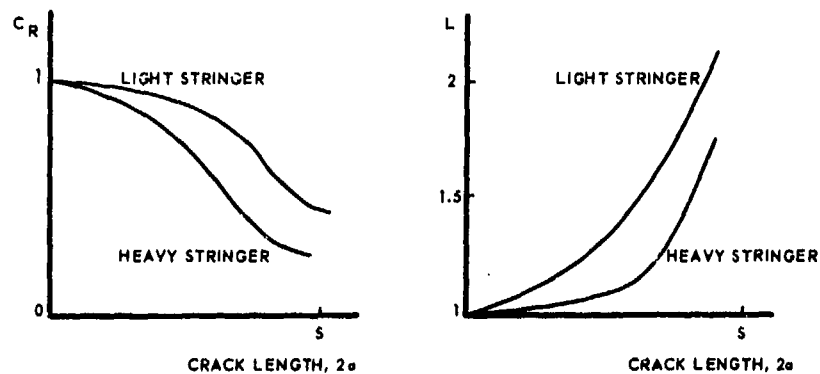
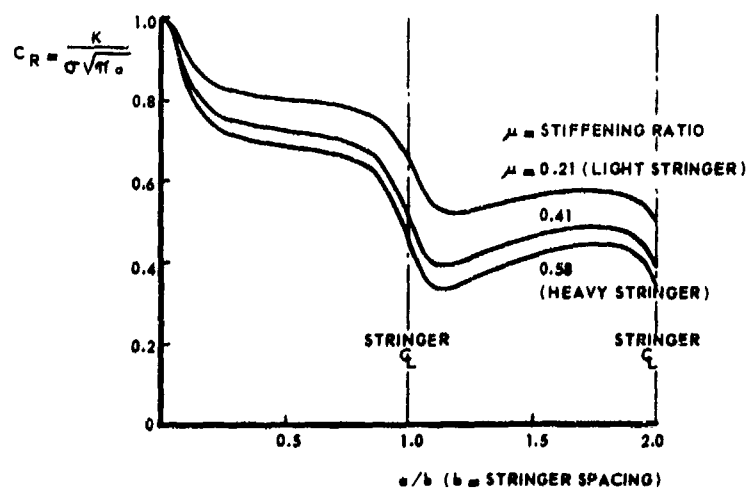
FIG. VB 16 SCHEMATIC ILLUSTRATION OF THE VARIATION OF  $C_R$  AND  $L$  FOR THE PANEL CONFIGURATION OF FIGURE II B 15.

FIG. VB 17 STRESS INTENSITY REDUCTION FACTOR (152 mm STRINGER SPACING) ACCORDING TO POE [27].

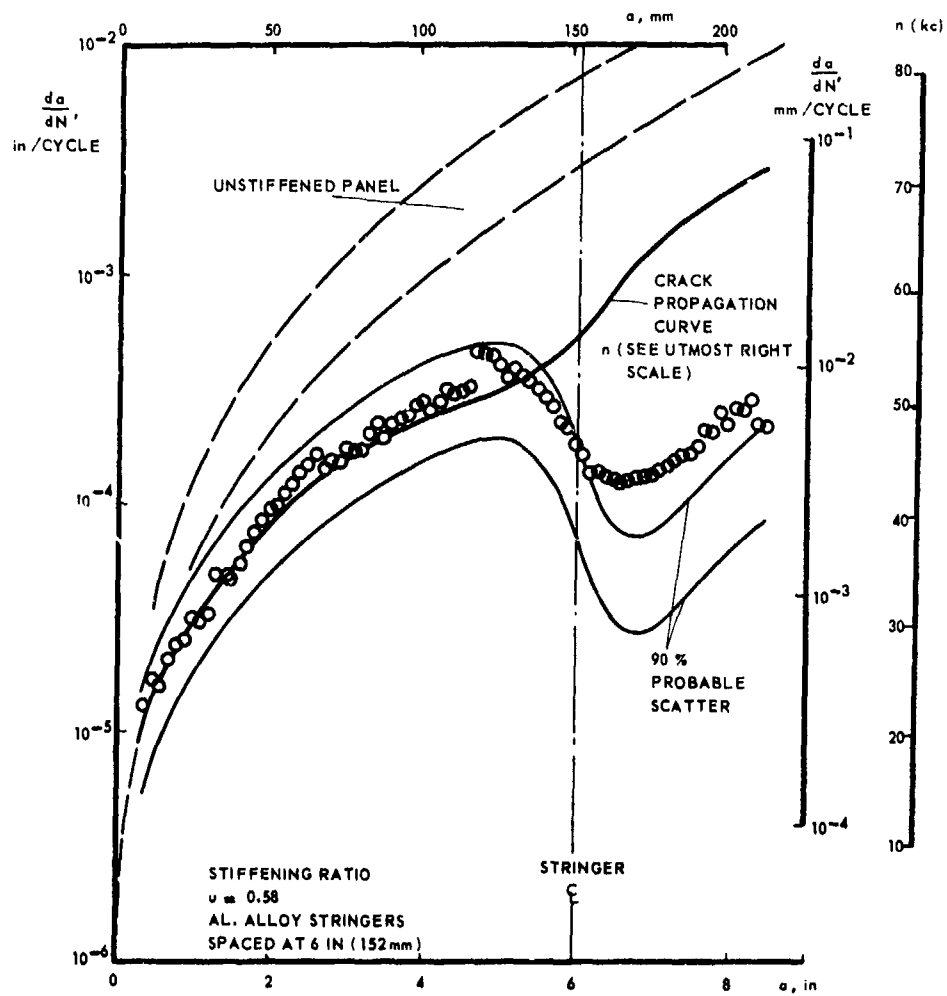


FIG. VB 18 FATIGUE CRACK GROWTH IN STIFFENED PANEL ACCORDING TO POE [28].

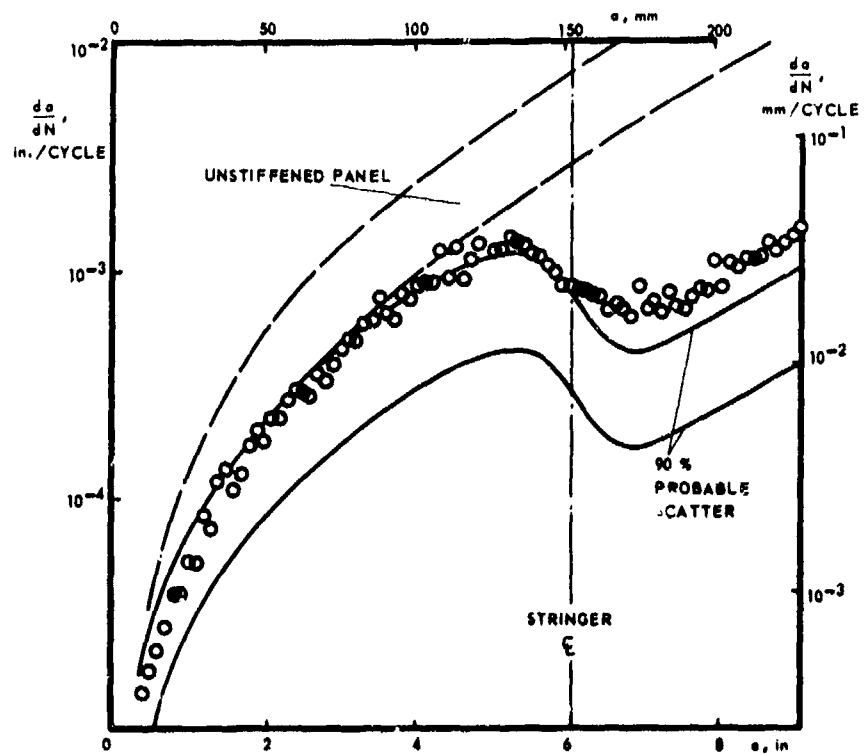


FIG. VB 19 FATIGUE CRACK GROWTH IN STIFFENED PANEL ACCORDING TO POE [28].

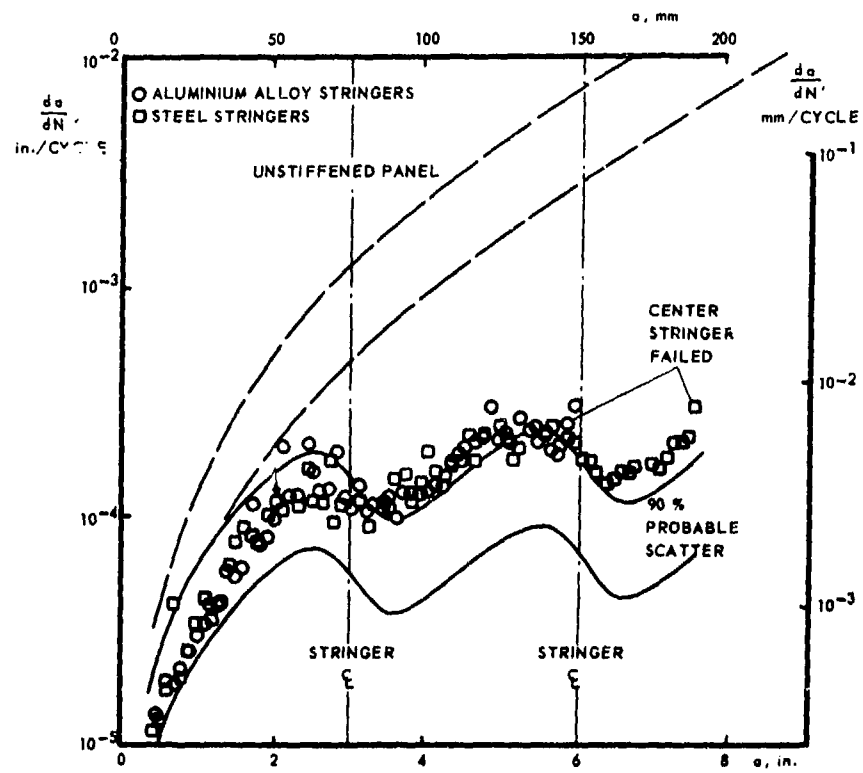


FIG. V B 20 FATIGUE CRACK PROPAGATION IN STIFFENED PANEL ACCORDING TO POE [28].

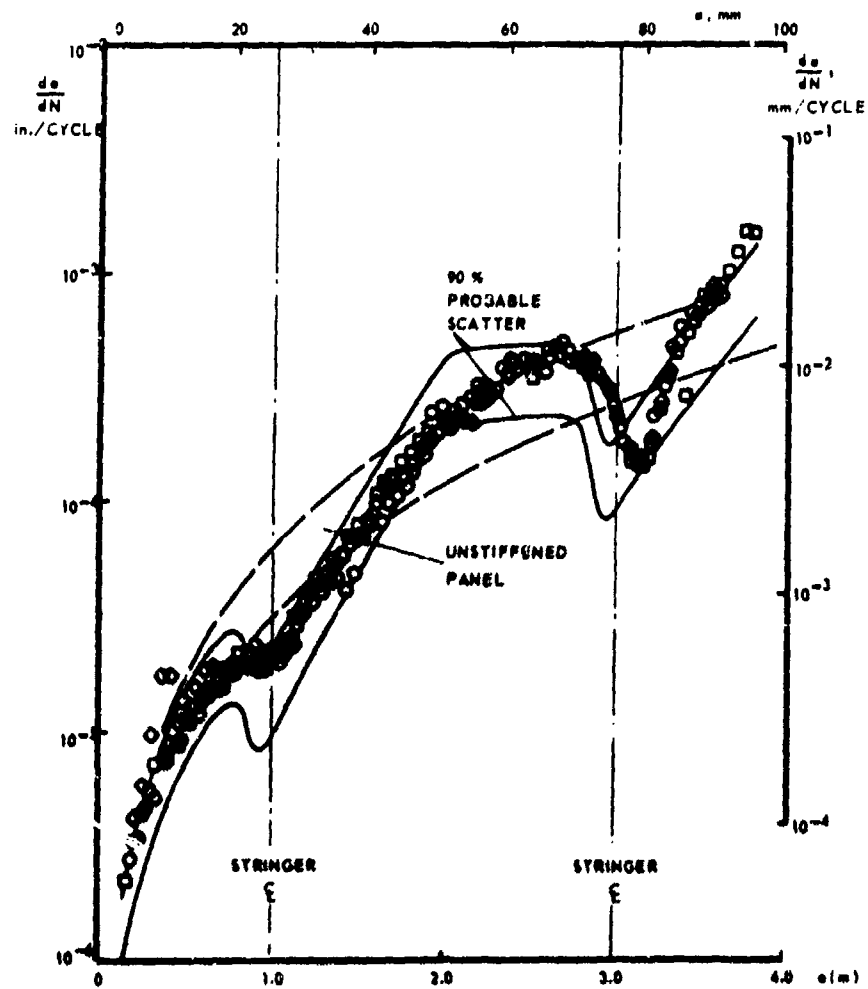


FIG. V B 21 FATIGUE CRACK PROPAGATION IN INTEGRALLY STIFFENED PANEL [28].



$L$ ,  $C_p$ , and fastener loads have been calculated for a wide variety of panel configurations, and include such cases as a crack emanating from a stringer (the stringer overlapping the crack), cracks growing between two fasteners, cracks growing through a fastener hole, and adhesively bonded stringers (chapter V.C.1). Further refinements of the analysis method should account for plastic deformation of the stringer, ovalization of rivet holes resulting from high bearing stresses, stringer eccentricity and other departures from the ideal case.

The applicability of this concept to fatigue crack propagation has been demonstrated by Poe [27]. He predicted the crack growth data in a stiffened panel on the basis of unstiffened panel data and compared his predictions with actual test data obtained from stiffened panels of different geometries. An example of such a comparison is given in figure VB 18. The two dashed curves give the scatter band of the crack rate data of the unstiffened panel. The two solid lines represent the predictions for the stiffened panel which are confirmed very well by the test data. As can be seen from equation (19) and figure VB 18, the stress intensity factor drops as the crack approaches the stringer and, hence, crack propagation should decelerate. When the crack has well passed the stringer, the stiffening effect decreases,  $K$  increases, and so does  $da/dn$ . This is also reflected in the crack propagation curve given in figure VB 18. This curve has been obtained by integration of Poe's  $da/dn$  data. It shows how crack growth is delayed in the vicinity of the stringer.

Poe's work contains many interesting results. Figure VB 19 shows that a light stringer causes a smaller deceleration of crack growth, since it brings about less reduction of the stress intensity factor. When the crack reaches the next stringer again a slow down can be observed as is depicted in figure VB 20. In the vicinity of the second stringer the reduction in propagation rate is in the order of a factor of ten. Similar observations were made by Smith et al [29] who studied the effect of adhesive-bonded tear straps on fatigue.

The skin crack causes a load concentration in the stringer, which enhances the likelihood of stringer fatigue failure. If this occurs skin crack propagation increases rapidly; the stringer is no longer effective in reducing the stress intensity factor and besides, the skin has to take the extra load from the failed stringer. Figure VB 20 illustrates this effect. In case of integral stiffeners the stiffening elements will always crack simultaneously with the skin. Therefore integral stiffening will cause little deceleration of crack growth as may be appreciated from figure VB 21.

The test results of Poe demonstrate that the method correctly predicts crack growth in stiffened panels. The observed growth rates were slightly higher than the predicted rates. The following factors may have contributed to this discrepancy:

- a) Fastener loads become very high when the crack approaches the stringer. The high bearing stresses cause bolt hole deformation and therefore the effective stiffness of the stringer is reduced, which implies that the stringer is less effective in reducing the crack tip stresses.
- b) The eccentricity of the stringer has not been accounted for in the prediction procedure. Stringer eccentricity slightly reduces the effect of the stringer. Finite element methods allow this effect to be determined.
- c) There may be an effect of stress history on crack propagation (see chapter V.B.4).

Stringers decelerate crack propagation in the skin due to crack tip stress reduction. A second deceleration effect occurs when the crack runs into a rivet hole. This will blunt the crack tip and further crack growth will be delayed until crack reinitiation. In the tests of Poe the row of rivets in the line of the crack were left out in order to prevent the crack from growing into a hole. In practice however, cracks will usually be initiated at a rivet hole and will follow a path through a row of holes. If the crack would pass between two holes the nearest rivets are very close to the crack and the stringer will be very effective in the reduction of crack tip stresses. If the crack passes through a hole, the nearest rivets are twice as far from the crack and therefore the stringer is less effective. For a given panel configuration (see chapter V.C.1) the difference in stress intensity factor may be in the order of 50 percent. The beneficial effect of crack tip blunting if the crack runs into a rivet hole, is therefore largely reduced by the much larger growth rate just before the hole is reached and after reinitiation. A test programme to investigate this effect seems highly worthwhile. From an investigation on fatigue crack propagation in full-scale wing center sections [30] it can be concluded that stop holes drilled at the crack tip did not have a large effect. Then it may well be, that there is little advantage of the crack running into a rivet hole above passage between holes, but of course, this depends upon hole size and other geometrical parameters.

In case of adhesive-bonded stringers the tip stress reduction can be larger; this case can be treated in a similar way as the riveted panel (chapter V.B.1). The tests of Smith et al [29] indicate that the method of prediction of crack growth as discussed in this section applies equally well in case of adhesive bonded tear straps.

### V.B.2.3 The sandwich panel

Also for a sandwich panel it is possible to calculate a value for the stress intensity factor [31]. If one of the faces is cracked, some load of the cracked face can be transmitted through the core into the other face. It implies that the stress intensity of the cracked face is reduced with respect to a similar unreinforced sheet. The reduction factor depends upon the core stiffness [31]. A more elaborate discussion of the calculation procedure is presented in chapter V.C.1.

As an example the reduction of the stress intensity factor for a central crack in one face as calculated by Bartelds and Vande Veer [31] is given in table V.B.3. The table considers two cases of the stiffness parameter

$$r = \frac{(1-\nu^2) E_c w^2}{\pi^2 E t c}$$

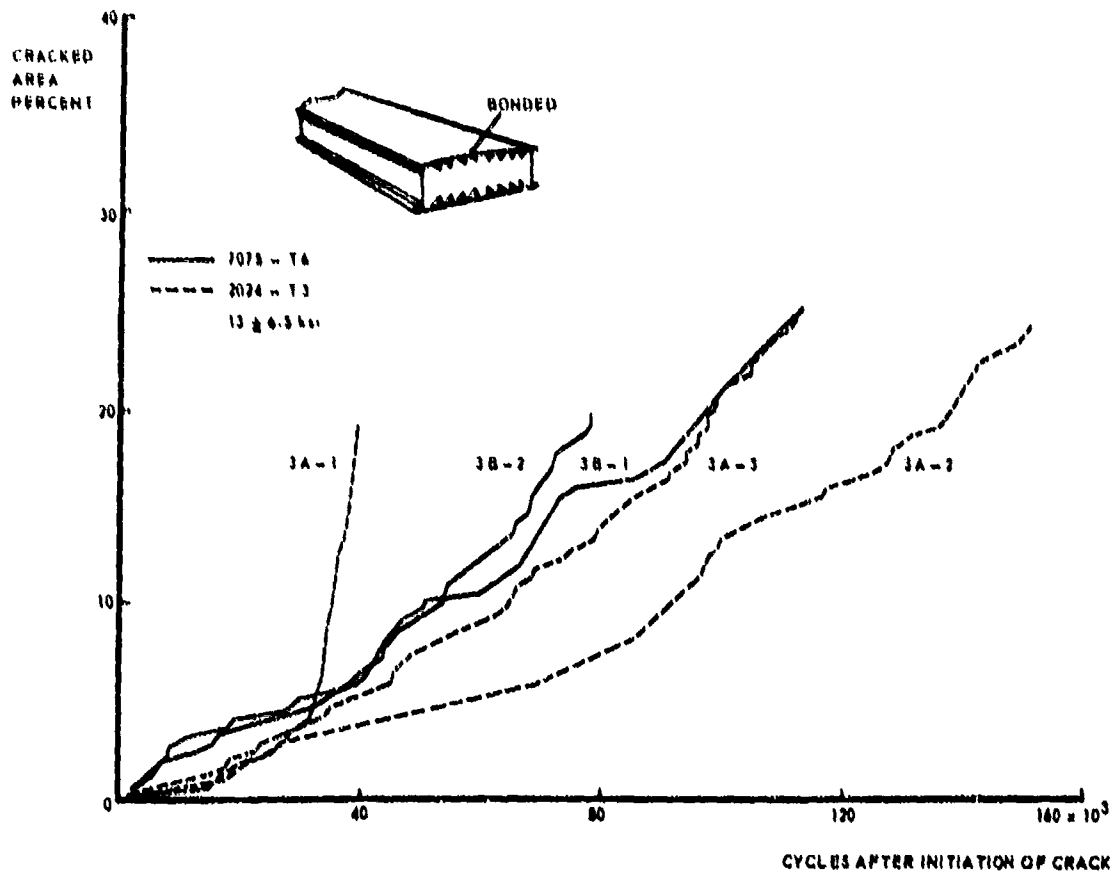
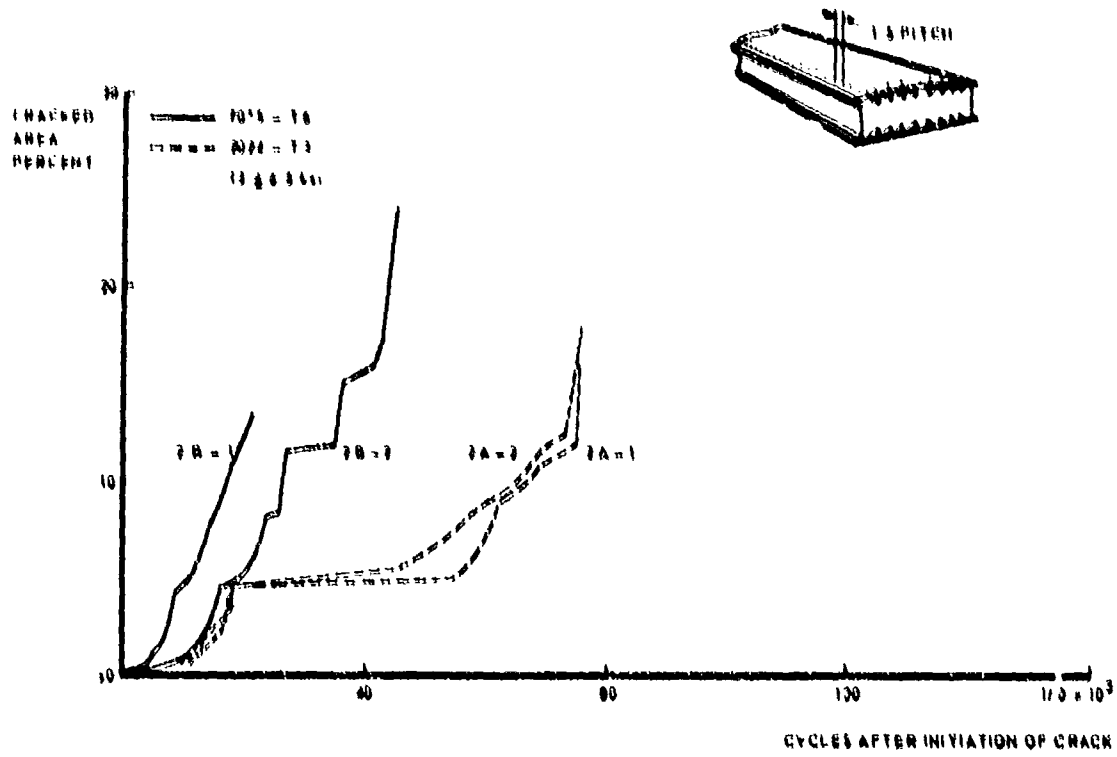


FIG. VB 22 DIFFERENCE BETWEEN REVETED AND ADHESIVE - BONDED STRINGERS (HARDRATH ET AL (32)).

in which  $G$  is the core shear modulus,  $E$  is Young's modulus,  $w$  is panel width,  $t$  is face thickness and  $c$  is core thickness. It appears that a fairly large reduction of the stress intensity can occur. This implies that fatigue crack propagation in sandwich panels will be somewhat slower than in comparable unreinforced sheets.

The stress intensity factor for sandwich panels as determined empirically by Smith et al [29] was lower as the core thickness decreased. This is in qualitative agreement with the calculations of Bartelds and Van de Veer. No fatigue crack propagation data are available to make a fair comparison between a sandwich panel and comparable cracked sheets in order to check whether the lower growth rates in the sandwich skin is in accordance with the reduction in  $K$ .

Table V.B.3

Stress intensity factor of sandwich panels according to Bartelds and Van de Veer [31], given as  $K_a/K_u$ , where  $K_a$  is the stress intensity of the sandwich with one face cracked and  $K_u$  is the stress intensity of a comparable unstiffened sheet.

a/w	Loaded edges supported		All edges supported	
	r = 4	r = 20	r = 4	r = 20
0.09	0.94	0.86	0.94	0.85
0.22	0.85	0.74	0.81	0.70
0.34	0.79	0.68	0.69	0.60
0.47	0.74	0.64	0.57	0.49

#### V.B.2.4 Crack propagation in aircraft structures

A fairly large amount of fatigue crack propagation data are available from tests on full scale aircraft structures. Analysis of these data is not very well possible within the scope of this survey for the following reasons:

- a) Data of comparable unstiffened panels are usually not available.
- b) Part of the tests were carried out at constant amplitude loading, another part at variable amplitude loading.
- c) Stiffening parameters for the various structures are largely different.
- d) Determination of stress intensity factors for all different structures would be a tremendous task.

For the benefit of the reader, who might be interested to analyse some of the data the most extensive reports on fatigue crack propagation tests in large aircraft structures are referenced [32 through 39].

#### V.B.2.5 Crack arrest

Crack arrest has two important aspects. The first is arrest of a fatigue crack, which after a dormant period may reinitiate and continue propagation. The second is arrest of a rapidly growing unstable crack which would have caused catastrophic failure if no arrest had occurred. Both aspects of crack arrest bear largely upon the same principles. The latter aspect of crack arrest receives ample attention in chapter V.C.1, where the problems of tip stress reduction are discussed.

The arrest of a fatigue crack can be achieved by structural means. Some crack stoppers are so-called "natural crack stoppers", others are called "artificial crack stoppers". The latter are often of the same character as the natural crack stoppers, but they are not essential to the structural integrity and they are introduced merely to act as crack stoppers in case cracks develop. In some cases artificial crack stoppers are introduced after a crack developed and was detected, to act as a provisory means, pending a more elaborate repair at a later time, more suitable to the operator. Both natural and artificial crack stoppers are discussed in this section without further attempts to distinguish the two. It should be emphasized that this section concerns itself solely with the prevention of further crack growth by fatigue. The arrest of crack growth under constant load is discussed in chapter V.C.1.

A discussion of means to arrest the growth of fatigue cracks is largely hampered by security measures, which do not allow publication of the available data. The unclassified literature on the subject is extremely scarce and hardly permits the compilation of some qualitative conclusions.

Crack arrest can be attained in three different ways:

- 1) Reduction of the crack tip stress intensity.
- 2) Reduction of the stress concentration.
- 3) Introduction of residual compressive stresses.

Reduction of the crack tip stress intensity can be achieved by load transmittal to other structural members, while the crack tip retains its residual compressive stress as may occur in a stiffened panel where the stringers take over some load of the cracked skin. This problem was discussed extensively in the previous sections of this chapter. A reduction of the stress intensity factor implies that the crack propagation rate is reduced, but there is no complete crack arrest. The reduction in growth rate can

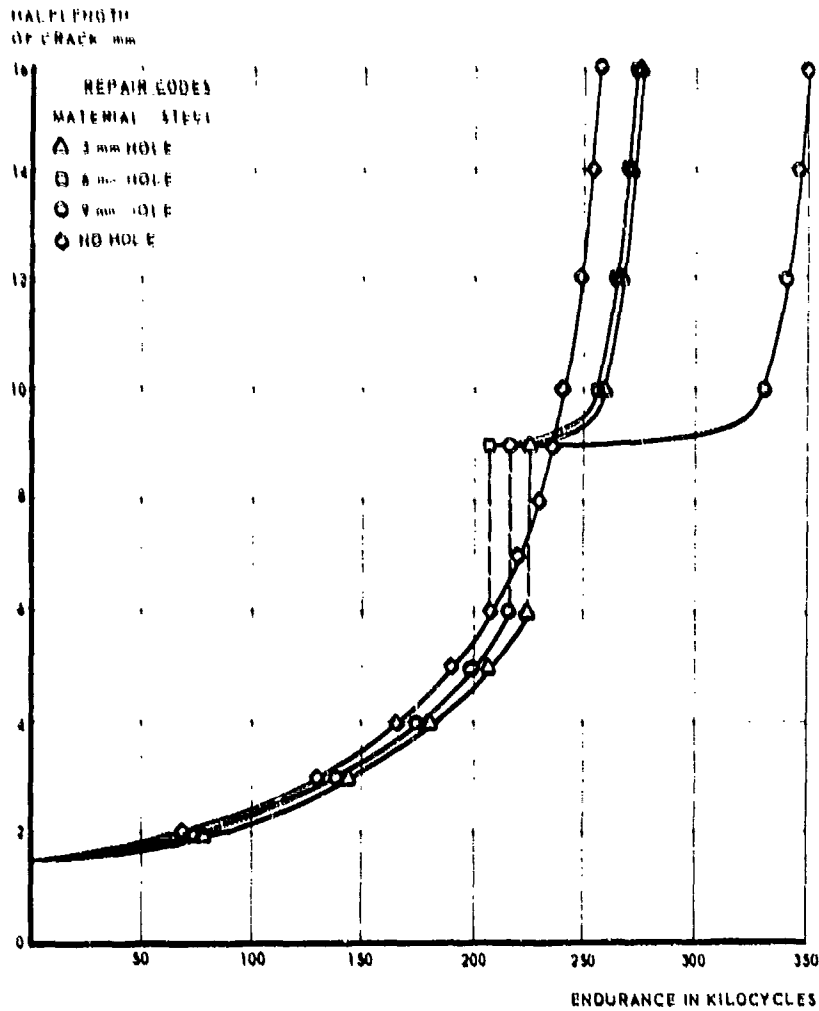


FIG. VB 23 EFFECT OF STOP HOLES ON CRACK GROWTH (VAN LEEUWEN [41]).

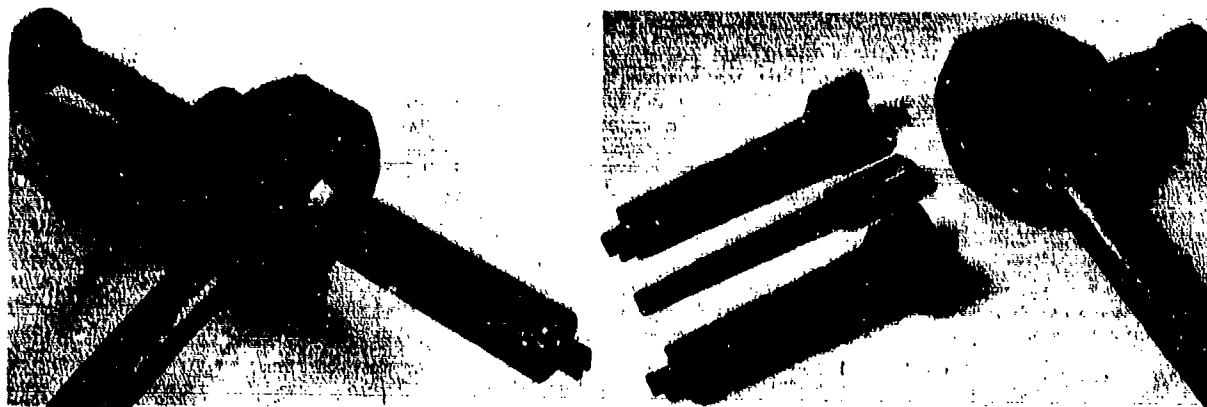


FIG. VB 24 COMPLETED TOOL (LEFT) AND COMPOSING PARTS (RIGHT) OF TOOL TO EXPAND HOLES [40, 41].

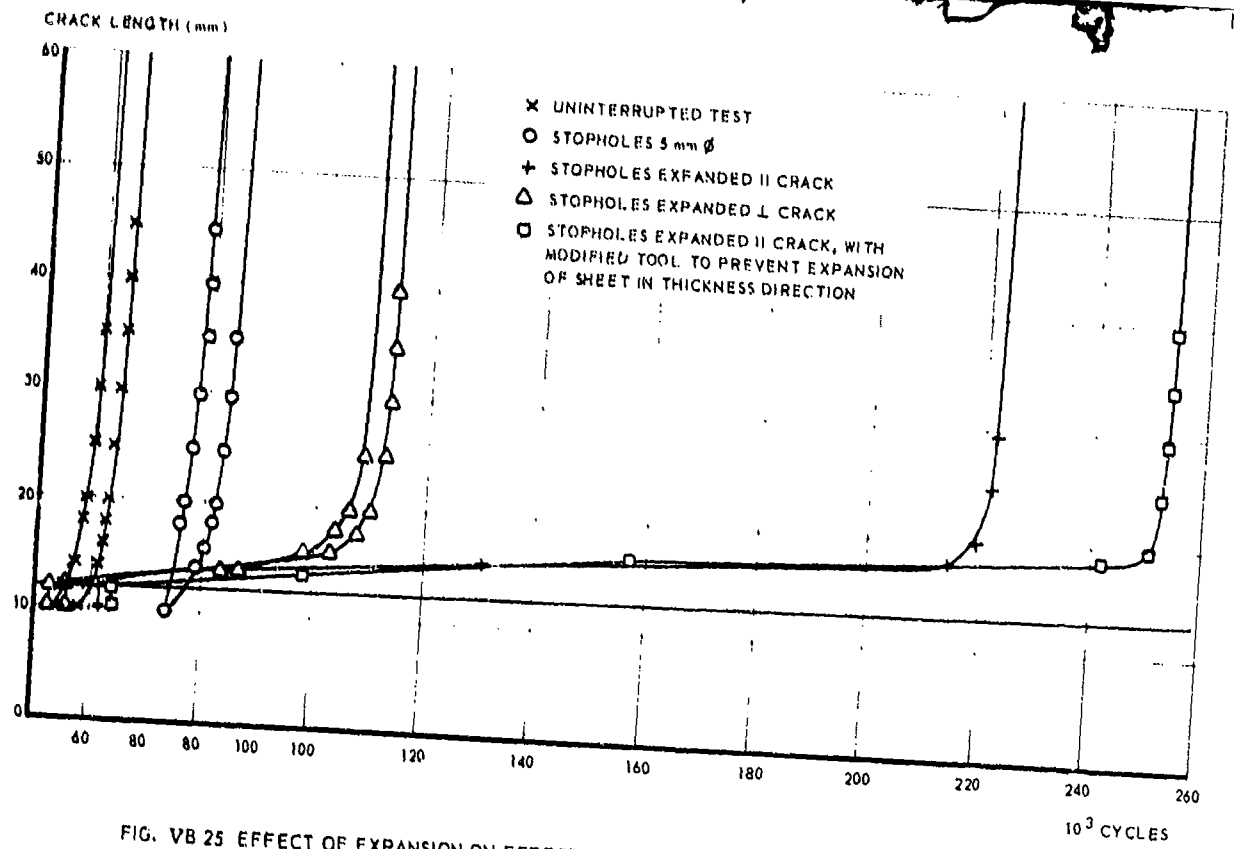


FIG. VB 25 EFFECT OF EXPANSION ON EFFECTIVITY OF STOP HOLES AFTER DE RIJK AND OTTER [42].

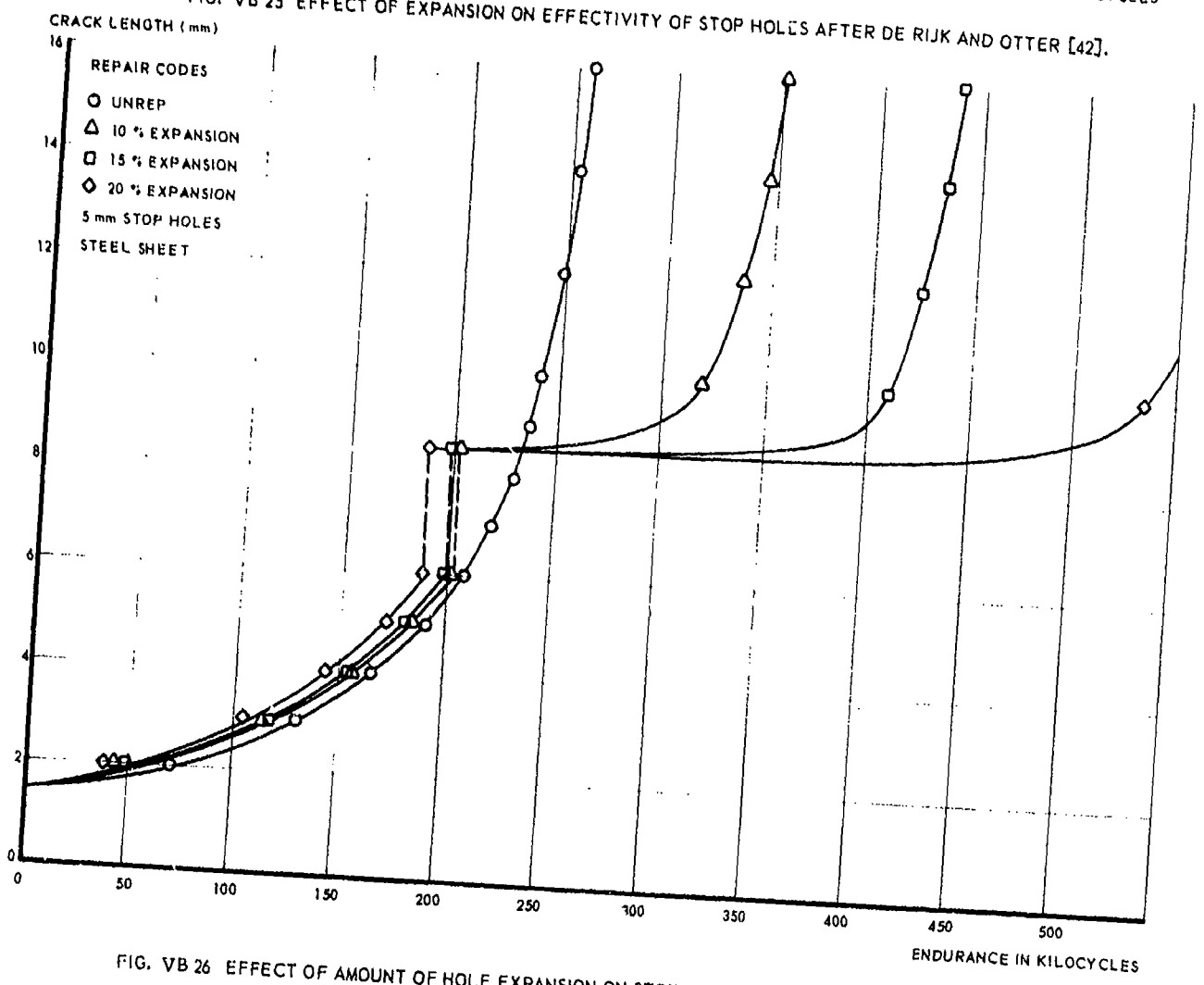


FIG. VB 26 EFFECT OF AMOUNT OF HOLE EXPANSION ON STOP HOLE EFFECTIVITY (VAN LEEUWEN) [41].



FIG. VB 27 EFFECT OF "BRINELL" DIMPLING ON CRACK GROWTH AFTER VAN LEEUWEN [41].

be rationally calculated and depends upon the nature of the stiffening elements as outlined in section V.B.2.

Reduction of the stress concentration occurs when the crack runs into a hole. As was discussed earlier the stress intensity factor then loses its meaning. An even larger reduction of stress concentration occurs when one of a series of parallel elements has completely cracked and reinitiation of cracking has to occur in a neighbouring element.

A crack may run into the hole of a rivet that connects the skin with a tear strap or stringer. This case was paid attention already in section V.B.2 and it was pointed out that this need not always be beneficial. The nearest rivets are further away from the crack tip and therefore the stringer is less effective in taking over load from the skin; consequently crack propagation before the arrest in the rivet hole and crack propagation after reinitiation is faster than in case the crack passes between two rivets. The latter effect may outweigh the gain of the dormant period necessary for crack reinitiation from the rivet hole, but this depends upon the size of the hole. A larger hole will give a larger reduction of the stress concentration and give a longer dormant period.

In case of adhesive - bonded tear-straps or stringers, crack arrest depends completely upon the reduction of the stress intensity factor. In fact there is no real crack arrest, but a reduction of crack growth rate. In figure V.B.22 derived from the work of Hardrath et al [32] on aluminium-alloy box beams, a comparison is made between identical riveted stringers and adhesive-bonded stringers. Crack arrest and dormant periods occurred in the riveted structure where the crack ran into a rivet hole. However, in total the crack-propagation is slower in the bonded structure.

Figure VB 22 confirms the statement made above that crack arrest in a rivet hole need not always be the best solution. On the other hand, it can be predicted on the basis of figure VB 22 that a bonded-and-riveted stringer might have given even better results. If the bonded stringers would have contained widely spaced rivets, crack arrest and a dormant period would have occurred in case the crack would have run into a rivet hole. This would not have impaired the effectiveness of the stringer in this case, since growth before and after arrest would have been as slow as in case of adhesive only. There are no data available to support this reasoning.

In tests on full scale wing center sections [30] it appeared that stop holes alone do not have a large effect. This was confirmed by tests by De Rijk and Otter [40] and by Van Leeuwen et al [41]. This again, shows that the reduction of stress concentration is not very effective and that crack-reinitiation will follow soon, as shown in figure VP 23. However, the situation can be greatly improved if the holes are expanded by cold deformation. This leads to the third means of crack arrest by the introduction of residual compressive stresses, which reduce the effective tension fatigue stress.

De Rijk and Otter [40] and Van Leeuwen et al [41] expanded the stop holes they drilled at the crack tip, by means of a device as depicted in figure VB 24. In essence it consists of a split cylinder which can be made to expand by means of a wedge that is pushed between the two halves of the cylinder. It is specially suited for applications where access to the structure is limited from the outside only. The effect of the method depends upon the amount of stretching as can be appreciated from figures VB 25 and VB 26.

Van Leeuwen et al [41] also studied the effect of filling the normal unexpanded stop hole by brazing a steel plug into the hole in a steel sheet. This proved to be better than an open hole, but it should be noted that brazing may be difficult to apply due to the heating involved.

Other methods of introducing residual stresses to reduce crack growth rates were investigated by Eggwartz et al [42] and by Van Leeuwen et al [41]. They pressed steel balls in the material, leaving a "Brinell" dimple of a certain diameter at the crack tip either at one or both sides of the sheets. Eggwartz et al [42] developed auxiliary equipment enabling application to aircraft structures where access to the structure is limited. The effect of the dimpling on crack growth can be appreciated from figure VB 27.

From the foregoing it may be concluded that the effect of natural crack stoppers depends largely upon the reduction in stress intensity which causes a reduction in crack growth. A smaller benefit has to be expected from a reduction of the stress concentration which causes a dormant period until crack reinitiation. It can also be concluded that artificial crack stoppers should preferably consist of adhesive-bonded tear straps. Their effectivity is based on growth rate reduction by stress reduction. The reduction will be larger if the stiffness of the straps is larger (chapter V.C.1), which may be achieved by a larger cross-section or by applying a strap material with a higher modulus than the skin material. The latter may cause difficulties if the coefficients of thermal expansion of the two materials differ largely. Tear straps will probably have their greatest effectivity if they are adhesive-bonded and riveted; then there will occur a dormant period in addition to the growth rate reduction, if the crack runs into a rivet hole.

If arrest of fatigue cracks depends upon holes or stop-holes the introduction of residual stresses is really necessary. In this respect it should be recommended to expand all those holes which lie in an expected crack path, although this may not be economically feasible. It should finally be noted that expansion of the hole due to riveting does introduce residual tensile stresses rather than compressive stresses. The riveting procedure is therefore not suitable to achieve the required expansion. The use of taper locks introduces residual tensile stresses around the hole. The latter act to increase the mean stress, but to decrease the amplitude of cyclic stresses, which usually also has a beneficial effect.

#### REFERENCES

1. Schijve, J. The analysis of random load-time histories with relation to fatigue tests and life calculations. *Fatigue of Aircraft Structures*, p. 115, Pergamon 1963.
2. Schijve, J. The accumulation of fatigue damage in aircraft materials and structures. AGARDograph No. 157 (1972).

3. De Jonge , J.B. The monitoring of fatigue loads. ICAS Congress Rome (1970) paper 70-31. Also NLR MP-70010 (1970).
4. Van Dijk , G.M. Statistical load data processing. ICAF Symp. Miami (1971). Also NLR MP 71004 (1971).
5. Buxbaum , D. Statistische Zählverfahren als Bindeglied zwischen Beanspruchungsmessungen und Betriebsfestigkeitsversuch. Lab. für Betriebsfestigkeit TR-TB-64, Darmstadt (1966).
6. Coleman , T.L.  
Hunter , P.A. Fatigue loadings on commercial transport airplanes. Air Force Conf. on Fract. and Fatigue (1969). AFFDL TR 70-144 (1970) pp. 123 - 130.
7. Jones , J.W. Airframe environment design considerations. The shape of the turbulence spectrum and probabilities of encountering given peak gust and rms values. Air Force Conf. on Fract. and Fatigue (1969). AFFDL TR 70-144 (1970) pp 159 - 171.
8. Palmgren , A. Die Lebensdauer von Kugellagen. Zeitschrift für Deutsche Ingenieure 68 (1924) pp 339-341.
9. Miner , M.A. Cumulative damage in fatigue. J. Applied Mechanics 12 (1945) pp. A 159 - A 164.
10. Von Euw , E.F.J. Effect of overload cycles on subsequent fatigue crack propagation in 2024-T3. Lehigh University, Ph.D. Thesis (1971).
11. Smith , G.R. Fatigue-service life prediction based on tests at constant stress levels. Proc. SESA 16 (1958) p. 9.
12. Crews , J.H. Elastoplastic stress-strain-behaviour at notch roots in sheet specimens under constant amplitude loading. NASA TN D-5253 (1969). Laboratory simulation of structural fatigue behaviour. ASTM STP 462 (1970) pp 74-91.
13. Morrow , J.D.  
Wetzel , R.H.  
Topper , T.H.
14. Impellizzerri , L.P. Cumulative damage analysis in structural fatigue. ASTM STP 462 (1970) pp. 40 - 68.
15. Schijve , J.  
Jacobs , F.A.
16. Schijve , J.  
Jacobs , F.A.  
Tromp , P.J.
17. Broek , D. Fatigue crack propagation in unnotched and notched aluminium alloy specimens. NLR TR M-2128 (1964).  
Crack propagation in aluminium alloy sheets under flight simulation loading.  
NLR TR-68117 (1968).  
Concepts in fail-safe design of aircraft structures.  
DMIC Memo 252 (1971).
18. Schijve , J.  
Broek , D.
19. Habibie , B.J. Crack-propagation tests based on a gust spectrum with variable amplitude loading. Aircraft Engineering 34 (1962) pp 314-316.  
Eine Berechnungsmethode zum Voraussagen des Fortschritts von Rissen unter beliebigen Belastungen. Messerschmitt-Bölkow-Blohm report UH-03-71. Hamburg (1971).
20. Forman , R.G.  
Kearney , V.E.  
Engle , R.M.
21. Hardrath , H. Numerical analysis of crack propagation in a cyclic loaded structure. ASME Trans. J. Basic Eng 89 D (1967) p. 459.  
A review of cumulative damage. Paper presented to Agard structures and Materials Panel (1965).
22. Schijve , J.  
De Rijk , P.
23. Schijve , J. Crack propagation in a full-scale wing structure under random flight simulation loading. NLR TR 71043 (1971).  
Fatigue tests with random flight-simulation loading.  
NLR MP 71908 (1971).
24. Grief , R.  
Sanders , J.L.
25. Vlieger , H.  
Broek , D.
26. Vlieger , H.
27. Poe , C.C. The effect of a stringer on the stress in a cracked sheet. Harvard University TR 18 (1963).  
Residual strength of cracked stiffened panels.  
NLR-TR-S.653 (1967).  
Residual strength of cracked stiffened panels. NLR-TR-71004 (1971).
28. Poe , C.C. Fatigue crack propagation in stiffened panels.  
ASTM STP 486 (1971) pp 79 - 97.  
The effect of riveted and uniformly spaced stringers on the stress intensity factor of a cracked sheet. Air Force Conf. on fracture and fatigue (1969). AFFDL-TR-70-144 (1970) pp 207 - 216.
29. Smith , S.H.  
Porter , T.R.  
Engstrom , W.L.
30. Broek , D. Fatigue crack propagation behaviour and residual strength of bonded stress reinforced, lamellated and sandwich panels. Air Force Conf. on fracture and fatigue. AFFDL-TR-70-144 (1970) pp 611 - 634.  
Crack propagation and residual strength of full scale wing center sections. NLR-TR-S-612 (1964).
31. Bartelds , G.  
V.d. Veer , I.
32. Hardrath et al , H.F. Elastic energy release rates in cracked sandwich panels.  
NLR-TR-72028 (1972).  
Fatigue crack propagation in aluminium alloy box beams. NACA TN 3856 (1956).
33. Hardrath , H.F.  
Leybold , H.A.
34. Foster , L.R.  
Whaley , R.E.
35. Mann , J.Y.  
Patching , C.A.
36. Parish , H.E.
37. Schijve , J.  
Broek , D.  
et al. Fatigue tests on Mustang wings under random loading.  
A.R.L. Struct. and Met. Note 268 (1961).  
Fatigue of 42 piston Provost-wings. S and T memo 1/65 (1965).  
Fatigue tests with random and programmed load sequences with and without ground-to-air cycles. A comparative study on full-scale wing center-sections. NLR-TR 613 (1965). AFFDL-TR-66-143 (1966).



38. Schijve , J. Fatigue-test results of two full-scale wing center-sections under ground-to-air cycle loading. NLR TR-S-635 (1965).
39. Schijve , J. Fatigue-test results of three full-scale wing center sections under constant amplitude loading. NLR TR-S-640 (1965).
40. De Rijk , P. Empirical investigation on some methods for stopping the growth of fatigue cracks. NLR TR 70021 (1970).
41. De Rijk , P. A.A.M. The repair of fatigue cracks in low-alloy steel sheet.
42. Van Leeuwen , H.P. NLR TR 70029 (1970).
43. Eggwirtz , S. Review of some Swedish investigations on fatigue during the period April 1967 to March 1969. FFA TN-HE-1270 (1969).
44. Wheeler , O.E. Spectrum loading and crack growth. ASME publication (1971). To be published in Journal of Basic Engineering.
44. Willenborg , J. A crack growth retardation model wing on effective stress concept. AFDDL-TM-71-1-FBR (1971).
- Engle , R.H.
- Wood , H.A.

## V.C. RESIDUAL STRENGTH

V.C.1	Built-up Sheet Structures, Wings . . . . .	195
	H. Vlieger and D. Broek	
V.C.1.1	Introduction . . . . .	195
C.1.2	Basic Fracture Behavior of A Cracked Stiffened Panel . . . . .	195
C.1.3	Principles of the Calculation of the Residual Strength Diagram . . . . .	197
C.1.4	Further Refinements, Practical Geometrics . . . . .	203
C.1.5	Crack Arrest . . . . .	205
C.1.6	Residual Strength of Stiffened Panels and Wings. . . . .	209
C.1.7	The R-Curve and the Residual Strength of Stiffened Panels . . . . .	215
C.1.8	Other Analysis Methods . . . . .	215
C.1.9	Sandwich Panels . . . . .	217
C.1.10	Appendix: Calculation of Fastener Forces. . . . .	219
C.1.11	Appendix: Finite Element Analysis of Cracked Panels (G. Bartelds). . . . .	222
	References . . . . .	225

## V.C.1 BUILT-UP SHEET STRUCTURES, WINGS

H. Vlieger and D. Broek

## V.C.1.1 Introduction

This chapter deals with the residual strength of sheet structures. This implies that it considers the condition of plane stress. In the next section the basic fracture behaviour of a stiffened panel is explained in a qualitative way. At present it is possible to calculate the residual strength of a stiffened panel to a high degree of accuracy, provided the residual strength behaviour of an unstiffened sheet of similar size is known. As outlined in the following section the latter requirement does not set any serious restrictions to the technical applicability of the method.

The principles of the calculation method are presented in section 3. Test results are provided to show the usefulness of the procedure to calculate the residual strength of stiffened panels, such as wing panels and tail plane panels. Some additional difficulties arise when the method has to be applied to curved panels loaded by internal pressure such as fuselages. This problem will be dealt with in a separate chapter (V.C.2).

The calculation procedure can be extended to complicated built-up sheet structures, with doublers, reinforcements, stringer run-outs etc. These particular configurations are paid attention in sections 4 and 6 of this chapter. Of course, the method can be further improved. Especially stringer eccentricity, deformation of fasteners and fastener holes will have to be accounted for in further refinements of the method, as is outlined also in section 4. Crack arrest and the usefulness of crack stoppers are treated in section 5. Basically, there is a possibility to incorporate the R-curve concept in the calculation procedure. This may be a worthwhile improvement, once the R-curve concept is better understood.

The last sections of the chapter deal with possible other means of analysis of stiffened panels and the special case of sandwich panels. The mathematics of the calculation procedures are presented in two appendices (sections V.C.1.10 and V.C.1.11).

## V.C.1.2 Basic fracture behaviour of a cracked stiffened panel

Since the calculation of the residual strength of a cracked stiffened panel is based on the residual strength properties of an unstiffened sheet, the behaviour of the latter will be considered briefly here (a more elaborate treatment is given in chapter V.B.3).

In a uniaxially loaded panel with a central transverse crack of length  $2a_0$ , the stress can be raised to  $\sigma_1$  and then the crack will start to grow slowly. This crack growth is stable, i.e. crack propagation can be maintained only if the load is raised further. Ultimately, at a stress  $\sigma_0$ , the crack will reach a length  $2a_c$  where it will propagate unstably at constant stress, resulting in final failure of the panel. The longer the initial crack, the lower the values of  $\sigma_1$  and  $\sigma_0$  as illustrated by the curves in figure V.C.1. The middle curve relates the fracture stress directly to the initial crack length  $2a_0$ . For the application to stiffened panels it is not strictly necessary that the events described obey a constant K concept, i.e.  $K_{II}$ ,  $K_{Ia}$  and  $K_{Ic}$  need not be constants (see chapter V.A.3), but it is useful to describe the events in terms of the stress intensity factor. This problem will be discussed in some more detail later in this chapter. (Note  $K_I$  is used here for opening mode cracking instead of  $K_{II}$ , since the problem is plane stress; this is done in accordance with chapter V.A).

When the panel is provided with stiffeners the stress distribution in the cracked region is different. The stringers provide extra stiffness that tends to decrease the stress at the crack tip by load transfer from sheet to stringer. In this connection two significant dimensionless parameters have to be introduced, namely the "tip stress reduction factor"  $C_R$  and the "stringer load concentration factor"  $L_B$ . The tip stress reduction factor  $C_R$  is defined as the ratio of the stress intensity factors for sheets with and without stringers

$$C_R = \frac{K_{\text{stiffened}}}{K_{\text{unstiffened}}} < 1 \quad (1)$$

The stringer load concentration factor is defined as the ratio of the maximum stringer load and the load in the stringer remote from the cracked section:

$$L_B = \left[ \frac{P_{\text{MAX}}}{P_{\infty}} \right]_{\text{stiffener}} > 1 \quad (2)$$

The values of  $C_R$  and  $L_B$  depend upon the stiffening ratio, the stiffness of the attachment, and the ratio of crack length to stringer spacing. As shown in section 3 of this chapter  $C_R$  and  $L_B$  can be calculated for various configurations of cracked stiffened panels. For the qualitative discussions in this chapter it is sufficient to know the parameters that affect  $C_R$  and  $L_B$ . Figure V.C.2 shows diagrammatically how  $C_R$  and  $L_B$  vary for the case of a central crack between two stiffeners. For cracks in the order of the stringer spacing the stringer is very effective leading to high  $L_B$  and low  $C_R$ .

Figure V.C.3 depicts the residual strength diagram of a simple panel with two stiffeners, containing a central crack. The behaviour of this panel will be analysed in detail below. In figure V.C.3 the lines a, b and c represent the residual strength curves for the unstiffened panel, like those in figure V.C.1. Because of the presence of the stringers the stress intensity factor will be reduced by a

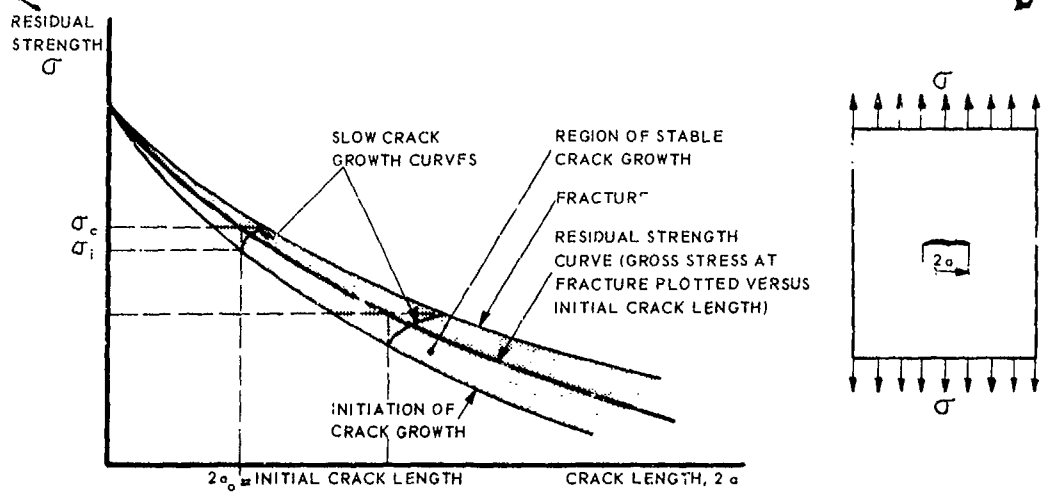


FIG. V C 1 RESIDUAL STRENGTH CURVE OF UNSTIFFENED PANEL.

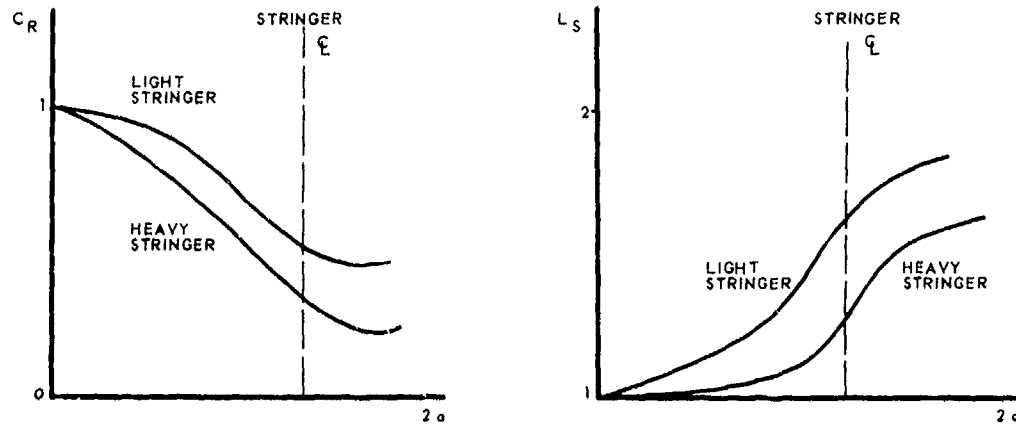


FIG. V C 2 VARIATION OF  $C_R$  AND  $L_S$  WITH CRACK LENGTH IN STIFFENED PANEL WITH CRACK BETWEEN STIFFENERS.

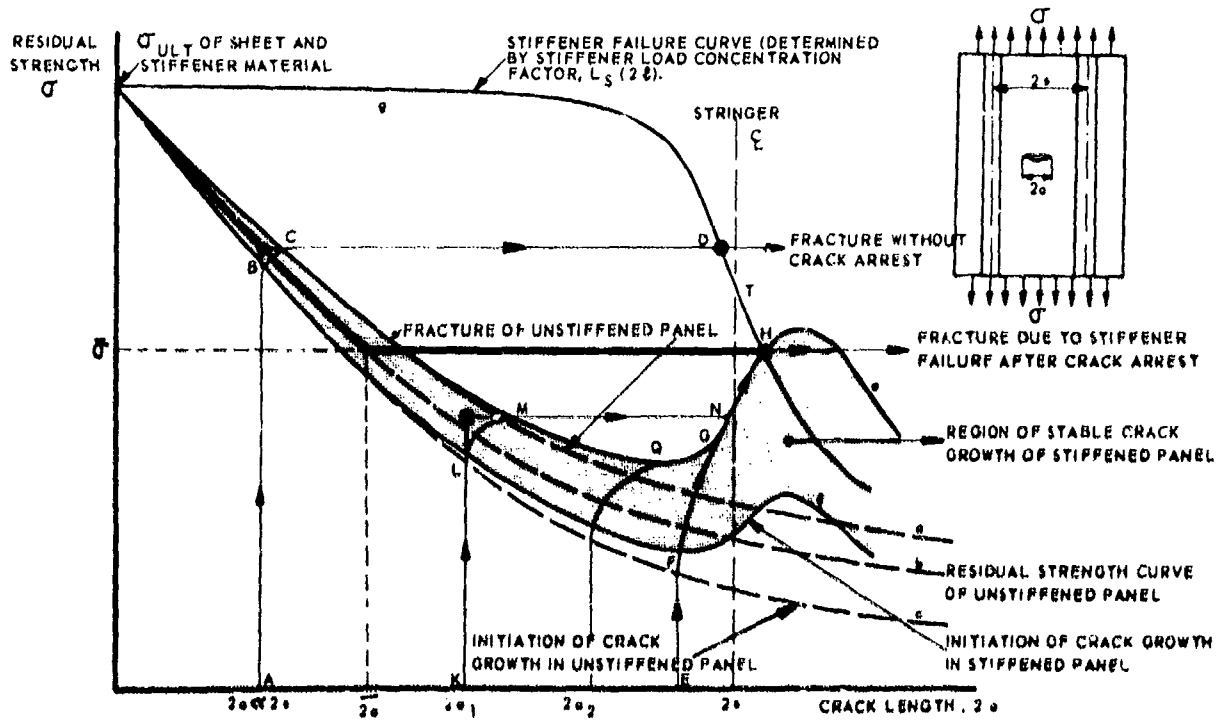


FIG. V C 3 RESIDUAL STRENGTH DIAGRAM FOR SIMPLE STIFFENED PANEL.

factor  $C_R < 1$ . Assuming that crack propagation in the stiffened panel occurs at the same stress intensity factor as in the unstiffened panel, the stress to propagate a crack will be increased by a factor  $1/C_R$ . This means that the lines e and c will be raised to e and f, respectively. These curves show a maximum for a crack slightly larger than the stringer spacing because the maximum tip stress reduction occurs when the crack extends slightly beyond the stringer center line (see Fig. V C.2).

However, in a stiffened panel also the possibility of stringer failure should be considered. Line g in figure V C.3 is the locus for stringer failure. When there is no crack ( $2a = 0$ ) the stringer will fail at its UTS. When the crack approaches the stringer, the load concentration factor  $L_g$  will increase, so that the stringer will fail at a lower nominal stress. Strictly speaking, the line g is determined by the equation

$$\sigma_{\text{failure}} = \frac{\sigma_{\text{UTS stringer}}}{L_g} \quad (3)$$

however as soon as the stringer starts to yield,  $L_g$  has to be corrected.

In case the crack is still small at the onset of instability ( $2a \ll 2s$ , where  $2s$  is stringer spacing) the stress condition at the crack tip will hardly be influenced by the stringers and the stress at unstable crack growth initiation will be the same as that of an unstiffened sheet of the same size. When the unstably growing crack approaches the stiffener, the load concentration in the stiffener will be so high that the stiffener fails without stopping the unstable crack growth (line ABCD in figure V C.3).

When the panel contains a crack extending almost from one stiffener to the other ( $2a \approx 2s$ ), the stringer will be extremely effective in reducing the peak stress at the crack tips ( $C_R$  small), resulting in a higher value of the stress at crack growth initiation at point P in figure V C.3. With increasing load, the crack will grow stably to the stiffener (EFGH) and due to the inherent increase of stiffener effectiveness, the crack growth will remain stable. (Actually, no unstable crack growth will occur for crack lengths larger than  $2a_s$ ). Fracture of the panel will occur at the stress level indicated by  $\bar{\sigma}$  due to the fact that the stiffener has reached its failure stress and the stress reduction in the skin is no longer effective after stringer failure.

For cracks of intermediate size ( $2a = 2a_s$ ), there will be unstable crack growth at a stress slightly above the fracture strength of the unstiffened sheet (point M), but this will be stopped under the stiffeners at N. After crack arrest the panel load can be further increased at the cost of some additional stable crack growth until H, where the ultimate stringer load is reached, again at the stress level  $\bar{\sigma}$ .

For the simple panel of figure V C.3 the actual residual strength curve is of the shape indicated by the solid line. This curve contains a horizontal part determined by the intersection of lines e and g. For initial cracks smaller than the stiffener spacing, this flat part constitutes a lower bound of the residual strength.

It has been outlined that  $C_R$  and  $L_g$  depend upon stiffening ratio (Fig. V C.2). In fact, this implies that the residual strength diagram of figure V C.3 is not unique. It shows the case that stringer failure is the critical event. For other stiffening ratios skin failure may be the critical event. This is depicted in figure V C.4. Due to a low stringer load concentration the curves e and g do not intersect. A crack of size  $2a_s$  will show stable growth at point B and become unstable at point C. Crack arrest occurs at D from where further slow growth can occur if the load is raised. Finally at point E the crack will again become unstable, resulting in panel fracture. Apparently, a criterion for crack arrest has to involve the two alternatives of stringer failure and skin failure, depending upon the relative stiffness of sheet and stringer.

It may be clear from the foregoing that it is not essential for crack arrest that the crack runs into a fastener hole. Crack arrest is basically a result of the reduction of crack tip stress intensity due to load transmittal to the stringer.

Figures V C.5 and V C.6 present some test data of Vlieger [2,3] for riveted panels with simple symmetric strip stiffeners. To achieve crack arrest in a rivet hole and between rivets, two locations of the line of the initial crack with respect to the nearest rivets were chosen: through and between rivet holes. However, in all cases the crack path at fracture extended through rivet holes in both directions independent of the location of the initial crack. So, in fact only specimens in which the crack path ran through rivet holes were investigated for this panel type. The test data confirm the predicted behaviour. The residual strength diagrams indeed contain a horizontal level. (Solid line indicated by  $\bar{\sigma}$ ). In case of a short crack (specimen 4 in figure V C.5) fracture instability occurs at a stress too high for crack arrest at the stringer. The panel failure stress is the same as for a comparable unstiffened sheet. Longer initial cracks show some slow crack growth and then a sudden fast crack growth. Crack arrest occurred at the stringer, after which the panel could be loaded to the horizontal level where final failure occurred.

In the following sections the methods to calculate the residual strength diagram will be considered and more test data for more practical panel configurations will be presented.

### V.C.1.3 Principles of the calculation of the residual strength diagram

Methods to calculate the tip stress reduction factor have been developed independently by Vlieger [1,2,3], Swift and Wang [4,5], Poe [6,7] and Creager and Liu [14]. Application of the tip stress reduction factor and the stringer load concentration factor to establish the residual strength characteristics of stiffened panels were proposed by Vlieger [2,3] and Swift and Wang [4,5].

In calculating  $C_R$  and  $L_g$  two different methods can be used viz., the finite element method and an analytical method. An analytical method has advantages over the finite element method in that the

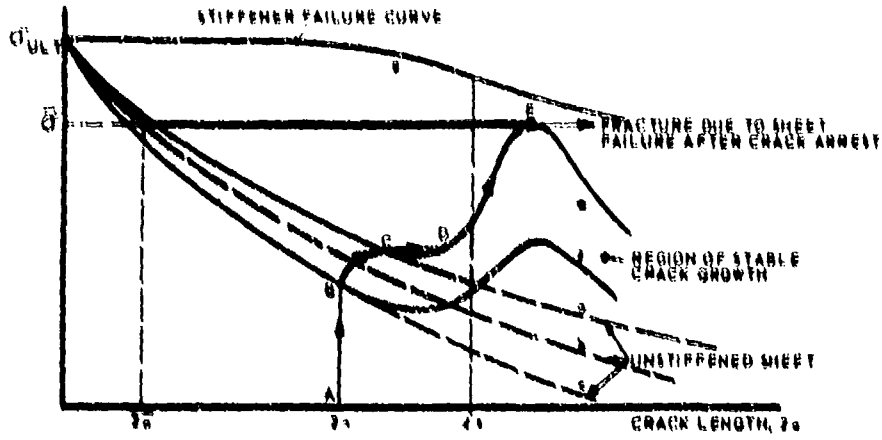


FIG. V C 4 PANEL CONFIGURATION WITH HEAVY STIFFENERS. "SKIN - CRITICAL." CASE.

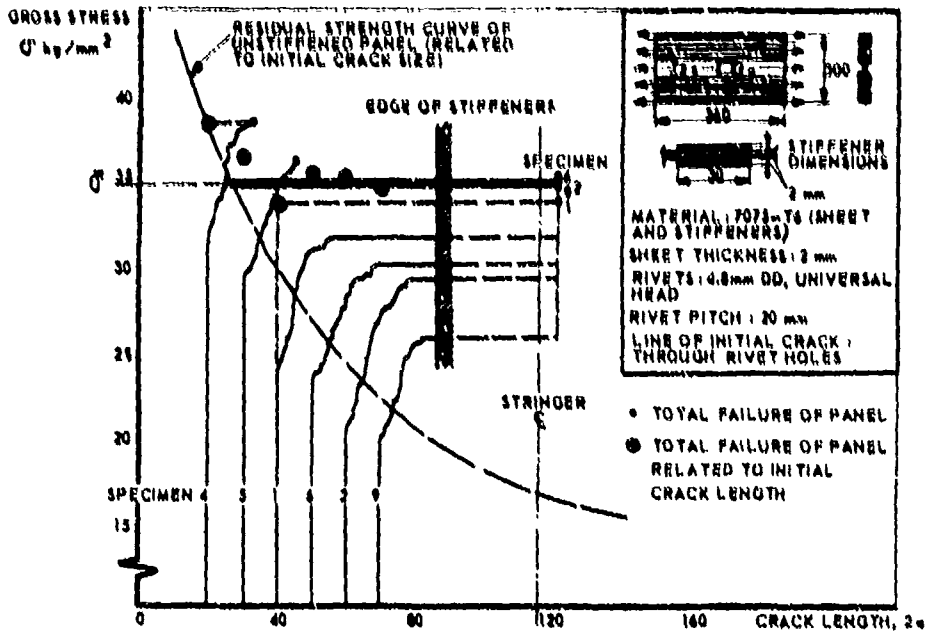


FIG. V C 5 RESIDUAL STRENGTH TEST DATA OF SIMPLE STIFFENED PANEL. LINE OF INITIAL CRACK THROUGH RIVET HOLES [2, 3].

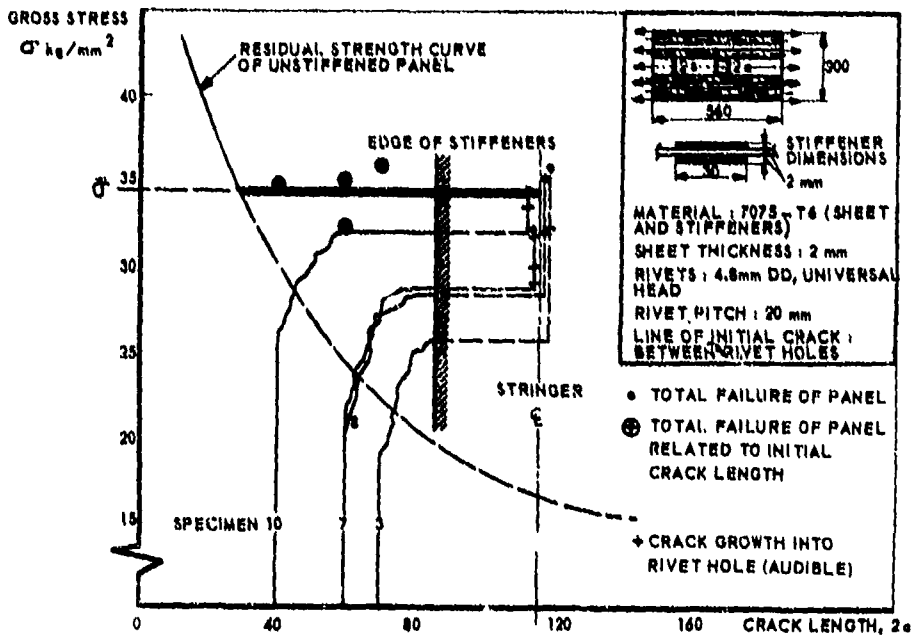
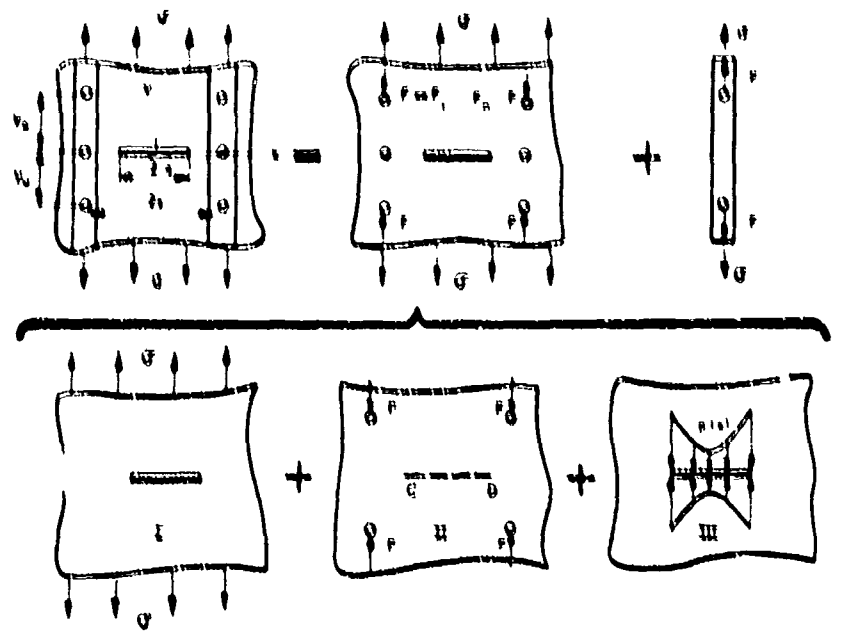


FIG. V C 6 RESIDUAL STRENGTH TEST DATA OF SIMPLE STIFFENED PANELS. LINE OF INITIAL CRACK BETWEEN RIVET HOLES [2, 3].



STRESS INTENSITY FACTORS

$$K_G = \sigma \sqrt{K_0}$$

$$K = 0$$

$$K_F = \frac{2\sqrt{K_0}}{\pi} \int_0^{\pi/2} \frac{p(\theta) d\theta}{\sqrt{1 - \sin^2 \theta}}$$

$$\text{WHERE } p(\theta) = \frac{F V_n}{\pi (V_0^2 + (a + b)^2)} \left[ \frac{3 + \nu}{2} - (1 + \nu) \frac{(a - b)^2}{V_0^2 + (a + b)^2} \right] +$$

$$\frac{F V_0}{\pi (V_0^2 + (a + b)^2)} \left[ \frac{3 + \nu}{2} - (1 + \nu) \frac{(a + b)^2}{V_0^2 + (a + b)^2} \right]$$

WHEN THE RIVET FORCES  $F$  ARE KNOWN IT FOLLOWS

$$L_s = 1 + \frac{F}{\sigma A_s} \quad C_R = \frac{K_G + K_F}{K_G}$$

Fig. V C 7 CALCULATION OF  $L_s$  AND  $C_R$  FROM THE ANALYTICAL METHOD

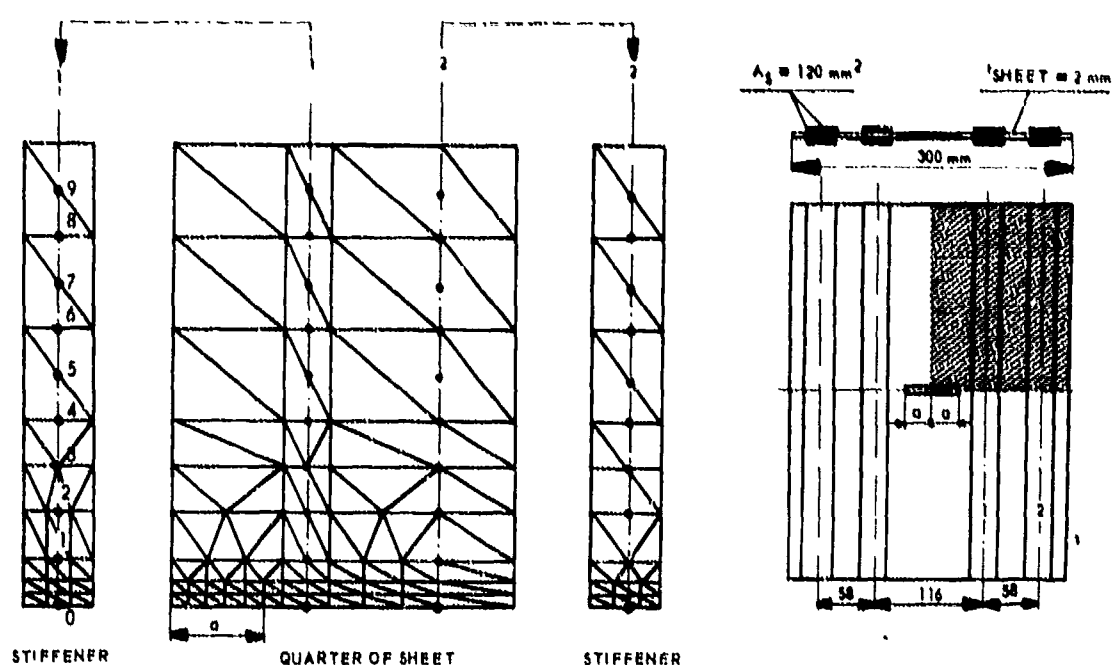


Fig. V C 8 IDEALIZATION OF CRACKED STIFFENED PANEL (451 NODAL POINTS, 196 TRIM - 6 ELEMENTS, 856 UNKNOWN) [2, 3]

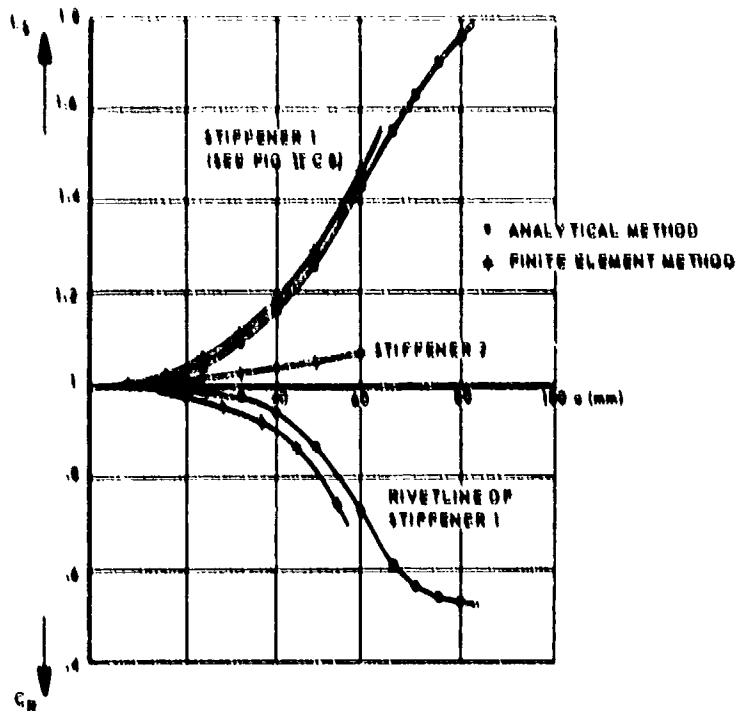


FIG. V C 9 COMPARISON OF FINITE ELEMENT METHOD AND ANALYTICAL METHOD ACCORDING TO VLIEGER [2, 3]

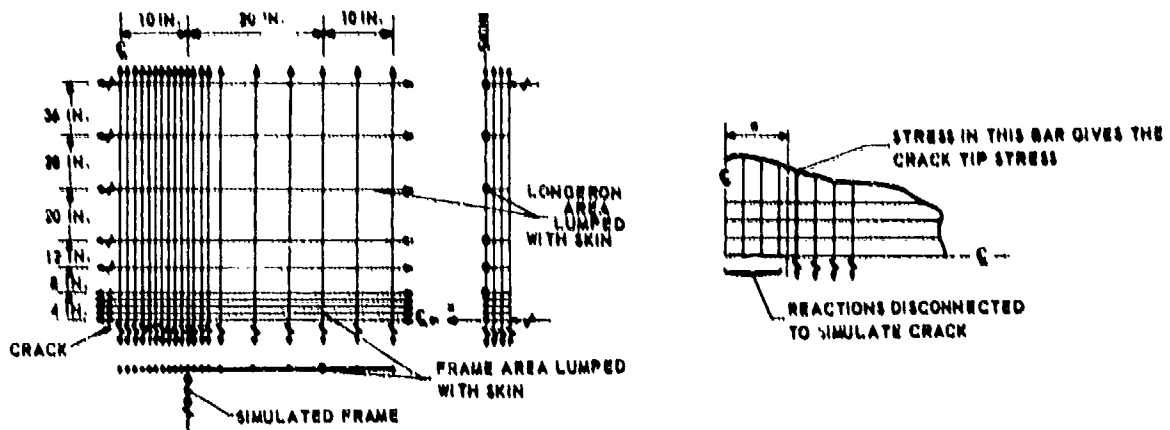


FIG. V C 10 FINITE ELEMENT ANALYSIS OF SWIFT AND WANG [4, 5]

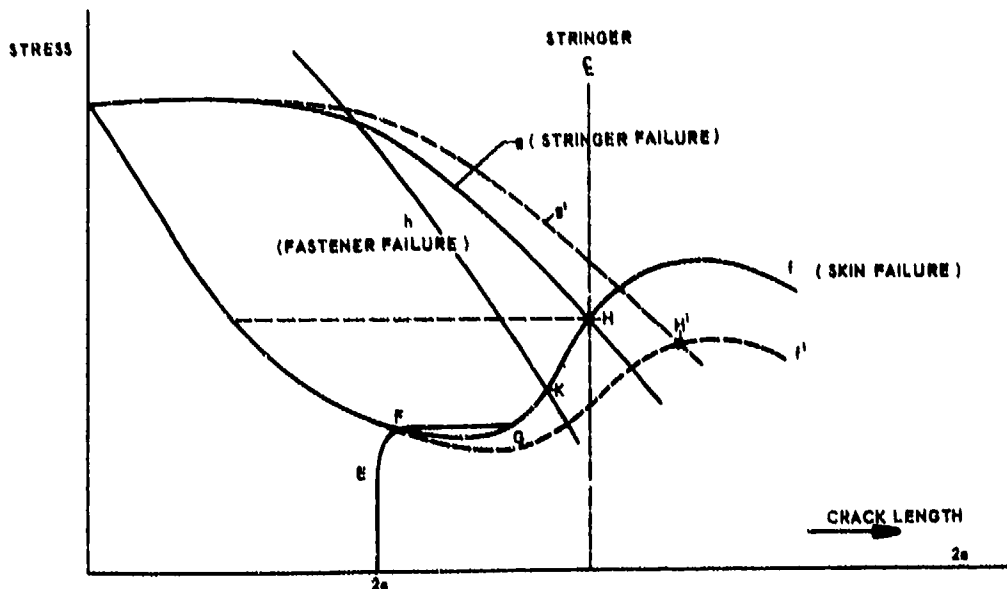


FIG. V C 11 CRITERION FOR FASTENER FAILURE



#### V.C.1.4 Further refinements practical assumptions

So far, the discussion was limited to skin critical and stringer critical configurations. Of course, a third criterion exists, which concerns fastener failure. Load transmittal from the skin to the stringer takes place through the fasteners (fastener loads  $F_1 \dots F_n$ ). If the fastener loads become too high, fastener failure may take place by shear. Fastener failure will reduce the effectivity of the stringer and therefore the residual strength will drop. The fastener loads  $F_1 \dots F_n$  follow from the calculations described in section V.C.1.10. The highest loads will be  $F_i$  on the fasteners adjacent to the crack path. The magnitude of  $F_i$  to fail the fasteners by shear can be calculated and the nominal stress in the panel to reach  $F_i$  then gives a third line  $h$  in the residual strength diagram depicted in figure V.C.1.1.

At zero crack length the fasteners do not carry any load, so line  $h$  tends to infinity for  $2a \rightarrow 0$ . For the particular case depicted in figure V.C.1.1 the residual strength is no longer determined by stringer failure solely (dashed horizontal line through point H) but possibly by fastener failure (point K). A crack of length  $2a$ , will show slow growth from E to F and instability from F to G. After crack arrest at G further slow growth occurs until at X the fasteners fail. The latter will probably cause panel failure, but this cannot be directly determined from the diagram. In fact a new residual strength diagram has now to be calculated, with omission of the first row of rivets at either side of the crack. Fastener failure will affect load transmittal from the skin to the stringer: line  $f$  will be lowered, line  $g$  will be raised. The intersection  $H'$  of the new lines  $g'$  and  $f'$  may still be above K and hence, the residual strength will still be determined by stringer failure at  $H'$ .

In reality the behaviour will be more complicated due to plastic deformation. Shear deformation of the fasteners, hole deformation and also plastic deformation of the stringers will occur before fracture takes place. This plastic deformation always leads to a reduction of the effectivity of the stringer to take load from the skin. This implies that line  $g$  will be raised and line  $f$  will be lowered. The intersection of the two lines (failure point) will not be affected to a great deal, however (compare points H and  $H'$  in figure V.C.1.1). This is the reason why the residual strength of a stiffened panel can still be predicted fairly accurately, even if plasticity effects are ignored [2,3]. Nevertheless a proper treatment of the problem requires that plasticity effects are taken into account. In case of the analytic method the plasticity effects can be accounted for in an approximate way as indicated by Creager and Liu [14]. They assumed in their calculations an infinite linear elastic skin and elastic, perfectly plastic tensile and shear elements for stringer and fastener, respectively. First the set of  $n$  independent equations (following from equal displacements in skin and stiffener of the  $n$  fasteners) corresponding to the elastic solutions is solved (see section V.C.1.10). This will deliver the  $n$  unknown fastener forces. This procedure is continued until either a fastener or a stringer yields. When one of both elements yields the equation following from the displacement of the concerning element is discarded. In case of yielding of one fastener  $F_i$  the remaining  $(n-1)$  equations can be solved, replacing in these equations the fastener force  $F_i$  by its yield force. In case of yielding of a stringer in the  $i$ th interval ( = interval between fasteners  $i$  and  $i+1$ ) the discarded equation is replaced by

$$\sigma + \frac{1}{A} \sum_{j=i+1}^n F_j = \sigma_{ys} \quad (5)$$

where  $A$  is stringer cross-sectional area and  $\sigma_{ys}$  is yield stress of stringer material.

Swift [5] and Swift and Wang [4] using a finite element analysis method take into account deformation of fastener and fastener holes. They use empirical relations. They apply the formula for the deflection  $b$  [4,5]:

$$b = \frac{F}{E_s d} \left[ 5.0 + 0.8 \left( \frac{d}{B} \frac{E_s}{E_s} + \frac{d}{R} \frac{E_s}{E_r} \right) \right] \quad (6)$$

in which  $F$  is the rivet force,  $d$  is the rivet diameter,  $B$  and  $R$  are the thicknesses of skin and reinforcement and  $E_s$ ,  $E_s$  and  $E_r$  are Young's moduli of attachment, skin and reinforcement, respectively. This formula is based on displacement measurements on simple lap splice specimens.

Another problem that has to be accounted for is stringer eccentricity. The eccentrically stiffened configuration differs from the symmetric strip arrangement in two respects:

- a) The eccentric stiffener has a lower effective stiffness and therefore less load is transferred from sheet to stiffener.
- b) The eccentrically loaded stiffener will cause bending of the panel in the region of the crack tip.

The eccentricity of the rivet forces with respect to the stiffener cross section gives rise to a non-uniform stress distribution which is shown diagrammatically in figure V.C.1.2. When shear deformations are neglected, a simple linear distribution results (Fig. V.C.1.2a). Shear deformations introduce an additional non-uniformity due to shear lag (Fig. V.C.1.2b). With regard to these effects the following qualitative remarks can be made:

- a) Stiffener bending is partly prevented by the pre-stress  $\sigma$  in both stiffener and sheet, and
- b) Shear lag and also stiffener bending reduce the effective stiffness of the stringer in the vicinity of the crack, resulting in a lower stiffener load (Fig. V.C.1.2b).

Both circumstances tend to reduce the maximum stringer stress and to neutralize the effects of stiffener eccentricity. The reduction of stringer stiffness due to shear lag will depend on the ratio between rivet pitch and developed stiffener width. As a result, for the dimensions of the Z-stringer under consideration, a larger reduction in stiffness and a lower stiffener load can be expected in case of a crack that runs through rivet holes, than in case of a crack between rivet holes. This is confirmed by test results of Vlieger [2,3] to be discussed in section V.C.1.5.

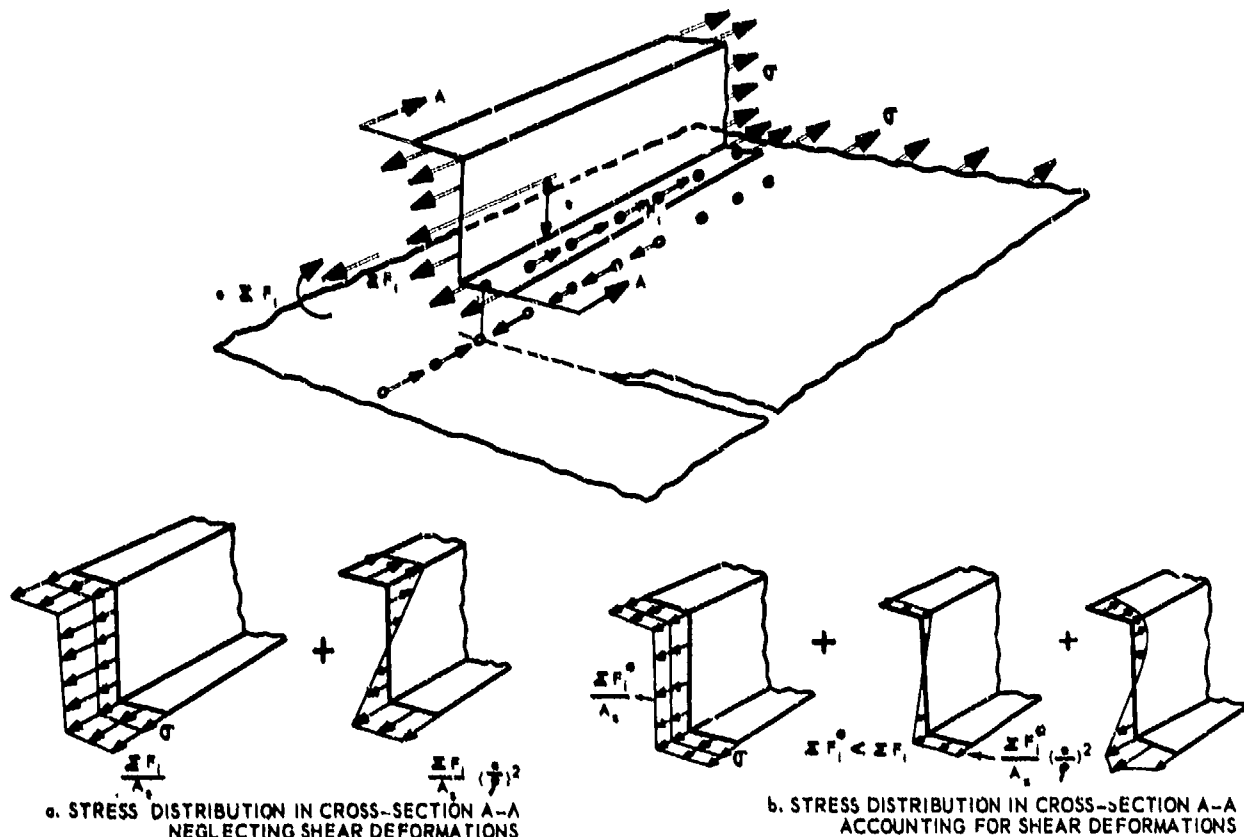


FIG. V C 12 EFFECT OF STRINGER SHEAR ON STRESS DISTRIBUTION.

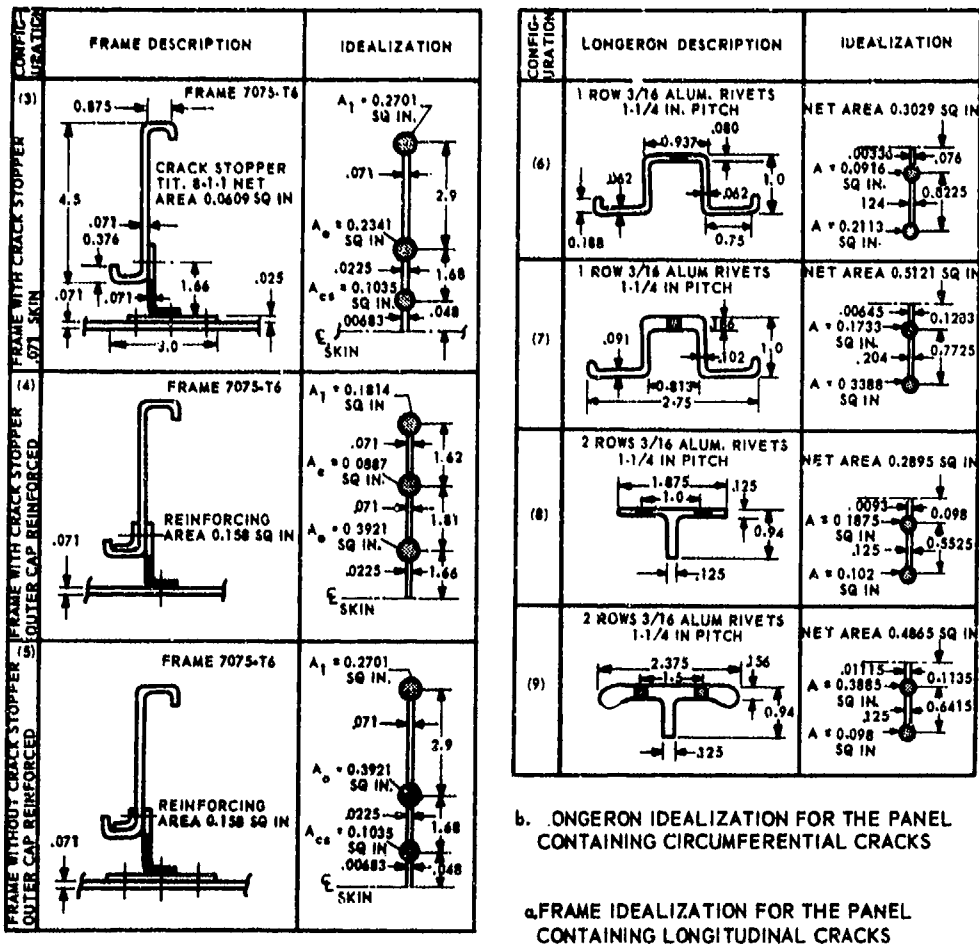


FIG. V C 13 IDEALIZATION OF STIFFENING ELEMENTS BY SWIFT AND WANG [4,5] (FINITE ELEMENT ANALYSIS)

#### V.C.1.4 Further refinements practical geometries

So far, the discussion was limited to skin critical and stringer critical configurations. Of course, a third criterion exists, which concerns fastener failure. Load transmittal from the skin to the stringer takes place through the fasteners (fastener loads  $F_1, \dots, F_n$ ). If the fastener loads become too high, fastener failure may take place by shear. Fastener failure will reduce the effectivity of the stringer and therefore the residual strength will drop. The fastener loads  $F_1, \dots, F_n$  follow from the calculations described in section V.C.1.10. The highest loads will be  $F_1$  on the fasteners adjacent to the crack path. The magnitude of  $F_1$  to fail the fasteners by shear can be calculated and the nominal stress in the panel to reach  $F_1$  then gives a third line h in the residual strength diagram depicted in figure V.C.11.

At zero crack length the fasteners do not carry any load, so line h tends to infinity for  $2a \rightarrow 0$ . For the particular case depicted in figure V.C.11 the residual strength is no longer determined by stringer failure solely (dashed horizontal line through point H) but possibly by fastener failure (point K). A crack of length  $2a$ , will show slow growth from E to F and instability from F to G. After crack arrest at G further slow growth occurs until at K the fasteners fail. The latter will probably cause panel failure, but this cannot be directly determined from the diagram. In fact a new residual strength diagram has now to be calculated, with omission of the first row of rivets at either side of the crack. Fastener failure will affect load transmittal from the skin to the stringer: line f will be lowered, line g will be raised. The intersection H' of the new lines g' and f' may still be above K and hence, the residual strength will still be determined by stringer failure at H'.

In reality the behaviour will be more complicated due to plastic deformation. Shear deformation of the fasteners, hole deformation and also plastic deformation of the stringers will occur before fracture takes place. This plastic deformation always leads to a reduction of the effectivity of the stringer to take load from the skin. This implies that line g will be raised and line f will be lowered. The intersection of the two lines (failure point) will not be affected to a great deal, however (compare points H and H' in figure V.C.11). This is the reason why the residual strength of a stiffened panel can still be predicted fairly accurately, even if plasticity effects are ignored [2,3]. Nevertheless a proper treatment of the problem requires that plasticity effects are taken into account. In case of the analytic method the plasticity effects can be accounted for in an approximate way as indicated by Creager and Liu [14]. They assumed in their calculations an infinite linear elastic skin and elastic, perfectly plastic tensile and shear elements for stringer and fastener, respectively. First the set of n independent equations (following from equal displacements in skin and stiffener of the n fasteners) corresponding to the elastic solutions is solved (see section V.C.1.10). This will deliver the n unknown fastener forces. This procedure is continued until either a fastener or a stringer yields. When one of both elements yields the equation following from the displacement of the concerning element is discarded. In case of yielding of one fastener  $F_i$  the remaining (n - 1) equations can be solved, replacing in these equations the fastener force  $F_i$  by its yield force. In case of yielding of a stringer in the i-th interval (- interval between fasteners i and i + 1) the discarded equation is replaced by

$$\sigma + \frac{1}{A} \sum_{j=i+1}^n F_j = \sigma_{ys} \quad (5)$$

where A is stringer cross-sectional area and  $\sigma_{ys}$  is yield stress of stringer material.

Swift [5] and Swift and Wang [4] using a finite element analysis method take into account deformation of fastener and fastener holes. They use empirical relations. They apply the formula for the deflection  $\delta$  [4,5]:

$$\delta = \frac{F}{E_s d} \left[ 5.0 + 0.8 \left( \frac{d}{B_s} \frac{E_s}{E_a} + \frac{d}{B_r} \frac{E_s}{E_r} \right) \right] \quad (6)$$

in which F is the rivet force, d is the rivet diameter,  $B_s$  and  $B_r$  are the thicknesses of skin and reinforcement and  $E_s$ ,  $E_a$  and  $E_r$  are Young's moduli of attachment, skin and reinforcement, respectively. This formula is based on displacement measurements on simple lap splice specimens.

Another problem that has to be accounted for is stringer eccentricity. The eccentrically stiffened configuration differs from the symmetric strip arrangement in two respects:

- The eccentric stiffener has a lower effective stiffness and therefore less load is transferred from sheet to stiffener.
- The eccentrically loaded stiffener will cause bending of the panel in the region of the crack tip.

The eccentricity of the rivet forces with respect to the stiffener cross section gives rise to a non-uniform stress distribution which is shown diagrammatically in figure V.C.12. When shear deformations are neglected, a simple linear distribution results (Fig. V.C.12a). Shear deformations introduce an additional non-uniformity due to shear lag (Fig. V.C.12b). With regard to these effects the following qualitative remarks can be made:

- Stiffener bending is partly prevented by the pre-stress  $\sigma$  in both stiffener and sheet, and
- Shear lag and also stiffener bending reduce the effective stiffness of the stringer in the vicinity of the crack, resulting in a lower stiffener load (Fig. V.C.12b).

Both circumstances tend to reduce the maximum stringer stress and to neutralise the effects of stiffener eccentricity. The reduction of stringer stiffness due to shear lag will depend on the ratio between rivet pitch and developed stiffener width. As a result, for the dimensions of the Z-stringer under consideration, a larger reduction in stiffness and a lower stiffener load can be expected in case of a crack that runs through rivet holes, than in case of a crack between rivet holes. This is confirmed by test results of Vlieger [2,3] to be discussed in section V.C.1.5.

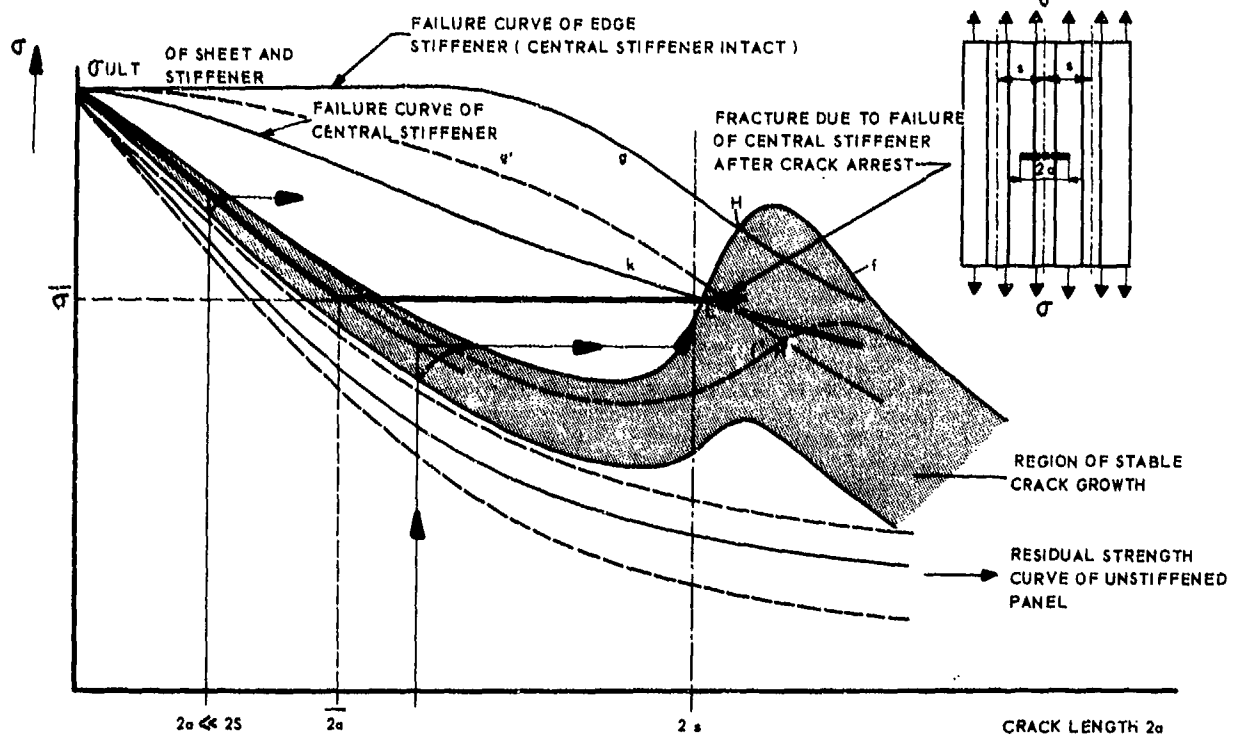


FIG. V C. 14 RESIDUAL STRENGTH DIAGRAM FOR A PANEL WITH THREE STIFFENERS AND A CENTRAL CRACK .

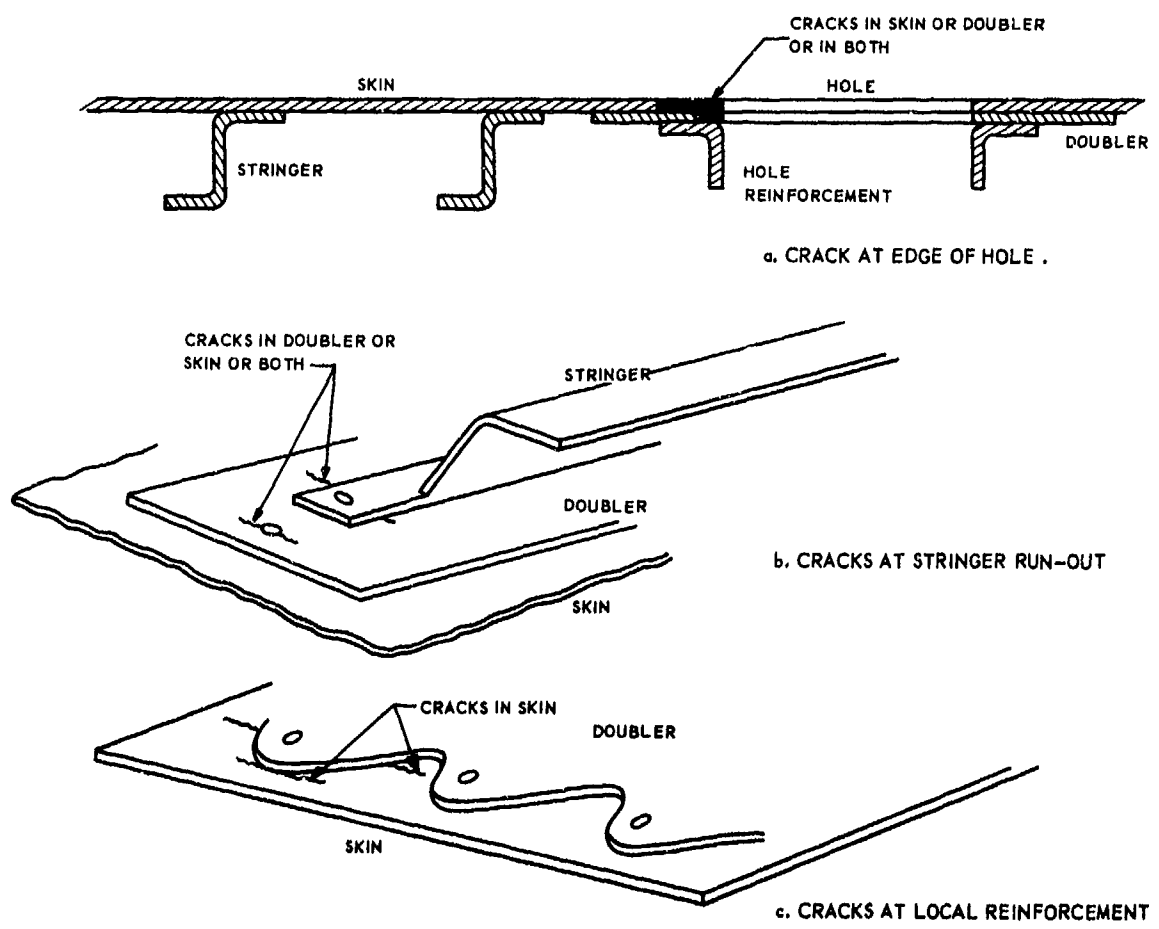


FIG. V C. 15. PRACTICAL CASES OF CRACKS IN BUILT-UP SHEET STRUCTURES

As pointed out already, stringer eccentricity can be easily accounted for in finite element methods. The idealisation of stringers by Swift and Wang [4,5] by lumped bars and shear panels has already been shown in figure V C.11. Swift and Wang also made analyses of more complicated geometries, such as skin-shear clipframe attachments. Figure V C.13 shows how they idealised various complicated arrangements of stiffening elements [4,5] by lumped bars and shear elements.

So far the discussion was limited to cracks between two stiffeners. In practice, however, cracks will usually start at a fastener hole and then there will be a stringer across the crack. This stringer will have a high load concentration factor. The problem can be dealt with in a similar way as the crack between stringers, either analytically or with finite element procedures. A schematic residual strength diagram for this case is presented in figure V C.14. Apart from the curve g for the edge stiffeners there will now be an additional failure curve k for the central stiffener. Failure of the panel may be determined by the intersection L of curves f and k where the central stringer fails. If that occurs the lines g and f are not valid any more, since both the skin and the edge stiffeners will have to take the extra load from the failed stringer; this will lower both the line g and f, to g' and f' and in general point H' will be lower than L. The latter will have to be checked in a complete analysis.

Due to the high load concentration, the middle stringer will usually fail fairly soon by fatigue (see section V.B.2.2) and therefore the lines g' and f' with the middle stringer failed will have to be used and the residual strength is determined by point H'. (Note that g', f' and H' will have different positions in the absence of the middle stringer; a cracked stringer will induce higher stresses in both the skin and the edge stiffener).

The case of a central stringer can still easily be treated with the analytical method if eccentricity effects are ignored. In practice, however, the geometries in which cracks occur will usually be so complicated that proper solution can only be arrived at by a finite element analysis. A few of such practical cases are shown in figure V C.15. The residual strength diagram of such cases will be somewhat different from those presented so far, but there will be no principal differences. In case of a skin crack with an intact doubler, the latter will take load from the skin and act in the same way as a stringer in the cases discussed here. If both skin and doubler are cracked, the doubler will transmit extra load to the skin and there will be an increase of the tip stress instead of a reduction.

It may be clear from the foregoing discussions that it is necessary to establish a complete residual strength diagram also for such practical cases depicted in figure V C.15. This implies that the situation has to be analyzed for various crack sizes, otherwise the behaviour of the structure cannot properly be checked. If for example in figure V C.3 one would only consider one crack size  $2a = 2s$ , then only the points N and T would be determined. These points give no information on the residual strength which is determined by H. When using finite element methods it is necessary to adopt such a procedure as the one used by Swift and Wang [4,5] where different crack sizes can be simulated by subsequently disconnecting successive elements in the crack path. Otherwise a completely new analysis would have to be made for another length of crack.

Finally this section will have to deal briefly with the case of adhesive bonded and integral stiffeners. In the analytical method these can be treated by assuming uniformly distributed fastener forces  $F_1 \dots F_n$  along the stringers. Similar procedures can be thought of for finite element methods. It should be noted that the criterion of stringer failure is not relevant in case of integral stiffeners, since the crack can run right through the stiffeners. In that case there will only be a skin crack propagation criterion, but this will still be different from the case of riveted stringers: the integral stringer will already be partly cracked if the crack size equals the stringer spacing.

In case of adhesively bonded stringers the criterion of fastener failure (or rather adhesive failure) will be important. Load transmittal from the skin to the stringer in the cracked area will set up high shear stresses in the bond. This may lead to decohesion and consequently, a decrease of the effectiveness of the stringer to take load from the skin; decohesion will alter the residual strength diagram as in the case of fastener failure discussed earlier in this section (Fig. V C.11).

#### V.C.1.5 Crack arrest

As pointed out in the foregoing sections, arrest of unstable crack growth at the next stringer is governed by three criteria:

- a) Stringer failure.
- b) Fastener failure or bond failure.
- c) Skin crack propagation.

If any of these three criteria are met, total failure will occur.

#### a. Stiffener failure criterion

According to equation (2) the ratio between the load in the stiffener in the cracked region ( $F_{max}$ ) and remote from the crack ( $F_{\infty}$ ), is defined as the load concentration factor  $L_S$  or

$$L_S = \frac{F_{max}}{F_{\infty}} = \frac{F_{max}}{\sigma A_s} \quad (7)$$

where  $\sigma$  is the uniform stress at the loaded end of the panel and  $A_s$  is the stiffener sectional area. Failure of the stiffener will occur when the value of  $F_{max}$  is equal to the ultimate strength of the stiffener ( $F_{ult}$ ), or when

$$F_{max} = F_{ult} = \psi \sigma_{ult} A_s \quad (8)$$

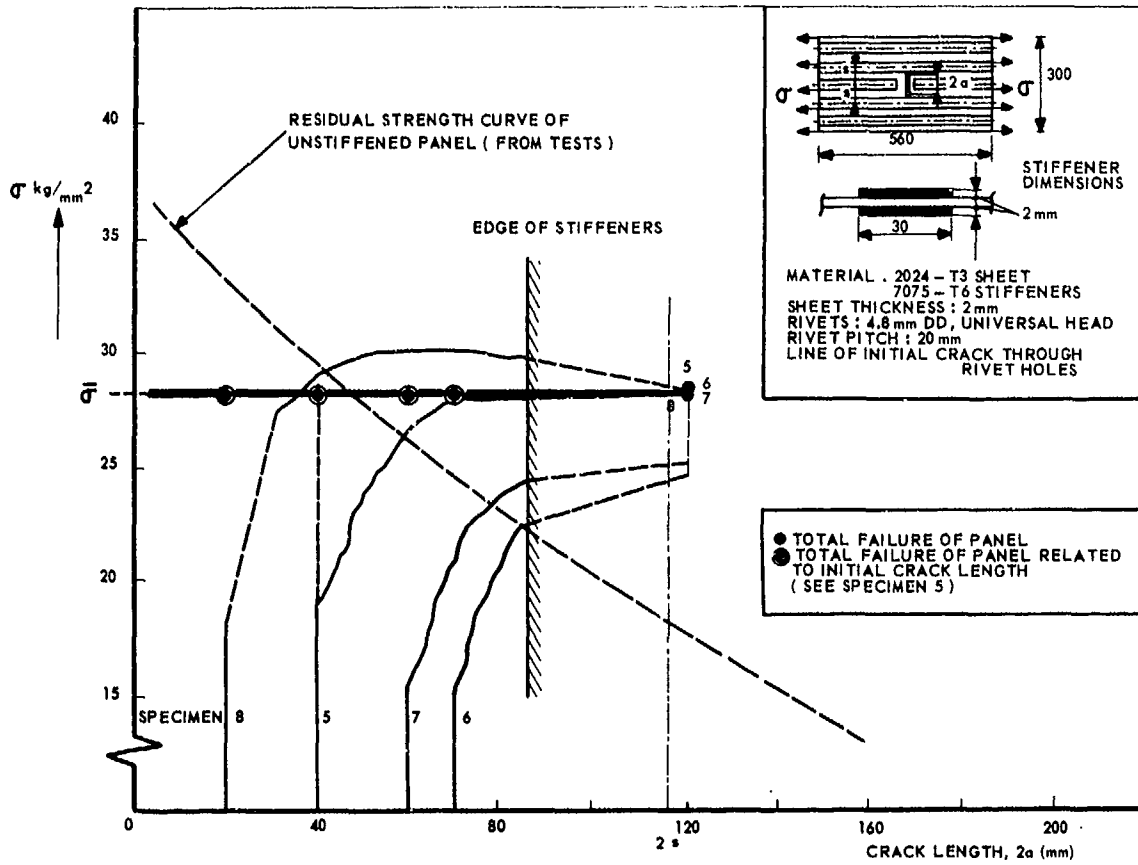


FIG. V C 16 TEST RESULTS OF STIFFENED PANELS WITH 2024 - T3 SKIN AND A BROKEN CENTRAL STIFFENER [3]

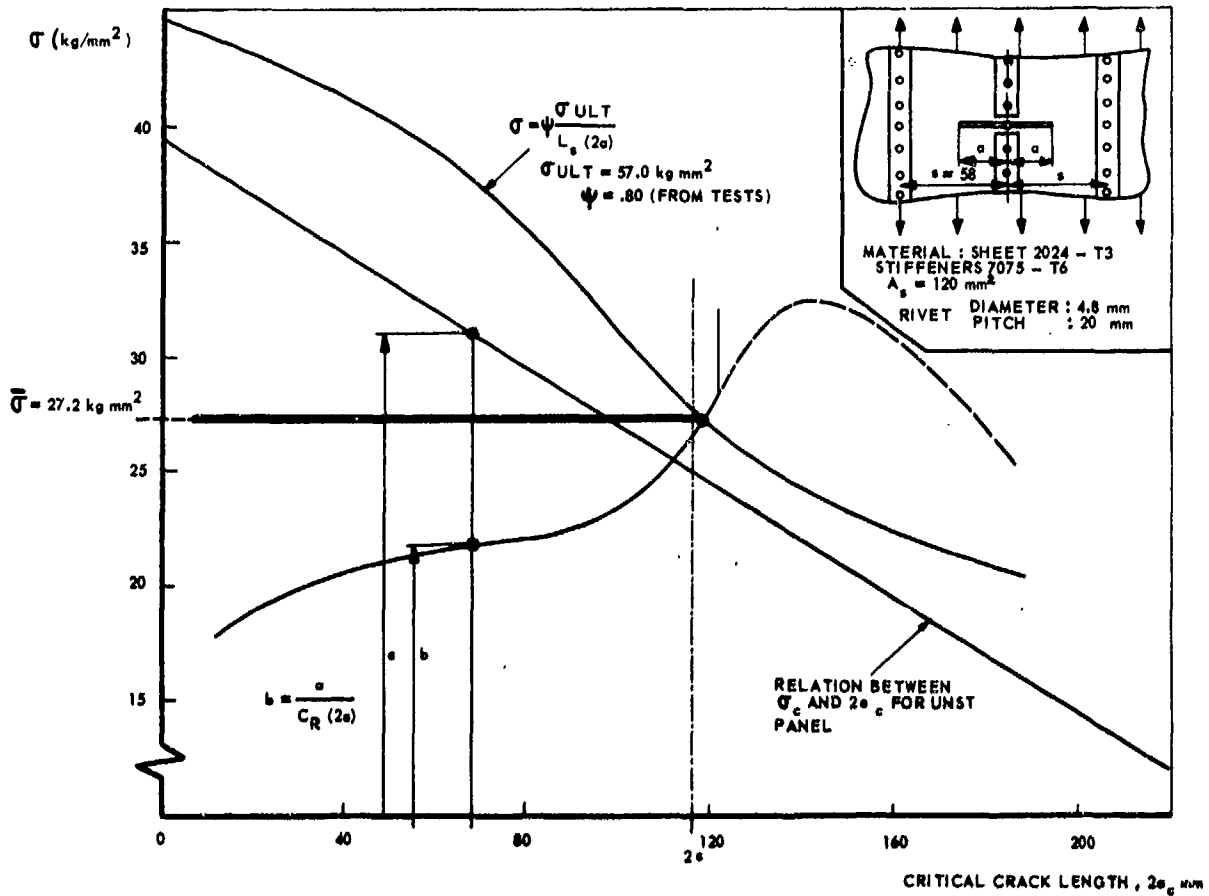


FIG V C 17 PREDICTED RESULTS FOR PANEL CONFIGURATION OF FIG. V C 16. [3]

where  $\sigma_{ult}$  is the ultimate tensile strength of the stiffener material and  $\psi \leq 1$  is a factor accounting for load eccentricity and notch effects in the stiffener. If there is a uniform stress distribution in the panel remote from the crack, then the stress in the stringer will equal the nominal stress  $\sigma$  in the skin, i.e.

$$F_{cs} = \sigma A_s \quad (9)$$

Combining equations (8) and (9) yields the following stiffener failure criterion:

$$\sigma = \psi \frac{\sigma_{ult}}{L_s} \quad (10)$$

#### b. Fastener failure criterion

Fastener failure will occur when the fastener forces  $F_1$  transmitted by the fasteners adjacent to the crack exceed the critical shear load of the fastener. The fastener failure criterion is then given by

$$F_1 = \frac{\pi}{4} d^2 \tau_{ult} \quad (11)$$

where  $d$  is the fastener diameter and  $\tau_{ult}$  is the ultimate shear stress of the fastener material. It has to be emphasized that fastener failure need not necessarily cause total failure of the panel as has been pointed out in the foregoing. If the fastener failure criterion is met, the values for  $L_s$  and  $C_R$  will change; the stringer failure criterion and the skin crack criterion will have to be re-checked in a new analysis.

#### c. Skin crack criterion

The intensity of the stress field in the neighbourhood of the crack tip of an unstiffened sheet is governed by the stress intensity factor  $K$  defined as

$$K_{unstiffened} = f \left( \frac{a}{w} \right) \sigma \sqrt{\pi a} \quad (12)$$

where  $f(a/w)$  is a width correction factor (Chapter V.B). According to equation (1) the effect of the stiffener on the stress condition at the crack tip is expressed by the tip stress reduction factor  $C_R$  defined as

$$C_R = \frac{K_{stiffened}}{K_{unstiffened}} \quad (13)$$

Hence the stress intensity factor of the stiffened sheet can be expressed as

$$K_{stiffened} = C_R f \left( \frac{a}{w} \right) \sigma \sqrt{\pi a} \quad (14)$$

Assuming that skin crack propagation occurs when  $K_{stiffened}$  has a value equal to the plane stress fracture toughness of the unstiffened sheet,  $K_{Ic}$ , then the stiffened skin crack resistance curve is given by the relation

$$\sigma_{skin} = \frac{K_{Ic}}{C_R f \left( \frac{a}{w} \right) \sqrt{\pi a_c}} \quad (15)$$

It has to be emphasized that the skin crack criterion need not necessarily be based on  $K_{Ic}$ . For the determination of the stiffened sheet failure stress a relation between  $\sigma$  and  $2a_c$  of the unstiffened panel has to be available; this relation need not be dictated by  $K_{Ic}$  = constant, since a simple data-plot will suffice. This data plot will give the failure stress  $\sigma_c$  of the unstiffened panel as a function of  $2a_c$

$$\sigma_c = f(2a_c) \quad (16)$$

In order to apply this to the stiffened panel the additional assumption is required that skin crack propagation in the stiffened panel will occur when the stress at the crack tip is the same as in the unstiffened sheet at the particular crack length under consideration. Hence, the skin crack criterion is given by

$$\sigma_{skin} = \frac{\sigma_c}{C_R} \quad (17)$$

This means that the skin crack resistance curve can be obtained by raising all points of the unstiffened panel curve by a factor  $1/C_R$  pertinent to the particular length of crack.

The latter procedure will usually have to be applied in case of 2024-T3 skin material for which an actual  $K_{Ic}$  value usually cannot be determined (except for extremely large panels). Comparison of the test data of figure V C.16 with the predicted results (figure V C.17) indicates that the procedure works satisfactorily. A comparison of results of tests and theory for panels with edge stiffeners and a 7075-T6 skin, which yields a valid  $K_{Ic}$ , can be made by considering figures V C.5 and V C.18b.

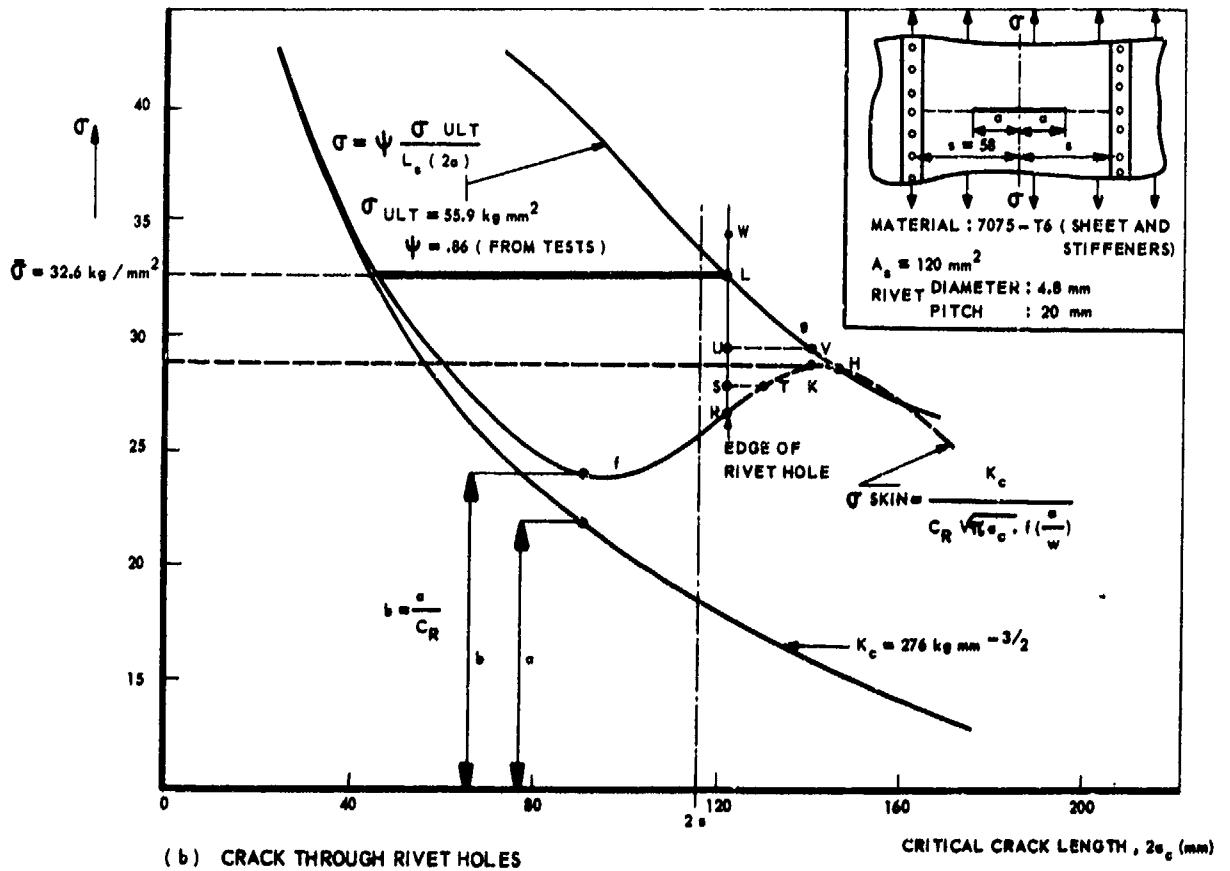
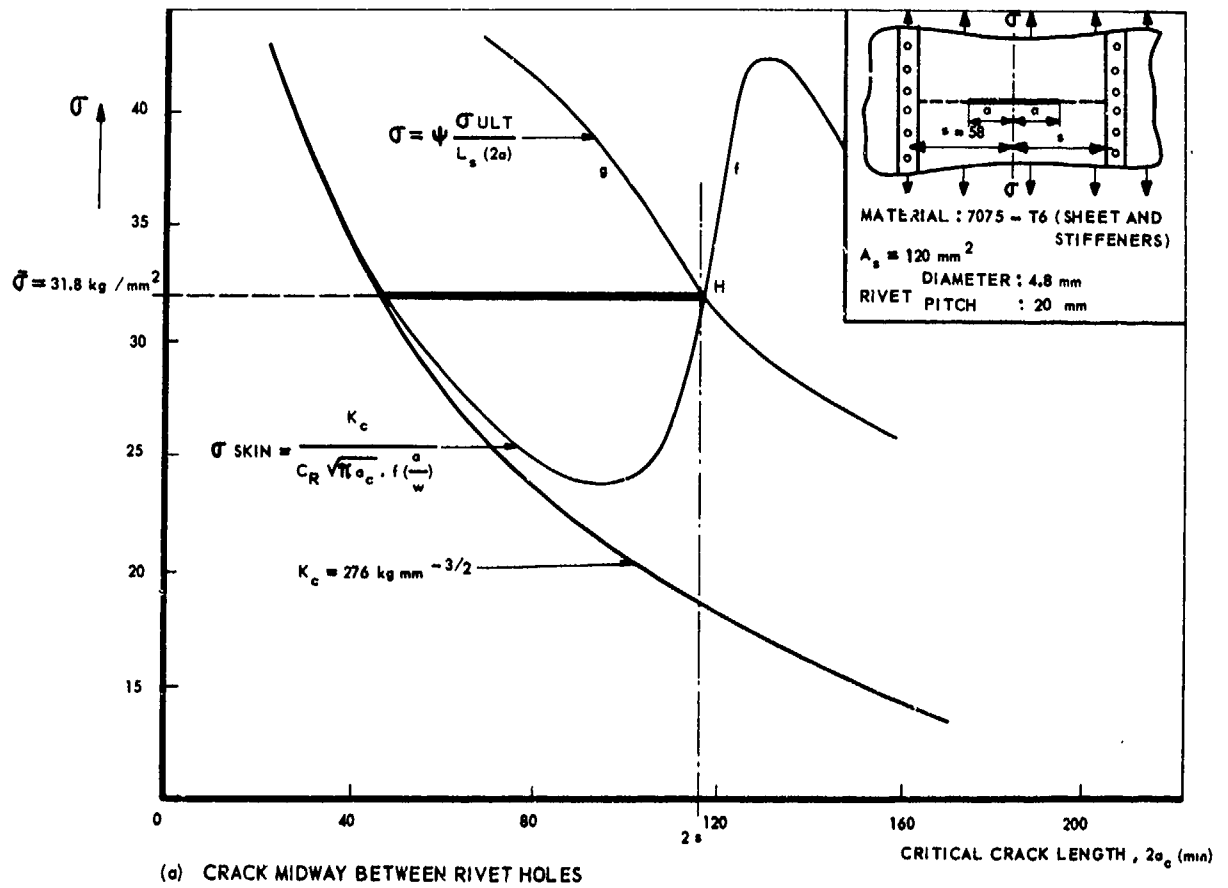


FIG. V C 18 EFFECT OF CRACK RUNNING INTO RIVET HOLE.



When discussing arrest of a fast - growing crack, the question arises, whether or not it makes any difference that the crack passes between rivet holes or runs into a rivet hole. A general answer to this question cannot be given, since it may differ for different geometries. Strictly speaking it is better that the crack passes between rivet holes; in that case the nearest rivets are at a distance  $y_0/2$  from the crack edges (if  $y_0$  is the rivet spacing). This means that the stringer is more effective in taking load from the skin and the tip stress reduction will be larger (small  $C_p$ ) at the cost of a higher load concentration in the stringer (high  $L_s$ ) and high fastener loads. If the crack runs into a rivet hole, the nearest rivets will be at a distance  $y_0$ , giving a smaller tip stress reduction ( $C_p$  larger) and lower stringer load (low  $L_s$ ) and lower fastener loads. Then of course, it will depend on the strength of stringers and fasteners and upon the crack resistance of the skin per se, which situation is preferable.

The problem is outlined for a particular sheet stringer combination in figure V.C.18. It is a case of a 7075-T6 skin with  $K_{IC} = 276 \text{ kg/mm}^{3/2}$  and 7075-T6 stringer with a UTS of  $55.9 \text{ kg/mm}^2$ . Formal analysis of this panel gives the residual strength diagrams of figure V.C.18a for a crack passing between rivets and of figure V.C.18b for a crack running into a rivet hole. Indeed, there is a much larger tip stress reduction if the crack passes between the holes, which is illustrated by the much higher skin crack propagation curve in a than in b. The failure criterion is stringer failure at point H in a at a stress of  $31.8 \text{ kg/mm}^2$ . In case b the fracture criterion is skin crack propagation at point K at a stress of about  $29 \text{ kg/mm}^2$ , followed by stringer failure at H at about the same stress.

Apparently the residual strength level is lower in case b than in case a according to this analysis. However, there is an additional benefit of the rivet hole, which has not yet been considered. If the crack runs into the rivet hole at point R the crack tip will be blunted. This implies that further crack growth will occur at a higher stress than suggested by curve f. The stress for further crack growth will be somewhere between point R and L and that depends upon the size of the hole. (See section V.A.3.5).

Suppose that the hole size will postpone crack growth until point S. Crack arrest will then occur again at T and slow growth until K where final failure takes place. In that case there is no beneficial effect of the rivet hole at all. This holds as long as further crack growth occurs at stresses lower than  $29 \text{ kg/mm}^2$ . If crack growth is postponed until U, there will be no further crack arrest and stringer failure occurs at V. The fastener hole might be so large that crack growth is postponed formally to W. This is insignificant, since at L stringer failure will occur, which of course gives total fracture. Consequently, the highest benefit that can be obtained is an increase of residual strength from K to L, where stringer failure triggers fracture. Depending upon the size of the fastener hole, failure will occur somewhere between K and L. Comparison with case a shows, that for this configuration there is no great benefit of cracks running into rivet holes; but as indicated in the previous discussion, each panel configuration requires a new analysis; there is no general rule. It has to be remarked here, that in the foregoing discussion further crack growth from the rivet hole was disregarded. In case a new fatigue crack starts at the rivet hole the beneficial effect of the rivet hole is cancelled and the residual strength is determined by point H. (See also sections V.A.3.5 and V.B.2.5).

#### V.C.1.6 Residual strength of stiffened panels and wings

This section is intended merely for the presentation of some more test results for stiffened panels and a few data that exist for complete wing structures. These data confirm the versatility and the power of the residual strength analysis method for stiffened panels.

Test data of Vlieger [2,3] on panels with simple strip stiffeners were presented already in figures V.C.5,6,16. Vlieger predicted the behaviour of these panels by means of the analytical method to an accuracy of 3 to 10 percent [2,3], which is considered very satisfactory for residual strength predictions. Besides, all his predictions were at the safe side. Vlieger also tested panels with Z-type stringers, some results of which are presented in figure V.C.19.

Swift and Wang [4,5] tested extremely large panels with longerons and frames. The latter were attached to the skin via shear clips, whereas in some cases extra tear straps were used as crack stoppers. Some of these configurations were shown here already in figure V.C.13. The longerons were either T or hat-sections. Some test data are shown in figure V.C.20. Swift and Wang predicted these data by means of the finite element analysis methods, discussed here in section V.C.1.3. Their predictions also have an accuracy of better than 10 percent, and better than 5 percent in most cases [4,5].

The residual strength characteristics of actual wing center sections of a civil aircraft [10,11] are shown in figure V.C.21. Test results of 11 wing center sections give a substantiation to the behaviour of built-up sheet structures: beyond a certain crack size there is always crack arrest at the stringers. Finally, some data of Vlieger [2,3] are presented for panels with adhesive bonded strip stiffeners or Z-stringers (Fig. V.C.22). When comparing these results with those of similar riveted panels (see fig. V.C.5,6,19), it appears that in the bonded panels in all cases unstable crack growth started at a higher load level, even when the initial crack tip was not close to a stiffener. This clearly indicates a much greater effectiveness of bonded stiffeners with regard to tip stress reduction, caused by the large rigidity of the adhesive joint. Further, in none of the bonded panels unstable crack growth was followed by crack arrest. This completely different behaviour compared with that of similar riveted panels might have been caused by decohesion of the adhesive layer close to the line of the crack due to the high shear loads in that region. This may occur particularly in case of Z-stringers due to the smaller bonded area compared with that of strip stiffeners. This progressive decohesion will result in an ever decreasing stringer effectiveness and consequently, a lower tip stress reduction. Finally, this may lead to unstable crack growth in the sheet followed by failure of the stiffener. A useful criterion for bond failure is not yet available and therefore the behaviour of adhesive bonded panels is difficult to predict. Nevertheless, the residual strength diagrams show the same horizontal part as those presented in other figures.

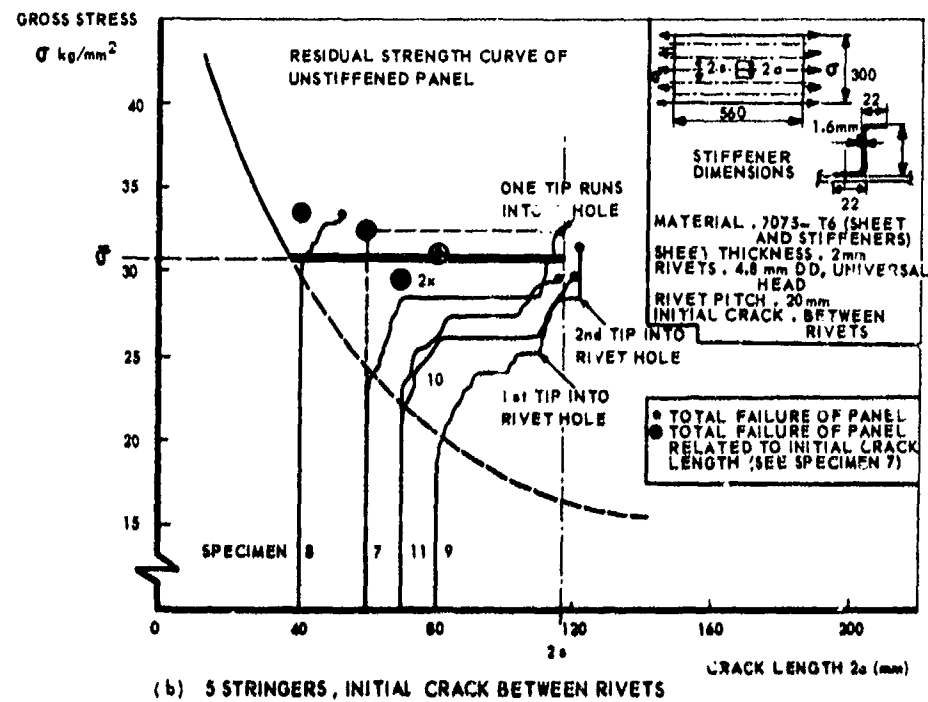
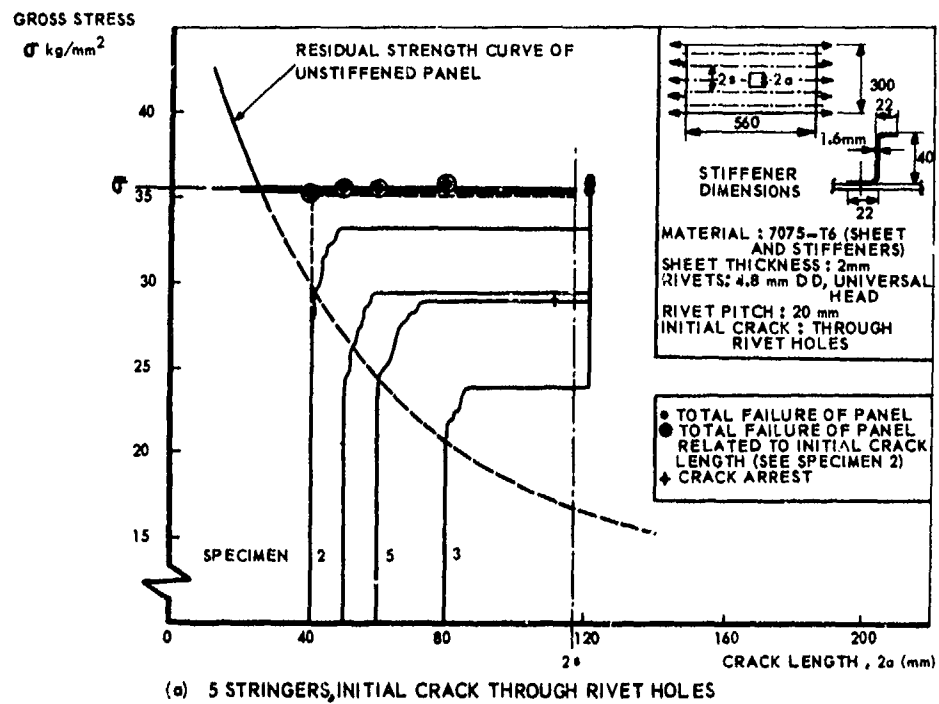
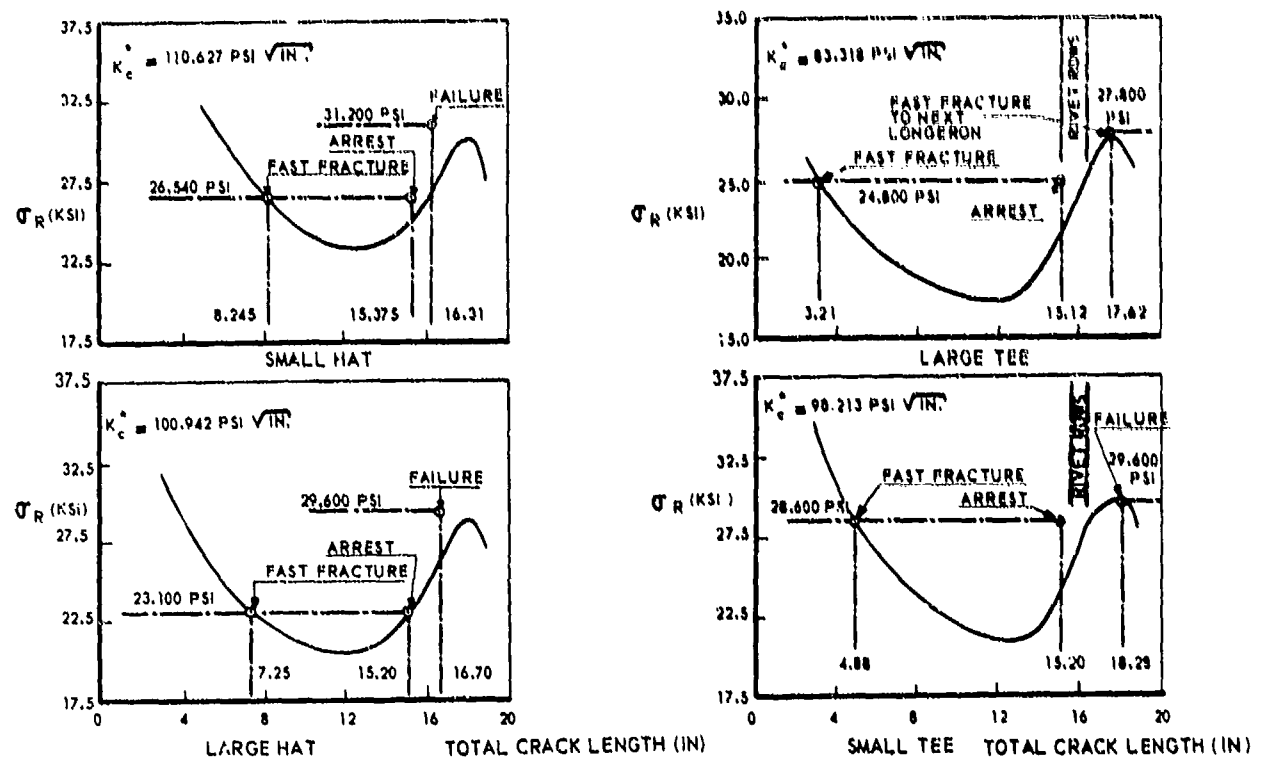


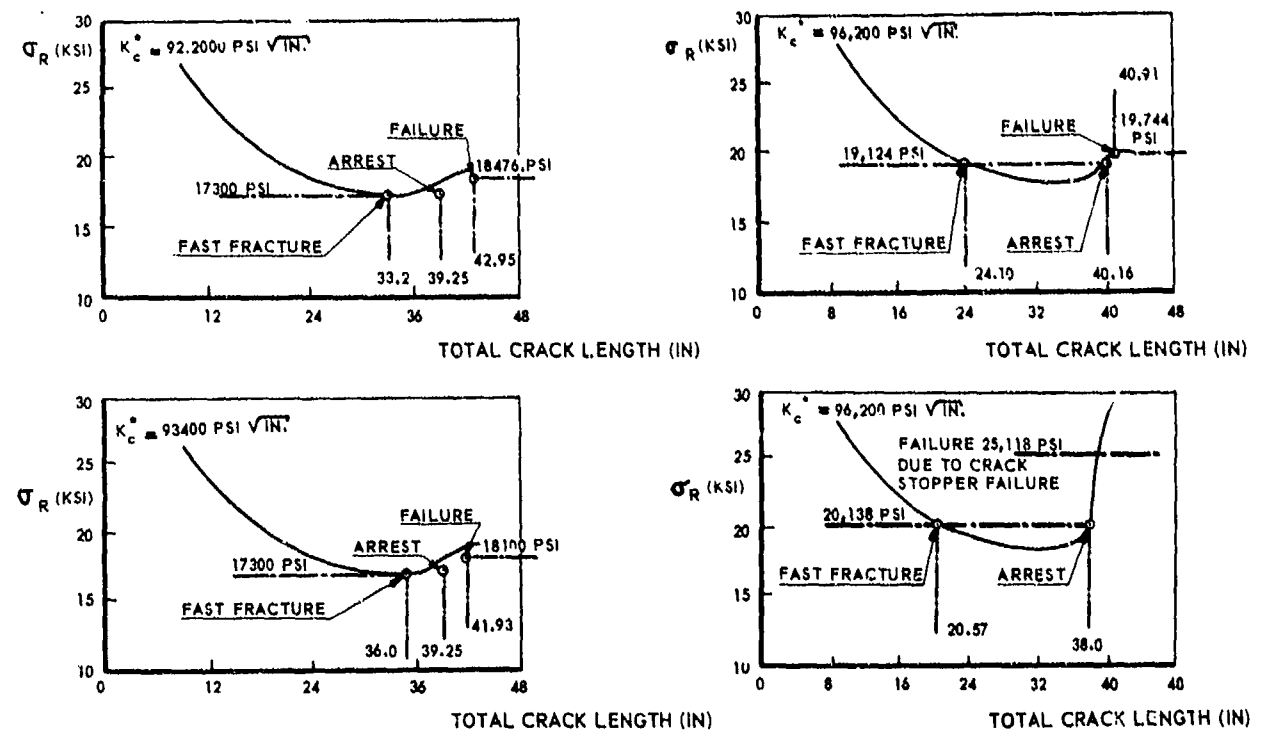
FIG. V : 19 TEST RESULTS OF VLIJGER [2,3]

○ TEST POINTS  
 — CALCULATED



a. GROSS RESIDUAL STRENGTH CURVES FOR CIRCUMFERENTIAL CRACKED FLAT PANELS (HAT SECTION LONGERONS)

b. GROSS RESIDUAL STRENGTH CURVES FOR CIRCUMFERENTIAL CRACKED FLAT PANELS (TEE SECTION LONGERONS)



c. GROSS RESIDUAL STRENGTH CURVES FOR LONGITUDINAL CRACKED FLAT PANELS

d. GROSS RESIDUAL STRENGTH CURVES FOR LONGITUDINAL CRACKED FLAT PANELS

FIG. V C 20 TEST RESULTS OF SWIFT AND WANG [4,5] ON 120 IN. WIDE PANELS WITH 7075 - T 73 SKIN

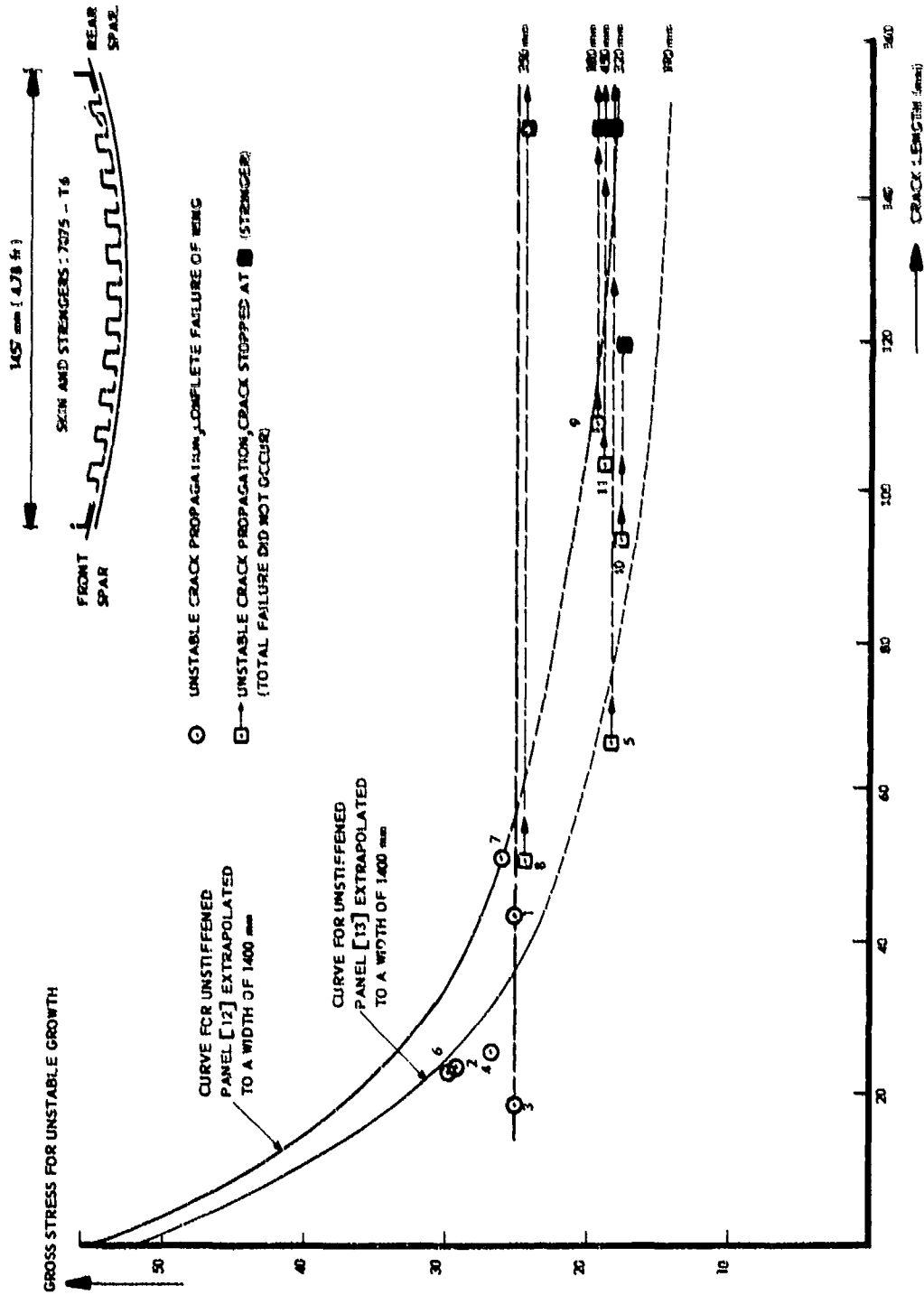
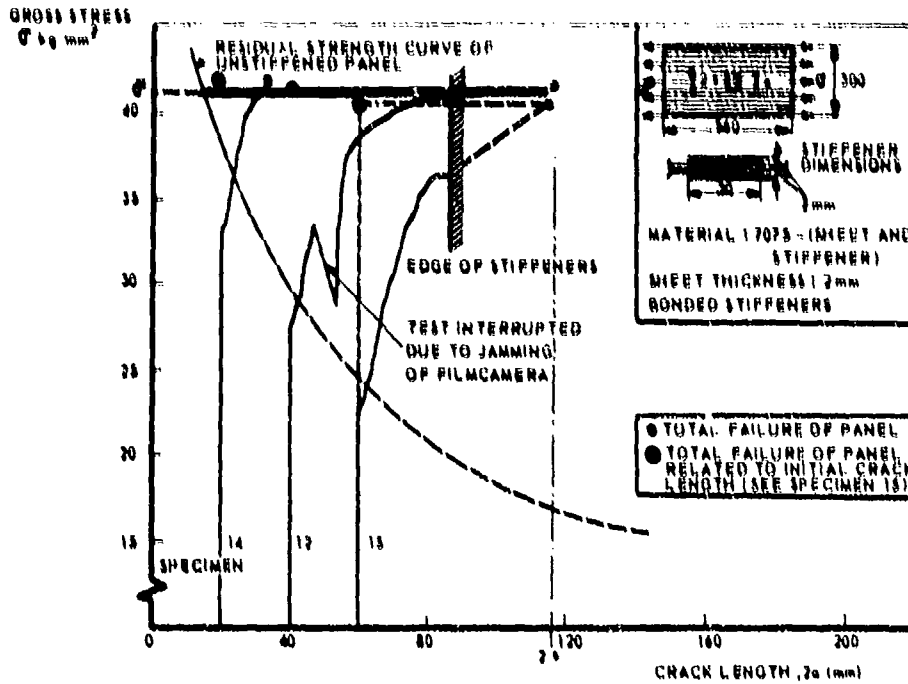
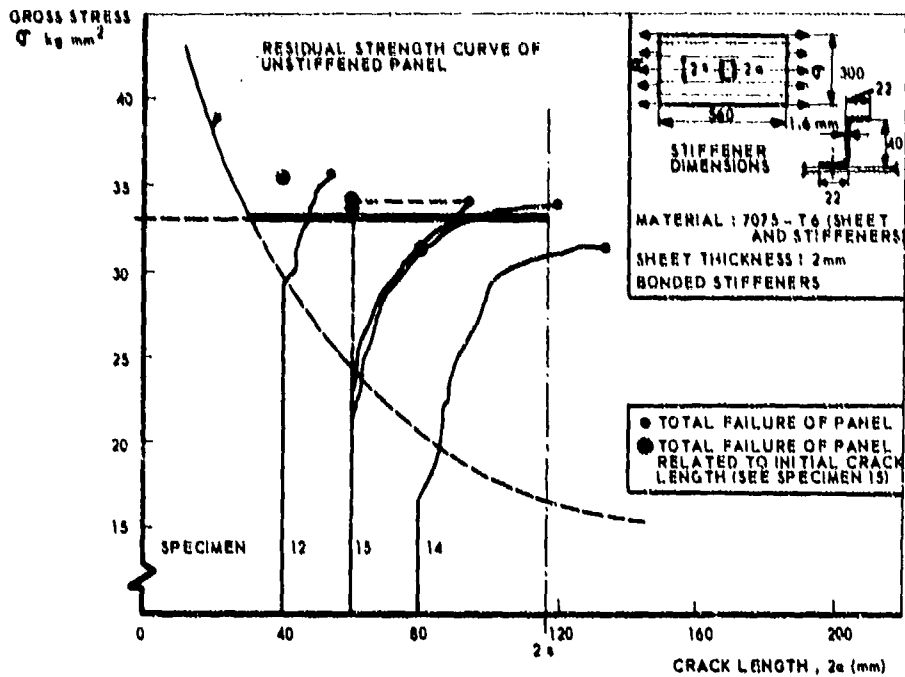


FIG. V C 21 RESIDUAL STRENGTH CHARACTERISTICS OF COMPLETE LOWER WING SKINS [10,11]



a. 4 STRIP STIFFENERS



b. 4 - Z STRINGERS

FIG. V C 22 RESULTS OF TESTS ON PANELS WITH ADHESIVE - BONDED STRINGERS [2,3]

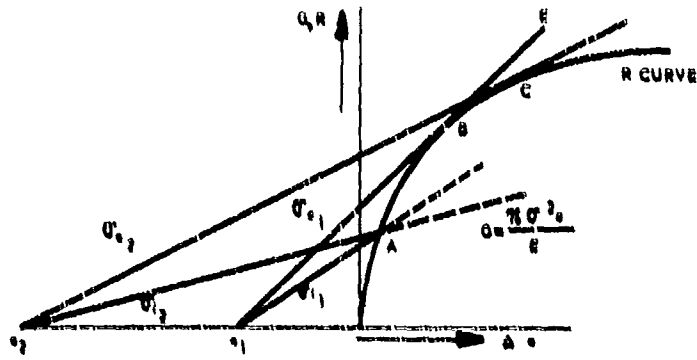


FIG. V C 23 R - CURVE CONCEPT FOR UNSTIFFENED PANEL

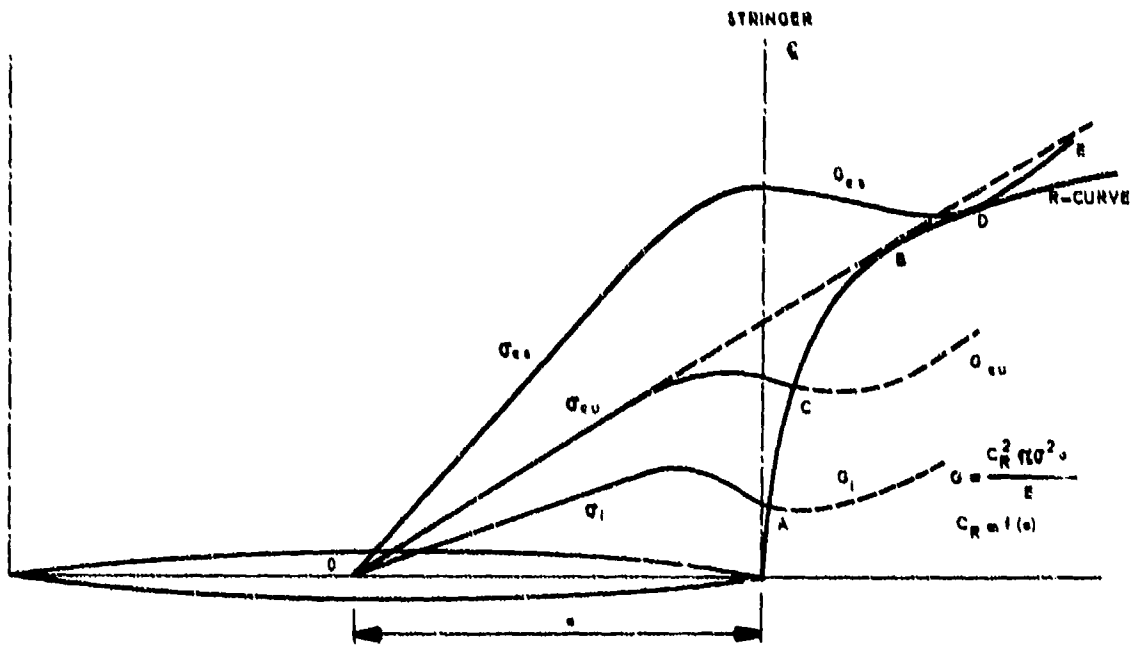


FIG. V C 24 R - CURVE CONCEPT FOR STIFFENED PANEL , CRACK EXTENDING TO STIFFENER

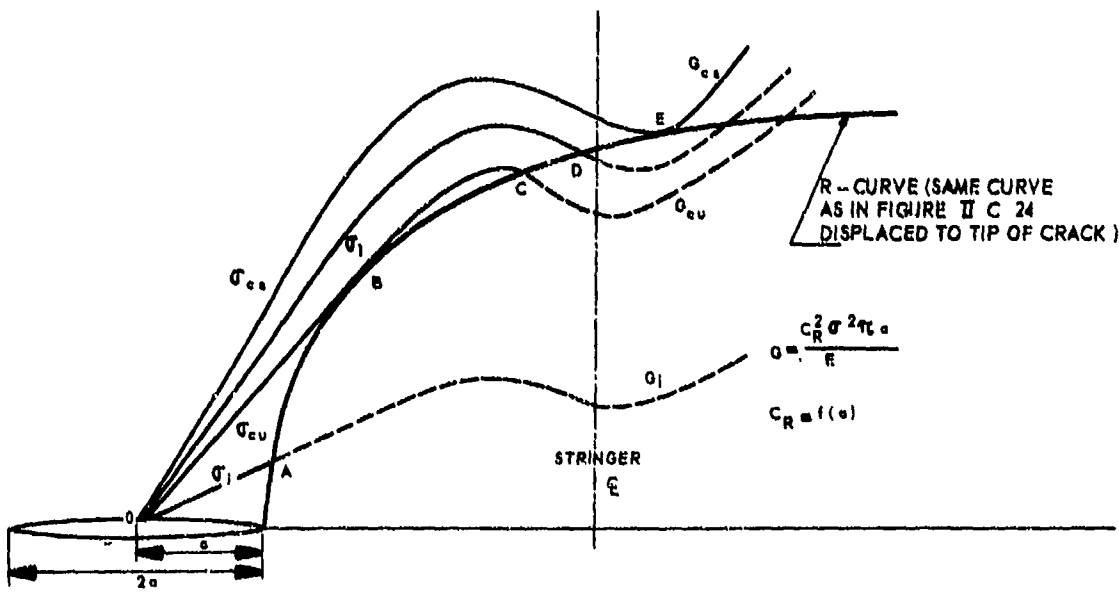


FIG. V C 25 R - CURVE CONCEPT FOR STIFFENED PANEL , SHORT CRACK WITH CRACK ARREST

### V.C.1.7 The R-curve and the residual strength of stiffened panels

In chapter V.B.3 it was shown that the R-curve concept can be very useful in the explanation of the fracture behaviour of sheet under plane-stress conditions. However, the concept has not yet found practical application in view of the difficulties in determining reliable and reproducible R-curves. Future developments may lead to practical usefulness. Therefore, it is useful to consider the applicability of the R-curve concept in case of built-up sheet structures or more specifically in case of stiffened panels. It will be shown below that the R-curve concept can easily be incorporated in the residual strength analysis of stiffened panels. A first attempt for the application to stiffened panels was made by Creager and Liu [14]. In order to facilitate comprehension the R-curve concept for unstiffened sheet will be reviewed very briefly. For a more elaborate treatment, reference is made to the pertinent chapters of this volume.

The case of an unstiffened sheet is depicted in figure V.C.23. The elastic energy release rate  $G = \pi \sigma^2 a/E$ , in case of constant stress, is proportional to the crack length, i.e. for a given stress,  $G$  can be represented by a straight line. Under the presence of a crack of length  $2a_1$  (semi-length  $a_1$ ) slow crack growth will commence at a stress  $\sigma_{c1}$ . The energy release rate is given by point A where  $G = R$ . Further increase of the stress will give slow crack growth to B at a stress  $\sigma_{c1}$ , where final failure occurs, since  $G$  remains larger than  $R$  (line BE). Similarly a crack of length  $a_2$  will give failure at a stress  $\sigma_{c2}$ , since the  $G$ -line  $a_2$ - $G$  is tangent to the R-curve.

Figure V.C.24 shows the simplest case of a stiffened panel where the crack extends to the stringer and the R-curve is indicated. In a stiffened panel the tip-stress intensity is reduced by a factor  $C_R$  (see eq 1). Since  $G = K^2/E$  the  $G$ -line for the stiffened panel will be given by  $G = C_R^2 \pi \sigma^2 a/E$ . This line is no longer straight, since  $C_R$  is a function of crack length (Fig. V.C.2). The deviation from the straight line will be the largest in the vicinity of the stringer. Slow crack growth will commence at a stress  $\sigma_c$  where in point A there is an energy balance  $G = R$ . Under the absence of the stringer, failure would take place at the stress  $\sigma_{cu}$  (at point B). Due to the curved  $G$  line, however, the stress  $\sigma_{cu}$  will only cause slow crack growth to point C in case of the stiffened panel. The stress can further be raised to  $\sigma_c$  (under simultaneous slow crack growth to D) before final failure takes place. At  $\sigma_{cs}$  the energy release rate  $G$  remains larger than  $R$  under constant stress (line D-E). This case was considered by Creager and Liu [14].

The situation is more complicated for a short crack in a stiffened panel. This case is depicted in figure V.C.25. Slow stable crack growth will start at a stress  $\sigma_c$ . The part OA of the curve  $G_c$  is still straight, since the stringer is remote. This means that slow growth commences at the same stress  $\sigma_c$  as in the unstiffened panel. At the stress  $\sigma_{cu}$  unstable crack growth occurs, since the line  $G_{cu}$  is tangent to the R-curve in point B. The part OB<sup>cu</sup> of the curve  $G_{cu}$  is also straight and hence unstable crack growth occurs at the same stress  $\sigma_{cu}$  as in the unstiffened panel. In case of the stiffened panel, however, crack arrest will occur at C, since the  $G$  curve bends downward in the vicinity of the stringer and dips under the R curve again. Further slow crack growth to D occurs if the stress is raised to  $\sigma_c$  and finally at  $\sigma_{cs}$  final fracture will occur since the  $G$  curve is tangent to the R-curve in E and  $G$  remains larger than  $R$  at constant stress.

The foregoing discussion has considered only the criterion for skin crack propagation. Apart from this the criteria for stringer failure and fastener failure would have to be considered also. The latter criteria are still given by eqs. (10) and (11). The  $G$ -curves follow immediately from the  $C_R$  values calculated with the procedures discussed in this chapter. Consequently, incorporation of the R-curve in the residual strength calculation of stiffened panels does not present essential difficulties and as soon as the R-curve concept will be properly established it can easily be used in design. It has to be noted, however, that it has been tacitly assumed in this discussion that the R-curve of the unstiffened panel and of the skin of a stiffened panel are the same. An objection against this assumption is that the R curve may be history dependent, since it is a measure for plastic energy consumption (chapter V.B.2); consequently the R curve of a stiffened skin and an unstiffened sheet may be different in view of the different stress history during crack propagation.

Finally, emphasis is placed on the fact that it is insufficient to consider only cracks that extend until a stiffener. Shorter cracks have to be considered also in order to analyse the possibilities of crack arrest. It may be clear that for other sizes of the initial crack similar diagrams as figure V.C.25 can be drawn. The same R-curve should be used, but it has to be displaced to the tip of the (other) initial crack.

### V.C.1.8 Other analysis methods

A few other methods have been proposed for the residual strength analysis of stiffened panels with cracks. Firstly, there is the finite width concept as proposed by Crichlow [12,15] which is a very simple and approximate engineering method for the unstiffened panel. Crichlow assumes the simplified stress distribution shown in figure V.C.26. From the equilibrium condition it follows

$$(\sigma_{tip} - \sigma_{nom}) 2w_e = 2a\sigma_{nom} \quad (18)$$

$w_e$  is called the effective width and is considered a material constant. Fracture is assumed to occur when  $\sigma_{tip}$  equals the ultimate tensile stress of the material  $\sigma_u$ , hence

$$\sigma_{tip} = \sigma_u \quad (19)$$

or

$$\sigma_c = \sigma_u \frac{1}{1 + a_c/w_e} \quad (20)$$

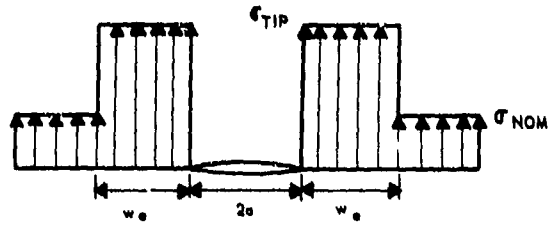


FIG. V C 26 EFFECTIVE WIDTH CONCEPT OF CRICHLAW [15, 16]

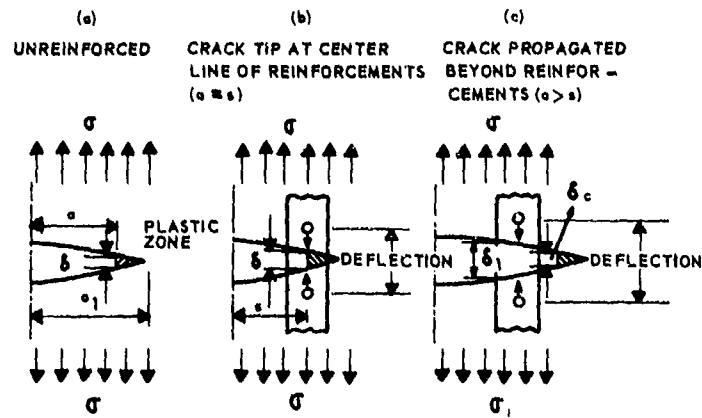


FIG. V C 27 CRACK OPENING DISPLACEMENT MODELS FOR RESIDUAL STRENGTH TESTS OF UNREINFORCED AND REINFORCED PANELS [17].

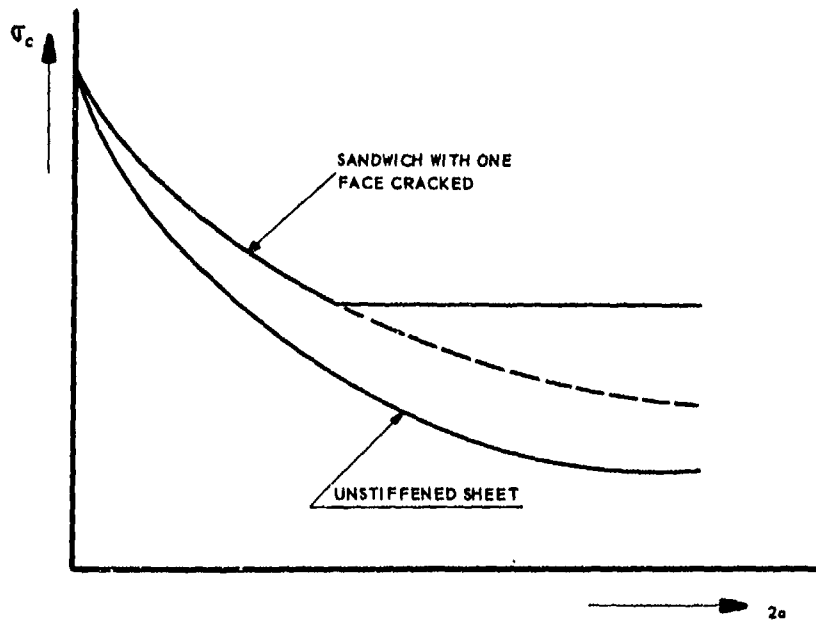


FIG. V C 28 BASIC RESIDUAL STRENGTH DIAGRAM OF ONE-FACE-CRACKED SANDWICH PANEL.



The effective width has to be determined from experiments.

In case there is a stringer at the crack tip eq (19) is modified into:

$$(\sigma_u - \sigma_{cs})(w_e B + \rho A) = \sigma_{cs} a_c B \quad (21)$$

where A is the stringer sectional area,  $\rho$  is a factor accounting for stringer eccentricity and B is skin thickness. The fracture stress is

$$\sigma_{cs} = \sigma_u \frac{1}{1 + \frac{a_c}{w_e + \rho A/B}} \quad (22)$$

A similar analysis was proposed by Troughton and McStay [16]. Crichlow tested stiffened panels and showed that the residual strength can be reasonably predicted if the crack extends to the stringer. In case of smaller cracks eq (20) would have to be used and crack arrest at the stringer would then be determined by eq (22), since  $\sigma_{cs} > \sigma_c$ .

Crichlow's method is useful to obtain a quick appraisal of the residual strength of a stiffened panel. If  $K_{1c}$  for the skin is known, one can calculate  $w_e$  for a crack equal to the stringer spacing ( $2a = S$ ) from

$$\sigma_c = \frac{K_{1c}}{\sqrt{\pi S/2}} \quad (23)$$

with eq (20)

$$\sigma_c = \sigma_u \left( \frac{1}{1 + a_c/w_e} \right)$$

leading to

$$2w_e = \frac{S}{\frac{\sigma_u \sqrt{\pi S/2}}{K_{1c}} - 1} \quad (24)$$

and then calculate the residual strength of the stiffened panel with eq (22). Of course, the more sophisticated analysis presented in the previous sections will be required to obtain a good impression of the residual strength behaviour and of the possibilities for crack arrest.

Another skin crack criterion was proposed by Liu and Ekvall [17]. They use the critical crack tip opening ( $\delta_{00}$ ) as a criterion for crack extension (see also chapter V.B.3). The crack tip opening displacement  $\delta$  can be given as (chapter V.B.3)

$$\delta = \frac{a}{\sigma_{ys}} \quad (25)$$

When the crack tip is under a stringer, the crack tip opening will be suppressed due to the extra stiffness of the stringer. Therefore the crack can continue to grow until  $\delta$  has reached the critical value  $\delta_c$  equivalent to that for an unstiffened panel (see figure VC.27). The situation will be governed by the deflection of the stringer between the two nearest rivets and therefore skin crack propagation will depend upon the elastic-plastic properties of the stringer material. This analysis method has not yet been developed to a quantitative prediction procedure, but a further development certainly seems worthwhile.

#### V.C.1.9 Sandwich panels

An analysis of the residual strength of cracked sandwich panels was made by Bartelds and van der Veer [18]. For the computation of elastic energy release rates in sandwich panels the face sheets were represented by linear strain, triangular elements, while the core layer was modelled by means of quadratic shear strain elements. Only sandwich panels of a basically symmetric structure were analyzed. The in-plane stiffness of the panel was described by means of TRIM6-elements. The bending and shear stiffness of the panel were modelled by means of a sandwich bending element, denoted as TRIB621 [19].

##### a Centrally cracked configuration

The uniformly loaded sandwich panel containing one centrally crack: 1 face sheet was treated in two conditions:

- Loaded edges simply supported, longitudinal edges free.
- All edges simply supported.

The face sheets of the panel were treated as isotropic membranes. The core layer was considered to have orthotropic shear stiffness properties as is typically true for honeycomb core materials. In-plane stiffness of the core layer was neglected.

In table 1 the energy release rate (note that the stress intensity factor follows from  $K^2 = G$ ) of the cracked sandwich panel,  $G_s$ , is compared with results obtained for a membrane under the same loading conditions,  $G_m$ , for two different values of the stiffness parameter  $r$ . This non-dimensional parameter relates the shear stiffness and the bending stiffness of the sandwich panel in the following manner

$$r = \frac{4b^2 E}{\pi^2 D} = \frac{8(1-\nu^2) \mu}{\pi^2} \frac{h}{E B_0} \quad (26)$$

In this relation  $E$  and  $\nu$  are Young's modulus and Poisson's ratio, respectively, of the face sheet material,  $B$  and  $c$  are the face layer and core layer thicknesses and  $b$  is the panel half-width.  $\mu$  is the geometric mean of the core shear moduli,  $\mu_1$  and  $\mu_2$ , for the two principal directions of core orthotropy (ribbon direction and lateral direction in case of a honeycomb material). Usually the core material will be oriented with the maximum shear stiffness direction parallel to the loading direction. Computations for different core orientations, that is for different values of the ratio  $\mu_1/\mu_2$  but for a fixed value of  $\mu = \sqrt{\mu_1 \mu_2}$ , revealed a negligible influence on the energy release rate in the situations studied.

Table 1 Normalized energy release rate for centrally cracked sandwich panel,  $G_s/G_m$

Crack aspect ratio, $\eta$	Loaded edges supported		All edges supported	
	$r = 4$	$r = 20$	$r = 4$	$r = 20$
	.03	.98	.95	.98
.09	.94	.86	.94	.85
.16	.90	.79	.87	.77
.22	.85	.74	.81	.70
.28	.82	.71	.75	.65
.34	.79	.68	.69	.60
.41	.76	.66	.63	.55
.47	.74	.64	.57	.49

From table 1 it is evident that the core layer considerably reduces the elastic energy release rate during crack propagation particularly in case of the largest  $r$ -value ( $r = 20$ ). This situation corresponds to a relatively stiff core and is more representative of actual sandwich construction than the weak core version ( $r = 4$ ). The test data of Smith, Porter and Engstrom [20] on sandwich panels with varying core thicknesses confirm this effect of core stiffness. They observed a decreasing stress intensity factor with decreasing core thickness.

#### b) Symmetric edge crack configuration

A similar set of computations was performed for a sandwich panel in which one of the face sheets contains two symmetric edge cracks. A comparison of energy release rates in the sandwich panel and in an equivalent membrane is made in table 2.

Table 2 Normalized energy release rate for edge-cracked sandwich panel,  $G_s/G_m$

Crack aspect ratio, $\eta$	Loaded edges supported		All edges supported	
	$r = 4$	$r = 20$	$r = 4$	$r = 20$
.03	.96	.88	.95	.85
.09	.88	.76	.84	.66
.16	.81	.69	.73	.53
.22	.77	.66	.64	.45
.28	.74	.64	.57	.40
.34	.73	.63	.51	.36
.41	.71	.63	.47	.33
.47	.73	.63	.43	.31

The decreasing energy release rate with increasing core stiffness, that is with increasing  $r$ -value, is obvious, although the reduction due to core support is, in general, more pronounced compared with the centrally-cracked configuration. It must be noted that an edge-cracked membrane exhibits a larger energy release rate than a centrally cracked sheet for the same value of the crack aspect ratio; this observation suggests that the effect of core support should be more pronounced in the edge cracked sandwich panel. Further, the pronounced beneficial effect of supporting the unloaded edges in comparison with the centrally-cracked configuration can be attributed to restricted panel bending. It is noted that cylindrical bending of a sandwich panel is possible without significant core shear deformations.

When considering the residual strength of the sandwich panel one can determine the stress intensity factor from

$$K_s = \sigma \sqrt{\pi a} f(\eta) h(\eta, r) \quad (27)$$

where the reduction factor  $h < 1$  is a function of crack aspect ratio and of the stiffness parameter  $r$ , defined in equation (26), relating core shear stiffness and extensional stiffness of the face sheets. Failure can be assumed to occur when  $K$  reaches  $K_{10}$  of the sheet material. When only one face of the sandwich contains a crack, then only this face will fail completely when  $K_s = K_{10}$  and the other remains intact. When bending effects are disregarded the residual strength will still be equal to half the strength of the uncracked panel (see figure VC.28). Of course the situation will be largely different with two faces cracked (has to be analysed).

The analytical procedure to determine the fastener forces in a cracked stiffened panel is based on the condition of equal displacements of the fastener points in sheet and stringer. The y-direction displacements in the cracked sheet and in the stringer due to the end loads and the fastener forces can be obtained by using the expressions derived by Romualdi, Frasier and Irwin [9]. This appendix considers the simple cases of a crack in a bay between two stringers, and of a crack across a central stiffener. These basic cases serve as a general outline of the procedure, which can equally well be applied to more complicated geometries.

a Crack extending between two stiffeners (Fig. V C.29)

The stiffened structure is split up into its composite parts as depicted in the upper line of figure V C.29. The displacement in the cracked sheet ( $v_a$ ) is composed of the separate components indicated in the second line of figure V C.29 ( $v_a$ ,  $v_b$  and  $v_c$ ). The displacement of the point ( $s, y_0$ ) of the cracked sheet due to the uniaxial stress  $\sigma$  (sketch a) can be obtained using a procedure suggested by Westergaard [21]:

$$v_a = \frac{\sigma}{E} \sqrt{\rho_1 \rho_2} \left[ 2 \sin \left( \frac{\theta_1 + \theta_2}{2} \right) - \frac{(1+\nu)y_0 r}{\rho_1 \rho_2} \cos \left( \theta - \frac{\theta_1 + \theta_2}{2} \right) \right] + \nu \frac{\sigma}{E} y_0 \quad (28)$$

The displacement of the point ( $s, y_0$ ) of the sheet due to the two pairs opposing fastener forces (sketch b) is obtained as follows. The displacement in y-direction of a point ( $x, y$ ) due to one pair of forces is given by Love [3] as (see sketch d):

$$v(x, y) = \frac{F(1+\nu)}{4\pi E B_1} \left[ (3+\nu) \ln \frac{r_1}{r_2} + (1+\nu) x^2 \left( \frac{1}{r_1^2} - \frac{1}{r_2^2} \right) \right] \quad (29)$$

where  $\nu$  is Poisson's ratio and  $B_1$  is the sheet thickness.

Equation (29) cannot be used in its present form to calculate the displacement in ( $0, y_0$ ) because of the logarithmic infinity of displacement in this point ( $r_1 = 0$ ). To avoid this singularity the force  $F$  is regarded to be uniformly distributed across the rivet diameter  $d$ . With this assumption and neglecting  $(d/y_0)^2$  in comparison to unity one obtains for the displacement in ( $0, y_0$ ) the expression

$$v(0, y_0) = \frac{F(1+\nu)}{4\pi E B_1} \left[ (3-\nu) \left( \ln \frac{d}{4y_0} - 1 \right) + 1 + \nu \right] \quad (30)$$

In case of sketch b the displacement of the point ( $s, y_0$ ) must be found for two pairs of forces. One pair is located at the point in question and causes a displacement as given by equation (30). The other pair, located a distance  $x = 2s$  from the point, causes displacement components as given by equation (29) in which  $r_1 = 2s$  and  $r_2 = \sqrt{4s^2 + 4y_0^2}$ . Consequently, the total displacement is:

$$v_b = \frac{F(1+\nu)}{4\pi E B_1} \left[ (3-\nu) \left( \ln \frac{d}{4y_0} - 1 \right) + (1+\nu) \left( 2 - \frac{s^2}{s^2 + y_0^2} \right) + (3-\nu) \ln \sqrt{\frac{s^2}{s^2 + y_0^2}} \right] \quad (31)$$

The displacement of the point ( $s, y_0$ ) due to stress distribution  $p(x)$  along the slit segment from  $x = a$  to  $x = -a$  is obtained as follows. The normal stress  $\sigma_y$  at any point  $x$  along the crack due to a pair of forces is according to Love [8], (see sketch d)

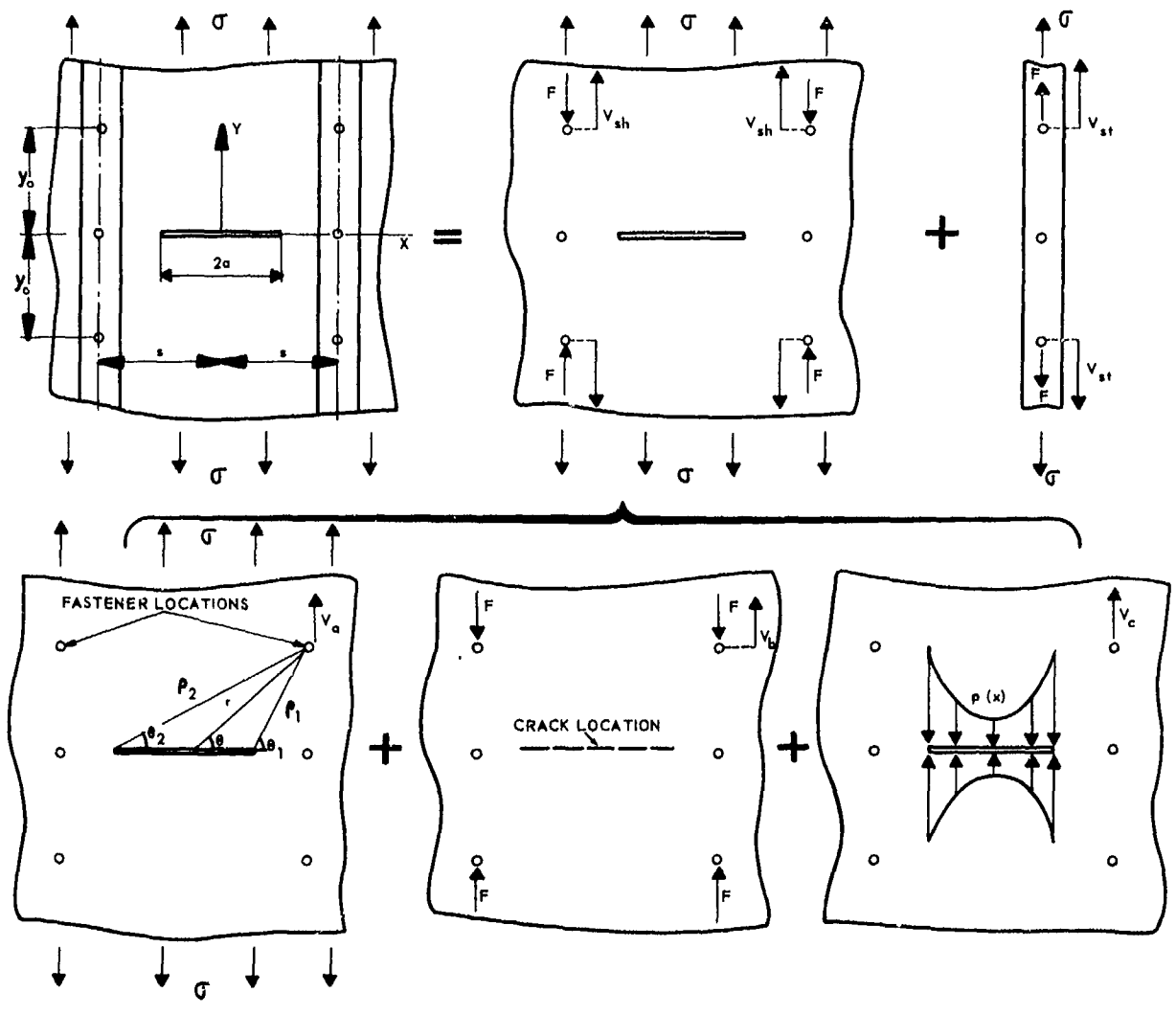
$$\sigma_y = \frac{F y_0}{\pi B_1 (x^2 + y_0^2)} \left[ \frac{3+\nu}{2} - (1+\nu) \frac{x^2}{x^2 + y_0^2} \right] \quad (32)$$

In case of sketch c the distribution of the stresses along the x-axis produced by two pairs of forces can be derived from expression (32) with the substitution of ( $x-s$ ) and ( $x+s$ ) respectively for  $x$ . This will yield

$$p(x) = \frac{F y_0}{\pi B_1 [y_0^2 + (x-s)^2]} \left[ \frac{3+\nu}{2} - (1+\nu) \frac{(x-s)^2}{y_0^2 + (x-s)^2} \right] + \frac{F y_0}{\pi B_1 [y_0^2 + (x+s)^2]} \left[ \frac{3+\nu}{2} - (1+\nu) \frac{(x+s)^2}{y_0^2 + (x+s)^2} \right] \quad (33)$$

In determining the displacement due to the stress distribution  $p(x)$  in sketch c the actual stresses along the crack are replaced (for simplicity) by a uniform stress distribution equal to the average of  $p(x)$  between the ends of the crack. The average stress  $\bar{p}$  along the crack is given by

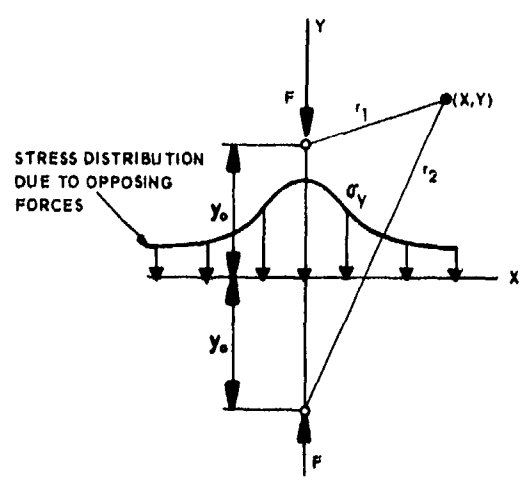
$$\bar{p} = \frac{1}{2a} \int_{-a}^{+a} p(x) dx \quad (34)$$



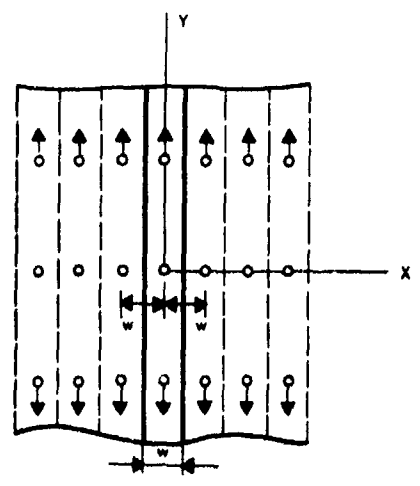
SKETCH a

SKETCH b

SKETCH c



SKETCH d



SKETCH e

FIG. V C 29 CALCULATION OF FASTENER FORCES FOR A CRACK BETWEEN TWO STIFFENERS

After integration it follows that

$$\bar{p} = \frac{F}{\pi a B_1} \left\{ \tan^{-1} \left( \frac{a+s}{y_0} \right) + \tan^{-1} \left( \frac{a-s}{y_0} \right) + \frac{y_0(1+\nu)}{2} \left[ \frac{a+s}{y_0^2 + (a+s)^2} + \frac{a-s}{y_0^2 + (a-s)^2} \right] \right\} \quad (35)$$

The displacement of the point  $(s, y_0)$  due to  $\bar{p}$  follows from the Westergaard solution for a crack containing internal (negative) pressure [21]. Its magnitude is given by

$$v_0 = -\frac{\bar{p}}{E} \left\{ 2 \left[ \sqrt{\rho_1 \rho_2} \sin \left( \frac{\theta_1 + \theta_2}{2} \right) - y_0 \right] - (1+\nu) y_0 \left[ \sqrt{\frac{F}{\rho_1 \rho_2}} \cos \left( \theta - \frac{\theta_1 + \theta_2}{2} \right) - 1 \right] \right\} \quad (36)$$

The displacement in the stiffener is composed of the displacement due to the forces  $F$  and that due to the stresses  $\sigma$ . The displacement due to a pair of forces of a point of the stiffener of width  $w$  is approached as follows. In a relatively narrow sheet the displacement of the point of force application cannot be properly represented by equation (30), since the boundary conditions are not satisfied. To account for the finite width of the stiffener Romualdi proposed to repeat the pair of forces at intervals  $w$  as shown in sketch e. The displacement is then expressed by a combination of equation (30) and a series of expressions of the form of equation (29), one for each pair of forces. The only other extension in the stiffener to be considered is that due to the uniform stress  $\sigma$ . The total displacement of point  $(0, y_0)$  in the stiffener is then

$$v_{st} = -\frac{F}{4\pi E B_2} (1+\nu) \left\{ \left[ (3-\nu) \left( \ln \frac{a}{4y_0} - 1 \right) + 1 + \nu \right] + 2 \sum_{n=1}^{\infty} \left[ (3-\nu) \ln \frac{nw}{\sqrt{n^2 w^2 + 4y_0^2}} + (1+\nu) \frac{4y_0^2}{n^2 w^2 + 4y_0^2} \right] \right\} + \frac{\sigma}{E} y_0 \quad (37)$$

where  $B_2$  is the stringer thickness.

#### b. Crack extending across a stiffener (fig. V C.30)

Referring to figure V C.29, sketch a, the displacement of the point  $(0, y_0)$  in the cracked sheet due to a uniaxial stress  $\sigma$  can be derived from equation (28) by substituting

$$\rho_1 = \rho_2 = \sqrt{a^2 + y_0^2} \quad r = y_0$$

and

$$\theta = \frac{\theta_1 + \theta_2}{2} = \frac{\pi}{2}$$

This will result in a displacement

$$v_a = \frac{\sigma}{E} \sqrt{a^2 + y_0^2} \left[ 2 - (1+\nu) \frac{y_0^2}{a^2 + y_0^2} + \frac{\nu y_0}{\sqrt{a^2 + y_0^2}} \right] \quad (38)$$

The displacement of the point  $(0, y_0)$  in the sheet due to opposing rivet forces located at  $(0, y_0)$  and  $(0, -y_0)$  (Fig. V C.30) is given by equation (30). The displacement in the cracked sheet due to the stress distribution  $p(x)$  along the crack is derived in a similar way as under case a. Using equation (32) in this case,  $\bar{p}$  will be

$$\bar{p} = \frac{F}{2\pi a B_1} \left[ 2 \tan^{-1} \left( \frac{a}{y_0} \right) + (1+\nu) \frac{a y_0}{a^2 + y_0^2} \right] \quad (39)$$

The displacement due to  $\bar{p}$  follows from Westergaard [21]:

$$v_0 = -\frac{\bar{p}}{E} \left[ 2 \left( \sqrt{y_0^2 + a^2} - y_0 \right) - (1+\nu) \left( \frac{y_0^2}{\sqrt{y_0^2 + a^2}} - y_0 \right) \right] \quad (40)$$

The displacement in the stiffener due to forces  $F$  and stresses  $\sigma$  has been derived as under case a and is given by equation (37).

Under a and b an outline of the procedure for the calculation of the displacements in sheet and stringer due to end-loads and fastener forces was given. For the sake of simplicity in the derivation of the equations only one fastener at either side of the crack was assumed to be active. However, the same procedure can be used when more rivets are active. By equating the displacements in corresponding points of sheet and stringer the compatibility condition yields

$$v_a + v_b + v_0 = v_{st} \quad (41)$$

Using the equations derived under a and b, after some arranging of terms, the following equation arises for fastener location  $y_1$  (in case of  $n$  active fasteners at either side of the crack)

$$a_{11} F_1 + a_{12} F_2 + \dots + a_{i1} F_i + \dots + a_{in} F_n = b_i \sigma \quad (42)$$

where the coefficients  $a_{ij}$  are functions of the panel characteristics (material, dimensions) and of the crack length. Writing down these equations for all  $n$  fastener locations will deliver a set of  $n$  independent equations of the shape of equation (42). Thus

$$\begin{array}{l} a_{11} F_1 + a_{12} F_2 + \dots + a_{1n} F_n = b_1 \sigma \\ a_{21} F_1 + \dots + a_{2n} F_n = b_2 \sigma \\ \vdots \\ a_{n1} F_1 + \dots + a_{nn} F_n = b_n \sigma \end{array} \quad (43)$$

Or in matrix notation

$$\begin{bmatrix} a_{11} & \dots & a_{1n} \\ \vdots & & \vdots \\ a_{n1} & \dots & a_{nn} \end{bmatrix} \begin{bmatrix} F_1 \\ \vdots \\ F_n \end{bmatrix} = \sigma \begin{bmatrix} b_1 \\ \vdots \\ b_n \end{bmatrix} \quad (44)$$

or, in contracted matrix notation

$$AF = \sigma B \quad (45)$$

Solving this equation will yield the  $n$  unknown fastener loads,  $F_1 \dots F_n$ .

In case of a panel configuration with three stiffeners (each attached with  $n$  fasteners) and a symmetric crack under the central stiffener, the same procedure as outlined above can be used in determining the fastener forces by a combination of the equations derived under a and b. In that case (due to symmetry) a set of  $2n$  independent equations for the calculation of the  $2n$  unknown fastener forces will arise. When in this case the central stiffener is broken the displacement of the fastener closest to the crack of this stiffener is determined solely by the stiffness of the sheet and therefore in that case from equal displacements in sheet and stringer a set of  $(2n - 1)$  equations will arise. The missing equation will be delivered by equilibrium of the central stiffener:

$$\sigma + \frac{1}{A} \sum_{i=1}^n F_i = 0 \quad (46)$$

where  $A$  is the cross-sectional area of the stiffener.

V.G.1.11 APPENDIX Finite element analysis of cracked panels by G. Bartelds.

### a Introduction

Application of finite element methods to linear fracture mechanics problems have been directed, in general, towards the determination of the elastic crack tip stress intensity factor,  $K$ . Basically, two different approaches are used, viz.

- a) The direct method by which the value of the stress intensity factor is derived from finite element results for the stress and deformation distributions near the crack tip.
- b) The indirect method by which the value of the stress intensity factor is derived from the energy release rate computed by repeated application of the finite element method to different crack length configurations.

Some of the earlier applications of the direct method [22,23] utilized the familiar constant strain or linear strain finite element. Obviously, the strain field singularity at the crack tip can not be represented in this case and mesh refinement and averaging procedures have to be used in order to extract an approximate  $K$ -value.

An improved accuracy was achieved by incorporating a stress or strain singularity by means of special finite elements [24,25,26] with the added advantage of a considerable reduction in the number of variables used.

In the indirect method [22,27] an approximate  $K$ -value is derived from the elastic energy release rate. This implies that in order to establish one  $K$ -value two energy computations must be carried out, for two lengths of crack slightly deviating from the particular crack size under consideration. Experience has shown, that there is no need to use a particularly fine mesh. Besides, the two computations can be organized in such a manner that the computer time used, is only slightly more than the time needed for one energy computation.

If a fracture mechanics problem associated with one particular crack configuration is to be studied, the direct method may be preferred, provided one has the necessary computer software (i.e. special finite element procedures) available. However, for an analysis of the influence of crack length on structural behaviour the indirect method is preferable.

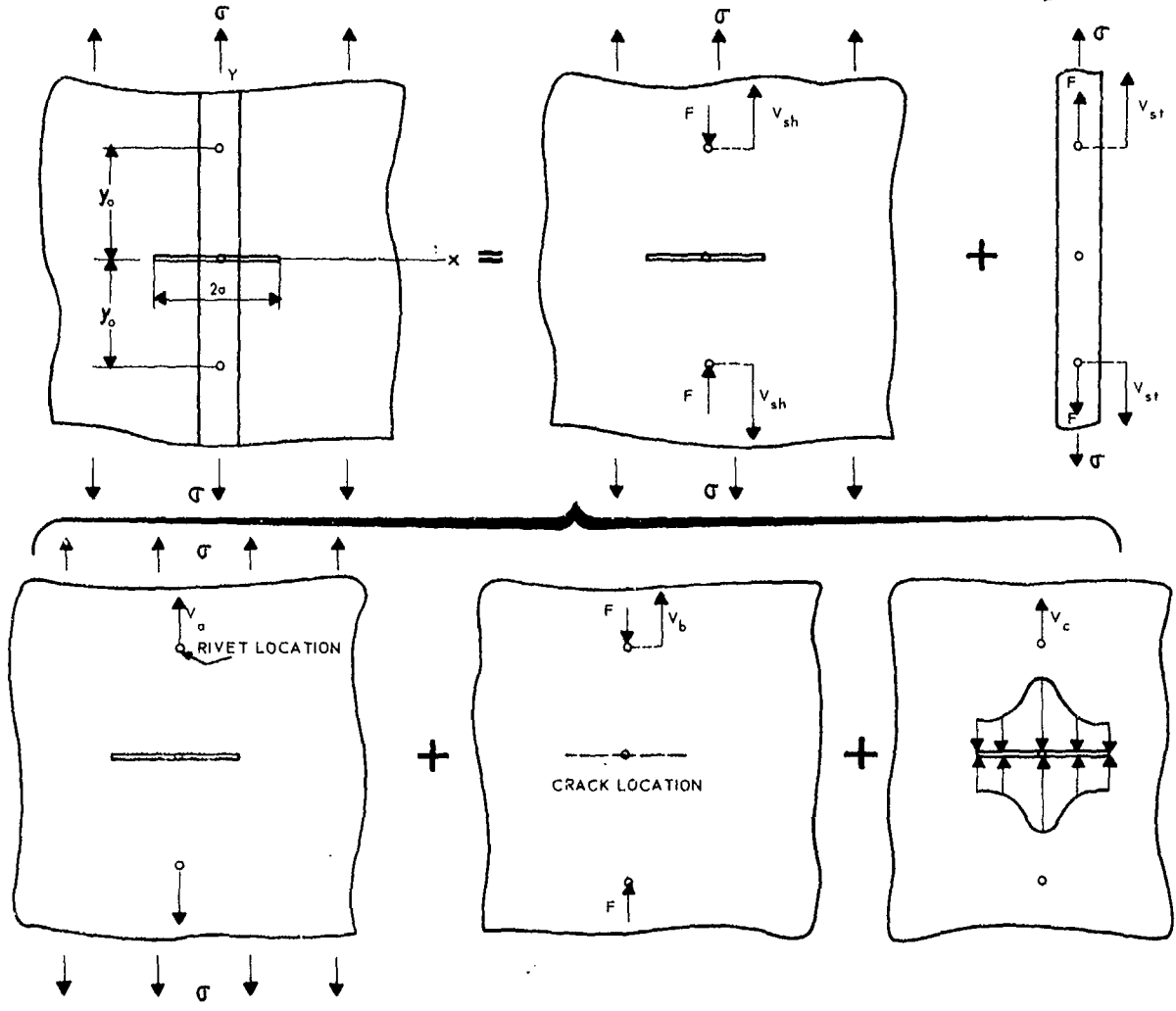


FIG. V C 30 CALCULATION OF FASTENER FORCES FOR A CRACK ACROSS A STIFFENER

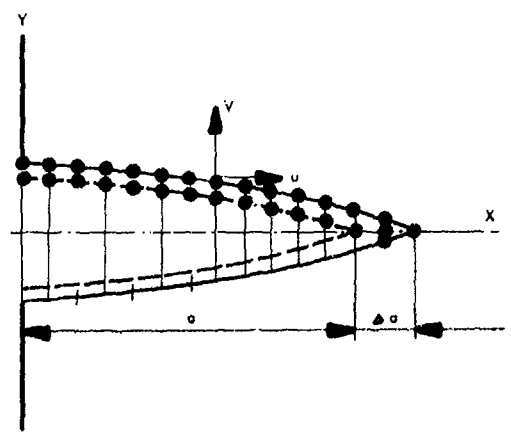


FIG. V C 31 CRACK CLOSURE BY NODAL POINT FIXATION.

**b The energy release method**

For a computation of the energy levels, associated with different crack lengths, in a structure under a given loading condition the finite element displacement method is extremely well suited.

In the displacement method the total potential energy functional expressed in terms of a vector,  $\bar{u}$ , of unknown displacements,

$$U - V = \frac{1}{2} \bar{u} K \bar{u} - \bar{u} \bar{p} \quad (47)$$

is minimized with respect to the vector  $\bar{u}$ . The procedure leads to a set of generalized equilibrium equations of the form

$$K \bar{u} = \bar{p} \quad (48)$$

that can be rapidly solved by means of efficient computer programs. In equation (48) the matrix  $K$  multiplying the displacements  $\bar{u}$  is called the stiffness matrix while  $\bar{p}$  is a vector of generalized loads. The adjective generalized is used to cover the case where the displacement vector does not contain displacement components exclusively but also includes rotations, curvatures or other "generalized displacements". In that case the local vector  $\bar{p}$  contains forces, moments and other "generalized loads".

Obviously the solution

$$\bar{u} = K^{-1} \bar{p} \quad (49)$$

can be used directly, together with the load vector  $\bar{p}$ , to compute the energy functional

$$U = \bar{u} \left( \frac{1}{2} K \bar{u} - \bar{p} \right) = - \frac{1}{2} \bar{u} \bar{p} \quad (50)$$

If this procedure is executed twice for two neighbouring values of the crack length  $a_1$  and  $a_2$ , the difference in energy levels is

$$\Delta U = U(a_1) - U(a_2) = - \frac{1}{2} [\bar{u}(a_1) - \bar{u}(a_2)] \bar{p} \quad (51)$$

Further, the differential quotient

$$\frac{\Delta U}{\Delta a} = - \frac{1}{2} \frac{\bar{u}(a_1) - \bar{u}(a_2)}{a_1 - a_2} \bar{p}$$

is a first approximation to the energy release rate  $\partial U / \partial a$  for a crack length  $a = (a_1 + a_2) / 2$ .

The extraction of a solution from a large set of equations is a formidable computational task even in case of a well-conditioned, positive-definite system. A considerable savings in computer time can be achieved, however, if the energy release computation is executed in the manner of a crack closure computation. In fact, the only differences between the consecutive configurations used in an energy release computation are associated with the boundary condition at the crack surface. As indicated in figure VC.31 a reduction of the crack length,  $a$ , by an amount  $\Delta a = a_1 - a_2$ , only involves the assignment of a prescribed value to the vertical displacement components at nodes situated "along  $\Delta a$ ". In the particular example shown, this simply amounts to setting the  $v$ -displacements of two nodes equal to zero.

This situation suggests a partitioning of the vector  $\bar{u}$ , and of the vector  $\bar{p}$  and the matrix  $K$ , in such a manner that all degrees of freedom affected by crack closure are grouped together in a vector  $\bar{u}_2$  while the remaining displacements are assembled into  $\bar{u}_1$ . Obviously, the size of  $\bar{u}_2$  is only a small fraction of the size of the complete vector  $\bar{u}$ . A straight-forward elimination of

$$\bar{u}_1 = K_{11}^{-1} (\bar{p}_1 - K_{12} \bar{u}_2) \quad (52)$$

then leads to a reduced system of equations

$$K_{22}^m \bar{u}_2 = \bar{p}_2^m \quad (53)$$

where  $K_{22}^m = K_{22} - K_{21} K_{11}^{-1} K_{12}$  and  $\bar{p}_2^m = \bar{p}_2 - K_{21} K_{11}^{-1} \bar{p}_1$ . The computer time involved in this elimination is comparable to the time required for one solution of the complete system.

The situation whereby none of the components of  $\bar{u}_2$  is prescribed now corresponds to the largest crack length. The crack is closed in a stepwise fashion by consecutively setting components of  $\bar{u}_2$  equal to zero. The associated solution of the reduced system of equation (53)

$$\bar{u}_2(a_1) = \left| K_{22}^m(a_1) \right|^{-1} \bar{p}_2^m \quad (54)$$

can be obtained by means of a fast in-core equation-solver algorithm. By use of equation (52) it follows from equation (50) that

$$U = - \frac{1}{2} (\bar{u}_1 \bar{p}_1 + \bar{u}_2 \bar{p}_2) = - \frac{1}{2} \bar{p}_1 K_{11}^{-1} \bar{p}_1 - \frac{1}{2} \bar{p}_2^m \bar{p}_2^m = U^m - \frac{1}{2} \bar{p}_1 K_{11}^{-1} \bar{p}_1 \quad (55)$$



where  $U^R$  is an energy quantity associated with the reduced system of equation (53). According to equation (55) it differs from  $U$  by a constant amount. Hence, the energy release rate

$$\frac{\Delta U}{\Delta a} = \frac{\Delta U^R}{\Delta a} = -\frac{1}{2} \frac{\bar{u}_2(a_i) - \bar{u}_2(a_{i+1})}{a_i - a_{i+1}} \frac{1}{P_2} \quad (56)$$

is determined completely by the reduced vectors utilized in the finite element crack closure computation. Thus, a set of discrete values of the energy release rate can easily be obtained by means of a simple addition to a standard linear system solution procedure.

#### REFERENCES

1. Vlieger, H.  
Broek, D. Residual strength of cracked stiffened panels. NLR report S-653, 1967.
2. Vlieger, H. Residual strength of cracked stiffened panels. NLR report TR-71004 (1971).
3. Vlieger, H. The residual strength characteristics of stiffened panels containing fatigue cracks. Accepted for publication in *Engineering Fracture Mechanics*.
4. Swift, T.  
Wang, D.Y. Damage tolerant design analysis methods and test verification of fuselage structure. Air Force Conf. on Fatigue and Fracture, 1969. AFFDL-TR-70-144 (1970) pp 653-683.
5. Swift, T. Development of the fail-safe design features of the DC-10. ASTM STP 486 (1971) pp 164-214.
6. Poe, C.C. The effect of riveted and uniformly spaced stringers on the stress intensity factor of a cracked sheet. Air Force Conf. on Fatigue and Fracture 1969. AFFDL-TR-70-144 (1970) pp 207-216.
7. Poe, C.C. Fatigue crack propagation in stiffened panels. ASTM STP 486 (1971) pp 79-97.
8. Love, A.E.H. A treatise on the mathematical theory of elasticity. New York, Dover, 4th Ed., 1944, p. 209.
9. Romualdi, J.P.  
Fraser, J.T.  
Irwin, G.R. Crack-extension-force near a riveted stringer. NRL Memo report no. 4956. (1957)
10. Broek, D. Crack propagation and residual strength of full-scale wing center sections. NLR report TR-S-612 (1964).
11. Schijve, J.  
Broek, D. et al. Fatigue tests with random and programmed load sequences on full-scale wing center sections. NLR report TR-S-615 (1965). Also: AFFDL-TR-66-143 (1966).
12. Crichlow, W.J. The ultimate strength of damaged structure. Full-Scale Fatigue Testing of Aircraft Structures. Plantema and Schijve ed. p. 149. Pergamon (1961).
13. Broek, D. The effect of finite specimen width on the residual strength of light alloy sheet. NLR report TR-M-2152 (1965).
14. Creager, H.  
Lui, A.F. The effect of reinforcements on the slow stable tear and catastrophic failure of thin metal sheet. AIAA Paper 71-113 (1971).
15. Crichlow, W.J. Stable crack propagation-fail safe design criteria-analytical methods and test procedures. AIAA Paper 69-215 (1969).
16. Troughton, A.J.  
McStay, J. Theory and practice in fail-safe wing design. Current aeronautical fatigue problems, pp 429-462. Schijve, Heath-Smith, Melbourne ed, Pergamon (1965).
17. Liu, A.F.  
Ekvall, J.C. Material toughness and residual strength of damage tolerant aircraft structures. ASTM STP 486 (1971) pp 98-121.
18. Bartelds, G. Elastic energy release rate in cracked sandwich panels. NLR-TR-72026 (1972).
19. Van der Veer, I.  
Bartelds, G. Finite element analysis of sandwich panels. Proc. IUTAM Symp. on "High Speed Computing of Elastic Structures", Liège, 1970.
20. Smith, S.H.  
Porter, T.R. Fatigue crack propagation behaviour and residual strength of bonded strap reinforced, laminated and sandwich panels. Air Force Conf. on Fatigue and Fracture, 1969. AFFDL-TR-70-144 (1970) pp 611-634.
21. Engstrom, W.L. Bearing pressures and cracks. *J. Appl. Mech.*, 6 (1939).
22. Westergaard, H.M.  
Watwood, V.B. The finite element method for prediction of crack behaviour. *Nucl. Eng. and Design*, 11 (1969), pp 323-332.
23. Chan, S.K.  
Tuba, I.S. On the finite element method in linear fracture mechanics. *Eng. Fract. Mech.*, 2 (1970), pp. 1 - 16.
24. Wilson, W.K.  
Tracey, D. Finite elements for determination of crack tip elastic stress intensity factors. *Eng. Fract. Mech.*, 3 (1971), pp 255-265.
25. Walsh, P.F. The computation of stress intensity factors by a special finite element technique. *Int. J. of Sol. and Struct.*, 7 (1971), pp 1333-1342.
26. Pian, T.H.H.  
Tong, P.  
Lak, G. Elastic crack analysis by a finite element hybrid method. 3rd Conf. on Matrix Meth. on Struct. Mech., Dayton (1971).
- Dukes, T.P. Proc. ISD/IS3C Symp. on Finite El. Techn., Stuttgart, (1969).

V.C.2 THE APPLICATION OF FRACTURE MECHANICS  
IN THE DEVELOPMENT OF THE DC-10 FUSELAGE

T. Swift

Summary . . . . .	227
Introduction . . . . .	227
Damage tolerance . . . . .	228
Longitudinal skin cracks . . . . .	228
Transverse skin cracks . . . . .	229
Configuration candidates . . . . .	229
Skin thickness . . . . .	231
Skin material . . . . .	231
Crack stopper straps . . . . .	231
Longeron geometric shape . . . . .	232
Analysis . . . . .	233
Analysis of cracked unstiffened panels . . . . .	233
Analysis of cracked stiffened panels . . . . .	233
Analysis results . . . . .	238
Skin fracture criterion . . . . .	240
Stiffener strength criteria . . . . .	242
Effect of attachment stiffness . . . . .	244
Bond delamination . . . . .	248
The threshold of slow stable crack growth . . . . .	249
Test program . . . . .	251
Curved panels . . . . .	252
Flat panels with longitudinal cracks . . . . .	252
Flat panels with circumferential cracks . . . . .	253
Test results . . . . .	255
Flat panels with longitudinal cracks . . . . .	255
Flat panels with circumferential cracks . . . . .	257
Curved panels . . . . .	268
Unstiffened cylinders . . . . .	268
Rivet shear deflection test results . . . . .	271
Stiffened panels, 30 inches wide . . . . .	271
Unstiffened panels, 30 inches wide . . . . .	274
Rivet shear load test . . . . .	274
Correlation . . . . .	277
Skin criteria . . . . .	277
Frame criteria . . . . .	277
Longeron criteria . . . . .	277
Flat panel versus curved panel testing . . . . .	279
Conclusions . . . . .	281
Longitudinal cracks . . . . .	281
Circumferential cracks . . . . .	282
Acknowledgment . . . . .	282
References . . . . .	282
Appendix: Format II Analysis . . . . .	283

## V.C.2 THE APPLICATION OF FRACTURE MECHANICS IN THE DEVELOPMENT OF THE DC-10 FUSELAGE

T. Swift

### SUMMARY

The degree of damage tolerance used in the design of the DC-10 fuselage pressure shell is discussed with reasons for its selection. Analysis methods are presented for the prediction of the residual strength of damaged, stiffened panels, based on the Matrix Force solution of an idealized structure combined with fracture mechanics equations. The effects of attachment flexibility, which play an important part in the residual strength of damaged structure, are accounted for. Crack growth retardation due to the plastic zone formed on high load cycles and its effect on propagation under spectrum loading is discussed. It is shown that the stress intensity at the threshold of slow stable growth is not only a material property but depends almost entirely on past load history. A description of the development test program to verify the analytical techniques and to substantiate the fail-safe strength of the fuselage shell is given together with the results of many of the tests.

### INTRODUCTION

With the introduction of the wide-bodied jet transport such as the McDonnell Douglas DC-10, fail-safe design has become increasingly important, particularly in the pressurized fuselage shell. The radial loading due to pressure has increased dramatically since the introduction of the first pressure shell design. This paper presents some of the steps taken during the development phases to ensure a fail-safe fuselage design.

The DC-10 aircraft is designed for a life of 120,000 hours which, based on a scatter factor of 2, represents 60,000 crack-free hours or 20 years of service at 3000 flight hours per year.<sup>1</sup>

A more realistic review of damage tolerance was required in which areas where fatigue damage is more likely to occur were considered. Analysis methods which included the capability to vary the degree of damage were developed to determine the residual strength of damaged, stiffened, structure. A self-propagating crack can be arrested in a region of low stress ahead of the crack tip by providing adequate circumferential and longitudinal stiffening. The crack-tip stress is reduced as the load is redistributed into the stiffeners. Various configurations were studied to produce an optimum structure, consistent with economy in manufacturing, which would not only provide fail-safe capability, but also would improve the service life of the fuselage shell.

In the past, the fail-safe design of aircraft structures incorporating the single element failure concept has proved inadequate. The introduction of fracture mechanics into aircraft design analysis methods has helped to overcome this inadequacy to some extent.

Plane strain fracture mechanics has almost become a science with the introduction of ASTM standard testing techniques, but much of the art remains with plane stress fracture of thin sheet components. This paper describes some of the methods used in applying linear elastic plane stress fracture mechanics to the design of stiffened, thin sheet fuselage structure.

This paper concentrates on three areas in which it is felt that significant error is introduced by present methods of analysis to predict crack propagation and residual strength of cracked stiffened panels:

- Effect of attachment flexibility
- Threshold of slow stable crack growth
- Flat panel versus curved panel testing

The attachment of the stiffener to the sheet and its flexibility are important in the prediction of stress distributions in stiffened crack panels. The assumption that the attachment is rigid and that the strains in the stiffener and skin are compatible can lead to considerable error.

The stress intensity at the threshold of slow stable crack growth has often been thought of as entirely a property of the material. It is, in fact, a function of the past loading history and the plastic zone ahead of the crack tip, introduced during previous loading cycles. The results of crack growth and residual strength tests on flat stiffened panels are presented, including the effects of high load cycles and slow stable crack growth. Crack growth rates  $da/dN$  versus the stress intensity factor range are presented for 2024-T3 clad sheet wide panels up to  $\Delta K$  values of 160 ksi  $\sqrt{\text{in.}}$ , approaching  $K_{IC}$  for the material.

A comprehensive test program was initiated to verify the analytical method and to study various configurations and materials. Both flat and curved panels were tested under uniaxial and biaxial loading, respectively. It was shown that while flat panel testing is in many ways adequate from a qualitative viewpoint, certain secondary effects are present while others are neglected which should be accounted for in the determination of allowable stresses.

## DAMAGE TOLERANCE

The degree of damage to be tolerated in a pressurized fuselage shell, without catastrophic failure, is not completely specified in any of the requirements of the regulating agencies. The FAA requires that the structure shall be capable of sustaining damage amounting to a single principal structural element when subjected to the loading for the fail-safe conditions listed in section 25.571, part 25, of the Federal Aviation Regulations. However, due to the large size of fuselage skin panels (approximately 400 by 80 inches for the DC-10), the single critical element is normally interpreted to mean one skin panel between any two longitudinal or circumferential stiffening members. This one-bay panel damage has been adopted by many designers in the past. In order to be realistic, however, one should consider how structural damage is initiated. Past experience has shown that the majority of damage incurred in service is due to fatigue, although isolated incidents such as engine cowls becoming detached, thrown engine parts, and small arms fire have been known to cause varying degrees of skin damage and should not be overlooked.

It was noted previously that the DC-10 is designed to be crack-free for 60,000 hours (including scatter factors), which represents about 20 years of service. However, imperfections in manufacturing such as badly driven rivets which do not fill holes properly, the preloading of parts due to mismatch, and scratches received in service can reduce fatigue life and thus the possibility of fatigue cracks occurring cannot be ignored.

## Longitudinal Skin Cracks

Cabin pressurization is the main source of loading causing longitudinal skin cracks. Figure 1 shows that radial loading due to internal pressure on the DC-10 is 3-1/2 times as high as that for the DC-6, which was the first pressurized aircraft designed at Douglas.

Testing on basic pressurized fuselage shell structure has indicated that longitudinal skin cracks are more likely to start in two critical locations, as follows:

1. Along the line of attachments which attach the outer fingers of a longitudinal splice member to the skin as shown in Figure 2: The radial tension stress due to pressure varies across a longitudinal skin bay and reaches a maximum value midway between frames. Transfer of load from the skin into the finger doubler causes a high attachment bearing stress which, when combined with the radial tension stress, may cause a fatigue crack in a longitudinal direction. A large number of configurations for the longitudinal splice shown in Figure 2 were fatigue tested. The configurations were changed until all failures occurred as shown in Figure 2 where they can be detected by visual inspection methods. Fatigue cracks hidden by splice plates could propagate a considerable distance before detection.

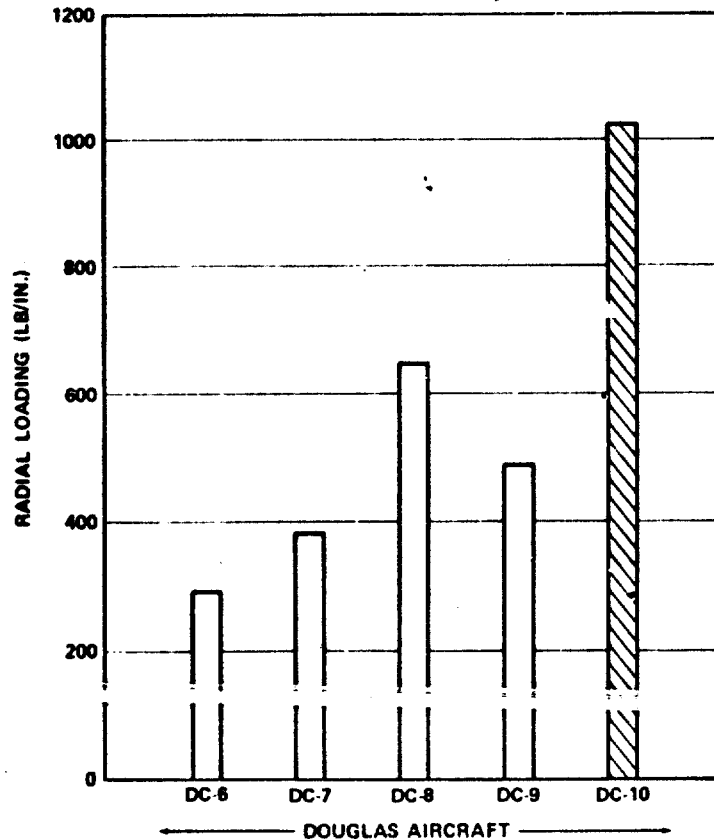


FIGURE 1. FUSELAGE SHELL RADIAL LOADING DUE TO NOMINAL CABIN PRESSURE

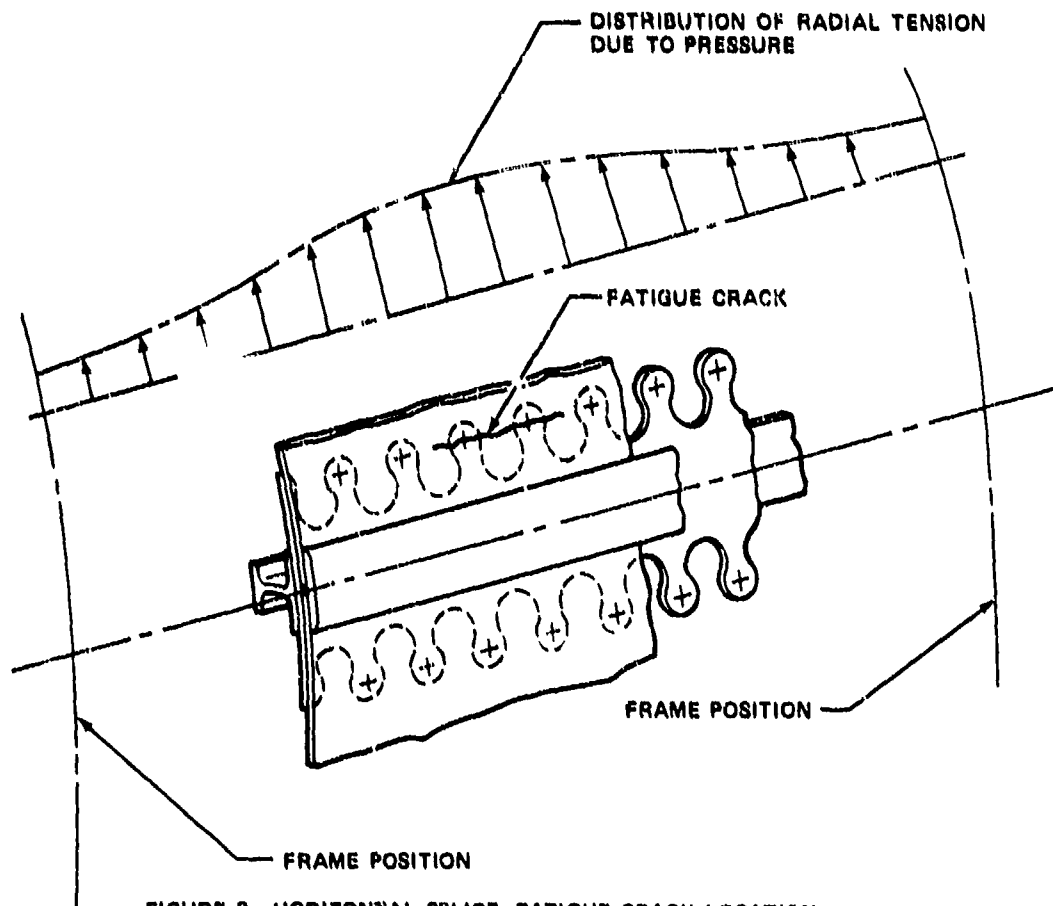


FIGURE 2. HORIZONTAL SPLICE, FATIGUE CRACK LOCATION

2. At the first attachment of a frame shear clip to skin joint as indicated in Figure 3: The stress  $\sigma_c$  in the region of the shear clip cutout is higher than the mid-bay stress due to the discontinuity of the clip. In addition, the skin may be carrying tension stress due to frame bending. The high local stress, combined with the bearing stress in the first attachment hole as the shear clip picks up load, can cause a fatigue crack in the skin. The skin crack shown in Figure 3a is just as likely to propagate into both adjacent bays as into one bay.

#### Transverse Skin Cracks

Testing under combined pressure and axial loads has indicated that transverse or circumferential skin cracks occur in two locations, as follows:

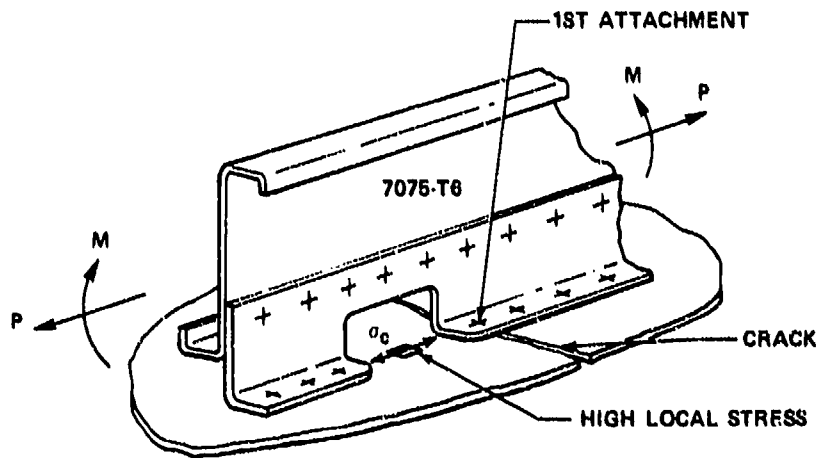
1. At the attachment of the skin to frame shear clip midway between longerons as shown in Figure 4: Local bending of the skin due to pressure, combined with axial stress due to fuselage bending, can cause skin cracks in a circumferential direction.
2. In the flanges where they attach to the frame as shown in Figure 4: Bending due to transfer of some of the pressure loading into the frame increases the axial tension stress in the longeron flanges locally, causing fatigue cracks. After failure of the longerons, the skin stress increases locally (Figure 13) causing fatigue cracks in the skin which propagate into the two adjacent skin bays.

In view of the above facts, it is evident that damage extending to two skin bays should be considered. Materials and stress levels are normally chosen so that cyclic crack growth rates are low and a propagating crack will be noticed within a reasonable inspection period and before reaching a critical length. However, hairline cracks are extremely difficult to find under zero load conditions and can easily escape detection. The design should, therefore, include the capability to arrest a crack after a fast fracture has occurred. The damage tolerance selected for the DC-10 fuselage shell was, therefore, as follows:

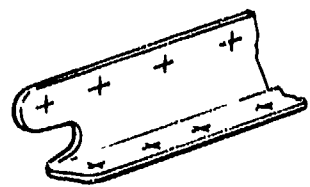
- Two-bay longitudinal crack with the center frame intact
- Two-bay circumferential crack with a center longeron failed

#### CONFIGURATION CANDIDATES

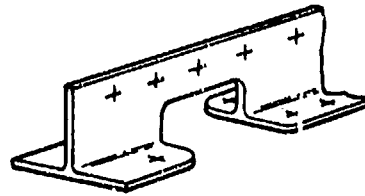
The basic shell configuration selection is the result of many trade studies conducted to satisfy a number of requirements such as shell general instability, frame flexibility and strength, as well as fatigue and fail-safe strength. The results of these studies indicated that the frame spacing should be 20 inches and longeron spacing should vary from 8 inches at the top of the shell to 6.5 inches at the bottom. The minimum bending stiffness of the frame section was set from general instability requirements. The outer and inner radii of the frame cross section were set by airplane performance and inside cabin dimension requirements, respectively. Although these basic dimensions were set for the minimum shell, several means were available to satisfy the fail-safe requirements to the damage toler-



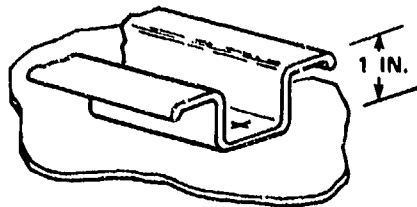
(a) MINIMUM FRAME SECTION  
(ANGLE SHEAR CLIP)



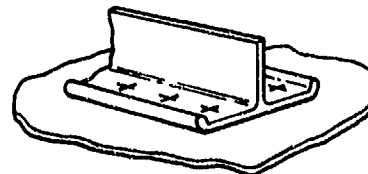
(b) EXTENDED SHEAR CLIP



(c) TEE SHEAR CLIP



(d) HAT LONGERON



(e) TEE LONGERON

FIGURE 3. FRAME AND LONGERON CONFIGURATIONS

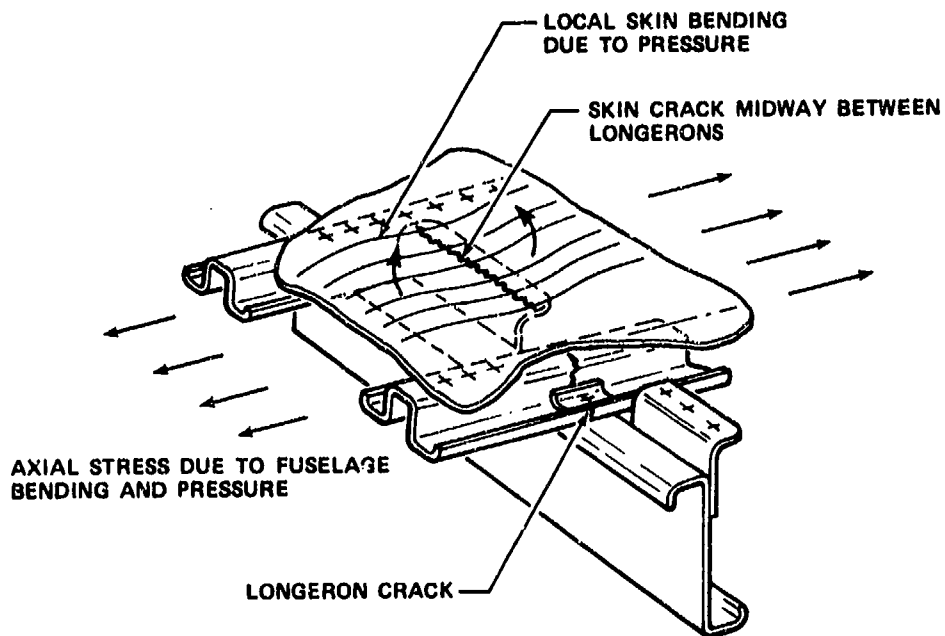


FIGURE 4. CRACK LOCATIONS, FUSELAGE SHELL

ance specified. These were the selection of (a) skin thickness, (b) skin material, (c) whether or not to use crack stoppers, and (d) longeron geometric shape.

#### Skin Thickness

The skin thickness selection for the minimum gage portion of the fuselage is particularly important for an aircraft such as the DC-10. The surface area of the shell is approximately 8700 square feet with 84 percent of this minimum gage. One gage variation can thus represent a weight change of approximately 950 pounds.

The most predominant loading condition for the minimum gage portion of the shell is due to pressurization. The fuselage is subjected to one full pressure cycle virtually every flight and, therefore, fatigue plays a vital part in the selection of the minimum gage. Hoop tension stresses should be kept to reasonably low limits to prevent failures in horizontal splices and in longeron-to-skin rivet lines. It should also be noted that local bending stresses due to pressure, in areas such as those illustrated in Figure 4, increase in inverse proportion to the skin thickness squared. Longitudinal crack propagation is decreased with decreasing hoop tension stress due to increasing skin thickness. Residual strength is increased to a lesser degree as will be illustrated later.

#### Skin Material

The skin material choice is perhaps the most important factor affecting the residual strength of a damaged fuselage shell. An independent research and development (IRAD) program on residual strength of stiffened flat wide panels<sup>2</sup> had resulted in the following values of plane stress fracture toughness  $K_{Ic}$  for four candidate materials: 52,700 to 63,500 psi  $\sqrt{\text{in.}}$  for 7075-T6, 70,000 psi  $\sqrt{\text{in.}}$  for 2014-T6, 90,000 psi  $\sqrt{\text{in.}}$  for 7075-T73 and as high as 158,000 psi  $\sqrt{\text{in.}}$  for 2024-T3. From a static strength standpoint, the ideal choice would be 7075-T6. In the past, 2014-T6 had been used successfully but in view of the increased radial loading (Figure 1) and the tendency to work to higher stress levels,<sup>1</sup> it was considered that a material with a higher fracture toughness would be more desirable. The two materials, 7075-T73 and 2024-T3, were therefore considered as candidates.

#### Crack Stopper Straps

The use of crack stopper straps is an effective means of increasing the residual strength of damaged panels. An unstable fast fracture can be confined to a local area by providing an area of low stress ahead of the crack tip. The crack tip stress is reduced as a large part of the redistributed load is transferred into the strap. The region of low stress can also be provided, to a lesser degree, by a frame connected to the skin by shear clips as indicated in Figure 3. The latter configuration would be desirable from a cost standpoint if the required residual strength could be attained.

When crack stopper straps are required, it has been Douglas policy to install them at a frame location, as illustrated by Figure 5, for several very good reasons. Without crack stopper straps, the skin stress level in the vicinity of the frames between shear clips (Figure 3) has been determined both from flat panel and curved panel pressure tests to be up to 18 percent higher than the mid-bay hoop stress. With crack stopper straps to provide continuity across the gap, the stress level in this critical area is reduced to 15 percent below the mid-bay stress, thus reducing the possibility of a fatigue crack starting. In addition, the crack stopper strap can be used as bending material to increase the frame stiffness and static strength. Tests have shown that after cutting a 3-inch-long slot in the skin over a titanium crack stopper strap that almost 14,000 cycles are required at 15,500 psi gross stress with a stress ratio  $R = 0.05$  to fail the strap. During this number of cycles, crack propagation was negligible until the crack stopper had failed. Prior to failure of the crack stopper, the increase in frame stress due to the crack was negligible, thus reducing the possibility of frame fatigue failure. With the strap at any other location, the possibility of starting a crack in the skin is increased, and, once a crack started, propagation would be much faster and the possibility of failing the frame in fatigue would be increased.

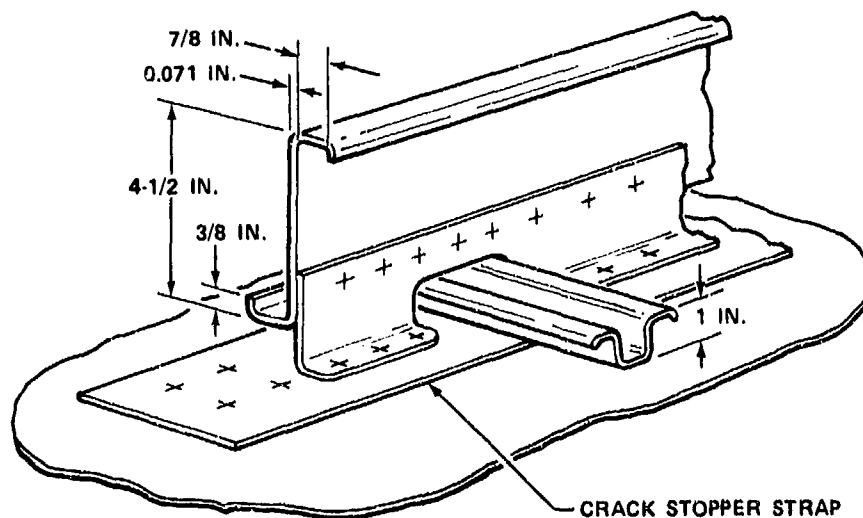


FIGURE 5. FRAME CRACK STOPPER CONFIGURATION

There is one advantage in placing the crack stopper midway between frames for cracks which start at frames. The crack would be confined to 20 inches in length. However, with this configuration the crack is more likely to start. If a mid-bay crack stopper is installed by riveting, a crack is just as likely to start at a rivet hole and propagate both ways. Tests have shown that before a crack propagates very far, the crack stopper would fail in fatigue due to the high load transfer into the strap. In highly loaded areas the adjacent frames (without crack stoppers) would be incapable of arresting the crack. The outer crack stoppers would therefore be required to arrest a 40-inch crack without the help of a backup frame. The possibility of starting a crack at a mid-bay crack stopper would be reduced if the strap were bonded to the skin without additional rivets. This configuration was considered for the DC-10 and abandoned for several reasons. The candidate material for crack stoppers was titanium and bonding of this material to aluminum was not considered as reliable as riveting. The bonding could easily become delaminated in service, especially under repeated shear loading of the skin panels and possible wrinkling due to tension field action. The longerons, passing over the bonded-on strap, would still require riveting through the strap. The bonding is subjected to delamination locally where the holes are drilled and the subsequent riveting operation is completed. Delaminations have been experienced where bonding is combined with riveting due to differences in the shear stiffness of the bonding material and the rivets. In addition, moisture seeping into the rivet holes and subsequently into the bonded surface has been known to cause delamination through corrosion.

Minimum weight structure with maximum reliability, consistent with the damage tolerance selected, was required. It should also be remembered that fatigue cracks, if they occur in service, usually form after many years of service. Techniques used to prevent rapid fracture should therefore be designed to perform other functions, for maximum economy, and yet be ready to stop a fast fracture without having deteriorated during service.

Another reason for abandonment of the bonding process and possibly the most significant is the distortion of the aluminum skin caused by thermal effects due to the difference in the coefficient of expansion of the titanium and the aluminum. A small test panel was fabricated as shown in Figure 6 and a strap of 0.025-inch thick titanium was bonded to it and cured at a temperature of 250°F (121°C). On cooling to room temperature, the panel curved to approximately 70-inch radius with the strap on the convex side. The panel was rolled to the correct radius with the strap on the concave side. The resulting anticlastic curvature due to residual stresses is illustrated in Figure 6. It was thought that this effect would be more severe on large panels, especially with longerons and frames assembled to the panels. The resulting quilted appearance of the shell would almost certainly be unacceptable to the customer.

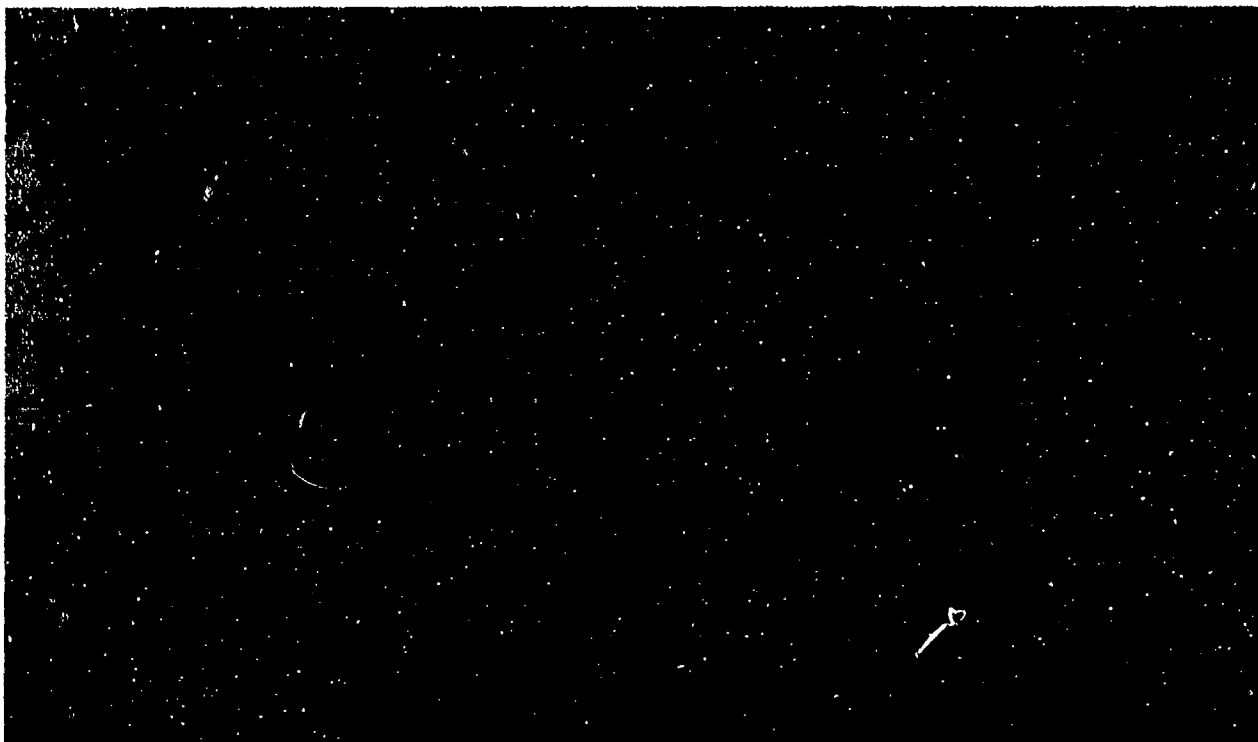


FIGURE 6. TEST PANEL DISTORTION DUE TO BONDING PROCESS

#### Longeron Geometric Shape

Hat-section longerons such as those illustrated in Figure 3d have been used on all previous Douglas aircraft. However, analysis indicated that for the damage tolerance selected for circumferential cracks, Tee-section longerons riveted to the skin with two rows of rivets would give higher allowable stresses. The Hat-section longerons were desirable from a cost standpoint because of the cost of the extra row of rivets required in the Tee-section longerons. Both Tee-section and Hat-section longerons were therefore chosen as candidates.

Both analysis and test programs were introduced to study the configurations.



## ANALYSIS

Analysis of the candidate configurations for the damage tolerance selected was highly desirable prior to starting the development test program. In early work at Douglas,<sup>3, 4, 5</sup> parametric lumped parameter analysis had been performed on 60-inch-wide panels with a single stiffening element containing a one-bay crack. Although this analysis proved to be extremely helpful in preliminary design work, further refinements were required to answer some of the questions listed below for panels containing two-bay cracks.

- How effective was the frame member working in conjunction with a crack stopper strap?
- How did the stress vary across the frame?
- What effect did a broken longeron have on the crack tip stress for a circumferential crack and how did the stress vary across the outer longeron cross section?

In view of this, the analysis described herein was initiated.

## Analysis of Cracked Unstiffened Panels

The most generally accepted equation for the fracture strength of unstiffened thin panels containing a central crack is (Reference 6)

$$\sigma_R = \frac{K_c}{C \sqrt{W \tan \frac{\pi a_c}{W}}} \quad (1)$$

where:

- $\sigma_R$  = Gross stress at failure
- $K_c$  = Plane stress fracture toughness, psi  $\sqrt{\text{in.}}$
- $C$  = Width correction factor<sup>7</sup>  $1.0 + 0.3 (2a/W)^2$
- $a_c$  = Half crack length at fast fracture
- $W$  = Panel width

For large panel widths, Eq (1) can be simplified as follows:

$$\sqrt{W \tan \frac{\pi a_c}{W}} = \left[ \pi a_c + \frac{W}{3} \left( \frac{\pi a_c}{W} \right)^3 + \frac{2W}{15} \left( \frac{\pi a_c}{W} \right)^5 + \dots \right]^{1/2}$$

For large values of  $W$  then

$$\sqrt{W \tan \left( \frac{\pi a_c}{W} \right)} \text{ approaches } \sqrt{\pi a_c}$$

$$\text{Therefore, Eq (1) reduces to } \sigma_R = \frac{K_c}{\sqrt{\pi a_c}} \quad (2)$$

## Analysis of Cracked Stiffened Panels

The effects of stiffeners on the fracture strength of stiffened panels can be determined by a Lumped Parameter Analysis of a structure representing the panel. The analysis is based on the Matrix Force Method of Structural Analysis<sup>8, 9</sup> and uses the Fortran Matrix Abstraction Technique (FORMAT)<sup>10</sup> to solve the matrix operations. Figures 7 and 8 show the idealized structure representing the stiffened panels for one- and two-bay longitudinal cracks, respectively. Figure 9 shows the idealized model for the two-bay circumferential crack. As illustrated, the panels are divided into a series of discrete bars and shear panels. The bars carry axial load and the panels carry shear load. The panels have the same thickness as the plate, and the bar areas are determined from the dimensions shown in Figure 8 as follows:

$$A_y = t(Z_1 + Z_2)/2 \text{ and } A_z = t(Y_1 + Y_2)/2$$

Loads are applied to the top of the panels, and reactions are provided at the bottom. The propagating crack is simulated by successive disconnection of the reactions in the skin at the horizontal centerline of the panel by an element modification procedure which is part of the computer program. The crack tip stress is defined by the stress in the last bar adjacent to the simulated crack as shown in Figure 7. The stiffening elements are represented by additional lumped bars connected to the main panel by a series of continuous shear panels.

A typical frame cross section with crack stopper strap is idealized by lumping areas as shown in Figure 10. As the crack propagates in the skin, the frame outer cap picks up load through the shear clip-to-frame attachment row. The area of the outer cap  $A_o$  is therefore calculated so that its cg lies on this attachment row. Frames without crack stoppers (Figure 3) are idealized by three lumped bars.

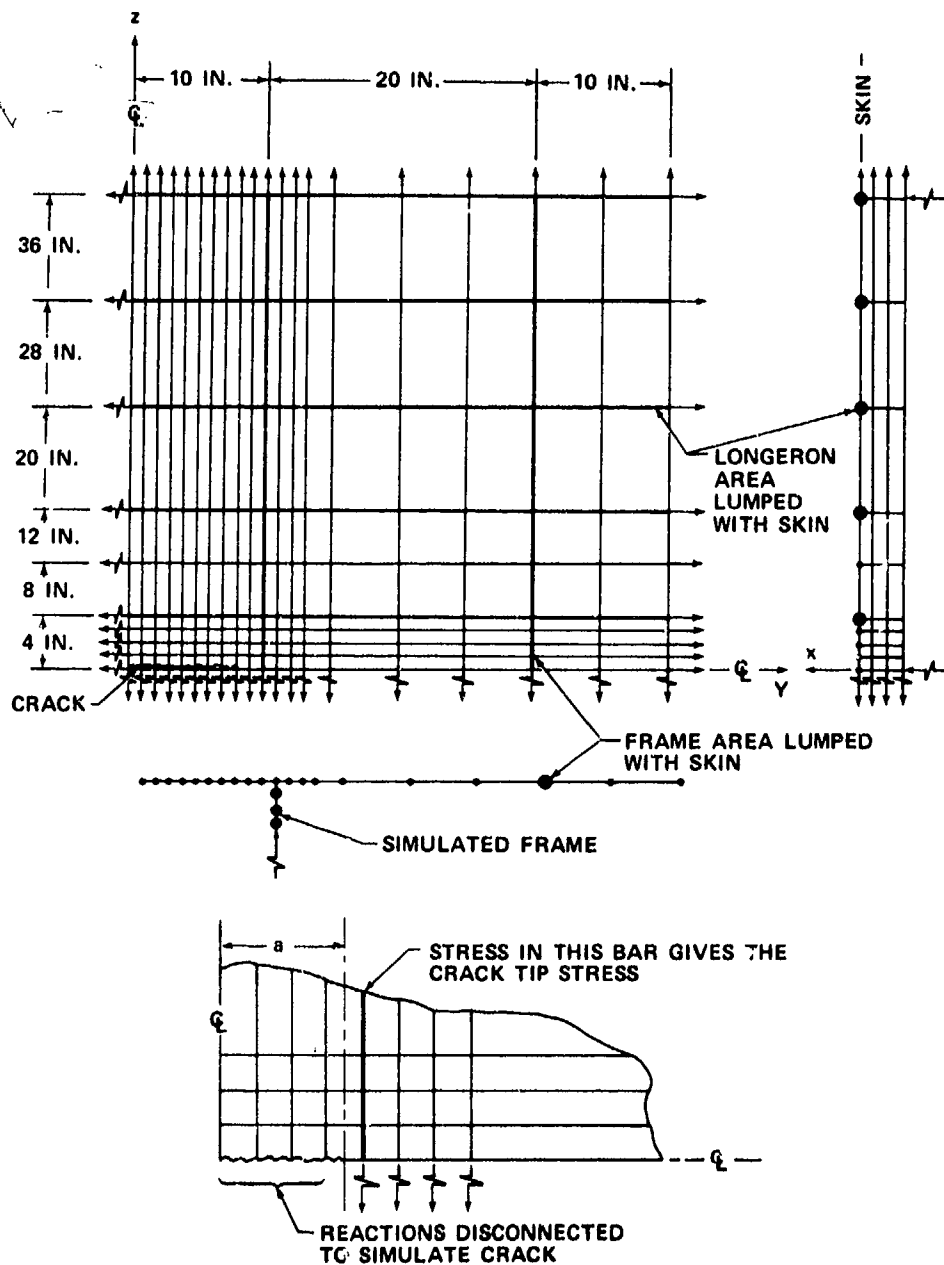


FIGURE 7. IDEALIZATION FOR ONE-BAY LONGITUDINAL CRACK

The stress intensity at the tip of the crack and the net section stress ahead of a crack tip are reduced when stiffeners are provided. As the crack extends, part of the load is transferred to the stiffeners and the remaining load is transferred to the skin ahead of the crack. If the stiffeners to skin attachment is infinitely flexible, no load will be transferred into the stiffener and the panel will behave like an unstiffened panel with no reduction in crack tip stress intensity. If, however, the attachment is rigid, a large portion of the load from the cracked sheet will be transferred to the stiffener, thus reducing the stress ahead of the crack tip with a consequent reduction in the crack tip stress intensity factor. It can be seen then that attachment flexibility must be accounted for if the proper stress distributions are to be determined.

Rivet shear deflection in aluminum alloy sheet is expressed as:

$$\delta = \frac{Pf}{E_a d} \quad (3)$$

where:

- $\delta$  = Deflection
- $P$  = Applied load
- $E_a$  = Modulus of aluminum
- $d$  = Rivet diameter

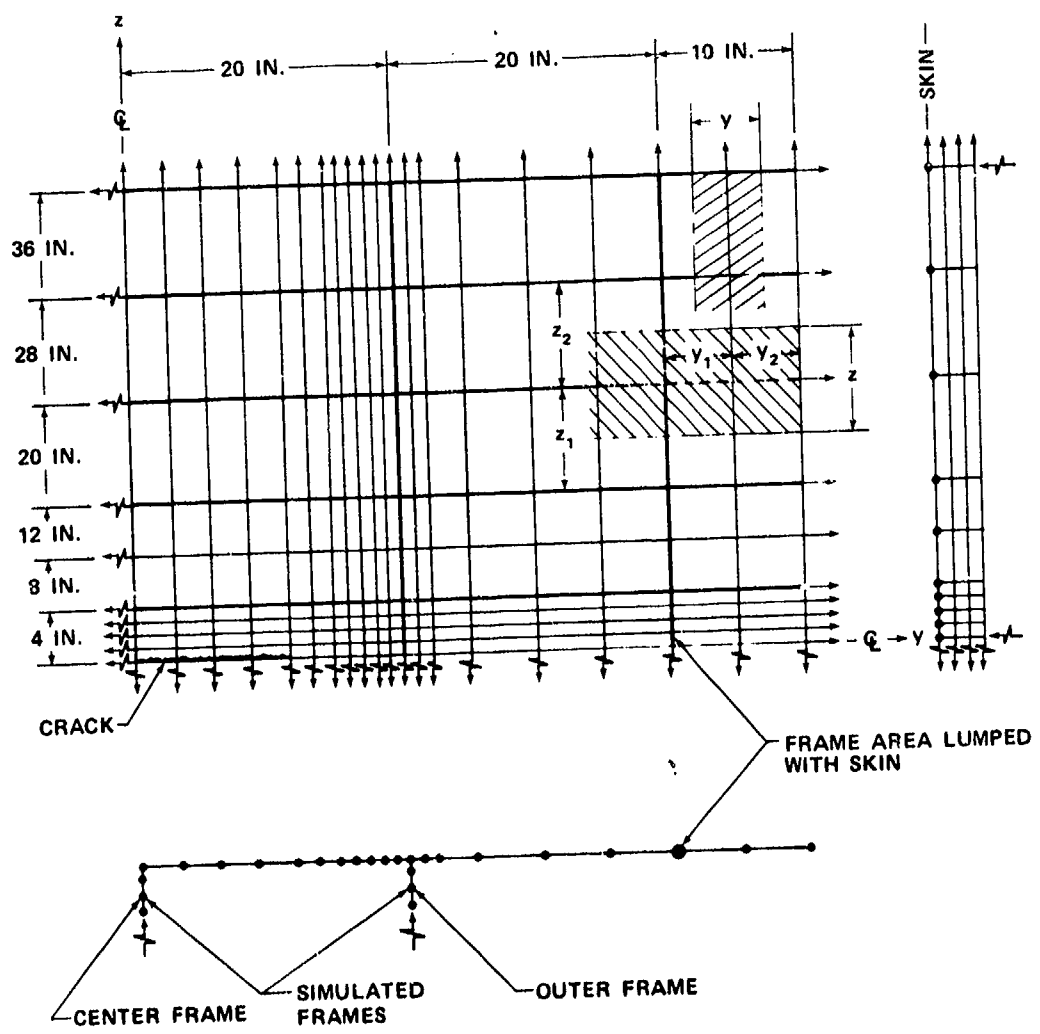


FIGURE 8. IDEALIZATION FOR TWO-BAY LONGITUDINAL CRACK

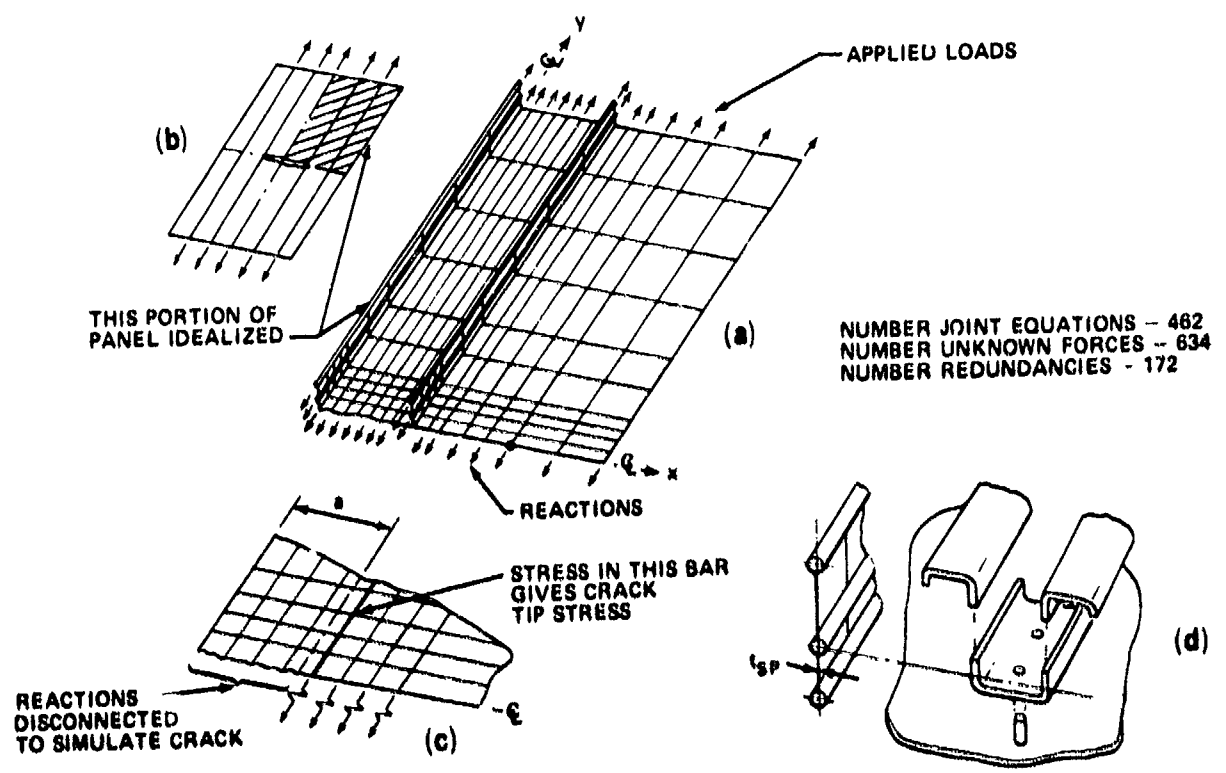


FIGURE 9. IDEALIZATION FOR TWO-BAY CIRCUMFERENTIAL CRACK

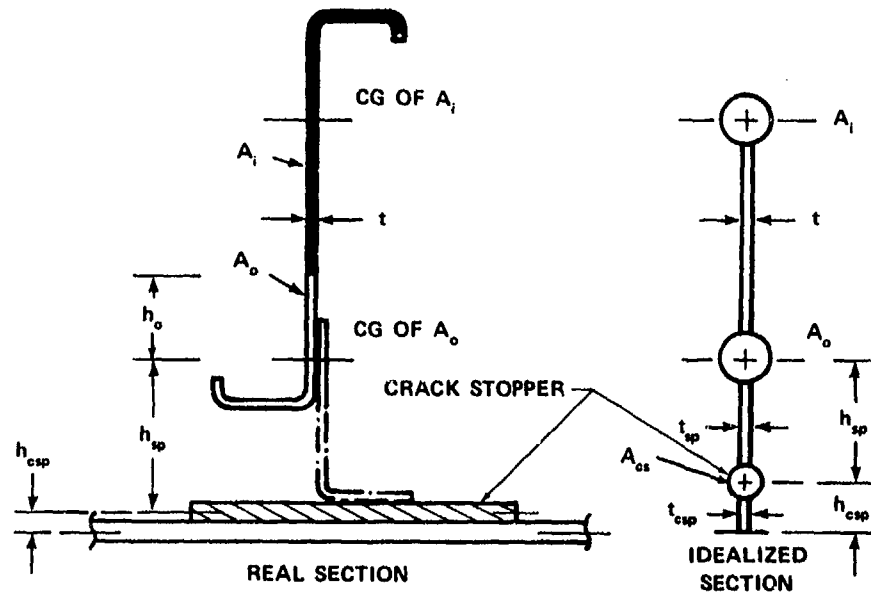


FIGURE 10. FRAME IDEALIZATION WITH CRACK STOPPER

and, for aluminum alloy rivets

$$f = 5.0 + 0.8 \left[ \frac{d}{t_1} + \frac{d}{t_2} \right] \quad (4)$$

where  $t_1$  and  $t_2$  are thicknesses of joined sheets.

For the shear clip to crack stopper and skin to crack stopper rivets,

$$f = 5.0 + 0.8 \left[ \frac{d}{t_1} + \frac{d E_a}{t_2 E_{cs}} \right] \quad (5)$$

where:

$E_{cs}$  = Modulus of crack stopper material.

These equations have been substantiated by test (Figure 50). The thickness of the idealized shear panels connecting the crack stopper to the skin is calculated as follows:

$$\text{Rivet deflection } \delta_R = \frac{Pf}{nE_a d}$$

where  $n$  = number of rivets between longerons.

$$\text{Idealized shear panel deflection } \delta_{csp} = \frac{Ph_{csp}}{Lt_{csp}G_a}$$

where:

$L$  = Distance between longerons

$G_a$  = Shear modulus of aluminum

However,  $\delta_R = \delta_{csp}$ , and equating deflections and solving for  $t_{csp}$ :

$$t_{csp} = \frac{h_{csp} n E_a d}{L G_a f} \quad (6)$$

The shear clip is idealized in a similar manner including both rows of rivets and the sheet metal clip.

For longitudinal bars located at longeron positions, the longeron area is included with the skin area in the plane of the sheet. Longerons in panels containing circumferential cracks are idealized into two lumped bars connected to the skin by a continuous shear panel. The thickness of the panel is determined using an equation similar to Eq (6).

Adhesive bonded joints are treated in a similar fashion. Referring to Figures 11d, 11e and 11f the thickness  $t_{sp}$  of the idealized shear panel of height  $h_{sp}$  is determined by equating the bond deflection  $\delta_b$  to the idealized shear panel deflection  $\delta_{sp}$

$$\delta_b = \frac{Pt_b}{W_b G_b}$$

where

- $W_b$  = bond width
- $t_b$  = bond thickness
- $G_b$  = shear modulus of adhesive bond material
- $\delta_b = \delta_{sp}$

$$t_{sp} = \frac{h_{sp} W_b G_b}{G_A t_b} \quad (7)$$

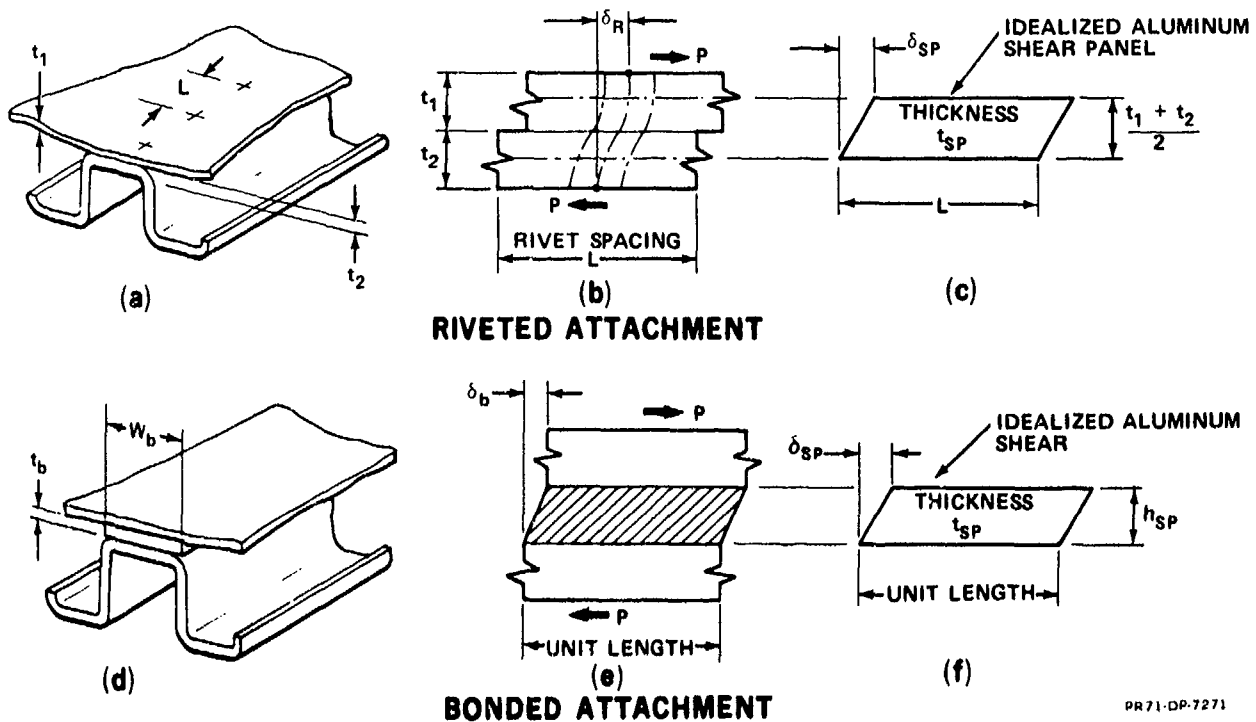


FIGURE 11. ATTACHMENT IDEALIZATION

The height  $h_{sp}$  would normally equal the bond thickness  $t_b$ . However, if a parametric study is required, it is often advantageous to obtain a unit solution with shear panel height constant and then modify the shear panel stiffness by changing its thickness using the element modification procedure outlined in the Appendix. In this way, any combination of crack length and stiffness up to a total of twelve can be made in one computer run.

The effect of stiffeners on the crack tip stress is determined by analyzing both unstiffened and stiffened panels having the same grid size and taking ratios between the crack tip stresses. The crack tip stress ratio, which is a function of crack length, is expressed as

$$R_{ct} = \frac{\sigma_{yct} \text{ in unstiffened panel}}{\sigma_{yct} \text{ in stiffened panel}}$$

where  $\sigma_{yct}$  is the stress in the y direction at the crack tip. Since Eq (1) and (2) are directly related to the plate net stress in the region of the crack tip, they can be rewritten to include the effects of stiffening.

The presence of secondary effects<sup>11</sup> such as crack buckling, makes the determination of  $K_c$  as a material parameter extremely difficult.  $K_c$  is, therefore, replaced by  $K_c^*$  which includes secondary effects. Thus, Eq (1) and (2) become, for finite width panels

$$\sigma_R = \frac{K_c^* R_{ct}}{C \sqrt{W \tan \frac{\pi a}{W}}} \quad (8)$$

and for infinite panels

$$\sigma_R = \frac{K_c * R_{ct}}{\sqrt{\pi a_c}} \quad (9)$$

$K_c$  determined from tests on stiffened panels of one configuration can be used to determine the fracture strength of a fuselage shell of another configuration by using Eq (9), provided  $R_{ct}$  versus crack length has been determined. The use of  $R_{ct}$ , determined from analysis of a finite panel, can be justified for use in Eq (9) for an infinite plate if the panel is wide enough. A comparison of the net section stress for the panel of Figure 7 to Westergaard's<sup>12</sup> equation for the net section stress of an infinitely wide plate is shown in Figure 12.

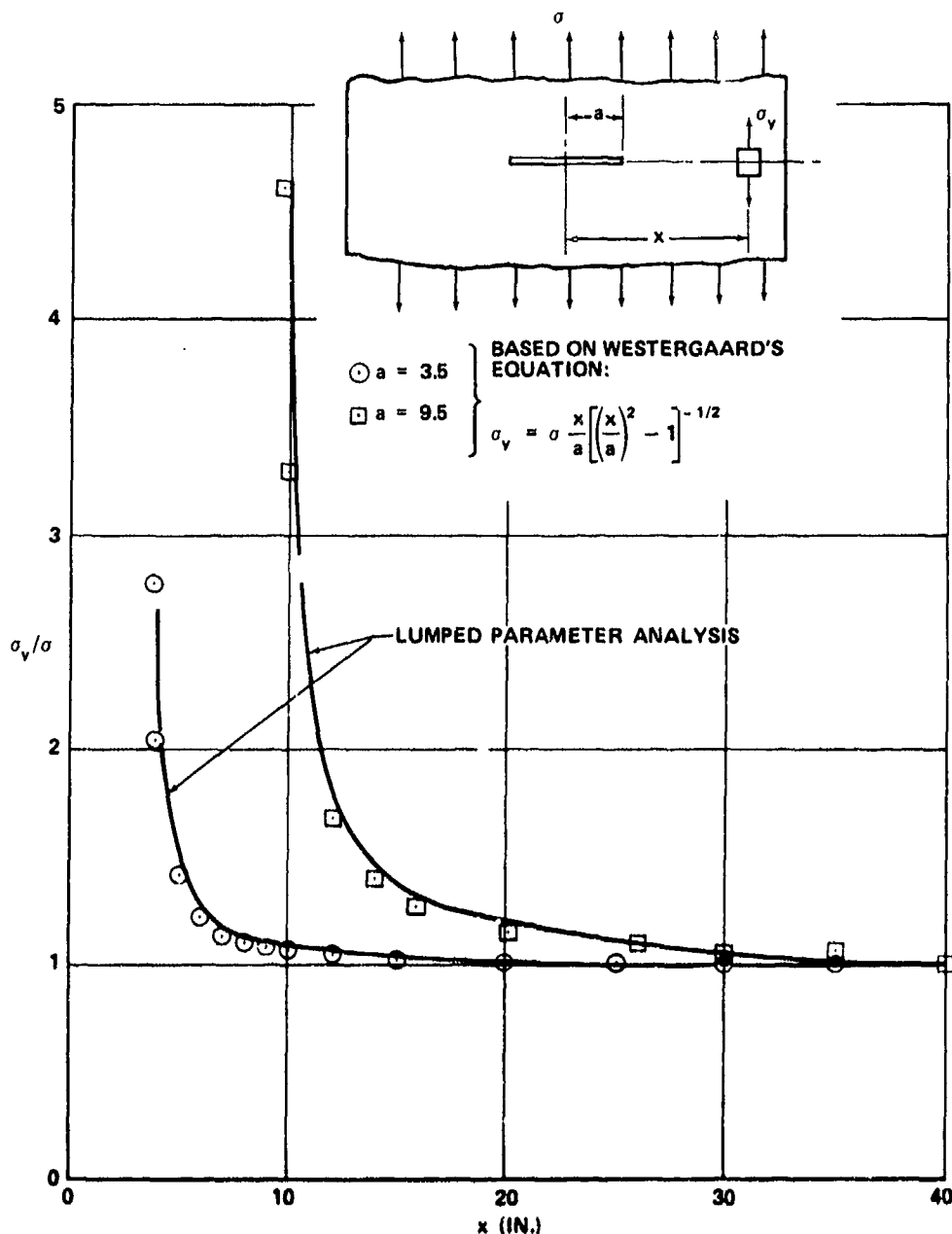


FIGURE 12. COMPARISON OF LUMPED PARAMETER ANALYSIS WITH WESTERGAARD'S EQUATION FOR INFINITELY WIDE PLATE

#### Analysis Results

Table 1 lists some of the more important analysis cases considered. Cases 1 to 9 and 10 to 12 are for two-bay and one-bay longitudinal cracks, respectively, where the frame members and circumferential crack stopper straps cause a reduction in crack tip stress. Cases 13 to 20 are for two-bay circumferential cracks with a broken central longeron where the outer longerons cause a reduction in the crack tip stress. For all of the cases listed in Table 1, a uniform stress level was applied to the upper boundary of the panels (shown in Figures 7, 8 and 9) to both skin and stiffening elements. The results of the analysis cases considered are listed in Tables 2, 3 and 4. The frame cross sections for cases 1 to 12 and the Hat-sections for cases 13 to 18 are similar to those shown in Figure 5. The stress ratio terms are defined below:

TABLE 1  
DESCRIPTION OF ANALYSIS CASES

CASE NO.	CASE DESCRIPTION	CRACK TYPE
1	FRAMES WITHOUT CRACK STOPPERS - 0.071 SKIN - CENTER FRAME INTACT	2 BAY LONGITUDINAL CRACK
2	FRAMES WITHOUT CRACK STOPPERS - 0.080 SKIN - CENTER FRAME INTACT	
3	FRAME WITH CRACK STOPPER - 0.071 SKIN - CRACK STOPPER 3 IN. BY 0.025 IN. TITANIUM WITH THREE ROWS 3/16 RIVETS - CENTER CRACK STOPPER INTACT	
4	SAME AS CASE 3 WITH CENTER CRACK STOPPER FAILED	
5	SAME AS CASE 3 WITH BOTH CENTER CRACK STOPPER AND CENTER FRAME FAILED	
6	FRAME WITH CRACK STOPPER - 0.071 SKIN - CRACK STOPPER 2.8 IN. BY 0.025 IN. TITANIUM WITH TWO ROWS 3/16 RIVETS - CENTER CRACK STOPPER FAILED.	
7	FRAME WITH CRACK STOPPER - 0.071 SKIN - CRACK STOPPER 2 IN. BY 0.02 IN. TITANIUM WITH TWO ROWS 3/16 RIVETS - CENTER CRACK STOPPER FAILED.	
8 <sup>a</sup>	FRAME WITH CRACK STOPPER - 0.083 SKIN - CRACK STOPPER 3.25 IN. BY 0.016 IN. TITANIUM WITH TWO ROWS 3/16 RIVETS - CENTER CRACK STOPPER FAILED.	
9	SAME AS CASE 8 WITH CENTER FRAME FAILED	
10	FRAMES WITHOUT CRACK STOPPERS - 0.071 SKIN	1 BAY LONGITUDINAL CRACK
11	FRAMES WITHOUT CRACK STOPPERS - 0.08 SKIN	
12	FRAMES WITH CRACK STOPPER - 0.071 SKIN - CRACK STOPPER 3 IN. BY 0.025 TITANIUM WITH THREE ROWS 3/16 RIVETS	
13	ROLLED HAT SECTION LONGERON - NET AREA 0.205 IN. <sup>2</sup> - 0.083 SKIN - ONE ROW 3/16 RIVETS AT 1-1/4 PITCH	2 BAY CIRCUMFERENTIAL CRACK WITH BROKEN CENTRAL LONGERON
14	SAME AS CASE 13 WITH 0.071 SKIN	
15	EXTRUDED HAT SECTION LONGERON - NET AREA 0.3029 IN. <sup>2</sup> - 0.071 SKIN - ONE ROW 3/16 RIVETS AT 1-1/4 PITCH	
16	SAME AS CASE 15 WITH 0.080 SKIN	
17	EXTRUDED HAT SECTION LONGERON - NET AREA 0.5121 IN. <sup>2</sup> - 0.071 SKIN - ONE ROW 3/16 RIVETS AT 1-1/4 PITCH	
18	SAME AS 17 WITH ONE ROW 3/16 STEEL ATTACHMENTS AT 1-1/4 PITCH	
19	EXTRUDED TEE SECTION LONGERON - NET AREA 0.2895 IN. <sup>2</sup> TWO ROWS 3/16 RIVETS AT 1-1/4 PITCH	
20	EXTRUDED TEE SECTION LONGERON - NET AREA 0.4865 IN. <sup>2</sup> TWO ROWS 3/16 RIVETS AT 1-1/4 PITCH	

<sup>a</sup>CASE 8 FRAME THICKNESS IS 0.063 IN. WITH DIMENSIONS AS SHOWN IN FIGURE 5.

- $\sigma$  = Gross stress applied to the upper boundary of the panel, psi
- $\sigma_{ccs}$  = Center crack stopper stress, psi
- $\sigma_{ocs}$  = Outer crack stopper stress, psi
- $\sigma_{occf}$  = Outer cap stress in the center frame, psi
- $\sigma_{iccf}$  = Inner cap stress in the center frame, psi
- $\sigma_{ocof}$  = Outer cap stress in the outer frame, psi
- $\sigma_{icof}$  = Inner cap stress in the outer frame, psi
- $\sigma_{of}$  = Longeron outer fiber stress, psi
- $\sigma_{if}$  = Longeron inner fiber stress, psi

All of the stresses shown are lumped stresses in the idealized members. The stress distributions in the sheet after a longeron is broken and prior to skin cracking is shown in Figure 13 for conditions 15 and 17 of Table 1.

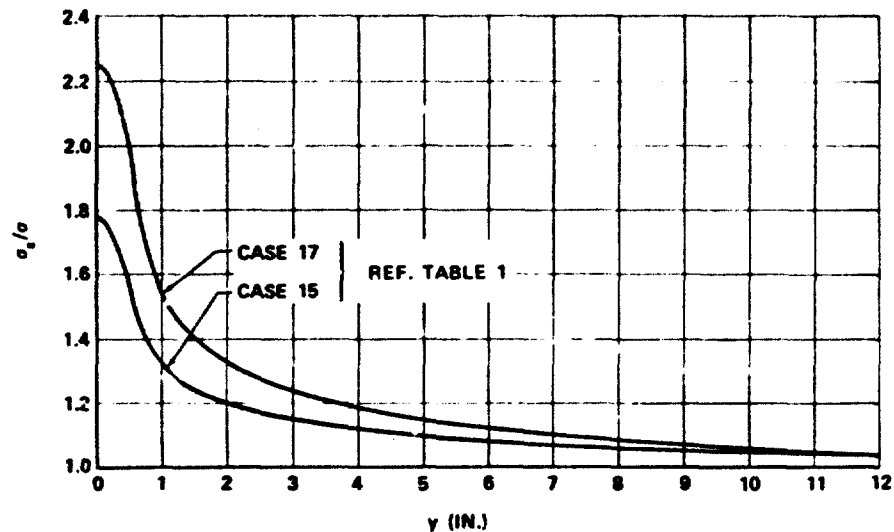
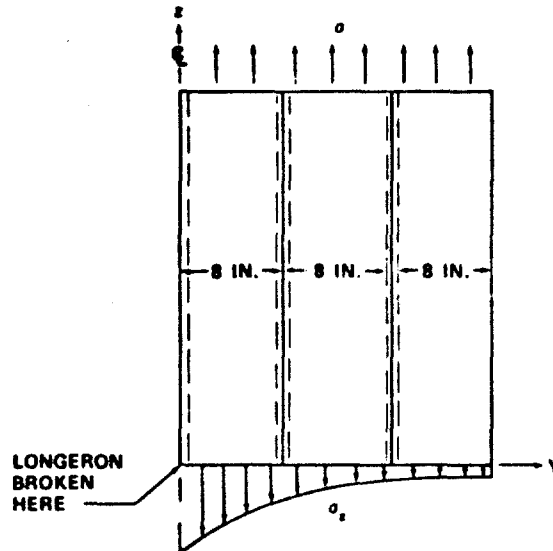


FIGURE 13. AXIAL SKIN STRESS IN THE VICINITY OF A BROKEN LONGERON

#### Skin Fracture Criterion

The presence of  $R_{ct}$  is illustrated in Figure 13 and represents the residual strength of a panel, based on skin criteria. The lower curve (dotted) represents an unstiffened panel and the upper two curves are for stiffened panels with longitudinal cracks plotted for cases 1 and 4 of Table 1. The change in slope of the curves for stiffened panels as the crack tip approaches the stiffener spacing is due to a reduction in crack tip stress as the stiffener picks up load. The maximum reduction in crack tip stress occurs in the region of the stiffeners as can be seen by the increase in  $R_{ct}$  values listed in Table 2.



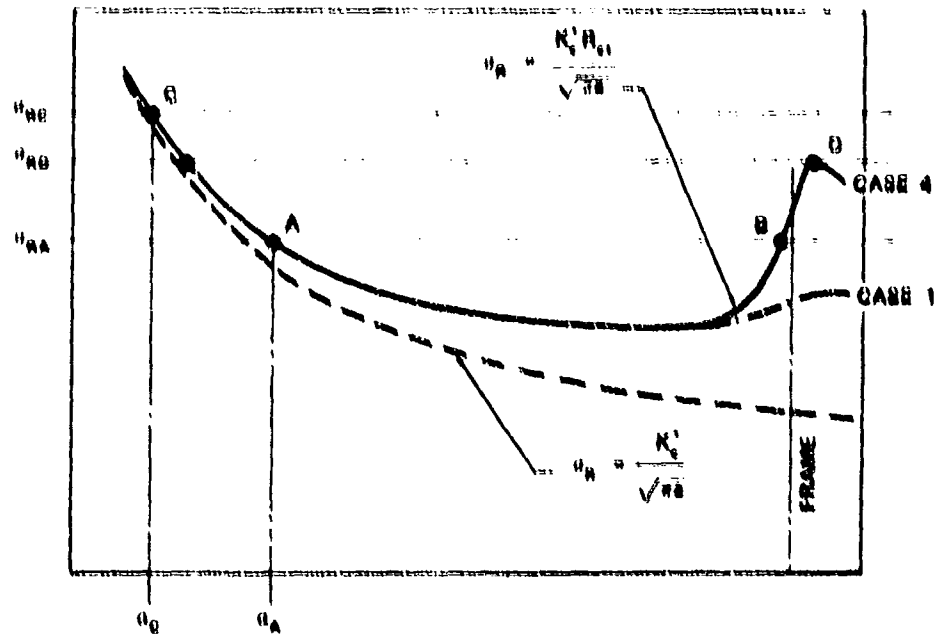


FIGURE 14. COMPARISON OF GROSS RESIDUAL STRENGTH CURVES FOR UNSTIFFENED AND STIFFENED PANELS, CASES 1 AND 4 OF TABLE 1

TABLE 2  
STRESS RATIOS FOR TWO-BAY LONGITUDINAL CRACKED PANELS

CASE	HALF CRACK LENGTH, a (IN.)										
	4.5	7.5	10.5	12.75	15.5	17.5	18.5	19.5	20.5	21.5	
$R_{c1}$	1	1.100	1.190	1.290	1.370	1.390	1.438	1.500	1.615	1.750	1.810
	2	1.088	1.128	1.182	1.227	1.378	1.438	1.480	1.550	1.704	1.721
	3	1.290	1.317	1.392	1.448	1.540	1.551	1.758	2.171	2.908	2.788
	4	1.084	1.123	1.197	1.248	1.339	1.448	1.551	1.931	2.618	2.538
	5	0.777	0.824	0.887	0.898	0.954	1.033	1.112	1.402	1.940	1.923
	6	1.064	1.122	1.195	1.245	1.338	1.442	1.541	1.888	2.437	2.415
	7	1.076	...	1.207	1.255	1.341	1.438	1.523	1.785	2.268	2.268
	8	1.043	1.104	1.175	1.233	1.338	1.444	1.538	1.833	2.318	2.299
	9	0.700	...	0.851	...	0.952	1.027	1.099	1.324	1.701	1.724
$a_{cct}/a$	3	5.822	7.448	9.149	10.00	11.45	12.42	12.86	13.24	13.40	13.50
$a_{cct}/a$	3	1.727	1.777	1.874	1.976	2.243	2.698	3.105	4.268	6.364	7.354
	1	1.750	1.825	1.988	2.087	2.417	2.980	3.529	4.772	7.141	8.249
	5	1.858	1.994	2.229	2.451	2.994	3.844	4.695	6.499	9.804	11.33
	6	1.749	1.824	1.983	2.084	2.408	2.934	3.481	4.549	6.690	7.767
	7	1.745	...	1.943	2.073	2.408	2.985	3.621	6.103	8.640	10.44
	8	1.743	1.811	1.938	2.089	2.402	2.944	3.489	4.607	6.942	8.159
	9	1.841	...	2.190	...	2.955	3.802	4.625	6.359	9.549	11.252
$a_{cct}/a$	1	1.643	2.104	2.576	2.851	3.281	3.598	3.710	3.845	3.988	4.050
	2	1.720	2.248	2.804	3.139	3.513	3.979	4.153	4.318	4.460	4.577
	3	1.251	1.447	1.688	1.782	1.955	2.099	2.160	2.213	2.238	2.251
	4	1.765	2.235	2.713	2.988	3.304	3.689	3.824	3.939	3.987	4.020
	5	1.760	2.224	2.698	2.969	3.372	3.685	3.800	3.916	3.972	4.011
	7	1.702	...	2.628	2.899	3.301	3.697	3.734	3.856	3.921	3.968
	8	1.672	2.113	2.574	2.844	3.245	3.638	3.674	3.792	3.855	3.899

TABLE 2  
STRESS RATIOS FOR TWO-BAY LONGITUDINAL CRACKED PANELS (CONT)

CASE	HALF CRACK LENGTH, $a$ (IN.)										
	4.5	7.5	10.5	12.75	15.5	17.5	18.5	19.5	20.5	21.5	
$\sigma_{ccf}/\sigma$	1	0.968	1.019	1.117	1.192	1.317	1.420	1.471	1.519	1.561	1.596
	2	0.933	0.976	1.069	1.143	1.262	1.361	1.411	1.460	1.503	1.539
	3	1.024	1.092	1.189	1.256	1.364	1.449	1.489	1.524	1.539	1.550
	4	1.000	1.076	1.191	1.271	1.400	1.501	1.549	1.591	1.609	1.622
	6	1.001	1.078	1.193	1.273	1.403	1.505	1.553	1.596	1.617	1.632
	7	0.996	...	1.183	1.263	1.393	1.497	1.547	1.592	1.617	1.635
	8	0.981	1.041	1.136	1.206	1.322	1.414	1.459	1.499	1.521	1.537
	9	1.022	1.057	1.119	1.175	1.304	1.470	1.596	1.781	2.082	2.325
$\sigma_{ocof}/\sigma$	2	1.015	1.048	1.108	1.168	1.294	1.463	1.596	1.797	2.139	2.402
	3	1.013	1.036	1.077	1.118	1.208	1.321	1.402	1.505	1.579	1.634
	4	1.024	1.058	1.115	1.167	1.291	1.419	1.516	1.636	1.722	1.784
	5	1.073	1.136	1.239	1.329	1.523	1.750	1.904	2.091	2.217	2.306
	6	1.023	1.057	1.114	1.165	1.277	1.412	1.506	1.623	1.716	1.784
	7	1.022	...	1.113	1.166	1.282	1.427	1.531	1.666	1.790	1.882
	8	1.021	1.054	1.109	1.161	1.259	1.407	1.499	1.614	1.713	1.788
	9	1.069	...	1.228	...	1.508	1.731	1.879	2.059	2.206	2.316
	10	1.031	1.079	1.152	1.210	1.311	1.393	1.427	1.447	1.434	1.429
$\sigma_{icof}/\sigma$	2	1.025	1.070	1.144	1.204	1.309	1.396	1.434	1.457	1.437	1.430
	3	1.017	1.047	1.095	1.135	1.208	1.271	1.302	1.325	1.327	1.331
	4	1.032	1.077	1.144	1.197	1.292	1.374	1.413	1.443	1.447	1.453
	5	1.101	1.184	1.309	1.406	1.581	1.734	1.807	1.865	1.878	1.891
	6	1.032	1.076	1.114	1.196	1.291	1.375	1.413	1.445	1.453	1.461
	7	1.030	...	1.142	1.195	1.292	1.376	1.416	1.448	1.454	1.462
	8	1.029	1.070	1.134	1.184	1.275	1.352	1.389	1.419	1.425	1.433
	9	1.096	...	1.292	...	1.552	1.697	1.768	1.826	1.844	1.862

If the panel contains a fatigue crack of half length  $a_A$ , and a gross stress of  $\sigma_{RA}$  is applied, then fast fracture will occur at A and the crack will be arrested at B. If, on the other hand, a gross stress of  $\sigma_{RC}$  is applied with half crack length equal to  $a_C$ , then fast fracture will occur at C and the crack will not be arrested. The residual strength of the panel is represented as  $\sigma_{RD}$  and any fracture at stress level higher than  $\sigma_{RD}$  will not be arrested and would represent an explosive failure in a pressurized shell. The value of the crack stoppers for case 4 can be seen by their influence on the residual strength when compared to case 1 for the panel without crack stoppers. The frame, connected to the skin by a flexible shear clip, is not as effective in picking up load as a crack stopper strap connected directly to the skin with three rows of rivets.

#### Stiffener Strength Criteria

In considering the gross residual strength of a stiffened panel, one must consider both skin fracture criteria and stiffener strength. Tables 2, 3 and 4 list stiffener stresses as a function of crack length. In order to maintain the skin fracture strength illustrated by Figure 14, the stiffeners must remain intact. In cases where the stiffener may be critical, yielding of the stiffener will take place prior to failure, resulting in an effective increase in the crack tip stress and a decrease in  $R_{ct}$ . Stiffener failure and skin fracture then occur simultaneously, but the failure is precipitated by stiffener criteria.

In order to obtain a balanced design, both skin and stiffener criteria must be considered. An example of this is illustrated in Figure 15. The curves shown represent gross residual strength for a flat panel, stiffened by frames and crack stoppers, and subjected to a uniform gross stress at the

Table 1 where the center crack stopper is intact and for case 4 where the center crack stopper is broken. The skin material is assumed to be 7075-T73 with  $K_{c*} = 90,000 \text{ psi} \sqrt{\text{in.}}^2$ . The crack stopper and frame are assumed to be titanium 8-1-1 and 7075-T6, respectively, with ultimate gross strengths 149,000 psi and 75,000 psi. If the damage tolerance criteria selected require that the center crack stopper should not fail, then for a half crack length of 20 inches, the gross strength would be limited to 11,000 psi from curve A of Figure 15; however, the residual strength based on skin criteria is 31,500 psi from curve B, resulting in an unbalanced design. If, however, the center crack stopper is allowed to break, leaving

**TABLE 3  
STRESS RATIOS FOR ONE-BAY LONGITUDINAL CRACKED PANELS**

CASE	HALF CRACK LENGTH, a (IN.)											
	1.5	3.5	4.5	5.5	6.5	7.5	8.5	9.5	10.5	11.5	12.5	
$R_{ct}$	10	1.004	1.016	1.026	1.038	1.056	1.081	1.110	1.102	1.287	1.363	...
	11	1.040	1.046	1.048	1.064	1.088	1.083	1.111	1.169	1.269	1.323	...
	12	1.006	1.019	1.030	1.047	1.070	1.106	1.172	1.443	1.946	2.017	...
$\sigma_{out}/\sigma$	17	1.720	1.806	1.882	1.991	2.163	2.406	2.882	3.840	6.749	6.713	7.418
$\sigma_{out}/\sigma$	10	1.009	1.046	1.076	1.118	1.174	1.249	1.353	1.509	1.765	1.989	2.183
	11	1.008	1.046	1.074	1.117	1.174	1.253	1.364	1.533	1.819	2.060	2.281
	12	1.008	1.040	1.067	1.103	1.149	1.210	1.289	1.389	1.482	1.518	1.571
$\sigma_{in}/\sigma$	10	1.008	1.040	1.064	1.093	1.126	1.169	1.191	1.214	1.209	1.210	1.217
	11	1.008	1.040	1.066	1.095	1.130	1.167	1.203	1.228	1.217	1.217	1.224
	12	1.007	1.036	1.068	1.088	1.116	1.150	1.184	1.213	1.218	1.226	1.236

**TABLE 4  
STRESS RATIOS FOR TWO-BAY CIRCUMFERENTIAL CRACKED PANELS  
WITH BROKEN CENTRAL LONGERON**

CASE	HALF CRACK LENGTH, a (IN.)											
	1.5	2.5	3.5	4.5	5.5	6.5	7.5	8.5	9.5	11.0	13.0	
$R_{ct}$	13	0.818	0.853	0.881	0.907	0.937	0.980	1.101	1.327	1.394	...	...
	14	0.843	0.867	0.892	0.916	0.943	0.983	1.092	1.298	1.362	...	...
	15	0.778	0.820	0.882	0.883	0.918	0.970	1.107	1.353	1.428	...	...
	16	0.798	0.836	0.865	0.894	0.926	0.972	1.092	1.306	1.378	...	...
	17	0.683	0.736	0.779	0.822	0.871	0.942	1.124	1.428	1.520	...	...
	18	0.681	0.713	0.782	0.827	0.880	0.966	1.370	2.062	1.966	...	...
	19	0.763	0.813	0.861	0.886	0.926	0.988	1.201	1.593	1.646	...	...
	20	0.682	0.727	0.778	0.826	0.881	0.967	1.241	1.704	1.766	...	...
$\sigma_{ot}/\sigma$	13	1.066	1.107	1.172	1.270	1.426	1.694	2.247	3.504	4.304	5.436	6.461
	14	1.063	1.104	1.168	1.268	1.426	1.699	2.269	3.606	4.476	5.741	6.848
	15	1.074	1.114	1.176	1.269	1.414	1.660	2.153	3.212	3.876	4.806	5.806
	16	1.069	1.109	1.170	1.263	1.408	1.653	2.143	3.230	3.937	4.968	5.830
	17	1.094	1.132	1.189	1.271	1.394	1.591	1.955	2.637	3.043	3.601	4.052
	18	1.109	1.152	1.216	1.311	1.462	1.740	2.423	3.441	3.867	4.449	4.932
	19	1.077	1.121	1.186	1.280	1.420	1.649	2.089	2.864	3.290	3.890	4.412
	20	1.100	1.143	1.202	1.284	1.398	1.568	1.855	2.273	2.496	2.810	3.080
$\sigma_{it}/\sigma$	13	1.074	1.107	1.164	1.214	1.287	1.373	1.465	1.518	1.573	1.619	1.637
	14	1.070	1.103	1.149	1.209	1.284	1.372	1.466	1.520	1.579	1.705	1.863
	15	1.088	1.120	1.165	1.223	1.292	1.372	1.465	1.497	1.542	1.639	1.769
	16	1.082	1.114	1.159	1.217	1.287	1.369	1.454	1.501	1.551	1.659	1.793
	17	1.119	1.161	1.193	1.246	1.306	1.372	1.432	1.444	1.465	1.517	1.588
	18	1.124	1.158	1.203	1.257	1.320	1.384	1.422	1.377	1.371	1.387	1.427
	19	1.080	1.113	1.168	1.210	1.267	1.317	1.318	1.180	1.123	1.079	1.081
	20	1.108	1.141	1.180	1.221	1.257	1.268	1.201	0.982	0.881	0.772	0.715

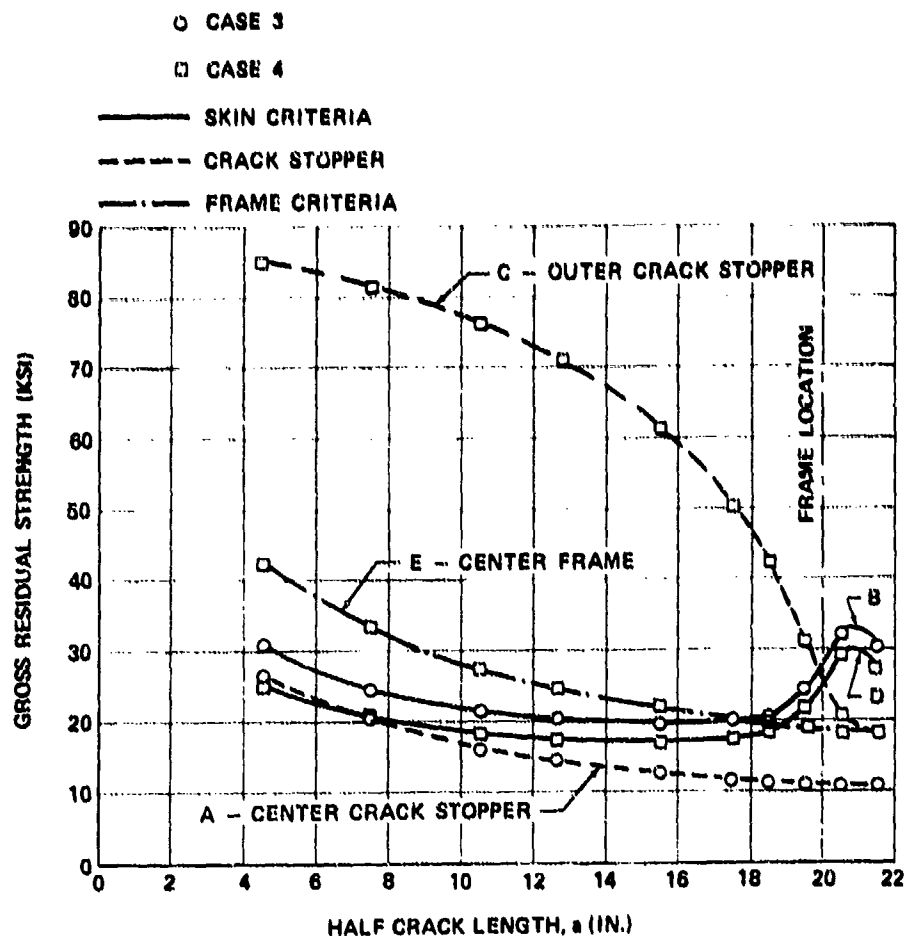


FIGURE 15. GROSS RESIDUAL STRENGTH FOR A TYPICAL FLAT PANEL WITH TWO-BAY LONGITUDINAL CRACK

the frame intact, the strength based on skin criteria would be reduced to 30,000 psi from curve D. However, the residual strength of the panel would be 19,000 psi for a half crack length of 20 inches based on center frame criteria. This is a case where increasing the damage tolerance would reduce the weight since the area of the crack stoppers would have to be more than doubled to maintain their continuity at a gross stress of 19,000 psi. The rivets attaching the crack stopper to the skin become highly loaded as the crack extends. Figure 16 shows outer crack stopper total rivet load as a function of crack length for cases 3, 4 and 6 of Table 1. Only the first and second rows are shown. For case 3, the rivets attaching the center crack stopper to the skin are extremely highly loaded analytically. For  $a = 21.5$ ,  $P_p/\sigma$  is 0.348.

#### Effect of Attachment Stiffness

In order to illustrate the effect of attachment stiffness, an analysis was performed on a panel 0.071 inch thick, having hat section stiffeners at 8-inch spacing with an area of 0.5121 square inch. The idealization for the panel was similar to that shown in Figure 9 with the center longeron assumed to be broken. Figures 17, 18, and 19 show the analysis results. Four different skin attachments were considered:

- Infinitely rigid
- Adhesive bond 1.0 inch wide, 0.01 inch thick with shear modulus  $G_b$  of 38,000 psi
- 3/16-inch-diameter steel attachments at 7/8-inch spacing
- 3/16-inch-diameter aluminum attachments at 1-1/4-inch spacing.

Figure 17 shows the crack tip stress intensity factor  $K$ , per unit gross stress, as a function of crack length. It can be seen that as the crack approaches the stiffener, the stress intensity is reduced. The lowest stress intensity factor occurs just beyond the stiffener for the infinitely rigid stiffener to skin attachment. This case assumes compatibility of strain between the stiffener and the sheet which is an assumption often made for other methods. In practice, however, appreciable deflection takes place in the rivets, resulting in a lower load transfer into the stiffener and a consequent increase in crack tip stress intensity. Considerable error may therefore be present with the rigid attachment assumption.

Figure 18 shows outer stiffener stress as a function of crack length for the four cases considered. The highest load transfer into the stiffener occurs with the rigid attachment. Outer and inner cap stresses are shown, indicating considerable bending in the stiffener due to eccentricity of load application from the sheet. The stiffener to skin attachment shear flow is shown in Figure 19 for the first 8-1/2 inches of idealized shear panel from the crack. It can be seen that the intensity of shear load is extremely high in the vicinity of the crack, particularly for the rigid and adhesively-bonded connection. The distributions are, of course, based on elastic analysis and do not show the effects of yielding of the first attachments on the remaining shear load distribution. The analysis results show that

RIVET LOAD =  $\begin{cases} P/3 \text{ FOR CASES 3 AND 4} \\ P/2 \text{ FOR CASE 6} \end{cases}$

——— CASE 3  
 - - - CASE 4  
 - · - CASE 6

REF. TABLE 1

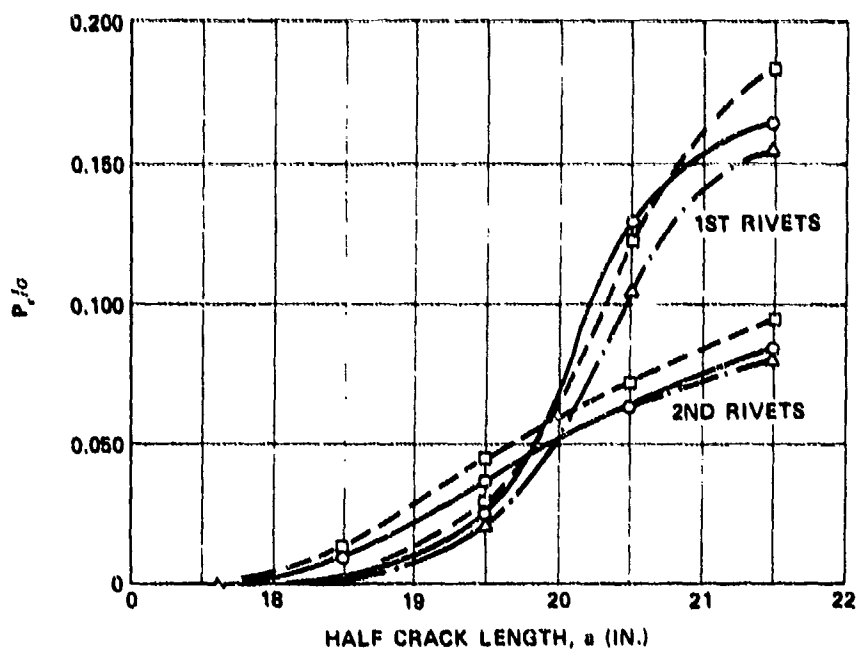
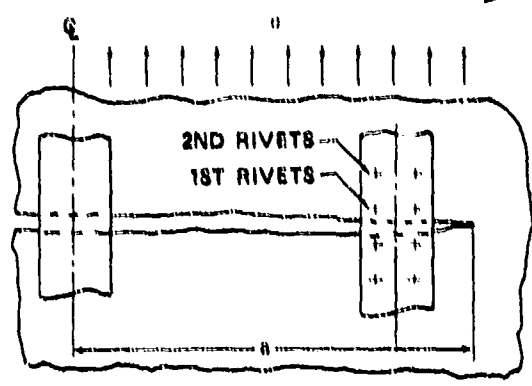


FIGURE 16. RIVET SHEAR LOAD, OUTER CRACK STOPPER TO SKIN RIVETS

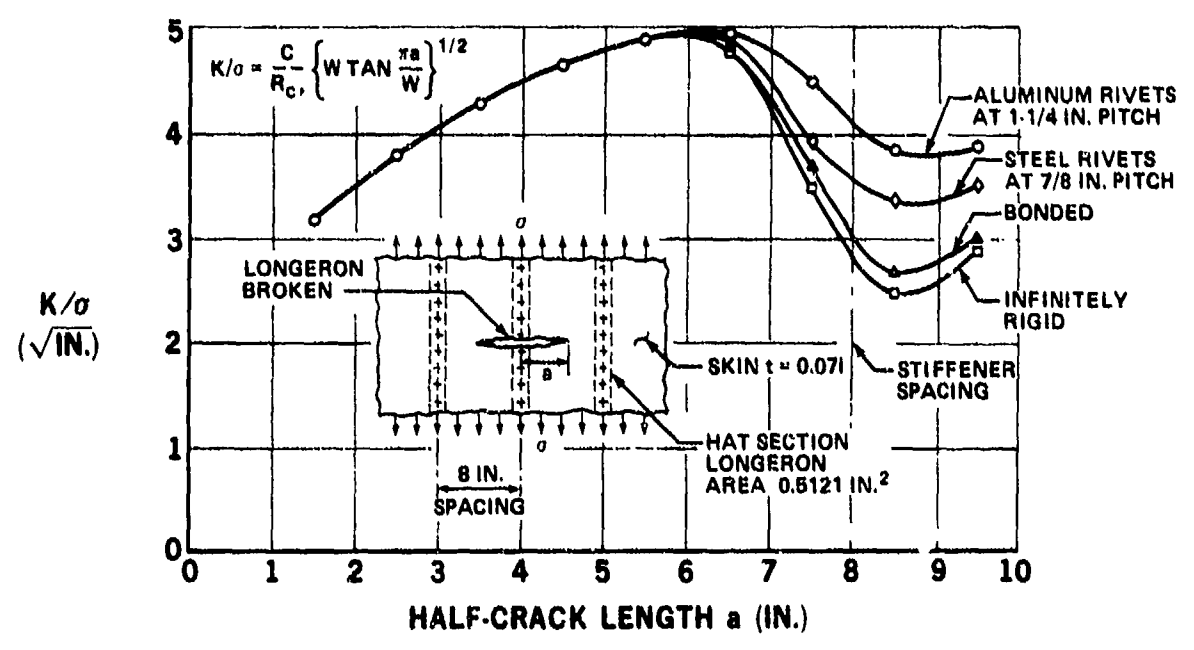
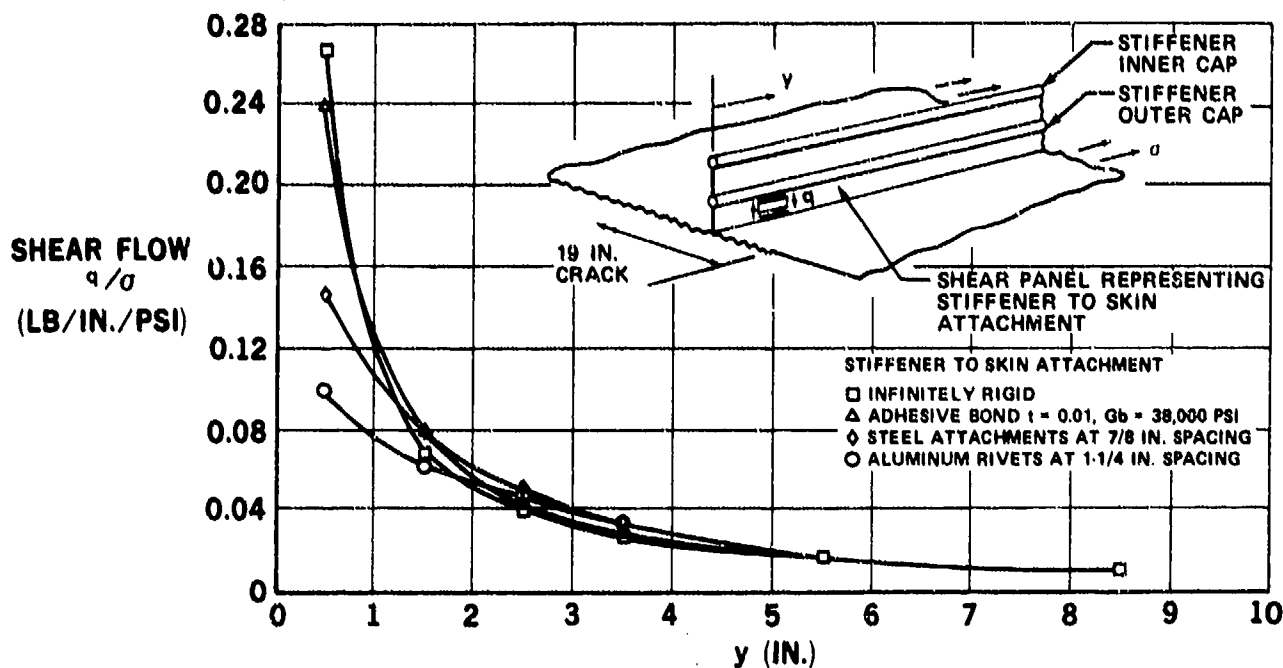
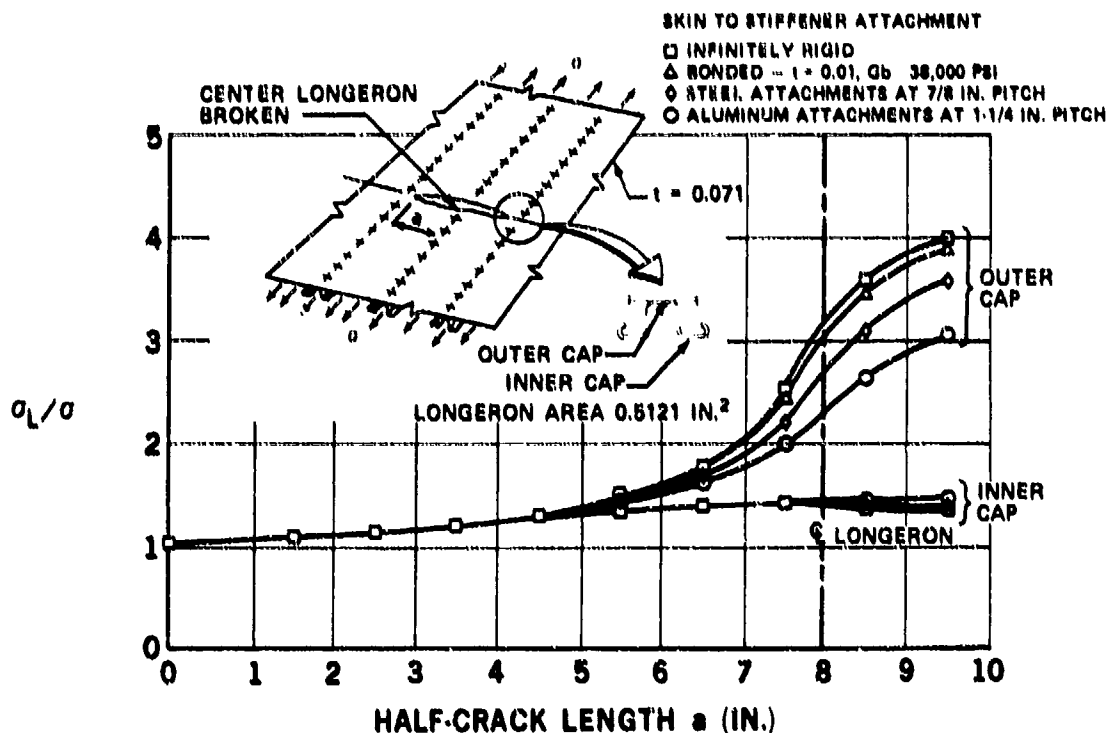


FIGURE 17. CRACK TIP STRESS INTENSITY FACTOR - CRACK LENGTH WITH VARIABLE STIFFENER TO SKIN ATTACHMENT



increasing the attachment stiffness increases skin strength but decreases stiffener strength. Care must be exercised, therefore, when choosing an attachment to obtain a balanced design. To illustrate this point the gross residual strength of the panel, based on both skin fracture and stiffener strength criteria, is shown in Figure 20. The skin fracture criteria have been plotted for two different skin materials:

- 2024-T3 clad sheet 0.071 inch thick with crack normal to the grain direction, and  $K_c$  of 192.4 ksi  $\sqrt{\text{in.}}$  obtained from wide panel tests.<sup>11</sup>
- 7075-T73 clad sheet 0.071 inch thick with  $K_c$  of 97.35 ksi  $\sqrt{\text{in.}}$ <sup>11</sup>

The stiffeners are 7075-T6 extrusion with allowable based on outer cap strength of 82,000 psi. The significance of the curves illustrating skin fracture criteria can be explained by referring to Figure 20. Consider the curve plotted for  $K_c = 97.35$  ksi  $\sqrt{\text{in.}}$  with stiffeners attached by an infinitely rigid connection. If the panel contains a crack of length  $a_1$  and a gross stress of  $\sigma$  is applied, then fast fracture will occur and the crack will be arrested at a crack length  $a_2$ .

The residual strength of the panel is given by  $\sigma_R$  at the peak of the curve. Compatibility between skin fracture and stiffener strength criteria exists when the stiffener allowable strength coincides with the skin residual strength at the peak of the skin residual strength curve.

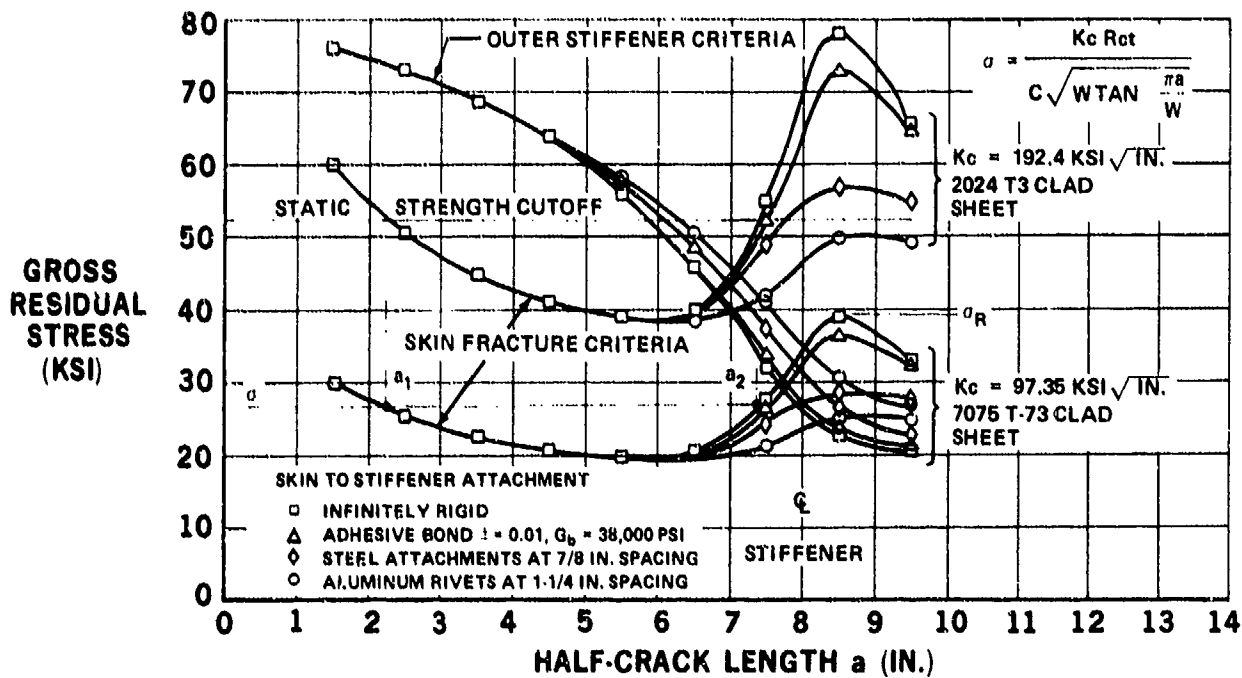


FIGURE 20. GROSS RESIDUAL STRENGTH VERSUS CRACK LENGTH

The residual strength of the 2024-T3 panel, based on skin criteria, is extremely high compared to the stiffener criteria, particularly for infinitely rigid or bonded attachment where the residual strength is higher than the static gross strength without crack. The design from a residual strength standpoint is more compatible when aluminum rivets at 1-1/4-inch spacing are used. Even so, failure of the panel would be precipitated by stiffener failure.

Figure 20 indicates that 7075-T73 skin material produces a more compatible design when combined with 7075-T6 extrusion for flat panels with the damage tolerance considered here. The configurations which show the least difference between skin and stiffener strength criteria are those two with steel or aluminum fasteners. Figure 21a shows gross residual strength based on skin criteria for the same panel containing a crack of length  $2a = 17$  inches with a broken center longeron. (The peak of the residual strength curve is at 17 inches. See Figure 20.) Gross strength is plotted against stiffener-to-skin attachment stiffness for various values of  $K_c$ . The stiffener strength curve is shown plotted over the curves. The intersection of the curves (illustrated by circles) indicates the optimum attachment stiffness for simultaneous failure of skin and stiffener. Figure 21b shows optimum attachment stiffness versus  $K_c$  derived from curves shown in Figure 21a.

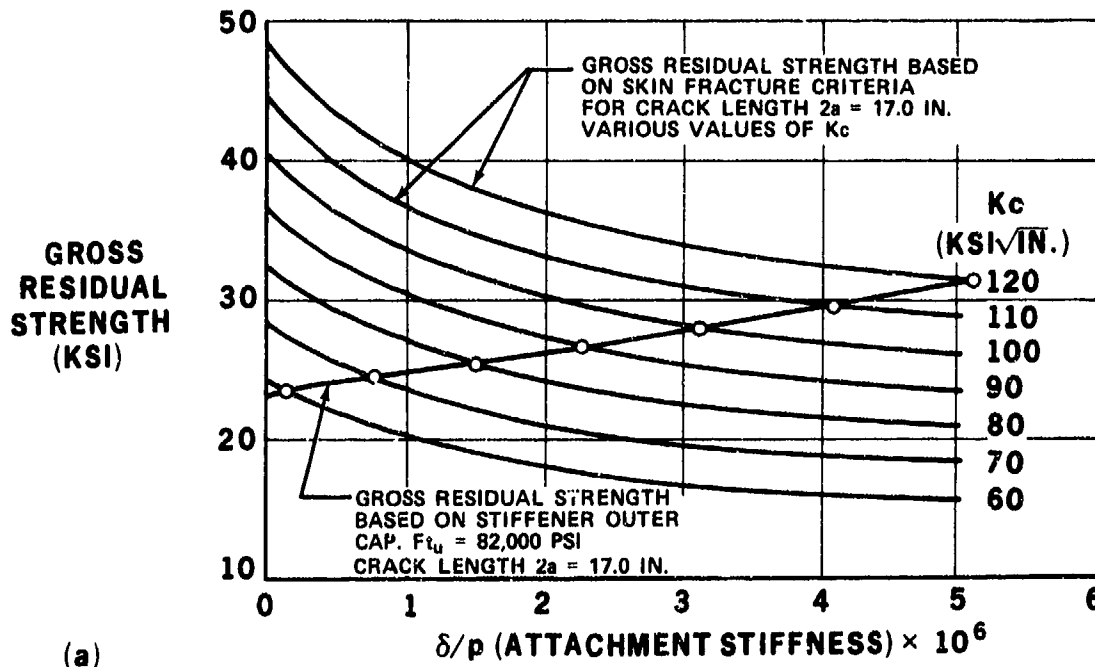
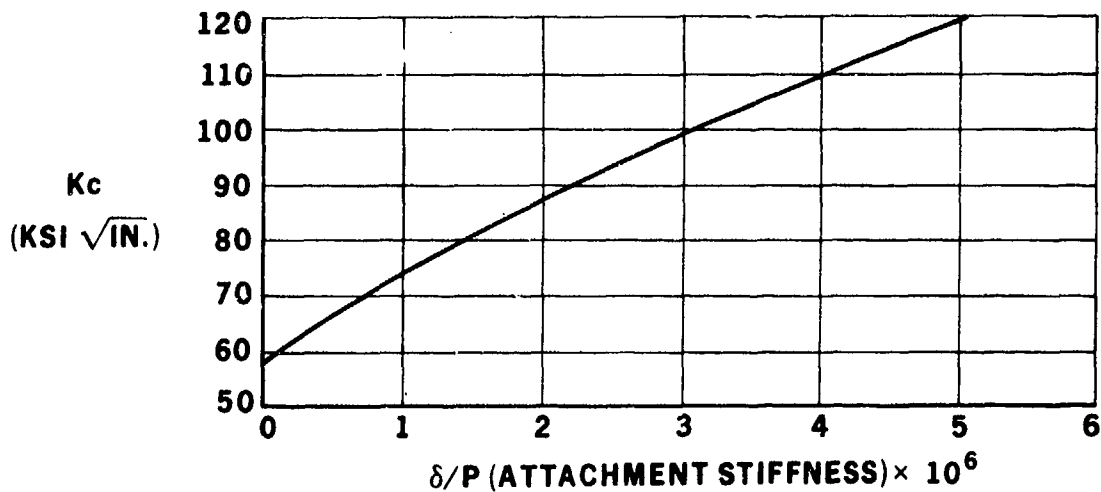


FIGURE 21a. OPTIMUM ATTACHMENT STIFFNESS



(b) OPTIMUM ATTACHMENT STIFFNESS vs  $K_c$  FOR SIMULTANEOUS FAILURE OF SKIN AND STIFFENER

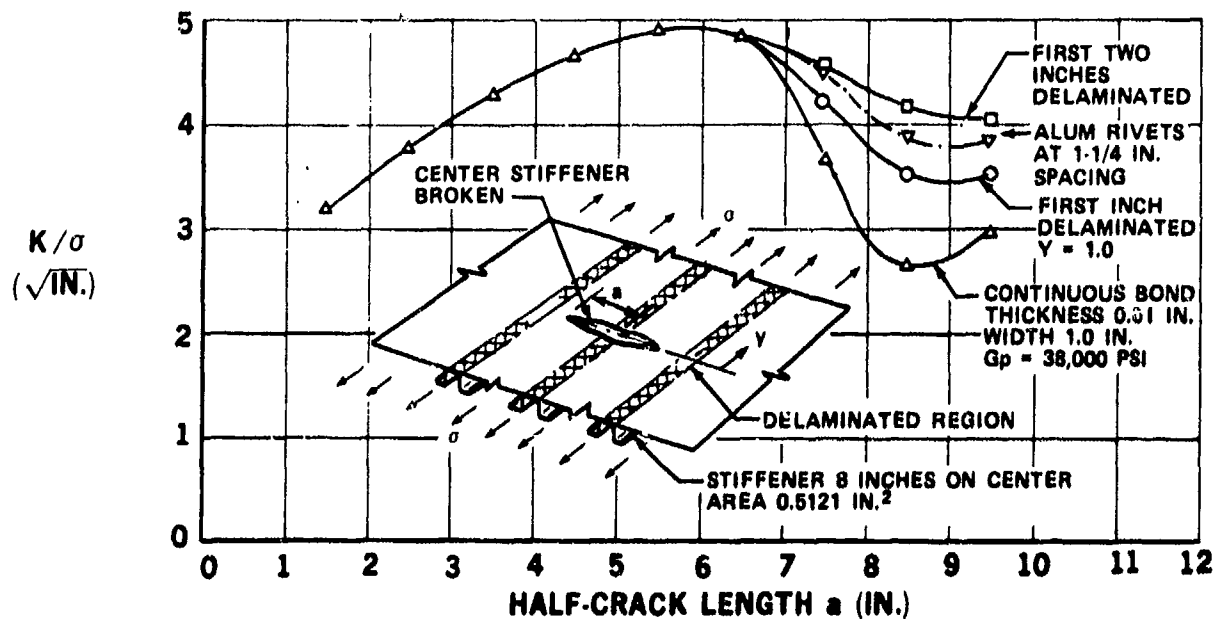
PR71-DP-7279

FIGURE 21b. OPTIMUM ATTACHMENT STIFFNESS (Continued)

## Bond Delamination

Considerable reduction in crack tip stress intensity is shown with bonded stiffeners, as illustrated in Figure 17. This is due to the high relative stiffness of the adhesive bond when compared to aluminum attachments. However, the load transfer through the bond material into the stiffener is extremely concentrated near the vicinity of the crack, as illustrated in Figure 19. This high concentration of shear load may cause bond delamination in the vicinity of the crack, thus reducing the effectivity of the stiffener. The effects of bond delamination can be easily accounted for in the FORMAT finite element analysis by using the element modification procedure outlined in the Appendix. The shear panels, which simulate the attachment of the stiffener to the skin, can be disconnected automatically during the crack propagation phase to represent bond delamination. The effects of delamination on the stress intensity factor are shown in Figure 22 for 1 and 2 inches of delamination on each side of the crack. Considerable increase in the crack tip stress intensity factor is shown with increasing delamination.

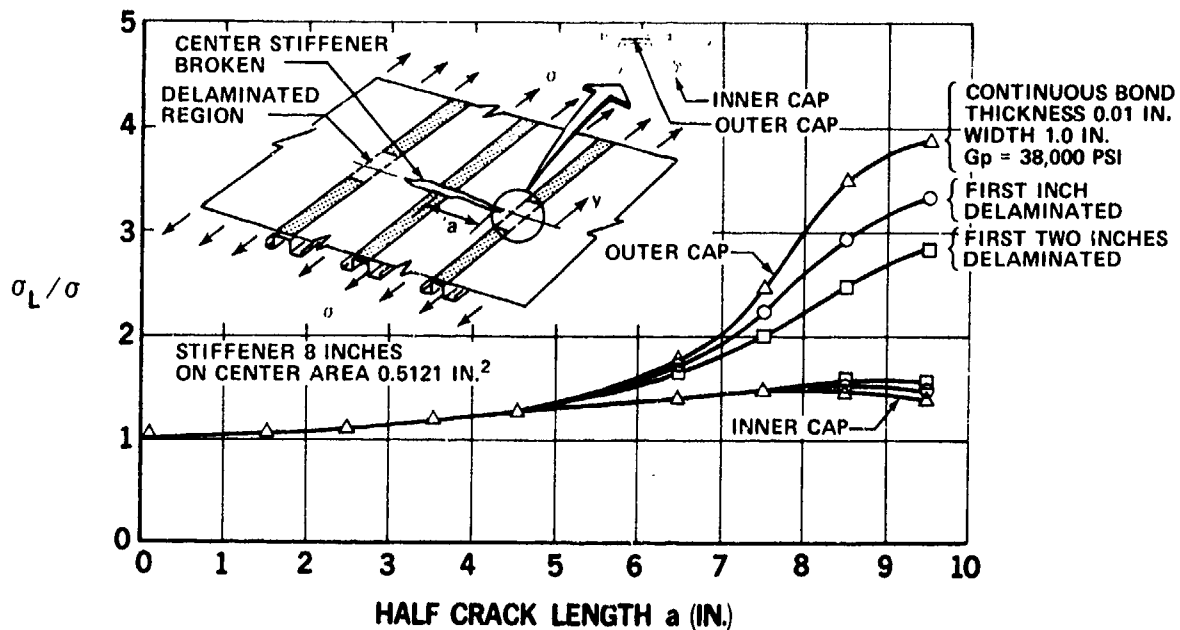
When delamination exceeds 1.5 inches on each side of the crack, the strength of the bonded panel will be lower than a panel with riveted stiffeners. Figure 23 shows that increasing bond delamination decreases the stiffener outer cap stress considerably and increases the inner cap stress slightly.



PR71-DP-7280

FIGURE 22. CRACK TIP STRESS INTENSITY VERSUS CRACK LENGTH WITH VARYING DEGREES OF BOND DELAMINATION





PR71-DP-7273

FIGURE 23. EFFECT OF BOND DELAMINATION ON OUTER STIFFENER STRESS

#### THE THRESHOLD OF SLOW STABLE CRACK GROWTH

Many equations have been proposed to determine the crack propagation rate under constant amplitude loading. Two of the most useful ones have been those proposed by Paris<sup>13</sup> and Forman<sup>14</sup>, respectively:

$$da/dN = C(\Delta K)^n \quad (10)$$

$$da/dN = \frac{C(\Delta K)^n}{(1-R)K_c - \Delta K} \quad (11)$$

Both of these equations have been integrated into computer programs to determine crack propagation under spectrum loading<sup>15</sup>. A method has been proposed to determine the effect of crack growth retardation due to high intermittent load cycles based on a reduced effective stress concept<sup>16</sup>. It is noted in this report that considerable conservatism exists in crack growth studies when this phenomenon is neglected. When considering materials with high ductibility such as 2024-T3, however, this conservatism may be offset to some extent by slow stable growth during the high load cycle. The use of Eq (10) and (11) in which parameters C and n have been determined from constant amplitude testing, in conjunction with the retardation model of Reference 16, may be insufficient to accurately predict the overall retardation effect. It is suggested that the effect of slow stable growth is significant and should be accounted for, particularly with 2024-T3 material.

Consider the panel shown in Figure 24a which contains a center, through crack that has been subjected to constant amplitude cyclic loading. During the load phase from A to B shown in Figure 24b, the gross stress is increased from  $\sigma_1$  to  $\sigma_2$ . At stress  $\sigma_2$  the crack tip stress intensity from Eq (1) is

$$K_B = \frac{\sigma_2 C}{R_{ct}} \sqrt{W \tan(\pi a_B / W)} \quad (12)$$

A plastic zone is formed at the crack tip of radius  $(1/2\pi)(K_B/\sigma_{ys})^2$  where  $\sigma_{ys}$  is the material yield strength. The plastic zone is surrounded by elastically strained material. Reducing the stress to  $\sigma_1$  at C causes a residual compressive stress to be imposed at the crack tip from the elastic material surrounding the plastic zone. On reapplication of the load at C, the residual stress will not be entirely relieved until a crack tip stress intensity equal to  $K_B$  is reached a little before the peak at D. At the peak D the crack tip stress intensity will be

$$K_D = \frac{\sigma_2 C}{R_{ct}} \sqrt{W \tan(\pi a_D / W)} \quad (13)$$

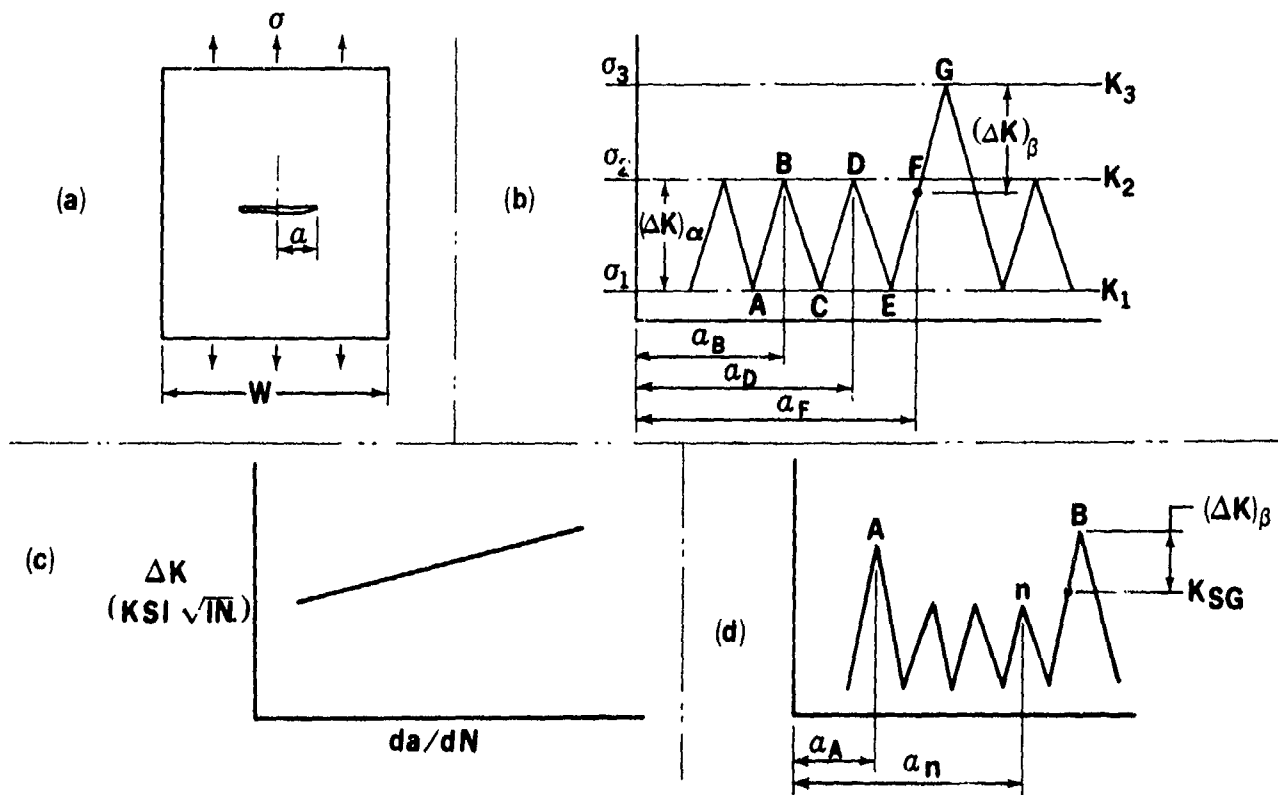


FIGURE 24. THRESHOLD OF SLOW STABLE CRACK GROWTH

The stress intensity factor range from C to D will be called  $(\Delta K)_\alpha$  and associated with this  $\Delta K$  will be a certain growth rate  $da/dN$ . For this particular type of growth rate, associated with constant amplitude stress, the zone ahead of the crack tip is always subjected to residual compressive stress imposed by the plastic zone from the previous load cycle. This kind of growth is normally seen plotted as  $\Delta K$  versus  $da/dN$ , similar to Figure 24c. Empirical or semi-empirical equations such as Eq (10) and (11) are written to fit the test data. As the gross stress level is increased from point E, the crack tip will again be subjected to residual compressive stress until a stress intensity  $K_D$  is reached at point F, which will be at a stress slightly less than  $\sigma_2$  (little error would be involved in assuming  $\sigma_2$ ). The crack growth from E to F would be  $(\Delta K)_\alpha$ -type growth, which is subject to residual stress from the previous load cycle. If the stress is increased to  $\sigma_3$  at point G, the zone ahead of the crack tip will be completely relieved of residual stress at point F, and the crack growth from E to G will not be the same kind of growth associated with residual stress from the previous load cycle. The stress intensity range from F (nearly equal to D) to G will be called  $(\Delta K)_\beta$  and can be several hundred times as great, depending on  $K_2$  and  $(\Delta K)_\alpha$ . This residual stress-free growth is defined as slow stable growth in this paper.

Suppose now that the history of load application has not been at a constant amplitude before the high load cycle was applied, and that a previous high load cycle A was applied followed by constant amplitude cycles, as shown in Figure 24d.

The crack propagation will be retarded until

$$a_n + \frac{1}{2\pi} \left( \frac{K_n}{\sigma_{ys}} \right)^2 = a_A + \frac{1}{2\pi} \left( \frac{K_A}{\sigma_{ys}} \right)^2 \quad (14)$$

$$\text{if } a_n + \frac{1}{2\pi} \left( \frac{K_n}{\sigma_{ys}} \right)^2 < a_A + \frac{1}{2\pi} \left( \frac{K_A}{\sigma_{ys}} \right)^2$$

then stable growth will not start to occur on the B high load cycle at a stress intensity  $K_n$  and will only start to occur when Eq (14) is satisfied.

$$\text{if } a_n + \frac{1}{2\pi} \left( \frac{K_n}{\sigma_{ys}} \right)^2 > a_A + \frac{1}{2\pi} \left( \frac{K_A}{\sigma_{ys}} \right)^2$$

then slow growth will start at a stress intensity  $K_n$ .

Let  $K_{SG}$  be the stress intensity at the threshold of slow stable growth on the high load cycle B. Then, to satisfy Eq (14)

$$K_{SG} = \sigma_{ys} \sqrt{2\pi[a_A - a_n + (1/2\pi)(K_A/\sigma_{ys})^2]} \quad (15)$$

and  $(\Delta K)_p = K_B - K_{SG} \quad (16)$

The  $K$ 's in each case are determined from Eq (1). The authors of Reference 14 suggested an additional crack growth curve to account for the transition from 90-degree tensile to 45-degree shear-type cracking. A third curve is suggested here to account for slow stable crack growth when spectrum type loading is being considered.

#### TEST PROGRAM

Extensive fatigue and fail-safe testing had been completed during the development of the DC-8 and DC-9 aircraft. The general philosophy during the DC-8 testing was to subject a panel or shell structure to pressure loading which would simulate a principal stress in the skin. Rotary saws were then inserted into the skin and advanced until rapid fracture occurred. This method is excellent for determining the crack arresting capability of the crack barriers but little information on fracture toughness is gained that can be used in future designs.

The methods changed during the DC-9 testing where saw cuts were made in the skin and cyclic pressure applied so that the saw cuts were converted to fatigue cracks prior to fast fracture. Fracture toughness can be determined from this type of testing if the crack length at fast fracture is known. All of these early data were extremely useful during the development of the DC-10 fail-safe capability. However, in order to produce the most efficient design, further development testing was required. Figure 25 illustrates some of the fail-safe development test specimens completed to date.

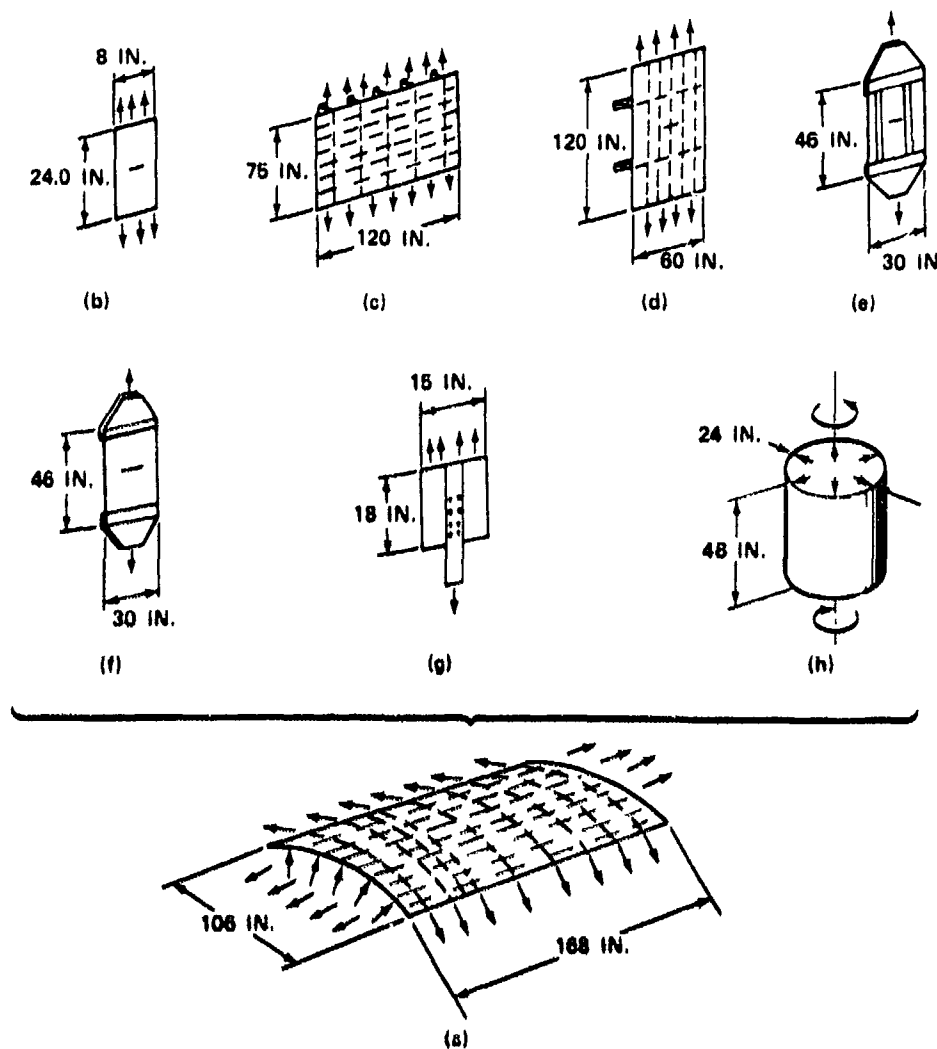


FIGURE 25. FUSELAGE FATIGUE AND FAIL-SAFE DEVELOPMENT TESTS

### Curved Panels

Figure 25a shows a large curved panel of radius 118.5 inches which is stiffened by eight frames and eleven longerons. Axial loading is applied by a series of whiffletrees attached to the ends of the panel. Pressure loading is applied to the under side of the panel by lowering a vacuum chamber onto the panel and evacuating the chamber. Both axial load and pressure loading can be cycled or applied statically. Transverse and longitudinal saw cuts can be made in the skin and propagated into fatigue cracks prior to applying static loading, to determine the effects of fast fracture and arrest.

The vacuum test machine was initiated during the DC-10 development and considerable effort was required to perfect its operation. The main innovations in this machine are the capability to apply axial load and the ability to observe the inner side of the panel during pressure loading. One circumferential and six longitudinal crack tests have been performed on two panels to date. Panel 15 was made from 0.080 7075-T73 clad sheet, with a frame configuration as shown in Figure 3a with a net area of 0.5042 square inch. Hat longerons were extruded as seen in Figure 3d with gross area 0.312 square inch. Panel 16 was made from 0.063 2024-T3 clad sheet with frame configuration as shown in Figure 5 but with thickness 0.063 and a net area 0.425 square inch. Crack stoppers were 3.25 by 0.016 titanium 8-1-1 and longerons were rolled Hat-section with gross area of 0.214 square inch. During the development of the vacuum test machine shown in Figure 26, all of the specimen types b to g of Figure 25 were tested to give early data to be incorporated into the larger curved panels. A view of the upper side of curved panel 16 is shown in Figure 27.

Figure 25b shows narrow specimens for material screening. Crack propagation and residual strength tests were performed on these specimens but the fracture toughness data obtained are not representative of very wide panels such as fuselage panels. This is illustrated by Liu who shows<sup>17</sup> the increase in plane stress fracture toughness  $K_{IC}$  with increasing panel width. This effect is particularly noticeable in 2024-T3 sheet.

### Flat Panels with Longitudinal Cracks

Figure 25c shows flat panels stiffened by longerons and frames. Fourteen tests were performed on six panels of this type. Frames on each of the panels were 7075-T6 with cross section as shown in Figure 3. Longerons were all 7075-T6 extruded Hat-section with a gross area of 0.312 square inch. A description of the panels is given in Table 5. Three-inch-wide titanium crack stoppers 0.025 inch thick were incorporated into panels 5 and 6 with three rows of rivets. Cracks were propagated under uniaxial cyclic loading from saw cuts in the skin to simulate one- and two-bay longitudinal cracks. Static loading was applied at predetermined crack lengths to fast fracture the skin. Cracks were normal to the frames and crack stoppers provided the crack barriers.

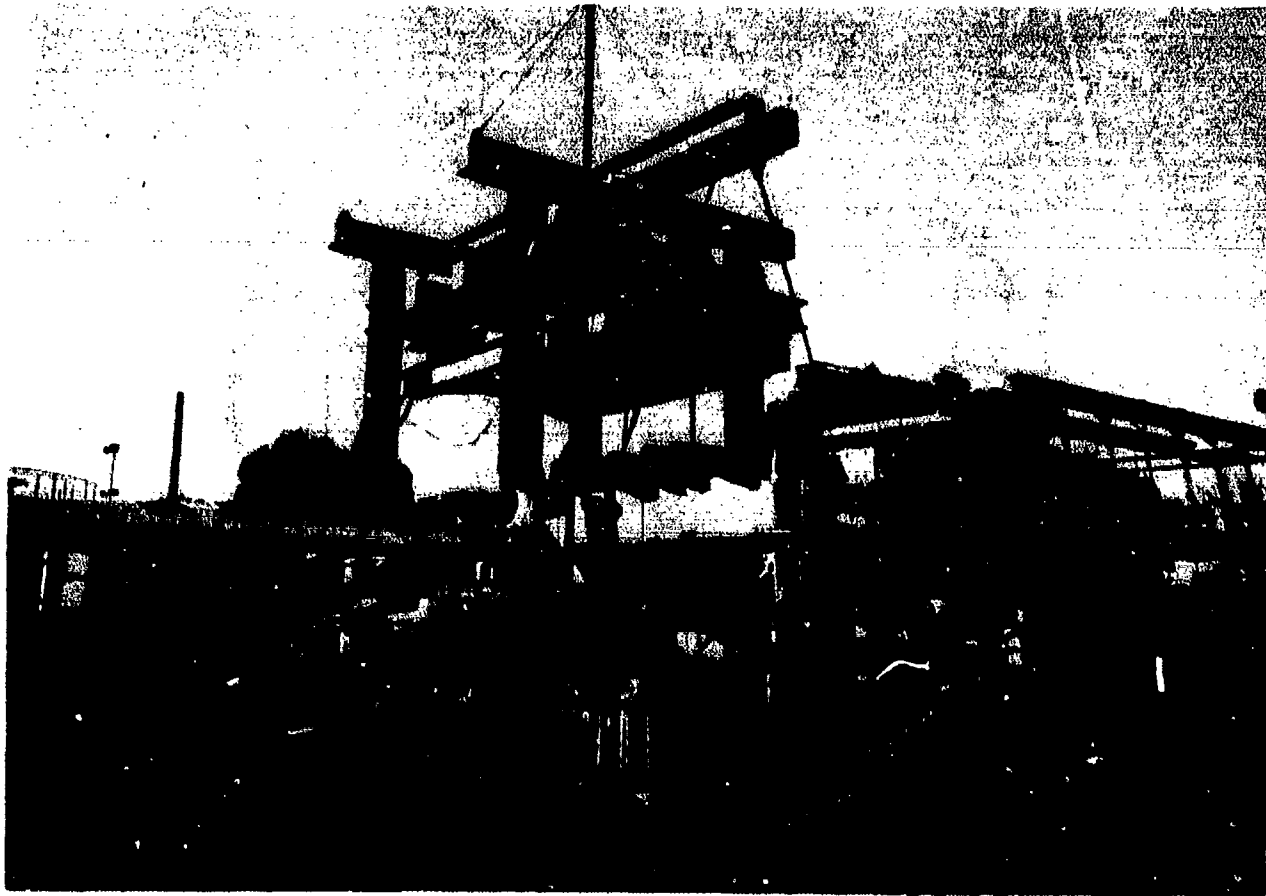


FIGURE 26. VACUUM TEST RIG FOR TESTING CURVED PANELS UNDER COMBINED PRESSURE AND AXIAL LOADING

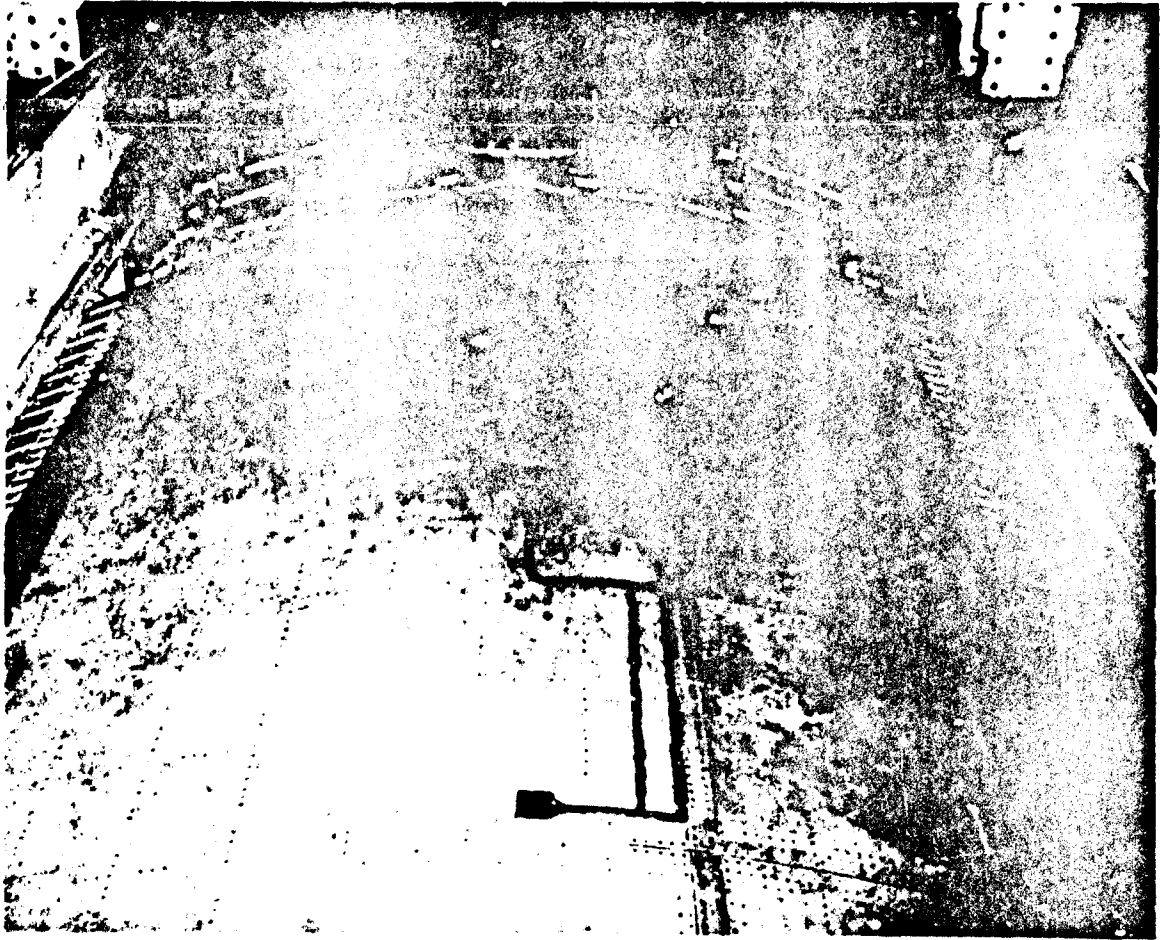


FIGURE 27. UPPER SIDE OF CURVED TEST PANEL 16

TABLE 5  
120-IN.-WIDE FLAT PANEL CONFIGURATION FOR LONGITUDINAL CRACKS

FRAME SPACING 20.0 IN.  
SKIN THICKNESS 0.071 IN.

PANEL NO.	SKIN MATERIAL	LONGERON		SHEAR CLIP TYPE*
		SPACING (IN.)	CRACK STOPPER	
1	7075-T73	6.5	NONE	(a)
2	7075-T73	8.0	NONE	(b)
3	7075-T73	6.5	NONE	(c)
4	7075-T73	8.0	NONE	(a)
5	7075-T73	8.0	3 IN. BY 0.025	(a)
6	2024-T3	8.0	TITANIUM B-1-1	(a)

\*REFER TO FIGURE 3

#### Flat Panels with Circumferential Cracks

Figure 25d shows flat panels stiffened by longerons and frames. Eighteen tests were performed on nine panels of this type. The configurations of eight of these panels, listed from 7 to 14, are shown in Table 6. Longerons were saw cut and cracks propagated into two adjacent bays under uniaxial cyclic loading to simulate a two-bay circumferential crack with a broken central longeron. At predetermined

TABLE 8  
60-IN.-WIDE FLAT PANEL CONFIGURATION FOR CIRCUMFERENTIAL CRACKS

LONGERON SPACING 8.0 IN.  
SKIN THICKNESS 0.071 IN.

PANEL NO.	SKIN MATERIAL	LONGERON TYPE*	LONGERON NET AREA (IN. <sup>2</sup> )	LONGERON TO SKIN ATTACHMENTS
7	7075-T73	HAT (d)	0.3029	NAS 1097 DD6
8	7075-T73	HAT (d)	0.5121	NAS 1097 DD6
9	7075-T73	TEE (e)	0.2895	RV 5176-6 7075-T73
10	7075-T73	TEE (e)	0.4865	NAS 1097 DD6
11	2024-T3	HAT (d)	0.3029	NAS 1097 DD6
12	2024-T3	HAT (d)	0.5121	NAS 1097 DD6
13	2024-T3	TEE (e)	0.2895	RV 5170-6 7075-T73
14	2024-T3	TEE (e)	0.4865	RV-5170-6 7075-T73

\*REFER TO FIGURE 3

crack lengths, static loading was applied to fast fracture the skin. Cracks were normal to the longeron so that the longerons acted as crack barriers.

Figure 25e shows flat panels stiffened by crack stopper straps. Six panels of this type were tested, made from 0.071 2024-T3 sheet with straps of various widths and thicknesses spaced 10 inches apart. The results of the two large flat panels with crack stoppers had indicated that perhaps two rivet rows were adequate, but in view of the high rivet loads predicted by the analysis (Figure 16), tests were needed to determine if the required load could be transferred without rivet failure. Nine-inch-long saw cuts were made in the skin with 1/8-inch-diameter holes drilled at the ends of the saw cut to delay any tendency to fast fracture the skin. Rivet edge distances were also varied since the large flat panels had indicated the crack stoppers to be more highly loaded on the side from which the crack was approaching. Increasing edge distance would reduce the tendency to overload one side of the strap. Static loading was applied to failure in all of the tests. Load input to the straps was measured by strain gages. Antibuckling guides were used on these tests.

Figure 25f shows 30-inch-wide unstiffened panels loaded uniaxially. During the early testing on the DC-8 where saw cuts were used, fracture toughness had been determined for 2024-T3 where the fracture had been initiated by a saw cut. Predictions were that for this material, no difference existed between fracture from a saw cut and fracture from a fatigue crack.<sup>18</sup> Two panels were tested for residual strength, one with a saw cut 9 inches long and the other with the same length of fatigue crack.

Figure 25g shows one of five small panels which had been cut from the fractured panels shown in Figure 25e. The purpose of these panels was to determine the crack stopper to skin rivet shear strength. Analysis had shown that the rivets between the ends of the crack were highly loaded and the possibility existed that these rivets could yield and redistribute load to the rivets away from the crack. Strain gages were installed between rivets and the load applied to the strap to failure. These panels were intended to simulate the case where the crack had propagated beyond the crack stopper.

Figure 25h shows one of 16 small unstiffened cylinders 24 inches in diameter and 48 inches long, made from 0.032 2024-T3 sheet. The purpose of these tests was to qualitatively assess the effects of shear and axial compression combined with pressure. The setup for testing the cylinders is illus-

trated in Figure 28. An internal pressure source was provided by water and compressed air. Torque loading, applied to the top of the cylinders, was provided by two servo-controlled hydraulic jacks. The system was capable of applying cyclic or static pressure and torque loading simultaneously. Both torque and pressure loading were monitored and recorded using oscillograph instrumentation. Axial constraint was provided on some of the cylinders by using long steel bolts to hold the two end flanges together. Relief to the axial tension stress due to pressure or the application of axial compression stress was provided. Rosette strain gages located on the cylinders were continuously recorded using oscillograph recorders. Longitudinal fatigue cracks, initiated from saw cuts, were propagated to pre-determined lengths by cyclic pressure loading. The test procedure subsequent to this operation is listed in Table 7.

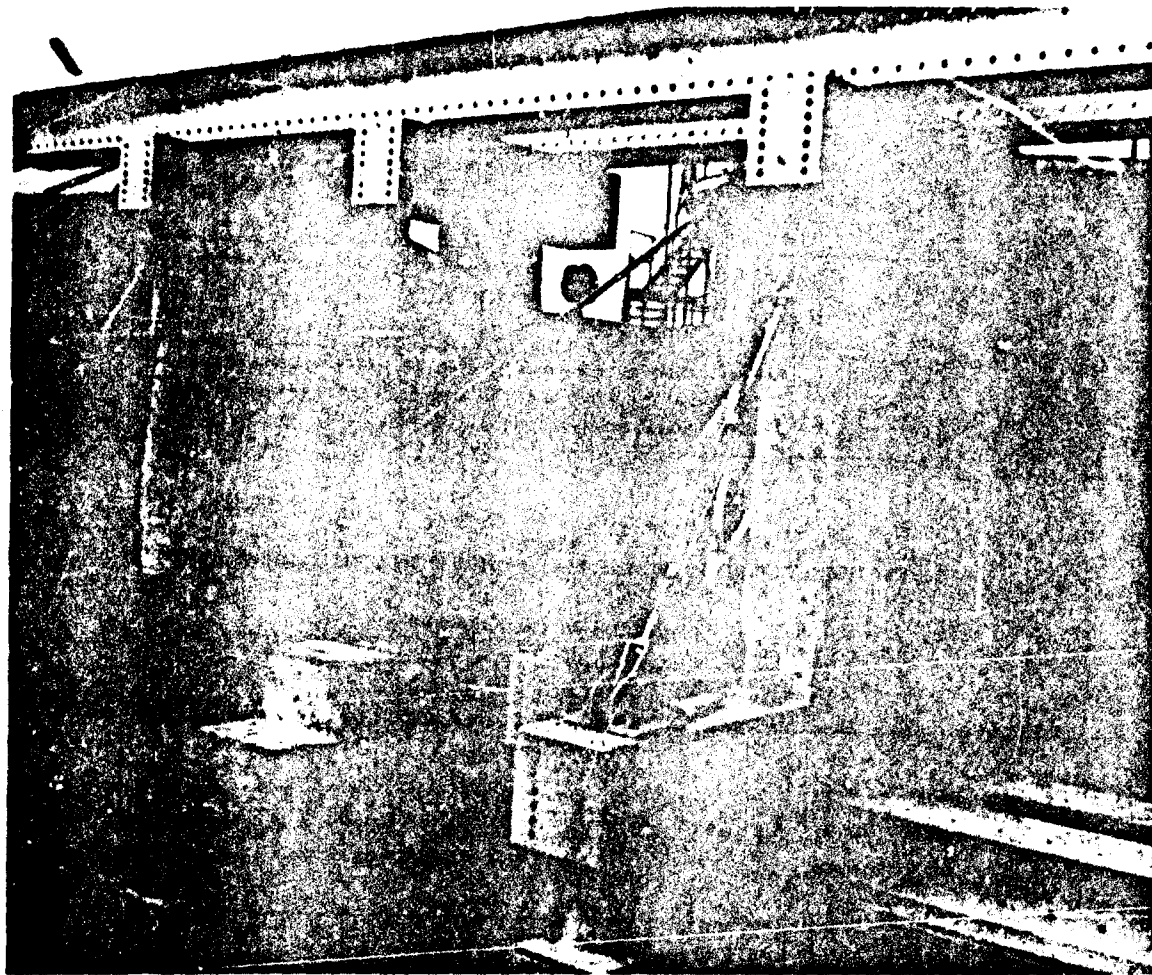


FIGURE 28. TEST FIXTURE FOR 24-INCH-DIAMETER CYLINDERS

TEST RESULTS

Flat Panels with Longitudinal Cracks

The results of tests on the 120-inch-wide flat panels are shown in Table 3. Symbols not yet defined and used in the tables are:

- $a_{ac}$  = Half crack length at crack arrest from calculation
- $a_{fc}$  = Half crack length at failure from calculation
- $\sigma_{Rc}$  = Gross stress at failure from calculation

Test values are the same with a sub T replacing the sub c. Fracture toughness  $K_{IC}$ , listed for panels 1 and 2, tests 1 and 2, panel 3 test 1, and the first part of test 2 on panel 6, is the maximum value applied without any tearing. For the two other tests on panels 2 and 5, the frame, central to the crack, was reinforced locally so that frame failure would not interfere with the skin critical criteria. Analysis had indicated (Table 2) that the frame could fail prior to the skin and this was substantiated very accurately by the strain gages on panel 4. Analyses were performed to account for the reinforcing so that accurate  $R_{pl}$  values shown in Table 8 were available to determine  $K_{IC}$ . Final failure of panels 1, 2, 3, 4 and 6 was due to skin fast fracture during static loading. In all cases where cracks had terminated in rivet holes, cyclic loading was applied to restart a fatigue crack. Final failure of panel 5 was due to outer crack reinitiation failure. Test 2 was performed on panel 6 with

**TABLE 7**  
**TEST PROCEDURE FOR 24-IN.-DIAMETER UNSTIFFENED CYLINDER TEST**

CYLINDER NUMBER	TEST PROCEDURE
1	CYCLE PRESSURE LOADING UNTIL FAILURE
2	INCREASE PRESSURE IN INCREMENTS TO FAILURE
3	
4	
5	INCREASE TORQUE AND PRESSURE IN INCREMENTS TO FAILURE TORQUE PRESSURE RATIO = 7750 IN <sup>3</sup>
6	
7	
8	INCREASE PRESSURE TO STABILIZE THE CYLINDER TIGHTEN DOWN THE TIE BOLTS TO PROVIDE AXIAL CONSTRAINT INCREASE PRESSURE TO FAILURE
9	
10	
11	
12	HOLD PRESSURE CONSTANT CYCLIC TORQUE APPLIED FROM ZERO TO A TORQUE/PRESSURE RATIO OF 7750 IN <sup>3</sup> UNTIL FAILURE.
13	
14	
15	INCREASE PRESSURE TO STABILIZE THE CYLINDER INCREASE TORQUE TO A CONSTANT VALUE CYCLE THE PRESSURE BETWEEN 8.5 PSI AND 13.85 PSI FOR CYLINDER 15 AND BETWEEN 9.0 PSI AND 21 PSI FOR CYLINDER 16
16	

**TABLE 8**  
**TEST RESULTS FOR 120-IN.-WIDE FLAT PANELS WITH LONGITUDINAL CRACK**

PANELS 1 TO 5 0.071 IN. 7075-T73 MATERIAL

PANEL 6 0.071 IN. 2024-T3 MATERIAL

ALL CRACKS PARALLEL TO GRAIN

PANEL NO.	TEST NO.	GROSS STRESS (PSI)	HALF CRITICAL CRACK LENGTH (IN.)	CALCULATED			TEST			TEST/CALCULATED					
				$R_{ct}$	C	$K^*_c$	$\sigma_{bc}$ (IN.)	$\sigma_{fc}$ (IN.)	$\sigma_{Rc AT}$ FAILURE	$\sigma_{bT}$ (IN.)	$\sigma_{fT}$ (IN.)	$\sigma_{RT AT}$ FAILURE	$\sigma_{bT}/\sigma_{bc}$ (IN.)	$\sigma_{fT}/\sigma_{fc}$ (IN.)	$\sigma_{RT}/\sigma_{Rc}$ (IN.)
1	1 <sup>a</sup>	19 410	8.90	1.145	1.006	> 91 000	...	...	...	...	...	...	...	...	...
	2 <sup>a</sup>	19 410	8.90	1.145	1.006	> 91 000	...	...	...	...	...	...	...	...	...
2	1 <sup>a</sup>	22 000	8.90	1.145	1.006	>103 137	...	...	...	...	...	...	...	...	...
	2 <sup>a</sup>	20 888	8.90	1.145	1.006	> 97 929	...	...	...	...	...	...	...	...	...
	3 <sup>b</sup>	17 300	16.90	1.430	1.023	92 000	18.30	21.50	19 000	19.63	21.48	18 476	1.072	0.999	0.972
3	1 <sup>a</sup>	19 410	8.90	1.145	1.006	> 91 000	...	...	...	...	...	...	...	...	...
	2 <sup>b</sup>	19 124	12.06	1.250	1.012	96 200	20.08	21.0	19 700	20.08	20.46	19 744	1.0	0.974	1.002
4	2 <sup>b</sup>	17 000	17.50	1.435	1.0255	93 400	18.63	21.50	19 000	19.63	20.97	18 100	1.064	0.975	0.953
5	2 <sup>b</sup>	19 000	16.325	0.98	1.0222	>145 500	...	...	...	...	...	...	...	...	...
6	2 <sup>b</sup>	19 000	16.325	0.98	1.0222	>145 500	...	...	...	...	...	...	...	...	...
	2 <sup>b</sup>	20 000	21.875	1.26	1.040	145 500	...	...	...	...	21 875	20 000	...	...	...

<sup>a</sup>ONE-BAY CRACK

<sup>b</sup>TWO-BAY CRACK



the center frame completely saw cut and final failure occurred with center frame, center crack stopper, and one outer crack stopper failed. Figure 29 shows the crack arrestment after fast fracture on panel 3. The fail-safe value of the separate shear clip frame configuration is illustrated by the crack in the clip leaving the main frame intact. If the frames were designed such that the clip were part of the main frame member, the crack would have propagated through the frame.

#### Flat Panels with Circumferential Cracks

These panels were tested in a servo-hydraulic universal testing machine capable of applying alternating loads up to 1.5 million pounds. Figure 30 shows two panels mounted in the machine.

Two tests were performed on each panel to simulate transverse or circumferential cracks with a broken center longeron. Uniaxial loads were applied to simulate shell inertia bending stresses and axial stresses due to pressure. Prior to the start of each test, one longeron was completely sawcut through and a crack starter slot with sharp ends placed in the skin directly over the longeron cut. The skin cracks were propagated to predetermined lengths under constant amplitude stress levels and then higher loads were applied to represent fail-safe stresses. The main purpose of the tests was to determine if there was any tendency to cause a fast fracture in the skin, and if such a tendency existed, were the longerons adequate as natural crack stoppers. The panels were repaired after the first test and tested to failure during the second test. Figure 31 shows Panel 12 after the second test.

The results of tests on the 60-inch-wide 7075-T73 panels are shown in Table 9. The results of testing on the four 2024-T3 panels are shown in Figures 32 through 40.

During Test 1 of Panel 11, the load was cycled by hand to give a maximum gross stress of 34.05 ksi with stress ratio equal to zero. Seventeen such cycles were applied which gave some ( $\Delta K$ )<sub>c</sub> - type crack growth data at extremely high stress intensity factors.

Crack growth versus cycles is shown in Figure 32. The highest stress intensity applied during this operation was 163.5 ksi  $\sqrt{\text{in}}$ . As the crack tip approaches the stiffener, the intensity factor K is reduced for the same gross stress, due to load transfer into the stiffener. Figure 33 shows the sawtooth appearance of the fracture during the seventeen high load cycles.

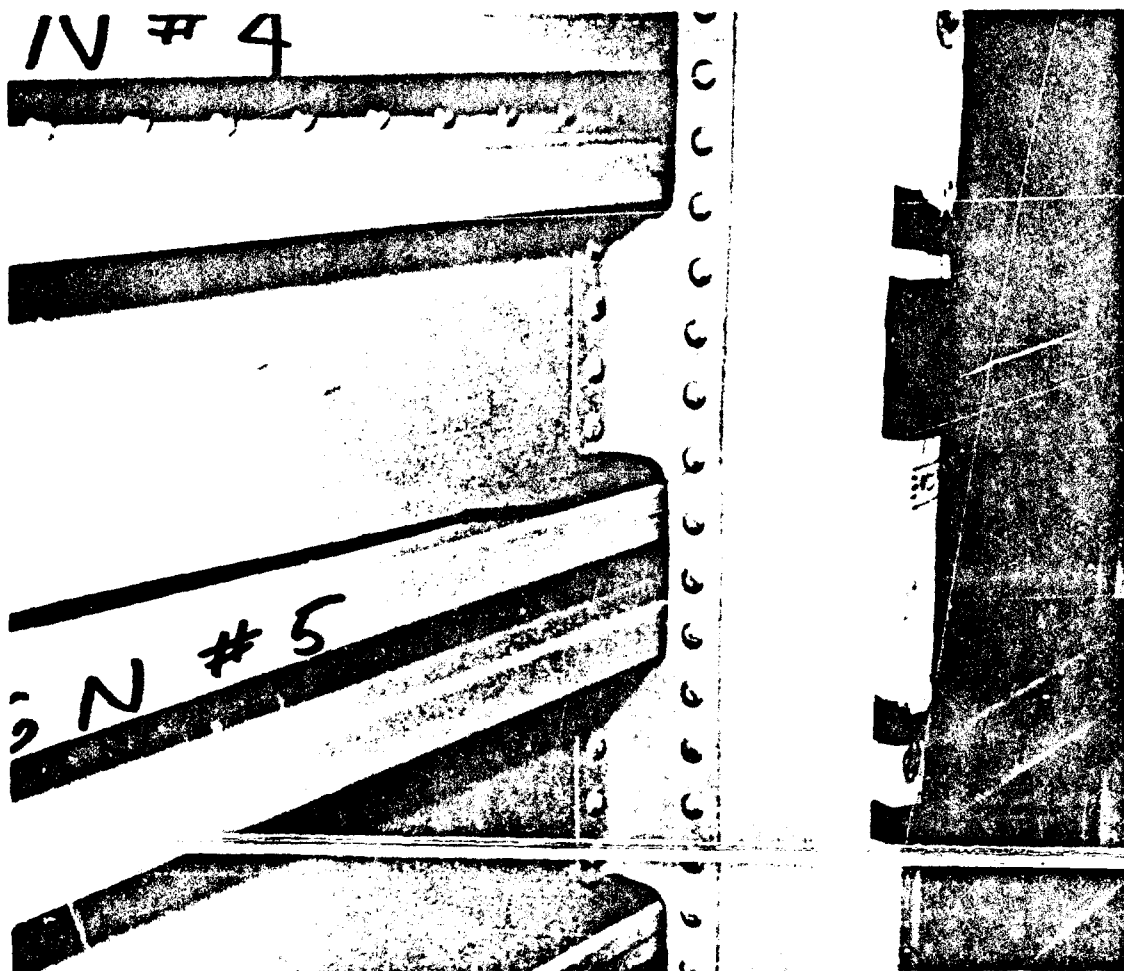


FIGURE 29. ARREST OF TWO-BAY LONGITUDINAL CRACK AFTER FAST FRACTURE, TEST 2, PANEL 3

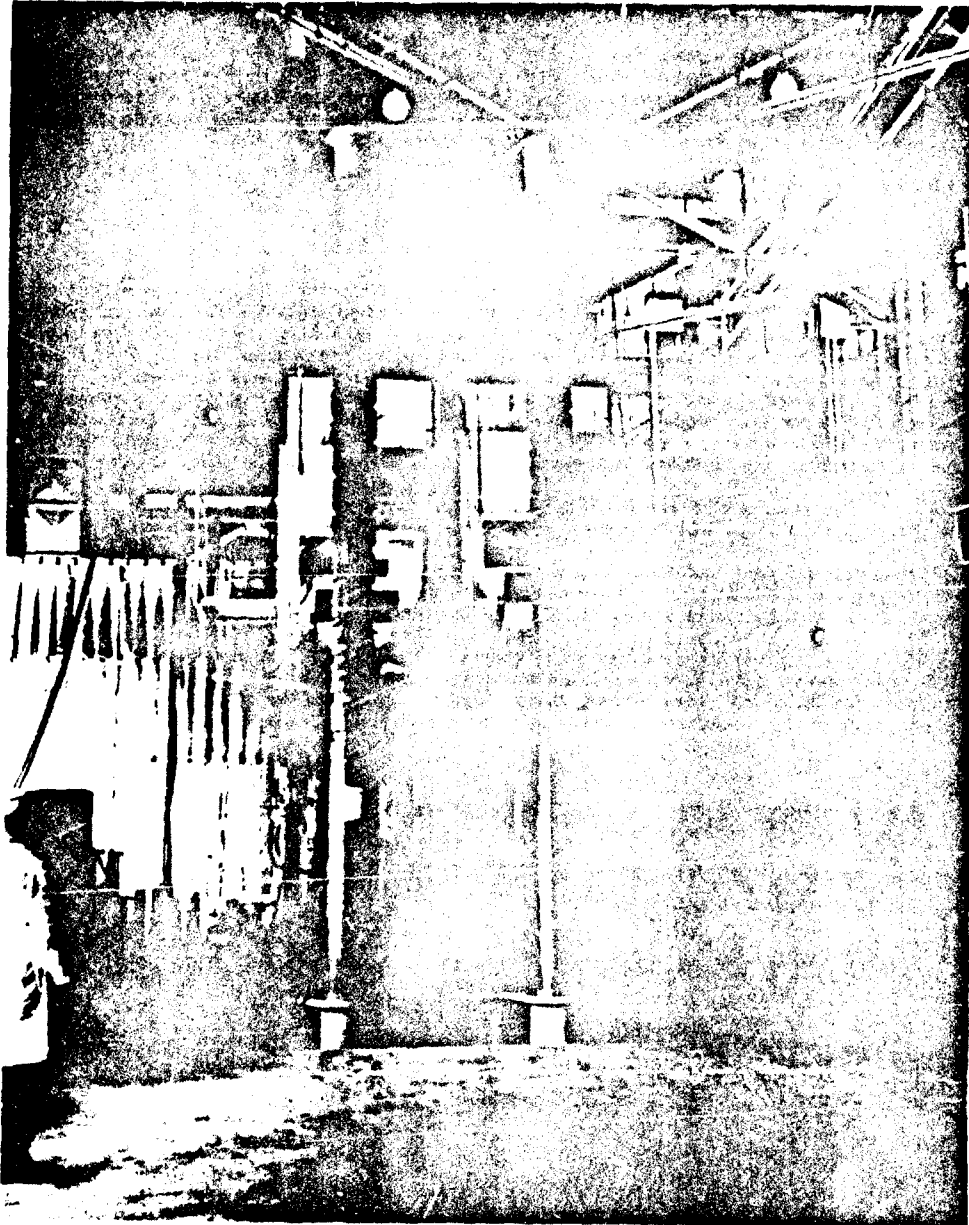


FIGURE 30. TEST PANELS MOUNTED IN 1.5-MILLION-LB MACHINE

The only fast fracture experienced on the 2024-T3 panels occurred during Test 2 of Panel 11. The results are shown in Figure 34. Fast fracture occurred at a gross stress of 40.0 ksi and a crack length of 12.41 inches giving a critical stress intensity factor  $K_c$  and fracture toughness for the material of 192.43 ksi  $\sqrt{\text{in}}$ . The fast fracture was arrested at a crack length of 14.75 inches. At this point, a further longeron was saw cut and the skin crack extended symmetrically about two broken longerons to 25.0 inches. Final failure occurred at a gross stress of 27.92 ksi and a crack length of 25.69 inches.

During the first test on Panel 12, static loads were applied, increasing in magnitude as shown in Figure 35. Slow stable crack growth was measured at each increment during static load application. Considerable retardation in crack propagation was experienced when cycling was resumed after each high static load application. Fast fracture of the skin did not occur during any of the high load cycles, and the highest crack tip stresses indicated by the strain gauges were 168 ksi  $\sqrt{\text{in}}$ .

Figure 36 shows the results of the second test on Panel 12. Higher cyclic stresses were applied and also static load applications with higher crack tip stress intensity factors. The highest  $K$  value reached without fast fracture was 168 ksi  $\sqrt{\text{in}}$ . at Point F. Hand cycling at high stress intensity factors was performed on Panel 13, Tests 1 and 2, and on Panel 14, Test 1 as shown in Figures 37, 38 and 39. During Test 2 of Panels 13 and 14, a second longeron was saw cut and the skin damage extended to three bays. The gross stress at failure of Panels 13 and 14 was 30.97 ksi and 34.29 ksi, respectively.

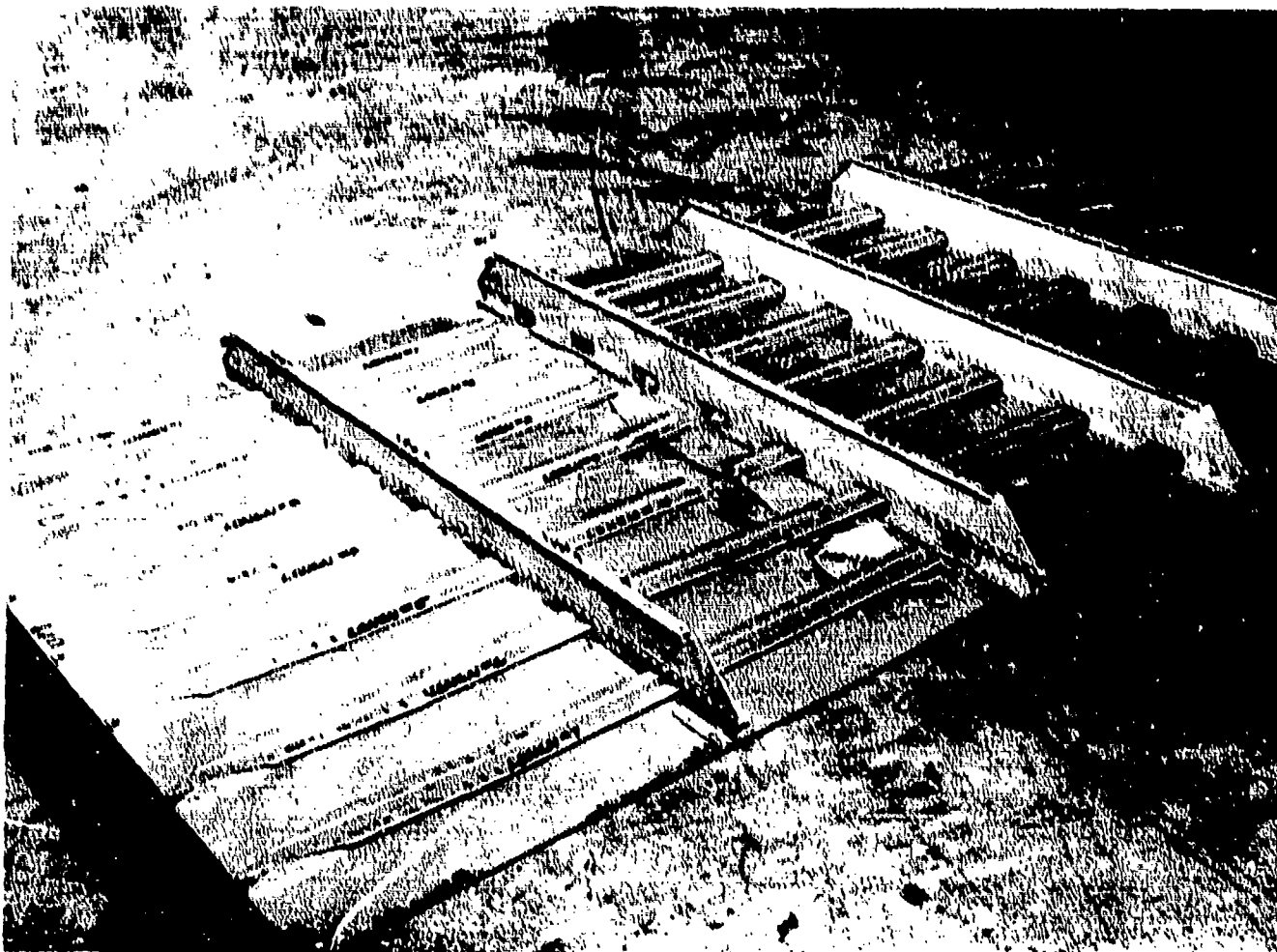


FIGURE 31. PANEL 12 AFTER FINAL FAILURE

TABLE 9  
TEST RESULTS FOR 60-IN.-WIDE FLAT PANELS WITH CIRCUMFERENTIAL CRACK

0.071 IN. 7075-T73 SKIN MATERIAL

CRACKS TRANSVERSE TO GRAIN

PANEL NO.	TEST NO.	GROSS STRESS (PSI)	HALF CRACK LENGTH (IN.)	$R_{ct}$	C	$K^*_c$	CALCULATED			TEST			TEST/CALCULATED		
							$a_{bc}$ (IN.)	$a_{fc}$ (IN.)	$\sigma_{Rc AT}$ FAILURE	$a_{bT}$ (IN.)	$a_{fT}$ (IN.)	$\sigma_{RT AT}$ FAILURE	$a_{bT}/a_{bc}$ (IN.)	$a_{fT}/a_{fc}$ (IN.)	$\sigma_{RT}/\sigma_{Rc}$ (IN.)
7	1	26 180	4.040	0.870	1.0054	104 368	8.100	...	...	8.095	...	...	0.999	...	...
	2	26 640	4.123	0.875	1.0067	110 627	8.100	9.000	30 100	7.688	8.165	31 200	0.949	0.906	1.036
8	1	23 080	3.275	0.770	1.0036	97 850	7.750	...	...	7.875	...	...	0.990	...	...
	2	23 100	3.625	0.780	1.0044	100 942	7.600	8.900	28 700	7.600	8.360	29 600	1.000	0.938	1.031
9	1	23 100	3.500	0.850	1.0128	91 760	7.700	...	...	7.375	...	...	0.958	...	...
	2	28 600	2.440	0.810	1.0020	98 213	8.250	9.000	29 600	7.600	9.140	29 600	0.921	1.015	1.000
10	1	24 000	1.880	0.685	1.0012	84 973	7.900	...	...	7.265	...	...	...	...	...
	2	24 800	1.605	0.670	1.0009	83 318	8.200	8.810	27 500	7.560	8.810	27 800 <sup>a</sup>	0.921	1.000	1.010

<sup>a</sup>FAST FRACTURE TO NEXT LONGERON FINAL FAILURE AT A GROSS STRESS 36 052 PSI WITH TOTAL CRACK LENGTH 32.67 IN. AND ONE BROKEN LONGERON.

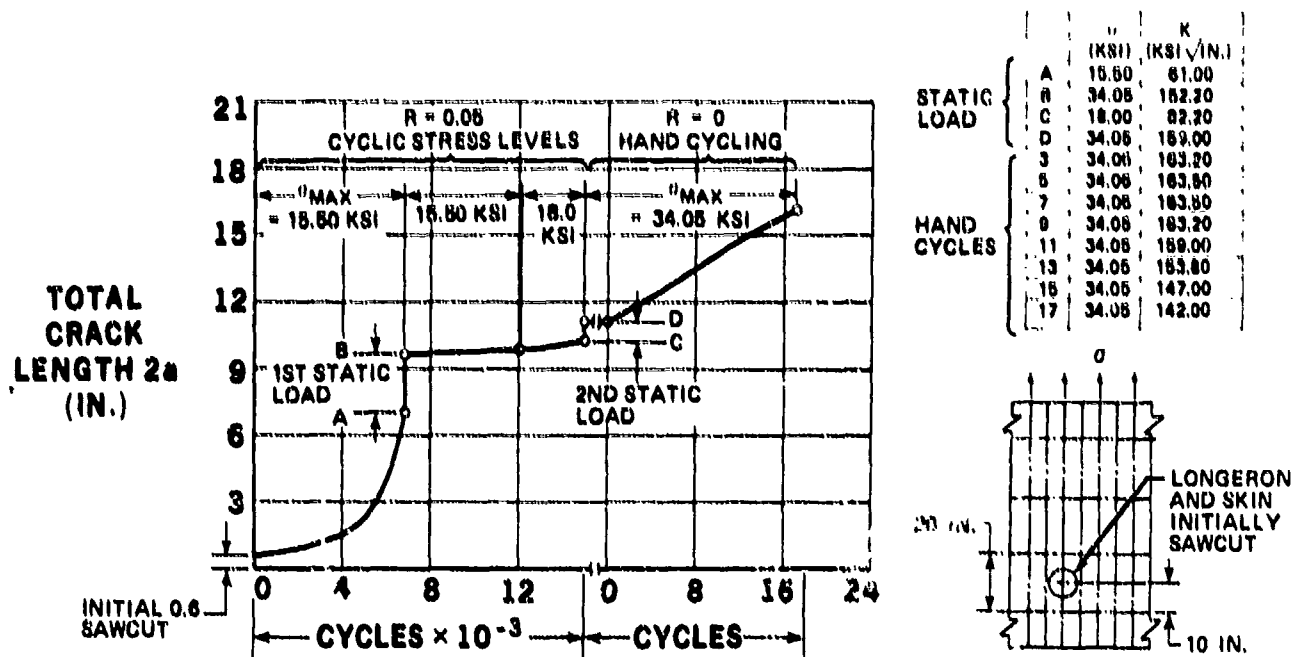


FIGURE 32. TEST RESULTS, PANEL 11 - TEST 1

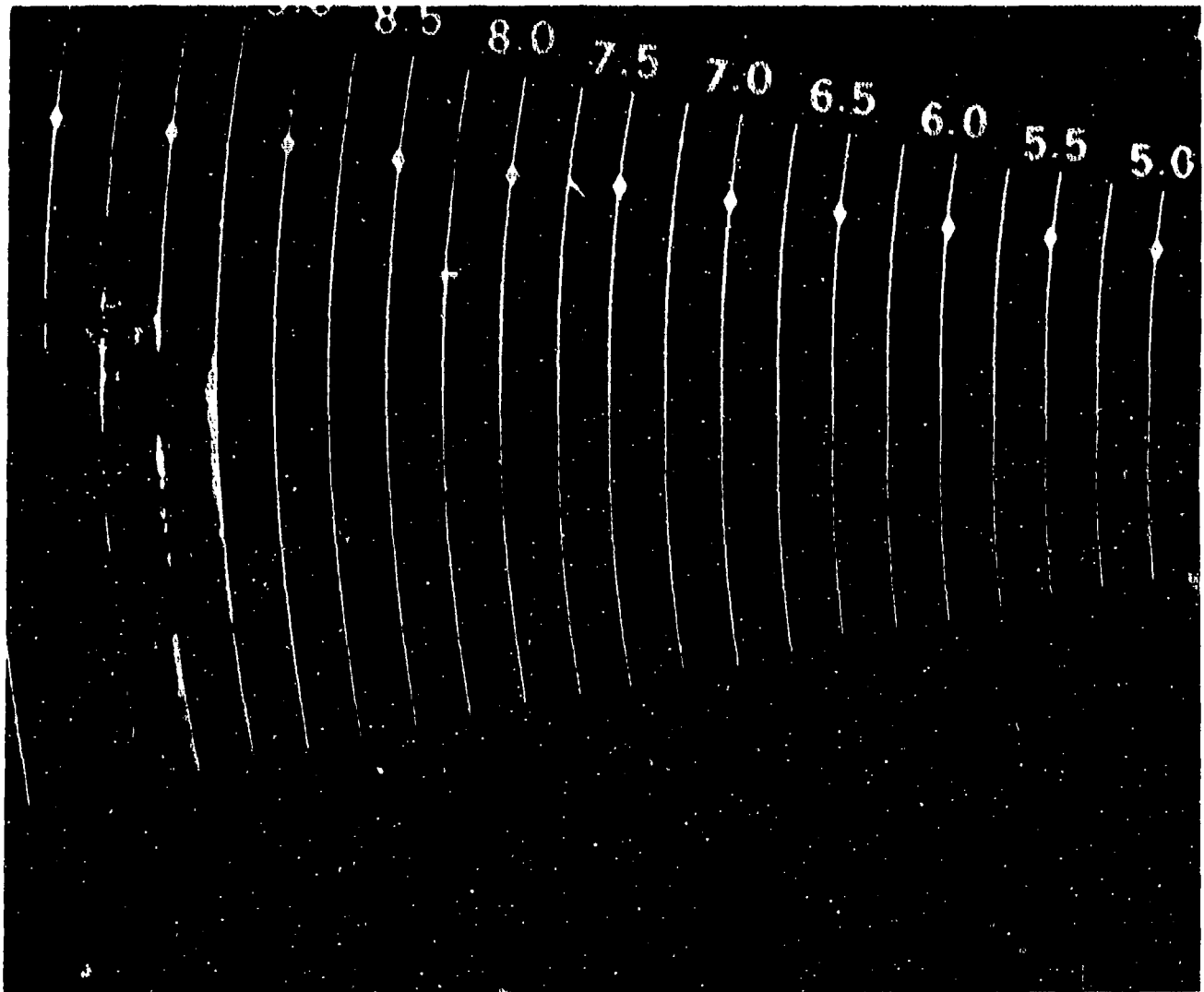


FIGURE 33. SAW TOOTH APPEARANCE OF CRACK DURING PROPAGATION AT HIGH STRESS INTENSITY

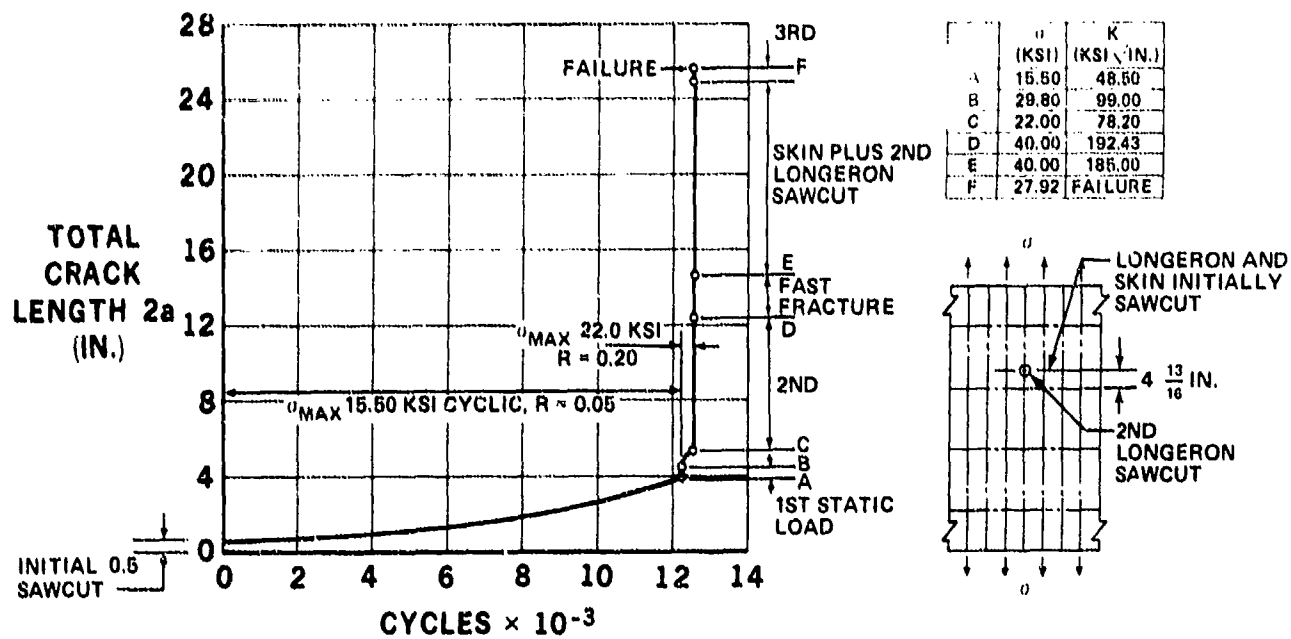


FIGURE 34. TEST RESULTS, PANEL 11 -- TEST 2

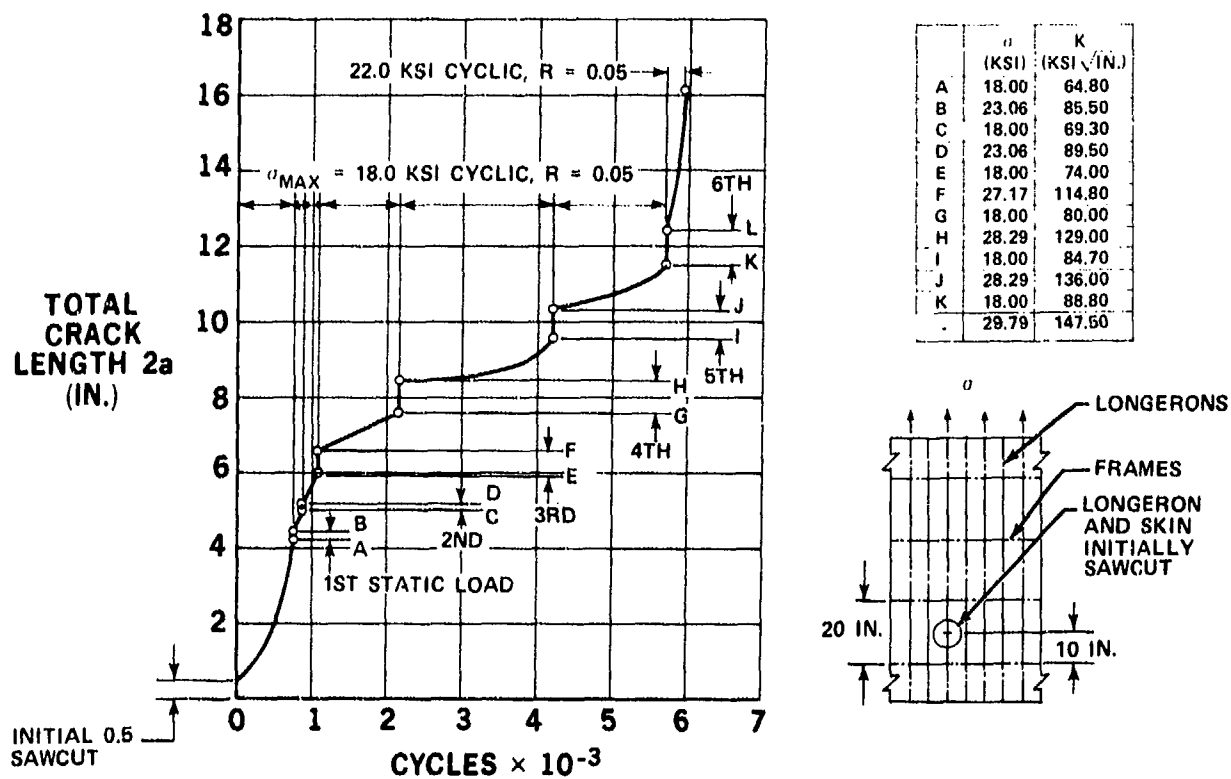


FIGURE 35. TEST RESULTS, PANEL 12 -- TEST 1

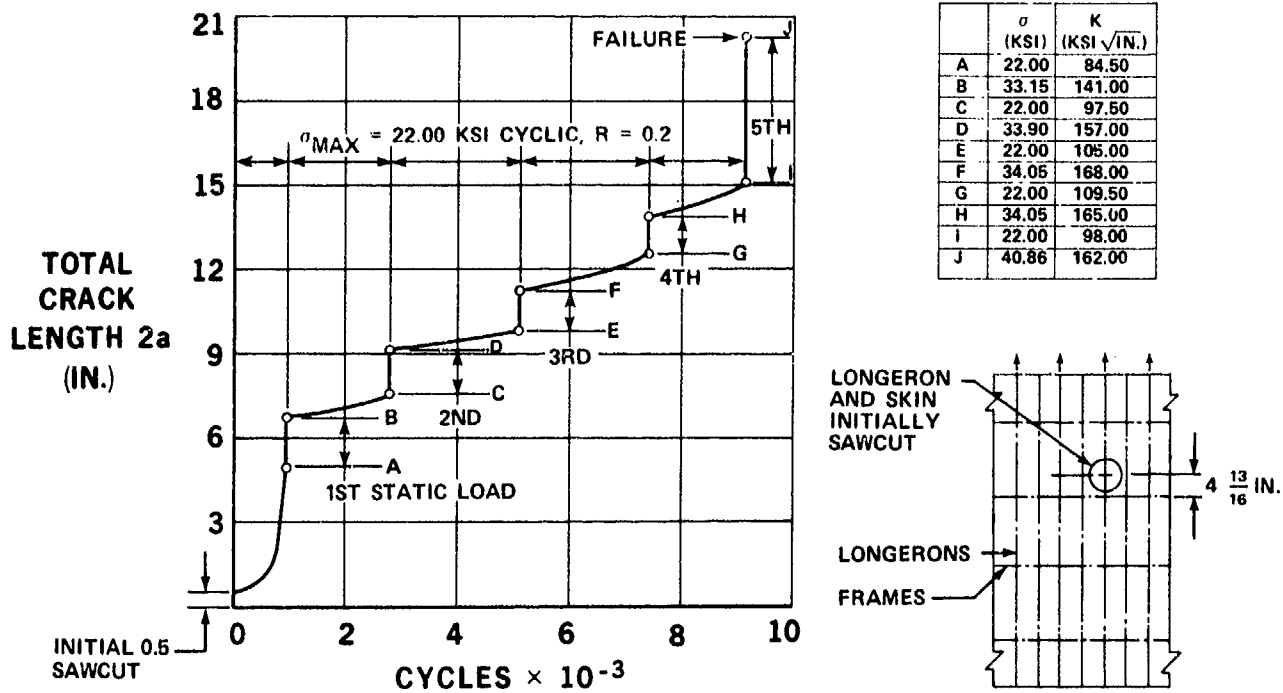


FIGURE 36. TEST RESULTS, PANEL 12 - TEST 2

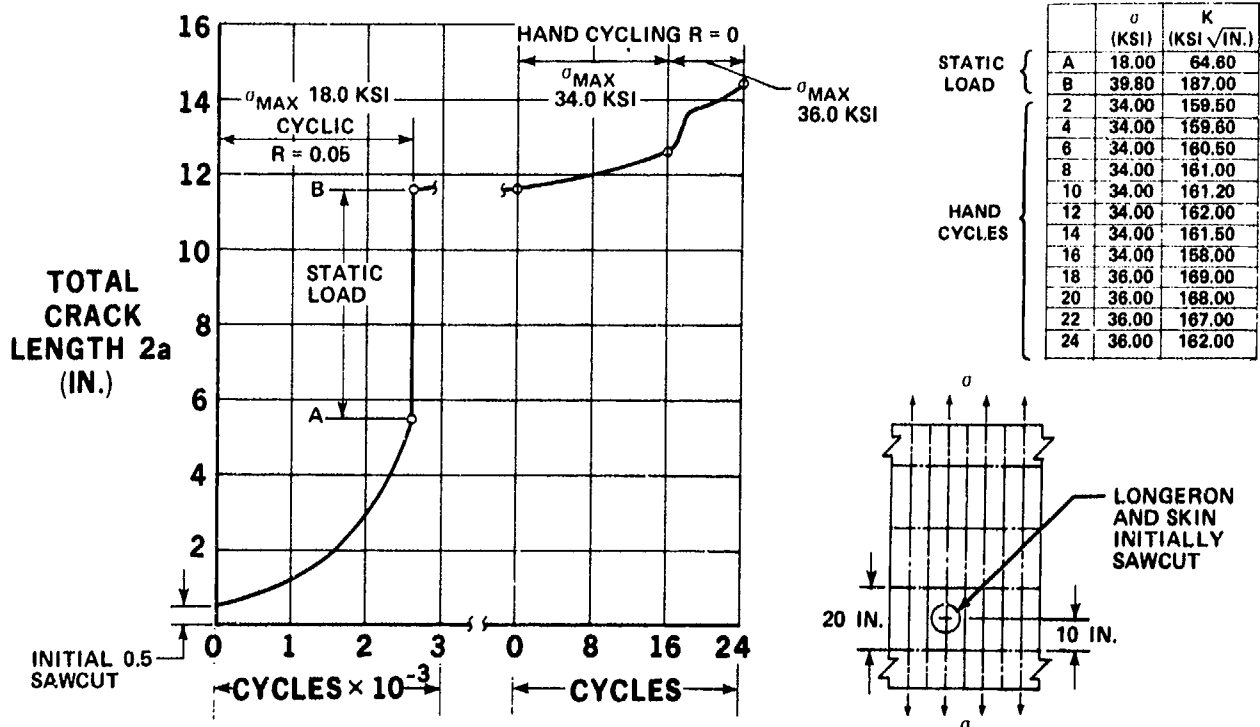


FIGURE 37. TEST RESULTS, PANEL 13 - TEST 1

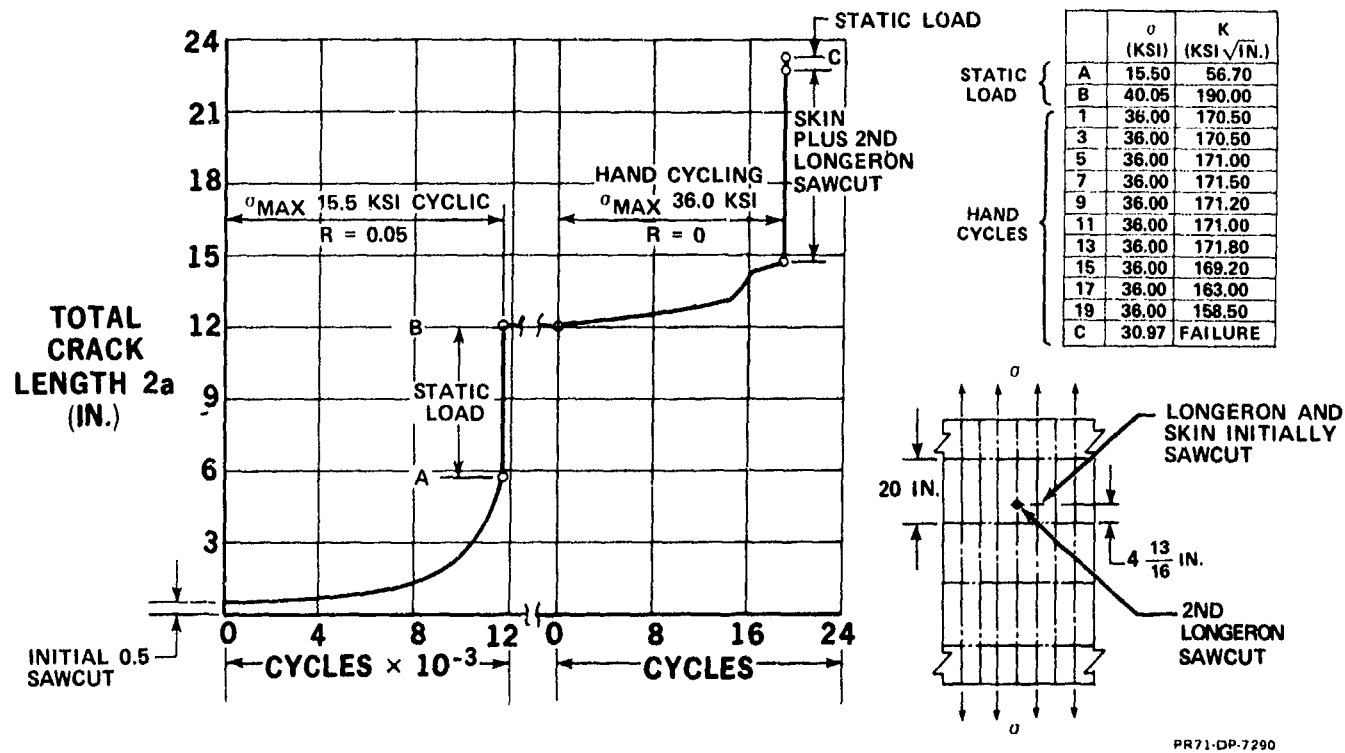


FIGURE 38. TEST RESULTS, PANEL 13 - TEST 2

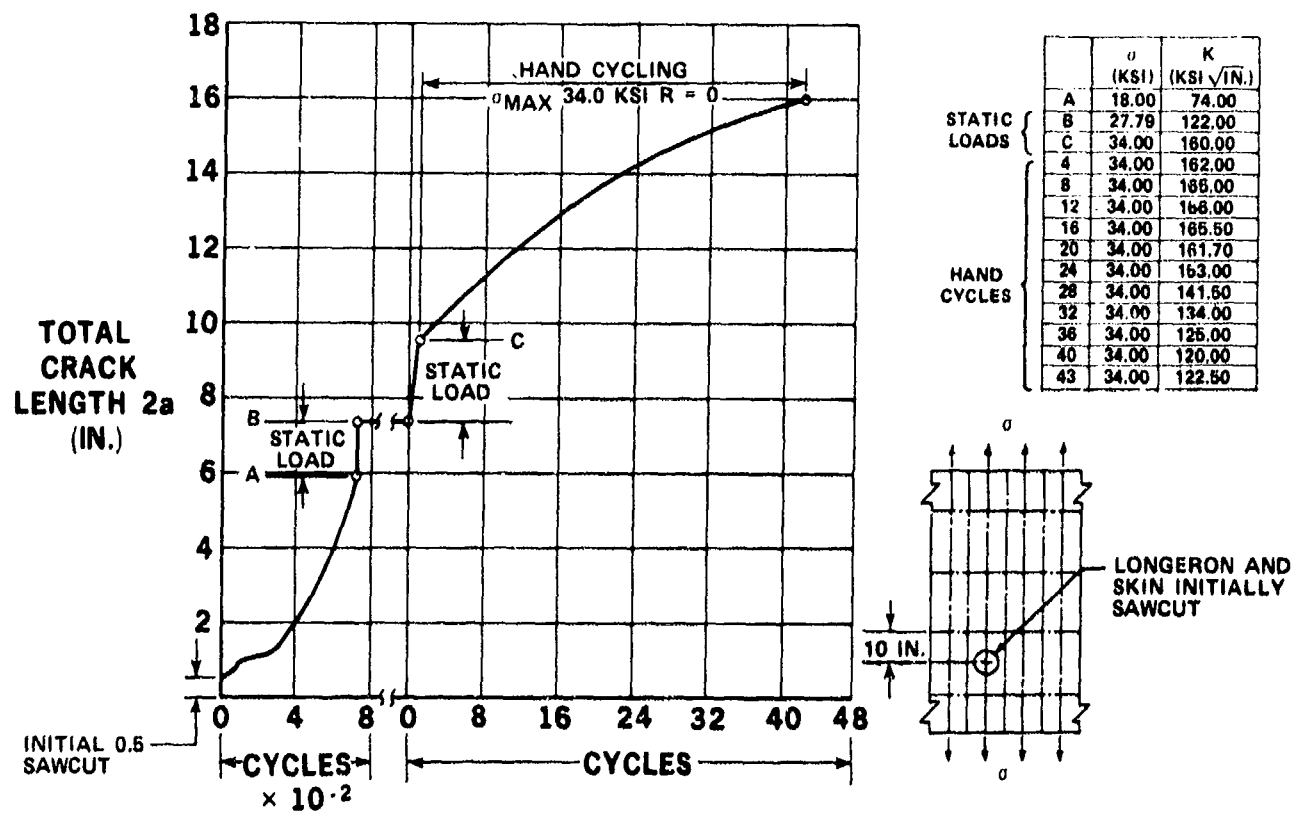


FIGURE 39. TEST RESULTS, PANEL 14 - TEST 1

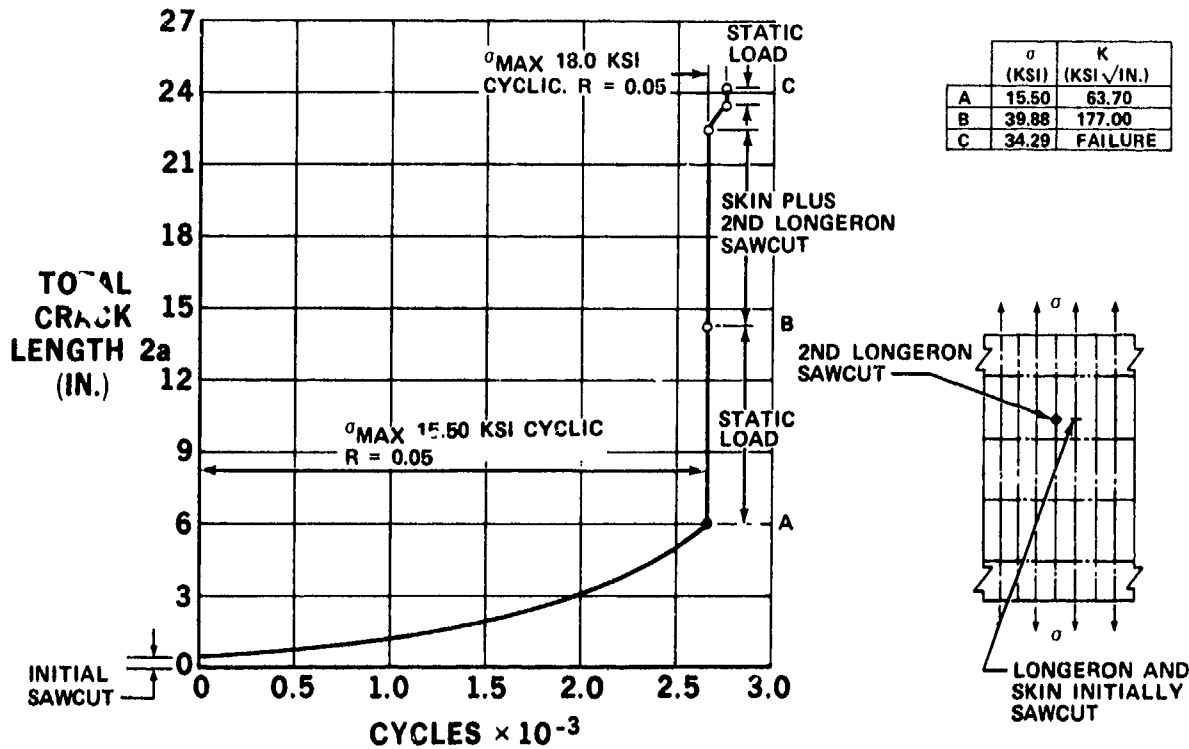
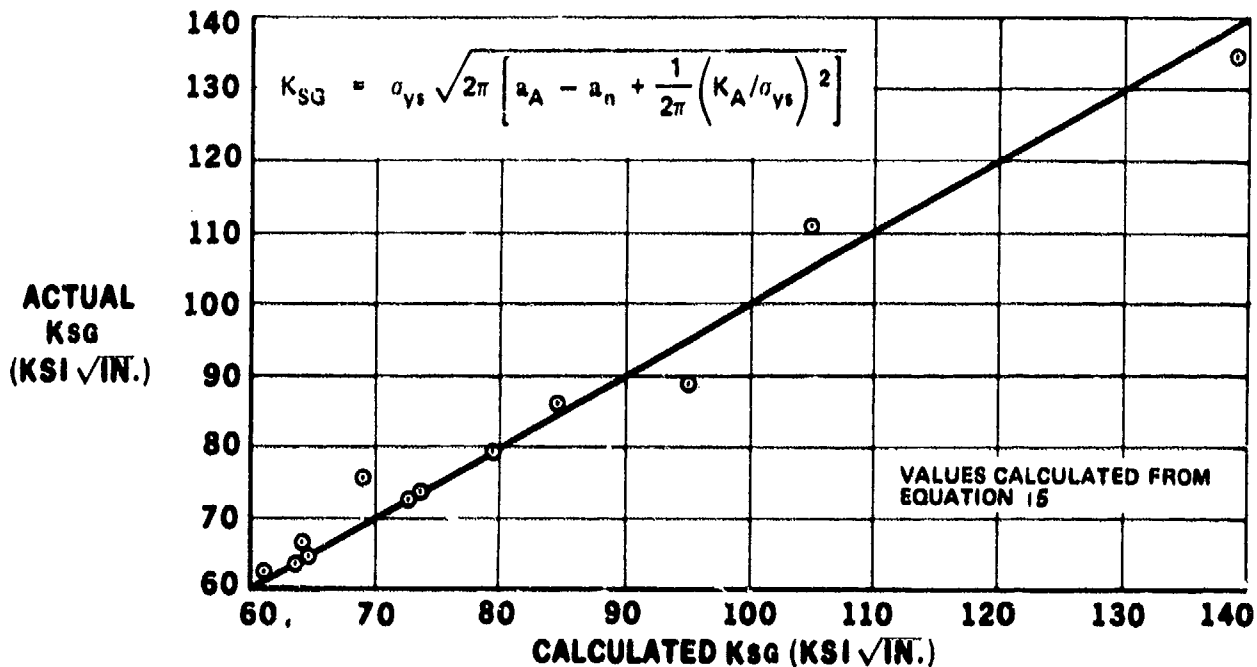


FIGURE 40. TEST RESULTS, PANEL 14 - TEST 2

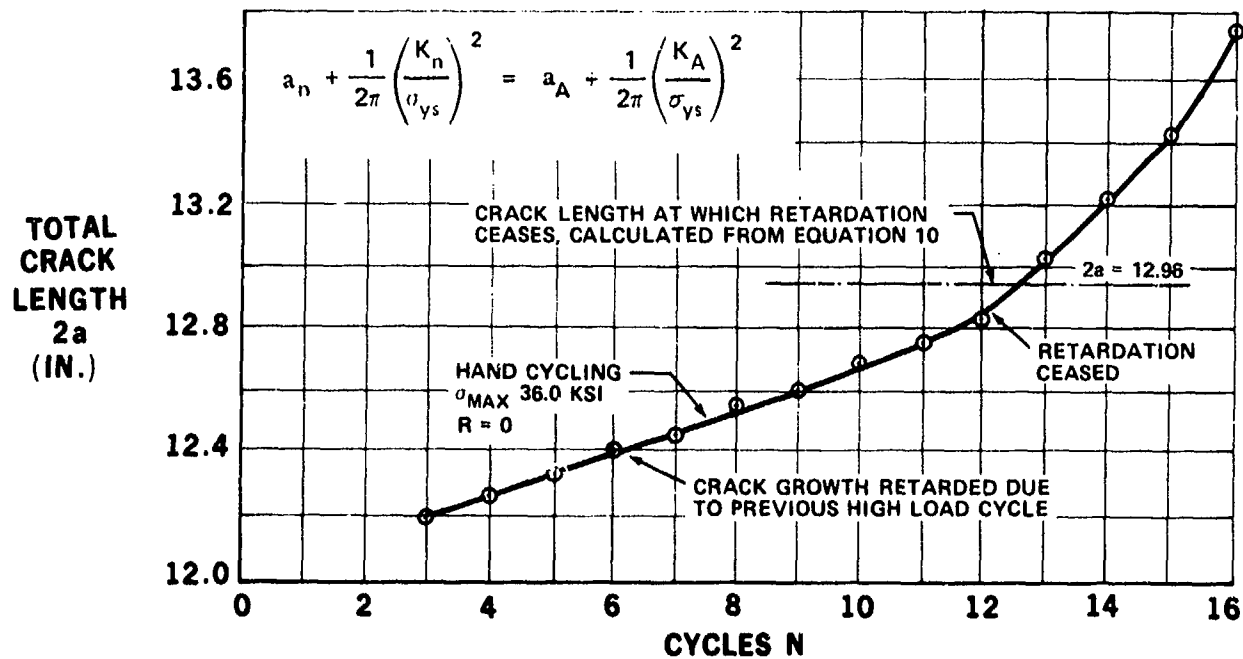
Verification of Eq (15), which gives the stress intensity at the onset slow stable growth as a function of the plastic zone size from the previous high load cycle, is shown in Figure 41a. It can be readily seen that the onset of slow growth is a function of previous load history and does not occur at a constant value. Figure 41b shows an enlargement of the crack growth versus hand cycles for Panel 13, Test 2, illustrated in Figure 38. A previous high load cycle had been applied at point B of Figure 38 up to a gross stress of 40.05 ksi and stress intensity of 190 ksi  $\sqrt{\text{in.}}$ . Hand cycles at a gross stress of 36.0 ksi were subsequently applied with growth rate retarded by the previous high load. Figure 41b shows a sharp increase in growth rate, as retardation ceases, at a crack length of 12.86 inches. The crack length at which retardation should cease (predicted from Eq (14) and (15) is 12.96 inches, indicating close agreement between analysis and test.



(a) ONSET OF SLOW CRACK GROWTH

FIGURE 41. ONSET OF SLOW GROWTH AND CRACK GROWTH RETARDATION





(b) TERMINATION OF CRACK GROWTH RETARDATION FROM PANEL 4 - TEST 2

FIGURE 41. ONSET OF SLOW GROWTH AND CRACK GROWTH RETARDATION (Continued)

Figure 42 shows crack growth rate  $da/dN$  versus  $\Delta K$  taken from all the tests. The data shown are not subjected to retardation due to high load cycles, having been tested by Eq (14) and (15). The data are  $(\Delta K)_c$ -type growth data where each cycle is subjected to preload from the previous load cycle, or constant cycle data. Values are shown up to extremely high  $\Delta K$  values where  $K$  is approaching  $K_C$  for the material. Equations of the Paris form, such as Equation 10, have been written to fit the data and it can be seen that a different equation is necessary when stress intensities approaching instability are applied. Figure 43 shows the same data with an equation of the Forman type, such as Eq (11), written to fit the data. It can be seen that a better fit is obtained in the region where stress intensities are approaching  $K_C$  for the material.

All of the stable growth data obtained from the panels have been plotted against stress intensity factor  $K$ , given by Eq (1). Curve A of Figure 44 represents data with the skin crack 4-13/16 inches from the lateral frame stiffeners and Curve B represents data for the crack midway between stiffeners. Considerably more lateral buckling of the sheet is experienced for the type A crack which causes a

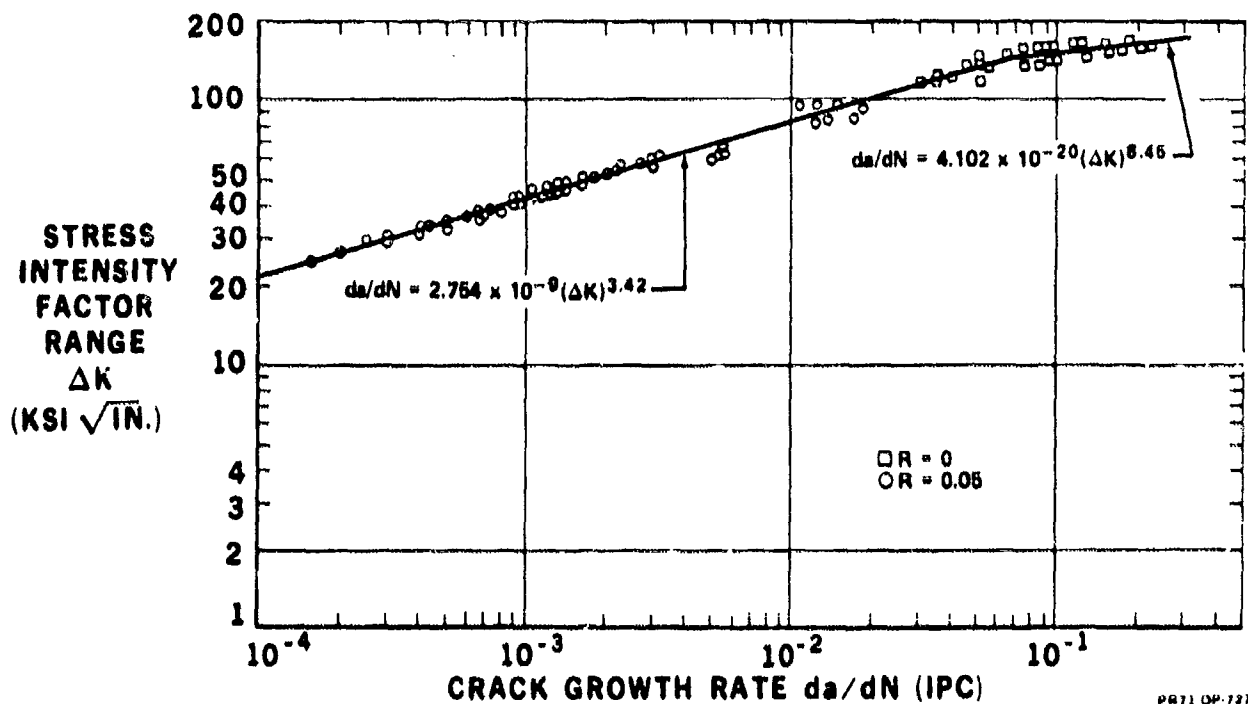


FIGURE 42. CRACK GROWTH RATE, 2024-T3 CLAD SHEET 0.071-THICK FITTED TO PARIS' EQUATION

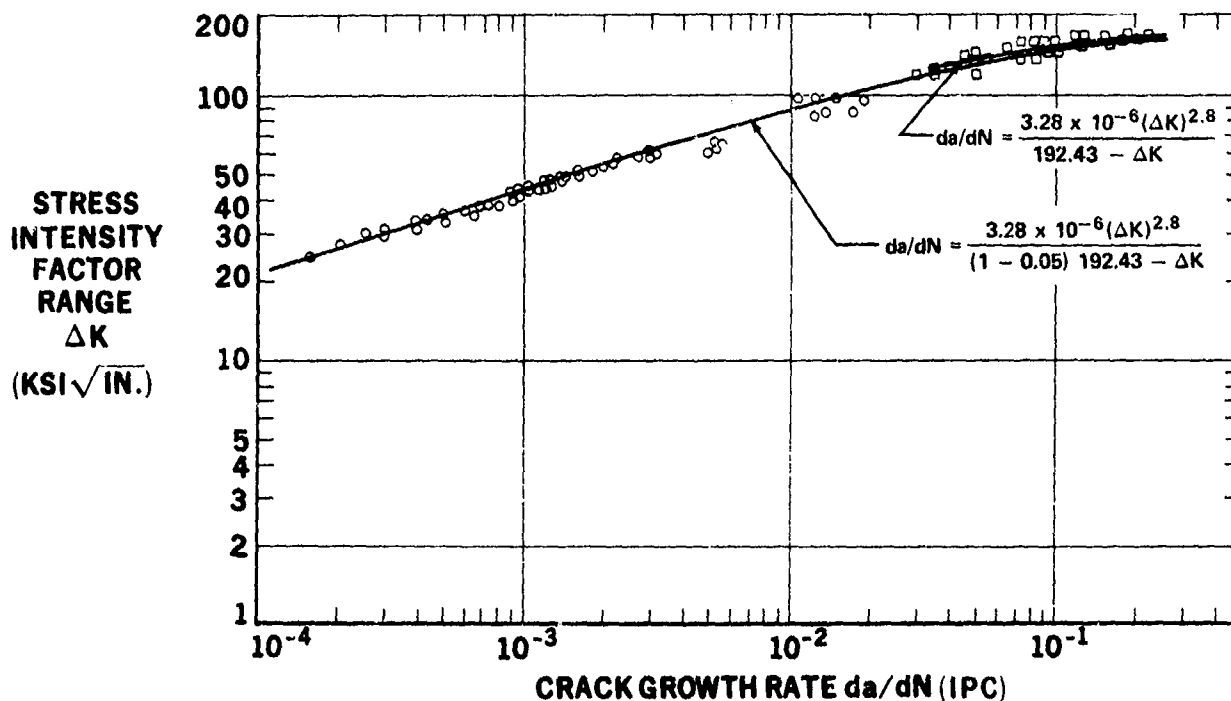


FIGURE 43. CRACK GROWTH RATE, 2024 T3 CLAD SHEET 0.071-THICK FITTED TO FORMAN'S EQUATION

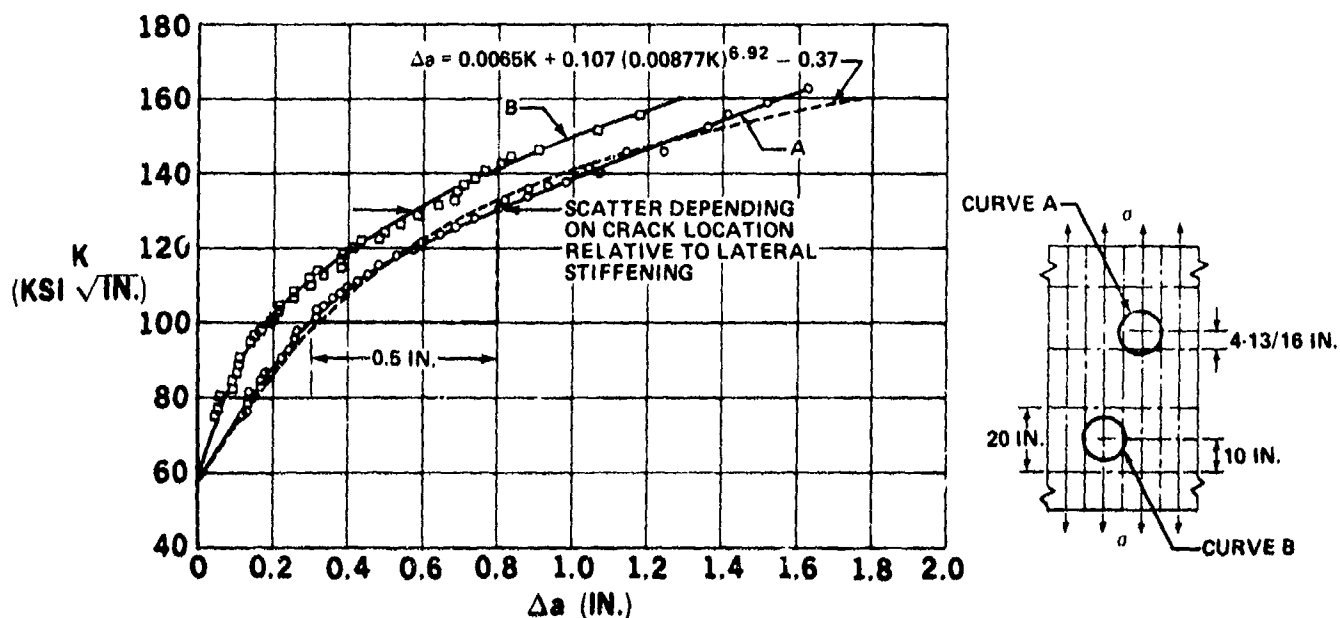


FIGURE 44. SLOW GROWTH VERSUS STRESS INTENSITY FACTOR (2024-T3 CLAD SHEET)

greater amount of crack extension per  $\text{ksi}\sqrt{\text{in.}}$  of stress intensity factor change due to interaction of Mode III-type stress intensity. The significance of the curves can be illustrated by the following example.

Consider the lower edge of the scatter band, Curve A. The crack is stable under a stress intensity of  $100 \text{ ksi}\sqrt{\text{in.}}$ . If the load is increased, slow growth will take place, and at  $130 \text{ ksi}\sqrt{\text{in.}}$ , with  $\Delta K$  equal to  $30 \text{ ksi}\sqrt{\text{in.}}$ , the half crack extension  $\Delta a$  will be 0.5 inch.

Because of the similarity of the slow stable growth curve to a stress strain curve, an equation similar to the Ramberg-Osgood equation (19) has been used to fit the lower edge of the scatter band. This equation is represented by the dotted line in Figure 44.

The onset of slow stable crack growth is shown to be at  $K = 57 \text{ ksi}\sqrt{\text{in.}}$ . But this is due to the limitations of the test data. It is hypothesized that slow stable growth would start as soon as load is applied, provided a fatigue crack could be formed at a maximum stress intensity of zero, which would be difficult. It has been shown by Eq (15) that the onset of slow stable growth is a function of the stress level previously applied. For example, if the maximum stress intensity at which crack propagation has taken place were  $2 \text{ ksi}\sqrt{\text{in.}}$ , then the onset of slow growth would be  $2 \text{ ksi}\sqrt{\text{in.}}$ , and if the crack had been propagated at a maximum stress intensity of  $30 \text{ ksi}\sqrt{\text{in.}}$ , the onset of slow growth would be  $30 \text{ ksi}\sqrt{\text{in.}}$ . In view of this, the family of curves has been plotted as shown in Figure 45. These curves are based on Curve A of Figure 44 and give the amount of half-crack extension per cycle versus stress intensity factor range ( $\Delta K$ ), as a function of the stress intensity at the onset of slow stable growth  $K_{SG}$ .

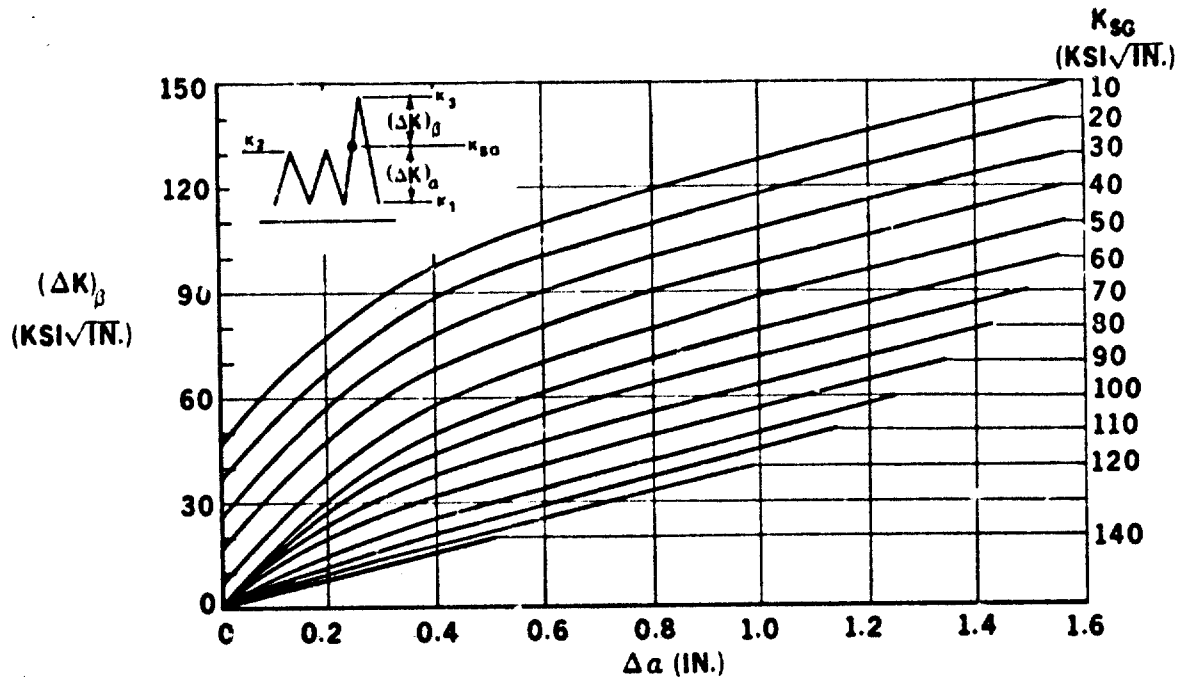


FIGURE 45. SLOW GROWTH VERSUS STRESS INTENSITY FACTOR RANGE BASED ON CURVE A

It can be readily seen by comparing the  $(\Delta K)_\beta$ -type growth of Figures 44 and 45 to the  $(\Delta K)_\alpha$ -type growth of Figures 42 and 43 that considerable error would be experienced if an equation such as Forman's equation were used for spectrum loading, where the parameters had been obtained from constant amplitude data. Considering Figure 24b, cycle EG, Forman's equation could be used from E to F, but between points F and G where stable growth is taking place, data such as that shown in Figure 44 should be used. The dividing line between  $(\Delta K)_\beta$  and  $(\Delta K)_\alpha$  types of growth should be determined by an equation such as Eq (15). The error may not be as pronounced in more brittle materials with lower fracture toughness values, but it is suggested that this phenomenon needs to be accounted for in crack propagation analysis of ductile materials such as 2024-T3.

In recent publications<sup>20, 21</sup>, the onset of slow stable growth has been included in the residual strength diagram for skin fracture criterion. This diagram shows two curves, one of which is based on  $K_{IC}$ , the fracture toughness of the material, and the other based on  $K_I$  described in Reference 21 as the threshold of slow crack growth and referred to in this paper as  $K_{SG}$ . However, the lower curve, describing the crack but in fact must be a function of the previous loading history.

Consider Figure 46. The upper Curve x has been plotted for Test Panel 11 using a fracture toughness value  $K_{IC}$  of 192.43 ksi  $\sqrt{\text{in.}}$  determined from Test 2, shown in Figure 34, and  $R_{ct}$  values from Table 4, for Case 15. The lower curve is plotted for the stress intensity at the threshold of slow stable growth, shown in Figure 44 as 57 ksi  $\sqrt{\text{in.}}$  which was limited by test data and may be lower as previously explained.

Consider the hypothetical case where a crack had been propagated at a gross constant amplitude maximum stress of 20.4 ksi, or lower, to a half-crack length  $a$  of 1.5 inches. On increasing the gross stress level, slow growth will start to take place at 20.4 ksi (as shown by point A of Figure 46) and follow curve AB (obtained from Figure 45) until point B is reached, where fast fracture will occur. If on the other hand the previous maximum constant amplitude stress was 32.0 ksi, then slow growth would not start until 32.0 ksi had been reached at point C in Figure 46 and would follow curve CD where fast fracture would take place at D. This hypothesis is substantiated to some extent by the results of Test 2 on Panel 11 shown in Figure 34. A crack had been propagated to a half-crack length  $a$  of 2.69 inches at a maximum gross stress of 22.0 ksi. Static load was gradually applied from zero and slow-crack growth started to occur at 23.32 ksi shown by point G in Figure 46.

Theoretically, to satisfy Eq (14) and (15), slow growth should have occurred at 22 ksi at point E, but the error is small. It did not, however, start at E on curve Y. Slow growth continued as the gross stress was increased (as shown by test points on Figure 46) until point G, where fast fracture occurred and the crack was arrested at point I.

Curve Y, therefore, has meaning only if the intersection of the maximum gross stress at which previous propagation has taken place and the half-crack length fall below the curve. It has been previously pointed out that the threshold of slow growth may in fact be as low as the lowest stress level at which it is possible to manufacture a fatigue crack.

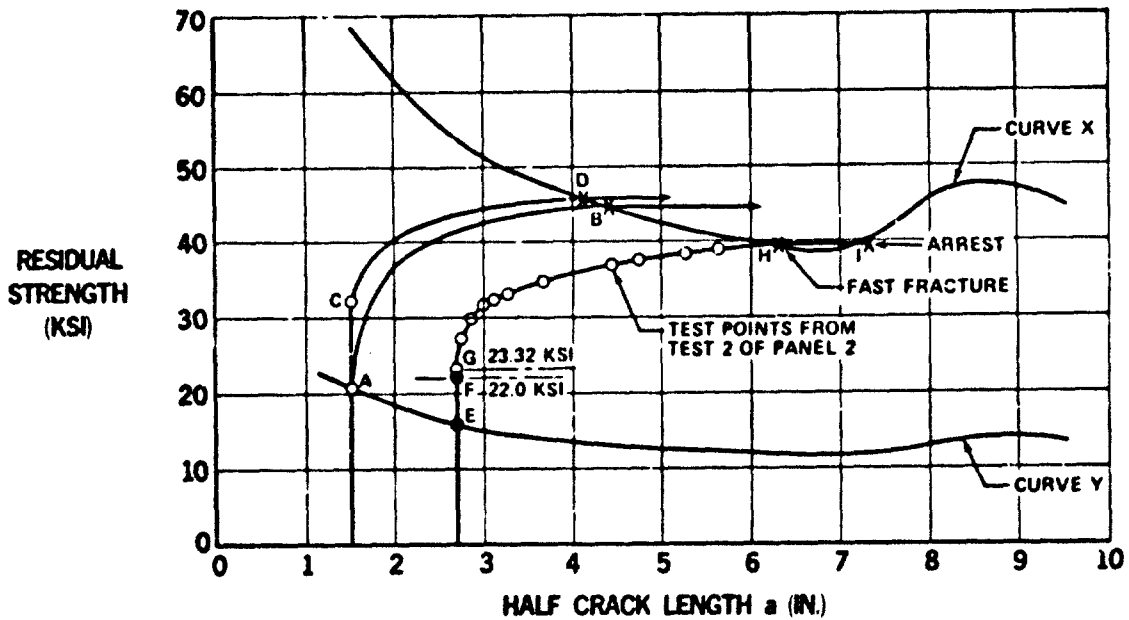


FIGURE 48. GROSS RESIDUAL STRENGTH AND THE THRESHOLD OF SLOW CRACK GROWTH

#### Curved Panels

The test results for curved panels 15 and 16 are listed in Table 10. Four tests were completed on panel 15. Saw cuts were made in the skin in a longitudinal direction, 1 inch away from a longeron in all cases. Cracks were propagated to predetermined lengths under cyclic loading and static load was applied to cause fast fracture. The skin stresses are functions of both pressure  $P$  and axial load per inch of length  $N_x$  due to Poisson's ratio effects of the biaxially loaded skin. The equations governing the stresses are determined using the methods of Flugge.<sup>22</sup> Tests 1 and 3 were performed with pressure load only while axial load was present in the case of tests 2 and 4. Fast fracture of the cracks occurred for all tests on panel 15 and in each case the cracks were arrested at the frames. It can be seen that the value of  $K_C^*$  is effectively increased by 8 percent when an axial stress of 2,500 psi is present and 23 percent with an axial stress of 28,495 psi. Axial compression stress parallel to the crack, which normally causes buckling, is minimized by axial tension stress and would be entirely cancelled out in the case of test 4. Figure 47 shows the crack arrested between rivets after test 1 of panel 15.

The crack stopper was completely saw cut and a cut made in the skin in a longitudinal direction on panel 16. Cyclic loading was applied to propagate the crack and several attempts were made at various crack lengths to cause fast fracture. The value of  $K_C^*$  listed in Table 10 for test 1 on panel 16 is the maximum stress intensity applied without fast fracture at the most critical crack length. The center frame was completely cut for test 2 and the skin crack extended to a 43-inch length. Failure occurred at 11.8 psi pressure due to outer crack stopper failure. Just prior to failure, the stress intensity in the skin was as listed for  $K_C^*$  during test 2. Analysis case 9 of Table 2 predicts a crack stopper stress of 183,000 psi with total crack length 45 inches and gross stress 16,300 psi. Typical values of  $F_{tu}$  from coupon tests show as high as 167,000 psi for titanium 8-1-1 so that the analysis was 10 percent conservative.

A two-bay circumferential crack test with a broken central longeron was conducted on panel 16. The equations governing the skin and longeron axial stresses, accounting for Poisson's ratio effects<sup>22</sup> are:

$$\sigma_{x_{skin}} = 11.25 N_x + 126.8 P$$

$$\sigma_{x_{long}} = 11.88 N_x - 298.6 P$$

Several attempts were made at total crack lengths up to 16.0 inches to cause fast fracture with axial load  $N_x = 2420$  lb/in. and pressure  $P = 9.1$  psi. Skin stress was 28,380 psi and longeron stress 23,600 psi. The maximum value of  $K_C^*$ , determined without fast fracture, was  $>131,700$  psi  $\sqrt{\text{in.}}$ . During this test it was not intended to fail the panel but merely to show a static capability to carry an axial load of 2420 lb/in. with a crack of 16.0 inches.

#### Unstiffened Cylinders

The prime purpose of this series of tests was to investigate the effects of shear combined with pressure on the residual strength of a cracked cylinder. The intention was to determine if the gross principal stress at failure, calculated from condition C of Figure 48, could be compared to the gross allowable stress obtained from condition A. As the presence of the biaxial tension stress  $\sigma_A$  improves the gross strength by cancelling some of the compression stress parallel to the crack edge, it would be more reasonable to determine the principal stress from condition B, neglecting the axial stress  $\sigma_A$ .

TABLE 10  
TEST RESULTS FOR LONGITUDINAL CRACK TESTS ON CURVED PANELS

PANEL NO.	TEST NO.	P (PSI) <sup>a</sup>	$\sigma_h$ (PSI) <sup>b</sup>	$\sigma_a$ (PSI) <sup>c</sup>	$\epsilon_c$ (IN.) <sup>d</sup>	$R_{ct}$	C	K <sup>e</sup> PSI √ IN.	CALCULATED			$\frac{\sigma_{ST}}{\sigma_{sc}}$	ANALYSIS CASE <sup>f</sup>
									$\sigma_{Rc}$ (PSI) <sup>g</sup>	$\sigma_{sc}$ (IN.)	$\sigma_{ST}$		
15	1 <sup>g</sup>	12.8	14 912	0	7.235	1.076	1.0023	66 460	14 750	10.60	10.06	0.95	11
	2 <sup>g</sup>	13.36	15 622	2500	8.050	1.071	1.0028	72 000	16 000	10.06	10.06	1.0	11
	3 <sup>h</sup>	10.80	12 600	0	12.10	1.210	1.0064	65 114	13 300	19.60	19.88	1.014	2
	4 <sup>h</sup>	11.55	15 380	28 495	12.825	1.230	1.0072	80 573	16 500	19.50	19.87	1.019	2
16	1 <sup>i</sup>	12.1 <sup>h</sup>	16 700	0	13.148	1.240	1.0075	> 88 000					8
	2 <sup>i</sup>	11.8 <sup>h</sup>	16 330	0	21.50	1.724	1.0200	> 81 544					9

- NOTES
- a PRESSURE AT FAST FRACTURE, ATTEMPTS AT FAST FRACTURE AND FAILURE
  - b  $\sigma_h$  = HOOP STRESS NORMAL TO CRACK =  $1165P + 0.597N_c$  FOR PANEL 15 AND  $1383P + 0.9714N_c$  FOR PANEL 16
  - c  $\sigma_a$  = AXIAL STRESS PARALLEL TO CRACK =  $8.4N_c + 121P$  FOR PANEL 15
  - d CRACK LENGTH AT FAST FRACTURE, ATTEMPTS AT FAST FRACTURE OR FAILURE
  - e  $\sigma_{Rc}$  = GROSS CALCULATED HOOP STRESS AT FAILURE
  - f REFERENCE TABLE
  - g ONE-BAY CRACK
  - h TWO-BAY CRACK WITH CENTER FRAME INTACT
  - i TWO-BAY CRACK WITH CENTER FRAME INTACT AND CENTER CRACK STOPPER CUT
  - j TWO-BAY CRACK WITH BOTH CENTER FRAME AND CRACK STOPPER CUT
  - k MAXIMUM PRESSURE APPLIED WITHOUT FAST FRACTURE
  - l FAILURE OCCURRED DUE TO OUTER CRACK STOPPER FAILURE

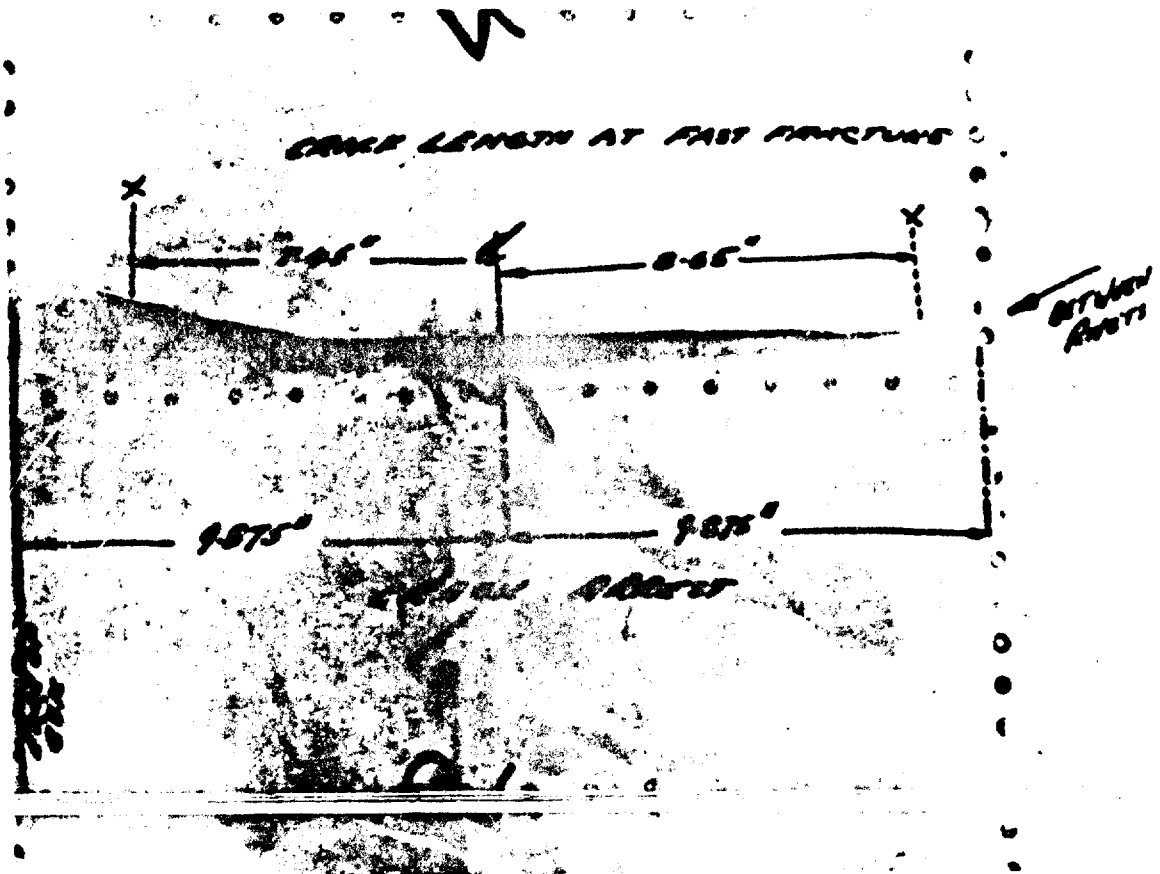


FIGURE 47. VIEW OF PANEL 15 SHOWING ARRESTMENT OF ONE-BAY CRACK

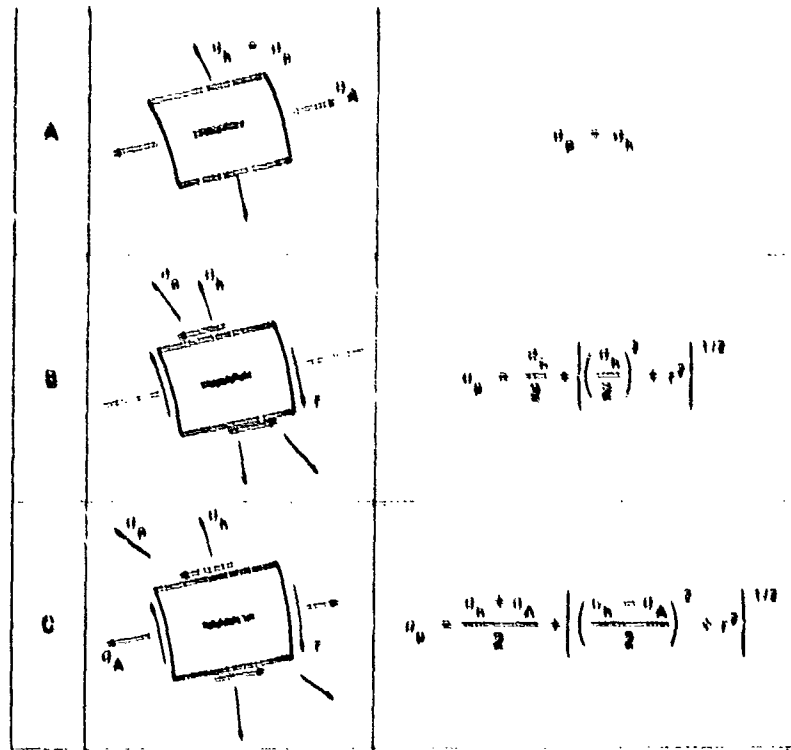


FIGURE 48. PRINCIPAL STRESS EQUATIONS FOR CASES A, B AND C

The terms appearing in Figure 48 are defined as follows:

- $\sigma_h$  = Hoop stress, psi
- $\sigma_A$  = Axial stress, psi
- $\tau$  = Shear stress, psi
- $\sigma_p$  = Principal stress, psi

The results of the tests are shown in Table 11 and plotted in Figure 49. It can be seen by comparing the results of the first six cylinders in Table 7, that the presence of shear reduces the gross residual strength. Comparing principal stress at failure of cylinders with applied shear to the allowable for cylinders without shear is conservative. However, the calculation of principal stress, neg-

- CONDITION A OF FIG. 24 CYLINDERS 1, 2, 3 AND 4
- CONDITION B OF FIG. 24 CYLINDERS 5, 6, 7, 12, 13, 14, 16 AND 18
- △ CONDITION C OF FIG. 24 CYLINDERS 5, 6, 7, 12, 13, 14, 15 AND 18
- ▲ CYLINDER 8 RELIEF OF AXIAL STRESS TO 467 PSI
- ⊕ CYLINDER 9 RELIEF OF AXIAL STRESS TO 1236 PSI
- ◇ CYLINDER 10 AXIAL COMPRESSIVE STRESS -2550 PSI
- ◻ CYLINDER 11 AXIAL COMPRESSIVE STRESS -2585 PSI

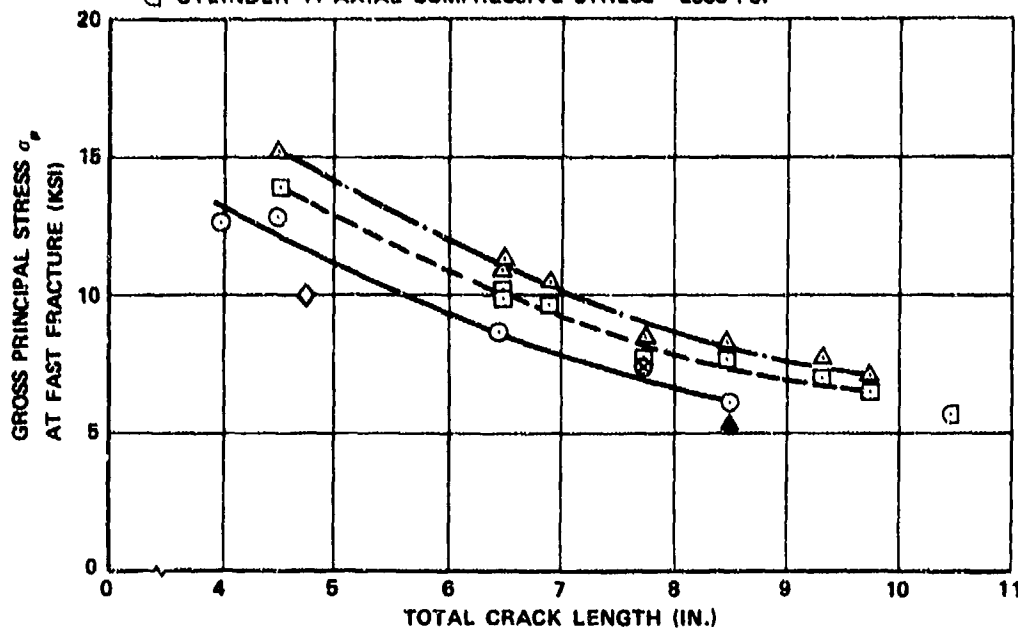


FIGURE 49. TEST RESULTS FOR 24-IN.-DIAMETER CYLINDER

TABLE 11  
TEST RESULTS OF 24-IN. DIAMETER CYLINDERS

CYLINDER NUMBER	CRACK LENGTH AT FAILURE (IN.)	LOADS AT FAILURE		STRESSES AT FAILURE			MAXIMUM PRINCIPAL STRESS AT FAILURE		CONDITION
		PRESSURE (PSI)	TORQUE (IN.-LB)	HOOP STRESS (PSI)	SHEAR STRESS (PSI)	AXIAL STRESS (PSI)	CASE C		
							CASE B $\sigma_A = 0$ (PSI) <sup>a</sup>	INCLUDING $\sigma_A$ (PSI) <sup>a</sup>	
1	4.00	34.0	0	12 750	0	6 275	12 750	12 750	P
2	4.50	34.3	0	12 880	0	6 440	12 880	12 880	P
3	6.44	23.0	0	8 630	0	4 315	8 630	8 630	P
4	8.50	16.1	0	6 030	0	3 015	6 030	6 030	P
5	4.50	27.3	209 250	10 250	7 240	5 125	13 995	15 368	P + T
6	6.88	19.0	147 250	7 125	5 085	3 563	9 772	10 732	P + T
7	8.44	15.0	116 250	5 625	4 020	2 813	7 719	8 478	P + T
8	8.50	14.5	0	5 440	0	467	5 440	5 440	P + C
9	7.70	20.0	0	7 500	0	1 235	7 500	7 500	P + C
10	4.75	27.0	0	10 130	0	-2 550	10 130	10 130	P + C
11	10.50	15.0	0	5 630	0	-2 585	5 630	5 630	P + C
12	9.75	13.0	93 000	4 875	3 210	2 435	6 468	7 089	P + T <sub>c</sub>
13	7.75	15.0	117 400	5 625	4 060	2 813	7 752	8 516	P + T <sub>c</sub>
14	6.50	20.0	159 650	7 500	5 520	3 750	10 423	11 455	P + T <sub>c</sub>
15	9.313	13.85	105 090	5 190	3 630	2 595	7 057	7 748	P <sub>c</sub> + T
16	6.47	20.9	133 145	7 840	4 600	3 920	9 964	10 880	P <sub>c</sub> + T

<sup>a</sup>REFERENCE FIGURE 24

CONDITION DEFINITION	}	P = STATIC PRESSURE ONLY
		P + T = STATIC PRESSURE + STATIC TORQUE
		P + C = STATIC PRESSURE + COMPRESSION
		P + T <sub>c</sub> = STATIC PRESSURE + CYCLIC TORQUE
		P <sub>c</sub> + T = CYCLIC PRESSURE + STATIC TORQUE

lecting axial stress (as in case B of Figure 48) gives a closer approximation to condition A than the calculation of principal stress from condition C.

#### Rivet Shear Deflection Test Results

In order to verify the rivet deflection Eq (3) and (5) for titanium and aluminum, several small tests were performed on lap splice specimens. Each specimen consisted of a strip of 6Al-4V single annealed titanium which was riveted to a strip of 0.071 2024-T3 clad sheet using RV-5197-6 countersunk rivets. The specimens were placed back to back as shown in Figure 50 to eliminate local bending. Three thicknesses of titanium were used, 0.016, 0.020 and 0.025 inch. The extension, under tension loading, was measured over a 2-inch gage length using an extensometer. Extension of the sheet was calculated and subtracted from the overall deflection so that actual rivet deflection would be obtained. The stiffness  $P/\delta$ , where P is the applied load and  $\delta$  is shear deflection of the rivet (obtained from the elastic portion of the resulting load deflection curve), is compared on Figure 50 to the value calculated from Eq (3) and (5).

#### Stiffened Panels, 30 Inches Wide

The test results for these panels are shown in Table 12. In all cases, the straps failed without failure of the rivets. The maximum load to be transferred to a strap in the DC-10 configuration is 4370 pounds for a 2.0-inch-long crack. It can be seen from Table 12 that the value of  $P_c$  in all cases is higher than this number so that strap failure will always precede rivet failure, even with two rivet rows.

0.071 2024-T3  
CLAD SHEET

0 AL-4V  
TITANIUM

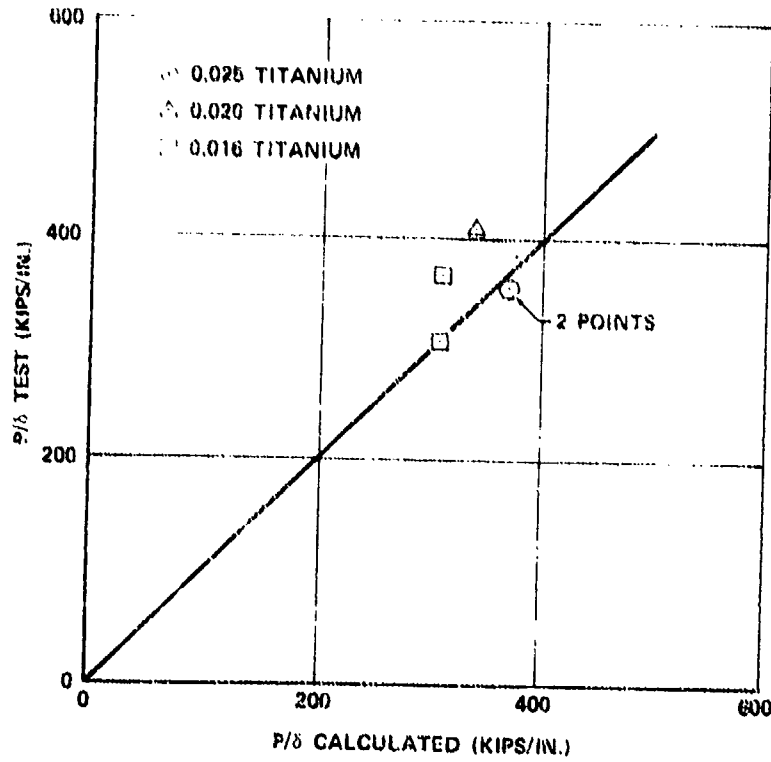
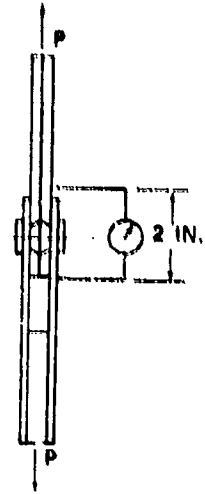
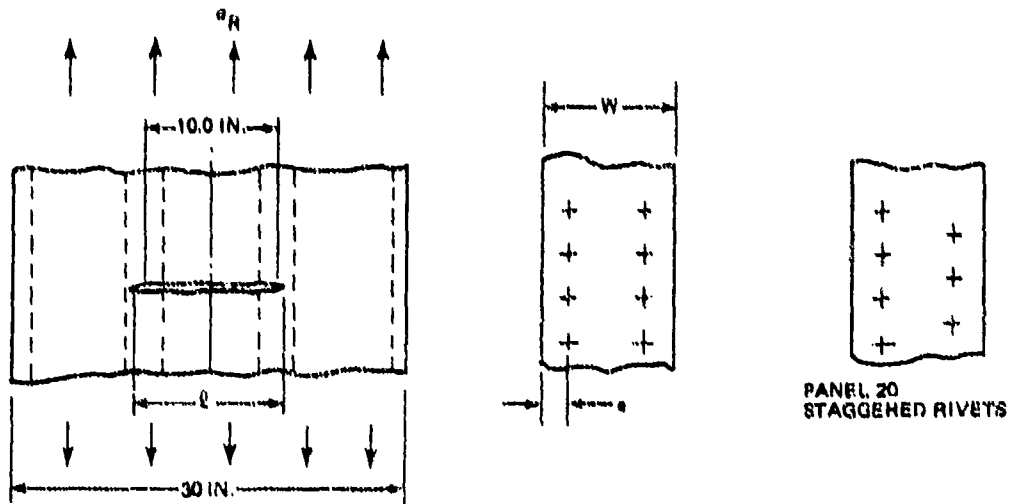


FIGURE 50. RIVET SHEAR DEFLECTION TEST RESULT CORRELATION



TABLE 12  
TEST RESULTS FOR 30-IN.-WIDE PANELS

0.071 2024-T3 CLAD SHEET  
TITANIUM STRAP GA1-4V



PANEL NO.	W	t	e (IN.)	P <sub>F</sub> (LB) (a)	L <sub>F</sub> (IN.) (b)	P <sub>C</sub> (c)	σ <sub>R</sub> (d)
17	2.813	0.025	11/16	89 000	11.45	6880	34 503
18	2.813	0.025	7/16	87 000	9.80	5725	33 727
19	3.438	0.020	7/8	94 000	10.50	5700	36 942
20	3.438	0.020	7/8	89 000	9.60	5380	34 977
21	4.188	0.016	1-1/16	80 000	10.60	5500	34 745
22 <sup>(e)</sup>	3.625	0.016	29/32	96,000	9.90	3000	36 185

- NOTES:
- (a) LOAD AT FAILURE
  - (b) CRACK LENGTH AT FAILURE
  - (c) LOAD TRANSFERRED TO CRACK STOPPER DUE TO CRACK
  - (d) GROSS STRESS AT FAILURE
  - (e) AM 350 STAINLESS STEEL STRAP

#### Unstiffened Panels, 30 Inches Wide

Two unstiffened panels made from 0.071 2024-T3 clad sheet were tested (Figure 51). A 9-inch-long central crack was propagated in the first panel and static load applied. Slow crack growth took place and final failure occurred at a gross stress of 24,600 psi with the crack 11.0 inches long. The second panel contained a 9-inch-long saw cut. Static load was applied and slow growth again took place to 11.0 inches before failure at the same gross stress of 24,600 psi. Antibuckling guides, set 1.0 inch apart, were used in both cases.  $K_C$  as determined for the final crack length from Eq (1) was 114,000 psi  $\sqrt{\text{in}}$ .

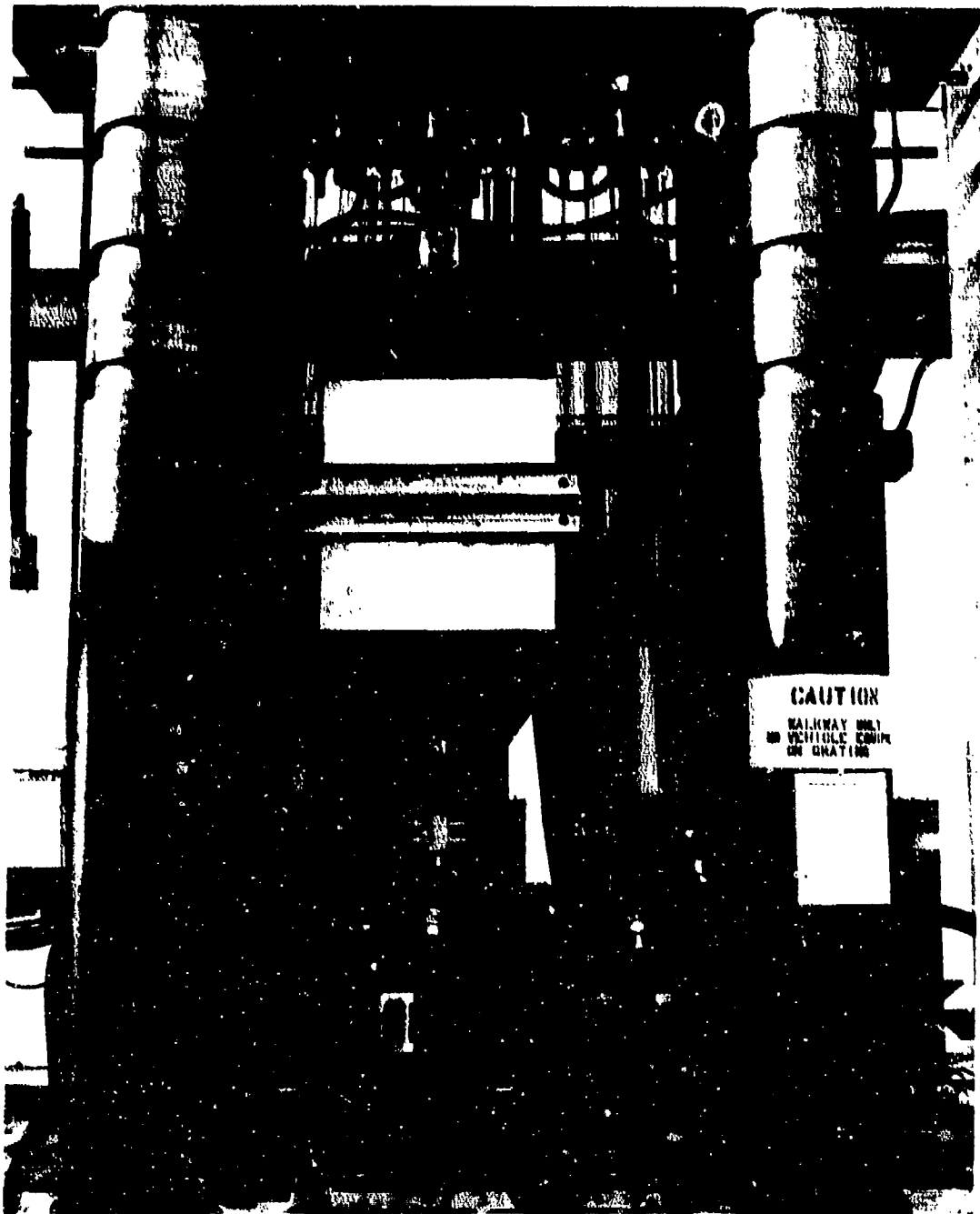


FIGURE 51. TEST SETUP FOR 30-INCH-WIDE PANELS

#### Rivet Shear Load Test

Figure 52 gives the results of tests performed on the small panels shown in Figure 25g to determine the crack stopper to skin rivet shear load.

A Lumped Parameter Analysis, to determine the rivet shear load, was performed on one of the panels with a 0.020 strap. This analysis is used for a comparison with the results for the three thicknesses of strap. It is not expected that the strap thickness variation, in the ranges considered,

will affect the calculated elastic load distribution to a high degree. The panel was divided into bars and shear panels similar to those shown in Figure 7. The rivet loads were determined from strain gage readings on the strap. The ordinate of Figures 52a to 52c is shown as shear flow in pounds/inch and since the rivets are spaced 1 inch apart, this load would, therefore, be rivet load. The shear flow shown is applied to two rivets. Figure 52a shows a comparison between test and elastic analysis for a 0.025 strap. It can be seen that the first rivets yield at a load between 3000 and 5000 pounds and more load is carried by the remaining rivets. Yielding occurred very early for both the 0.020 and 0.016 straps as shown in Figures 52b and 52c. Figure 52d shows applied load versus shear load in the first rivets for tests on two panels with 0.025 straps. The maximum load transferred from the skin to crack stopper for DC-10 loading with a crack 42 inches long is 4370 pounds. This is determined from case 6 of Table 1 with cabin pressure 9.2 psi and skin stress 80 percent of  $PR/t$  hoop stress, where  $R$  is 118.5 inches. It can be seen from Figure 52d that little or no loss in first rivet load is experienced at this applied load. However, due to early yielding of the first rivets in the 0.020 and 0.016 straps shown in Figures 52b and 52c, a loss in the crack tip stress ratio  $R_{ct}$  could be expected if 0.020 or 0.016-inch-thick straps were used.

P (LB)	CALCULATED	TEST
1000	○—○	○—○
3000	□—□	□—□
5000	△—△	△—△
7000	▽—▽	▽—▽

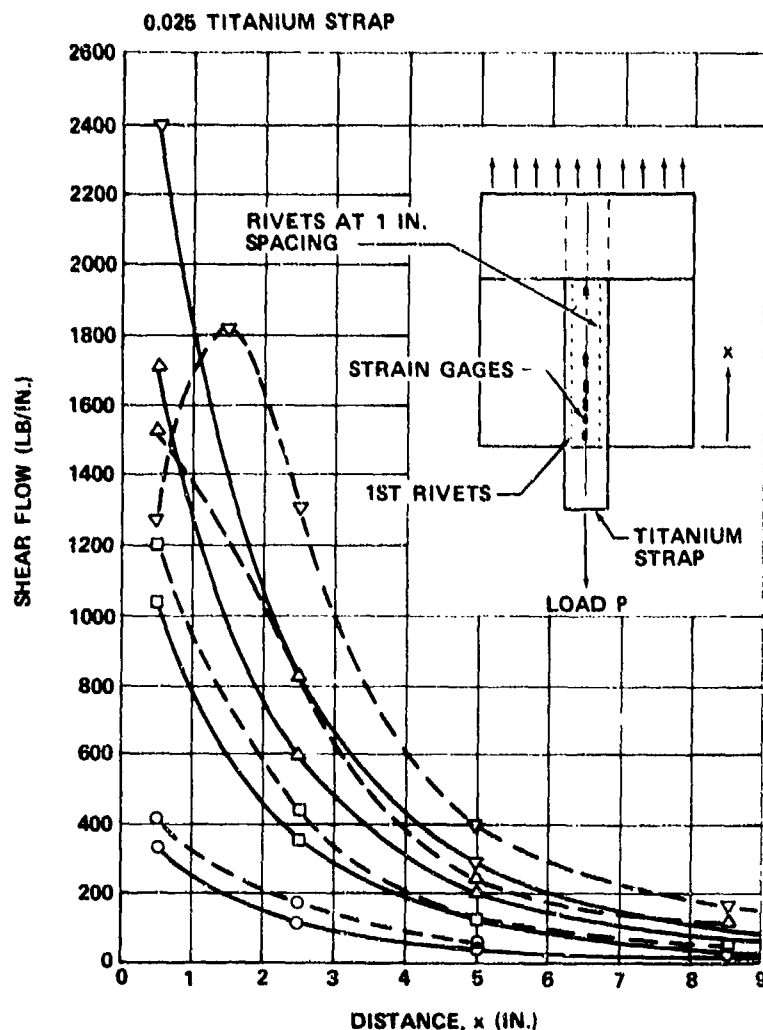


FIGURE 52a. RIVET SHEAR LOAD - ANALYSIS, TEST CORRELATION - 0.025 TITANIUM STRAP

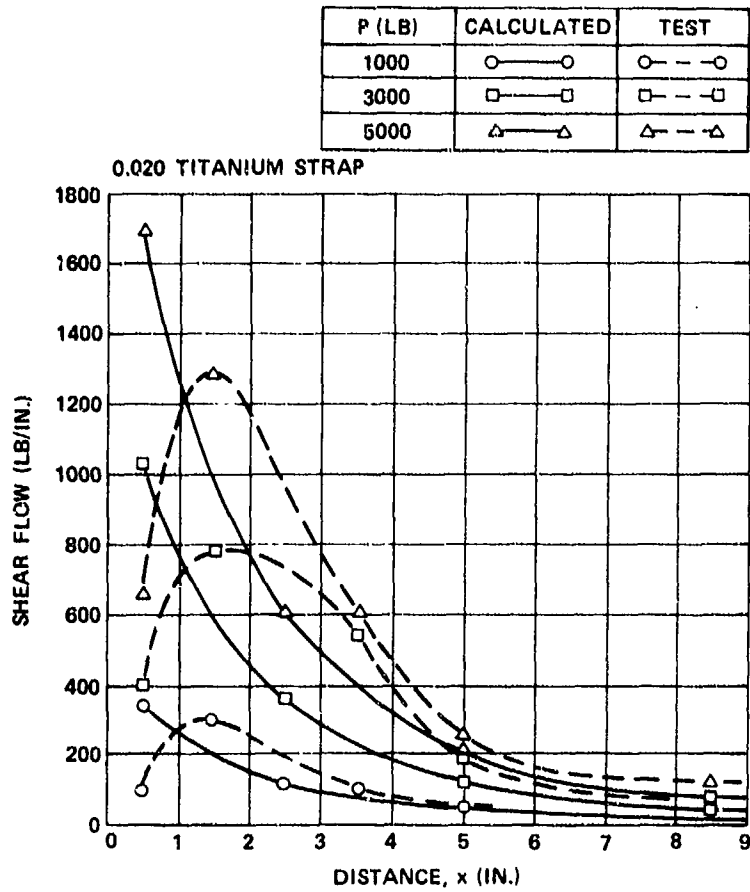


FIGURE 52b. RIVET SHEAR LOAD - ANALYSIS, TEST CORRELATION - 0.020 TITANIUM STRAP

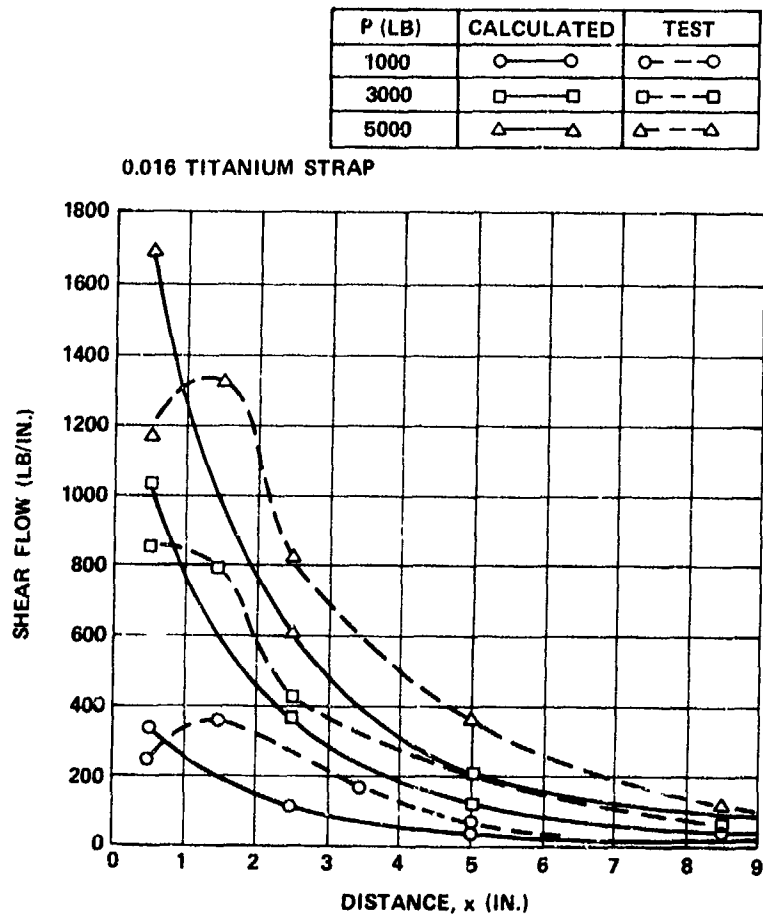


FIGURE 52c. RIVET SHEAR LOAD - ANALYSIS, TEST CORRELATION - 0.016 TITANIUM STRAP

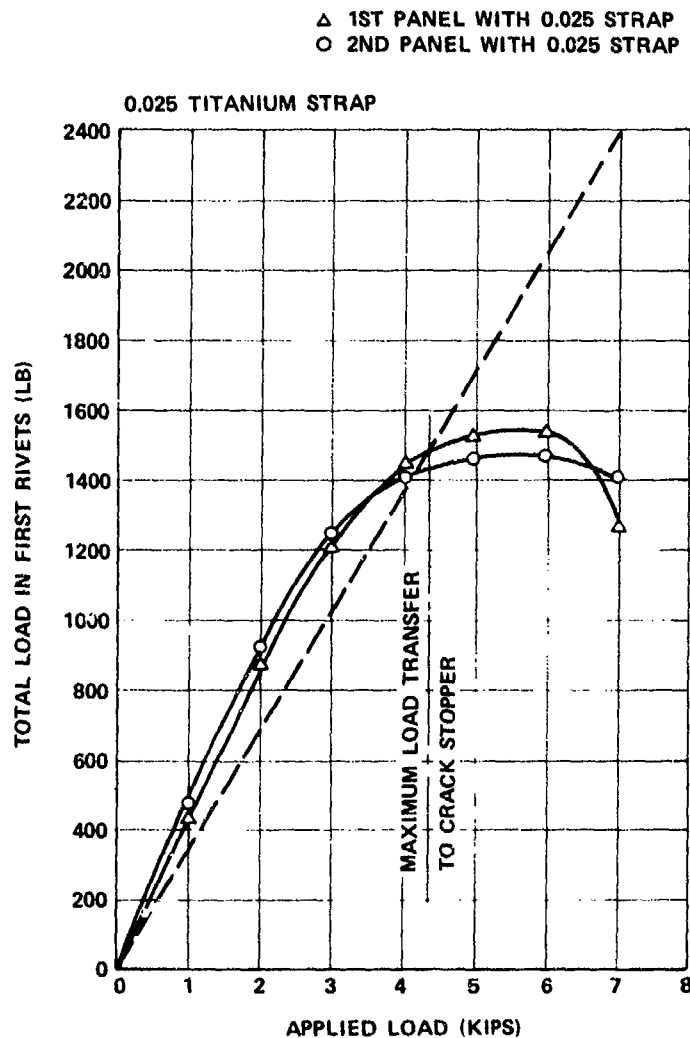


FIGURE 52d. RIVET SHEAR LOAD - ANALYSIS, TEST CORRELATION - 0.025 TITANIUM STRAP

#### CORRELATION

##### Skin Criteria

Space limitations prevent illustrations such as Figure 14 for every test. Figure 53 shows the results of test 2 on panel 3. The shape of the curve is determined by analysis of case 1 of Table 1 and the height by  $K_C^*$  at fast fracture. The curve is plotted from Eq (8). Correlation is shown with the analysis at crack arrest and final failure where the data points fall on the curve. For other tests where fast fracture, arrest and failure occurred, the correlation is shown in the tables of test results by comparing calculated crack arrest lengths and failure stresses with those obtained from test.

##### Frame Criteria

An example of frame stress correlation is shown in Figure 54 for panels 5 and 6. The outer cap stresses are extremely close to the analysis but the inner cap stresses are lower. This kind of correlation is typical of all the tests performed. The outer, more critical cap stresses were always extremely close to the analysis results.

##### Longeron Criteria

Longeron bending stresses were not predicted accurately on any of the tests on flat panels 7 to 14. Secondary effects due to center longeron bending influenced the test results. Figure 55 shows that at some distance from the crack, the longeron load  $P$  is acting at the centroid of the section. This load is reacted eventually by the skin ahead of the crack and is thus transferred a distance  $e$  which causes the longeron to bend inwards. The induced bending in the center longeron for a uniaxial loading case causes the outer longerons to be loaded as shown in Figure 55b. The resultant bending in the outer longerons tends to cancel out the bending caused by transfer of load from the cracked skin as indicated in Table 4. The load input to the longeron, however, is accurately predicted by the analysis for the flat panels as illustrated by Figure 56 for panels 8 and 12. If the panel section shown in Figure 55b were a section of a pressurized shell, then the inward bending of the center longeron would be relieved by the cabin pressure and the loading  $W$ , causing relief to the outer longeron bending, would not be present. This illustrated by Figure 57 which shows outer longeron stress correlation for the circumferential crack test on panel 10. It can be seen that the analysis predicts quite accurately the longeron stress for the pressurized panel. It can be seen that testing flat panels to determine fail-safe

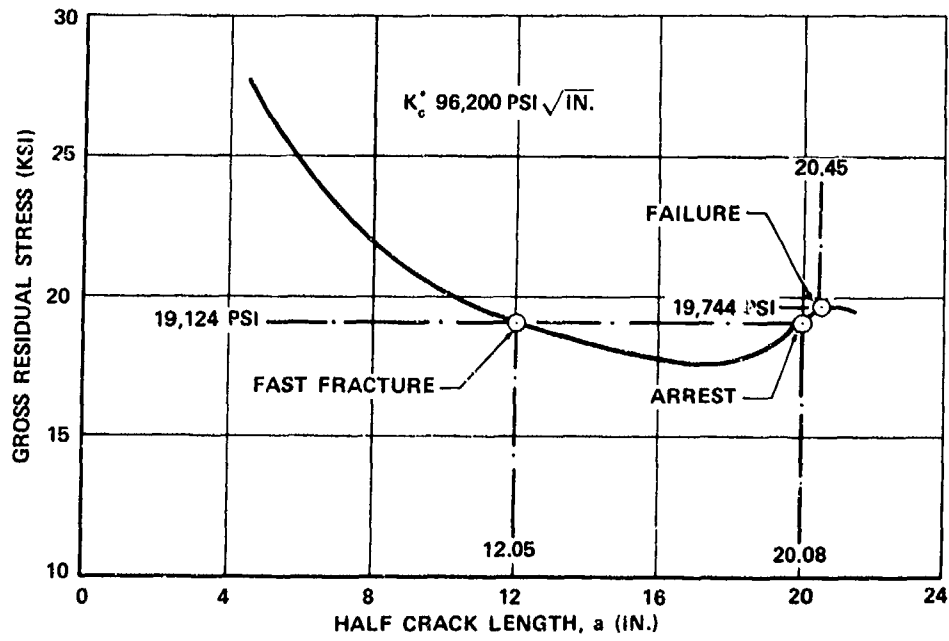


FIGURE 53. GROSS RESIDUAL STRENGTH CURVE, TEST 2, PANEL 3

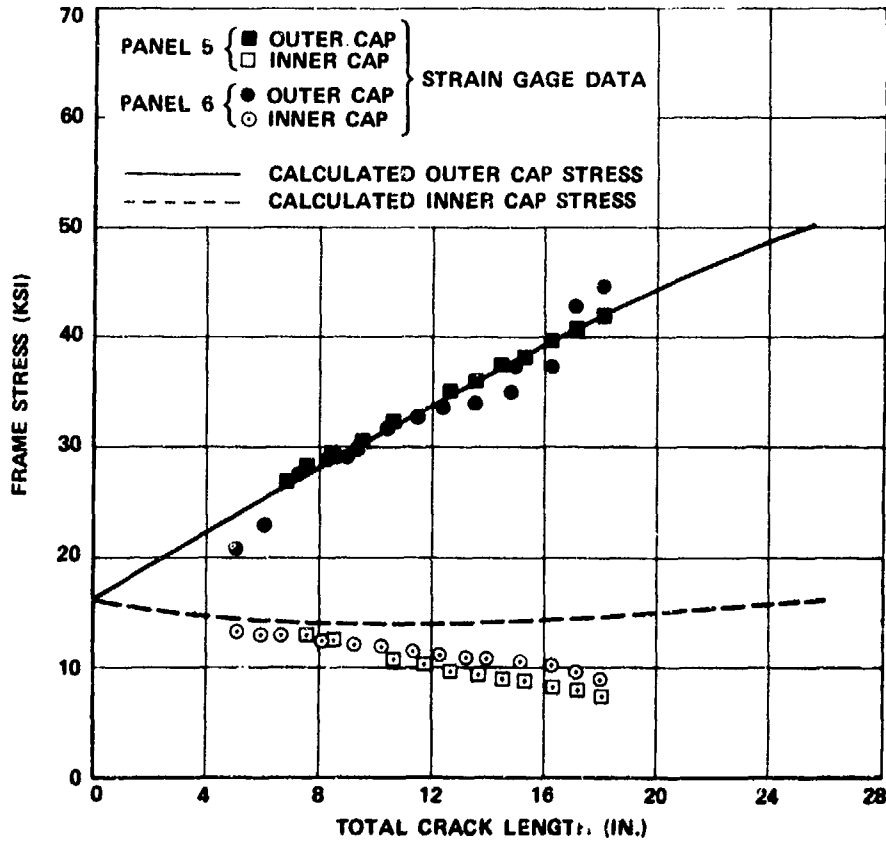
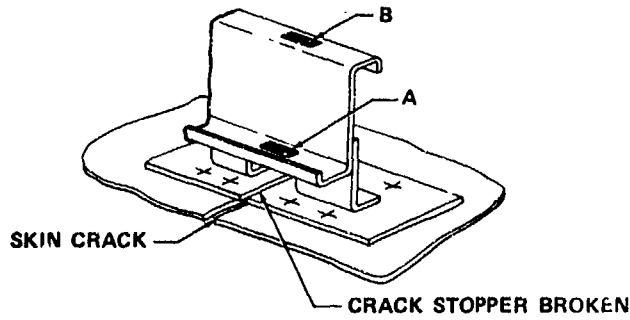


FIGURE 54. CENTER FRAME STRESS CORRELATION TWO-BAY CRACK TEST, PANELS 5 AND 6, TEST 2, GROSS STRESS 16,400 PSI

allowable stresses for curved panels under pressure for this condition should be treated with caution, particularly if the residual strength is determined by stiffener criteria. The relief due to longeron bending will produce allowable stresses higher than would be obtained from a curved panel test.

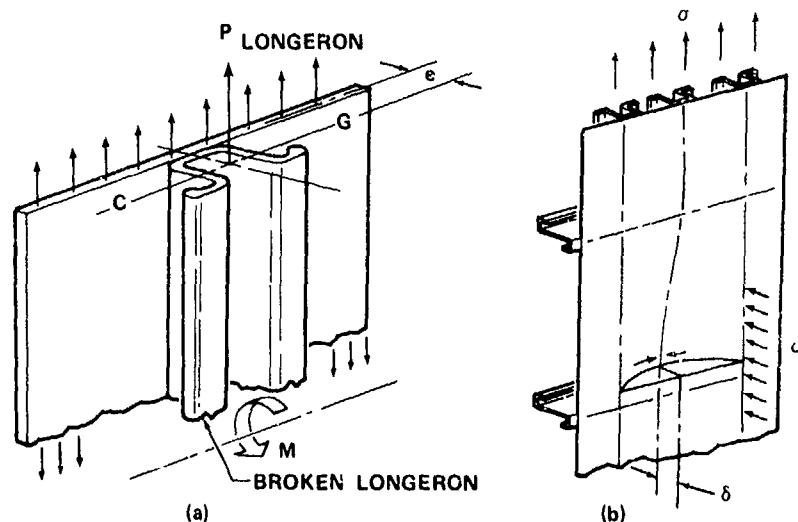


FIGURE 55. CENTER LONGERON BENDING

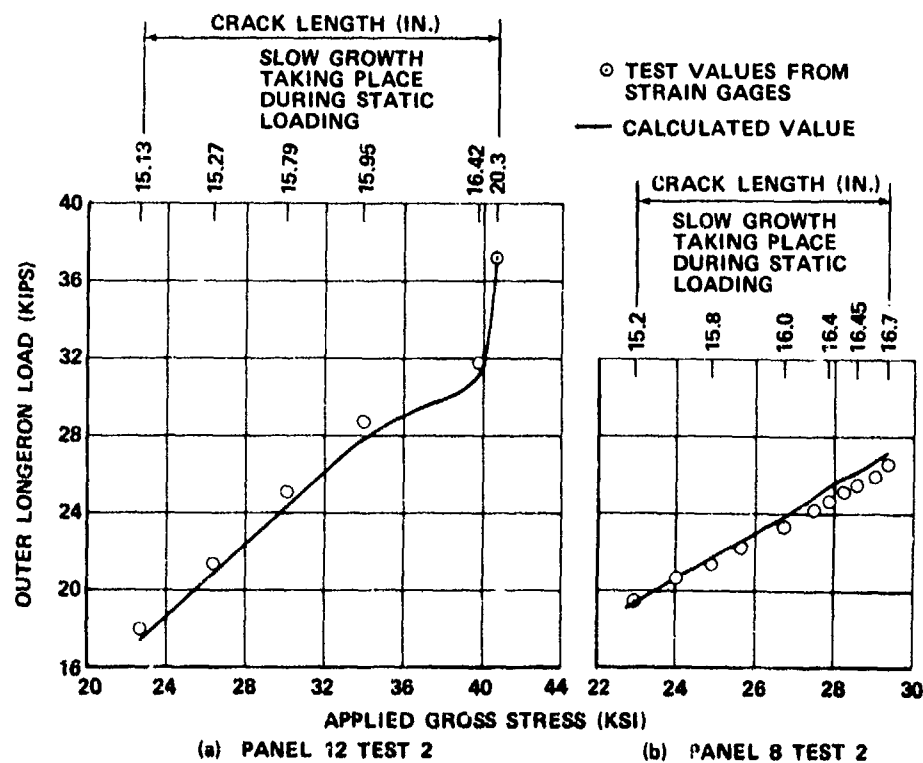


FIGURE 56. OUTER LONGERON LOAD. FLAT PANEL WITH CIRCUMFERENTIAL CRACK

#### FLAT PANEL VERSUS CURVED PANEL TESTING

Residual strength and crack propagation tests are often performed on flat, stiffened panels to simulate fatigue-damaged curved pressurized fuselage structure. This method of testing panels loaded uniaxially is far more inexpensive than testing large curved stiffened panels under biaxial loading conditions combined with pressure.

Much can be learned from the results of flat panel testing, but care must be exercised in the interpretation of results. For example, the bulging effect caused by pressure loading when a longitudinal crack is propagated in a pressurized shell cannot be exactly simulated by flat panel testing. The bulging causes an increase in crack tip stress intensity, particularly when the crack tips are in the region midway between stiffeners. Tests are often performed on flat panels and the results adjusted by bulging coefficients similar to the one proposed in Reference 23.

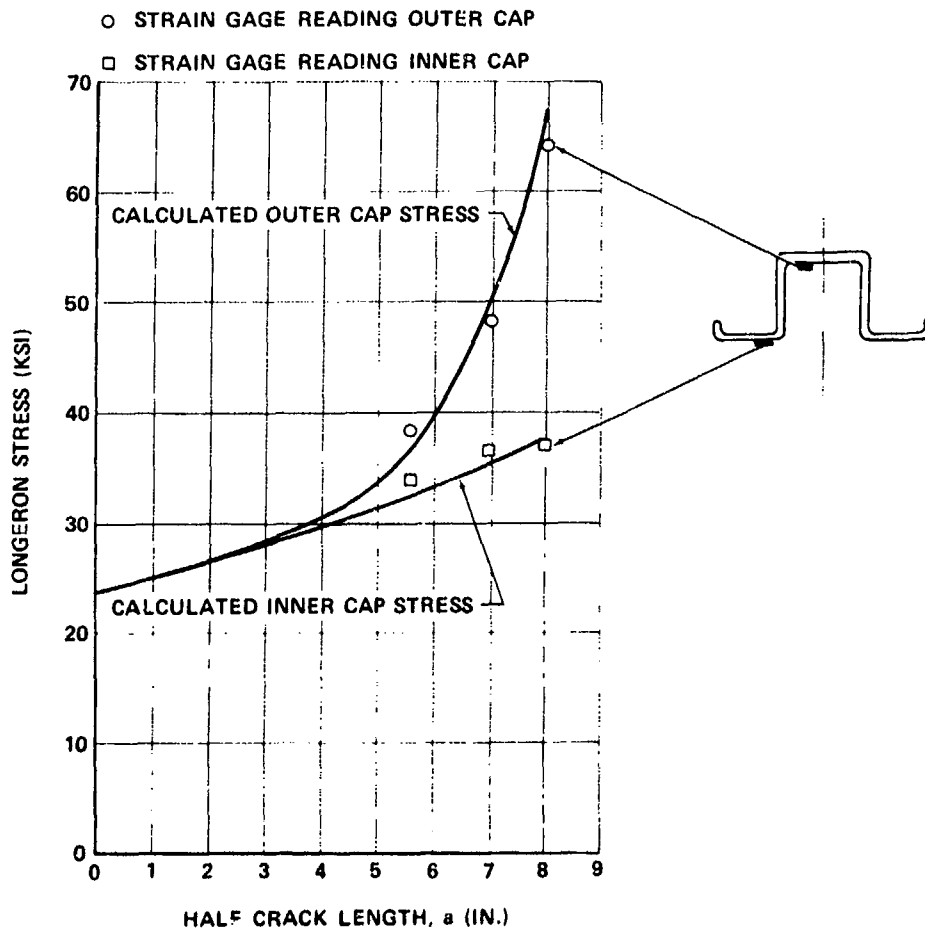


FIGURE 57. OUTER LONGERON STRESS CORRELATION CIRCUMFERENTIAL CRACK TEST, PANEL 16

$$(K_c)_{\text{CURVED}} = \frac{(K_c)_{\text{FLAT}}}{(1 + 10a/R)} \quad (17)$$

It has been shown by curved panel testing conducted at Douglas that when a two-bay longitudinal crack is propagated with the center frame intact, the stress intensity at the crack tip can be approximated to Eq (17), provided the total crack length is divided by two. The center stiffener remaining intact reduces the bulging to a degree equivalent to a one-bay crack. This bulging coefficient, however, is only valid when the crack tip is sufficiently remote from the stiffener. It has been found that with a full two-bay crack, when the crack tips are in the vicinity of the outboard stiffener, the bulging may be ignored and flat panel data used to determine residual strength. It should be noted, however, that this has only been substantiated on panels with titanium crack stoppers located at frame positions which help to reduce bulging in the vicinity of the frame.

Figure 58 shows a comparison between crack growth in a curved panel subjected to biaxial load combined with pressure, and that of a flat panel. The crack in the skin extends into two bays, and the center longeron is broken in each case. The panels are both made from 2024-T3 clad sheet 0.071 inch thick with identical frames and longeron stiffeners. The longeron has a net area of 0.3029 square inch with a configuration similar to Configuration 6 in Figure 11, Reference 11. Stress intensity factors can be determined from the data for Case 15 in Table 4. The gross average axial stress levels are the same in each case with the same stress ratio except that the curved panel is also subjected to a cyclic maximum pressure of 9.3 psi. The crack growth is faster in the curved panel due to the skin working at a higher stress than the longeron. In a pressurized shell, where the skin is biaxially loaded and the stiffeners are uniaxially loaded, the skin works at a higher stress than the longeron due to strain compatibility. For the panel in question the skin axial stress is given by

$$\sigma_{x_s} = 9.183 N_x + 1.1332 N_\phi \quad (18)$$

and the longeron stress by

$$\sigma_{x_L} = 8.902 N_x - 2.058 N_\phi \quad (19)$$

where



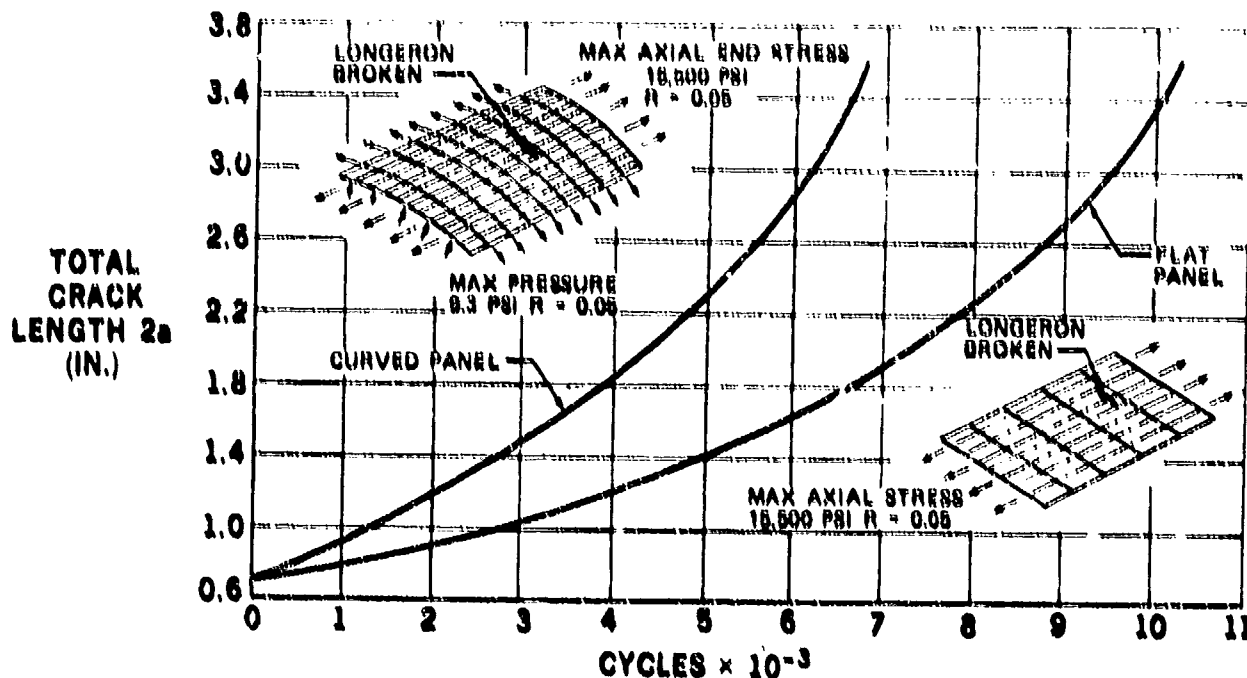


FIGURE 58. COMPARISON OF CRACK PROPAGATION CURVED VERSUS FLAT PANELS, SKIN MATERIAL 2024-T3

- $N_x$  = the axial load per inch  
 $N_y$  = the radial load per inch due to hoop tension =  $PR$   
 $P$  = pressure (psi)  
 $R$  = shell radius (in.)

In this case, the skin axial stress is 16,920 psi and the longeron stress is 12,930 psi, whereas the skin and longeron stress in the flat panels are both 15,900 psi.

#### CONCLUSIONS

Fracture mechanics analysis was successfully applied during the fail-safe structural development program for the DC-10. During this program, several factors were uncovered in which significant error could be experienced if not considered in analytical procedures.

The effects of attachment flexibility on the stress intensity factors in stiffened panels are significant and should be accounted for in crack propagation and residual strength analysis.

The threshold of slow stable crack growth and the amount of growth in 2024-T3 clad sheet is almost entirely a function of the past load history. Crack growth during high load cycles, where pre-load from the previous cycle has been relieved, is an order of magnitude greater than the type of growth experienced during constant amplitude loading and should be accounted for in spectrum crack growth analysis.

Care should be exercised when using the results of flat panel tests to predict allowable stresses for curved sheet structure.

The test results of the 24-inch-diameter cylinders, although qualitative due to their comparatively diminutive size, do at least indicate that shear stresses reduce the residual strength in the presence of fatigue cracks. Figure 49 indicates that principal stresses determined from condition B of Figure 48 are slightly conservative when compared to the allowables determined from condition A. It was decided to account for shear by comparing the results of panels symmetrically loaded to a principal stress determined from condition B of Figure 48 which neglects axial stress. The effects of axial tension increase the allowable stress as seen from the results of tests 2 and 4 of panel 15 listed in Table 10.

Many factors, other than the general ones mentioned above, influenced the final configuration selection and some of these are discussed below as they apply to the damage tolerance criteria for longitudinal and transverse cracks.

#### Longitudinal Cracks

The highest limit design principal stress in the minimum gage portion of the shell is approximately 19,000 psi from hoop stress and shear. It was desirable to show the structure to be fail-safe for limit values to satisfy foreign requirements. The gross residual strength from flat panels 2, 3 and 4 without crack stoppers and with 7075-T73 skin, range from 18,100 to 19,744 psi as listed in Table 8. The various shear clips on these panels shown in Table 5 and illustrated in Figure 3 do not

vary the strength significantly. The results of tests on curved panel 15 indicate a 30-percent loss in strength due to bulging from pressure. This is indicated by  $K_C^*$  values from flat panels listed in Table 8, compared to those for curved panel 15 for tests without axial load listed in Table 10. It can be seen that 7075-T73 skin on panels without crack stoppers would, at best, only produce an allowable gross stress of 13,800 psi. With 2024-T3 skin without crack stoppers, using  $R_{CT}$  for  $a = 21.5$  of 1.81 (from case 1 of Table 2) and  $K_C^*$  of 88,090  $\mu\text{si} \sqrt{\text{in.}}$  (from Table 10), the gross allowable stress is just a little over 19,000 psi. In view of this, it was decided to use both 2024-T3 skin 0.071 thick and crack stopper straps for the minimum gage portions of the shell. Test 2 on panel 5 listed in Table 8 had indicated a gross stress of 25,118 psi could be applied without failure of the crack stopper to skin rivets. It was decided, therefore, to use only two rows of rivets since the load transfer into the crack stopper would only be based on a gross stress from hoop tension in the region of 12,000 psi. Tests on 30-inch-wide panels listed in Table 12 had indicated that the required load could be transferred to the crack stopper with two rows of rivets. Reducing the crack stopper thickness from 0.025 inch was considered but tests on panels shown in Figure 25g, with results plotted on Figures 52a to 52c, indicated that the first rivets yield early on all thicknesses other than 0.025.

Figure 52d shows that adequate load can be transferred before rivet yield. The gross residual strength of this configuration is approximately 26,000 psi using  $R_{CT}$  from case 6 of Table 2. Titanium was chosen for crack stopper material because of its high strength-to-weight ratio and resistance to fatigue which ensures skin cracking before crack stopper cracking.

#### Circumferential Cracks

For the longitudinal crack case 2024-T3 material had been chosen. This choice was substantiated by tests on 2024-T3 panels 11 to 14 of Figures 32 through 40 compared to 7075-T73 panels 7 to 10 of Table 9.  $K_C^*$  values are shown to be almost double those of 7075-T73. Comparing allowables for the same longeron, for example, panel 8, using 7075-T73, failed at 29,600 psi (Table 9). Panel 12 with a similar longeron but with 2024-T3 skin failed at 40,855 psi. Hat-section longerons, in conjunction with 2024-T3, were therefore chosen for the circumferential crack condition. This configuration gives more than adequate fail-safe capability for the selected damage tolerance.

#### ACKNOWLEDGMENT

The author wishes to express his appreciation to R. E. Darling and R. G. Eastin who performed some of the computer analyses included in this paper.

#### REFERENCES

1. Stone, M., "Structural Reliability Through Detail Design and Development Testing," Air Force Conference on Fatigue and Fracture of Aircraft Structures and Materials, Miami Beach, Florida, 15-18 December 1969, AFFDL TR-70-144.
2. Wang, D. Y., "An Investigation of Fatigue Crack Propagation and Fail-Safe Design of Stiffened Large Aluminum Alloy Panels With Various Crack Stoppers," Proc. 10th ASME/AIAA Structures, Structural Dynamics and Materials Conference, New Orleans, La., April 1969.
3. "Crack Propagation Prediction and Crack Stopper Techniques for Stiffened and Unstiffened Flat Sheet in a Supersonic Environment," ASD-TDR-63-773.
4. Hunt, R. T., "Residual Strength and Crack Propagation in Stiffened Panels," Douglas Report LB 31837.
5. Eide, G. R., "Fail-Safe Design of Stiffened Panels," Douglas Report LB 32056.
6. Irwin, G. R., "Analysis of Stresses and Strains Near the End of a Crack Traversing a Plate," J. Appl. Mech., September 1957.
7. Allen, F. C., "Stress Analysis of Centrally Cracked Plates," presented to ASTM Committee E24, March 1969.
8. Denke, P. H., "A General Digital Computer Analysis of Statically Indeterminate Structures," Douglas Paper 834, September 1959.
9. Denke, P. H., "A Computerized Static and Dynamic Structural Analysis System; Part III. Engineering Aspects and Mathematical Formulation of the Problem," Douglas Paper 3123, presented to the SAE International Automotive Congress and Exposition, January 1965.
10. Picard, J. and Morris, R. C., "Format 11 - Second Version of Fortran Matrix Abstraction Technique," AFFDL-TR-66-207, Vol. 1, 1966.

- 11. Swift, T. and Wang, D. Y., "Damage Tolerant Design-Analysis Methods and Test Verification of Fuselage Structure," presented to Air Force Conference on Fatigue and Fracture of Aircraft Structures and Materials, Miami, Florida, December 15-18, 1969, AFFDL TR 70-144.
- 12. Westergaard, H. M., "Bearing Pressures and Cracks," J. Appl. Mech., June 1959.
- 13. Paris, P. and Erdogan, F., "A Critical Analysis of Crack Propagation Laws," Journal of Basic Engineering, Trans. of ASME, Series D, Vol. 85, December 1963.
- 14. Forman, R. G., Kearney, V. E. and Engle, R. M., "Numerical Analysis of Crack Propagation in Cyclic Loaded Structures," Journal of Basic Engineering, Trans. of ASME, Vol. 89, September 1967.
- 15. Engle, R. M., "Cracks - A Fortran IV Digital Computer Program for Crack Propagation Analysis," AFFDL-TR-70-107, October 1970.
- 16. Willenborg, J., Engle, R. M., Wood, H. A., "A Crack Growth Retardation Model Using an Effective Stress Concept," TM 71-1-FBR Air Force Flight Dynamic Laboratory.
- 17. Liu, A. F., "Statistical Variation in Fracture Toughness Data of Airframe Materials," presented to Air Force Conference on Fatigue and Fracture of Aircraft Structures and Materials, Miami, Florida, December 15-18, 1969.
- 18. Broek, D., "The Residual Strength of Aluminum Alloy Sheet Specimens Containing Fatigue Cracks or Saw Cuts," C.G.L. Class C 311; C 331, Report NLR-TR M. 3143 "National Lucht - En Ruimtevaartlaboratorium" National Aero Space Laboratory NLR Amsterdam.
- 19. Ramberg and Osgood, "Description of Stress Strain Curves of 3 Parameters," NACA TN 903.
- 20. Vlieger, H., "Residual Strength of Cracked Stiffened Panels," National Aerospace Laboratory NLR, The Netherlands, NLR TR 71004u.
- 21. Broek, D., "Concepts in Fail-Safe Design of Aircraft Structures," Battelle Memorial Institute, March 1971.
- 22. Flugge, W., "Stress Problems in Pressurized Cabins," NACA T. N. 2612.
- 23. Kuhn, P., "Notch Effects on Fatigue and Static Strength," Published in "Current Aeronautical Fatigue Problems," Pergamon Press.
- 24. Swift, T., "Development of the Fail-Safe Design Features of the DC-10," ASTM Symposium on Damage Tolerance in Aircraft Structures, Toronto, Ontario, Canada, 21-26 June 1970, ASTM STP-486.
- 25. Swift, T., "The Application of Fracture Mechanics to the Design of Damage-Tolerant Stiffened Aircraft Structure," Presented to ASM 1972 WESTEC Conference, Los Angeles Convention Center, Los Angeles, California, 13-17 March 1972.

APPENDIX

FORMAT II ANALYSIS

Unit Solution

A unit solution to the stress distributions in an uncracked idealized panel is obtained using the Force Matrix Method of structural analysis.<sup>8,9</sup> This method is based on the formulation of matrix equations of equilibrium and Maxwell-Mohr equations of continuity. A solution to the matrix equations is obtained using the Second Version of Fortran Matrix Abstraction Technique (FORMAT II)<sup>10</sup>. The basic matrix equations solved in the unit solution by FORMAT II are:

$$F = f_x X + f_o \tag{A1}$$

$$\Delta = f_o^T D f_o \tag{A2}$$

where

F = Matrix of element forces in the statically indeterminate structure resulting from unit values of external loads

Δ = Matrix of deflections in the statically indeterminate structure resulting from unit values of external loads

f<sub>x</sub> = Matrix of element forces resulting from unit values of the redundancies

f<sub>o</sub> = Matrix of statically determinate element forces resulting from unit values of external loads

$$X = -(f_x^T D f_x)^{-1} (f_x^T D f_o)$$

D = Matrix of element flexibilities

The superscript T represents transposition of the matrix.

The matrix of element forces in the statically indeterminate structure due to external loads is:

$$FKOI = F, KO \quad (A3)$$

The matrix of deflections in the statically indeterminate structure due to external loads is:

$$DEFKOI = \Delta, KO \quad (A4)$$

where KO is the matrix of external loads.

The matrices required from the unit solution to be used in the second stage or modification analysis are:

Eq (A1)

Eq (A2)

$f_N$

$$\delta_{NN}^{-1} = (f_N^T D f_N)^{-1}$$

$f_0$

D

The matrix of element forces - Eq (A1) takes the form:

$$F = \begin{matrix} & \left[ \begin{array}{c} \text{Reactions} \\ \text{Bar Forces} \\ \text{Panel Forces} \end{array} \right]^n \\ m & \end{matrix}$$

where m is the number of element forces and n is the number of external load vectors. Typical values of m and n are:

m = 1087  
n = 43      1-Bay Longitudinal Crack

m = 1233  
n = 47      2-Bay Longitudinal Crack

m = 1043  
n = 39      For idealization of Figure 9

Extractor matrices are also required in the modification analysis to extract the reactions, bar forces, panel shear forces and panel shear flows from the matrix F. These matrices are defined in the unit analysis and saved for use in the modification analysis. They are defined as follows:

GR = Reaction extractor matrix

GB = Transposed bar force extractor matrix

GP = Panel shear force extractor matrix

GPF = Panel shear flow extractor matrix

#### Element Modification

The effects of crack propagation in the sheet are determined by disconnecting the reactions in the skin at the horizontal centerline as illustrated in Figure 9. This function is performed by an element modification procedure which requires the solution to the following matrix equations:

$$FM = FKOI + FE, C, EO \quad (A5)$$

$$DM = DEFKOI + DE, C, EO \quad (A6)$$

where

FM = Matrix of element forces in modified structure

DM = Matrix of element deflections in modified structure

- FKO1 = Matrix of element forces in unmodified structure  
 DEFKO1 = Matrix of element deflections in unmodified structure  
 FE = Matrix of element forces in unmodified structure due to unit deformations of elements to be modified  
 DE = Element deflections in unmodified structure due to unit deformations of elements to be modified  
 C = Column extractor matrix  
 $FE = -f_x \delta_{xx}^{-1} f_x^T EM$   
 $\delta_{xx}^{-1} = (f_x^T D f_x)^{-1}$  called DXXINV  
 EM = Matrix defining unit deformations of elements to be modified

$f_x$  is redefined FX

$f_o$  is redefined FO

$$FE = -FX, DXXINV, FX^T, EM \quad (A7)$$

$$DE = FO^T (D, FE + EM) \quad (A8)$$

$$EO = \left[ (\Delta D_{mm})^{-1} = R, FE, C \right]^{-1} R, FKO1 \quad (A9)$$

$$= A^{-1}, R, FKO1$$

R is a row extractor matrix

$$(\Delta D_{mm})^{-1} = \left[ D(D_{mli}/D_{li} - 1) \right]^{-1}$$

$D_{mli}$  = Original value of area, thickness or I value of element to be modified

$D_{li}$  = Modified value of area, thickness or I value of element to be modified

D = Value of original element flexibility obtained from D matrix of original run

For multiple modification, the basic equations are expanded as shown. Three modifications are demonstrated.

$$A = \left[ (\Delta D_{mm})^{-1} - (Rmm_1, FE, Cmm_1 + Rmm_2, FE, Cmm_2 + Rmm_3, FE, Cmm_3) \right]$$

$$EOM = A^{-1} (Rmm_1 + Rmm_2 + Rmm_3) FKO1$$

$$FMM = \left[ FKO1 : FKO1 : FKO1 \right] + FE \left[ Cmm_1 EOM : Cmm_2 EOM : Cmm_3 EOM \right]$$

$$DMM = \left[ DEFKO1 : DEFKO1 : DEFKO1 \right] + DE \left[ Cmm_1 EOM : Cmm_2 EOM : Cmm_3 EOM \right]$$

These equations, written generally for r modifications, are:

$$A = (\Delta D_{mm})^{-1} - \sum (Rmm_r, FE, Cmm_r) \quad (A10)$$

$$EOM = A^{-1} \sum (Rmm_r) FKO1 \quad (A11)$$

$$FMM = \left[ FKO1 : FKO1 : \dots \right]_r + FE \left[ Cmm_1 EOM : Cmm_2 EOM : \dots \right]_r \quad (A12)$$

$$DMM = \left[ DEFKO1 : DEFKO1 : \dots \right]_r + DE \left[ Cmm_1 EOM : Cmm_2 EOM : \dots \right]_r \quad (A13)$$

For a problem which includes only disconnecting reactions,  $\Delta D_{mm}$  is infinitely large  $[(\Delta D_{mm})^{-1} = 0]$  and is therefore neglected. However, the capability exists to change bar areas and panel thicknesses by retaining  $\Delta D_{mm}$ .

The number of modifications in any one computer run is generally 12. This means that successive disconnections of 12 reactions take place in one computer run. The solution to the modification matrix equations is obtained using the FORMAT II abstraction instructions.<sup>10</sup>

To familiarize the reader with the solution to the equations, an example is given for four modifications using FORMAT abstraction statements for disconnect only -  $(\Delta D_{mm})^{-1} = 0$ .

	FKO1	= F. MULT. KO	
	DEFKO1	= DELTA. MULT. KO	
Eq (A7)	FXTEM	= FX. TMULT. EM	
	XEM	= -DXXINV. MULT. FXTEM	
	FE	= FX. MULT. XEM	
Eq (A8)	DFE	= D. MULT. FE	
	DFEM	= DFE. ADD. EM	
	DE	= FO. TMULT. DFEM	
Eq (A10)	RFWUN	= RMMWUN. MULT. FE	
	AWUN	= RFWUN. MULT. CMMWUN	
	RFTWO	= RMMTWO. MULT. FE	
	ATWO	= RFTWO. MULT. CMMTWO	
	SUMWUN	= -AWUN. ADD. -ATWO	
	RFTRE	= RMMTRE. MULT. FE	
	ATRE	= RFTRE. MULT. CMMTRE	
	SUMTWO	= -ATRE. ADD. SUMWUN	
	RFFOR	= RMMFOR. MULT. FE	
	AFOR	= RFFOR. MULT. CMMFOR	
	A	= AFOR. ADD. SUMTWO	
		Let $\Sigma$ (RMM <sub>r</sub> )	= RMT
	Eq (A11)	SWUN	= RMMWUN. ADD. RMMTWO
STWO		= SWUN. ADD. RMMTRE	
RMT		= STWO. ADD. RMMFOR	
RMTFKO		= RMT. MULT. FKO1	
EOM		= A. SEQEL. RMTFKO	
	Let EMM	= Cmm <sub>1</sub> EOM : Cmm <sub>2</sub> EOM, etc.	
Eq (A12)	EKWUN	= CMMWUN. MULT. EOM	
	EKTWO	= CMMTWO. MULT. EOM	
	ADWUN	= EKWUN. ADJOIN. EKTWO	
	EKTRE	= CMMTRE. MULT. EOM	
	ADTWO	= ADWUN. ADJOIN. EKTRE	
	EKFOR	= CMMFOR. MULT. EOM	
	EMM	= ADTWO. ADJOIN. EKFOR	
	Let FOM	= [FKO1 : FKO1 -]	
	B	= FKO1. RENAME.	
	BWUN	= FKO1. ADJOIN. B	
	BTWO	= BWUN. ADJOIN. B	
	FOM	= BTWO. ADJOIN. B	
	FEEMM	= FE. MULT. EMM	
	FMM	= FOM. ADD. FEEMM	

Let DOM = DEFKO1 : DEFKO1 -  
 C = DEFKO1.RENAME  
 CWUN = DEFKO1.ADJJOIN.C  
 CTWO = CWUN.ADJJOIN.C  
 DOM = CTWO.ADJJOIN.C  
 DEEMM = DE.MULT.EMM  
 DMM = DOM.ADD.DEEMM

FMM is the matrix of element forces in the modified structure:

$$FMM = \begin{bmatrix} \text{Reactions} \\ \text{Bar Forces} \\ \text{Panel Forces} \end{bmatrix}^n_m$$

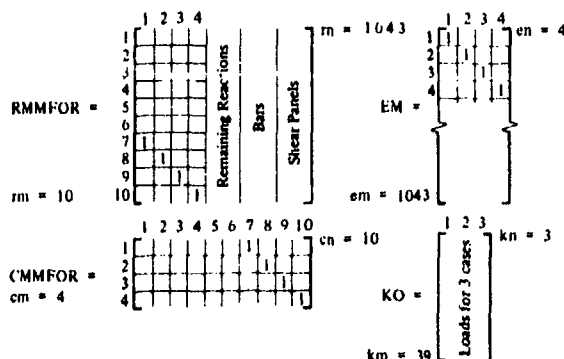
Reactions, bar forces, panel forces and shear flows can be extracted from this matrix using extractor matrices GR, GBT, GP, GPF saved from the unit analysis.

Joint external reactions: FREACT = GR.MULT.FMM  
 Bar forces: FBAR = GBT.MULT.FMM  
 Panel shear forces: FPANEL = GP.MULT.FMM  
 Panel shear flows: FFLOW = GPF.MULT.FMM

The four basic input matrices to the modification program are RMMr, CMMr, EM and KO. RMMr and CMMr are row and column extractor matrices for the multiple modification procedure. EM is a matrix of unit deflections for the elements to be modified. KO is a matrix of external loads.

A simple example will serve to illustrate the form of these matrices. Consider the idealization of Figure 9. Suppose it is required to disconnect, one at a time, the first four reactions from the vertical centerline in the skin, to simulate a propagating crack for three different loading conditions. There will be four RMM and CMM matrices, one EM matrix and one KO matrix. The fourth RMM and CMM matrices only are shown for illustration. The row and column sizes for these matrices m and n are:

- rm = Number of rows in the RMM matrix: total number of modifications to be made (10 in the example)
- rn = Number of columns in the RMM matrix: total number of element forces (1043 for the idealization of Figure 9)
- cm = Number of rows in the CMM matrix: number of elements to be modified (4 in the example, i.e., 4 reactions)
- cn = Number of columns in the CMM matrix: total number of element modifications to be made (10 in the example)
- em = Number of rows in the EM matrix: total number of element forces (1043 in the example)
- en = Number of columns in the EM matrix: number of elements to be modified (4 in the example)
- km = Number of rows in the KO matrix: number of load vectors (39 for the idealization of Figure 9)
- kn = Number of columns in the KO matrix: number of load cases considered (3 in the example)



## V.C.3 HEAVY SECTIONS

W. T. Kirkby

V.C.3.1 Introduction . . . . .	288
C.3.2 Residual Strength of Welded Fitting . . . . .	288
C.3.3 Residual Strength of Main Spar Booms Containing Cracks . . . . .	291
References . . . . .	293

## V.C.3.1 Introduction

This chapter is concerned with the prediction of the residual strength of relatively thick structures for which the analysis may be undertaken on the assumption of plane strain conditions. In essence the problem is to obtain the best estimate of stress intensity, for a given nominal stress state in the member concerned, and to relate this to the appropriate fracture toughness value (e.g.  $K_{Ic}$ ) for the material concerned. The problems of estimating stress intensity in thick sections differ from those encountered in dealing with thin sheet materials in so far as the 'through the thickness' dimensions and geometry of the crack have to be considered in addition to the length of the surface crack. The general problems in such plane strain conditions are discussed in relation to heavy members with surface flaws, corner cracks at holes, and other natural cracks, in section V.A above, principally in relation to the prediction of crack growth - in this latter case the predicted stress intensity is related to crack growth data for the material concerned, rather than to fracture toughness data.

It is not intended therefore to repeat the general discussion of the prediction of stress intensity given in V.A.2 - suffice to say that the best choice of available mathematical solution must first be made in relation to the practical case being considered - almost invariably the best solution available falls short of representing the complexity of the real situation and a considerable element of experience and judgement is involved. Guidance on available solutions may be obtained from V.A.2 above and from the comprehensive list given in Appx to V.C.1 - it will be noted that some twenty solutions are listed for crack geometries involving through-the-thickness parameters. In treating complex geometrical situations, one or more of the solutions listed may be compounded (or superimposed)<sup>1</sup> to give a better match to the real situation.

In the paragraphs which follow two practical examples are given to illustrate applications of fracture mechanics in relatively thick sections - the first relates to a design problem discussed by Wilhem<sup>2</sup> and the second gives a comparison between predicted and observed residual strength values, taken from work by Faulkner.

## V.C.3.2 Residual strength of welded fitting (Fig.1)

In cases where there may be a crack traversing from the edge of a hole or at an angle to the loading direction, it becomes necessary to introduce an equivalent or effective crack length rather than the absolute measure of the crack length. In most cases, the equivalent crack length is the same as the absolute crack length plus the discontinuity, for the crack and hole situation. However, for particular applications, estimates should be made of effective length magnitude, and compared with the absolute crack length. The requirements for calculating equivalent crack length will be indicated in the following section.

## The crack at a hole

A design for a proposed feed-through arm is shown in Fig.1. In its center is a hole with a tubular insert welded at the top and bottom surface. Fatigue is a consideration, particularly if a brittle weld condition occurs. Inspection dictates that a  $\frac{1}{8}$ -inch crack can be detected at regular inspection periods (we will assume a through-the-thickness crack). The arm material is  $\frac{1}{2}$ -inch thick 2219-T851 aluminium with a yield of 51.2 ksi, a plane strain\* fracture toughness of 32.6 ksi $\sqrt{\text{inch}}$ , and an operating stress environment of 35 ksi prevails.

Question: Can this design be considered safe in the presence of an inspectable crack, at a 25% overload condition due to pressure pulses at P? What design modifications would be recommended?

STEP 1. Assuming the worst fatigue crack condition, i.e. the tube has split along the crack axis, it can be seen that this situation then becomes the Bowie crack solution (see equation given on Fig.2).

In this case, to solve the stress intensity equation, an equivalent crack length should be introduced. In other words, an equivalent 'Griffith' crack length must be found for the geometry in question.

As the importance of the effective or equivalent crack length has many implications in fracture analysis, we will present this typical example which will have direct bearing on our problem.

The stress intensity for a crack or cracks at a hole in an infinite plate in uniform tension is from Fig.2.

$$K_I = \sigma \sqrt{\pi a} f\left(\frac{a}{r}\right)$$

and the stress intensity for a central crack in an infinite plate in uniform tension is (from Equation VII-1, Ref.1)

$$K = \sigma \sqrt{\pi a_e}$$

where  $a_e$  is the equivalent crack. By equating these two solutions, the equivalent crack length is determined by

\* The plane strain ( $K_{Ic}$ ) fracture toughness value is applicable in this case with  $\frac{1}{2}$ -inch thick plate material. It would be a safe assumption that plane strain fracture behaviour predominates.



$$a_e = a \left[ f \left( \frac{a}{r} \right) \right]^2$$

and the values  $f \left( \frac{a}{r} \right)$  are shown in Fig.2.

At this point, a comparison can be made of the effective crack length and the actual crack length of the Bowie geometry. For a 1.0-inch diameter hole, the equivalent crack lengths are shown in Fig.3. For the half-crack length of interest (0.25 inch, see Fig.1), it can be seen that the effective crack length is the hole radius plus actual crack length. Beyond a crack length of 0.12 inch, there is a little difference between the equivalent crack lengths computed by the Bowie solution or the crack length plus radius approximation.

STEP 2. The equivalent crack length for the feed-through arm has been found to be

$$a_e \cong a + r = 0.25 \text{ inch} + 0.50 \text{ inch}$$

or

$$a_e \cong 0.75 \text{ inch}$$

STEP 3. Compute the finite geometry correction factor for the problem using the equivalent crack length. The crack aspect ratio is (from Fig.1)

$$\frac{2a}{W} = \frac{1.5 \text{ inches}}{6 \text{ inches}} = 0.25$$

From Fig.1,  $\lambda = 1.04$  for a crack aspect ratio of 0.25.

STEP 4. Solve the basic stress intensity equation for critical conditions; i.e.  $a_e \rightarrow a_{ec}$ ,  $\sigma \rightarrow \sigma_c$ , and  $K \rightarrow K_{Ic}$  in plane strain. Therefore,

$$\sigma_c = \frac{K_{Ic}}{\sqrt{\pi a_{ec}} \lambda} = \frac{32.6 \text{ ksi}\sqrt{\text{inch}}}{\sqrt{\pi(0.75 \text{ inch})} (1.04)}$$

$$\sigma_c = 20.5 \text{ ksi}$$

Clearly this design will not tolerate an inspectable crack at the anticipated operating conditions.

What would be the least tolerable crack for this design? The answer to this question can be obtained through fracture mechanics by assuming bounds on the crack length parameter. For example, manipulation of the basic stress intensity equation, again assuming critical conditions at the operating stress, 35 ksi,

$$a_e = \frac{1}{\pi} \left[ \frac{K_{Ic}}{\sigma_c \lambda} \right]^2$$

gives the solution for equivalent critical crack length. However, the finite width correction,  $\lambda$ , is also a function of crack length. For this crack geometry, an estimate can be made as  $\frac{2a}{W} \rightarrow 0$ ,  $\lambda \rightarrow 1.00$ , so the smallest equivalent critical crack length will be 0.276 inch. Referring to Fig.2, an equivalent crack length of 0.276 inch would be a crack less than 0.05-inch long from the edge of the 1-inch diameter hole. This perhaps would correspond to a slight nick caused by a tool at the hole edge; therefore, a re-evaluation of the design is inevitable.

It may be possible to introduce four reasonable design modifications which, as alternatives, could assure a fracture safe part. They are:

- (1) Reduce allowable operating stress,
- (2) Reduce hole diameter,
- (3) Use a different material (higher  $K_{Ic}$ ),
- (4) Reduce plate thickness and *still meet stress criteria*.

In many cases it is difficult to change the configuration to satisfy new operating parameters. Items 1 or 2 could satisfy the design requirements,  $\sigma_c \geq 35 \text{ ksi}$ , for the inspectable crack. But, we have already seen that the smallest tolerable crack for this geometry is very small ( $< 0.05 \text{ inch}$ ), which is an undue restriction; and the operating stress level may be invariant.

This brings us to the third or fourth alternatives. Changing to a tougher material (higher  $K_{Ic}$ ) will solve the problem. However, by increasing the material plane strain fracture toughness, one may gain some of the necessary fracture resistance, but not enough for the given operating stress and inspectable crack. This leaves the remaining fourth alternative as a consideration.

It will be remembered that by reducing the plate thickness, one takes advantage of the material's ability to fracture by net section yielding. In other words, a brittle fracture behaviour had been assumed and by reducing the thickness a mixed mode or possibly plane stress fracture would result. This would tend to result in higher values of fracture toughness. Plane stress ( $K_c$ ) fracture toughness values of  $\approx 113 \text{ ksi}\sqrt{\text{inch}}$  have been reported for this 2219 material in 0.10-inch thick sheet. This value reflects the influence of plastic zone size. In this problem we could safely assume that for a reduction in plate thickness to  $\frac{1}{2}$  inch, we would gain  $\approx 50\%$  of the plane stress fracture toughness, or  $56.5 \text{ ksi}\sqrt{\text{inch}}$ . (This would be a conservative estimate and would imply that full plastic zone development or total plane stress behaviour would not be realized.)

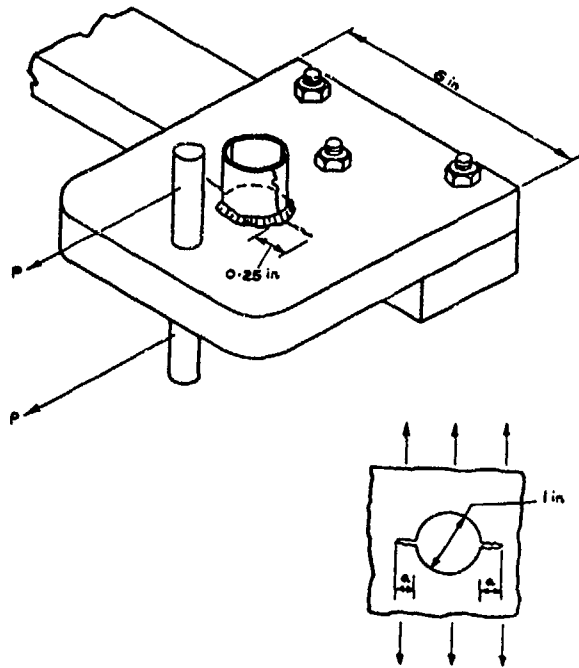


Fig. 1 Feed through arm with welded support base

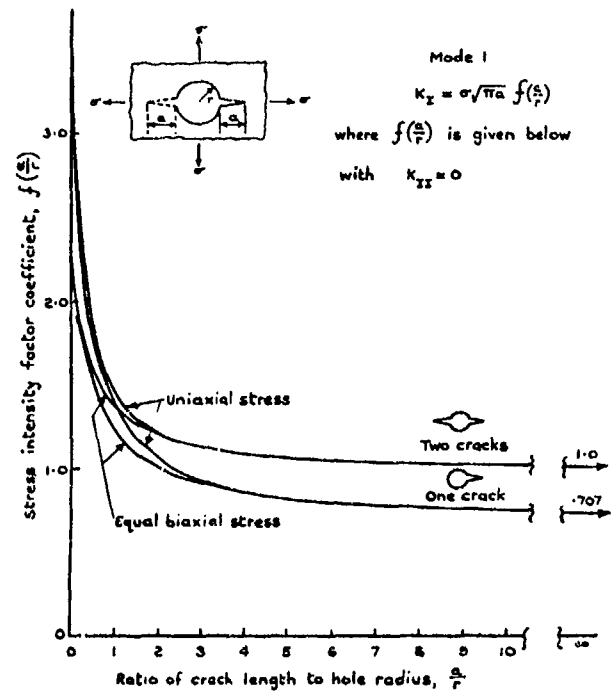


Fig. 2

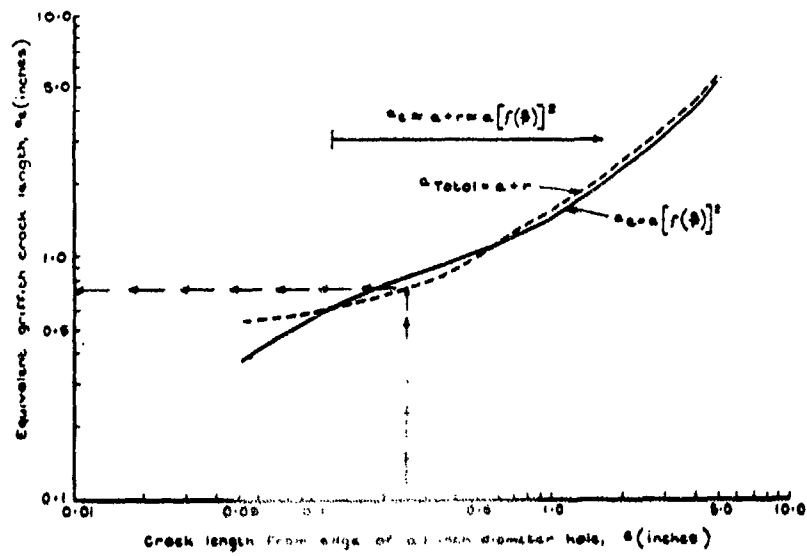


Fig. 3 Equivalent crack length for cracks at a 1 inch diameter hole

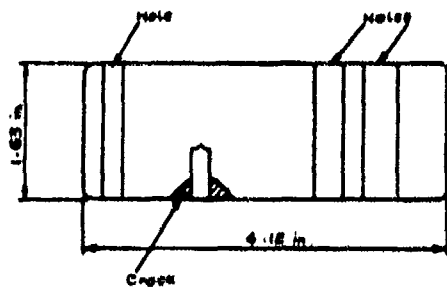
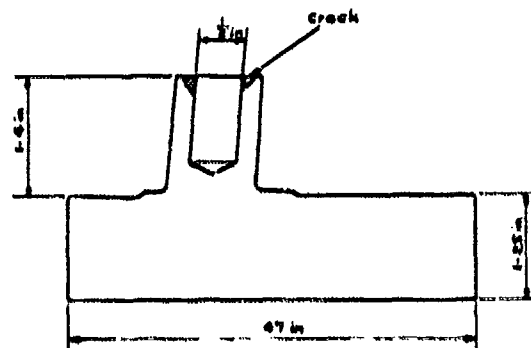


Fig. 4 Type 1 Tooling hole test specimen

Fig. 5 Type 2 Top flange specimen  
(section through boom)

Design with reduced thickness

STEP 5. Compute the new critical fracture stress based on a mixed mode type of failure with a reduced plane stress fracture toughness,  $\bar{K}_c \cong 57 \text{ ksi}/\sqrt{\text{inch}}$ .

$$\sigma_c = \frac{\bar{K}_c}{\sqrt{\pi a_{ec}} \lambda} = \frac{57 \text{ ksi}/\sqrt{\text{inch}}}{\sqrt{\pi(0.75 \text{ inch})} (1.04)}$$

$$\sigma_c = 36 \text{ ksi}$$

Therefore, this re-design (assuming a 35 ksi operating stress) would be considered fracture safe for the  $\frac{1}{4}$ -inch crack condition, but not for the 25% overload condition. However, compensation must be made for the reduction in area caused by the reduction in thickness.

The designer and stress analyst must now decide on the basis of stress analysis of this re-design if a reduction in plate thickness will meet static strength requirements, and other stress criteria, for example. This is where the interplay between material/stress and fracture parameters enters the picture, and trade-offs are selected.

#### V.C.3.3 Residual strength of main spar booms containing cracks

The information presented in this section was obtained from residual strength calculations and associated laboratory tests on main spar booms of extruded section in aluminium alloy. The cross-sections of the spars considered and the crack geometries are shown in Figs.4-8. The five configurations are designated Types 1-5.

##### Details of theoretical calculations

The following assumptions and generalisations have been made in the calculations:-

(1) In all cases the cracks have been considered to be corner cracks and a solution for this type of crack taken from a Boeing document<sup>3</sup> has been used. This solution is as follows:-

$$K = 0.795\sigma \sqrt{\pi a}$$

where  $a$  is the crack length measured along the surface and  $\sigma$  is the stress.

The assumption that the cracks could be considered as corner cracks has been taken to apply both to true corner cracks and also in the case of cracks growing from both sides of a hole. However, in the detail tests on Type 5 a number of the specimens had cracks grown from one side of a relatively small hole only and thus the restraint imposed on the crack in these cases would obviously affect the stress intensity at the crack tip. Consideration of solutions available for similar geometries for sheet conditions suggest that a correction factor in the order of 1.75 needed to be applied and thus the solution used for this case is:-

$$K = \frac{0.795\sigma}{1.75} \sqrt{\pi a} = 0.454\sigma \sqrt{\pi a}$$

(2) The  $K_{Ic}$  values used in the calculations were those determined using specimens cut from the detail residual strength specimens.

For the specimens Types 1, 2 and 3, the values of  $K_{Ic}$  for a total of 16 specimens cut from two residual strength specimens, ranged between 24.6 to 31.8 ksi/ $\sqrt{\text{inch}}$  and the majority of the Type 4 and 5 results fell between 24 and 35 ksi/ $\sqrt{\text{inch}}$  for a total of 36 specimens cut from 9 booms.

##### Presentation of results

In Fig. 9, two scatter bands have been drawn. These represent the range of the *calculated* crack lengths against stress level for the two crack geometries considered. The width of the scatter band being determined by the scatter in  $K_{Ic}$ .

The measured crack lengths and stress levels for all the relevant specimens available have been plotted on this graph. (No results are plotted on this figure for Type 3 specimens - see below.)

In Table 1, the results are also presented in tabular form. Included in this table are a number of cracks present in the Type 3 residual strength specimen which did not prove to be critical, and thus the actual failing load can only be said to be in excess of that attained during the test.

Due to the amount of bending present in the specimens, the stress level plotted is not the average stress over the whole of the boom area but the more local stresses measured during the various tests. Also, in the case of the Type 4 specimens with cracks in the lower flange, the crack length considered is that measured in the body of the boom as some difficulty was experienced in deciding which crack dimension to take as the critical length. It should be noted however that in these cases, the whole of the bottom flange was also cracked.

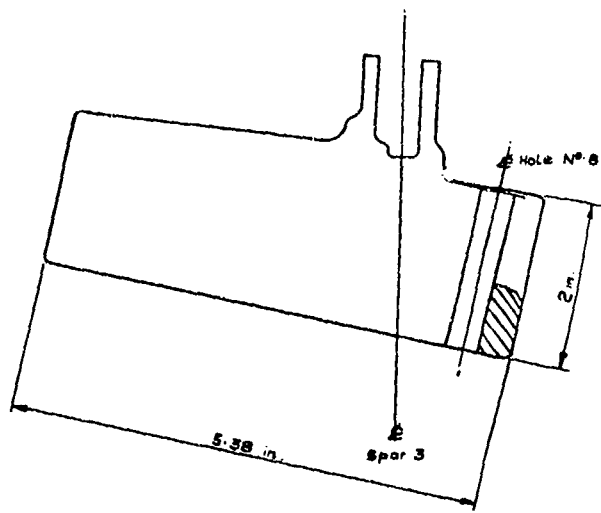


Fig. 6 Type 3 Hole N° 8 specimen

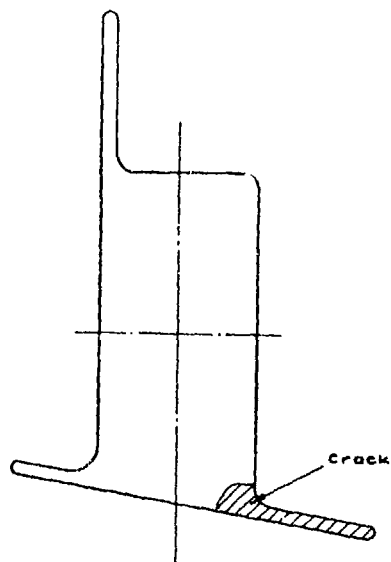


Fig. 7 Type 4 Flange test specimen  
(section through boom)

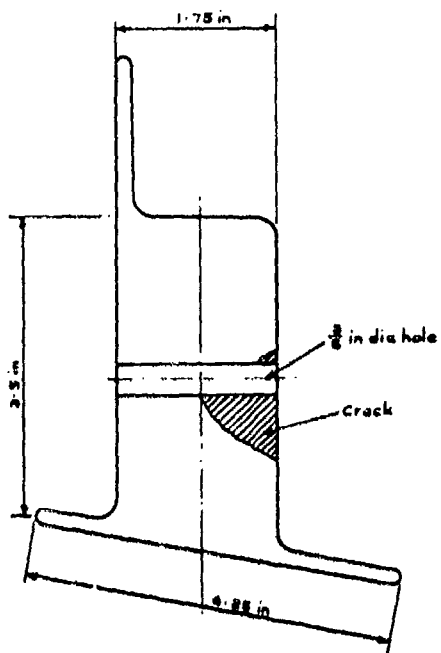


Fig. 8 Type 5 Body test specimen  
(section through boom)

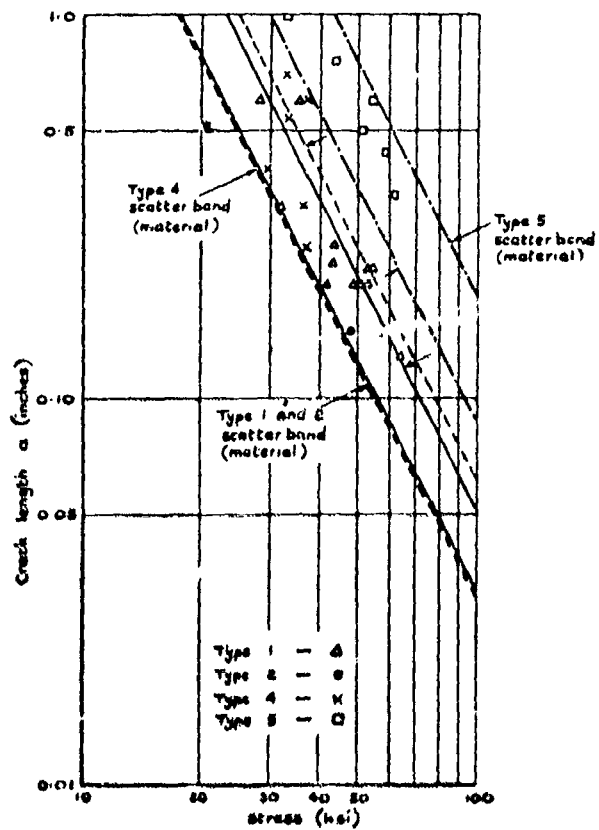


Fig. 9 Comparison of predicted and achieved residual strength

Table 1  
COMPARISON OF ACTUAL AND THRORETHECAL FAILING LOADS

Type of specimen	Length of crack	Strength %	FFDL*		
		Actual	Calculated		
			Min.	Max.	
1	0.6	50 to 62	40	52	
	0.13	In excess of 66	85	110	
	0.13		86	114	
	0.15		99.5	79	105
	0.2		73.8	69	89
	0.2		87.4		
	0.2		89.6		
	0.2		93.4		
	0.22		94		
	0.22		94.8	66	86
	0.23		75.6	64	84
	0.26		84	61	79
0.32	53.8	55	71		
2	0.14	66	62	80	
3	0.75 total	In excess of 62	58	74	
	0.3 total	In excess of 66	90	115	
4	0.15	121.6	101	148	
	0.25	87.8	78	114	
	0.32	88.2	69	102	
	0.4	70.4	62	90	
	0.54	81.9	53	78	
	0.6	86.5	51	74	
	0.7	79.6	47	69	
5	0.34	160	140	205	
	0.44	154	122	180	
	0.5	137.8	115	170	
	0.6	142	105	155	
	0.75	112.5	94	138	
	1.0	86	82	120	

\* Fully factored design load.

REFERENCES

- 1 D.J. Cartwright and D.P. Rooke. Stress intensity factors - a review. Presented at the Annual Conference of the Stress Analysis Group of the Institute of Physics University of Leicester, UK. September 1971.
- 2 D.P. Wilhem. Fracture mechanics idelines for aircraft structural applications. Technical Report AFFDL TR-69-111. February 1970.
- 3 F.W. Smith. Stress intensity factors for a semi-elliptical surface flaw. Boeing Company, Structural Development Research Memorandum No.17 August 1966.

## V.C.4. AEROSPACE PRESSURE VESSELS

C. F. Tiffany

Summary . . . . .	294
Introduction . . . . .	294
Important Considerations in Preventing Failures . . . . .	295
Evaluating Cyclic and Sustained Flaw Growth . . . . .	295
Validating the Stress Intensity Approach . . . . .	296
Combined Cyclic and Sustained Stress Flaw Growth . . . . .	297
Proof Tests on Actual Pressure Vessels . . . . .	299
Conclusions . . . . .	300
References . . . . .	311

## SUMMARY

During the development of the many pressure vessels used in the Apollo Program several serious failures were encountered. Also, such failures have occurred in other aerospace programs. Even with relatively inert environments failures have occurred after only a few pressure cycles. In some cases through-the-thickness cracks formed and the vessels leaked. In other cases, unfortunately, small surface or embedded flaws grew to critical size prior to growing through the thickness of the vessel wall and catastrophic failure ensued.

Considering the severe consequence of a pre-launch or in-flight failure of a launch vehicle or spacecraft pressure vessel, the National Aeronautics and Space Administration has, during the past several years, devoted much attention to this fracture control problem. Research programs have been sponsored for the purpose of investigating failure mechanisms, obtaining static fracture toughness and subcritical flaw growth data, and developing fracture mechanics analysis methods applicable to both thick and thin walled vessels. The role of the proof pressure test in failure prevention was investigated and was implemented as one of the more important facets of the pressure vessel fracture control plan used in the Apollo Program. Other important facets include rigid controls on test fluids, test pressures, pressure cycles, pressurization and depressurization rates, and hold times at proof pressure. Close surveillance of actual pressure vessel histories was also an essential part of the plan.

This chapter reviews several of the different types of pressure vessel failures which have been encountered, and presents a discussion of the important considerations and the general technical approach being used to prevent such failures in the future. This encompasses many considerations ranging from initial material selection through the final acceptance of individual batches of propellant based on the results of fracture specimen tests. Examples of static fracture toughness and subcritical flaw growth data, which have been obtained on various research programs are included. Cyclic lives, times to failure and flaw growth rates are discussed in the context of linear elastic crack tip stress intensity factors. It is shown how the proof test is used to provide assurance of subsequent service life for both thick and thin walled vessels, and test procedures are recommended which should minimize potential damaging effects of the test which can occur as a result of flaw growth.

Because of the many factors involved it is unlikely that service failures of pressure vessels can be completely eliminated in the immediate future. However, with continued improvement it is believed that the general design approach outlined herein provides the best opportunity of achieving this goal.

Introduction

Pressure vessels generally contain flaws or defects which are either inherent in the materials or introduced during a fabrication process. Relatively large flaws can cause failure to occur during initial proof testing. Smaller flaws can survive proof testing, but with pressure cycles and/or after a period of time of sustained pressure loading, they may grow until a particular flaw is of the minimum size necessary to cause failure. From an economic standpoint it is important that the failure of aerospace pressure vessels during proof testing be minimized. From the standpoint of economic and personnel safety, it is important that operational failures be prevented.

During the past several years some costly proof test failures have occurred which were directly attributable to pre-existing flaws. Probably one of the most spectacular examples was the failure of a 260-  
 (Reference 1) Several NDT methods had been applied to this case including visual, dye penetrant, and ultrasonic inspection of all weldments and weldment repairs. The pre-existing flaw which served as the primary fracture origin is shown in the insert in Figure 1. Failure occurred at a stress level less than fifty percent of the material tensile yield strength. Other examples of proof test failures can be cited from tests of large aluminum propellant tanks and smaller auxiliary tanks used in the Apollo program.

Failures have occurred in the preflight checkout or storage condition stages. After only 21 hours of sustained pressurization, an inclusion in the parent metal of a welded high pressure helium tank grew to 150 percent of its initial size, and caused catastrophic failure. This failure was in a relatively

inert environment. Hostile environments (e.g.,  $N_2O_4$ , methanol, and water) have caused many more failures in high strength vessels. In many of these cases, post mortem examination revealed that the initial flaws were extremely small (below 10 percent of the critical size), and, as might have been expected, they escaped detection because they were below the limits of nondestructive inspection capability. Flaw growth under the action of both loading and environment played the predominant role in these cases. An example of one such failure is the Apollo service module fuel tank shown in Figure 2. This failure occurred after one hour and fifty minutes of 245 psi, using methanol. The design burst pressure for the vessel was 360 psig and a proof test had been conducted at 320 psig. The tank was fabricated from forged 6Al-4V titanium and was solution treated and aged to a tensile ultimate strength of 165 ksi minimum. Examinations of the fracture showed that a stress corrosion crack had extended to a depth of about 60% of the thickness at which time it became unstable and complete fracture occurred. The fracture origin is also shown in Figure 2. The approximate depth and length of the stress corrosion crack is indicated in the figure.

From the above examples it is clear that the prevention of pressure vessel failures involves the understanding and control of many interrelated factors. Nondestructive inspection will not prevent failures if the techniques used cannot detect the flaw that must be detected; the proof test does not provide assurance against subsequent failure if the environment to which the vessel is exposed induces an excessive amount of crack growth; and the often used practice of using high design factors of safety to obtain pressure vessel reliability is not necessarily the answer. For example, the design factor would have had to been nearly twice as high as that used to prevent the motor case failure shown in Figure 1.

It is obvious that failures such as those described have provided substantial incentive to develop and apply pressure vessel fracture control measures. During the past several years a considerable amount of attention has been devoted to this problem. The primary effort has been directed towards the development and application of fracture mechanics techniques. This chapter reviews these techniques and discusses the usefulness and limitations of the proof pressure test as it relates to reliable service performance.

#### Important Considerations in Preventing Failures

The three major considerations in the prevention of proof test and service failures of metallic pressure vessels are, the initial flaw sizes, the critical flaw sizes (i.e., the sizes required to cause fracture at a given stress level) and the subcritical flaw growth characteristics. (See the block diagram in Figure 3.) The prevention of proof test failure is dependent upon the actual initial flaw sizes being less than the critical flaw sizes at the proof stress level. In order to obtain confidence that the vessel will not fail in service, it is necessary to show that the largest possible initial flaw in the vessel cannot grow to critical size during the required life span. The significant parameters affecting critical flaw sizes are the applied stress levels, the material fracture toughness values, the pressure vessel wall thickness, the flaw location, and the flaw orientation. For surface and imbedded flaws in a tension loaded elastic stress field the stress intensity factor associated with the critical flaw size is denoted as  $K_{Ic}$ . The determination of actual initial flaw sizes depends upon the use of nondestructive inspection procedures. The stress intensity factor associated with the initial flaw size is denoted  $K_{Ii}$ . As will be discussed, a successful proof pressure test can provide a measure of the maximum possible  $K_{Ii}/K_{Ic}$  in the vessel when it is placed into service.

Subcritical flaw growth can occur as a result of cyclic loading, sustained stress loading and combined sustained stress and cyclic loading. When the sustained stress flaw growth is environmentally induced, it is often termed stress corrosion and combined cyclic and sustained stress growth is called corrosion fatigue. Because of the potentially high rates of flaw growth, the problems of sustained stress and combined cyclic and sustained stress growth are of major importance in the design of aerospace pressure vessels.

#### Evaluating Cyclic and Sustained Stress Flaw Growth

Of the many types of laboratory specimens used for obtaining fracture toughness values and subcritical flaw growth data, those which involve plane strain cracking are of most interest to pressure vessel designers. Specimens containing through-the-thickness cracks must be relatively thick for most materials in order to develop plane strain conditions at the crack tip. This limitation can and has restricted the use of such specimens. As applied to the problem of predicting critical flaw sizes and evaluating subcritical flaw growth in both "thick and thin walled" aerospace pressure vessels, the surface flawed or "part-through" type cracked specimen has probably found the widest use. (Reference 2, 3, and 4). With this specimen the initial flaw closely simulates the type of flaws often encountered in service, and it can be oriented to suit the flaw growth characteristics desired. Unlike the through-the-thickness crack, however, continuous "on line" measurement of crack length or flaw size is not possible.

A procedure for the evaluation of cyclic flaw growth using surface flawed specimens is schematically illustrated in Figure 4a. The  $K_{Ic}$  for the material is first determined from static pull tests of a surface flawed specimen. A series of flawed specimens are then placed into test, each specimen being cycled to a different maximum applied initial stress intensity. Typically, a zero-full tension-zero loading profile, such as illustrated on the figure insert, is applied but other loading profiles appropriate to specific situations may also be used. The number of cycles required to cause failure of each specimen is determined and a relationship between initial applied stress intensity and cycles to failure is established by the complete set of specimens. The applied stress levels should be sufficiently high (and the specimens

\*When the wall thickness is large enough and/or the  $K_{Ic}$  is low enough so that the critical depth for a long surface flaw is less than  $1/2t$ , the vessel is herein termed "thick-walled". Where the critical depth of a long surface flaw is greater than  $1/2t$ , the vessel is herein termed "thin-walled".

sufficiently thick) that failure will occur before the crack depth has exceeded one half the specimen thickness to ensure that the crack growth occurs under conditions of maximum constraint. The data can be replotted in a completely equivalent manner as shown on Figure 4b. The rate of crack growth as a function of the applied stress intensity can then be established by determination of the slopes of the crack length versus cycle plots at a series of selected stress intensity values. A typical result obtained for titanium cycled at 70°F is shown in Figure 5.

The procedure for evaluating sustained stress flow growth with surface flawed specimens is similar in principle to that used for the cyclic stress flow growth determinations. The process is illustrated schematically in Figure 6a. As before, the  $K_{Ic}$  of the material is determined and a series of flawed specimens are placed into the test environment and loaded to various fractions of  $K_{Ic}$ . The time required for fracture is noted for those specimens which fail within some reasonable time, (e.g., specimens 3 and 4) it is still possible to obtain flow growth information by "marking" the crack front (applying a number of low stress fatigue cycles) and then pulling the specimen apart. The fracture face will usually permit direct measurement of sustained load growth by separation of the striated areas produced by the cyclic loading operations. The fracture surface preceded by such a sequence is shown in Figure 6b. The striated area produced by the initial flow sharpening operation and the area produced by the final working operation are separated by a clearly visible area representing the crack growth during the sustained load test.

A point is finally reached that neither failure nor flow growth occur, (e.g., specimens 5 and 6.) the highest level of  $K$  for which this condition obtains, is called the threshold stress intensity,  $K_{th}$  (or  $K_{Isc}$  if due to stress corrosion cracking - Reference 5).

Another method of obtaining  $K_{th}$  values using surface flawed specimens is through the use of a single wire strain gage, which measures the flow opening as a function of time. See Figure 7. The flow opening measurement is used to provide an indirect indication of flow growth as a function of time at load (i.e., the deeper the flaw the larger the opening strain). The highest applied stress intensity at which there is no indication of flow growth is then designated as the threshold value.

Such flow opening measurements can also be used to obtain an estimate of flow growth rate as a function of stress intensity level, however, in the interpretation of flow opening measurements it should be recognized that the change in flow opening with time at load may be due to both flow growth and plastic deformation at the flaw tip. This is illustrated in Figure 8. As shown on the figure, the portion of the flow opening strain due to plastic deformation should approach zero when the plastic zone size,  $w$ , is small compared to the remaining ligament thickness,  $t_n$ . This can generally be accomplished by testing shallow flaws in relatively thick specimens. The proportionality constant in the expression relating the change in strain,  $\Delta \epsilon$ , with flow growth,  $\Delta(a/Q)$ , can be determined from partial growth specimens as shown in Figure 9. The procedure for obtaining flow growth rate as a function of stress intensity level from flow opening strain versus time records is schematically illustrated in Figure 10. Some actual oscillograph records of flow opening strain versus time for 6Al-4V titanium (STA) in helium gas are shown in Figure 11. From these records the growth rate curves shown in Figure 12 were obtained. It is interesting to note that over a considerable range in stress intensity the growth rate is nearly constant. A similar curve for 6Al-4V titanium (STA) in freon TF is shown in Figure 13. At an applied stress intensity level of about 59% of the  $K_{Ic}$  value the growth rate is approaching zero. This stress intensity is thus considered to be the threshold level.

The discovery of a unique  $K_{th}$  for a given material and environment is the key to the design of safe pressure vessels subjected to sustained loading. While  $K_{th}$  can be 80 percent of  $K_{Ic}$  or higher in inert environments, (e.g., the titanium in helium gas) more hostile media (e.g., the freon TF) can significantly reduce this value. In general, it has been found that  $K_{th}$  values decrease with increasing yield strength in steel alloys (References 6 and 7). Also, there is considerable evidence to indicate that sustained load flow growth is most severe under conditions of plane strain (Reference 5). Reference 8 shows that  $K_{th}$  values, determined from through-the-thickness cracked specimen tests, increase with decrease in specimen thickness.

Studies of flow growth and stress intensity in aggressive environments (Reference 7, 9, 10, 11, and 12) indicate an ever increasing growth rate with increasing stress intensity, however, as shown in Figure 13 it may be relatively constant over an appreciable range in stress intensities. In these tests for  $K_{th}$ , one often encounters wide scatter, abnormally short times to failure and very marked dependence on environmental characteristics (media and temperature), and even on minor changes in chemical composition, (References 3 and 13).

In chemically inert environments the crack growth rate initially decreases with increasing stress intensity. If the initial stress intensity is sufficiently low, the crack may halt. At higher stress intensities, the crack growth rate passes through a minimum and then increases steadily to an instability. Such flow growth behavior was reported by Johnson (Reference 6) for AM 350 steel in a purified argon environment. This behavior was also noted in Reference 2 for SA1-2.5Sn(ELI) titanium and 2219-T87 aluminum.

From these remarks, it is apparent that the service condition must be carefully simulated. During the past few years a considerable amount of sustained load flow growth data have been obtained on a number of different material-environment combinations. A summary of some  $K_{th}$  information is given in Table I.

#### Establishing the Stress Intensity Approach

Probably the most convincing evidence that the stress intensity factor,  $K$ , is the controlling mechanical parameter in cyclic and sustained stress flow growth are the correlations obtained between various types of fracture specimens and between specimens and actual pressure vessels.



### a. Correlation Between Various Specimen Types

Brown and Beachem (Reference 14) explored sustained stress flow growth behavior using three different specimen types:

1. The center-cracked plate
2. The surface-flawed plate
3. The precracked cantilever beam

for 4340 steel in dilute NaCl solution. The same  $K_{th}$  value was obtained for all three types. However, there were differences in failure at a given level of  $K_I$  greater than  $K_{th}$ . This can be explained by the different functional relationships between crack length and associated stress intensities. The more rapid the increase in  $K$  with crack length, the shorter the failure time. For this reason, the cantilever beam specimens exhibited the shortest failure times, while the center-cracked specimens were the slowest in cracking.

In cases where the stress intensity decreases with crack length (e.g., wedge force loading for a center-cracked specimen)  $K_{th}$  is rather simple to evaluate. Smith, Piper, and Downey (Reference 9) obtained values of 20 to 25 ksi  $\sqrt{in}$  for crack initiation, and 20 to 22 ksi  $\sqrt{in}$  for crack arrest, using this procedure with Ti-8Al-1 Mo-1V alloy in a 3.5 percent salt solution.

For end loaded specimens under constant load, both stress intensity factor and net section stress increase with increasing crack length; with wedge-force loading, the net section stresses increase whereas the stress intensity decreases with increasing crack length. The excellent agreement between initiation and arrest  $K_{th}$  values clearly shows that it is the stress intensity parameter and not net section stress that is the controlling parameter in sustained stress crack growth.

Reference 15 shows correlations between two types of specimens used to obtain cyclic flow growth data. In this investigation round notched bars and surface flawed specimens were tested to obtain  $K_{II}/K_{IC}$  versus cycle curves for Ladish D6AC steel. The results showed close agreement between the two specimen types with the data scatter being somewhat larger for the round notched bar specimens. This data scatter was attributed to eccentric crack growth.

### b. Correlation Between Specimens And Pressure Vessels

Correlations between sustained stress flow growth in surface flawed fracture specimens and pressure vessels subjected to cyclic and sustained pressurization are shown in References 2, 16 and 17. In References 2 and 16 aluminum and titanium vessels containing small initial fatigue cracks were tested in environments of room temperature air, liquid nitrogen, and liquid hydrogen and the results were compared with the fracture specimen data. Reference 17 shows results of Inconel 718 fracture specimens and pre-flawed pressure vessel sustained stress tests in the environment of high pressure (5,000 psig) gaseous hydrogen at room temperature. Figures 14 and 15 show comparisons between some of the pre-flawed pressure vessel and specimens tests. Similar results were previously obtained for Ladish D6AC steel pressure vessels, and are shown in Reference 15. In none of the tests was there any significant differences in flow growth characteristics between the biaxially stressed vessels and the uniaxially stressed specimens.

In addition to laboratory specimen-pressure vessel comparisons, there have been a number of instances during the past several years where sustained stress fracture specimen data and fracture mechanics analyses have been used to describe conditions leading up to service failures and were used to arrive at corrective actions. For example, service failure correlations involving a 4330 steel hydraulic actuator failure in a water environment are shown in References 18 and 19, and titanium pressure vessel failures with  $N_2O_4$  propellant in Reference 20. The Apollo service module fuel tank failure shown in Figure 2 also illustrates the usefulness of fracture specimen testing in a service failure analysis. Laboratory tests on uniaxial surface flawed specimens made from material from the failed vessel resulted in the sustained stress flow growth curve shown in Figure 16. As can be seen from this figure the  $K_{th}$  for the material in the methanol environment is about 24 percent of  $K_{IC}$ . The average  $K_{IC}$  values for the material was about 44ksi  $\sqrt{in}$ . The resulting predicted critical flow size curve is shown in Figure 17. Also shown on this figure is the threshold stress intensity curve. As can be seen from the figure an initial flaw or defect greater than about 2.5 mils deep would result in a stress intensity above the threshold value at the test pressure level of 245 psig. In that machining grooves have been observed on Apollo pressure vessels in excess of this depth it is reasonable to assume that the subject vessel also contained such initial defects. During the one hour and 50 minutes at the 245 psig pressure the initial defect grew in size and catastrophic failure occurred when the stress corrosion crack attained the critical size. From the curve shown in Figure 17 the predicted critical depth is 0.31 inches. This predicted size corresponds closely with that observed at the actual fracture origin as shown in Figure 2.

### Combined Cyclic and Sustained Stress Flow Growth

As previously described, the cyclic life for a given cyclic load profile and environment depends primarily on the ratio of initial to critical stress intensity. A large number of pressure vessel materials have been investigated and a significant amount of cyclic flow growth data obtained. Some such data was shown in the specimen-pressure vessel correlations previously discussed. Another set of typical data is illustrated in Figure 18. In this figure both a best fit curve and a statistically determined lower bound curve are shown.

#### a. Implications for Design

If the maximum initial stress intensity at the operating stress level in a pressure vessel is known, it can be entered in the ordinate of  $K_{II}/K_{IC}$  versus cycle plot and the cycles to failure (i.e.,

cycles to increase  $K_{II}$  to  $K_{IC}$  read off the abscissa. However, this assumes that either the vessel is cycled at a frequency comparable to that used in generating the specimen data or that cyclic frequency is not important. In Reference 18, it was hypothesized that below the sustained stress threshold stress intensity value ( $K_{th}$ ) cyclic frequency (or hold time at maximum load) probably would not have a major effect on the cyclic flaw growth rate, but above  $K_{th}$ , it could have a large effect. In other words, the minimum cycle life was limited to the number of cycles required to increase the initial stress intensity  $K_{II}$  to the  $K_{th}$  value and that above the  $K_{th}$  level failure could occur in one additional cycle if the hold time were sufficiently long. On a  $K_{II}/K_{IC}$  versus log cycles curve, this is represented by the difference between the cycles at  $K_{II}/K_{IC}$  and  $K_{th}/K_{IC}$ .

#### b. Effect of Long Hold Times

From an experimental standpoint, if one were to test a series of specimens with very long hold times at maximum load, the total cyclic life for each specimen would be expected to be reduced by an incremental number of cycles,  $N_0$ , corresponding to that at the  $K_{th}/K_{IC}$  level for data obtained at a relatively high cyclic frequency. These predicted upper and lower bound curves for very short and long hold times at maximum load are illustrated schematically in Figure 19a.

To date there is only a limited amount of experimental data to substantiate this prediction. Some of these data were developed for NASA Lewis Research Center on 2219-T87 aluminum and 5Al-2.5Sn(ELI) titanium in the relatively inert environment of liquid nitrogen and are shown in Reference 2. Data for the titanium alloy are reported in Figure 19b. These, as well as the other data in Reference 2 tend to support the original Reference 18 hypothesis. When materials are subjected to more aggressive environments (i.e., those resulting in low  $K_{th}/K_{IC}$  values) there is considerable doubt as to the general validity of the hypothesis. There is some data on 8Al-1Mo-1V titanium in salt water which indicates that cyclic frequency has no significant effect on growth rate at stress intensity levels below  $K_{th}$ . These data are shown in Figure 20. On the other hand, investigations by Barsom (Reference 21), and Wei (Reference 22) have shown that for some material-environment combinations, both the environment and the cyclic frequency can affect the growth rates at stress intensity values below  $K_{th}$ . For example, Barsom has shown that, for 12Ni steel in salt water, cyclic growth rates are higher than in a dry environment, and progressively increase with decreasing cyclic frequency (i.e., from 600 cpm to 6 cpm) at stress intensity ( $K_{max}$ ) levels less than  $K_{th}$ . A complete explanation of this type of behavior has yet to be obtained, however, it is apparent that additional research on environmentally enhanced fatigue growth (i.e., corrosion fatigue) is required.

If it is necessary to use materials with low threshold values (less than 70 or 80%  $K_{IC}$ ) in the expected operating environment, the effect of environment and cyclic frequency on cyclic flaw growth rates should be determined and the appropriate rates used in the pressure vessel life estimations. As mentioned above, the minimum allowable cyclic life should be limited to the number of cycles required to increase the initial stress intensity  $K_{II}$  to the  $K_{th}$  value.

#### c. Effect of Wall-Thickness

The technique for using  $K_{II}/K_{IC}$  versus time data to estimate pressure vessel life are dependent upon pressure vessel wall thickness. For "thick-walled" vessels the  $K_{II}/K_{IC}$  curves can be used as indicated above. For "thin-walled" vessels the task is somewhat more complicated. When the depth of a surface flaw becomes large with respect to the wall thickness, the stress intensity is higher than that predicted by the original Irwin surface flaw equation (Reference 23) and as a result, the subcritical flaw growth rates will be higher and the total life shorter than that obtained from  $K_{II}/K_{IC}$  curves of the type shown in Figure 18. (It should be noted that shallow surface flaw specimens are used in generating the basic  $K_{II}/K_{IC}$  data.) The increase in stress intensity for long surface flaws and for semicircular surface flaws, which become deep with respect to the wall thickness have been approximated by Kobayashi (Reference 24) and Smith (Reference 25), respectively. For thin-walled vessels, Reference 26 provided a method for estimating cyclic flaw growth rates using shallow flaw data by inclusion of the deep flaw stress intensity magnification. Using this method flaw growth rate curves are obtained by differentiating the  $K_{II}/K_{IC}$  versus cycle curve. For a given vessel design, the flaw growth rate curves are then arithmetically integrated using the Kobayashi approximation to account for the increase in stress intensity as the flaw approaches the free surface.

In an attempt to obtain a better insight into the behavior of deep surface flaws in thin walled vessels and to evaluate the validity of the method for predicting cyclic flaw growth suggested in Reference 26, NASA initiated an experimental investigation of a titanium and an aluminum alloy under Contract NAS3-10290. While the results of this work are reported in detail in NASACR-72606 two significant findings were as follows:

1. For very long surface flaws (i.e., small  $a/2c$  values) the Kobayashi approximation tended to underestimate the magnitude of the deep flaw stress intensity magnification. As seen in Figure 21 this is particularly true for the titanium alloy.
2. Cyclic flaw growth rates can in some cases be significantly higher than those predicted from shallow flaw data corrected for stress intensity magnification. This appears to be the case when the crack tip elastic zone is large compared to remaining ligament between the flaw tip and the back surface.

A complete understanding and explanation of these preliminary findings is not yet available and as a result improved (i.e., more precise) life prediction procedures for thin walled vessels cannot yet be firmly established. However, it is important to recognize that the procedure presented in Reference 26 can under certain conditions result in unconservative life estimates and that it is possible to avoid this unconservatism. Specifically, the use of the procedure can result in an excessively high estimate of cyclic life for the situation when the threshold flaw size is very deep with respect to the wall thickness (i.e.,

approximately one plastic zone size from the back surface). Likewise, it can result in an unconservative (but not necessarily dangerous) estimate of the number of cycles for a flaw to grow through the wall thickness for the situation when the critical flaw depth actually exceeds the wall thickness. To avoid unconservative estimates in these situations it appears desirable to experimentally obtain cyclic life data using test specimens with the same thickness as the actual vessel and containing long surface flaws.

It is hoped that with further research both the deep flaw stress intensity magnification and growth problems will be clarified so that improved life and failure mode prediction procedures can be recommended.

### Proof Tests on Actual Pressure Vessels

#### a. Initial Stress Intensity Factors in Service

A key factor then in the application of sustained stress and combined cyclic and sustained stress flow growth data is prior knowledge of initial flaw size or more specifically, initial stress intensity ( $K_{II}$ ) levels within the vessel. The actual  $K_{II}$  values are a function of both the actual initial flaw shapes and location. If initial flaw size and stress levels can be defined, the stress intensity can usually be determined with a reasonable degree of accuracy using available stress intensity solutions or approximations (References 23, 27, 28 and 29). Determination of actual initial flaw sizes is dependent upon non-destructive inspection.

A measure of the maximum possible initial stress intensity can be obtained from a properly designed and successful proof pressure test. Some comments on nondestructive inspection are given in Appendix I.

It was originally pointed out in Reference 30 that a successful proof test to a pressure  $\alpha$  times the maximum operating pressure indicates that the maximum possible  $K_{II}/K_{IC}$  at the maximum operating pressure is equal to  $1/\alpha$  and that this value could then be used in conjunction with  $K_{II}/K_{IC}$  versus cycles data to estimate minimum life. Additionally it was pointed out in Reference 18 that the validity of the minimum life prediction was not dependent upon an accurate knowledge of either the actual applied stress levels or the finite fracture toughness ( $K_{IC}$ ) values, both of which vary throughout a given vessel. However, the accuracy of the prediction is dependent upon the validity of the sustained stress and combined cyclic and sustained stress flow growth data and this in turn emphasized the need for determining the areas of the vessel (i.e., welds, parent metal, etc.) which exhibit the highest growth rates and lowest  $K_{II}$  values. Also, it is important to make sure that compositional changes and/or both batch to batch variations in propellants and test fluids used in the vessels will not result in lower  $K_{II}$  values than those used in the original analysis (or design) of the vessel. The control procedures used in Apollo pressure vessels are discussed in Appendix II.

#### b. The Test Factor

From the standpoint of initial design the minimum required proof test factor for a pressure vessel is  $\alpha = 1 + \text{allowable } K_{II}/K_{IC}$  and in order to prevent delayed time failure the allowable  $K_{II}/K_{IC}$  must be less than the minimum  $K_{II}/K_{IC}$ . The amount less depends upon the pressure cycle requirements.

#### c. Undesirable Flaw Growth During the Proof Test

Since the initial introduction of the concept, there have been concerns expressed about possible damaging effects of the proof test and speculation as to whether the test could actually cause an operational failure of a vessel which otherwise might have performed satisfactorily. Also, there have been numerous questions about the value of the test as a function of pressure vessel wall thickness, the selection of the test temperature, test media, pressurization and depressurization rates, time at maximum pressure, multiple proof test cycles and the need to simulate service loads other than internal pressure.

Subcritical flaw growth can and often does occur even in relatively inert environments. It is therefore likely that during the time required to perform a proof test initial flaws or defects in the vessel can increase in size (or possibly even new flaws could be opened up). In fact, if the proof test is not properly designed (e.g.,  $\alpha$  is  $< 1 + \text{allowable } K_{II}/K_{IC}$ , depressurization rates which are too slow or the test being conducted with an aggressive test media), the flaw growth occurring during the test can be sufficient to cause a subsequent operational failure, which otherwise may not have occurred.

#### d. Non-Service Test Temperature

If the proof test is performed at a temperature which is different from the operating temperature, the required minimum proof test factor is as follows:

$$\alpha = \frac{1}{\text{allowable } K_{II}/K_{IC}} \times \frac{K_{IC} \text{ at Proof Temperature}}{K_{IC} \text{ at Operating Temperature}}$$

The advantage of testing at a temperature where the  $K_{IC}$  is lower than at the operating temperature is that either a lower proof test factor can be used or a larger operational life can be assured. The disadvantages are possible increased risks of proof test failure and the need for an accurate knowledge of how  $K_{IC}$  varies with temperature for all of the materials in the vessel.

\* The plastic zone size can be estimated from the expression  $\frac{\pi}{16} \left( \frac{K_{II}}{\sigma_{ys}} \right)^2$

#### e. Effect of Thickness

From analysis, it can be shown that regardless of the pressure vessel wall thickness, the required minimum proof test factor,  $\alpha$ , should be  $1/\alpha$  allowable  $K_{II}/K_{IC}$ , however, the value of the proof test in providing assurance against service failure changes with decreasing wall thickness and/or increasing fracture toughness,  $K_{IC}$ , as does the predicted pressure vessel failure mode. This is illustrated in Figure 22.

#### f. Dangers of Slow Rates of Pressurization and Depressurization

If the pressure vessel is pressurized at a slow rate or if the proof pressure is sustained for a prolonged period of time, the probability of a proof test failure is increased, because of possible slow flaw growth. However, subsequent to a successful test it can still be said that the maximum  $K_{II}/K_{IC}$  at the operating pressure is equal to  $1/\alpha$ . On the other hand, if the vessel is slowly depressurized such that the flaw which was just smaller than critical size at the proof stress level continues to grow, the maximum possible  $K_{II}/K_{IC}$  after the test will be greater than  $1/\alpha$ . In fact, it appears that if the positive  $dK/dt$  due to flaw growth is greater than the negative  $dK/dt$  due to reduction in stress the vessel could even fail during depressurization.

The amount of flaw growth which will actually occur during depressurization is dependent on the actual  $K_{II}/K_{IC}$  ratio (or initial flaw size) at the start of depressurization, the depressurization rate, and the sustained stress flaw growth characteristics of the vessel materials in the proof test media. It is apparent that in order to minimize the flaw growth one should use a test fluid which is relatively inert, and use a high rate of depressurization. If it is assumed that the  $K_{II}/K_{IC}$  ratio at the start of depressurization approaches unity (i.e., the vessel is just about to fail) and if sustained stress flaw growth rate data for the material-environment are available, it is then possible to determine the maximum possible  $K_{II}/K_{IC}$  at the start of the vessel's operational life as a function of depressurization time.

##### (1) An Example with Titanium Alloy

This was done for 6Al-4V titanium pressure-vessel proof tested with gaseous helium (i.e.,  $K_{th} \sim .90 K_{IC}$ ) and the results are shown in Figure 23. In this study the negative  $dK/dt$  due to reduction in stress was based on an assumed linear reduction in pressure with time (i.e., the dashed lines in Figure 23). The solid curves in Figure 23 represent the actual reduction in  $K_{II}/K_{IC}$  for various depressurization times. These curves account for the change in stress intensity due to flaw growth above the  $K_{th}$  value due to stress reduction. The growth rate data shown in Figure 12 was used in determining these curves. The locus of  $K_{II}/K_{IC}$  values at the given depressurization times represent the maximum possible  $K_{II}/K_{IC}$  values in the vessel when it is put into service.

#### g. Multiple Proof Tests

In general, very little can be gained by performing multiple proof test cycles. Even after the last cycle all that can be said is that the maximum possible  $K_{II}/K_{IC} = 1/\alpha$ , and the cycles performed subsequent to the first cycle could have done some amount of needless damage to the vessel as a result of cyclic flaw growth. However, occasionally special circumstances dictate the need or make it desirable to conduct more than one proof test. Such special circumstances include the following cases:

- (1) A single proof test cannot be designed to envelop the critical operational pressure, temperature and external loading combinations.
- (2) The vessel was modified or repaired subsequent to the initial test and the modified and repaired areas need to be proof tested.
- (3) It is desired to extend the guaranteed life of the vessel after it has had a period of service usage.
- (4) From an economical standpoint it is desired to test components (e.g., bulkheads) of the vessel prior to initiating final assembly.
- (5) To minimize the risk of failure at the design temperature it has been shown (by laboratory experiments on preflawed simulated parts or specimens) that a prior test at a higher temperature is advantageous.

#### h. Pressure and Other Service Loadings Combined

For those pressure vessels which are critical for internal pressure combined with flight loads it may not be possible to envelop the operational stress levels in the vessel with internal pressure alone. In such cases it appears desirable to include provisions in the test setup to apply simulated flight loads combined with internal pressure.

#### Conclusions

Both safety and economic considerations require the prevention of additional delayed time failures of aerospace pressure vessels. It is believed that compliance with the technical approach based on the use of laboratory specimen test data, fracture mechanics analyses, and the use of well designed proof tests can provide confidence that such operational failures will not occur.

If the proof test is properly conceived and executed, operational failures should be substantially diminished. When considering the impact of a possible service failure, the need for a

meaningful proof test appears mandatory. The information gained far outweighs the potential damage done by the test. Furthermore, it should be noted that in a well designed proof test, this potential damage can be minimized.

At the present time we know of no acceptable alternate to this approach in pressure vessel certification, and thus conclude that it should be used. It has been and is in use on the Apollo program and is expected to be used on other NASA programs.

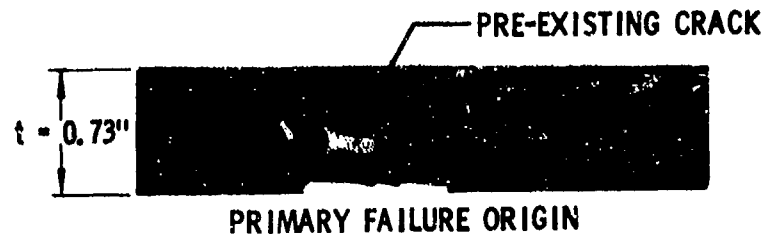


Fig.1 260" diameter motor case failure

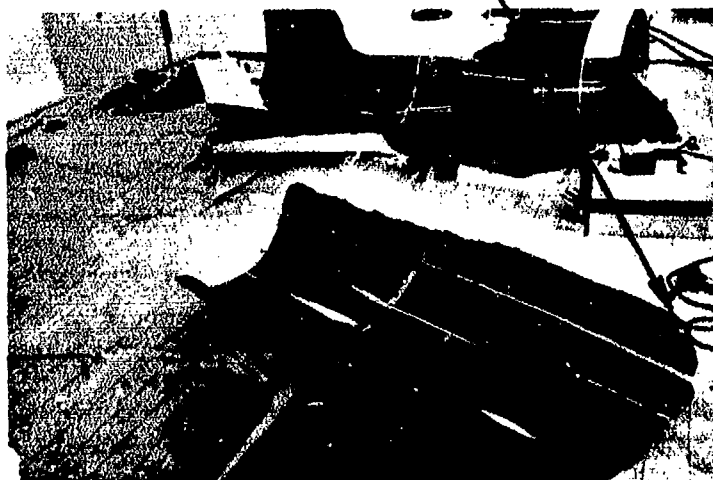
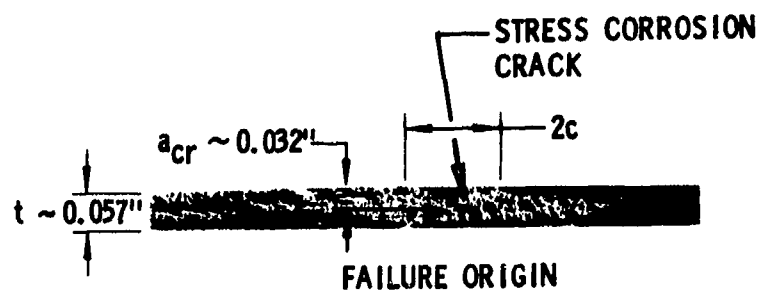


Fig.2 Apollo service propulsion system fuel tank failure

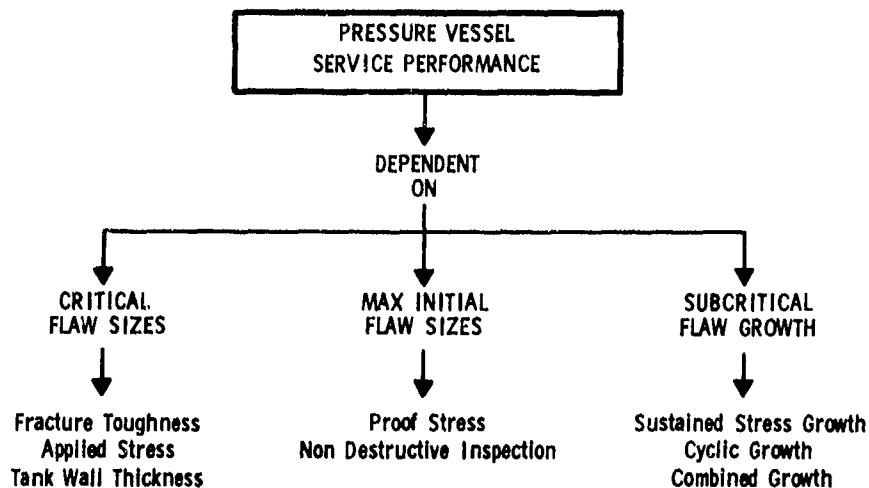


Fig.3 Technical approach

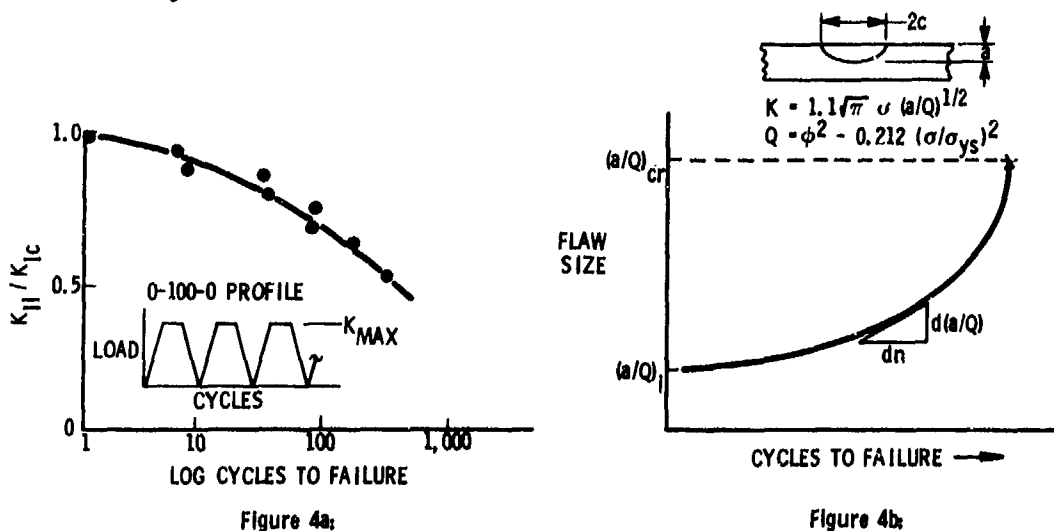


Fig.4 The evaluation of cyclic flaw growth (schematic representation)

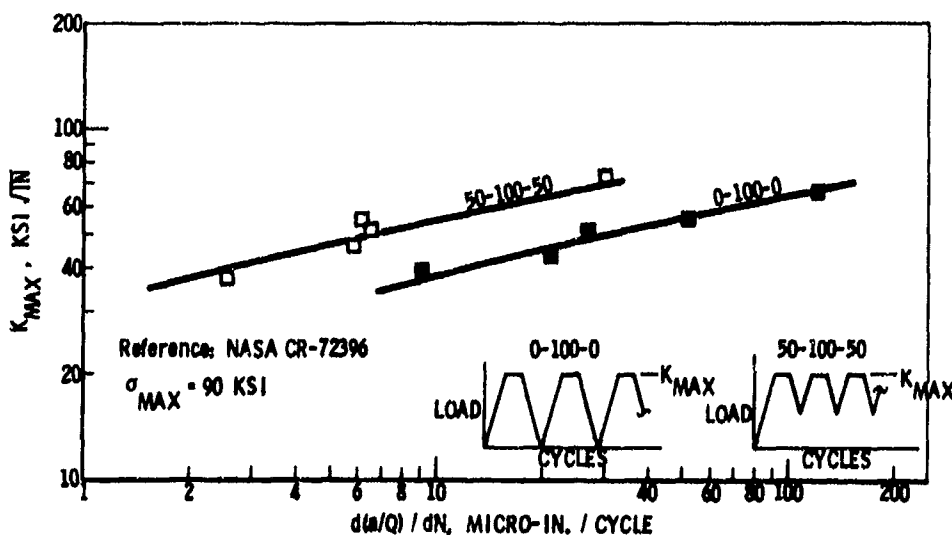


Fig.5 Flaw-growth-rate curves for 6Al-4V (ELI) titanium base metal in ambient air

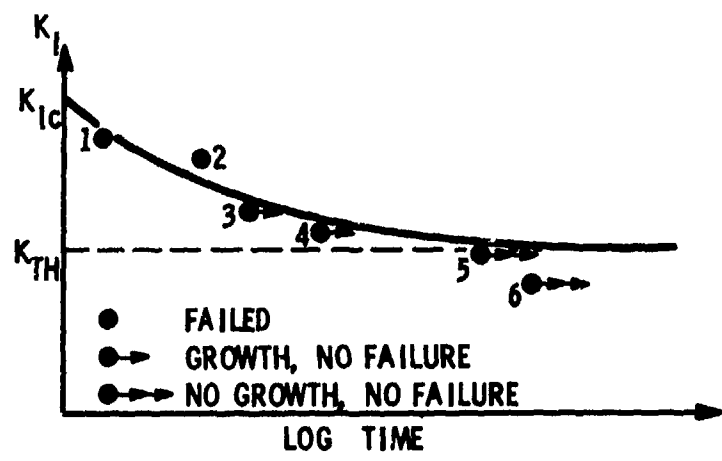
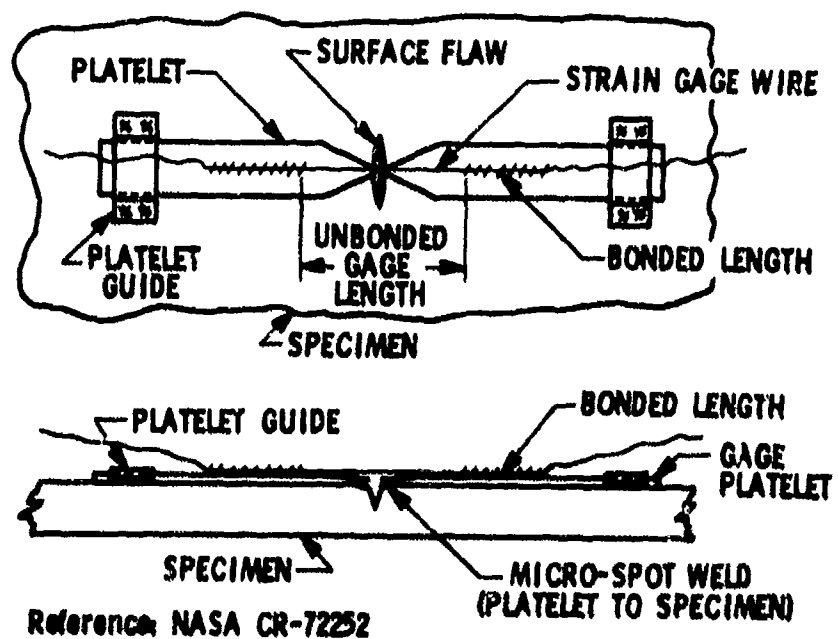
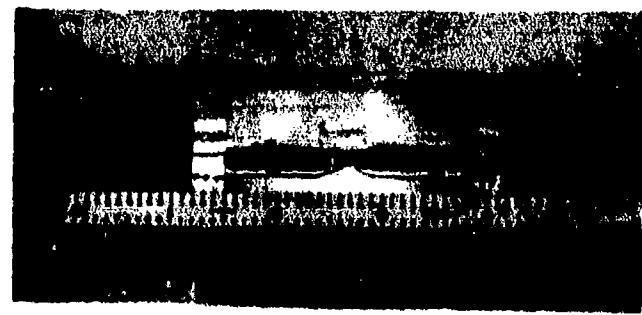


Fig.6(a) Flaw growth data (schematic)

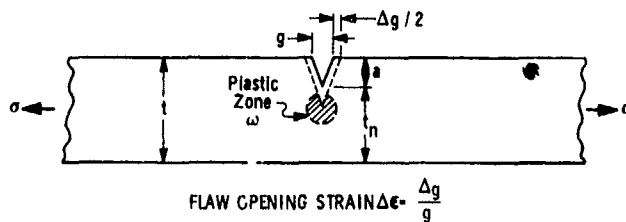


Fig.6(b) Fracture face of surface flaw specimen



Reference: NASA CR-72252

Fig.7 Instrumentation for measuring flaw opening displacement



FLAW OPENING STRAIN  $\Delta\epsilon = \frac{\Delta g}{g}$

$\Delta\epsilon = \Delta\epsilon_a + \Delta\epsilon_p$

WHERE:

$\Delta\epsilon_a$  - Change in Strain Due to Flaw Growth

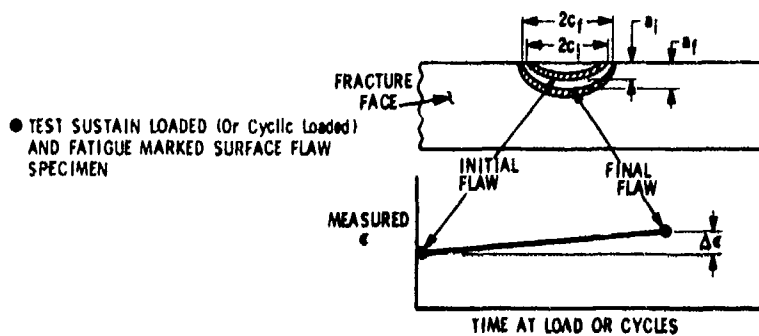
$\Delta\epsilon_p$  - Change in Strain Due to Plastic Deformation at the Flaw Tip

$\Delta\epsilon_a = C \sigma \Delta \left( \frac{a}{\sqrt{Q}} \right)$  FROM THEORETICAL ANALYSES BY GREEN, SNEDDON AND IRWIN

$\Delta\epsilon_p$  - UNKNOWN BUT BELIEVED TO  $\rightarrow 0$  WHEN  $\omega/t_p$  IS SMALL FOR SPECIMENS TESTED  $\omega/t_p \rightarrow 0$  IN MOST CASES

$\Delta\epsilon = \Delta\epsilon_a$

Fig.8 Components of flaw opening strain (thick specimens)



● TEST SUSTAIN LOADED (Or Cyclic Loaded) AND FATIGUE MARKED SURFACE FLAW SPECIMEN

● FROM FRACTURE FACE

Measure:  $a_i, 2c_i, a_f$  and  $2c_f$

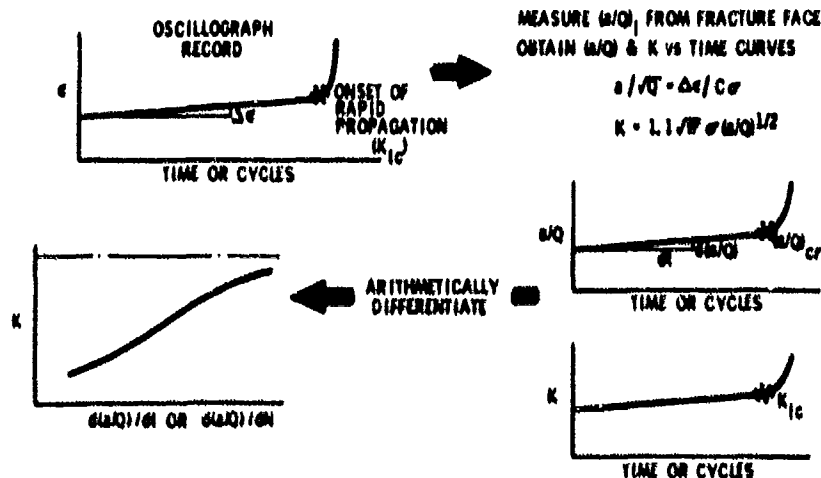
Compute:  $(a/\sqrt{Q})_i$  and  $(a/\sqrt{Q})_f$

$\Delta(a/\sqrt{Q}) = (a/\sqrt{Q})_f - (a/\sqrt{Q})_i$

● COMPUTE C

$C = \frac{\Delta\epsilon}{\sigma \Delta(a/\sqrt{Q})}$

Fig.9 Evaluation of constant relating flaw opening strain to flaw growth



MEASURE  $(a/Q)_i$  FROM FRACTURE FACE OBTAIN  $(a/Q)$  & K vs TIME CURVES

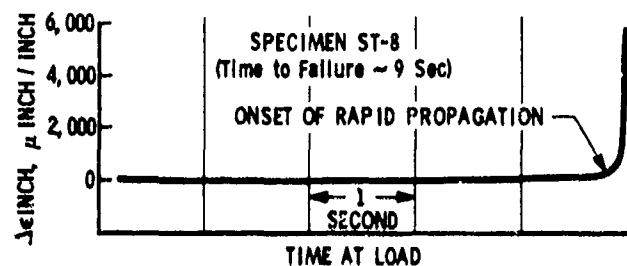
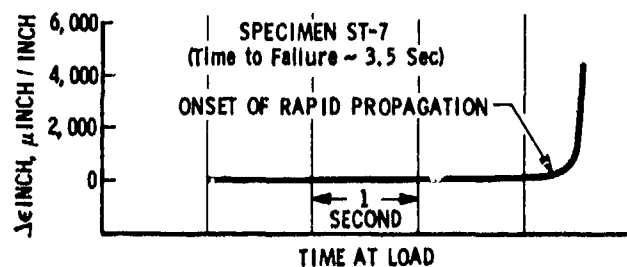
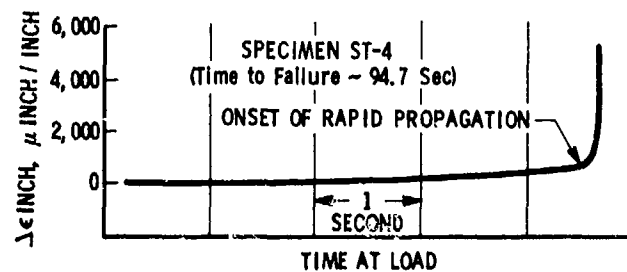
$a/\sqrt{Q} = \Delta\epsilon/C\sigma$

$K = 1.1\sqrt{W} \sigma (a/Q)^{1/2}$

ARITHMETICALLY DIFFERENTIATE

Fig.10 Determination of K versus  $d(a/Q)/dt$  curves





Reference: NASA CR-99632 \*SPECIMEN THICKNESS 0.4"

Fig.11 Oscillograph records for "thick" specimens (last 4 to 5 seconds prior to failure)

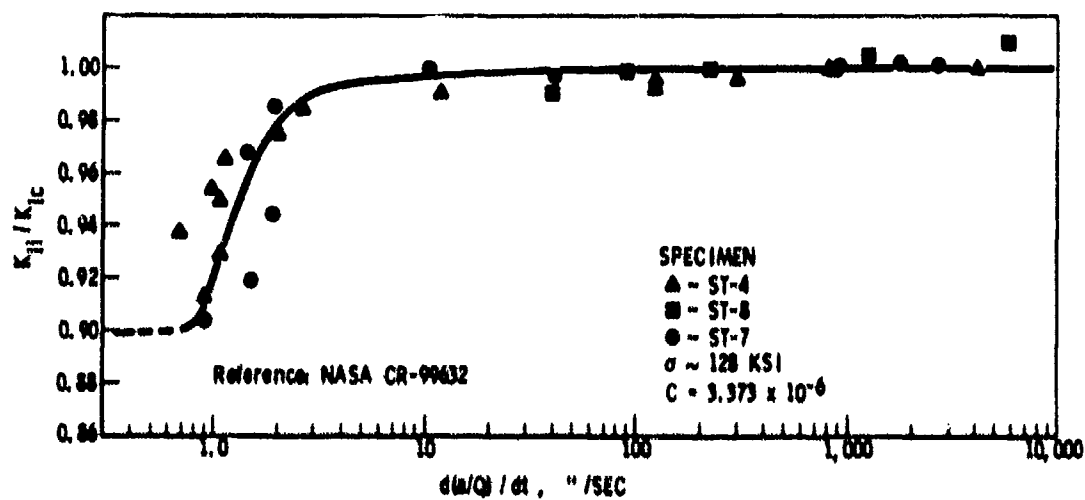


Fig.12 Sustained load flaw growth rate data for "thick walled" 6Al-4V titanium pressure vessels in GHe at room temperature

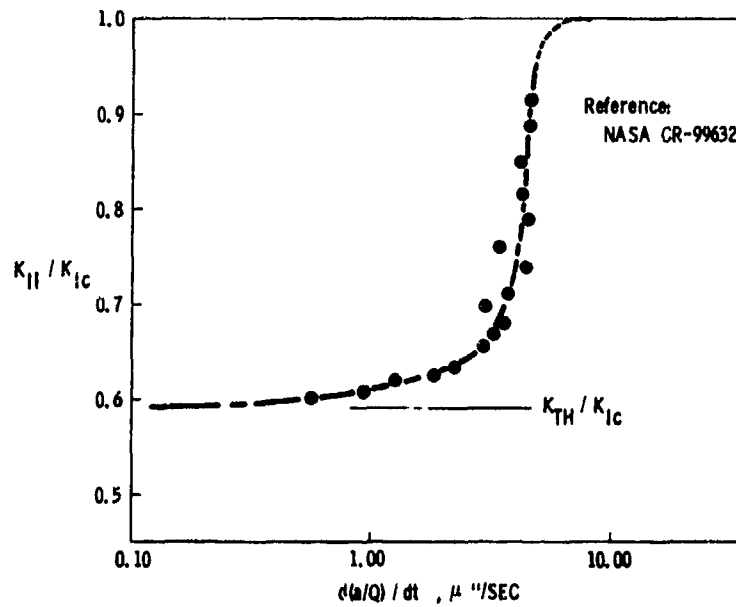


Fig.13 Sustained load crack growth rates for 6Al-4V titanium weld in Freon T.F.

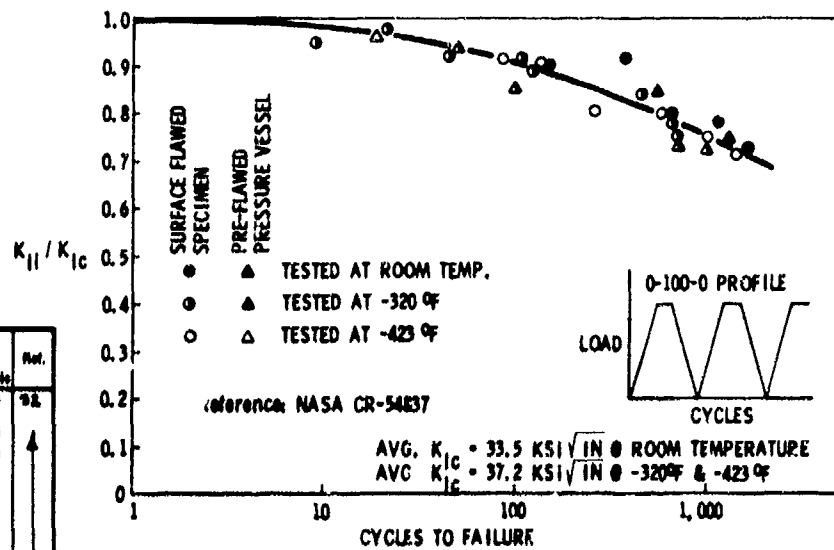


Fig.14 Cyclic crack growth data for 2219-T87 aluminium

Material	Temp. °F	σ <sub>ys</sub> Ksi	Fluid Environment	$K_{TH}/K_{Ic}$	Ref.
6Al-4V Titanium Forging-ETA	R.T.	100	Methanol	.26	92
	R.T.	100	Freon M.F.	.50	
	R.T.	100	H <sub>2</sub> O <sub>2</sub> (.30% HO)	.74	
	R.T.	100	H <sub>2</sub> O <sub>2</sub> (.50% HO)	.83	
	R.T.	100	H <sub>2</sub> O + Sodium Chromate	.83	
	R.T.	100	H <sub>2</sub> O	.86	
	R.T.	100	Nitrogen, Air or BOK	.86	
	R.T.	100	Aerocast 50	.82	
	80	100	H <sub>2</sub> O <sub>2</sub> (.30% HO)	.71	
	100	100	Monomethylhydrazine	.76	
110	100	Aerocast 50	.75		
6Al-4V Titanium Weldments (Heat Affected Zone)	R.T.	125	Methanol	.30	
	R.T.	125	Freon M.F.	.48	
	R.T.	170	H <sub>2</sub> O	.83	
	R.T.	125	H <sub>2</sub> O + Sodium Chromate	.82	
6Al-3 1/2 Sn (SL) Titanium Plate	320	100	LH <sub>2</sub> (σ < Prop. Limit)	> .90	
	320	100	LH <sub>2</sub> (σ > Prop. Limit)	.82	
	423	210	LH <sub>2</sub>	> .90	
2219-T87 Aluminium Plate	R.T.	66	Air	.80*	
	320	66	LH <sub>2</sub>	.82*	
	423	72	LH <sub>2</sub>	> .85*	
4340 Steel	R.T.	204	Water	.24	
4340 Steel	R.T.	> 200	Salt Water	< .28	
ATA Welds:					
1004 (200) Steel	R.T.	200	Salt Water Spray	> .70	
1004 (250) Steel	R.T.	230	Salt Water Spray	> .70	
1704-6C-200 Steel	R.T.	170	Salt Water Spray	> .70	
6061-4C-2.5C Steel	R.T.	170	Salt Water Spray	> .70	
Inconel 718	R.T.	180	Deionized Hydrogen at 1000 psi	< .25	98.

\* No Failure K<sub>TH</sub>. Some Growth Observed at Lower Values. See Ref.

Table 1 Typical threshold stress intensity data for various material - environment combinations

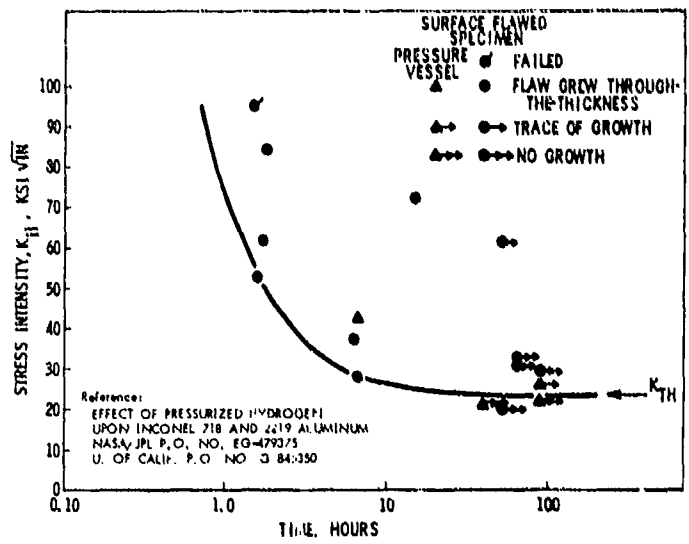


Fig. 15 Sustained load flow growth data for Inconel 718 in 5200 psig hydrogen gas at room temperature

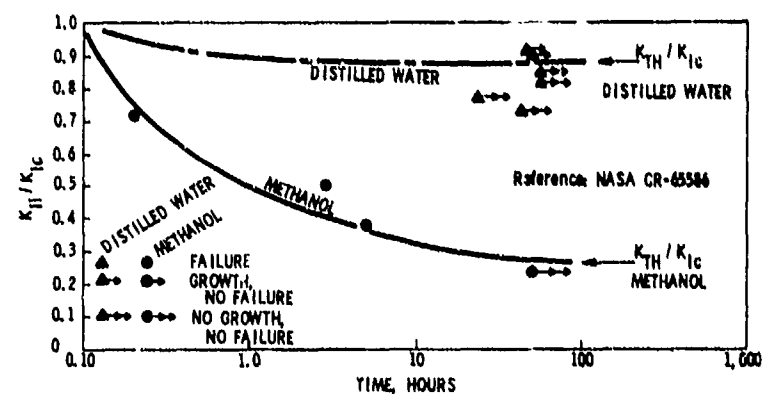


Fig. 16 Sustained load flow growth data for 6Al-4V titanium S.T.A. forging at room temperature

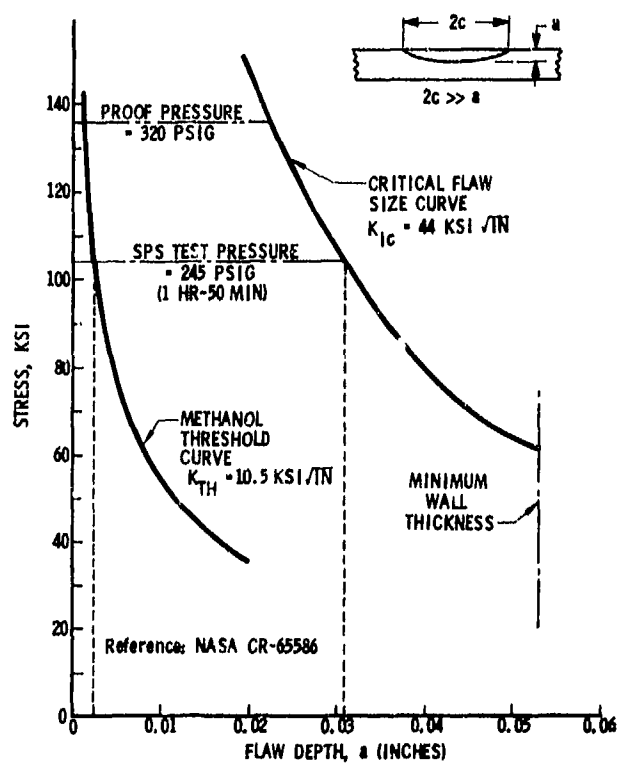


Fig. 17 Critical and threshold flaw size curves (SPS fuel tank cylinder)

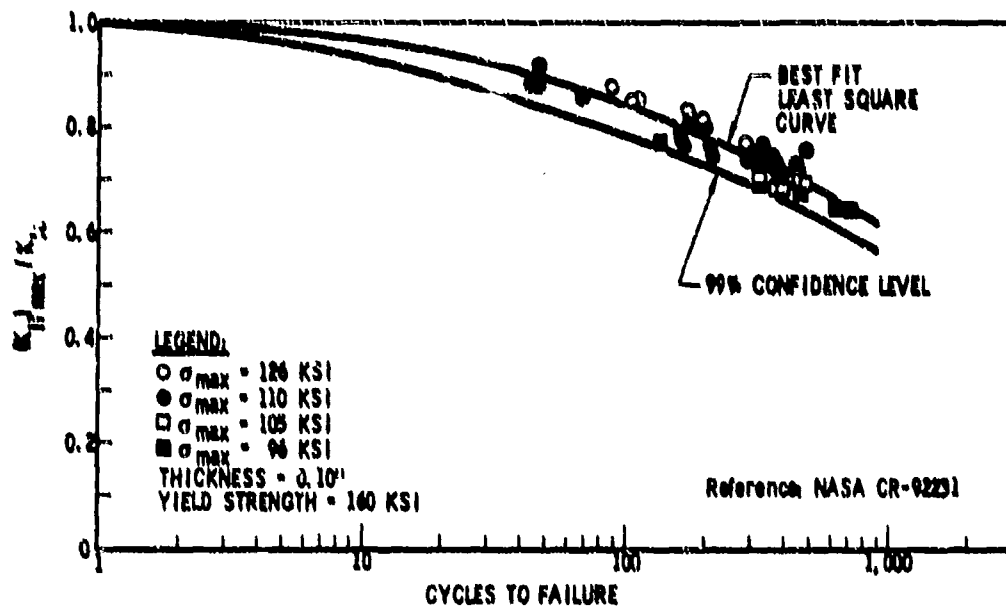


Fig. 18 Cyclic flaw growth data for heat treated 6Al-4V titanium  
R = 0.10 environment = R.T. air

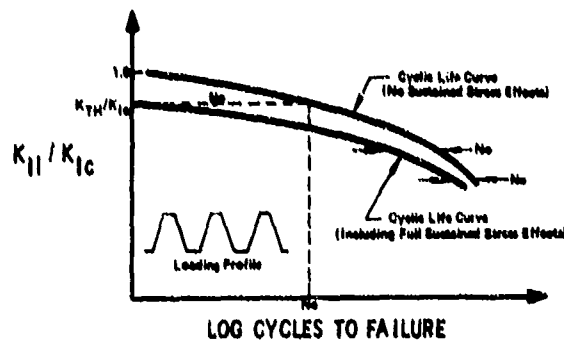


Fig. 19(a) Estimated cyclic life bounds for combined cyclic and cyclic and sustained stress flaw growth

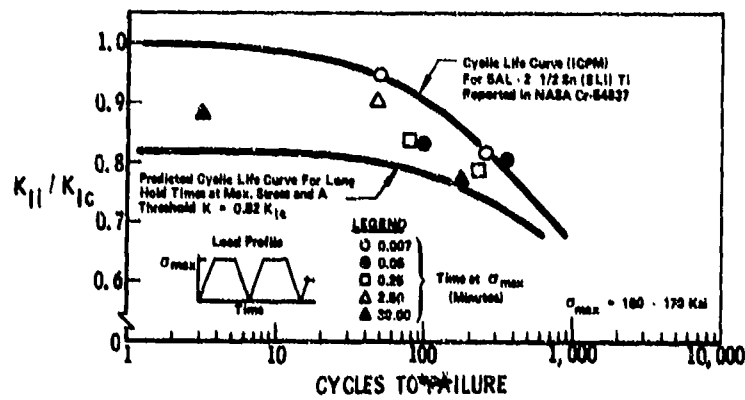


Fig. 19(b) Combined sustained and cyclic stress life data (5Al-2.5Sn (BLI) titanium at -320°F)

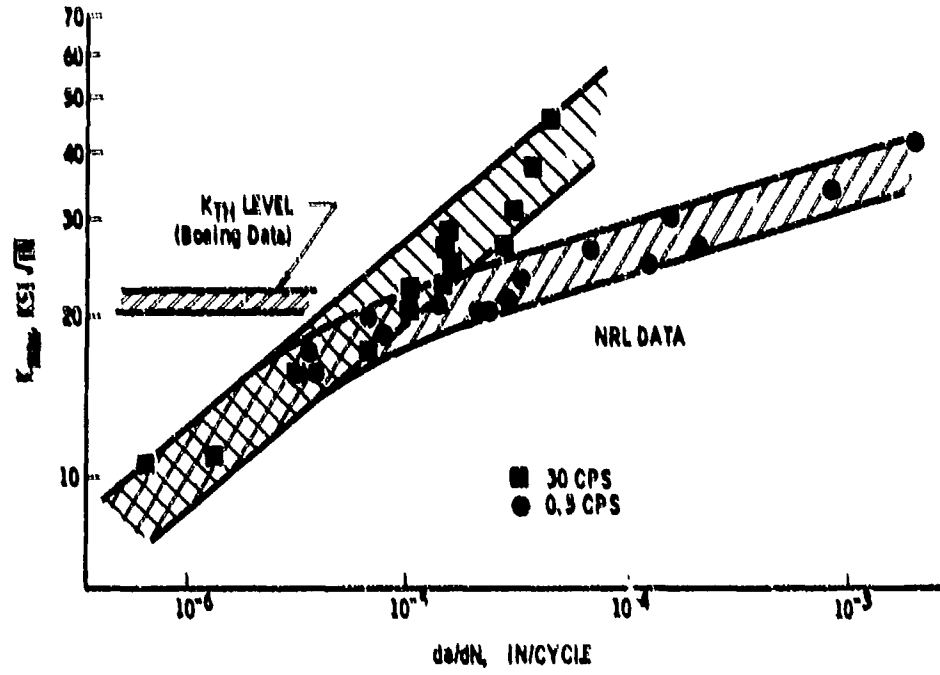
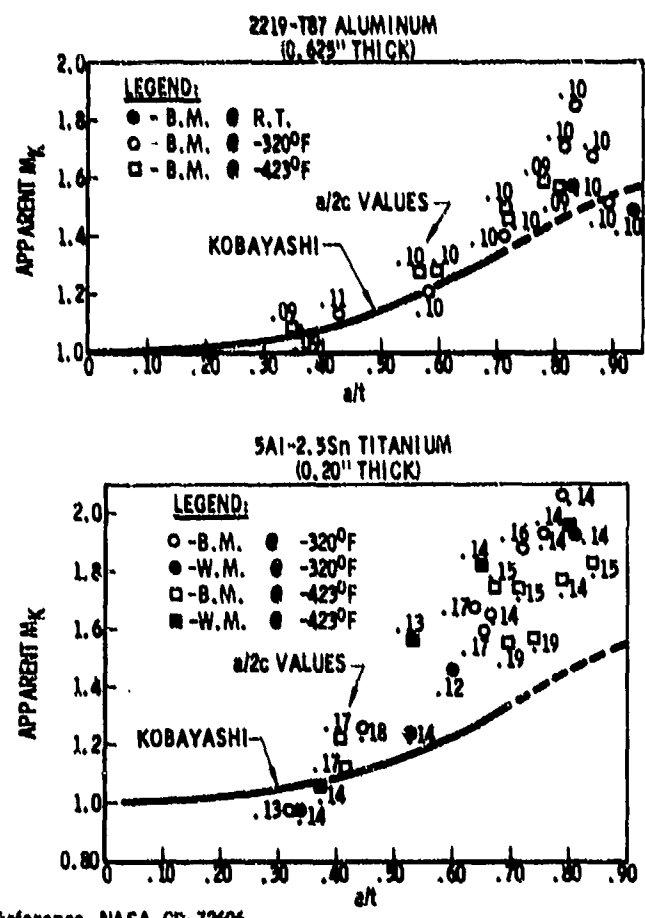


Fig.20 Aggressive environment flaw growth (8Al-1Mo-1V-Ti in saltwater at R.T.)



Reference: NASA CR-72606

Fig.21 Deep flaw stress intensity magnification

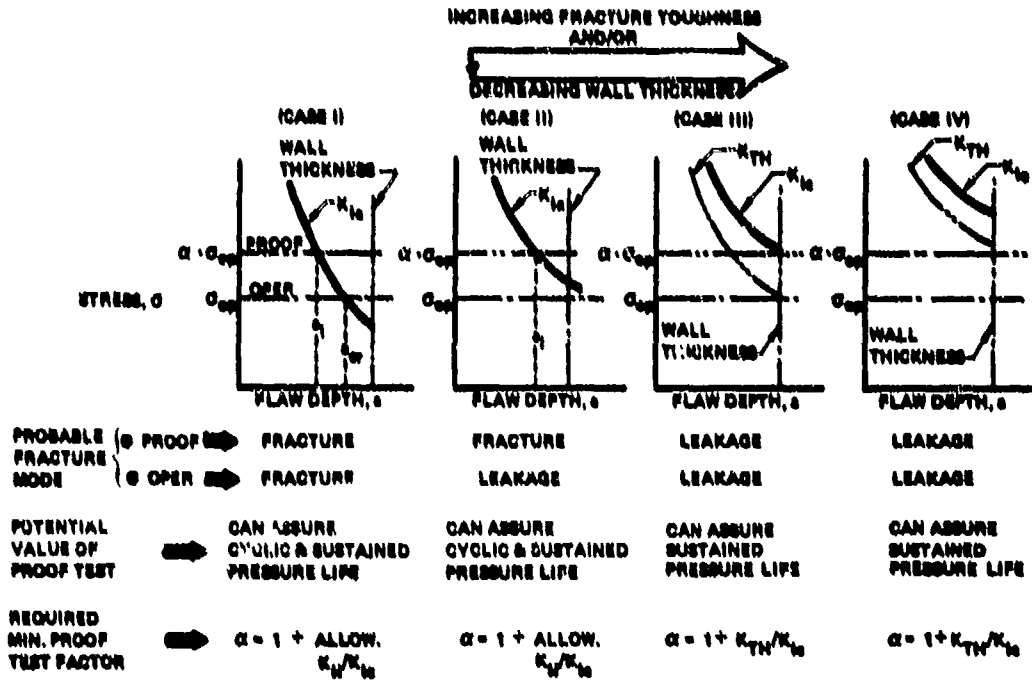


Fig.22 The effect of wall thickness on value of the proof test

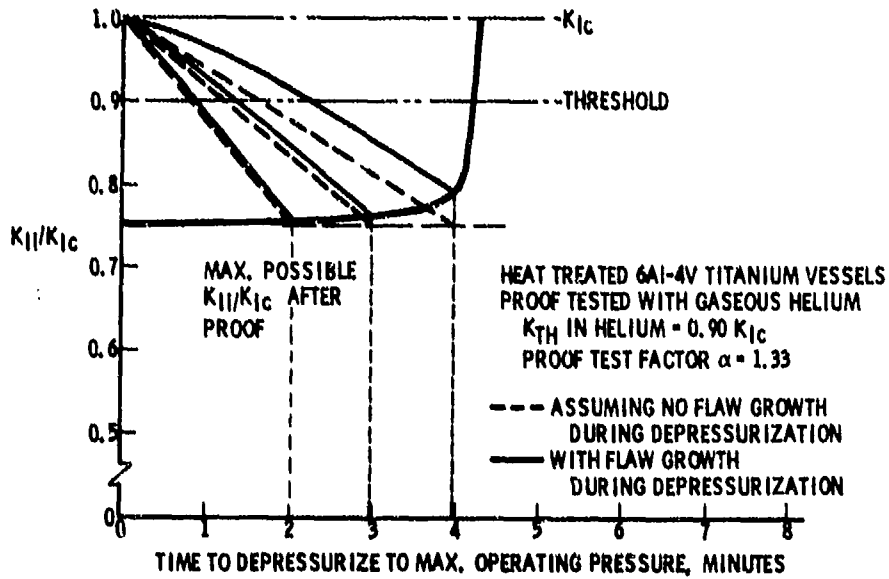


Fig.23 The effect of depressurization time on value of the proof test (thick walled tanks)

## REFERENCES

1. Srawley, J. E.; and Regar, J. B.: Investigation of Hydrotest Failure of Thiokol Chemical Corporation 260-inch Diameter SL-1 Motor Case, NASA TM X-1194, 1966.
2. Tiffany, C. F.; Lorenz, P. M.; and Shah, R. C.: Extended Loading of Cryogenic Tanks. NASA CR-72252, 1967.
3. Tiffany, C. F.; and Masters, J. N.: Investigation of the Flaw Growth Characteristics of 6Al-4V Titanium Used in Apollo Spacecraft Pressure Vessels. NASA CR-65586, 1967.
4. Hall, L. R.: Plain Strain Cyclic Flaw Growth in 2014-T62 Aluminum and 6Al-4V (ELI) Titanium. NASA CR-72396, 1968.
5. Brown, B. F.: A New Stress Corrosion Cracking Test Procedure for High Strength Alloys. Paper presented at the ASTM Arsenal Meeting at Purdue University (Lafayette, Ind.), June 13-18, 1965.
6. Johnson, H. H.; and Paris, P. C.: Subcritical Flaw Growth. Engineering Fracture Mechanics, Vol 1, No. 1, June 1968, pp. 3-45.
7. Peterson, M. H.; Brown, B. F.; Newbegin, R. L.; and Grover, R. E.: Stress Corrosion Cracking of High Strength Steel and Titanium Alloys in Chloride Solutions at Ambient Temperature Corrosion, Vol. 23, No. 5, May 1969, pp. 142-148.
8. Piper, D. E.; Smith, S. H.; and Carter, R. V.: Corrosion Fatigue and Stress Corrosion Cracking in Aqueous Environments. Metals Engineering Quarterly, Vol. 8, Aug. 1968, pp. 50-63.
9. Smith, H. R.; Piper, D. E.; and Downey, F. K.: A Study of Stress Corrosion Cracking by Wedge Force Loading Engineering Fracture Mechanics, Vol 1, No. 1, June 1968, pp. 123-128.
10. Johnson, H. H.; and Willner, A. M.: Moisture and Stable Crack Growth in a High Strength Steel. Applied Materials Research, Vol. 4, No. 1, Jan. 1965, pp. 34-40.
11. Steigerwald, E. A.; and Benjamin, W. D.: Stress Corrosion Cracking Mechanisms in Martinitic High Strength Steels. Third Quarterly Progress Report, Contract AF 33(615)-3651, Air Force Materials Laboratory, 1967.
12. Irwin, C. R.: Moisture Assisted Slow Crack Extension in Glass Plate. Memorandum Report 1678, Naval Research Laboratory. 1966.
13. Masters, J. N.: Cyclic and Sustained Load Flaw Growth Characteristics of 6Al-4V Titanium. NASA CR-92231, 1968.
14. Beachem, C. D.; and Brown, B. F.: A Comparison of Three Specimens for Evaluating the Susceptibility of High Strength Steel to Stress Corrosion Cracking. Internal Report, U.S. Naval Research Laboratory, 1967.
15. Tiffany, C. F.; and Lorenz, P. M.: An Investigation of Low-Cycle Fatigue Failures Using Applied Fracture Mechanics. Report ML-TDR-64-53, May 1964.
16. Tiffany, C. F.; Lorenz, P. M.; and Hall, L. R.: Investigation of Plane Strain Flaw Growth in Thick-Walled Tanks. NASA CR-54837, 1966.
17. Lorenz, P. M.: Fracture Toughness and Sustained Flaw Growth Characteristics of Inconel 718 in the Environment of Pressurized Gaseous Hydrogen. Report D2-114404-1, The Boeing Co., Oct. 1968.
18. Tiffany, C. F.; and Masters, J. N.: Applied Fracture Mechanics. Fracture Toughness Testing and Its Applications. ASTM Spec. Tech. Publication No. 381, 1965, pp. 249-277.
19. Koetje, E. L.: Report on Failure of T. E. Actuator. Report D2-16676-1, The Boeing Co., July 1965.
20. Haese, W. P.: Investigation of Fracture of 6Al-4V Titanium in  $N_2O_4$ . Report D2-24057-1, The Boeing Co., Dec. 1965.
21. Barsom, J. M.: Corrosion-Fatigue Crack Propagation Below  $K_{ISCC}$ . Paper presented at the National Symposium on Fracture Mechanics at Lehigh University (Bethlehem, Pa.), Aug 26, 1969.
22. Wei, R. P.: Some Aspects of Environment-Enhanced Fatigue Crack Growth. Paper presented at ASTM Fall Meeting (Atlanta, Ga.), Oct. 3, 1968.
23. Irwin, G. R.: Crack Extension Force for a Part-Through Crack in a Plate. Trans. ASME, J. Appl. Mech., Series E, Vol. 29, No. 4, Dec. 1962, pp. 651-654.
24. Kobayashi, A. S.: On the Magnification Factors of Deep Surface Flaws. Structural Development Research Memorandum No. 16, The Boeing Co., Dec. 1965.
25. Smith, F. W.: Stress Intensity Factor for a Semi-Elliptical Flaw. Structural Development Research Memorandum No. 17, The Boeing Co., Aug. 1966.
26. Tiffany, C. F.; Masters, J. N.; and Pall, F.A.: Some Fracture Considerations in the Design and Analysis of Spacecraft Pressure Vessels. Paper presented at the ASM National Metals Congress (Chicago), Oct. 1966.

REFERENCES (CONT'D)

27. Shah, R.C.; and Kobayashi, A.S.: Stress Intensity Factor for an Elliptical Crack Under Arbitrary Normal Loading. Paper presented at the Second National Symposium on Fracture Mechanics at Lehigh University (Bethlehem, Pa.), June 17-19, 1968.
28. Kobayashi, A.S.; Ziv, M.; and Hall, L. R.: Approximate Stress Intensity Factor for an Embedded Elliptical Crack Near Two Parallel Free Surfaces, Int. J. of Fracture Mechanics, Vol 1, No. 2, June 1965, pp. 81-95.
29. Shah, R. C.; and Kobayashi, A. S.: On the Parabolic Crack in an Elastic Solid. Engr Fracture Mechanics, Vol 1, No. 2, Aug 1968. pp. 309-325.
30. ASTM Special Committee on Fracture Testing of High-Strength Metallic Materials: Progress in the Measurement of Fracture Toughness and the Application of Fracture Mechanics to Engineering Problems. Materials Research and Standards, Vol 4, No. 3, Mar. 1964, pp. 107-119.
31. Johnson, H. A., et al: Large Motor Case Evaluation. Annual Progress Report, Vol 11, USAF Contract AF33(615)-1623, June 1965.
32. Tiffany, C. F.: Fracture Control of Metallic Pressure Vessels, NASA SP-8040, 1970.

ACKNOWLEDGEMENTS

The author wishes to acknowledge the contributions of Mr. G. Smith of NASA Lewis Research Center, Cleveland, Ohio, and Mr S. Glorioso of NASA Manned Space Flight Center, Houston, Texas. Mr Smith has been intimately involved in many of the technical research programs cited in this chapter and directly contributed to a portion of the text. Mr Glorioso was involved with the Apollo pressure vessel work cited in this chapter and likewise contributed to the text.

At the time this chapter was originally drafted the author was in charge of the Structures and Materials Research organization of the Boeing Company's Aero-Space Group, Seattle, Washington.

## APPENDIX I

Nondestructive Inspection (NDT) Applied to Pressure Vessels

The more common inspection procedures used in the inspection of aerospace pressure vessels are radiographic, ultrasonic, penetrant, and magnetic particle. Other laboratory techniques, which have been investigated for potential production usage, include eddy current and infrared (Reference 31). A number of studies have been performed during the past several years for the purpose of evaluating the capabilities of these various techniques to detect the different types of flaws found in pressure vessels (Reference 1 and 31). The results of these studies combined with actual pressure vessel inspection experience lead to the following general conclusions:

1. With the use of multiple inspection systems (e.g., X-ray, ultrasound, and penetrant) most surface and internal flaws encountered in pressure vessels can be, and generally are detected. However, it is unsafe to assume that all potentially dangerous flaws will be found all of the time (e.g., tight cracks are particularly difficult to detect).
2. The lower limits of inspection detection capability (i.e., the largest initial flaw sizes which can escape detection) cannot be confidently established.
3. The inspection procedures commonly in use do not provide the precise measure of initial flaw sizes (i.e., length and depth) necessary for use in obtaining a reliable minimum life estimation.
4. Regardless of the limitations, there is no practical alternative but to rely on non-destructive inspection in the prevention of proof test failures of most high strength pressure vessels.



## APPENDIX 2

Acceptance of Apollo Propellants and Fluids Based on Fracture Specimen Tests

All fluids to which Apollo pressure vessels are exposed are compatibility tested with 6Al-4V titanium solution treated and aged using precracked, PTC, type specimens. The crack growth threshold of the fluid and the maximum possible flaw which can exist in the pressure vessel based on the proof test plus subsequent cyclic flaw growth determines the maximum pressure at which the fluid can be utilized. Some fluids such as inhibited nitrogen tetroxide and trichlorotrifluoroethane (Freon TF) have been found to have threshold values which vary significantly from batch to batch. In some instances fluids had to be disposed of and replaced.

For flight fluids such as inhibited nitrogen tetroxide and Aerozine 50, the hypergolic oxidizer and fuel, respectively, a sample is extracted at each spacecraft-fluid distribution system interface. This sample would include any contamination which might be introduced anywhere in the storage or propellant loading system. Also, it would be representative of possible depletion of crack growth inhibitors such as nitrous oxide in the nitrogen tetroxide.

Results on the fluids used on the Apollo flights to date have shown the nitrogen tetroxide threshold varied from 72 to 81 percent  $K_{Ic}$ . The Aerozine 50 has varied from 76 to 84 percent of  $K_{Ic}$ .

In ground tests, the oxidizer and fuel are simulated using Freon TF and water, respectively. The water which has varied slightly in Ph and halide content has had a threshold spread from 71 to 80 percent of  $K_{Ic}$ . Generally, the Freon TF has been found to have a threshold in excess of 59 percent; however, in one instance a threshold of 46 percent was determined and this fluid was discarded.

In summary, small amounts of contamination or subtle differences in chemistry have resulted in significant differences in slow crack growth characteristics. It has been found in the Apollo program that utilizing fracture specimen tests as an added means of fluid quality control has been necessary to preclude exposing pressure vessels above a threshold based on the maximum possible flaw which could exist in the vessel.

## V.C.5 AN EXAMPLE OF A METHOD FOR PREDICTING FAILURE

G. H. Haslam

V.C.5.1	Introduction . . . . .	314
C.5.2	Approach . . . . .	314
C.5.3	Stress Intensity Factor . . . . .	314
C.5.4	Crack Propagation Life . . . . .	315
C.5.5	Fatigue Limit . . . . .	315
C.5.6	Comparison with Experimental Results . . . . .	317
C.5.7	Design Curves . . . . .	319
C.5.8	Yield Criteria . . . . .	319
C.5.9	Discussion . . . . .	322
C.5.10	Conclusions . . . . .	322

## V.C.5 AN EXAMPLE OF A METHOD FOR PREDICTING FAILURE

G.H. Haslam

## V.C.5.1 Introduction

In this chapter a method is put forward for estimating the life to failure of a cylindrical pressure vessel subjected to repeated internal pressure. Design curves are obtained by which the fatigue life of such a cylinder may be estimated from a knowledge of the transverse uniaxial fatigue limit and fracture toughness properties of the cylinder material, as well as the diameter ratio of the cylinder and the repeated pressure. Examples are given of the application of the method and close correlation is demonstrated between estimated and actual behaviour.

## V.C.5.2 Approach

Paris and Erdogan<sup>1</sup> proposed that, since the elastic stress field and the size of any plastic zone around a crack tip are proportional to the stress intensity factor  $K_I$ , the rate of crack propagation of a fatigue crack should be a function of  $K_I$ . They found that a large body of experimental data could be fitted by an expression of the form

$$\frac{da}{dN} = B(\Delta K)^m \quad (1)$$

Frost<sup>2</sup> observed fatigue crack growth in sheet specimens of a wide range of materials. He found that the initial rate of crack growth of a central transverse crack in a sheet specimen subjected to the loading cycle  $\sigma_m \pm \sigma_a$ , where  $\sigma_m > \sigma_a$ , was given by

$$\frac{da}{dN} = A\sigma_a^3 \quad (2)$$

Owing to the inherent scatter in the observed results, both equations (1) and (2) may be applied with equal confidence, although equation (1) is applicable to a wider range of crack lengths. Indeed, Frost's results have been re-analysed (Frost, Pook and Denton<sup>3</sup>) in terms of the range of stress intensity factor ( $\Delta K$ ) and it was concluded that this analysis could be regarded as an alternative to the use of the parameter  $\sigma_a^3$ .

In the method presented, the crack propagation life of a cylinder subjected to repeated internal pressure is estimated by means of the range of stress intensity factor as used in equation (1). The stress intensity factor used is a simplified approximation to that which would be expected under the complex conditions at the bore of a pressurized cylinder. The effect of the high pressure oil in contact with the bore surface is taken into account by considering high local effective stresses at the crack.

## Notation

A	} material constants describing fatigue crack growth
B	
C	
m	
a	current crack length
a <sub>c</sub>	final crack length
a <sub>0</sub>	initial crack length
b	transverse uniaxial fatigue limit in repeated tension
K <sub>I</sub>	stress intensity factor
L	$\left[ \frac{1}{\left( \frac{R^2+1}{R^2-1} + \frac{5}{R+1} \right) \sqrt{\left( \frac{R^2+1}{R^2-1} + \frac{5}{R+1} \right)^2 + 1}} \right]^{3/2}$
N	fatigue life
P	internal pressure
P <sub>L</sub>	internal pressure at fatigue limit
P <sub>y</sub>	internal pressure to cause yield at bore
R	outer/inner diameter ratio
$\sigma$	range of maximum principal stress
$\sigma_e$	local effective maximum principal stress at the fatigue limit
$\sigma_m, \sigma_a$	mean stress and stress amplitude in crack propagation relationship
$\sigma_y, \tau_y$	yield stresses in uniaxial tension and shear
$\Delta K$	range of stress intensity factor

## V.C.5.3 Stress intensity factor

The stress intensity factor for a straight-fronted edge crack, length  $a$ , in a semi-infinite plate subjected to stress  $\sigma$ , is given by Paris and Sih<sup>4</sup> as

$$K_I = 1.1\sigma(\pi a)^{1/2}$$

and for a semi-circular fronted edge crack by

$$K_I = 1.1\sigma(\pi a)^{1/2} 0.69$$

The crack front profile observed on fatigue tests on thick-walled cylinders under pulsating internal pressure approximates to a semi-ellipse. The value of  $K_1$ , therefore, would be expected to be within the above limits, and is assumed to be approximately

$$K_1 = \sigma(\pi a)^{1/2} \quad (3)$$

In deriving an accurate expression for the stress intensity factor around a crack in a cylinder wall, further complications arise owing to the finite wall thickness and the stress gradient in the wall. The finite wall thickness causes the value of  $K_1$  to increase, but the stress gradient causes a decrease in  $K_1$ . Since most of the fatigue crack propagation life is spent on propagating a crack over a small distance from the bore surface, the above conditions in the cylinder wall will have only a secondary effect. Therefore, in the present analysis, their combined effect is neglected. Hence, the expression used for stress intensity factor is that given by equation (3).

#### V.C.5.4 Crack propagation life

By substituting equation (3) in equation (1) and integrating, the following expression for crack propagation life of the cylinder is obtained.

$$N = \frac{2}{2-m} \frac{1}{B\sigma_0^m \pi^{m/2}} \left( a^{(2-m)/2} \right)_{a_0}^{a_c} \text{ cycles} \quad (4)$$

When a fatigue crack propagates through the wall of a cylinder, bursting occurs by fast fracture before the crack has propagated to the outer surface. However, the current rate of crack propagation when the crack is long enough to cause fast fracture is such that relatively few extra cycles would have been required to cause the crack to propagate throughout the wall thickness. In equation (4), therefore, the final crack length  $a_c$  is taken as the cylinder wall thickness.

The original crack length  $a_0$  is taken as the length of crack which will just fail to propagate at the fatigue limit. Frost<sup>2</sup> showed that this was given by

$$a_0 = \frac{C}{(\frac{1}{2}\sigma_e)^3} \quad (5)$$

where  $C$  is a material constant, and  $\sigma_e$  is the effective local hoop stress range at the fatigue limit of the cylinder.

Morrison, Crossland and Parry<sup>5</sup> have shown that the fatigue limit of a cylinder subjected to pulsating internal oil pressure is reduced when the oil is in intimate contact with the bore surface. This decrease in fatigue strength was considered to be caused by local stresses at the fatigue crack due to oil penetration. Haslam<sup>6</sup> proposed that the local effective hoop stress was given by

$$\sigma = P \left( \frac{R^2 + 1}{R^2 - 1} + \frac{5}{R + 1} \right) \quad (6a)$$

and, at the fatigue limit,

$$\sigma_e = P_L \left( \frac{R^2 + 1}{R^2 - 1} + \frac{5}{R + 1} \right) \quad (6b)$$

Haslam also showed<sup>6</sup> that the repeated pressure at the fatigue limit was given by

$$P_L = \frac{b}{\sqrt{\left\{ \left( \frac{R^2 + 1}{R^2 - 1} + \frac{5}{R + 1} \right)^2 + 1 \right\}}} \quad (7)$$

Hence

$$\sigma_e = \frac{b}{\sqrt{\left\{ 1 + \left( \frac{R^2 + 1}{R^2 - 1} + \frac{5}{R + 1} \right)^2 \right\}}} \quad (8)$$

In equation (4), the value of  $\sigma$  is taken as the effective local hoop stress at a crack in the bore surface, as given by equation (6a).

The values of  $B$  and  $m$  in equation (4) may be obtained from the experimental data presented by Frost, Pook and Denton<sup>3</sup>.

#### V.C.5.5 Fatigue limit

From equation (7), it is possible to estimate the fatigue limit of a cylinder subjected to repeated internal pressure. This equation is shown plotted in Fig.1, in terms of  $P_L/b$  against  $R$ . From this curve, knowing the transverse fatigue strength of the cylinder material, it is possible to estimate the fatigue limit of a cylinder of a given diameter ratio.

Thus, by using equations (4) and (7), it is possible to obtain a theoretical fatigue curve from the fatigue limit up to gross yielding at the bore of the cylinder. The selection of a criterion to define yielding at the bore is discussed later.

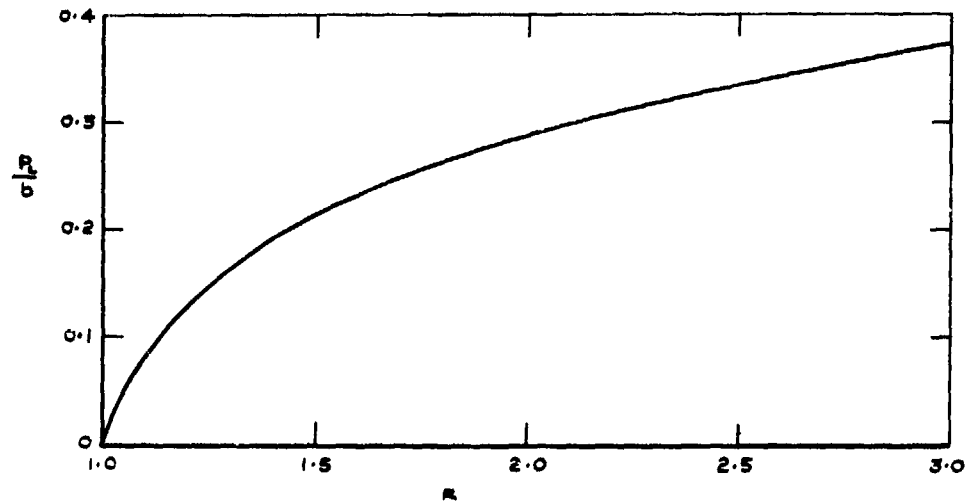


Fig. 1 Fatigue limits of thick-walled cylinders subjected to repeated internal pressures

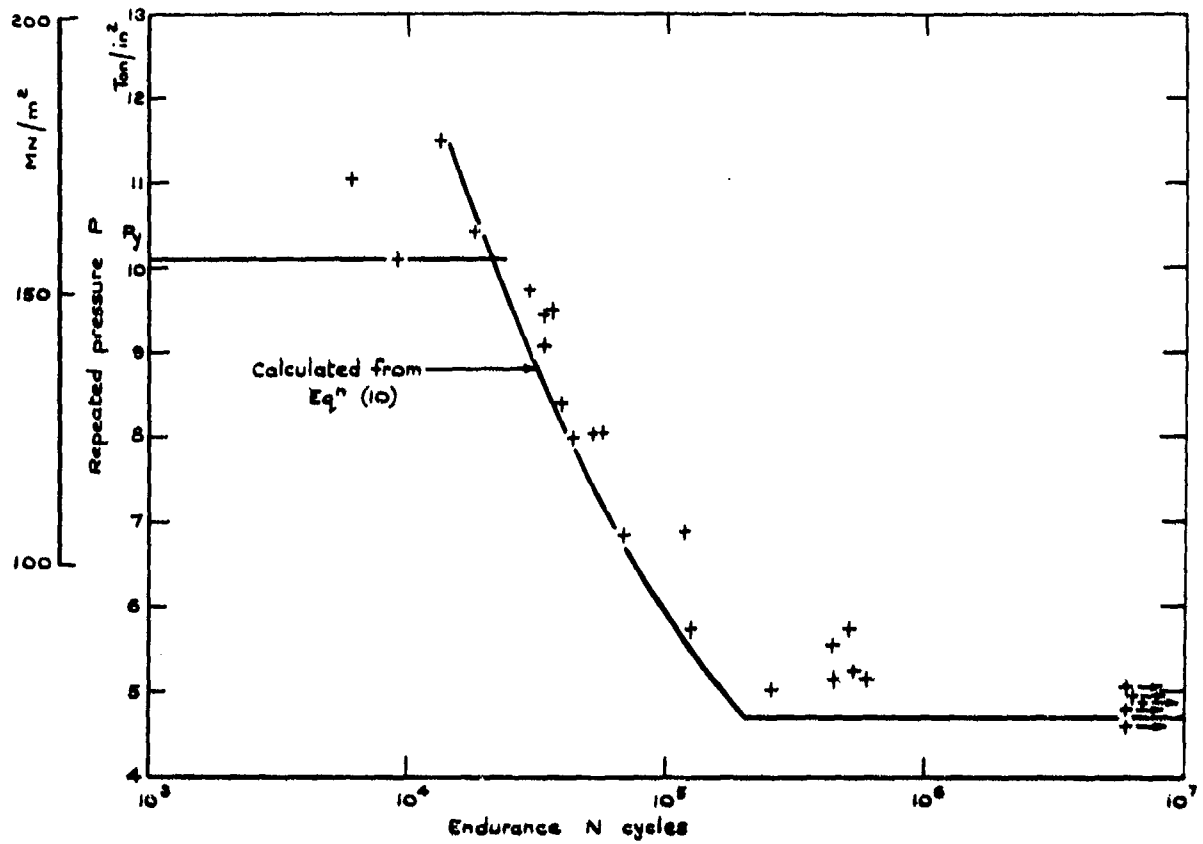


Fig. 2 Estimated fatigue curve for En 26 steel cylinders,  $R = 1.2$

### V.C.5.6 Comparison with experimental results

Frost, Pook and Denton<sup>3</sup> have presented values of  $\Delta K$  for crack growth rates of  $0.025 \mu/c$  ( $10^{-6}$  in/c), and of  $m$  for various materials. From these data, fatigue crack propagation lives may be estimated as given in equations (9)-(16), where the coefficients are applicable when the parameters are in ton/in units.

For mild steel, subjected to a repeated tensile stress,  $m = 3$ , and  $\Delta K = 16.6 \text{ h bar cm}^{1/2}$  ( $6.74 \text{ ton in}^{-3/2}$ ) for  $da/dN = 0.025 \mu/c$  ( $10^{-6}$  in/c).

From equation (1)

$$\frac{da}{dN} = B(\Delta K)^m$$

Solving for  $B$ , and substituting in equation (4), we get

$$N = \frac{110}{\sigma^3} \left( \frac{1}{\sqrt{a_0}} - \frac{1}{\sqrt{a_c}} \right) \times 10^6 \quad \text{cycles} \quad (9)$$

where  $\sigma$  is in ton/in<sup>2</sup> and  $a_0$  and  $a_c$  are in inches.

Fatigue tests have been carried out on cylinders of En 26 steel with a diameter ratio of 1.2. The results presented in (6) may now be compared with the estimated fatigue curve given by equation (9). For this material, the transverse uniaxial fatigue limit,  $b$ , was  $0.573 \text{ MN/m}^2$  ( $0.37 \text{ ton/in}^2$ ). Therefore, for  $R = 1.2$ , equation (8) gives

$$\sigma_s = 567 \text{ MN/m}^2 \quad (36.7 \text{ ton/in}^2)$$

For steel specimens, subjected to repeated tensile stress, the value of  $C$  in equation (5) is  $65 (\text{MN/m}^2)^3 \text{ m}$  ( $0.7 (\text{ton/in}^2)^3 \text{ in}$ ) (Frost and Greenan<sup>7</sup>).

From equation (5),  $a_0 = 28.75 \times 10^{-4} \text{ mm}$  ( $1.132 \times 10^{-4} \text{ in}$ ). The wall thickness of the cylinders,  $a_c$ , was  $2.5 \text{ mm}$  ( $0.1 \text{ in}$ ).

From equation (6a),

$$\sigma = P \left( \frac{R^2 + 1}{R^2 - 1} + \frac{5}{R + 1} \right)$$

for  $R = 1.2$ ,  $\sigma = 7.81P$ . Substituting these values in equation (9) gives

$$N = \frac{20.98}{P^3} \times 10^6 \quad \text{cycles} \quad (10)$$

Equation (10) is shown plotted in Fig.2, in terms of  $P$  against  $\log N$ , the experimental results are also shown for comparison. The estimated fatigue limits shown in Fig.2 are obtained from equation (7).

Further fatigue tests were carried out on cylinders of the same material, with  $25.4 \text{ mm}$  ( $1.0 \text{ in}$ ) bore and  $50.8 \text{ mm}$  ( $2.0 \text{ in}$ ) outer diameter. For these cylinders,  $\sigma_s = 548 \text{ MN/m}^2$  ( $35.5 \text{ ton/in}^2$ ),  $a_0 = 32 \times 10^{-4} \text{ mm}$  ( $1.258 \times 10^{-4} \text{ in}$ ),  $a_c = 12.7 \text{ mm}$  ( $0.5 \text{ in}$ ) and  $\sigma = 3.33P$ . In equation (9) this gives

$$N = \frac{261}{P^3} \times 10^6 \quad \text{cycles} \quad (11)$$

The estimated fatigue curve and experimental results are shown in Fig.3.

Fatigue tests have been carried out by Morrison, Crossland and Parry<sup>5</sup> on thick-walled cylinders of En 25 steel, 'Hykro' steel and 0.15 per cent C mild steel. The results have been compared with the estimated fatigue curves given by equation (9) and it was found that in each case the theory gave good correlation with the experimental results. Most of these results were obtained in the vicinity of the fatigue limit and have not been included in the present paper. However, further work was done by Austin and Crossland<sup>6</sup> on En 25 steel cylinders with diameter ratios of 1.4 and 1.8. The experimental results obtained by both teams of investigators for these cylinders are shown in Figs.4 and 5, compared with the estimated fatigue curve from equations (7) and (9).

Morrison, Crossland and Parry<sup>5</sup> have presented results of fatigue tests on aluminium alloy DTD 364 and commercially pure titanium cylinders. From the data given by Frost, Pook and Denton<sup>3</sup>, it is found that, for the aluminium alloy,  $\Delta K = 5.71 \text{ h bar cm}^{1/2}$  ( $2.32 \text{ ton/in}^{-3/2}$ ) for  $da/dN = 0.025 \mu/c$  ( $10^{-6}$  in/c),  $m = 3.7$  and  $C = 2.8 (\text{MN/m}^2)^3 \text{ m}$  ( $0.03 (\text{ton/in}^2)^3 \text{ in}$ ).

Solving for  $B$  and substituting in equation (4), we get

$$N = \frac{2.94}{\sigma^4} \left( \frac{1}{a_0} - \frac{1}{a_c} \right) \times 10^6 \quad \text{cycles}$$

for  $m = 4$ , and

$$N = \frac{5.57}{\sigma^3} \left( \frac{1}{\sqrt{a_0}} - \frac{1}{\sqrt{a_c}} \right) \times 10^6 \quad \text{cycles}$$

for  $m = 3$ .

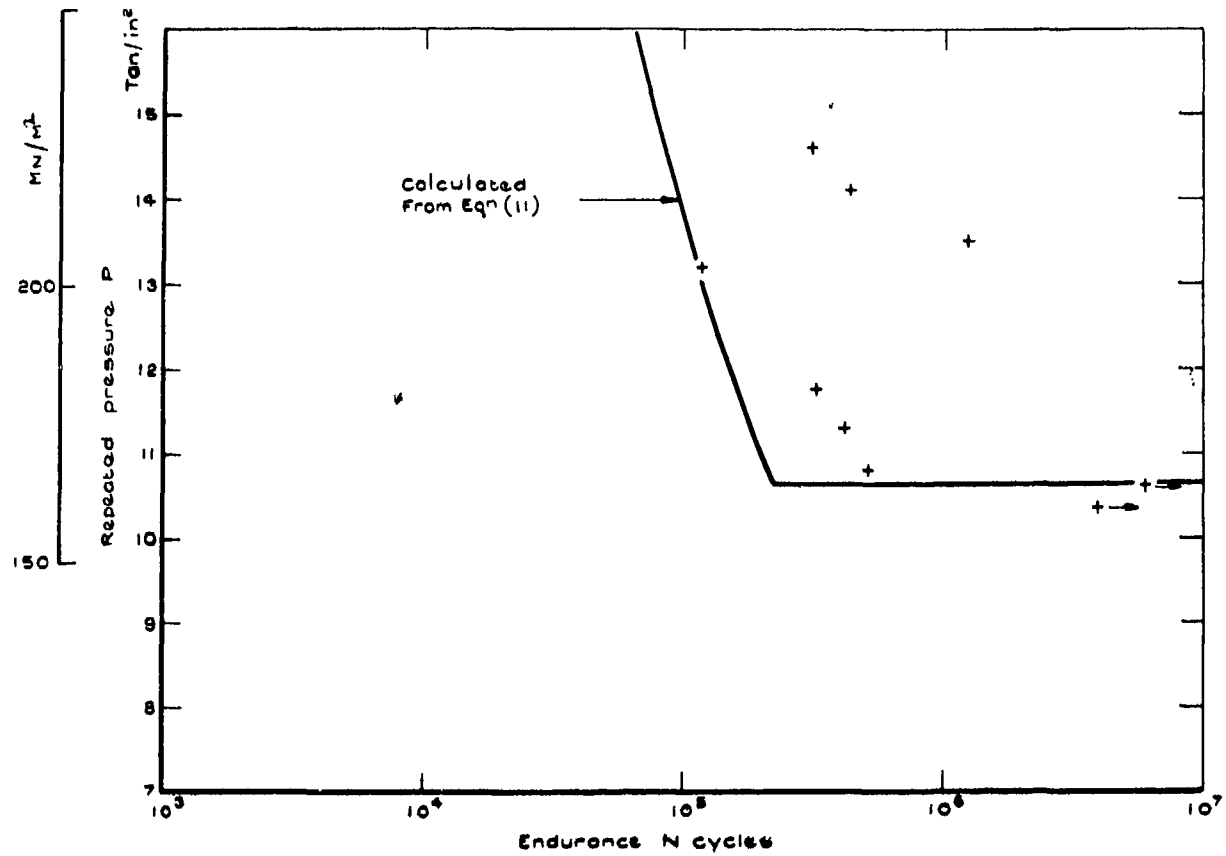


Fig.3 Estimated fatigue curve for En 26 steel cylinders,  $R = 2.0$

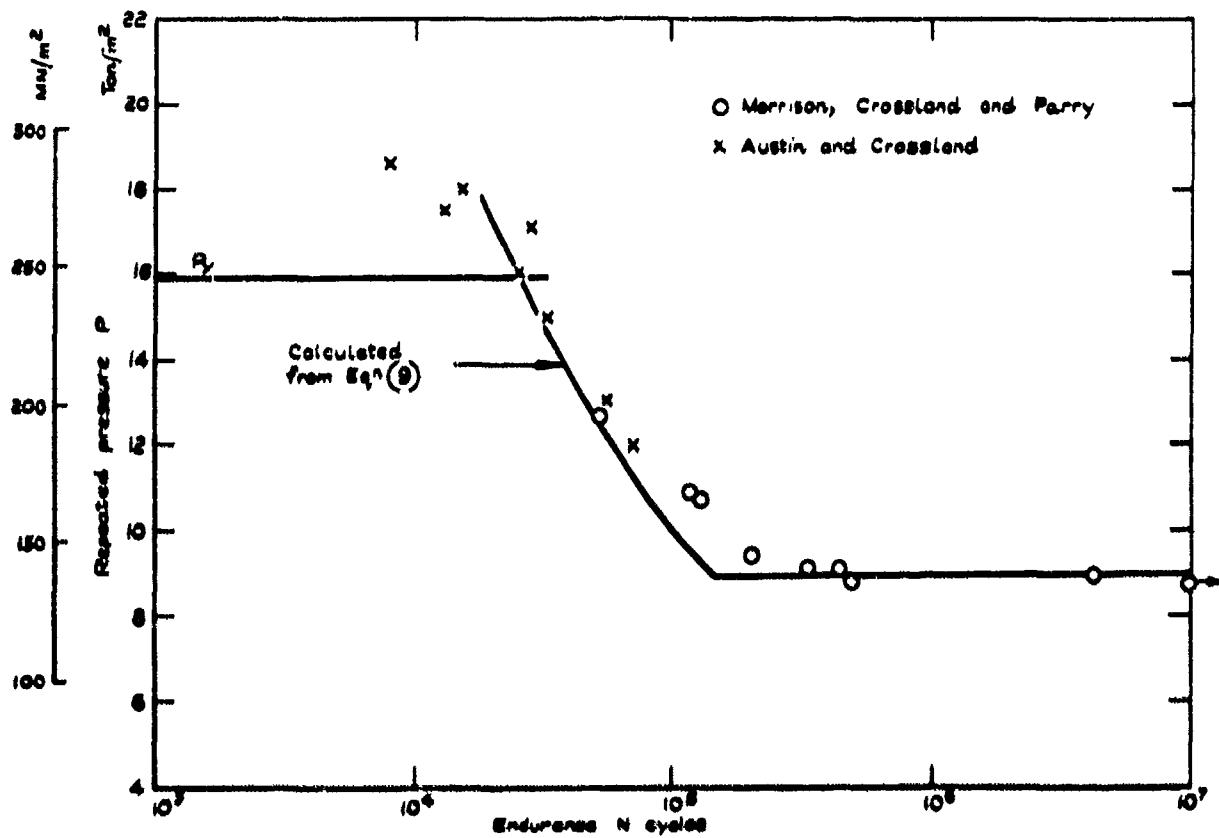


Fig.4 Estimated fatigue curve for En 25 steel cylinders,  $R = 1.4$

The cylinders had a diameter ratio of 2.0 and a wall thickness of 12.7 mm (0.5 in). The transverse fatigue limit of the material was 0-330 MN/m<sup>2</sup> (0-21.4 ton/in<sup>2</sup>). Thus,

$$\begin{aligned}\sigma_e &= 317 \text{ MN/m}^2 \text{ (20.5 ton/in}^2\text{)} \\ a_0 &= 8.25 \times 10^{-4} \text{ mm (0.325} \times 10^{-4} \text{ in)} \\ a_c &= 12.7 \text{ mm (0.5 in)} \\ \sigma &= 3.33P.\end{aligned}$$

Therefore,

$$N = \frac{733.8}{P^4} \times 10^6 \text{ cycles} \quad (12)$$

for  $m = 4$ .

$$N = \frac{26.22}{P^3} \times 10^6 \text{ cycles} \quad (13)$$

for  $m = 3$ .

Fig.6 shows the theoretical fatigue curves for  $m = 3$  and  $m = 4$ . Comparing these with the experimental results, it is seen that a safe fatigue life may be estimated by using  $m = 3$ .

For commercially pure titanium,  $m = 4$ ,  $\Delta K = 6.48 \text{ h bar cm}^{1/2}$  (2.63 ton/in<sup>-3/2</sup>) for  $da/dN = 0.025 \text{ } \mu\text{/c}$  ( $10^{-6} \text{ in/c}$ ) and  $C = 9.3 \text{ (MN/m}^2\text{)}^3 \text{ m}$  (0.1 (ton/in<sup>2</sup>)<sup>3</sup> in) (Frost, Pook and Denton<sup>3</sup>). This gives

$$N = \frac{161.1}{P^4} \times 10^6 \text{ cycles} \quad (14)$$

for  $R = 1.4$ , and

$$N = \frac{1.373}{P^4} \times 10^6 \text{ cycles} \quad (15)$$

for  $R = 2.0$ .

Unfortunately, there are few experimental results available for titanium cylinders. These are shown in Figs.7 and 8, compared with the theoretical fatigue curves.

#### V.C.5.7 Design curves

From equation (9), the fatigue crack propagation curve for steel cylinders is given by

$$N = \frac{1.101 \times 10^8}{\sigma^3} \left( \frac{1}{\sqrt{a_0}} - \frac{1}{\sqrt{a_c}} \right) \text{ cycles}$$

From typical values of  $a_0$  and  $a_c$ , given above, it is seen that  $a_0^{-1/2}$  is negligible compared with  $a_c^{-1/2}$ . Thus, neglecting  $a_0^{-1/2}$ , and substituting the expression for  $\sigma$  and  $\sigma_e$  given in equations (6a) and (6b), we get

$$N = 46.5L \left( \frac{\sqrt{b}}{P} \right)^3 \times 10^6 \text{ cycles} \quad (16)$$

where

$$L = \left[ \frac{1}{\left( \frac{R^2 + 1}{R^2 - 1} + \frac{5}{R + 1} \right) \left( \frac{R^2 + 1}{R^2 - 1} + \frac{5}{R + 1} \right)^2 + 1} \right]^{3/2}$$

Fig.9 shows the fatigue crack propagation curve given by equation (16) for  $R = 1.2$ , together with the experimental results for En 25 and En 26 steel cylinders. The fatigue limits shown in Fig.9 are as given by equation (7) for these materials. In Fig.10, the crack propagation curve for steel cylinders with  $R = 1.4$ , as given by equation (16), is shown compared with the experimental results for cylinders of various steels. The fatigue limits have been omitted from Fig.10 for clarity.

Comparing Figs.9 and 10 with Figs.2 and 4, it is seen that neglecting the term  $a_0^{-1/2}$  in equation (9) has made no significant difference in the estimated fatigue curves.

Fig.11 shows design curves for estimating the crack propagation life of steel cylinders with diameter ratios for 1.2-3.0. Hence, by the use of Figs.1 and 11, it is now possible to obtain an estimated fatigue curve of thick-walled steel cylinders based on the transverse fatigue strength of the cylinder wall. For non-ferrous cylinders, design curves similar to those given in Fig.11 may be obtained, as shown in Figs.6, 7 and 8.

#### V.C.5.8 Yield criteria

The crack propagation life has been estimated using the rate of crack propagation based on linear elastic fracture mechanics theory. It would be expected that this method of estimating the fatigue life

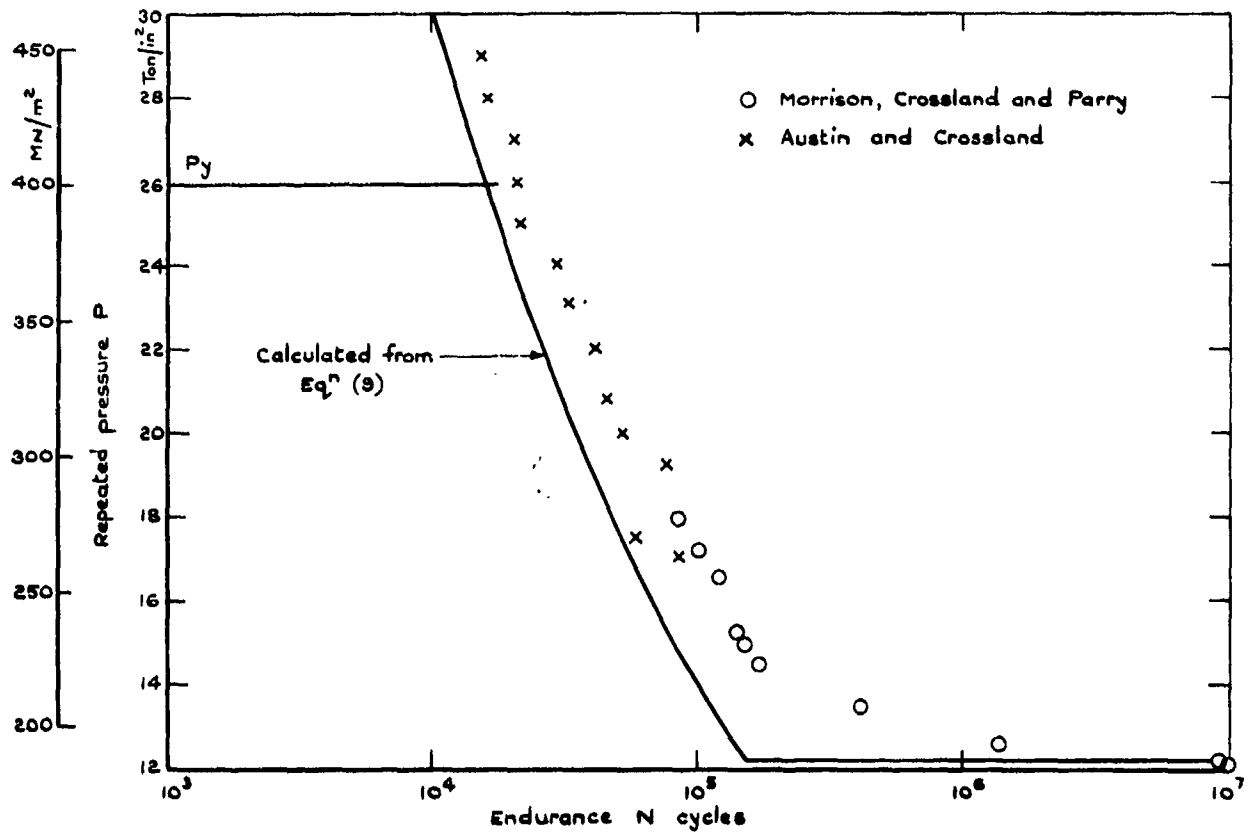


Fig.5 Estimated fatigue curve for En 25 steel cylinders, R = 1.8

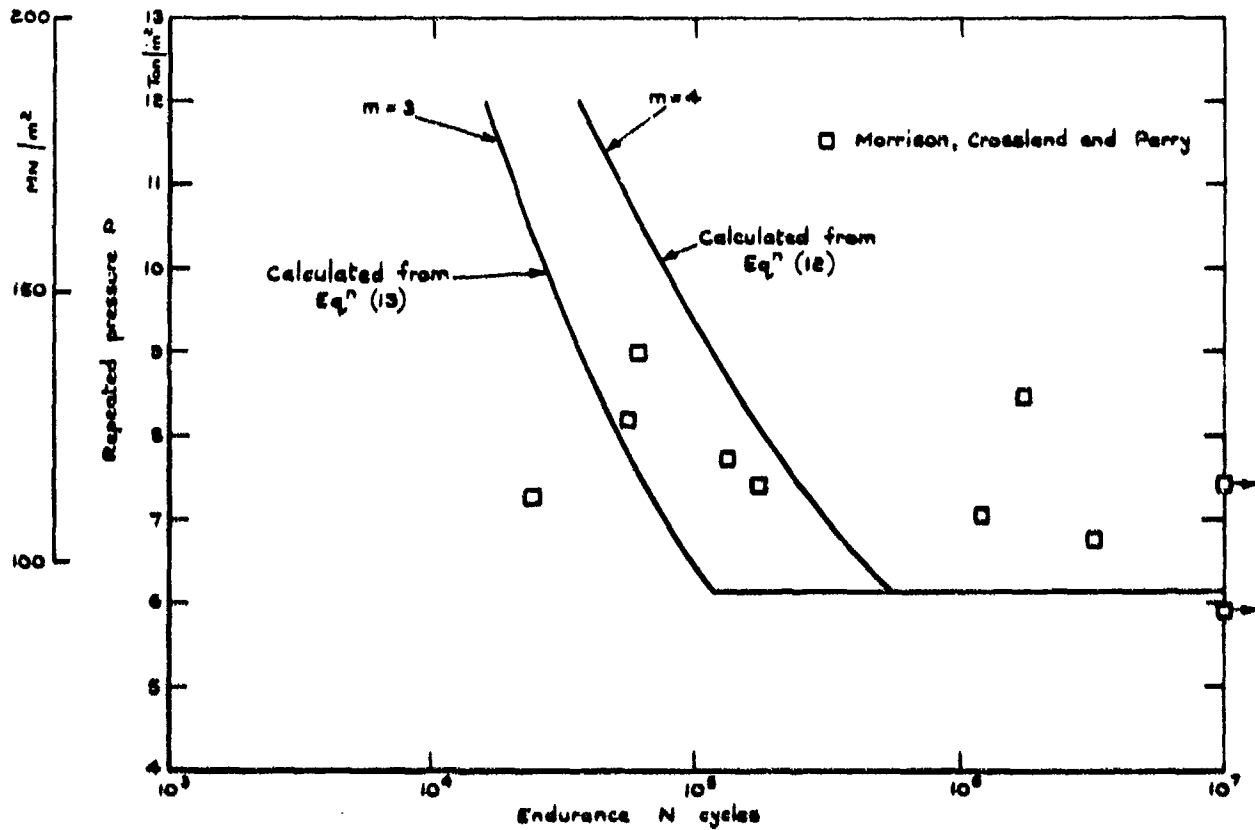


Fig.6 Estimated fatigue curve for aluminium alloy DTD 364 cylinders



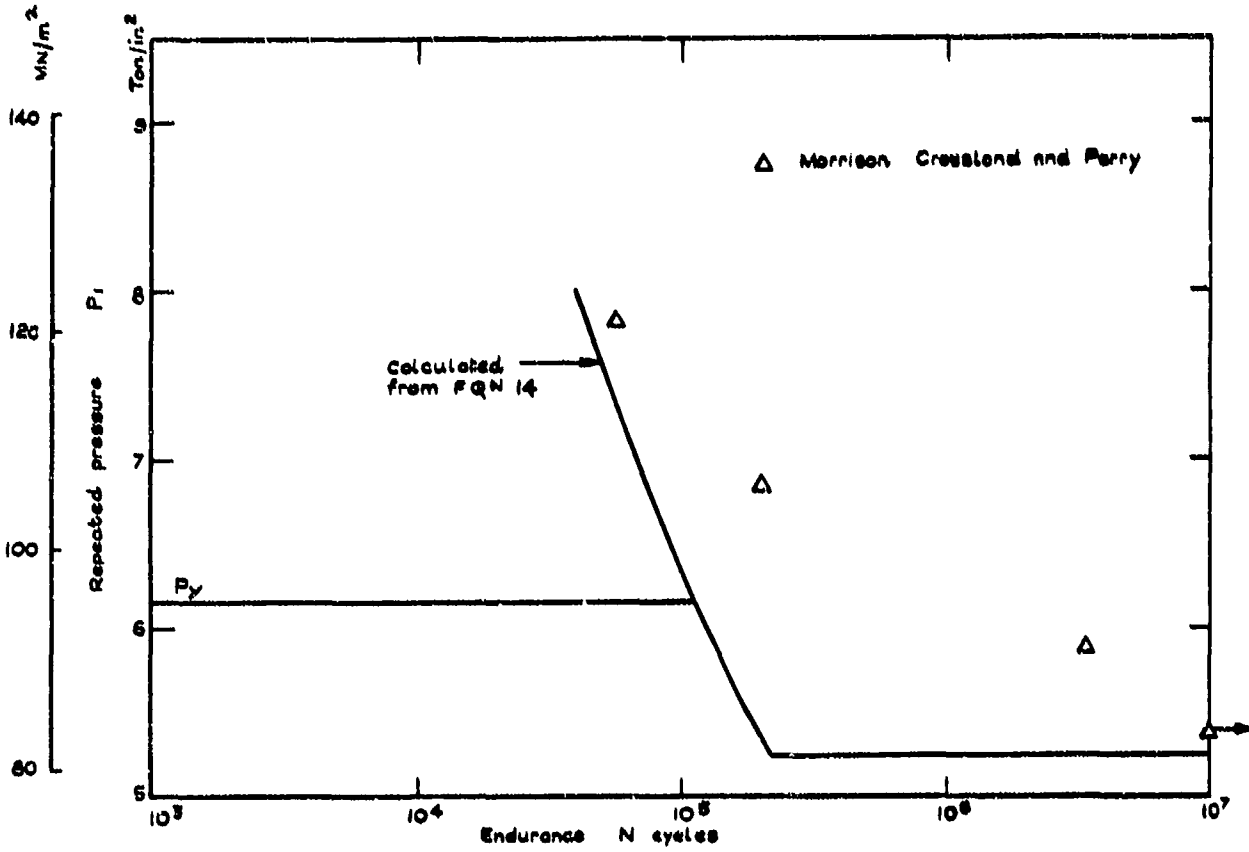


Fig.7 Estimated fatigue curve for commercially pure titanium cylinders,  $R=1.4$

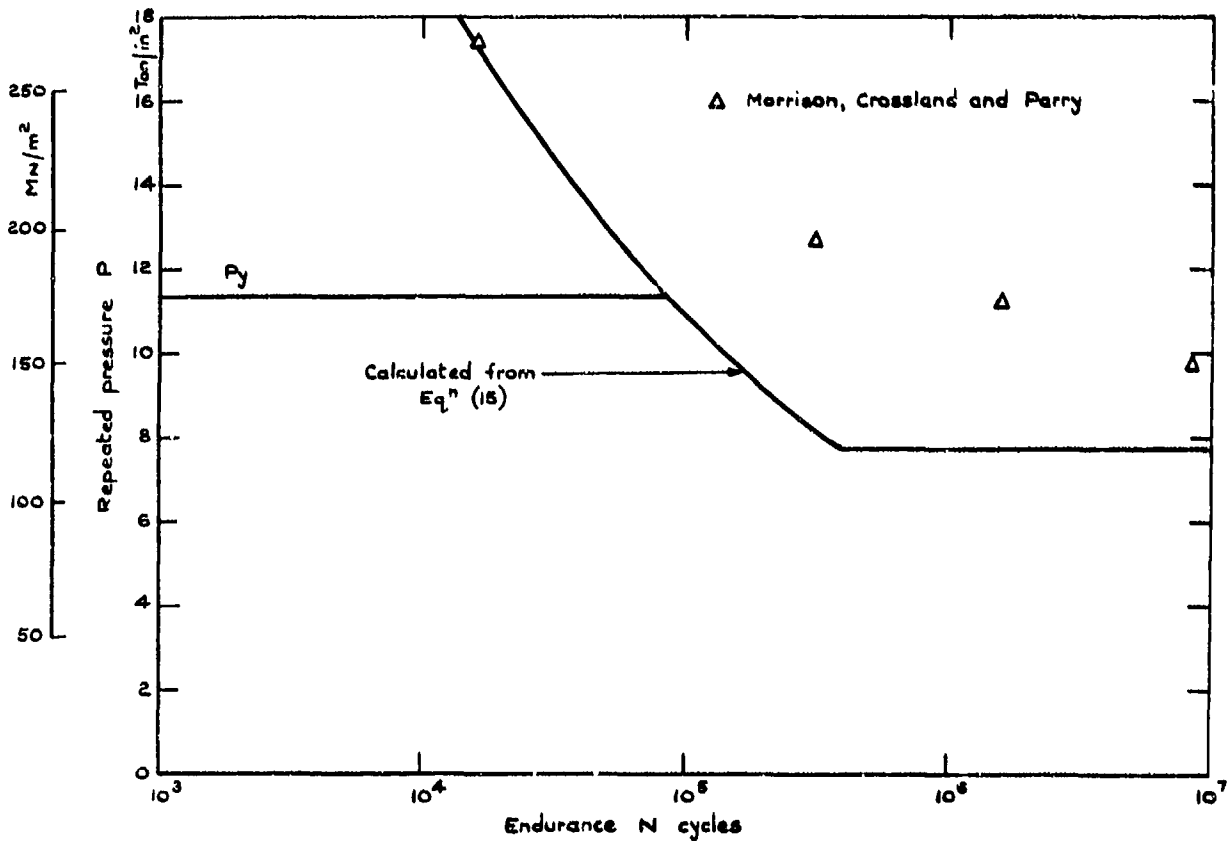


Fig.8 Estimated fatigue curve for commercially pure titanium cylinders,  $R=2.0$

is applicable only in the elastic range of the material. It is necessary, therefore, to define a yield criterion which describes the upper limit of the range of application of the above theory.

Three yield criteria were examined.

- (1) Maximum shear strain energy (von Mises)

$$P_y = \frac{\sigma_y (R^2 - 1)}{\sqrt{3R^4 + 1}}$$

- (2) Maximum principal stress (Rankine)

$$P_y = \frac{\sigma_y (R^2 - 1)}{R^2 + 1}$$

- (3) Maximum shear stress (Tresca)

$$P_y = \frac{\tau_y (R^2 - 1)}{R^2}$$

where  $\sigma_y$  is the yield stress in uniaxial tension,  $\tau_y$  is the yield stress in shear, and  $P_y$  is the internal pressure to cause yield at the bore.

Although the von Mises criterion is normally accepted as applicable to the static yield of ductile metals, it does not give the best fit to the experimental results in this case. The highest yield pressure is given by the maximum principal stress criterion and this is shown in Figs. 2, 4, 5 and 7. As can be seen, the deviation of the experimental points from the theoretical line in all cases occurs above this level. The maximum principal stress is therefore suggested as the most suitable criterion for defining the upper limit of applicability of the proposed method.

In the case of the titanium cylinders (Figs. 7 and 8) the yield pressure given by the maximum principal stress criterion is rather lower than the safe range of the estimated fatigue curve.

Thus, it appears that the crack propagation curve given by equation (4) may be used to estimate the fatigue lives of cylinders subjected to repeated internal pressures not greater than that required to cause yielding in the hoop direction. However, to verify this, further results are required in the high pressure-short endurance region for cylinders with diameter ratios of 2 and greater.

#### V.C.5.9 Discussion

By using an approximate value for stress intensity factor, and considering a high local effective hoop stress at the crack due to oil penetration, it has been possible to estimate satisfactorily the finite fatigue lives of cylinders subjected to repeated internal pressure. To do this, it was necessary to know only the transverse uniaxial fatigue limit of the cylinder material, the diameter ratio of the cylinder and the magnitude of the repeated pressure.

As the theoretical fatigue lives have been obtained using linear elastic fracture mechanics theory, it would be unsafe to use equation (4) to estimate the fatigue life of a cylinder subjected to gross plastic yielding. The maximum principal stress criterion has been used to define yield at the bore of the cylinder.

For thick-walled steel cylinders, it has been shown feasible to neglect the final crack length; thus a simplified equation for the crack propagation life is obtained. By making this simplification, it is suggested that the fatigue life is dependent on the diameter ratio, but is only slightly effected by the actual wall thickness. This has been demonstrated experimentally by Parry<sup>9</sup> who tested En 25 steel cylinders of 2.0 diameter ratio, with bore sizes from 9.52 to 25.4 mm (0.375 to 1.0 in) and found no significant change in fatigue life.

Since the rate of crack propagation is independent of the strength of the steel, but is governed by the value of Young's modulus (Frost<sup>2</sup>), it has been possible to present design curves to give estimated crack propagation lives of steel cylinders of a common Young's modulus.

#### V.C.5.10 Conclusions

Simple fracture mechanics theory, together with a knowledge of the high local stresses due to oil penetration into cracks, may be used to give satisfactory estimates of the fatigue life of a thick-walled cylinder subjected to repeated internal pressure.

When used in conjunction with a previous method of predicting the fatigue limit<sup>6</sup>, this theory provides complete theoretical fatigue curves which give good correlation with the experimental results.

The proposed method is applicable to cylinders subjected to elastic stresses, but is liable to predict unsafe estimates of the fatigue life of a cylinder in which gross plastic yielding occurs.

In the case of thick-walled cylinders of high-strength steel it is feasible to assume an infinite final crack length. Thus, design curves are obtained which give estimated fatigue lives of steel cylinders of various diameter ratios.

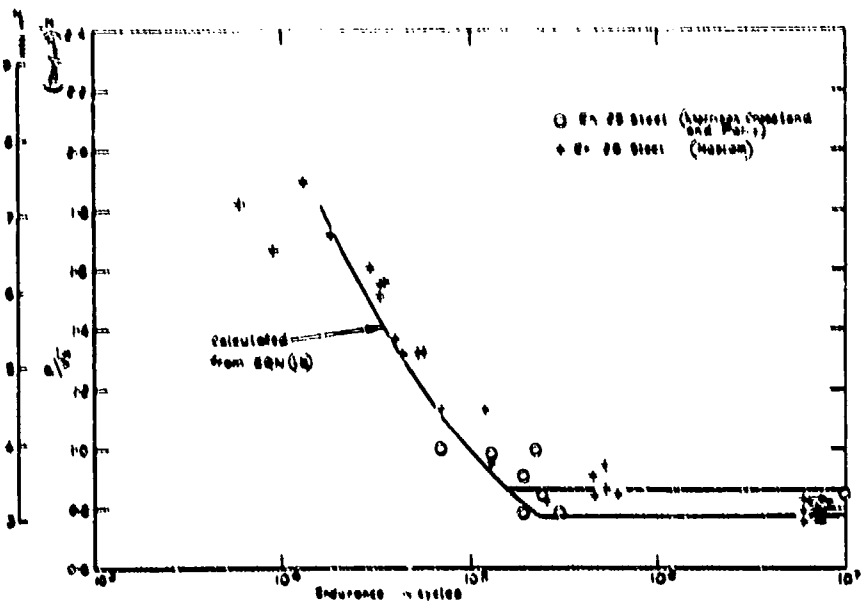


Fig. 9 Estimated fatigue curve for steel cylinders, R = 1.2

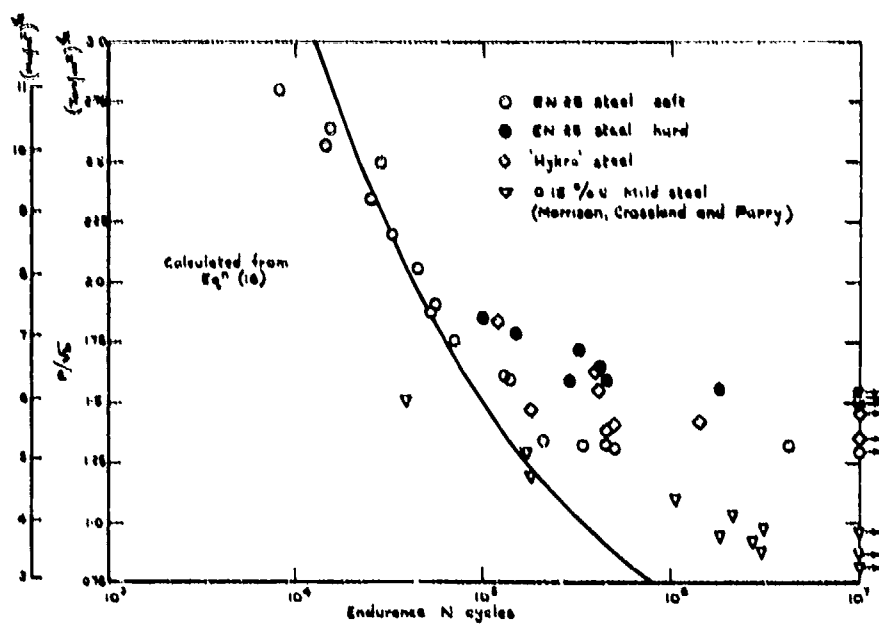


Fig. 10 Estimated fatigue curve for steel cylinders, R = 1.4

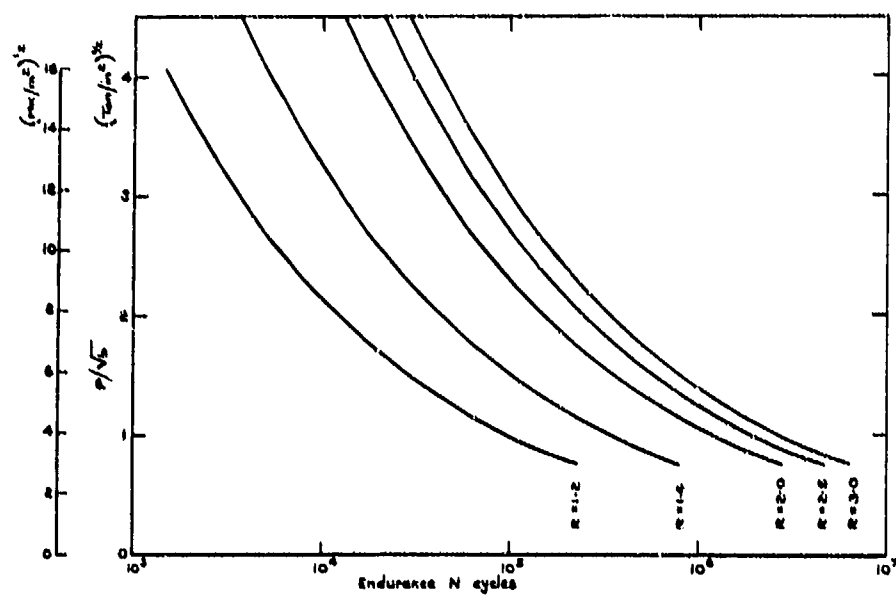


Fig. 11 Estimated fatigue curves for steel cylinders subjected to repeated internal pressure

## Acknowledgements

This chapter is Crown copyright and is reproduced by permission of the Controller of Her Majesty's Stationery Office.

## REFERENCES

- 1 P.C. Paris and F. Erdogan. A critical analysis of crack propagation laws. *J. bas. Engrg.* 1963 85 (4), 528.
- 2 N.E. Frost. The growth of fatigue cracks. *1st Int. Conf. on Fracture* 1965 3, 1433.
- 3 N.E. Frost, L.P. Fook and K. Denton. A fracture mechanics analysis of fatigue crack growth data for various materials. *Engrg. Fracture Mech.* (to be published).
- 4 P.C. Paris and G.C. Sih. Stress analysis of cracks. *Fracture toughness testing and its application ASTM STP 381*, 1965 30.
- 5 J.L.M. Morrison, B. Crossland and J.S.C. Parry. Strength of thick cylinders subjected to repeated internal pressure. *Proc. Instn. mech. Engrs.* 1960 174 (2), 93.
- 6 G.H. Naslam. The fatigue limit of cylinders subjected to repeated internal pressures. *High temperatures: High pressures* 1969 1 (6), 705.
- 7 N.E. Frost and A.F. Greenan. Effect of a tensile mean stress on the alternating stress required to propagate an edge crack in mild steel. *J. mech. Engrg. Sci.* 1967 9 (3), 233.
- 8 B.A. Austin and B. Crossland. Low endurance fatigue strength of thick-walled cylinders: development of a testing machine and preliminary results. *Proc. Instn. mech. Engrs.* 1965 180 (1), 43.
- 9 J.S.C. Parry. Fatigue of thick cylinders: further practical information. *Proc. Instn. mech. Engrs.* 1965 180 (1) 16, 387.

## V.D SERVICE FAILURES AND LABORATORY TESTS

V.E SHORT SURVEY ON POSSIBILITIES OF FATIGUE LIFE  
ASSESSMENT OF AIRCRAFT STRUCTURES BASED ON  
RANDOM OR PROGRAMMED FATIGUE TESTS

W. Barrois

Summary . . . . .	325
V.D.1 Introduction . . . . .	325
D.2 Low temperature brittleness of steels . . . . .	326
D.3 Stress corrosion and related phenomena . . . . .	334
References . . . . .	343
Summary . . . . .	346
V.E.1 Introduction . . . . .	346
E.2 Needs of the designer . . . . .	346
E.3 Representativeness of fatigue tests . . . . .	347
E.4 Prediction and analysis methods for constant amplitude Loadings . . . . .	349
4.1 Loading types and their intensities . . . . .	351
4.2 Reference structures . . . . .	351
E.5 Damage evaluation of fatigue loadings on structures by simplified representation of the random load spectrum . . . . .	351
E.6 Fatigue test acceleration or interpretation of test results in case of changes in service load levels . . . . .	359
6.1 Notched specimens . . . . .	361
6.2 Riveted or bolted assemblies . . . . .	361
E.7 Tests under random loadings . . . . .	363
E.8 Conclusion on designer's needs relative to fatigue test results . . . . .	364
References . . . . .	365

V-D SERVICE FAILURES AND LABORATORY TESTS

W. Barrois

## SUMMARY

The object of this section is to emphasize, from the point of view of the structural engineer, some significant differences between the conditions of certain laboratory tests and the service environment. Low-temperature brittleness and hydrogen embrittlement of steels, and intergranular- or stress-corrosion of aluminum alloys are reviewed in relation to various causes of service or manufacturing damages and to service environment.

## V-D. 1 INTRODUCTION

Formerly, laboratory tests on small normalized specimens were not very representative of the service behaviour of structures. In spite of continuous improvements, it seems necessary to examine the present state of this matter. Some of the differences between service failures of structures and laboratory test results were mainly attributable to the intricacies of actual problems compared with the extreme simplification of certain laboratory tests which were in the first place designed to control the regularity in quality of manufactured materials, and not to supply design data. Furthermore, researches and investigations carried out by scientists and metallurgists were often devoted to gaining a clearer understanding of the influence of a particular parameter, and their character was related to the Cartesian analytic method rather than to a synthesis of the structure behaviour in service.

Now, an additional germ of common language for designers and metallurgists is afforded by Fracture Mechanics which favours their co-operation to deal in a more rational way with the problems arising from the service behaviour of structures. However, differences in immediate objectives and interpretation are justifying an attempt to examine the representative character of laboratory tests, from the designer's viewpoint.

For a designer, the main objectives of tests should be directed along the following lines:

- Significant representation of service behaviour, taking into account undetected manufacturing defects or service damages,
- consideration of research parameters governing service behaviour,
- definition and rapid checking of basic data to permit corrective action,
- lowering of test prices and allowed test times.

In general, a metallurgy laboratory is responsible for the following:

- carrying out investigations on control tests for material acceptance,
- investigation of heat-treatments and their control,
- design of tests to select materials,
- appraisal of damages on parts removed from service or rejected from production, to meet requests of Production-, After-Sales-, or Design-Departments.

In Research Laboratories, and in each sub-specialty of materials and structures tests, the scientist attempts to study each topic in depth in order that invariant physical quantities related to intrinsic material properties may be defined, and subsequently used as data in the application of general theories based on as many test results as possible to give improved predictions. In this scientific activity, financial limitations, as well as the desire to separate the studied variables, necessitate carrying out tests in stylistic conditions that are not very representative of actual problems which are always intricate.

In applied research, and a fortiori in engineering studies, costly investigations are sponsored only when a deficiency has been revealed by serious service failure: problems arising from service or manufacturing operations. Then more representative test types are investigated until a new test is defined to detect the kind of failure observed in service. After being normalized, this test becomes the new credo of

specialized laboratories until, from developments of techniques and of service operations, new failures arise that are unpredictable with usual test types.

Studies of failures and their remedies are essentially interdisciplinary. Most of the severe failures are due to a combination of several causes of weakness, e.g. the material not locally meeting specified requirements even though simultaneously treated specimens showed good properties; defects due to forging, casting, machining, or protection defects locally existing in parts; existing severe stress concentrations that should have been avoided; maintenance inspections not having been frequent enough or sufficiently detailed; and finally, overloads in service resulting from "abnormal" manoeuvres. The multiplicity of specialties concerned in the foregoing causes of damage explains why it is difficult to gather synthetical views on these problems, and why some failures are only explainable in terms of gaps existing between specialties or by the particular trends of the various specialists to minimize or to overestimate the effect of certain damage causes.

Wording itself generates some difficulties in communication. For example the term "brittle" when applied to a material has not only one meaning. Designers sometimes consider a part to be brittle when, in presence of a sharp notch or of a crack, its residual strength becomes abnormally low. For the strength test specialist, brittleness is related to the macroscopic appearance of the fractured cross-sectional area: a grained transverse fracture is said to be brittle, whereas a fibrous fracture or a fracture showing 45° bevel lips is considered ductile. In microfractography, a transverse fracture is said to be brittle only if electron microscope shows that cleavage decohesion is preponderant; fracture is termed semi-brittle in presence of microcraters separated by thin ligaments fractured after noticeable plastic straining; fracture is considered as being ductile in the case of large plastic elongation occurring before 45° lips appear at the failure time.

The same situation exists in fatigue. The designer speaks of fatigue when the strength of a part under repeated loadings is lower than in the case of a single load application. Severely notched parts can be damaged by as few as some tens of high level load cycles. Fifteen years ago, those in metallurgical test laboratories spoke of fatigue only in connection with stressing for a large number of cycles ( $10^4$  to  $10^8$ ), and fatigue corresponded to fracture without macroscopic appearance of plastic distortions; they have more recently been obliged to create the new term of "low cycle fatigue" after service incidents in thermal fatigue had led COFFIN to investigate the effects of lower number of cycles (2 to  $10^4$ ). On some occasions, statements of test laboratory people, who are experts on fractures, were that these latter type of fractures were not due to fatigue, meaning only that the fractures did not present features that are usual after  $10^5$  to  $10^8$  fatigue cycles, but were similar to static fractures. From these statements, designers were led to believe that fractures were caused by single applications of high loads, whereas they were actually caused by low cycle fatigue. For the time being, fracture inspection by means of electron scanning microscopes will avoid the possibility of this kind of mistake but wording difficulties may persist on other topics.

In the case of high strength materials the term "stress-corrosion" is often used for hydrogen embrittlement induced by corrosion in high strength steels as well as for liquid metal embrittlement or for true stress corrosion in aluminium alloys and titanium alloys. The term "stress corrosion without corrosion" has appeared in the technical literature to describe a fracture having the appearance of one produced by stress corrosion but in which no corrosion mechanism was involved.

Here, we are only interested in causes which lower the strength of notched or cracked parts. The scientific field concerned with these problems tends to divide into sections each of which concentrates on one of the various aspects such as low-temperature brittleness, fatigue cracks, stress-corrosion, and hydrogen embrittlement.

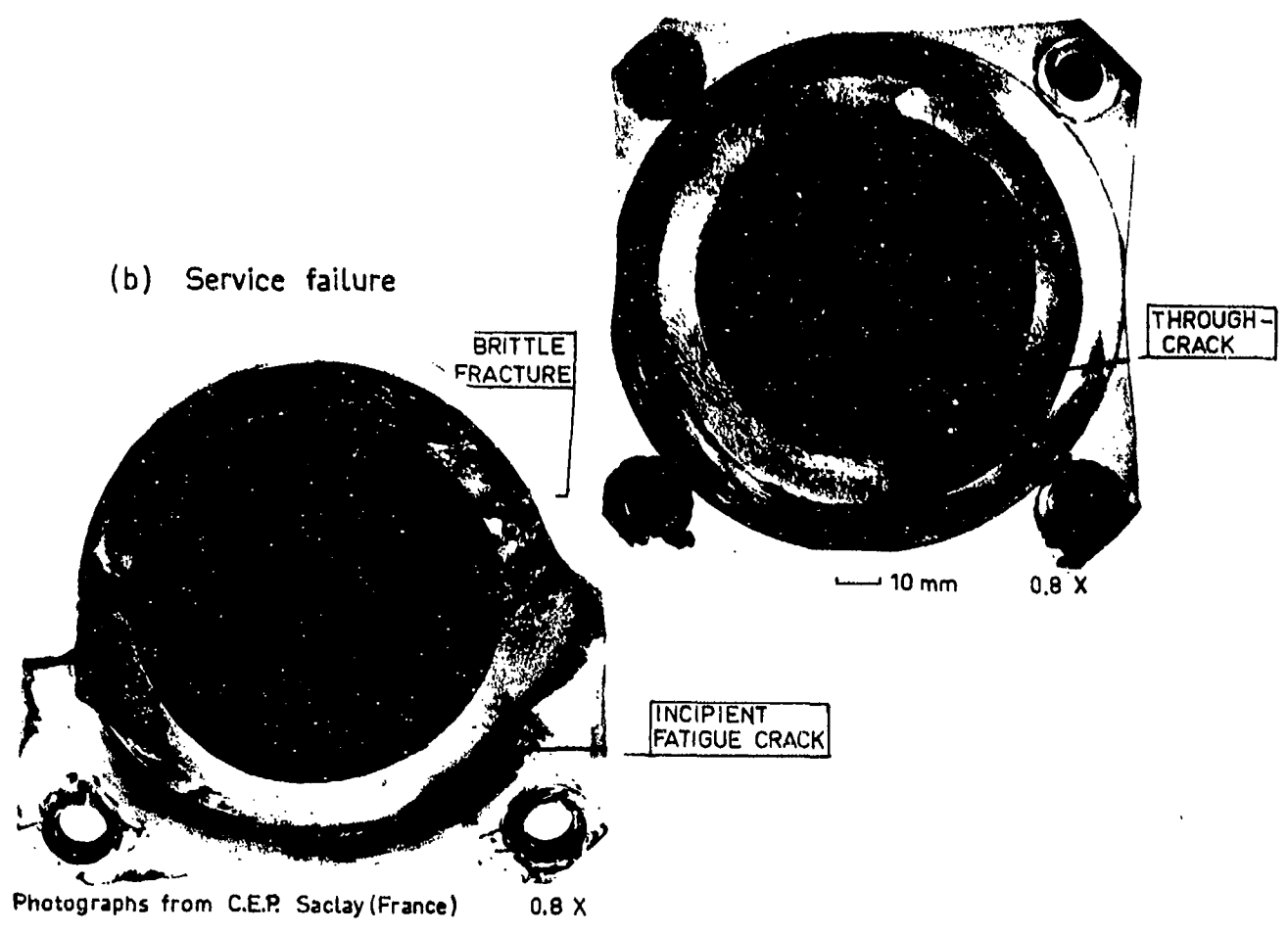
#### V-D. 2 LOW-TEMPERATURE BRITTLENESS OF STEELS

For economical reasons, general metal industries use cheap carbon steels that become brittle at the lower end of the operation temperature range, while the aircraft industry is using high-strength steel alloys that are assumed not to become more brittle at the lowest temperature developed in flight. However, brittleness is strongly dependent upon the acuteness of notches, manufacturing defects and fatigue cracks that may be undetected after control operations or maintenance inspections.

We will discuss a fairly recent example of low-temperature brittleness which occurred in service on a landing gear axle trunnion the design of which had been substantiated by satisfactory fatigue tests which were terminated by static failure after the fatigue crack had slowly propagated on a peripheral length of 60 mm and extended deeply inside the tube (see Figure V-D.1a). The rupture load was much higher than the service loads developed during hard landings. Figure V-D.1b relates to a brittle fracture that occurred in service under normal taxiing conditions after a moderately severe impact. The temperature conditions on the ground and the brittle fracture surface, as well as the very small initial fatigue crack, have led to the suspicion that the 15-CDV6 French steel (same as American Vascojet 90), treated to an ultimate tensile strength of 145,000 lb/in<sup>2</sup>, may be brittle at low temperature, even though the conventional notch impact tests on key-hole 10-mm Charpy specimens (see Figure V-D.1c) had revealed no particular brittleness at the lowest operating temperature.

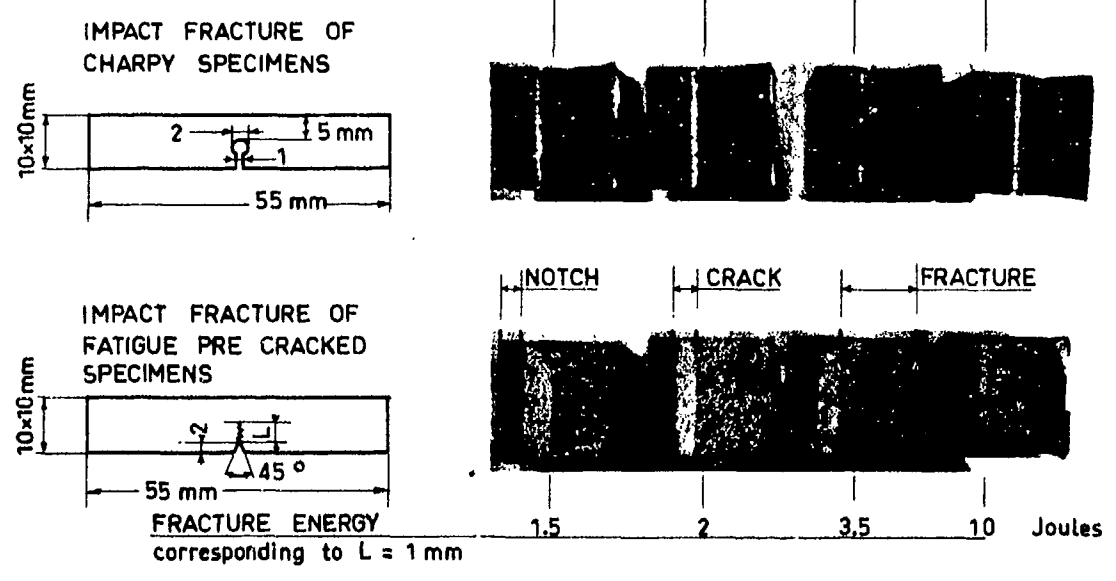
(a) Fatigue test

(b) Service failure



Photographs from C.E.P. Saclay (France) 0.8 X

TEMPERATURES	$\theta = -40$	$-30$	$0$	$+20$	$^{\circ}\text{C}$
IMPACT ENERGIES $K_{UF}$	$= 75$	$60$	$80$	$85$	$\text{J}/\text{cm}^2$



(c) Low-temperature brittleness of the 15 CDV 6 Steel.

Fig.V-D.1 Fracture of axles

Notch impact tests on "Manlabs" specimens with a V-notch prolonged by a fatigue crack have shown that, like high-strength steels, the strength of this medium-strength steel is considerably reduced at approximately 0 °C in the presence of a fatigue crack.

Fracture occurred in the neighbourhood of the weld seam between a small-height shoulder, machined during the preliminary lathe machining of the tube, and the square flange. The low strength, therefore may be ascribed to an exhaustion of the original ductility during the heating and cooling phases of welding, as well as to residual welding stresses and to the effect of fatigue in service. This illustrates a bad selection of material and production processes based on acceptance tests that were not representative of the service behaviour with regard to possible fatigue crack and to material condition.

Before we consider more appropriate test types, we must review the factors of significance that increase the transition temperature between brittle and ductile modes of fracture, which are

- acuteness of notches or stress intensity factors of cracks,
- thickness of the stressed part area,
- fatigue, and cold- and hot-working effects,
- steel content in alloying elements,
- heat-treatments.

General trends in strength reduction at low temperatures are well illustrated by WESSEL'S tests<sup>2</sup> on a commercial Ni-Mo-V steel forging for which the decreases in strength appear below temperature of -180 °C in smooth specimens, -120 °C in 10.8-K<sub>n</sub> notched specimens, and within temperatures from +10 °C to +50 °C in fatigue precracked specimens.

Therefore, in addition to the design stress concentrations, care should be taken of hidden strong stress concentrations resulting from such manufacturing defects as forging laps, quenching cracks, local lack of weld in welded joints, as well as of service fatigue cracks. Undetected cracks or flaws may be sufficient to shift the brittle-ductile transition temperature and to alter normally satisfactory performance of a steel to totally bad performance.

It should be emphasized that notched specimens are increasingly being replaced by precracked specimens in investigations on brittleness. Figure V-D.2, from test results of MAYNOR and MUELLER<sup>3</sup>, shows the effect of test temperature on static strength for an H-11 steel. It is seen that the low temperature at which a significant reduction in critical values of the stress intensity factor  $K_{Ic}$  occurs, is not as low in the case of thicker sheets treated to higher strength (240,000 lb/in<sup>2</sup>). The strength decreases and the brittle-ductile transition temperature increases with increasing thickness.

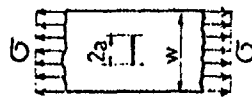
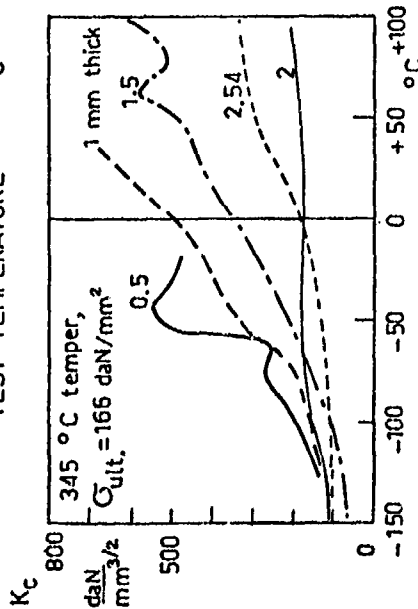
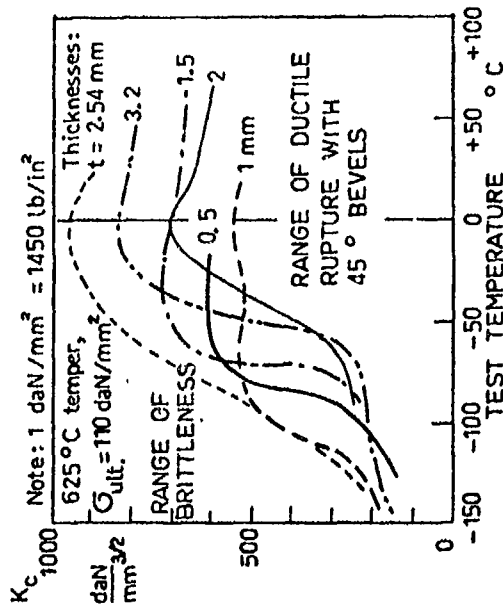
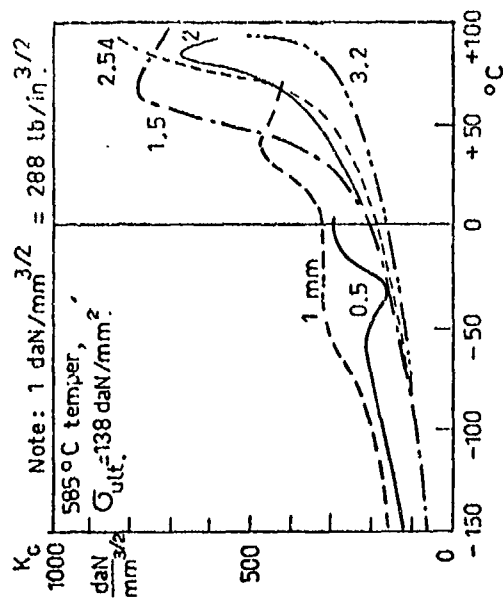
It is worth noting that the so-called brittle fracture appearance transition temperature is strongly dependent on thickness for a geometric reason. This corresponds to the appearance on the fractured surface of ductile shear lips or a fibrous area which form a fixed percentage (e.g. 50%) of the total fractured area and contrast with the brittle grained fracture area. Indeed, in the fracture of a sharply notched or precracked component, even when made from a very ductile material, the crack initiation presents a transverse fracture of brittle appearance. Incipient shear lips widen progressively from the external surface, giving a "thumbnail" appearance to the crack initiation, and then tend to reach a limited width irrespective of the thickness if the latter is large enough. Therefore, as underlined by BLUHM<sup>3</sup>, the percentage ratio in brittle- to total-surface area is dependent on both temperature and thickness.

Catastrophic effects of brittleness suggest a material property at the small scale of grains and precipitates, and probably at the still smaller scale of point defects such as vacancy clusters and pile-ups or intersections of dislocations that are stabilized by stranger solute atoms. This property, unlikely to be measurable, could be conceived as the local elongation that nucleates microcracks or promotes the merging of several neighbouring pre-existent microcracks into a larger one.

As proved by the test results of VISHNEVSKY and STEIGERWALD<sup>4</sup> plotted in Figure V-D.3 and concerning a 0.35% C, 3% Ni, Cr-Mo-V martensitic steel treated to a room-temperature yield stress of 160,000 to 180,000 lb/in<sup>2</sup>, the true fracture strain correlates well with the maximum stress intensity factor of precracked Charpy specimens only in tests performed at room temperature; at -196 °C, the toughness was independent of fracture strain.

The effect of a fatigue pre-treatment on the brittle-ductile transition temperature of steel was first investigated by MacGREGOR and GROSSMAN<sup>5</sup> on SAE 1020 steel treated to a tensile strength of 65,470 lb/in<sup>2</sup>. The relation between the transition temperature in slow bend tests using notched ( $D = .33$  in.,  $d = .2676$  in.,  $r = .01$  in.) MOORE specimens that had been pre-fatigued in rotating bending, was expressed by analytic relations of the form





H-11 STEEL SHEETS  
 Austenitized at 1010 °C; oil quenched;  
 double temper 2 x 2 hr.  
 Results from MAYNOR and MUELLER<sup>3</sup>.

$$K_c = \sigma_c \sqrt{\frac{\pi a}{1 - (2a/w)^2}}$$

$a = a_3$  is defined by the ASTM as the half-crack length for instability;  
 $\sigma_c$  = critical fracture stress.

Fig.V-D.2 Fracture toughness ( $K_{c3}$ ) of H-11 steel sheets as a function of treatment and test temperature

$$\left[ \log_{10} \frac{\phi_1 N}{n} \right] \cdot \left[ \frac{1}{T_0} - \frac{1}{T} \right] = K$$

where N was the number of cycles to fatigue failure, n the number of fatigue pre-treatment cycles,  $\phi_1$  a factor depending upon the fatigue stress level,  $T_0$  the transition temperature of virgin specimens, and T that of pre-fatigued specimens. An investigation of the possible causes for the large effects found suggested the tentative conclusion that strain hardening and ageing during fatigue test were responsible.

A similar series of tests was performed by LESSELLS and JACQUES<sup>6</sup> on two medium carbon shipbuilding steels of Navy grade 4885 treated to tensile strength of about 60,000 lb/in<sup>2</sup>. The specimen used was a notched (D = .5 in., d = .4 in., r = .005 in.) MOORE specimen pre-fatigued in rotating bending and fracture tested in impact. As testing proceeded, it was found that fatigue cracks were developing at the base of the notch both above and below the endurance limit. When specimens were cyclically tested in order to avoid fatigue cracks, the resulting transition curve showed little deviation from the original curve presumably due to the low stress of the prior fatigue. A series of specimens were prestrained in tension prior to testing in impact with a marked shift of the transition curve resulting. Authors concluded that the following phenomena, in their order of importance, produce a marked effect on the impact transition curves:

1. Fatigue damage accompanied by high stress concentrations associated with fatigue cracks.
2. Gross plastic deformation resulting probably in an increase of the micro (small scale) stress concentrations.
3. Fatigue damage which does not result in macro stress concentration but which is undoubtedly associated with micro plastic deformation.

Insofar as the fatigue effect is concerned, as we have previously stated elsewhere,<sup>7</sup> initially cold-worked materials firstly soften while relaxing residual stresses at the scales of grains, subgrains and precipitates, then some cavities are created due to the displacement and meeting of vacancies that pre-exist or that are due to piling-up and intersections of dislocations, and finally microcracks are produced. Thus, it can be assumed that the fatigue effect is likely to cause, first of all, an increase in ductility, then a decrease in ductility. This would result in a moderate transition temperature drop followed by a transition temperature increase up to higher values during the fatigue progress. This is the trend shown by SALKIN's tests<sup>8</sup> on low alloy steels as treated to an ultimate strength of 100,000 lb/in<sup>2</sup> with a rupture elongation of 26% and a reduction in area of 70% at room temperature. Fatigue pre-treatment was performed in axial tension-compression on specimens from which V-notched Charpy specimens were machined. In the case of pre-fatigue at 20 °C, Figure V-D.4a shows a correlation trend of the transition temperature for a 50% brittle fracture appearance with a quantity that is roughly proportional to the cycle ratio n/N; it seems that the fatigue embrittlement passes through a minimum in the low cycle ratio range. Figure V-D.4b shows that this fatigue effect is more pronounced after a fatigue pre-treatment at 300 °C.

An investigation by HOLDEN<sup>9</sup> dealt with the dependence of yield stress at 20 °C and fracture stress at -196 °C upon grain size for 0.09% C mild steel before and after prolonged cyclic stressing at the fatigue limit which was increased by step-increasing the fatigue stress (coaxing process). The yield stress at 20 °C and the fracture stress at -196 °C were found to be increased after fatigue treatment. After cyclic stressing, the transition temperature  $T_0$  was found to be constant, irrespective of the grain size. Figure V-D.5 is to be compared with Figure V-D.3. The cyclic hardening and embrittlement were not adequately accounted for by processes of ageing and precipitation on the slip planes active in fatigue. Note that the concept of activation energy used is based upon an average of local phenomena that are assumed to be statistically independent, a hypothesis no longer exact in fatigue phenomena (see reference 5, Section 2.5.2).

WEISZ and ERARD<sup>10</sup> have investigated the low temperature brittleness of a 0.14% C, Mn-Mo low alloy steel. After a first fatigue treatment (n/N = 0.5) at various temperatures, the ultimate strength of -196 °C was only slightly modified by a low cycle fatigue pre-treatment at room temperature, whereas fatigue pre-treatment at 300 °C caused the strength at -196 °C to be a minimum with an important scatter. In the case of fatigue pre-treatment at 300 °C, the strength at -196 °C decreased linearly as the logarithm of the number of fatigue cycles increased. In order to elucidate whether the embrittlement was to be attributed to fatigue microcracks, two groups of fatigue pre-treated specimens were submitted to special treatments. The first group was normalized by heat-treatment at 900 °C in order to retain microcracks but to eliminate crystal distortions; the second group was machined to a depth of 0.5 mm to eliminate microcracks while maintaining crystal distortions due to fatigue. At -196 °C the first group showed the virgin material strength whereas the second group had the strength of the fatigued material. Moreover, fatigue at 300 °C yielded a shift of the transition temperatures for fracture elongation and reduction in area, the maximum values of each being significantly lowered.

In a review on an explanation of fracture initiation close to welds by exhaustion of ductility after hot straining, MYLONAS and ROCKEY<sup>11</sup> stated: "Numerous tests confirm that a small amount of cold extension may not exhaust the ductility in tension to the same degree as a precompression. Tests show that plastic compression at temperatures up to about 370 °C greatly reduces the ductility in subsequent extension at 24 °C and

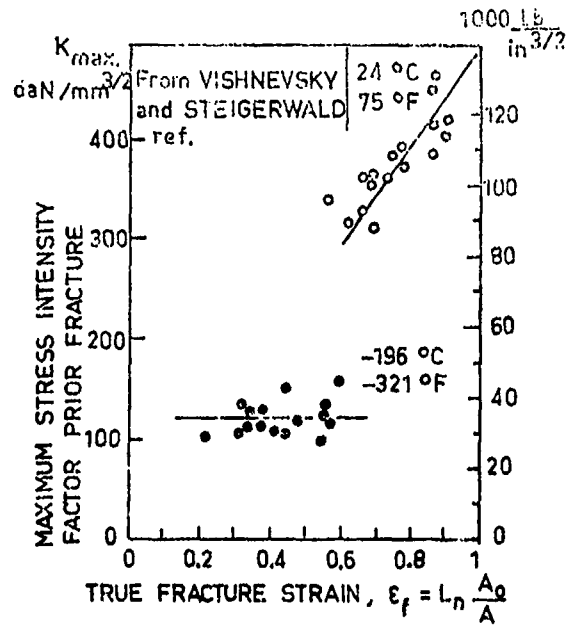


Fig.V-D.3 Effect of tensile ductility on notch-bend fracture toughness at two testing temperatures. From Vishnevsky and Steigerwald<sup>4</sup>

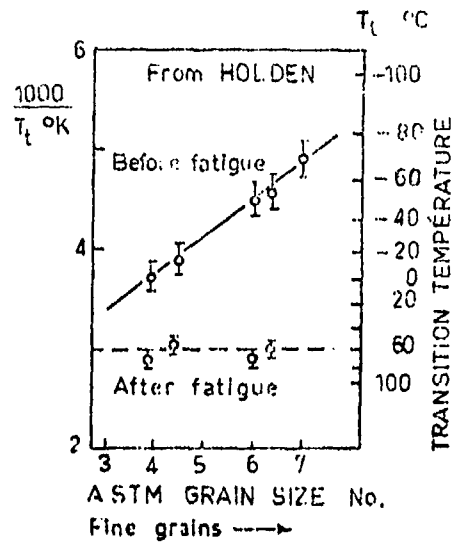


Fig.V-D.5 Effect of stressing at fatigue limit on transition temperature of mild steel. From Holden<sup>9</sup>

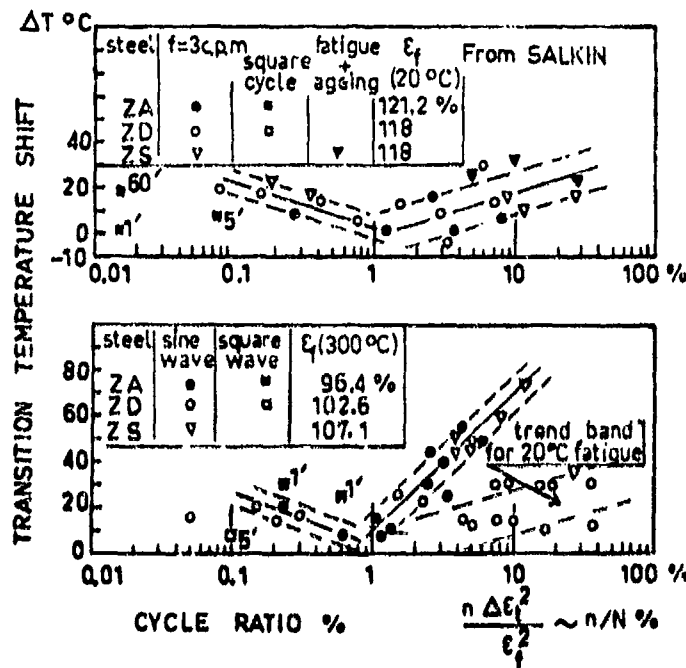


Fig.V-D.4 Effect of fatigue at 20°C and 300°C on 50% fibrous transition temperature. From Salkin<sup>8</sup>

at -26 °C". MYLONAS<sup>12</sup> performed tests on pre-compressed notched plates submitted to localized lateral pressings to remove the residual tensions, and showed that the residual stresses did not contribute significantly in the initiation of brittle fracture. Brittle fracture was due to the exhaustion of ductility in subsequent tension, this being produced by compressive prestraining and ageing.

It is generally accepted that exhaustion of ductility in tension after precompression is due to the flattening and alignment of flaws or cavities in a direction perpendicular to the final tension. This process accounts for the effect of hot-precompression but not for the low stress level fatigue effect in HOLDEN's tests and the high stress level fatigue effect in WEISZ and ERARD's tests. We propose the more general complementary process we have previously considered in fatigue and phenomena related to Bauschinger's effect (see reference 5, Section 2.1.3). It may be stated that: a range of temperatures exists in which fatigue or reversed straining changes the distribution in stability of crystal lattice distortions by relieving low stability distortions and increasing the stability of distortions that are not eliminated; these remaining distortions become thus very stable under subsequent loading at low temperature that is overloading them and creating microcracks which decrease the local ductility. Fatigue or precompression at room temperature would be insufficient to cause elimination of a significant part of lattice distortions whereas fatigue or precompression at a high enough temperature could eliminate a number of distortions, thus leaving a free region for the low temperature subsequent loading to create under plastic strain a new set of lattice distortions with continuous distribution of higher stability level which limits the plastic elongation and favours formation of microcracks.

Aircraft structures may be exposed to widely varying strain rates. In precracked components, local strain rates at crack tips are higher than nominal strain rates over the net cross-sectional areas, which is due to high negative stress gradients which cause the strain rate in a point ahead of the crack tip to be dependent on its distance from the crack tip and on the crack propagation velocity.

A distinction should be made between the onset of slow crack propagation during which the crack propagation velocity mainly depends upon the loading rate, and the rapid crack propagation velocity beyond the critical crack length in which the much higher crack propagation velocity mainly depends upon elastic energy stored in the whole specimen and its loading system.

It may be suggested that the loading rate effect is likely to be significant only at the onset of slow crack propagation. This is well supported by tests performed by BROEK and NEDERVEEN<sup>13</sup> on 2024-T3 clad and 7075-T6 clad aluminium alloy sheets, using 2-mm thick and 300-mm wide specimens containing 45-mm and 90-mm long centre jeweller's sawed slots. These tests showed a decrease of about 20% in net stress at the onset of slow crack propagation for decreasing test durations from 1800 sec to 2 sec, whereas critical lengths and residual strengths were not significantly modified for loading durations from 1800 sec to 0.4 sec. During fast crack propagation to fracture, crack propagation velocities were of the order of 100 m/sec in 2024-T3 aluminium alloy sheets, and of 1500 m/sec in 7075-T6 aluminium alloy sheets.

FORD, RADON and TURNER<sup>14</sup> have investigated the fracture toughness of a medium strength steel ( $\sigma_{ult} = 100,000$  lb/in<sup>2</sup>,  $\sigma_y = 83,000$  lb/in<sup>2</sup>, fracture elongation = 23%, and reduction in area = 53%). Tests on V-notch (deepened or not in fatigue) bend specimens, under slow static loading and under impact loading, showed that the results depend on absolute sizes and thickness of specimens, and on the loading rate. Loading rate effects occurred only with the large thickness specimens which fractured, when test temperatures were sufficiently low under stresses below corresponding yield stresses. The 50% shear appearance transition temperature in the fracture of small precracked specimens varied from -55 °C in slow tests to -17 °C in impact tests.

The loading rate effect on the low-temperature strength of fatigue-precracked specimens is more pronounced than in the case of notched specimens although in tests performed by BRADLEY and BEACHEM<sup>15,16</sup> on 422-martensitic stainless steel sheets, the decrease in net strength of about 20% was accompanied by a more fibrous aspect of the fractured area.

MARGSHALL<sup>17</sup> has reviewed the metallurgical aspects of brittle fracture problems evolved from using steels heat-treated to an ultimate tensile strength near the maximum attainable. Metallurgical factors affecting the brittle-ductile transition temperature and the low-temperature toughness of steels are related to:

- carbide particle dispersion in the ferrite matrix,
- the chemical composition in dissolved elements, grain size and submicroscopic structure of the ferrite matrix,
- the amount of retained austenite,
- the distribution of nonmetallic inclusions.

In quenching steels from the austenite condition to produce martensite, the cooling rate in certain areas of a part may not be fast enough to avoid the formation of some pearlite, bainite and "free" ferrite (i.e., ferrite formed prior to the martensite transformation of austenite). After tempering the brittle-ductile transition temperature

of these mixed structures are inferior to those of an entirely martensitic structure.

Certain steels such as the American 4340 steel are more brittle when tempered near 260 °C than if tempered at slightly lower or slightly higher temperatures. This can be overcome by the addition of one to two per cent of silicon in the steel alloy.

For mild steel containing 0.02% carbon, the brittle-ductile transition temperature of ferrite is higher with larger grain and subgrain sizes. However, for ingot iron, the transition temperature increases with a decreasing size of subgrains.

For annealed ship steels, OWEN et al.<sup>18</sup> observed that the transition temperature increased with ferrite grain size, pearlite patch size, and the related parameters of austenite grain size. The correlation was found to be the strongest with ferrite grain size. In normalized structures, the variation of transition temperature could not be explained in terms of the above metallographic parameters. It was concluded that cooling rate, and probably differences in composition, could produce effects which influence the transition temperature but which could not be measured by light microscopy.<sup>19</sup> Electron microscopy might reveal significant details such as density and location of dislocation clusters.

For high-strength martensitic steels of fine grain size, the size of martensite platelets is associated with the grain size. Fine martensite platelets correspond not only to better fracture transition properties, but also to higher strengths than coarse platelets. We assume that good properties are due to martensite platelets small enough to maintain lattice coherence with the ferrite matrix.

Exposure of certain steels to a temperature below the austenite-ferrite transformation range, but not high enough to modify the carbide dispersion and room-temperature properties, may increase the brittle-ductile transition temperature, but no satisfactory explanation is available and an ordinary microstructural examination of these steels does not reveal any related indication on structural changes.

In other cases, tempering at temperatures within 370 °C to 570 °C produces a significant increase of the brittle-ductile transition temperature with little or no effect on ultimate tensile strengths and without any visible structural change (temper embrittlement). Blue brittleness is exhibited by some steels after being heated to some temperature within 160 °C to 300 °C, and more especially if the steel is wrought at the elevated temperature. Fairly completely deoxidized ("killed") steels are free of blue brittleness.

Strain-ageing embrittlement of mild steels occurs after cold-working followed by ageing at room temperature or at moderately elevated temperatures up to 260 °C. This is not accompanied by any visible structural change. It may be suggested that this results from the effect of cold-working and ageing on the distribution of slip barriers, some of them being eliminated, and the stability of others being increased by local ordering of interstitial solute atoms.

The influence of elements dissolved in ferrite on the brittle-ductile transition temperature has been investigated by REES et al.<sup>20 to 23</sup> at the National Physical Laboratory in England from 1951 to 1954. Various elements including oxygen, silicon, nickel, chromium, molybdenum, manganese and carbon were added to high-purity iron. It seems that interstitial elements, carbon and oxygen, are more effective in modifying the transition temperature than are substitutional elements. It has been suggested that the main role of alloying elements is to control or tie up interstitial elements.

Previously quoted tests performed by VISHNEVSKY and STEIGERWALD<sup>4</sup> on a 0.35% C, 3% Ni, Cr-Mo-V base steel with various contents in alloying elements, C, Mn, Cr, Ni, Mo, V and Al, and using precracked V-notch-bend specimens, have shown that C, Mn, Cr and Mo elements raise the transition temperature whereas V and Ni lower it and improve the notch strengths at low temperatures.

From the above short review on low-temperature properties of notched parts, we will underline that the low-temperature brittleness of steels or other susceptible materials should be investigated preferably on precracked specimens of representative thickness, and if possible, machined from actual forgings or rough materials having undergone all heat- and strain-treatments used for actual parts. Test conditions should be representative of service environment, temperature and loading rate conditions. Our preference is for toughness measurements on slow bend fatigue-precracked specimens on condition that preliminary tests results show correlation with full-scale tests on actual parts in which damage or production defects will have been simulated.

Designers are mainly interested in quantities or parameters directly related to service behaviour of structures. Therefore, even in investigations aimed to select metallurgical treatments and using impact tests on V-notched fatigue-precracked specimens, it is considered necessary to verify the correlation between impact energy and toughness in the whole field.

Cases of in-flight catastrophic failure of a F-111 American military aircraft and premature failure during full-scale structural fatigue tests in a forged steel part of the wing carry through box made from high-strength steel treated to an ultimate strength of about 220,000 lb/in<sup>2</sup>, have caused full-scale proof-tests to be carried out on all aircraft after some period of service. In order to represent possible brittle

conditions at low temperatures undergone in flight at high altitudes, each aircraft was proof-tested to design limit load conditions in a very large chamber cooled down to  $-40^{\circ}\text{C}$ . From structural investigations on the F-111, HINDERS<sup>24</sup> stated that "metallurgical examination near the hole area where the fatigue crack originates had revealed that there was an area of untempered martensitic grain structure at the surface of the hole and that the hole itself was drilled and reamed in a local hard spot which resulted in dulling the drill and generating the excessive heat which caused the untempered martensite. This very brittle material then cracked as the interference fit "taperlok" bolt was drawn up into place. Experience with steel used in the F-111 has shown a great sensitivity of stress intensity factor to failure to heat treatment variables. The heat-treatment processes of normalizing, austenizing and quenching could produce wide variation in  $K_{Ic}$  values even within a single part or from heat to heat of the same part". In this case, two specimens of D6ac steel from different heats might possess the same measured  $\sigma_y$  and yet have a two to one range of  $K_{Ic}$ .

Fatigue precracked parts made from high-strength aluminium alloys suffer no additional embrittlement effect at low temperatures. HALL and FINGER<sup>25</sup> have investigated the toughness of fatigue precracked 25.4-mm thick 2014-T62 aluminium alloy plates that were tested in ambient air, in liquid nitrogen at  $-196^{\circ}\text{C}$ , and in liquid hydrogen at  $-253^{\circ}\text{C}$ . With specimens containing a centre surface flaw and loaded in the long direction,  $K_{Ic}$  was found to be fairly independent of the test temperature, showing that no low-temperature effect exists for this aluminium alloy. Titanium alloys also are only slightly sensitive to low temperatures<sup>25, 26</sup>.

Except for some fatigue pre-treatment in the material close ahead of the crack tip due to high level flight loads, the residual static strength in service differs little from that shown in laboratory tests performed on similar parts containing a sharp notch deepened in fatigue.

Ten years ago, we were concerned with investigations on two catastrophic in-flight failures of old military aircraft that occurred in lower booms of the wing forward spars made from 2014 aluminium alloy forgings. In one case, brittle fracture originated from a fatigue crack of very small extent (0.5% of the total lower boom cross-sectional area) that was initiated by fretting at a bolt hole edge (see Figure V-D.6). In the other case, an initial flaw existing at an external sharp angle only covered about 0.4% of the total cross-sectional area. In both cases, fracture surfaces showed no evidence of stress corrosion and the circumstances of the accidents led to the assumption that a reduction of at least 30% in ultimate rupture strength had occurred.

Figure V-D.7 shows the fracture surface of a wing attachment fitting made from a 7079-T6 aluminium alloy forging, the fracture of which occurred during a laboratory full-scale fatigue test of the aircraft structure. Small fatigue areas are visible on both sides of the bolt holes. The total fatigue area is only 2.8% of the net cross-sectional area of the lower flange. These small fatigue cracks caused such a considerable loss in bending strength that failure occurred at 98.3% of the design limit load after a fatigue test life corresponding to 2138 flight hours of fighter operations.

KIRBKY and EYNON<sup>27</sup> have made investigations on a multibolt joint to establish the relationship between fatigue damage and residual static strength. The joints consisted of a bar made from extruded British L 65 aluminium alloy (similar to 2014-T6). Joints which had previously been subjected to varying histories of fatigue loading were fractured under static loads. It was found that joints which showed no evidence of fatigue cracking, when fracture surfaces were examined to the naked eye, retained their original static strength. Figure V-D.8 show the relationship between the percentage of the cross-sectional area precracked in fatigue and the residual static strength expressed as a percentage of the original strength. It also appeared that there was no large reduction in strength until more than 80% of the fatigue life had been consumed.

We assume that the greater reduction experienced in parts made from forgings may be due to the varying metallurgical condition of different part areas, and possibly the consequence of machining that causes grain direction to form an angle with external machined surfaces.

We believe that tests on small specimens are of interest only if specimen thickness, material conditions, and the locations of initial cracks are representative of actual problems. Too frequently, scientists seeking an invariant property and being desirous to compare their results with those of other laboratories are planning test conditions that are different from any service condition. In this connection, tests of HALL and FINGER<sup>25</sup> on thick plates containing surface cracks at the hole edges are simulating well some of the more important service conditions. However, it would be worth noting that service fractures often appear following stress-corrosion crack propagation originating from manufacturing flaws, fatigue cracks, fretting damages or corrosion pits.

### V-D. 3 STRESS-CORROSION AND RELATED PHENOMENA

As in the fatigue test field, but more recently, the situation in stress-corrosion testing is evolving toward more representative tests. In fatigue testing, it was possible to contract test duration with little effect on results, except when corrosion, thermal stresses or dynamic response were present. On the contrary, it is difficult to accelerate stress-corrosion tests without modifying the investigated phenomena. However, since tests would take too long if they were performed in real time, accelerated methods that were

CENTRE ORIGINATED  
BRITTLE FRACTURE

Photograph from Service Technique Aéronautique, Paris,

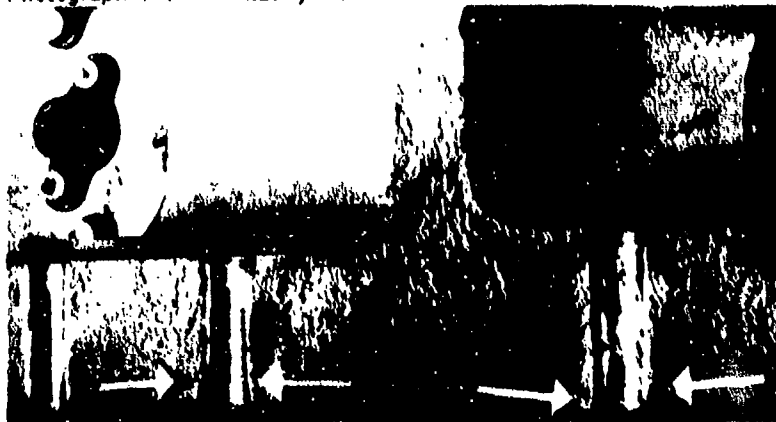


HERRING - BONE  
BRITTLE FRACTURE

FATIGUE CRACK ORIGIN

Fig.V-D.6 In-flight brittle failure in the lower boom of the wing main spar of a bomber aircraft

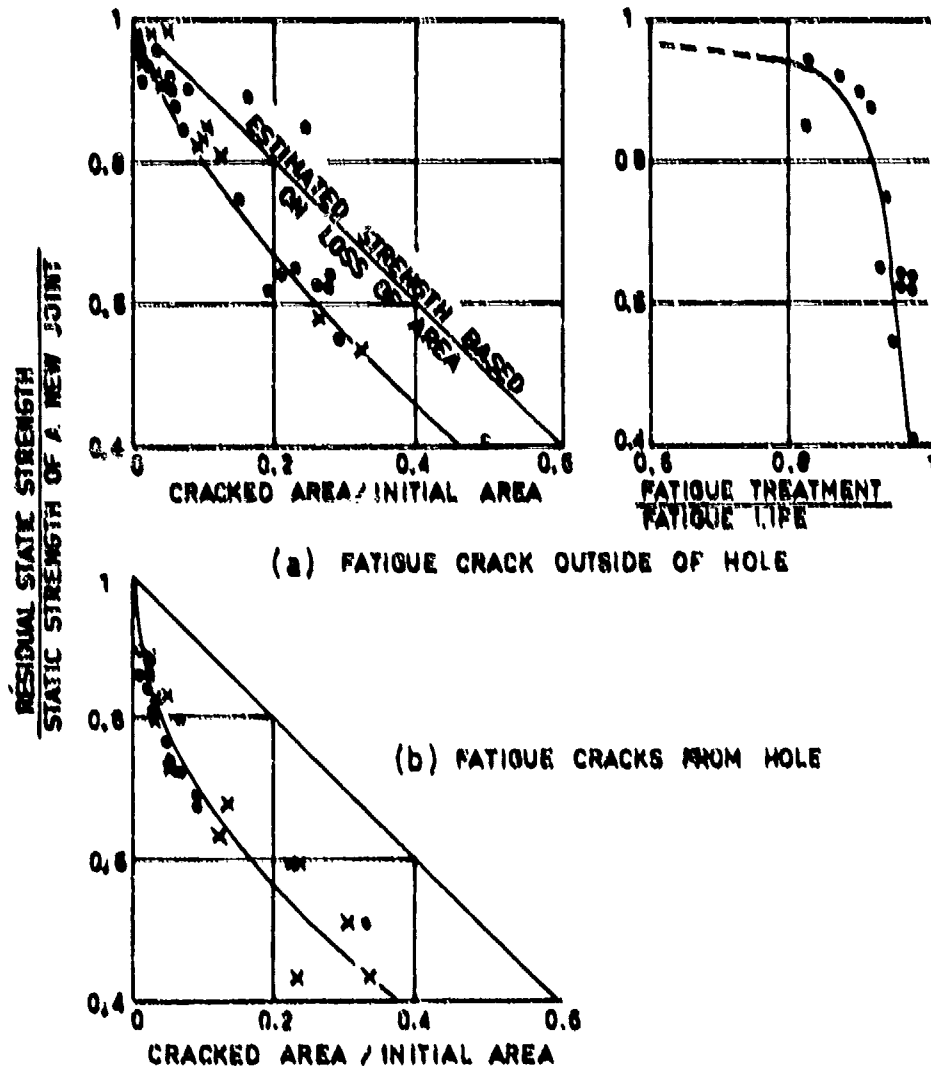
Photograph from I.A.B.G., Ottobrunn



Arrows indicate fatigue cracks.

Fig.V-D.7 Brittle failure in a full-scale fatigue test

PREVIOUS HISTORY OF ;  
 • PROGRAMME LOADING  
 x CONSTANT LOADING



(a) FATIGUE CRACK OUTSIDE OF HOLE

(b) FATIGUE CRACKS FROM HOLE

Fig.V-D.8 Residual static strength of a bolted joint cracked in fatigue<sup>17</sup>



assumed of comparative value have been generally used. Earlier laboratory stress-corrosion tests were carried out on smooth specimens in the presence of a 20% NaCl aqueous solution even though most service difficulties experienced in aircraft structures were due to slightly acid or slightly alkaline condensed water. Later, the most used alkaline environment consisted of 3.9% NaCl in water. As actual corrosion involves an important action of oxygen, the usual practice is now to carry out stress-corrosion tests by effecting a so-called "alternate immersion" sequence of successive immersions into and emersions from a 3.9% NaCl aqueous solution. These tests seldom last for more than 90 days, after which it is assumed that stress-corrosion risks no longer exist.

Certain disillusioning service behaviour of alloys that had satisfied specifications through conventional tests revealed that most of the dangerous corrosions of aircraft structures in operation are due to alternate water condensation into assembly interstices from which air escapes at high altitude while the part is cooled down, and then on rapid descent to landing, when hot air enters and water vapour condenses. The corrosion process is one of differential aeration and involves electrochemical reactions quite different from those acting in conventional laboratory tests.

Moreover, a distinction must be made between initiation and propagation phases of stress-corrosion. Incipient stress-corrosion is delayed by surface protection of actual parts, whereas it can occur at a number of neighbouring pits on bare specimens. In the latter case, it may be questioned whether tests performed under fixed deflections are of significance since a number of incipient cracks decrease the stresses produced by the fixed deflections, whereas stress-corrosion crack propagation in actual parts often have well localized origins such as scratches, scores, protection defects, fretting, wear, or fatigue cracks. Data on duration of the propagation phase are less scattered than initiation data and correspond better to actual service phenomena where initiation is generally due to one or several of the above mentioned causes or may be even pre-existent.

For these reasons, surface corrosion initiation should be considered in connection with the various protective coatings and with the maintenance processes. On the contrary, once an incipient crack exists, its propagation under stress-corrosion depends only on material, stress field and environmental conditions.

Although the statement has often been made that material should be sufficiently protected against corrosion pitting so that a stress-corrosion crack will not initiate under service conditions, it must be observed that surface protection is mainly aimed at restricting the number of areas where corrosion pits can form and so minimize the possibility of stress-corrosion in vital areas.

It should be noted that certain heat-treatments modify the relative importance of the initiation and propagation phases of stress-corrosion. For example, the T6 ageing of 2024 aluminium alloy increases pitting sensitivity while decreasing risks of intergranular corrosion. As stated by DRUMMER et al.<sup>28</sup> for the 7075 aluminium alloy, the overaging T73 treatment can induce a great resistance to crack initiation while stress-corrosion crack propagation is little modified.

From pH and corrosion potential measurements performed at crack tips under applied stresses, DAVIS<sup>29</sup> stated that 5456-H117 and 7075-T651 aluminium alloys should both be considered susceptible to stress-corrosion, although 5456-H117 had previously been considered immune to stress-corrosion while 7075-T651 was considered very susceptible.

BORCHERS and TENCKHOFF<sup>30</sup> have investigated the influence of surface condition on the stress corrosion of an Al-Mg-Zn aluminium alloy casting and have shown that the improvement effected by shot peening results not simply from surface compressive residual stresses but working deformation destroys grain boundaries at the surface. In high-strength aluminium alloys, the almost general feature in stress corrosion is intergranular cracking. Therefore, the stress corrosion process can only begin when the cold-worked surface layer, which shows no well-defined grain boundary structure, has been penetrated by pitting corrosion, and grain boundaries of the deeper material are exposed. Note that the "Hailby layer" of the surface cold-worked material is more anodic and will protect the bulk material until pits are deep enough to act as crevices in which electrolyte acidifies and corrosion potential evolves in the active direction.

The importance of surface condition is well supported by an investigation of COCKS<sup>32</sup> who appraised the degree of conjoint action between stress and corrosion in stress corrosion, using a new test procedure which consists of measuring the reduction in subsequent stress corrosion lifetime after a precorrosion without application of stress. Stress corrosion index (SCI) is defined as

$$SCI = 1 + \frac{dy}{dx}$$

where y is the time to failure after precorrosion and x is the time during which the specimen was exposed to precorrosion without stress. For the corrosion of 7075 aluminium alloy in a deaerated one normal NaCl aqueous solution buffered to pH 4.7 at 30 °C with an anodic current density of 0.3 mA/cm<sup>2</sup>, and a stress of about 90% of the yield value applied in the short transverse direction, the stress corrosion index was found to be SCI = 1 for electropolished specimens in which precorrosion plays no part. For as-machined specimens, stress corrosion lifetime was about five times that of electropolished specimens but precorrosion reduced it to the preceding value while maintaining the total time under corrosion. Specimens reheated and retreated had similar behaviour

but stress corrosion lifetime was only three times that of electropolished specimens. This proves that a surface layer is involved and therefore underlines the need to investigate the various surface conditions obtained in the actual manufacturing processes.

In high-strength steels, brittle fracture may be caused by hydrogen induced embrittlement due to a deficiency in the degassing process that must follow electrolytic cadmium plating. Fast crack propagation may also occur by a progressive embrittlement due to the hydrogen evolving during stress-corrosion. Porous cadmium plating can present difficulties in degassing but the pores should be then filled with a polymer in order to avoid hydroxyl ions re-entering the pores and serving as a very efficient electrolyte for the cadmium-steel "battery" at each interface-deep pore (from ANDERSON<sup>13</sup>).

To increase service safety, it is still useful to choose materials having low sensitivity to stress-corrosion and to brittle fracture. The designer's aim is to ensure both slow stress-corrosion crack propagation and that cracks may become large enough to be detectable before they cause a significant drop in static strength.

Service behaviour and laboratory tests could be considered according to the following headings:

1. Causes of initial defects.
2. Influence of the corroded area location in the structure on the electro-chemical process involved.
3. Selection of materials having possibilities for trade-off between pitting, intergranular and stress-corrosion sensitivities, tensile strength and fatigue strength characteristics.
4. Effects of the stress distribution and of its variation during crack propagation.
5. Brittleness of cracked parts.

Some non-limitative examples of initial protection defects in steels are:

- Undetected quenching flaws due to tensile stresses produced by rapid cooling, the levels of which depend on factors such as steel hardness, cooling rate and stress concentration in the part. Figure V-D.9 shows a sketch of an in-flight incident in a screwed-down bolt caused by fatigue crack propagation originating from a quenching flaw. Before tempering, the roughly machined part had a sharp angle between head and shank. Quenching induced tensile stresses of a level high enough to cause a surface flaw which was partially eliminated by the final machining, leaving very small cracks in the fillet.
- Chromium plating of steels causing passivation by oxidizing so that they behave as noble electro-positive metals. Such a chromium-plated steel pin in contact with an unprotected steel bushing may cause the bushing surface to corrode.
- Contact with more active metals causing hydrogen cracking, as described by HENTHORNE<sup>11</sup> for martensitic precipitation hardening stainless steel in contact with aluminium alloys.
- Defects in cadmium plating that create a local cathodic area. This was the case of the high-strength H-11 steel bolt which suffered an in-flight fracture as illustrated in Figure V-D.13.
- Pitting by acid solution to initiate a stress-corrosion crack. This is illustrated in Figure V-D.14 which shows a brittle fracture that occurred during a static proof-test under internal pressure of a reinforcement ring of a rocket nozzle.
- Poisonous elements such as H<sub>2</sub>S or As can accelerate hydrogen evolution in stress-corrosion processes of steel.

In aluminium alloys, initial defects may be:

- Cracks induced by cold-working correction of bending or warping deflections arising from previous heat-treatments.
- Rupture of the paint film at edges of external rivet heads by relative displacements in assemblies, and subsequent corrosion of vermicular appearance extending into the aluminium cladding, if any exists, or possibly, in absence of any anodic cladding or spraying, crevice corrosion between rivet shanks and bores.
- Cracks around rivet heads in the alumina film of anodized sheets.

In all alloys the following kinds of defect may be encountered:

- Damage by concentrated sharp contact as illustrated in Figure V-D.10.

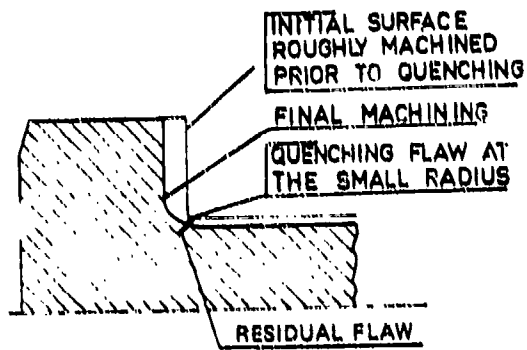
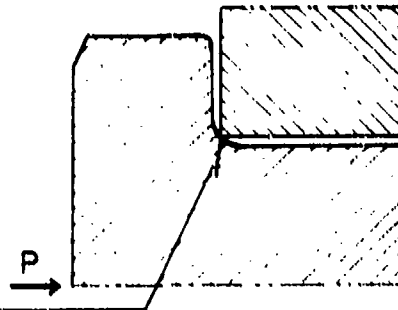
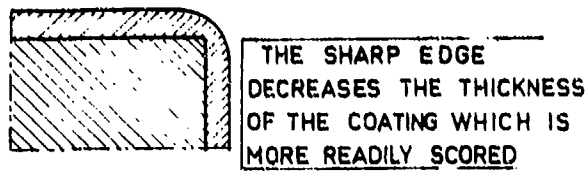


Fig.V-D.9 Quenching flaw



THE SHARP EDGE OF THE HOLE DAMAGES THE FILLET OF THE SCREWED-DOWN PART AND GENERATES AN INCIPIENT CRACK

Fig.V-D.10 Damage by concentrated sharp contact in a fillet



THE SHARP EDGE DECREASES THE THICKNESS OF THE COATING WHICH IS MORE READILY SCORED

Fig.V-D.11 Thinned protective coating on a sharp edge

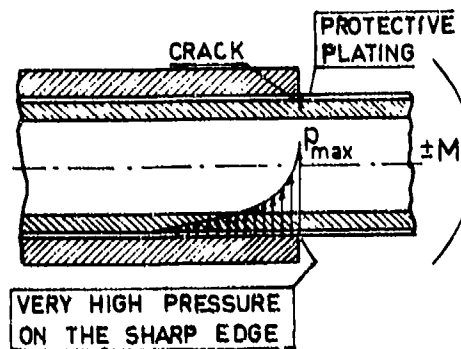


Fig.V-D.12 Fretting damage in bending due to a sharp edge

- Figure V-D.11 illustrates the thinning of the protective coating layer around a sharp edge, giving a weaker protection and a higher probability of damage.
- Surface damage by wear or fretting inflexed or movable assemblies. Figure V-D.12 illustrates the case of a brittle failure that occurred during a fatigue test on a tubular element made from high-strength 35 W C D 16 steel (similar to 4340 US steel) tempered for a tensile ultimate strength of 260,000 lb/in<sup>2</sup>. Under the action of a bending load, the electrolytic chromium plating was removed at the sharp edge of the encasing. A crack was then propagated under corrosion-fatigue conditions.
- Pitting during inter-operations storages in manufacture.
- Scratches and scores resulting from handling during assembly or maintenance operations.
- Unprotected areas due to hand-filing at the time of final assembly of parts into structure.
- Short transverse cracking by stress-corrosion or by fatigue under local vibrations may become dangerous in parts loaded longitudinally under general fatigue loads that cause the direction of crack propagation to change.
- In a similar way, a fatigue crack due to local vibrations may be relayed by stress-corrosion.

Most frequently, stress-corrosion damages occur close to parting lines in die forgings where forging fibres are cut by machining, and more generally in areas where tensile stresses exist continuously in the short transverse direction. Figure V-D.15 illustrates the failure of a forging made from 2014 aluminium alloy and submitted to ground load under the aircraft weight. The forging had a tubular shape in the cracked region and was assembled with an inner steel tube shrink-fitted in liquid nitrogen. The fracture, 250 mm long, occurred suddenly while the aircraft was at a standstill. The brittle aspect of the fracture is shown in Figure V-D.15 b. The fracture was caused by surface cracks due to intergranular stress-corrosion and originated from the inner surface of the part in contact with the steel tube and was close to the die-forging parting line. Figure V-D.15 c shows a large number of subsidiary cracks in the region near the fracture. Figure V-D.15 d is a micrograph which shows the crack path in the direction of grain flow.

Corrosion is governed by the action of an electrolyte, which is often aqueous, in the presence of surface differences resulting from heterogeneities in composition and in chemical and physical properties. Besides micro-differences existing in the material itself, corrosion-generative differences can be influenced by the location of the corroded area in the structure.

In aircraft structures, corrosion by differential aeration is the most frequent case. The local electrolyte is generally provided by condensation of atmospheric water vapour onto a cold surface. Pitting corrosion of metallic materials, bare or passivated by an oxide film, is favoured by drop condensation of water.

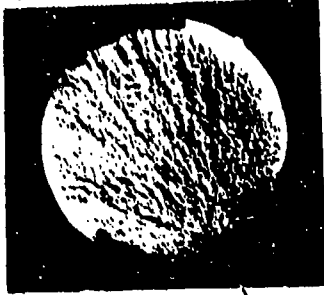
In numerous cases, corrosion cells in storage tanks result from sludge deposits or from stratification of liquids having different densities. The microbiological corrosion at the bottom of aircraft fuel tanks is due to the presence of water, deposits of sludge, and to bacterial growth that releases acid products of metabolism. Heterogeneities in aeration and acidity create corrosion cells.

Gasket materials or thermic- and acoustic-insulating materials able to leach chloric or sulphuric products at room temperature or, by accident, at elevated temperatures, may cause corrosion. In certain cases, electrolytes result from leakage of aggressive products such as acid vapours from batteries, alkaline or acid liquids escaping from galleys and toilets in passenger airplanes, leakage or emission of foods or chemical compounds from the freight, as well as traces of contamination arising from the fabrication which the cleaning and protection processes have not removed.

In aircraft, condensed water accumulates in the cold zones of poor ventilation such as bottom of fuselage, stringer of closed top-hat shaped cross-section, or low situated cavities and recesses. Because of the contraction and expansion of air due to variation in altitude and temperature, water vapour enters easily into all cavities and gaps. When cavities are colder than the environmental atmosphere, condensed water can spread and remain there for a time long enough to produce corrosion damage. Particularly, paint or varnish films are always porous. When they cover interstices or when blisters form due to local defects of adhesion, water enters the cavities, and the corrosion products raise the film, and extend the peeling of the film to failure and subsequent scaling. Attachment of equipment onto a cold metallic surface may provide a gap which will retain condensed water and favour corrosion.

Internal condensation of water can destroy the aluminium honeycomb sandwich material, when joints show evidence of manufacturing defects or in the presence of fatigue cracks, due to the corrosion of the honeycomb walls of the sandwich core. Further

Photo. CEP Saclay, France.



STRESS CORROSION CRACK

H-11 steel treated to 175 daN/mm<sup>2</sup> (250,000 lb/in<sup>2</sup>). Cadmium-plated, 12-mm dia. shank of a 16-mm dia. bolt screwed tight under a 25-mmdaN torque.

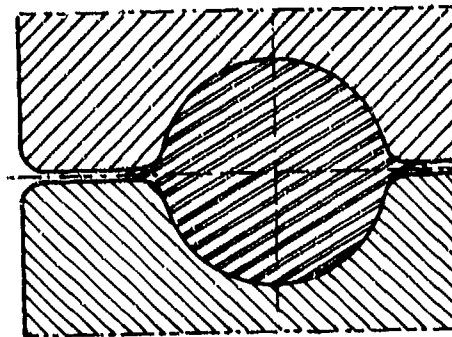
Fig.V-D.13 Stress-corrosion service failure of a high-strength steel bolt

Photograph Nord Aviation, France

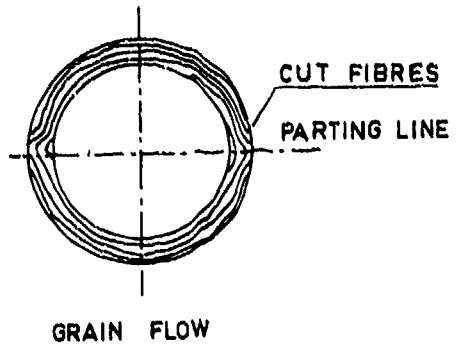


CORROSION PIT  
STRESS CORROSION CRACK  
BRITTLE FRACTURE

Fig.V-D.14 Stress-corrosion of steel part treated to 198 daN/mm<sup>2</sup> (280 000 lb/in<sup>2</sup>)



DIE FORGING

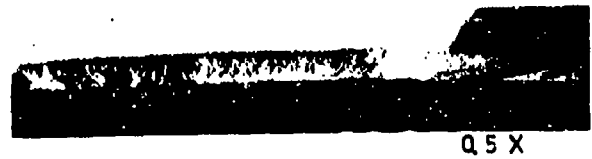


GRAIN FLOW

(a) Die forging fibres are cut by machining.

Photographs from C.E.P., Saclay, France.

(b) Fractured surface.



0.5 X

(c) Arrows indicate stress-corrosion near the fractured surface as viewed from inside.



4 X

(d) Micrograph shows intergranular cracks.



120 X

Fig.V-D.15 Stress-corrosion in a high-strength aluminium alloy part near the parting line of die forging

damage can occur from expansion of the water when it changes to ice.

Crevice corrosion can result from a deep pit but more often occurs in gaps or assembly clearances as well as under fouling deposits or sludge. In a pre-existent crevice, oxygen diffuses toward the cathodic surface and the difficulty of oxygen renewal causes the crevice bottom to remain anodic. Although corrosion phenomena are of very various natures, it is worth noting the relative importance of crevice or gap corrosion.

The resistance of materials to crevice and gap corrosion cannot be appraised from conventional corrosion tests of coupons to salt spray or to exposure in sea or industrial atmosphere. Accelerated tests or long time tests have no significance in this case. The problem of the correct representation of corrosion in crevices or gaps might be investigated in two ways. First, it is possible, as proposed by ANDERSON<sup>33</sup> to use a special short specimen containing a central hole; an axial compressive loading causes the hole wall to yield in compression, and on unloading residual tensile stresses will be produced. Then, the self-stressed specimen may be submitted to appropriate environments, either in this condition, or after affixing lateral plates with a fastener to represent crevice corrosion conditions. After pH and corrosion potential measurements of electrochemical conditions existing in a particular case of crevice corrosion, a systematic study of the surface conditions may be performed on coupons by controlling aeration, pH and electrochemical potential to simulate the pitting conditions existing in a crevice. Secondly, tests of the two preceding sorts should be checked by more representative tests using simplified types of assembly submitted to a varying environment and simulating service variation in air pressure and temperature.

An example of problems that arise from material selection was the choice that had to be made for the 2024 aluminium alloy extrusions between the T3 treatment which favours scaling intergranular corrosion from protection defects in service, and the T6 treatment which favours pitting corrosion and necessitates careful protection during inter-operation storages.

Another example concerns stringers in upper skins of wing box beams. High compressive stresses that are developed by flight loads make buckling strength an important factor. Besides, tensile stresses due to taxiing loads are often moderately high and any fatigue problem occurs only in very flexible wings. In general, upper skin stringers are made from 7075-T651 aluminium alloy extrusions that have high yield compressive strength. However, sensitivities to pitting corrosion and then to intergranular corrosion and/or stress corrosion may lead to difficulties if rivet and bore surfaces are not protected. In wing box regions that are also integral fuel tanks, the necessary tightness was often obtained using wet-installing of bolts and rivets by coating them with a rubberlike sealing product or with zinc chromate paint or cement. In most cases this also ensures against risks of pitting corrosion and subsequent damages.

Tightness may also be secured by dry-installed taper bolts. In some cases, their service behaviour was disillusioning due to the fact that residual installing stresses aggravated by eccentricity defects of the conical bores introduced fatigue risks under taxiing loads in particularly flexible wings, the same defects leaving a gap too small to permit fuel leakage but into which water vapour enters, condenses and may cause pitting corrosion.

Another means to secure tightness in automatic riveting operations consists of forming rivet heads by slow crushing of cylindrical rivet wire sections into bores which are shaped to conform to special rivet heads. In slow forming, rivet shanks fill the bores better than in hammer riveting; residual pressure exists between rivet shanks and bores and secures tightness, at least during early phases of service operations. The necessity to avoid any defect in automatic riveting has led to an improvement in the automatic grinding of drills, thereby improving the quality of bore surfaces and probably delaying pitting corrosion.

In these sort of problems, it is quite difficult to define laboratory tests that are able to assess the corrosion implications involved in the selection of materials and of manufacturing processes that are initially based on weight saving and financial reasons. Since crevice corrosion in gaps depends on the surface condition, laboratory tests should be performed with small assembly specimens made from the same materials and manufactured by the same means as planned for the structure under consideration. Moreover, since fatigue in service, even under compressive loads, is able to produce fretting damages and to decrease the level of residual riveting stresses and so to increase clearances between rivets and bores, pitting corrosion tests should be carried out after a fatigue pretreatment and should consist of repeated immersions under load into an electrolyte (for example, 3.5% NaCl aqueous solution) and of lasting periods without loading. Specimens would be cut through rivets at various test durations in order to examine surface pitting corrosion of rivets and bores.

In assessing whether a stress-corrosion test is representative of the actual structure behaviour, attention must be paid to the correct realization of the stress field, first in initial distribution and in distribution variation while the crack propagates, secondly in intensity variation simulating variations in service condition. Of course, materials and grain flow direction must be as in the actual element.

The first point may be clarified by considering, for example, residual stresses around a interference-fitted pin. As crack propagation diminishes the initial

installing pressure, the stress intensity factor at the crack tip first increases, then passes through a maximum level and finally decreases, possibly resulting in a non-propagating crack. Current tests are effected either by applying a steady load or by imposing an initial deflection, whereas in many actual circumstances crack propagations modify the initial load or deflection conditions. Care should be taken to load the development specimen similarly to the actual part.

The second point may be illustrated by the general case of attachment lugs assembled by conical expansion bolts or containing interference-fitted bushings. For example, the lug of a RR-58 aluminum alloy clevis used as a wing attachment fitting on a passenger aircraft exhibited intergranular corrosion cracks which were attributed to residual tensile stresses produced by the tightening torque of a conical expansion pin. Laboratory measurements indicated a residual tensile stress of 3,600 to 5,800 lb/in<sup>2</sup>, depending on the tightening torque of the nut. At the same location, the tensile stress resulting from the horizontal-flight equilibrium loads was about 15,000 to 20,000 lb/in<sup>2</sup>. Now, while the residual stresses had been applied for eight years, i.e., for 70,000 hours, the additional stresses in flight had been applied each year for 10 hours per day during 300 days, i.e., for 24,000 hours.

During stress-corrosion, overload effects may be imagined as follows:

1. First, the overload causes the crack to propagate in the material damaged by intergranular corrosion until the crack front is straightened and an equilibrium depth is reached in the sound ductile material.
2. The ductile material then elongates and, after unloading, some compressive residual stresses remain and exert a retardation effect on the propagation of the stress corrosion crack under a lower load.
3. Finally, static failure occurs under the highest load at a crack depth smaller than that observed under the low steady load.
4. If the highest load is applied long enough at each loading, it may cause damage through stress corrosion by itself; if the time of application is too short, the improving effect of the load may increase the time to failure despite the smaller crack depth at final fracture.

On this point, the situation will remain uncertain, just as it was until recently with regard to fatigue, as long as no systematic study is made of the effect of high loads in the loading programmes used for stress corrosion tests. Need for this has been pointed out by several authors and recently emphasized by ANDERSON<sup>33</sup>.

Besides, for investigations on actual parts, different types of specimens may be used in different critical locations, with the best specimen shape chosen with regard to local condition. For example, in an investigation by LEHMANN<sup>34</sup> on the comparative stress corrosion behaviour of die forgings made from 7079-T6 and AZ-74.61 (German Al-Zn-Mg-Ag alloy) aluminum alloys, specimens were taken at the following locations:

- C-ring specimens around a jack point-hole,
- tension smooth specimens in a fitting area, and
- double cantilever beam (DCB) specimens in the parting line area.

Comparative tests using different types of specimens may result in different quality classification as was the case for corrosion tests of aluminum alloys in seawater by DANER<sup>35</sup>.

#### REFERENCES

1. VIALATTE, M.; Centre d'Essais des Propulseurs de Saclay (France), Laboratoire de Métallurgie, Report No. 4129-L-69, 1969.
2. WESSEL, E. T.: The influence of pre-existing sharp cracks on brittle fracture of a Nickel-Molybdenum-Vanadium forging steel, Trans. ASM, Vol. 52, p. 277, 1960.
3. MAYNOR, H. W. Jr., MUELLER, R. E.: The effect of thickness and tempering temperature on fracture appearance transition temperature and critical toughness of high-strength steel sheet - Part I. Final Technical Report No. 2, May 30, 1963, Auburn University, AD 411781, see beginning of the study in Proc. ASTM, 1962.
4. VISHNEVSKY, C., STEIGERWALD, E. A.: Influence of alloying elements on the low-temperature toughness of martensitic high-strength steels, Trans. ASM, Vol. 62, No. 2, p. 305, June 1969.
5. MacGREGOR, C. W., GROSSMAN, N.: Some new aspects of the fatigue of metals brought out by brittle transition temperature tests, The Welding Journal, March 1948, pp. 133-s to 144-s.
6. JESSELLS, J. M., JACQUES, H. E.: Effect of fatigue on transition temperature of

- steel, The Welding Journal, Feb. 1950, pp. 74-s to 83-s.
7. BARROIS, W.: Manual on Fatigue of Structures - Fundamental and Physical Aspects, AGARD-MAN-8-70, See Sections 2.5.3 and 5.3.4., 1970.
  8. SALKIN, R.V.: How low cycle fatigue embrittles pressure vessel steels, C.N.R.M., No. 8, Sept., 1968.
  9. HOLDEN, J.: The hardening and embrittlement of mild steel by cyclic stressing at the fatigue limit, Acta Metallurgica, Vol. 7, June 1959.
  10. WEISZ, M., ERARD, M.: Contribution a l'etude de la fragilisation par deformations alternées d'un acier pour caisson de réacteur, Revue de Metallurgie, Mémoires scientifiques, LXIII, No. 2, p. 180, 1966.
  11. MYLONAS, C., ROCKEY, K. C.: Exhaustion of ductility by hot straining - An explanation of fracture initiation close to welds, Welding Journal, July 1961, Research supplement, p. 306-s.
  12. MYLONAS, C.: Static brittle fracture initiation without residual stresses, Welding Journal, Nov., 1961, Research supplement, p. 516-s.
  13. BROEK, D., NEDERVEEN, A.: The influence of the loading rate on the residual strength of aluminium alloy sheet specimens, Report NLR-TR M.2154, National Aerospace Laboratory NLR, Amsterdam, Oct. 1965.
  14. FORD, G., RADON, J. C., TURNER, C. E.: Fracture toughness of a medium strength steel, Imperial College of Science and Technology, Department of Mechanical Engineering, London, 1967, Private communication; see also: RADON, J. C., Turner, C. E.: Note on the relevance of linear fracture mechanics to mild steel, J. Iron and Steel Institute, Vol. 204, p. 842, Aug. 1966.
  15. SRAWLEY, J. E., BEACHEM, C. D.: Crack propagation tests of high-strength sheet steels using small specimens, NRL Report 5127, April 9, 1958.
  16. SRAWLEY, J. E., BEACHEM, C. D.: Effect of rate of loading on high-strength sheet tensile and crack propagation tests, NRL, Code 6322, June 16, 1959.
  17. MARSCHALL, C. W.: The factors influencing the fracture characteristics of high-strength steels, DMIC Report 147, Battelle Memorial Institute, Columbus, Ohio, Feb. 6, 1961.
  18. OWEN, W. S., WHITMORE, D. H., COHEN, MORRIS and AVERBACH, B. L.: Relation of Charpy impact properties to microstructure of three ship steels, The Welding Journal, 36, No. 11, p. 503-s, Nov. 1957.
  19. HARTBOWER, C. E., ORNER, G. M.: Metallurgical variables affecting fracture toughness in high-strength sheet alloys, Report ASD-TDR-62-868, Wright-Patterson Air Force Base, Ohio, June 1963.
  20. REES, W. P., HOPKINS, B. E., TIPLER, H. R.: Tensile and impact properties of iron and some iron alloys of high purity, J. Iron and Steel Inst., Vol. 169, p. 157, 1951.
  21. REES, W. P., HOPKINS, B. E.: Intergranular brittleness in iron-oxygen alloys, J. Iron and Steel Inst., Vol. 172, p. 403, 1952.
  22. ALLEN, N. P., REES, W. P., HOPKINS, B. E., TIPLER, H. R.: Tensile and impact properties of high-purity iron-carbon and iron-carbon-manganese alloys of low carbon content, J. Iron and Steel Inst., Vol. 1970, p. 108, 1953.
  23. REES, W. P., HOPKINS, B. E., TIPLER, H. R.: Tensile and impact properties of Fe-Si, Fe-Ni, Fe-Cr, and Fe-Mo alloys of high-purity, J. Iron and Steel Inst., Vol. 177, p. 93, 1954.
  24. HINDERS, U. A.: F-111 Design experience - Use of high-strength steel, AIAA Paper No. 70-884, AIAA 2nd Aircraft Design and Operation Meeting, Los Angeles, Cal, July 20-22, 1970.
  25. HALL, L. P., FINGER, R. W.: Fracture and fatigue growth of partially embedded flaws, AFFDL TR 70-144 Proc. Air Force Conference on Fatigue and Fracture of Aircraft Structures and Materials, Miami Beach, 1969.
  26. Anonymous: Review of current data on the tensile properties of metals at very low temperatures, DMIC Report 148, Battelle Memorial Institute, Columbus, Ohio, Feb. 14, 1961.
  27. KIRKBY, W. T., EYNON, G. R.: The residual static strength of a bolted joint cracked in fatigue, Royal Aircraft Establishment, TR-66-111, Structures Department, Farnborough, April 1966.
  28. BRUMMER, S. B. et al.: Study of the general mechanism of stress corrosion of



aluminium alloys and development of techniques for its detection, TYCO Laboratories, Feb. 1969, quoted by NASA under No. N69-14011.

29. DAVIS, J. A.: pH and potential measurements during stress corrosion of aluminum alloys, Bell Aerospace Company, Textron Division, Buffalo, N.Y., USA; presented at AGARD S. M. Panel Meeting, Brussels, Oct. 1971.
30. BORCHERS, H., TENCKHOFF, E.: Über den Einfluss des Oberflächenbeschaffenheit auf das Spannungsrisskorrosion-Verhalten von AlZnMg-Gusslegierungen, Z. Metallkunde, Vol. 59, No. 1, Jan 1968.
31. HENTHORNE, M.: Stress corrosion cracking of martensitic precipitation hardening stainless steel, Carpenter Technology Corporation, Reading, Penn., USA; presented at the AGARD S. M. Panel Meeting, Brussels, Belgium, Oct. 1971.
32. COCKS, F. H.: Measuring the degree of conjoint action between stress and corrosion in stress corrosion, TYCO Laboratories, Waltham, Mass., USA; presented at the AGARD S. M. Panel, Brussels, Oct. 1971.
33. ANDERSON, W. E.: Engineering utility and significance of stress corrosion cracking data, Battelle Pacific Northwest Laboratories, Richland, Wash., USA, Report BNWL-SA-4073; presented at AGARD S. M. Panel Meeting, Brussels, Oct. 1971.
34. LEHMANN, W.: Results of comparative stress corrosion tests on Al-Zn-Mg-Cu alloys using different types of specimens, I.A.B.G., Ottobrunn; presented at AGARD S. M. Panel Meeting, Brussels, Oct. 1971.
35. DANEK, G. J.: Influence of test method on stress-corrosion behavior of aluminum alloys in seawater, AGARD S. M. Panel Meeting, Brussels, Oct. 1971.

W. Barrois

#### SUMMARY

The survey is an attempt to answer the question: "What information is needed in terms of load spectrum and test conditions, to extend the results of laboratory tests to the prediction of service fatigue life of aircraft structures?" After considering designers' needs and detailing the various physical parameters that are significant in the fatigue behaviour of specimens and structures, several types of fatigue tests are reviewed from the viewpoint of their representativeness. A short survey is then made of the present prediction methods of structure fatigue life from fatigue tests of components, assemblies and structures undergoing constant amplitude loadings. Then, after considering fatigue tests under programmed loadings, the case of random loadings is briefly discussed. It is concluded that describing random loadings by their root mean squares is not sufficient to predict the fatigue lives of structures even when the shape of the load power spectrum is known, except in cases of comparative prediction where the only change is the general intensity of the spectrum. The possibility of test acceleration by increasing the general loading intensity is considered. The necessity of a more complete treatment of every partial result of structural fatigue tests is emphasized as well as the usefulness of broad co-operation in this field in order to extend the amount of fatigue data able to be used by designers.

#### V-E. 1 INTRODUCTION

For several years, problems in acoustic fatigue and those implied by aircraft dynamic responses to random loadings defined by power spectra, have drawn attention of designers to possibilities of fatigue life assessment from results of fatigue tests under programmed or random loadings that simulate actual random loadings in flight. In these tests, the stress spectrum shapes in relation to statistical frequencies of occurrence and dynamical frequencies may be quite different either due to different excitations or to very different structural responses. Intensity of every loading is defined either by the maximum load or by the quadratic mean load.

Often, these tests are carried out only for purposes of fatigue strength substantiation of particular structures. Their possible use in fatigue life prediction of other structures may entail extensive tests on simple components or elementary assemblies. Before planning costly tests, it may be useful to study how such results might be used by designers.

That leads to the necessity to define designer's requirements and to review briefly fatigue prediction methods using results of conventional tests under constant amplitude loadings, and then to consider two cases of random fatigue tests, either in fatigue at low frequencies or with frequencies within the acoustic range.

#### V-E. 2 NEEDS OF THE DESIGNER

In a previous survey<sup>1</sup>, we have attempted to show that for technical reasons and due to fundamental and physical causes, it is difficult to assess fatigue life of an aircraft structure sufficiently accurately through elasticity analysis and allowable stress design values related to the particular material. Useful analyses consist only of comparative or interpolative computations based on fatigue test results of structures, assemblies or components. However, even within this restricted field, the computation size is often a heavy burden in practice. Various analytical methods of increasing complexity have been proposed. In order to assess their practical usefulness, two kinds of distinction have to be made:

- (i) Firstly, certain methods quickly yield a rough classification of assemblies; they may supply a provisional assessment at the preliminary design stage, at the expense of costly previous analyses on a large number of fatigue test results on actual and similar structures, or assemblies made from the same material through the same manufacturing processes. On the contrary, other more analytical methods imply computations that are tailored for each particular case but can be used only when detailed drawings are available.
- (ii) Secondly, the selected method and its degree of accuracy must correspond to the particular needs of the designer.

---

\*Reprinted from AGARD Conference Proceedings No. 118.

At the preliminary design stage, assembly modes and manufacturing processes that entail the minimum of fatigue problems and a design with geometries that make possible further local reinforcements the incorporation of which do not imply extended design changes, would be selected. In addition, the structure must be "fail-safe" against fatigue or other causes of damage. The fail-safe requirement may lead to vital attachment being oversize locally, such that the fatigue problem disappears.

At the prototype design stage, a first comparative analysis should supply a rough classification of the various assembly areas of the structure according to the following degrees of decreasing fatigue strength:

- certainly sufficient,
- doubtful,
- certainly insufficient.

Areas of "certainly insufficient" strength should precipitate immediate design changes. "Doubtful" areas should be assessed again by means of another more accurate computation based on previous fatigue tests. In case of a doubt persisting, development tests on representative assemblies or partial structures should be carried out under the estimated particular loading programme of the aircraft.

At the production design stage, an interpretative third analysis on development test results might take account of changes in aircraft loading, weights and performances, design and sizing, since the prototype stage. Moreover, some areas previously classified as sufficiently strong may become doubtful, and other development tests should be carried out and analyzed by means of a previously demonstrated computation method.

Finally, after the full-scale fatigue tests, interpretative computations are necessary in order to substantiate the fatigue evaluation of operational aircraft, taking into account the latest design changes and inflight load measurements performed in actual operations on the first operational airplanes.

Designers' needs may be summarized as follows:

Interpretative computations that enable re-assessment to be made of the fatigue life of a structure for a new loading programme significantly different from the testing programme.

"A priori" subjective classification of fatigue strength of structural assembly areas with respect to the fatigue strength of structures previously known to be sufficient or insufficient. This implies computations that define the fatigue quality of each structure tested and the quality needed to withstand the particular loading programme that corresponds to the aircraft studied and to its foreseen operational use.

Prediction analysis should take into account detail shapes and sizing. Computations of local stresses near stress raisers and assessment of the allowable intensity value of the load spectrum are needed. Empirical coefficients to use in computations would be obtained by the same computation methods from test results of simple assemblies representative of stress raisers and of current design of joints.

#### V-E J REPRESENTATIVENESS OF FATIGUE TESTS

In order to study the possibilities of assessing life in service from test results, it is first fitting to examine the representativeness of the tests. Obviously, the service behaviour can be considered to be the most representative test.

- (a) Indoor full-scale fatigue tests carried out by the Swiss "Fabrique Federale d'Avions" at Emmen are fairly close to service operation in that the loads applied to wing, tail surfaces, fuselage and landing gears are controlled by continuous recording which was performed during service operations for a time long enough for the statistical sampling to be considered as stationary. However, the environment is not so representative from the corrosion point of view. This type of test can begin only after some time of service operations, hence its purpose is only a final verification yielding results after a long time of service operation has elapsed.
- (b) Conventional full-scale fatigue tests carried out indoors or, better still, in the open, are often performed on a flight-by-flight basis with loading programmes deduced from general statistical data confirmed by sampling measurements carried out on the prototype aircraft or the first production aircraft. The loading programme may be simplified to consist of a reduced number of load levels by means of "equivalent" damage calculation based on fatigue test results of "fairly" representative specimens. It may also be randomized in replacing the continuous curve of the cumulative frequencies of occurrence by a stepped diagram resulting in a discrete number of level classes of flight and ground loads, the application sequence of which is randomized. In some cases the fuselage is immersed into a water tank and filled with water. Other tests are carried out with air pressurization, the fuselage being filled with rigid plastic foam. Outdoor tests are recommended as being more representative from the corrosion point of view.

- (c) Full-scale fatigue tests of incomplete structures are carried out in the laboratory, either under a simplified loading programme from service measurements, or more frequently under constant amplitude loadings when it is possible to compare several versions of design, materials or manufacturing processes.
- (d) Systematic fatigue tests of assembly elements such as sheet joints by means of one or several rivet lines, lug loaded by a pin, etc., are generally performed under constant amplitude loads for several intensities in order to plot a mean S-N curve and to appraise the scatter.
- (e) Systematic fatigue tests of notched specimens under constant amplitude loads of several intensities and with several values of the alternating-to-steady component ratio and several geometrical notch factors give results which are often used as middle term of comparison to assess the fatigue behaviour of structures under loading programmes differing from those under which they were tested.
- (f) Research fatigue tests of elementary assembly specimens or notched specimens appraise the influence of different loading programme types assumed to be equivalent in damage when based on the Miner-Palmgren rule.

In order to determine what the representativeness of these types of tests may be, i.e., how realistic they are, and what degree of confidence to ascribe to them, it must be noted which are the parameters of significance in the fatigue behaviour and how these parameters are represented in every fatigue test type.

Broadly considering the initiation phase of fatigue cracking, the governing parameters are as follows:

- (i) The alternating component of the surface stress which gives rise to alternating plastic shear strains which modify the cold-worked condition of the surface material and which create clusters of vacancies and pileups of dislocations, as well as surface crevices, from which microcracks originate.
- (ii) The maximum value of the tensile surface stress which plays an important part in the growth of micro- and macro-cracks.
- (iii) The stress gradient in the direction perpendicular to the surface which governs the material depth within which plastic distortions are significant.
- (iv) Intensity, gradient and stability of surface residual stresses which, when they are tensile, decrease the duration of the fatigue crack initiation phase, whereas they have a delaying effect when they are compressive.
- (v) The geometrical roughness of the surface, and the metallurgical condition of the surface material.
- (vi) The beneficial effect of a small enough number of high loads that create favourable residual stresses at notch roots but do not yet create microcracks when applied.
- (vii) The corrosion sensitivity of the material and, in assemblies, the fretting behaviour which can create surface damage that may seriously shorten the crack initiation phase.

The fatigue crack propagation phase depends on the stress distribution in the crack area and on the changes in this distribution due to the crack propagation. It also depends on loading sequences through the beneficial effect of rarely occurring overloads. A corrosive environment may also substantially increase the crack propagation rate. Crack propagation may be impeded when the load is transferred from the cracked area into another assembled part (fail-safe). It may nevertheless give rise to a static fracture. In the case when the propagation of a fatigue crack ceases, further crack propagation may take place due to stress corrosion or intergranular corrosion.

Final static fracture occurs with a smaller and less easily detectable crack the more brittle the material and the thicker the part. It is worth noting that the material is often more brittle in the short transverse direction.

Preceding features imply that to be representative of service behaviour, every full-scale fatigue test should be carried out with a structure made from the same materials, having undergone the same treatments, manufacturing and protection processes, and the same inspection and maintenance procedures as the operational structure. This kind of test is costly and takes too long to complete. Its application is therefore restricted to final fatigue strength substantiations carried out in accordance with the tests of types (b) and (c) previously reviewed.

However, due to discrepancies between the test loading programme and load statistics from measurements performed during actual service operations, or subsequently to change in operational conditions such as freight weight, aircraft speed, etc., or again after an important development of the aircraft without general modification of the primary structures, a reassessment of the fatigue behaviour may be necessary without

the possibility of carrying out a full-scale fatigue test. This raises a problem of selection between partial fatigue tests of weak areas and of systematic tests the results of which will be used in comparative calculations.

All computation methods are based on tests that are performed under conditions more or less representative of actual service environments. Corrosion had no influence in the very rare laboratory tests performed in a vacuum or in a neutral atmosphere, e.g., in dry argon. In normal indoor tests, the corrosion effect is generally fairly small, except during the crack propagation phase in materials susceptible to stress-corrosion. In full-scale fatigue tests performed in the open and in those carried out in water-tanks, the test duration of more than one year achieves a sufficiently severe simulation of the corrosion environment. Corrosion often has a significant but moderate influence on the test duration, measured in real time, and on the fatigue life which is measured in number of cycles, flight hours or number of flights.

Another time effect is due to dynamic resonance of the structure that modifies the stress intensities and distributions. A distinction should be made between random loads at low frequencies which excite vibration modes of the whole structure, and high frequency random loads which excite only local vibration modes of small structure areas.

In discussing prediction methods, the following cases of random loading are to be considered:

- Very low dynamic frequencies for which the structure behaves quasi-statically. The loading spectrum mainly depends on the aircraft mission.
- Frequencies within the range of fundamental vibrations modes of the whole aircraft which excite structural vibration modes, but for which corrective computations can bring the problem back to the case of quasi-static loading. Loading spectra depend on aircraft missions and dynamical properties on the whole structure. Slow fatigue test results can be used in the assessment of fatigue life, and the number of flights is the more logical fatigue life unit.
- Acoustic frequencies excite locally small structural elements. Stress spectra depend on excitations and local dynamical properties of the structure. They are different from those applied to the whole structure. Numbers of cycles to consider are generally very large compared with those of loadings that concern the whole structure.

#### V-E 4 PREDICTION AND ANALYSIS METHODS FOR CONSTANT AMPLITUDE LOADINGS

Computation methods which use fatigue test results of notched specimens disregard possible damage by fretting due to relative micro-displacements at the contact surfaces of assembled materials.

Computation methods based on tests of assemblies are also questionable due to the fact that materials, although nominally defined, may differ from those used in the structure. For example, differences may be associated with heat treatment, grain texture, surface condition and corrosion protection.

Computations should, therefore, introduce empirical coefficients resulting from laboratory tests on representative assemblies, which should then be modified after outdoor full-scale fatigue tests and possibly reviewed in the light of service behaviour.

The earlier method of fatigue life assessment of a notched component was based, for comparison, on the higher surface fatigue stress in the notch, so that the favourable effect of the stress gradient in depth was disregarded. This method is very conservative if the data used are from axial fatigue tests on smooth specimens; it is simple and may be used to check whether or not the fatigue strength can definitely be considered sufficient. However, fatigue strength may be overestimated when using rotating bending results of small-diameter smooth specimens. This method fails in the case of fretting or of superimposition of undefined stress raisers.

An improvement of this method was made by taking stress gradients into account and by using fatigue test results of a set of notched specimens with several notch factor values. This permitted curves to be drawn showing fatigue life as a function of alternating and steady components of the higher surface stress for several values of the relative stress gradient,  $(1/\sigma)\partial\sigma/\partial n$ , in the direction perpendicular to the surface<sup>1,4</sup>.

In 1959, Hayes<sup>3</sup> proposed to use fatigue test results of notched specimens with several values of the  $K_T$  notch factor in order to define by interpolation an "equivalent notch factor" from one fatigue test of the studied component. Then, the interpolation of curves from test results on notched specimens using this equivalent notch factor enables an assessment to be made of the component fatigue behaviour under any loading programme.

In 1962, an improvement by Benoff<sup>4</sup> was based on the approximate correlation between the test specimens between the maximum fatigue stress of a notched specimen and that of smooth specimens. This correlation was found to be independent of the alternating-to-steady stress ratio and to encompass a large range of cycles, but was not valid for round specimens. The correlation varies with each notch factor,  $K_T$ ,

but the fatigue notch factor,  $K_F$ , varies with  $K_T$  and the notch radius,  $r$ , according to an empirical relation.

$$K_F/K_T = f(r).$$

From this, Deneff derived an interpolation method to obtain the diagrams,

$$N = f(\sigma_a, \sigma_m),$$

corresponding to fixed values of  $K_T$  and  $r$ . He applied its method to fatigue strength computation on sheet assemblies where, for the stresses at edges of holes, a distinction was made between stresses resulting from the local load transferred by each fastener and those by-passing the fasteners.

To compute local stresses in a multi-riveted statically-redundant assembly, each assembly sheet was idealized by a system of rectangular meshes according to network lines, the nodes of which were at hole centres. These network lines were assumed to be axially loaded bars transferring shear loads to rectangular sheet elements. Deformations due to bearing stresses in holes and to rivet bending were disregarded. Computation, restricted to the elastic range, yielded nominal stresses applied near each hole and local loads transferred by each rivet. Allowable values of these loads and stresses were drawn from fatigue tests on elementary elements.

In 1969, a first attempt was made by Jarfall<sup>5</sup> to take account of the bending of rivets and hole bearing deformations which vary with sheet thickness, fastener diameter, and with the material. He used elasticity methods of assembly analysis previously investigated from 1944 to 1947 by Vogt<sup>6</sup>, Manford et al.<sup>7</sup>, and Rosenfeld<sup>8</sup>. In this field it is worth noting a recent paper by Harris et al.<sup>9</sup> that recognizes the possibilities afforded by modern digital computers.

In order to take into consideration the plastic behaviour under fatigue stressing, i.e., changes in stress-strain cycles, creation or relaxation of residual stresses, surface condition in holes, axial tightening and diametral interference or clearance of fasteners, Jarfall introduced two empirical coefficients to be determined in partial fatigue tests. Using these coefficients, he called the "Stress Severity Factor - SSF" the ratio of the higher local stress at a hole edge to a reference stress chosen to be the nominal stress near the hole assuming the hole was reduced to a zero diameter.

To determine empirical coefficients, it was postulated that, for a fixed fatigue life of  $N$  cycles, the fatigue failure of different elements would occur for the same value of the higher local stress, i.e., for the same value of the product of the nominal stress to failure after  $N$  cycles and the SSF-factor. Hence, this factor has some similarity with the fatigue notch factor  $K_F$ . It is valid only within a certain range or number of cycles which would have to be determined by experience. It might still be called "Fatigue notch factor equivalent to the assembly detail" and designated  $K_F$ . Three specimens are needed to obtain two ratios each of which supply one coefficient. Jarfall used flat sheet specimens containing a circular hole with three loading modes: axially loaded specimens with free hole or hole filled by a fastener, and specimens fixed at one end and loaded at the hole by means of a pin. Then, in fatigue tests of assemblies, local values of the Stress Severity Factor were determined for each incipient crack. Knowing the SSF of various areas of an assembly, it is possible to compute its fatigue life under any loading programme and then, knowing its service behaviour, to define allowable values of the SSF for each particular class of design and of operational service.

Crichlow and his collaborators<sup>10</sup> have proposed the so-called "Fatigue Quality Index" method that comprehensively characterizes the fatigue behaviour of an assembly and implicitly takes account of details and materials. The fatigue quality index is the geometrical notch factor chosen from amongst, or interpolated from, those of a set of simple notched specimens, made from a reference material that has yielded  $N = f(\sigma_a, \sigma_m, K_T)$ -curves, in order to have same fatigue life as the tested component for the same values of the nominal fatigue stress,  $\sigma_a$  and  $\sigma_m$ , near the notch or the assembly junction. If the component is tested under a loading programme, fatigue durations of reference specimens are computed and plotted against the loading programme intensity, and, through the point representing the component fatigue test, one interpolation is made to define the  $K_T$ -value of the notch factor equivalent to the component. Since the material of the tested component may differ from that of the reference specimens, one no longer speaks of equivalent  $K_T$  but only of Fatigue Quality Index  $K$ . As in Jarfall's tests, structure tests are carried out considering all intermediate durations until cracks appear, the repair of which allow the fatigue test to continue and more useful results for further prediction purposes to be obtained. This is supported by the fact that in the absence of a "fail-safe" design, the duration for a crack to be detectable is in practice often close to the total fatigue life to failure. For aluminium alloys, 2024-T3 aluminium alloy sheet material is used as the reference.

All previously mentioned methods are based on the assumption that, by means of comparative, comprehensive testing made through parameters the knowledge of which enables prediction to be made of the fatigue behaviour of another structure or of an element assumed to be similar to the local area under investigation. In the different cases, attempts are made to describe design and loading conditions of more or less complex structural details in order to bring every problem back to one which has been previously tested. However,

because manufacturing processes and metallurgical conditions are playing an important part, it may be expected that the prediction accuracy will be limited by the difficulty to exactly describe all significant conditions. At the very best, it may be hoped that quite good prediction will be possible from a first full-scale fatigue test on the structure being studied when the evaluation aim will be only to appraise the effect of slight changes in sizing and loading on the fatigue life.

The comparisons can be defined along the following lines:

1. Loading types and their intensities

Loading may be of three types, namely, constant amplitude, programmed, or random. Intensities of each of them may be measured respectively, as amplitude, higher load and load distribution, and quadratic mean load.

2. Reference structures

They may be as follows:

- (a) Another structure of same detail design, materials and manufacturing processes.
- (b) Structural assembly details having same features.
- (c) Notched specimens of same relative stress gradient, material and manufacturing processes.
- (d) Smooth specimens made from the same material.

The following comparison parameters may be used:

- (i) The "Equivalent notch factor -  $K_T$ ", the "Stress Severity Factor - SSF" and the "Fatigue Quality Index -  $K$ " are used with reference structures of the types (a) and (b).
- (ii) Nominal design stresses around stress raisers are to be used in connection with tests on reference representative details.
- (iii) Surface stresses and their relative stress gradients in depth direction.
- (iv) Surface stresses alone.

Table I shows a simplified description of prediction methods.

A valuable extension of these studies would be the establishment of prediction means, consisting of banks of data on fatigue strengths of conventional structures and elements, and suitable as input data for digital computers for strength or optimization analyzes. All items of these data would be provided by accurate analyzes of test results on full-scale structures, partial structures, and components and assemblies representative of various designs under constant amplitude loadings. The cases of fatigue life prediction under random loading would be treated by means of the Miner-Palmgren rule.

V-E 5 DAMAGE EVALUATION OF FATIGUE LOADINGS ON STRUCTURES BY SIMPLIFIED REPRESENTATION OF THE RANDOM LOAD SPECTRUM

In most full-scale fatigue tests of aircraft structures, the applied load system is simplified with respect to random service loads. The first problem to deal with consists of defining a test load system that is equivalent to service loads with regard to fatigue damage. Figure 1 which concerns the full-scale fatigue test of the "Caravelle" structure, schematizes the general course of computations from gust velocity statistics and one estimate of ground loads to define the load programme to be applied during a test cycle which represents one mean type flight. Figure 1(a) shows gust velocity statistics by sections of altitude, drawn from acceleration recording on an aircraft of comparable type and performances (Comet 1) during a world-round trip. Figure 1(b) illustrates the estimated type flight of the Caravelle with values of air-speed, altitude and aircraft weight that are varying during the flight. For each flight section, constant values are assumed, and partial statistics of acceleration increments,  $\Delta n$ , at the gravity centre are determined. They are corrected to give the same loads when applied to the reference take-off weight. Figure 1(c) shows the sum of these partial statistics as one curve of cumulative frequency in  $10^4$  flights to reach or exceed  $\Delta n$ -values. Then it is assumed that the wing structure, in the areas of high stresses, has the same fatigue properties as the notched specimens, the constant amplitude fatigue properties of which are represented in Figure 1(d); in this particular case, these stresses depended on the acceleration increment  $\Delta n$  as follows:

$$S = 8.1 \pm 8.1\Delta n \text{ daN/mm}^2.$$

The load spectrum of the figure 1(c) was decomposed into a series of constant amplitude fatigue loads,  $S_i = 8.1 \pm S_{ai}$ , each of them being applied for  $N_i$  cycles and producing a partial damage.  $N_i/N_{Ri} \cdot N_{Ri}$  is the number of cycles to failure under the load  $S_i$ , taken from the Figure 1(d). Numerical data and computation results are reported in Table II.

Partial damage due to ground loads during landing and taxiing, as well as that due to ground-air-ground transition from the lowest negative stress to the highest positive stress can be computed from appropriate load statistics. In the case of the Caravelle, at the beginning of the full-scale fatigue test, the total computed damage was 0.84 for 10<sup>4</sup> flights. The test was carried out for 100,000 cycles without noticeable actual damage. This first test phase was followed by a last phase under a simplified load programme of 210 higher load level for 3,000 cycles corresponding to 4400 flights. It was shown that the test "damage" was lower than 0.1 for 10<sup>4</sup> cycles and that a life of 20,000 flights was substantiated with a scatter factor of 5.

In addition to the fact that the structure under investigation may have a better fatigue strength than the reference notched specimen (here,  $K_T=4$ ), the discrepancy between damage prediction and full-scale test results is partially explained by the beneficial effect of the supplementary "fail-safe" cycles in which the higher load corresponds to an occurrence frequency of about ten times in 10,000 flights, i.e., to a load defined by  $n = 2.56$  and a corresponding maximum stress level of 20.8 daN/mm<sup>2</sup>, whereas the maximum stress levels in the other test cycles were of 12 daN/mm<sup>2</sup> in normal cycles applied up to 20,000 cycles, and of 16.2 daN/mm<sup>2</sup> up to test completion.

In fact, computation had only been used to replace the loads of the average flight in the Figure 1(e) by the "equivalent" test loads of the Figure 1(f), in which the load reached or exceeded on average one time per flight had been kept. In actual service, up to 15,000 flights, the fatigue damages were negligible. Detected damage which did not affect the flight safety was due to unpredicted taxiing loads but such damage concerned only the wing rib at the main landing gear attachment.

This general course of fatigue computation has been retained in France for the Falcon 20 and the Nord 262 civil aircraft, as well as for the military transport aircraft Transall C-160, designed and manufactured in a French-German co-operation. The statistics used for gust loads were those of the RAS Data Sheets. In the case of the Transall aircraft, measurements in flight at low altitude have yielded load statistics used in the interpretation of fatigue test results.

Several causes of error exist in this kind of computation:

- (i) Certain load statistics are unknown at the time of test. This was the case for the asymmetrical loads on tail surfaces of the Caravelle type which used thrust reversal after touch-down. In the 707 Boeing aircraft operations, taxiing afforded unpredicted repeated tension stresses in the upper wing skin.
- (ii) Fatigue test data from notched specimens or from structures of old design and of war-time manufacture represent badly the properties of the structure under investigation. To cope with this difficulty, some fatigue tests on assembly elements representative of the structure may be carried out under a standardized load spectrum.
- (iii) The beneficial effect of design limit loads that could be encountered very clearly in service, or their detrimental effect when applied after a crack initiation, are not represented in tests. The beneficial effect due to a premature application of high loads must be avoided, whereas the detrimental effect would shorten the fatigue life only slightly, due to the exponential course of the crack propagation in fatigue.
- (iv) The principle on using an average flight loading is questionable since a number of flights are carried out without noticeable gust loading and also because gust loads concentrated during few flights are less damaging due to the lowering by application of the first high gust of residual tensile stresses created by taxiing loads. When the loading spectrum includes compressive stresses, the damage under a service loading may be less severe than under an average loading programme, as far as the statistics of turbulent and quiet flights are concerned.

As long as the final true load spectrum differs but little from the spectrum used in the structural fatigue test, corrective computations may be made for the areas damaged by the applied loads or, in default of damage, in conservatively assuming damage beginning just at the conclusion of the test.

When the true load spectrum is unknown, comparative experimental investigation of several designs or manufacturing processes may be carried out, or the fatigue strength of a particular structure may be appraised, under a standardized approximate spectrum. In development tests based on a standardized shape of a spectrum of cumulative frequencies of level crossings, a distinction should be made between aircraft components loaded similarly to a wing, i.e., under a loading programme having two mean load values, and components with a loading programme having only one mean load value.

For the first loading case, typical of wings, D. Schütz<sup>12</sup> has proposed the standardized load spectrum shape shown in the Figure 2. It corresponds to a mean load spectrum drawn through flight measurements carried out on DC-9, Boeing 737, BAC-111 and Transall aircraft. Flight loads measured on the Air-France's Caravelles are plotted at the lower limit of the scatter band. It must be pointed out that these loads are deduced from vertical acceleration measurements at the gravity centre by means of a



**TABLE I**  
Fatigue Prediction Methods for Structures Submitted to Loading Programmes

STUDIED A-STRUCTURE (LOADING PROGRAMME)	REFERENCE STRUCTURE B*		COMPARISON PARAMETERS	TYPES OF CALCULATION	EXPERIMENTAL DATA	
	TYPE	LOADING			SPECIAL TEST ON B	GENERAL DATA
FULL-SCALE	FULL-SCALE a	PROGRAM.	EQUIVALENT $K_T$ JARFALL'S SSP FATIGUE QUALITY INDEX K	DAMAGE (A, B) ELASTICITY (A, B) DAMAGE (A, B)	YES YES YES	S-N NOTCH CURVES OF THE MATERIAL  S-N- $K_T$ REFERENCE CURVES
ASSEMBLY	LOCAL FITTING b	PROGRAM.	NO	NO ANALYSIS, SAME STRESSES ON A AND B.	YES	NO
		CONSTANT AMPLITUDE	DAMAGE  NOMINAL STRESSES	DAMAGE (A, B)  DAMAGE (A, B)	YES  NO	TESTS OF B, CONSTANT AMPLITUDE LOADS.
COMPLEX NOTCHED COMPONENT	NOTCHED SPECIMENS c	CONSTANT AMPLITUDE	SURFACE STRESS AND GRADIENT	ELASTICITY PLOTTING OF S-N-RELATIVE GRADIENT CURVES	NO	S-N NOTCH CURVES AND SIZE EFFECT LAW.
$K_T$ NOTCHED COMPONENT	SMOOTH OR NOTCHED SPECIMENS d	CONSTANT AMPLIT.	SURFACE STRESS	ELASTICITY DAMAGE	NO	S-N CURVES OF SMOOTH OR NOTCHED ( $K_T + K_{T_A}$ ) SPECIMENS.

**TABLE II**  
Damage Computations for the Caravelle Wing Under Gust Loads

U, ft/sec., RAS.	7.5	10	15	20	25	30	35	40	45
$\Delta n$ to $P_d$	0.242	0.322	0.403	0.644	0.803	0.966	1.120	1.29	1.45
N cumulative	88,800	35,174	6,610	1,584	426	188	66	34.5	1
$\Delta n$	0.282	0.402	0.563	0.724	0.905	1.046	1.207	1.37	1.53
$N_1$	51,426	28,564	5,016	1,188	238	122	31.5	33.5	1
$S_{d1}$ (daN/mm <sup>2</sup> )	2.28	3.25	4.55	5.9	7.15	8.45	9.75	11.1	12.4
$N_{R1}$	$2 \times 10^6$	$5 \times 10^5$	$10^5$	$4.5 \times 10^4$	$2.5 \times 10^4$	$1.4 \times 10^4$	$8.4 \times 10^3$	$5.4 \times 10^3$	$3.6 \times 10^2$
$N_1/N_{R1}$	0.0257	0.0572	0.0503	0.0258	0.0095	0.0087	0.0038	0.0062	0.003
Total gust damage for $10^4$ flights = $\sum N_1/N_{R1} = 0.1875$									

**TABLE III**  
Distributions of Occurrence of Level Crossings

$H/H_0$	$10^{-7}$	$10^{-6}$	$10^{-5}$	$10^{-4}$	$10^{-3}$	$10^{-2}$	$10^{-1}$	0.3	0.5	1
EXPONENTIAL	1.167	1	0.833	0.667	0.500	0.333	0.167	0.117	0.083	0
GAUSSIAN	1.085	1	0.908	0.795	0.672	0.529	0.335	0.210	0.136	0
RAYLEIGH	1.08	1	0.913	0.817	0.710	0.580	0.408	0.296	0.224	0
LOG-GAUSSIAN	1.215	1	0.804	0.622	0.470	0.335	0.216	0.162	0.137	0.10

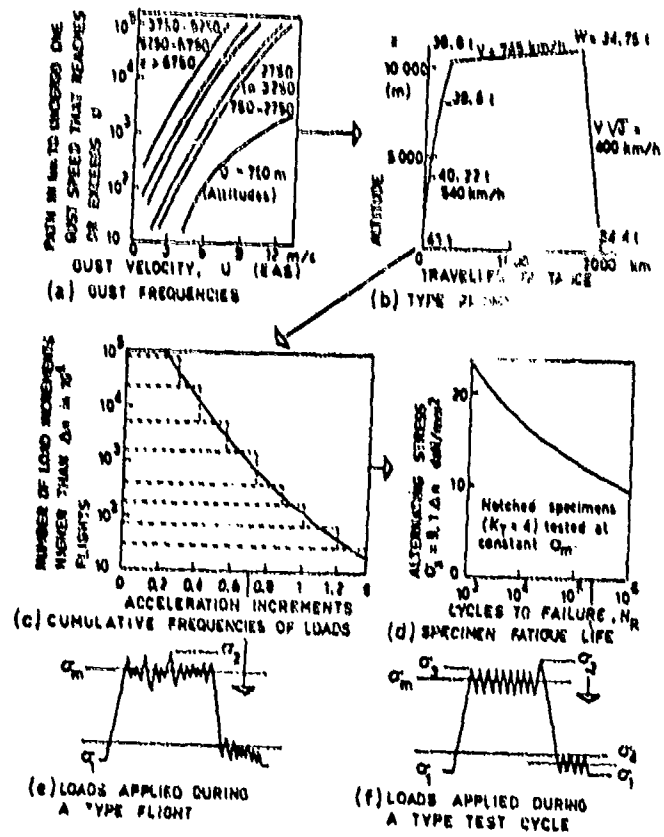
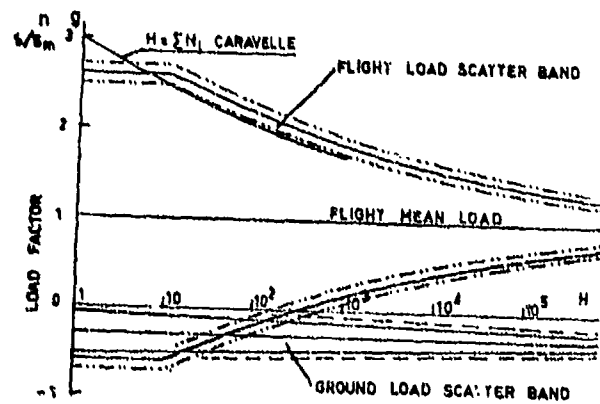


Fig.1 Evaluation of fatigue test loads



count method in which level crossings are counted only one time between two crossings of the zero acceleration. This method neglects a certain percentage of low level loads but the number of positive maximums is close to that of zero crossings with positive slope. The mean curve of level crossings in flight is quite well represented by a gaussian-logarithmic distribution of the ratio of the alternating load to the mean load,  $S_a/S_m$ , of total number of cycles  $H_0 = 2 \times 10^7$ , passing through the points  $P = 0.5$ ,  $S_a/S_m = 0.085$  and  $P = 5 \times 10^{-7}$ ,  $S_a/S_m = 1.6$  (see the B-straight line in Figure 4).

Figure 3 shows the level crossing spectrum of vertical accelerations measured at the gravity centres of ten Caravelles of Air-France during 47,000 flights and plotted for 20,000 flights. Positive accelerations,  $An_1$ , are more severe than the negative accelerations,  $An_2$ ; that may be due to different pilot responses in presence of severe gusts, and to the asymmetry of manoeuvres. This fact corresponds to a varying mean load. Figure 3 shows the alternating overloads  $An$  around the mean load, as well as the quantity  $1 + S_a/S_m$ , where  $S_a$  is proportional to  $An$  and  $S_m$  is proportional to  $(An_1 - An_2)/2$ .  $S_a$  and  $S_m$  are not true stresses since the stress spectrum is not exactly proportional to the spectrum of load factors at the gravity centre of the aircraft. The statistic of level crossings of  $S_a/S_m$  values are represented by a straight line 'A' in Figure 4 in assuming for the positive values a total number of level crossings,  $H = 2 \times 10^6$ , in order to compute the occurrence frequencies. The abscissae scale is the normal Gaussian distribution of probability  $P(x > a)$  such that  $\log_{10}(x = S_a/S_m)$  be higher than a fixed value  $\log_{10} a$ . With  $H_0 = 2 \times 10^6$ ,  $H = 10^6$  corresponds to the frequency 0.5. This straight line is easily prolonged, thus permitting an appraisal of the high and very rare overload values as well as frequencies of loads lower than the measurement threshold.

To evaluate the fatigue damage, the load spectrum may be replaced by a stepped diagram or may be broken down into a sum of component spectra for which fatigue results are available. To illustrate the procedure, the Caravelle  $S_a/S_m$  spectrum will be broken down into stepped components of constant amplitude or into Gaussian components in order to use LBF results of fatigue tests on notched specimens in the case of constant amplitude loads and in the case of load programmes having a Gaussian distribution of level crossings.

Figure 7 shows  $S_a - N_R$  curves for a mean stress  $S_m = 8.1 \text{ daN/mm}^2$ , from Mustang wing tests of 2024-T3 aluminium alloy, and LBF fatigue tests on notched specimens ( $K_T = 3.1$ ,  $r = 2 \text{ mm}$ )<sup>14</sup> made from German 3.1354.5 aluminium alloy. Lockheed results of fatigue tests<sup>15</sup> on notched specimens ( $K_T = 4$ ,  $r = 2.5 \text{ mm}$ ) made from 7075-T6 aluminium alloy are quite comparable to the Mustang results. With the Caravelle spectrum replaced by a 17-level stepped spectrum, between  $H = 10$  and  $H = 10^6$ , damage computations yield

$$\begin{aligned} \epsilon n_i / N_{Ri} &= 0.224 \text{ from Mustang curves, and} \\ &= 0.207 \text{ from LBF S-N curves for } K_T = 3.1. \end{aligned}$$

Figure 5 illustrates the break-down of the Caravelle spectrum into two Gaussian components, each of them defined by the maximum value,  $S_a/S_m$ , and by their sizes, namely  $10^6$  for the I-component of maximum level  $S_a/S_m = 0.9$ , and  $1.45 \times 10^4$  for the II-component of maximum level 1.3. The I-component is tangential to the overall spectrum, while the II-component passes through the point  $P_1$  on the I-component at the distance  $\log_{10} 2$  from the overall spectrum. To complete, one stepped rectangular III-component of constant level amplitude, 1.34, and of size 10, is used; it passes through the point  $P_2$  of the II-component at the distance  $\log_{10} 2$  from the overall spectrum.

In development fatigue tests of motor-vehicle components that are loaded by the dynamic response to road irregularities, Gassner and W. Schütz<sup>11</sup> have used their standardized LBF programme consisting in eight constant amplitude load steps, the levels of which are interpolated from the binomial distribution  $C_j^{10}$  with  $j = 0, 1, 2, \dots, 10$ . The level of each load step is measured by the ratio of its alternating load,  $S_a$ , to the highest load value of the programme,  $\bar{S}_a$ ; the mean load,  $\bar{S}_m$ , the same for all steps, is defined by the ratio  $R = (\bar{S}_m - \bar{S}_a) / (\bar{S}_m + \bar{S}_a)$ . Occurrence frequencies of loads are:

$S_a/\bar{S}_a = 1$	0.95	0.85	0.725	0.575	0.425	0.275	0.125
$\Delta N_i = 2$	16	280	2720	20,000	92,000	280,000	605,000,

with  $H_0 = \epsilon \Delta N_i = 1,000,610 \approx 10^6$ , and a RMS stress of the  $S_a$ -amplitudes,  $S_e$ , such that  $(S_e)^2 = 0.055(\bar{S}_a)^2$ . For the instantaneous sine-shaped stress  $S$ , the quadratic mean would be  $\sigma^2 = (S_e)^2/2$ . This standardized LBF-distribution is very close to the binomial distribution  $C_j^{10}$  which corresponds to  $H_0 = 1,048,576$  and to  $(S_e)^2 = 0.05357(\bar{S}_a)^2$  or  $S_e = 0.231\bar{S}_a$ . It is nearly equivalent to the gaussian distribution of highest level  $1.06\bar{S}_a$  and of size  $10^6$  which is represented by a straight line in a  $P(x > a) - S_a/\bar{S}_a$  diagram; the straight line passes through the points  $S_a = 0$ ,  $P = 0.5$  or  $H = 10^6$ , and  $S_a = \bar{S}_a$ ,  $P = 2 \times 10^{-7}$  or  $H = 4$ . The RMS of this distribution is  $S_e = 0.230\bar{S}_a$ .

With this Gaussian distribution of programmed loads defined by the highest load,  $\bar{S}_a$ , LBF's fatigue tests on notched specimens ( $K_T = 3.1$ ) are plotted in Figure 8 and may be represented by straight lines

$$\log \bar{N}_F = a - K \log \bar{S}_a,$$

where  $\bar{N}_F$  is the total number of cycles of all load levels to failure, and  $\bar{R} = (\bar{S}_m - \bar{S}_a) /$

$(\bar{S}_m + \bar{S}_a)$  is the fatigue ratio for the highest loads. In case of a same  $\bar{S}_m$ -value for every programme loading of various  $\bar{S}_a$ -values, an interpolation has been performed by plotting dotted straight lines through exact points located on R-curves. With these test results, the break-down of alternating flight loads of the Caravelle spectrum that is illustrated in Figure 6 yields the following "damage" values:

I-component:  $\bar{S}_a = 0.9 \times 8.1 = 7.3 \text{ daN/mm}^2$ ,  $N = 10^6$ ,  $N_F = 8 \times 10^6$ ,  $d_I = N/N_F = 0.125$ ;

II-component:  $\bar{S}_a = 1.3 \times 8.1 = 10.5 \text{ daN/mm}^2$ ,  $N = 1.45 \times 10^4$ .

For a size of  $10^6$ , the fatigue would be  $N_F = 1.7 \times 10^6$ , the B-curve corresponds to an occurrence frequency of  $S_a$  equal to  $1.45 \times 10^4$ , i.e., from Gassner and Schützli, to a conversion factor 0.22 such as  $N_F$  becomes  $0.22 \times 1.7 \times 10^6 = 3.75 \times 10^5$ . The damage of the II-component would be  $d_{II} = 0.0385$ ;

III-component:  $\bar{S}_a = 1.34 \times 8.1 = 10.85 \text{ daN/mm}^2$ ,  $N_F = 4 \times 10^4$ ; and  $d_{III} = 0.00025$ .

The total computed damage would be  $D = 0.1637$ .

Taking into account the gaussian-logarithmic distribution of the Caravelle's flight alternating loads, it would have been preferable to compute the damage value from LBF's fatigue tests of notched specimens under this kind of loading programme. This has not been possible in the absence of an exact knowledge of the LBF log-normal distribution.

Consider now Figure 6 where the distribution of flight alternating loads approximate closely to a straight line component of cumulative occurrence frequencies equal to 2.5 times those of the straight line defined by the points  $S_a = 0$ ,  $H_0 = 10^6$ , and  $S_a/S_m = 1$ ,  $H = 1$ . Most of the load spectra of civil and military transport aircraft have a shape which lends itself to a simple approximation by an exponential function represented by a straight line in a diagram  $S - \log H$ . Therefore, that is this kind of spectrum shape that should be the basis for programmed or random fatigue tests aimed to the design of transport aircraft structures.

On the contrary, for fighter aircraft, flight load spectra are better approached by analysis into Gaussian components, or Rayleigh components such as

$$H = H_0 e^{-\frac{(S_a/S_m)^2}{2}}$$

where  $H_0$  is the total number of zero crossings with positive slope, and  $S_m = \sigma/\sqrt{2}$  is the RMS of the initial gaussian process when the number of positive maxima equals  $H_0$ . The Rayleigh distribution is represented by a straight line in the diagram  $(S_a)^2 - \log H$ .

Figure 9 illustrates the approximation of the flight load spectrum of the Mirage III RS aircraft measured in Swiss operations<sup>16</sup>, by means of only one Rayleigh distribution for positive and negative accelerations. The approximation by a Gaussian distribution is less exact.

Figure 10 and Table III give the shapes and ordinates of the four types of loading spectra previously mentioned. The semi-logarithmic distribution is more suitable for an easy approximation of flight loadings in the case of transport airplanes, due to the possibilities afforded by its variable slope which permit a precise adjustment in the range from medium level to low level loads. The Gaussian distribution of logarithms of load levels (log-normal) might seem better appropriate if it was not often difficult and sometimes not possible to make its adjustment to certain measured loading spectra. The adjustment criteria is that in all points, the approximation curve have a less concavity than the investigated spectrum.

In the case of fighter aircraft, the Rayleigh and Gaussian distributions may be convenient. However, it is more easy to adjust Rayleigh straight line (in a diagram  $(\text{load})^2 - \log_{10} H$ ).

However, aircraft flight loads always include the transition at each flight of the mean load from the flight condition to the lower value, negative for the wing, during the taxiing at low speed. The effect of this transition is more to be ascribed to a change in residual stresses than to its direct fatigue damage. The last load applied just before a stress change in sign has a predominant effect on the damage afforded by the following loads (see Schijve<sup>16</sup>). This effect may aggravate the influence of ground loads which produce tensile stresses in the wing upper skin, as in the case of certain transport airplanes having a particularly flexible wing. Figure 11 illustrates the inversion in sign of the loads of upper and lower skins of a wing. In wing upper skins, repeated compressive stresses due to flight loads tend to create tensile residual stresses at the stress raisers and reinforce the damaging effect of repeated tensile stresses due to ground loads.

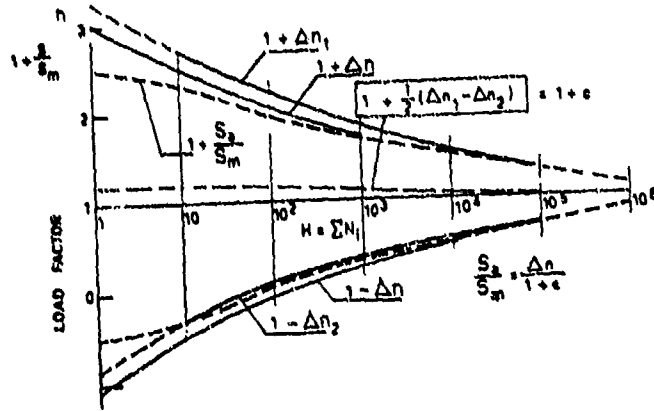


Fig.3 Caravelle flight load spectrum for 20,000 flights

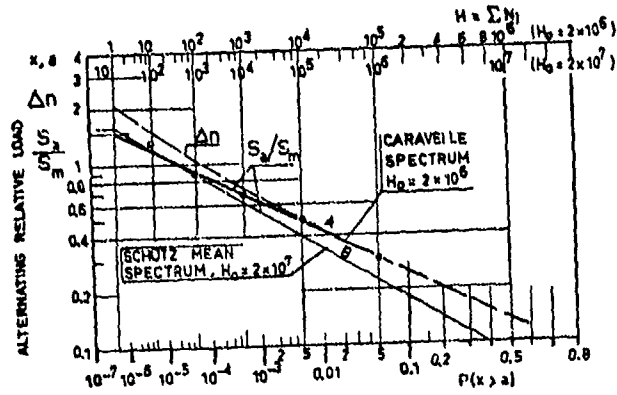


Fig.4 Linear plotting of log-normal distributions. Caravelle data for 20,000 flights

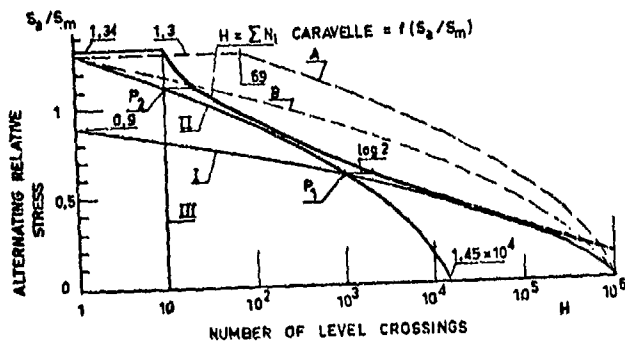


Fig.5 Gaussian components of the Caravelle spectrum

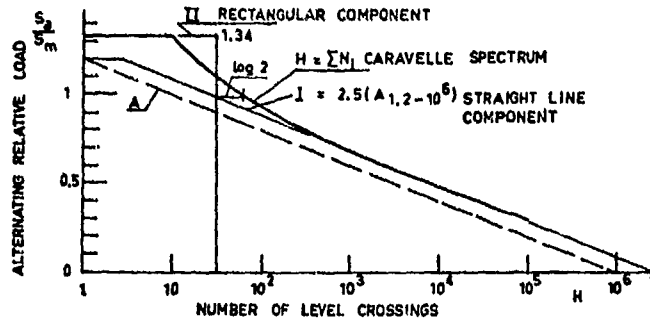


Fig.6 Straight line component of the Caravelle spectrum

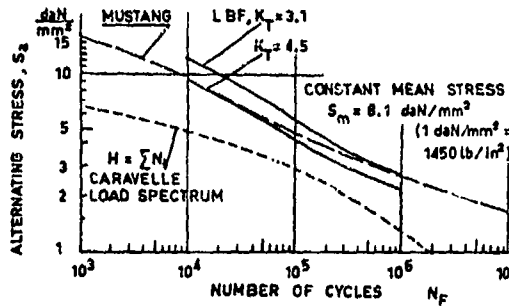


Fig.7 Constant amplitude fatigue test results

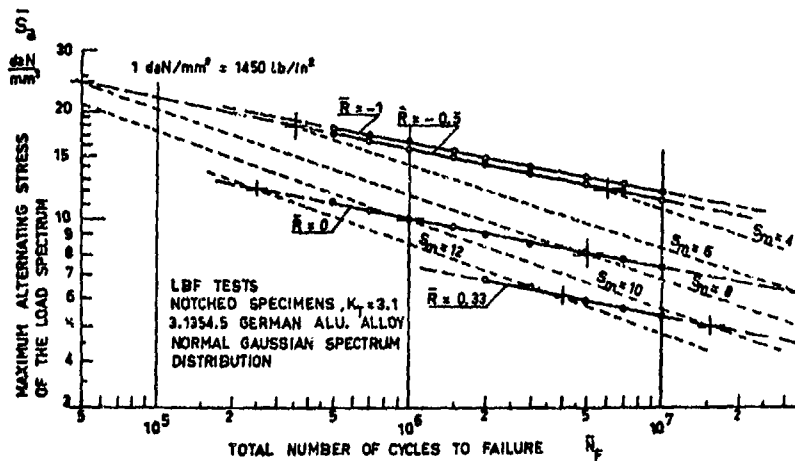


Fig.8 LBF  $\bar{S}_a - \bar{N}$  curve of 3.1 -  $K_T$  notched specimens under Gaussian load distribution

In order to take account of ground-air-ground transition, we have proposed<sup>17</sup> to break-down the diagram of loads during one flight into one fundamental component defined by the highest and the lowest loads applied during the flight, and complementary alternating loads. That attributes to the ground-air-ground transition an importance comparable to the actual importance. To our knowledge no other method supported by comparative and statistically significant tests is available to replace this rough mode of assessment.

In full-scale fatigue tests, the following procedures to represent the ground-air-ground transition have been considered.

- Tests of Swiss type<sup>2</sup>, controlled by tapes of statistical measurements recorded in actual operations. This method implies that fatigue test results enable, at the very most, late changes to be made in manufactured aircraft and in a number of components under manufacture.
- Tests under random loading with random times for the passage from the flight to the ground conditions. In this case, loads may be generated either by one or several Gaussian processes, or by a program where the sequences of application of individual loads will have been determined randomly.
- Tests under random loads, on a flight-by-flight basis, the overall spectrum being broken down into partial spectra for each flight, the severity of which being distributed according to the extreme values of the loads, on a flight-by-flight basis. In the case of the military aircraft, Transall, Figure 12 illustrates this possibility. Straight lines correspond to a Gaussian distribution between the flights of the logarithms of additional wing bending moments reached or exceeded  $n$  times per flight. This result, similar to that obtained by Baxbaum<sup>18,19</sup> from other flights and other measurements on the same aircraft, shows that the individual flight spectra are distributed as the extreme values. This kind of result only concerns gust loads; it would be useful to know if other aircraft behave similarly.

V-E 6 FATIGUE TEST ACCELERATION OR INTERPRETATION OF TEST RESULTS IN CASE OF CHANGES IN SERVICE LOAD LEVELS

In the statical strength of aircraft structures, possible service overloading with respect to design loads and the possible weakness of a particular structural component are palliated by a safety factor arbitrarily taken to be equal to 1.5. In the realm of the fatigue strength of these structures, safety is ensured by a life scatter factor quite variable, according to technical circumstances, the Authority and the Country. In France, a value of 5 has been proposed; it is lessened to 3 for secondary structure and for vital components the fail-safe of which has been proved<sup>20</sup>. Its minimum value is 2.

In helicopter components, the very large number of load cycles to consider in service put an obstacle to laboratory tests under the low stresses corresponding to actual number of cycles. Whereas, one should consider service loads applied in the number of cycles range from  $10^8$  to  $10^{10}$ , fatigue tests are carried out with higher load levels in the range of  $10^6$  cycles. Test results are extrapolated to a very large number of cycles in order to obtain the so-called endurance limit,  $S_e$ . To compare this fatigue limit strength to applied loads, loads are multiplied by a safety factor the order of magnitude of which may reach 3.

In general, life scatter is fairly constant in ratio along the steeper sections of S-N curves and is rapidly increasing toward the larger number of cycles. Gassmann's tests<sup>21</sup> in axial tension-compression of smooth hour-glass shaped specimens made from a low alloy Cr-Ni-Mo steel, in which the static strength was measured by means of tensile specimens taken from the fatigue specimens in the vicinity of the end fittings, have proved that the main part of the fatigue scatter may be ascribed to the scatter in tensile properties, and that the corrected S-N curve was a straight line in a diagram  $\log S - \log N$ , from  $N = 10$  to  $N = 10^5$ . Then, for  $N \geq 10^5$ , the straight line was lower than test results indicated. For aluminium alloys which have no well-defined endurance limit, it is probable that the straight line would pass through results up to a larger number of cycles. It might be accepted that the scatter in fatigue strength is proportional to that of the static strength, and that it may be better evaluated by means of a regression straight line, except in case of initial damage by fretting.

When a fatigue test has been performed with the loading foreseen for the production aircraft at the time of the prototype manufacture, it frequently happens that the actual loading of production aircraft and, a fortiori, those corresponding to later type developments, are more severe. That implies a need to carry out interpretative analyses by which existent fatigue life margins are transformed into load margins. If life margin is not available, a reinforcement will be substantiated by transforming a lowering of local design stresses into a load margin. In order to be better placed for later interpretation of fatigue test results, and to obtain results more early, it is proposed to reduce the supplementary test duration corresponding to the scatter factor by increasing the general load level, according to this apparent reduction of the scatter factor. This first test phase would permit substantiation of the service operations of the first aircraft, and the test would be possibly resumed to substantiate an actual increase in operational loads. In the initial phase, inspections should be more frequent, due to

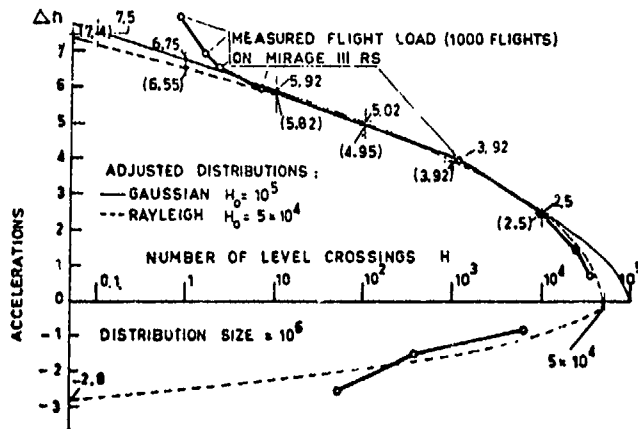


Fig.9 Flight loads on a fighter aircraft

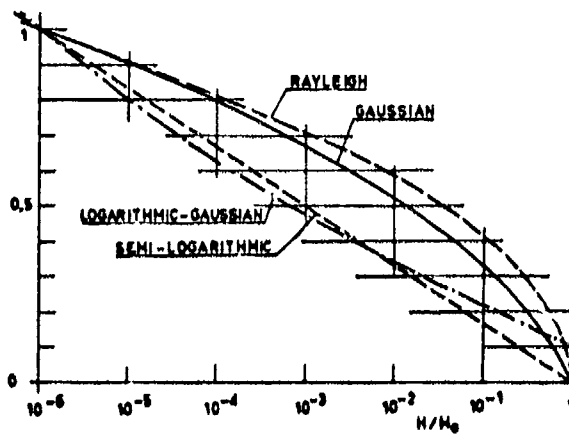


Fig.10 Distribution shapes

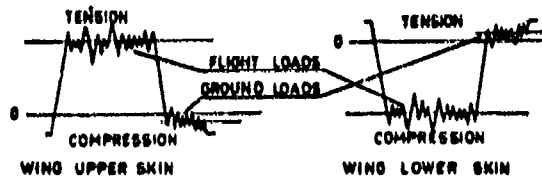


Fig.11 Service stressing of wing upper and lower skins



the fact that crack occurrence should be detected for smaller crack lengths (divided by the squared factor of load increase). In the following, we make an attempt to evaluate the test duration reduction which would correspond to an increase of 10% in load level.

From fatigue tests performed in Australia on Mustang wings<sup>13</sup>, it has been proposed that the results could be considered to be similar to those obtained by the NACA on notched specimens made from 2024-T3 aluminium alloy sheet with a notch factor of 4. This kind of comparison is questionable for the following reasons.

- (a) The local fatigue behaviour depends, not only on the stress concentration factor, but also on the stress gradient in the depth direction, particularly in the case of high loads and low fatigue cycles.
- (b) In the case of a complex structure, the ratio between the higher stress and the nominal stress is the product of the local stress concentration factor and of the load concentration factor, which is the ratio between the local load and the mean load in the considered area. It stands to reason that the stress gradient corresponding to the local stress concentration should be associated with the overall stress concentration in the prediction of the local fatigue behaviour of the structure.
- (c) In actual structures, fretting damage plays a more important part in decreasing the fatigue life in the range of large number of cycles and low stresses; it is absent in tests on notched specimens.

Local shapes of S-N curves may be characterized by their slopes in logarithmic coordinates:

$$k = - \frac{\partial \log N}{\partial \log S}$$

This slope varies along the S-N curve; this is likely to be due to the scatter of the material properties as was the case in the Gassmann's tests. Hence, in tests of assemblies using at the very most two or three specimens per load level, the plotted S-N curve will be questionable, and its slope will be still more questionable. For example, Figure 13 shows fatigue test results from Morfin and Halsey<sup>22</sup>, on box-beams made from 7075-T6 aluminium alloy. From  $10^2$  to  $8 \times 10^4$  cycles, with R positive but low, k shows the successive rough values 4.8 - 2.25 and 4.8, of mean value 3.9. Using other test results of the same specimens, a mean straight line of slope  $k = 4.5$  may be plotted, thus showing that the erratic slope variation was due to scatter.

A short survey of published results yields the following values of k.

#### 1. Notched specimens

In tests under constant amplitude of the alternating stress, the mean stress increases the slope of the  $\log S_a - \log N$  curve. Round notched specimens made from A-U2GN aluminium alloy thick sheet and tested at the "Etablissement Aéronautique de Toulouse", yielded:

$$K_T = 1.7, \text{ relative stress gradient } g = \frac{1}{S} \frac{\partial S}{\partial z} = -1, S_m = 0, k = 4.8;$$

$$K_T = 3.3, g = -5.7 \text{ mm}^{-1}, S_m = 0 \quad 10.5 \quad 21 \text{ daN/mm}^2$$

$$k = 4.9 \quad 3.6 \quad 3.1.$$

These values concern the range from  $10^4$  to  $10^5$  cycles.

In the same range of number of cycles, tests of LBF (Report 1079) on flat notched specimens made from the German 3.1354.5 aluminium alloy give:

$$K_T = 3.1 \text{ and } g = -1 \text{ mm}^{-1}; S_m = 0 \quad 4.7 \quad 9 \quad 15.5 \text{ daN/mm}^2$$

$$k = 3.3 \quad 2.8 \quad 2.4 \quad 2.3.$$

With the same specimens and the same alloy, test results plotted in Figure 8 correspond to:  $S_m = 0, k = 7.6$ ;  $S_m = 8 \text{ daN/mm}^2, k = 4.8$ . It is seen that k is somewhat higher in case of tests under a load spectrum.

#### 2. Riveted or bolted assemblies

Among numerous tests, we will quote some of them on small assemblies made from 2024-T3 aluminium alloy sheet. From  $10^4$  to  $10^5$  cycles, test by Schütz (LBF Report F-47) for countersunk rivets yielded:

$$k = 3 \text{ for constant amplitude loading, and}$$

$$k = 5.6 \text{ for programmed loading spectrum.}$$

In EAT's tests (Report 8388/MY),  $k = 4$  was obtained for countersunk rivets,

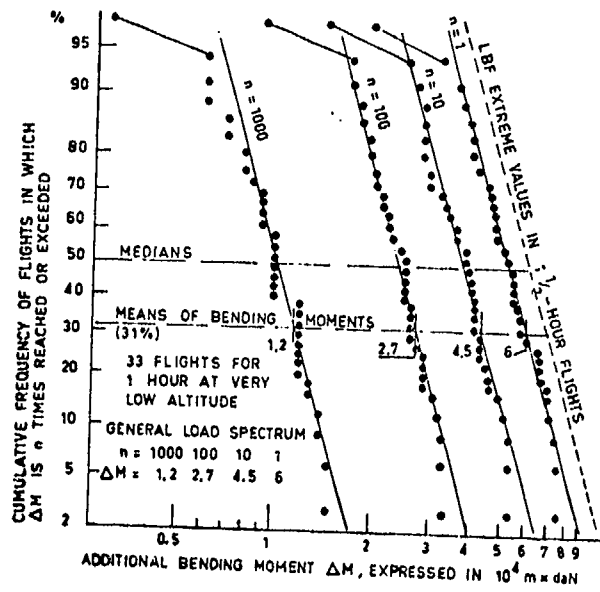


Fig.12 Flight distribution in severity of flight load spectra of Transall aircraft at low altitudes

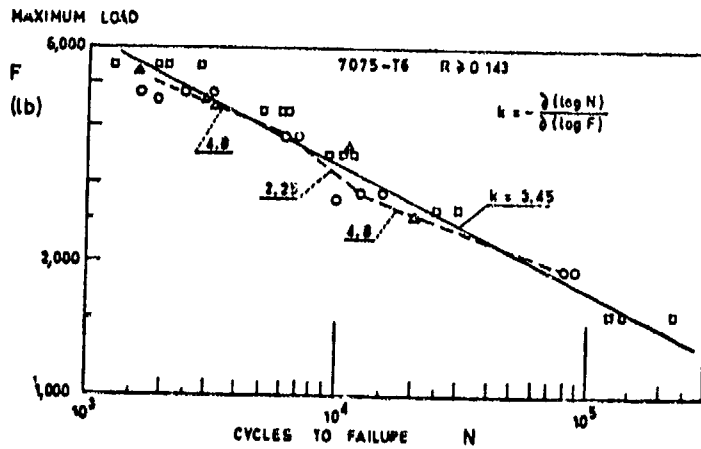


Fig.13 Fatigue test results of 7075-T6 aluminum alloy beams, from Mordfin and Halsey<sup>23</sup>

whereas  $k = 7$  for round head rivets.

In NLR's tests (TN M. 3104) with round head rivets:  $k = 4$  for heat treated sheet with  $S_{0.2} = 19.4 \text{ daN/mm}^2$  and  $k = 2.1$  for cold-worked sheet having  $S_{0.2} = 25 \text{ daN/mm}^2$ .

It is obvious that the fretting plays a part varying in the different cases, and that this entails a large range of variation of  $k$ . Moreover, a part of the variation is due to the scatter and to the small number of specimens tested at each load level.

### 3. Structures

Under constant amplitude loads, Mustang wings<sup>13</sup> yield between  $10^4$  and  $3 \times 10^5$  cycles:  $F_{min.} = R = 0$ ,  $k = 5$ ;  $F_{m.} = 0$ ,  $R = -1$ ,  $k = 6$ .

Other results are:

- NACA TN 4137, 2024 aluminium alloy box-beams:  $k = 3.7$ .
- NACA TN D-547, quoting NACA TN 4132, C-46 wings under constant amplitude loads, between  $10^4$  and  $10^5$  cycles:  $k = 3.98$ .
- Tests by Mordfin and Halsey on 7075-T6 aluminium alloy box-beams:  $k = 3.45$  as shown in Figure 13. Tests by Rosenfeld (ASTM STP 338) yield  $k = 4$ .

In general,  $k$  is quite variable but probably higher than 3 for constant amplitude tests, 4 for programmed tests with zero mean load, and 5 for programmed tests with noticeable mean load.

On condition that a sufficient number of specimens are available for each loading level, the analyses of tests on various assembly types would permit a better answer to be obtained to the problem. Conservatively, we are assuming that an increase of 100 in load level, in a programmed fatigue test, would correspond to a reduction of 330 in duration.

### V-E 7 TESTS UNDER RANDOM LOADINGS

The quite recent development of fatigue tests of notched specimens under random loads is first the consequence of practical possibilities afforded by the test devices electronically controlled using input signals from analogue devices, or from a computer, such as those used by Swanson<sup>23</sup> and by Melcon and McCulloch<sup>24, 25</sup>.

Secondly, the prediction of the dynamical response of aircraft in continuous turbulence and to ground irregularities through the power spectral density method give results that are expressed as a sum of Rayleigh distributions weighted by the RMS of each distribution. Melcon and McCulloch have investigated the fatigue life of flat notched specimens ( $K_T = 4$ ,  $g = -0.8 \text{ mm}^{-1}$  and  $K_T = 7$ ,  $g = -3.2 \text{ mm}^{-1}$ ) made from 7075-T6 aluminium alloy under random or programmed (low-high loads) loading spectra obtained by superimposing elementary spectra. The resulting programme was applied about 10 times. The loadings had the same distribution in cumulative frequency of occurrence in the two test types, random or under programme. These spectra were representative for loadings of fighter aircraft. The discrepancies of results between random or programmed loadings seem ascribable only to the count method applied to the random signal, which disregarded numerous low amplitude variations of the load between two successive zero crossings.

This difference has been avoided in tests by Jacoby<sup>25</sup>, in which random or programmed loads were digitally defined by a computer controlling the sequence of their application. Specimens made from 2024-T3 aluminium alloy were of the type with centre notch ( $K_T = 3.1$ ,  $g = -1.82 \text{ mm}^{-1}$ ). The loading spectra used were based on flight and ground loads of a transport airplane. The considered sequences were:

- (a) Random sequence of maxima and minima, the only condition being that a maximum follows a minimum;
- (b) Random sequence of alternating loads around mean loads in flight and on the ground, with random transition from the flight condition to the ground condition;
- (c) Flight-by-flight programme with high-low-high sequence of flight loads;
- (d) Flight-by-flight programme with low-high-low sequence of flight loads;

Relative durations were:

Sequences	a	b	c	d
Life durations	1	0.9	0.8	1.6.

We believe that although service loads are not truly alternating and that they often result from multi-modal response giving rise to beating, their representation by alternating loads is likely to represent sufficiently closely actual behaviour when the lower resonance frequencies of the structure are fairly distinct. When the flight alternating

load spectrum is known and in the case where the distribution of extreme values per flight is unknown, the most simple test mode consists of creating flight and ground alternating sequences, and to determine randomly the times of the ground-air-ground transition.

If the overall loading spectrum and the extreme value distribution by flight are both known, it will be possible to use random sequences of programmed loads by flight, their intensities being distributed between the flights as extreme values.

The knowledge of the load spectrum computed by means of the power spectral density method as a superimposition of several Rayleigh distributions (case of gust loads) affords no change in the problem since it does not prejudice on any distribution between flights and the fatigue test on a flight-by-flight basis is certainly fundamental both with programmed and random loadings.

Another problem occurring mainly in fatigue tests at acoustical frequencies related to vibrations of structural sheet panels, is that of the possible definition of a spectrum of cumulative frequency of level crossing by the RMS of a load or a stress.

If the highest value of the load is fixed, if the spectrum is complete, and if its irregularity coefficient  $H_0/H_1$  is known, the RMS,  $S_e$ , is a comparison term as valuable as another ( $H_0$  is the number of zero crossings with positive slope, while  $H_1$  is the number of positive maximums). However,  $S_e$ , often is only known from an electric measurement on a random signal, the maximum values of which are not known. Test results which give place to a  $S_e-N$  curve are often obtained from the generation of the random loads by exciting the structure vibrations by a white noise having a power spectral density fairly constant between two cut-off frequencies. It seems difficult to use this kind of result for fatigue life prediction of another different element under an excitation corresponding to a power spectrum having different cut-off frequencies. From Clevenson and Steiner<sup>26</sup>, the spectrum shape would have little influence on the fatigue life; the used spectra were well defined, that being not the case in practical problems. Moreover, fretting and ground-air-ground transition were not represented. In the case of aircraft primary structures, the ratios of the highest spectrum loads to the RMS loads vary with the general shape of spectra, therefore vary with the aircraft type, transport or fighter.

Finally, it must be noted that two types of root mean squares of a random load are to be considered, namely:

- (a) the time root mean square,  $\sigma$ , which depends on the frequency distribution of oscillating loads and that occurs in computations by the method of the power spectrum, and
- (b) the root mean square,  $S_e$ , of peak loads.

The relation  $S_e^2 = 2\sigma^2$  is only valid when only one gaussian process exists.

#### V-E 8 CONCLUSION ON DESIGNER'S NEEDS RELATIVE TO FATIGUE TEST RESULTS

In the matter of fatigue life prediction, the designer generally lacks reliable data to supplement the laboratory test results on simple notched specimens--few test results may be available on simpleriveted or bolted assemblies under constant amplitude load or, more rarely, under programmed loading. The best possibility of prediction still consists of using comparative damage computations using standard fatigue data of notched specimens to analyze a fatigue test result on a structure in order to predict the fatigue life of another structure or some particular design conception and some manufacturing process. The final result depends on the choice of representative structural element to be used in prediction and on the designer judgment, which is unfortunate in case of bad prediction. This state of affairs may be permanent. Any attempt to progress should be international with regard to the importance of test facilities and general means of use.

A practical effort to standardize fatigue tests of components, assemblies and structures has been made by Gassner and his collaborators. Their standardized spectrum is well suitable to represent flight loads of fighter aircraft and general ground loads, its use to represent flight loads of transport aircraft is less convenient. In this latter case, the exponential relation

$$H = H_0 e^{-c(S_a)^2}$$

seems better suited. Hence, it would be possible to perform fatigue development tests by using only two distribution types, namely:

- Exponential.

With each of these distributions, it would be useful to carry out fatigue tests in order to know the influence of the ground-air-ground transition for each type of

technological detail. As first proposed by Gassner, each distribution would be defined by the value,  $S_0$ , of the highest load of the spectrum, the value,  $S_m$  of the mean load, and the spectrum size, i.e., the total number of mean level crossings. The convenient sizes would be  $10^6$  for applications to transport aircraft, and  $10^4$  for fighter aircraft.

The Gaussian-logarithmic distribution is badly suited to adjustment with actual spectra and would be considered only if there were reliable data to demonstrate that the same distribution would be usable for a large class of aircraft. Taking account of the possible application of the Rayleigh distribution to certain problems of acoustic fatigue, it would be judicious to consider this distribution as a substitute of the Gaussian distribution. In this case, the RMS value would be defined by the distribution instead of defining the distribution by the measured RMS of an electrical signal.

Acoustic fatigue tests are excluded from the present short survey, however, if fatigue tests at high frequency concern specimens of stiffness such that the stress distribution depends on the frequency, it would be useful to standardize these tests by defining the highest load and the shape of the level crossing spectrum.

In returning to the designer's needs, it may be stated that before systematic fatigue test results of assemblies under standardized loading spectra become available, a useful fatigue quality classification of assemblies and structures could be carried out along the line of approach used by Crichlow and his collaborators, or by Jarfall.

In the present survey, the general framework of the problem is outlined and tentative suggestions are put forward for discussion, rejection or to be followed-up.

#### REFERENCES

1. Barrois, W.: Manual on Fatigue of Structures - Fundamental and Physical Aspects. AGARD-MAN-8-70, Paris, June 1970.
2. Branger, J.: Ein Simulator der Ermüdungsgeschichte für Grossobjekte (Fatigue History Simulator) im Eidg. Flugzeugwerk (F + W). Schweizer Archiv für angewandte Wissenschaft und Technik, Heft 8, 1966.
3. Hayes, J. E.: An Analytical Method for Predicting Aircraft Fatigue Life. Proceedings of the WADC Symposium 1959 on Fatigue of Aircraft Structures, WADC Report TR 59-107, Wright-Patterson, Ohio, August 1959.
4. Deneff, G. V.: Fatigue Prediction Study. Technical Report WADD TR 61-153, Wright-Patterson AF Base, Ohio, January 1962.
5. Jarfall, L.: Fatigue Cycling of Riveted or Bolted Joints. FFA Report HF-1239, Stockholm, June 1969.
6. Vogt, F.: The Load Distribution in Bolted or Riveted Joints in Light-Alloy Structures. Report SME 3300, Royal Aircraft Establishment, Farnborough, October 1944; also in NACA TM 1135.
7. Manford, B. T. and Rosenfeld, S. J.: Preliminary Investigation of the Loads carried by Individual Bolts in Bolted Joints. NACA TM 1051, May 1946.
8. Rosenfeld, S. J.: Analytical and Experimental Investigation of Bolted Joints. NACA TN 1458, October 1947.
9. Harris, H. G. et al.: Stress and Deflection Analysis of Mechanically Fastened Joints. Report AFFDL-TR-70-42, Wright-Patterson AF Base, Ohio, May 1970.
10. Crichlow, W. J. et al.: An Engineering Evaluation of Methods for the Prediction of Fatigue Life in Airframe Structures. Lockheed California Company, Report ASD-TR-61-434, Wright-Patterson AF Base, Ohio, March 1962, Abstract number N62-12760.
11. Gassner, E. and Schütz, W.: Evaluating Vital Vehicle Components by Programme Fatigue Tests, FISITA, Ninth International Automobile Technical Congress, 1962, Inst. Mech. Engineers London.
12. Schutz, D.: Establishment of a Standardized Flight-By-Flight Program for Aircraft Wings. ICAF Conference, Stockholm, 1969; also in LBF Report S-81, p. 4/20.
13. Scale Testing Pergamon Press, ICAF-AGARD Symposium proceedings, Amsterdam 1959; edited by Plantema and Schijve.
14. Gassner, E. and Schütz, W.: Assessment of the Allowable Design Stresses and the Corresponding Fatigue Life. Pergamon Press, ICAF-AGARD Symposium, Munich 1965; edited by Gassner and Schütz.

15. McCulloch, A. J. et al.: Investigation of the Representation of Aircraft Service Loadings in Fatigue Tests. Report ASD-TR-61-435, Wright-Patterson Air Force Base, Ohio, January 1962.
16. Schijve, J.: The Accumulation of Fatigue Damage in Aircraft Materials and Structures. AGARD-AG-157, January 1972.
17. Barrois, W.: Sur la Fatigue des Cellules d'Avions. Métaux-Corrosion-Industries, no. 364, December 1955. See also: Physical Interpretation of Metal Fatigue. 5th Conference ICAF, Bruxelles, October 1957.
18. Buxbaum, O.: Betriebsbeanspruchungen des Militar-Transportflugzeuges. Transall A04, LBF Report 1966, not published.
19. Buxbaum, O.: Extreme Value Analysis and its Application to CG Vertical Accelerations Measured on Transport Airplanes of the Type C-130. AGARD Report No. 579, March 1971.
20. Barrois, W.: Les Essais Statiques et de Fatigue des Structures des Avions en France et à l'Etranger. First Part, DOC-AIR-ESPACE, No. 110, May 1968, Paris.
21. Gassmann, H.: Schädigung und Schadensakkumulation bei hochfestem Stahl. Thesis, Technischen Hochschule Stuttgart, 1966.
22. Mordfin, L. and Halsey, N.: Programmed Manoeuvre-Spectrum Fatigue Tests of Aircraft Beam Specimens. ASTM STP No. 338, 1963.
23. Swanson, R. et al.: Crack Propagation in Clad 7070-T6 Aluminium Alloy Sheet under Constant and Random Amplitude Fatigue Loading. ASTM STP 415, July 1966.
24. Melcon, M. A. and McCulloch, A. J.: Simulation of Random Aircraft Service Loadings in Fatigue Tests. Pergamon Press, ICAF-AGARD Symposium, Rome, 1963.
25. Jacoby, G. H.: Comparison of Fatigue Lives under Contentional Program Loading and Digital Random Loading. ASTM STP 462, October 1968.
26. Clevenson, S. A. and Steiner, R.: Fatigue Life under Random Loading for Several Power Spectral Shapes. NASA TR R-266, September 1967.

## V F. OUTLOOK, FUTURE DEVELOPMENTS

D. Broek

### V F.1 Introduction

In concluding chapter V on fail-safe design it is necessary to consider the achievements made so far and to emphasize their shortcomings. Throughout chapter V it has appeared that really none of the tools available to design fail-safe is in a state of relative perfection, although some parts of the procedures have been brought to an acceptable stage of reliability. Fail-safe design requires a solution to the following problems.

- a) Determination of the minimum detectable crack length.
- b) Prediction of the residual strength of the structure in cracked condition, o.g. determination of the critical crack length at the required fail-safe load.
- c) Establishment of expected load spectrum.
- d) Determination of the crack propagation from the minimum detectable crack size to the critical crack length, in order to set safe inspection intervals (or in rare cases safe intervals for proof testing or periodic stripping).
- e) Knowledge of locations, liable to develop cracks.
- f) Reliable service inspection, taking into account the accessibility of the parts or structures under consideration.

This volume presents useful engineering solutions to all of these problems, but it has appeared that these solutions still have conspicuous shortcomings. One important shortcoming is that often insufficient data are available to use a certain procedure, although the method in itself is ready for engineering applications. Section F.2 gives a survey of the data that should be made available in order to allow a proper application of the fail-safe design procedures in their present stage of development.

Other shortcomings are due to an insufficient knowledge of fracture and fatigue mechanisms, basically, as well as in its applications to structural design. Further basic and empirical research is required together with a further development of prediction procedures. Basic research is not considered here, as this chapter deals with practical fail-safe concepts. Empirical investigations are necessary because there are still a number of practical questions waiting for an answer. Areas that require further exploration in that respect are discussed in the following sections.

### V F.2 Required basic data for fail-safe design at present state of knowledge.

The fail-safe design procedure described in detail in chapter V will certainly see further development in the near future. On the basis of the limited experimental evidence yet available, the engineering approach is useful, despite its shortcomings, but has to be refined at certain points and has to be substantiated by further testing. The method is expected to find application in current designs.

For application of the procedure in its present form, the designer needs the following information:

- a) Reliable data plots of  $da/dn$  versus  $\Delta K$  for various stress ratios ( $R$ ) so that no extrapolation is required. The data plots should be available for a wide variety of materials, thicknesses, and for different environments like water, humid air, dry air, and fuel. Effects of low and slightly elevated temperatures should be involved. The data should allow an appraisal of the scatter.
- b) Reliable residual strength curves are required. Again, data for a wide variety of materials and thicknesses have to be available. Some data are required to allow an appraisal of the effects of temperature, machining procedures, and manufacturing procedures.
- c) In order to simplify procedures in the early design stage of stiffened sheet structures, plots of  $U_r$  (stress intensity reduction factor) and  $L$  (stringer load factor) showing the effects of such parameters as rivet size and spacing and stringer-skin ratio would prove to be worthwhile. (For the definitive design, exact calculations would have to be made).
- d) The prediction of fatigue crack growth in the design phase, requires information about expected load-time histories. Problems involved are associated with measurement techniques, and statistical analysis in relation to fatigue damage accumulation.
- e) Service experience can give useful information. Such data are obtained under realistic conditions with respect to load-time histories and environment. The statistical reliability may be high if many aircraft are involved. Collection and availability of such data would be useful.

data would be worthwhile.

### V F.3 Areas that require further exploration.

As pointed out in chapter V.B.1 on Fatigue-Crack Propagation, the integration procedure needs further exploration. Preferably, random load history crack-propagation tests should be carried out and predictions made, by using different integration procedures, and the predictions compared with the

test results. This approach would allow an evaluation of the merits of the various procedures and it could lead to certain recommendations. The tests should involve different materials, since it is likely that one integration method would apply better to a particular material, whereas another integration method would apply better to another material.

Random load testing to explore the differences in behaviour under various gust and maneuver spectra are required since, as yet, there is no good appreciation of how conservative the crack growth predictions are for these two spectra. The generation of data of spectrum load tests could ultimately lead to a stage where the integration procedure is no longer necessary, since the result could be derived immediately from spectrum test data. (A fatigue specimen is, of course, the best damage-integrating computer). A handbook with a compilation of flight simulation data may be useful for estimating fatigue properties. Moreover, it could be a reference for comparative testing in order to judge the fatigue quality of a new design.

In the area of the residual strength problem in plane stress there is one point that deserves particular attention. If the curve for onset of unstable crack growth is to be used for stiffened structures, there should be a standard procedure to generate this curve. First, there is a pronounced effect of panel size, and, second, it is not easy to define the critical crack length. At the end of the slow growth period, the crack rate accelerates, and it is hard to define the point of instability. The result of the test depends on the testing technique, as far as critical instability is concerned. Some agreement has to be made to standardize testing procedures in order to insure that the designer knows what the curve really means.

Further exploration of the crack growth resistance curve is recommended, because it may lead to a better understanding of the physical processes. Incorporation of the crack-growth resistance curve in the analysis of stiffened panels is basically possible. This approach certainly needs attention, since it may evolve into more sophisticated design methods. The methods to calculate the residual strength of stiffened panels needs further improvement. Such factors as stringer eccentricity, fastener deformation and hole deformation should be accounted for in the calculations.

As for the residual strength under plane strain conditions the applicability to complicated geometries and natural cracks needs further attention. Stress intensity factors for such geometries are gradually being made available, but there is a shortage of test data to prove their applicability for the prediction of the residual strength on the basis of  $K_{Ic}$  as determined from a standard test. Exploration of the usefulness of the J-integral to fracture toughness problems is certainly necessary. It may lead to a more sophisticated fracture toughness test. The use of the J-integral or a modified J-integral for crack propagation has to be investigated. A positive result would make the J-integral apply to plane stress problems (slow crack growth) also.

#### V F.4 Fail-safe design and structural integrity.

It has been pointed out in chapter V that an improvement of the fracture toughness (plane stress as well plane strain) is less effective than improvement of inspection techniques and crack propagation properties. For a certain prescribed fail-safe load an improvement of the fracture toughness by 40 per cent, increases the critical crack length by a factor 2 (in case of built-up sheet structures it may be even less). An increase of the critical crack length gives a longer crack propagation life, but crack propagation rates in this range are already high. A reduction of the minimum detectable crack length by a factor 2 due to improved inspection technique will give a much larger increase of the crack propagation period available for crack detection. An improvement of inspection techniques will be especially useful, because cracks are small during the greater part of their crack propagation life. At the moment the crack is somewhat larger, the greater part of the propagation life is expired and there is only little time left for detection. In this connection, it is clear that improvement of crack propagation properties is important.

Fail-safe design has long been a matter of qualitative engineering judgement. The time has arrived now that reasonable quantitative predictions can be made, especially with respect to residual strength. It must be expected that progress will be made in the near future to improve the situation with respect to fatigue crack propagation. Then it seems appropriate that airworthiness requirements will set more severe demands to the proof of fail-safety.

With the present state of the art it seems feasible to demand a proof by analysis and supporting tests. The amount of fatigue damage to be considered must be defined on the basis of crack propagation properties in conjunction with the inspection periods envisaged, taking into account the inspectability of the particular structure.

Supporting tests will remain necessary and have to be conducted on full scale components, representative for the complete structure. Test specimens should include attachment fittings, major joints and splices, discontinuities, cut-outs and stringer run-outs etc. In fatigue testing, flight simulation tests will have to be carried out, including gust and maneuver-loading. Proof loads, fail-safe loads and other high loads, the occurrence of which is remote, may not be applied until the test is completed. The fatigue critical locations should be determined as well as the crack propagation characteristics and inspection procedures. Inspection techniques should be evaluated for their effectivity.

Residual strength tests must be carried out after completion of the cyclic test. The test article should be loaded to the required fail-safe load while it contains realistic damage. In contrast to the residual strength calculation, where the maximum allowable extent of the damage is determined, in the residual strength test it has to be shown that the structure can sustain the prescribed fail-safe load under the presence of realistic fatigue damage. In determining the amount of damage the following factors should be taken into account:



- a) Accessibility of the area for the detection of cracks.
- b) The effectiveness of the inspection technique and the minimum detectable crack length.
- c) Frequency of inspection envisaged. (Superficial daily and pre-flight inspections should not be considered).
- d) The rate of crack propagation during cyclic loading.

In order to make fail-safety a reality all information should be made available to the aircraft operator. Results of analysis and tests should be systematically documented, with special emphasis on critical locations, crack propagation rates and residual strength. The following information should be supplied to purchasers:

- a) Compilation of critical locations.
- b) The nature of the cracks that occurred in the tests and the order in which they occurred.
- c) Inspection periods for all critical locations.
- d) Means of inspection including e.g. instrument or X-ray tube settings to obtain highest sensitivity for the area under consideration.
- e) Warning that service should be discontinued if a crack is found, until corrective measures have been taken.

A final plea is related to the dissemination of information, which has also been made by Schijve in his compilation on cumulative fatigue damage (Agardograph 157, 1972). Several times it occurs that good solutions are not reached because of insufficient knowledge, although the information is available somewhere. Equally regretful is the situation where prejudice discards improved solutions and progress is impeded by traditions. The problem is greatly a matter of education and divulgence of information. Hopefully, the present volume may be helpful by outlining the various aspects of the aircraft fail-safe problem.

VI EXPERIMENTAL TECHNIQUES FOR DETERMINING  
FRACTURE TOUGHNESS VALUES

Walter Schütz  
Wolfram Oberparleiter

Summary . . . . .	371
1. Introduction . . . . .	371
2. Methods for Determining Fracture Toughness $K_{IC}$ Under Plane Strain Conditions . . . . .	371
2.1 ASTM Standardized Method of Test for Plane Strain Fracture Toughness of Metallic Materials . . . . .	372
2.1.1 Specimen Geometrics . . . . .	372
2.1.2 Discussion of Some Criteria for Valid Test Results of the ASTM Standard Method . . . . .	373
2.1.3 Statistical Evaluation of $K_{IC}$ Values . . . . .	375
2.2 Standard Method of Sharp Notch Tension Testing of High Strength Sheet Materials . . . . .	375
2.3 Non Standard Methods with Various Specimens . . . . .	377
2.3.1 K-Calibration of Specimen . . . . .	377
2.3.2 The Dynamic Tear Test . . . . .	382
3. Methods for Determining Critical Stress Intensity Factor $K_C$ . . . . .	383
3.1 Critical Crack Length Obtained by Filming . . . . .	384
3.2 Computing $K_C$ and Critical Crack Length $2l_C$ Based on Nonlinear Effects . . . . .	386
3.3 Computing $K_C$ at Small Crack Lengths . . . . .	386
4. Testing Fracture Toughness of Weldments . . . . .	386
5. Environmental Effects on Fracture Toughness . . . . .	388
5.1 Fracture Toughness Tests at High or Low Temperatures . . . . .	388
5.2 Fracture Toughness in Corrosive Environments . . . . .	389
5.2.1 Salt Water Corrosion . . . . .	389
5.2.2 Hot Gas Corrosion . . . . .	390
5.2.3 Embrittlement due to Temperature Cycling . . . . .	390
6. Effect of Strain Rate on $K_{IC}$ Values . . . . .	390
7. Closing Remarks . . . . .	391
References . . . . .	393

## VI. EXPERIMENTAL TECHNIQUES FOR DETERMINING FRACTURE TOUGHNESS VALUES

Walter Schütz  
Wolfram Oberparleiter

### SUMMARY

Two standard methods - The Standard Method of Test for Plane Strain Fracture Toughness of Metallic Materials and the Standard Method of Sharp Notch Tension Testing of High Strength Sheet Materials, both published by the ASTM - are described and some details which are important for carrying out the test are discussed. Apart from these standardized procedures a number of problems have to be solved which are not covered by these standard procedures. Therefore a series of nonstandard test methods are explained which mainly use different specimen shapes. Advantages and disadvantages of these test methods are discussed and comparisons of the test results with results obtained from the ASTM standard specimen are made. Also test equipment for testing fracture toughness of weldments, under environmental conditions (low temperature, salt water corrosion) and high strain rates are described. Finally the various sources of scatter for the  $K_{IC}$  values are pointed out and a method for statistical evaluation of  $K_{IC}$  is given.

### 1. INTRODUCTION

At the present time the materials constants necessary for the calculation of static strength of cracked structure still have to be determined experimentally. While for the plane strain condition a Standard Method of Test has been published by ASTM [1] and SAE [2] in the United States and by BISRA [3] in the United Kingdom it must be recognized that these standards cover only a small percentage of the many practical problems facing the engineer concerned with the residual static strength of structures and materials.

Other conditions which are not covered by the ASTM standard but may have a large influence on the behaviour of cracked structure in service are:

- In many structural applications the thickness requirements of the plane strain conditions are not met.
- Environmental effects: low or high temperatures, corrosion in its many forms e. g. stress corrosion (including hot salt stress corrosion), hot gas corrosion, salt water corrosion etc. Some of these effects occur simultaneously. Moreover they can act synergistically, that is, their effects cannot be linearly superimposed.
- Metallurgical variables: grain direction, product form, heat treat cycles etc.
- Strain rate effects, for example in gun tubes.
- Fracture toughness of joints (weldments, riveted or bonded connections).
- The material changes in the course of the service life, i. e. embrittlement due to start-stop-operation in gas turbines or nuclear radiation.

These remarks are in no way intended to detract from the importance of the above mentioned standards, but do show that apart from the standardized procedures a number of other problems must be solved by the test engineer. But in any case the engineer first should try to use the ASTM Standard Method of Test; only if this is not possible, he should look for another method for his special application.

Besides some remarks on the ASTM Standard Method of Test for plane strain fracture toughness of metallic materials this paper describes in the following some other non-standard methods of testing which have been published in the literature or used by the authors at IABG. Also advantages or disadvantages of the various test methods are discussed.

2. METHODS FOR DETERMINING FRACTURE TOUGHNESS  $K_{IC}$  UNDER PLANE STRAIN CONDITIONS2.1 ASTM Standard Method of Test for plane strain fracture toughness of metallic materials

As mentioned above the materials constant  $K_{IC}$  has to be determined experimentally. Therefore its measurement has been the subject of extensive research over the past years. All this work has been coordinated by the ASTM Committee E-24 and has resulted in the development of a Standard Method of Test which is standardized in the Annual Book of ASTM Standards as Designation E 399-72 T 17. This method covers the determination of plane strain fracture toughness of metallic materials by a bend or a compact tension test using a notched and fatigue precracked specimen. It provides for very specific limits on the minimum specimen dimensions and fatigue crack length. The overall purpose of the requirements of the ASTM Standard Method is to assure that the  $K_{IC}$  values thus obtained will be essentially the same as the  $K_{IC}$  values from test specimens of unlimited size. Only then the values of  $K_{IC}$  can be considered a materials constant and are not a function of the test method used.

2.1.1 Specimen geometries (Standard specimen)

Two types of standard specimen are used, the bend specimen, single-edge-notched and loaded by three point bending (fig. 1) and the compact tension specimen also single-edge-notched but pin loaded in tension (fig. 2). The width to thickness ratio  $W/B$  used for the standard specimen is 2.0 for  $B > 12,7$  mm and 4.0 for  $B \leq 12,7$  mm.

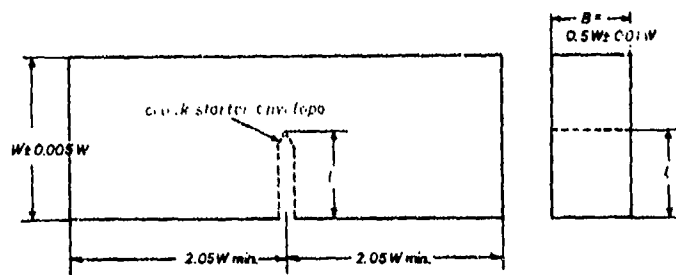


Fig. 1: Bend specimen  
- standard proportions  
and tolerances

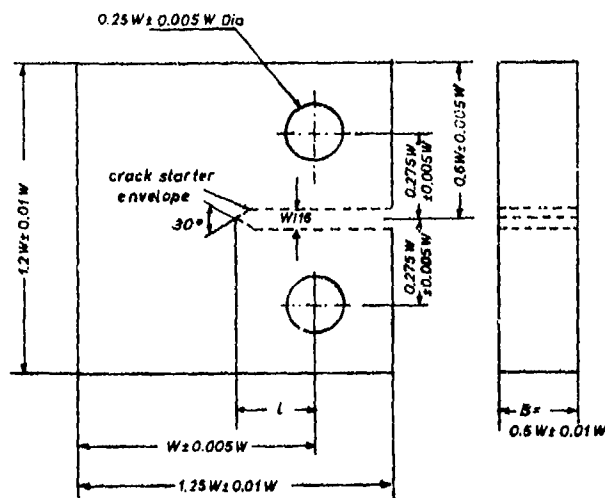


Fig. 2: Compact tension specimen  
- standard proportions  
and tolerances

Note: Dimensions and tolerances in mm.  
Surfaces shall be perpendicular and parallel as applicable to within 0.002 W TIR

If the form of available material may be better adapted to alternate specimen shapes than to the standard specimen, alternative bend specimen may have  $W/B = 1.0$  to  $4.0$  and alternative compact specimen  $W/B = 2.0$  to  $4.0$ . The limit  $W/B = 1.0$  for the bend specimen leads to the square notch bend specimen SNB with a square cross section. This smaller cross section of the SNB produces a higher fracture stress to cause the onset of  $K_{IC}$  instability than is produced by the standard notch bend specimen NB for the same material [47]. This results in a higher fracture-stress-to-yield-stress ratio and effectively decreases the measuring capacity of the SNB specimen. At fracture-stress-to-yield-stress ratios of 1.1 or less for the SNB, the  $K_{IC}$  value was in close agreement with values measured by the standard NB specimen.

## 2.1.2 Discussion of some criteria for valid test results of the ASTM Standard Method of Test

In some applications particular requirements of the ASTM Standard Method of Test cannot be met or are violated in the test. The following paragraphs give some ideas what can be done in these cases.

### 2.1.2.1 Criteria for thickness of test specimen

The specifications of the ASTM Standard for the specimen geometry, especially the thickness, have been one of the major problems for standardization. If no estimation for  $K_{IC}$  is available at the beginning of the test series the thickness  $B$  of the first test specimen should be dimensioned by  $\sigma_{YS}/E$  according to a table in ASTM Designation E 399-72. Having obtained a valid  $K_{IC}$  value the thickness  $B$  calculated from

$$B \geq 2.5 \cdot (K_{IC}/\sigma_{YS})^2$$

will give a considerably smaller specimen as shown in table 1.

Material [-]	Thickness of specimen [mm]	$\sigma_{YS}$ [Rp/mm <sup>2</sup> ]	$\sigma_{YS}/E$ [-]	$K_{IC}$ [Rp/mm <sup>3/2</sup> ]	B according to $\sigma_{YS}/E$ [mm]	$B \geq 2.5 \cdot \left(\frac{K_{IC}}{\sigma_{YS}}\right)^2$ [mm]
3.1354 - T 851	25	45.3	0.006	83.1	63	8.4
3.1354 - T 851	50	39.6	0.0052	90.0	75	13.0
3.4364 - T 7351	25	40.5	0.0055	110.5	75	18.6
3.4364 - T 7351	50	41.0	0.0056	119.8	75	21.3
3.4354.7	28	49.6	0.0067	91.8	44	8.6
3.4364 - T 73	28	40.8	0.0055	112.1	75	19.0
T16A14V annealed	25	92.3	0.0082	195.1	20	11.2
T16A14V STA	25	104.7	0.0095	215.2	12.5	10.6
T16A16V2Sn annealed	25	101.3	0.0080	239.0	20	13.9
T16A16V2Sn STA	25	126.9	0.0115	100.0	6.5	1.6

Table 1: Comparison of specimen thicknesses determined from

$$\frac{\sigma_{YS}}{E} \text{ and } 2.5 \cdot \left(\frac{K_{IC}}{\sigma_{YS}}\right)^2$$

Some tough materials require very large specimens to obtain a valid  $K_{IC}$  value. Therefore in some cases difficulties in producing standard specimens arise due to the limited thickness available. These can sometimes be avoided by welding or brazing extension pieces to the test section, fig. 3 [5, 6]. The material of the extension pieces should

have a similar Young's modulus  $E$  and a similar  $\sigma_{ys}$  to avoid undesirable stresses at the bond line of the two materials. Tests have shown that the  $K_{IC}$  values obtained from the standard compact tension specimen and the welded or brazed compound specimens are identical [5].

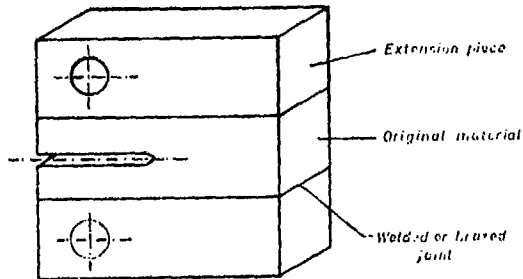


Fig. 3: Compound specimen

#### 2.1.2.2 Fatigue crack initiation and propagation

Crack initiation will be facilitated by spark machining of the notch. This may be the most useful method for manufacturing the notch in high strength steels. A straight through notch, if it is spark machined will almost certainly be sharp enough for successful crack initiation. But unless the alignment is controlled very closely there is some tendency for the cracks to grow eccentrically from a straight through notched specimen. Therefore the use of a chevron notch in general is believed to be the more desirable method, for the initiation of fatigue crack growth usually takes place in the center of the specimen thickness and the crack then advances symmetrically across the entire front [7].

To initiate and grow the fatigue crack in a reasonable time, fatigue precracking should be started at higher loads than specified for the last 2.5 percent of the notch plus crack length. However the difference between the initial and the final fatigue loads must not be too large because preceding high loads may retard crack propagation under subsequent low loads. The load distribution during fatigue cracking should be symmetrical. However due to grain flow imperfections especially in hand forgings [8], it is nevertheless possible to get an asymmetrical crack front (fig. 4). If this is noticed early enough shimming during fatigue cracking may save the specimen.

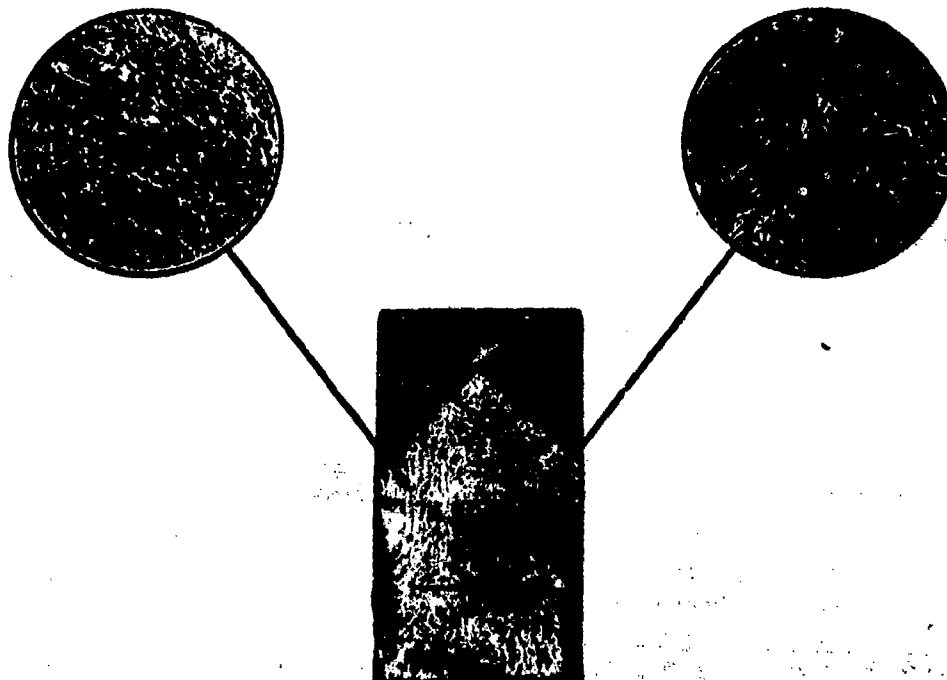


Fig. 4: Asymmetric fatigue crack front of a standard bend specimen caused by different microstructure

### 2.1.2.3 Criteria for length and straightness of the fatigue crack

The ASTM Standard states as follows:

If the difference between any two of the crack measurements exceeds 5 percent of the average, or if any part of the crack front is closer to the machined notch root than 5 percent of the average crack length or 1.3 mm minimum, also if the length of either surface trace of the crack is less than 90 percent of the average crack length, as defined, the test is invalid.

Tests at Dayton University [9] have shown that on aluminium alloys (2024-T851) there is no effect on  $K_{IC}$  values if the first and third criterion for the straightness of the fatigue crack is violated. For other materials the percentage of the deviation should be noted and if it is small and the statistical evaluation - described in the following paragraph - has shown the  $K_{IC}$  values to be insignificantly different from the valid ones the values may be used in the opinion of the authors.

### 2.1.3 Statistical evaluation of $K_{IC}$ values

If a sufficient number of test results is available a statistical evaluation should be carried out. The arithmetic mean can be calculated from 2 to 5 specimens. For more than 5 test results Gaussian normal probability paper should be used; the probability of survival of the individual specimen can be calculated according to [10]

$$P_S = \frac{3m - 1}{3n + 1}$$

where  $m$  = total number of specimens  
 $n$  = number of individual  $K_{IC}$  values, arranged in descending order

The results usually fit a straight line over a considerable range of probabilities of survival. However it should be recognized that unless a very large number of test results is available and fit a straight line the Gaussian Normal Distribution is not necessarily valid. Therefore one should be cautious to extrapolate very far.

If a sufficient number of valid and invalid  $K_{IC}$  values is available, the two samples can be tested for the hypothesis of a common parent population [11]. If neither the variances nor the means differ significantly at the chosen level of confidence, the nominally invalid values may be accepted.

A measure of the scatter of fracture toughness values is the Standard Deviation  $\sigma$

$$\sigma = \sqrt{\frac{1}{(N-1)} \sum_{i=1}^N (X_i - \bar{X})^2}$$

where  $N$  = number of  $K_{IC}$  values  
 $\bar{X}$  = arithmetic mean of the available  $K_{IC}$  values

One Standard Deviation  $\sigma$  can also be read off the straight line as the difference between the mean ( $P_S = 50$  percent) and  $P_S = 84$  percent or  $P_S = 16$  percent respectively (fig. 5).

## 2.2 Standard method of sharp notch tension testing of high strength sheet materials

For high strength sheet materials it is not possible to determine valid  $K_{IC}$  values with the ASTM Standard Method of Test, because the minimum size requirement of  $B > 6.4$  mm is not met. In these cases it may be possible to obtain a qualitative indication of the material strength by using ASTM Standard Method Designation E 338-68 [12]. The specimens used are either sharp edge-notch specimens or fatigue center-cracked specimens (fig. 6). Since the notch strength may depend on sheet thickness and specimen width, the method is restricted to one specimen width (generally suitable for evaluation of high strength materials) and to sheet materials not less than 0.64 mm and not more than 6 mm in thickness. The length of the specimen is specified to be 300 mm. The specimens are pin loaded in tension. Comparison of different materials and material conditions must be based on tests with specimens having the same thickness.

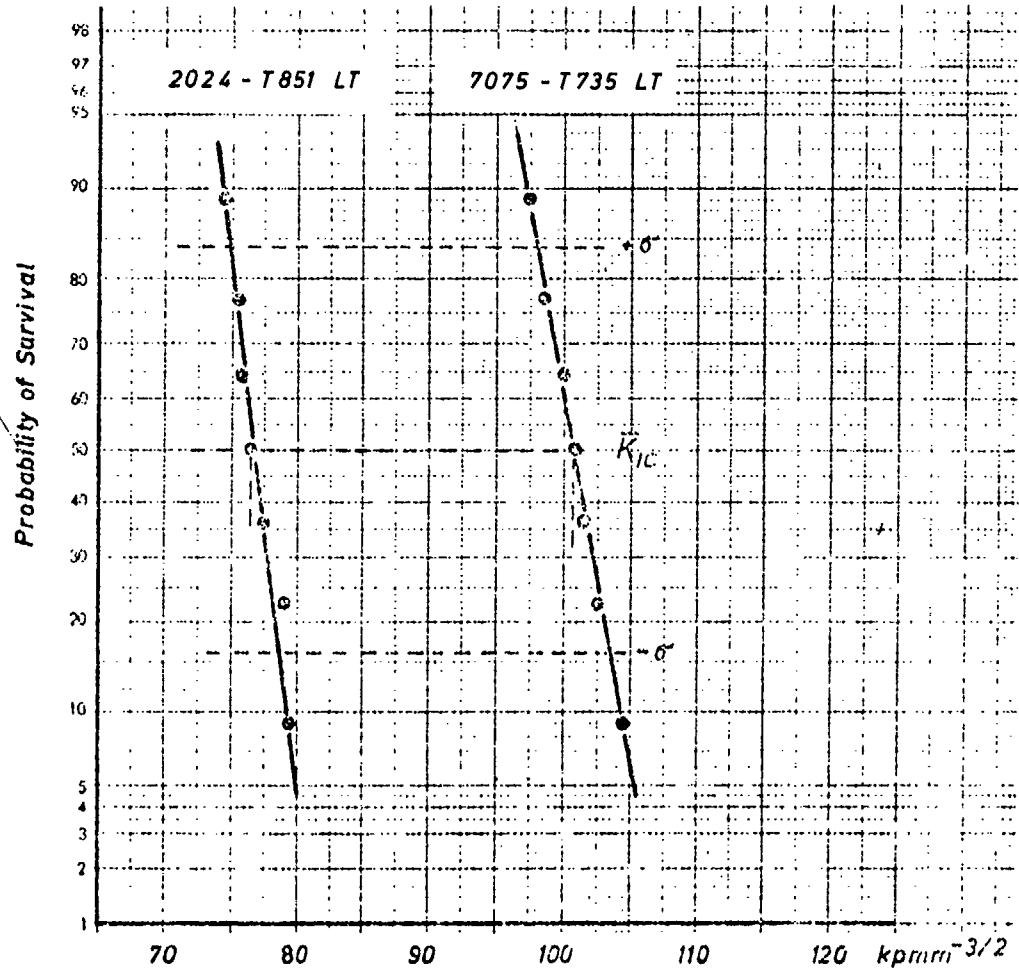


Fig. 5: Statistical evaluation of  $K_{IC}$  values

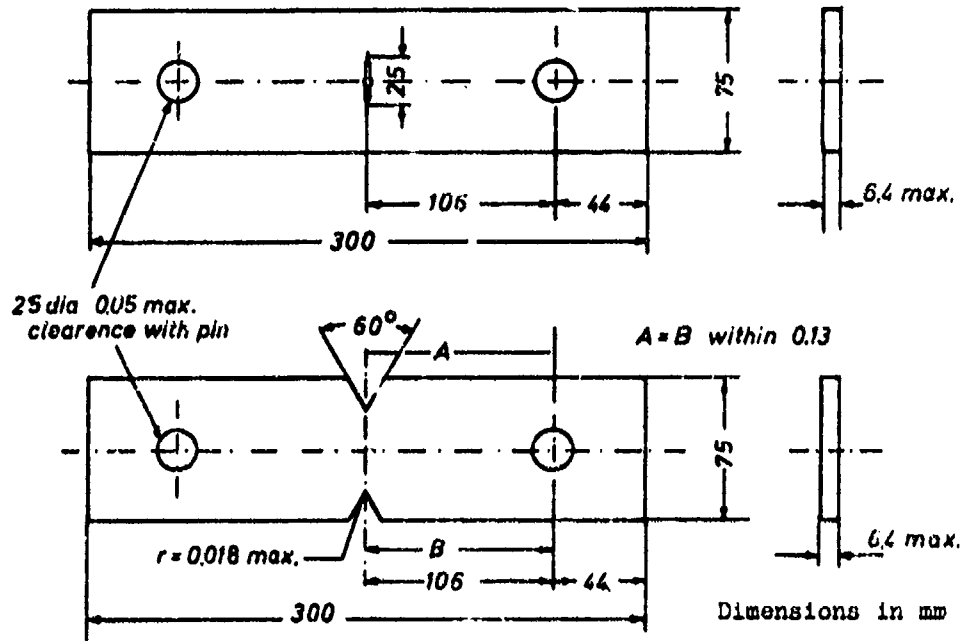


Fig. 6: Fatigue center crack and machined sharp edge-notch specimen



This method provides a comparative measure of the resistance of sheet materials to unstable fracture originating from the presence of cracks or crack-like stress concentrators. It is not intended to provide an absolute measure of resistance to crack propagation which might be used in calculations of the strength of structures. However the test is useful for

- studying the effects of variables of composition, heat-treatment in research and development of materials
- comparison of the relative crack-propagation resistance of several materials which are equally suitable for an application
- specifications of acceptance and manufacturing control if a minimum acceptable sharp notch strength can be established

The calculation of the sharp notch strength takes no account of any crack extension which may occur during the test. It is analogous to the tensile strength of a standard tension test. The precision of sharp-notch-strength measurement should be equivalent to that of an ordinary tensile strength of a sheet specimen; also the test should be conducted in a similar manner. However the sharp-notch strength is more sensitive to local flaws and normally shows more scatter. This should be reduced at least by testing duplicate specimens and averaging the results. The sharp notch strength may decrease rapidly through a narrow range of decreasing temperature. This temperature range and the rate of decrease depend on the material and its thickness. The temperature of specimen during each test shall therefore be controlled and recorded. Tests shall be conducted throughout the range of expected service temperatures to ascertain the relation between notch strength and temperature. Care shall be taken that the lowest and the highest anticipated service temperature are included.

### 2.3. Non standard methods with various specimen geometries

For special applications or because it is often not possible to machine one of the standard specimens from a given component configuration, some other specimen geometries have been used for plane strain fracture toughness testing. A number of different types of specimens have been developed, but the expressions for  $K_I$  of these specimens are more complicated. The dimensions of the specimens in relation to crack dimensions are not large enough to neglect the effect of specimen boundaries on the crack stress field.  $K$  calibrations of the specimens have to be done.

#### 2.3.1 K - Calibration of specimen

The commonly used method of  $K$ -calibration is the measurement of compliance  $c = (v \cdot B)/P$  of a specimen having a crack which opens when a load is applied. The results of the compliance tests are shown as a function of crack length (fig. 7) and fitted by a polynomial expression  $c = f(l)$ . Furthermore in a mathematical stress analysis the specimen has to be idealized into a sufficiently simple model. According to Irwin [13] the crack extension force

$$G = \frac{1}{2} \cdot \left[ \frac{P}{B} \right]^2 \cdot \frac{dc}{dl} \quad \begin{array}{l} v = \text{displacement} \\ P = \text{applied load} \end{array}$$

together with the relationship between crack extension force and stress intensity factor  $K = (G \cdot E)^{1/2}$  yields the expression for  $K$ :

$$\frac{KB}{P} = \left[ \frac{E}{2} \cdot \frac{dc}{dl} \right]^{1/2}$$

where  $dc$  is the derivation of the compliance function and  $E$  is Young's modulus.

In the following paragraphs some special specimen geometries are described including the results of  $K$  - calibrations.

##### 2.3.1.1 Center cracked and double or single edge cracked plate

The main standard method of Test E 399-72 T requires a minimum thickness of 6.4 mm. For plane strain crack toughness testing of ultra high strength metallic materials another type of specimen - the plate specimen in tension - with rectangular cross section and through thickness cracks has been developed [6]. These plates have rectangular shapes and are center cracked or double or single edge cracked; they are pin loaded in tension (fig. 8).

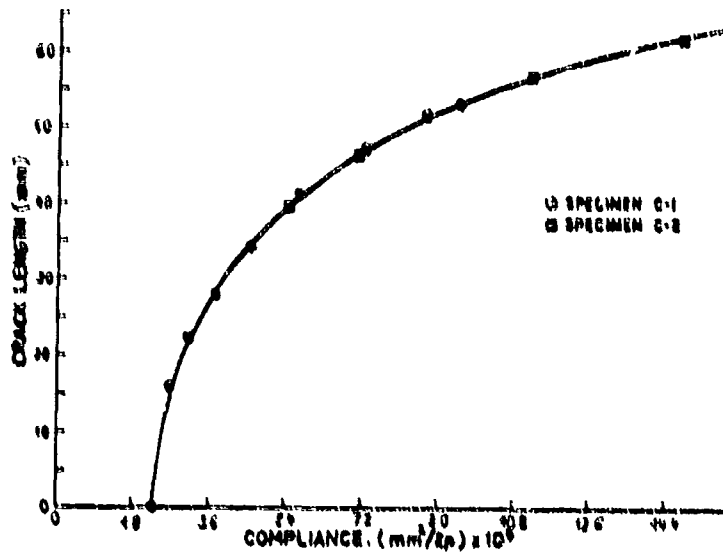


Fig. 7: Compliance test results

To get a valid  $K_{IC}$  value the same size requirements apply as for the ASTM standard specimen (see paragraph 2.1.2.1). Because of the high loads and materials requirements these specimens are not used much except for ultra high strength materials and the determination of crack extension resistance curves.

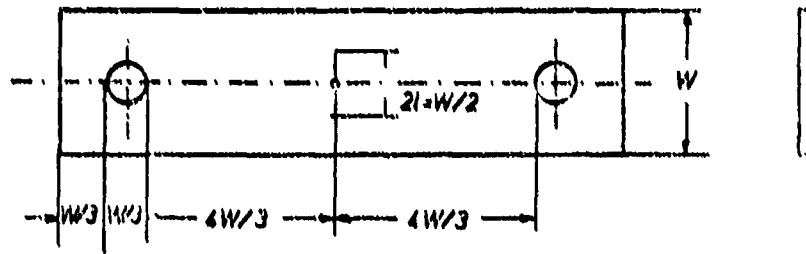
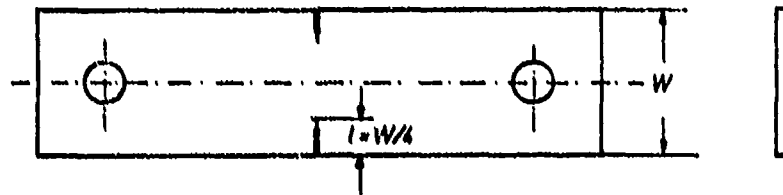


Fig. 8a: Center cracked plate



preferred thickness  $W/2$  to  $W/4$

Fig. 8b: Double edge cracked plate

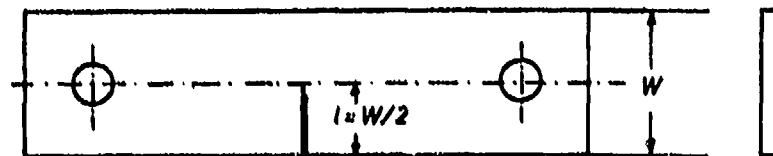


Fig. 8c: Single edge cracked plate (tension)

### 2.3.1.2 Circumferentially cracked round bar T47

This specimen (fig. 9) has the advantage that notches of a particular contour may be produced to close tolerances very easily by cylindrical grinding or lathe turning. However the control of the crack front which must be concentric to the load axis is difficult. Just as with the center cracked plate the fracture load is very high. Therefore the cracked round bar is used only for particular applications, i. e. investigation of the effect of cracks at the base of screw threads or of the influence of notch sharpness. The K expression obtained is

$$K = \frac{P}{D^{3/4}} \cdot \left[ 1.72 \frac{D}{d} - 1.27 \right]$$

Test results obtained from Standard ASTM specimens and circumferentially cracked round bars have been shown by some researchers to be very similar T47.

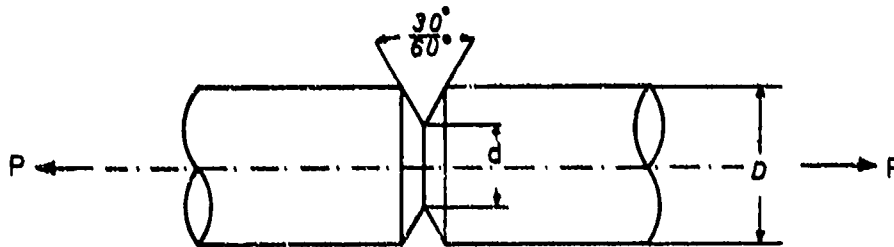


Fig. 9: Circumferentially cracked round bar

### 2.3.1.3 The C-shaped specimen T27

This specimen type is very useful for determining the fracture toughness of thick walled tubes like pressure vessels or gun tubes. In many of these applications wall thickness and curvature of the tube prevent the use of the standard ASTM specimen.

The C-shaped specimen (fig. 10) is pin loaded in tension and utilizes the available material most efficiently.

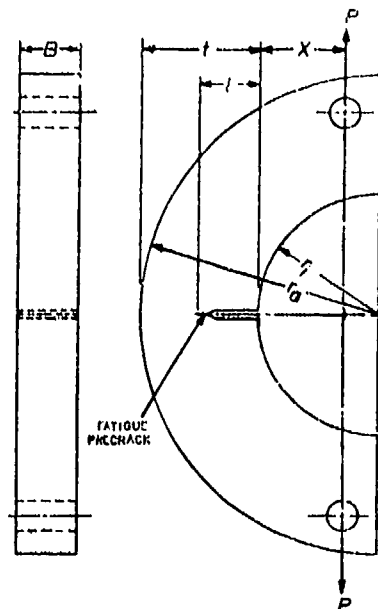


Fig. 10: "C" - shaped fracture toughness specimen

The expression for K

$$K = \frac{\sqrt{l} \cdot P}{B \cdot (r_a - r_i)} \left[ Y_T + 6 \cdot \left( \frac{X}{r_a - r_i} + \frac{1}{2} \right) \cdot Y_B \right]$$

was obtained by a compliance test combined with a mathematical model. The result was checked by a finite element calculation. The polynomial functions  $Y_T$  and  $Y_B$  are identical with those of the ASTM bending and compact tension tests and can be taken from ASTM E 399-72 T [17]. Also fatigue cracking and size requirements and the determination of  $K_{IC}$  should be taken from E 399-72 T.

Results of comparative fracture toughness tests using C-shaped specimens and the ASTM standard bend specimens made of 4340 steel agree within 2 percent, which is within the experimental error [12].

#### 2.3.1.4 Round CT-specimen

Most of the fracture toughness specimens have a rectangular shape. The round CT specimen can be easily fabricated from round semiproducts. The stress geometry of this specimen shape (fig. 11) is similar to the stress geometry of the proved standard compact tension specimen. The expression for K from a K-calibration is:

$$K = \frac{P}{B \cdot W} \cdot \sqrt{l} \cdot \sqrt{\frac{E \cdot B}{2 \cdot (1/W)} \cdot \frac{dc}{d(1/W)}}$$

where c is the compliance.

Tests with this kind of specimen geometry have been done for a high-strength hot work tool steel of German designation 90MnV8 and the aluminium alloy 7075-T6 [16]. The experimentally determined K expression is

$$K = Y \cdot \frac{P}{W \cdot B} \cdot \sqrt{l}$$

with

$$Y = 29.6 - 162.36 (1/W) + 492.6 (1/W)^2 - 663.6 (1/W)^3 + 405.55 (1/W)^4$$

valid in the range  $0.3 \leq 1/W \leq 0.7$ .

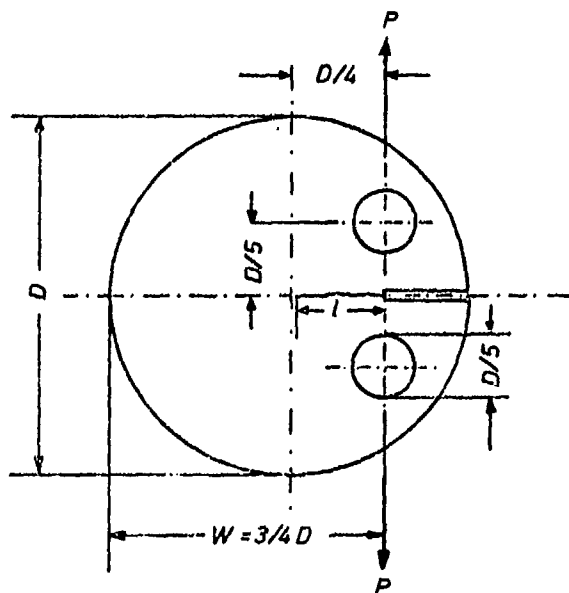


Fig. 11: Round compact tension specimen

### 2.3.1.5 The double cantilever beam specimen [17]

The determination of plane strain fracture toughness data on low strength high toughness materials using the specimens described before e. g. notch bend, single or double edge cracked plate etc. requires a specimen size large enough to provide the restraints for plane strain conditions to be satisfied. For these materials the required size is unduly large for primarily two reasons:

- limited size in a test equipment for testing environmental effects on  $K_{IC}$
- limited source of specimen material

Because of certain advantages of the double cantilever beam specimen it is used in conjunction with fracture mechanics as a substitute for the ASTM Standard specimen under stringent space conditions. A typical DCB specimen and method of loading is shown in (fig. 12a).

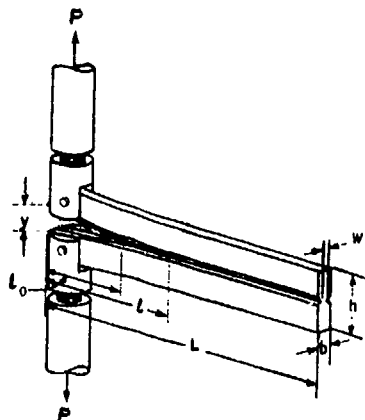


Fig. 12a: Typical double cantilever beam specimen and method of loading. The saw cut  $l_0$  facilitates starting the crack

As the name implies the DCB specimen may be considered as a pair of cantilever beams which are fixed to an elastic base. Considering that the compliance of this specimen depends on the crack length  $l$ , the moment of inertia  $I$  of the specimen arms about the axis of rotation and the beam depth  $h$ , the relationship between the applied force  $F$  and the total deflection  $y$  of both arm is

$$y = \frac{P}{E} \cdot \phi \quad (1)$$

where  $E$  is the modulus of elasticity and  $\phi$  is a function of crack length  $l$ , moment of inertia  $I$  and the beam depth  $h/2$

$$\phi = \frac{C_1}{I} \cdot l^n \quad (2)$$

where  $C_1$  and  $n$  are constants and depend only on beam depth; they are calculated from the relationship between  $\phi$  and  $l$  which is determined from the slope of the load-extension line  $y/P$  from recording of the extensometer (fig. 12b) and from the measured crack length.

Thus equation (1) can be written as

$$y = \frac{P \cdot C_1 \cdot l^n}{E \cdot I} \quad (3)$$

Irwin and Kies [18] have shown that for the application of fracture mechanics in absence of a mathematical analysis the determination of the strain energy release rate  $G$  for a specimen may be accomplished experimentally. Using equation (1)

$$G = \frac{P^2}{2 \cdot W \cdot E} \cdot \frac{d\phi}{dl}$$

and substituting equation (2) and (3)

$$G = \frac{n \cdot y^2 \cdot E \cdot I}{2 \cdot W \cdot C_1} \left[ \frac{C_1 \cdot P}{E \cdot I \cdot y} \right]^{\frac{n+1}{n}}$$

G may then be converted to the plane strain fracture toughness  $K_{IC}$  by the well known relationship

$$K = \left[ \frac{E \cdot G}{1 - \nu^2} \right]^{1/2}$$

where  $\nu$  = Poisson's ratio.  
Thus  $K_{IC}$  is then

$$K_{IC} = \left\{ \frac{E^2 \cdot I \cdot n \cdot \nu^2}{2 \cdot W \cdot C_1 \cdot (1 - \nu^2)} \left[ \frac{C_1 \cdot P}{E \cdot I \cdot \nu} \right]^{\frac{n+1}{n}} \right\}^{1/2}$$

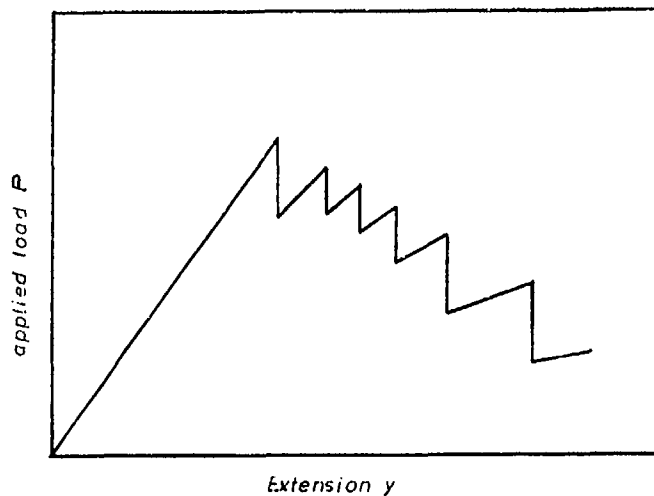


Fig. 12b: Typical DCB specimen fracture behavior at constant crosshead speed. Each vertical segment represents an unstable crack propagation event.

### 2.3.2 The dynamic tear test

The dynamic tear test is designed to measure the energy required to propagate a moving crack under conditions of the characteristic fracture mode of the metal. A major requirement of the test is the simulation of a sharp natural crack for the initiation of fracture. In contrast to the ASTM standard method of test an embrittled electron beam weld is introduced into the bend specimen instead of a chevron notch (fig. 13a). When the specimen is impact loaded the embrittled weld is fractured and provides a sharp crack which propagates into the test material.

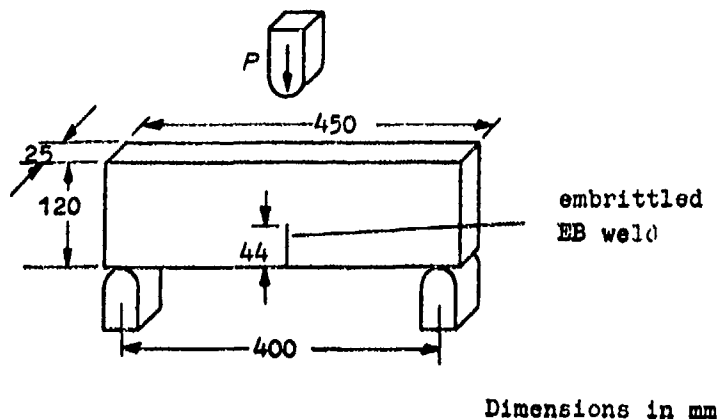


Fig. 13a: Dynamic tear test specimen for testing a 25 mm thick plate

This method has several features which show its importance as an engineering fracture toughness test [47]:

- For many aluminium, steel and titanium alloys a high degree of correlation between fracture toughness  $K_{IC}$  and DT-energy was found [19]. This correlation permits the use

of the simple and less expensive DT test to estimate  $K_{IC}$  values.

- Furthermore plane strain fracture mechanics procedures cannot be applied to metals in which crack instability occurs concomitant with large plastic zones (elastic-plastic case). Through extrapolation of the  $K_{IC}$  - DT correlation  $K_C$  can be estimated even when the metal is well within the elastic-plastic region.
- The dynamic tear test specimen utilizes the full thickness of the plate in contrast to the ASTM Standard Method specimen where the chevron notch plus crack length places the zone of maximum stress intensity at the center of the plate. The DT test therefore integrates any variation in toughness from the center to the surface of the plate.
- The correlation of  $K_{IC}$  and DT-energy is also influenced by the strain rate. The effective crack toughness of many metals, sensitive to strain rate, decreases to a lower limit as the crack velocity increases. The impingement of a high velocity crack in the DT-test on the test material provides a measure of material toughness under the most severe conditions the metal may experience in service. Problems of this kind may be present in gunbarrels.

The DT-test is an example of a test which requires a correlation with a real fracture mechanics test before it may be effectively employed. The value determined by the DT-test cannot be used directly to calculate the strength of a material or structure in the cracked condition, but can be used for itself only for comparative purposes, unless a valid correlation between DT-energy and  $K_{IC}$  is known as in (fig. 13b).

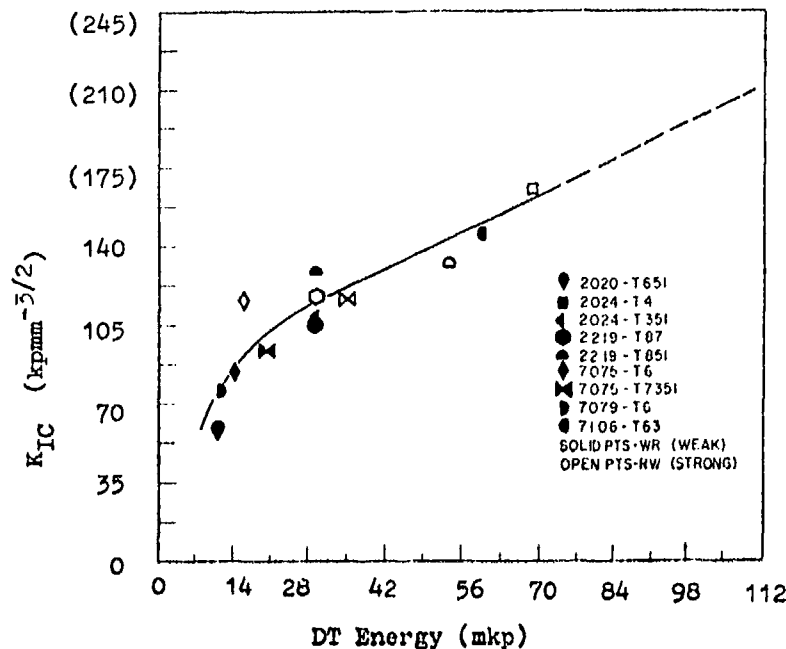


Fig. 13b: Correlation of  $K_{IC}$  with DT energy

3. Methods for determining critical stress intensity factor  $K_C$  under plane stress conditions using the critical crack length  $l_C$

In some structural applications the thickness requirements of the ASTM Standard Method of Test (Paragraph 2.1.2.1) cannot be met, especially if thin sheet is to be tested. Linear elastic fracture mechanics do not apply and therefore the critical stress intensity factor  $K_C$  is not a material constant but depends on sheet thickness  $[20]$  (fig. 14). For calculation of  $K_C$  the knowledge of the critical crack length and the load at fracture is necessary and one difficulty is to determine the exact critical crack length.

Two methods are described for determining this critical crack length. Both utilize rectangular center cracked specimen containing a fatigue crack produced by previous fatigue crack propagation tests and loaded in tension as already described in paragraph

2.3.1.1. Unless it is the purpose of the test to determine the effect of sheet width on  $K_C$ , the width of the specimen should be 160 mm and the length about 400 mm; this is a convenient size for standard test machines and a lot of comparable data are available from the NLR [21] and the IABG [22, 23] based on this specimen size.

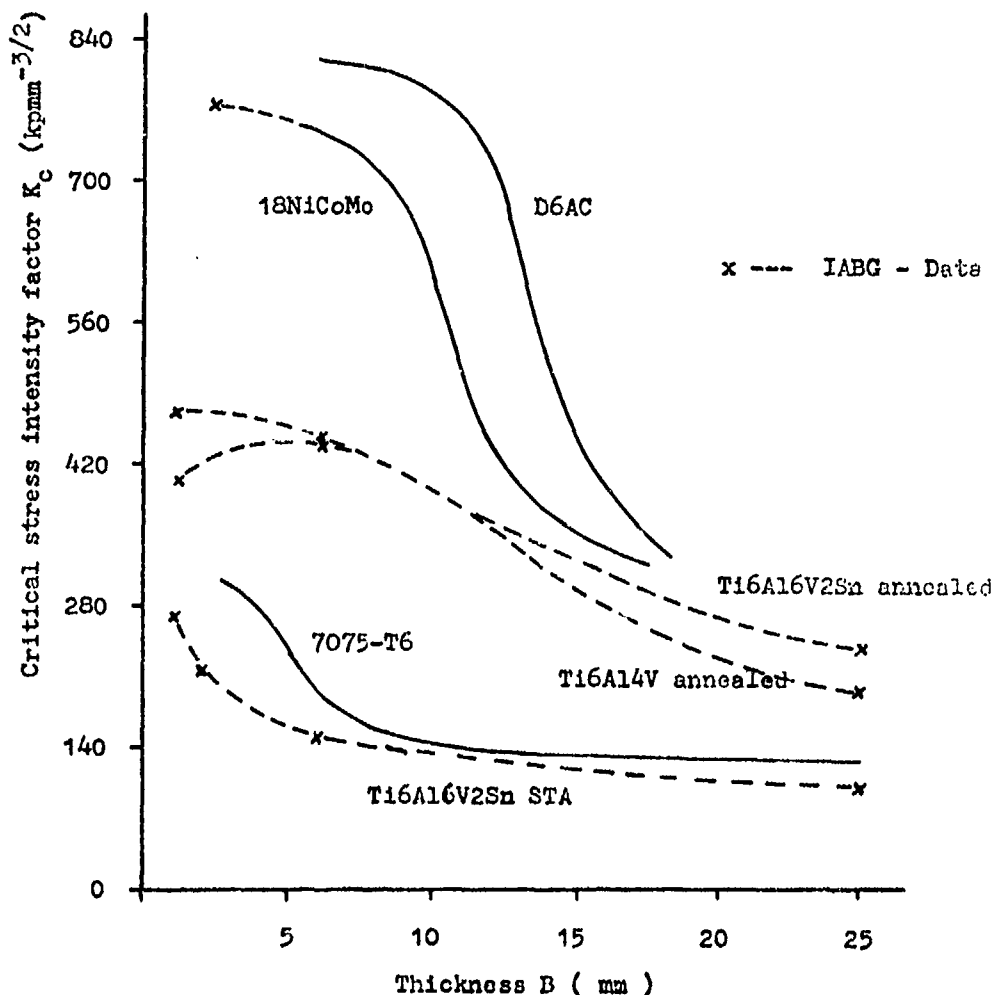


Fig. 14: Critical stress intensities for several materials as a function of thickness (Data from IABG and others)

### 3.1 Critical crack length obtained by filming (fig. 15)

Tests have shown that on tension loading of fatigue center-crack specimen slow stable crack propagation occurs if the load exceeds a certain value, and stops again, if the load is kept constant. Filming this crack growth at the tension test, the critical crack length  $2l_C$  can be obtained from the last frame before fracture (fig. 16); a film speed of 20 frames per second usually is high enough.

$K_C$  then should be calculated using Feddersen's equation [24]

$$K_C = \frac{F_C}{W \cdot B} \cdot \sqrt{\pi \cdot l_C \cdot \sec \frac{\pi \cdot l_C}{W}}$$

where

$F_C$  = load at fracture  
 $l_C$  = half crack length at fracture  
 $W$  = specimen width  
 $B$  = specimen thickness

$K_C$  has been found to be approximately constant and independent of crack length if the critical crack length  $2l_C$  taken from this film is used. The previously used  $K_{CO}$ -value calculated from the crack length  $2l_0$  at the beginning of the tension test decreases with crack length below about  $2.5 \cdot (K_{IC}/\sigma_{0,2})^2$ . Also the  $K_C$ -values are higher than the  $K_{CO}$ -values.



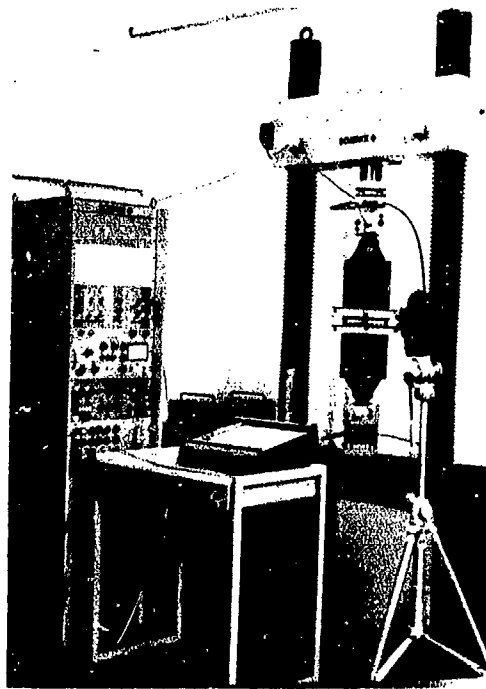
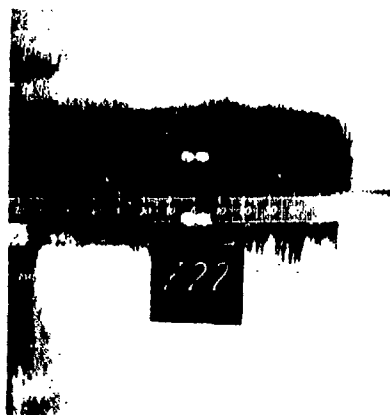


Fig. 15: Test equipment for determining  $K_{IC}$  of thin fatigue-center-cracked sheet



unloaded  
 $2l = 67 \text{ mm}$



$2l = 78 \text{ mm}$



$2l = 89 \text{ mm}$



fracture

Fig. 16: Slow stable crack propagation during tension loading of fatigue center cracked thin sheet

### 3.2 Computing $K_C$ and critical crack length $2l_C$ based on nonlinear effects

The load displacement records of fatigue center cracked thin sheet specimens show a larger deviation from linear elastic behaviour at higher tension load than thick specimens; this is caused by plasticity effects at the crack tip and a larger plastic zone than in plane strain conditions.

The method published by Liebowitz and Eftis [25] is using this nonlinear load displacement record. This record is approximated by an analytical function  $v = f(F)$  considering the linear and nonlinear part. This relationship between tension force  $F$  and displacement  $v$  is used to calculate the total energy release rate  $\tilde{G}$ , consisting of the elastic and the nonlinear contribution. Comparing this total energy release to Irwin's elastic energy release rate  $G$  leads to

$$\tilde{G} = C \cdot G$$

where  $C$  is the nonlinear correction factor which considers plasticity. The corrected stress intensity factor  $\tilde{K}_C$  is then

$$\tilde{K}_C = K_C \cdot \sqrt{C}$$

This method is also practicable for materials where the ratio of residual static strength to yield strength  $\sigma_{B,R}/\sigma_{0,2}$  exceeds 0.8. This condition is not met by tough materials. Also for very small cracks the corrected  $K_C$ -values are too high according to the experience of the authors. As pointed out in paragraph 3.1 the length of the fatigue crack should exceed  $2.5 (K_C/\sigma_{0,2})^2$ . Considering this requirement the  $\tilde{K}_C$ -values obtained by this method show good agreement with the  $K_C$ -values computed with  $2l_C$  taken from film, as described in paragraph 3.1.

### 3.3 Computing $K_C$ at small crack lengths

As shown in paragraph 3.1 and 3.2 the  $K_C$  values decrease with crack length smaller than about  $2.5 (K_C/\sigma_{0,2})^2$  if Feddersen's or Irwin's equation

$$K_C = \frac{F_C}{W \cdot B} \cdot \sqrt{W \cdot \tan\left(\frac{\pi \cdot l}{W}\right)}$$

are used.

Deriving Feddersen's or Irwin's equation it is assumed that the distance  $r$  in front of the crack at which the stress is measured, is very small in relation to the half crack length  $l$ . This does not appear to be a valid assumption when the crack is small and therefore  $K_C$  reduces with crack length.

Allen [26] has shown that  $K_C$  remains essentially constant if the following equation is used (Fig. 17)

$$K_C = \frac{F_C}{W \cdot B} \cdot \left\{ 1 - \left( \frac{\sin(\pi \cdot l/W)}{\sin(\pi/W)(a + 1/2 \cdot \pi)} \right)^2 \right\}^{-1/2} \quad (1)$$

If  $r^2/l^2$  is small relative to unity a simplified equation

$$K_C' = \frac{F_C}{W \cdot B} \cdot \sqrt{W \cdot \tan\left(\frac{\pi \cdot l}{W}\right) + 1}$$

can be used which is a very close approximation to equation (1).

## 4. Testing fracture toughness of weldments

Techniques for measuring fracture toughness of weldments are not different from those for testing base materials. Two techniques are used mainly: The ASTM Standard Method using a bend specimen (see paragraph 2.1) and the technique using a three-point bend specimen. But some additional aspects for fracture toughness testing of weldments should be noted too:

$K_{IC}$  -values of weldments are affected by the position of the notch (fig. 18). In general the center of the weld has the lowest  $K_{IC}$ , the heat affected zone HAZ has the highest

and the base material is falling into the intermediate position [27, 28]. The limited size of the heat affected zone sometimes presents difficulties. This zone is usually not perfectly straight, and therefore the fatigue crack front may penetrate a portion of the weld metal and fracture may initiate in it. The measured  $K_{IC}$  value is then characteristic of the weld metal and not of the HAZ. As it is difficult to predict just where cracks will start in service in weldments, specimens with fatigue cracks in all three possible locations should be tested. The lowest  $K_{IC}$  value then obtained should be used for calculations.

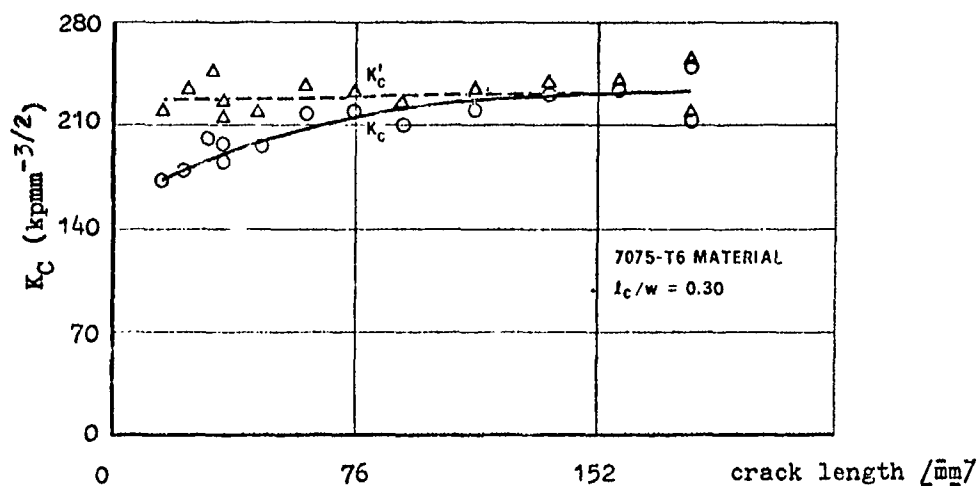
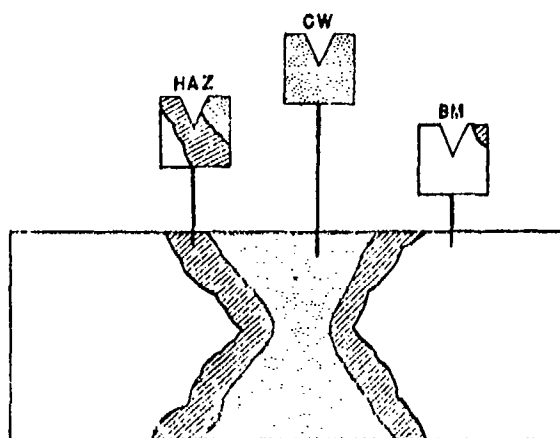


Fig. 17: Variation of  $K'_{IC}$  and  $K_{IC}$  with crack length



CW = Center of Weld  
 HAZ = Heat affected Zone  
 BM = Base Material

Fig. 18: Cross section of weld area showing different locations of starting notch

Also the kind of welding should be noted (TIG, MIG, short arc, electron beam, plasma, narrow gap etc.) because a comparison of  $K_{IC}$  tests on some steels has shown that TIG welds have higher  $K_{IC}$  values in the center of the weld than MIG and short arc welds. In the heat affected zone, however, short arc welds have the highest  $K_{IC}$  values [27].

The report also should contain the welding parameters; for example for electron beam welds welding velocity, vacuum and voltage. Last but not least the size of the welding beam and the quality of welding examined by metallurgical procedures should be noted.

## 5. Environmental effects on fracture toughness

The requirements of the ASTM Standard Method of Test are sufficient only for tests in air and under various temperatures. For fracture toughness tests conducted under other environmental conditions additional requirements must be defined in order to obtain comparable results in different laboratories.

### 5.1 Fracture toughness tests at high or low temperatures

For heating or cooling of the standard ASTM specimen copper plates or chambers should be used which are in contact with the sides of the specimen (fig. 19). Cooling the specimen is possible by liquid nitrogen down to about  $-160^{\circ}\text{C}$ , where the liquid nitrogen partly evaporates in the cooling chambers. The temperature in the chamber depends on the ratio of liquid and gaseous nitrogen; this ratio can be controlled by the flow rate. The use of liquid baths should be avoided unless it is established that the liquid has absolutely no effect on  $K_{IC}$  or unless it is the purpose of the test to explore the effect of the fluid itself on  $K_{IC}$ . The temperature distribution in the critical, cracked section of the specimen should be calibrated at the beginning of the test series by at least 3 thermocouples, one in a hole near the crack tip, one each on the sides of the specimen. It is the experience of the authors that the equipment described above will give a quite uniform temperature distribution (about  $\pm 1.5^{\circ}\text{C}$ ) over the critical section even for materials which have a poor thermal conductivity like titanium.

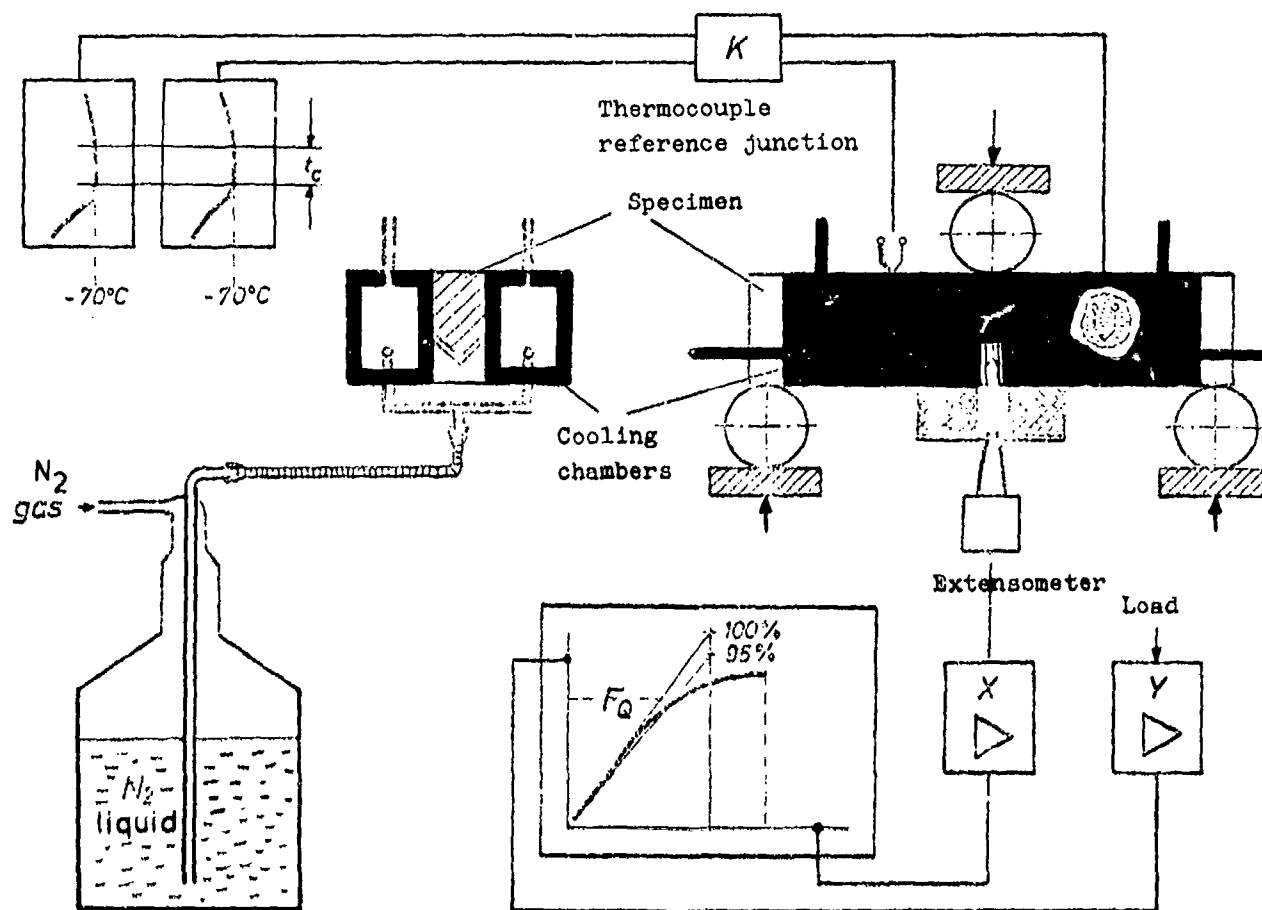


Fig. 19: Testing equipment for  $K_{IC}$  testing at low temperature

For the tests themselves two thermocouples are sufficient: One on a part of the surface not touched by the cooling chambers and one in a hole in the center of the specimen. Fatigue cracking of the specimen may be conducted at room temperature. However the maximum  $K$  during fatigue loading,  $K_f \text{ max}$ , should not exceed

$$0.6 \cdot (\sigma_{0.2} / 2 \cdot \sigma_{0.2,1}) \cdot K_Q \quad \square$$

( $\sigma_{0.2,1}$  = 0.2 offset yield strength at temperature  $T_1$ )

5.2 Fracture toughness in corrosive environments

5.2.1 Salt water corrosion

The ASTM Standard Method of Tests provides no information on the composition of corrosive media and duration of fracture tests in a corrosive medium. Therefore for comparison of  $K_{IC}$  values obtained from different corrosion tests the exact composition of the salt water used should be known or "synthetic sea water" as described for example in the German standard DIN 50 900 should be used. Moreover it is urgently necessary to control the pH-value and the temperature of the salt water continuously during the test and keep it constant. To avoid potential voltage between the test specimen in sea water (fig. 20) and the test equipment, the test specimen should be electrically isolated from the testing equipment. This can be done for example by making the rollers out of non metallic materials i. e. ceramic or granite and all seawater containers of plastic.

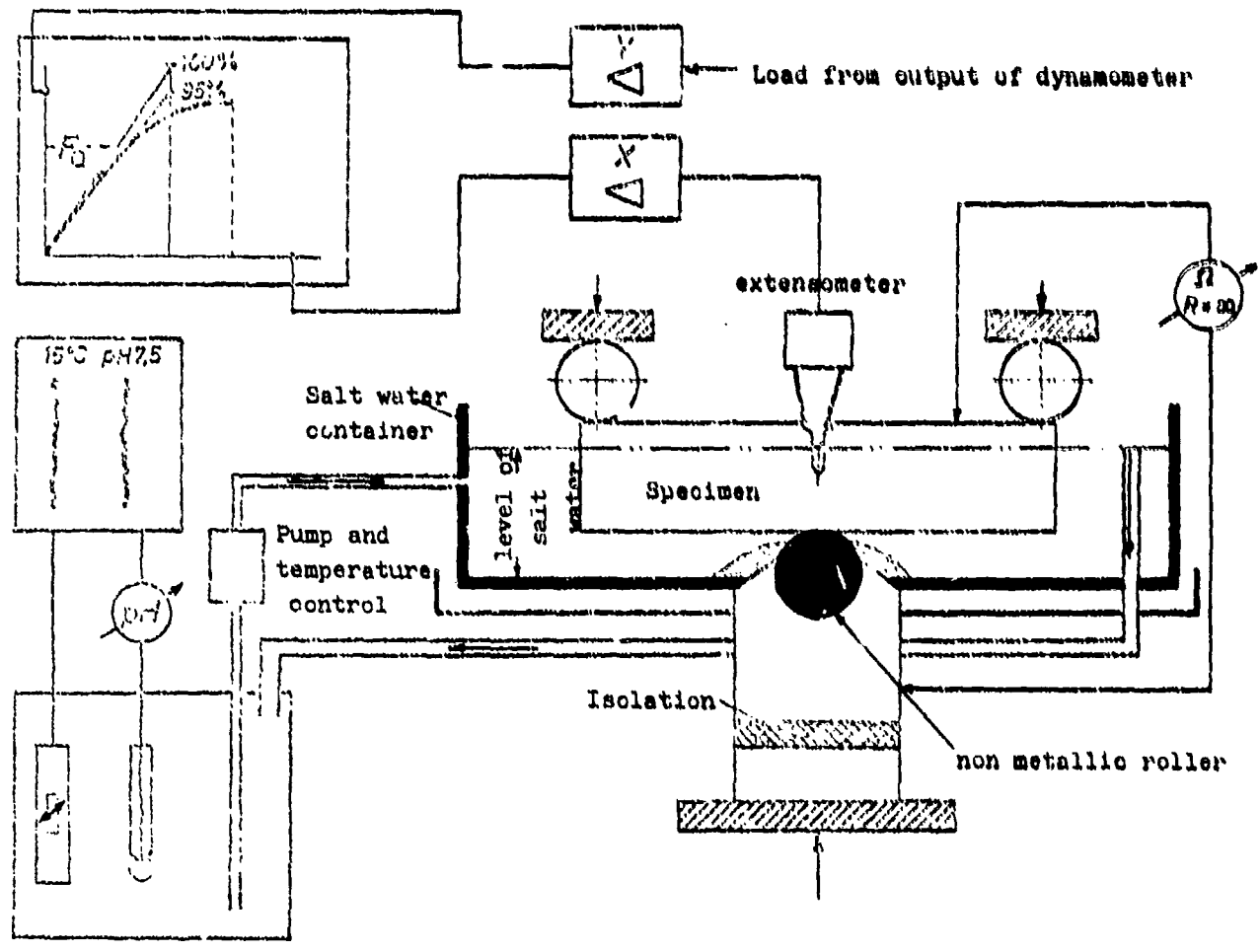


Fig. 20: Testing equipment for  $K_{IC}$  testing under corrosive media

Another important factor is the time under load spent by the specimen in the corrosive environment. Using the requirement of the ASTM Standard Method of Test for the strain rate  $K_Q/t$ , this time is too short for any corrosion effects.

Two types of tests are possible: (1) short duration (about 1 hour), step loaded tests for subcritical crack growth under sustained loading, that is, the applied load is held constant for a certain time and then increased stepwise [29]. (2) The specimen is loaded for a certain time at some fraction of the estimated load at failure in the corrosive environment. After this time it is broken,  $K_{IC}$  is determined and it is examined for subcritical crack growth. This is thought to be a better approximation to loading in service [30] at least for the lower wing surface of aircraft.

### 5.2.2 Hot gas corrosion

Just as for salt water there is no standard in composition of "synthetic corrosive gases". While a more or less standardized equipment is used for hot corrosion tests [31], the fuel burned in these test rigs greatly influences the results. The corresponding test parameters, such as temperature, sulphur content of fuel, fuel-air-ratio etc. therefore have to be noted carefully in order to enable valid comparisons to be made. In tests conducted at Motoren- und Turbinen-Union (MTU), Munich, the specimens have been placed into the hot gas stream of a jet engine and the fatigue crack developed. Afterwards the specimens are broken in the hot gas stream. Because of the high temperatures involved no displacement gage was used up to now. For calculating  $K_{Ic}$  and  $K_{Ic}$  the maximum load  $P_{max}$  is used.

### 5.2.3 Embrittlement due to temperature cycling

Most gas turbine materials which undergo start-stop operations in service tend to embrittle due to the corresponding temperature variations. In order to be meaningful, fracture toughness tests ought to be carried out on suitably embrittled specimens.

## 6. Effect of strain rate on $K_{Ic}$ values

For calculating the residual strength and critical crack length in some special applications (gun tubes for example) the conventional ASTM Standard Method of Test which involves static tests for determining  $K_{Ic}$  is not entirely satisfactory. Because of the high strain rates occurring at the discharge of the guns the crack toughness behaviour of steels may be different from that at normal rates. The instrumented impact test on precracked Charpy V-Notched or bend specimens provides an inexpensive but also inaccurate procedure for determining dynamic fracture toughness. In fig. 21 gage No. 1 was used as a crack detector to determine the time of crack initiation. The nominal elastic strain at gage No. 2 was experimentally recorded as the crack initiated. This strain was then used to calculate the corresponding nominal elastic stress at the point where the gage is situated. Using the elementary strength-of-materials formula  $\sigma = Mc/I = \epsilon_{max} \cdot E$ , the moment and corresponding equivalent static load necessary to give this stress was calculated. With this equivalent static load which occurred at the time of crack initiation, the dynamic  $K_{Ic}$  value can be calculated for the test condition from

$$K_I = Y \cdot \frac{\sigma \cdot M \cdot \sqrt{l}}{B \cdot W^2}$$

For the strain rates and steels tested by some investigators [32, 33] the dynamic  $K_{Ic}$  value decreased with increasing strain rate at a constant temperature, see (fig. 22).

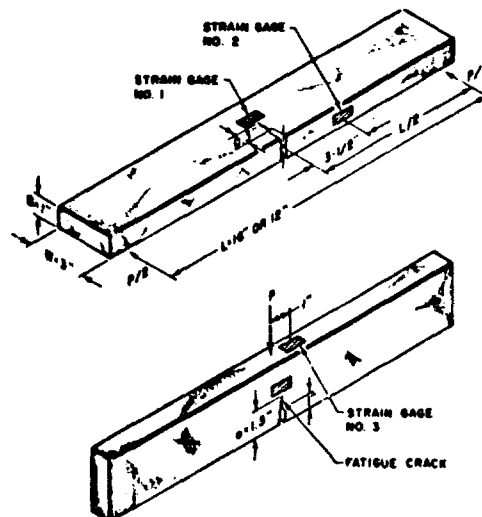


FIG. 21. Instrumented beam specimen for dynamic fracture toughness testing.

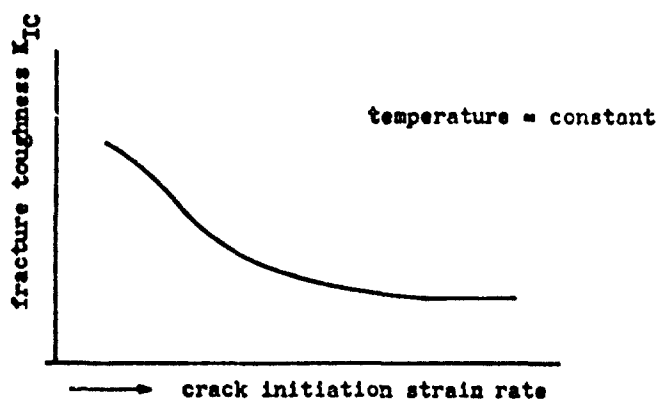


Fig. 22: Variation of  $K_{IC}$  with increasing strain rate

To the writers' knowledge a normal ASTM Standard test at the high strain rates involved (i. e. about 5 msec from zero to maximum load) has not yet been carried out but this test method is to be preferred. Such tests which should be possible using fast servohydraulic cylinders, are planned at the IABG.

#### 7. Closing remarks

Two ASTM Standard Methods of Tests for determining fracture toughness and a series of nonstandard tests for special applications have been described and advantages and disadvantages have been discussed. But using these methods and even the ASTM Standard Methods it must be realized that a  $K_{IC}$  or a  $K_C$  value is a material property and as such subjected to considerable scatter. This may be caused by material effects or different test equipments such as:

- test scatter caused by material inhomogeneity. Determination of the average of  $K_{IC}$  and the limits are discussed in paragraph 2.1.3.
- scatter among valid  $K_{IC}$  values obtained from tests conducted at different laboratories on the same material. This scatter may be caused by using different test equipment or methods [34] e. g. by test machine response [32].
- scatter due to different heat treatments of nominally identical material. Especially for titanium and high strength steels (D 6 A C) large differences in  $K_{IC}$  have been reported [36] although the static strength  $F_{tu}$  and  $F_{ty}$  have been within specifications.
- scatter due to product form, for example different semiproducts as sheet material, plates, handforgings, dieforgings, extrusions a.s.o. Grain direction may have a large influence.
- scatter among  $K_{IC}$  values obtained from specimens which are taken from different positions within a thick plate or a large forging. For the titanium alloy Ti6Al6V2Sn the differences in  $K_{IC}$  values are shown in (fig. 23). [37].

Considering all these points mentioned above for critical aerospace applications the specimen for determining  $K_{IC}$  should be taken out of the component itself.

For rough calculations  $K_{IC}$  values of nominally identical materials tested by the ASTM Standard Method of Test may be used, for these values are obtained on the same basis. This may be of help in the design stage. In the near future it should be a requirement to the materials manufacturer that he guarantees the  $K_{IC}$  value just as at present  $F_{tu}$  and  $F_{ty}$  and show proof of compliance by including it in the materials sheet.

Material : Ti-6Al-6V-2Zn annealed

Thickness of semiproduct: 98 mm (plate)

Specimen thickness : 6 mm

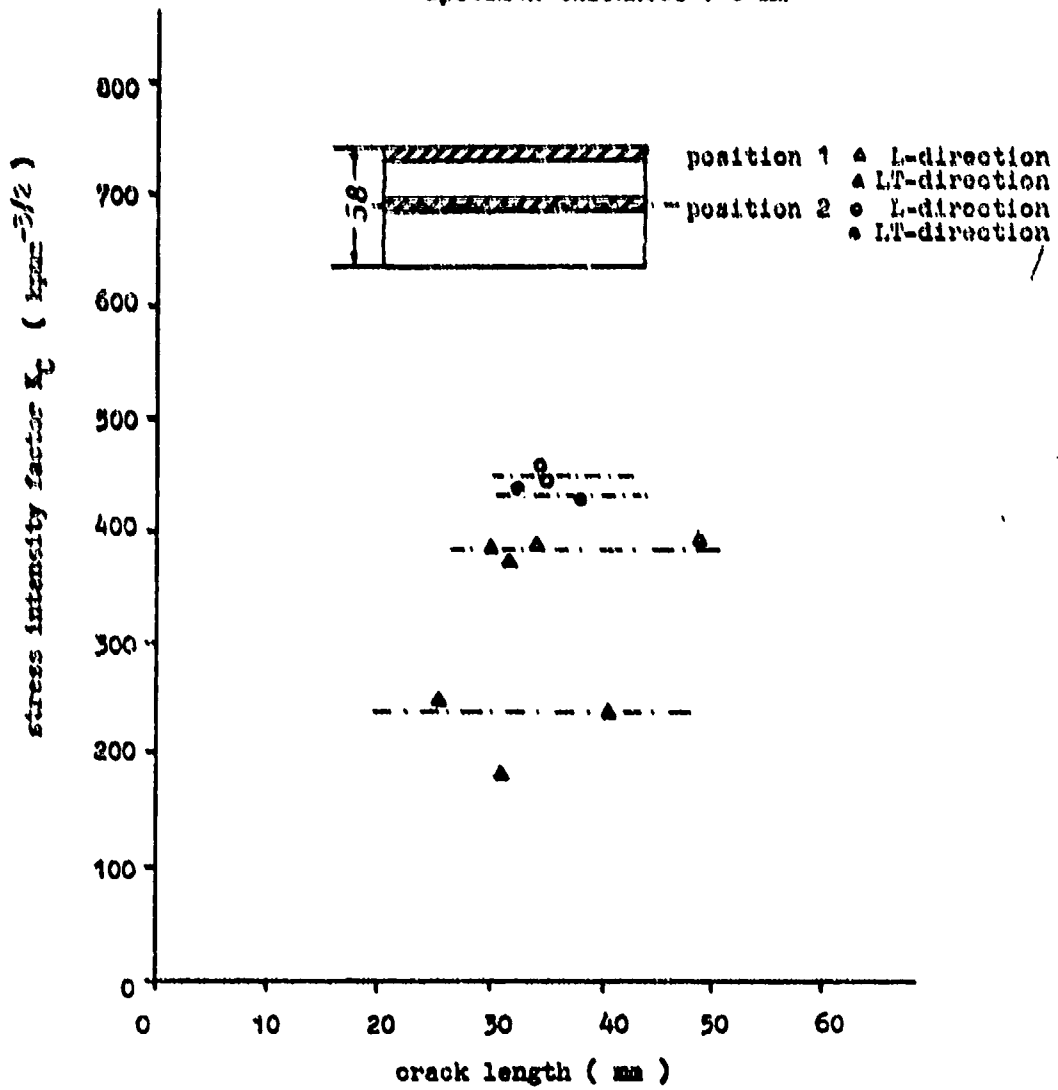


Fig. 23: Scatter of  $K_I$  between specimens taken from different positions within a thick plate



REFERENCES

- [1] Standard Method of Test for Plane Strain Fracture Toughness of Metallic Materials. Annual Book of ASTM Standards 1972, Designation E 399 - 72 T, pp. 955 - 974
- [2] Plane Strain Fracture Toughness Testing of High Strength Metallic Materials Using a Fatigue Cracked Bend Specimen. Aerospace Material Document AMD 23 DD, Society of Automotive Engineers, New York 9. Jan. 1968
- [3] Walker, E. F. and M. J. May: The Fracture Properties of a Ni-Cr-Mo-V-Steel. BISRA open Report MQ/A/91/68
- [4] Freed, C. N., R. J. Goode and R. W. Judy Jr.: Comparison of Fracture Toughness Test Procedures for Aluminium Alloys. Engineering Fracture Mechanics 1971, Vol. 2, pp. 359 - 371
- [5] Klausnitzer, E.: Messung der Bruchzähigkeit ( $K_{IC}$ ) metallischer Werkstoffe mittels Verbundproben. Atomwirtschaft Jhrg. XVI, Nr. 4 (April 1971), S. 3 - 4
- [6] Brown, W. F. Jr. and J. E. Srawley: Plane Strain Crack Toughness Testing of High Strength Metallic Materials. ASTM Special Technical Publication No. 410, December 1967
- [7] Kaufmann, J. G.: Fracture Toughness Testing. Advanced Testing Techniques, ASTM STP 476, American Society for Testing and Materials, 1970, pp. 96 - 111
- [8] Sprowls, D. O. and J. G. Kaufman: Discussion on Fracture Toughness and Stress Corrosion Properties of Aluminium Alloy Hand Forgings. Journal of Materials JMLSA Vol. 7 no. 2, June 1972, pp. 263 - 265
- [9] Petrak, G. J.: A Note on Fatigue Crack Front Straightness in  $K_{IC}$  Testing. Engineering Fracture Mechanics, 1972, Vol. 4, pp. 311 - 313
- [10] Rossow, E.: Eine einfache Rechenschiebernäherung für die den normal scores entsprechenden Prozentpunkte. Zeitschrift für wirtschaftliche Fertigung 59 (1964) Heft 12, Dezember, S. 596 - 597
- [11] Comparison of Samples, Engineering Science Data Unit, The Royal Aeronautical Society, 4 Hamilton Place, London W. 1, ITEM No. 68016, Febr. 1968
- [12] Standard Method of Sharp - Notch Tension Testing of High - Strength Sheet Materials. Annual Book of ASTM Standards, Part 31, Juli 1970, Designation E 338 - 68, pp. 847 - 854
- [13] Irwin, G. R.: Structural Aspects of Brittle Fracture. Application Materials Research, 3. April 1964, pp. 65 - 81
- [14] Clark, W. G. Jr.: Fracture Mechanics in Fatigue. Experimental Mechanics, September 1971, pp. 422 - 428
- [15] Kendall, D. P. and M. A. Hussain: A New Fracture Toughness Test Method for Thick Walled Cylinder Material. Experimental Mechanics, April 72, Vol. 12 Nr. 4
- [16] Feddern, G.: Eine neue Probenform für bruchmechanische Experimente. Institut für Werkstoffkunde I, Universität Karlsruhe (not published)
- [17] Hoagland, R. G.: On the Use of the Double Cantilever Beam Specimen for Determining the Plane Strain Fracture Toughness of Metals. ASME-Paper No. 67-Met-A (1967)
- [18] Irwin, G. R. and J. E. Kies: Critical Energy Rate Analysis of Fracture Strength. Welding Journal 33, 193 - 198, 20 - 24 (1964)
- [19] Freed, C. N. and R. J. Goode: Correlation of Two Fracture Toughness Tests for Titanium and Ferrous Alloys. Naval Research Laboratory, NRL Report 6740, January 16th 1969
- [20] Nelson, F. G., P. E. Schilling and J. G. Kaufmann: The Effect of Specimen Size on the Results of Plane Strain Fracture Toughness Tests. Engineering Fracture Mechanics, 1972, Vol. 4, pp. 33 - 50
- [21] Broek, D.: The Effect of Finite Specimen Width on the Residual Strength of Light Alloy Sheet. NLR - TR 2151, September 1965
- [22] Leis, H. and W. Schütz: Bewertung neuer Flugzeugbauwerkstoffe mit den Methoden der Bruchmechanik. Luftfahrttechnik - Raumfahrttechnik 16 (1970) Nr. 10, S. 247 - 251
- [23] Schütz, W. and W. Oberparleiter: Rißfortschritts- und Restfestigkeitsverhalten von Flugzeugbauwerkstoffen. IABG-Versuchsbericht Nr. TF 236, Januar 1972

- [24] Feddersen, C. E.: Discussion to: Plane Strain Crack Toughness Testing. ASTM STP 410 (1967)
- [25] Liebowitz, H. and J. Eftis: On Nonlinear Effects in Fracture Mechanics. Engineering Fracture Mechanics, Vol. 3 (1971) pp. 267 - 281
- [26] Allen, F. C.: The Effect of Thickness on the Fracture Toughness of 7075 Aluminium in the T6 and T73 Conditions. From Damage Tolerance in Aircraft Structures, ASTM STP 486, 1971, pp. 16 - 38
- [27] Kies, J. A., H. L. Smith, H. E. Romine and H. Bernstein: Fracture Testing of Weldments. ASTM STP 381, American Society of Testing and Materials, 1965, pp. 328 - 356.
- [28] Gentilicore, V. J., A. W. Pense and R. D. Stout: Fracture Toughness of Pressure Vessel Steel Weldments. Welding Journal, Research Supplement, October 1970
- [29] Clark, W. G. and E. T. Wessel: Influence of a Synthetic Seawater Environment on the Fracture Behaviour of HP 9 - 4 - 25 and HP 9 - 4 - 20 Alloy Steels. Materials Performance and the Deep Sea, ASTM STP 445 (1969) pp. 93 - 114
- [30] Schütz, W. and D. Mertens: Ermittlung von Werkstoffkennwerten an elektronenstrahlgeschweißten Ti-Legierungen. IABG-Versuchsbericht Nr. TF 273, Juni 1972
- [31] Hot Corrosion Problems Associated with Gas Turbines. ASTM STP 421, American Society for Testing and Materials (1967)
- [32] Shoemaker, A. K. and S. T. Rolfe: Static and Dynamic Low Temperature  $K_{IC}$  - Behaviour of Steels. Journal of Basic Engineering, September 1969, pp. 512 - 518
- [33] Server, W. L. and A. S. Tetelman: The Use of Precracked Charpy Specimens to Determine Dynamic Fracture Toughness. UCLA Report ENG - 7153, University of California, Los Angeles
- [34] Heyer, R. H. and D. E. McCabe: Evaluation of a Method of Test for Plane Strain Fracture Toughness Using a Bend Specimen. ASTM STP 463, American Society for Testing and Materials, 1970, pp. 22 - 41
- [35] Swanson, S. R.: The Validity of Fracture Toughness Data as Influenced by Test Machine Response. Paper Presented at the Conference on Fracture Toughness of High Strength Steels. University of Sheffield, March 25 - 25, 1968
- [36] Wood, H. A.: Fracture Control Procedures for Aircraft Structural Integrity. Presented to the International Committee on Aeronautical Fatigue, Miami Beach, Florida, May 13/14, 1971
- [37] Schütz, W. and W. Oberparleiter: Rißfortschritt und Restfestigkeit an 6 mm dicken Titanplatten. IABG-Versuchsbericht TF - 258, April 1972

## VII. FLAW DETECTION METHODS

VII.A. RELIABILITY OF THE DETECTION OF FLAWS AND OF THE DETERMINATION  
OF FLAW SIZE

Ekkart Knorr

Summary . . . . .	396
1. Problem . . . . .	396
2. Description of Investigations . . . . .	397
2.1 Definition of Fatigue Cracks through Nondestructive Testing . . . . .	397
2.2 Eddy Current Testing of Bolt Holes . . . . .	401
2.3 Ultrasonic Testing Below Heads of Rivets in Sheet Material . . . . .	404
3. General Valuation of NDI-Methods with Respect to Reliability . . . . .	408
3.1 Remarks to Above Described Investigations . . . . .	408
3.2 Sequence of NDI Methods. . . . .	408
3.2.1 Preface . . . . .	408
3.2.2 Flaw Detection in Sheet Material . . . . .	409
3.2.3 Flaw Detection in Solid Metallic Parts . . . . .	409
3.2.4 Determination of Flaw Size. . . . .	410
References . . . . .	412

VII.A. RELIABILITY OF THE DETECTION OF FLAWS AND OF THE DETERMINATION  
OF FLAW SIZE

Ekkart Knorr

SUMMARY

Three laboratory investigations concerning reliability of crack detection and determination of crack size which represent the state of the art to the authors knowledge are shortly described. All three are typical applications of nondestructive inspection to structural parts of aircraft:

- inspection of flat surfaces with fatigue cracks, using ultrasonic, X-ray, dye penetrant, magnetic particle and eddy current methods
- crack detection below rivet heads with an ultrasonic shear wave technique and
- crack detection in bore holes of a forged part using a manual eddy current method;

the second and the third one with statistical evaluation of probability of success. An evaluation of the conventional NDI-methods regarding reliability is performed.

1. PROBLEM

Not only availability of any nondestructive testing method for flaw detection in structural parts with known flaw critical points, but also reliability of detection of flaws above a certain length or of flaw size measurement, are essential conditions for every statement about fixation of intervals of inspection or in general about flight safety when flying with (always existent) flaws.

Although the hitherto known nondestructive-inspection (NDI-) methods in their principles are elaborated very exactly and some thousands of different applications are described in the literature, there exist only a few systematic experimental investigations about reliability of flaw detection and determination of flaw size for the practice of maintenance of aircraft (reliability in manufacturing NDI-methods is excluded here).

All known NDI-methods for detecting and measuring flaws have their limits from their basic physics, from mechanical arrangements, from apparatus, from type of tested materials, from accessibility to the point where crack is starting or moving and these limits are combined with human limitations of the testing personnel as interest, experience, fitness and intellect; consequently, the success of any NDT cannot be 100 %, i.e. not all flaws are detected or too many "flaws" are indicated which do not exist. In the first case results a technical risk, in the second one it may be uneconomical.

General tendency in NDI goes to full or partly automatically working testing apparatus to eliminate the human factor and/or to accelerate work. But in aircraft maintenance quantity of test piece series usually is not as large, that automatic inspection apparatus is profitable; on the other hand inspection problems vary quickly, and well experienced inspection personnel are a more adaptable element of NDI-test unity than specialized apparatus.

To get information about reliability of inspection for flaws in aircraft structures, reliability defined here as experimentally found and statistically proven probability of detection of flaws or determination of flaw size, it is absolute precondition to know the real status of flaw existence or flaw dimensions. No one of the nondestructive methods until today is able to give this actual status of flaw. Therefore only destructive methods combined with optical evaluation give the reference-basis to get the status of flaws; in most cases by breaking up the flaw of the damaged part to determine crack area and its length at surfaces by aid of a microscope (if possible electron beam microscope), sometimes by preparing the surface of the part around the

crack tip mechanical and/or chemical and following optical measurement of crack length. ("Optical" is a limitation too, but the least.)

Destruction of all or of a representative cross section of all parts in service in practical applications e.g. is nonsense only to get information about reliability of inspection methods; consequently reliability investigations are usually only possible performing practice-oriented laboratory tests.

Extrapolation to maintenance of structures in the field is possible but should be done critically, regarding the influence of the differences in test conditions such as accessibility, temperature, working overhead and others. (The extrapolation generally is done based on experience from similar cases, i.e. emotional; recently we try to get factors for these influences.)

From principle, these remarks are valid for all types of flaws, p.e. fatigue cracks, stress corrosion cracks, inclusions, tool marks, o.a.; but it is known that type of flaw influences the precision of some NDI-methods. Therefore, when using results of literature their specific preconditions have to be regarded.

## 2. DESCRIPTION OF INVESTIGATIONS

Following three laboratory investigations about reliability of detection of flaws and of determination of flaw size are described briefly: Inspection of flat surfaces, below rivet heads and in bore holes.

### 2.1 Definition of fatigue cracks through nondestructive testing (Inspection of flat surfaces)

In 1968 Packman, Pearson, Owens and Young presented results of a systematical experimental investigation about reliability of nondestructive inspection with special view to fracture mechanics [1]. The ability for crack detection, location and crack measurement of X-ray, ultrasonic-, penetrant-, eddy current- and magnetic particle techniques was tested in laboratory; surface fatigue cracks were originated in 3" diameter and 1/4" thick tubes of 4330 steel and 7079-T6511 aluminium material in a constant amplitude fatigue test.

The results for sensitivity (percentage of cracks found in dependence of crack length at the surface), accuracy (of the crack length) and assurance index (a combination of factors as accuracy, sensitivity, precision) are repeated in fig. 1 - 6. They are based on optical measurement of crack length after destruction of the tested part. The typical crack area was a thumbnail form, which is important to know for the valuation of the different nondestructive methods, for they all depend from area of the crack (ultrasonic), area and width (volume of the penetrating oil, X-ray) or the course of the crack below the surface near the crack tip (penetration depth of eddy current, magnetic particle inspection). For their special case the authors give a sequence of sensibility of the chosen methods for both materials for two ranges of length: from zero to 0.15 or 0.2 inches and from 0.2 to 0.5 inches.

For aluminium cylinders the sequence was for less than 0.2" crack length: ultrasonics, penetrant, X-ray, for lengths 0.2" to 0.5": penetrant, ultrasonics, X-ray. For steel tubes and crack lengths less than 0.15": ultrasonics, magnetic particle, penetrant and X-ray, for lengths between 0.15" to 0.5": ultrasonics and magnetic particle method changed their position. For eddy current no curves are given, but it is valued less sensitive than ultrasonics for cracks lengths between 0.2" and 0.5".

General conclusion is that reliability of NDT needs to be improved, for the maximum assurance index obtained was 90 %.

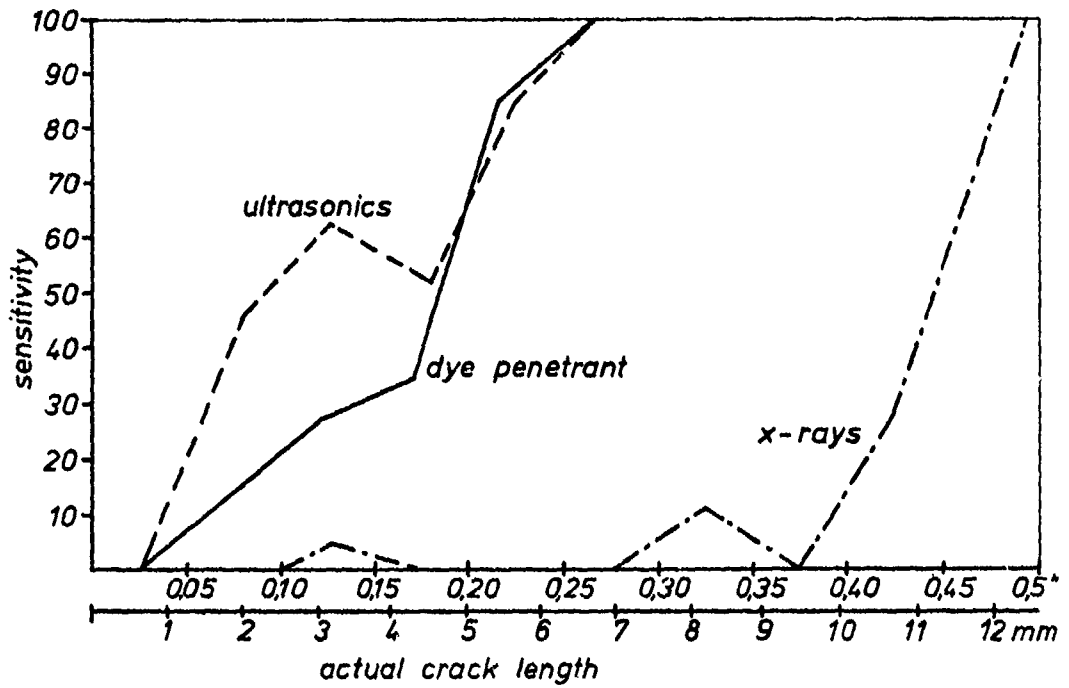


Fig. 1: Sensitivity of NDT-methods in detecting surface fatigue cracks in 7075-76511 aluminium [1]

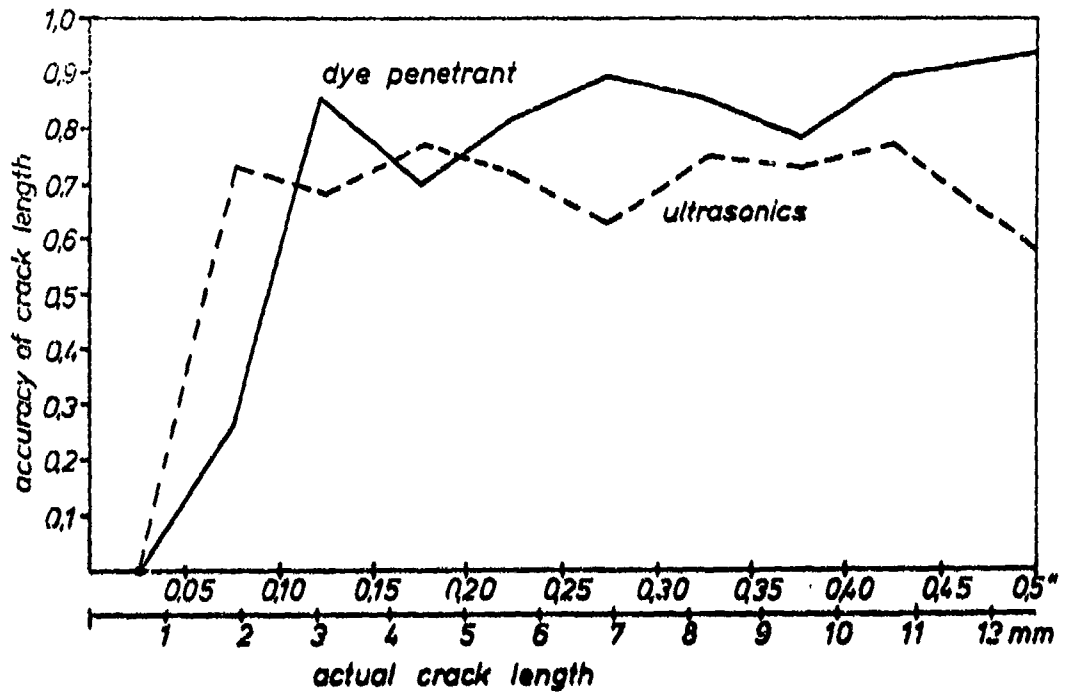


Fig. 2: Accuracy of crack length, indication by NDT in 7075-T6511 aluminium [1]

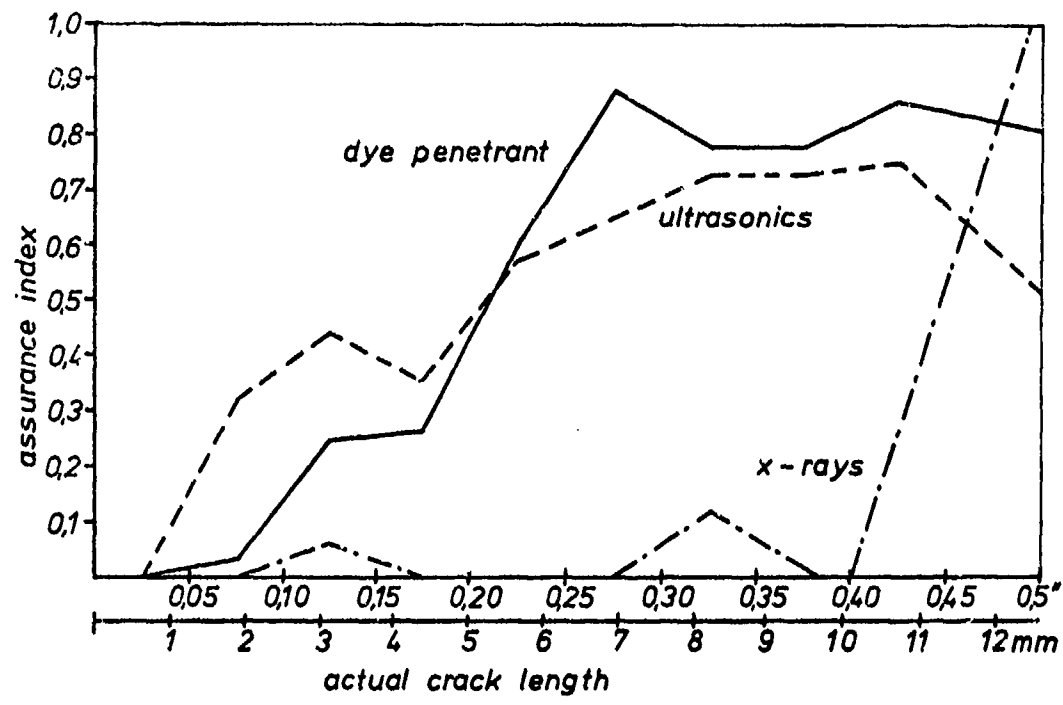


Fig. 3: Assurance index of NDT measurements in 7075-T6511 aluminium [U]

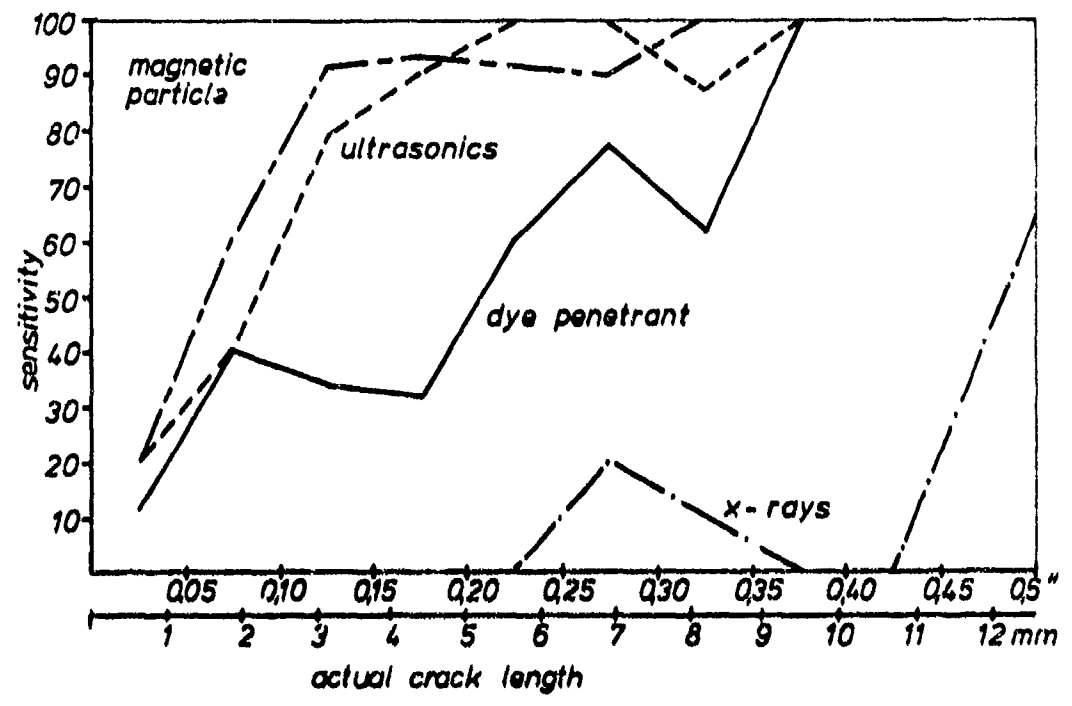


Fig. 4: Sensitivity of NDT methods in detecting surface fatigue cracks in 4330 V modified steel heat treated to 220 to 240 ksi ultimate strength [U]

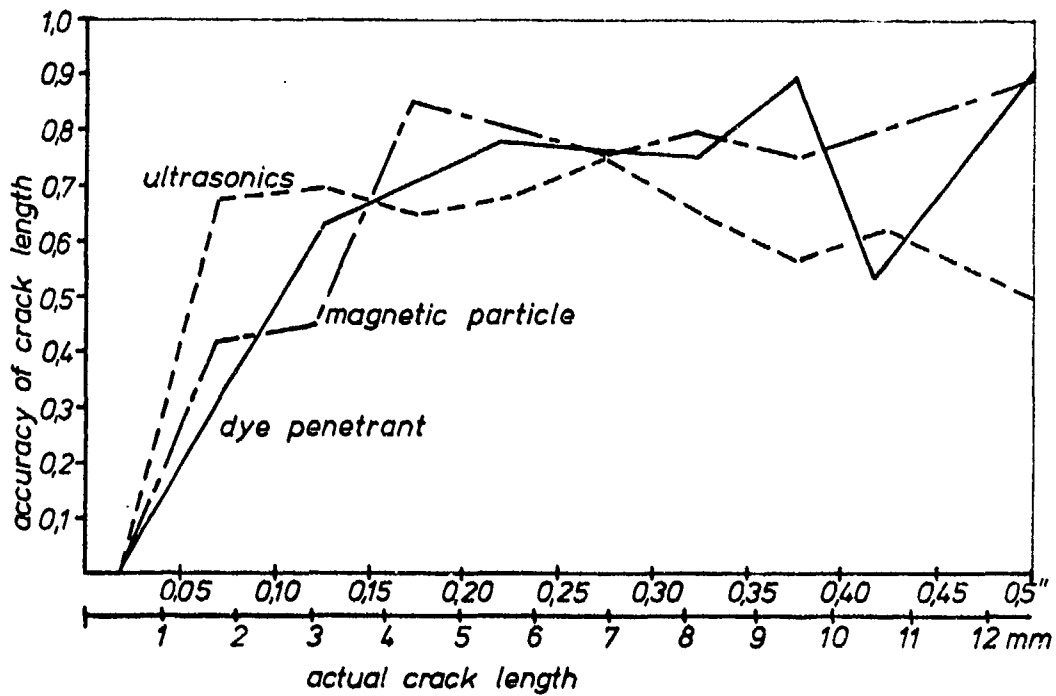


Fig. 5: Accuracy of crack length, indication by NDT in 4330 V modified steel heat treated to 220 to 240 ksi ultimate strength [7]

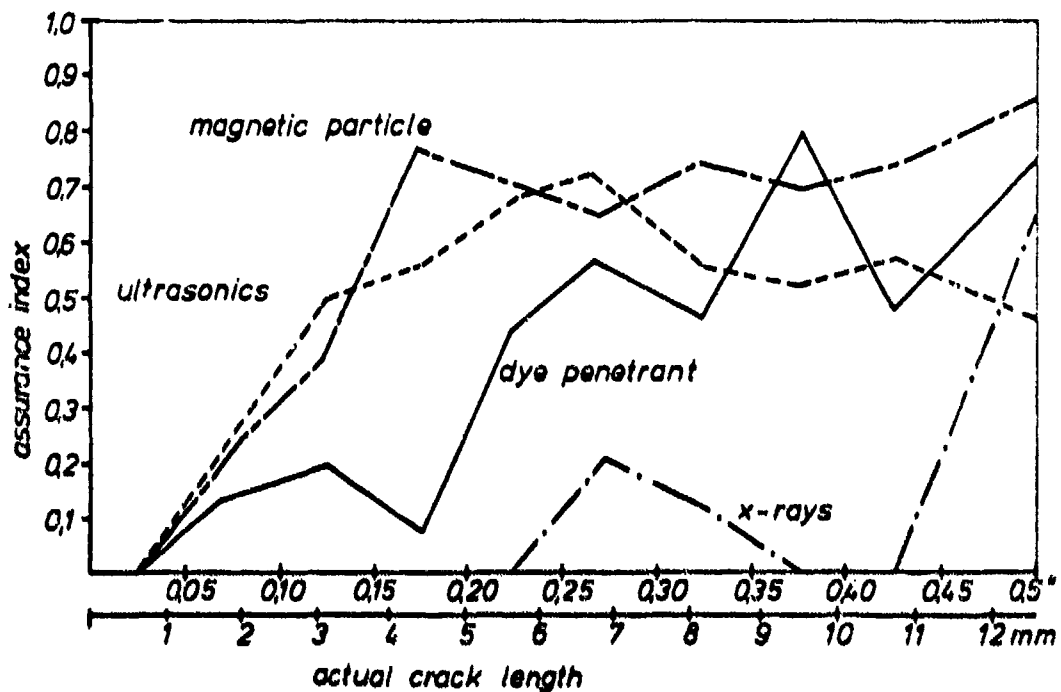


Fig. 6: Assurance index of NDT measurements in 4220 V modified steel heat treated to 220 to 240 ksi ultimate strength [7]



## 2.2 Eddy current testing of bolt holes

In 1970 IABG developed a manual inspection method for a special bolt hole of the lower side of a wing-to-fuselage-fitting of an aircraft in service (see fig. 7), the fitting forged of high strength material and margin of safety zero. Inspection had to be done at the airport without dismantling, except taking out the screw bolt itself, i.e. fitting was covered from wing skin. The testing personnel had to work over head. The bolt hole had a depth of 1 inch and a diameter of 5/16 inch, but method can be applied to nearly all hole diameters.

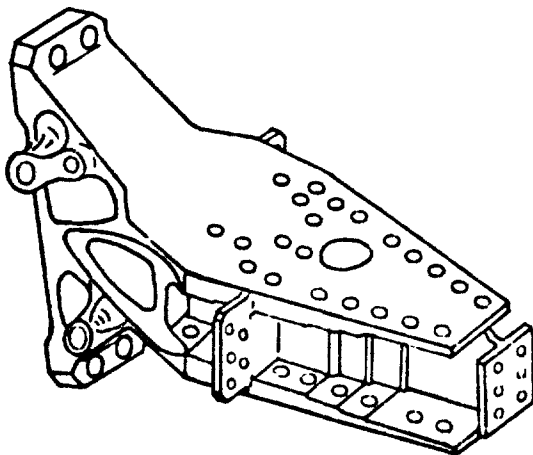


Fig. 7: Wing-to-fuselage-fitting of an aircraft with critical bolt holes

Testing method was optimized with view to

- detection of cracks as soon as possible
- the available testing device and the present testing personnel
- a tolerable time for inspection.

The principle of the method was to drive around at three different depths of the hole, so that the eddy current influenced areas were overlapping. If any crack was detected its length was measured in a second step by eddy current and controlled by optics using endoscopes.

To get a valid statement for the probability of success of these manual inspections and to make a certain training, everyone of those 9 inspectors, who had to inspect the aircraft later on, had to test independent of the others about 200 bolt holes of fittings fatigued in laboratory tests, 80 of the holes having fatigue cracks of different lengths (see fig. 8). It has to be mentioned that testing conditions were better in laboratory: normal temperature, no working overhead, sitting while working, no skin above the fitting plane. This is important, if extrapolations of the results are made to inspections in the field.

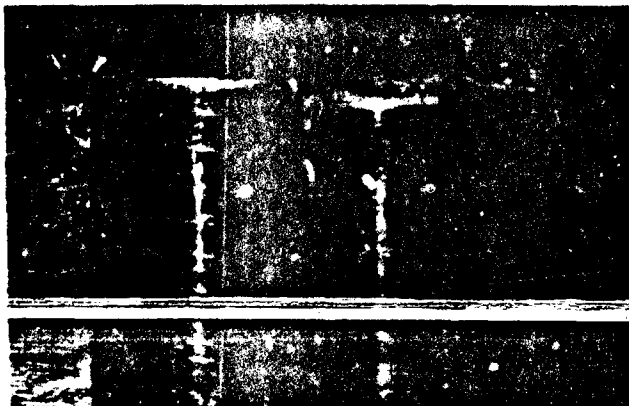


Fig. 8: Examples of fatigue cracks in 5/16" diameter bore holes of fittings

The results are shown in figures 9 - 13. They are based on the effective crack areas determined optically (by microscope) after breaking up most of these bolt holes when nondestructive inspection was finished. Fig. 9 shows that in most cases crack size range was determined correct, with a light tendency to underestimate crack size. Only 2 % of the holes were designated as cracked, which really had no cracks. And these 2 % always were near minimal detectable crack length or were confused with existent scratches.

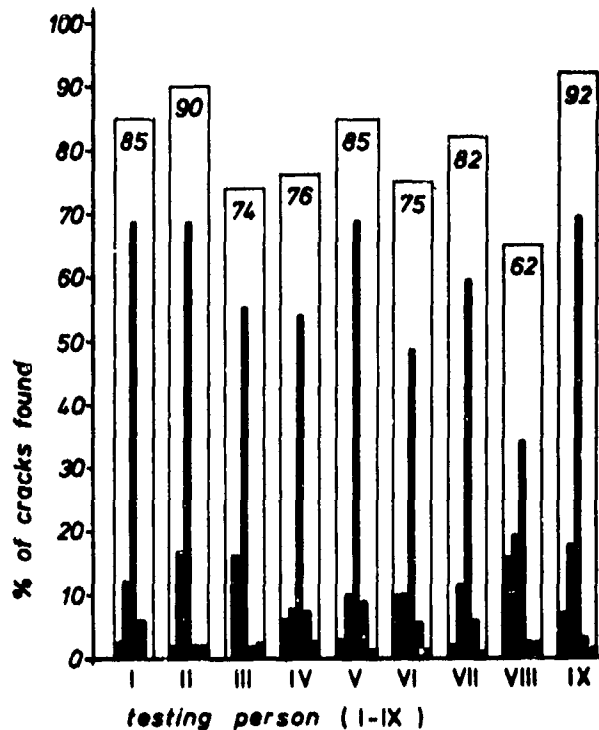


Fig. 9: Percentage of cracks found by 9 inspectors. The central bar gives the percentage of correct determined crack sizes, on the left hand cracks valued to small for one respectively more than one classes, on the right side cracks valued to large.

The percentage of cracks found in dependence of crack area (in classes) is given in fig. 10 for each one of the testers. This figure not only allows a first estimation of reliable found crack area, but gives very much information about the qualification of the testing personnel; or consequently, which one needs more training or is eliminated from further inspection.

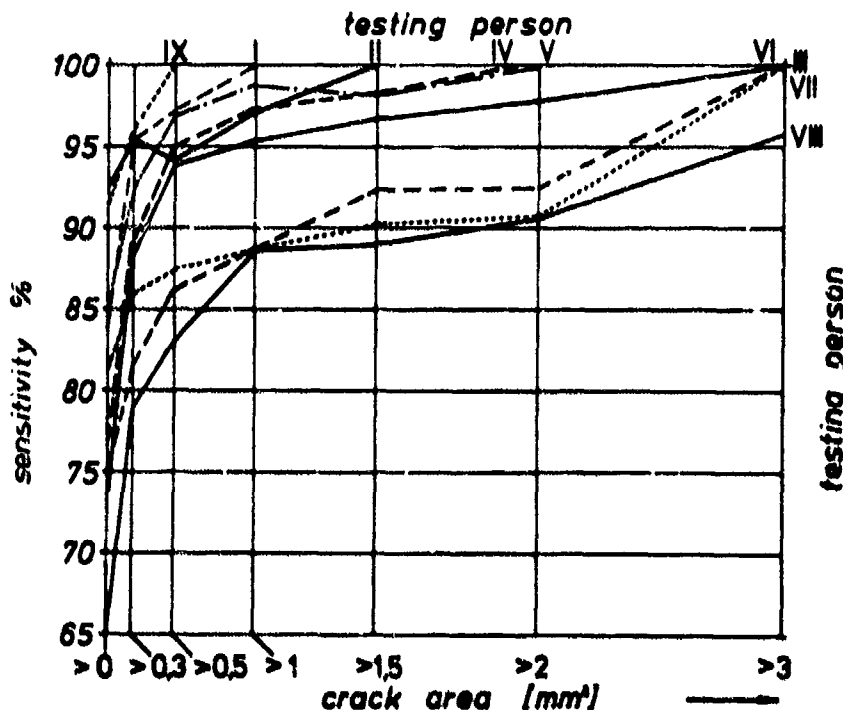


Fig. 10: Sensitivity of eddy current method in detecting fatigue cracks in bore holes of 7075-T6 aluminium found independent by 9 testing persons.

For further evaluation it is presupposed (and has been controlled), that these 9 inspectors define a normal distributed totality. Fig. 11 shows the mean probability of crack detection in dependence of the percentage of found cracks for the chosen classes of crack areas. For example, if it is requested to detect 90 % of the cracks with areas  $\leq 0.3 \text{ mm}^2$ , only for 5.5 % this request is satisfied.

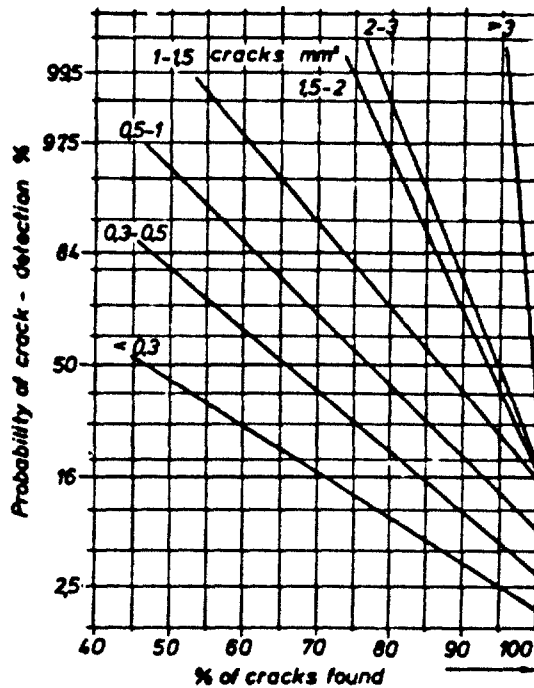


Fig. 11: Mean probability of crack detection using manual eddy current method, dependent from crack areas

Not only mean values are of interest, but too the scatter factor. In fig. 12 (a-c) the 95 % area of confidence is shown for different classes of crack areas, i. e. 95 % of all real cases of crack detection are between these limits.

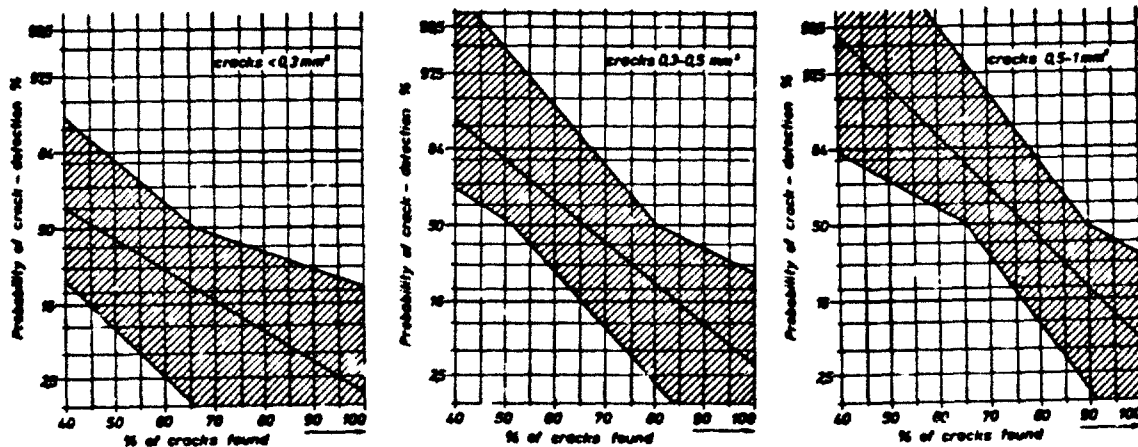


Fig. 12: Mean probability and zone of confidence for different classes of crack areas, found by eddy current

- a) all cracks up to  $0.3 \text{ mm}^2$     b) crack areas  $0.3$  and  $0.5 \text{ mm}^2$   
 c) crack areas  $0.5 - 1 \text{ mm}^2$

It is of more practical interest to know the probability of crack detection for cracks above a minimum size. This is given in fig. 13 (a-c) for all detectable cracks and for cracks above 0.3 and 0.5 mm<sup>2</sup> minimum size. Fig. 13c demonstrates increase of reliability, if only the 6 best inspectors perform this inspection; or from another point of view: with equal total costs only with 50 % more available time for these 6 best inspectors this inspection was done either with more probability of success or - with equal probability - the certain detectable area of crack is less. This leads to the consequence known from experience that an urgent action (i. e. lack of time) has less reliability.

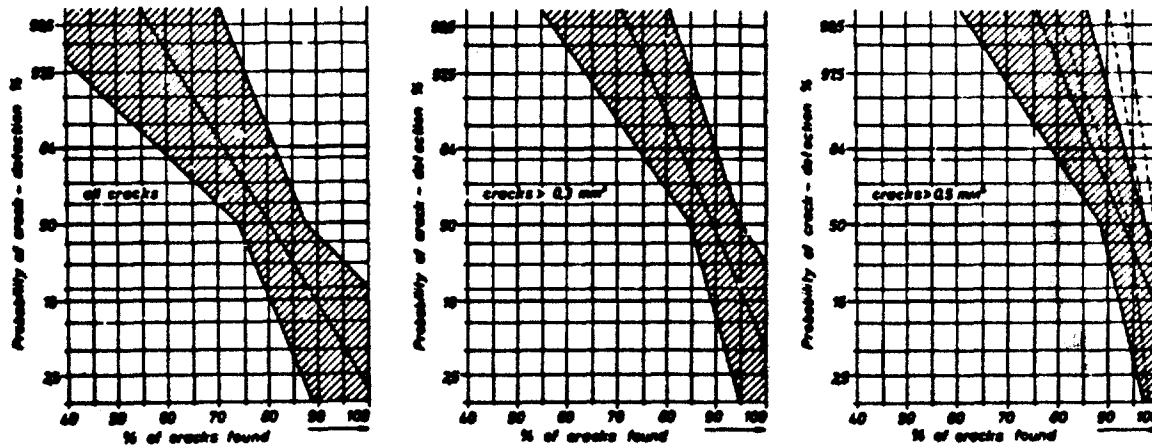


Fig. 13, a - c: Mean probability and zone of confidence for cracks above a given minimum size in bolt holes, using eddy current testing. The dotted lines in 13 c show improvement, if only the best 6 of the tested 9 inspectors would carry out this inspection.

Later on, to have an inspection document and to eliminate as far as possible the human factor in this inspection, we developed an automatically working eddy current sensor, driven by a motor, which helically scans the complete wall of the hole. When moving forward (into the hole), the profile of crack(s) is automatically written on a card of about 7.5 x 4.7 inches; when returning helically it writes the angular direction of the crack(s). With this device similar but shortened tests have been done at some fittings, with about 30 fatigue cracks, but from only one inspector.

### 2.3 Ultrasonic testing below heads of rivets in sheet material (carousel method)

Fatigue cracks often initiate below heads of rivets or of Yo-bolts. For a special case where cracks originated below heads of countersunk rivets at the points shown in fig. 14 in a 0.25" thick wing skin of high strength aluminium material (7075-T6), we worked out an optimal ultrasonic inspection method. The principle is that the maximum intensity of an ultrasonic beam (impulse reflection by transverse waves) is directed to a point between the crack-critical areas below the head and moved concentrically around the rivet center. Spacing of the beam assures, that all 4 critical areas are enveloped (see fig. 14). To control the practical efficiency or say the probability of success for given personnel apparatus methodical and environmental conditions (testing in field without removing of any rivet, working over head), we performed laboratory tests.

In test bars of 7075-T6 sheet material 0.25" thick with altogether 600 countersunk holes of 5/16" diameter we generated about 300 fatigue cracks of different crack areas (for ultrasonic shear wave reflection not crack lengths but crack area and its microstructure is decisive). Everyone of the same 7 inspectors, who later on had to do the inspection of the aircraft, with 5 ultrasonic devices (type Krautkrämer, USIP 11 and USIP 10W), equal ultrasonic probes (4 MHz) and different mounting supports (for the circular move-

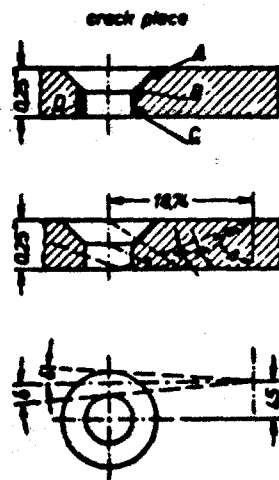


Fig. 14: Crack-critical points in sheet material with holes (above) and principle of ultrasonic test method. Divergence of sonic beam cares for detecting of cracks in all critical points in only one test

The results shown in the next figure are based on optical microscopic measurement of crack areas after breaking up the holes. Fig. 15 gives some information about the connection between real cracks not found and faults identified. (These are either cracks below the given limit, scratches or misinterpretation of "grass".) In this arrangement of the testing persons in fig. 15 the generally known tendency is confirmed that the higher the percentage of real cracks identified by a specific inspector when number of inspection points is given, the higher is the percentage of indicated flaws. Or more practical, an inspector too cautious is very expensive before he causes elimination of intact structural parts; the same effect results, if the fracture mechanist prescribes cracks, to be found by NDI, too close to the minimum detectable crack size.

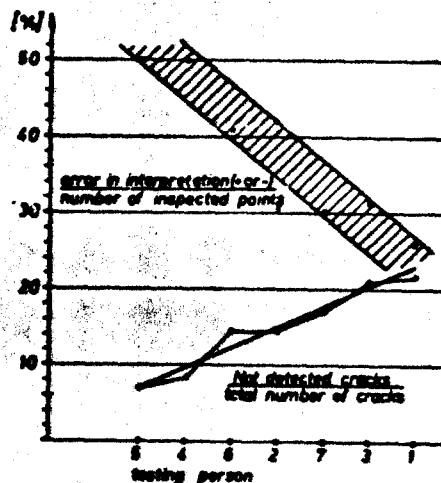


Fig. 15: Connection from misinterpretations in total with not found real cracks for 7 testing persons

Fig. 16 shows the sensitivity of this ultrasonic method, comparing the results of the seven tested inspectors with those of more experienced laboratory personal. The influence of experience is obvious.

Crack length normally is the reference quantity for fracture mechanics calculations, but ultrasonic indication depends from area of crack. The connection between crack length and crack area for the tested special geometry is given in fig. 17.

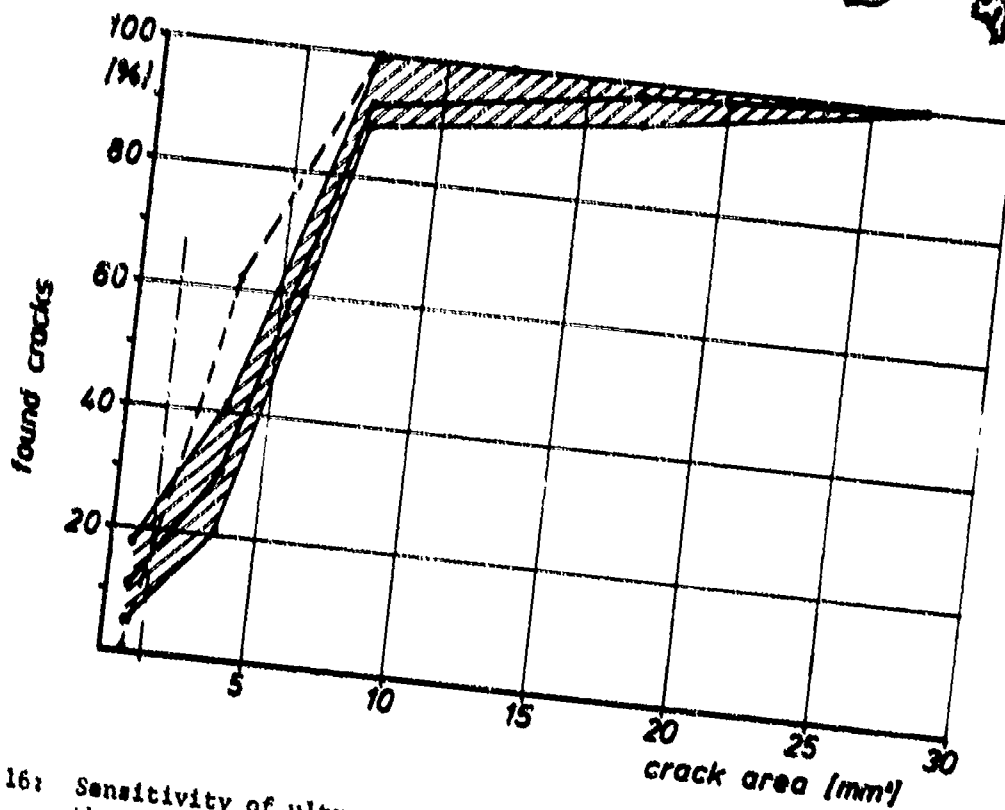


Fig. 16: Sensitivity of ultrasonic carousel method. The scatter band includes the results of 7 testers, the dotted line shows the results of an experienced laboratory inspector

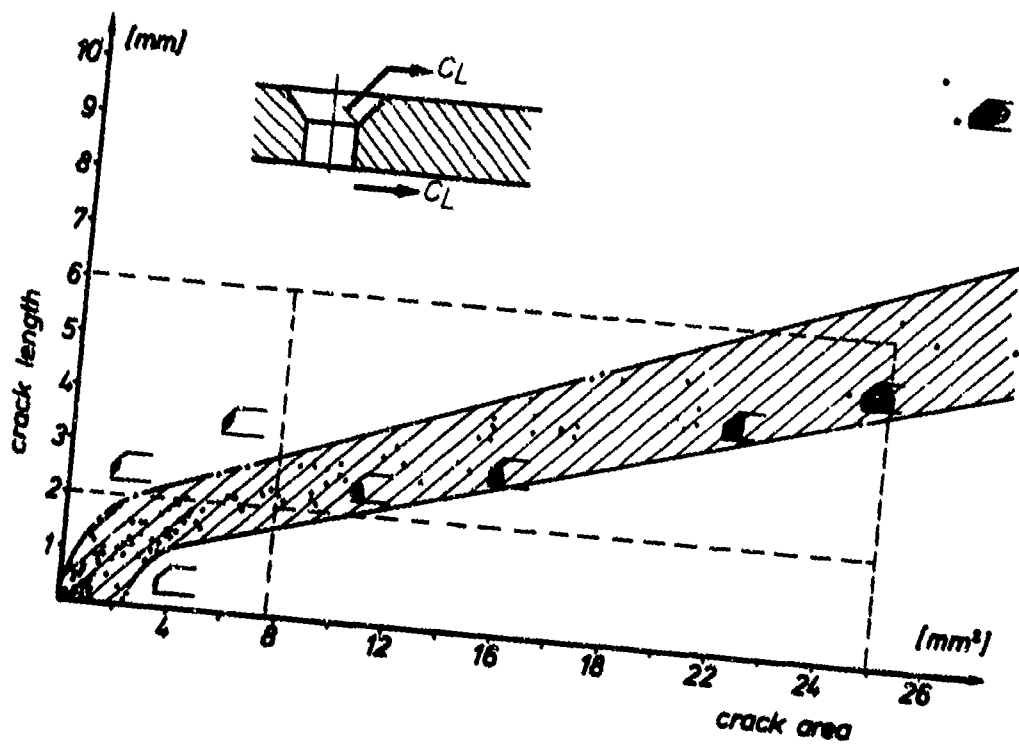


Fig. 17: Connection between crack area and crack length as an aid for valuing ultrasonic indication from carousel method.

The width of the scatter band is caused - beside the human factor, little errors in calibrations and little differences of the probes - essentially by the dependence of form of the crack area from the point, where the crack has started. Data - points near the upper limit of the scatter band belong to cracks originated at the edge between the cylindrical and the conical part of the countersunk - hole, data points near the lower limit from cracks which started at the edge from cylindrical hole and plane surface to the sheet. In total is obvious that definition of crack length for short cracks by ultrasonic inspection is uncertain and for computing purposes not well suitable, but for crack detection it is better than any other method we know.

Fig. 18 (a-c) shows the mean probability of success for detection of cracks and its 95 % range of confidence for different classes of crack areas.

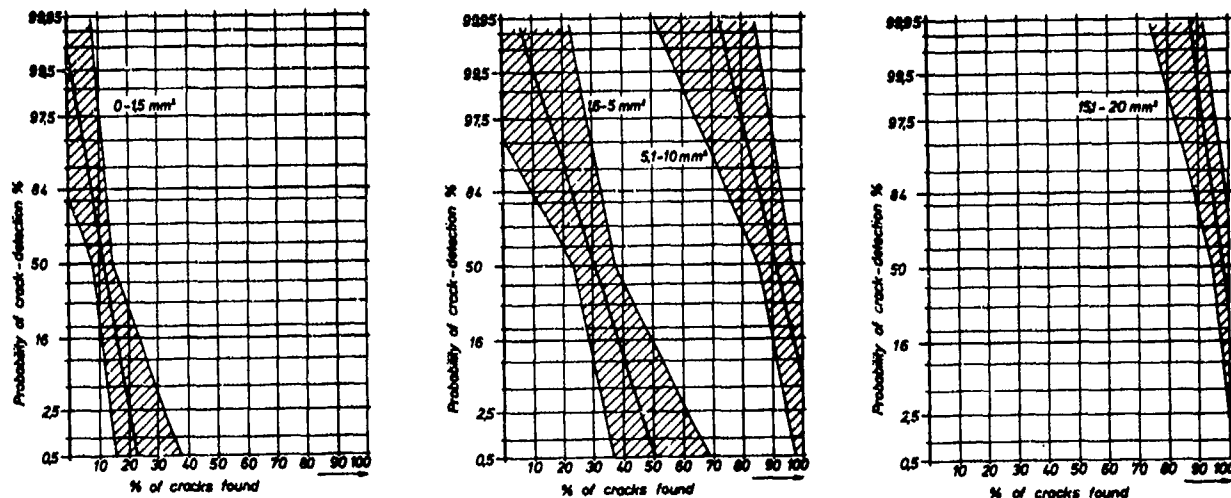


Fig. 18, a-c: Probability and zones of confidence for different classes of crack areas, using ultrasonic carousel method in aluminium sheet material

In analogy fig. 19 (a-c) shows the probabilities of success, with which cracks above a prescribed size are detected.

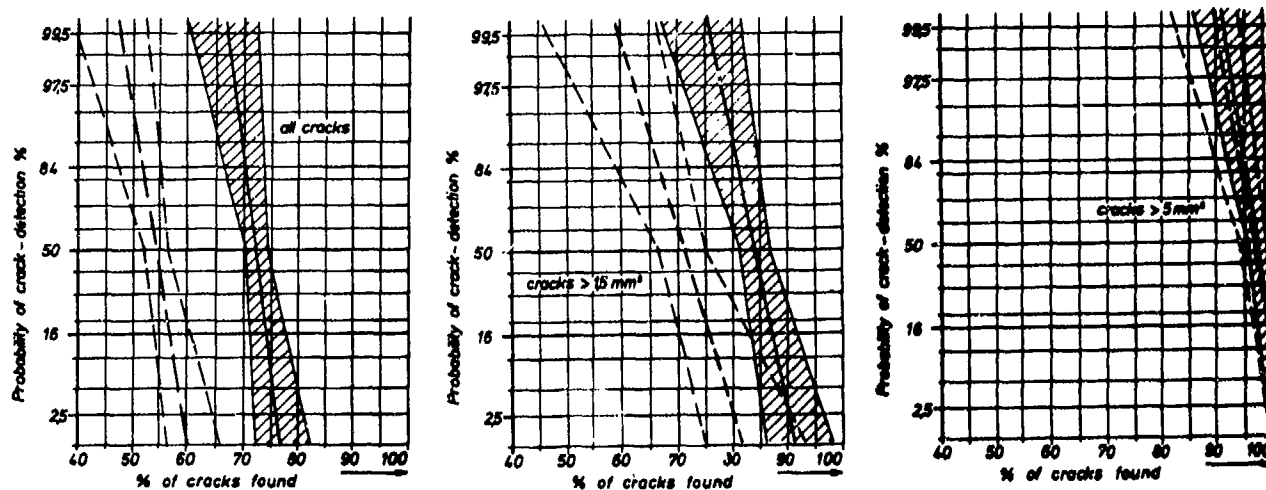


Fig. 19. a-c: Probability and zones of confidence for ultrasonic carousel method, if cracks above a prescribed crack area have to be found. Shaded areas show the distribution of the different crack sizes in test, dotted lines refer to a uniform distribution of crack areas.

These probabilities are valid only for the accidental distribution of crack size in our laboratory tests. For extrapolation to crack detection in the field the distribution of crack sizes in field should be known, but they are not. Nevertheless to give a comparison the dotted lines in fig 19 (a-c) show the reliabilities and their zone of (95 %) confidence for a uniform distribution of crack sizes to any class of crack area (see fig. 20).

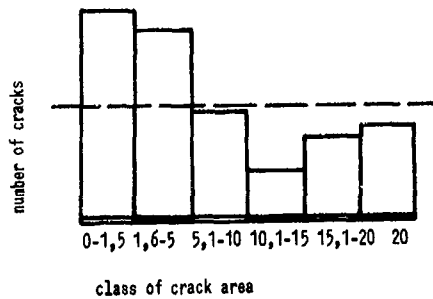


Fig. 20: Accidental distribution of crack sizes in our laboratory test; dotted line indicates equal number of cracks in any class of crack area.

Finally it can be expected, that improvements are possible in detectability (not measurement of length) using focused ultrasonic beam.

### 3. GENERAL VALUATION OF NDI-METHODS WITH RESPECT TO RELIABILITY

#### 3.1 Remarks to above described investigations

The three investigations described above give some indication for three typical applications in aircraft structures: NDI in free accessible flat surfaces, below rivet heads and in bolt holes of solid parts (p.e. forgings). They are the single systematic investigations concerning reliability of practical crack detection and measurement of crack size known to the author.

They show:

- .1 The men of practice of NDI estimated rates of reliability too high until now, reliability of crack detection is until today poor and insufficient.
- .2 By application of more specialized methods higher rates of reliability are reachable, or respectively smaller cracks can be found and determined reliable.
- .3 If possible from technique and economy nondestructive testing methods should be fully automatized to reduce the human factor.
- .4 For every specific application optimization of testing method is necessary which includes: comparative qualification test of all known NDI-methods, elaboration of the most suitable one, control of efficiency using equivalent parts with equivalent cracks, investigation of reliability in laboratory or - at least - estimation of reliability using own experience and literature.
- .5 It would be useful, to analyse the statistical distribution of crack sizes after performing inspections in the field, to get in hand the factors of extrapolation from reliability - investigations in laboratory and effective reliability in the field.
- .6 Location of cracks in accessible surfaces is sufficient, in unaccessible regions (cracks found by ultrasonics or X-ray) improvements are needed.
- .7 Reliable detection of tiny flaws requires a lot of further developments not only of testing devices, but primarily of techniques of application. There is a vast field.
- .8 Determination of exact flaw size using NDI is not possible; crack lengths often are indicated too short. The ultrasonic method which is crack area indicating shows great uncertainties in determination of crack size.

#### 3.2 Sequence of NDI-methods regarding reliability for typical applications in aircraft structures

##### 3.2.1 Preface

Generally distinction has to be made for:

- .1 Testing problem: - detection of cracks in large areas when crack starting point is unknown
  - detection of cracks when critical area is known
  - measurement of crack length
  - determination of crack area



- .2 Shape of tested area:
  - flat
  - moderately curved (positive or negative)
  - extremely curved (radius, positive or negative)
- .3 accessibility:
  - flaw in the external side of a good accessible surface
  - flaw at the inner surface of a part accessible from outside
  - flaw in a part covered from all sides
- .4 material:
  - metallic, magnetizable (p. e. steels)
  - metallic, not magnetizable (p. e. aluminium alloys)
  - non metallic (homogeneous, not homogeneous)
- .5 methods (classification to what is indicated):
  - .5.1 crack area is indicated from:
    - ultrasonics (longitudinal and transversal waves)
    - eddy current (for crack depth only between 0.05 mm and 1 mm)
    - X-ray (inaccurate, but for all crack areas above ca. 50 mm<sup>2</sup>)
    - holographics (anomalies of deformation)
  - .5.2 crack length primarily is indicated by:
    - optics (magnifying lenses, microscopes, endoscopes)
    - eddy current (very sensitive, but depends from shape of crack area directly below the surface)
    - penetrant
    - magnetic particle (limited to magnetizable materials)
    - crack wires (automatic acting, the most reliable method we know, critical region has to be known before, limited by accessibility for installation of the wires).

3.2.2 Flaw detection in sheet material  
(including results of pos. 2 and IABG-experience; numerical data estimated)

- 3.2.2.1 Flaw detection in large areas, critical points unknown, flat or moderately curved, with a lot of potential crack points, metallic sheet material and free accessibility leads to the following sequence of reliability
- if crack direction is unknown: dye penetrant (ultraviolet light, sure detectable crack length > 6 mm), optics (crack length > 10 mm), X-ray (crack length > 13 mm)
  - if crack direction is known: ultrasonics (Rayleigh waves, crack length > 5 mm, shear waves, crack areas > 20 mm<sup>2</sup>), dye penetrant (crack length > 5 mm), optics (crack length > 10 mm), X-ray (crack length > 13 mm), holographics (possible, but no experience).

- 3.2.2.2 Flaw detection in surfaces, when crack-critical area (1 - 4 sq.in.) is known from stress analysis or experience, metallic sheet material, surface flat or moderately curved, free accessible,
- without notches: eddy current (crack length > 3 mm, crack area > 1 mm<sup>2</sup>), ultrasonics (Rayleigh waves, crack length > 4 mm), ultrasonics (shear waves, crack length > 6 mm or crack areas > 20 mm<sup>2</sup>), magnetic particle (crack length > 6 mm), dye penetrant (crack length > 7 mm), optics (crack length > 10 mm, dependent from crack opening), X-ray (crack length > 13 mm)
  - with a few notches (cylindrical holes, countersunk holes, radius): eddy current (crack length > 3 mm, if edge effect can be compensated), magnetic particle (crack length > 6 mm), dye penetrant (crack length > 7 mm), optics (crack length > 9 mm), ultrasonics (shear waves, crack areas > 20 mm<sup>2</sup>), X-ray (crack length > 20 mm);
  - with notches, but cracks hidden p. e. below rivet head: ultrasonics (shear waves, crack areas > 20 mm<sup>2</sup>), all other methods only later on, when crack tip reaches one of the parallel surfaces of the sheet (crack length as above).

- 3.2.2.3 Flaw detection in extremely curved surfaces (down to 2 mm radius) of metallic sheet material, free accessible surface, with or without notches: ultrasonics (Rayleigh-waves, crack length > 4 mm), eddy current (crack length > 5 mm, but only if device permits compensation), magnetic particle (crack length > 6 mm), dye penetrant (crack length > 7 mm).

3.2.3 Flaw detection in solid metallic parts  
(p. e. forgings as landing gears, fittings, spars)

Attention has to be paid to the effect of grain flow in forgings to NDI-indications. We had examples, where X-ray and ultrasonics (Rayleigh-waves, shear waves and longitudinal waves) indicated a "flaw", but eddy current and metallographic investigation stated, there was no discontinuity of material!

Therefore: For control of an X-ray-indication ultrasonics are not always a sufficient aid.

3.2.3.1 Flaw detection in solid metallic parts at external surfaces, when free accessible, and critical areas are not known (i. e. detection of flaws all over the surface): magnetic particle (crack length  $> 5$  mm), dye penetrant (crack length  $> 8$  mm), optics (crack length  $> 10$  mm), ultrasonics and eddy current possible too, but in general uneconomical.

3.2.3.2 Flaw detection in solid metallic parts at external surfaces, free accessible, but critical areas (1 - 4 sq.in.) known: eddy current (crack area  $> 1$  mm<sup>2</sup>, crack length  $> 3$  mm), ultrasonics (surface waves, crack length  $> 4$  mm), magnetic particle (crack length  $> 6$  mm), ultrasonics (shear waves, crack length  $> 7$  mm, crack area  $> 25$  mm<sup>2</sup>) dye penetrant (crack length  $> 7$  mm), optics (crack length  $> 10$  mm), X-ray (crack length  $> 13$  mm).

3.2.3.3 Flaw detection in solid metallic parts at internal surfaces, none or bad accessibility, critical areas unknown: No reliability with any method.

3.2.3.4 Flaw detection in solid metallic parts at internal surfaces, critical areas known, none or insufficient accessibility (accessibility normally decides choice of method, not reliability): ultrasonics (shear waves, crack area - dependent from distance between acoustic source and point of crack - not less than 40 mm<sup>2</sup>), optics (with mirrors or stiff endoscopes, crack length  $> 15$  mm, with flexible endoscopes  $> 18$  mm), eddy current and X-ray (crack length  $> 20$  mm).

#### 3.2.4 Determination of flaw size

Little information is available about accuracy of crack length measurement (where accuracy is defined as relationship from crack length measured by NDT-methods to real crack length got from destructive determination).

Crack length, which is a part of the formulas to compute failure stress is a plain expression for the influence of crack-geometry to residual static strength, which in every case presupposes a specific and typical form of the crack.

From the physical point of view all NDT-methods (except optics) are measuring form - or material-properties, which are combined in a very different manner to those geometry values, which characterize the form of a crack: crack length at a surface, crack depth, crack area, course of crack tip and spacing of the crack flanges all over the crack area.

More practical: none of the NDI-methods (except optics) measures directly the wanted crack length, only destructive testing gives full information above geometry, but except spacing. (The latter may be neglected, for it does not influence fracture mechanics computing.) Therefore many assumptions and calibrations are necessary to give any reliable value of crack size.

From a practical point of view a differentiation into two essential different ranges of accuracy seems suitable:

The first range is that of crack detection, with reliabilities from 0 to 100 %. The second range includes all flaw sizes above the sure detectable minimum size of crack, i. e. 100 % reliability in detection. In this second range the task is reduced to the problem, to determine the point of the crack tip as precise as possible and to know the form of the crack.

Except from [1] for this second range no literature is available, therefore only estimated accuracies of IABG-experience can be added to [1].

##### 3.2.4.1 Determination of crack size at free accessible surfaces

The following methods can be used:

- . optics (with magnifying lenses or microscopes)
- . eddy current
- . dye penetrant
- . magnetic particle
- . ultrasonics

- Optical inspection is the single method which measures directly crack length at the surface. Accuracy of 0.5 mm is reachable when using microscopes up to a magnification of 40-80x on chemically prepared clean surfaces, which is practicable only in laboratory.  
In the field crack length in general is underestimated, at clean surfaces with 8 - 10 x magnifiers of about 2 mm, with the naked eye to 8 mm. Accuracy reached is extremely dependent of human factor.
- Eddy current is the next sensitive from our experience. It measures the change of conductivity against the nondisturbed state and is - seen from numerical data - an integral of the distribution of intensity in and short below the material surface, i. e. the course of crack tip until a depth of about 1 mm below the surfaces influences the indication.  
For calibration of distance between coil and crack tip consequently the course of the crack front a) has to be known and b) has to be constant. If these conditions are fulfilled, an accuracy of  $\pm 1$  mm is reachable. A practical advantage of this method is, that (thin) corrosion protective coatings or other plastic coverings do not have to be removed.
- Dye penetrant accuracies are remarkably less. Because indication depends on penetrated volume of the liquid, accuracy depends from crack width, crack depth and form of crack area.  
Consequently, there may be great differences between crack tip indicated and real crack tip, with underestimation up to 7 mm and overestimation up to 5 mm. Accuracy depends much on exact following to the test procedure, especially from penetrating and developing time.
- Magnetic particle testing leads to similar faults in determination of crack size. These faults are caused by inhomogeneity of the magnetic field in combination with the influences of the crack form. For our experience crack lengths in most cases are underestimated, i. e. real crack length is greater than indication.
- Ultrasonic methods using Rayleigh-waves, transversal or longitudinal waves, although best suitable for detection of flaws, are less convenient for determination of crack length in surfaces. The relative best result is got using Rayleigh-waves (surface waves); transversal and longitudinal wave indications depend from crack area, from inclination between ultrasonic beam and crack plane, from microstructure of crack (p. e. fatigue crack gives another reflection than a stress corrosion crack of the same area) and from distance between ultrasonic source and crack. Deviation from real crack length can be reduced to  $\pm 6$  mm, when distances are about 50 mm, using Rayleigh-waves. The other wave forms show deviations up to  $\pm 10$  mm for the same distance.

#### 3.2.4.2 Determination of crack size at non accessible surfaces of solid parts

In this case only two methods may be useful:

Ultrasonics (shear waves and longitudinal waves) and X-ray. Both lead to insufficient results regarding accuracy.

- Ultrasonics: Since many years great efforts are made to get good accuracy from the ultrasonic inspection method. For a lot of materials DGS-diagrams have been developed, which display the interrelation between echo amplitudes, distance between ultrasonic source and flaw, and the flaw size. (Such flaws are normally idealized, are plane, have well defined form and vertical angle of incidence. In practice of aircraft inspection, none of these presumptions is given.) Ultrasonic echo impulse cannot discern between crack length and depth, and therefore gives large faults in crack length determination. The good results of the carousel method described in pos. 2.3 cannot be generalized. Deviation of  $\pm 15$  mm is to take into account for distances of about 70 mm. Less deviation can be expected, when the form of the crack is known.
- X-ray: X-ray-techniques principally underestimate the crack length. Indication depends from differences in absorption, i. e. for a crack from crack-opening, and demands knowledge of crack-area inclination. Fatigue cracks therefore often are not found at all, stress corrosion cracks show better detectability, just as inclusions, cavities and impurities. A general estimation of accuracy for X-ray-inspection cannot be given.

REFERENCES

- [1] P.F. Packmann, H.S. Pearson, J.S. Owens and G. Young: Definition of Fatigue Cracks through Nondestructive Testing. Journal of Materials, IMLSA, Vol 4, No. 3, Sept. 1969, pp. 666 - 700
- [2] G. Wernimont: Precision and Accuracy of Test Methods. ASTM-Spec., Techn. Publ. No. 103, 1950
- [3] S.J. Klima, D.J. Lesco and J.C. Freche: Application of Ultrasonics to Detection of Fatigue Cracks. Exp. Mech. 6, March 1956, pp. 154/161
- [4] H.A. Wood: Fracture Control Procedures for Aircraft Structural Integrity. 6. ICAF-Symposium, held at Miami Beach, Mai 13 - 14, 1971. pp. 437 - 483: Advanced Approaches to Fatigue Evaluation.

## VII.B NONDESTRUCTIVE TESTING (NDT) AND FRACTURE MECHANICS

Enrico Bolis

Summary . . . . .	413
1. Introduction . . . . .	413
2. NDT Specifications and Criteria . . . . .	413
3. Recent Progress in NDT Techniques . . . . .	414
4. Current NDT Methods . . . . .	415
5. Survey of Methods . . . . .	415
References . . . . .	417

## SUMMARY

The basic concepts of nondestructive testing (NDT) are reviewed in relationship with fracture mechanics concepts. The necessity of correlating basic differences between ordinary destructive mechanical tests and NDT is considered. The use of NDT for assessment of integrity of aircraft components and structures, after fabrication and during service life is discussed. Inherent limitations of NDT and necessity of interdepartmental team work are reviewed. General information on routine and advanced methods is included.

## 1. INTRODUCTION

Nondestructive testing of materials is to be considered a conceptually different technique from the standard testing of materials used in the laboratory. This basic difference does not rely on the sole characteristic of destructiveness or nondestructiveness of specimens subject to test. The really discriminating feature between the two systems is that properties of prime importance for constructional materials - such as strength, fracture toughness, fatigue or corrosion resistance - are directly measured by standard testing of materials. With nondestructive testing, it is possible to reach positive assessments on features that are different - but not less significant - from those earlier defined as primary. The results of both systems of testing - destructive and nondestructive - need to be correlated through appropriate laboratory programs. Magnetic permeability of steel or its capability to be penetrated by X-rays do not bear direct relationship to the capability to withstand loads and environment as expected by the designer. Variability of these physical properties of the materials enable nonhomogeneities and discontinuities to be detected in the piece and these are obvious suspect features that may have an important influence on the performance of the structure. From these points, it appears that both systems of material testing are to be considered as complementary rather than exclusive methods and that the correlation work must take into account the characteristics of each method, each material and each design configuration.

The results of NDT are seldom direct; they need interpretation. This interpretative skill should be delegated to a team of specialists rather than left to the sole judgment of the NDT inspector. This team would be composed of a stress engineer, a material technologist, a laboratory expert and an NDT specialist. The final decision to accept a part after the completion of the fabrication cycle must be referred to an acceptance standard. Acceptance standards will be discussed in the following paragraph. A very valuable feature of NDT is the possibility of extending the inspection to 100% of the production and to 100% of the parts during service life to the condition monitored. It should be clearly stated that the concept of the acceptance standard applies only to the fabrication cycle of the parts. In this case the standard of acceptance is a necessity. During service life no general standard is possible for assessing the residual life of the inspected part.

## 2. NDT SPECIFICATIONS AND CRITERIA

All materials called for in technical documents (procurement, design, fabrication) are supposed to be free from detrimental defects. These defects may have origin in the rough material itself or in the fabrication process of the part; they are correlated with internal discontinuities or inhomogeneities varying in size from an atomic lattice up to a size directly apparent in the surface of the same part. These internal configurations of materials are generally seen by modern NDT methods, whose sensitivity and powers of discrimination are so effective that they may provide data and features that may have no practical relevance, at least in the part that is undergoing test. Whether the configuration put in evidence by NDT is to be considered acceptable or not is a question of acceptance standards and quality level. It is clear that acceptance standards are a mandatory tool in production quality control procedures, but to prepare this tool with proper directions for use, is not a simple job. Owing to the physical principles on which they rely, NDT techniques have usually a built-in limitation: in the majority of cases they can indicate defect (or flaw) size, rather than measure size absolutely. For example, in the surface inspection test (liquid penetrant or magnetic-particle) the defect length is well defined but the depth of the defect is not well defined. For internal defects - detected by X-rays or ultra sonic testing - the measure of the critical spot is not absolute, even though the best techniques are used and all the pertinent parameters that may influence the test results are included. The determination of absolute dimension and exact location of the defect in the internal region of the manufactured part is sometimes possible through a complex operation of integration between different methods of NDT. The geometrical configuration of the part plays an important role in defect assessment. Complex geometric configurations may be

associated with defect characteristics which may have originated in the fabrication process. Some of these defects may not be relevant to NDT techniques notwithstanding their high sensitivity but because of their orientation dependence. In any case, we have called a "defect" what is referred to generally as a flaw. Whether this flaw is to be considered a defect or not, is a question pertaining to the acceptance standard.

The criteria on which the determination of these standards is based may be classified as follows:

- theoretical considerations of stress analysis - material and fabrication technology;
- correlation with classical direct destructive tests;
- quality level of similar parts successfully accepted in the past - same material, stress level and environment.

Quality standards beyond that which is justified by tests and practical experience would be costly and potentially harmful because they could obscure better ways of achieving realistic safety levels. Realistic progress in material technology properly nondestructively monitored, may lead to a significant improvement in aircraft design. Many good specifications have been written incorporating NDT acceptance levels. There are three major sources of NDT specifications: military, technical societies and industry.

A good workable specification should include:

- method of test
- test procedure
- objective criteria of acceptance/rejection with reference standard.

The defect location and orientation are more compelling reasons for rejection, rather than size alone. The best NDT specifications are for specific parts. The more general the specification, the more difficult becomes its use. The basic concept is that one usually finds what one is looking for; and what is to be looked for is to be established after exhaustive preliminary study. The method of test must refer to a reference standard, the method and the standard being strictly interrelated. These reference standards must be, when practicable, substantiated in physical elements on which is induced an artificial flaw, to be taken as reference. Examples: ultrasonic test block standards and penetrometers for X-ray inspection. These physical elements may not always be produced. Reference standards for penetrant inspection are not available because it proved practically impossible to produce two samples with identical artificial defects typical for penetrant detection. When, as in this example, physical elements to be used as reference standards are not practical, the NDT specification should include sketches, photos, or clear verbal descriptions of acceptance/rejection limits.

### 3. RECENT PROGRESS IN NDT TECHNIQUES

Improvements in sensitivity, selectivity, and discriminating power - have advanced the possibility of detecting critical deterioration in aircraft components during service life. The built-in capabilities of NDT methods would seem to warrant this result, at least to some extent. Unfortunately, generally speaking, this goal is to be considered practically unattainable, if we are referring to an ideal and automatic method. Deterioration of components can be detected during service life provided an integrated maintenance-inspection program is organized rationally from the early beginning of service life. In this programme the role of NDT is relevant and will contribute substantially to the building of flight safety. It is not to be maintained that NDT should be an automatic lifeguard and panacea. When a definite deterioration is detected, the evaluation of the capability of the element to withstand project loads for a certain time, depends on the integration of the following fields:

- laboratory tests, properly programmed and interpreted during the qualification phase of the prototype;
- consideration of fracture mechanics applied to specific part, with failure mode identification;
- result of a programme of NDT well tailored to the specific problem.

It is possible to foresee that this integration among the three different fields should be started right in the project phase and this seems to be the trend of modern engineering. With such an approach the designer, the material engineer and the NDT representative are all involved at the design stage for the purpose of early detection of deterioration. From the failure modes study of the sensitive areas of the structure, with reference to a certain type of defect likely to be expected from similar previous experience, it is possible to determine, for example the critical crack length which will cause failure in that particular component of the structure. This critical crack length will be determined from calculations and experiments, substantiated by failure history of similar components. The concept of similarity applies to geometrical configuration, material fabrication cycle, standard of acceptance, and defect orientation. The relationship of the mechanism of crack extension to critical length is to be investigated in terms of fracture mechanics concepts.

With all these facts available, a positive programme of NDT can be arranged and the sensitivity to be expected from NDT can be made a requirement. Modern NDT techniques in fact do make available methods whose sensitivity is adequate to an early detection of

fatigue cracks in structures. These methods can be used to detect small fatigue cracks during the course of fatigue tests in the laboratory and can also be successfully applied in the field. As orientation, we can quote that with ultrasonic reflection techniques fatigue cracks that ranged in length from 0.0005 to 0.0025 in. were detected in 2014 aluminum alloys. It must be considered that fatigue is not the sole factor to be considered in the evaluation of deterioration of aircraft structures during services life. Corrosion, local wear, surface deterioration, and change in residual stress configuration, also play important roles in the behaviour of structures and these can be monitored on condition by NDT. A maintenance plan is supposed to take into account deterioration possibilities and NDT detection capabilities in different areas. During the progress of utilisation of the aircraft concerned, continuous reassignments of inspection plans and reevaluation of life expectancy are to be considered and worked out on a complex feedback basis. The maintenance plan should be such to satisfy general criteria of reliability which are applicable to system maintenance. Specific NDT instructions will be issued to monitor the condition of items that have demonstrated criticality at laboratory level during the qualification stage and also to substantiate the absence of other critical points not previously foreseen. It is clear that a too complicated burden of NDT requirements should be permitted only in the early field intensive trials. Every point that confirms its criticality during the first phase of utilization of the aircraft should undergo adequate and well substantiated modification plans. When considerable service time has elapsed a new NDT Program could help to predict practical service life time. In any case it is assumed that every nondestructive inspection should be performed following the direction of a specific technical Order.

#### 4. CURRENT NDT METHODS

The methods of NDT may today be considered as a host of technological tools based on very diversified physical principles. Some of these methods are routine methods at shop and laboratory levels both in manufacturing and servicing facilities. Other methods, referred to as advanced methods, are still in the development phase and routine application can hardly be foreseen at this time. The present state of the art may indicate a general reorganization of this tooling, taking also into account the requirements of modern bonded structures and new composite materials. Many of the techniques of NDT are so well advanced with regard to sensitivity that they may produce more uncertainties than sound judgments. Therefore, the establishment of central consultation laboratories are advocated to help review and double check diagnoses in doubtful cases. It may be said that almost every measurement of physical constants in metals has originated a particular NDT method and that local or overall variability of physical constants may be correlated with elastic and ultimate properties of metals. The five most commonly used methods for nondestructive evaluation of materials may be classified as follows:

- radiographic
- magnetic-particle
- liquid-penetrant
- eddy current
- ultrasonic

Each of these methods shows in itself a great variety of modes of application and practically every method is available in a very diversified variety of hardware and software. Other techniques are currently undergoing development and many show promise as standard applications in the future. These include optical and acoustic holography, acoustic emission and thermal methods. Other methods, such as X-ray diffraction, probably will remain confined to the laboratory level. With the development of new radio isotope sources, nuclear techniques once restricted to laboratory use, are becoming available for quality control in the field. Examples of these brand new applications: coating-thickness measurements in inaccessible parts.

#### 5. SURVEY OF METHODS

The present survey is merely intended to be an orientation on what and how the host of NDT techniques may contribute to making assessments on the internal configuration of materials and fabricated parts and on potentially detrimental defects. In this respect NDT methods are a tool whose utilization is in many cases mandatory and whose importance cannot be over emphasized. Information gathered through NDT both at the manufacturing level and during service life, are to be processed by means of theoretical and experimental concepts of fracture mechanics. The inspection of metal surfaces is a principal application for NDT. As a matter of fact exterior surfaces are inherently weaker as far as bonds are concerned; generally the result of manufacturing may create on the surface many types of stress raisers. Last but not least, the surface is much exposed to environmental damage during service life. The physical principles on which hardware and software of NDT rely are extremely diversified and practically cover all the provinces of modern applied physics. Quantitative data on sensitivity and on resolving power are not given. This information will be found in a physics handbook.

Liquid Penetrant. Liquid having very low surface tension is allowed to penetrate into microcavities and discontinuities opened on the surface of the part. After the penetrating period, the excess of penetrant is removed and powdered material for development is applied. Indications are viewed with white light or under "black light" (fluorescent additives to the developer). Penetrant inspection is an important and sensitive tool of NDT, but is not applicable to surfaces having high porosity or roughness. Previous surface cleaning of the part is necessary. The equipment is available as simple portable equipment

or larger stationary equipment. While the method is suitable both at the manufacturing level and field levels, the acceptable standards are not generally defined. The reliability of judgment in its use is based on the thoroughness and visual and mental acuity of the operator.

**Magnetic Particle.** This is a standard NDT method for detecting surface and sub-surface discontinuities in ferromagnetic materials. It consists in establishing a suitable magnetic field in the test object. Parts to be inspected are previously cleaned and dried. Many types of magnetizing current can be used (d.c. and a.c. magnetization). The proper value of flux density (strength of magnetizing field) is critical, and the direction of the magnetizing field is most important. Detection capability is selective to field orientation. The method is very sensitive if the controlling factors are properly monitored. When strength of field or direction of magnetic field is inadequate, important discontinuities may be missed. After inspection, demagnetizing of parts is required. The standard methods are applicable both at the manufacturing level and in field tests. Qualification of personnel is required.

**Eddy Current.** The basic principle lies in the variation of magnetic permeability correlated with internal or surface inhomogeneities. The variation of magnetic permeability is detected by intensity and phase of the internal current. A coil carrying a high frequency alternating current, placed near an object capable of conducting an electrical current, induce in the object an electrical current which cause a magnetic field. Any flaw or variation in mechanical, physical or chemical properties of the object affect this magnetic field whose variations are measured and correlated with the shape and size of the defect. This method is particularly useful for checking fastener holes for cracks and to test the integrity of bonded structures. Recent applications include the sorting of gears for improper heat treatment.

**Thermal Methods.** Heat is applied over the specimen (heat source, electrical current, infrared heat source). The distribution of temperature is noted and a "hot spot" will appear at the specimen indicating a defect somewhere below the surface hot spot. The method is a very indirect one; the correlation between the defect and the surface temperature distribution pattern is very problematic. This method is practically useful provided this correlation is properly set up and there is some previous knowledge of possible defects. The instrumentation technique is critical. The latest development in surface temperature detection utilizes liquid crystals. These indicators are very sensitive and some experiments demonstrated that they can monitor strain heat to indicate potential fracture. Thermal techniques are best suited for detecting flaws reasonably near the surface; definition suffers if the flaw is deep, because the hot spot tends to diffuse as it travels to the surface.

**X-Radiography.** The basic method is in continuous development. The most recent techniques allow use on component thicknesses over 20 inches. It is the most suitable method for inspecting complex structures with low accessibility; applicable to all metallic materials for detecting flaws, voids, porosity, inclusions, corrosion. It is also usable for inspecting welded parts and bonds in sandwich structures. Practically this method allows the detection of the most common defects. Qualified personnel and equipment are required, and safety regulations are mandatory. Generally, this method is not applicable to forged parts, and orientation of defects versus radiation is critical. Reference standards are available.

**Gamma Rays.** Gamma radiography is similar in many respects to X-radiography. Gamma rays are shorter than X-rays and thus have greater penetrating power; they interact with materials in much the same way and the recording media and techniques are basically the same. Gamma rays require a radioactive source. Safety precautions and qualifications are mandatory.

**Neutron Radiography.** A stream of neutrons (from a proper source) passes through the test object, is partially absorbed and the emergent beam is recorded. N-radiography is somewhat similar to X-radiography but N-rays have far different characteristics. This process supplements rather than replaces X-radiography. The special feature of this method is that a stream of neutrons is readily absorbed by hydrogen bearing materials and by such materials as boron and lithium. The method has been used to check castings and welds for potential hydrogen embrittlement and for inspection of hydraulic systems (presence of deteriorated O rings and contaminants).

**Ultrasonic.** This is a widely accepted method and the range of applications are extremely broad. High frequency mechanical vibrations are induced in the part, usually by means of piezoelectric transducers. Transmitted or reflected energy is converted to electric signals and displayed on a cathode ray tube or pen recorder. The reflected ultrasonic energy may be absorbed in the viscoelastic layer, converted to heat, and observed as a color display through a liquid-crystal layer (acoustography). Ultrasonic waves (Rayleigh waves) may be launched along the surface of the metal and reflected back from cracks at right-angles to their path. Ultrasonic inspection is very sensitive and has good penetrating power. It has proved to be a suitable tool to detect crack initiation and crack propagation prior to failure. Specimen geometry and orientation of defect can be limiting factors. Interpretation of ultrasonic displays or recording require very skilled personnel; the same skills are required to select proper techniques and sensitivity for different applications. Qualifications of personnel and equipment are mandatory. Standards are available.



**Acoustic Emission.** Deforming materials generate stress waves giving rise to low intensity inaudible sounds. Microphones are used to detect these signals, whose frequency and amplitude are recorded and analyzed. It is a promising technique under development. Recent applications were used to monitor welding; flaws such as porosity, inclusions, incomplete fusion and cracks, create emission during the welding process because of the stress surrounding them. Through acoustic emission, impending failure during a structural test may be detected. Stress corrosion, fatigue crack and hydrogen embrittlement emit identifying sounds long before they cause failure.

**Other Methods.** Other methods should be mentioned, at this moment being under development both for routine and for special purposes. The very important problem to detect non-destructively the residual stress configuration and its variations during service life deserves special attention. X-ray diffraction and magnetic methods for ferromagnetic materials (Barkhausen noise) seem to be the most promising methods. Recent application of holography methods are also to be mentioned. These methods consist basically in superposition of two images taken by coherent light of an object in more than one state: at rest and under some state of deformation. The difference of the two images shows up as interference fringes or patterns at points of discontinuities.

Some nondestructive testing techniques have been discussed while others like liquid crystal and kryptonated tests are not included in this manual. This manual had the main objective of treating fracture mechanics techniques and consequently was concerned chiefly with such material while referring in a cursory way to nondestructive techniques. However, some reports that may be of interest in the area of nondestructive testing are:

(1) U.S. Army Materiel Command, "Guidance to Nondestructive Testing Techniques," AMC Pamphlet 702-10, April 1970

(2) \_\_\_\_\_ "Guide to Specifying NDT in Materiel Life Cycle Applications," AMC Pamphlet 702-11, November 1970

(3) R.C. Zubinskas, "State of the Art Survey on Holography and Microwaves in Nondestructive Testing," Army Materials and Mechanics Research Center, AMMRC MS 72-9, September 1972

#### REFERENCES

- |                         |   |
|-------------------------|---|
| BIRCHON                 | "Leo, a plan for NDT" - British Journal of NDT - Sept. 1970   |
| KLIMA, LESCO, FRECHE    | Application of ultrasonics to detection of fatigue cracks - Experimental Mechanics - March 1966   |
| GROVER                  | Using fatigue information in design - Experimental Mechanics May 1972   |
| KLEINF, HASEMALER       | Relationship of Standards and Specifications to nondestructive testing - Materials evaluation August 1965<br>Commonly used specifications and standards for nondestructive testing - Materials evaluation - March 1966. |
| ENGINEERING OUTLINE 108 | Nondestructive testing - Engineering - Jan 18, 1968   |
| LAVOIX                  | Nondestructive testing - Design guide - Machine design - Sept. 1969.  |
| R.C. McMaster           | Nondestructive testing Handbook - Edited for the Society for nondestructive testing - New York.   |

## VII.C. DETECTION AND DETERMINATION OF FLAW SIZE BY ACOUSTIC EMISSION

C. E. Hartbover

Foreword . . . . .	419
Introduction . . . . .	419
Proof-Testing Concepts . . . . .	421
Case Histories . . . . .	421
Fracture Mechanics Concepts in Proof Testing . . . . .	423
Acoustic Emission As a Nondestructive Inspection Method . . . . .	425
Low Cycle High-Stress-Intensity Fatigue . . . . .	425
Stress Corrosion Cracking and Hydrogen Embrittlement . . . . .	434
Strain-Aging Embrittlement . . . . .	438
Delayed Weld Cracking . . . . .	440
Acoustics Emission from Welded Aluminum . . . . .	451
Continuous In-Service Surveillance . . . . .	453
Acoustic Emission as a Precursor of Fracture . . . . .	453
Isolation of an Acoustic-Emission Source from Extraneous Noise . . . . .	459
Instrumentation for In-Field Flaw Detection . . . . .	462
Summary of Theoretical and Experimental Limitations . . . . .	465
Correlation of Acoustic Emission with Size of Crack and Crack Growth rate . . . . .	465
Flaws too Small to be Detected by Conventional Nondestructive Inspection . . . . .	468
Electrical Disturbances . . . . .	468
White Noise . . . . .	468
Extraneous Noise from Metallurgical Sources . . . . .	471
References. . . . .	471

## VII.C. DETECTION AND DETERMINATION OF FLAW SIZE BY ACOUSTIC EMISSION\*

C. E. Hartbower

Foreword

However defect-free a structure may appear to be when it enters proof test and service, if there are active mechanisms for subcritical crack growth, such as fatigue, stress corrosion, hydrogen embrittlement, and/or strain aging, the life of the structure will be shortened. How much it is shortened will depend upon the rate of subcritical crack growth and the critical crack size of the material as determined by its fracture toughness. Proof testing provides a measure of maximum defect that can be present at the start of service. The difference between the critical crack size and the defect size at the start of service is the amount of slow crack growth that can be tolerated. Without acoustic emission as a non-destructive inspection procedure, structures are needlessly lost in proof test and service. When a crack approaches critical size, at the onset of crack instability, the increase in crack-growth rate unmistakably heralds imminent fracture through the generation of an abrupt increase in acoustic emission count.

Available acoustic emission instrumentation systems are so sensitive that it is possible to detect each stage of the failure process starting with deformation (dislocation pileups), crack propagation and, finally, the onset of instability -- all in real time. Moreover, in the second and third stage of the failure process, as described above, it is possible by triangulation to locate the source of the signal. In some applications, the practical limitation for use of acoustic emission as a nondestructive inspection method has been and will continue to be extraneous noise. However, most noise problems are solved by the effective use of band-pass filters or special isolation techniques involving computer solutions.

INTRODUCTION

The use of acoustic emission as a nondestructive inspection technique has been under development for over a decade. The technique is based upon the elastic energy which is spontaneously released when a material undergoes plastic deformation and/or cracking. Thus, acoustic emission constitutes a unique non-destructive inspection method in that the material defect when propagating, transmits its own signal, with the sensor acting as the receiver. In other words, the material undergoing crack growth both generates and transmits the signal (acoustic emission) which then can be detected by suitable instrumentation and the source located using seismic techniques.

The first well documented investigation of acoustic emission in metals was made in Germany by Kaiser<sup>(1)\*\*</sup> in 1950. He reported that all metals examined (zinc, steel, aluminum, copper, and lead) exhibited the emission phenomenon. Working with polycrystalline specimens, Kaiser concluded that acoustic vibrations originate in grain boundary interfaces. Emissions were believed to be associated with the interaction induced between interfaces by applied stress. He noted that, for a given material, characteristic spectra of frequency and amplitude existed and were related to the stress level.

In the U.S.A., the researches of Schofield, et al<sup>(2-4)</sup> and studies at Aerojet-General Corporation<sup>(5-28)</sup> were largely responsible for triggering the current high activity in this new field of nondestructive inspection. Schofield, in 1955, initiated an extensive investigation of acoustic emission phenomena. He found that the emissions did not originate entirely from grain boundaries, as single crystals also emitted. Also, characteristic spectra of frequency and amplitude were not found, from which Schofield concluded that frequency and amplitude were not the correct fundamental quantities to characterize the emission process. Tatro<sup>(29)</sup> started his investigations of acoustic emission in 1956 and explored the possibility of detecting slip in metals with sonic techniques. From studies on single-crystal aluminum, Tatro and Liptai<sup>(30)</sup> reported that emission activity was related to pileup and breakaway of dislocations. Anodic surface layers applied to aluminum crystals changed the emission spectra and acted as effective barriers to dislocation and slip-band formation at the surface. Thus, work at Michigan State University started in this field prior to 1960<sup>(29-32)</sup>. Work with acoustic emission at Aerojet began in the early 1960s; the first practical application was in the proof testing of glass-wound Polaris rocket motor cases<sup>(5)</sup>.

Dunagan<sup>(33-37)</sup> at the University of California Lawrence Radiation Laboratory also did pioneering work with acoustic emission, but most of his early research was for the U.S. Atomic Energy Commission and, therefore, was not publicized. Most early studies of acoustic emissions were associated with plastic deformation or crack propagation in metals. The frequency range used in most investigations was below 60 KHz; a significant advance in experimental technique was the extension of experiments into the 100 KHz and 1 MHz ranges, first reported by Dunagan, Tatro and Harris<sup>(33)</sup>. This eliminated the need for elaborate soundproof facilities by minimizing the effects of extraneous laboratory noise in the study of continuous-emission

\*This chapter deals with a new technology. Questions and comments are invited.

\*\*References appear at the end of text.

Since the middle 1960s, applications of acoustic emission techniques to materials research, material evaluation, nondestructive testing, and structural evaluation have increased rapidly. Impetus has been given this new technology by graduate studies (29,31,32,38-48) at several universities, including in particular, Michigan State, University of Michigan, Arizona University and Washington State.

Acoustic emission is the detectable elastic energy which is spontaneously released when materials undergo plastic deformation and/or fracture. The phenomenon of sound emitting from metals undergoing deformation is discussed in the literature at least as early as 1928 and the phenomenon of "tin cry" is believed to date to antiquity. Audible sounds or "clicks" noted during heat treatment of steels have been related to the martensitic transformations; studies have shown that the martensitic transformation is a copious emitter of acoustic emission<sup>(37)</sup>.

Both metals and non-metals have been investigated, although most of the work published to date has been concerned with metal test specimens or structures. Analogous studies have been conducted on geologic materials (rocks, etc.), where the terms "microseismic activity" or "rock noise" are commonly used rather than acoustic emission.

For metals, the observed acoustic signals are often reported as being of two types: a quasi-continuous signal and a burst-type signal which is of a damped sinusoid form. The frequencies attending these waves have been reported to range from audible "clicks" up to 50 MHz; thus, the spectrum extends over more than four decades. Acoustic emission signal levels are such as to require amplification factors ranging from about  $10^4$  to  $10^7$ , depending upon the sensitivity desired. Thus, extraneous electrical and mechanical noise may be a problem in monitoring acoustic emission. One other factor, which is not always recognized by experimenters, is that the observed frequency spectrum of acoustic emission is significantly influenced by the resonance and transmission characteristics of both the specimen (geometry as well as acoustic properties) and the sensing method.

Early work by Schofield led him to hypothesize that acoustic emission was primarily due to the formation of slip lines on the specimen surface. His later experiments caused him to alter this view, and by 1964 he had concluded that it was due to an internal mechanism and that the sample surface and its condition, play only a secondary role in influencing emission response. He also noted that the continuous-type signal was strain-rate sensitive, and hypothesized that it was the result of dislocation pinning and cross slip. He thought that the burst-type signal was related to the rapid deformation mechanisms responsible for the formation of stacking faults and mechanical twins. Subsequent work by other investigators has only partially substantiated these hypotheses. Investigators at Aerojet-General Corporation deliberately set the sensitivity of their system to preclude detection of plastic-deformation, focusing their attention on crack-growth processes. Their work showed that high energy bursts are detected as cracks propagate.

Acoustic emission differs from other nondestructive techniques in one significant respect. It is a passive monitoring method and depends entirely on changing internal stresses within the sample or structure to provide the excitation function. Another feature encountered in certain metals is that once a given stress, or load, has been applied, and the acoustic emission from accommodating this stress has ceased (in the absence of a subcritical-crack-growth mechanism), no more emission will occur until this stress level is exceeded. If the load is completely removed, when the load is re-applied, no emission occurs until the previous load has been exceeded. This often useful and sometimes troublesome behavior is called the Kaiser effect in honor of Dr. Kaiser who first observed it. For many metals, the Kaiser effect offers a simple, yet effective, method of determining the approximate maximum stresses to which a part or structure has been subjected.

The usual instrumentation for obtaining acoustic emission data consists of sensors, amplifiers, band-pass or high-pass filters, signal conditioning circuits, and a high frequency magnetic tape recorder. Auxiliary instrumentation, to assist in displaying and analyzing the signals, includes oscilloscopes, total-count and count-rate devices, X-Y recorders, strip-chart recorders, audio-amplifier-speaker monitors, and various types of frequency-spectrum and pulse-height analyzers. Digital and analog computers are occasionally used for post-test or real-time signal analysis and triangulation.

The sensor which has found the widest use in detecting acoustic emission from stressed structures is the accelerometer. Although accelerometers have a limited frequency response, they provide a reliable and reproducible output which is of considerable value for structures testing. Other sensors which have been successfully used include high-frequency, ultrasonic-type, piezoelectric transducers, phonograph cartridges, and crystal and capacitive microphones.

Throughout the literature, various terms are used interchangeably, sometimes even within a given paper. Some of the terms treated in the literature as being synonymous can lead to confusion. A list of acoustic-emission jargon (terminology) is presented below; the first term is generally preferred and will be used in the following chapter.

Acoustic Emission:	stress-wave-emission (SWE), acoustic wave, stress-wave, acoustic pulse.
Continuous Emission:	high-frequency emission, quasi-continuous emission
Acoustic-Emission Bursts:	stress-wave-emission bursts, jumps, pulses.
Emission Rate:	burst rate, pulse rate, count rate, stress-wave-emission rate, emission occurrence rate, frequency, repetition rate.
-----	-----
Emission Amplitude:	stress-wave amplitude, emission height, amplitude, pulse height.

## PROOF-TESTING CONCEPTS

### Case Histories

Examination of failed rocket motor cases has indicated the typical failure origin to be a small crack or crack-like flaw. The flaw is sometimes sufficiently large to cause fracture on initial loading and sometimes it is so small that the structure can withstand many load cycles or a prolonged period of sustained stress before the flaw attains critical size for failure. From service-failure analyses, it is clear that fabricated structures and even raw materials contain defects of various kinds. Service life therefore is controlled by (1) the initial flaw size, (2) the rate of slow crack growth in the environment of the proof test and/or service, and (3) the flaw size (critical crack size) to cause fracture at the operating stress. The latter is determined by a quantitative measure of fracture toughness. The rate of subcritical crack growth and the threshold stress intensity below which slow crack growth will not occur ( $K_{Isc}$ ) are determined by laboratory evaluation and can be monitored by nondestructive inspection based on acoustic emission. Initial flaw size is estimated by quality control and verified by proof test.

The basic philosophy of the proof test is that once a pressure vessel has withstood the proof pressure, subsequent loading to a lesser pressure will not produce failure. Obviously, this assumes that there will be no fatigue cracking in service and no slow crack growth of existing subcritical defects due to time-dependent mechanisms such as hydrogen, stress corrosion and/or strain aging. However, experience shows that without the detection of acoustic emission, failure can occur in proof testing as a result of undetected subcritical crack growth. Moreover, when a material is susceptible to slow crack growth, the concept of the proof test is invalid; i.e., after proof testing, tankage can fail at a lesser load if stress-corrosion, strain aging, hydrogen or cyclic loading are involved in service. There are numerous examples to illustrate the fact of subcritical crack growth in proof testing as well as in service.

Consider the 6A1-4V titanium second-stage Minuteman, a 42-in.-dia solid-propellant rocket motor case which was proof tested with inhibited water with three cycles of ninety seconds each to 1.1 of the mean expected operating pressure (MEOP). One chamber failed "prematurely" during the fourth cycle (a test-rig malfunction of the first cycle necessitated a fourth cycle to proof pressure). The failure occurred after 40 seconds at pressure during the last cycle of proof testing. Thus, the chamber withstood a total of 220 seconds at maximum pressure. The fabricator's failure analysis reported that failure initiated in the inside-diameter surface, in the fusion and heat-affected zone of the center girth weld. No cracks were found by nondestructive inspection prior to proof testing. The only explanation for such a failure is subcritical crack growth during proof testing.

Consider also the alloy-steel first stage solid-propellant Polaris rocket motor case which was proof tested with inhibited water at 1150 psig and held at pressure for 180 seconds, with two or more pressure cycles. In the early development of the Polaris, there were numerous failures in proof test, and some had all the characteristics of subcritical crack growth. One chamber, for example, failed after 120 seconds at proof pressure on the second test cycle. The chamber had been inspected by magnetic-particle, dye-penetrant, radiographic and visual procedures; all failed to reveal cracking. Another Polaris chamber failed after the second proof cycle during the first few seconds of depressurization, after withstanding a total of 260 seconds at proof pressure.

The above examples show that incipient flaws in a pressure vessel can increase in size as a result of proof testing. The concern here is not only with those pressure vessels that fail during proof test (an economic loss) but also with those that suffer subcritical crack growth without failure in the proof test. The latter then enter service with enlarged cracks which may be subject to additional slow crack growth at service loads. However, if the proof test does not fail the pressure vessel, and if a system is employed to detect and locate flaw(s) undergoing subcritical crack growth, the information gained from the proof test outweighs the damage done by slow crack growth. Furthermore, with the safeguard of acoustic-emission detection, proof testing significantly above the pressure anticipated in service can be advantageous. For example, if a vessel survives the first cycle to 1.5 times the mean expected operating pressure (1.5 MEOP), then the largest flaw that can be present in the successfully proof-tested tankage is smaller than that at 1.1 MEOP<sup>(49)</sup>. Thus, a vessel which survives the first cycle at a proof pressure of 1.5 MEOP is less likely to fail in service because of the significantly smaller defects demonstrated to be present by the proof test. However, if acoustic emission is not used to detect flaw growth and permit unloading before a crack reaches critical size, the higher proof pressure (1.5 MEOP) will increase the probability of failure in the proof test itself.

The examples of subcritical crack growth cited in earlier paragraphs involved high-strength materials. Some who are primarily concerned with lower-strength materials may take comfort in this. However, one other example should be considered. During the routine air-leak test of a large steel pressure vessel, a catastrophic brittle failure occurred at a pressure of about 3,200 psig, even though the vessel previously had passed two hydrostatic tests at 7,500 psig. The pressure vessel was in the form of a sausage-shaped flask, about 15-ft long with a 19-1/2-in. inside diameter and a 1-1/4-in. minimum wall thickness; it was manufactured in accordance with ASTM Spec. A372 Class 4, modified to a minimum yield strength requirement of 80,000 psi. Investigation of the failure<sup>(50)</sup> revealed that, following the hydrostatic tests, prior to leak test, the pressure vessel had been galvanized twice, including a five to eight hour warm-acid-stripping operating prior to the second galvanize. Hydrogen embrittlement arising from the acid stripping was suspected to be a factor contributing to the brittle failure. Standard Charpy V-notch impact tests revealed the 15-ft-lb transition to be plus 100°F and the FATT to be plus 125°F; the drop-weight NDT was approximately plus 80°F. Thus, the brittle condition of the steel was confirmed by the high transition temperatures of the pressure-vessel material. Nevertheless, the failure was considered to be unusual inasmuch as the pressure vessel had successfully passed two cycles of proof test to 7,500 psig and then failed at 3,200 psig in a routine air-leak test.

Aluminum also has been involved in slow-crack-growth proof-test failures. On 1 December 1966, a Saturn S-II liquid hydrogen tank (CBTT) fabricated of 2014-T6 aluminum ruptured at 33.4 psig (measured at the apex of the dome), damaging the common bulkhead assembly beyond repair. The CBTT margin of safety was based on 39 psig at room temperature measured at the forward bulkhead apex. The failure initiated in the LH<sub>2</sub> tank wall from an undetected crack in a recirculation-pump mounting boss. A study of the cyclic history of the CBTT up to the time of failure revealed prior cycles to higher pressure than the cycle that produced failure<sup>(51)</sup>. The maximum pressure achieved in the failure cycle at room temperature was 45.5 psig (measured at the point of failure). A higher pressure of 47.1 psig (measured at the same point) had been reached in a prior liquid-nitrogen (LN<sub>2</sub>) certification test of the forward liquid-hydrogen bulkhead. Thus, the CBTT experienced highest pressure in the LN<sub>2</sub> testing, but failed at a lower pressure under hydrostatic testing in water at room temperature. The tank failed under a rising pressure; 88 minutes were involved in rising from 30 psig to failure at 38.4 psig (0.6 psig below the intended maximum test pressure of 39 psig). This was the only pressurization with water subsequent to component proof testing.

The prior cycles at liquid-nitrogen temperature would have caused catastrophic propagation of the existing cracks in a material embrittled by cryogenic temperature; i.e., in many structural materials at liquid-nitrogen temperature, the fracture toughness would be lower, and with pressurization the critical crack size would have been reached, producing unstable crack propagation. Thus, in many materials, proof-testing at cryogenic temperature is more severe than proof testing at room temperature. However, in 2014-T6, which does not suffer a transition temperature, proof testing in LN<sub>2</sub> was less severe than proof testing in water at room temperature.

Based on an investigation of the failure<sup>(51)</sup>, it was concluded that flaws similar to those found in the CBTT recirculation-pump mounting boss may exist in flight hardware. These could propagate to failure during the S-II life cycle unless detected and removed. In this connection, it was noted that failure of the CBTT did not initiate in the regions of the LH<sub>2</sub> tank cylinder longitudinal weldments, which were predicted by analysis to be the most critical structural area and were the basis on which test-pressure limitations had been established. Based on stress analysis, it was reported that the recirculating-pump mounting area was under sufficiently low stress to have precluded failure in sound material, unless (a) an unknown flaw of critical size existed which was not detected by the original inspection techniques, or (b) an unknown, low-cycle, high-stress life cycle limit has been exceeded. The possibility of slow-crack growth as the result of stress corrosion cracking in water was not discussed.

A 260-IN. DIAMETER SOLID-PROPELLANT ROCKET MOTOR chamber fabricated from air-melted grade-250, 18% nickel maraging steel, using the submerged-arc-welding process<sup>(52)</sup>, failed in proof test at 56% of the proof pressure due to undetected flaws. Thus, the proof test was "successful" in revealing the undetected flaws, but at great cost.

The chamber consisted of a 260-in.-dia cylindrical section approximately 510-in. long between the forward and aft equators, a hemispherical forward head and a hemispherical aft head with a 183-in.-dia nozzle attachment flange. The nozzle shell attached to the chamber during hydrotest was approximately 114-in. long with a minimum dia of 76 in. and an aft dia of 112 in. The overall length of the chamber and nozzle-shell assembly was approximately 71.5 feet.

The findings of an Investigating Committee<sup>(53)</sup> showed that the failed case design was based on a plate yield strength of 230,000 psi and a weld efficiency of 90% for a design strength in the welds of 207,000 psi. Using a factor of safety of 1.3 for the welds resulted in a nominal plate thickness of 0.73-in. in the cylindrical section and 0.477-in. in the hemispherical domes. In the weld area, a mismatch of 10% of the thickness was allowed, but it was not to exceed 0.060-in. The eccentricity of membrane forces from this mismatch in a longitudinal weld results in an elastic-stress magnification factor of 1.25.

The hydrotest fluid was water inhibited by the addition of 0.73 lb of sodium dichromate in each 1000 gal of water, with a caustic soda addition to achieve pH neutrality. The water was heated by the addition of steam during filling to give a temperature of approximately 62°F.

The maximum hydrotest pressure planned was 960 psi, 10% above the maximum expected operating pressure of the motor. An initial 300-psi pressurization permitted instrumentation and pressurization system checkout, while a second 350-psi pressurization verified the status of the instrumentation. During the final pressurization, there were 5 minute holds at 300 to 500 psi in order to record strain-gage readings.

Failure of the chamber occurred at 542 psi (approximately 56 percent of proof pressure). Investigation showed that the failure originated from a defect that was not detected by nondestructive inspection prior to aging. There was no nondestructive inspection between aging and hydrotest. The defect causing the failure was in the heat-affected zone of a longitudinal submerged-arc-weld on the cylindrical section of the motor case. The area where the defect was located had been repaired by a manual tungsten-arc inert-gas (TIG) weld. The defect, which was submerged within the vessel wall and oriented longitudinally, was approximately 1.4-in. long and had a depth of about 0.10 in. Four other undetected defects of significant size were discovered after the motor case failure. All of these defects were also located beneath manual TIG-weld repairs. The presence of undetected defects in weld-repair regions is unexpected since weld repairs are normally subjected to extraordinary quality control. One of these defects, which was in the same longitudinal weld as the defect causing the motor-case failure, was involved in the fracture as a secondary origin. The other defects were discovered during reinspection of all welds by nondestructive testing techniques after hydroburst.

Stress intensity values ( $K_{I1}$ ) were calculated for both defects at the fracture origin by Tiffany and Masters<sup>(54)</sup>. An analysis of the stress field in the vicinity of the fracture origin indicated a maximum hoop fiber stress at the primary origin to be 93 ksi plus or minus the bending stress (13 ksi) for the cusp. Using this assumed stress and the dimensions of the "clean" origin, gave a maximum applied stress

intensity of 55 ksi-in.<sup>1/2</sup>. Boeing Company tests of submerged-arc-weld test plates supplied by the chamber fabricator indicated the plane-strain fracture toughness ( $K_{Ic}$ ) as measured from tests of surface-flaw specimens to be approximately 55 ksi-in.<sup>1/2</sup> at the yield strength of 215 to 220 ksi<sup>(54)</sup>. Thus, the proof test failure of this chamber, unlike any of those previously described, did not require slow crack growth to produce failure; the proof-test failure was the result of an undetected flaw exceeding the critical crack size at the failure pressure\*.

#### Fracture-Mechanics Concepts in Proof Testing

Positive assurance of the structural integrity of pressure vessels depends upon determination of (1) the initial flaw size, (2) the rate at which pre-existing flaws grow under operating conditions, and (3) the maximum flaw size the material can tolerate under operating conditions. Before proof testing, the only basis for estimating the initial flaw size is a knowledge of the quality-control procedures employed during fabrication. For example, if X-ray is the nondestructive inspection method used, then the largest undetected crack in the pressure vessel at the time of proof testing might be estimated as being 2 percent of the thickness. If the critical crack size at the proof pressure is less than 2 percent of the wall thickness, then the pressure vessel may fail during proof test. (With acoustic emission as a nondestructive inspection method employed during proof test, one should be able to detect the growth of such a defect at loads well below the proof pressure and discontinue the proof test before failure occurs.) If the pressure vessel does not fail in proof test, i.e., if there are no cracks in the pressure vessel of critical size at proof pressure, then one can estimate the largest flaw at the start of service to be no larger than the critical crack size at the proof pressure. This then is the estimated initial flaw size.

With pressure cycling and/or time at stress, an initial flaw may grow until it reaches critical size at the operating stress level. The pressure vessel will then fail catastrophically or develop a leak. The flaw-growth potential (in inches) is equal to the critical size minus the initial size. The life of the vessel is directly dependent upon this flaw-growth potential and the subcritical-flaw-growth characteristics of the tankage material.

Determination of the initial flaw size generally relies upon the use of nondestructive inspection procedures; however, the conventional proof test can be one of the most positive inspection procedures available, if used in conjunction with linear elastic fracture mechanics. A successful proof test actually defines the maximum possible initial flaw size that exists in the vessel. This results from the following functional relationship between stress level and flaw size as defined by the critical stress intensity ( $K_{Ic}$ )

$$K_{Ic}^2 = 1.21 \pi (a/Q) F^2$$

where  $a$  is the depth of a part through crack,  $Q$  is the flaw shape normalizing factor, and  $F$  is the applied stress.

Tiffany and Pall<sup>(49)</sup> point out that the critical flaw size at the proof-pressure stress level may be regarded as the largest possible initial flaw size that can be retained by the pressure vessel before it enters service. If the proof pressure is equal to  $\alpha$  times the operating pressure, it can be seen that for "thick-walled" vessels, the critical flaw size at the proof stress level,  $(a/Q)_{cr-proof}$ , or the maximum possible initial flaw size at the operating stress level,  $\max(a/Q)_{i-oper}$ , is as follows:

$$(a/Q)_{cr\ proof} = \max(a/Q)_{i-oper} = [K_{Ic} / \alpha F_{oper}]^2 / 1.21 \pi$$

and the critical flaw size at the operating stress level is:

$$(a/Q)_{cr\ oper} = [K_{Ic} / F_{oper}]^2 / 1.21 \pi$$

The ratio of the maximum possible initial flaw size to the critical size is then

$$\max(a/Q)_{i-oper} / (a/Q)_{cr} = 1/\alpha^2$$

For example, if a vessel successfully passes a proof test of 1.1 MEOP, the maximum initial flaw size which can exist immediately after the test is no larger than  $1/1.1^2$  or 83% of the critical size at the operating pressure. Failure of the vessel would occur when and if the flaw grows from this initial value to the critical value at the operating pressure.

The growth of subcritical flaws has been found to be primarily a function of the magnitude of the initial stress intensity as compared to the critical value. After a successful proof test, the maximum possible initial stress intensity in any one given area of the vessel, as compared to the critical value in that same area, is as follows:

$$\frac{\max K_{Ii}}{K_{Ic}} = \frac{(1.21 \pi)^{1/2} F_{oper} (a/Q)_{i-oper}^{1/2}}{(1.21 \pi)^{1/2} F_{oper} \alpha (a/Q)_{i-oper}^{1/2}} = \frac{1}{\alpha}$$

Consequently, with experimentally determined critical stress intensity, and cyclic and sustained-stress flaw growth data for the vessel materials (parent metal, welds, etc.), the maximum operational life of the vessel can be determined<sup>(49)</sup>.

\* Two 260-in.-dia motors, fabricated by Aerojet from vacuum-arc-remelted grade-200 18% nickel maraging steel have been successfully proof tested in inhibited water, pressurized at 50 psig per min to 200, 300, 400, 500, and 600 psig, held for 120 seconds at each pressure, then raised to 738 psig proof pressure for 120 seconds, all in one cycle. Fracture toughness measurements indicated  $K_{Ic}$  value over 3 times higher (165 ksi-in.<sup>1/2</sup>) than measured in the failed chamber.

It is important to note that the validity of the minimum life prediction (and the proof test factor determination) is not dependent upon accurate knowledge of the actual applied stress levels in the vessel nor the absolute fracture toughness values, both of which will vary throughout the pressure vessel. The accuracy of the life prediction is dependent only upon the validity of the flaw-growth data. This, of course, emphasizes the importance of careful simulation of service environment in the laboratory flaw-growth tests and the need for determining the component of the tank (i.e., weld, forging, plate, etc.) which will exhibit the highest flaw-growth rates<sup>(49)</sup>.

Previously cited examples of proof-test failures during periods of sustained pressure or as a result of multiple cycles have demonstrated that initial flaws or defects in a vessel may be increased in size by proof testing and, thus, the actual operational life of the vessel can be somewhat less after the proof test than it was before. However, if the pressure vessel survives the proof test, the information gained from the proof test far outweighs the damage that may have been done by flaw growth.

For materials that are sensitive to environmentally induced flaw growth (and most materials are affected to some degree), the test media and test duration are important considerations. For example, a number of high-strength motor-case steels have been found to be very sensitive to flaw growth in water and proof-test failures have occurred as a result of flaw growth during pressurization and/or during the period of sustained load at proof pressure. Although it might have been possible to eliminate these failures by use of a faster pressurization rate and immediate depressurization upon attaining the proof-pressure level, it is apparent a corrosion-inhibited test media is highly desirable. Prior to the final selection of a test media to be used in the proof test, it is important to perform sustained-stress flaw-growth tests in the proposed media to assure that flaw growth during proof testing will not be a major problem.

Also, it appears that there is very little to be gained by holding the chamber at the proof-test pressure any longer than is necessary to assure that the required level is attained. While it can be argued that if the pressure is held for a long enough time, the maximum possible initial flaw size is that size corresponding to the threshold stress intensity ( $K_{Isc}$ ) for the chamber material in the hydrotest environment, this is not a safe assumption. Initial flaws which have a stress intensity only slightly above the threshold value can still grow nearly to critical size and not fail, regardless of the duration of the proof test<sup>(49)</sup>.

Also, in general, very little can be gained by performing multiple-proof-test cycles. Actually, the cycles performed subsequent to the first cycle may do needless damage to the vessel as a result of cyclic flaw growth. In effect, multiple-proof-test cycling is a low-cycle fatigue test with a known ratio of applied stress intensity to critical stress intensity

$$K_{I1}/K_{Ic} = 1/d$$

or for proof testing at 1.1 MEOP,

$$K_{I1} = 0.91 K_{Ic}$$

This assumes an undetected surface flaw just short of critical size at proof pressure. Since fatigue crack growth rate is strongly dependent upon the magnitude of the maximum applied stress intensity as compared to the critical stress intensity, one would expect a high fatigue crack growth rate in most metals at  $0.9 K_{Ic}$ .

Consider, on the other hand, proof testing at 1.5 MEOP. If a vessel survives the first cycle to 1.5 MEOP, then the largest flaw that can be present in the proof-tested vessel is smaller than that at 1.1 MEOP and, consequently, the maximum applied stress intensity in proof testing at 1.5 MEOP is

$$(K_{I1})_{1.5 \text{ MEOP}} = 0.67 K_{Ic}$$

Thus, a vessel which survives the first cycle at a proof pressure of 1.5 MEOP is less likely to see significant crack growth in multiple proof-test cycling than a vessel proof tested at 1.1 MEOP. However, the higher proof pressure (1.5 MEOP) will increase the probability of failure in the first cycle of proof test.

From the above discussions, it is apparent that slow crack growth is an important consideration in determining pressure-vessel performance. Extensive studies have been undertaken to investigate slow-crack-growth phenomena; these are discussed later in this chapter. Moreover, acoustic emission is shown to be a unique nondestructive test method for use in hydrotest both to detect slow crack growth during proof test and to provide a precursor of crack instability.

When a pressure vessel fails on rising load before reaching the proof pressure, the failure is caused by a defect that escaped nondestructive inspection; i.e., a defect of critical size at the failure pressure. When a pressure vessel fails during a period of sustained load at the proof pressure or fails on rising load after previously sustaining one or more proof cycles, there is no known explanation other than slow crack growth.

Research on slow crack growth based on acoustic emission has demonstrated both the utility of acoustic emission for monitoring crack growth and the various mechanisms producing slow crack growth. Of the mechanisms investigated, hydrogen and/or stress-corrosion cracking are the most likely causes of slow crack growth during proof test. Spontaneous strain aging also should be suspect in any proof test involving even slightly elevated temperature.

Unfortunately, the concept of proof test is not valid if after proof test there is slow crack growth in the pressure vessel in storage or in service. Likewise, the concept of proof test is not valid if there is an embrittlement of the plastic zone formed at the flaw boundary during proof test, so that on reloading to MEOP in service there is a sudden extension of the crack.



Slow crack growth can occur in the period between proof testing and service loading as a result of hydrogen embrittlement and/or stress-corrosion cracking if there is sufficient internal pressure and/or residual welding stresses to produce such growth while in storage. Furthermore, if there are cracks which do not reach critical size in proof testing, the plastic zone formed at 1.1 MEOP may be subject to embrittlement during storage if there is elevated temperature involved in the storage (strain aging). If the critical crack size ( $a_{cr}$ ) at the service MEOP is equal to or less than the sum of the crack length present after proof test and the plastic-zone diameter ( $2 r_y$ ),

$$(a_{cr})_{1.0 \text{ MEOP}} \leq (a_{cr})_{1.1 \text{ MEOP}} + 2 r_y$$

the pressure vessel will fail at or before reaching the service MEOP if the plastic zone is embrittled during storage.

In the proof test, itself, since there is no way to know how large a defect may be present at the start of the test, there is no way to calculate the amount of slow crack growth that can be tolerated during proof test. Therefore, it is essential that one carefully inspect for defects before starting the proof test, and make sure that the proof-test environment will inhibit stress-corrosion cracking. Because neither nondestructive inspection nor control of hydrotest environment provides assurance of "zero defects", there is a very real need for an inspection method that will provide positive information on slow crack growth. Acoustic emission provides such a method.

#### ACOUSTIC EMISSION AS A NONDESTRUCTIVE INSPECTION METHOD

##### Low Cycle High-Stress-Intensity Fatigue

In practice, conventional nondestructive inspection is not as reliable as one might expect. Experience has shown that occasionally a dangerous flaw will escape detection and cause premature failure in service. Some of these flaws are detected in proof testing; if the proof test is "successful" the structure is destroyed in proof test before it gets into service. However, not all structures are suitable for proof testing (an airplane wing, for example). Furthermore, proof testing may cause subcritical crack growth, and sometimes subcritical crack growth occurs in service after proof test. Obviously, however thorough and effective the conventional nondestructive inspection method, subcritical crack growth is a serious complication to quality control. Fatigue is one of the best known mechanisms of subcritical crack growth.

Harris, Dunegan and Tetelman<sup>(55)</sup> have discussed the prediction of fatigue life by the combined use of fracture mechanics and acoustic emission. They proposed periodic proofing to loads greater than the working load while simultaneously monitoring for acoustic emission. Prediction of fatigue life is based on the observation that acoustic emission from a crack is directly related to the stress-intensity factor, as also is the fatigue-crack-growth rate and, therefore, it is possible to directly correlate acoustic emission, crack growth and number of fatigue cycles.

Electron fractography has provided much information on how fatigue cracks grow. However, the expense of electron fractography both in terms of equipment and skill required, severely limits the use of this tool. The use of stress-wave emission promises to be much cheaper and provides a dynamic real-time measurement of crack growth. Coupling the two techniques, electron fractography and stress-wave emission, will greatly enhance both methods.

A need for more detailed information on the fatigue cracking process has been recognized for over a decade. Weibull<sup>(56)</sup> in 1961 discussed this subject. "In any fatigue damaging process, continued until final rupture, various stages of quite different character can be distinguished. From an engineering aspect, it may be convenient to divide the process into an initiation period, ending with the appearance of a visible crack, and a propagation period, ending with the final rupture".

Studies of crack growth based on the appearance of fracture surfaces also were discussed by Christensen<sup>(57)</sup> in 1961. Findings from such studies "...support the general conclusion that the crack-propagation phase of fatigue damage is more predictable and less subject to scatter than the crack nucleation phase. Most scatter in fatigue data results from scatter in the micro-crack nucleation period... The transition from crack nucleation to the crack propagation phase is a rather difficult and complex stage for which limits should be defined. Although this has been recognized and discussed by many researchers, the point of view taken here is based on field experiences where it has been found that a crack one-fourth inch to one-half inch long is about the smallest flaw that can be readily detected in working structures. This is reasonable for structures composed of many members and alternate load paths. Moreover, it may be fortunate that most metals research programs have taken this practical viewpoint of assuming the existence of cracked members. In the later stages of cracking which the designer encounters he is far more concerned with crack growth and fracture characteristics in structures than with the crack nucleating period. On the other hand, the designer must also focus his attention on crack nucleation in his efforts to design fatigue resistant structures. Nevertheless, it is well to separate the two phenomenon for study. Unless fatigue data are properly evaluated and separated in these respects, it becomes too diluted, and gives rise to more speculation than understanding".

It is interesting to note that Christensen was one of the first to use stress-wave emission in the study of cracking. At the Cranfield Symposium in 1961, Christensen described his setup for measuring microsounds that accompany microcracking in stressed metal as follows: "As the microcrack occurs, it sets up a vibrational wave that propagates through the metal. A crystal accelerometer, cemented to the test panel in a direction perpendicular to the loading, picks up this component of the wave motion traversing the panel in the same manner as a seismograph in recording earthquakes. The magnitude of the early microcracks that were recorded in this particular test were in the order of 0.004 g's. These micro metal quakes can be converted into sound pressures and received on conventional headsets. If a value of zero db is

considered as the threshold of unaided hearing and 80 db the level of normal conversation then this will represent a latitude from 1 to 10,000. The micro sounds that have been recorded in experiments are believed to be far below this threshold value and therefore the magnification has been many times more than 10,000. The physical significance of these observations is that the occurrence and generation of heretofore undetected cracks were probably formed very early in the useful life of structures. The growth and extension of such cracks then will increase with the continued use of randomly loaded parts or members. To date these studies have indicated that microcracking can occur on the application of a load as low as 25% of the load that would normally fracture the part. Of equal significance is the fact that this was observed in the relatively notch-resistant material, RENE' 41.

"It is possible that with the aid of more sensitive equipment, microcracking can be detected at much earlier stages than reported here. It may also be practical to use this technique to prove the existence of an early crack formation period in elevated temperature fatigue. This technique also suggests a method for detecting and evaluating microcracking during proof loading of manufactured parts. For example, from the frequency of the microcrack sounds that occur during the loading to destruction of a few typical flash-welded parts it may be possible to classify marginal parts for service use. Having established a level of reliability in this manner, all subsequent proof-tested parts then will have far greater degrees of confidence for prolonged service use".

Much has been said about sporadic crack growth in fatigue. For example, with programmed loading, it has been observed that in certain instances, when stepwise loading is decreasing, there is a delay before crack propagation resumes, and when the stepwise loading is increasing, cracks propagate immediately and apparently at a greater rate than would be otherwise expected. Also, periods of constant load at elevated temperature may be attended by creep which, on resumption of cyclic loading, sometimes causes a pronounced decrease in the rate of crack growth for a short period of time. These phenomena can be studied using acoustic emission in greater detail than heretofore possible on a cycle-to-cycle basis.

The application of acoustic emission for the detection of fatigue crack growth has been investigated at Aerojet<sup>(58)</sup>. The materials involved in the study of acoustic emission from low-cycle, high-stress-intensity fatigue, as shown in Table 1, included D6aC tempered at 600 and 1100°F and 7075-T6 aluminum.

Table 1. Materials and Properties

Material	Modulus psi x 10 <sup>6</sup>	Yield Strength (ksi)	Toughness	
			K <sub>Ic</sub> (a)	K <sub>c</sub> (b)
D6aC	30			
600 temper		230	58	100
1100 temper		200	108	285
7076-T6	10.4	80	31	52

- (a) Plane-strain toughness based on COD pop-in in SEN-tension  
 (b) Apparent fracture toughness at failure load for 0.1-in. thick material

Test Procedure. The acoustic emission system used in this study<sup>(58)</sup> is shown in Figure 1. The test specimen was the precracked single-edge-notch tension specimen (see Figure 2). Gross cracking was monitored by means of the crack-opening-displacement (COD) gage, while microcracking, cycle-by-cycle, was monitored with acoustic-emission sensors. The sensors were bonded to the test specimen using quartz wax. The gain was increased at the totalizer until the background noise level was within a few millivolts of the threshold acoustic-emission level. The output signals of the totalizer and the COD gage were recorded on a strip chart. The COD gage had a sensitivity of 0.0013-in. when recorded on the 10-in. wide strip chart. With a dual-pen strip chart, it was a simple matter to determine where in the load cycle the bursts of stress-wave emission occurred. This is illustrated in Figure 3 using data from D6aC (600°F tempered) specimen 6842. Note that the pen recording the COD was 0.1 in. behind the pen recording the stress-wave emission count. The arrows indicate the position on the COD record where cracking started in each cycle.

A closed-loop Materials Test System (MTS) was used to fatigue test SEN-tension specimens at six (6) cycles per minute. The single-edge-notch (SEN) tension specimens consisted of 3 x 12-in. panels containing an electric-discharge-machined edge notch, extended and sharpened by tension-tension fatigue. The stress intensity for the fatigue precracking operation was approximately one-half the estimated critical plane-strain stress intensity (K<sub>Ic</sub>). The stress intensity was calculated from the expression published by ASTM Committee E24<sup>(59)</sup>; viz.,

$$K_I = Y P a^{1/2} / BW$$

where Y = 1.99 - 0.41 (a/W) + 18.70 (a/W)<sup>2</sup> - 38.48 (a/W)<sup>3</sup> + 53.85 (a/W)<sup>4</sup>, P = load, a = crack length, B = specimen thickness, and W = specimen width. Each specimen was first step loaded to provide in-test calibration of the COD gage<sup>(60)</sup> and to determine the noise level at load. The set point (gain) of the emission totalizer was determined at the maximum load for cyclic testing. The specimen was then unloaded to the mean cyclic load, all instrumentation checked, and then the cyclic loading started. In general, maximum load corresponded to the COD deviation-from linearity.

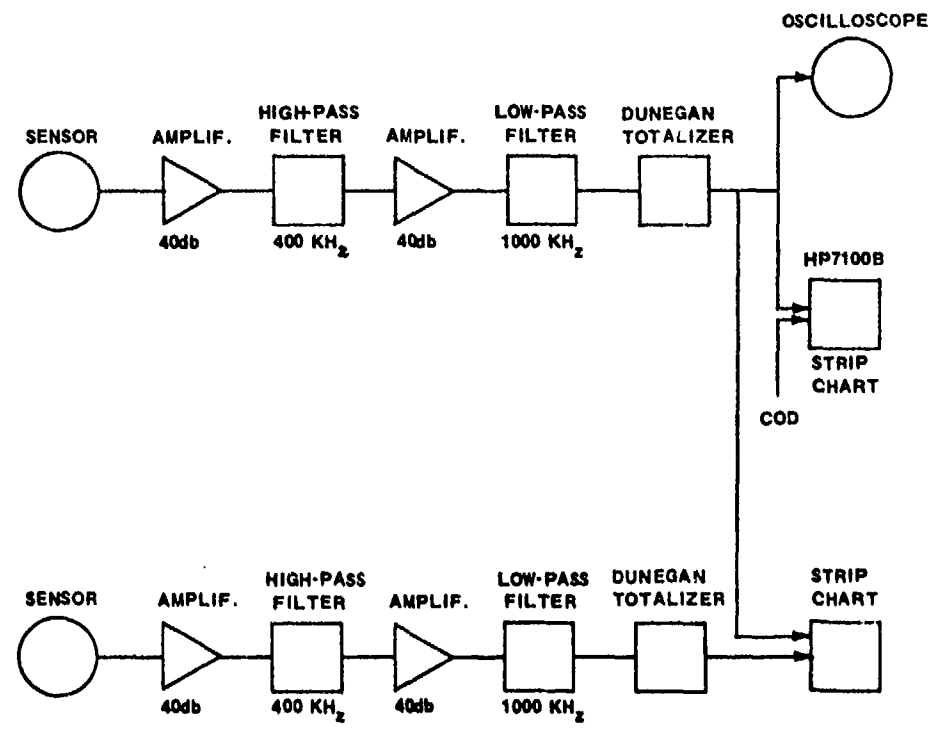


Figure 1. Acoustic Emission Monitoring System for Low-Cycle High-Stress-Intensity Fatigue

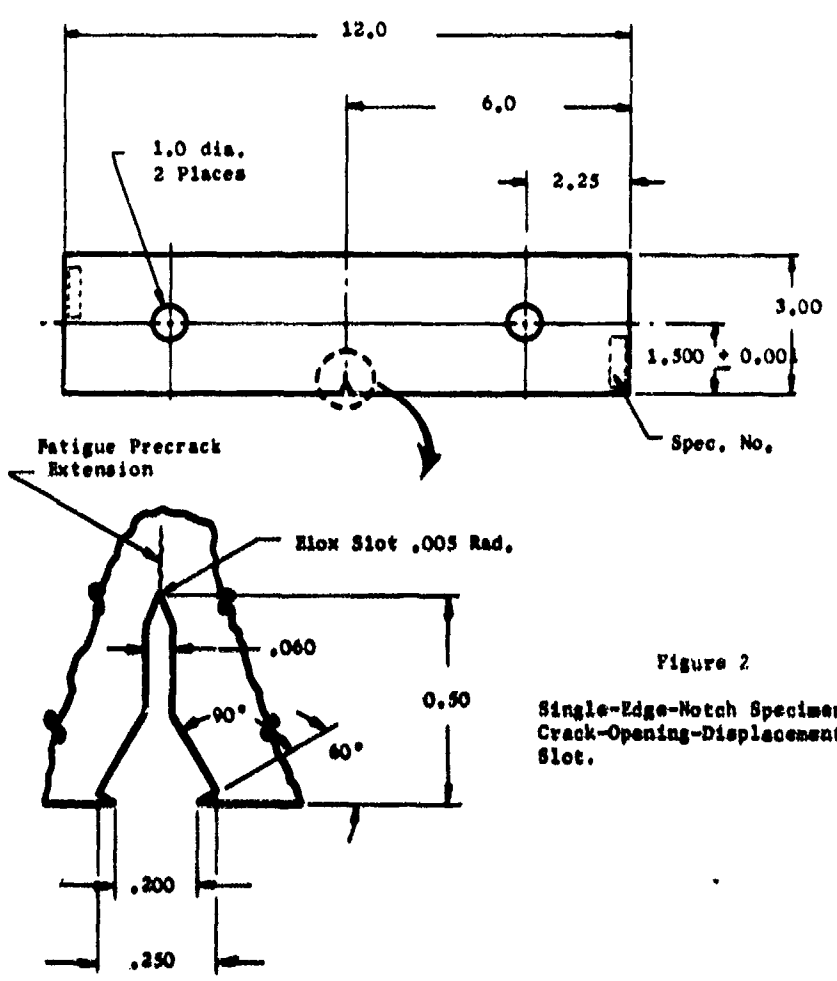


Figure 2  
Single-Edge-Notch Specimen and  
Crack-Opening-Displacement  
Gage Slot.

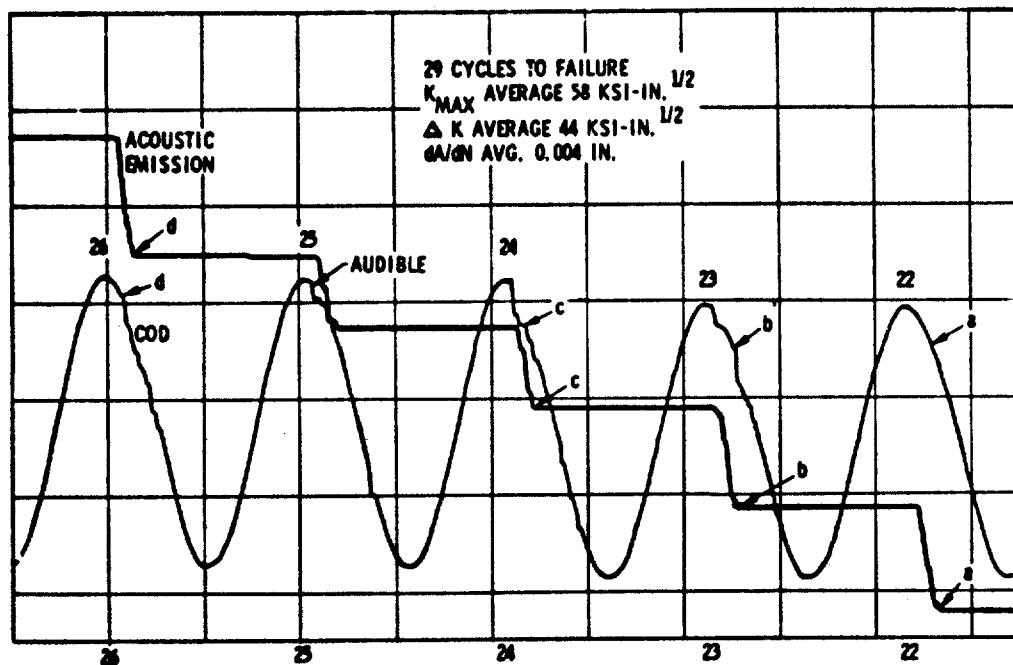


Figure 3. Fatigue Cracking in 600°F Tempered D6aC Specimen 6842 - 0.29-in. Thick

**Test Results - D6aC Steel.** Specimens of D6aC steel in two thicknesses and two tempering conditions were tested in low-cycle high-stress intensity fatigue. The D6aC steel was obtained in the mill annealed condition as 0.1 in. and 0.3 in. thick surface-ground sheet and plate. The chemical composition (weight percent) and heat numbers of each are shown below.

Thickness	Heat	C	Mn	Si	P	S	Ni	Cr	Mo	V
0.1-in.	3910262 (a)	0.45	0.75	0.21	0.004	0.005	0.55	1.08	0.99	0.09
	Check (b)	0.47	0.70	0.23	-	-	0.54	1.08	0.94	0.12
0.3-in.	3952092 (a)	0.48	0.74	0.23	0.005	0.006	0.56	1.07	1.00	0.09
	Check (b)	0.49	0.78	0.23	-	-	0.51	1.01	0.97	0.09

(a) Supplier Analysis  
(b) AGC Check Analysis

The heat-treat procedure employed for processing the D6aC is shown below. The indicated tempering cycles were employed to produce widely varying strength levels and fracture toughness. In order to prevent carburization, decarburization or other surface attack, austenitization was performed using a neutral salt bath followed by quenching directly to room temperature in agitated oil. Tempering was performed in an air atmosphere at the indicated temperature and time.

<u>Austenitize</u>	- 1700°F - 30 minutes at temperature
<u>Quench</u>	- Agitated oil at room temperature
<u>Temper</u>	- High Strength/Low Toughness: 600°F - 2 hours
	- Low Strength/High Toughness: 1100°F - 2 hours

Table 2 summarizes the tests and stress-intensity factors at fracture. Note that the critical stress intensity values calculated from fatigue testing were approximately the same as those obtained from a single cycle, i.e., rising load to failure.

Figure 4 is a plot of the cumulative stress-wave count (TSWE) versus cycle number for 0.1-in.-thick specimen 6826; the computer-plotted curve shows the last 20-30 cycles. At the cycling rate of 6 cpm there was more than ample time to unload the test specimen if one wished to avoid fracture. Figure 5 shows the plot of stress-intensity factor ( $K_{max}$ ) versus cumulative stress-wave count for each successive cycle. Note that  $K_{max}$  - TSWE was approximately a linear relationship.

Specimen 6827, also 0.1-in.-thick, was tested in the same manner as 6826 except that the notch of the single-edge-notch (SEN) tension specimen was filled with water after the specimen had been cycling for some time. The specimen went 500 cycles after the water was added, before it failed. Figure 6 is a plot of the COD data obtained in the last 60 cycles of the test, with the stress-wave-count per cycle cursor of failure.

Table 2. Critical Stress-Intensity in Fatigue

Material	Thickness	Critical Stress Intensity		Fatigue Specimen
		Rising Load	Fatigue	
1100 D6aC	0.294	204 - 251 Avg(3) <u>227</u>	222	6S46
	0.292		265 <sup>(a)</sup>	6S47
	0.101	275 - 287 Avg(3) <u>285</u>	240	6S26
	0.100		265 <sup>(b)</sup>	6S27
600 D6aC	0.293	92 - 107 Avg(3) <u>100</u>	65	6S42
	0.104	94 - 104 Avg(4) <u>100</u>	116	6S22
	0.101		112 <sup>(c)</sup>	6S23

- 
- (a) last 290 cycles with water in the notch; because the COD in the last cycle was lost, the  $K_C$  value is for one cycle before failure.  
 (b) water in the notch; the  $K_C$  value is for one cycle before failure.  
 (c) last 188 cycles with water in the notch; the  $K_C$  value is for one cycle before failure.

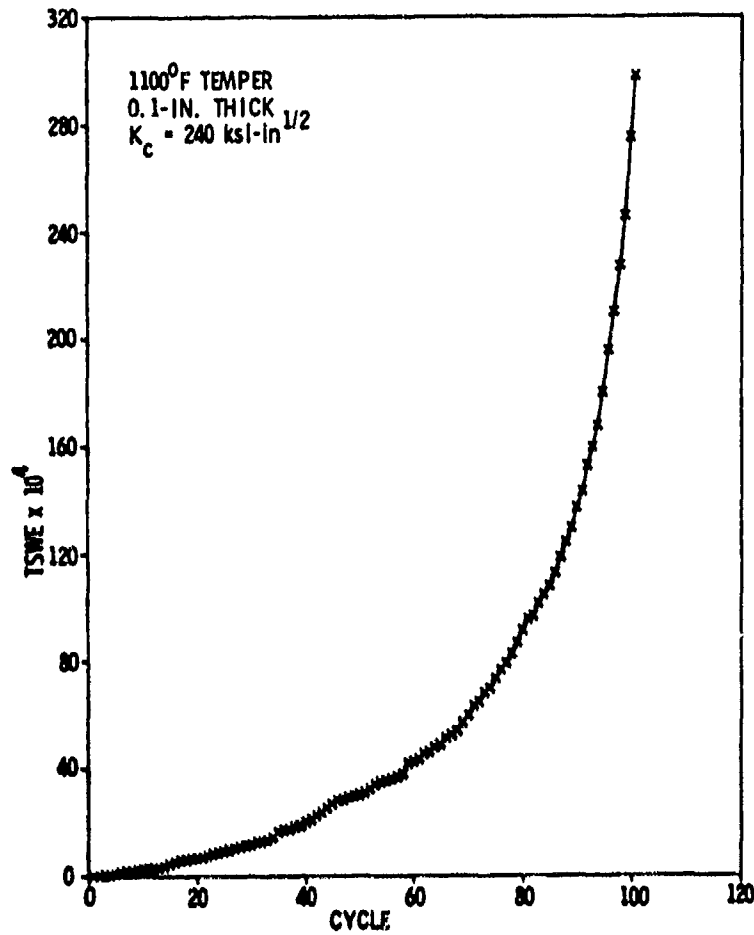


Figure 4. Relationship Between TSWE and Cycle Number for 1100°F Tempered D6aC 0.1-in.-Thick Specimen 6S26

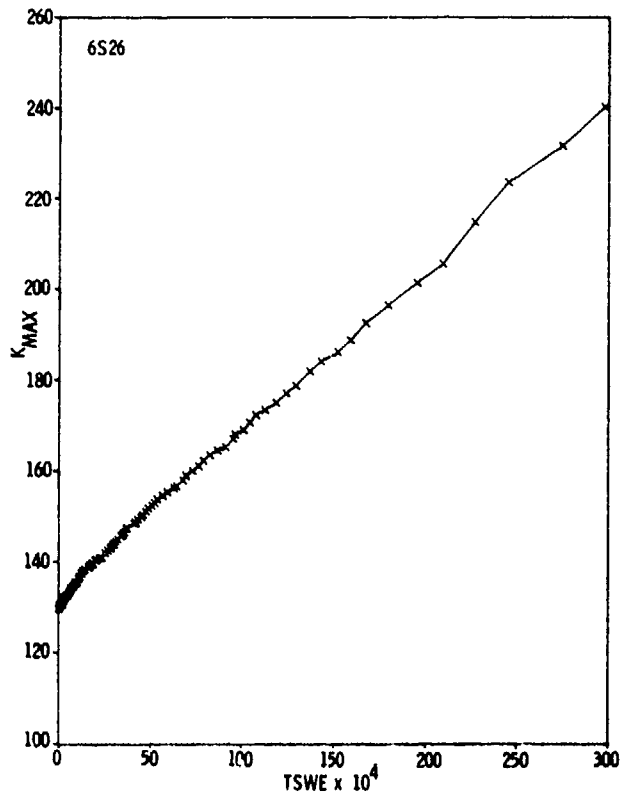


Figure 5. Relationship Between Maximum Stress Intensity and Acoustic-Emission Count in 1100°F Tempered D6aC 0.1-in.-Thick Specimens 6S26 and 6S27.

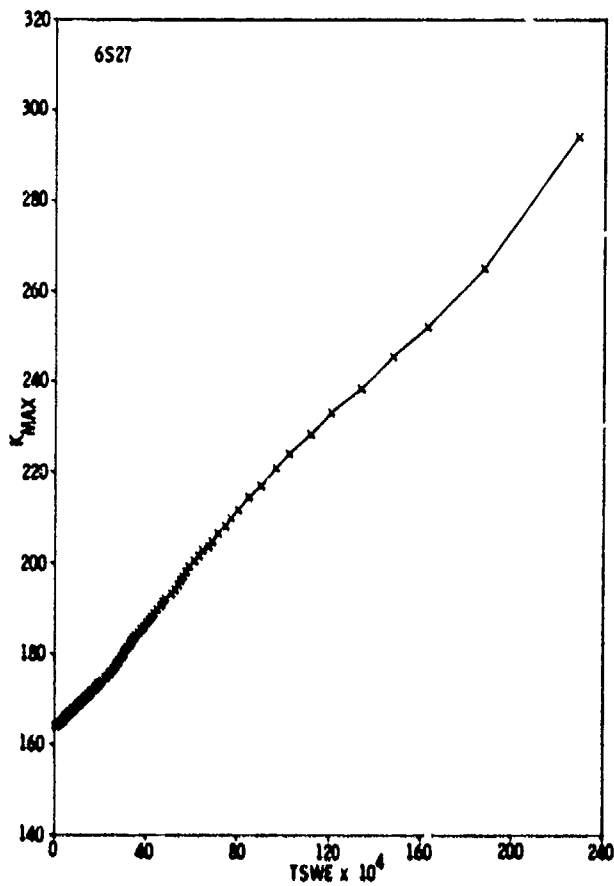
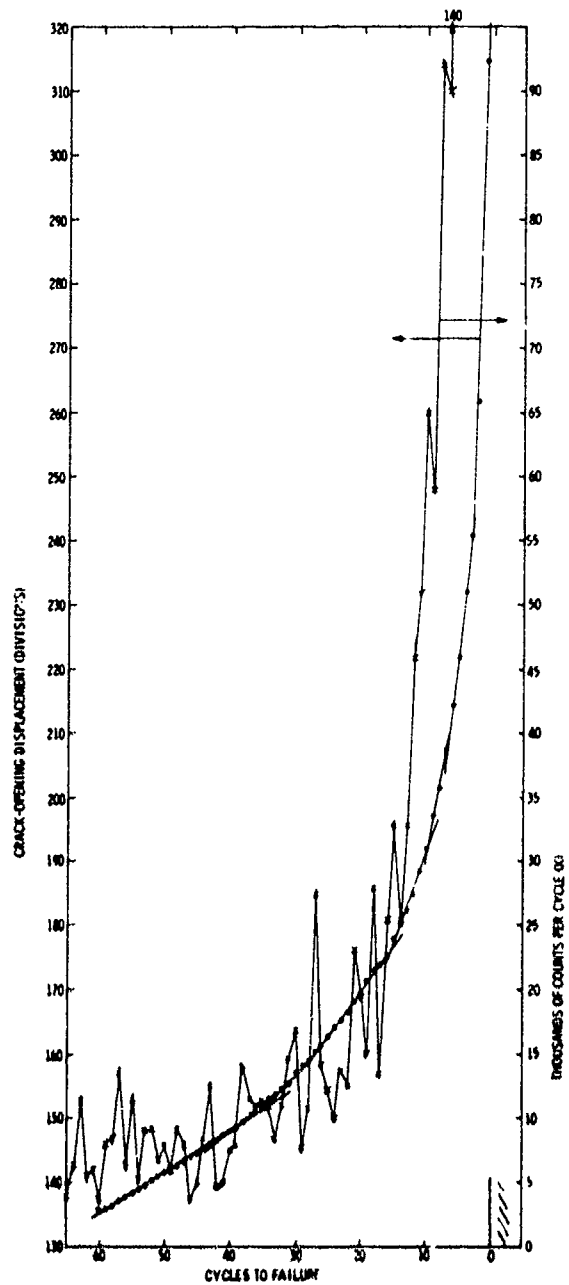


Figure 6. Correlation Between COD and TSWE as a Function of Cycle Number in 1100°F Tempered D6aC 0.1-in.-Thick Specimen 6S27 Subjected to Corrosion Fatigue.



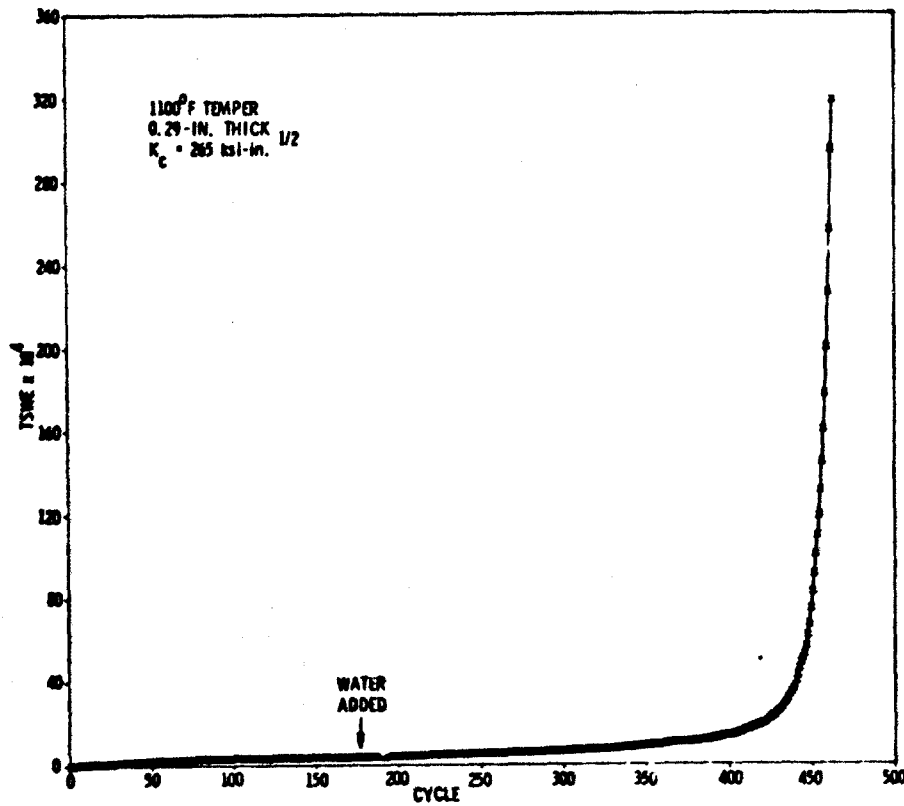


Fig. 7. Relationship Between TSWE and Cycle Number in D6aC Specimen 6S47 Subjected to Corrosion Fatigue

Specimen 6S47 was tested initially in a low-humidity air-conditioned laboratory. However, after 178 cycles, the edge notch was filled with water. After 290 cycles with water in the notch, the specimen failed. Figure 7 shows an unmistakable precursor of failure in the last 30 to 40 cycles, but no apparent effect from the addition of water.

Specimen 6S22 was cut from 600°F tempered D6aC steel; this specimen was tested in the same manner as the specimen described above, with water inserted in the notch after 163 cycles in low-humidity air. In the 600°F tempered material, the water was extremely detrimental. Figure 8 is a plot of TSWE versus cycle number. Note that at the point where water was added, there was an increase in the stress-wave count rate. A comparison between Figures 7 and 8 shows the marked difference in behavior between the 600 and 1100°F tempered material; recall that in obtaining the data in Figure 7, water was added after 178 cycles with very little, if any, effect. In Figure 9, note the short periods of dormancy in the plot of data taken before adding water, followed by marked and nearly continuous activity after adding the water.

Specimen 6S22 was first subjected to a maximum load of 3010 lb (630-lb minimum), tested in a low-humidity air-conditioned laboratory. There were occasional small bursts of stress-wave emission around maximum load. A sample of these data are shown in the following tabulation (only the cycles producing stress-wave data are shown in the tabulation):

Cycle Number	Stress-Wave Count/Cycle	Cycle Number	Stress-Wave Count/Cycle
13	100	73	750
16	600	75	200
22	1100	77	100
27	2700	79	370
29	1650	94	2500
31	950	95	4400
32	170	96	2300
37	200	110	420
71	200		

Thus, there were periods of dormancy interspersed with varying sizes of bursts. However, the crack-opening displacement did not increase significantly in these 100 cycles and, therefore, the crack growth was very small.

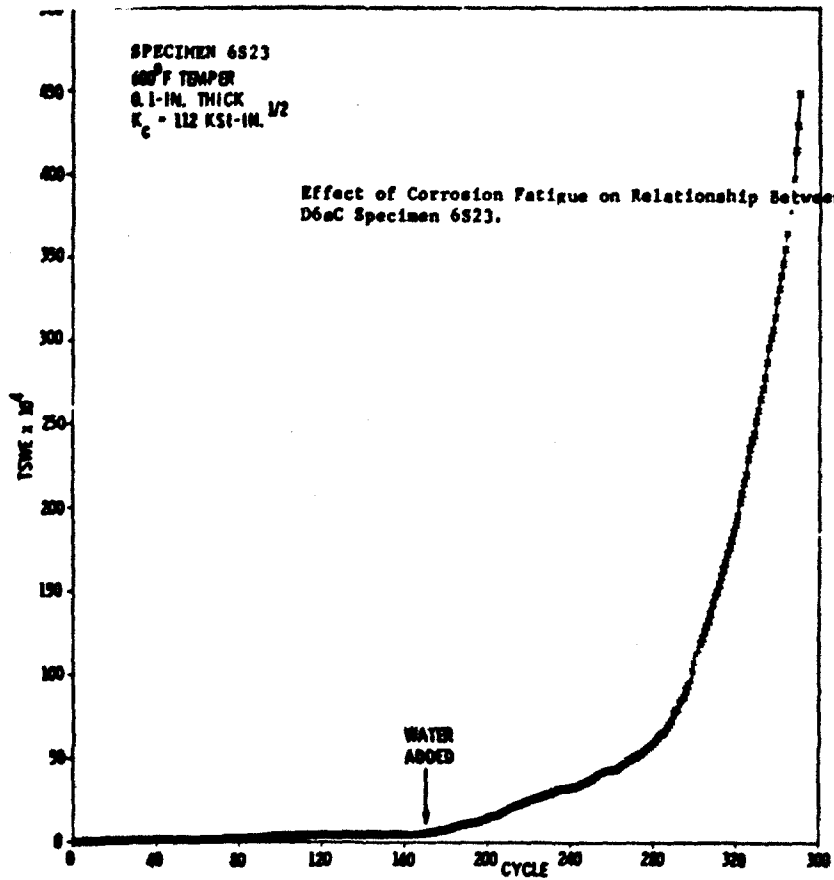
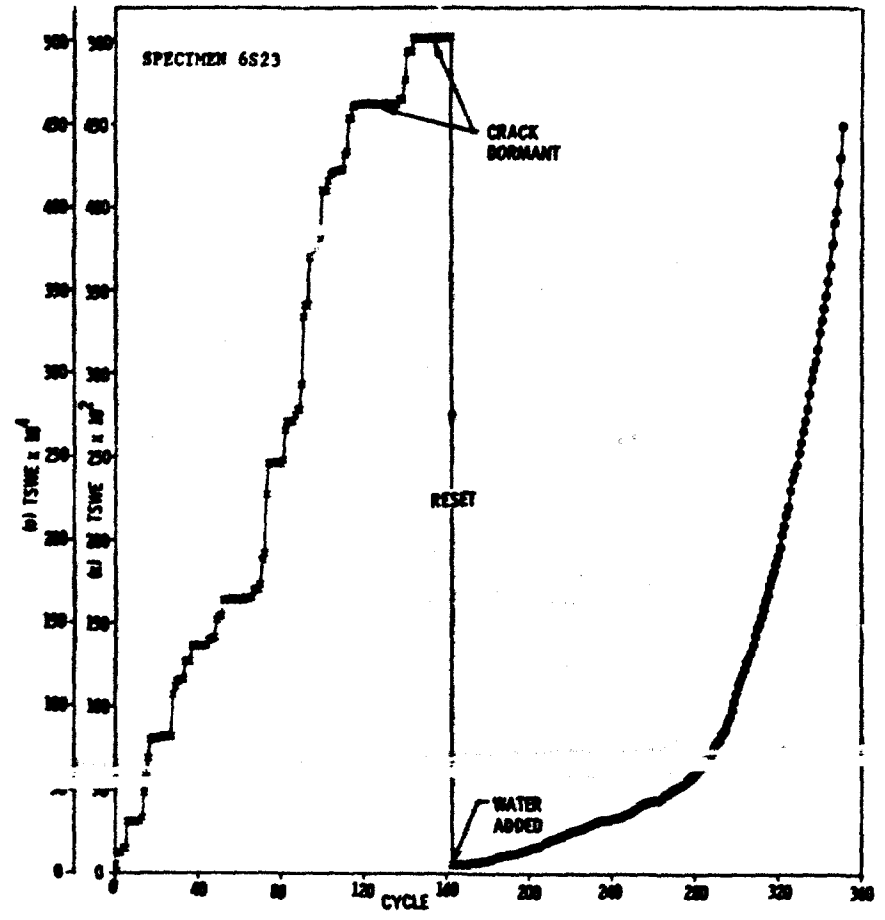


Figure 8

Figure 9





After 398 cycles, the notch was filled with water and cycling continued at 3.0 kips maximum load. There was some increase in stress-wave activity but still no significant increase in crack-opening displacement. The following tabulation shows the stress-wave activity recorded in the first twenty-five cycles after adding the water:

Cycle Number	Stress-Wave Count/Cycle	Cycle Number	Stress-Wave Count/Cycle
1	2220	12	100
2	1400	13	2300
3	280	14	600
4	2100	15	400
6	300	17	1050
7	830	18	3200
8	600	19	2000
		20	2500
10	200		
11	150	25	2400

The average count per cycle for the data sample tabulated for dry air was 171 counts per cycle; after adding water the average count per cycle based on the data sample tabulated above was 913 counts per cycle. Thus, stress-corrosion cracking was taking place as shown in Figure 8.

**7075-T6 Aluminum.** Specimen BS-1 was tested in the same manner and with the same system as in the steel testing. After approximately 200 cycles in an air-conditioned low-humidity laboratory, a 3 percent NaCl solution was placed in the notch of the SEN tension specimen. The stress intensity at the time of adding the solution was 28.5 ksi-in.<sup>1/2</sup> ( $\Delta K$  was 26.3 ksi-in.<sup>1/2</sup>). In 216 additional cycles, the specimen fractured; the stress intensity at fracture was 32.1 ksi-in.<sup>1/2</sup>. The cumulative stress-wave count before and after adding the 3% NaCl solution is shown in Figure 10. Note the two-orders-of-magnitude change of scale in plotting the count after stress-corrosion cracking was initiated. Data were

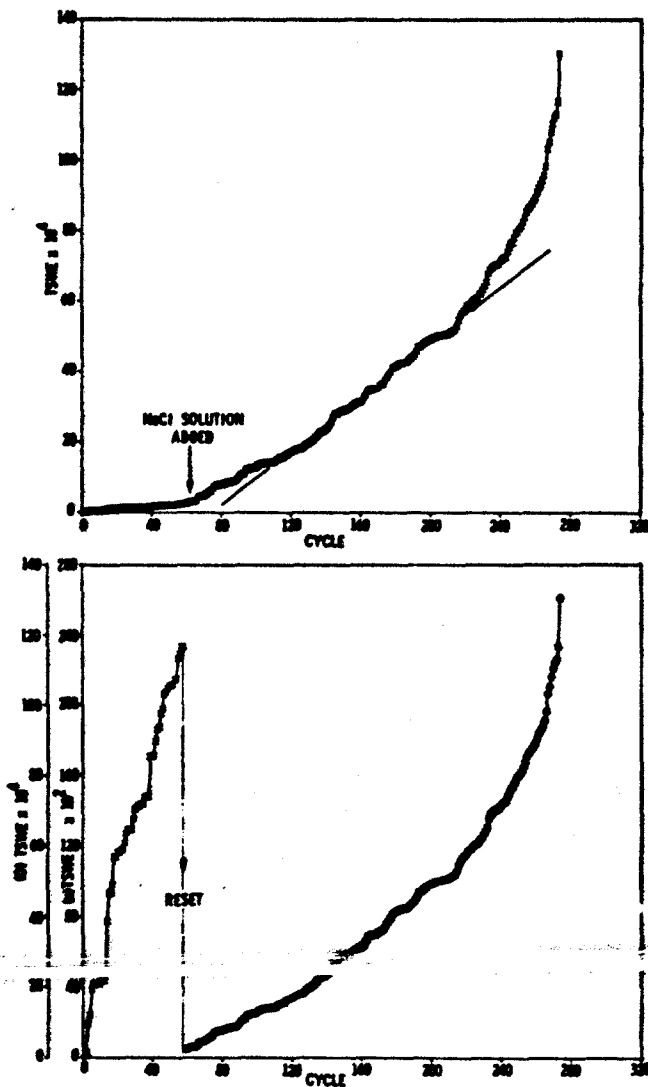


Figure 10

Relationship Between TSWE and Cycle Number in 7075-T6 Aluminum 0.26-in.-Thick Specimen BS-1 Subjected to Corrosion Fatigue.

tabulated for a total of 58 cycles before adding the solution; note the unmistakable change after 58 cycles. Table 3 is a tabulation of the average count rate and the average crack growth in each successive 10 cycles before and after adding the 3% NaCl. Note that there was an order of magnitude increase in stress-wave count rate after adding the salt solution. The increase in crack growth rate was not as dramatic but nevertheless unmistakable after adding the salt solution. Note that approximately 50 cycles before failure occurred, there was a marked increase in the count rate and in the crack growth rate. In Figure 10, the change of slope would serve as the precursor of failure (approximately 50 cycles before fracture). From Figure 11 note the linear relationship between TSWE and  $K_{max}$ .

#### Stress Corrosion Cracking and Hydrogen Embrittlement

A series of papers has been published in the open literature in which acoustic emission was used for the crack detection of stress-corrosion cracking and hydrogen embrittlement. Because the details can be obtained from respective publications, only the highlights of these researches will be reviewed here.

One paper (61) describes a study of slow crack growth in D6aC steel as influenced by hydrogen and stress-corrosion using acoustic emission (stress waves) as a new technique for monitoring incremental crack growth. In this study it was found that the D6aC steel was susceptible to slow crack growth both when hydrogenated and tested in distilled water. Over a given period of slow crack growth, there was a direct relationship between the number of stress waves and crack growth rate and, alternately, there was an inverse relationship between secondary-incubation time and crack-growth rate. As the crack lengthened under constant load, the stress intensity increased and the rate of stress-wave emission (SWE/sec) increased at a relatively gradual rate until a sudden increase in rate occurred corresponding to the start of rapid crack growth. Crack growth was found to occur in discontinuous steps for all test conditions investigated. A synergistic effect was noted when hydrogenated D6aC steel was tested in water. Hydrogen diffusion appeared to be the controlling mechanism in both types of embrittlement.

The conclusions of this research based on tests in an aqueous environment and/or after the deliberate addition of hydrogen were as follows:

1. D6aC low-alloy steel heat treated to produce a variety of microstructures and strength levels is susceptible to slow crack growth under sustained load when tested in the hydrogenated condition and/or in an aqueous environment.

2. A crack-opening-displacement (COD) gage in conjunction with a constant-speed strip chart, provides a sensitive measurement of average crack-growth rate during sustained-load tests. However, on an increment-by-increment basis, only gross movements of the crack front are detectable on the COD chart.

3. Stress wave emission as measured by an appropriate instrumentation system is a highly sensitive device for monitoring increment-by-increment growth of a crack. In many instances where SWE shows incremental crack growth with definite time intervals between jumps, the COD chart indicates continuous crack growth.

4. It was found that over a given period of slow crack growth, there is a direct relationship between the number of stress waves and the crack-growth rate,  $da/dt$ ; or alternatively, there is an inverse relationship between secondary incubation time  $\Delta t$ , and  $da/dt$ .

5. As the crack lengthens under constant load, the stress intensity increases and both  $1/\Delta t$ , and  $da/dt$  increase at a relatively gradual rate. At a critical crack size, both  $1/\Delta t$ , and  $da/dt$  suddenly increase producing an easily identified inflection in the curves of SWE per second vs time-at-load; the inflection corresponds to the start of rapid crack growth.

6. In hydrogenated D6aC low-alloy steel heat treated to low toughness (1550/400):

a. The crack growth rate ( $da/dt$ ) increases with increasing crack length until at an intermediate stress intensity level,  $da/dt$  becomes constant or even decreases slightly before increasing to the point of crack instability. At high stress-intensity levels, the data from hydrogenated specimens tested in water approach the curve relating  $K$  and  $da/dt$  for nonhydrogenated material tested in water.

b. Hydrogenated material baked for 1/2 hr at 300°F was found to have lower crack growth rates than material baked for 3 hr at 300°F. No explanation was found for this apparently anomalous result; the various tests of 1/2 hr baked material were consistent, however, in showing this behavior.

c. Hydrogenated material baked for 3 hr at 300°F and tested in water has a greater rate of crack growth than would be predicted by tests of hydrogenated material tested in air and nonhydrogenated material tested in water, i.e., the combination of hydrogenation and aqueous environment has a synergistic effect.

7. In hydrogenated D6aC low-alloy steel heat treated to high toughness (1750/1100):

a. The crack-growth rate ( $da/dt$ ) increases with increasing crack length until at an intermediate stress intensity level, the rate of increase of  $da/dt$  suddenly increases, with  $da/dt$  for the material tested in air and in water increasing at approximately the same rate.

b. Hydrogenated material baked for 1/2 hr at 300°F and tested in water has the same crack-growth rate as the non-hydrogenated material tested in water. Thus, in this material condition, the embrittling effect of water appears to be the controlling mechanism.

c. Hydrogenated material baked for 3 hr at 300°F has the same accelerated crack-growth rate whether tested in air or water; thus, there was no evidence of a synergistic effect with the combination of hydrogenation and water. In fact, hydrogen appears to be the controlling mechanism since adding water does not increase the crack growth rate.

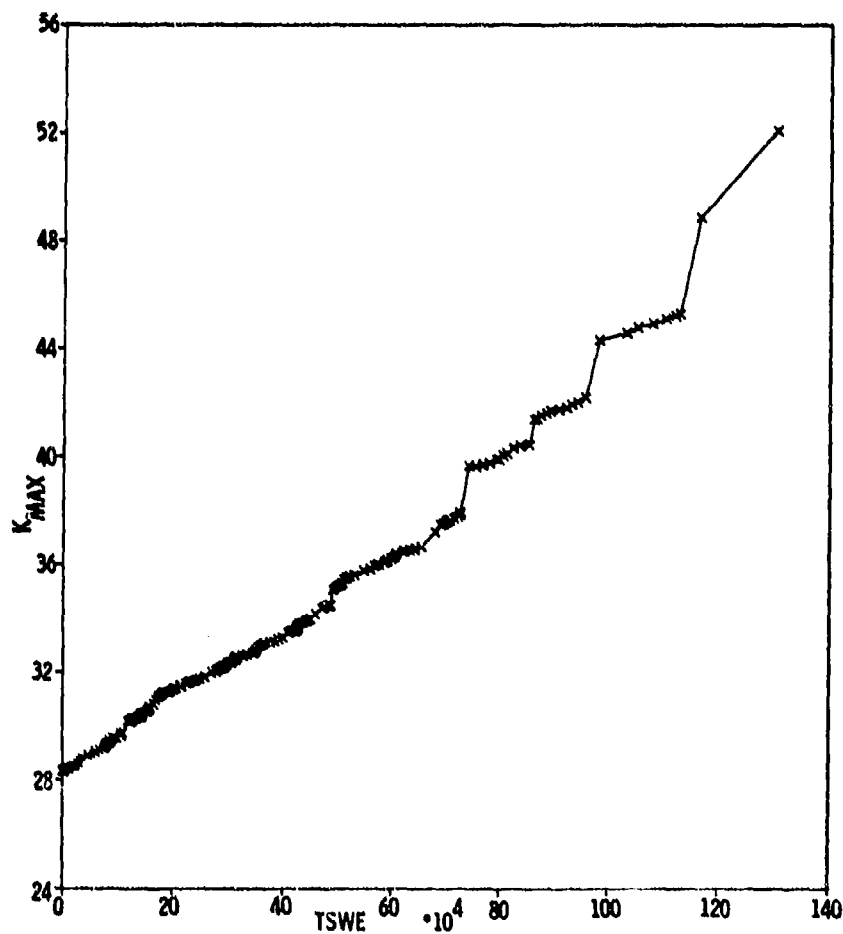


Figure 11. Relationship Between  $K_{max}$  and TSWE in 7075-T6 Aluminum 0.26-in.-Thick Specimen RC-1.

TABLE 3. AVERAGE COUNT AND CRACK-GROWTH RATES, 7075-T6

<u>Cycle Range</u>	<u>Average Count Rate</u> SWE per Cycle	<u>Average Crack Growth</u> in. per Cycle x 10 <sup>-3</sup>
50 - 40	563	0.142
40 - 30	316	0.141
30 - 20	186	0.141
20 - 10	583	0.000
10 - 0	269	0.000

3% NaCl ADDED

0 - 10	2057	0.973
10 - 20	3191	0.948
20 - 30	1182	0.794
30 - 40	3676	1.704
40 - 50	1760	0.494
50 - 60	2230	1.089
60 - 70	2060	1.174
70 - 80	4410	0.913
80 - 90	5270	1.221
90 - 100	2550	0.651
100 - 110	4350	0.849
110 - 120	4820	1.037
120 - 130	3050	1.011
130 - 140	5520	1.472
140 - 150	2020	1.709
150 - 160	5510	1.277
160 - 170	4980	1.234
170 - 180	9400	2.606
180 - 190	6490	4.056
190 - 200	9560	3.088
200 - 210	11820	5.426
210 - 217	26360	14.53

A more recent study of stress-corrosion cracking<sup>(62,63)</sup> provides additional evidence of the utility of acoustic emission as a method for monitoring stress-corrosion cracking. One phase of this study, heretofore not reported in the open literature is described in the following paragraphs. The material was 6Al-4V titanium in the solution treated and aged condition and the environment was circulating distilled water at 65 and 165°F. The criterion used in evaluating the crack-growth process was primary incubation time as determined by acoustic emission. Water at 165°F induced stress-corrosion cracking; whereas, at 65°F, there was no subcritical crack growth in the periods investigated (up to 19 hours at 0.9 K<sub>c</sub>).

**Material Investigated.** In this investigation, a single heat of 6Al-4V titanium was used for the study of slow crack growth. The chemistry of the heat follows:

6.0% Al, 4.1% V, 0.13% Fe, 0.023% C, 0.110% O, 0.0050% H, 0.015% N

The mill-annealed tensile properties as obtained from the titanium producer were:

135,000 psi F<sub>ty</sub>, 142,000 psi F<sub>tu</sub>, 15.5% elongation

The room-temperature properties obtained from the material after a conventional solution treating and aging treatment (1765°F/15 min, water quench and age at 1100°F for 8 hr) was as follows:

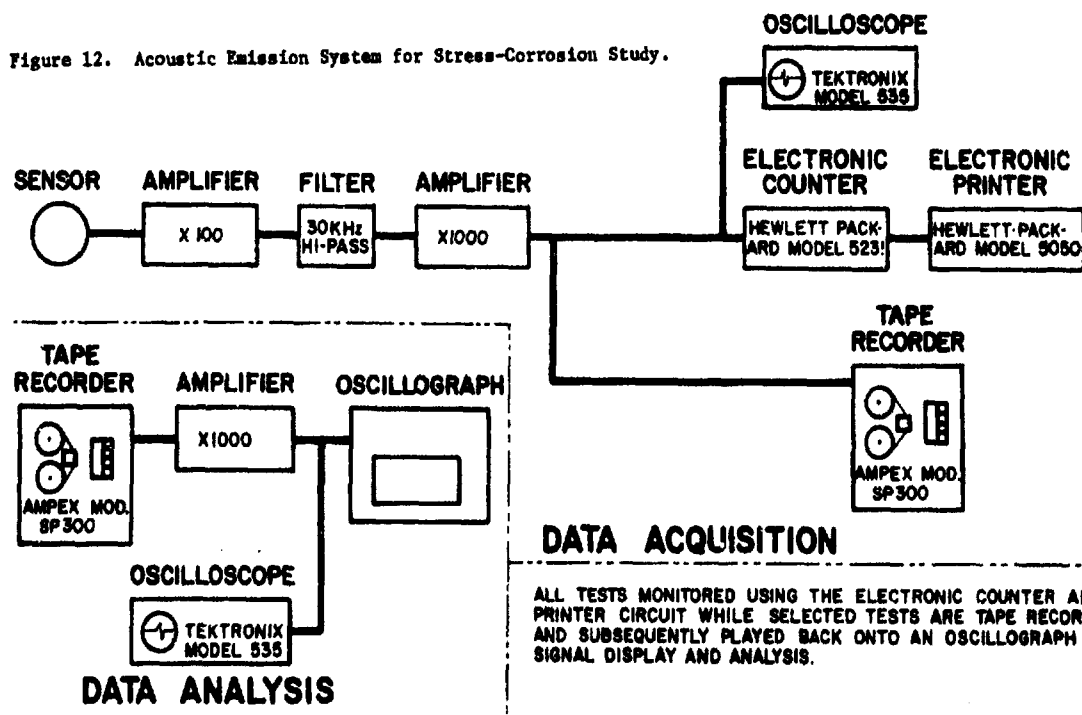
6Al-4V Titanium Microstructure	0.2% Offset Yield (ksi)	Ultimate Strength (ksi)	Stress Intensity at Failure (ksi-in. <sup>1/2</sup> )
Equiaxed-Alpha	147 - 155 Av(3) 152	166 - 169 Av(3) 168	80 - 97 Av(3) 90

**Test Procedure.** The single-edge-notch (SEN) tensile specimen, the crack-opening displacement gage, the experimentally determined calibration curve for converting crack-opening-displacement measurements to crack length and the K calibration as published by ASTM were the same as those used in the low-cycle-fatigue study, previously described.

The acoustic-emission monitoring system is shown schematically in Figure 12. As indicated in this figure, the system consisted of accelerometers, amplifiers, filters, tape recorders, and an electronic counter and digital printer. The accelerometers were attached to the specimens using a linear-force coiled-spring technique. The electronic counter, instead of counting a stress wave as an individual event, recorded every cycle above an arbitrary trigger level set on the basis of background noise and held constant for a given series of tests. With this characteristic, a large stress wave results in more cycles above the trigger level than a small stress wave; thus, a greater acoustic-emission printout-number would be obtained for a large emission than for a small emission. In other words, the electronic counter provided an integration of size and number of emissions rather than a one-for-one count.

As indicated in Figure 12, two basic systems were used for data acquisition. The electronic counter system provided a real-time record of the emission (both cumulative count and rate of emission) throughout each test period. The high-pass filter in the system eliminated a major portion of the extraneous low-frequency noises which tended to mask very small amplitude emissions. A second data acquisition system also was used for a limited number of tests. This system used the same amplification and filtering components but incorporated a magnetic tape recorder. The data were collected by recording each test and subsequently analyzed through playback as shown in Figure 12.

Figure 12. Acoustic Emission System for Stress-Corrosion Study.



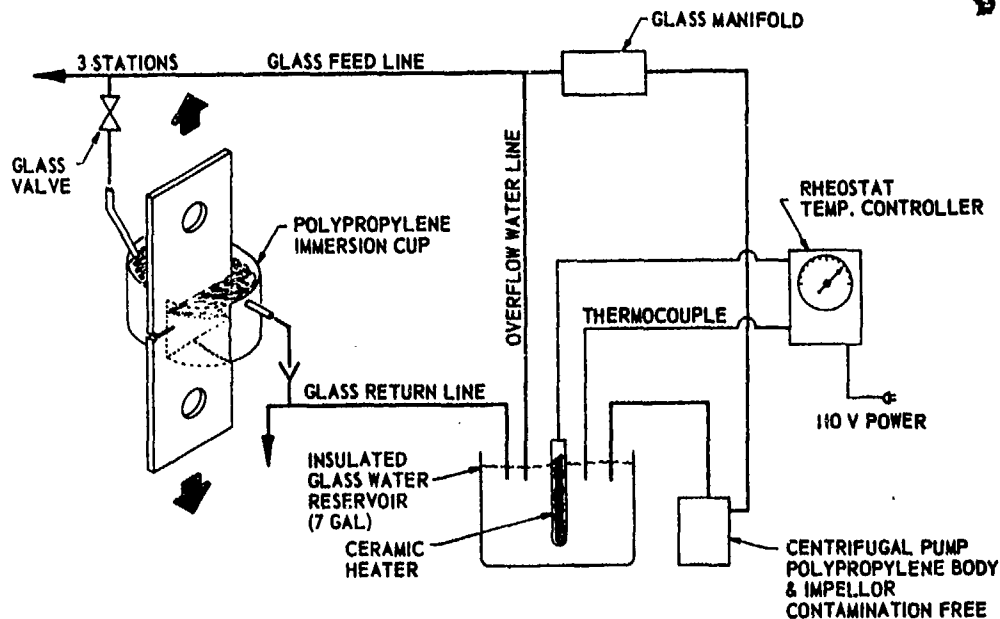


Figure 13. Environmental System for Stress-Corrosion Cracking Study

The data-acquisition system utilized 100X amplification, followed by a 30 KHz high-pass filter and then 1000X amplification. With this system, a 38 KHz input signal (approximately the resonance frequency of the mounted accelerometer) was amplified 5000X. Also, with the electronic counter, two levels of stress-wave amplitude were recorded. The counter strip-chart printout recorded both cumulative count and count per unit time (count rate). By a voltage setting, the count-rate printout was adjusted to read signals just above the background noise level; count rate, then, was recording small emissions, while cumulative count was set to record the larger emissions, approximately 5 times those of the count-rate printout.

Environmental Testing. Because of the test times in this phase of the investigation, a circulating system was installed with a 7-gal reservoir. To maintain the chemistry of the water as constant as possible, the entire system was made of glass or chemically stable plastic. The system is shown schematically in Figure 13.

Specimens were loaded in a test machine actuated by a two-way air cylinder. The essential feature of the system was the ability to hold a constant load over extended test periods.

The general procedure for fracture testing the 3 by 12-in. SEN-tensile specimens was as follows:

- a. Under a continuously rising load (10,000 psi/min.) determine the apparent critical stress intensity factor for each material condition when tested in air.
- b. Then, under constant load, test each material condition in the following manner:
  - (1) hold in room-temperature water, at 0.8 of the critical stress intensity ( $K_{IC}$ ) determined in step a.
  - (2) hold in room-temperature water at either 0.9 or 0.7  $K_{IC}$ , depending on the time to fracture in step b.(1), and
  - (3) hold in 165°F water, at the stress-intensity level selected in the preceding steps.

Experimental Results. When the titanium was exposed to water at room temperature at an applied stress intensity of 78 ksi-in.<sup>1/2</sup> (0.9  $K_{IC}$ ), failure did not occur in a test period of 80 hours. When specimens were instrumented for the detection of acoustic emission, no subcritical crack growth was observed in test periods of up to 20 hours in room-temperature water.

In 165°F water, on the other hand, the primary incubation time was 17,160 seconds (4.76 hours) at an applied stress intensity of 75 ksi-in.<sup>1/2</sup> (0.8  $K_{IC}$ ). When the stress intensity was increased to 85 ksi-in.<sup>1/2</sup> (0.9  $K_{IC}$ ) the primary incubation time was reduced to 2,640 seconds and failure occurred in approximately one hour.

When a modified microstructure at an applied stress intensity of 102 ksi-in.<sup>1/2</sup> (0.8  $K_{IC}$ ) was exposed to 165°F water, the primary incubation time was 3,360 seconds and failure occurred in approximately one hour. From Figure 14 it will be seen that the first large burst of stress waves occurred after 3340 sec at load. The stress waves for the first 70 sec at load are attributed to a creep phenomenon which is often observed at constant load. Thus, the primary incubation time at an applied stress intensity of 102 ksi-in.<sup>1/2</sup> was indicated to be 56 min. At 105 ksi-in.<sup>1/2</sup> (10:18:00 clock time), there was a large burst of stress waves which is believed to be the plane-strain, pop-in ( $K_{IC}$ ) instability. The time increment between stress waves after pop-in averaged 40 seconds.

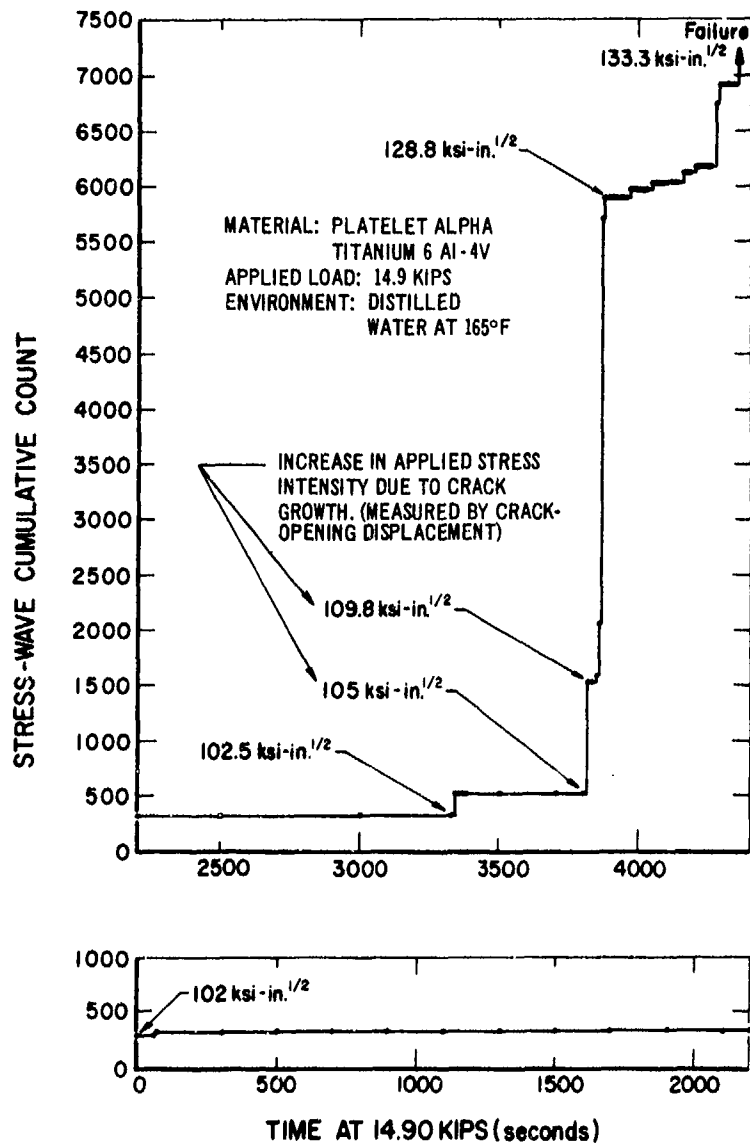


Figure 14. Subcritical Cracking in Platelet-Alpha 6Al-4V Titanium in 165°F, Circulating, Distilled Water (Specimen A2)

#### Strain-Aging Embrittlement

Strain aging has been investigated as a less-known mechanism of slow-crack growth in steel using acoustic emission<sup>(64)</sup>. In steel, strain-aging embrittlement occurs as the result of a combination of stress at the crack tip and elevated temperature in the range of 300 to 800°F<sup>(65)</sup>. Many service applications involve moderately elevated temperature, and in weld fabrication sometimes there are low-temperature stress-relieving operations or preheat-postheat operations where residual stress, time and temperature provide the necessary conditions for spontaneous strain aging and resulting slow crack growth.

The spontaneous strain aging embrittlement mechanism in steel is generally considered to involve the diffusion of carbon and/or nitrogen as a necessary condition. This has been experimentally confirmed in high-strength steels by Steigerwald and Hanna<sup>(66)</sup>. Their investigation concentrated on the kinetics of the process which allowed an activation energy to be determined. This was found to be best represented by the diffusivity of carbon in iron. Their investigation, however, did not allow a detailed description of the slow crack-growth process.

Acoustic emission, on the other hand, provided the means for following step-by-step the discontinuous movement of the crack front. The emissions provided information on both the size of the crack step<sup>(14,67)</sup> and the time interval between steps.

Compared to hydrogen embrittlement and stress-corrosion cracking, the embrittlement at elevated temperature was attended by relatively few movements of the crack front. Light and electron fractography confirmed that the large stress waves occurring during the periods of sustained load were associated with gross movement of the crack front. At the start of the holding period the time between stress waves ( $\Delta t_s$ ) was short, with  $\Delta t_s$  increasing with time at load until finally a steady-state condition was

reached where the secondary incubation time was relatively constant. After the D6aC heat treatment which effectively solutionized the carbides (1750 for 1/2 hr), the steady-state secondary incubation time was approximately 80 sec, as compared to 1650 sec in the heat-treat condition with massive carbides (1550°F for 1/4 hr). The crack growth rate also varied by a factor of 20 for the two heat-treat conditions.

The conclusions of this investigation<sup>(64)</sup> based on acoustic emission data and fracture surface measurements in single-edge-notched tensile specimens exposed to moderately elevated temperature (400 to 500°F) under sustained load were as follows:

1. In general, embrittlement at elevated temperatures is attended by relatively few movements of the crack front (as compared with hydrogen embrittlement).
2. Large stress waves in the sustained-load period were associated with a gross movement of the crack front as identified by both electron and light fractography.
3. Immediately after the sustained load was reached, the time between large stress waves was found to become increasingly longer. After this initial period, a steady-state condition evolved where the secondary incubation time (denoted as  $\Delta t_{ss}$ ) was relatively constant.
4. In microstructures associated with relatively small amounts of carbon in solid solution, the value of  $\Delta t_{ss}$  at 500°F was found to average 1650 sec. In the condition with a greater amount of carbon in solid solution (austenitized at 1750°F for 1/2 hr), the corresponding secondary incubation time was only 84 sec. The crack-growth rate also varied by a factor of 20;  $da/dt$  for the material with relatively little available carbon averaged 190  $\mu$ -in./min as compared with 3880  $\mu$ -in./min in the 1750/800 condition.
5. Secondary incubation times at 370 and 500°F for the condition most sensitive to embrittlement indicated that carbide precipitation was the embrittling mechanism.
6. A fracture mechanism is hypothesized based upon carbides precipitating on the large number of nucleation sites present at the crack tip. The basic premise is that the crack increment in the embrittled region is about equal in size to the theoretical crack-tip displacement.
7. Preliminary findings indicate that the embrittlement process is more temperature dependent than stress dependent. The crack growth rate during the slow-crack-growth process may be approximated by:

$$da/dt \approx 2v_c / \Delta t_s$$

where  $2v_c$  is the theoretical crack-tip displacement and  $\Delta t_s$  is the secondary incubation time. The secondary incubation time is highly dependent upon both test temperature and concentration of carbon in solid solution.

In a subsequent investigation<sup>(23)</sup>, center-notch panels were tested at various loading rates as well as single-edge-notch tensile specimens tested under sustained load.

The basic instrumentation system was comprised of accelerometers, a charge amplifier, a band-pass filter, a tape recorder, and an oscilloscope. Two accelerometers, one ranged to 0.1g sensitivity and one to 1.0g sensitivity, were employed during the testing of each specimen. The signal from the accelerometer was tape-recorded as raw, unfiltered data, and also displayed on an oscilloscope while tape recording. The signal from the tape recorder was filtered for display on the oscilloscope. Likewise, on subsequent playback of the tape-recorded raw data, the signals were filtered to eliminate extraneous noise. This was accomplished using a band-pass filter with upper and lower frequency separately variable in the range of 20 to 20,000 cps. For data playback, low and high cut-off frequencies of 5000 to 20,000 cps were used.

Based on this phase of the investigation, Gerberich<sup>(23)</sup> made the following observations:

1. Spontaneous strain-aging embrittlement occurs in 0.48 percent carbon D6aC steel at temperatures ranging from 400 to 600°F when tempered at 400°F.
2. This embrittlement occurs under both sustained-load and rising-load conditions with 0.02 to 1.0 in. of slow crack growth being observed in failure times ranging from 68 to 7230 sec.
3. It was found that the crack growth could be described by

$$da/dt \approx mK \sigma^n e^{-H/kT}$$

where

- $m$  is a constant of unity having dimensions of in.<sup>1/2</sup>/psi-sec
- $K$  is the applied stress-intensity level in psi-in.<sup>1/2</sup>
- $H$  is the activation energy for carbon diffusion in steel
- $T$  is the absolute temperature

4. Incorporation of this crack-growth rate equation into analyses for sustained-load and rising-load behavior allowed description of the time to failure from  $t_f = f(\sigma, d\sigma/dt, T, a)$ .

5. SWE and electron fractographic observations demonstrated that the growth process was discontinuous and predominantly intergranular, and that the average jump distance could be described by

$$l_j = \frac{l^* + d}{2}$$

where  $l^*$  is related to the theoretical crack tip displacement and  $d$  is the average grain size.

6. An activation energy, based upon the time between these crack jumps, was determined to be 21.0 kcal/mole which points to carbon clustering and/or carbide precipitation as the embrittlement mechanism.

#### Delayed Weld Cracking

Notvest appears to be the first to use stress-wave emission in the study of weld cracking. His study was concerned with the crack susceptibility of D6aC steel during and after welding. A piezoelectric transducer attached to the weld plate detected signals associated with weld cracking which then were amplified and tape recorded. Recording was continuous through the welding and post-heat cycles. With this technique, cracking was found to be associated with transformation reactions. The test welds were considered crack-free when adjustments in weld procedure eliminated the acoustic emission. The system used by Notvest was reported to be sensitive enough to detect the austenite to martensite transformation. Without post heat, acoustic crack indications were detected as soon as the weld zone cooled below 500°F. Increasing preheat only served to delay cracking until an equivalent temperature was reached in the cooling curve. If sufficient weld preheat and post heat was provided, the cooling curve for a weld could intersect the region of bainite transformation and no visible or acoustic crack indications were detected (68).

Jolly (69) has described the use of stress-wave emission as a means to detect weld cracking in stainless steel. The welding was done by tungsten inert-gas. It was found that crack growth could be detected during welding without interference from the noise of the welding arc. Jolly found that crack growth sometimes continued from weld solidification until the weld approached thermal equilibrium with the welded structure. He found the rate of emission from single-pass welds to be about an order of magnitude less than from multipass welds. The onset of emission was found to occur 20 to 45 seconds after the deposited weld metal began to solidify. Furthermore, the emission rate was found to increase as the weld cooled; the normalized emission rate reached a maximum at approximately 400°C, indicating that a major portion of the emission in the stainless steel welds was due to hot cracking.

Hartbower (70) evaluated weld cracking in HY-80 steel based on stress-wave emission. A multi-pass square-butt weld was prepared by the tungsten-arc process with deliberate incomplete penetration to assure cracking. There was no attempt to record stress-wave emission during welding. After welding, stress-wave activity was greatest in the first seven hours, with 7078 counts; in the following 24-hr period, there was an increase of only 29 counts and in the next 24-hr period there was only one additional count. This suggested that delayed cracking might be completed in approximately three days. However, it was noted that the gross cracking which occurred during welding may have largely stress relieved the weldment and, thus, shortened the period of delayed cracking.

An acoustic-emission study was undertaken for the U.S. Navy to quantify the duration of delayed weld cracking, particularly in 100-ksi yield strength materials (71). Cracking was induced by means of the cruciform. The cruciform has been discussed as a test for heat-affected zone cracking by Potest and Warner (72), Winterton and Nolan (73) and Rathbone, et al (74). All welding was done in a heavy-construction shop to assure that the findings of the investigation would be representative of shop practice and skills. Both manual welding with covered electrodes and semi-automatic welding with the metal-inert-gas (MIG) process were investigated. With the exception of controlled experiments with electrode deliberately exposed to moisture, the covered electrodes were stored in an oven at 250°F up to time of use, in accord with approved shop practice. Likewise, to assure that the findings would be meaningful in terms of heavy-construction shop practice, multipass welding was used together with controlled preheat and interpass temperature.

The objectives of the program were met by monitoring the weldments for acoustic emission during and immediately after welding, and for periods up to eighteen days. Stress-wave indications of delayed cracking were subsequently correlated with metallographic findings in selected weldments.

Materials and Welding Procedure. One of the materials investigated in the Navy study was a 100-ksi yield strength constructional alloy supplied in two composition types as shown in Table 4. The weldments were made with both covered electrode and semi-automatic MIG welding. The covered electrode was 3/16-in.-dia. MIL-12018, and the bare electrode used in MIG welding was 1/16-in. dia., MIL-TYPE B88. Shop procedure calls for a maximum energy input of 55,000 joules per linear inch of weld in thicknesses of 1/2-in. or greater. The welds were preheated to 150°F and the interpass temperature was held at approximately 250°F. Tack welding was not used; the weldments were dogged to the work table as shown in Figure 15. Welding was done in a systematic manner, always proceeding from a to b to c to d (see Figure 15) in accord with Army Ordnance procedure.

Table 4. Chemistry and Tensile Properties

Code		Composition (Weight percent)										Tension (ksi)		
		C	Mn	P	S	Si	Ni	Cr	Mo	V	Ti	Cu	FTY	FTU
B7748	B	.15	.33	.010	.019	.27	2.43	1.35	.29	.003	.001	.15	105	120
5P3524	P	.10	.79	.005	.010	.28	3.36	.90	.41	.09	-	-	110	124



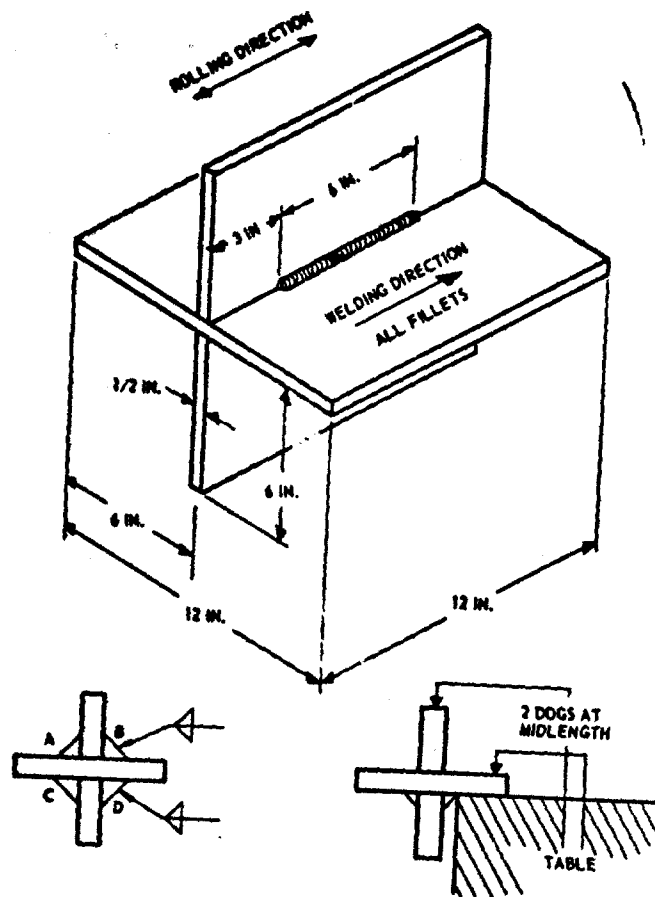


Figure 15. Typical Cruciform Details and Clamping Arrangement.

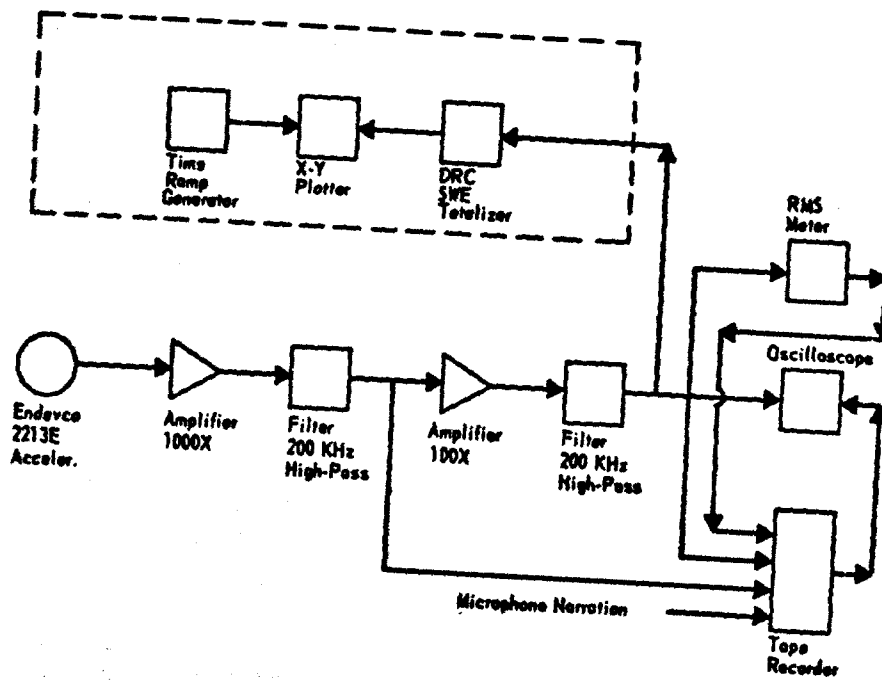


Figure 16. SWAT Instrumentation Used in Monitoring Cracking in the Fabrication Shop.

Acoustic Emission During and Immediately After Welding. One objective of this study was to determine the feasibility of using acoustic emission as a supplementary nondestructive inspection method to detect cracking during welding. For this purpose the system shown in Figure 16 was used. In general, the first weldment to be completed on a given day was monitored, starting with the last weld pass and continuing for approximately two hours after the completion of welding. In the case of the cruciforms welded with covered electrode, data were collected from the as-deposited joint, and then the slag was removed from the weld and monitoring continued for the remainder of the two-hour period.

For those cruciforms welded with covered electrode, during welding and for the first few minutes after welding there was a very large stress-wave emission (SWE) count rate which was found to be in large part the result of cracking slag. For example, as shown in Figure 17, in the first 5-minutes after welding was completed, the cruciform generated over 1,500,000 counts; whereas, on removal of the slag, the count in the next 5-minute period increased by only 70,000. The data as seen on an oscilloscope before and after removing the slag were typical of metal cracking. Thus, slag cracking was found to preclude the use of acoustic emission as an inspection method for cracking during welding where covered electrode is used. After this fact had been established, the slag was removed immediately after welding. In the MIG welds, the data recorded during and immediately after completing the last weld pass is assumed to be the combined result of martensite transformation<sup>(68)</sup> and/or short-time cold cracking.

Figure 18 shows the data collected from the last two passes in MIG welding a 1-in.-thick cruciform. Note that while the second pass was being deposited (200 KHz high-pass filtering) approximately 2,500,000 counts were recorded over a period of 30 seconds. The signals observed on the oscilloscope were characteristic of stress-wave emission; few electrical disturbances were observed with 200 KHz high-pass filtering. When the weld pass was completed, the filtering was dropped to 100 KHz. For 22.5 seconds after the weld pass was completed, the stress-wave-emission rate was very high; this was followed by an abrupt reduction in the rate of stress-wave emission.

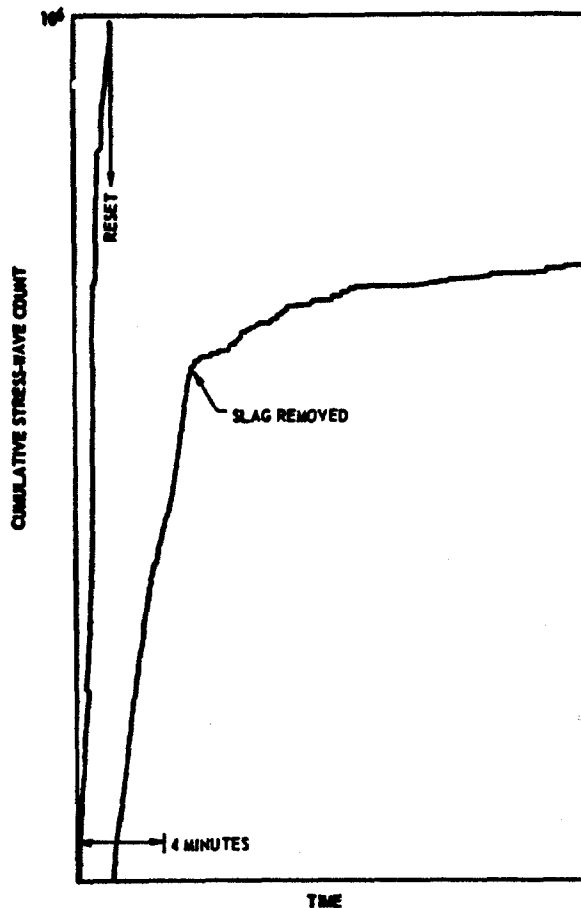
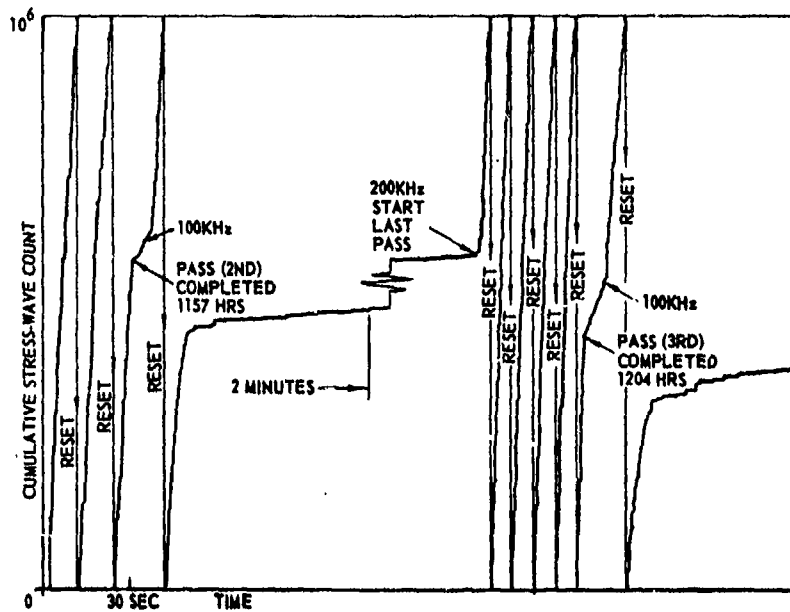


Figure 17. Cumulative Stress Wave Count Before and After Slag Removal

Figure 18, Cumulative Stress-Wave Count During and Immediately After MIG-Welding the Heat-B Cruciform.



Approximately 5 minutes after completing the 2nd pass, the 3rd pass was started. Again, the filter was set at 200 KHz during welding; approximately 5,000,000 counts were recorded over a period of 35 seconds while the 3rd pass was being deposited. The filter was then dropped to 100 KHz; for 21.5 seconds after the weld was completed, the stress-wave emission rate continued to be very high. This again was followed by an abrupt decrease in the rate of stress-wave emission.

From Table 5, when heat B was welded with the MIG process, in the period between 5 and 10 minutes after the weld was completed, the average SWE count-rate was 14,000 per minute, and in the 10 to 15 minute period, the count rate was 7,400 per minute.

Table 5. Summary of Stress-Wave Count Rate Between 5 & 15 Minutes After Welding

Date	Plate		Electrode	Joint	Test	Time After Welding (Minutes)	SWE Count	
	Thick.	Code					Increase (count)	Rate (SWE/min.)
20 Aug	1-in.	B	bare	IP (a)	#26	5-10	70,000	14,000
						10-15	37,000	7,400
27 Aug	1-in.	P	bare	IP	#27	5-10	157,000	31,400
						10-15	43,000	8,600
10 Sept	2-in.	P	covered	IP	#30	5-10	232,500	46,500
						10-15	78,000	15,600
17 Sept	1-in.	P	covered	IP	#32	5-10	223,000	44,600
						10-15	90,000	18,000

(a) Incomplete-penetration fillet weld

When heat P was welded with the MIG process, in the 5-10 minute period after welding was completed, the average SWE count rate was 31,400 per minute, and between 10 and 15 minutes, the count rate was 8,600 per minute.

Figure 19 shows the stress-wave activity recorded as soon as the slag was removed from the last pass of 2-in. heat P welder with covered electrode. Note that the activity was high at first but then decreased rapidly over a period of approximately 15 minutes. Thereafter, as seen in Figure 20, there were only occasional bursts of stress-wave activity. In the second and third hour of recording, occasional bursts of stress-wave emission were evident, with the cracking continuing at a more or less constant rate over the two-hour period.

From Table 5, in the period between 5 and 10 minutes after completing the last fillet weld, the average SWE count rate was 46,500 per minute, and in the 10 to 15-minute period, the count rate was 15,600 per minute. Cruciform No. 32, prepared from 1-in.-thick heat P, generated a count rate of 44,600 per minute between 5 and 10 minutes and 13,000 per minute between 10 and 15 minutes after welding. Thus, the stress-wave activity immediately after welding was almost the same for the two weldment thicknesses.

**Delayed Crack Detection.** After two to three hours of continuous monitoring immediately after welding, the cruciforms were moved from the fabrication site to the Aerojet plant in Sacramento, a distance of approximately 75 miles. During this period, no data were taken, the time lost traveling between the fabrication site and setting up in the Aerojet plant was generally about four hours.

Upon return to the Aerojet plant, the program plan called for continuous monitoring from 1600 hours Thursday until 0800 hours on Monday, a total of 88 hours. The system used in this data collection is shown in Figure 21. Note that the filter level used after welding was finished was much lower than that used during welding (see Figure 16).

Figure 22, a plot of cumulative stress-wave count versus time, is typical of these data; the material in Figure 22 is 2-in.-thick plate welded with a 12018 electrode. Note that with delayed cracking, the data were predominantly burst type. The data in Figure 22 are from cruciform No. 30; see Figures 19 and 20 for the data recorded immediately after welding.

In addition to being displayed on an X-Y plotter, the data were printed on a strip chart showing the number of counts recorded in each 1-minute period. Table 6 illustrates the detailed information that can be obtained from the acoustic emission strip chart. The time between stress-wave bursts ( $\Delta T$ ) provides a measure of crack-incubation time. In that the electronic-counter system integrates the number of stress waves and the size of the stress wave, the rate of stress-wave emission (number of counts per minute) is considered to be an indication of the crack-growth rate. The cumulative (total) count provides an overall indication of the amount of cracking. The time over which the stress wave activity occurs gives the duration of cold cracking. In Table 6, note the large number of occurrences in the first 10 hours and long intervals between bursts toward the end of the data collection period (for purposes of illustration, only the data in the first 10 hours and after 350 hours are tabulated here). To summarize the strip-chart data, tables were prepared to show the activity occurring in successive 10-hour periods.

Table 7 summarizes the data presented in Table 6, based on count rates of 100 and 500 per minute. A change in count rate is tantamount to changing the sensitivity of the system; i.e., if counts of 500 or greater are used, the smallest increments of crack growth are disregarded. Until a thorough metallographic investigation is made of the extent of actual cracking in each weldment, the size of burst that is associated with "meaningful" crack extension is not known. Note, from Table 7, that the cruciform prepared from heat B using stick electrode generated a much higher count than the cruciform prepared from heat P regardless of the count-rate used.

To eliminate the complication of different data-collection periods, the average count per burst was calculated on the basis of counts of 500 per minute or greater. Table 8 shows that the average count per burst was remarkably constant; this is attributed to either a characteristic of the system or a characteristic of the type of cracking. If the latter is correct, this would indicate that each of the conditions and materials tested generated the same size of crack increment per burst.

**Correlation of Acoustic Emission and the Extent of Cracking.** The prime objective of the Navy study was to determine quantitatively the duration of delayed cracking in the 100-ksi yield strength weldments as a function of constraint and welding conditions. The study showed that stress-wave emission occurred in some weldments throughout the entire period of investigation, and this appeared to be irrespective of constraint or welding process. Without metallographic examination, a question remained as to the size of the defect source generating the stress-wave emission. Moreover, with more than one weld in the cruciform, there could have been multiple stress-wave sources which would preclude meaningful incubation-time measurements. In other words, the high count rate observed during the first several hours after welding could have been the result of any one or a combination of the following sources: (1) discontinuous growth of a few large cracks, (2) grain-by-grain cracking along an enlarging crack envelope and/or (3) a myriad of small cracks. Moreover, different cracking mechanisms may have been involved while the weldment was cooling as opposed to after the weldment was cold. While the weldment was hot and cooling, micro-cracking may have been occurring in the weld metal over the entire length of the deposit, and after the weld was cold the stress-wave emission may have been from one or more cracks in the weld and/or HAZ. Also, with high amplification and sensitivity in the SWAT system, the count rate observed during welding, and continuing for a short time after the welding, may have been, at least in part, generated by the martensite transformation<sup>(68)</sup>.

Two weldments were selected for metallographic examination. The sectioning was in accord with the procedure used by Army Ordnance<sup>(72)</sup> except that the weldments were not stress relieved and the etchant had to be modified. Two percent nital was used. The weldments selected were cruciforms 31 (heat B) and 32 (heat P); these were 1-in. thick, welded with covered electrode and monitored for 440 hours (approx. 18 days). Based on macro-examination, weldment 31 with over 200,000 counts was found to be cracked over the entire length of the d weld. Based on a decreasing depth of crack in each successive section, the

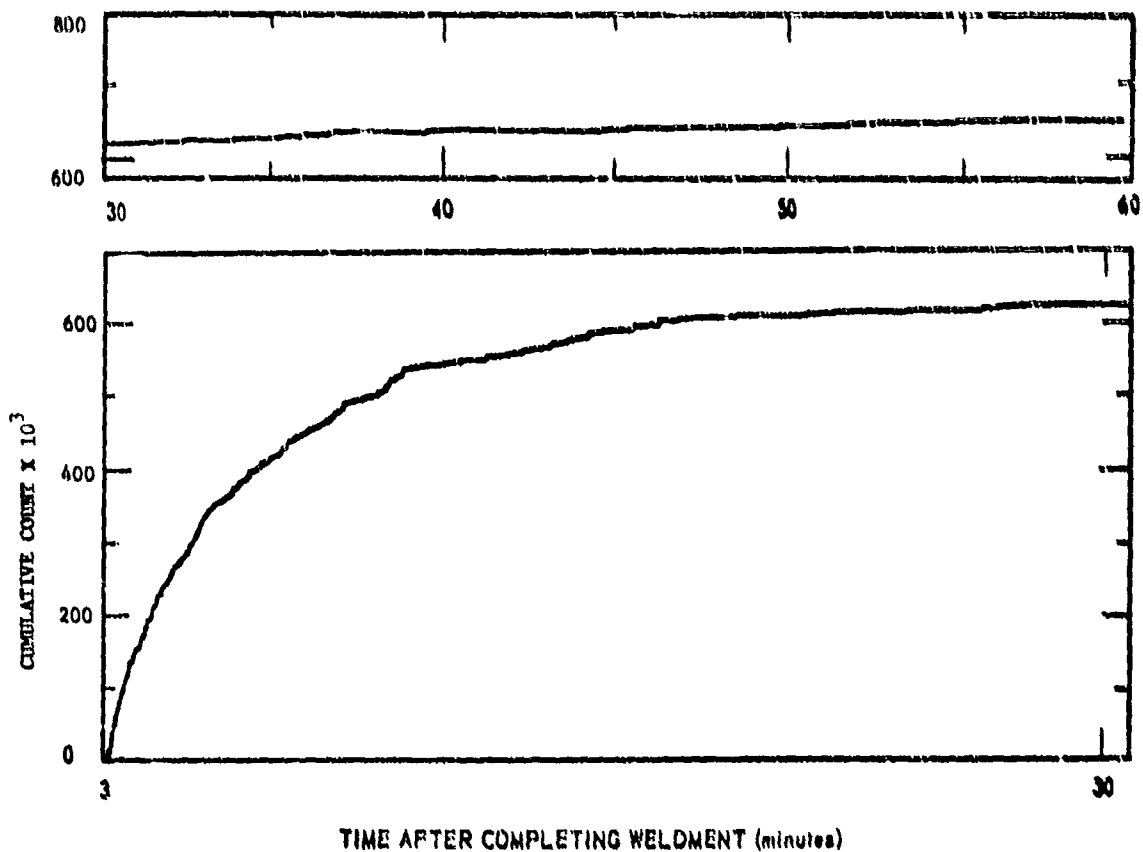


Figure 19. Cumulative Stress Wave Count in the First Hour After Welding the Heat P Cruciform with Covered Electrode (incomplete penetration cruciform slag removed)

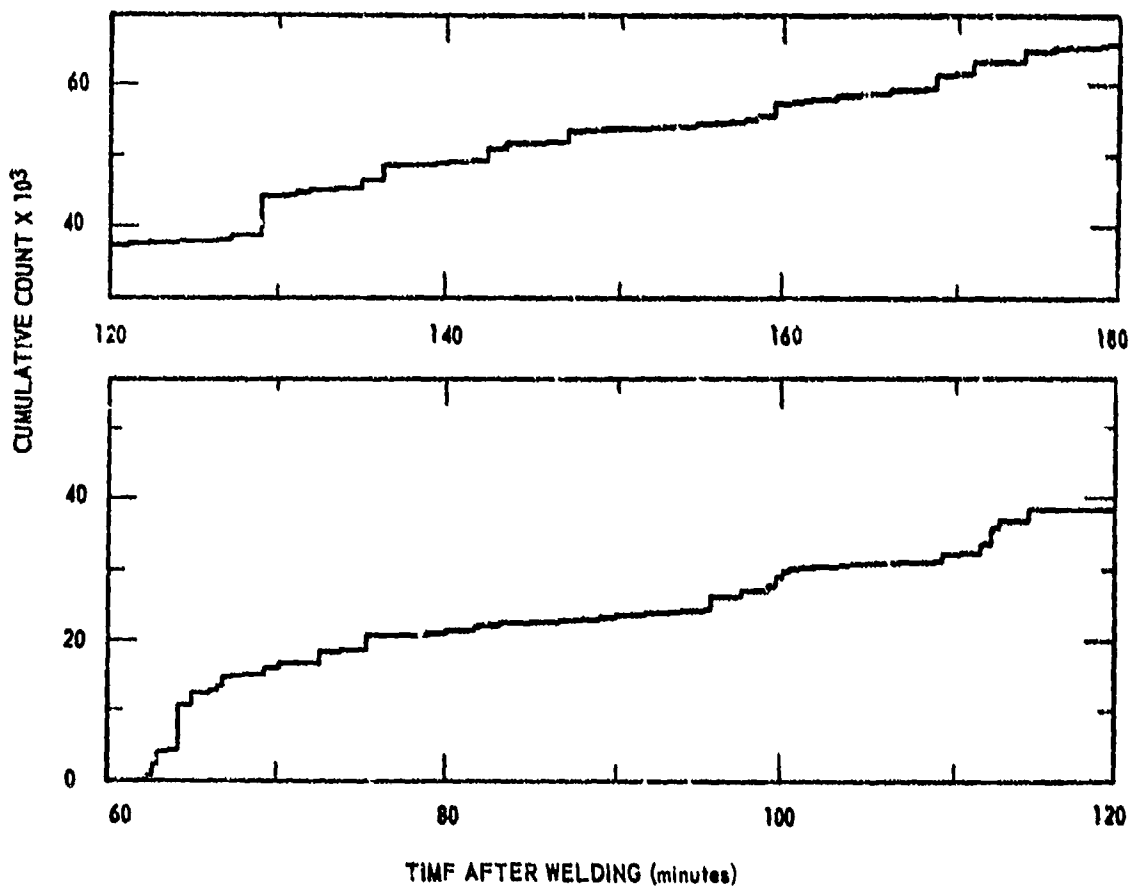


Figure 20. Cumulative Stress Wave Count in the Second and Third Hour After Welding Heat P with Covered Electrode (same cruciform as Fig. 19).

TABLE 6 - 1-IN. PLATE WELDED WITH 12018 COVERED ELECTRODE  
INCOMPLETE-PENETRATION FILLETS

DATE 1970	CODE B, HEAT B7748				CODE P, HEAT 5P3524			
	TIME		EMISSION		TIME		EMISSION	
	CLOCK	$\Delta T$	RATE	TOTAL	CLOCK	$\Delta T$	RATE	TOTAL
17 Sept					1002			
	1117							
	1440							
		Welding Complete						
		System On						
					1440			
					1450		147	147
					1458	8	130	277
					1500	2	100	377
					1501	1	779	1156
					1508	7	1485	2641
					1511	3	660	3301
	1512		1293	1293	1512	1	894	4195
					1513	1	1656	5851
					1514	1	237	6088
	1518	6	5242	6535	1518	4	2939	9027
					1519	1	357	9384
					1524	5	754	10138
					1526	2	130	268
	1527	9	145	6680	1544	18	190	458
					1549	5	2581	13039
	1550	23	722	7402	1551	2	685	724
					1552	1	2307	16031
	1553	3	1163	8565	1553	1	1396	17427
					1600	7	480	907
					1604	4	3199	21106
					1606	2	1980	23086
	1608	15	230	8795	1608	2	253	339
	1610	2	1089	9884	1610	2	8516	31855
	1611	1	2949	12833	1612	2	139	994
					1614	2	188	32182
	1614	3	6692	19525	1622	8	368	550
					1628	6	213	763
	1625	11	117	19642	1632	4	161	32924
	1630	5	102	19744	1636	4	1046	33970
	1634	4	12208	31952	1645	9	432	34402
					1651	6	3764	38166
	1651	17	1608	33560	1701	10	100	266
					1735	34	157	423
					1739	4	797	39220
					1744	5	1199	40419
					1747	3	303	722
					1808	21	367	41089
	1820	89	894	34454	1820	12	175	264
					1827	7	306	570
	1841	21	142	34596	1856	29	2394	43964
	1846	5	157	34753	1838	2	180	44144
					1859	1	1008	45152
					1902	3	1568	46720
	1987	21	410	35163	1907	5	724	47444
					1918	11	620	48064
	1942	35	1510	36673	1927	9	1199	49263
	1950	8	972	37645	2002	10 hrs after welding		
					2019	52	688	49951
	2032	42	182	37747				
	2055	3	687	39434	2044	11	669	52564
	2047	12	6990	45424	2105	21	212	776
	2117	- 10 hrs after weld completion						

TABLE 6 (Continued)

DATE 1970	CODE B, HEAT B7748				CODE P, HEAT 5P3524			
	TIME		EMISSION		TIME		EMISSION	
	CLOCK	$\Delta T$	RATE	TOTAL	CLOCK	$\Delta T$	RATE	TOTAL
2 Oct	0117	- 350 hrs after welding			0002	- 350 hrs after welding		
	1117	- 360 hrs after welding			1002	- 360 hrs after welding		
	1308	1518	168	875	1730	1308	109	811
	1839	331	783	323658	1737	7	152	963
	2117	- 370 hrs after welding			2002	- 370 hrs after welding		
3 Oct	0215	456	634	324292	0602	- 380 hrs after welding		
	0216	1	3755	328047				
	0717	- 380 hrs after welding			1602	- 390 hrs after welding		
	1105	529	154	201	1952	135	176	100139
	1111	6	103	304	2028	36	727	866
	1410	179	177	481				
	1717	- 390 hrs after welding						
	2012	362	140	621				
	2056	44	104	725				
	4 Oct	0055	239	126	851	0202	- 400 hrs after welding	
0254		119	1881	330732				
0317		- 400 hrs after welding			1202	- 410 hrs after welding		
0507		133	136	868	1501	1113	125	991
0512		5	121	989	2202	- 420 hrs after welding		
0520		8	125	331114				
1301		461	472	586				
1317		- 410 hrs after welding						
1506		125	192	778				
2317		- 420 hrs after welding						
5 Oct	0128	622	144	331922	0812	- 430 hrs after welding		
	0917	- 430 hrs after welding			0917	1096	305	101296
					0924		121	417
					0932		227	644
					0940		109	753
	1010	System Off			1010	System Off		
	1917	- 440 hrs after welding			1802	- 440 hrs after welding		

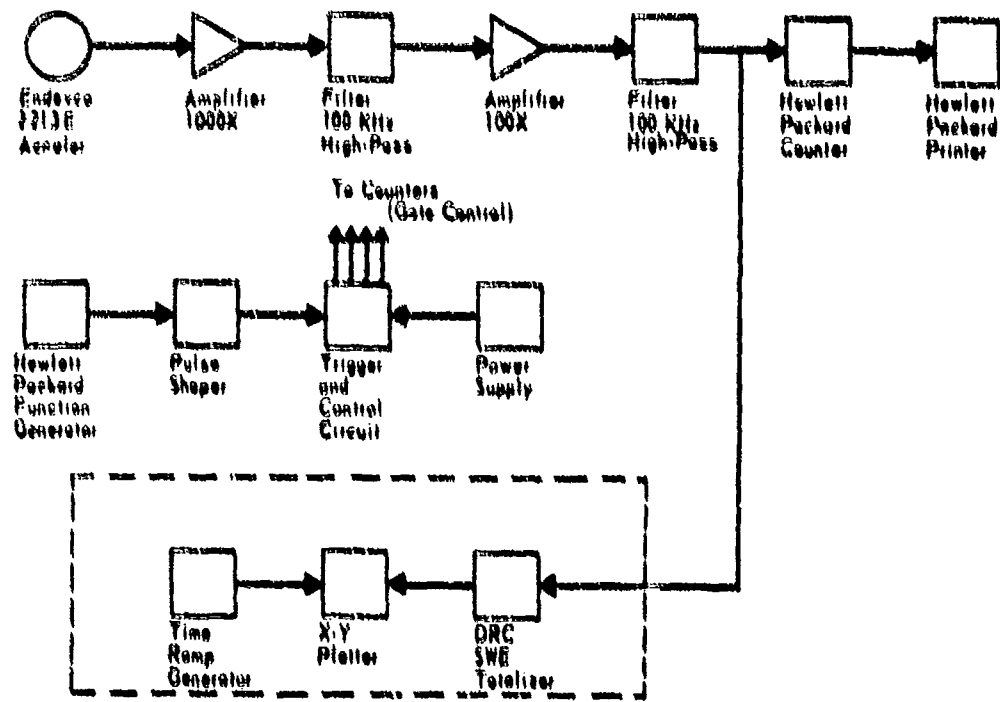


Figure 31. SHAT Instrumentation Used in Monitoring Delayed Cracking at Aerojet.

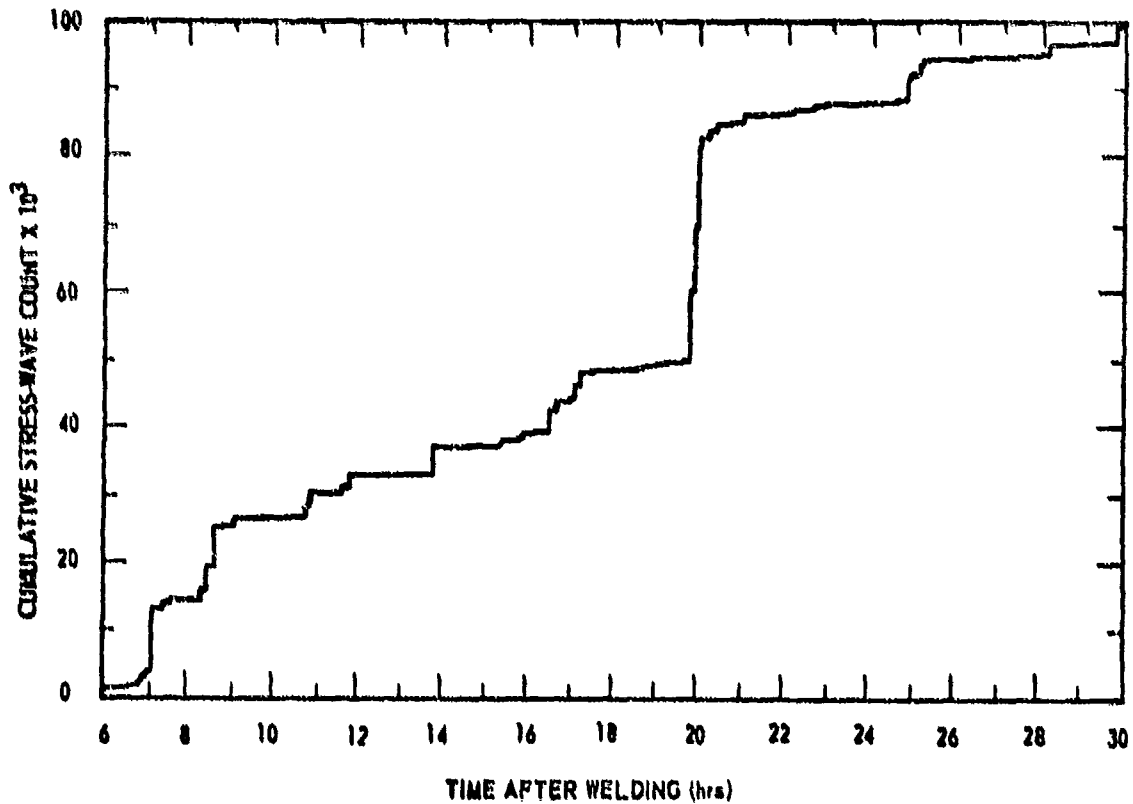


Figure 32. Cumulative Stress Wave Count from 6 to 30 h after Welding Next P with Covered Electrode.



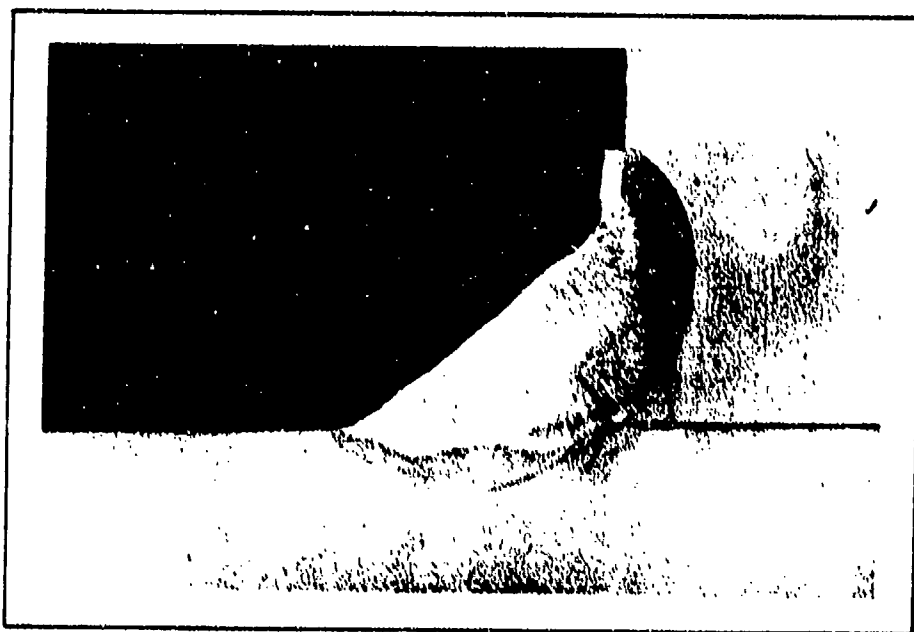
Table 7. Stress-Wave Emission from 1-in. 100-ksi Yield Strength Cruciforms Welded with 12018 Covered Electrode.

Period (hr)	BASED ON A RATE OF 500 COUNTS PER MINUTE OR GREATER				BASED ON A RATE OF 100 COUNTS PER MINUTE OR GREATER			
	Plate B		Plate F		Plate B		Plate F	
	No. Bursts	SWE Count	No. Bursts	SWE Count	No. Bursts	SWE Count	No. Bursts	SWE Count
10-20	2	1,700	9	21,637	4	2,279	14	22,892
20-30	19	29,313	7	15,407	50	36,319	16	17,307
30-40	8	14,702	1	1,641	28	18,715	4	2,133
40-50	5	86,791	0	0	18	90,197	0	0
50-60	4	5,798	0	0	6	6,106	0	0
60-70	6	17,109	0	0	14	19,037	0	0
70-80	0	0	0	0	7	1,331	0	0
80-90	1	508	0	0	5	1,202	0	0
90-100	4	20,395	1	1,050	10	22,048	1	1,050
100-110	2	7,363	0	0	6	8,469	0	0
110-120	2	1,034	0	0	3	1,234	0	0
120-130	8	25,632	0	0	15	27,099	1	200
130-140	0	0	0	0	0	0	0	0
140-150	5	3,242	1	956	18	5,593	1	956
150-160	0	0	0	0	5	1,339	0	0
160-170	1	1,334	0	0	3	1,846	0	0
170-180	2	2,763	0	0	4	3,339	1	111
180-190	0	0	0	0	3	938	0	0
190-200	1	933	0	0	1	933	0	0
200-210	1	881	0	0	3	1,311	0	0
210-220	7	13,272	0	0	8	13,612	0	0
220-230	1	1,334	0	0	7	3,010	0	0
230-240	0	0	0	0	2	333	0	0
240-250	0	0	0	0	0	0	0	0
250-260	0	0	0	0	0	0	0	0
260-270	0	0	0	0	0	0	3	303
270-280	2	1,911	0	0	9	3,738	10	1,838
280-290	2	3,084	0	0	5	3,997	5	946
290-300	0	0	0	0	3	333	0	0
300-310	1	769	0	0	3	1,481	0	0
310-320	0	0	1	604	0	0	2	803
320-330	1	668	0	0	1	668	0	0
330-340	0	0	0	0	2	612	0	0
340-350	0	0	0	0	0	0	9	1,420
350-360	0	0	0	0	1	168	0	0
360-370	1	783	0	0	1	783	2	261
370-380	2	4,389	0	0	2	4,389	0	0
380-390	0	0	0	0	3	431	0	0
390-400	1	1,881	1	727	4	2,231	2	903
400-410	0	0	0	0	4	834	0	0
410-420	0	0	0	0	1	192	1	123
420-430	0	0	0	0	1	144	0	0
430-440	0	0	0	0	0	0	4	762
Total	89	248,289	21	42,112	260	286,360	76	52,490

Table 8. Number of Bursts, Total Count (Bursts of 500 or More Counts), and Average Count per Burst

Weldment Thick.	Process	Plate B		Plate F	
		No. Bursts	SWE Count	No. Bursts	SWE Count
1-in.	Stick	89	248,289	21	42,112
		Avg.	2,790	Avg.	2,000
2-in.	Stick	30	58,188	27	54,052
		Avg.	1,980	Avg.	2,000
1-in.	MIG	68	111,573	97	169,323
		Avg.	1,640	Avg.	1,750
2-in.	MIG	35	57,410	29	40,801
		Avg.	1,640	Avg.	1,410

cracking began at the starting end of the d weld. Figure 23 shows the crack at approximately midlength of the d weld (Section 31-D4). Weldment 32, on the other hand, with approximately 40,000 counts was found to be cracked only in the section nearest the finishing end of the d weld. Figure 24 shows microcracking (250X magnification) in the next to the last section (32-D5). Micro-examination revealed crack initiation in several of the welds examined, i.e., welds a, b and c, as well as d starting at the root of the incomplete-penetration fillet welds.



31-D4

Figure 23. D-Weld Cracking at Approx Mid Length of Cruciform No. 31  
(4X Magnification)



32-D5 MAG. 250X

Figure 24. Microcracking in Section 5 of Cruciform No. 32.

Acoustic Emission from Welded Aluminum

One characteristic of acoustic emission is that once a given stress, or load, has been applied, and the acoustic emission associated with the resulting creep has ceased, in the absence of a subcritical-crack-growth mechanism, no more emission will occur until this stress level is exceeded. If the load is removed, and then reapplied, no emission occurs until the previous load has been exceeded. This is the so-called Kaiser effect.

Figure 25 is a comparison of data from two 2219 longitudinally welded, unnotched, tension specimens. Note that an increase in stress-wave activity is indicated in the range of 5 to 10 kips load on the first application of load. When the specimens were loaded for a second time, the activity in this range completely disappeared. This behavior is consistent with the Kaiser effect.

One of the specimens (No. 27 shown in Figure 25) was subjected to a third load cycle. For the third cycle, a model 2213 accelerometer was spring mounted on the specimen. The data were filtered at a band width of 60 KHz with approximately the same gain as in the previous cycles, viz., 100 db. The following tabulation of stress-wave-count data illustrates the marked drop in count in each successive cycle at a given load and the marked increase in count just before failure in the 3rd cycle (the precursor of fracture):

Specimen	Cycle	Date	Load	Count	Max. Load	Total Count
27	1	11-3-70	36.85	134,000(a)	36.85	134,000(a)
	2	11-3-70	36.85	3,200(b)	38.30	3,500(b)
	3	9-29-71	36.85	730(b)	40.65	610,000(c)

- (a) High count resulting largely from the peak in stress-wave activity at 10 kips
- (b) Kaiser effect
- (c) Precursor of failure

Figure 26 shows the precursor as seen in the 3rd cycle; the specimen fractured at 40 kips. Note that as a result of the Kaiser effect, the stress-wave activity did not begin until about 38 kips, the maximum load of the 2nd cycle.

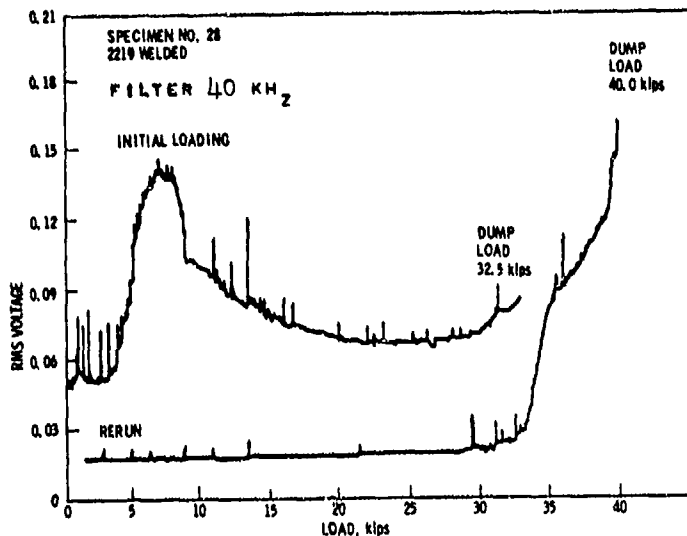
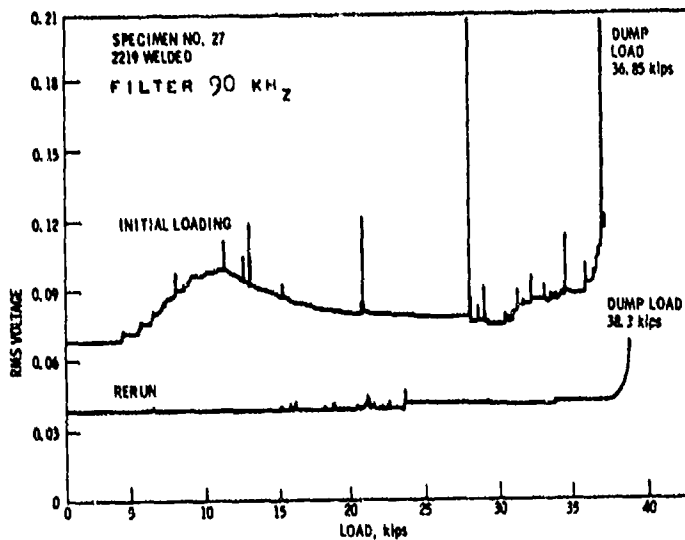


Figure 25

Kaiser Effect in Longitudinally Welded, Unnotched, Tension Specimen.

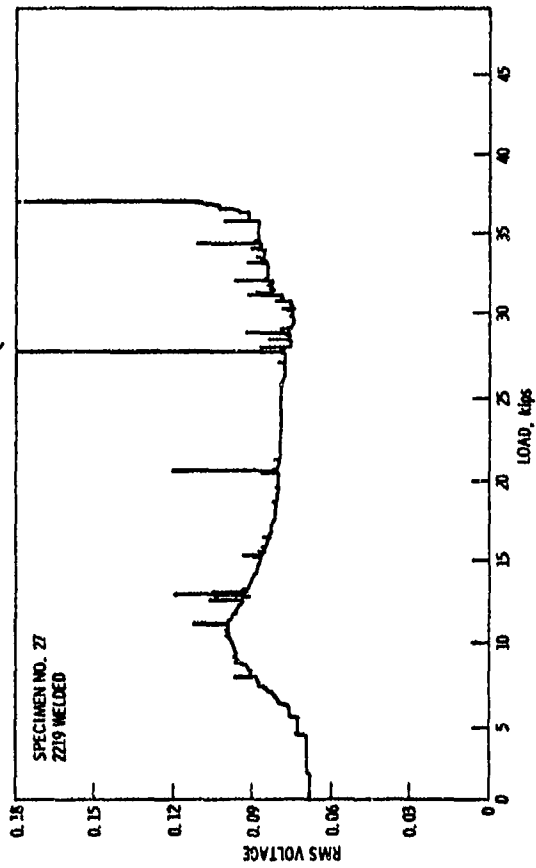
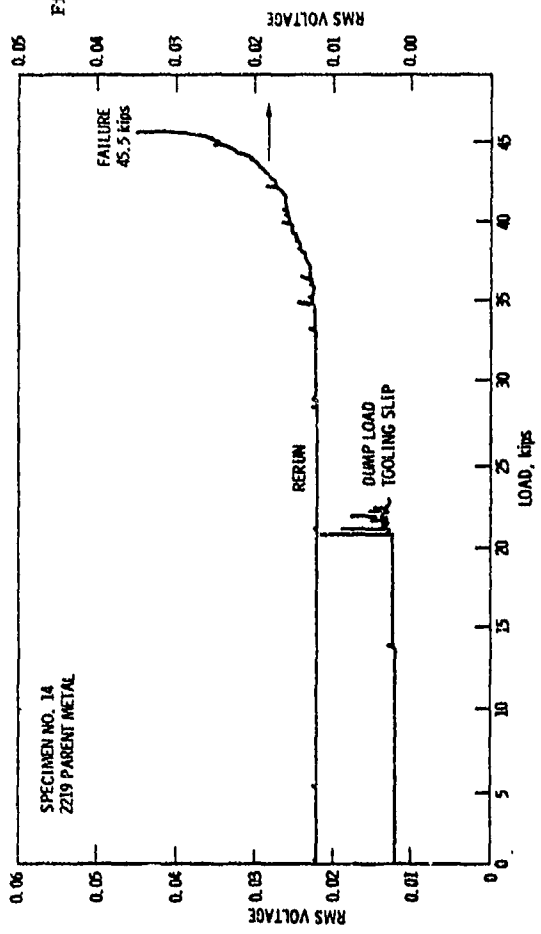


Figure 27. Comparison of Welded and Unwelded, Unnotched Specimens Tested at Room Temperature.

Figure 26. Kaiser Effect in Third Cycle of Specimen No. 27 (second cycle to 38 kips).

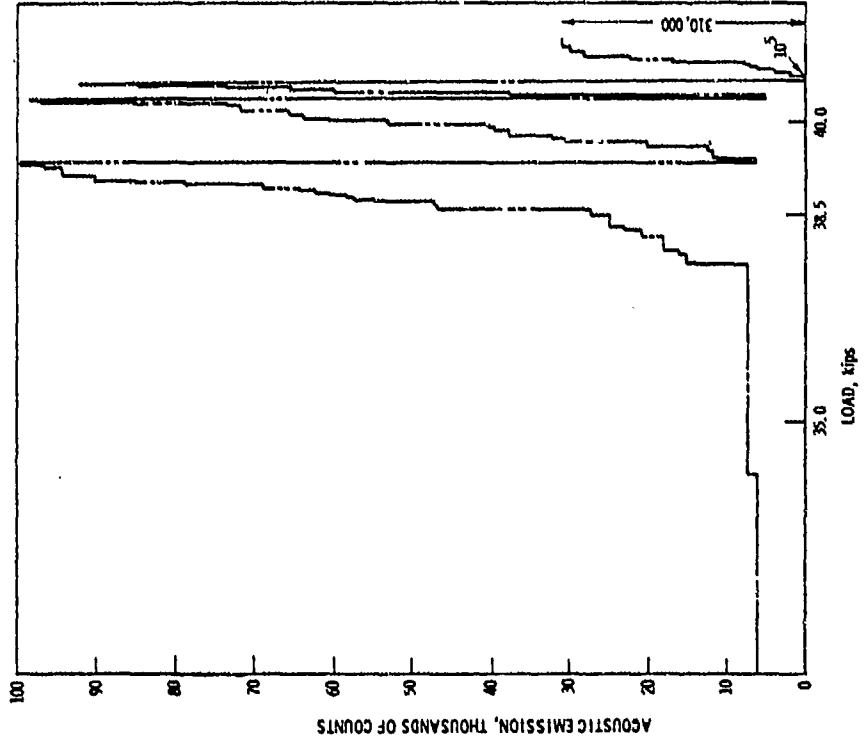


Figure 27 is a comparison of unnotched, welded and unwelded, room-temperature tests. Note that the parent-metal specimen showed virtually no stress-wave activity until there was a tooling problem, at which time the specimen was unloaded, the situation corrected and then reloaded. The fact that there was an increase in stress-wave activity at about 10 kips in welded specimens but not in unwelded (parent-metal) specimens suggests that the change in stress wave activity at low load on 2nd loading could be the relief of residual welding stresses rather than the Kaiser effect.

A comparison of data from precracked specimens also indicated an increase in stress-wave activity in the range of 5 to 10 kips load. These were part-through-crack (PTC), longitudinally welded, tension specimens of 2219 aluminum. From Figure 28 note that when the filter level was reduced from 90 KHz to 40 KHz, the evidence of activity at 10 kips was markedly increased, and when the specimen was loaded a second time, the activity completely disappeared. This behavior is consistent both with the Kaiser effect as well as with the behavior that would be expected if the first load cycle had produced a stress relief.

Effect of Filter Level. Band-pass filtering has long been recognized as an essential part of any acoustic-emission detection system. Variations in machine or environmental noise from day to day sometimes necessitates changes in the filtering level; however, an attempt is made to minimize such changes in the filtering level because of the effect of filter level on the cumulative count. Consider, for example, the following data for unnotched, 2219-T87 longitudinally welded, tension specimens No. 27 and 28, and also 2219-T87, longitudinally welded, PTC-tension specimens No. 29 and 30.

Specimen No.	Test Temperature (°F)	High-Pass Filter KHz	Trigger Level (set Point)	Cumulative SWE Count
27	75	90 + 90	8.5	$0.13 \times 10^6$
28	75	40 + 40	5.0	$2.02 \times 10^6$
29	75	90 + 90	8.0	$0.08 \times 10^6$
30	75	40 + 40	5.0	$1.18 \times 10^6$

As seen from these data, reducing the filter level from 90 KHz to 40 KHz increased the cumulative count by more than an order of magnitude. The difference in set point was an adjustment in signal gain in the Dunegan system, and not a change in trigger level. In the Dunegan system, the trigger level is fixed at 0.707 volt. When filtering at 40 KHz, more background noise was detected and therefore less gain was required to bring the signal up to a level just under the 0.707-volt trigger level. Figure 29 schematically illustrates this condition. With the quieter system provided by 90 KHz filtering, a higher set point (gain) was required to bring the signal up to a level just under the 0.707-volt trigger level.

#### CONTINUOUS IN-SERVICE SURVEILLANCE

##### Acoustic Emission as a Precursor of Fracture

Office of Naval Research Study<sup>(19)</sup>. From single-edge-notched tensile tests of 7075-T6 aluminum, HY-80 and HY-150 constructional steels, D6aC low-alloy high-strength steel, and 6Al-4V titanium, it was found that stress-wave amplitude and repetition rate are recognizable, reproducible stress-wave characteristics which can be used as precursors to crack instability. SEN tensile tests of 7075-T6 aluminum involving a range of widths, thicknesses and crack depths all showed essentially the same stress-wave behavior. However, marked differences in stress-wave characteristics were observed as a function of material toughness. In highly tough HY-80, HY-150, D6aC (austenitized at 1750°F and tempered at 1100°F), and 6Al-4V (aged at 1250°F) where there was no detectable pop-in by either crack-opening-displacement gage or stress-wave emission, the failure process was identified by an increasing stress-wave count, starting at approximately the load corresponding to deviation from linearity in the crack-opening-displacement chart. In the more brittle D6aC steel (austenitized at 1750°F and tempered at 600°F) and 7075-T6 aluminum, plane-strain instability was identified by an order-of-magnitude increase in stress-wave amplitude and the final failure process was identified by an increasing stress-wave count, generally starting at approximately the plane-strain pop-in. In the extreme embrittlement of D6aC austenitized at 1550°F, fracture occurred directly from the plane-strain pop-in with only two or three stress waves before the final unstable burst of crack growth. Subsequent studies at Aerojet showed that acoustic-emission can be used to not only presage plane-stress instability but also plane-strain instability.

Acoustic Emission as a Precursor of Plane-Strain Instability. Much of the materials testing done at Aerojet using acoustic emission for monitoring crack growth has been at room or elevated temperature. One observation common to all the studies, regardless of the material investigated, was that the stress-wave-emission signals have characteristics which serve as a precursor of failure; viz., (1) a marked increase of the amplitude of the signals as observed in real time on an oscilloscope, (2) a marked increase in the signal repetition rate (count per second) and (3) a marked increase in the slope of the cumulative count-versus-load plot.

In the Office of Naval Research (ONR) study, the plane-strain ( $K_{Ic}$ ) instability was identified by acoustic emission but the acoustic emission monitoring system used did not have sufficient amplification and/or sensitivity to detect a precursor for the  $K_{Ic}$  instability. However, in a more recent study for the Advanced Research Projects Agency<sup>(75)</sup>, an improved acoustic-emission detection system demonstrated that acoustic emission can also provide warning of the plane-strain ( $K_{Ic}$ ) instability.

In the ONR study, the stress-wave instrumentation utilized an accelerometer and tape recorder. The signal from the accelerometer was tape recorded as unfiltered data. On subsequent playback of the tape recording, a filter was used to eliminate noise below 10,000 cps. The tape recorder used for this

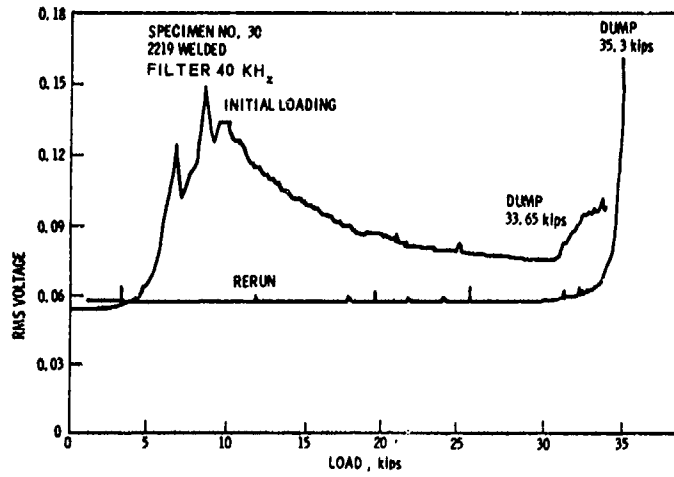
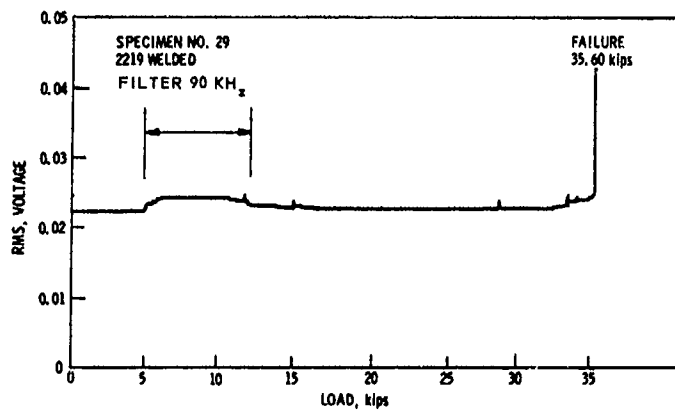


Figure 28. Kaiser Effect in Longitudinally Welded PTC-Tension Specimens.

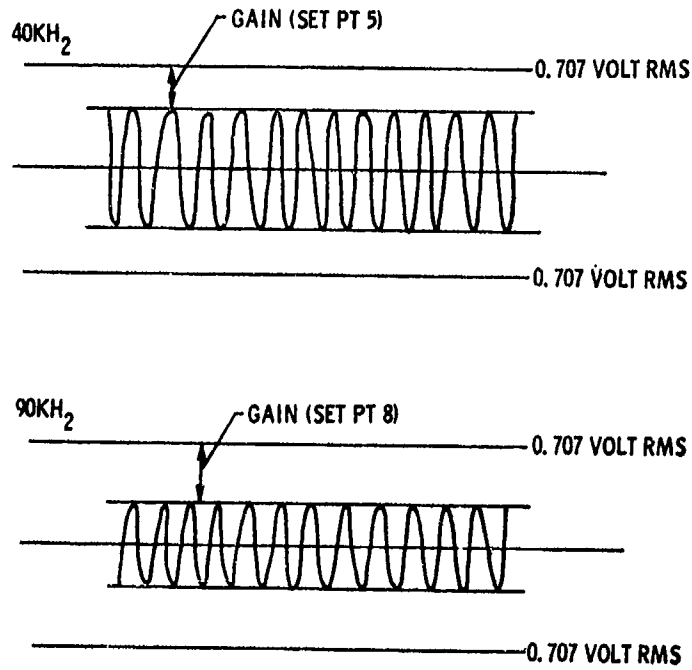


Figure 29. Adjustment in Gain to Compensate for Variations in Background Noise (trigger level fixed at 1 volt).

work was a portable, seven-track, instrumentation recorder (IRIG track dimensions) with frequency response in the direct-record-reproduce system of 50 to 40,000 cps at 15 ips and 50 to 20,000 cps at 7-1/2 ips tape speed. Data analysis was accomplished by tape playback through an oscilloscope and by re-recording on an oscillograph. The latter had the advantage of providing both a permanent record and time-base expansion. With the data recorded at 15 ips and played back at 3-3/4 ips, the effective frequency response of the oscillograph was approximately 32,000 cps. The distribution of stress waves throughout the loading of each specimen was evaluated by means of a B&K level recorder and an electronic counter.

In the ONR study, the fact that the emission data did not provide a precursor of the plane-strain instability was considered to be a serious limitation from the standpoint of nondestructive inspection, particularly for applications where leak-before-burst can not be tolerated (as in a fuel tank) or in materials and material conditions where pop-in results in catastrophic failure (no crack arrest). In these situations, emission data are of little value if there is no precursor of the plane-strain instability. They can only be used to locate the flaw but will not indicate the precursor to instability.

In the ARPA-sponsored study, a higher-sensitivity emission detection system was used. It was hypothesized that if the emission sensors would be capable of detecting crack growth before the plane-strain instability and, in particular, presaging the onset of plane-strain instability, then SWAT would be an important NDI method for those applications where a leak can not be tolerated or where material toughness is such that catastrophic failure results directly from plane-strain pop-in.

The instrumentation used in the ARPA-sponsored study is shown in Figure 30. The counter system used to develop the rate and cumulative-emission totals had a frequency capability to 10 MHz; the overall counting-system response was down 3 db at 700 KHz. The data recorded on magnetic tape were limited in upper frequency to the tape recorder capability of 300 KHz.

The data obtained during each test were plotted versus applied load and consisted of rate of emission, cumulative-total count (TSWE), and emission signal-level in RMS volts. The emission sensors were preloaded against the specimen surface through the use of constant-force springs. These are springs which maintain a constant force, independent of extension. The contact side of each sensor was lightly coated with silicon vacuum grease to provide a good couplant between sensor and specimen. Prior to the beginning of each test and with all systems activated, the ambient noise level of the system was reconfirmed. This simple check was the key to assuring system performance. For any given test, deviation from the ambient noise level established at the beginning of the program was an indication that something was not operating properly in the system. For example, the low-noise battery-driven amplifiers were a potential problem as the battery became discharged; however, the ambient-noise-level check always detected this condition. By this procedure, each test was conducted under identical conditions. Total system gain for these tests was set at 20,000:1.

Figure 31 illustrates the precursor in a plane-strain part-through-crack (PTC) tension test of 2014-T6 at room temperature. Figure 32 was obtained from a -320°F cryogenic test of 7039-T61 aluminum using a compact tension specimen (WOL configuration, 1-in. thick, 2-in. wide). This specimen gave over 220,000 counts before it failed and the plot provided a more or less typical precursor to failure. However, it is apparent that the counter trigger level affected the precursor<sup>(76)</sup>.

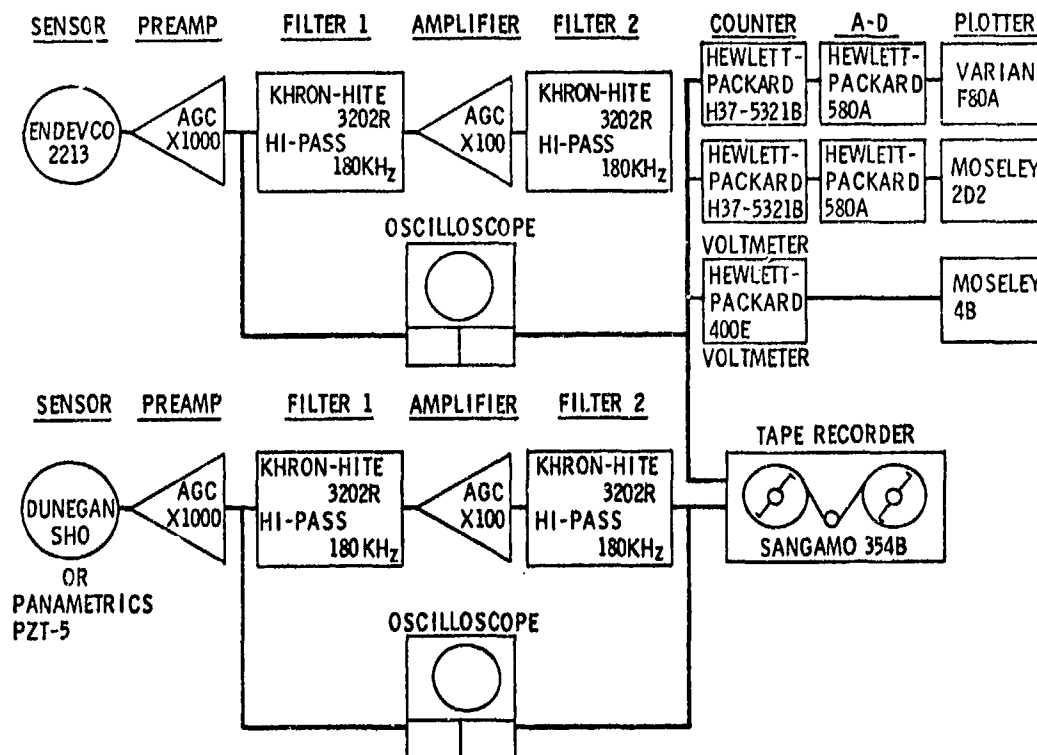


Figure 30. Instrumentation System for Fracture Testing

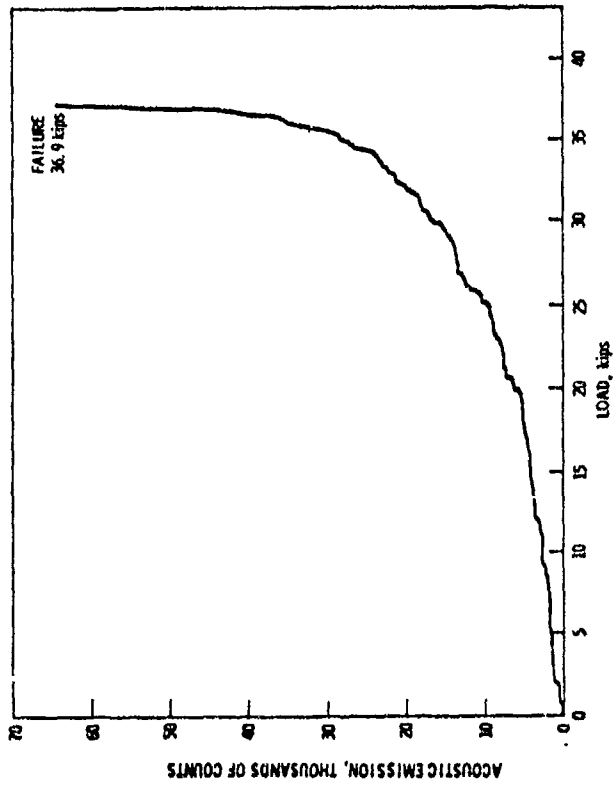
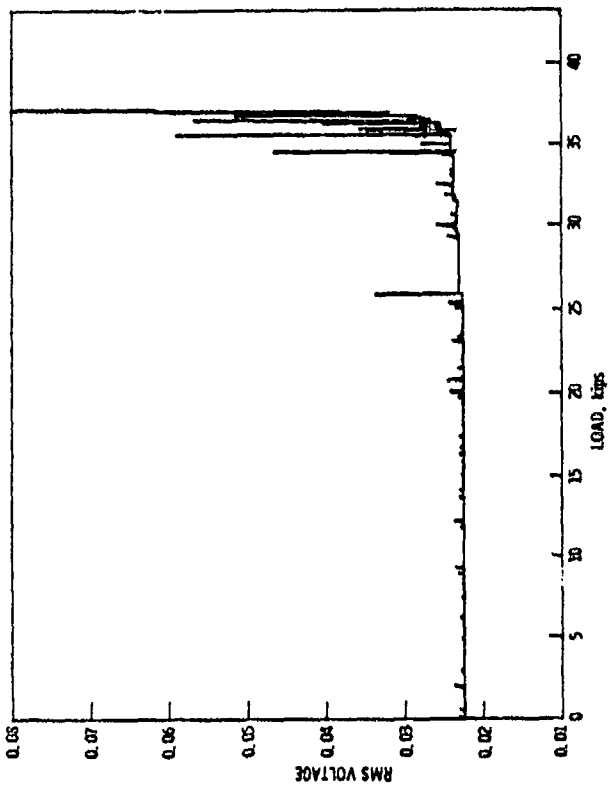


Figure 31. Precursor of Plane Strain Fracture of 2014-T6 PTC-Tension Specimen Tested at Room Temperature.

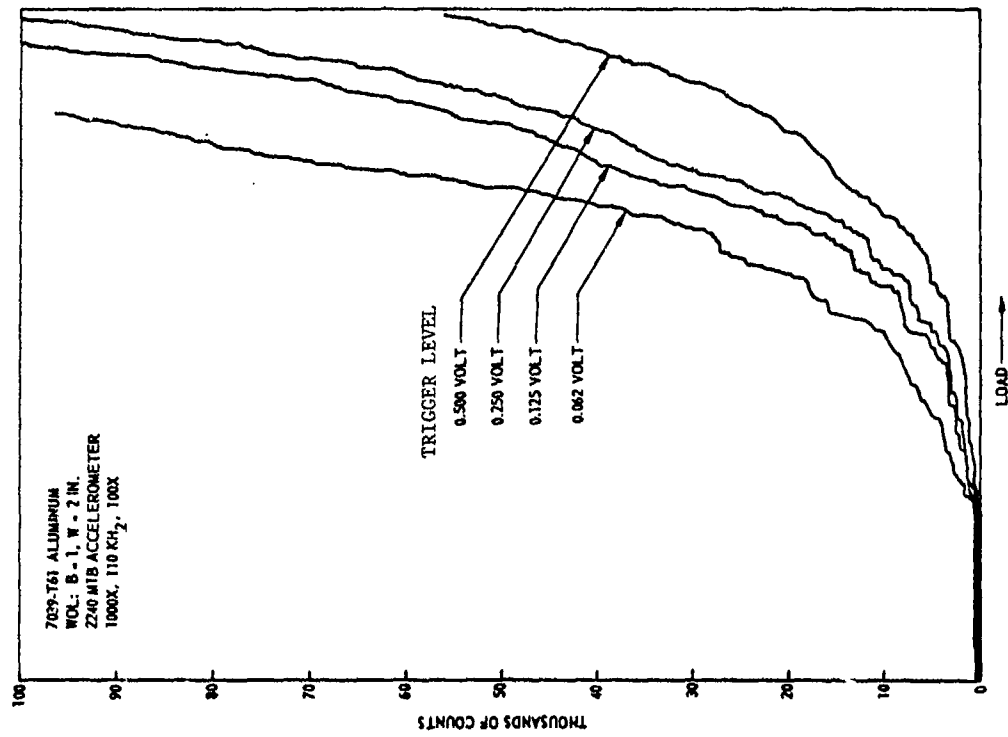


Figure 32. SWL Precursor in a 7039-T61 WOL Tension Specimen



**Effect of Trigger Level.** When the effect of trigger level on the precursor was investigated, it was found that the trigger level used in counting the stress-wave emissions had a marked effect on the precursor. For example, in Figure 33 the data from 2014-T6 specimen 8-8, tested at 73°F, were played back at trigger levels of 0.059, 0.070, 0.090 and 0.12 volt. Note that at the lowest trigger level (0.06 v), the precursor appeared to occur at about 25% of the failure load; whereas, at the highest (least sensitive) trigger level, the precursor was small and occurred only just before failure. In Figure 34, it will be seen that at an 0.15-volt trigger level, the 2219-T87 specimen showed no precursor whatsoever; whereas, at an 0.07-volt trigger level there was an unmistakable precursor. Because the choice of trigger level is arbitrary, selection of a quantitative value of load corresponding to the onset of crack instability does not appear to be meaningful.

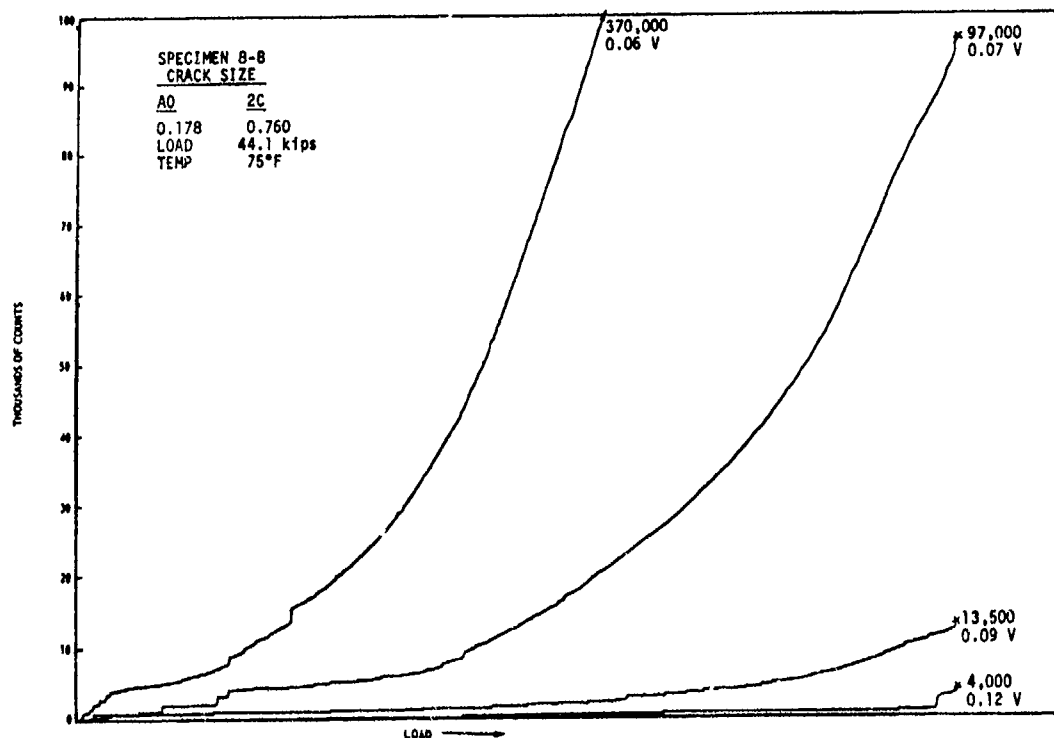


Figure 33. Effect of Trigger Level on Precursor in a PTC-Tension Test of 2014-T6 at 75°F.

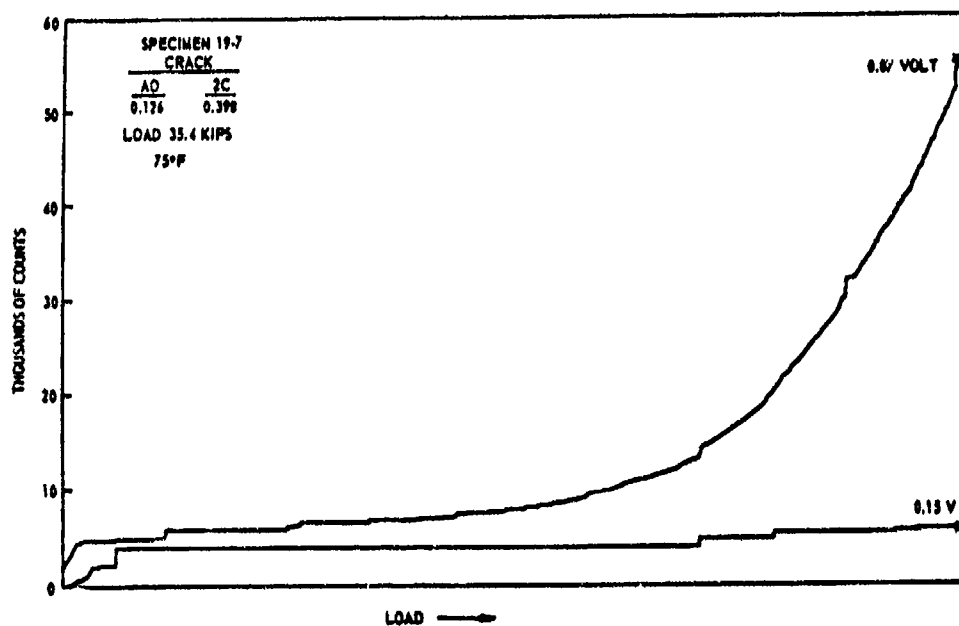


Figure 34. Effect of Trigger Level on Precursor in a PTC-Tension Test of 2219-T87 at 75°F.

The effect of trigger level on the precursor is best understood by a consideration of the background "noise" level. If the background noise increases (band widens) as the load is increased, the stress-wave count could be affected if, at the start of the test, the triggering voltage is set just above the background "noise" level. Comparisons between the background "noise" band widths at the start of loading and near fracture are shown in Figure 35. At low load, in the elastic region, the background "noise" produced a relatively narrow signal band; while at loads near fracture, in the plastic region, the band was significantly widened. Likewise, in comparisons between room and cryogenic test temperatures, at low temperature where plastic deformation is minimized, the width of the band was essentially the same near fracture as at the start of loading. This suggests that the broadened band near fracture in the 75°F tests was the result of plastic-zone formation. No attempt was made to photograph burst-type stress waves; when they appeared in the photographs, it was by chance. Figure 36 schematically shows the effect of background "noise" at three triggering levels for room-temperature tests. As the load increased, the net section yielding and the plastic zone at the crack tip increases and, consequently, the continuous emission increases. At a low-voltage trigger level, the background "noise" increases to trigger-level one at a relatively low load, producing an anomalously low precursor. At trigger-level three, the specimen is practically at the failure load before the background "noise" has increased to the trigger voltage, giving little or no precursor (see Figure 33 for actual test data).

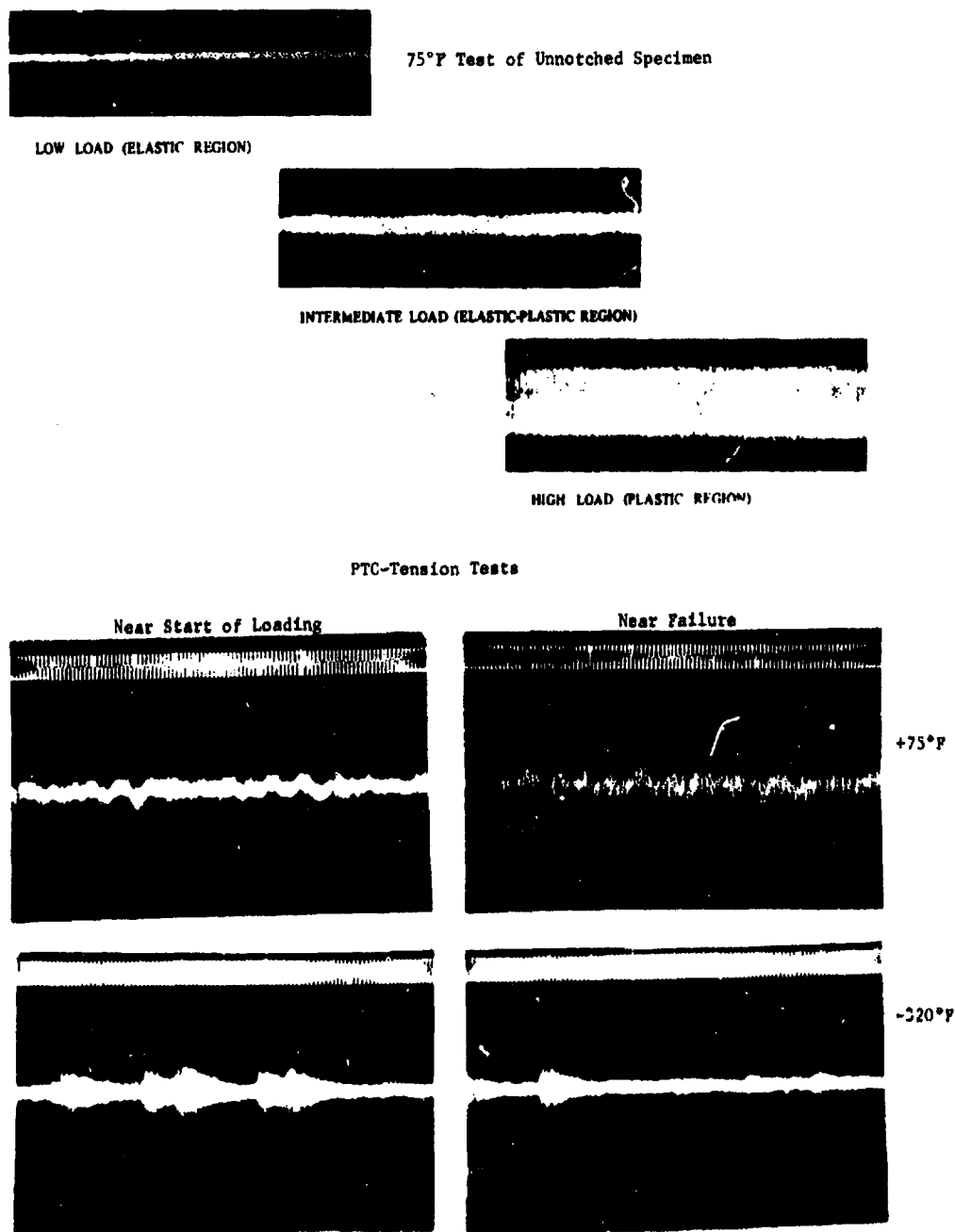


Figure 35. Background "Noise" at Various Stages of Notched and Unnotched Tension Tests.

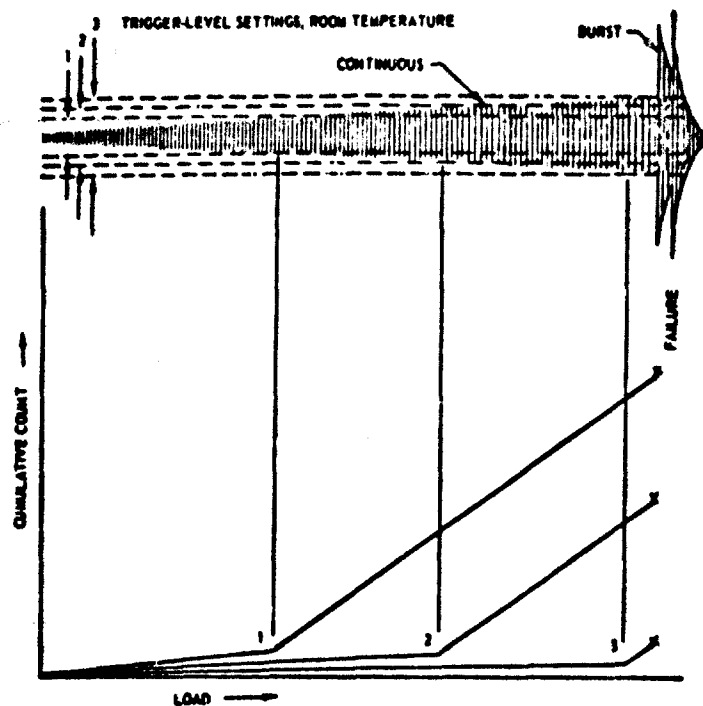


Figure 36. Schematic of the Effect of Trigger-Level Setting on the Precursor Isolation of an Acoustic-Emission Source from Extraneous Noise

**D6aC Aircraft Fittings.** Indications of low fracture toughness in a D6aC steel wing-pivot-support structure aroused interest in the possible use of acoustic emission as a nondestructive inspection method for aircraft. Aerojet was requested to instrument a D6aC wing-pivot fitting during fatigue test in an aircraft structural test facility. The objective of the test was to (1) determine if acoustic emission could be detected and separated from the inherent noise of full-scale fatigue testing, and (2) demonstrate the location of stress-wave origins by sensor-zoning techniques. An Aerojet computerized system was used for this purpose. The preselected "sphere of interest" was a taper-lock-fastened door in the wing carry-through structure. Sensors were positioned so as to monitor a sphere of interest of approximately 2-ft dia. Thus, sensors 1, 5, 8 and 9 established a circle in the horizontal plane, while 1, 3, 8 and 11 established a circle in the fore-and-aft vertical plane. The third plane was established by sensors 3, 5, 9 and 11. Figure 37 shows sensor No. 2 at the center of the sphere.

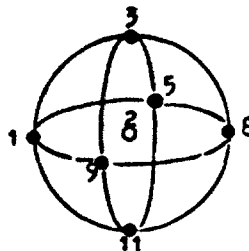


FIGURE 37 - SPHERE OF INTEREST SENSOR ARRAY.

Cracking within the zone of interest was defined by the time of stress-wave arrival at the various sensor positions. Stress waves originating at or near the center of the sphere of interest arrive first at the center sensor and later at the circumferential sensor locations. Conversely, stress waves or extraneous noise originating outside the sphere of interest arrive first at the circumferential sensor positions and later at the center. Equipment which automatically displays the sequence and time differentials clearly defined activity originating from the primary area of interest. The computerized system housed in a van performed this function.

BASED ON THIS WORK, THE FOLLOWING CONCLUSIONS WERE DRAWN: (a) STRESS-WAVE ORIGIN from crack growth in D6aC steel can be detected in selected areas during test; (b) test system noises can be accounted for and separated from crack growth by at least two means; viz., (1) spheres of interest are developed by preselected sensor arrays which serve to isolate specific areas of the test structure and

(2) mechanical noises generally have a slower rise time than the transient stress-wave pulse which provides another means of discriminating noise from crack extension; and (c) automated control of the load-release mechanism may be used to avoid catastrophic failure from areas being monitored during structural testing of aircraft and components.

**Monitoring a Known Crack in a Steel Structure.** A large steel structure under construction was found to contain a crack. The cracked girder consisted of a 2-in.-thick, 30-in.-wide tension flange with a 7/8-in.-thick web. While construction was shut down, it was possible to monitor the structure for subcritical crack growth using the system shown in Figure 38. When there was extraneous noise in the structure, it was necessary to utilize a computerized system with an array of four accelerometers to distinguish between signals generated by the known crack and those from elsewhere in the structure. With a computerized system it was possible to discount any stress wave emanating from a source other than the crack under investigation.

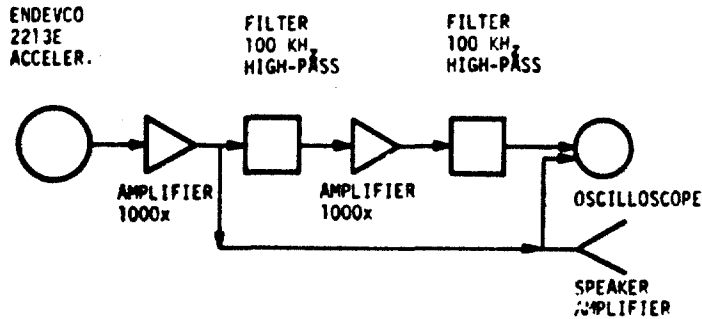


Figure 38. Schematic of the System Used in Monitoring a Cracked Girder in a Large Steel Structure.

Isolation of the known defect from extraneous stress-wave sources was accomplished in the following manner: a pulser which simulates stress waves in the metal was placed in the immediate vicinity of the known crack. Then four sensors were positioned in an array around the crack and pulser so that sensor No. 1 received the pulser signal first, sensor No. 2 received the signal second, etc. With a computer logic system to determine the difference in time of arrival ( $\Delta t$ ) between sensors, and a computer to receive, store and print the data by teletype, it was possible to distinguish between stress waves emanating from the known crack (or structural element) and extraneous "noise". Whenever the teletype printout showed a sensor sequence other than 1, 2, 3, 4, and with  $\Delta t$  values significantly different from those determined with the pulser, the data were rejected as not coming from the known crack.

An example of the data print-out from the pulser with the pulser positioned close to the known crack is shown in Table 10. Figure 39 shows the position of the sensors and pulser relative to the known crack. From Table 10 note that the difference in time of arrival between sensors 1 and 2 was 80 microseconds, between sensors 1 and 3 was 170 microseconds and between sensors 1 and 4 was approximately 390 microseconds. The number in the first column of the teletype printout is the sensor that first receives the signal. When signals were generated by a source other than the known crack, columns (a), (b), (d) and (g) of the teletype printout indicated the sensor position out of sequence.

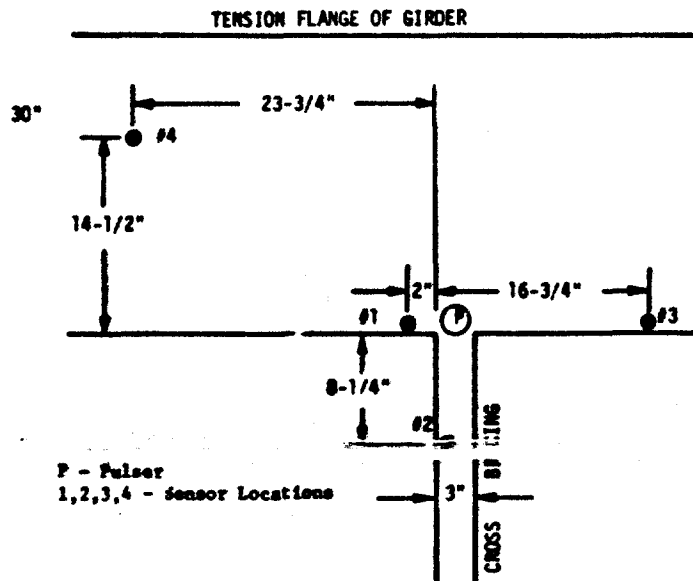


Figure 39

Location of Sensors on a Girder Element Containing a Known Flaw.

TABLE 10 COMPUTER RESULTS FOR PULSED-GENERATED SIGNAL

SENSOR NO. (a)	SENSOR NO. (b)	TIME $\Delta T$ (c)	SENSOR NO. (d)	TIME $\Delta T$ (e)	TIME $\Delta T$ (f)	SENSOR NO. (g)	TEST TIME (h)
1	2	6	3	17	42	4	23.36
1	2	6	3	17	42	4	23.37
1	2	6	3	17	39	4	23.37
1	2	6	3	17	39	4	23.37
1	2	6	3	17	39	4	23.37
1	2	6	3	17	39	4	23.37
1	2	6	3	17	39	4	.00
1	2	6	3	17	39	4	.00
1	2	6	3	17	39	4	.00
1	2	6	3	17	39	4	.00
1	2	6	3	17	39	4	.01
1	2	6	3	17	39	4	.01
1	2	6	3	17	42	4	.01
1	2	6	3	17	42	4	.01
1	2	6	3	17	42	4	.01
1	2	6	3	17	42	4	.01
1	2	6	3	17	42	4	.02
1	2	6	3	17	42	4	.02
1	2	6	3	17	42	4	.02
1	2	6	3	17	39	4	.02
1	2	6	3	17	39	4	.03

-----  
 (a) number of the 1st sensor to receive signal  
 (b) number of the 2nd sensor to receive signal  
 (c) time differential between (a) and (b) in microseconds x 10  
 (d) number of the 3rd sensor to receive signal  
 (e) time differential between (a) and (d) in microseconds x 10  
 (f) time differential between (c) and (e) in microseconds x 10  
 (g) number of the 4th sensor to receive signal  
 (h) time at which signal was received

TABLE 11

TYPICAL COMPUTER PRINTOUT RECORDING  
 STRESS WAVE EMISSION

SENSOR NO. (a)	SENSOR NO. (b)	TIME $\Delta T$ (c)	SENSOR NO. (d)	TIME $\Delta T$ (e)	TIME $\Delta T$ (f)	SENSOR NO. (g)	TEST TIME (h)
1	4	9	2	.75	EEZ	3	.25
2	1	1	4	3	EEZ	3	.26
3	1	36	4	101	EEZ	3	.37
1	4	14	2	91	EEZ	3	.57
1	4	13	3	29	EEZ	2	1.07
1	4	31	2	37	54	3	1.14
1	2	50	4	121	EEZ	3	1.29
4	1	14	2	61	63	3	1.32

Pulse check at location of beam crack

1	2	6	3	9	11	4	2.21
1	2	6	3	9	10	4	2.21
1	2	6	3	9	11	4	2.22

-----  
 (a) number of the 1st sensor to receive signal  
 (b) number of the 2nd sensor to receive signal  
 (c) time differential between (a) and (b) in microseconds x 10  
 (d) number of the 3rd sensor to receive signal  
 (e) time differential between (a) and (d) in microseconds x 10  
 (f) time differential between (c) and (e) in microseconds x 10  
 (g) number of the 4th sensor to receive signal  
 (h) time at which signal was received

Examples of the teletype printout for emissions from sources other than the known crack are shown in Table 11. Note that stress-wave emission originating from locations other than the known crack resulted in a variety of sensor sequences. EEE on the teletype printout signifies a time differential in excess of a preset arbitrary maximum. The test-time printout (column h) is the time from the start of the data collection in hours. Thus, from Table 11 at 0.25 hours test time, sensor No. 1 first received a stress wave, sensor No. 4 received the signal 90 microseconds later, sensor No. 2 received the signal 1750 microseconds after sensor No. 1, and finally, sensor No. 3 received the signal but too late to be recorded. The sequence 1, 4, 2, 3 indicated a source other than the known crack. The difference in pulser time checks between Tables 10 and 11 is the result of a small change in the pulser and sensor positioning.

#### Instrumentation for In-Field Flaw Detection

Pressure Vessel Monitoring. The Aerojet mobile laboratory has been used in the qualification testing of large pressure vessels. In addition to an array of accelerometers, four pulsers are located on the pressure vessel to provide a means of introducing an artificial stress wave while the vessel is under pressure. The hydrotest procedure consisted of three cycles, with the pressure reduced to low value between each cycle. The media was water; the material was 2219 aluminum with a nominal wall thickness of 0.190 in. The van and tank are shown in Figure 40.

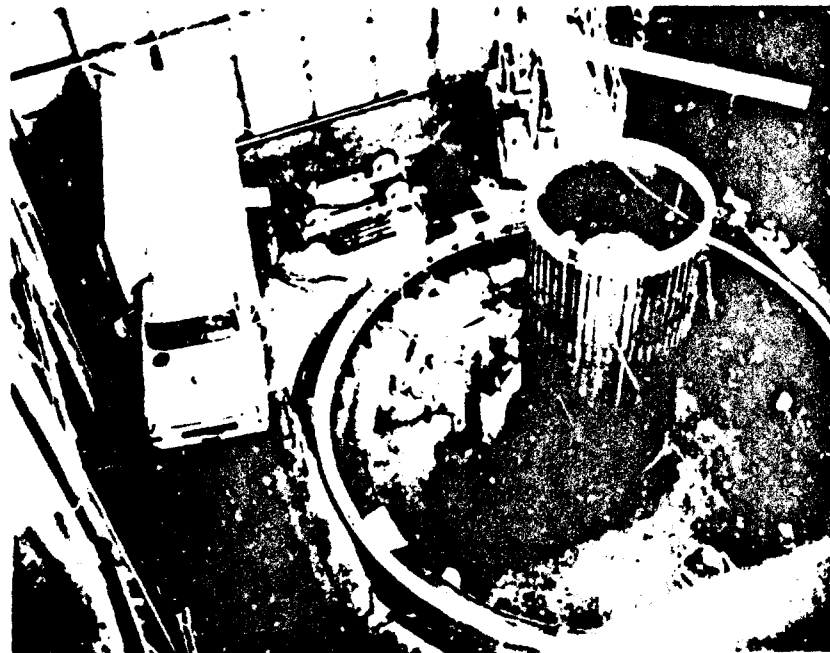


Figure 40. Van and Pressure Vessel Prior to Test.

The pulsers were used as an overall system check. An electrical signal was fed into the pulsers, which transformed the electrical signal into mechanical energy and then transmitted the energy to the wall of the pressure vessel. The simulated stress wave transmitted by the pulser propagated through the pressure vessel and was detected by the 15 sensors. Thus, the pulsers provided a check of the detection sensitivity and the reliability of the electronic components as well as an evaluation of the software of the computer. With pulsers located in different positions on the pressure vessel, the pulsers also provided a check of the system capability for detection and location of a stress-wave source. During test, when there is no crack growth, no solutions are posted by the computer and, therefore, without the pulsers, the operator has no way of knowing at any given time if the system is in peak operating condition. With the pulsers, on the other hand, the operator periodically can make an in-test, at load, overall system check.

The trigger level of the system was set 20 millivolts above the background noise level, and the signal amplification was set to provide a 60-db gain. The mechanical noise of the hydrotest system was sufficiently low that the filters were set at 30 KHz high-pass.

Data display was by visual and graphical means in real time during the test. The video display was on a television monitor which also showed the sensor locations on an overlay plan view of the pressure vessel. The arrival of detected stress waves were posted on the screen of the monitor so that their location could be determined as a function of time. Particular attention was paid to areas indicating multiple emissions since this can be indicative of subcritical crack growth. Video tape records of the monitor display also were made for posttest data analysis if required.

Analog records were made of the stress waves recorded by each of thirteen of the fourteen channels used to monitor the pressure vessel. These were recorded using a fourteen-channel tape recorder operating in a direct mode. The fourteenth channel was used for tape synchronous control. In addition, a totalizer system was used to plot the cumulative stress-wave-emission count vs pressure for each hydrotest cycle. The output from channels 9, 10, 11 and 12 were mixed and plotted as a single output.

The hydrotest produced no significant increase in stress-wave rate during the pressure cycling. The background noise (amplitude and frequency) encountered during the hydrotest was very low with 30 KHz high-pass filtering. Multiple emissions were detected from two areas. These suspect areas were checked using other nondestructive inspection methods to ensure that no defects of significant size were present. Only random impulses were detected from the remainder of the pressure vessel.

Defects Too Small to be Verified by Conventional NDI. When acoustic-emission sources are located and then found by conventional nondestructive inspection (NDI) methods to be too small to require repair (or are too small to be located at all by the available NDI technique), the suspect location(s) can be monitored continuously using a simple, compact, non-computerized, data-conditioning system which utilizes a high-frequency transducer attached to the pressure vessel at the center of the suspect area. Because of the inherently high attenuation of stress waves in the megahertz range, only those signals emitting from the source in the immediate vicinity of the transducer will be recorded. This concept is an alternative to the technique of using an array of transducers, calibrated with a pulser signal, and data processed by computer. Another alternative is a system based on two sensors which will accept only those signals that originate from sources that lie on a line between the two sensors. Thus, if a weld is indicated to contain the stress-wave-emission source, two sensors can be attached to the pressure vessel at an appropriate distance apart along the weld.

Real-Time Computer-Based Systems. Examples of real-time computer-based systems are shown in Figures 41 and 42. Figure 41 is a view of the 16-channel system housed in a truck, thus providing a mobile laboratory; it was this system that was used in the applications described in previous paragraphs. A more recent 10-channel system is shown in Figure 42. Operation of this system is relatively simple due to the inclusion of self-checking circuits in the Digital Analyzer and software. The application of the system is initiated by locating the sensor-preamplifier packages on the test vehicle. This is done at the test site using conventional surveying procedures. The number and arrangement of the sensors are

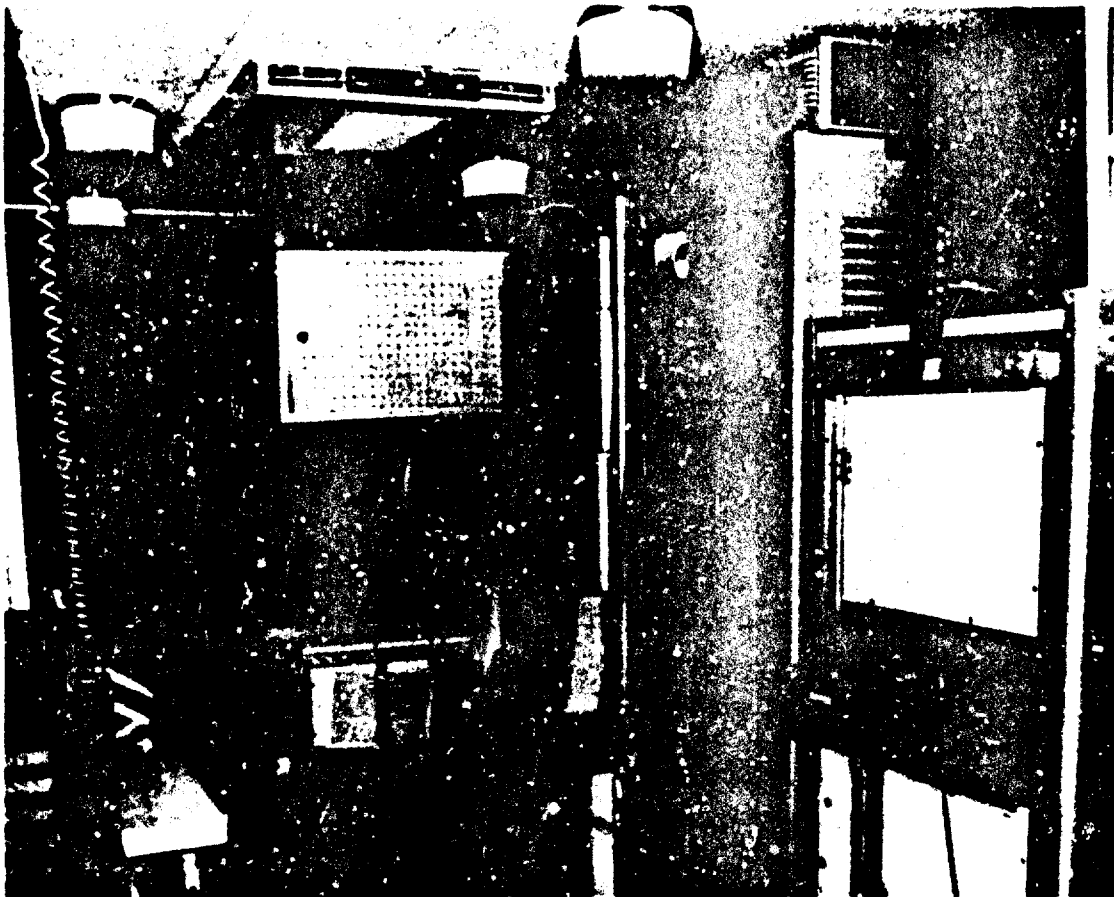


Figure 41. Interior View of Mobile Acoustic-Emission Laboratory

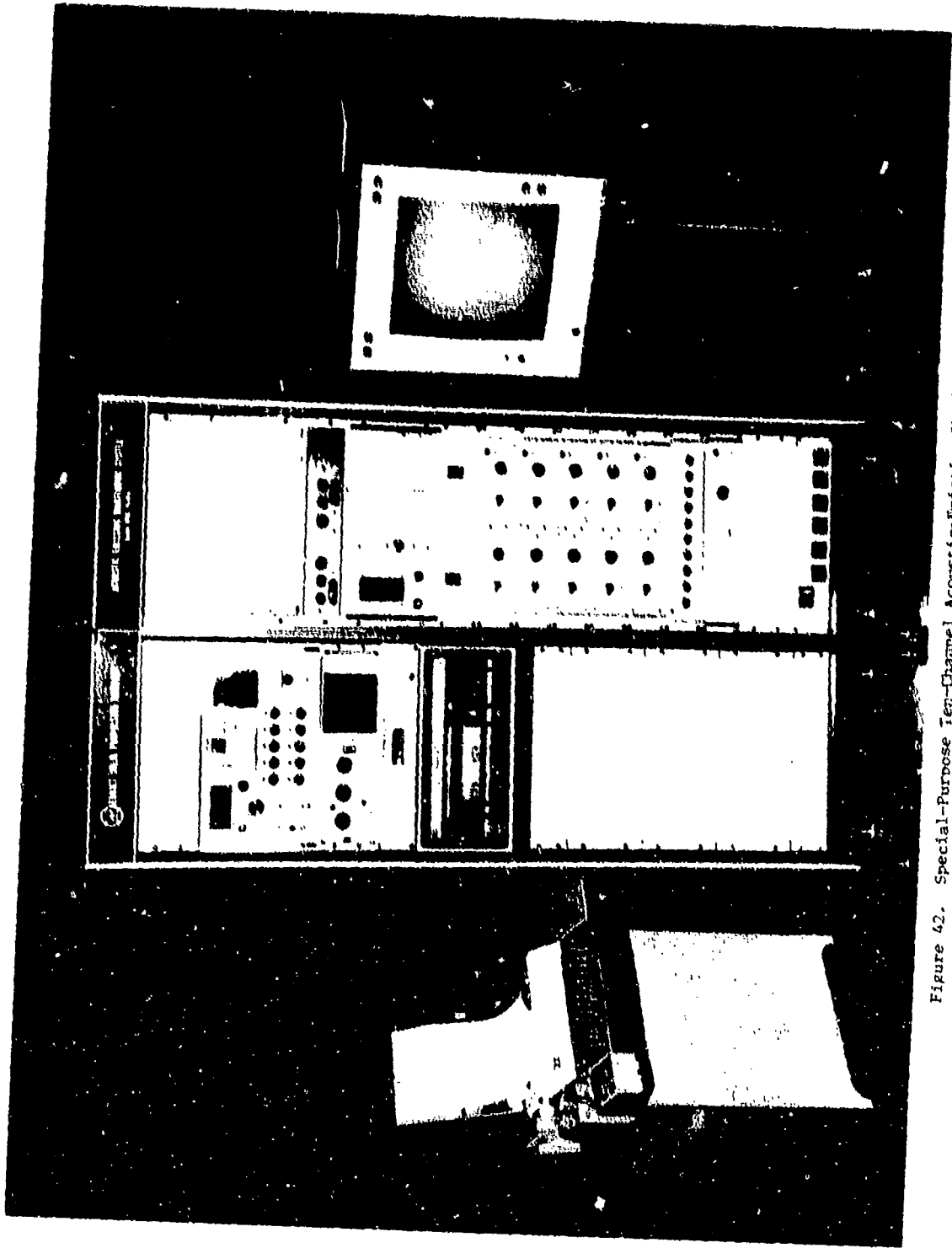


Figure 42. Special-Purpose Ten-Channel Acoustic-Mission Monitoring System



determined by the size and shape of the pressure vessel up to the maximum available in this system of 10 channels. The sensor packages are connected by coaxial cables to the patch panel of the main acoustic emission instrumentation consoles. These consoles contain all other components except the teletype and remote-video display. The latter is a self contained unit which can be located up to fifty feet from the main instrumentation consoles.

#### SUMMARY OF THEORETICAL AND EXPERIMENTAL LIMITATIONS

Schofield, in a recent publication devoted to acoustic emission<sup>(77)</sup>, directed attention to the plight of the acoustic-emission investigator at the current state of the art in the following hypothetical situation:

"A large pressure vessel has been in service for several years and is to be tested for pressure integrity. Certain areas of the vessel are physically inaccessible for the more general ultrasonic and radiographic inspection methods because of structural configuration, insulation, concrete, radiation and other factors. Of course, a prime motive for employing acoustic emission is that immediate proximity to the area is not necessary, but also, more often than not these inaccessible areas contain discontinuity regions associated with relatively high local stresses.

"The investigator begins to receive a number of distinct burst signals on his monitor. The rate that these signals occur provide important information on the defect propagation rate, while the time delays of the signals arriving at the transducers provide the data for computation of emission-source location. How does the investigator distinguish between the rapid propagation of a large, critically growing crack, and the simultaneous emission from several smaller insignificant cracks, all in the near vicinity of each other?"

First, with regard to the question posed by Schofield. It has been shown<sup>(19)</sup> that when a crack approaches instability (near critical size), the attendant acoustic-emission rate is markedly increased over that for subcritical crack growth. However, the observation is qualitative because engineering judgement is required in establishing the trigger level for the electronic counter system. In addition to the question posed by Schofield, there are several related questions that further point up the experimental limitations of using acoustic emission as a nondestructive test method. The additional related questions that the acoustic-emission investigator must take into consideration are (1) what if there is a single source which repeatedly emits but shows no sign of instability?, (2) what if subsequent conventional nondestructive inspection is incapable of detecting the source?, (3) will the electronics distinguish between extraneous electrical disturbances which produce high-rise-time, single-pulse, signals?, (4) what is to be done if there is white noise in the system?, and (5) will the system distinguish between crack growth and metallurgical complications such as phase transformation, creep, twinning and slip-line development?

Not all these questions can be answered in a satisfactory manner at this time. However, the more troublesome of the limitations are discussed in the following paragraphs.

#### Correlation of Acoustic Emission with Size of Crack and Crack Growth Rate

One of the most significant assets of acoustic emission is the ability to detect the presence of active defects in structures and by the use of special (systems) techniques to physically locate the defect in the structure. A major shortcoming in the practical application of this asset is the present inability to determine the size of the defect with reasonable accuracy. To date there have been no conclusive results reported from which the size and propagation rate can be determined<sup>(77)</sup>.

Potentially one of the most important observations derived from acoustic-emission technology is that the emission characteristics of flawed specimens are highly dependent upon the stress intensity of the flaw present. The first evidence obtained at Aerojet of a relationship between stress-wave emission and stress intensity factor came from a study of fatigue cracking in 1/8 x 8 x 24 in. D6aC through-cracked, center-notched panels<sup>(9)</sup>. As shown in Figure 43, the crack growth rate in low-cycle high-stress-intensity fatigue was directly proportional to the summation of stress-wave amplitude in each cycle.

At about the same time, Dunegan, Harris and Tatro at the University of California Lawrence Radiation Laboratory (LRL) showed that with the count trigger level set to record plastic deformation (dislocation activity), most of the emission occurs during and shortly after yielding, then decreases as further straining takes place. Based on the volume of metal being strained in the plastic zone at the tip of a crack, Dunegan assumed that the acoustic emission count rate would be proportional to the rate of increase of the volume of metal producing the acoustic emission. This led to the prediction that if all the acoustic-emission pulses are added up as the test proceeds, then at any time the total number of counts will be proportional to the fourth power of the stress-intensity factor associated with the flaw at the time. Figure 44 from the work of Dunegan and Harris, shows the relationship between stress-intensity factor and acoustic emission cumulative count in rising-load-to-failure tests of 7075-T6 aluminum. Note that data obtained from four initial crack lengths grouped into a single curve fitting the theoretical fourth-power curve. Unfortunately, the plots of such data did not always conform to a fourth power curve; in another study, Dunegan and Harris reported the exponent to vary between the 6th and 8th power. Later studies at Aerojet<sup>(23)</sup> indicated a direct proportionality between stress-intensity

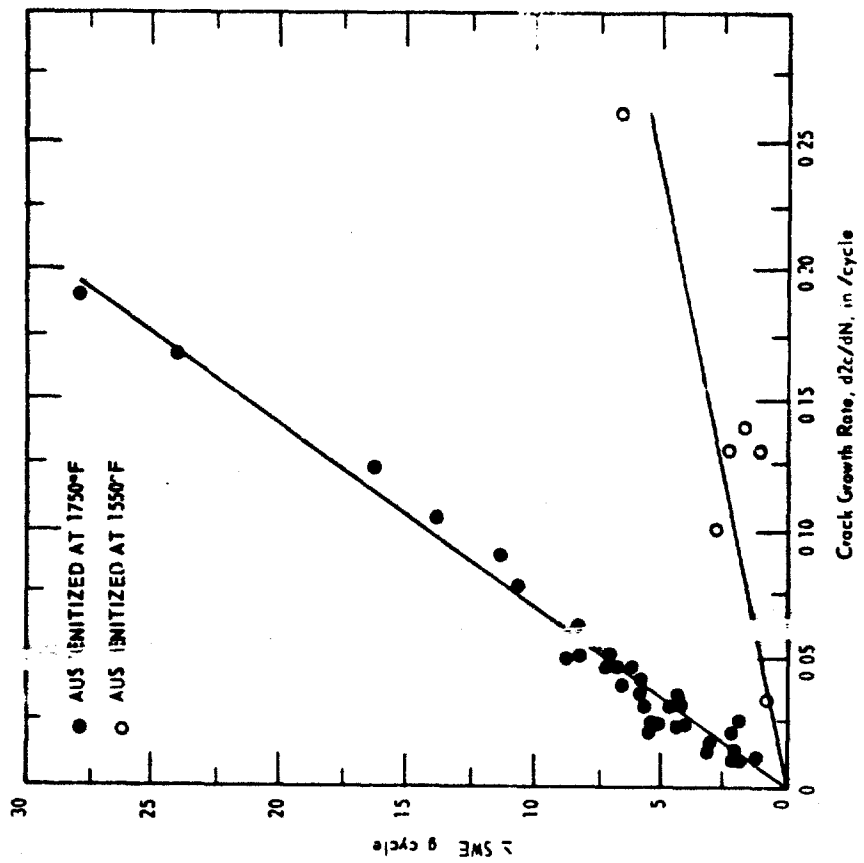


Figure 43. Relationship Between Fatigue Crack Growth Rate and Stress Wave Emission for Two Conditions of 70516 Steel

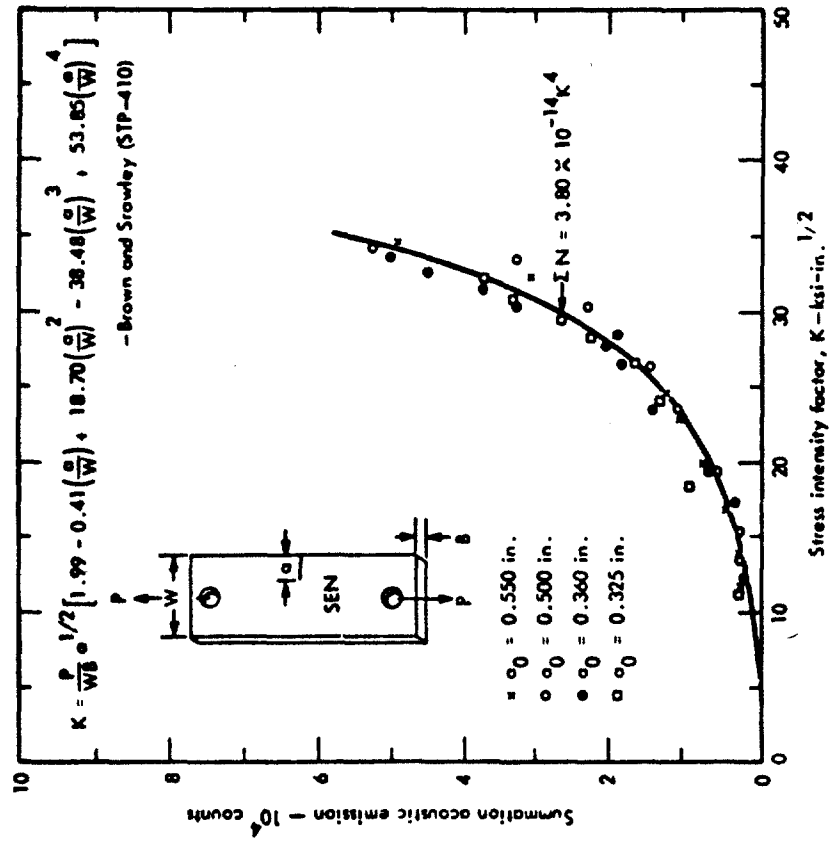


Figure 44. Summation of Acoustic Emission as a Function of Stress-Intensity Factor-70516

factor and cumulative stress-wave count in single-edge-notch tension specimens (Figure 45). It was hypothesized that the difference between the LRL and Aerojet test results could be the result of a difference in trigger level. At LRL the counter trigger level was set to include the continuous emission produced by plastic deformation; whereas, in most Aerojet studies, the trigger level was set above the continuous emission, focusing on the burst-type stress-wave emission associated with incremental crack growth. However, differences from test to test, even with a supposedly constant data-acquisition system, have been encountered and as yet not explained.

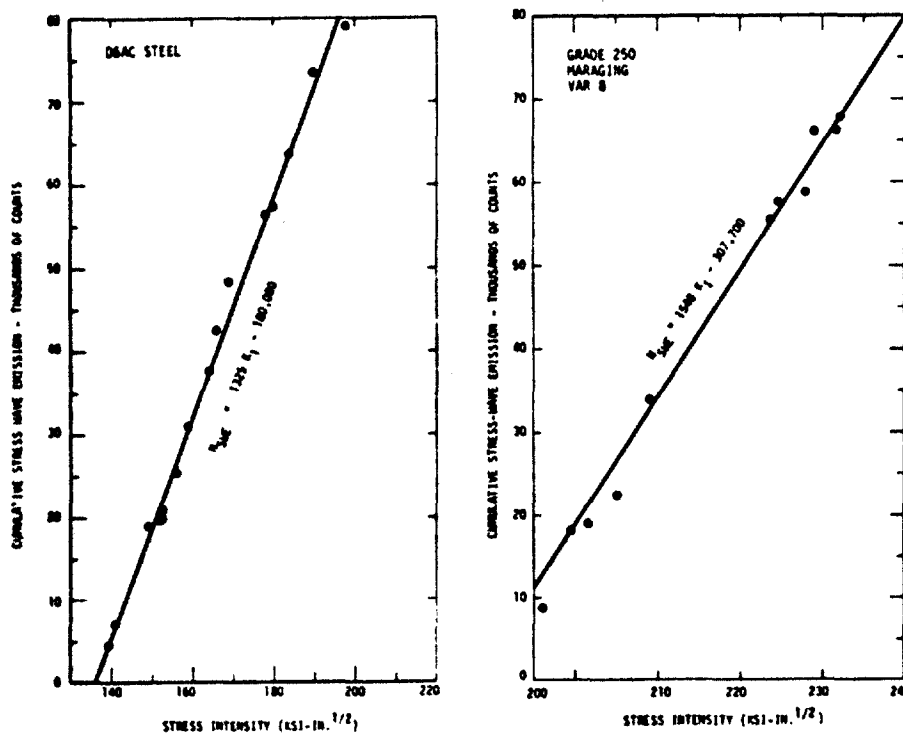


Figure 45. Relationship Between Stress Intensity and Cumulative Count for Materials Under Constant Load and Subjected to Stress-Corrosion Cracking in 70°F Water.

The importance of the relationship between stress intensity factor and acoustic emission lies in the possibility of estimating flaw sizes and failure load based on in-service, real-time, nondestructive inspection of a flawed structure utilizing acoustic emission. However, before this can be realized, much has to be learned about the variables affecting the count-versus-K relationship. To facilitate comparisons between results obtained in the various studies at Aerojet, a computer program was used to calculate stress-intensity values from empirically determined values of load and COD, and to plot various relationships. These relationships were based on the following fracture-mechanics parameters<sup>(78)</sup>:

$$G = K^2/E$$

$$(COD)E/(1-\nu^2) = \frac{2K}{\pi} (2\pi r)^{1/2}$$

$$r = \frac{1}{2\pi} \left(\frac{K}{FTY}\right)^2$$

where  $G$  is the stress-field energy release rate (in.-lb/in.<sup>2</sup>),  $K$  is the stress intensity factor (ksi-in.<sup>1/2</sup>),  $E$  is the modulus (psi),  $COD$  is crack-opening-displacement (in.),  $\nu$  is Poisson's ratio,  $r$  is the plastic-zone (in.) and  $FTY$  is the 0.2 percent offset yield strength (psi).

It was hypothesized that if the electronic counter integrates size and number of the stress-wave emission, the count can be assumed to be proportional to the stress-field energy release rate,  $G$ . Based on this assumption, it can be shown that the above fracture-mechanics parameters should provide a proportionality between TSWE and  $K^2/E$  and between COD and  $(1-\nu^2) TSWE/FTY$ , where  $TSWE$  is the cumulative stress-wave-emission count.

A computer program was used to calculate the stress-intensity values from empirically determined values of load and COD, and to plot the semi-empirical relationships. The relationship  $K$  versus

A single heat of Grade-250 maraging steel, split to provide part as air-melt (AM) and part as vacuum-arc-remelt (VAR) provided encouraging results as will be seen from Figures 46-47.

Figure 48 presents data from three tests of high-toughness D6aC material 0.1-in. thick, tempered at 1100°F. Figure 49 shows the results for the same heat of D6aC but heat treated to a higher-strength, lower-toughness condition (600°F temper).

From such studies as described above, it will be seen that in the present stage of development, acoustic emission is not capable of determining quantitatively the size of a source defect except at the onset of crack instability and then only if the fracture toughness (critical stress intensity) is known. Thus, acoustic emission must be used in conjunction with conventional nondestructive inspection to determine the size and orientation of the source defect. Relationships between cumulative stress-wave count and applied stress-intensity factor have been observed in the laboratory and show great promise. However, the work has been done with simple test specimens; application of the relationship to prototype structures remains as one of the most important objectives of future research and development. If the relationship can be applied to actual structures and tankage, then it will be possible to calculate the crack size from the cumulative stress-wave count and the known stress.

#### Flaws Too Small to be Detected by Conventional Nondestructive Inspection

When acoustic emission sources are located and then found by conventional nondestructive inspection (NDI) methods to be too small to require repair (or are too small to be located at all by the available NDI technique), the suspect location(s) can be monitored continuously using a simple, compact, non-computerized, data-conditioning system which utilizes a high-frequency transducer attached to the pressure vessel at the center of the suspect area. Because of the inherently high attenuation of stress waves in the megahertz range, only those signals emitting from the source in the immediate vicinity of the transducer will be recorded. This concept is an alternative to the technique of using an array of transducers, calibrated with a pulser signal, and data processed by computer. Another alternative is a system based on two sensors which will accept only those signals that originate from sources that lie on a line between the two sensors. Thus, if a weld is indicated to contain the stress-wave-emission source, two sensors can be attached to the pressure vessel at an appropriate distance apart along the weld.

#### Electrical Disturbances

Switches can often be a source of trouble by producing a single high-rise-time spike which will be counted electronically as though it were a stress wave. The essential difference between an electrical pulse and acoustic emission is in the ring down seen as an exponential decay in the stress wave as viewed on an oscilloscope, whereas the electrical signal is seen as a single pulse devoid of ring down. One method for eliminating this problem is to incorporate an electronic device in the counting system which counts only when the ring-down phenomenon is present. Another approach is to ignore signals which reach several sensors simultaneously. It is characteristic of the extraneous electrical signal in a given circuit to appear in all sensor outputs on that circuit simultaneously. In laboratory testing where computerized source location is not used, a dummy sensor is used (mounted on a plate devoid of cracking). When the test plate and the dummy plate simultaneously show an increase in count, the signal is discarded as being electrical.

#### White Noise

Metal-to-metal rubbing and escaping gas are two examples of phenomena which generate noise containing all frequencies and, therefore, are difficult if not impossible to eliminate by band-pass filtering. If the source of the white noise can not be eliminated, mechanical signature analysis can be used. This technique is well known and has been used widely for detecting wear in rotating parts; e.g., in bearings. The noise under normal service (with no worn or defective parts) is recorded and later compared at regular intervals during service. When the noise changes appreciably, it is a warning of the presence of a defective part or cracking.

The transducers used in acoustic-emission studies are well suited to mechanical signature analysis. If a crack is approaching instability, a marked increase in count rate will occur, over and above the normal count rate produced by the inherent noise.

#### Extraneous Noise from Metallurgical Sources

The transformation of austenite to martensite as a weld cools will produce signals that appear to be weld cracking. The transformation will occur along an isotherm starting at the  $M_s$  temperature and ending at the  $M_f$  temperature; the isotherms will progress across the plate as it is being welded at a distance behind the traveling arc. With a system of two sensors which will accept only those signals that originate between the two sensors and continuously report where the source is located along that line, the phase-transformation can be identified by correlating the acoustic emission data with temperature measurements in the plate.

Twinning and slip-line development per se are difficult to distinguish from cracking since plastic deformation is inherent at the crack tip. The stresses for slip or twinning are not a constant for a given material, but vary with test temperature, strain rate, alloy content, grain size and other variables. In most materials having a BCC structure, the yield stress for slip increases sharply with decreasing temperature, whereas, the twinning stress is relatively independent of temperature. At high loading rates or at low temperature, twinning is the preferred mode for deformation in BCC metals. There is considerable evidence that twinning is an extremely effective deformation mode for nucleating cleavage cracks. Green (79) has pointed out that such cracks will then grow slowly, by plastic deformation, until

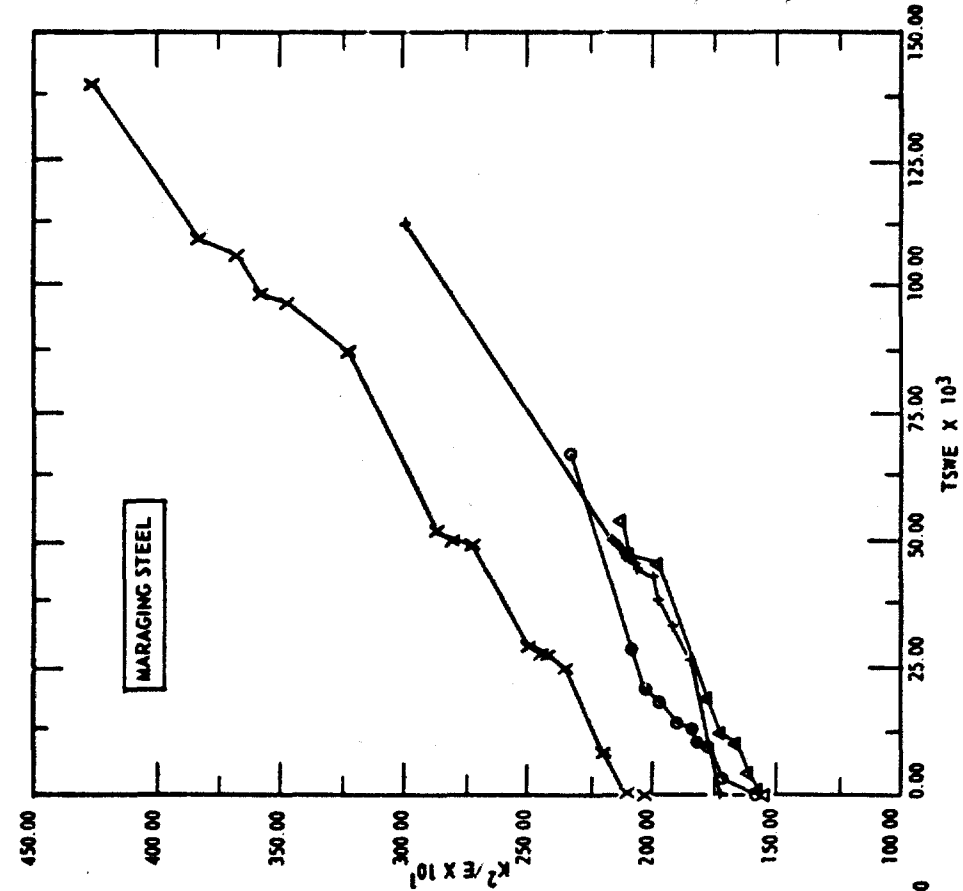


Figure 46. Relationship Between  $K$  and Count for 182 Michel Maraging Steel Under Constant Load (crack growth produced by water at 70 and 65°F).

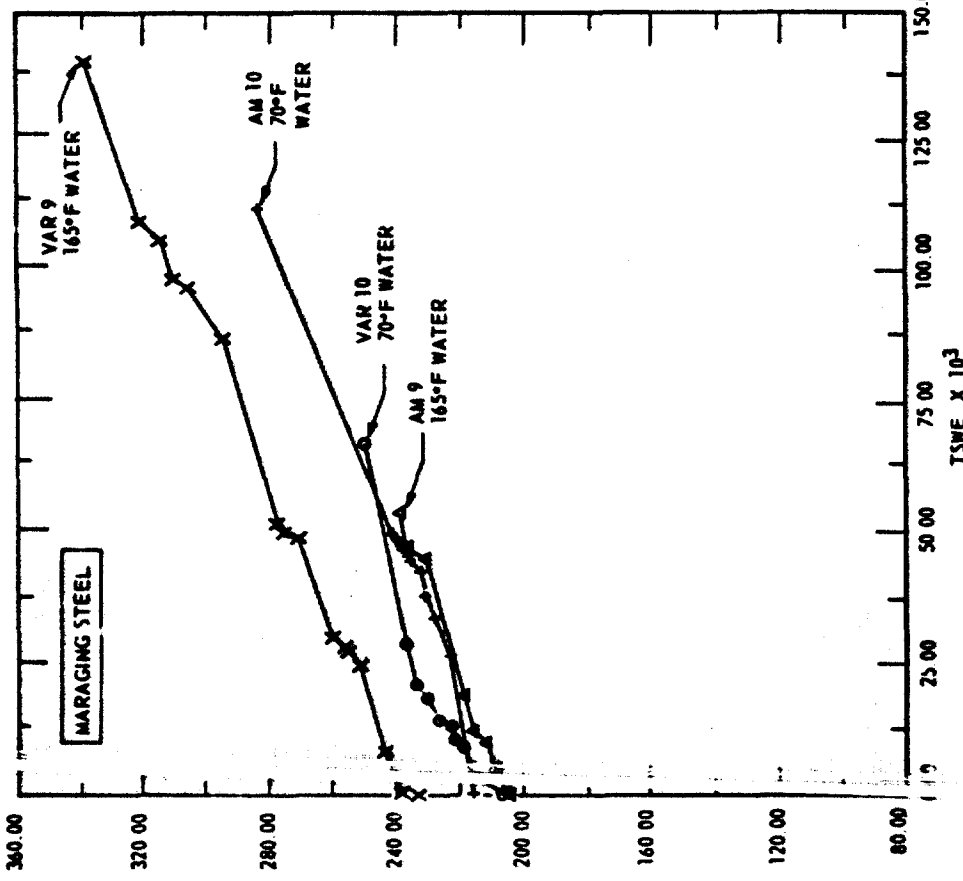


Figure 47. Relationship Between  $K^2/E$  and Count (same test as in Figure 46)

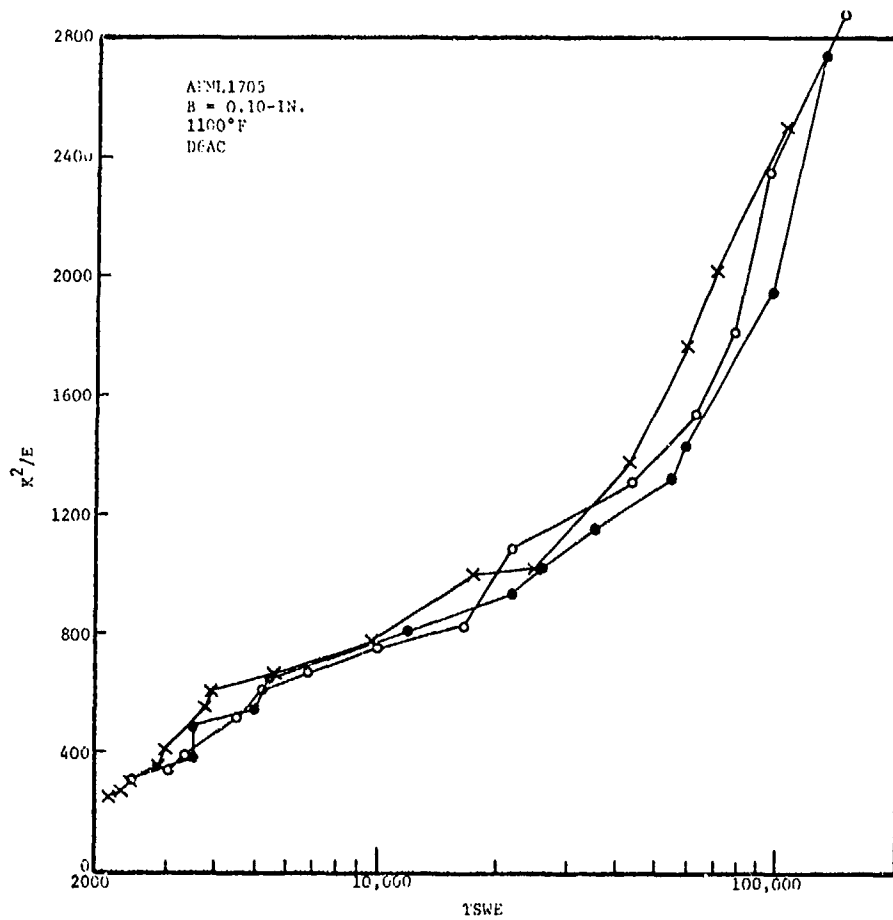


Figure 48. Relationship Between  $K^2/E$  and Count in Rising Load Tests of 1100°F Tempered D6aC Steel 0.10-in. Thick.

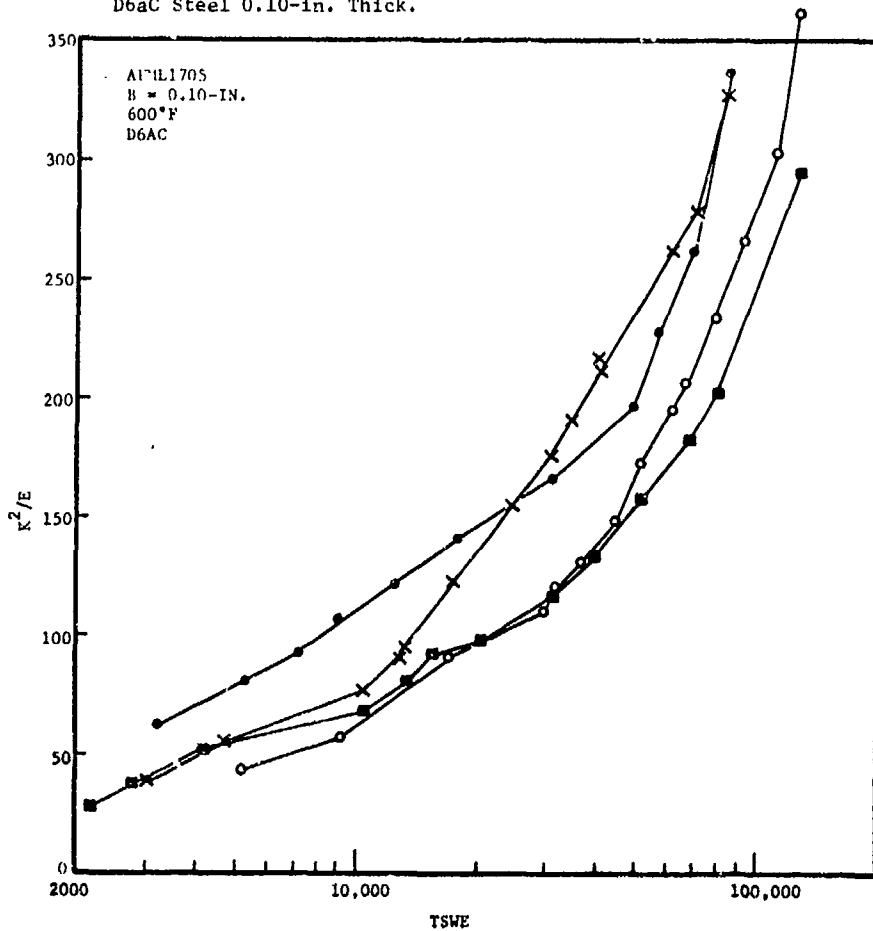


Figure 49. Relationship Between  $K^2/E$  and Count in Rising Load Tests of 600°F Tempered D6aC Steel 0.10-in. Thick.

subcritical crack growth such as stress corrosion, fatigue or strain aging, there will be slow crack growth until the point of instability is reached. Thus, in the present state of the art, there is no known way to distinguish between twinning per se and crack growth.

When materials are subjected to a rising load at room temperature, followed by a period of sustained load, as in proof testing, acoustic emission commonly shows a continuing but decreasing rate of emission for a short period of time. The phenomenon has been likened to room-temperature creep; the mechanism has not been identified. However, in the presence of a crack, at net-section loads well under the proportional-limit stress, when this phenomenon is observed it is believed to be associated with plastic-zone formation at the crack tip and, therefore, can be used to locate the crack. Moreover, when there is troublesome noise during rising load, by interrupting the loading process periodically, this phenomenon can be utilized to detect and locate the growing crack.

#### REFERENCES

1. J. Kaiser, "Untersuchungen uber das auftreten Gerauschen beim Zugversuch", PhD. Thesis, Technische Hochschule, Munich (1950); see also Arkiv Fur das Eisenhüttenwesen, 24, 43-45 (1953).
2. Schofield, B. H., "Acoustic Emissions Under Applied Stress", Aeronautical Research Lab., Office of Technical Services, U.S. Dept. of Commerce, Washington, D.C., Rept. ARL-15" (1961). Also Schofield, B. H., Barress, R. A. and Kyrola, A. A., "Acoustic Emission Under Applied Stress", ASTIA Document No. AD 155674, WADC Technical Rept. 58-194 (1958).
3. B. H. Schofield, "Acoustic Emission from Metals, Its Detection, Characteristics, and Source", Proceedings of the Symposium on Physics and Nondestructive Testing, San Antonio, Texas, Southwest Research Institute, October 1963.
4. Schofield, B. H., "Acoustic Emission Under Applied Stress", Aeronautical Research Lab., Wright-Patterson AFB, Ohio, Contract No. AF33(616)-5640, Project No. 7021, Task No. 70663, ASD-TR-53-509, Part I, April 1963, Part II, May 1964.
5. A. T. Green, C. S. Lockman, and R. K. Steele, Modern Plastics, 41, July 1964, 137-139.
6. A. T. Green, C. E. Hartbower, and C. S. Lockman, "Feasibility Study of Acoustic Depressurization System", Report NAS 7-310, Aerojet-General Corporation, February 1965.
7. C. E. Hartbower, W. W. Gerberich, and P. P. Crimmins, WELD IMPERFECTIONS, Menlo Park, California, Addison-Wesley, 1968, 371-389.
8. C. S. Lockman, A. T. Green, and R. K. Steel, WELD IMPERFECTIONS, Loc cit. 361-370.
9. C. E. Hartbower, W. W. Gerberich and P. P. Crimmins, "Characterization of Fatigue-Crack Growth by Stress-Wave Emission", NAS 1-4902, June 1966. Available from NASA, P.O. Box 5700, Bethesda, Maryland 20014. Report CR-66303.
10. A. T. Green, C. S. Lockman, S. J. Brown, and R. K. Steele, "Feasibility Study of Acoustic Depressurization System", NASA CR-55472, March 1966.
11. A. T. Green, "Stress-Wave Detection, Saturn S-II", NASA CR-61161, December 1966.
12. W. W. Gerberich and C. E. Hartbower, Int. J. of Fracture Mechanics, 3 (3), September 1967, 185-192.
13. W. W. Gerberich and C. E. Hartbower, "Monitoring Crack Growth of Hydrogen Embrittlement and Stress Corrosion Cracking by Acoustic Emission", Conference on Fundamental Aspects of Stress Corrosion Cracking, Ohio State University, September 1967.
14. C. E. Hartbower, W. W. Gerberich, and P. P. Crimmins, "Mechanisms of Slow Crack Growth in High-Strength Steels", AFML-TR-67-26, Vol. 1, Aerojet-General Corp., February 1967. Also WELDING JOURNAL, 47(1), Jan. 1968, 1-s. Received the Spraragen Award as best research paper published in the WELDING JOURNAL in the year 1968.
15. A. T. Green, "Testing of 10-inch Glass Hemispheres Using Stress-Wave Analysis Technique", N00014-67-C-1033, Naval Ship Research and Development Center, September 1967.
16. A. T. Green and C. E. Hartbower, "Stress-Wave Analysis Technique for Detection of Incipient Failure," Aerojet-General Corp., Presented at ONRL Conference on Incipient Failure Diagnosis for Assuring Safety and Availability of Nuclear Power Plants, Gatlinburg, Tennessee, October 1967. Published in the PROCEEDINGS of the AEC Conference.
17. W. G. Reuter, A. T. Green, C. E. Hartbower and P. P. Crimmins, "Monitoring of Crack Growth in Ti-6Al-4V Alloy by the Stress Wave Analysis Technique", Report on NASA Houston Contract NAS 9-7759, Dec. 1968.
18. C. E. Hartbower, W. W. Gerberich, and P. P. Crimmins, WELDING JOURNAL, 47(10), Oct. 1968, 433-443-s.
19. C. E. Hartbower, W. W. Gerberich, and H. Liebowitz, Engineering Fracture Mechanics, 1(2), August 1968, 291. Also C. E. Hartbower, W. W. Gerberich, W. G. Reuter, and P. P. Crimmins, "Stress-Wave Characteristics of Fracture Instability in Constructional Alloys", AD-674-881, Aerojet-General Corp., July 1968; IIW Doc. IX-700-70.
20. C. S. Baker, "Acoustic Emission and Prefracture Processes in High-Strength Steels," AFML-TR-67-266, Aerojet-General Corporation, Wright-Patterson AFB, March 1968. USAF Contract AF33(615)-5027.
21. C. E. Hartbower and P. P. Crimmins, "Fracture of Structural Metals as Related to Pressure-Vessel Integrity and In-Service Monitoring," presented at the ICRPG/AIAA 3rd Solid Propulsion Conference (AIAA Paper 68-501), Atlantic City, June 1968.
22. W. W. Gerberich and W. G. Reuter, "Theoretical Model of Ductile Fracture Instability Based on Stress-Wave Emission", ONR Contract Report N00014-66-C0340, Aerojet-General Corp., Sacramento, California, February 1969.

23. C. E. Hartbower, W. G. Reuter and P. P. Crimmins, "Mechanisms of Slow Crack Growth in High-Strength Steels and Titanium", Final Technical Report AFML-TR-67-26, Vol. II, June 1969 on Contract AF33(615)-2788 for the period April 1967 - April 1969, 199 pages.
24. A. T. Green, "Development of a Nondestructive Testing Technique to Determine Flaw Criticality", ARPA Contract F33615-68-C-1705, Aerojet-General Corp., Sacramento, California, August 1969.
25. C. E. Hartbower, WELDING JOURNAL, 35(2), Feb. 1970, 54-s.
26. C. E. Hartbower, F. J. Climent, C. Morais, and P. P. Crimmins, "Stress-Wave-Analysis Technique Study of Thick-Walled Type A302-B Steel Pressure Vessels", NASA NAS9-7759, Aerojet-General Corp., July 1969.
27. A. T. Green, Nuclear Safety, 10, January-February 1969, 4-18.
28. A. T. Green and C. E. Hartbower, "Development of a Nondestructive Testing Technique to Determine Flaw Criticality", Interim Technical Report on ARPA Contract F33615-68-C-1705 (ARPA Order No.1244, Code 8D10), May 1970.
29. Tatro, C. A., "Sonic Techniques in the Detection of Crystal Slip in Metals", Division of Engineering Research, College of Engineering, Michigan State University, East Lansing, Mich., Status Rept., 1959.
30. C. A. Tatro and R. G. Liptai, "Acoustic Emission from Crystalline Substances", Proceedings of the Symposium on Physics and Nondestructive Testing, San Antonio, Texas, Southwest Research Institute, October 1962, 145-153.
31. R. G. Liptai, "An Investigation of the Acoustic Emission Phenomenon", Ph.D. Thesis, Michigan State University, East Lansing, Michigan, 1963.
32. R. B. Engle, "Acoustic Emission and Related Displacements in Lithium Fluoride Single Crystals", Ph.D. Thesis, Michigan State University, East Lansing, Michigan, 1966.
33. Dunegan, H. L., Tatro, C. A., and Harris, D. O., "Acoustic Emission Research, Lawrence Radiation Laboratory, Livermore, Rept. UCID-4868, Rev. 1, 1964.
34. H. L. Dunegan and C. A. Tatro, Review of Scientific Instruments, 38, 8, August 1967.
35. H. L. Dunegan, D. O. Harris, and C. A. Tatro, Engineering Fracture Mechanics, 1(1), June 1968, 105-122.
36. H. Dunegan and D. Harris, Ultrasonics, 7, July 1969, 160-166.
37. Liptai, R. G., Dunegan, H. L. and Tatro, C. A., Int. J. Nondestruct. Test. 1, 1969, 213.
38. L. D. Mitchell, "An Investigation of the Correlation of the Acoustic Emission Phenomenon with the Scatter in Fatigue Data", Ph.D. Thesis, University of Michigan, 1965.
39. J. N. Kerawalla, "An Investigation of the Acoustic Emission from Commercial Ferrous Materials Subjected to Cyclic Tensile Loading", Ph.D. Thesis, University of Michigan, 1965.
40. A. B. L. Argarwal, "An Investigation of the Behavior of the Acoustic Emission from Metals and a Proposed Mechanism for its Generation", Ph.D. Thesis, University of Michigan, 1968.
41. J. R. Frederick, "Use of Acoustic in Nondestructive Testing", Semi-Annual Report O1971-2-T, March-August 1969, University of Michigan, November 1969.
42. N. G. Sankar, "Unload Emission Behavior of Material and Its Relation to the Bauschinger Effect", Ph.D. Thesis, University of Michigan, 1969.
43. R. C. Bill, "An Acoustic Emission Study of the Deformation Mechanisms of Polycrystalline Aluminum and Copper", Ph.D. Thesis, University of Michigan, 1970.
44. J. R. Frederick and D. K. Felbeck, "Dislocation Motion as a Source of Acoustic Emission", ACOUSTIC EMISSION, ASTM STP 505, American Society for Testing Materials, 1972, 129-139.
45. D. M. Egle, "A Comprehensive Analysis of an Acoustic Emission Detection System", Ph.D. Thesis, Tulane University, New Orleans, Louisiana, 1965.
46. R. H. Chambers, "New Techniques in Nondestructive Testing by Acoustical and Exo-electron Emission", AD-691-230, Arizona University, Tucson, Arizona, July 1969.
47. C. K. Day, "An Investigation of the Plastic Bursts of Microstrain in Zinc as Sources for Acoustic Emission", M.S. Thesis, Washington State University, Pullman, Washington, 1969.
48. J. C. Spanner, "A Selective Review on the Utilization of Acoustic Emission Techniques for Materials Research and Structural Integrity Analysis", M.S. Thesis, Washington State University, Pullman, Washington, 1970.
49. C. F. Tiffany, F. A. Pall, "An Approach to the Prediction of Pressure Vessel Minimum Fatigue Life Based Upon Applied Fracture Mechanics", Boeing Doc. D2-22437 (1963). Also Materials Research & Standards, 4(3), March 1964.
50. R. C. Bates and H. D. Greenberg, "A Study of the Fracture Resistance of Steel Pressure Vessels by Means of Charpy, Drop-Weight, and Full-Size Burst Tests", AIME Met. Soc. Conf., APPLICATION OF FRACTURE TOUGHNESS PARAMETERS TO STRUCTURAL METALS, Vol. 31, Edited by H. D. Greenberg, Chairman of the Symposium Committee, New York, Gordon and Breach Sci. Pub. 1964.
51. C. D. Crockett and W. R. Mason, "CBTT Incident Report, Structures Working Group", NASA Report SID 67-29, Jan. 1967.
52. C. E. Hartbower, "The Role of Weld Toughness in the Performance of a 260-in.-Dia Rocket Motor Case", International Institute of Welding 1969 Annual Assembly, Public Session, July 14, 1969, Kyoto, Japan.
53. J. E. Srawley and J. B. Esger, "Investigation of Hydrotest Failure of Thiokol Chemical Corporation 260-In.-Dia SL-1 Motor Case", NASA TM X-1194, Jan. 1966.



54. J. E. Srawley and J. B. Egar, Appendix by Tiffany and Masters, Ibid.
55. D. O. Harris, H. L. Duneagan and A. S. Tetelman, "Prediction of Fatigue Lifetime by Combined Fracture Mechanics and Acoustic Emission Techniques", University of California, Lawrence Radiation Laboratory, Report UCRL-71760.
56. W. Weibull, "The Effect of Size and Stress History on Fatigue Crack Initiation and Propagation," PROCEEDINGS OF THE CRACK PROPAGATION SYMPOSIUM, Cranfield, England, 2, September 1961, 271.
57. P. H. Christensen, "Cracking and Fracture in Metals and Structures", Ibid., 326.
58. C. E. Hartbower, C. F. Morais, W. G. Reuter and P. P. Crimmins, "Acoustic Emission from Low-Cycle High-Stress-Intensity Fatigue", Symposium on FRACTURE AND FATIGUE, May 3-5, 1972, George Washington University, Washington, D.C.
59. Brown, W. F. and Srawley, J. E., Plane-Strain Crack Toughness Testing of High-Strength Metallic Materials, ASTM STP 410, American Society for Testing and Materials, 1966, 12.
60. W. G. Reuter and C. E. Hartbower, ENGINEERING FRACTURE MECHANICS, 4 (1), March 1972, 183.
61. C. E. Hartbower, W. W. Gerberich and P. P. Crimmins, WELDING JOURNAL, 47(1), Jan. 1968, 1-18-s.
62. C. E. Hartbower, W. G. Reuter and P. P. Crimmins, "Mechanisms of Slow Crack Growth in High-Strength Steels and Titanium", Technical Report AFML-TR-67-26, Vol. II, June 1969 under USAF Contract AF 33(615)-2788.
63. W. G. Reuter and C. E. Hartbower, ENGINEERING FRACTURE MECHANICS, 3(4), Dec. 1971, 493-510.
64. W. W. Gerberich and C. E. Hartbower, WELDING JOURNAL, 47(10), Oct. 1968, 433-443-s.
65. Troiano, A. R., Trans. ASM, 52, 1960, 54-80.
66. Steigerwald, E. A., and Hanna, G. L., Trans. Quart. ASM 36(3), Sept. 1963, 656.
67. Gerberich, W. W., and Hartbower, C. E., Int. J. of Fracture Mechanics, 3(3), 1967, 185.
68. Notvest, K., WELDING JOURNAL, 45(4), April 1966, 173-178-s.
69. Jolly, W. D., Ibid., 48(1), Jan. 1969, 21-27.
70. Hartbower, C. E., WELDING JOURNAL, 49(2), Feb. 1970, 54-s.
71. C. E. Hartbower, W. G. Reuter, C. F. Morais and P. P. Crimmins, "Acoustic Emission for the Detection of Weld and Stress Corrosion Cracking", ACOUSTIC EMISSION, ASTM STP 505, American Society for Testing and Materials, 1972, 187.
72. Poteat, L. E. and Warner, W. L., WELDING JOURNAL 39(2), Feb. 1960, 70-76-s.
73. Winterton, K. and Nolan, M. J., Ibid., 77-72-s.
74. Rathbone, A. M., Conner, L. P., and Gross, J. H., Ibid., 43(12), Dec. 1964, 551-563-s.
75. C. E. Hartbower, C. F. Morais, W. G. Reuter and P. P. Crimmins, "Development of a Nondestructive Testing Technique to Determine Flaw Criticality", Final Report AFML-TR-71-218, on Contract F33615-68-C-1705, January 1972.
76. W. G. Reuter, private communication.
77. B. H. Schofield, "Research on the Sources and Characteristics of Acoustic Emission", ACOUSTIC EMISSION, ASTM-STP-505, American Society for Testing and Materials, 1972, 11-19.
78. Irwin, ENGINEERING FRACTURE MECHANICS, 1(2), 1968, 241-257.
79. E. Crowan, FRACTURE, B. L. Averbach, et al. eds., MIT, Wiley, New York, 1959, 147.

## VII.D SURFACE DYE PENETRANTS

Wolfgang Hansen

## SUMMARY

In the manufacture of parts for high-stress duty, maximally reliable and economic inspection for irregularities has become a mandatory procedure. For the detection of near-surface discontinuities, two penetrant inspection processes have won general acceptance: one using red dye; and the other, fluorescent penetrant.

With a few exceptions, these inspection processes lend themselves ideally to use on practically all metallic and non-metallic materials.

Fundamentals . . . . .	475
Performance . . . . .	475
1. Precleaning . . . . .	475
2. Penetration . . . . .	477
3. Removal of Penetrant . . . . .	477
4. Drying . . . . .	477
5. Developing . . . . .	480
6. Assessment . . . . .	480
Applicability of Process - Limitations . . . . .	480
Intensifying the Sensitivity . . . . .	480
Exceptional Cases . . . . .	482
Fabricated Sheet or Plate . . . . .	482
Difference between Red and Fluorescent Penetrants . . . . .	483
Qualification of Inspection Materials . . . . .	483
Qualification of Penetrant Inspector . . . . .	484
Bibliography . . . . .	484

## VII.E MAGNETIC PARTICLE TESTING

Eberhard Dickhaut

## SUMMARY

Whereas the penetrant inspection processes are suitable for testing very nearly all the materials utilized in the air industry, the magnetic particle inspection methods are restricted to use on ferro magnetic materials. Notwithstanding this limitation the magnetic flaw detection methods are preferred wherever the size and the material of the components will admit of its application. This preference is attributed to the greater simplicity and ease of process and detection over penetrant inspections.

Fundamentals . . . . .	485
Process Procedure . . . . .	485
1. Magnetising Methods . . . . .	485
1a. Current Flow Method . . . . .	485
1b. Threading Bar Method . . . . .	488
1c. Current Induction Method . . . . .	488
2. Pole Magnetising . . . . .	488
2a. Yoke Magnetising . . . . .	488
2b. Magnetisation using Coils . . . . .	489
Preparing the Parts . . . . .	489
Magnetisation . . . . .	489
De-magnetisation . . . . .	489
Ink Concentration versus Current Intensity . . . . .	489
Sampling the Test Media . . . . .	490
Usefulness of Process . . . . .	490
Bibliography . . . . .	490

## PART I

## VII.D. SURFACE PENETRANT DYES

Wolfgang Hansen

## FUNDAMENTALS

For conclusive inspection, a high contrast is needed between the defect and the sound background of the part. To this end, red or fluorescent dye suspended normally in oil is allowed to penetrate the defects. The discontinuities must be open to the surface. Penetration is attributed to capillary action, where a crack is likened to a tube of microscopic calibre. (FIG. 1).

When this capillary tube is placed in a vessel holding a wetting liquid, the liquid will rise in the tube. The rise is characterised by the following relationship: )<sup>1</sup>

$$h = \frac{2p}{r \cdot \gamma \cdot g}$$

where  $h$  = elevation in tube, comparable with depth of penetration in cm

$p$  = force of liquid acting on circumference of tube, surface tension in dyn.cm<sup>-1</sup>

$r$  = one-half the internal diameter of tube in cm

$\gamma$  = specific weight of liquid in g.cm<sup>-3</sup>

$g$  = acceleration due to gravity  $\sim 9,81 \text{ m}\cdot\text{s}^{-2}$

(FIG. 2)

As it will become readily apparent from the foregoing expression, the elevation in the tube relates to three quantities. Of these, tension  $p$  and specific weight  $\gamma$  are considered material constants. The greater the magnitude of  $p$ , the higher the elevation. The relationship also connotes that a decline in calibre and specific weight produces a rise in elevation.

Inasmuch as a crack may properly be considered a capillary tube squeezed flat, the implications for the inspection process are these:

the narrower the crack, the higher the elevation of the penetrant. It follows that there is a limit to penetration when the width of crack is somewhere near two to five times the size of molecule in the penetrant. The readability of the penetrant indication is determined by the sensitivity threshold of the human eye, so that perception will be precluded when the amount of dye drops below a certain minimum. )<sup>2</sup> The inspection medium, then, must be selected to

— maintain the specific weight of the penetrant at a minimum

— give a maximum of surface tension.

These properties cannot be varied arbitrarily; considerations such as the solubility of the basic dye and the desired degree of creep of the penetrant all compel a compromise which ultimately dictates the final properties.

## PERFORMANCE

1. Precleaning

Irregularities to be revealed by the use of a penetrant must be surface-connected. By this token, the defects must be free from grease, oil carbon, acids, alkalis or any other contaminants.

Pre-cleaning by grinding or abrasive blasting is normally not tolerated; it tends to plug voids, to peen the edges of discontinuities and so to seal the defects. (FIG. 3).

All parts are thoroughly pre-cleaned. On oily dirt, perchloroethylene or tri vapour gives good results. Stubborn dirt can be overcome by prior washing in warm alkali solution. Thereafter the part is thoroughly rinsed, cleaned and then dried to remove water from the discontinuities.

Some and carbon deposits can normally be eliminated with a suitable solvent.

Failing this, abrasive blasting may be employed as a last resort and must then be performed with all possible caution.

Abrasive blasting must be as brief as possible.

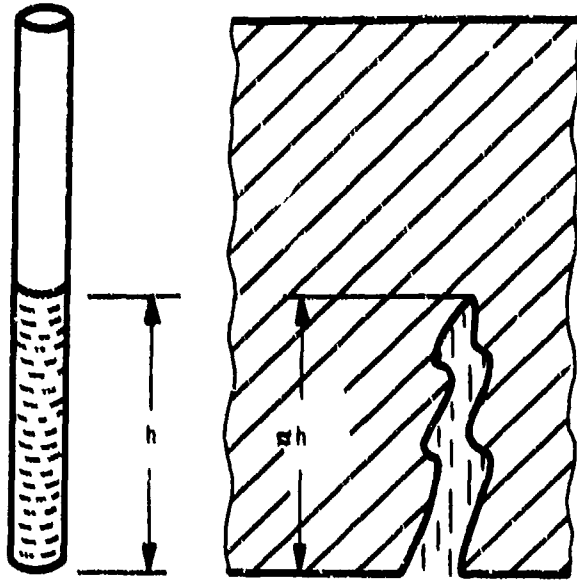


Fig. 1

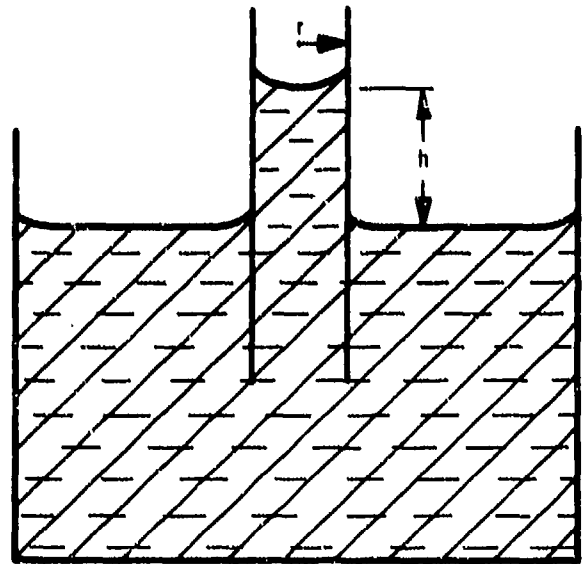
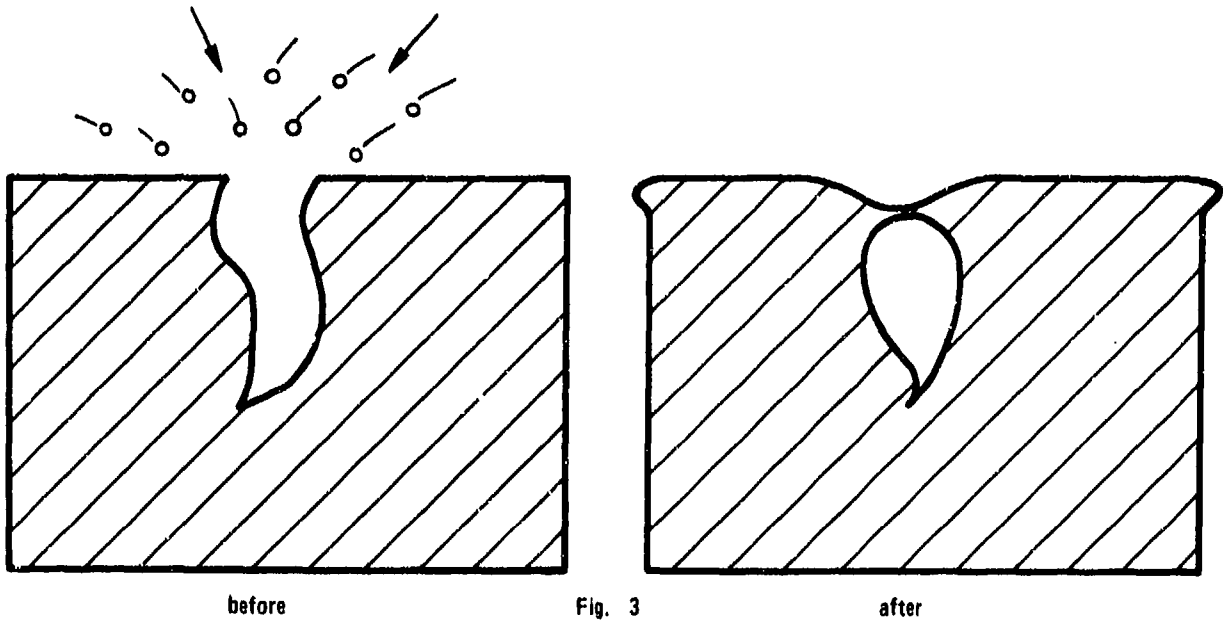


Fig. 2



before

Fig. 3

after

Blasting will almost always seal the more close-lipped discontinuities. Access of the penetrant to the defect is then achieved by etching the material with an acid or alkali. This removes a modest amount of material, enough to reopen the discontinuity. (FIG. 4).

Where materials are susceptible to intergranular corrosion, electrolytic etching, such as electrolytic polishing, has been finding increasing use in exposing defects sealed by abrasive blasting.

## 2. Penetration

After cleaning, the surface is wetted with the penetrant. (FIG. 5).

While any of the commonly practiced methods of application will normally give entire satisfaction, dipping is preferred in series production, where the parts are stacked in baskets and run through a succession of baths.

For spot inspection, spray cans are being used to advantage.

The penetrant dwell time is selected to suit the material under inspection so as to ensure adequate depth of penetration.

A penetration time of 10 minutes will be sufficient on castings of light-metal alloys exhibiting comparatively coarse defects, whereas 20 minutes is recommended for forgings and steels having occasionally very fine cracks.

For economy, the dipping method allows the penetrant to drip off during the last five minutes to recover some of the expensive penetrant.

## 3. Removal of Penetrant

For contrast between the defect and the sound material, the penetrant is removed from the surface of the part to remain only in the discontinuity. Depending on the method, the surplus penetrant is rinsed off with water either directly or after the application of an emulsifier. Use of a gentle stream of water is important for good cleaning. Water-washable penetrants come with a built-in emulsifier for immediate rinsing. Rinsing is limited to the minimum time necessary to remove all of the surplus penetrant from the surface, for the penetrant in the discontinuities is easily disturbed by rinsing. To alleviate this condition, a clock-operated washing process is employed where the water in a tank is whirled with air under pressure. The optimum rinsing time is determined experimentally. In this, the surface is checked under white or ultraviolet light every 15 seconds for exactly the moment that freedom from penetrant is achieved.

Post-emulsifiable penetrants are not water-washable but require the use of an emulsifier before they can be rinsed off in the shape of an emulsion.

What remains, when the emulsifier dwell time and all other conditions are just right, is a crack filled with penetrant exactly to the surface. When the dwell time is short, some of the penetrant refuses to emulsify and will cling to the surface. When the dwell time is long, the effect of emulsification reaches down into the discontinuity and rinsing will then carry away an excessive amount of penetrant. (FIG. 6).

During emulsification, penetrant is inevitably carried into the emulsifier tank, so that the emulsifier suffers from an increasing degree of contamination with penetrant. This will in some measure extend the normally necessary emulsifier dwell time. The still tolerable degree of contamination is about 20% for the commonly used emulsifiers.

For the purpose of experimentally deducing the proper emulsifier dwell time and the degree of contamination, a test plate size 100x100x3 mm of stainless steel, such as X10CrNiTi18 9, is used. It incorporates a 5 mm dia hole drilled through one of its corners.

Its surface is blasted with quartz grit for a mean 16 $\mu$ m profile. The plate is wetted with penetrant and then suspended for a duration of five minutes to allow the penetrant to drain. Thereafter the proper emulsifier is applied in accordance with manufacturer's instructions. The exact emulsifier dwell time is recorded. After the prescribed dwell time, the plate is rinsed immediately under a water spray, drained and developed (see 5.). Inspection should then disclose no indications other than the dotted impressions caused by grit blasting. Red or fluorescent background haze is indicative of deficient emulsification, and the plate is then reprocessed, with the emulsifier dwell time extended, and again checked for proper background.

This procedure is iterated until the exact time when the plate is just turning clean is ascertained. The minimum emulsifier dwell time is then determined analogously.

Then when emulsifiers of precisely known degrees of contamination are tested, a curve can be plotted to give the proper emulsifier dwell time at various degrees of contamination. (FIG. 7).

## 4. Drying

After washing, the part is dried. In the production of small-size or series items, good results are obtained with a thermostatically controlled oven drier operating on circulating air.

To combat corrosion, a continuous supply of fresh air is indispensable. The drier temperature is preferably about 65°C, higher temperatures tending to dull the fluorescent indication once the 80°C mark is exceeded. Loss of fluorescence relates directly to temperature and time, so that

removed layer, approx. 10 - 50  $\mu\text{m}$

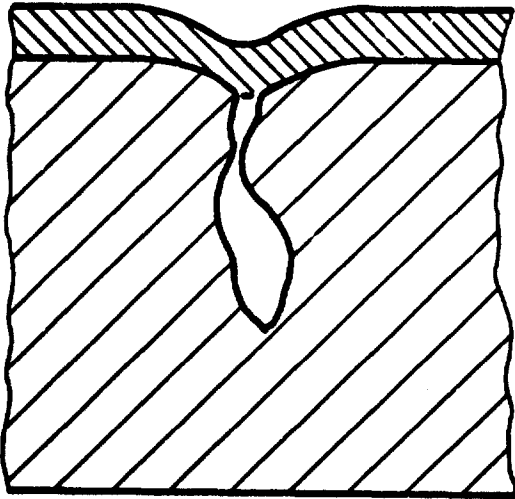


Fig. 4

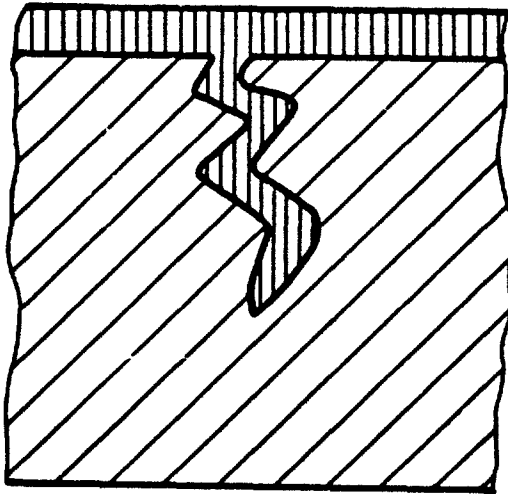


Fig. 5

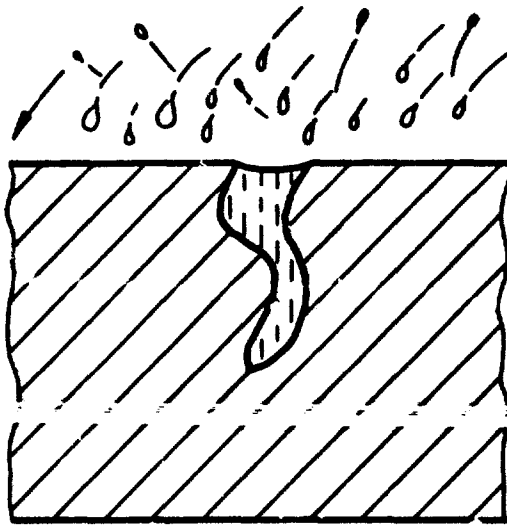
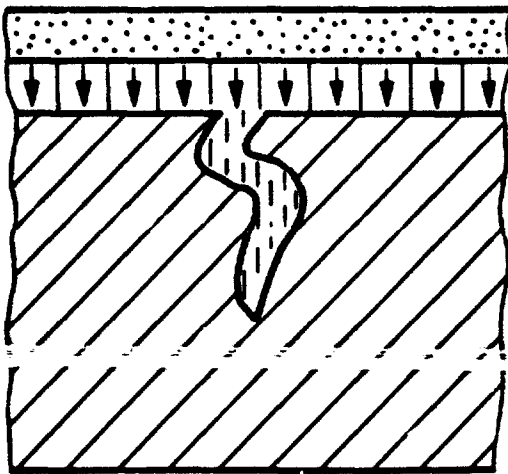
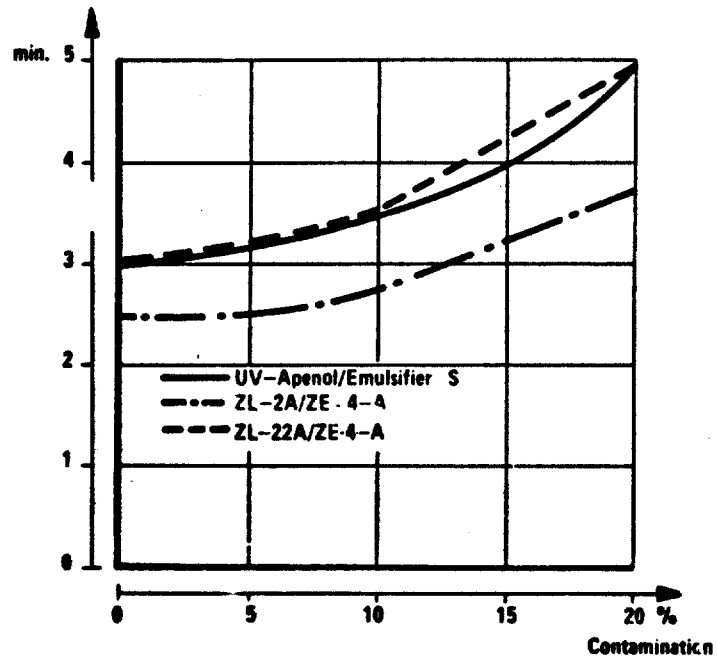


Fig. 6



Emulsifying time as a function of contamination

Fig. 7

the delicate indications are the first to disappear. For ease of drying bulky parts, a good procedure is to pass hot-air jets around the work, again avoiding overheating.

#### 5. Developing

In many cases the amount of dye in the discontinuity is not sufficient to form a contrast high enough to reveal the defect. When this happens, the indication must be intensified and resort is then made to a developer, a white powder, which is applied to the surface of the part. The developer is heavily porous in structure and so produces a countercapillary force which when contrasted with the penetrant operates to retract part of the dye from the defect. This forms an indication which is many times the width of the actual defect. In this manner, defects are easy to spot. (FIG. 8).

Various types of developer are in current use.

In conjunction with fluorescent dyes, preference often goes to developers in the shape of light, dry powders. They are normally applied in whirling cabins. Surplus powder is removed from the part before inspection commences. Another type is the aqueous wet developer, where the part is dipped in the developer solution after washing and when still wet, after which the developer is briefly allowed to drain from the part and the part is then dried. This type of developer ensures improved contrast with the penetrant in the defect. For use in conjunction with red dyes, the developers are mostly dispensed from pressurised cans. In this process, the contrast must be intensified as well as the indication, so that the developer is designed to produce a white background. This is achieved by adding to the contents of the spray can, next to the pressure agent, a volatile penetrant solvent. When the solvent contacts with a defect, the penetrant is diluted and increased in volume for a larger indication. This solvent type of developer must be sprayed sparingly, the right intensity of application being achieved when after the solvent has evaporated, the surface of the part is still barely perceptible as a faint shine through the developer. Otherwise, when the developer is put on too thick, delicate indications low in dye may not be able to spread to the surface, and safe evidence of the condition of the part is prevented. (FIG.9).

The developer must be allowed sufficient time to form an indication. When the contact with the penetrant is poor, developing time must be extended to suit.

Practical experience indicates a developing time of 15 minutes for dry developers, while aqueous wet developers require a time of approximately 25% in excess of their drying time. Nonaqueous wet developers require 5 minutes.

#### 6. Assessment

Evaluation of the indications requires perfect lighting conditions. The time allowed for observation of the part under inspection is limited to a brief period; some of the test media begin to bleed heavily shortly upon application and make a considered judgement difficult. The penetrant inspector must be dark conditioned for at least one minute before exploring ultraviolet indications.

Inspection takes place under the filtered light of ultraviolet lamps giving not less than 125 watts. These mercury vapour lamps wear comparatively fast and need periodic inspection.

As a minimum requirement the intensity of illumination in  $\mu\text{W}/\text{cm}^2$  and when measured at a distance of 300 mm from the filter glass shall be 75% of the performance in the virgin condition. Non-focussed lamps should never be allowed to fall below an output of  $350 \mu\text{W}/\text{cm}^2$ .

The test unit used for verification is sensitized in the wave length band of 365 nm.

#### Applicability of Process - Limitations

Where parts exhibit a comparatively rough surface profile resulting from a particular operation in their manufacture, the disclosure of exceedingly fine irregularities is frequently not the condition actually sought. The employment of high-sensitivity processes will cause the rough surface to emerge as a heavily dyed background which makes it all but impossible to spot defects, considering that the process as here described rests on the contrasting effect of the high-lighted defect against the sound background.

In instances like these - chiefly when alloy castings are under inspection - a process is required which duly allows for the condition of the surface. Preference is then accorded to water-washable penetrants. This process ignores extremely delicate defects but safely reveals microshrink and casting cracks.

Titanium or steel parts are not likely to produce poor backgrounds due to rough surfaces. Another consideration here is that the cracks or discontinuities are wholly disparate in nature, the cracks being notably finer, owing to the different material. This calls for an inspection process by which the threat of washout is minimized. Resort is then made to post-emulsifying penetrants. These refuse to wash off with water.

For cleaning the part, use must then be made of a separate emulsifier which causes the penetrant oil to transform, within a precisely prescribed period of time, and become soluble in water. The dye can then be rinsed off with water, forming an emulsion. The remaining treatment is akin to that of the first-named process.

#### Intensifying the Sensitivity

Although post-emulsifying penetrants largely prevent washout, there are still some parts which



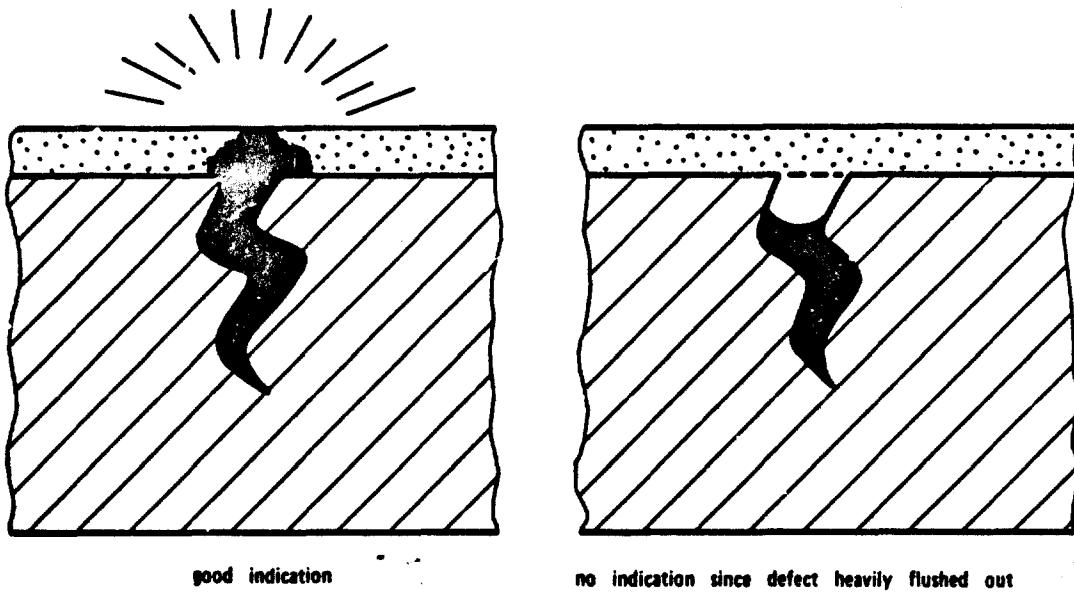


Fig. 8

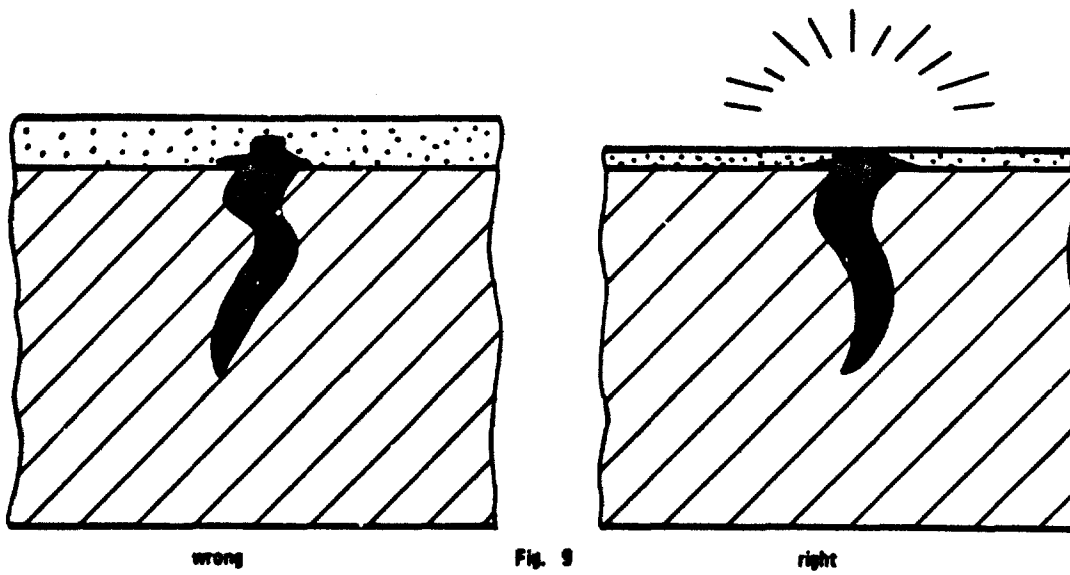


Fig. 9

must be free from even the slightest of defects. For these applications, the sensitivity of the process must be enhanced, which is achieved in several stages.

Use of a high-dye penetrant to form indications of greater dye intensity.

Use of a very slow acting emulsifier to alleviate the risk of overemulsifying.  
(For various reasons the chemical make-up of the oil puts a limit to the promotion of sensitivity offered by this expedient).

Use of a hydrophilic emulsifier.

This process involves a change in the sequence.

After the application of the penetrant, the part is thoroughly sprayed with water. This being a post-emulsifiable penetrant which will not dissolve in water, the operation is not anticipated to produce a 100% clean surface; the cleaning action is merely mechanical and as might be obtained with a rag.

A hydrophilic emulsifier - a 5% aqueous solution on wetting agent base - is then employed to remove the remaining traces of penetrant. The high, 95% water content prevents emulsification from spreading down into the crack to any significant degree. This ensures that the entire interior of the crack remains filled with dye and amenable to inspection. This is the normal procedure for rotating parts, such as rotor discs, shafts and blades, which are machined all around.

Use of a nonaqueous wet developer.

Exceedingly fine cracks accommodate only minute amounts of dye, so that a readily visible indication cannot form. The solution content in the nonaqueous developer then dilutes the dye and increases its volume. This promotes the contact between the developer and the penetrant for improved visibility.

The so improved sensitivity permits cracks in widths below  $1\mu\text{m}$  and depths of  $5/100\text{ mm}$  to be revealed with assurance.

#### Exceptional Cases

Certain parts defy the commonly practiced inspection processes or media.

#### Fabricated Sheet or Plate

Fabricated constructions incorporating spot welds or other overlaps imposed by their design give considerable trouble in the standard dip method. In dipping, the penetrant enters not only the discontinuities but also such cavities as may be formed by spot welded or riveted joints. Assessment in this condition is then difficult if not impossible considering the pools of penetrant collecting in the wrong places.

Cavities, once they are filled with penetrant, cannot be cleaned out with entire satisfaction. If nothing else, attempts to clean with tri or per vapour may result in an aggregate mixture of penetrant constituents, water and solvent. Subsequent treatment at temperature may then cause the solvents to decompose and hydrochloric acid to form, so that severe corrosion may ensue. In cases like these it is recommended that the penetrant be applied as sparingly as possible. Inasmuch as mere traces of penetrant will give adequate indication of cracks, it will be sufficient to just wet the part with the dye.

While this amount of dye will be sufficient to penetrate cracks, it will not be enough to flood the joints.

In this, the electrostatic method of penetrant application has been found useful, where the penetrant is fed from a tank to an atomizer gun through a hose, with 30 to 100 kV applied to the spray nozzle of the gun. The penetrant particles are charged in the electrostatic field and now travel to the grounded opposite pole, the part, along the electric field lines. Inasmuch as all penetrant droplets are subjected to this force, the process is marked by its notable economy. For good results, the surface should be barely wetted.

Emulsifier cannot be applied in this fashion for the reason that the amount of emulsifier would then have to be about quadrupled to ensure adequate emulsification. Use is therefore made of a highly sensitive water-washable penetrant.

The developer powder is applied electrostatically and dosed in minute amounts, so that the dust issuing from the atomizer is practically invisible. The layer on the part should likewise be barely visible. The electrostatic effect operates to compact the powder to a substantial degree. This improves the contact between the penetrant and the developer and so serves to achieve a much greater sensitivity than would otherwise be possible with the conventional method of spraying.

-----  
spray inspection appear as mere dots will in the electrostatic method emerge in distinct, continuous outline.

#### Liquid Oxygen Containers

When containers are intended for the storage of liquid oxygen, they must never be brought in

contact with organic substances for the reason that liquid oxygen will give rise to explosive oxidation when it meets with organic substances. Crack inspection using the conventional penetrants, which consist of organic substances, are therefore disallowed. This has led to the development of special inspection media containing aqueous dye solutions. These are not entirely free from organic substances, such as dyes or wetting agents, but are so low in them that careful cleaning will avert the risk of contact with the liquid oxygen. During the performance of the inspection proper, contact of the parts with organic substances must be meticulously avoided.)<sup>3</sup>

#### Difference between red and fluorescent Penetrants

The difference between red and fluorescent penetrants is chiefly in the contrast they give.

Red lines on a white background are more difficult to detect than fluorescent indications of a bright yellowish green against a dark, very nearly black background.

It can be shown experimentally that even very delicate cracks can be evidenced by red penetrant, capillary attraction being a law which applies to either type of penetrant.

For good results, the developer must be sprayed on sparingly so as to permit all indications, even the faintest, to reach the surface of the comparatively thick layer of developer. This, however, prevents a pure white background and makes for a grayish surface which impairs the contrast and makes assessment difficult.

Accordingly, a process utilizing red dye is not safe enough when the defects to be indicated are very delicate, and it is then discouraged. The concurrent use of red and fluorescent dye on a part is not allowed. Owing to the strong capillary forces it is difficult to remove penetrant from cracks once it has entered. Nor will different penetrants dispel others from the defects. Fluorescent inspection, therefore, is not conclusive evidence when it is preceded by red penetrant inspection of the same defects.

#### Qualification of Inspection Materials

The sensitivity category, the process operation and the quality assurance all impose certain requirements on the materials used in the inspection.

The document ruling investigations along these lines is LTF 6850-001.)<sup>4</sup>

This is the air industry standard governing acceptance tests on the various penetrant materials. It is used in the determination of physical data and in the testing of given comparative substances on specimens.

The manufacturer of the materials can, upon successful completion of the test series, file with the MBL)<sup>5</sup> for approval. For quality assurance, the user should periodically test the materials in the pot and on the shelf to give an early warning of any deterioration in the quality or of exhaustion of the emulsifier.

#### Qualification of Penetrant Inspector

The penetrant inspector should have normal vision and be conversant with the basics of inspecting and reading indications.

His sight, both near and far, and his colour discrimination, should be examined by an optician before the inspector is employed on the work and once every year thereafter.

The conscientious performance and evaluation of the inspection is closely linked with the integrity of the penetrant inspector. His expertise and judgement should therefore be expanded by continual training.

The basic knowledge, theoretical and practical alike, should be imparted in courses at yearly intervals.

A written examination eliciting solutions to reasonably practical problems has given full satisfaction.

It is essential that the inspector under examination be given an opportunity to discuss his answers with the instructor so as to imbue him with a keen awareness of the skills in his trade.

An inspector should be employed on the work only after he has demonstrated a minimum capability for it. His qualification should be revoked any time that his supervisors suspect that he may be negligent on the job.

BIBLIOGRAPHY

- 1.) E.A.W. Müller, Handbuch der zerstörungsfreien Materialprüfung  
Verlag, R. Oldenburg, München 1965
- 2.) R. Alburger, Specification-Technical Data-Penetrant Parameters  
Shanon Luminous Materials Co. Los Angeles, Calif.
- 3.) C.E. Bats, Principles of Penetrants,  
Magnaflex Corp. Chicago 1963
- 4.) LTF 6850-001 Luftfahrttauglichkeitsforderungen für RiBprüfmittel
- 5.) Musterprüfstelle der Bundeswehr für Luftfahrtgeräte

VII.E MAGNETIC PARTICLE TESTING

Eberhard Dickhaut

FUNDAMENTALS

When a magnetic field is created in a ferritic material, the molecular magnets will align in the direction of the field. The stronger the field, the greater the number of molecular magnets aligned. This holds true until saturation is achieved, when the molecular magnets are aligned in their entirety. Beyond that point, continued intensification of the magnetic field ceases to affect the magnetised material. When the magnetic field collapses, the molecular magnets will not all revert to their disordered state but will in part remain in orientation, leaving the material with a certain amount of remanent magnetism. When the magnitude of the induced magnetic field is plotted versus the progressive intensity of magnetisation, and then the condition charted at regressive magnetisation, a leg of the hysteresis loop is formed where the ascending curve extends to saturation point M and the descending curve to the point of remanence B<sub>r</sub>.(FIG. 1).

It is essentially irrelevant whether the magnetic field is created with the aid of a permanent magnet or an electric current, so that either method is finding use in current material inspection practice.

The magnetic field created in the part under inspection can be visualized in the shape of lines of force passing through the part on their shortest path from one pole to the other.(FIG. 2).

When a defect lies at right angles to the lines of force, the field is distorted and the lines are deflected. The magnetic field builds up in the remaining sound cross section. The lines of force passing directly under the surface are forced to the surface where they form a localized leakage field.(FIG. 3).

Since the magnetic conductivity of iron is appreciably greater than that of air, small magnetic particles in the shape of, say, iron dust are avidly attracted by the lines of force where they come through the surface in the leakage field. As a result, a visible magnetic bridge is formed. In this manner, parts can be dusted with an iron powder for evidence of discontinuities lying at substantially right angles to the direction of the field. The place of iron dust is normally taken by finely ground ferric oxide dyed various colours for maximally high contrast in specific applications.

Process Procedure

For conclusive indication, it is essential that the lines of force are made to run in a direction normal to the direction of the discontinuity. Accordingly, a part of bar stock requires magnetisation in two different directions to evidence flaws in both the longitudinal and the circumferential directions.

1. Magnetising Methods

1a. Current Flow Method

When it is intended to detect a flaw lying along the length of the part, the plane of the magnetic field must be at right angles to it. Now wherever a current is passed along a conductor of a non-ferritic material, such as copper, a circular magnetic field is associated with it, the lines of force running in closed concentric loops around the conductor over its entire length. This phenomenon is expediently exploited. (FIG. 4).

For when this field is applied to a ferritic conductor by passing a current through the part, the lines of force will be entirely internal owing to the superior magnetic conductivity of the material. (FIG. 5).

So when a current of electricity passes through a part, a defect lying at right angles to the direction of the field gives rise to a leakage field which indicates its presence. (FIG. 6)

For inspection, the part is placed between the contact pads of a current flow machine. Where this is not practicable the current can be passed through the part using suitable clamps and cables. To prevent burning, the contact pads should be faced with soft lead or copper braid.

A satisfactory degree of magnetisation can usually be created by using a current of 300 amps A.C. for each 10 mm in diameter of the part measured at right angles to the current flow. (Formula 1). When D.C. is used, this should be 400 amps for each 10 mm in diameter. (Formula 2).

$I_a = \frac{300 \cdot D}{10}$  Formula 1

$I_d = \frac{400 \cdot D}{10}$  Formula 2 )1

- I<sub>a</sub> = current intensity A.C.
- I<sub>d</sub> = current intensity D.C.
- D = diameter or diagonal of part, in mm.

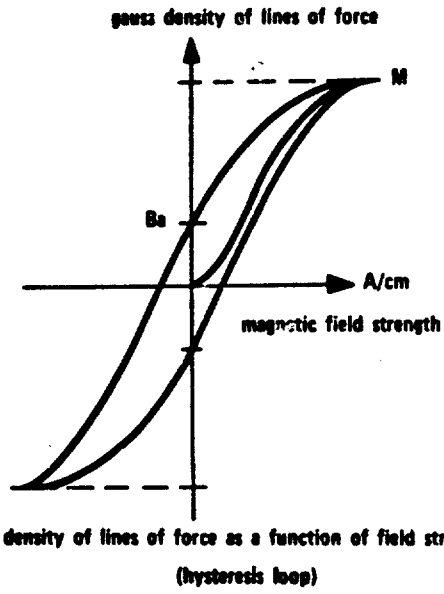


Fig. 1

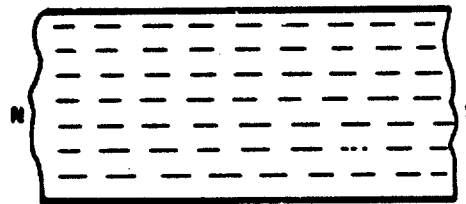


Fig. 2

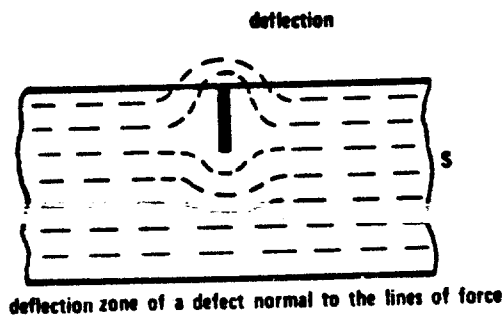
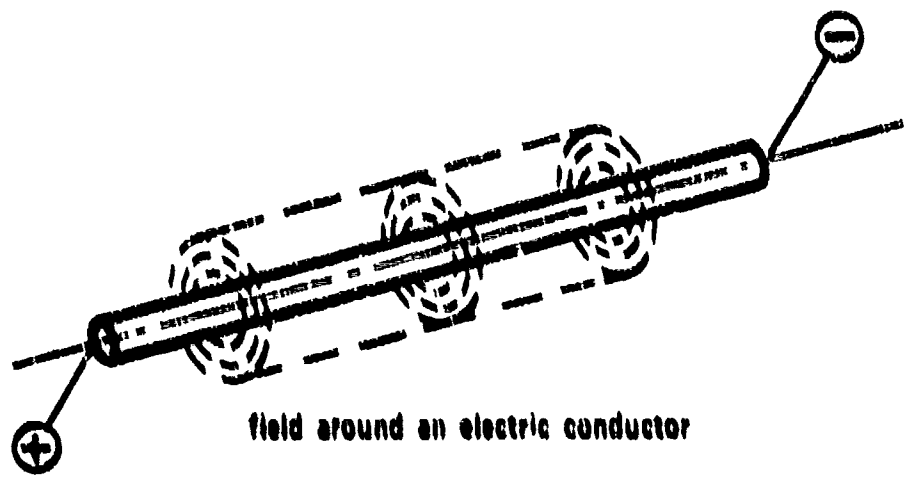
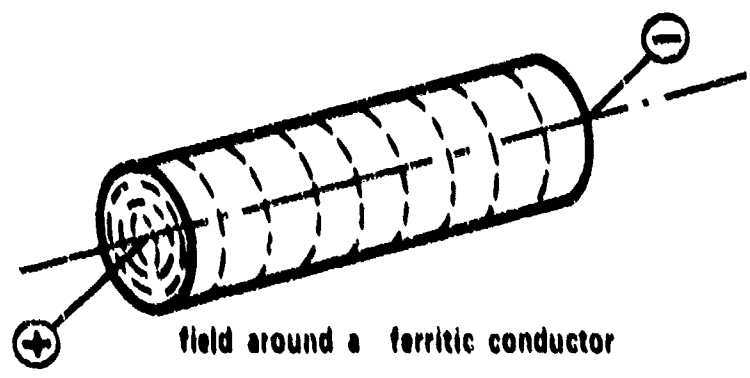


Fig. 3



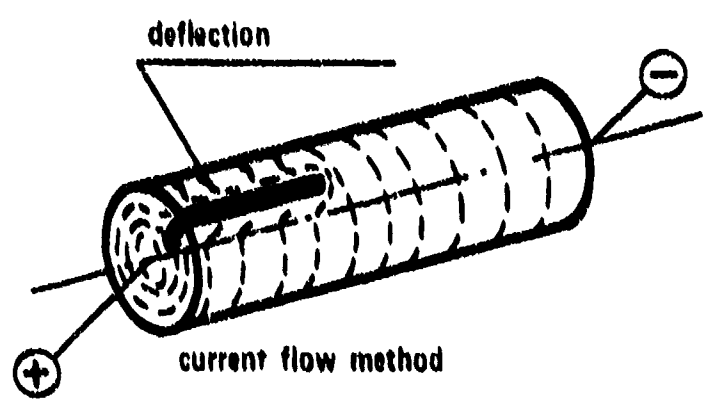
field around an electric conductor

Fig. 4



field around a ferritic conductor

Fig. 5



current flow method

Fig. 6

These figures are admittedly approximate and relate only to parts of simple geometry. The proper amps for complex shapes must be confirmed by trial. A tangential field-intensity meter will be a useful tool in this.

The steels currently finding use in the air industry (no gray cast materials) normally call for 24 amps/cm at the surface. It should be remembered, though, that different diameters will give different figures at one and the same current value. The readings should never be short of the specified figure. When 30 amps/cm is exceeded locally, a new revised magnetising value must be determined for that diameter. As a rule, inspection should commence with the smallest magnetising figure so as to avert trouble from remanence.

Where an annular component is to be tested by passing a current diametrically across it, when it is clamped between the pads in a plane parallel to its diameter, it should be recalled that the current will divide and the current passing through each half of the ring will only be half that indicated on the meter of the current flow machine.

#### 1b. Threading Bar Method

Tubular or circular parts can be tested by centrally threading them on a copper bar and passing a current of electricity through the bar. The magnetic field created around the bar will then concentrate in the component. This permits the indication of defects which extend approximately in parallel to the axis of the copper conductor and radially at the faces. The particular merit of this method is that it will help detect defects also at the inner surfaces of the component. (FIG. 7).

Burns are normally safely prevented.

Long components should be held clear of the copper conductor by insulators, so that arcing is avoided. The conductor should have the maximum cross section still compatible with the inking and assessment requirements on the internal diameter.

#### NOTE:

In the current flow and threading bar methods, the defects revealed will lie parallel and radial to the direction of the current. The direction of the magnetic field is at right angles to the peripheral flow of the current.

For magnetisation, the length of the part under inspection is no consideration as long as the intensity of the current is maintained at the proper magnitude.

#### 1c. Current Induction Method

When an annular component is taken as a single turn, untapped secondary winding of a transformer, a current can be induced free of contact into the component which will vary according to, among others, the cross-sectional area of the component and of the current inducing laminated iron core. Inasmuch as the faults detected in parts through which a current is passed are invariably in the direction of the flow of the current, this method reveals all peripheral flaws no matter on what surface they may be located. (FIG. 8).

Good results have been obtained from the induction method through the use of an induction machine where the yoke is excited with A.C., inasmuch as in this arrangement only a laminated core is clamped between the poles of the yoke. This core, when fitted with an additional copper conductor, can simultaneously be used as an auxiliary conductor for passing the current. )2

This method of testing is particularly suited to parts of a less rigid nature or where clamping of the part is difficult. It is not recommended for parts where the radial dimension is far in excess of the sectional thickness.

Since the iron core must be a considerable cross section to be able to pass the necessary currents, the internal diameter of the part is a consideration in the selection of this test method.

The current in the ring can be measured using a grip current tester. The magnetising value at the surface should be 24 - 30 amps/cm.

#### NOTE:

By induction magnetising, the flow of current in annular components is circumferential. Defects are detected in parallel to the direction of current flow.

### 2. Pole Magnetising

#### 2a. Yoke Magnetising

To avoid remanence, the component is magnetised by means of an electromagnet (yoke). The current flowing in the electromagnet serves the sole function of creating the magnetic field and does not pass through the part under inspection. The risk of burning is here precluded. (FIG. 9).

The suitable intensity of field, which is read in ampere turns, is satisfactorily ascertained using a tangential intensity tester as described in the section on current flow techniques. It should be remembered, again, that different cross sections make for different values of magnetisation. Where a part is of stepped section, it may be necessary to make an inspection for



each section.

When the component is clamped between the pads of the yoke by means of a mandrel, it should be noted that air greatly resists the magnetic field and that the distance between the pads and the part should therefore be held as close as practicable.

#### 2b. Magnetisation using Coils

Parts of markedly stepped cross section are preferably inspected inside a coil.

Only the length of a part which lies actually within the coil is efficiently magnetised.

Repeat tests are therefore necessary when inspecting long components.

Coils must be insulated to avoid shorting. The intensity of magnetisation is dependent on the number of turns. All other factors being equal, the intensity of field is doubled when either the current or the number of turns is doubled. The intensity is measured best with a tangential intensity meter.

#### NOTE:

The magnetic field created when magnetisation is by yoke or coil lies in an axial plane, and detection is provided of defects which lie at right angles to the field or the axis of coil.

#### Preparing the Parts

The part must be positively free from grease and scale. In the case especially of fluorescent detector inks, the smallest degree of contamination by grease or oil may cause a change in the fluorescence of the carrier liquid, and a loss of sensitivity will then ensue. Scale or air-borne rust particles will likewise bear negatively on the sensitivity inasmuch as these particles are subject to magnetic effect. They may displace the detector ink at discontinuities but will remain invisible for lack of dye. Electrolytically deposited coatings are recognized as a further cause of poor sensitivity.

When the coating thickness is about 10  $\mu$ m or over, detection obviously suffers. This has also been noted where the material is coated with varnish.

#### Magnetisation

Shortly before magnetisation the part is completely wetted with the carrier liquid containing the indicating medium. The flux is then switched on for the duration of one second while inking continues. Inking is halted just before the first shot of magnetising current is completed. Two more shots of current are then applied, each one second in duration, but inking must definitely cease. Thereafter the liquid is allowed one minute to drain from the part, and the part is ready for assessment. Care must be exercised to prevent contact with other magnetised parts before inspection.

#### De-magnetisation

De-magnetisation after inspection is mandatory. A de-magnetising method in frequent use is to keep reversing the poles of the magnetic field until after about 20 shots the field is gradually reduced to zero intensity. (FIG. 10).

De-magnetisation often gives trouble where components are magnetised to the core, when D.C. was used for magnetisation. This then requires the use of special equipment of high output and exceedingly low reversal rate (less than 1 cps).

As a result, the use of A.C. for magnetisation is developing. In this process the skin effect or the concentration of electrical current on the outer surface of a conductor limits magnetisation to the surface and simultaneously improves detection on parts of changing section. De-magnetisation can then rely on substantially less complex equipment.

#### Ink Concentration versus Current Intensity

Proper concentration of the test medium is a determinant of sustained success in magnetic flaw detection. When an artificial flaw is tested and the quality of indication plotted as a function of concentration and intensity of current, a diagram much like FIG. 11 will result.

It will become apparent from the foregoing graph that for a discontinuity lying 0.5 mm under the surface, the amperes must be increased 50% when the concentration is lowered from 3 grams a liter to 0.3 grams a liter. The recommended concentration of fluorescent test media has therefore been rated at 3 to 5 grams/liter. In this, a small amount of background fluorescence is tolerated if only the sensitivity is a maximum.

It should be noted here that in pastes and liquid concentrates, the effective content of the test medium is a mere 25 to 30% of the total weight.

A useful method of sampling the concentration employs a centrifugal tube per ASTM D96-63)<sup>2</sup>. Considering the slow rate of precipitation, the practice is often to load the liquid at the end of the workday and check the results the morning after.

### Sampling the Test Media

The test media, notably when these are fluorescent, will deteriorate as the dye segregates from the oxide particles. The concentration, as tested, will therefore not tell the whole story. For evidence of the remaining efficacy of the ink, MTU are using a test piece designated No. 3, which is 50 mm in diameter and 10 mm in thickness. It incorporates a number of coarse grinding cracks as well as minute fissures resulting from stress corrosion. The plate is magnetised once using 30 amps/cm by the threading bar method and then allowed to operate entirely on remanent magnetism. It is merely wetted with ink and given a minute for the liquid to drain from it. When the test medium is sufficiently active, the cracks and fissures will show up in their entirety. When the strength of the ink is exhausted, only the coarse grinding defects are indicated. It will be sufficient evidence to focus attention on a certain zone on the plate and re-examine the self-same zone for changes whenever a sampling inspection is made. (FIG. 12).

### Usefulness of Process

The inspection process essentially lends itself to use in the ready detection of all surface flaws up to a width of less than  $1\mu\text{m}$  and a depth of about  $10\mu\text{m}$ . This is the order of magnitude of the finest cracks in the test plate No. 3 MTU are using. This will hold only when the surface is either ground or dressed smooth; otherwise, the indications of machining imperfections will overshadow the evidence of true defects.

When use is made of less potent inks, the sensitivity can be dulled to a point where the only flaws indicated are such rough defects as may stem from forging or rolling operations. Concerning the formation of indications it appears that the two types of dye, black or fluorescent, give entirely equivalent results. The differences which in the case of fluorescent powder are caused by the thickness of varnish layer on the oxide particles are too small to have any practical consequence. The fluorescent indication nevertheless makes for substantially higher contrast which greatly facilitates assessment and obviates the need for special aids to interpretation.

The detection of subsurface flaws still poses formidable problems and its success hinges largely upon the shape of the defect. Drilled 0.5 mm diameter holes can still be revealed at depths of about 1.5 mm under the surface; fissures, at about 2.5 mm. At greater depths than these, the indication becomes so obscure that conclusive analysis is precluded.

### Bibliography

- 1) Dr. E.A.W. Müller, Handbuch der zerstörungsfreien Materialprüfung  
Verlag R. Oldenburg, München
- 2) Zerstörungsfreie Werkstoffprüfung,  
Mitteilungen der Firma Karl Deutsch, Wuppertal Nr. 5 März 1971
- 3) ASTM D 96 - 63 Band 17/64 Petroleum Products.

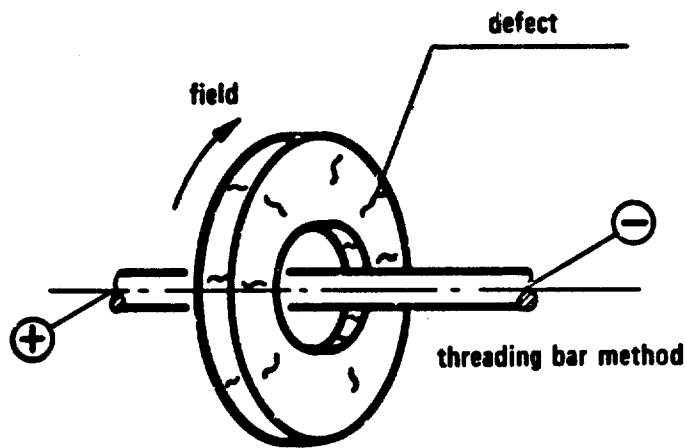


Fig. 7

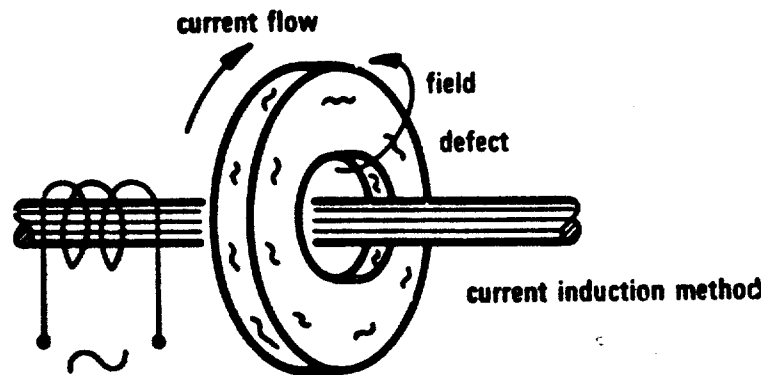


Fig. 8

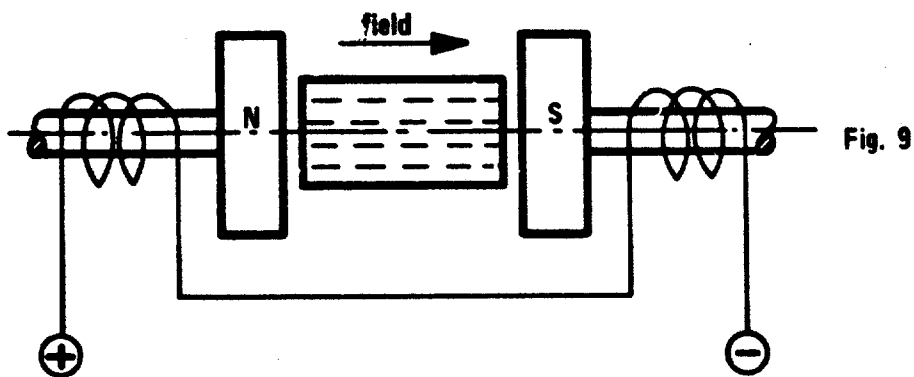


Fig. 9

yoke magnetizing method

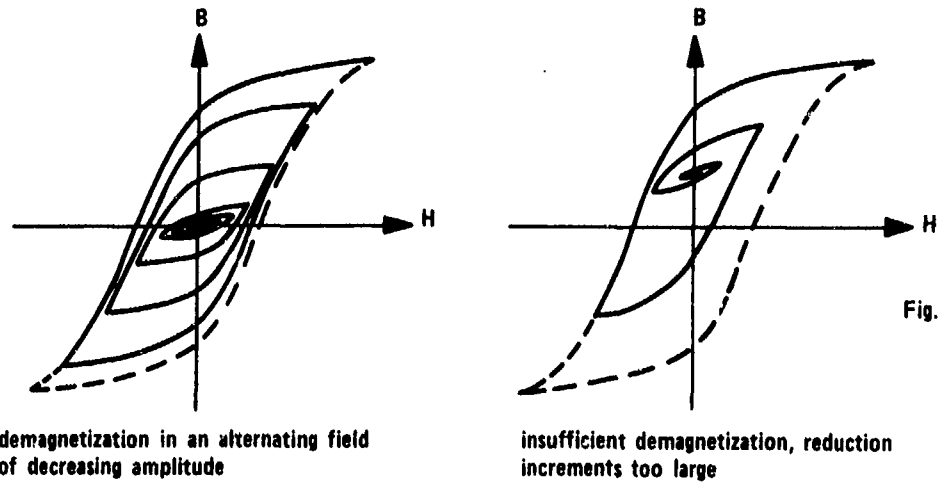


Fig. 10

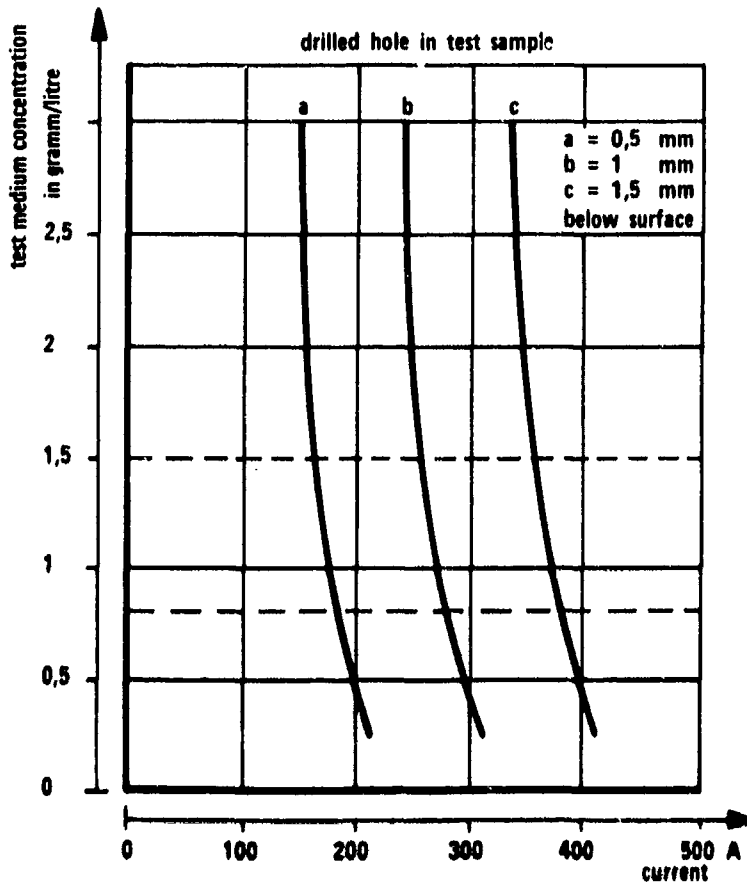


Fig. 11

Flaw indication as a function of current and concentration of test medium

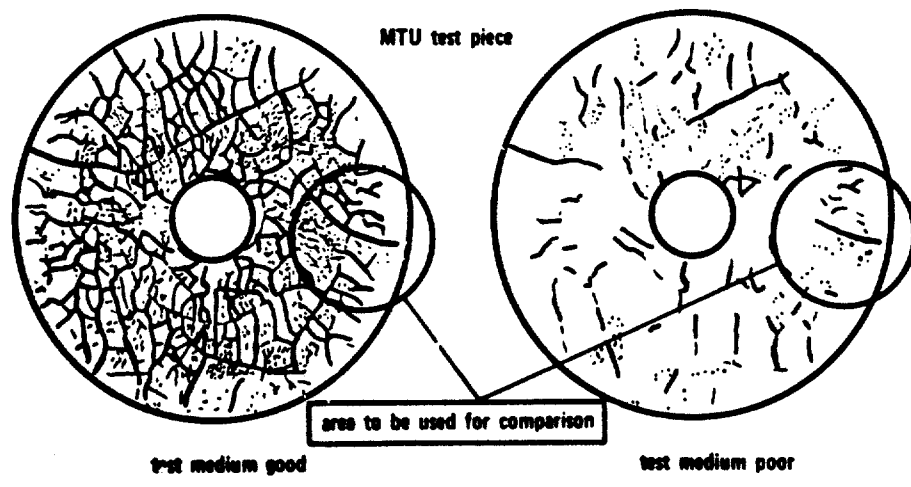


Fig. 12

## VII.F FLAW DETECTION BY MEANS OF HOLOGRAPHIC INTERFEROMETRY

Klaus Grünewald

I. Optical Interferometry and NDT . . . . .	494
II. Principles of Holography . . . . .	495
III. Holographic Interferometry . . . . .	496
IV. Some Results of Holographic Flaw Detection Measurements . . . . .	499
V. Limitations of the Method . . . . .	501
References . . . . .	501

## SUMMARY

In the past years, holographic interferometry developed into an effective test method. Proceeding from brief descriptions of optical measuring principles and of holography, the theoretical and experimental aspects of holographic interferometry are discussed. References are made with respect to quantitative interpretation of interferograms. The possibilities of flaw detection are illustrated by some experimental examples.

## 1. OPTICAL INTERFEROMETRY AND NDT

Optical methods of investigations utilizing the wave nature of light have at all times been superior by very accurate information on geometric dimensions or changes of the tested objects. This feature results from the fact that the light passing different optical paths can lead to interference. A classic example for such an interferometric test method is the Michelson interferometer at which the path-length difference between two mirrors arranged at right angles is interferometrically measured. The monochromatic light beam of a point source falls on the two reflecting mirrors via a beam splitter. The two reflected beams of about the same intensity are combined again at the beam splitter and are observed in an observation telescope. If both beams covered the same optical path length, they are in phase at the observation point, i.e. they lead to maximum intensity. In case one or both mirrors is displaced normal to its surface by  $\lambda/4$ , the amount of a quarter of wave length of the light, the interference in the observation point results in an extinction. Measurement of mirror displacement consists, therefore, in counting the n-extinctions occurring during the displacement by  $\Delta x$ . The displacement  $\Delta x = n \cdot \lambda/2$  can, therefore, be measured with an accuracy of  $\lambda/4$ .

With increasing  $\Delta x$ , the relative error is steadily decreasing; at a displacement of 50 cm, n is about  $2 \cdot 10^8$  ( $\lambda = 500$  nm) and the error  $\pm 2,5 \cdot 10^{-5}$  %.

While the high accuracy of the interferometric measurements is rendered possible by the wave length stability of the light, another feature of the light limits the measuring range and, therefore, the applicability of these interferometers.

The light emitted by single atoms consists always of wave trains, the length of which is given by the radiation period of the atoms of about  $10^{-8}$  s. Different wave trains emitted successively are, however, no longer coherent, i.e. their phase relation is not stable but random.

The wave trains of a single atom can lead to the formation of interference phenomena. If these wave trains are split into two partial waves which lead to interference after passing two different paths, the phases of the partial waves are given by

$$\varphi_1(x_1) = kx_1 + \delta_1$$

$$\varphi_2(x_2) = kx_2 + \delta_2$$

$k = 2\pi/\lambda$  and  $\delta_1$  is the initial phase shift of the successive wave trains identified by the index 1. The phase difference  $\Delta\varphi$  of the partial waves which is important for the interference remains therefore constant over several periods:

$$\Delta\varphi = \varphi_1(x_1) - \varphi_2(x_2) = k(x_1 - x_2)$$

provided that  $|x_1 - x_2|$  is smaller than the length of the wave trains being abt. 1 m.

In the practical experiment not only one atom is used for light generation but a considerable number of radiating atoms. Since their phase shift  $\delta$  is different among one another, coherence of the light is limited. An undisturbed interference is only possible if the coherence condition of Verdet is met:

$$a \sin \theta \ll \frac{\lambda}{2}$$

a is the lateral expansion of the light source and  $\theta$  the aperture angle at which the observed beam emerges.

This condition limits the practical possibility of the classic interferometry by the fact that a great coherence length is always connected with a small a or a small  $\theta$ , respectively, and, therefore, with low light intensity.

The laser is a radiation source not underlying this restriction. When generating light in the laser, the "stimulated emission" from the atoms are no longer uncorrelated. Emission is rather made in the way the wave trains emitted by all atoms have a stable

phase relation among one another. In this case, light of high intensity is obtained with a great coherence length. The coherence length is limited then by the width of line of the emitted radiation ascribed for example to instabilities of the resonator.

Now with such light sources it is not only possible to carry out interferences with tight light beams, i.e. spatially concentrated wave fields, but to lead wave fields emanating from spatially expanded objects to interference.

Holography, an invention of the Hungarian physicist Gabor [1], is a suitable method to record such interference phenomena. This enables one to record and reconstruct coherent wave fields. The interfering wave fields are ascribed to object positions realized at different times. The practical significance of this method results among others from the applicability in the range of nondestructive testing. The holographic interferometry measures the deformation of an object on its surface. The deformation itself, however, is defined by the properties of the material varying more or less considerably at the defects.

## II. PRINCIPLE OF HOLOGRAPHY

The essential point of the holographic method is the full identity of the reconstructed object wave with the initial object wave. The physical processes these facts are based on can be illustrated by the simple example of recording a spherical wave emanating from a point with a plane wave (Martienssen [2]).

For better understanding of the method, the mathematical relations (see e.g. Gabor [3]) shall be briefly represented according to fig. 1.

The object wave which is represented in fig. 1 by the wave in the (x,y) plane from one object point is given by the complex amplitude

$$G(x,y) = g(x,y) \exp \{i(\omega t + \varphi_G)\} \quad \text{with } \varphi_G = \frac{2\pi}{\lambda} l_G + \delta_G$$

$\sigma$  being a real variable. The phase  $\varphi_G$  is composed of a constant phase term  $\delta_G$  and a term which depends on the path length  $l$  the wave has travelled to a certain point (x,y).  $\lambda$  is the wave length and  $\omega$  the frequency of the monochromatic light.

At the position of hologram plate H, this wave is superimposed by the coherent reference wave

$$R(x,y) = r(x,y) \exp \{i(\omega t + \varphi_R)\} \quad \text{with } \varphi_R = \frac{2\pi}{\lambda} l_R + \delta_R$$

The superposition of both waves results in a stationary interference pattern and the following intensity distribution is recorded in the points at the hologram plate (fig. 1a):

$$I(x,y) = |G(x,y) + R(x,y)|^2 = (G + R)(G^* + R^*) = g^2 + r^2 + GR^* + RG^*$$

$g^2$  and  $r^2$  represent the intensity of both waves,  $G^*$  and  $R^*$  are the complex conjugate of  $G$  and  $R$ , respectively. If the developed hologram plate is again transmitted at its initial position by the reference wave, hence results the following wave field behind the plate:

$$W = I(x,y) \cdot R(x,y) = (g^2 + r^2)R + r^2G + G^*R^2$$

The first term is the damped reference wave, the second is the damped object wave and the term

$$G^*R^2 = gr^2 \exp \{i(\omega t + 2\varphi_R - \varphi_G)\}$$

leads to a real image of the object.

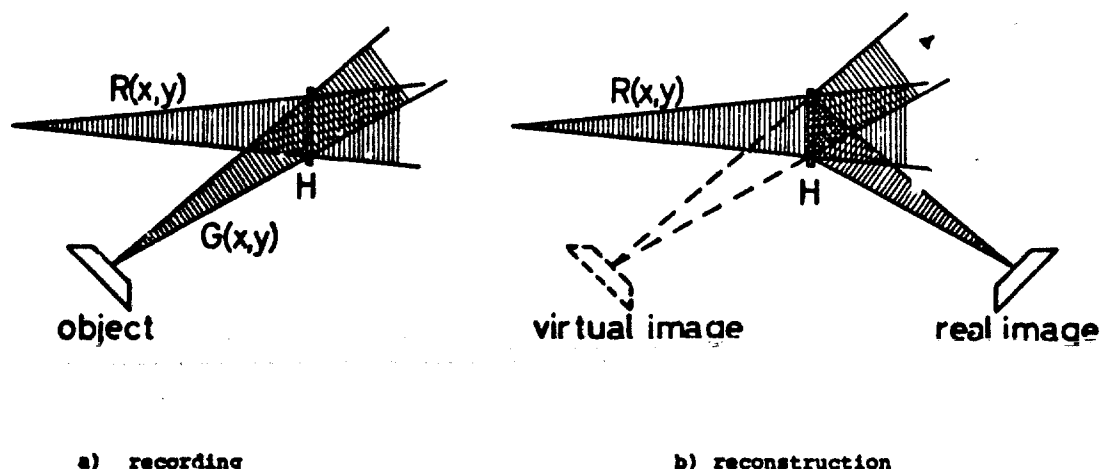


Fig. 1: Schematic Holographic Arrangement

Fig. 1b illustrates the shape of the single wave fields with the reconstruction described by the above formula. A more illustrated description of the process bases on the fact that the reference wave is diffracted with the reconstruction at the hologram plate the interference pattern of which acts as a diffraction screen. The zero order of diffraction represents the damped reference wave and the two first orders give the virtual and real image of the object.

The complete reconstruction of the object wave field gives a complete three-dimensional reproduction of the object. Moreover, it is possible to observe the virtual image in the scope of the expansion of the hologram plate in various views. This means, however, that every part of the hologram plate contains the complete information on the wave field.

Without entering into further theoretical aspects of holography and its application (see [4,5,6]), some criteria for the practical feasibility of this method are stated.

Coherence as an essential feature of the light used for holography has already been discussed in detail. Therefore, only the laser is in consideration for light sources, its capacity ranging between 1 and 1000 mW according to the size of the objects to be holographed, to the sensitivity of the recording photo plates, and to the exposure time considered practicable.

Besides the sensitivity of the photo plates which must not meet general demands, their resolving power has to be high enough to enable separate recording of interference lines occurring with superposition. When considering the superposition of two plane waves which are tilted against each other by an angle  $\theta$ , they form parallel interference fringes the distance of which is given by

$$d = \frac{\lambda}{\sin \theta}$$

The greater  $\theta$  gets, the less  $d$  will be, and can minimally be equal to  $\lambda$ . Therefore, a hologram plate should resolve at least 2000 lines per millimeter (in this case  $\lambda$  was assumed to 0.5  $\mu\text{m}$ ).

Another important demand is the stability of the experimental arrangement. Since recording is made by the reference wave through the interference of the object wave, the phases of both waves must not shift by more than  $\sim \lambda/10$  against each other during exposure time. This means that the object and all optical components have to be stable within these limits during the recording period. This condition can for example be met by using vibration dampers and heavy table plates.

### III. HOLOGRAPHIC INTERFEROMETRY

The above described method enables the storing of wave fields and their reconstruction at any later time. When returning a developed hologram in its initial position and regarding the object through the hologram, the information on the object is received twice by the eye; on the one hand through the reconstructed object wave, and on the other hand directly from the object which is still in its initial position. The observer cannot distinguish between both wave fields and sees one object. When slightly displacing the original object or the hologram plate, both pertaining wave fields shift accordingly and regular interference fringes occur at the object. The described method has for the first time been used by Collier, Doherty and Pennington [7] and Powell and Stetson [8] to measure and visualize smallest deformations.

The formation of interference fringes shall be explained by fig. 2. In this case, the object to be holographed is a plane plate square with the paper plane. The plate is illuminated by point I; O is the observation point, and H is the hologram plate containing the information on the plate in its initial position. When turning the plate by a small angle, so that  $P_1$  changes into  $P'_1$ , the distance the light is covering from I via  $P_1$  to O changes by certain path lengths.



Fig. 2: Object Movements and Optical Path Differences



When assuming that

$$\overline{IP_1} + \overline{P_1O} = x_1$$

$$\overline{IP_1'} + \overline{P_1'O} = x_1 - \frac{\lambda}{2}$$

then the waves scattered at the homologous points  $P_1$  and  $P_1'$  in direction O have a phase shift of  $\lambda/2$ . They extinguish and this point of the surface appears dark. The following shall be valid for the other points:

$$\begin{array}{ll} \overline{IP_2} + \overline{P_2O} = x_2 ; & \overline{IP_2'} + \overline{P_2'O} = x_2 - \frac{3\lambda}{2} \\ \overline{IP_3} + \overline{P_3O} = x_3 ; & \overline{IP_3'} + \overline{P_3'O} = x_3 - \frac{5\lambda}{2} \\ \overline{IP_4} + \overline{P_4O} = x_4 ; & \overline{IP_4'} + \overline{P_4'O} = x_4 - \frac{7\lambda}{2} \end{array}$$

On this condition, extinction appears at all these points, while an intensification occurs between the points. When assuming moreover that the distance from observation and illumination point to the plate is great against the expansion of the plate, horizontal equally spaced parallel fringes occur at this plate, the distance of which is equal to that of the points  $P_1$ . The fringe distance is thus a measure for the angle between both positions of the plane.

In case of general movements and objects of any shape, an order N can be ascribed to every interference fringe, where the optical path changed by  $(N - 1/2)\lambda$  due to the change of position of the observed point.

If there are areas of higher fringe density in an interferogram that is totally covered with regular fringes, this refers to a significant different deformation at these points and thus to an inhomogeneity of the material. At these points, the surface of the object is more or less considerably deformed than the surrounding area.

Holographic interferometry as a method of nondestructive testing is based therefore on the fact that a slight deformation in the  $\mu$ -range is so exactly measured as to recognize and localize different deformations to be attributed to defects.

With the above described real-time method it is possible to observe directly the influence of the deformation on the formation of the interference pattern. This method will therefore always be applied when reference values on the optimum load are not yet known or when dynamic processes are to be observed. In this case, recording is made by direct photographing through the hologram. Should these values be known, then it is more appropriate to carry out the investigation according to the double exposure method. In this case, a hologram plate is twice exposed and the object deformation is made between both exposures. A hologram repositioning at a larger scale or an in situ development of the holograms, respectively, are thus unnecessary. When reconstructing these holograms both object waves and thus the interference pattern can be recorded at any later time.

The time-average method used with vibration analyses is a third possibility of interferometric recording. With this the object is stimulated to resonant vibration and holographed. During exposure time which is long against the time of vibration, a great number of object positions is recorded. The object positions contribute at a different degree to the density of the hologram plate according to the hold-up time given by the sine-shaped vibration. As for example Fryer [9] reports there will be an interference pattern showing light fringes at the vibration nodes and closed interference fringes at the antinodes, the intensity variation of which is described by the square of a zero order Bessel function. Fig. 3 shows as example of such a measurement, the vibration image of a GFRP-diaphragm.

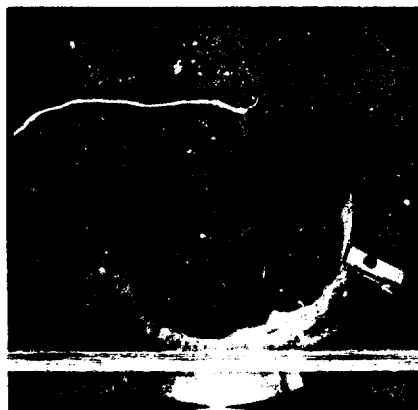


Fig. 3: Vibration Modes of a GFRP-Plate at 533 Hz

In the present paper, the problems arising with defects localizing due to displacement of resonance frequency and to the disturbance of vibration modes shall not be discussed in detail.

The problem of applying stress to test objects is moreover of basic significance to obtain interferograms with a good evidence. The object has to be loaded in a way that a reproducible deformation of the object surface occurs in the order of some  $\mu$ ; furthermore internal defects must necessarily take effect in a different deformation of the surface, as to detect these defects.

Normally the following methods are used:

1. compressive load, 2. tensile stress, 3. bending strain, 4. thermal load and 5. acoustic stimulation.

Compressive load can always be applied when containers or tubes capable to be loaded for internal pressure are tested. This method proved itself generally with such tests.

Plane plates or stripes can be deformed by means of tensile stress. In this case, conclusions can be drawn for the stress variation by holographic measurement of the deformation. The difficulty is, however, that deformation takes place in the plane of the plate. Concerning vertical observation and illumination, this direction is rather insensitive with respect to the change of the optical path. Slight disturbing movements square thereto proved to be sensitive. Such disturbances occurred for example with the investigations of flat GFRP-plates [10].

These difficulties are not apparent in the case of bending strain, where the deformation lies in the direction of observation and illumination. Besides the defect localization, this method has been applied for measuring the Poisson's ratio [11].

With respect to thermal stress, the object is slightly heated (or cooled) between the exposures, causing an expansion. This method is reasonable as soon as areas of different thermal expansion have to be localized. Also with massive objects, often no other stress can be applied; in this case there is however the basic difficulty that internal defects will no longer take effect in a different deformation of the surface.

It has already been pointed out how material or production defects effect the pattern of holographic interferograms. Now the question arises, according to which criteria the interferograms will be evaluated, i.e. according to which aspects can local or integral deviations from the basic pattern ascribed to an undisturbed test object be recognized. On principle, there are two methods: on the one hand clear defects can be identified phenomenologically on the basic pattern, and on the other hand, the interferograms can be subjected to a quantitative analysis.

The first step of the quantitative analysis shall clarify the characteristics of the basic pattern to be assigned to the faultless test object. For this purpose, an interferogram has theoretically been calculated for the optical arrangement available in the experiment and for certain assumptions on the static-free deformation of the object.

This calculation is based on the considerations of Sollid [12] and Ennos [13] leading to the following relation

$$(1) \quad N = \frac{2}{\lambda} d \cos\theta \cos\psi$$

$N$  represents the fringe order at a point of the surface for which the angle between observation and illumination direction amounts to  $2\theta$  and the displacement vector  $\vec{d}$  with the angle bisector between observation and illumination direction includes the angle  $\psi$ . In vector notation this relation is:

$$N = \frac{1}{\lambda} \left( \frac{(\vec{r}-\vec{r}')\vec{d}}{|\vec{r}-\vec{r}'|} + \frac{(\vec{o}-\vec{r}')\vec{d}}{|\vec{o}-\vec{r}'|} \right)$$

In this equation  $\vec{r}$  is the vector of the observed object point,  $\vec{r}'$  the vector of the illumination point, and  $\vec{o}$  the vector of the observation point in a Cartesian coordinate system.

Fig. 4 shows the interference pattern of a cylindrical tube calculated according to this relation. The tube deformation has been outlined by a peripheral expansion constant at the overall length and an axial upset connected therewith. Furthermore, it has been assumed that the left tube end has been fixed and observation and illumination point are located on the level of the left tube end.

Some further calculations showed the influence of the optical arrangement, the mounting support of the tube and various variations of peripheral and axial expansions on the basic pattern. A good conformity between calculated and pertaining experimental interferograms was stated in all respects [14].

In a further step of interpretation the displacement field of the object surface should be calculated from the experimental interferogram.

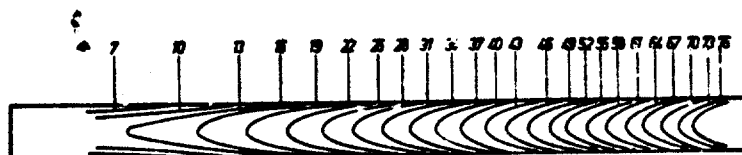


Fig. 4: A Calculated Interferogram of a Cylindrical Tube

As illustrated in Eq (1), the component of the displacement vector in direction of the angle bisector between observation and illumination direction contributes to the phase shift between the light waves emanating from one object point at both exposures. This component being  $d_{\psi}$ , hence follows

$$d_{\psi} = d \cos \gamma \quad \text{and} \quad N = \frac{2}{\lambda} d_{\psi} \cos \theta.$$

Since  $\theta$  is given by the optical arrangement, it is always possible to determine  $d_{\psi}$  according to this relation as soon as the absolute order of a fringe is known on the interference image. Such a fringe can be detected when parts of the object are visible which are not moved; for the first fringe adjacent to this area  $N$  equals 1.

Besides the limitation on such cases at which the absolute fringe order can be determined, this evaluation is also unsatisfactory inasmuch as only in a few cases the real displacement vector  $\vec{d}$  can be calculated by  $d_{\psi}$ . This is for example possible for the simple rotation of a plane through an axis. For all other more irregular displacement fields this evaluation is of less importance.

In order to obtain a general determination of  $\vec{d}$ , it is necessary to record the interference pattern at the same time from several directions. When recording simultaneously for instance four holograms from various directions and considering four fixed points on all four interferograms, the differences in the fringe order between the four points furnish the 12 coefficients of a linear equation system, the solution of which results in the 12 components of the displacement vectors at the four points. If they are known, the vectors at any object point can be determined by similar calculations.

The accuracy of this method depends on the accuracy of the determination of  $N$  at the single points. If the accuracy is indefinitely high,  $\vec{d}$  can also be exactly determined independent of the selection of the optical arrangement of the four holograms. If it is assured that  $N$  can only be determined by one digit after the decimal point, then the accuracy determining  $\vec{d}$  will very strongly be influenced by the optical arrangement. This was shown by some calculations of  $\vec{d}$  from theoretical interferograms.

#### IV. SOME RESULTS OF HOLOGRAPHIC FLAW DETECTION MEASUREMENTS

Since its introduction in 1965, holographic interferometry has been tested at first in different fields of materials testing to prove generally which flaws can be detected in which materials. In the second step, these problems have to be cleared up each time for a certain object as far as particulars can be given for the performance of a holographic test method. Up to now, it is not yet possible to comment definitely on the problems of flaw detection and determination of flaw size. The following deals rather with some special results with respect to these problems.

Vest et al. [15] tested holographically microcracks in steel and compared the results with those of other methods, such as magnaflux, eddy current and X-ray inspection. The microcracks are artificially introduced into the test object. Several 5/16 in. holes are drilled into a rib of 0.13 in. thickness of a channel. Then radial cracks of 0.01 to 0.44 in. length have been applied into several holes.

The application of stress required for holographic inspection had been made in a different manner. The best method was to tap a tapered bolt with a certain initial loading and to brace this bolt additionally prior to the second exposure of the hologram. The results show that cracks up to a length of 0.1 in. can be detected and localized, while cracks of 0.1 to 0.03 in. length could be detected but not localized.

With respect to the other methods, there was a comparable result only with magnaflux. The more tedious preparation of the object with this method has however been pointed out.

First results of flaw detection for glass fibre reinforced plastics (GFRP) are now in hand. With these composite materials, cracks can occur either in the fibre during the manufacturing process or in resin for instance by alternating loads.

In order to test the influence of the flaws in the fibre on the deformation of the object and thus on the disturbance of the interference pattern, test objects of different geometry have been provided with artificially applied fibre cuts.

Level plates of 280 x 280 mm<sup>2</sup> were produced by laminating bidirectional linen texture layers [10]. The interferogram represented in fig. 5 originates from tensile stress of a plate consisting of 5 layers and containing a cut of 60 mm through all layers. The cutting point in the figure center can clearly be seen on the basic pattern which is not very regular in itself. The length of the cut can also be determined therefrom.

For the purpose of the present investigation a plate of the same diameter consisting of 5 layers and containing a cut of 25 mm through one layer in the plate center. In this case, the plate was clamped at the outer surface and stress was applied so that the space behind the plate was evacuated. The well reproducible basic pattern consists of concentric circles which are only at the outer areas slightly disturbed by clamping effects. The cutting point is clearly to be seen at the division of the inner dark interference patch. The length of the cutting can, however, only be determined by a greater failure.

Cuts in the fibre of filamentary wound cylindrical tubes can also clearly be recognized with the holographic method [14]. Fig. 7 represents a part of a 9-layer tube containing a cut of 25 mm through 3 layers. The basic pattern shows clearly a deviation at the flaw position indicating a different deformation of the tube at internal compression stress. The cut length can also be estimated.

The discussed examples show that flaws of the fibre of reinforced plastics can be detected. With respect to the determination of flaw size, it has been referred only to flaw geometry. Further systematic investigations shall clear up the effect of flaws of different size on the interferograms and the significance of these flaws with respect to the demands on certain components.

The examination of the cylindrical tubes showed already that some holographically detected flaws led to a reduction of the bursting strength of these tubes and that flaws of varying size and in different layers of the tube took a different effect on the disturbance of the basic pattern.

Fig. 8 represents the crack formation in the resin of a GFRP tank ascribed to compression stress. The differential pressure applied between both exposures of a series of experiments was mounted always to 0.05 at. The basic pressure has, however, been varied from 0.3 to 10 at. The above tank has been holographed at a basic pressure of 10 at, and only at this pressure the interference pattern disturbance of horizontal shape could be seen in the tank center. Later on this disturbance could clearly be assigned to a slight crack round the tank which occurred at a stress of 10 at.



Fig. 5: A Flaw in a GFRP-Plate

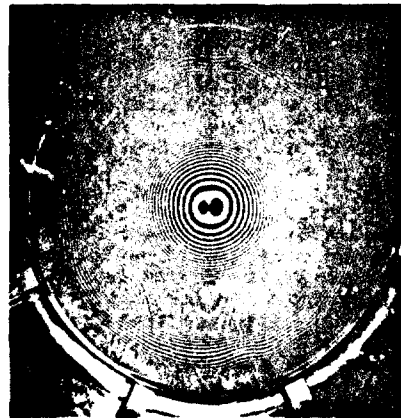


Fig. 6: A Flaw in the Center of a GFRP-Disk

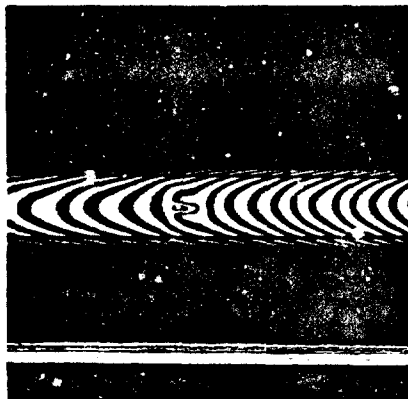


Fig. 7: Part of a GFRP-Tube with a Flaw

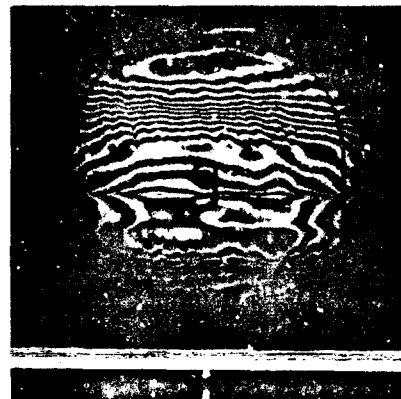


Fig. 8: GFRP-Tank with a Horizontal Crack at the Tank Center

## V. LIMITATIONS OF THE METHOD

Holographic interferometry proved to be a sensitive method in non-destructive testing. Although some problems are far from being cleared up already - a pre-condition for simple and secure application on different objects - it can be reported that this method represents a very good supplement to existing test methods in some fields.

It also proved, however, that there are fundamental limitations which can partly be deferred by an increased experimental expense. These limitations are connected with the sensitivity of the method, with the possibilities of the object loading and with the nature of the coherent light.

Since the holographic method reacts extremely sensitive on any deformation, involuntary movements or deformations of the object which are superimposed on the intended deformation, take a strongly disturbing effect. These phenomena have for instance been observed at components of GFRP disposing only of low thickness. In this case, variations in the percentage of resin can either lead to inherent stress or cause the different contents of resin to make varying deformations. Then it is no longer possible to identify the interference pattern with a theoretically calculated basic pattern, since both outline different object movements. Moreover, the variations in the percentage of resin being irregular, the flaw detection is complicated. A flaw of a certain size still to be observed on a regular basic pattern can then no longer be detected on the disturbed basic pattern. Only flaws of a greater size can be detected.

The uniformity of reproduction of the objects and a deformation behaviour to be described by general relations in the range required for the holographic interferometry are the pre-condition for a sensitive flaw detection. This means for example that an internal compression stress applied to a cylindrical tube will result in an axially symmetrical peripheral expansion independent of the axial position.

The second directly reasonable limitation of the method has already been mentioned above. Any object containing a flaw somewhere in its body must dispose of a suitable stress. This stress has to be selected so that the flaw within the body causes a different deformation on the object surface. The bigger the component, the less this condition is complied with. In this case, a localization of the flaw and finally also the qualitative detection can no longer be carried out.

A third limitation is connected with the light features requiring for instance the mentioned mechanical stability of the object during exposure. This condition can only be met as long as the objects are not too big to be put on the holographic table. Moreover, they have to be stable in themselves as not to get stimulated by vibrations of atmospheric disturbances. The demand for object stability can only be circumvented by reducing essentially the exposure time and the time between both exposures. This is rendered possible by using double-impulse lasers emitting 2 impulses of abt. 20 nsec each in the interval of abt. 100 usec.

There are also limitations with small objects. The natural granulation makes itself so strongly felt that only very few interference fringes can be resolved on a surface of some mm<sup>2</sup>. To circumvent this fact, methods of granulation reduction must additionally be used.

## REFERENCES

- |      |  |  |
|------|--|--|
| [1]  | GABOR, D.  | Nature, 161, 777, 1948   |
| [2]  | MARTIENSSEN, W.                                    | VDI Nachrichten 38, 4, 1967  |
| [3]  | GABOR, D.  | Rep. Prog. Phys. 32, 395, 1969   |
| [4]  | SMITH, H.M.  | Principles of Holography, Wiley Interscience, 1969                               |
| [5]  | KIEMLE, H.<br>ROSS, D.                             | Einführung in die Technik der Holographie, Akad. Verlagsanstalt, Frankfurt, 1969 |
| [6]  | COLLIER, R.J.<br>BURCKHARD, C.B.<br>LIN, L.H.      | Optical Holography Academic Press  |
| [7]  | COLLIER, R.J.<br>DOHERTY, E.T.<br>PENNINGTON, K.S. | Appl. Phys. Lett. 7, 223, 1965   |
| [8]  | POWELL, R.L.<br>STETSON, K.A.                      | J. Opt. Soc. Am. 55, 612, 1965   |
| [9]  | FRYER, P.A.  | Rep. Prog. Phys. 33, 489, 1971   |
| [10] | not yet published                                  |  |

- [11] YAMAGUCHI, J.  
SAITO, H. Jap. J. of Appl. Phys. 8, 768, 1969
- [12] SOLLID, J.E. Appl. Optics 8, 1587, 1969
- [13] ENNOS, A.E. J. Sci. Instr. (J. of Phys. E) Serie 2, 1, 731, 1968
- [14] GRÜNEWALD, K.  
KALETSCH, D.  
LEHMANN, V.  
WACHUTKA, H. Optik, to be published
- [15] VEST, C.M.  
MEKAGUE, E.L.  
FRISCHEN, A.A. Trans. of the ASME J. of Basic Engineering  
June 1971, p. 237

VII G. AN ANALYSIS OF A TEST FATIGUE FAILURE  
BY FRACTOGRAPHY AND FRACTURE MECHANICS

C. J. Peel

Summary . . . . .	503
Introduction . . . . .	503
Impeller History . . . . .	503
Fractographic Examination . . . . .	503
Fatigue Crack Growth Rate Extrapolation . . . . .	503
Fatigue Stress Analysis . . . . .	505
Fatigue Life Assessment . . . . .	505
Discussion . . . . .	508
Conclusions . . . . .	508
Acknowledgements . . . . .	508
References . . . . .	508

SUMMARY

The fracture surfaces of two fatigue cracks, that had caused the failure of an engine impeller during a fatigue substantiation test, were examined by electron microscopy to find the number of fatigue crack growth cycles. This was done by measuring the spacings of fatigue striations on the fracture surface as a function of crack depth and by subsequent integration of the striation spacing versus crack depth expression. The measured striation spacings were compared with laboratory crack growth data to determine the fatigue stress intensity range as a function of crack depth and hence the fatigue stress range. The number of crack initiation cycles was then found by comparing the fatigue stress range and number of crack growth cycles with further laboratory data and the total fatigue life was calculated to have been approximately 50,000 cycles. This identified the fatigue loading that had caused the failure as having been the 29179 cycles of engine acceleration and deceleration that had been applied during the test.

INTRODUCTION

The failure<sup>(1)</sup> of a gas turbine engine impeller occurred during a fatigue substantiation test, in which the engine was repeatedly accelerated and decelerated until pieces of the impeller broke away and the test had to be stopped. An examination of the impeller revealed that several semi-elliptical fatigue cracks (Figs 1, 2) had initiated and grown through the impeller disc until final rapid failure occurred. It was necessary to find out whether the engine acceleration-deceleration cycle or some other form of loading, such as resonance of the impeller, had caused the fatigue cracking. To do this the number of crack growth cycles was determined by measurement of fatigue striation spacings as a function of crack depth and integration of the derived expression. Laboratory data<sup>(2-7)</sup> relating fatigue crack growth rates to stress intensity ranges and fatigue crack initiation periods<sup>(8)</sup> to fatigue stress ranges was then used to determine the total fatigue life of the impeller.

IMPELLER HISTORY

The impeller had been machined from an aluminum alloy forging to DTD 731 specification, an alloy of the RR58 or AA2618 type. The engine testing cycle was:-

- a. 3 seconds at 10,000 rpm
- b. Acceleration to 36,200 rpm in 17 seconds
- c. 3 seconds at 36,200 rpm
- d. Deceleration to 10,000 rpm in 17 seconds

The engine impeller failed after 29,179 of these cycles had been applied.

FRACTOGRAPHIC EXAMINATION

Dye penetrant revealed that, as well as the fatigue cracks that had broken through completely, there were cracks at each point where an impeller vane met the impeller disc. All the fatigue cracks initiated at the inside radius of a balance ring. (Fig 3). This ring on the face of the impeller disc reduced the bending moment acting on the impeller caused by the asymmetry of the impeller in a radial plane. One fatigue crack (A in Fig 1) that had grown to its critical depth of 4.0mm was examined in a scanning electron microscope and striation spacings were measured as a function of crack depth. A shorter crack (B), that was diametrically opposite crack A, was broken open by hand after the test and found to be only 1.0mm deep. This crack was examined by a carbon replica technique in a transmission electron microscope.

FATIGUE CRACK GROWTH RATE EXTRAPOLATION

Striations were not detected on either fracture surface at crack growth rates below 0.09µm/cycle or above 1.0µm/cycle. Thus to determine the total number of crack growth cycles extrapolation of crack growth rates over the first 0.4mm and the last 1.0mm of crack depth was necessary. The errors possible in this extrapolation were greatest at the shorter crack lengths. At crack depths greater than 3.0mm crack A was growing faster than 1.0µm/cycle and the last 1.0mm of crack growth to rapid failure must have taken less than 1000 cycles.

Linear elastic fracture mechanics was used as the basis of the extrapolation method since it has been found<sup>(2)</sup> that the fatigue crack growth rate  $\frac{da}{dn}$  can be related to the range in stress intensity ( $\Delta K$ ) of the fatigue cycle: -

$$\frac{da}{dn} = B \Delta K^m \quad (1)$$

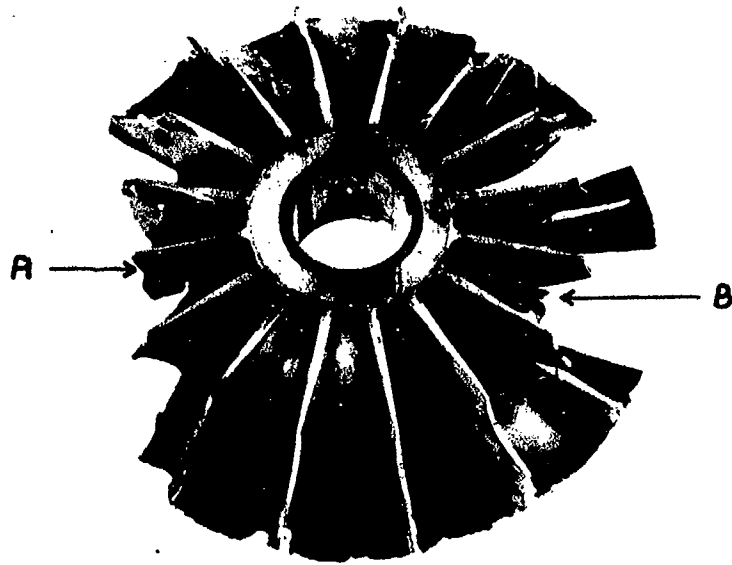


Fig.1 The broken impeller showing the positions of cracks "A" and "B"



Fig.2 The fatigue crack "A" viewed along arrow "A" in Figure 1



B and m are constants. Provided the section has infinite width the stress intensity range is proportional to the square root of the crack depth (a) and to the stress range ( $\Delta\sigma$ ):-

$$\Delta K \propto \Delta\sigma \sqrt{a} \quad (2)$$

Thus 
$$\frac{da}{dn} = C a^{m/2} \quad (3)$$

Before equation (3) was used to extrapolate the crack growth rates, it had to be proved that equations (1) and (2) were applicable to the fatigue crack growth in the impeller. By comparison of the striation spacings with fatigue crack growth rates that had been measured (4) optically at increasing values of  $\Delta K$  (Fig 4), a graph of  $\Delta K$  versus crack depth was plotted on logarithmic scales for cracks A and B (Fig 5). An R value of 0.05 (Fig 4) was considered for inspection purposes to be the most applicable since R, the ratio of minimum stress intensity to maximum stress intensity of the fatigue cycle was equal to the ratio of the squares of the minimum and maximum engine speeds:-

$$R = \frac{\text{minimum stress intensity}}{\text{maximum stress intensity}} = \frac{10,000^2}{36,200^2} = 0.077$$

The data for crack A and for some of the depth of crack B fitted a slope of 0.5 (Fig 5) reasonably well that is:-

$$\Delta K \propto \sqrt{a} \quad (4)$$

The crack depth (a) was taken as the sum of the fatigue crack depth ( $a_f$ ) and a notch depth ( $a_0$ ). That is the balance ring was considered to have been acting as a notch of depth  $a_0$  (Fig 3). A value of 1.2mm for  $a_0$  was found to give a good fit to the straight line in Fig 5 and seemed reasonable, being slightly less than half the thickness of the balance ring.

Initially corrections (9) were made to equation (2) to correct for finite section width and crack front curvature, but as these corrections were small (<10%) and tended to cancel each other they were subsequently ignored.

Since equation (2) was applicable to the impeller, particularly for the crack A that grew to final fracture, a graph of crack growth rates against crack depth was plotted on logarithmic scales (Fig 6). It was found that a straight line of slope 2.06 (ie  $m = 4.12$ ) fitted the data well, especially when extra weight was given to crack A. Thus to determine the number of cycles  $a_1 N^{a_2}$  that was taken to grow from depths  $a_1$  to  $a_2$ , equation (3) can be rewritten and integrated:

$$a_1 N^{a_2} = \int_{a_1}^{a_2} C^{-1} a^{-m/2} da \quad \text{cycles} \quad (5)$$

However in equation (2) when the crack depth was zero  $\Delta K$  and thus  $\frac{da}{dn}$  should have been zero, that is the fracture mechanics approach breaks down at very short crack depths. The solution adopted was to assume an incubation depth of 0.125mm, where the fracture mechanics approach did not apply. This incubation depth corresponded to experimental work (8) in which the number of cycles to form the first detectable crack was measured for varying stress ranges and notch geometries, the minimum detectable crack depth being approximately 0.125mm. Thus from equation (5) the number of cycles to grow crack A from an incubation depth of 1.325mm (1.2 + 0.125mm) to the final critical crack depth of 5.2mm (4.0 + 1.2mm) was found to be 9930 cycles. The value of C was taken as the value of the crack growth rate when  $a = 1.0$ mm. (Fig 6)

#### FATIGUE STRESS ANALYSIS

The two modes of loading thought to be the most applicable to the engine case were tension and bending. For a straight fronted crack in a section of infinite width the relationship (8) is:-

$$\Delta K = 1.1 \Delta\sigma \sqrt{a} \quad (6)$$

holds for both these types of loading. Again ignoring the various corrections (1) for finite section width, crack front shape and plastic zone size, the stress range  $\Delta\sigma$  was determined by solution of equation (6). For example at a nominal crack depth of 1.0mm  $\Delta K$  was  $9.7 \text{ MNm}^{-3/2}$  (Fig 5). Hence the total stress range whether tension, bending or mixed mode was  $157 \text{ MNm}^{-2}$  and the maximum stress  $\sigma_{max}$  of the fatigue cycle was  $170 \text{ MNm}^{-2}$  since R was 0.077.

#### FATIGUE LIFE ASSESSMENT

The number of cycles to grow the crack from the incubation depth to final rapid failure was calculated to have been 9,930 cycles. Data published by Pearson (8) suggested that for a stress range of  $160 \text{ MNm}^{-2}$  and the blunt notch at the root of the balance ring the initiation and incubation stage, that is the number of cycles to form a crack 0.125mm deep, should have occupied approximately 80% of the total fatigue life. (Fig 7).

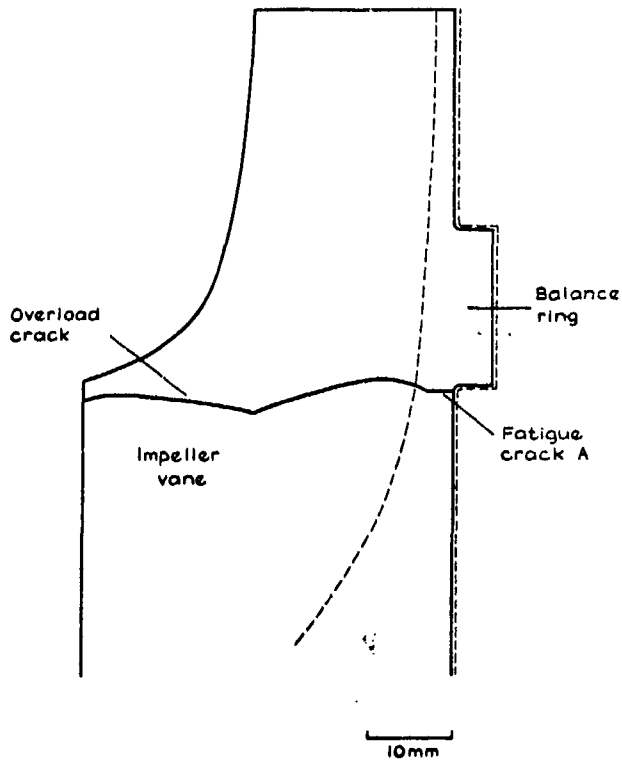


Fig.3 Two superimposed radial sections taken through the outer regions of the impeller. A section in the plane of an impeller vane is shown in continuous lines, a mid-vane section in dashed lines

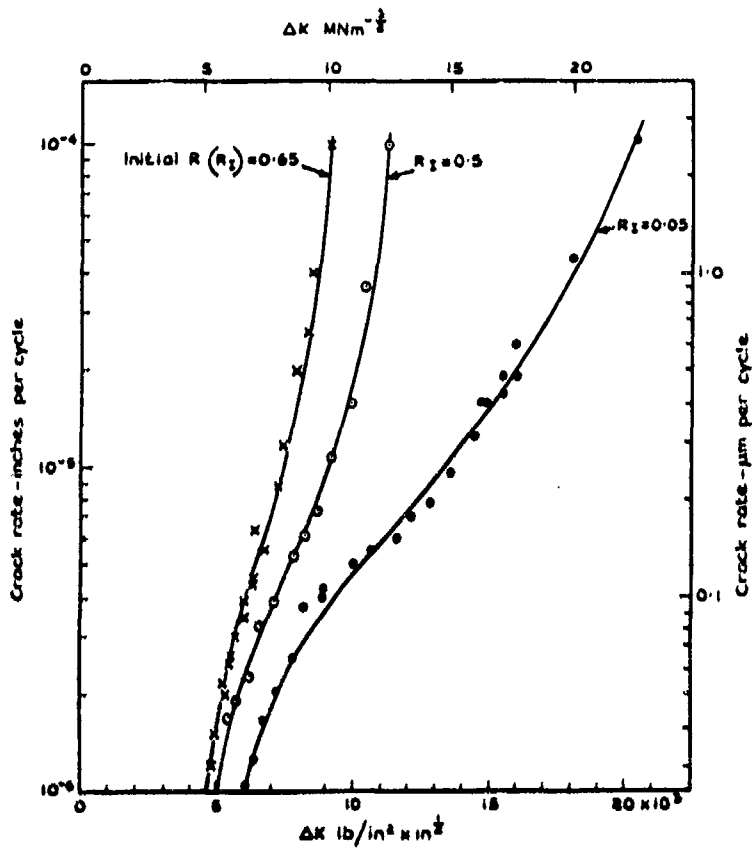


Fig.4 Crack growth rates versus stress intensity ranges for 3 inch RR 58 plate at three ratios R of minimum to maximum stress. (Taken from Reference 4)

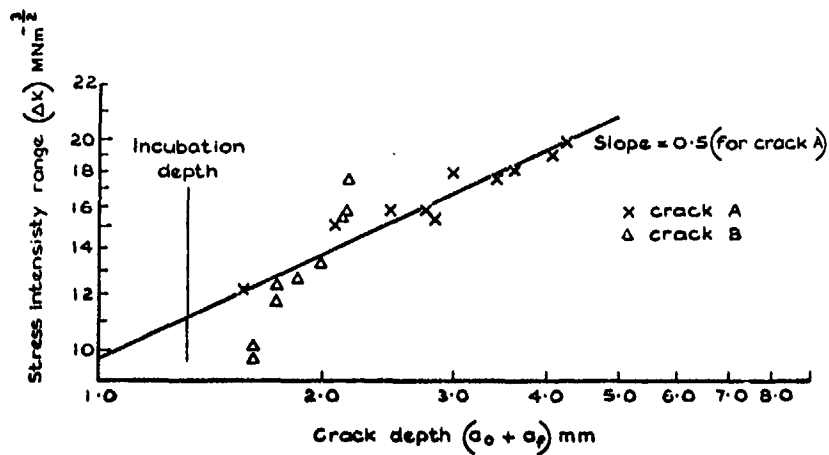


Fig. 5 Stress intensity range versus crack depth for cracks A and B

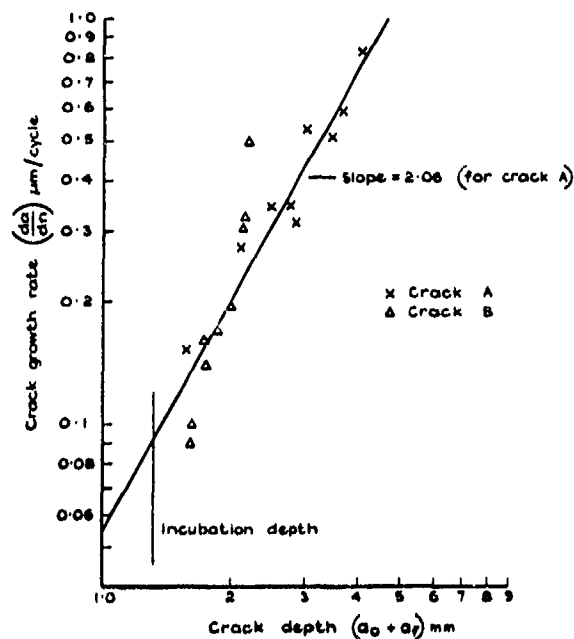


Fig. 6 Crack growth rates versus crack depths for cracks A and B

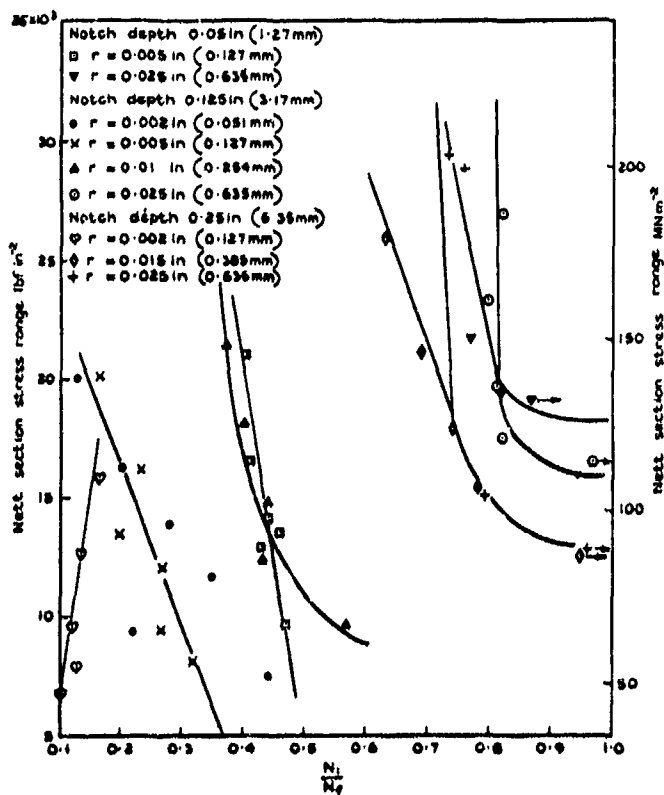


Fig. 7 Plot of the fraction  $\frac{N_i}{N_f}$  of the fatigue life  $N_f$  that is taken in forming a detectable crack ( $\sim 0.125$  mm deep) against nett section stress range for various notch depths and notch root radii  $r$  (from Reference 8)

Thus the total fatigue life of the impeller would have been 49650 cycles, which is in good agreement with the number of applied acceleration-deceleration cycles (29179) of this impeller test.

#### DISCUSSION

Failures of components that occur under service conditions are frequently analyzed qualitatively by fractographic techniques. In this case of a uniformly loaded fatigue fracture, quantitative analysis was possible in that the total fatigue life and the fatigue stress range were determined for the impeller simply from fractographic evidence in the form of fatigue striations.

Some further information was revealed by the fracture analysis and has not yet been presented. Firstly the fatigue crack growth rate of crack A was increasing rapidly as the crack grew to the critical crack depth of 4.0mm (ie  $a_0 + a_f = 5.2\text{mm}$  in Fig 5) suggesting that the fracture toughness of the impeller alloy for this cracking direction was approximately  $24 \text{ MNm}^{-3/2}$ . A calculation of the fracture toughness based on equation (6) using  $\sigma_{\text{max}}$  and including crack front shape and finite width corrections resulted in a value of approximately  $25 \text{ MNm}^{-3/2}$ .

The effect of the balance ring in acting as a notch depth  $a_0$  should also be noted. In the absence of this blunt notch a fatigue stress range of  $160 \text{ MNm}^{-2}$  should have given a fatigue life in excess of  $10^6$  cycles.

#### CONCLUSIONS

- (1) Fatigue striation spacings and hence fatigue crack growth rates were measured at increasing crack depths on the fracture surface of a fatigue crack that had caused total failure of an engine impeller. From these growth rates, calculations revealed that the fatigue crack had taken 9,930 cycles to grow from a depth of 0.125mm to a critical depth of 4.0mm.
- (2) The fatigue stress intensity range, which was found to increase with the square root of the crack depth, was determined by comparison of the striation spacings with laboratory crack growth data. From this stress intensity range, the fatigue stress range was found to have been approximately  $160 \text{ MNm}^{-2}$ .
- (3) Using this value of the stress range and the number of crack growth cycles, the total fatigue life of the impeller was estimated by comparison with laboratory data to have been approximately 50,000 cycles.
- (4) This total fatigue life identified the fatigue loading as having been the 29,179 cycles of engine acceleration and deceleration that were applied during testing.

#### ACKNOWLEDGMENTS

The author is indebted to his colleagues in the Materials Department, Mr. D. P. Rooke, Dr. F. J. Bradshaw and particularly Mr. S. Pearson who supplied Figs 4 and 7.

#### REFERENCES

1. C. J. Peel "An analysis of a test fatigue failure by fractography and fracture mechanics". Royal Aircraft Est Technical Report 72034 (1972)
2. P. C. Paris  
F. Erdogan "A critical analysis of crack propagation laws". Jnl Basic Engineering Trans ASME 85 p528 (1963).
3. R. W. Hertzberg  
P. C. Paris Proc 1st Int Conference on Fracture Sendai Japan p459 (1965).
4. S. Pearson "The effect of mean stress on the fatigue crack propagation in half inch thick specimens of aluminum alloys of high and low fracture toughness." Engineering Fracture Mechanics 4 p9 (1972)
5. J. C. McMillan  
R. W. Hertzberg Electron Fractography ASTM STP 436 p89 (1968)
6. R. C. Bates  
W. G. Clark Jnr Trans ASM 62 p380 (1969)
7. J. Kershaw  
H. W. Liu "Electron Fractography and Fatigue crack propagation in 7075-T6 Aluminum sheet." Int Jnl Fracture Mechanics 7 No3 p269 (1971)
8. S. Pearson "Fatigue crack initiation and propagation in half inch thick specimens of an aluminum alloy" Royal Aircraft Est Technical Report 71109 (1971)
9. W. F. Brown  
J. E. Srawley "Plane strain crack toughness testing of high strength metallic materials." ASTM STP 410.

## APPENDIX 1

## TYPICAL PLANE STRAIN FRACTURE TOUGHNESS OF AIRCRAFT MATERIALS

W.T. Matthews

## CONTENTS

INTRODUCTION . . . . .	511
DEFINITION OF SYMBOLS . . . . .	512
REFERENCES . . . . .	512
<b>A. Steel . . . . .</b>	<b>516</b>
<u>i Low Alloy . . . . .</u>	<u>516</u>
Table 1 AISI 4330M, EN30B . . . . .	516
2 35NCD 16, EN40C . . . . .	517
3 H-11 . . . . .	518
4 AISI 4140 . . . . .	519
5 AISI 4340 . . . . .	520
6 300M . . . . .	522
7 D6AC . . . . .	524
8 EN24, Ni-Cr-Mo-V . . . . .	526
<u>ii Nickel Steels . . . . .</u>	<u>527</u>
9 9Ni-4Co-.3C . . . . .	527
10 9Ni-4Co-.45C . . . . .	528
11 10 Nickel . . . . .	529
<u>iii Maraging Steel . . . . .</u>	<u>530</u>
12 12 Nickel . . . . .	530
13 18 Ni-200 Grade . . . . .	531
14 18 Ni-250 Grade, DTD5212, G100, G110, Marval 18 . . . . .	532
15 18 Ni-300 Grade, G125 . . . . .	535
16 18 Ni-350 Grade . . . . .	536
<u>iv Stainless Steel . . . . .</u>	<u>537</u>
17 17-4 PH . . . . .	537
18 17-7 PH . . . . .	538
19 PH15-7Mo . . . . .	539
20 PH13-8Mo, FV520B . . . . .	540
21 AM355, APC-77 . . . . .	541
<b>B. Titanium Alloys . . . . .</b>	<b>542</b>
<u>i <math>\alpha</math> Alloy . . . . .</u>	<u>542</u>
22 5Al-2.5Sn . . . . .	542
<u>ii Near <math>\alpha</math> Alloys . . . . .</u>	<u>543</u>
23 IMI 679, 8Al-1Mo-1V, 6Al-2Sn-4Zr-2Mo . . . . .	543
<u>iii <math>\alpha</math>-<math>\beta</math> Alloys . . . . .</u>	<u>544</u>
24 IMI 550 . . . . .	544
25 IMI 680 . . . . .	545
26 4Al-3Mo-1V, 7Al-4Mo . . . . .	546
27 6Al-4V . . . . .	547
28 6Al-6V-2Sn . . . . .	549
29 6Al-6V-4Zr-4Mo, 6Al-2Sn-4Zr-6Mo, 6Al-2Sn-2Zr-2Mo-2Cr . . . . .	551

	<u>iv <math>\beta</math> Alloys</u>	.553
Table 30	13V-11Cr-3Al, 8Mo-8V-2Fe-3Al, 11.5Mo-6Zr- 4.5Sn	.553
C.	<u>Aluminum Alloys</u>	.555
	<u>i Copper Alloys</u>	.555
31	2014, DTD5020, HID66, BS L77, BS L93, GB-26S	.555
32	2020	.557
33	2021, 2219	.558
34	2024, DTD5090, A-U4G1	.560
35	2618, RR58, DTD731, CM003/4D, A-U2GN	.562
	<u>ii Zn-Mg Alloys</u>	.563
36	7001, 7049	.563
37	7007,	.565
38	7075, DTD 5050, DTD 5074, BS L95, AZ74, 7175	.566
39	7178, DTD 363	.570
	<u>iii Zn-Mg-Mn Alloys</u>	.572
40	7039, 7005.	.572
41	7079	.573
42	DTD 5024, DTD 5094	.574
43	7080, M-75S	.575
	<u>iv Other Aluminum Alloys</u>	.576
44	6061, DTD 5050, A-U4G1	.576
D.	<u>Beryllium</u>	.577
45	S-200	.577
46	v $K_C$ Data (Figure 1)	.578

## APPENDIX I. TYPICAL FRACTURE TOUGHNESS OF AIRCRAFT METALLIC MATERIALS

### INTRODUCTION

The fracture toughness values presented in this appendix are expressed in terms of linear elastic fracture mechanics. The general tabulation includes only values measured under plane strain conditions. These plane strain  $K_{IC}$  values have been obtained by the ASTM E399-72 "Standard Method of Test for Plane Strain Fracture Toughness Testing of Metallic Materials" or a similar method. This data compilation includes materials manufactured in the USA and Europe. Factors involved in the selection and interpretation of the  $K_{IC}$  values will be discussed in the latter sections of this introduction.

### Plane Stress of Mixed Mode $K_c$ Data

$K_c$  values have not been tabulated in this appendix because at present they are not suitable for general use in design. There are difficulties associated with the measurement of  $K_c$  and with its use as a fracture criterion in structural applications. As a consequence,  $K_c$  measurement methods have not been standardized. In contrast to  $K_{IC}$ , the plane stress value is a function of several structural or specimen related variables such as the material thickness, the crack length, the crack length to width ratio, the stiffness of a structural part or specimen and the stiffness of the system applying load in a structural application or of a laboratory materials testing system. There are also uncertainties in defining and measuring the critical crack length at instability which must be obtained in order to evaluate  $K_c$ . However, it is of importance to quantitatively illustrate the extent of the increase in fracture toughness which typically occurs when the material thickness is reduced and plane strain restraint decreases. In figure 1, section V, curves illustrate this effect for a steel alloy, 300 Grade Maraging; a titanium alloy, 4Al-3Mo-IV; and an aluminum alloy, 7075-T7351.

### Characteristics of Selected $K_{IC}$ Materials

Toughness values are shown for materials which have a high strength to weight ratio. In general such materials have the following room temperature yield strengths: Steel, 180 KSI (1241 MN/m<sup>2</sup>); Titanium 130 KSI (896 MN/m<sup>2</sup>) and Aluminum 50 KSI (345 MN/m<sup>2</sup>).

### Testing Conditions

The material values shown correspond to quasi-static loading of approximately one to three minutes duration. The environment is a neutral laboratory environment in which no aggressive chemicals or extremes of humidity are intentionally introduced.

### Specimen Types

$K_{IC}$  values shown have been obtained from ASTM recommended Bend and Compact Tensile Specimens and from a variety of other specimens: Four Point Bend, Double Cantilever Beam, Wedge Opening Loading, Side Edge Notched, Center Cracked specimens and a few Double Edge Cracked and Notched Round specimens. Surface Cracked Specimen data is not included in the appendix since although this configuration is extremely important in applications, criteria for validity of  $K_{IC}$  measurements of Surface Cracked Specimens have not been established.

### Criteria for Validity of Typical $K_{IC}$ Values

The ASTM E399-72 requirements are taken as the general guide for validity. However, since complete details of factors cited by ASTM are usually not available, personal judgment must be exercised. For example, although all data listed pertain to fatigue cracked specimens, the range of imposed  $K_I$  during fatiguing is usually not reported. In addition the crack front curvature and the orientation of the crack plane with respect to the loading axis are also unknown. Other typical unknowns are the critical crack length, the details of selection of the critical load value, the appearance of the fracture surfaces, the details of fixture design to minimize friction and the linearity of the displacement gage. Therefore, it is often necessary to assume that in general the test measurements have been carried out according to good practice. In terms of specific criteria for inclusion in this appendix, the ASTM requirement of thickness greater than  $2.5 (K_{IC}/\sigma_{YS})^2$ , was applied. Virtually all of the data satisfied this requirement. Although it would be desirable to require that crack length exceed  $2.5 (K_{IC}/\sigma_{YS})^2$ , this criterion was not rigidly imposed. The minimum reported crack length for data presented in this appendix is  $1.25 (K_{IC}/\sigma_{YS})^2$ .

### Accuracy of $K_{IC}$ Values

In general the  $K_{IC}$  values shown are averages of several tests. The range of typical data may be interpreted to be the average shown  $\pm 10\%$ . In cases where the range of toughness values was large, either the entire range is shown or the extremely high values were excluded before computing the average.

### Parameters Influencing $K_{IC}$

Where available the influence, whether significant or negligible, of material form and thickness, composition, heat treatment, testing temperature and material anisotropy and yield strength upon  $K_{IC}$  is shown by the series of data entered in the tables. In most cases where a particular heat treatment produces both the highest yield strength and toughness, data for other heat treatments are omitted. It

which leads to the highest toughness is not included in this compilation. In those instances it is not possible to obtain valid  $K_{IC}$  measurements for the particular material thickness of interest. There are additional parameters which may also influence  $K_{IC}$  values which are not shown in these tables since they are rather infrequently reported. These include melting practice, heat treating practice such as the size of quenching bath relative to the material size and the amount of material straining during forging.

## Units, Symbols and Nomenclature

Data is presented in the customary units used in the USA with accompanying International System Units (SI) in parentheses. The definition of units and symbols for specimen orientation and type are given preceding the tabulations.

## DEFINITION OF SYMBOLS AND UNITS

## a) Composition and Heat Treatment Codes

Code Form: Letter, Number

Letter - Identifies Composition

Number - Identifies Heat Treatment

Detailed descriptions of Composition and Heat Treatment are at the bottom of each table. The compositional values are measured values in terms of percentage by weight, except when designated "ppm" parts per million.

When only specified composition is available, the nominal specified levels are followed by the letter "N" and the maximum levels of other elements are followed by "M".

## b) Orientation of Specimens

Code: First Letter: Direction of Loading

Second Letter: Direction of Crack Propagation

L: Direction Parallel to Primary Grain Flow Direction of Plate, Forging or Extrusion

T: Direction Parallel to Largest Dimension in Plane Transverse to L Direction

S: Direction Parallel to Smallest Dimension in Plane Transverse to L Direction

ST4: Direction 45° Between Directions of Largest and Smallest Dimension in Plane Transverse to L Direction

R: Radial Direction

C: Circumferential Direction

If a direction is ambiguous in terms of two of the above definitions, then both directions are shown.

## c) Specimen Identification

Bend: 3 point Bend Specimen

Bend (4 pt): 4 point Bend Specimen

CT: ASTM Compact Tensile Specimen

WOL: Similar to CT, but with different dimensions

CC: Remotely Loaded Flat Tensile Specimen with Center Notch

DEC: Remotely Loaded Flat Tensile Specimen with Double Edge Cracks

SEN: Remotely Loaded Flat Tensile Specimen with a Single Edge Crack

NR: Round Tensile Specimen, Circumferentially Notched

DCB: Double Cantilever Beam Specimen

## d) Units

Temperature: F - Degrees Fahrenheit

K - Degrees Kelvin

Stress: KSI - Kips per Square Inch

MN/m<sup>2</sup> - Mega Newtons per Square Meter

Stress Intensity: KSI  $\sqrt{\text{in}}$  - Kips per Square Inch Times Square Root Inches

MN m<sup>-3/2</sup> - Mega Newtons times (Meters)<sup>-3/2</sup>

Length: in, mm - Inches, Millimeters

ft, m - Feet, Meters

## REFERENCES

1. Kendall, D. P., Materials Research and Standards Vol 10, No. 12, p 14.
2. Baker, A. J., Lauts, F. J., and Wei, R. P., Structure and Properties of Ultra High Strength Steels ASTMSTP370, 1965, p 3.
3. Guthrie, J. L., "High Strength Steel Evaluation for Supersonic Aircraft," Boeing Co., AD818490, March 1967.
4. Vishnevsky, C. and Steigerwald, E. A., Fracture Toughness Testing at Cryogenic Temperatures ASTMSTP496, 1971, pp. 3-26.
5. Irani, J.J., et al, "The Effect of Thermal and Thermomechanical Treatments on Temper Embrittlement of Low Alloy Steels", BISR A MG/A/81/67, NTIS PB 180448.
6. Jones, M. H., and Brown, W. F. Jr., Review of Developments in Plane Strain Fracture Toughness Testing, ASTMSTP463, 1970, pp. 63-101.
7. Steigerwald, E. A., Eng. Fracture Mech, Vol 1, No. 3, 1969, pp. 473-494.
8. Kula, E. B., and Anctil, A. A., J. Matls, N.Y. Vol 4, No. 4, Dec 1969, pp. 817-841
9. Srawley, J. E., Jones, M. H., and Brown, W. T. Jr., Materials Research and Standards, Vol 7, No. 6, June 1967, pp261-266.
10. Shoemaker, A.K. and Rolfe, S.T., "The Static and Dynamic Low Temperature Crack Toughness Performance of Seven Structural Steels," Eng. Fracture Mech, Vol. 2, No. 4, June 1971, p 319.



11. Wessel, R. T., et al, "Engineering Methods for Design and Selection of Materials Against Fracture," Westinghouse Research Laboratories report to U.S. Army Tank-Automotive Center, AD601005.
12. Amateau, M. P., and Steigerwald, H. A., "Fracture Characteristics of Structural Metals," TRW Inc. AD611873, January 1965.
13. Bullock, D.P., et al, "Evaluation of the Mechanical Properties of 9 Ni-4Co Steel Forgings," Boeing Co., Air Force Materials Laboratory Report AFML-TR-68-87 March 1968. AD 833 650.
14. Brown, W. F. Jr., and Srawley, J. B., Plane Strain Crack Toughness Testing of High Strength Metallic Materials, ASTM STP 410, 1967, p 18 & p 60.
15. Srawley, J. B., Fracture, Chapman and Hall, 1969.
16. Hubsy, R. T. and Brown, W. F. Jr., "Crack Toughness Characteristics of Several Alloys For Use in Heavy Sections of High Speed Aircraft," NASA-TN-D-4998, January 1969, N69-17275.
17. Carter, C. S., Met. Trans., Vol 1, No. 6, June 1970, p 1551.
18. Pendleberry, S. L., et al, "Fracture Toughness and Crack Propagation of 300M Steel," Lockheed-California Co., AD 676573, August 1968.
19. "Mechanical Property Data, 300M Steel," Battelle Memorial Institute, AD 700072, 1969.
20. Amateau, M. P. and Steigerwald, H. A., "Test Methods for Determining Fracture Toughness of Metallic Materials," TRW Inc., Air Force Materials Laboratory Report AFML-TR-67-145, September 1967, AD823594.
21. Freed, C. N. and Goode, R. J., "Correlation of Two Fracture Toughness Tests for Titanium and Ferrous Alloys," Naval Research Laboratories, NRL 6740, January 1969. AD 683 639.
22. Heitman, G. H., Coyne, J. B., and Galipeau, R. P., Metals Engineering Quarterly, ASM, Vol 8, No. 3, August 1968, pp. 15-18.
23. Leis, H. and Schütz, W., Luftfahrttechnik-Raumfahrttechnik, B 15, Nr. 7, 1969, S180/84.
24. Freed, C.N., Eng. Fracture Mech., Vol 1, No. 1, June 1968, p 173.
25. DeSisto, T. S., and Hickey, C. F., Proceedings, ASTM, Vol 65, 1965, pp. 641-653.
26. Shannon, J. L. Jr., and Brown, W. F. Jr., Applications Related Phenomena in Titanium Alloys, ASTMSTP432, 1968, pp. 33-63.
27. Leis, H. and Schütz, W., Luftfahrttechnik-Raumfahrttechnik, B16, Nr10, 1970, S247/251.
28. Hanna, G. L., and Steigerwald, H. A., "Fracture Characteristics of Structural Metals," TRW, Inc., June, 1963, AD411509.
29. Greenlee, M. L., "Evaluation of T1-8Mo-8V-2Fe-3Al Die Forging, Wyman-Gordon Co.," Titanium Metals Corp. of America, Case Study M-61, February 1969.
30. Bohanek, E., "Heat Treatability of IMI 680, Beta III, and T1-8Mo-8V-2Fe-3Al in Heavy Sections," Titanium Metals Corp. of America, Report No. 31, June 1968.
31. Broadwell, R. G., "The Fracture Toughness-Tensile Property Relationships of Several Deep Hardenable Titanium Alloys." TMCA, Presented at AIME Annual Meeting, Las Vegas, Nevada, May 1970.
32. Petorsen, V.C., Guernsey, J. B. and Buehl, R.C., Air Force Materials Laboratory Report AFML-TR-69-171. AD 856 670.
33. Feeney, J. A. and Blackburn, M. J., Met. Trans., Vol 3, No. 1, January 1972, p 340.
34. Curtis, R. E. and Spurr, W. F., Trans. Am. Soc. Metals, Vol 61, No. 1, March, 1968, pp. 115-127.
35. Carman, C. M. and Katlin, J. M., Applications Related Phenomena in Titanium Alloys, ASTMSTP432, 1968, pp. 124-144.
36. Hall, L. R., Fracture Toughness Testing at Cryogenic Temperatures, ASTMSTP496, 1971, pp. 40-60.
37. Kaufman, J. G., Schilling, P.B., and Nelson, F. G., Metals Engineering Quarterly, Vol 9, No. 3, August 1969.
38. Kaufman, J. G., Nelson, F. G., and Holt, M., Eng. Fracture Mech., Vol 1, No. 2, 1968, p 259.
39. Nelson, F. G., and Kaufman, J. G., Fracture Toughness Testing at Cryogenic Temperatures, ASTMSTP496, 1971, pp. 27-39.
40. Judy, R. W., Goode, R. J., and Freed, C. M., "Fracture Toughness Characterization Procedures and Interpretations to Fracture-Safe Design for Structural Aluminum Alloys," Welding Research Council Bulletin, No. 140, May 1969.
41. Brownhill, D. J., et al, "Mechanical Properties Including Fracture Toughness and Fatigue, Corrosion Characteristics and Fatigue Crack Propagation Rates of Stress-Relieved Aluminum Hard Forgings," Air Force Materials Laboratory Report AFML-TR-70-10, February 1970. AD 868 376.

42. Brownhill, D. J., Davies, R. E., and Sprowls, D. O., Air Force Materials Laboratory Report AFML-TR-68-34, February 1968. AD 828 772.
43. Westerlund, R.W., et al, "Development of High Straight Aluminum Alloy Readily Weldable in Plate Thickness and Suitable for Applications at -423°F", ALCOA Contract No. NAS-8-5452, October 1967 NTIS, N68-14135.
44. Heyer, R. H. and McCabe, D. E., Review of Developments in Plane Strain Fracture Toughness Testing, ASTM STP 463, 1970, pp. 22-41.
45. Wilson, W. R., Clark, W. G., and Wessel, E. T., "Fracture Toughness Testing for Combined Loading and Low to Intermediate Strength Metals," Westinghouse Research Laboratories, U. S. Army Tank-Automotive Command Report 10276, November 1968, AD 682 754.
46. Hanna, G. L., and Steigerwald, E. A., "Development of Standardized Test Methods to Determine Plane Strain Fracture Toughness," Air Force Materials Laboratory Report AFML-TR-65-213, September 1965, AD 475 012.
47. Walker, E. F., and May, M. J., "Single Edge Notch Specimens of Two High Strength Martensitic Steels Tested in Tension and Bending," BISRA-The Inter-Group Labs. of British Steel Corp., MG/EB/337/67, 1968, PB 180 455.
48. Davis, S. O., Tupper, N. G., and Niemi, R. M., "Plane Strain Fracture Toughness Properties of Three Aluminum Alloys as a Function of Specimen Geometry," Air Force Materials Laboratory Report AFML-TR-65-150, July 1965, AD 470 276.
49. Davis, S. O., Tupper, N. G., and Niemi, R. M., Eng. Fracture Mech., Vol 1, No. 1, 1968, p 213.
50. "Thick Section Fracture Toughness," Technical Document Report ML-TDR-64-236, Boeing-North American, 1964, AD 452 824.
51. Peddersen, C. D., Moon, D. O., and Hyler, W. S., "Crack Behavior in D6AC Steel," MCIC Report 72-04, Jan 1972, AD 737 779.
52. Gunderson, A. W., "Preliminary Mechanical Property Evaluation of D6AC Steel in Support of the F-111 Aircraft Recovery Program," Air Force Materials Laboratory Technical Memorandum MAA 70-6, July 1970.
53. Hoenie, A. F., et al, "Determination of Mechanical Property Design Values for 18Ni-Co-Mo 250 and 300 Grade Maraging Steels," Air Force Materials Laboratory Report AFML-TR-65-197, July 1965.
54. Steigerwald, E. A., Review of Development in Plane Strain Fracture Toughness Testing, ASTM STP 463, 1970, pp. 102-123.
55. Bates, R. C., and Clark, W. G. Jr., Trans. Am. Soc. Metals, Vol 62, No. 2, June 1969, pp. 380-389.
56. Nelson, F.G., Schilling, P.E., and Kaufman, J.G. Eng. Fracture Mech. Vol 4, No. 1, p 51, March 1972.
57. May, M.J., Review of Developments in Plane Strain Fracture Toughness Testing, ASTM STP 463, 1970, pp. 41-62.
58. Swartzberg, F.R., et al. "Cryogenic Alloy Screening" NASA CR-72733 Nov. 1970, NTIS N71-10447.
59. Carter, C.S., "Evaluation of a High Purity 18% Ni (300) Maraging Steel Forging", AFML-TR-70-139, June 1970 AD 871 979.
60. Sertour, G., Societe Nationale Industrielle, Aerospatiale-Laboratoire Central, Suresnes, France, Private Communication.
61. Kaufman, J.G., et al, "Fracture Toughness, Fatigue and Corrosion Characteristics of X7080-TE41, 7178-T651, Plate 7075-T6510, 7075-T73510, X7080-T7E42 and 7178-T6510 Extruded Shapes" AFML-TR-69-255.
62. Kirkby, W.T., Royal Aircraft Establishment, Farnborough, Hants, U.K., Private Communication.
63. Braithwaite, A.A., Unpublished Work UK MOD (P.E.).
64. Rea, M.J., "Research into the Improvement of Fracture Toughness of High Strength Titanium Alloys and the Reduction of Cracking Susceptibility in Aqueous Environment", HAD Ltd. Rsch. Div. Rep. No. ISX5663/1, March 1971.
65. Armitage, M.R., BAC Preston, U.K., Private Communication.
66. Lee, K.T. and Hubbard, R.J., "Relationship Between Fracture Toughness, Plain Tensile Properties and Metallurgical Structure of a Titanium Alloy," Iron and Steel Inst. Publication 120, Fracture Toughness of High Strength Materials, 1970.
67. Norwood, J.I., "A Comparison of the Strength and Tensile Properties of Several High Strength Steels", BSC Report SSD 33/70 P 25/PD Oct. 1970.
68. McDermid, D.S., Unpublished work, UK MOD (P.E.).
69. Bayliss, J., Baker, T.J. and Dewey, M.A., "The Effect of Microstructure on the Crack Propagation Resistance of High Strength Steels for Aircraft Applications", Fulmer Rsch. Inst. Rep. R 30/2/Dec. 1970.
70. Maraging Steels, Firth Brown Ltd. Publication, Nov. 1970.

71. Roberts, C. "Fractography and Fracture Mechanics", U.K. MOD (NVEE Report No. 70505, May, 1970.
72. Binning, M.S., Unpublished Work, U.K. MOD (PE).
73. Carlholm, T. and Reuter, P., "Plane Strain Fracture Toughness of Electron Beam Welds in HD 66, 54 and 46 Aluminum Alloy Plate", Weld and Met Fab, Vol 39, No. 6, June 1971, pp. 235-241.
74. Peel, C.J. and Forsyth, P.J.E., "Fracture Toughness of Al-Zn-Mg-Mn Alloys to DTD 5024" RAE Tech. Rep. 70162, Sept. 1970.
75. Peel, C.J. and Forsyth, P.J.E., Unpublished Work, U.K. MOD (PE).
76. Simpson, A.R. and Fielding, J., "Aluminum Alloy Plates - An Evaluation of the Scatter in  $K_{IC}$  Values", HSA Report ER/MISC/MAN/1050, July 1971.
77. Webster, D., Trans. Am. Soc. Metals, Vol. 62, No. 3. Sept. 1969, p 759.
78. Fisher, D.M. and Repko, A.J., J. Matis, N.Y., Vol. 7, No. 2, June 1972, pp. 167-174.
79. Hauser, J.J. and Wells, M.G.H., "Inclusions in High Strength and Bearing Steels", AFML-TR-69-339, AD 867.824.
80. Mravic, B. and Smith, J.H. "Development of Improved High Strength Steels for Aircraft Structural Components" AFML-TR-71-213, AD 736 812.
81. Judy, R.W., et al, "Fracture Characteristics of Ti-6Al-2Mo and Ti-6Al-4V in 3 inch Thick Sections", Naval Research Lab Report MR-2156, August 1970, AD 711 856.
82. Goode, R.J., et al, "Metallurgical Characteristics of High Strength Structural Materials", Naval Research Lab Report 6405, Nov. 1965.
83. Johnson, F.A., and Radon, J.C., Int. J. of Fract. Mech, Vol. 8 No. 1, March 1972.
84. "Mechanical Property Data 7049 Aluminum T73 Forgings", Battelle Memorial Institute, Dec. 1969.
85. Rolfe, S.T. and Novak, S.R., "K<sub>IC</sub> Testing of Medium Strength High Toughness Steels", U.S. Steel, Project No. 39.01A-007(11), August 1967, AD 817 373L.
86. Jones, M.H., Bubsey, R.T., and Brown, W.F. Jr., "Crack Toughness Evaluation of Hot Pressed and Forged Beryllium", NASA TMX67967, 1971, N72-14546.
87. Peddersen, C.E., and Hyler, W.S., "Fracture and Fatigue Characteristics of 7075-T7351 Aluminum Alloy Sheet and Plate", Battelle Memorial Institute, March 1970, AD 714019.
88. Spaeder, G.J. and Murphy, W.J., J of Mtlis, N.Y., Vol. 3, No. 1, March 1968, pp. 116-133.
89. Freed, C.N., Sullivan, A.M. and Stoop, J., "Effect of Sheet Thickness on the Fracture Resistance  $K_c$  Parameter for Titanium Alloys", Naval Research Laboratory, To be published.
90. Webster, D. Trans. Am. Soc. Met., Vol. 69, No. 4, Dec. 1968, p 816.
91. Robinson, J.N. and Tuck, C.W., Eng. Fracture Mech., Vol. 4, No. 2, 1972, pp. 377-392.
92. Coyne, J. E., "The Beta Forging of Titanium Alloys", The Science, Technology and Application of Titanium, P97, Pergamon Press, 1970
93. Hunter, D.B. and Arnold, S.V., "Metallurgical Characteristics and Structural Properties of Ti-8Mo-8V-2Fe-3Al Sheet, Plate and Forgings". The Science Technology and Applications of Titanium, p959, Pergamon Press 1970, also U.S. Army Materiels Research Agency Report WALTR 405/2-14 October, 1966, AD 648 244.
94. Boeing Co., Commercial Supersonic Transport Program, Phase II-C Report FA-SS-66-5, 1966, AD 806 980
95. Curtis, R.E. et al Trans Am. Soc. Metals, Vol. 62, p457, 1969
96. Heitman, G.H., J of Metals, May 1971, p37.
97. Jones, R.E., "Mechanical Properties of 7049-T73 and 7049-T76 Aluminum Alloy Extrusions at Several Temperatures" AFML-TR-72-2, Feb. 1972.
98. Nelson, F.G. and Kaufman, J.G., "Fracture Toughness of Plain and Welded 3 in. Thick Aluminum Alloy Plate", Presented at ASTM Sixth National Symposium on Fracture Mechanics, Philadelphia, Pa., August 1972.
99. Jones, R.E. "Fracture Toughness and Fatigue Crack Growth Properties of 7175-T736 Aluminum
100. TIMET Div of Titanium Corp. of America, Project 99-4, Report No. 44, Aug. 1, 1970.
101. Seagle, S.R., et al, Development of a Deep-Hardenable Alloy for Intermediate Temperature Applications" RMI Co., Presented at the Second International Conference on Titanium, Cambridge, Mass; May 2-5, 1972. (To be published in proceedings)
102. Wood, R.A. and Favor, R.J., "Titanium Alloys Handbook," MCIC-HB-02, Battelle, Dec. 1972

Steel, Low Al W: AISI 4330M, EN30B

Form	Composition, Heat Treatment	Test Orientation	Temp °F (°C)	Yield Strength KSI (MN/m <sup>2</sup> )	Typical K <sub>IC</sub> KSI/√in (MN m <sup>-3/2</sup> )	2.5 (K <sub>IC</sub> <sup>2</sup> / σ <sub>ys</sub> ) <sup>2</sup> in (mm)	Specimen			Ref.
							Type	Thickness in (mm)	Width in (mm)	
<b>AISI 4330M</b>										
Cylindrical	A,1	C-R	70(294)	181(1248)	120(131)	1.10(27.9)	WOL 1.0 (25.4)	2.75(69.8)	---	1
15.5 in. (39 mm) OD	A,1	C-R	-20(244)	---	120(131)	---	WOL 1.0 (25.4)	2.75(69.8)	---	
6.5 in. (16. mm) ID	A,2	C-R	70(294)	157(1082)	120(131)	1.47(37.5)	WOL 1.0 (25.4)	2.75(69.8)	---	
35 ft (10.7 m) Long	A,2	C-R	-60(222)	---	45(49)	---	WOL 1.0 (25.4)	2.75(69.8)	---	
Plate: 1 in (25.4 mm) Thick	B,3	L-T	70(294)	210(1448)	55(60)	0.17(4.3)	NR D=	0.353(19.9)	---	2
		L-T	-100(200)	---	40(44)	---	NR D=	0.353(19.9)	---	
Forging: 3 in. (76.2 mm) Thick	C,4	L-T	70(294)	198(1365)	84(92)	0.45(11.4)	Bend0.48 (12.2)1.5 (38.1)0.3 (7.6) 4pt			3
		L-T	-65(219)	---	64(70)	---	Bend0.48 (12.2)1.5 (38.1)0.3 (7.6) 4 pt			
<b>EN30B</b>										
Bar: 0.56 in. (14.2 mm) Square	D,5	L-ST	70(294)	198(1365)	68(75)	0.295(7.5)	Bend0.313(7.8) 0.5 (12.7)0.25 (6.4)			5
	D,6	L-ST	70(294)	207(1427)	65(72)	0.247(6.3)	Bend0.315(8.0) 0.5 (12.7)0.26 (6.6)			
	D,7	L-ST	70(294)	216(1489)	56(62)	0.168(4.3)	Bend0.315(8.0) 0.5 (12.7)0.21 (5.3)			
	D,8	L-ST	70(294)	232(1600)	74(81)	0.254(6.5)	Bend0.315(8.0) 0.5 (12.7)0.25 (6.4)			
	D,9	L-ST	70(244)	248(1710)	68(75)	0.188(4.8)	Bend0.315(8.0) 0.5 (12.7)0.22 (5.6)			
COMPOSITION										
HEAT TREATMENT										
1.	1550F (1117K), Oil Quench; Temper 1050F (839K), 4 Hr									
2.	1550F (1117K), Salt Quench to 600F (589K); Temper 1050F (839K), 4 Hr									
3.	1700F (1200K), 1 Hr, Oil Quench; Temper 600F (589K), 1 Hr, Air Cool									
4.	1575F (1130K), 1 Hr, Oil Quench; Temper 500F (533K), 3 Hr, Air Cool									
5.	Hot Rolled, Air Cooled; 1525F (1103K), 1 Hr, Oil Quench; Temper 391F (473K), 1 Hr									
6.	Heated at 54F (30K)/sec to Ac3 Temp, Quench; Temper 661F (623K), 1 Hr									
7.	Heated at 54F (30K)/sec to Ac3 Temp, Quench; Temper 391F (473K), 1 Hr									
8.	1796F (1253K), 1 Hr, Quench in Lead Bath 931F (773K); Ausformed, 70% Reduction, Air Cooled; Temper 750F (672K), 1 Hr.									
9.	1796F (1253K), 1 Hr, Quench in Lead Bath 931F (773K); Ausformed, 70% Reduction, Air Cooled; Temper 391F (473K), 1 Hr									

	C	Si	Mn	S	P	Mo	Ni	Cr	V
A	0.34	0.22	0.50	0.011	0.012	0.58	3.08	1.15	0.13
B	0.31	1.59	---	---	---	0.40	1.80	2.04	0.07
C	0.28	0.38	0.80	0.007	0.009	0.44	1.84	0.90	0.08
D	0.32	0.20	0.49	0.009	0.012	0.24	4.09	1.22	---

Steel Low Alloy 35NiCr 16, EN40C

Table 2

Norm	Composition, Heat Treatment	Test Orientation	Temp °P (°K)	Yield Strength ksi (N/mm <sup>2</sup> )	Typical $K_{IC}$ ksi√in (MN/m <sup>3/2</sup> )	$2.5 \left( \frac{K_{IC}}{\sigma_{ys}} \right)^2$ in (mm)	Specimen			Ref.
							Type	Thickness in (mm)	Width in (mm)	
<b>35NiCr 16</b>										
Bar: Vac. Anneal										
A,1	L-R	70(294)	191(1317)	72(79)	0.355 (9.0)	(a)	---	---	---	67
A,2	L-R	70(294)	202(1393)	72(79)	0.318 (8.1)	(a)	---	---	---	
A,3	L-R	70(294)	211(1455)	67(74)	0.252 (6.4)	(a)	---	---	---	
C,-	T-S	70(294)	208(1434)	74(81)	0.316 (8.04)	Bend 0.5 (12.7)	1.0 (25.4)	---	---	60
C,-	T-S	70(294)	216(1489)	72(79)	0.278 (7.1)	Bend 0.5 (12.7)	1.0 (25.4)	---	---	
C,-	T-S	20(294)	222(1531)	71(78)	0.256 (6.5)	Bend 0.5 (12.7)	1.0 (25.9)	---	---	
<b>EN40C</b>										
Bar: 0.56 in (14.2 mm) dia										
B,4	L-R	70(294)	218(1503)	60(66)	0.189 (4.8)	Bend 0.313(8)	0.5 (12.7)	0.23(5.8)	0.15(3.8)	5
B,5	L-R	70(294)	239(1648)	59(65)	0.152 (3.9)	Bend 0.313(8)	0.5 (12.7)	0.15(3.8)	0.21(5.3)	
B,6	L-R	70(294)	260(1793)	55(61)	0.112 (2.8)	Bend 0.313(8)	0.5 (12.7)	0.12(3.0)	0.12(3.0)	
B,7	L-R	70(294)	317(2186)	44(48)	0.048 (1.2)	Bend 0.313(8)	0.5 (12.7)	0.12(3.0)	0.12(3.0)	

(a) Specimen in accordance with ASTM Recommendations.

COMPOSITION

	C	Mn	P	S	Al					
A	1.35	0.27	0.33	5.99	1.69	0.44	0.05	0.009	0.009	0.026
B	1.37	0.26	2.54	0.13	2.98	0.90	0.23	0.013	0.015	---
C	1.35N	0.4M	0.35N	4.0N	1.75N	0.45N	--	0.03M	0.03M	--

HEAT TREATMENT

1. 171 (1203K), Air Cool; 1606F (1148K), Air Cool; -95F (203K); Temper 751F (673K), 2 Hr
2. 171 (1203K), Air Cool; 1606F (1148K), Air Cool; -95F (203K); Temper 661F (623K), 2 Hr
3. 171 (1203K), Air Cool; 1606F (1148K), Air Cool; -95F (203K); Temper 427F (493K), 2 Hr
4. 161 (1172K), Oil Quench; Temper 571F (573K), 1 Hr
5. Heat at 54F (30K)/sec to A<sub>3</sub> Temp, Immediate Quench to 70F (294K); Temper 571F (570K), 1 Hr
6. 171 (1253K), 1 Hr, Quench in Lead Bath 1021F (823K); Ausformed 70% Reduction, Air Cooled; Temper 571F (473K), 1 Hr
7. 171 (1253K), 1 Hr, Quench in Lead Bath 1021F (823K); Ausformed 70% Reduction, Air Cooled; Temper 571F (573K), 1 Hr

STEEL, Low Alloy: H-11, H-11M

Table 3

Form	Composition, Heat Treatment	Test Orientation	Temp $\sigma_y$ (°F)	Yield Strength KSI (MN/m <sup>2</sup> )	Typical $K_{IC}$ KSI√in (MPa√m)	$2.5 \left( \frac{K_{IC}}{\sigma_y} \right)^2$ in (mm)	Specimen			Ref.	
							Type	Thickness in (mm)	Width in (mm)		Crack Length in (mm)
Plate: 0.0065 in (2.2 mm) Thick	A,1	L-T	75(297)	243(1675)	40(44)	0.068( 1.7)	CC	0.085( 2.2)	1.75( 4.44)	0.7 (17.8)	54
		L-T	-100(200)	257(1760)	35(38)	0.046( 1.2)	CC	0.085( 2.2)	1.75( 4.44)	0.7 (17.8)	
		L-T	75(297)	231(1590)	35(38)	0.057( 1.4)	CC	0.085( 2.2)	1.75( 4.44)	0.7 (17.8)	
		L-T	-100(200)	240(1555)	31(34)	0.042( 1.1)	CC	0.085( 2.2)	1.75( 4.44)	0.7 (17.8)	
		L-T	200(367)	202(1393)	55(60)	0.185( 4.7)	Bend	0.5 (12.7)	1.0 (25.5)	0.23( 5.8)	7
Plate: 0.5 in (12.7 mm) Thick	B,3	L-T	75(297)	212(1462)	34(37)	0.064( 1.6)	Bend	0.5 (12.7)	1.0 (25.5)	0.28( 7.1)	
		T-L	75(297)	204(1407)	32(35)	0.061( 1.5)	Bend	0.5 (12.7)	1.0 (25.5)	0.26( 6.6)	
		L-T	-50(238)	216(1489)	23(25)	0.028( 0.7)	Bend	0.5 (12.7)	1.0 (25.5)	0.26( 6.6)	
		L-T	-100(200)	228(1572)	21(23)	0.021( 0.5)	Bend	0.5 (12.7)	1.0 (25.5)	0.23( 5.8)	
		L-T	200(367)	198(1365)	81(89)	0.418(10.6)	Bend	1.03 (26.2)	0.94(23.8)	0.24( 6.1)	
Bar: 1 in (25.4 mm) Thick	C,4	L-T	-50(238)	210(1448)	25(28)	0.035( 0.9)	Bend	0.75 (19.1)	0.75(19.1)	0.13( 3.3)	
		L-T	-100(200)	220(1517)	23(25)	0.027( 0.7)	Bend	1.0 (25.4)	1.0 (25.4)	0.28( 7.0)	
		T-L	70(294)	189(1303)	45(49)	0.142( 3.6)	Bend	0.48 (12.2)	1.5 (38.1)	0.3 ( 7.6)	3
		T-L	-65(219)	---	35(38)	---	Bend	0.48 (12.2)	1.5 (38.1)	0.3 ( 7.6)	
		T-L	70(294)	225(1551)	38(41)	0.071( 1.8)	Bend	0.75 (19.1)	0.75(19.1)	0.15( 3.8)	12
Forging: 3 in (76.1 mm) Thick	D,5	T-L	70(294)	194(1338)	73(80)	0.35 ( 8.9)	Bend	0.75 (19.1)	0.75(19.1)	---	
		T-L	-65(219)	---	---	---	Bend	0.48 (12.2)	1.5 (38.1)	0.3 ( 7.6)	
Forging: 8 in (203 mm) Square	E,1	T-L	70(294)	225(1551)	38(41)	0.071( 1.8)	Bend	0.75 (19.1)	0.75(19.1)	0.15( 3.8)	12
		T-L	70(294)	194(1338)	73(80)	0.35 ( 8.9)	Bend	0.75 (19.1)	0.75(19.1)	---	

COMPOSITION	HEAT TREATMENT										
	C	Mn	Si	Cr	Mo	V	P	S			
A	0.43	0.25	0.96	5.12	1.33	0.57	0.010	0.007	1. 1850F (1283K), 20 min; Temper 2 Hr + 2 Hr, 1050F (839K)		
B	0.39	0.31	0.90	4.91	1.30	0.51	0.016	0.010	2. 1850F (1283K), 20 min; Temper 2 Hr + 2 Hr, 1100F (867K)		
C	0.38	0.35	0.96	4.99	1.36	0.50	0.010	0.007	3. 1850F (1283K), in Salt, Oil Quench; Temper 1 Hr + 1 Hr, 1080F (856K)		
D	0.37	0.28	0.93	5.15	1.20	0.43	0.009	0.008	4. 1850F (1283K), in Salt, Oil Quench; Temper 1 Hr + 1 Hr, 1100F (867K)		
E	0.40	0.35	0.87	4.90	1.27	0.51	0.021	0.008	5. 1550F (1117K), 1 Hr, Oil Quench; Temper 2 Hr + 2 Hr, 950F (783K), Air Cool		

Steel, Low Alloy: AISI4140

Table 4

Form	Composition, Heat Treatment	Test Orientation	Temp °F (°K)	Yield Strength KSI (MN/m <sup>2</sup> )	Typical K <sub>IC</sub> KSI√in (MN m <sup>3/2</sup> )	2.5 (K <sub>IC</sub> <sup>2</sup> / σ <sub>ys</sub> ) in (mm)	Specimen			Ref.	
							Type	Thickness in (mm)	Width in (mm)		Crack Length in (mm)
Bar: 1 in (25.4 mm) Thick	A,1	L-T	200(367)	173(1193)	65(72)	0.353 (9.0)	Rend	1.03 (26.2)	1.0 (25.4)	0.321 (8.2)	7
	A,1	L-T	75(297)	190(1310)	72(79)	0.359 (9.1)	Bend	1.03 (26.2)	1.0 (25.4)	0.225 (5.7)	
	B,1	T-L	75(297)	---	70(77)	---	Bend	1.02 (25.9)	1.0 (25.4)	0.3 (7.6)	
	B,1	L-T	-50(228)	200(1379)	65(72)	0.324 (8.2)	Bend	1.02 (25.9)	1.0 (25.4)	0.33 (8.4)	
	B,1	L-T	-100(200)	205(1413)	52(57)	0.161 (4.1)	Bend	1.02 (25.9)	1.0 (25.4)	0.24 (6.1)	
	C,2	T-L	70(294)	177(1220)	90(99)	0.782 (19.9)	SEN	1.0 (25.9)	4.5 (114)	1.6 (40.6)	21
Plate: 1 in (25.4 mm) Thick											

COMPOSITION										
	C	Mn	P	S	Si	Cr	Mo	Ni	V	
A	0.37	0.75	0.010	0.019	0.26	0.85	0.15	---	---	
B	0.38	0.81	0.008	0.025	0.27	0.91	0.17	---	---	
C	0.43	0.98	0.013	0.030	0.19	1.04	0.21	0.01	0.08	

HEAT TREATMENT	
1.	Austenitize 1550F (1117K) in Salt, Oil Quench, Temper 800F (700K), 2 Hr
2.	Austenitize 1550F (1117K), 1 Hr, Oil Quench, Temper 900F (756K), 2 Hr + 2 Hr, Air Cool

Form	Composition, Heat Treatment	Test Orientation	Temp °F (°K)	Yield Strength KSI (MN/m <sup>2</sup> )	Typical K <sub>IC</sub> KSI√in (MN m <sup>3/2</sup> )	2.5 (K <sub>IC</sub> /σ) <sup>2</sup> in (mm)	Specimen			Ref.	
							Type	Thickness in (mm)	Width in (mm)		Crack Length in (mm)
Plate: 0.125 in (3.2 mm) Thick	A,1	L-T	200(567)	220(1517)	40(44)	0.083 (2.1)	CC	0.10 (2.5)	3.0 (76.2)	1.2 (30.5)	8
	A,2	L-T	-100(200)	220(1517)	40(44)	0.083 (2.1)	CC	0.10 (2.5)	3.0 (76.2)	1.2 (30.5)	
Plate: 0.375 in (9.5 mm) Thick	B,3	L-T	200(567)	208(1435)	60(66)	0.208 (5.3)	Bend	0.390(9.9)	1.0 (25.4)	0.4 (10.1)	7
	E,3	L-T	75(297)	226(1517)	52(57)	0.149 (3.6)	Bend	0.390(9.9)	1.0 (25.4)	0.4 (10.1)	
	F,3	T-L	75(297)	223(1538)	53(58)	0.141 (3.6)	Bend	0.377(9.6)	0.9 (22.9)	0.37 (9.4)	
Plate: 0.500 in (12.6 mm) Thick	E,3	L-T	-50(228)	235(1620)	40(44)	0.072 (1.8)	Bend	0.390(9.9)	1.0 (25.4)	0.4 (10.1)	
	E,3	L-T	-100(200)	240(1655)	32(35)	0.044 (1.1)	Bend	0.390(9.9)	1.0 (25.4)	0.4 (10.1)	
	H,10	T-L	75(297)	231(1593)	68(75)	0.217 (5.5)	Bend	0.500(12.7)	1.0 (25.4)	0.4 (10.1)	80
Plate: 0.625 in (15.9 mm) Thick	C,4	L-T	75(297)	204(1504)	78(86)	0.371 (9.4)	SEN	0.523(13.3)	2.0 (50.8)	0.67 (17.0)	12
	D,5	L-T	70(294)	182(1255)	106(116)	0.850 (21.6)	Bend	1.0 (25.4)	2.0 (50.8)	1.0 (25.4)	6
Plate: 1 in (25.4 mm) Thick	D,6	L-T	70(294)	213(1469)	68(75)	0.255 (6.5)	Bend	1.0 (25.4)	1.0 (25.4)	0.5 (12.7)	
	B,7	L-T	-50(228)	203(1380)	65(71)	0.256 (6.5)	Bend	1.0 (25.4)	1.0 (25.4)	0.2 (5.1)	7
Billet: 4x4.5 in (102x 114 mm) Vac. Arc Remelted	D,8	L-T	-100(200)	206(1400)	50(55)	0.148 (3.8)	Bend	1.0 (25.4)	1.0 (25.4)	0.2 (5.1)	
	D,7	L-T	75(297)	230(1586)	52(57)	0.128 (3.3)	Bend	0.25 (6.3)	1.0 (25.4)	0.5 (12.7)	9
	D,7	L-T	75(297)	206(1400)	80(88)	0.38 (9.7)	Bend	0.95 (24.2)	2.0 (50.8)	1.0 (25.4)	44
Forged Bar: 5 in (127 mm) Thick	G,9	L-T	72(296)	241(1662)	53(58)	0.121 (3.1)	Bend	0.90 (22.9)	1.8 (45.7)	0.9 (22.9)	79
	T,11	T-S	72(296)	240(1655)	54(59)	0.127 (3.2)	Bend	0.90 (22.9)	1.8 (45.7)	0.9 (22.9)	
	J,11	T-S	70(294)	191(1317)	80(88)	0.136 (3.5)	Bend	0.90 (22.9)	1.8 (45.7)	0.9 (22.9)	69
	J,12	T-S	70(294)	230(1586)	49(53)	0.439 (11.1)	(a)	---	---	---	
						0.113 (2.9)	(a)	---	---	---	

(a) Specimen in accordance with ASTM Recommendations



STEEL, Low Alloy: AISI 4340 (Sheet 2 of 2) Table 5

Form	Composition, Heat Treatment										Yield Strength KSI (MN/m <sup>2</sup> )	Typical K <sub>IC</sub> KSI√in (MN m <sup>3/2</sup> )	2.5 (K <sub>IC</sub> <sup>2</sup> / σ <sub>ys</sub> ) <sup>2</sup> in (mm)	Specimen			Ref.
	C	Mn	P	S	Si	Ni	Cr	Mo	Test Orientation	Temp °F (°K)				Type	Thickness in (mm)	Width in (mm)	
	A	0.41	0.72	0.015	0.009	0.33	1.83	0.78	0.26								
	B	0.43	0.84	0.006	0.005	0.27	1.78	0.78	0.26								
	C	0.43	0.65	0.010	0.005	0.30	1.85	0.82	0.26								
	D	0.42	0.71	0.010	0.012	0.25	1.77	0.80	0.23								
	E	0.40	0.75	0.005	0.010	0.29	1.77	0.79	0.25								
	F	0.41	0.69	0.018	0.012	0.29	1.87	0.78	0.22								
	G	0.42	0.84	0.008	0.005	0.25	1.71	0.82	0.24								
	H	0.38	0.74	0.001	0.005	0.28	1.86	0.84	0.26								
	I	0.43	0.63	0.013	0.004	0.24	1.56	1.03	0.30								

## COMPOSITION

## HEAT TREATMENT

1. Normalize 1600F (1144K), 1 Hr; Austenitize 1550K (1117K), 1 Hr, Oil Quench; Temper 1 Hr, 400F (478K)
2. Normalize 1600F (1144K), 1 Hr, Austenitize 1550F (1117K), 1 Hr, Oil Quench; Temper 1 Hr, 700F (664K)
3. 1550F (1117K) Salt; Oil Quench; Temper 1 Hr + 1 Hr, 500F (533K)
4. 1500F (1089K), 1 Hr; Temper 1 Hr + 1 Hr, 700F (644K)
5. 1500F (1089K), 0.5 Hr; Oil Quench; Temper 1 Hr, 925F (770K)
6. 1500F (1089K), 0.5 Hr; Oil Quench; Temper 1 Hr, 750F (672K)
7. 1550F (1117K) Salt, Oil Quench; Temper 1 Hr + 1 Hr, 800F (700K)
8. 1500F (1089K), 0.5 Hr, Oil Quench; Temper 1 Hr, 600F (589K)
9. 1650F (1172K), 1 Hr, Air Cool; 1550F (1089K), 1 Hr, Oil Quench; -321F (77K), 0.5 Hr Min; 400F (478K), 2 Hrs
10. 1600F (1144K), 0.5 Hr, Air Cool; 1500F (1089K), 0.5 Hr, Oil Quench; -320F, 0.5 Hr, 400F (478K), 6 Hr, Air Cool; 250F (394K), 24 Hr, Air Cool
11. 1543F (1113K), 0.5 Hr, Oil Quench; Temper 841F (723K), 0.75 Hr
12. 1543F (1113K), 0.5 Hr, Oil Quench; Temper 571F (573K), 1 Hr

Table 6

Form	Composition, Heat Treatment	Test Orientation	Temp °F (°K)	Yield Strength KSI (MN/m <sup>2</sup> )	Typical K <sub>IC</sub> KSI√in (MN m <sup>3/2</sup> )	2.5 (K <sub>IC</sub> /σ <sub>ys</sub> ) <sup>2</sup> in (mm)	Specimen			Ref.	
							Type	Thickness in (mm)	Width in (mm)		Crack Length in (mm)
Forging: 6 x 10 in (152 x 254 mm)	A,1	L-T	70(294)	246(1703)	69(75)	0.195 (5.0)	Bend	---	---	19	
Forging: 4.5 x 4.5 in (114 x 114 mm) Vac. Arc Remelt	B,2	L-T	70(294)	243(1675)	60(65)	0.152 (3.9)	Bend	0.50 (12.7)	1.0 (25.4)	0.5 (12.7)	16
Forging: 1 x 13 x 34 in (25.4 x 330.2 x 863.6 mm)	C,3	L-T	70(294)	240(1655)	88(96)	0.336 (8.5)	CC	0.372(9.4)	5.0 (127)	1.90 (1.90)	18
	C,4	L-T	70(294)	234(1613)	74(81)	0.250 (6.4)	CC	0.370(9.4)	5.0 (127)	2.05 (52.1)	
	C,5	L-T	70(294)	205(1413)	74(81)	0.326 (8.3)	CC	0.370(9.4)	5.0 (127)	1.75 (44.4)	
Forging: 3 x 9 in (76.2 x 229.6 mm) Hot Rolled 2300F (1533K) Forged 2100F (1422K)	D,6	T-L	70(294)	233(1606)	79(87)	0.287 (7.3)	Bend	0.480(12.2)	1.5 (38.1)	0.30 (7.6)	3
		I-L	-65(219)	233(1606)	53(58)	---	4 pt Bend	0.480(12.2)	1.5 (38.1)	0.30 (7.6)	
Forging: 20 in (508 mm) dia Ingot Forged at 2125F (1456K) to 3 x 9 in (76.2 x 228.6 mm)	L,6	T-L	70(294)	236(1627)	68(74)	0.208 (5.3)	Bend	0.480(12.2)	1.5 (38.1)	0.30 (7.6)	
		T-L	-65(219)	---	45(49)	---	4 pt Bend	0.480(12.2)	1.5 (38.1)	0.30 (7.6)	
Billet: 3 in (76.2 mm)	F,7	L-TS	70(294)	142(976)	111(122)	1.53 (38.8)	(a)	---	---	---	67
	F,8	L-TS	70(294)	185(1275)	111(122)	0.9 (22.9)	(a)	---	---	---	
	F,9	L-TS	70(294)	206(1418)	78(86)	0.358 (9.1)	(a)	---	---	---	
Bar: Vacuum Arc Remelted 1 in (25.4 mm) Dia	F,10	LR	70(294)	238(1643)	68(75)	0.209 (5.3)	(a)	---	---	---	67
Forged Bar: Vac Remelt 5 in (127 mm) Dia	G,11	CR	70(294)	255(1755)	45(50)	0.078 (2.0)	(a)	---	---	---	68
Billet: 4 x 4.5 in (101 x 114 mm)	H,12	L-T	72(296)	259(1785)	52(57)	0.101 (2.6)	Bend	0.9(22.9)	1.8 (45.7)	0.9 (22.9)	79
		T-L	72(296)	255(1758)	56(62)	0.121 (3.1)	Bend	0.9(22.9)	1.8 (45.7)	0.9 (22.9)	79
		T-L	72(296)	255(1758)	58(64)	0.129 (3.3)	Bend	0.9(22.9)	1.8 (45.7)	0.9 (22.9)	79

(a) Specimen in accordance with ASTM Recommendations

Table 6

Form	Composition, Heat Treatment						Test Orientation	Temp °F (°C)	Yield Strength KSI (MN/m <sup>2</sup> )	Typical K <sub>IC</sub> KSI/√in (MN m <sup>-3/2</sup> )	2.5 (K <sub>IC</sub> <sup>2</sup> / σ <sub>ys</sub> ) <sup>2</sup> in (mm)	Specimen			Ref.
	C	Si	Mn	S	P	Mo						Ni	Cu	V	
A	0.43	1.68	0.70	0.010	0.010	0.39	1.93	0.79	0.07	0.15					
B	0.41	1.77	0.81	0.003	0.007	0.40	1.85	0.83	0.08	-					
C	0.40	1.60	0.83	0.006	0.007	0.41	1.82	0.83	0.09	-					
D	0.39	1.55	0.82	0.009	0.012	0.43	1.73	0.86	0.09	-					
E	0.43	1.62	0.85	0.006	0.014	0.41	1.74	0.94	0.08	-					
F	0.42	1.45	0.73	0.006	0.009	0.40	1.82	0.98	0.11	0.029					
G	0.44	1.69	0.81	0.006	0.005	0.38	1.34	0.85	0.09	-					
H	0.42	1.59	0.80	0.006	0.006	0.37	1.81	0.79	0.08	-					

**COMPOSITION**

**HEAT TREATMENT**

- 1600F (1144K), Quenched Max Oil; Double Temper 2 + 2 Hr, 575F (575K)
- 1700F (1200K), 3 1/2 Hr, Air Cool; 1600F (1144K), 1 1/2 Hr; Salt Quenched to 1000F, Hold 1 Hr; Oil Quenched; 110F, 1/2 Hr; Double Tempered 575F (575K), 2 + 2 Hr Air Cool
- 1700F (1200K), 1 1/2 Hr, Air Cool; 1600F (1144K), 1 1/2 Hr, Oil Quenched; Double Temper, 2 + 2 Hr, 500F (533K)
- 1700F (1200K), 1 1/2 Hr, Air Cool; 1600F (1144K), 1 1/2 Hr, Oil Quenched; Double Temper, 2 + 2 Hr, 675F (630K)
- 1700F (1200K), 1 1/2 Hr, Air Cool; 1600F (1144K), 1 1/2 Hr, Oil Quenched; Double Temper, 2 + 2 Hr, 975F (797K)
- 1600F (1144K), 1 Hr, Oil Quenched; Double Temper, 3 + 3 Hr, 600F (589K), Air Cool
- 1705F (1205K), Air Cool; 1777F (1243K), Oil Quench; 1200F (922K), 2 + 2 Hr
- 1705F (1205K), Air Cool; 1777F (1243K), Oil Quench; 1111F (875K), 2 + 2 Hr
- 1705F (1205K), Air Cool; 1777F (1243K), Oil Quench; 1021F (823K), 2 + 2 Hr
- 1705F (1205K), Air Cool; 1777F (1243K), Oil Quench; 481F (523K), 2 + 2 Hr
- 1705F (1205K), Air Cool; 1615F (1243K), Oil Quench; 571F (574K), .5 + .5 Hr
- 1700F (1200K), 1 Hr, Air Cool; 1600F (1144K), 1 Hr, Oil Quench, -321F (77K), 0.5 Hr Min; 600F (589K), 2 + 2 Hr

STEEL, Low Alloy: D6AC (Sheet 1 of 2)

Table 7

Form	Composition, Heat Treatment	Test Orientation	Temp °F (°C)	Yield Strength KSI (MN/m <sup>2</sup> )	Typical $K_{IC}$ KSI√in (MN m <sup>-3/2</sup> )	$2.5 \left( \frac{K_{IC}}{\sigma_{ys}} \right)^2$ in (mm)	Specimen			Ref.	
							Type	Thickness in (mm)	Width in (mm)		Crack Length in (mm)
Plate: 0.095 in (2.4 mm) Thick	A,1	T-L	75(297)	236(1628)	46(50)	0.095(2.4)	CC	0.095(2.4)	1.75(44.4)	0.7(17.8)	12
		L-T	-100(200)	253(1745)	37(41)	0.053(1.3)	CC	0.095(2.4)	1.75(44.4)	0.7(17.8)	
		L-T	-200(144)	263(1815)	36(40)	0.047(1.2)	CC	0.095(2.4)	1.75(44.4)	0.7(17.8)	
Plate: 0.5 in (12.7 mm) Thick	B,2	L-S	70(294)	203(1400)	110(120)	0.734(18.6)	Bend	0.75(19.1)	1.5(38.1)	0.368(9.3)	20
		L-S	70(294)	231(1593)	61(66)	0.174(4.4)	Bend	0.257(6.5)	0.486(12.3)	0.245(6.2)	
Plate: 0.75 in (19.1 mm) Thick	B,1	---	70(294)	247(1703)	67(74)	0.735(18.7)	Bend	0.75(19.1)	0.75(19.1)	---	46
		---	175(353)	211(1455)	92(101)	0.475(12.1)	CT	0.75(19.1)	1.5(38.1)	0.75(19.1)	51
Plate: 0.8 in (20.3 mm) Thick	C,3	---	70(294)	217(1496)	94(103)	0.469(11.9)	CT	0.75(19.1)	1.5(38.1)	0.75(19.1)	
		---	-20(244)	226(1558)	72(79)	0.254(6.4)	CT	0.75(19.1)	1.5(38.1)	0.75(19.1)	
		---	175(353)	211(1455)	92(101)	0.475(12.1)	CT	0.75(19.1)	1.5(38.1)	0.75(19.1)	
Plate: 1.5-1.8 in (38.1-45.7 mm) Thick		---	70(294)	217(1496)	79(87)	0.331(8.4)	CT	0.75(19.1)	1.5(38.1)	0.75(19.1)	
		---	-20(244)	226(1558)	50(55)	0.122(3.1)	CT	0.75(19.1)	1.5(38.1)	0.75(19.1)	
		---	-65(219)	228(1572)	46(51)	0.102(2.6)	CT	0.75(19.1)	1.5(38.1)	0.75(19.1)	
Forging: 0.8 in (20.3 mm) Thick 1.5-1.8 in (38.1-45.7 mm) Thick		---	70(294)	214(1476)	97(107)	0.514(13.0)	CT	0.75(19.1)	1.5(38.1)	0.75(19.1)	
		---	70(294)	214(1476)	90(99)	0.442(11.2)	CT	0.75(19.1)	1.5(38.1)	0.75(19.1)	
Billet: 3 in (76.2 mm) Dia	D,4	LR	70(294)	208(1434)	105(115)	0.637(16.2)	CT	0.75(19.1)	1.5(38.1)	0.75(19.1)	67
		LR	70(294)	215(1482)	84(92)	0.382(9.7)	CT	0.75(19.1)	1.5(38.1)	0.75(19.1)	
COMPOSITION											
A	C	Mn	P	S	Si	Ni	Cr	Mo	V	Al	
0.47	0.85	0.007	0.005	0.005	0.20	0.57	1.07	1.01	0.08	0.06	
0.45	0.69	0.008	0.006	0.006	0.026	0.55	1.08	1.01	0.08	0.07	
0.475N	0.75N	0.015N	0.015N	0.015N	0.22N	0.55N	1.0N	1.0N	0.12N	---	
0.47	0.90	0.010	0.007	0.007	0.30	0.55	1.0	0.92	0.10	0.026	

STEEL, Low Alloy: D6AC (Sheet 2 of 2)

Table 7

Form	Composition, Heat Treatment	Test Orientation	Temp $T_p$ (°K)	Yield Strength KSI (MN/m <sup>2</sup> )	Typical $K_{Ic}$ KSI√in (MN m <sup>3/2</sup> )	$2.5 \left( \frac{K_{Ic}}{T_p} \right)^2$ in (mm)	Specimen			Ref.
							Thickness in (mm)	Width in (mm)	Crack Length in (mm)	
	1. 1650F (1172K), 1550F (1117K), Oil Quenched 150F (339K); Temper 1 Hr + 1 Hr, 500F (533K)									
	2. 1550F (1117K) in Salt, 20 min, Oil Quench; Temper 1 Hr + 1 Hr, 500F (533K)									
	3. 1700F (1200K); Quench in Furnace to 975 ± 25F (797 ± 14K) at 6F (3.3K) per minute from 1350 to 1150F (1026 to 894K), Oil Quench 140F (334K); Temper 1000-1025F (811-823K), 1 Hr + 1 Hr									
	4. 1705F (1203K), Air Cool; 1615F (1153K), Oil Quench at 363F (457K), 1 Hr; Temper 841F (723K), 2 Hr									
	5. 1705 (1203K), Air Cool; 1615 F (1153K), Oil Quench at 363F (457K), 1 Hr; Temper 1021F (823K), 2 Hr									

## HEAT TREATMENT

STEEL, Low Alloy: EN24, Ni-Cr-Mo-V

Table 8

Form	Compo- sition, Heat Treat- ment	Test Orienta- tion	Temp °F (°K)	Yield Strength KSI (NKK/m <sup>2</sup> )	Typical K <sub>1C</sub> MSI/√in (MN √m <sup>3/2</sup> )	2.5 (K <sub>1C</sub> σ <sub>ys</sub> ) <sup>2</sup> in (mm)	Specimen			Ref.	
							Type	Thickness in (mm)	Width in (mm)		Crack Length in (mm)
<b>EN24</b>											
Ingot: 5 in (127 mm) Sq.	A, 1	L-ST	70(294)	231(1590)	64(70)	0.192 (4.9)	Bend	0.492 (12.5)	0.984 (25)	91	
	A, 2		70(294)	220(1520)	37(41)	0.071 (1.8)	Bend	0.482 (12.5)	0.984 (25)		
	A, 3		70(294)	206(1420)	75(83)	0.331 (8.4)	Bend	0.482 (12.5)	0.984 (25)		
	A, 4		70(294)	206(1420)	41(45)	0.099 (2.5)	Bend	0.482 (12.5)	0.984 (25)		
	A, 5		70(294)	186(1285)	71(78)	0.364 (9.3)	Bend	0.482 (12.5)	0.984 (25)		
	B, 6	L-T	70(294)	263(1837)	45(48)	0.074(1.9)	Bend	0.187(4.7)	0.75(19.1)	47	
	B, 7	L-T	70(294)	251(1753)	49(53)	0.096(2.4)					
	B, 8	L-T	70(294)	241(1683)	51(56)	0.112(2.8)					
	C, 9	L-T	70(294)	247(1725)	67(73)	0.185(4.7)					
	C, 10	L-T	70(294)	236(1648)	63(69)	0.180(4.6)					
<b>Ni-Cr-Mo-V</b>											
Bar: 1.0 x 0.312 in (25.4 x 7.9 mm)											
<b>COMPOSITION</b>											
	C	Mn	Si	P	S	Ni	Cr	Mo	Cu	Al	V
A	0.39	0.57	0.28	0.021	0.038	1.76	1.10	0.24	0.023	0.16	0.020
B	0.45	0.44	0.79	0.012	0.008	1.72	1.31	0.88	-	-	0.23
C	0.39	1.15	1.45	0.008	0.006	1.80	0.09	0.50	-	-	0.24
<b>HEAT TREATMENT</b>											
1. 1543K (1113K), Hold 40 Sec. Oil Quench, 7 cycles; 1596F (1133K), Hold 1 min, Oil Quench, 3 cycles; 661F (623K), 4 Hr											
2. 1561F (1123K), 1 Hr, Oil Quench; 481F (523K), 1 Hr											
3. 1561F (1123K), Hold 1 min, Oil Quench, 4 cycles; 661F (623K), 4 Hr											
4. 1561F (1123K), 1 Hr, Oil Quench; 661F (623K), 1 Hr											
5. 1561F (1123K), 1 Hr, Oil Quench, 841F (723K), 1 Hr											
6. 1690F (1193K), Oil Quench; refrigerated at -95F (203K); Tempered 481F (523K)											
7. 1690F (1193K), Oil Quench; refrigerated at -95F (203K); Tempered 571F (573K)											
8. 1690F (1193K), Oil Quench; refrigerated at -95F (203K); Tempered 661F (623K)											
9. 1561F (1123K), Oil Quenched; Temper 706F (648K)											
10. 1561F (1123K), Oil Quenched; Temper 481F (523K)											

Table 9

Form	Composition, Heat Treatment	Test Orientation	Temp $T_F$ ( $^{\circ}F$ )	Yield Strength KSI ( $10^6 N/m^2$ )	Typical $K_{IC}$ KSI $\sqrt{in}$ ( $10^6 N/m^2$ )	$2.5 \left( \frac{K_{IC}}{\sigma_{ys}} \right)^2$ in (mm)	Specimen				Ref.
							Type	Thickness in (mm)	Width in (mm)	Crack Length in (mm)	
Plate: 1.5 in (38.1 mm) Thick	A,1	T-L	-100(200)	198(1365)	132(1145)	4.11 (26.2)	Bead	1.4 (35.5)	2.8 (71.1)	1.4(35.5)	4
	A,1	T-L	-321( 78)	240(1655)	49( 54)	0.104( 2.6)	Bead	1.4 (35.5)	2.8 ( 71.1)	1.4(35.5)	
Forging: 4.5 x 4.5 in (114.3 x 114.3 mm)	B,2	L-T	70(394)	223(1535)	99(110)	0.49 (12.5)	DEC	0.50(12.7)	3.0 (76.1)	0.5(12.7)	16
	L-T	L-T	-100(200)	202(1392)	64( 69)	0.25 ( 6.4)	DEC	0.50(12.7)	3.0 (76.1)	0.5(12.7)	
Forging: 3 in (76.2 mm) Thick	C,3	T-L	150(339)	175(1186)	108(121)	0.95 (24.2)	WOL	2.0 (50.8)	5.1 (130)	1.8(45.7)	11
	T-L	T-L	70(294)	177(1220)	142(156)	1.61 (41.0)	WOL	2.0 (50.8)	2.25(57.3)	2.0(25.4)	
	T-L	T-L	70(294)	177(1220)	100(110)	0.798(20.3)	WOL	2.0 (50.8)	5.1 (130)	1.6(45.7)	
	T-L	T-L	0(255)	167(1289)	105(114)	0.788(20.0)	WOL	2.0 (50.8)	5.1 (130)	1.8(45.7)	
	T-L	T-L	-40(233)	188(1296)	111(121)	0.871(22.1)	WOL	2.0 (50.8)	5.1 (130)	1.8(45.7)	
	T-L	T-L	-75(214)	188(1296)	112(122)	0.888(22.6)	WOL	2.0 (50.8)	5.1 (130)	1.8(45.7)	

COMPOSITION

	C	Mn	Co	Mo	Cr	Ni	P	S	Si
A	0.21	8.90	4.24	0.20	0.74	0.099	0.007	0.01	
B	0.32	7.62	4.25	0.16	1.03	0.025	2.007	0.01	
C	0.26	8.41	3.9	0.33	0.40	0.028	0.708	0.01	

HEAT TREATMENT

1. Normalize 1650F (1172K), 1.5 Hr, Air Cool; Austenitize 1500F (1088K), 1.5 hr, Water Quench; Temper 1025F (552K), 6 Hr
2. 1125F (807K) 16 Hr, Air Cool; 1700F (1200K) 1 Hr, Air Cool; 1550F (1115K), 0.5 Hr, Salt Quench to 460F (232K); Hold 7 Hr.
3. 1550F (117K), 2 Hr; Double Temper, 2 Hr + 2 Hr, 1000F (511K)

Table 10

Form	Compositional Transmittance	Yield Strength (ksi)	Temp (°F)	Type of Defect	Type of Specimen	2.5 (1/4) in (6.35 mm)		Type	Specimens			
						Yield Strength (ksi)	Temp (°F)		Yield Strength (ksi)	Temp (°F)		
Plate: 0.95 in (2.4 mm) Thick	A,1	220(1510)	75(297)	L-1	CC	0.125(3.2)	75(297)	CC	0.105(2.6)	1.75(44.8)	0.17(4.3)	12
	Y-1	224(1545)	75(297)	Y-1	CC	0.124(3.2)	75(297)	CC	0.105(2.6)	1.75(44.8)	0.17(4.3)	12
	L-1	223(1540)	-100(200)	L-1	CC	0.124(3.2)	-100(200)	CC	0.105(2.6)	1.75(44.8)	0.17(4.3)	12
	L-1	220(1535)	-200(146)	L-1	CC	0.106(2.7)	-200(146)	CC	0.105(2.6)	1.75(44.8)	0.17(4.3)	12
	Y-1	235(1610)	75(297)	Y-1	Round	0.575(14.6)	75(297)	Round	0.575(14.6)	1.75(44.8)	0.17(4.3)	12
Forging: 9 x 9 x 24 in (228.6 x 228.6 x 609.6 mm)	C,3	198(1365)	70(296)	L-1	CC	0.725(18.7)	70(296)	CC	1.0(25.4)	9.0(228.6)	1.6(40.6)	12
	L-1	211(1453)	-110(196)	L-1	CC	0.172(4.3)	-110(196)	CC	1.0(25.4)	9.0(228.6)	1.6(40.6)	12
Forging: 3 x 9 x 24 in (76.2 x 228.6 x 609.6 mm)	E,4	225(1550)	70(296)	L-1	Round	0.4(10.2)	70(296)	Round	0.400(10.2)	1.5(38.1)	0.32(8.1)	12
	L-1	---	-65(219)	L-1	4 PC Round	---	-65(219)	4 PC Round	0.400(10.2)	1.5(38.1)	0.32(8.1)	12
Forging: 3 x 9 x 24 in (76.2 x 228.6 x 609.6 mm)	E,5	185(1314)	100(422)	L-1	Round	0.455(11.5)	100(422)	Round	0.400(10.2)	1.5(38.1)	0.32(8.1)	12
	L-1	225(1550)	75(297)	L-1	4 PC Round	0.372(9.4)	75(297)	4 PC Round	0.400(10.2)	1.5(38.1)	0.32(8.1)	12
Forging: 3 x 9 x 24 in (76.2 x 228.6 x 609.6 mm)	L-1	240(1655)	-65(219)	L-1	4 PC Round	0.344(8.7)	-65(219)	4 PC Round	0.400(10.2)	1.5(38.1)	0.32(8.1)	12
	Y-1	---	-65(219)	Y-1	4 PC Round	---	-65(219)	4 PC Round	0.400(10.2)	1.5(38.1)	0.32(8.1)	12
	S-1	---	-64(219)	S-1	4 PC Round	---	-64(219)	4 PC Round	0.400(10.2)	1.5(38.1)	0.32(8.1)	12
	L-1	243(1675)	-110(196)	L-1	4 PC Round	0.365(9.3)	-110(196)	4 PC Round	0.400(10.2)	1.5(38.1)	0.32(8.1)	12
	Y-1	---	---	Y-1	4 PC Round	---	---	4 PC Round	0.400(10.2)	1.5(38.1)	0.32(8.1)	12

COMPOSITION

	C	Mn	Co	Ni	Mo	Cu	V	P	S	Si
A	0.45	8.76	3.76	0.12	0.30	0.30	0.06	0.005	0.009	0.01
B	0.43	8.00	4.0	0.42	0.08	0.09	0.12	---	---	0.01
C	0.43	8.00	3.81	0.13	0.11	0.13	0.09	0.005	0.009	0.01
D	0.45	7.90	4.26	0.09	0.22	0.33	0.10	0.005	0.011	0.01
E	0.44	7.79	4.05	0.19	0.29	0.32	0.08	0.010	0.009	0.02

HEAT TREATMENT

1. 1450F (793C). 600 Quench; Temper 1 Hr @ 1 Hr. 600F (316C).
2. 1400F (760C). Air Cool; 1450F (793C) (1 Hour) @ 0.5 Hr. Soak; Soak.
3. 1400F (760C). 6 Hr. Air Cool; 1400F (760C). 1 Hr. Air Cool; 1450F (793C). 30 min.
4. Salt Quench, 450F (232C). 6 Hr. Air Cool; 1450F (793C) 1 Hr @ 1 Hr. 700F (377C).
5. 1500F (816C). 1 Hr. Soak; Quench 675F (358C) 6 Hr; 1450F (793C) (117-11720) 2 Hr. Air Cool; 1450F (793C) 30 min; 1450F (793C) 2 Hr. 400F (204C) Soak; Soak.
6. Hr. Air Cool



STEEL: 10 Nickel

Table 11

Form	Compositional Heat Treatment	Test Orientation	Temp °F	Yield Strength (ksi)	Typical $\frac{K_{IC}}$ (ksi√in)	$2.5 \left(\frac{K_{IC}}{S_y}\right)^2$ (in)	Specimens			
							Type	Thickness (in)	Width (in)	Length (in)
Plate: 0.5 in (12.7 mm) Thick	A, 1	L-1	70(204)	257(1772)	51(565)	0.28 (7.5)	Round	0.5 (12.7)	1.0 (25.4)	0.5 (12.7)
		T-1	70(204)	256(1765)	52(577)	0.105 (2.6)	Round	0.5 (12.7)	1.0 (25.4)	0.5 (12.7)
	B, 2	T-1	70(204)	256(1765)	87(973)	0.352 (8.9)	Round	0.5 (12.7)	1.0 (25.4)	0.5 (12.7)
	C, 2	T-1	70(204)	277(1975)	73(800)	0.216 (5.5)	Round	0.5 (12.7)	1.0 (25.4)	0.5 (12.7)
	D, 3	T-1	70(204)	257(1772)	77(855)	0.618 (15.7)	Round	0.5 (12.7)	1.0 (25.4)	0.5 (12.7)

COMPOSITION

	C	Mn	P	S	Si	Cr	Ni	Al	N	O	Co	
A	0.26	0.15	0.001	0.003	0.12	10.08	2.09	0.06	0.008	0.002	0.01	15.2
B	0.23	0.13	0.001	0.002	0.13	9.66	1.94	0.06	0.002	0.005	0.001	12.3
C	0.25	0.14	0.002	0.003	0.11	10.10	1.99	1.01	0.004	0.002	0.003	14.6
D	0.25	0.11	0.001	0.003	0.12	16.0	1.57	0.79	0.004	0.003	0.002	12.6

HEAT TREATMENT

- 1650F (1172K), 1 Hr, Water Quenched; 1500F (1093K), 1 Hr., Water Quench; Temper 950F (783K), 1 Hr Water Quench
- Heat to 1050F (839K), Hold, Heat to 1550F (1117K), Hold, Water Quench, Repeat Cycle 4 Times, Temper 950F (783K), 5 Hr
- Heat to 1120F (879K), Hold 6 Sec, Heat to 1650F (1062K), Hold 8 Sec, Water Quench, Repeat Cycle 4 Times, Temper 400F (478K), 5 Hr

Table 12

Form	Composition, Heat Treatment	Test Orientation	Temp °F (°K)	Yield Strength KSI (MPa)	Typical $K_{IC}$ KSI√in (MPa√m)	$2.5 \left( \frac{K_{IC}}{Y} \right)^2$ in (mm)	Specimens			Ref.	
							Type	Thickness in (mm)	Width in (mm)		Crack Length in (mm)
Plate: 1 in (25.4 mm) Thick	A,1	L-T	70(294)	271(1179)	100(110)	0.86 (21.8)	SEM	1 (25.4)	4.5 (114.3)	1.6 (40.7)	21
	B,1	T-L	70(294)	185(1276)	120(132)	1.175 (29.9)	SEM	1 (25.4)	4.5 (114.3)	1.6 (40.7)	
Plate: 2 in (50.8 mm) Thick	C,1	L-T	20(294)	175(1207)	125(136)	1.28 (32.5)	Beam	2 (50.8)	5.95 (151)	1.6 (40.7)	85
	D,2	-	70(294)	186(1282)	147(162)	1.56 (39.6)	Beam	2 (50.8)	2 (50.8)	-	85

COMPOSITION

	C	Mn	P	S	Si	Ni	Cr	Mo	Ti	Al
A	0.033	0.08	0.007	0.005	0.07	12.5	4.81	3.55	0.21	0.16
B	0.033	0.08	0.007	0.005	0.07	12.5	4.71	3.65	0.21	0.16
C	0.23	0.068	0.004	0.008	0.094	12.1	5.21	2.86	0.24	-
D	0.24	0.044	0.007	0.013	0.042	11.72	5.58	3.18	0.30	0.47

HEAT TREATMENT

- 1500F (820K); Temper 900F (756K), 3 Hr
- 1500F (820K); Temper 900F (756K), 30 Hr

STEEL: 18Ni: Maraging: 200 Grade

Table 13

Form	Composition, Heat Treatment	Test Orientation	Temp °F (°K)	Yield Strength KSI (MN/m <sup>2</sup> )	Typical $K_{IC}$ KSI√in (MN m <sup>3/2</sup> )	$2.5 \left( \frac{K_{IC}}{\sigma_{ys}} \right)^2$ in (mm)	Specimen			Ref.	
							Type	Thickness in (mm)	Width in (mm)		Crack Length in (mm)
Plate: 1 in (25.4 mm) Thick	A,1	L-T	-321(18)	241(1662)	115(127)	0.569 (14.5)	Bend	1.0 (25.4)	3.0 (76.2)	1.6 (40.6)	10
Plate: 2 in (50.8 mm) Thick	-2	L-T	75(297)	187(1289)	152(167)	1.65 (42.0)	Bend	2.0 (50.8)	4.0 (101.6)	1.5 (38.1)	85
Plate: 2 in (50.8 mm) Thick	-3	L-S	70(294)	197(1356)	104(114)	0.697 (17.7)	(a)	---	---	---	71
		L-T	70(294)	192(1324)	100(110)	0.687 (17.2)	(a)	---	---	---	
		T-S	70(294)	194(1334)	78(86)	0.404 (10.3)	(a)	---	---	---	
		T-L	70(294)	195(1347)	75(83)	0.370 (9.4)	(a)	---	---	---	
		S-L	70(294)	198(1365)	70(75)	0.312 (7.9)	(a)	---	---	---	
Plate: 2.13 in (54mm) Thick	B,4	T-L	75(297)	206(1420)	170(187)	1.7 (43.2)	Bend	2.0 (50.8)	4.0(101.6)	2.0(50.8)	
		T-L	-100(200)	229(1580)	164(179)	1.28 (32.5)	Bend	2.0 (50.8)	4.0(101.6)	2.0(50.8)	
		T-L	-321(78)	271(1870)	79(87)	0.21 (5.3)	Bend	2.0 (50.8)	4.0(101.6)	2.0(50.8)	
Plate: 4.25 in (108 mm) Thick Con.El. Vac Remelt, Hot Rolled at 2300F (1553K)	C,5	L-T	75(297)	234(1613)	92(101)	0.386 (9.8)	Bend	3.94 (100)	7.89(200)	4.0 (102)	78
	C,6	L-T	75(297)	211(1455)	103(113)	0.596 (15.1)	CT	3.94 (100)	6.31(160)	3.22 (81.8)	
	C,7	L-T	75(297)	190(1310)	129(142)	1.152 (2.93)	Bend	3.94 (100)	7.87(200)	3.92 (99.6)	
	C,8	L-T	75(297)	174(1200)	180(198)	2.675 (68.0)	Bend	3.93 (100)	7.86(200)	3.98 (101)	
	C,9	L-T	75(297)	166(1145)	187(206)	3.173 (80.6)	CT	3.93 (100)	6.31(160)	3.20 (81.3)	

HEAT TREATMENT

- 1500F (1089K), 93 Min, Water Cooled; 1160F (899K), 93 Min, Water Quench
- 1500F (1089K), Aged 900F (756K), 3 Hr
- Aged 895F (753K), 3 Hr
- 1650F (1172K), 2 Hr, Air Cool; 1450F (1060K), 2 Hr, Air Cool:
- Aged 900F (756K), 2 Hr
- 1650F (1172K), 4.5 Hr, Air Cool; 850F (728K), 100 Hr
- 1650F (1172K), 4.5 Hr, Air Cool; 1000F (811K), 6 Hr
- 1650F (1172K), 4.5 Hr, Air Cool; 1050F (839K), 6 Hr
- 1650F (1172K), 4.5 Hr, Air Cool; 1100F (867K), 6 Hr
- 1650F (1172K), 4.5 Hr, Air Cool; 1100F (867K), 24 Hr

(a) Specimen in accordance with ASTM Recommendations

COMPOSITION

	C	Mn	P	S	Si	Ni	Co	Mo	Ti	Al	Cr
A	0.003	0.02	0.003	0.007	0.005	17.90	7.73	2.96	0.20	-	-
B	0.005	0.03	0.005	0.008	0.02	18.40	8.50	3.34	0.20	0.07	0.10
C	0.02	0.07	0.001	0.009	0.08	17.78	7.07	4.46	0.185	-	-

STEEL, 18 Ni Maraging: (250 Grade), DTD 5212, G100, G110, Marvel 18 (Sheet 1 of 3) Table 14

Form	Composition, Heat Treatment	Test Orientation	Temp °F (°C)	Yield Strength KSI (N/m <sup>2</sup> )	Typical $K_{IC}$ KSI√in (MN m <sup>3/2</sup> )	$2.5 \left( \frac{K_{IC}}{\sigma_{ys}} \right)^2$ in (mm)	Specimen			Ref.	
							Type	Thickness in (mm)	Width in (mm)		Crack Length in (mm)
<b>250 Grade</b>											
Plate: 1 in (25.4 mm) Thick	A,1	L-T	70(294)	259(1786)	68(74)	0.172(4.3)	Bend	0.250( 6.4)	2.0 (50.8)	---	14
Rolled to 2 in (50.8 mm) thickness from Press Forged Slab	B,2	L-T	70(294)	227(1565)	96(105)	0.447(11.3)	Bend	1.8 (45.7)	3.75(95.3)	---	15
	B,2	L-T		232(1600)	85( 93)	0.336( 8.5)	Bend	1.8 (45.7)	3.75(95.3)	---	
	B,3	L-T		259(1786)	84( 92)	0.263( 6.7)	Bend	1.8 (45.7)	3.75(95.3)	---	
	B,4	L-T		259(1786)	80( 87)	0.239( 6.1)	Bend	1.8 (45.7)	3.75(95.3)	---	
Forging: 3 in (76.2 mm) Thick	C,5	T-L	70(294)	243(1675)	99(108)	0.415(10.5)	Bend 4 pt	0.480(12.2)	1.5 (38.1)	0.3 ( 7.6)	3
	T-L		-65(219)	---	90( 98)	---	Bend 4 pt	0.480(12.2)	1.5 (38.1)	0.3 ( 7.6)	
Plate: 1 in (25.4 mm) Thick	D,6	-	70(294)	246(1696)	105(114)	0.455(11.6)	Bend	1.00 (25.4)	3.0 (76.2)	---	10
	-		0(255)	250(1724)	72( 78)	0.207( 5.3)	Bend	1.00 (25.4)	3.0 (76.2)	---	
	-		-100(200)	300(2068)	75( 82)	0.156( 4.0)	Bend	1.00 (25.4)	3.0 (76.2)	---	
	-		-200(144)	260(1834)	52( 57)	0.100( 2.5)	Bend	1.00 (25.4)	3.0 (76.2)	---	
	-		-385( 75)	230(1586)	40( 44)	0.075( 1.9)	Bend	1.00 (25.4)	3.0 (76.2)	---	
Forging: 4.5 x 4.5 in (114.3 x 114.3 mm) Vacuum Arc Remelt	E,7	L-T	-110(194)	273(1882)	86( 94)	0.248( 6.3)	SEN	0.250( 6.4)	1.0 (25.4)	0.500(12.7)	16
	T-L		-110(194)	272(1875)	80( 87)	0.216( 5.6)	SEN	0.250( 6.4)	1.0 (25.4)	0.500(12.7)	
Forging: 13 x 13 in (330.2 x 330.2 mm) Vacuum Arc Remelted	E,7	L-S	-110(194)	259(1786)	82(89)	0.251(6.4)	SEN	0.250( 6.4)	1.0(25.4)	1.500(12.7)	16
	TL		-110(194)	260(1793)	80(87)	0.237(6.0)	SEN	0.250( 6.4)	1.0(25.4)	0.500(12.7)	
	S-T		-110(194)	262(1806)	82(89)	0.245(6.2)	SEN	0.250( 6.4)	1.0(25.4)	0.500(12.7)	
	ST4-ST4		-110(194)	262(1806)	72(78)	0.189(4.8)	SEN	0.250( 6.4)	1.0(25.4)	0.500(12.7)	

STEEL: 18 Ni Maraging (250 Grade), DTD 5212, G100, G110, Marval 18 (Sheet 2 of 3) Table 14

Form	Composition, Heat Treatment	Test Orientation	Temp °F (°K)	Yield Strength KSI (N/mm <sup>2</sup> )	Typical $K_{IC}$ KSI/√in (MN m <sup>-3/2</sup> )	$2.5 \left( \frac{K_{IC}}{\sigma_{ys}} \right)^2$ in (mm)	Specimen			Ref.	
							Type	Thickness in (mm)	Width in (mm)		Crack Length in (mm)
Plate: 1.5 x 25 in (38.1 x 330.2 mm)		LS	-110(194)	262(1806)	83(90)	0.251(6.4)	SEN	0.250( 6.4)	1.0(25.4)	0.500(12.7)	16
		TL	-110(194)	267(1841)	73(80)	0.187(4.7)	SEN	0.250( 6.4)	1.0(25.4)	0.500(12.7)	
		ST	-110(194)	267(1841)	69(75)	0.167(4.2)	CT	0.500(12.7)	1.0(25.4)	0.500(12.7)	
Plate: 0.5 in (12.7 mm) Thick		TL	-110(194)	264(1820)	84(92)	0.253(6.4)	SEN	0.250( 6.4)	1.0(25.4)	0.500(12.7)	
<b>DTD 5212</b>											
Forged Plate: 2.5 in (63.5 mm) Thick	F, 8	L-T	70(294)	246(1696)	91(100)	0.342(8.7)	(a)	---	---	---	65
<b>G100</b>											
Forged Bar: 5 in (127 mm) Thick	H, 11	T-S	70(294)	204(1407)	88(97)	0.465 (11.8)	(a)	---	---	---	69
	H, 12	T-S	20(294)	225(1551)	82(90)	0.332 (8.4)	(a)	---	---	---	
	H, 13	T-S	70(294)	248(1706)	83(92)	0.280 (7.1)	(a)	---	---	---	
<b>G110</b>											
Bar: 4.9 in (125 mm) Thick, Vac. Melted	G, 9	L-ST	70(294)	*262(*1806)	92(101)	---	(a)	---	---	---	70
	G, 9	ST-L	70(294)	*260(*1793)	85(93)	---	(a)	---	---	---	
Bar: 8 in (203) Sq Double Vac. Melted	G, 9	ST-L	70(294)	*266(1834)	82(90)	---	(a)	---	---	---	
Plate:	G, 9	---	70(294)	235(1620)	80(88)	0.290 (7.4)	Bond	0.715(18.2)	1.0(25.4)	0.47 (11.9)	57
<b>Marval 18</b>											
	---	T-S	70(294)	245(1689)	100(110)	0.416 (10.6)	Bond	0.5 (12.7)	1.0 (25.4)	---	60

(a) Specimen in accordance with ASTM Recommendations

\* Tensile Ultimate Values

Form	C	Mn	Si	P	S	Ni	Mo	Co	Yield Strength KSI (MN/m <sup>2</sup> )	Typical K <sub>IC</sub> KSI√in (MN m <sup>3/2</sup> )	2.5 (K <sub>IC</sub> <sup>2</sup> / σ <sub>ys</sub> ) <sup>2</sup> in (mm)	Specimen			Ref.		
												Thickness in (mm)	Width in (mm)	Crack Length in (mm)			
Composition	Temp °F (°K)	Test Orienta- tion	Temp °F (°K)		Yield Strength KSI (MN/m <sup>2</sup> )		Typical K <sub>IC</sub> KSI√in (MN m <sup>3/2</sup> )		2.5 (K <sub>IC</sub> <sup>2</sup> / σ <sub>ys</sub> ) <sup>2</sup> in (mm)		Type	Thickness in (mm)	Width in (mm)	Crack Length in (mm)	Ref.		
A	.020	0.05	0.09	0.006	0.005	18.35	5.32	7.18	0.04	0.32	-	-	-	-	-	-	-
B	0.006	0.06	0.01	0.006	0.007	18.47	4.81	7.40	0.11	0.40	0.002	0.01	0.05	-	-	-	-
C	0.030	0.10	0.10	0.005	0.008	18.05	5.08	7.66	0.15	0.40	-	-	-	-	-	-	-
D	0.003	0.002	0.003	0.002	0.004	17.1	4.65	7.60	-	0.50	-	-	-	-	-	-	-
E	0.020	0.05	0.03	0.003	0.003	18.20	4.71	7.38	0.14	0.42	0.003	0.016	0.05	-	-	-	-
F	0.015	0.04	0.01	0.01	0.01	18.0	4.5	7.75	0.10	0.45	-	-	-	-	-	-	-
G	0.01	0.05	0.05	0.005	0.005	17.5	4.85	8.0	0.1	0.5	-	-	-	-	-	-	-
H	0.003	0.05	0.05	0.005	0.004	18.3	4.72	7.64	0.119	0.8	-	-	-	-	-	-	-

COMPOSITION

HEAT TREATMENT

1. Mill Anneal; 900F (756K) 3 Hr
2. 1500F (1089K), Air Cool; Aged 800F (700K) 6 Hrs
3. 1500F (1089K), Air Cool; Aged 1000F (811K) 6 Hrs
4. 1500F (1089K), Air Cool; Aged 900F (756K) 6 Hrs
5. 1500F (1089K), Air Cool; Aged 900F (756K) 24 Hrs
6. 1650F (1172K), 1 Hr, Water Quench; 1525F (1103K) 1 Hr, Water Quench; Aged 900F (750K) 5 Hr, Water Quench
7. 1500F (1089K), Air Cool; Aged 950F (783K) 3 Hr, Air Cool
8. 1489-1525F (1083-1103K), Air Cool; 904F (758K), 3 Hr, Air Cool
9. 1507F (1093K), Air Cool; 895F (753K), 3 Hr, Air Cool
10. 1507F (1093K), Aged 913F (763K)
11. 1471-1650F (1073-1173K), Air Cool; 796F (698K), 1.5 Hr
12. 1471-1650F (1073-1173K), Air Cool; 895F (753K), 1.25 Hr
13. 1471-1650F (1073-1173K), Air Cool; 895F (753K), 2.5 Hr

STEEL, 18 Ni Maraging: 300 Grade and G125

Table 15

Form	Composition, Heat Treatment	Test Orientation	Temp °F	Yield Strength KSI (MN/m <sup>2</sup> )	Typical K <sub>IC</sub> KSI√in (MN m <sup>-3/2</sup> )	2.5 (K <sub>IC</sub> <sup>2</sup> /σ <sub>ys</sub> ) in (mm)	Specimen			Ref.					
							Type	Thickness in (mm)	Width in (mm)		Crack Length in (mm)				
<b>300 Grade</b>															
Plate: 0.5 in (2.7 mm) Thick	A,1	T-L	600(589)	236(1627)	80(87)	0.287 (7.3)	CC	0.25 (6.4)	3.0 (76.2)	1.0 (25.4)	53				
		T-L	70(294)	280(1931)	68(74)	0.147 (3.7)	CC	0.25 (6.4)	3.0 (76.2)	1.0 (25.4)					
		T-L	-100(200)	305(2103)	42(46)	0.047 (1.2)	CC	0.25 (6.4)	3.0 (76.2)	1.0 (25.4)					
Plate: 1 in (25.4 mm) Thick	B,2	L-ST	70(294)	285(1965)	52(57)	0.083 (2.1)	Bend	0.25(6.4)	1.0 (25.4)	—	14				
		L-T	70(2 94)	299(2062)	68(75)	0.129 (3.3)	Bend	0.5(12.7)	1.0 (25.4)	0.5 (12.7)	59				
Forging: 8 in (203) Dia Con. Elec. Vac. Reheat	C,3	T-L	70(294)	300(2068)	68(75)	0.128 (3.3)	Bend	0.5(12.7)	1.0 (25.4)	0.5 (12.7)					
		T-L	-65(219)	---	54(59)	---	Bend	0.5(12.7)	1.0 (25.4)	0.5 (12.7)					
		L-T	70(294)	280(1931)	83(91)	0.326 (8.3)	Bend	0.5(12.5)	1.0 (25.4)	0.5 (12.7)					
		T-L	70(294)	280(1931)	77(85)	0.189 (4.8)	Bend	0.5(12.5)	1.0 (25.4)	0.5 (12.7)					
<b>G125</b>															
Plate: 0.75 in (19 mm) Thick	E,4	L-T	70(294)	*296(2020)*	63(69)	---	(a)	---	---	---	70				
		T-L	70(294)	*296(2020)*	60(66)	---	(a)	---	---	---	40				
<b>COMPOSITION</b>															
	C	Mn	Si	P	S	Ni	Mo	Co	Al	Ti	B	Zr	Cr	Cu	* Tensile Ultimate Values
A	0.03	0.06	0.07	0.003	0.007	18.00	4.77	9.16	0.12	0.70	0.005	0.01	-	-	
B	0.03	0.021	0.06	0.003	0.010	18.53	4.64	8.89	0.15	0.69	-	-	-	-	
C	0.003	0.002	0.01	0.002	0.004	18.51	4.84	9.11	0.15	0.84	0.002	0.011	0.002	0.01	
D	0.014	0.05	0.02	0.004	0.004	18.25	4.79	8.87	0.10	0.60	0.004	0.010	-	-	
E	0.01	0.05	0.05	0.005	0.005	18.5	4.85	9.00	0.10	0.75	-	-	-	-	
<b>HEAT TREATMENT</b>															
1. 1650F (1172K), 1 Hr, Air Cool; Age 850F (728K), 3 Hr															
2. 1500F (1089K), Age 900F (756K), 3 Hr															
3. Double Anneal, 1700F (1200K), 1 Hr, Fan Cool to 200F (367K), 1500F (1089K), 1 Hr, Fan Cool to 200F (367K), Aged 900F (756K), 6 Hr															
4. 1507F (1093K), Air Cool; 895F (753K), 3 Hr, Air Cool															

STEEL, 18Ni: Maraging: 350 Grade

Table 16

Form	Composition, Heat Treatment	Test Orientation	Temp °F (°K)	Yield Strength KSI (MN/m <sup>2</sup> )	Typical $K_{IC}$ KSI√in (MN m <sup>-3/2</sup> )	$2.5 \left( \frac{K_{IC}}{\sigma_{ys}} \right)^2$ in (mm)	Specimen			Ref.	
							Type	Thickness in (mm)	Width in (mm)		Crack Length in (mm)
Billet: 4 in (102mm) Sq. Cons. Elec. Vac. Remelt	A, 1	S-T	70(294)	338(2330)	37(40)	0.030 (0.8)	Bend	0.394(10)	0.394 (10)	0.15 (3.8)	17
		S-L	70(294)	---	37(40)	---	Bend	0.394(10)	0.394 (10)	0.15 (3.8)	
		L-S	70(294)	334(2302)	36(39)	0.029 (0.7)	Bend	0.394(10)	0.394 (10)	0.15 (3.8)	

COMPOSITION

C	Mn	Si	P	S	Ni	Mo	Co	Al	Ti	B	Zr	
A	0.005	0.01	0.010	0.002	0.005	18.61	4.64	11.93	0.13	1.36	0.001	0.01

HEAT TREATMENT

1. Double Anneal, 1700F (1200K), 1 Hr; 1500F (1089K), 1 Hr; Aged 900F (750K), 8 Hr



STAINLESS STEEL: 17-4 PH

Table 17

Form	Composition, Heat Treatment	Test Orientation	Temp $\sigma_f$ ( $^{\circ}$ F)	Yield Strength KSI ( $\text{MN}/\text{m}^2$ )	Typical $K_{IC}$ KSI $\sqrt{\text{in}}$ ( $\text{MN m}^{3/2}$ )	$2.5 \left( \frac{K_{IC}}{\sigma_y} \right)^2$ in (mm)	Specimen			Ref.
							Type	Thickness in (mm)	Width in (mm)	
Plate: 0.5 in (12.7 mm) Thick	B,1	L-T	200(367)	161(1110)	81(88)	0.633(16.1)	Bend 0.510(13)	1.0 (25.4)	---	7
	A,1	L-T	70(294)	168(1158)	46(50)	0.187( 4.7)	Bend 0.510(13)	1.0 (25.4)	---	
	A,1	T-L	70(294)	---	36(40)	---	Bend 0.510(13)	1.0 (25.4)	---	
	B,1	L-T	70(294)	170(1172)	37(41)	0.118( 3.0)	Bend 0.510(13)	1.0. (25.4)	---	
	B,1	T-L	70(294)	---	40(44)	---	Bend 0.510(13)	1.0 (25.4)	---	
	B,1	L-T	-50(228)	189(1303)	28(31)	0.055( 1.4)	Bend 0.510(13)	1.0 (25.4)	---	
	A,1	L-T	-50(228)	183(1262)	29(32)	0.063( 1.6)	Bend 0.510(13)	1.0 (25.4)	---	
	A,1	L-T	-100(200)	190(1310)	23(25)	0.057( 1.0)	Bend 0.510(13)	1.0 (25.4)	---	
	B,1	L-T	-100(200)	195(1344)	27(29)	0.048( 1.2)	Bend 0.510(13)	1.0 (25.4)	---	
Bar, 1/2 in (12.7 mm) Thick	C,1	L-T	70(294)	209(1441)	52(57)	0.177( 4.5)	Bend 0.635(16.1)	0.635(16.1)	---	
<b>COMPOSITION</b>										
	<u>C</u>	<u>Mn</u>	<u>P</u>	<u>S</u>	<u>Si</u>	<u>Cr</u>	<u>Ni</u>	<u>Co</u>	<u>Ta</u>	<u>Cb</u>
A	0.036	0.24	0.018	0.016	0.58	15.8	4.31	3.46	0.02	0.21
B	0.037	0.28	0.019	0.013	0.60	15.7	4.37	3.29	0.01	0.21
C	0.038	0.22	0.018	0.018	0.64	15.7	4.27	3.46	0.01	0.21
<b>HEAT TREATMENT</b>										
1. 1400F, (1033K) 1 1/2 Hr; Cool to 55F (286K), Age 900F (756K) 1 Hr										

STAINLESS STEEL: 17-7 PH

Table 18

Form	Composition, Heat Treatment	Test Orientation	Temp °F (°K)	Yield Strength KSI (MN/m <sup>2</sup> )	Typical $K_{IC}$ KSI√in (MN m <sup>3/2</sup> )	$2.5 \left( \frac{K_{IC}}{\sigma_{ys}} \right)^2$ in (mm)	Specimen			Ref.
							Type	Thickness in (mm)	Width in (mm)	
Plate: 0.5 in (12.7 mm) Thick	A <sub>1</sub>	L-T	75(297)	164(1131)	66(72)	0.405(10.3)	Bend 0.5 (12.7) 1.0 (25.4) 0.374(9.5)	4 pt	7	
	A <sub>1</sub>	T-L	75(297)	153(1055)	64(70)	0.436(11.1)	Bend 0.5 (12.7) 1.0 (25.4) 0.203(1.9)	4 pt		
	B <sub>2</sub>	L-T	75(297)	183(1262)	63(69)	0.295( 7.5)	Bend 0.5 (12.7) 1.0 (25.4) 0.269(6.8)	4 pt		
	C <sub>2</sub>	L-T	75(297)	176(1212)	67(74)	0.363( 9.2)	Bend 0.5 (12.7) 1.0 (25.4) 0.236(6.0)	4 pt		
	A <sub>1</sub>	L-T	-50(228)	178(1227)	43(47)	0.146( 3.7)	Bend 0.5 (12.7) 1.0 (25.4) 0.260(6.6)	4 pt		
	C <sub>1</sub>	L-T	-50(228)	155(1069)	51(56)	0.271( 6.9)	Bend 0.5 (12.7) 1.0 (25.4) 0.223(5.7)	4 pt		
	D <sub>1</sub>	L-T	-50(228)	179(1234)	45(99)	0.159( 4.0)	Bend 0.5 (12.7) 1.0 (25.4) 0.252(6.4)	4 pt		
	A <sub>1</sub>	L-T	-100(200)	180(1241)	43(47)	0.143( 3.6)	Bend 0.5 (12.7) 1.0 (25.4) 0.206(5.2)	4 pt		
	C <sub>1</sub>	L-T	-100(200)	180(1241)	47(52)	0.170( 4.3)	Bend 0.5 (12.7) 1.0 (25.4) 0.211(5.4)	4 pt		
	D <sub>1</sub>	L-T	-100(200)	190(1310)	45(49)	0.141( 3.6)	Bend 0.5 (12.7) 1.0 (25.4) 0.234(5.9)	4 pt		
	E <sub>2</sub>	L-T	75(297)	164(1130)	56(61)	0.291( 7.4)	Bend 0.223(5.7) 1.0 (25.4) 0.246(6.2)	4 pt		
	E <sub>2</sub>	L-T	-50(228)	168(1158)	38(42)	0.128( 3.3)	Bend 0.223(5.7) 1.0 (25.4) 0.242(6.1)	4 pt		
	E <sub>2</sub>	L-T	-100(200)	175(1207)	32(35)	0.084( 2.1)	Bend 0.223(5.7) 1.0 (25.4) 0.252(6.4)	4 pt		
	F <sub>2</sub>	L-T	-100(200)	186(1283)	47(52)	0.159( 4.0)	Bend 0.197(5.0) 0.910(23.1) 0.263(6.7)	4 pt		
G <sub>2</sub>	L-T	-100(200)	168(1158)	49(54)	0.212( 5.4)	Bend 0.202(5.1) 0.930(23.6) 0.216(5.5)	4 pt			
H <sub>2</sub>	L-T	75(297)	206(1420)	69(76)	0.294( 7.5)	Bend 0.610(15.5) 0.616(16.6) 0.153(6.0)	4 pt			
Plate: 0.188 in (4.8 mm) Thick										
Bar: 1 in (25.4 mm) Thick										
COMPOSITION										
A	0.060	16.9	6.85	1.50	0.75	0.26	0.011	0.013		
B	0.060	16.9	7.85	1.39	0.75	0.26	0.011	0.013		
C	0.078	16.9	7.38	1.36	0.62	0.25	0.023	0.008		
D	0.076	17.0	7.17	1.22	0.66	0.32	0.019	0.007		
E	0.073	16.7	7.20	1.05	0.72	0.43	0.028	0.005		
F	0.069	17.2	7.29	1.08	0.63	0.36	0.017	0.012		
G	0.077	16.7	6.96	1.11	0.78	0.50	0.032	0.013		
H	0.072	17.3	7.19	0.90	0.68	0.54	0.028	0.005		
HEAT TREATMENT										
1. 1400F (1033K), 1.5 Hr; Cool to 555F (564K); Age 1050F (839K), 1.5 Hr										
2. 1750F (1228K), 10 min; Cool to -110F (194K); 8 Hr; Age 950F (783K), 1 Hr										

STAINLESS STEEL: PH 15-7 Mo

Table 19

Form	Composition, Heat Treatment	Test Orientation	Temp °F (°C)	Yield Strength KSI (N/mm <sup>2</sup> )	Typical $K_{IC}$ KSI√in (MPa m <sup>1/2</sup> )	$2.5 \left( \frac{K_{IC}}{\sigma_{YS}} \right)^2$ in (mm)	Specimen			Ref.	
							Type	Thickness in (mm)	Width in (mm)		Crack Length in (mm)
Plate: 0.5 in (12.7 mm) Thick	A,1	L-T	+200(367)	196(1351)	88( 96)	0.504(12.8)	Bend 4 pt	0.520(13.2)	1.0(25.4)	0.300(7.6)	7
	B,1	L-T	+200(367)	191(1337)	65( 71)	0.290( 7.4)	Bend 4 pt	0.520(13.2)	1.0(25.4)	0.347(8.8)	
	A,1	L-T	70(294)	207(1427)	45( 49)	0.118( 3.0)	Bend 4 pt	0.520(13.2)	1.0(25.4)	0.257(6.5)	
	B,1	L-T	70(294)	203(1400)	50( 55)	0.152( 3.9)	Bend 4 pt	0.520(13.2)	1.0(25.4)	0.276(7.0)	
	A,2	L-T	70(294)	195(1344)	76( 83)	0.569(14.4)	Bend 4 pt	0.510(13.0)	1.0(25.4)	0.238(6.0)	
	A,2	L-T	70(294)	185(1262)	74( 81)	0.409(10.4)	Bend 4 pt	0.510(13.0)	1.0(25.4)	0.287(7.3)	
	A,2	L-T	-50(228)	203(1400)	53( 58)	0.170( 4.3)	Bend 4 pt	0.510(13.0)	1.0(25.4)	0.381(9.7)	
	A,1	L-T	-50(228)	218(1503)	28( 31)	0.041( 1.0)	Bend 4 pt	0.510(13.0)	1.0(25.4)	0.160(4.1)	
	B,2	L-T	-50(228)	184(1250)	46( 50)	0.625(15.9)	Bend 4 pt	0.510(13.0)	1.0(25.4)	0.269(6.8)	
	B,1	L-T	-100(200)	232(1600)	29( 32)	0.039( 1.0)	Bend 4 pt	0.510(13.0)	1.0(25.4)	0.300(7.6)	
	B,2	L-T	-100(200)	203(1400)	46( 50)	0.13 ( 3.3)	Bend 4 pt	0.510(13.0)	1.0(25.4)	0.282(7.2)	
	A,2	L-T	-100(200)	200(1379)	47( 51)	0.138( 3.5)	Bend 4 pt	0.510(13.0)	1.0(25.4)	0.281(7.2)	
Bar: 1 in (25.4 mm) Thick	C,3	L-T	75(297)	173(1193)	53( 58)	0.236(6.0)	Bend 4 pt	0.750(19.1)	0.750(19.1)	0.3 ( 7.6)	
	D,3	L-T	75(297)	178(1228)	50( 55)	0.197(5.0)	Bend 4 pt	0.750(19.1)	0.750(19.1)	0.236(6.0)	

COMPOSITION:

	C	Cr	Mn	Al	Mn	Si	P	S
A	0.070	15.3	7.71	2.30	1.28	0.61	0.012	0.009
B	0.070	15.1	7.31	2.37	1.19	0.52	0.018	0.012
C	0.055	14.5	7.33	2.16	1.15	0.75	0.018	0.016
D	0.060	14.6	7.43	2.21	1.22	0.74	0.015	0.013

HEAT TREATMENT:

1. 1400F (1033K) 1.5 Hr; Cool to 55F (286K); Age to 1050F (839K), 1 Hr
2. 1400F (1033K) 1.5 Hr; Cool to 55F (286K); Age to 1130F (883K), 1.5 Hr
3. 1400F (1033K) 1.5 Hr; Cool to 55F (286K); Age to 1080F (856K), 1.5 Hr

STAINLESS STEEL: PH13-8 MO and FV 520B

Table 20

Form	Composition, Heat Treatment	Test Orientation	Temp °F (°K)	Yield Strength KSI (MN/m <sup>2</sup> )	Typical K <sub>IC</sub> KSI√in (MN m <sup>-3/2</sup> )	2.5 (K <sub>IC</sub> /σ <sub>ys</sub> ) <sup>2</sup> in (mm)	Specimen			Ref.	
							Type	Thickness in (mm)	Width in (mm)		Crack Length in (mm)
PH13-8MO Forging: 4.5 x 4.5 in (114.3 x 114.3 mm) Double Vacuum Melted	A, 1	L-T	70 (294)	206 (1420)	92 (100)	0.500 (12.7)	DEC	0.500 (12.7)	3.0 (76.2)	0.500 (12.7)	16
		L-T	-110 (194)	229 (1579)	43 (47)	0.088 ( 2.2)	SEN	0.250 (6.4)	1.0 (25.4)	0.500 (12.7)	
		T-L	-110 (194)	227 (1565)	41 (45)	0.081 ( 2.1)	SEN	0.250 (6.4)	1.0 (25.4)	0.500 (12.7)	
		L-T	-110 (194)	224 (1544)	53 (58)	0.146 ( 3.7)	SEN	0.250 (6.4)	1.0 (25.4)	0.500 (12.7)	
		T-L	-110 (194)	218 (1503)	57 (62)	0.171 ( 4.3)	SEN	0.250 (6.4)	1.0 (25.4)	0.500 (12.7)	
		L-T	-110 (194)	219 (1510)	47 (51)	0.115 ( 2.9)	SEN	0.250 (6.4)	1.0 (25.4)	0.500 (12.7)	
		T-L	-110 (194)	226 (1558)	47 (51)	0.108 ( 2.7)	SEN	0.250 (6.4)	1.0 (25.4)	0.500 (12.7)	
		L-TS	70 (294)	205 (1412)	89 (98)	0.468 (11.9)	CN	1.0 (25.4)	8.6 (21.8)	---	50
		L-TS	-110 (194)	219 (1510)	42 (46)	0.092 ( 2.3)	CN	1.0 (25.4)	8.6 (21.8)	---	
		FV520B Bar: 6 in (152 mm) Dia	C, 2	L-R	70 (294)	170 (1172)	119 (131)	1.225 (31.1)	(a)	---	---

(a) Specimen in accordance with ASTM Recommendations

COMPOSITION

	C	Si	Mn	S	P	Mo	Ni	Cr	Al	Cu	Nb
A	0.042	0.02	0.02	0.004	0.003	2.06	8.07	12.58	1.11	-	-
B	0.043	0.31	0.10	0.004	0.003	2.14	8.40	12.72	0.96	-	-
C	0.07N	0.64	1.0N	0.025N	0.035N	1.6N	5.4N	13.7N	-	1.6N	0.35N

HEAT TREATMENT

- 1700F (1200K) 1 Hr, Air Cool; Refrigerated at -110F (194K), 16 Hrs; Aged 1000F (511K), 4 Hr, Air Cool
- 1921F (1323K); 1561F (1123K); 841F (723K), 3 Hr.

STAINLESS STEEL: AM355 and AFC-77

Table 21

Form	AM355	Composition, Heat Treatment	Test Orientation	Temp °F (°K)	Yield Strength KSI (MN/m <sup>2</sup> )	Typical K <sub>IC</sub> KSI√in (MN m <sup>3/2</sup> )	2.5 (K <sub>IC</sub> /σ <sub>YS</sub> ) <sup>2</sup> in (mm)	Specimen			Ref.
								Type	Thickness in (mm)	Width in (mm)	
Plate: 0.5 in (12.7 mm) Thick	A,1	L-T	-50(228)	178(1227)	80(88)	0.505 (12.8)	Bend 0.775(19.7)	0.793(20.1)	0.22 (5.6)	7	
Plate: 0.625 in (15.9 mm) Thick	A,2	L-T	-100(200)	180(1241)	54(59)	0.225 (5.7)	Bend 0.775(19.7)	0.793(20.1)	0.22 (5.6)		
Forging: 9x9 in (230 x 230 mm)	B,3	L-T	70(294)	201(1366)	74(81)	0.359 (8.6)	Bend 0.625(15.9)	1.0 (25.4)	---	58	
		L-T	70(294)	167(1151)	63(69)	0.356 (9.0)	CC 1.0 (25.4)	9.0 (229)	1.5 (38.1)		
		L-T	-110(193)	203(1400)	24(70)	0.35 (8.9)	CC 0.575(9.5)	6.0 (152)	0.5 (12.7)		
AFC-77											
Bar: 3 in (76.2 mm) Dia Air Melted	C,4	T-L	70(294)	192(1324)	91(100)	0.56 (14.2)	Bend 0.48 (12.2)	1.5 (38.1)	---	90	
		L-T	70(294)	222(1531)	74(81)	0.278 (7.1)	Bend 0.48 (12.2)	1.5 (38.1)			
		T-L	70(294)	210(1448)	65(76)	0.270 (6.9)	Bend 0.48 (12.2)	1.5 (38.1)			
		L-T	70(294)	277(1910)	106(117)	0.366 (9.3)	Bend 0.48 (12.2)	1.5 (38.1)			
Plate: 0.56 in (14.2 mm) Thick	C,7	L-T	70(294)	200(1379)	110(121)	0.75 (19.1)	Bend 0.5 (12.7)	1.5 (38.1)	0.5 (12.7)	77	

COMPOSITION

	C	Si	Mn	S	P	Al	Cr	Mo	V	Co	N
A	0.113	0.32	1.08	0.006	0.012	4.06	15.08	2.82	-	-	-
B	0.12	0.44	1.21	0.009	0.015	4.49	15.02	2.76	-	-	-
C	0.16	0.15	0.18	0.021	0.015	0.21	14.0	5.02	0.23	13.41	0.04

HEAT TREATMENT

- 1710F (1206K), Water Quench; -100F (200K), 3 Hr; Age 1600F (811K), 3 Hr
- 1710F (1206K), 10 min; Temper 925F (770K), 3 Hr
- 1925F (1325K), 0.5 Hr; Oil Quench; -100F (200K), 3 Hr; Temper 850F (728K), 2 Hr; Oil Quench; -100F (200K), 3 Hr, 850F (728K), 1 Hr, Air Cool
- 1900F (1311K), 1 Hr, Oil Quench; -100F (200K), 0.5 Hr; Temper 700K (644K); 2 Hr + 2 Hr, Air Cool
- 1900F (1311K), 1 Hr, Oil Quench; -100F (200K), 0.5 Hr; Temper 800F (706K), 2 Hr + 2 Hr, Air Cool
- 2000F (1367K), 1 Hr, Oil Quench; -100F (200K), 0.5 Hr; Temper 500F (533K), 2 Hr, 10% Cold Reduction by Rolling; Temper 700F (644K), 2 Hr + 2 Hr, Air Cool
- Cold Roll 1/4 from 1.12 in (28.5 mm) Plate to 0.56 in (14.2 mm) in 5 stages with Intermediate Anneal, 1400F (1053K); 1900-1675F (1255-1297K), 1 Hr, Oil Quench; -100F (200K), 0.5 Hr, Temper 500F (533K), 2 Hr + 2 Hr

TITANIUM,  $\alpha$  Alloy: SA1-2.5 Sn

Table 22

Form	Composition Heat Treatment	Test Orientation	Temp $t_p$ (°C)	Yield Strength (ksi) (980 N/mm <sup>2</sup> )	Typical $K_{IC}$ (ksi√in) (MN√m)	$2.5 \left( \frac{K_{IC}}{\sigma_{YS}} \right)^2$ (in (mm))	Specimens			
							Type	Thickness (in (mm))	Width (in (mm))	Crack Length (in (mm))
Plate: 0.5 in (12.7 mm) Thick (ELI)	A, 1	L-T	-329(78)	175(1207)	65(73)	0.345(8.8)	Round	0.250(6.4)	0.500(12.7)	---
		T-L	-329(78)	171(1179)	56(55)	0.284(7.2)	Round	0.250(6.4)	0.500(12.7)	---
		L-T	-423(71)	205(1415)	55(60)	3.280(8.5)	Round	0.250(6.4)	0.500(12.7)	---
Plate: 0.5 in (12.7 mm) Thick (Commercial Grade)	B, 1	T-L	-423(71)	209(1441)	52(57)	0.355(9.0)	Round	0.250(6.4)	0.500(12.7)	---
		L-T	-320(78)	205(1490)	26(28)	0.044(1.1)	Round	0.250(6.4)	0.500(12.7)	---
		T-L	-320(78)	204(1487)	50(55)	0.250(6.4)	Round	0.250(6.4)	0.500(12.7)	---
Plate: 0.8 in (20.3 mm) Thick (ELI)	C, 2	L-T	-423(71)	233(1659)	25(27)	0.059(1.5)	Round	0.250(6.4)	0.500(12.7)	---
		T-L	-320(78)	173(1195)	62(66)	0.322(8.2)	Round	0.400(10.2)	0.75(18.8)	1.25(31.5)
		T-L	-423(71)	187(1299)	65(65)	0.302(7.7)	Round	0.400(10.2)	0.75(18.8)	1.25(31.5)

COMPOSITION

	Al	Sn	Fe	S	C	Ni	W	Mo	Cu	Pb
A	5.0	2.6	0.16	0.01	0.025	---	---	---	---	---
B	5.1	2.3	0.34	0.015	0.023	---	---	---	---	---
C	5.1	2.50	0.19	---	0.02	---	---	---	---	---

HEAT TREATMENT

- 1500F (1069K) Furnace Cooled
- 1500F (1117K), 16 Hr, Furnace Cooled

TITANIUM, Near - Alloys: BEI 679, 6A1-25a-IV, 6A1-25b-IV, 6A1-25c-IV

Form	Composition, Heat Treatment	Test Orientation	Temp (°F)	Yield Strength KSI (N/mm <sup>2</sup> )	Typical $K_{IC}$ KSI√in (MPa√m)	$\frac{K_{IC}}{\sqrt{a}}$ in (mm)	Specimens				
							Type	Thickness in (mm)	Width in (mm)	Crack Length in (mm)	
BEI 679											
Forging: 0.625 in (15.9 mm) Thick A,1 β Processed Z100F (1422 K)		(a)	70(294)	141(975)	31(36)	0.319(12.9)	Round	0.5(12.7)	---	---	
Forging: 0.625 in (15.9 mm) Thick A,1 α + β Processed 1675F (1186 K)		(a)	70(294)	135(1855)	26(28)	0.372(14.6)	Round	0.5(12.7)	---	---	
Forging: 1.25 in (31.8 mm) Thick E,5 β Forged 1890 F (1255K)		(a)	70(294)	135(1931)	57(62)	0.445(17.5)	Round	0.5(12.7)	---	---	
TI-6Al-4V-IV											
Plate: 1 in (25.4 mm) Thick											
Forging: 0.625 in (15.9 mm) Thick C,2 Thick β Processed Z100F (1422K)		L-T	70(294)	132(951)	67(74)	0.589 (15.0)	Round	0.5 (12.7)	5 (12.7)	1.7 (43.3)	
Forging: 0.625 in (15.9 mm) Thick C,3		(a)	70(294)	126(868)	57(65)	0.532 (13.0)	Round	0.5 (12.7)	---	---	
Forging: 0.625 in (15.9 mm) Thick C,3 Thick α+β Processed 1890F (1255K)		(a)	70(294)	143(985)	34(37)	0.367 (4.5)	Round	0.5 (12.7)	---	---	
Forging: 0.625 in (15.9 mm) Thick D,4 Thick β Processed Z100F (1422K)		(a)	70(294)	146(1056)	52(57)	0.387 (8.1)	Round	0.5 (12.7)	---	---	
Forging: 0.625 in (15.9 mm) Thick D,4 Thick α+β Processed 1750F (1228K)		(a)	70(294)	160(1155)	32(32)	0.400 (2.5)	Round	0.5 (12.7)	---	---	
COMPOSITION											
	Al	Mo	V	Sn	Zr	Fe	Si	C	O	N	H
A	2.3	0.9	-	11.1	5.0	0.06	0.21	0.023	-	-	-
B	7.96	0.92	1.0	0.15	-	0.12	0	0.049	0.07	0.613	0.006
C	7.7	1.1	1.0	-	-	0.07	-	0.022	-	-	-
D	5.0	2.0	-	2.1	3.9	0.06	-	0.024	-	-	-
E	2.25	1.0	-	11.0	5.0	-	0.2	-	-	-	-
HEAT TREATMENT											
	1. 1450F (1172K), Water Quench; 500F (272K), 14 Hr, Air Cool 2. 1800F (1255K), 1 Hr, Water Quench; 1100F (867K), 2 Hr, Air Cool 3. 1625F (1186K), 1 Hr, Water Quench; 1100F (867K), 2 Hr, Air Cool 4. 1775F (1242K), 1 Hr, Water Quench; 1100F (867K), 2 Hr, Air Cool 5. 1495F (1196K), 1 Hr, Air Cool; 450F (772K), 24 Hr, Air Cool										

(a) Test orientation is not specified, but loading and crack propagation directions are in a plane where maximum grain flow is approximately radially symmetric.

TITANIUM,  $\alpha$ - $\beta$  Alloy: BMI 550

Table 24

Form	Composition, Heat Treatment	Test Orientation	Temp °F (°C)	Yield Strength KSI (N/mm <sup>2</sup> )	Typical $K_{IC}$ KSI- $\sqrt{in}$ (MPa- $\sqrt{cm}$ )	$Z_{1/2}$ (in) (mm)	Specimens			Ref
							Type	Thickness in (mm)	Width in (mm)	
Bar: 3.37 x 0.625 in (85.7 x 15.9 mm)	A, 1	L-T	70(294)	137(946)	61(67)	0.496 (12.6)	(a)	---	---	64
	A, 1	T-L	70(294)	135(928)	60(65)	0.484 (12.5)	(a)	---	---	64
	A, 2	T-L	70(294)	135(935)	59(64)	0.494 (12.5)	(a)	---	---	65
Bar: 2 x 3.5 in (50.8 x 88.9 mm)	B, 3	L-S	70(294)	137(945)	52(57)	0.360 (9.2)	(a)	---	---	65
	T-1	T-L	70(294)	150(1054)	34(37)	0.128 (3.3)	(a)	---	---	---
	T-5	T-S	70(294)	150(1054)	44(49)	0.215 (5.5)	(a)	---	---	---
	S-1	S-L	70(294)	121(854)	49(54)	0.410 (10.4)	(a)	---	---	---
	S-T	S-T	70(294)	121(854)	33(36)	0.186 (4.7)	(a)	---	---	---
Plate: 0.63 in (16 mm) Thick	C, 4	T-L	70(294)	160(1105)	74(81)	0.535(13.6)	Bend	0.5(12.7)	1.5(38.1)	95
	C, 5	T-L	70(294)	177(1220)	49(54)	0.192(4.9)	Bend	0.5(12.7)	1.5(38.1)	---

(a) Specimen in accordance with ASTM Recommendations

COMPOSITION

	Al	Mo	Sr	Fe	Si	H
A	4.0	5.95	2.19	0.12	0.54	0.003
B	4.0	4.0	2.0	0.24	0.5	0.0154
C	4.0	4.3	2.1	0.09	0.50	0.005

HEAT TREATMENT

- 1795F (1253K), 1 Hr, Air Cool; 1650F (1172K), 1 Hr, Air Cool; 931F (773K), 24 Hr
- 1795F (1253K), 1 Hr, Air Cool; 1597F (1143K), 1 Hr, Air Cool; 931F (773K), 24 Hr
- 1650F (1173K), Air Cool; 931F (773K), 24 Hr
- 1650F (1173K), 0.5 Hr, Air Cool; 800 F (708K), 24 Hr, Air Cool; 952F (773K), 24 Hr, Air Cool
- 1650F (1173K), 0.5 Hr, Air Cool; Cold Rolled 20% Reduction; 932F (773K), 24 Hr, Air Cool



TITANIUM:  $\alpha$ - $\beta$  Alloy: IMI 680

Table 25

Form	Composition, Heat Treatment	Test Orientation	Temp		Yield Strength KSI (98N/m <sup>2</sup> )	Typical $K_{IC}$ KSI $\sqrt{in}$ (MPa $\sqrt{m}$ )	$2.5 \left( \frac{K_{IC}}{Y} \right)^2$ in (mm)	Specimen			Ref.
			°F	(°K)				Type	Thickness in (mm)	Width in (mm)	
Bar: 2 x 1.3 in (50.8 x 33 mm)	A <sub>1</sub>	L-T	70 (294)		179 (1234)	29 (32)	0.066 (1.7)	(a)	---	---	---
Forging: 0.75 in (19mm) Thick Disc	A <sub>2</sub>	---	70 (294)		140 (965)	59 (65)	0.444 (11.3)	(a)	---	---	65
	A <sub>3</sub>	---	70 (294)		143 (984)	50 (55)	0.306 (7.8)	(a)	---	---	---
	A <sub>4</sub>	---	70 (294)		159 (1093)	40 (44)	0.158 (4.0)	(a)	---	---	---
	A <sub>5</sub>	---	70 (294)		163 (1123)	32 (35)	0.96 (2.4)	(a)	---	---	---
	A <sub>6</sub>	---	70 (294)		174 (1200)	19 (21)	0.29 (0.76)	(a)	---	---	---
	A <sub>7</sub>	---	70 (294)		192 (1321)	15 (16.5)	0.15 (0.39)	(a)	---	---	---
	A <sub>8</sub>	L-T	70 (294)		166 (1145)	45 (49)	0.184 (4.7)	Bend	0.50 (12.7)	1.5 (38.1)	0.35 (8.9)
Forging: 4x6.2 in (105x158 mm) Thick	A <sub>9</sub>	T-S	70 (294)		138 (951)	69 (76)	0.625 (4.7)	Bend	0.5 (12.7)	1.0 (25.4)	60
	A <sub>10</sub>	T-S	70 (294)		150 (1034)	54 (59)	0.333 (8.5)	Bend	0.5 (12.7)	1.0 (25.4)	---

(a) Specimen in accordance with ASTM Recommendations

COMPOSITION

A 2.25N 4.0N 11.0N 0.2N 0.2N 0.013M

HEAT TREATMENT

- 1471-1501F (1073-1123K); 931F (773K), 24 Hr, Air Cool
- Forged at 1831F (1273K); 1606F (1148K), Furnace Cool; 967F (793K), 24 Hr, Air Cool
- Forged at 1696F (1198K); 1606F (1148K), Furnace Cool; 967F (793K), 24 Hr, Air Cool
- Forged at 1831F (1273K); 1498F (1088K), Water Quench; 967F (793K), 24 Hr, Air Cool
- Forged at 1696F (1198K); 1498F (1088K), Water Quench; 967F (793K), 24 Hr, Air Cool
- Forged at 1606F (1148K); 1606F (1148K), Water Quench; 967F (793K), 24 Hr, Air Cool
- Forged at 1831F (1273K); 1606F (1148K), Water Quench; 967F (793K), 24 Hr, Air Cool
- 1490F (1083K), 1 Hr, Water Quench; 930F (772K), 24 Hr, Air Cool

Table 26

TITANIUM,  $\alpha$ - $\beta$  Alloys: 4 Al-3 Mo-IV, 7Al-2.5 Mo, 7Al-4 Mo

Temper	Form	Composition, Heat Treatment	Test Orientation	Temp °F (°K)	Yield Strength KSI (MN/m <sup>2</sup> )	Typical $K_{IC}$ KSI√in (MN m <sup>-3/2</sup> )	$2.5 \left( \frac{K_{IC}}{\sigma} \right)^2$ in (mm)	Specimen			Ref.																																																						
								Type	Thickness in (mm)	Width in (mm)		Crack Length in (mm)																																																					
<b>Ti-4Al-3Mo-IV</b>																																																																	
Plate: 0.5 in (12.7 mm) Thick		A,1	L-T	70 (294)	155 (1069)	72 (78)	0.539 (13.7)	Bend 0.5 (12.7)	1.5 (38.1)	0.3 (7.6)	34																																																						
		A,2	L-T	70 (294)	161 (1110)	63 (69)	0.382 (9.5)	Bend 0.5 (12.7)	1.5 (38.1)	0.3 (7.6)																																																							
Plate 0.5 in (12.7 mm) Thick		A,5	T-L	70 (294)	175 (1207)	66 (72)	0.356 (9)	Bend 0.5 (12.7)	1.5 (38.1)	0.3 (7.6)	94																																																						
Forging: 0.625 in (15.9 mm) Thick β Processed 2100F (1422K)		B,3	(a)	70 (294)	146 (1007)	49 (53)	0.282 (7.2)	Bend 0.5 (12.7)	---	---	22																																																						
<b>Ti-7Al-2.5 Mo</b>																																																																	
Plate: 0.5 in (12.7 mm) Thick		E,7	T-L	70 (294)	152 (1048)	52 (57)	0.293 (7.4)	Bend 0.5 (12.7)	1.5 (38.1)	0.35 (8.9)	95																																																						
		E,8	T-L	70 (294)	136 (938)	65 (71)	0.571 (14.5)	Bend 0.5 (12.7)	1.5 (38.1)	0.35 (8.9)																																																							
Plate: 0.5 in (12.7 mm) Thick		D,6	T-L	70 (294)	145 (1000)	33 (36)	0.129 (3.3)	Bend 0.5 (12.7)	1.5 (38.1)	0.3 (7.6)	94																																																						
Forging: 0.625 in (15.9 mm) Thick β Processed 2100F (1422K)		C,4	(a)	70 (294)	155 (1069)	41 (45)	0.175 (4.4)	Bend 0.5 (12.7)	---	---	22																																																						
<p>(a) Test orientation is not specified, but loading and crack propagation directions are in a plane where maximum grain flow is approximately radially symmetric.</p>																																																																	
<b>HEAT TREATMENT</b>																																																																	
<p>1. 1875F (1297K), 1 Hr, Air Cool; 1725F (1214K), 1 Hr, Water Quench; 1050F (839K), 8 Hr, Air Cool</p> <p>2. 1800F (1255K), 1 Hr, Water Quenched; Aged 1100F (867K), 8 Hr, Air Cooled</p> <p>3. 1725F (1214K), 1 Hr, Water Quench; 1050F (839K), 4 Hr, Air Cool</p> <p>4. 1750F (1228K), 1 Hr, Water Quench; 1050F (839K), 4 Hr, Air Cool</p> <p>5. 1875 F (1297K), 1 Hr, Water Quench; 1100F (867K), 8 Hr, Air Cool</p> <p>6. Mill Annealed</p> <p>7. 1800F (1255K), 0.5 Hr, Water Quench; 1100F (867K), 8 Hr, Air Cool</p> <p>8. Mill Annealed; Hot Rolled 50% Reduction at 1750F (1228K)</p>																																																																	
<b>COMPOSITION</b>																																																																	
<table border="1"> <thead> <tr> <th></th> <th>Al</th> <th>Mo</th> <th>V</th> <th>Fe</th> <th>C</th> <th>H</th> <th>O</th> <th>N</th> </tr> </thead> <tbody> <tr> <td>A</td> <td>4.5</td> <td>3.3</td> <td>1.0</td> <td>0.10</td> <td>0.03</td> <td>0.006</td> <td>0.11</td> <td>0.009</td> </tr> <tr> <td>B</td> <td>4.4</td> <td>3.1</td> <td>1.1</td> <td>0.08</td> <td>0.02</td> <td>---</td> <td>---</td> <td>---</td> </tr> <tr> <td>C</td> <td>6.9</td> <td>4.0</td> <td>-</td> <td>0.12</td> <td>0.023</td> <td>---</td> <td>---</td> <td>---</td> </tr> <tr> <td>D</td> <td>6.9</td> <td>3.7</td> <td>-</td> <td>0.15</td> <td>0.02</td> <td>0.005</td> <td>0.15</td> <td>0.007</td> </tr> <tr> <td>E</td> <td>6.8</td> <td>2.4</td> <td>-</td> <td>0.04</td> <td>0.02</td> <td>0.004</td> <td>0.06</td> <td>0.008</td> </tr> </tbody> </table>													Al	Mo	V	Fe	C	H	O	N	A	4.5	3.3	1.0	0.10	0.03	0.006	0.11	0.009	B	4.4	3.1	1.1	0.08	0.02	---	---	---	C	6.9	4.0	-	0.12	0.023	---	---	---	D	6.9	3.7	-	0.15	0.02	0.005	0.15	0.007	E	6.8	2.4	-	0.04	0.02	0.004	0.06	0.008
	Al	Mo	V	Fe	C	H	O	N																																																									
A	4.5	3.3	1.0	0.10	0.03	0.006	0.11	0.009																																																									
B	4.4	3.1	1.1	0.08	0.02	---	---	---																																																									
C	6.9	4.0	-	0.12	0.023	---	---	---																																																									
D	6.9	3.7	-	0.15	0.02	0.005	0.15	0.007																																																									
E	6.8	2.4	-	0.04	0.02	0.004	0.06	0.008																																																									

TITANIUM,  $\alpha$ - $\beta$  Alloy: 6Al-4V (Sheet 1 of 2)

Table 27

Form	Composition, Heat Treatment	Test Orientation	Temp (°K)	Yield Strength KSI (MN/m <sup>2</sup> )	Typical $K_{IC}$ KSI $\sqrt{in}$ (MN $\sqrt{m}$ )	$2.5 \left( \frac{K_{IC}}{\sigma_{ys}} \right)^2$ in (mm)	Specimen			Ref.	
							Type	Thickness in (mm)	Width in (mm)		Crack Length in (mm)
Plate: 0.5 in (12.7 mm) Thick ( $\beta$ Processed)	A,1	L-T	75(297)	148(1020)	46(50)	0.240( 6.1)	Bend	1.0 (25.4)	1.0 (25.4)	0.290( 7.4)	7
		T-L	75(297)	---	42(46)	---	Bend	1.0 (25.4)	1.0 (25.4)	0.3 ( 7.6)	
		L-T	-50(228)	---	46(50)	---	Bend	1.0 (25.4)	1.0 (25.4)	0.3 ( 7.6)	
		L-T	-100(200)	185(1276)	47(51)	0.161( 4.1)	Bend	1.0 (25.4)	1.0 (25.4)	0.26 ( 6.6)	
		L-T	75(297)	148(1020)	48(52)	0.263( 6.7)	Bend	1.0 (25.4)	1.0 (25.4)	0.303( 7.7)	
Plate: 0.75 in (19.1 mm) Nominal Thickness	C,2	L-T	-50(228)	177(1220)	53(58)	0.224( 5.7)	Bend	1.0 (25.4)	1.0 (25.4)	0.267( 6.8)	
		L-T	-100(200)	173(1193)	54(59)	0.246( 6.2)	Bend	1.0 (25.4)	1.0 (25.4)	0.208( 5.3)	
		L-T	75(297)	133( 916)	75(82)	0.792(20.1)	Bend	0.781(19.8)	1.5 (38.1)	0.3 ( 7.6)	20
Plate: 1.0 in (25.4 mm) Thickness ( $\beta$ Processed)	D,5	T-L	75(297)	150(1034)	45(49)	0.225( 5.7)	Bend	0.9 (22.9)	1.8 (45.8)	0.45 (11.4)	4
		T-L	-321( 78)	227(1565)	36(39)	0.063( 1.6)	Bend	0.9 (22.9)	1.8 (45.8)	0.45 (11.4)	
Plate: 0.5 in (12.7 mm) Thick	E,3	L-T	70(294)	148(1024)	70(77)	0.56 (14.2)	Bend	0.5 (12.7)	1.5 (38.1)	---	34
		(b)	75(297)	146(1007)	60(65)	0.422(10.7)	Bend	0.5 (12.7)	---	---	22
Forging: 0.625 in (15.9 mm) Thick $\beta$ Processed ZrO <sub>2</sub> FF (1422K)	F,4	(b)	75(297)	150(1034)	46(50)	0.235( 6.0)	Bend	0.5 (12.7)	---	---	
		(b)	75(297)	150(1034)	61(66)	0.413(10.5)	Bend	0.55 (14)	1.02 (26)	0.55 (14)	23
Handforging: 1.0 in (25.4 mm) Thick	J,6	L-T	70(294)	148(1020)	55(60)	0.345( 8.8)	Bend	1.0 (25.4)	2.0 (50.8)	1.0 (25.4)	
		T-L	70(294)	127( 875)	78(86)	0.942(23.9)	WOL	2.0 (50.8)	6.2 (15.8)	1.8 ( 4.6)	11
Forging: 3.0 in (76.1 mm) Thick	G,2	T-L	150(339)	140( 966)	81(89)	0.837(21.3)	WOL	2.0 (50.8)	2.25(57.2)	0.5 (12.7)	
		L-T	-75(214)	159(1097)	68(75)	0.457(11.6)	WOL	2.0 (50.8)	6.2 (15.8)	1.8 ( 4.6)	
Bar: 2.26 x 1.2 in (57.5 x 30.5 mm)	H,7	L-T	70(294)	128(883)	71(78)	0.769(19.5)	( $\alpha$ )	---	---	---	63
		L-T	70(294)	140(968)	58(63)	0.429(10.9)	( $\alpha$ )	---	---	---	
Bar: 2 in (50.8 mm) Dia	I,8	L-S	70(294)	147(1014)	55(60)	0.350( 8.9)	Bend	0.5 (12.7)	1.0 (25.4)	---	60
		T-S	70(294)	147(1014)	55(60)	0.350( 8.9)	Bend	0.5 (12.7)	1.0 (25.4)	---	

Form	Composition, Heat Treatment	Test Orientation	Temp °F	Temp (°K)	Yield Strength KSI (MN/m <sup>2</sup> )	Typical $K_{IC}$ KSI $\sqrt{in}$ (MN m <sup>3/2</sup> )	$2.5 \left( \frac{K_{IC}}{\sigma_{ys}} \right)^2$ in (mm)	Specimen			Ref.	
								Type	Thickness in (mm)	Width in (mm)		Crack Length in (mm)
Plate: 3 in (76.1 mm) Thick	K, 9	T-L	70 (294)		122 (841)	101 (111)	1.713 (43.5)	Bend	3.0 (76.1)	6.0 (152.2)	3.0 (76.1)	81

(a) Specimen in accordance with ASTM Recommendations

(b) Test orientation is not specified but loading and crack propagation directions are in a plane where maximum grain flow is approximately radially symmetric.

## COMPOSITION

	Al	V	Fe	C	Si	O	N	H
A	6.2	4.2	0.15	0.020	-	-	-	-
E	6.3	4.3	0.15	0.026	-	-	-	-
C	5.83	3.78	0.16	-	-	-	0.022	0.006
D	6.1	4.12	0.13	0.024	-	0.16	0.013	0.008
E	6.4	3.9	0.17	0.03	-	0.15	0.018	0.003
F	6.3	4.1	0.09	0.025	-	-	-	-
G	6.3	4.1	0.13	0.023	-	0.17	-	0.004
H	6.18	3.91	0.07	-	-	-	-	0.001
I	6.54	4.24	0.7	-	0.16	-	0.007	0.002
J	6.13	4.0	0.3M	0.1M	-	-	-	-
K	6.0	4.1	0.5	0.023	-	0.07	-	0.008

## HEAT TREATMENT

- 1700F (1200K) Air Cool; Age 1000F (811K), 4 Hr
- 1750F (1228K) 1 Hr, Air Cool; Age 1000F (811K), 4 Hr
- 1850F (1283K) 30 Min, Water Quenched, Aged 1250F (950K) 4 Hr
- 1725F (1214K) 1 Hr, Water Quenched; Aged 1050F (839K) 4 Hr, Air Cool
- 1725F (1214K) 1 Hr, Water Quenched; Aged 1000F (811K) 4 Hr, Air Cool
- Solution Treated and Aged
- 1741F (1223K), 1 Hr, Air Cool; 1246F (948K), 1 Hr, Air Cool
- 1291F (973K), Air Cool
- 1750F (1228K), 3 Hr, Water Quenched; Aged 1100F (867K), 4 Hr, Air Cool

Form	Composition, Heat Treatment	Test Orientation	Temp °F (°K)	Yield Strength KSI (MM/m <sup>2</sup> )	Typical $K_{IC}$ KSI√in (MN m <sup>-3/2</sup> )	$2.5 \left( \frac{K_{IC}}{\sigma_{ys}} \right)^2$ in (mm)	Specimen			Ref.	
							Type	Thickness in (mm)	Width in (mm)		Crack Length in (mm)
Plate: 1.0 in (25.4 mm) Thick	A,1	L-T	75(297)	186(1283)	33(37)	0.079( 2.0)	SEN	1.0 (25.4)	5.0 (12.7)	1.6 (40.6)	24
	A,2	L-T	75(297)	167(1151)	60(65)	0.323( 8.2)	SEN	1.0 (12.7)	5.0 (12.7)	1.6 (40.6)	
Plate: 1.0 in (25.4 mm) Thick	B,3	L-T	75(297)	179(1234)	30(35)	0.070( 1.8)	BEND	0.250(12.7)	0.500(12.7)	0.200( 5.1)	25
ELI Grade	B,4	L-T	75(297)	171(1179)	34(37)	0.099( 2.5)	BEND	0.250(12.7)	0.500(12.7)	0.200( 5.1)	
	B,4	L-S	75(297)	---	38(42)	---	Bend	0.250(12.7)	0.500(12.7)	0.200(5.1)	
	B,4	L-T	-321(77)	258(1779)	23(25)	0.020(0.5)	Bend	0.250(12.7)	0.500(12.7)	0.200(5.1)	
	B,4	L-S	-321(77)	259(1786)	25(27)	0.023(0.6)	Bend	0.250(12.7)	0.500(12.7)	0.200(5.1)	
Bar, 4.5 in (114.3 mm) Dia Commercial Grade	G,5	L-C	75(297)	184(1269)	31(34)	0.070(1.8)	Bend	0.250(12.7)	0.500(12.7)	0.200(5.1)	
	G,5	L-C	-321(77)	270(1862)	23(25)	0.018(0.5)	Bend	0.250(12.7)	0.500(12.7)	0.200(5.1)	
Forging: 0.625 in (15.8 mm) Thick $\beta$ Processed 2100F (1422K)	C,3	(a)	75(297)	170(1172)	38(41)	0.125( 3.2)	BEND	0.500(12.7)	---	---	22
Forging: 4.5 x 4.5 in (114.3 x 114.3 mm) Vacuum Arc Remelt	D,5	L-T	75(297)	149(1027)	60(65)	0.405(10.3)	DEC	0.500(12.7)	3.0 (76.2)	1.0 (25.4)	26
Forging: 4.5 x 4.5 in (114.3 x 114.3 mm) Vacuum Arc Remelt	D,5	L-ST	-110(194)	181(1248)	56(61)	0.239( 6.1)	SEN	0.250( 6.4)	1.0 (25.4)	0.500(12.7)	16
	D,5	ST-L	-110(194)	184(1269)	50(55)	0.180( 4.6)	SEN	0.250( 6.4)	1.0 (25.4)	0.500(12.7)	
Plate: 1.5 in (38.1 mm) Thick	D,6	L-S	-110(194)	195(1344)	41(45)	0.110( 2.8)	SEN	0.250( 6.4)	1.0 (25.4)	0.500(12.7)	
	D,6	L-T	-110(194)	195(1344)	32(35)	0.068( 1.7)	SEN	0.250( 6.4)	1.0 (25.4)	0.500(12.7)	
	D,6	TS-TS	-110(194)	195(1344)	25(27)	0.043( 1.1)	CT	0.500(12.7)	1.0 (25.4)	0.500(12.7)	
Plate: 0.5 in (12.7 mm) Thick	D,6	L-T	-110(194)	210(1448)	33(36)	0.063( 1.6)	SEN	0.250( 6.4)	1.0 (25.4)	0.500(12.7)	
	D,6	T-L	-110(194)	208(1434)	30(33)	0.053( 1.3)	SEN	0.250( 6.4)	1.0 (25.4)	0.500(12.7)	
Handforging: 1.0 in (25 mm) Thick	F,7	L-T	75(297)	180(1241)	29(32)	0.065( 1.7)	BEND	0.55 (14)	1.02 (26)	0.55 (14)	23
	F,7	T-L	75(297)	186(1282)	26(28)	0.049( 1.2)	BEND	1.0 (25.4)	2.0 (50.8)	1.0 (25.4)	

(a) Test orientation is not specified but the loading and crack propagation directions are in a plane where maximum grain flow is approximately radially symmetric.

(b) Specimen in accordance with ASTM Recommendations

TITANIUM,  $\alpha$ - $\beta$  Alloy: 6Al-6V-2Sn (Sheet 2 of 2)

Table 28

Form	Composition, Heat Treatment	Test Orientation	Temp		Yield Strength KSI (MN/m <sup>2</sup> )	Typical K <sub>IC</sub> KSI√in (MN m <sup>3/2</sup> )	2.5 (K <sub>IC</sub> <sup>2</sup> / $\sigma_{ys}$ ) in (mm)	Specimen			Ref.	
			°F	(°K)				Type	Thickness in (mm)	Width in (mm)		Crack Length in (mm)
β Forged: 4.92 in (125 mm) Dia	E, 8	L-C	70	(294)	139(958)	60(65)	0.466 (11.8)	(b)	---	---	---	63
	E, 9	L-T	70	(294)	178(1227)	32(35)	0.08 (2.1)	(a)	---	---	---	---
	E, 10	L-T	70	(294)	194(1338)	29(32)	0.056 (1.4)	(a)	---	---	---	---
	F, --	T-S	70	(294)	163(1124)	47(51)	0.200 (5.1)	Bend 0.5 (12.7)	0.5(12.7)	1.0 (25.4)	60	---

COMPOSITION										
	Al	V	Sn	C	Fe	Cu	O	N	H	
A	5.5	5.5	2.0	0.024	0.69	0.73	0.08	0.010	0.003	
B	5.33	5.34	1.96	0.015	0.59	0.65	0.081	0.018	0.005	
C	5.4	5.3	2.0	0.022	0.63	0.6	-	-	-	
D	5.5	5.4	1.9	0.025	0.65	0.64	0.12	0.012	0.005	
E	5.4	5.4	2.0	-	0.53	-	0.015	0.004	0.002	
F	5.5	5.5	2.0	0.05M	0.68	0.68	0.2M	0.04M	0.015M	
G	5.64	5.52	2.26	0.021	0.59	0.56	0.172	0.007	0.016	

HEAT TREATMENT	
1.	1550F (1117K), 1 Hr, Water Quenched; Aged 900F, (756K), 4 Hr, Air Cool
2.	1625F (1158K), 1 Hr, Water Quenched; Aged 1200F, (922K), 2 Hr, Air Cool
3.	1600F (1144K), 1 Hr, Water Quenched; Aged 1050F, (839K), 4 Hr, Air Cool
4.	1650F (1172K), 1 Hr, Water Quenched; Aged 1125F, (881K), 4 Hr, Air Cool
5.	1650F (1172K), 1 Hr, Water Quenched; Aged 1050F, (839K), 4 Hr, Air Cool
6.	1550F, (1117K), 1/2 Hr, Water Quenched; Aged 1050F, (839K), 4 Hr, Air Cool
7.	Solution Annealed and Aged
8.	1400F (1033K), Air Cooled
9.	1561F (1123K), 1 Hr, Water Quench; 967F (793K), 4 Hr, Air Cool
10.	1741F (1223K), 1 Hr, Water Quench; 967F (793K), 4 Hr, Air Cool

Table 29

(Sheet 1 of 2) TITANIUM,  $\alpha$ - $\beta$  Alloys: 6Al-6V-4Zr-4Mo, 6Al-2Sn-4Zr-6Mo and 6Al-2Sn-2Zr-2Mo-2Cr

Form	Composition, Heat Treatment	Test Orientation	Temp °F (°K)	Yield Strength KSI (N/mm <sup>2</sup> )	Typical $K_{IC}$ KSI√in (MN m <sup>3/2</sup> )	$2.5 \left( \frac{K_{IC}}{\sigma_{ys}} \right)^2$ in (mm)	Specimen			Ref.
							Type	Thickness in (mm)	Width in (mm)	
6 Al-6V-4 Zr-4Mo Die Forging: 3.5 in (88.9 mm) Thick, $\beta$ Forged 1750F (1228K)	A,1	C-R	70 (294)	157 (1082)	40 (44)	0.162 (4.1)	Bend 0.5 (12.7) 4 Pt	1.5 (38.1)	0.35 (8.9)	96
$\alpha$ - $\beta$ Forged 1575F (1130K)	A,1	C-S	70 (294)	156 (1075)	46 (50)	0.217 (5.5)	Bend 0.5 (12.7) 4 Pt	1.5 (38.1)	0.35 (8.9)	
Forging: 4.25X6in (108X152 mm), $\alpha$ - $\beta$ Forged 1575F (1130K)	A,1	C-R	70 (294)	170 (1172)	51 (56)	0.225 (5.7)	Bend 0.5 (12.7) 4 Pt	1.5 (38.1)	0.35 (8.9)	
Forging: 4.25X6in (108X152 mm), $\alpha$ - $\beta$ Forged 1575F (1130K)	A,1	C-S	70 (294)	168 (1158)	62 (68)	0.340 (8.6)	Bend 0.5 (12.7) 4 Pt	1.5 (38.1)	0.35 (8.9)	
Forging: 4X6.2 in (102X158 mm), $\alpha$ - $\beta$ Forged 1540F (1112K)	B,2	L-T	70 (294)	160 (1103)	49 (54)	0.234 (5.9)	Bend 0.5 (12.7) 4 Pt	1.5 (38.1)	0.35 (8.9)	
6 Al-2Sn-4Zr-6Mo Forging: 1.5 in (38.1 mm) Sq $\beta$ Forged 1800F (1255K)	C,4	---	70 (294)	*180 (1241)	46 (50)	---	---	---	---	100
Forging: 2 in (50.8 mm) Thick $\beta$ Forged 1800 F (1255K)	C,4	---	70 (294)	*168 (1158)	60 (66)	---	---	---	---	
Forging: 3.5 in (88.9 mm) Thick $\beta$ Forged	C,2	C-R	70 (294)	169 (1165)	22 (24)	0.042 (1.1)	Bend 0.5 (12.7) 4 Pt	1.5 (38.1)	0.35 (8.9)	96
Forging: 4.3X6 in (108X152 mm) $\alpha$ - $\beta$ Forged, 1650F (1172K) Max	C,3	L-T	70 (294)	158 (1089)	41 (45)	0.168 (4.3)	Bend 0.5 (12.7) 4 Pt	1.5 (38.1)	0.35 (8.9)	31
	C,2	L-T	70 (294)	174 (1200)	25 (27)	0.052 (1.3)	Bend 0.5 (12.7) 4 Pt	1.5 (38.1)	0.35 (8.9)	

\*Ultimate Strength Values

TITANIUM,  $\alpha$ - $\beta$  Alloys: 6Al-6V-4Zr-4Mo, 6Al-2Sn-4Zr-6Mo and 6Al-2Sn-2Zr-2Mo-2Cr

Form	Composition, Heat Treatment	Test Orientation	Temp °F (°K)	Yield Strength KSI (MN/m <sup>2</sup> )	Typical $K_{IC}$ KSI $\sqrt{in}$ (MN m <sup>3/2</sup> )	$2.5 \frac{K_{IC}^2}{\sigma_{ys}}$ in (mm)	Specimen			Ref.			
							Type	Thickness in (mm)	Width in (mm)		Crack Length in (mm)		
<b>6Al-2Sn-2Zr-2Mo-2Cr</b>													
Bar: 4in(101.6mm) Dia													
	D,5	L-R	70(294)	160(1103)	62(68)	0.376(9.6)	CT	1.0(25.4)	2.0(50.8)	1.0(25.4)	101		
		R-L	70(294)	164(1131)	51(56)	0.242(6.1)	CT	1.0(25.4)	2.0(50.8)	1.0(25.4)			
	D,6	L-R	70(294)	161(1110)	58(64)	0.325(8.2)	CT	1.0(25.4)	2.0(50.8)	1.0(25.4)			
		R-L	70(294)	169(1165)	45(49)	0.177(4.5)	CT	1.0(25.4)	2.0(50.8)	1.0(25.4)			
	D,7	---	70(294)	158(1089)	74(81)	0.548(13.9)	CF	1.0(25.4)	2.0(50.8)	1.0(25.4)			
	D,7	---	70(294)	160(1103)	59(65)	0.340(8.6)	CT	1.0(25.4)	2.0(50.8)	1.0(25.4)			
Forging: 1 in (25.4 mm) Thick, $\alpha$ - $\beta$ Forged													
$\alpha$ - $\beta$ Forged													
<b>COMPOSITION</b>													
	Al	V	Zr	Mo	Sn	Cr	C	Fe	Cu	H	O	N	Si
A	6.18	5.74	4.07	4.20	---	---	---	0.07	0.012	0.014	0.12	0.012	---
B	6.0N	6.0N	4.0N	4.0N	---	---	---	---	---	---	---	---	---
C	5.0N	---	4.0N	6.0N	2.0N	---	0.04M	0.15M	---	0.15M	0.15M	0.02M	---
D	6.0N	---	2.0N	2.0N	2.0N	2.0N	---	---	---	---	---	---	0.25N
<b>HEAT TREATMENT</b>													
	1.	1525F(1103K), 4 Hr, Air Cool; 950F(873K), 8 Hr, Air Cool											
	2.	1600F(1144K), 1 Hr, Water Quench; 1100F(867K), 8 Hr, Air Cool											
	3.	1600F(1144K), 1 Hr, Air Cool; 1100F(867K), 8 Hr, Air Cool											
	4.	1675F(1186K), 1 Hr, Air Cool; 1100F(867K), 8 Hr, Air Cool											
	5.	1745F(1225K), 1 Hr, Water Quench; 1000F(811K), 4 Hr, Air Cool											
	6.	1745F(1225K), 1 Hr, Oil Quench; 1000F(811K), 4 Hr, Air Cool											
	7.	1745F(1225K), 1 Hr, Air Cool; 1000F(811K), 4 Hr, Air Cool											



TITANIUM,  $\beta$  Alloys: 13V-11 Cr-3Al, 8Mo-8V-2Fe-3Al, 11.5Mo-6Zr-4.5Sn (Sheet 1 of 2) Table 30

Form	Composition, Heat Treatment	Test Orientation	Temp $\sigma_f$ ( $^{\circ}$ F)	Yield Strength KSI ( $\text{MN}/\text{m}^2$ )	Typical $K_{IC}$ KSI/ $\sqrt{\text{in}}$ ( $\text{MN}/\text{m}^{3/2}$ )	$2.5 \left( \frac{K_{IC}}{\sigma_f} \right)^2$ in (mm)	Specimen			Ref.
							Type	Thickness in (mm)	Width in (mm)	
<b>13V-11Cr-3Al (G120 VCA)</b>										
Bar: 1 in (25.4 mm) Diameter	A,1	L-ST	300(422)	159(1096)	39(43)	0.150(3.8)	NR	Do=.505(12.8)	Di=.375( 9.5)	28
	A,1	L-ST	70(294)	181(1248)	32(35)	0.078(2.0)	NR	Do=.505(12.8)	Di=.375( 9.5)	
		L-ST	-45(230)	200(1379)	28(31)	0.049(1.2)	NR	Do=.505(12.8)	Di=.375( 9.5)	
Forging: 0.625 in (15.9mm) Thick B,2 $\alpha+\beta$ Processed: 1675F (1186K)		(a)	70(294)	178(1227)	43(47)	0.146(3.7)	Bend	0.500(12.7)	---	22
Forging: 0.625 in (15.9mm) Thick B,2 $\beta$ Processed: 2100F (1422K)		(a)	70(294)	176(1213)	41(45)	0.136(3.5)	Bend	0.500(12.7)	---	
<b>8 Mo-8V-2Fe-3Al</b>										
Closed Die Forging 0.5 in (12.7 mm) Thick	C,3	T-L	70(294)	181(1248)	38(41)	0.110(2.8)	Bend	0.500(12.7)	1.5 (38.1)	0.300(7.6) 29
2.5 in (63.5 mm) Thick		T-L	70(294)	178(1227)	41(45)	0.133(3.4)	Bend	2.5 (63.5)	1.5 (38.1)	0.300(7.6)
Forged Bar: 3 in (76.2 mm) Square	F,3	L-T	70(294)	165(1138)	52(57)	0.248(6.3)	Bend	(b)	---	30
Forging: 4 in (102 mm) Thick 11.5 Mo-6Zr-4.5Sn (B111)	F,3	L-T	70(294)	176(1213)	63(69)	0.317(8.1)	Bend	0.5 (12.7)	1.5 (38.1)	0.350(8.9) 31
Forging: 4 in (102 mm) Thick	E,4	L-T	70(294)	182(1255)	61(66)	0.280(7.1)	Bend	0.500(12.7)	1.5 (38.1)	0.35 (8.9) 31
Plate: 0.5 in (12.7 mm) Thick	D,5	T-L	70(294)	174(1200)	61(66)	0.305(7.7)	Bend	0.500(12.7)	1.5 (38.1)	---
Plate: 0.640 in (16.3 mm) Thick	E,6	---	70(294)	166(1145)	51(56)	0.236(5.9)	Bend	0.525(13.3)	1.5 (38.1)	---

(a) Test orientation is not specified, but loading and crack propagation directions are in a plane where maximum grain flow is approximately radially symmetric.  
 (b) Specimen in accordance with ASTM Recommendations

TITANIUM - B Alloys: 13V-11 Cr-3A, 8Mo-8V-2Fe-4Al, 11.5Mo-6Zr-4.5Sn (Sheet 2 of 2) Table 30

Form	Composition, Heat Treatment		Test Orientation	Temp $\sigma_f$ (°F)	Yield Strength KSI (MN/m <sup>2</sup> )	Typical $K_{IC}$ KSI $\sqrt{in}$ (MN m <sup>-3/2</sup> )	$2.5 \left( \frac{K_{IC}}{\sigma_{ys}} \right)^2$ in (mm)	Specimen			Ref.						
	V	Cr						Al	Fe	C		Mo	Zr	Sn	Type	Thickness in (mm)	Width in (mm)
A	13N	11N	3N	-	0.05M	-	-	-	-	-	-	-	-	-	-	-	-
B	13.5	10.5	3.1	0.16	0.17	-	-	-	-	-	-	-	-	-	-	-	-
C	7.81	-	2.95	2.17	-	7.91	-	-	-	0.006	0.122	0.006	-	-	-	-	-
D	-	-	-	0.03	-	10.71	4.12	4.60	-	-	-	-	-	-	-	-	-
E	-	-	-	-	-	11.5	6	4.6	-	-	-	-	-	-	-	-	-
F	8.0N	-	3.0N	2.0N	0.05M	8.0N	-	-	-	0.08M	0.014	0.015M	-	-	-	-	-

COMPOSITION:

HEAT TREATMENT

- 1425F (1047K), 15 min; Aged 900F (756K), 72 Hr
- 1350F (1006K), 2 Hr, Air Cool; 1450F (1061K), 1/2 Hr, Water Quench; 900F (756K), 20 Hr, Air Cool
- 1475F (1075K), 1 Hr, Water Quench, Aged 1000F (811K), 8 Hr, Air Cool
- 1325F (992K), 1 Hr, Water Quench, Aged 950F, 8 Hr, Air Cool
- 1320F (1006K), 15 min, Delay 15sec, Water Quench; Aged 950F (783K), 8 Hr
- 1600F (1144K), 1 Hr, Water Quench; Aged 900F (756K), 8 Hr



ALUMINUM, Copper Alloys: 2014, UTD 5020, HTD 66, BS L77, BS L93, GP-265 (Sheet 2 of 2) Table 31

Temper	Form	Composition, Heat Treatment	Test Orientation	Temp °F (°C)	Yield Strength KSI (N/mm <sup>2</sup> )	Typical $K_{IC}$ ESI/√in (MPa√in)	7.5 $\left(\frac{K_{IC}}{\sigma_{YS}}\right)^2$ in (mm)	Specimen			
								Type	Thickness 1/2 in (mm)	Width 1/2 in (mm)	Crack Length 1/2 in (mm)
<b>H14-56</b>											
WP	Plate: 0.5 in (12.7 mm) Thick	D, S	L-S	70 (294)	62 (425)	23 (25)	0.344 (8.7)	(B)	---	---	---
			T-S	70 (294)	62 (425)	19 (21)	0.235 (6.0)	(B)	---	---	---
<b>BSL-77</b>											
WP	Forging:	E, S	T-S	70 (294)	65 (445)	20 (22)	0.239 (6.7)	(B)	---	---	---
			S-L	70 (294)	64 (440)	17.5 (19)	0.187 (4.7)	(B)	---	---	---
<b>BSL-93</b>											
WP	Plate: 1.5 in (38.1 mm) Thick	E, 2	L-T	70 (294)	63 (437)	23 (25)	0.353 (9.5)	(B)	---	---	---
			T-L	70 (294)	62 (428)	21 (23)	0.287 (7.5)	(B)	---	---	---
			S-L	70 (294)	60 (414)	19 (21)	0.251 (6.8)	(B)	---	---	---
<b>GP-265</b>											
W	Plate: 2.5 in (63.5 mm) Thick	F, S	T-L	70 (294)	41 (285)	19 (21)	0.54 (13.6)	10B	1.5 (38.1)	10	1.8 (45.7)

(a) Fabrication and Heat Treatment in accordance with Applicable Military, Federal, ASTM or Aluminum Association Specifications.  
 (b) Specimen in accordance with ASTM specifications.

COMPOSITION

	Cu	Mg	Si	Fe	Mn	Zn	Cr	Ti	Ni	Pb
A	4.5N	0.5N	1.0N	1.0N	1.0N	0.25M	0.1M	0.15M	-	-
B	4.58	0.69	0.94	0.22	0.72	0.08	0.01	0.04	-	-
C	4.41	0.50	0.97	0.24	0.73	0.14	0.01	0.04	-	-
D	4.3N	0.62N	0.75N	1.0M	0.8M	0.2M	-	-	0.2M	-
E	4.45	0.5N	0.7N	0.5M	0.8N	0.2M	-	-	0.2M	0.05M
F	4.04	0.66	0.81	0.42	0.74	-	-	0.04	-	-

HEAT TREATMENT

- Solution Heat Treated, Cold Worked and Artificially Aged in accordance with MIL Specification MIL-B-60000 and Aluminum Standards and Test.
- 940F (773K), Water Quench; 1.5-2.5 hr; Age 310-375F (155-185C)
- 931F (773K), Water Quench; Age 310-360F (155-155C)
- 940F (773K), Water Quench; Stretch 1.5-3%; Age 340F (165C), 8-22 hr
- 931F (773K), Water Quench; Age 310-375F (155-185C)
- 941F (773K), 3 hr, Quench; Age 310F (155C), 10 hr

ALUMINUM, Copper Alloy: 2020

Table 32

Temper	Form	Composition, Heat Treatment	Test Orientation	Temp °F (°C)	Yield Strength ksi (N/mm <sup>2</sup> )	Typical K <sub>IC</sub> ksi√in (MPa√m)	2.5 $\left(\frac{A}{b}\right)^2$ in (mm)	Specimen			
								Type	Thickness in (mm)	Width in (mm)	Gage Length in (mm)
T651	Plate: 1.375 in (34.9 mm) Thick	A, (e)	L-T	70(294)	76(524)	22(24)	0.209 (5.3)	Band	1.375(34.9)	3.0 (76.2)	---
			T-L	70(294)	77(531)	19(21)	0.152 (3.9)	Band	1.375(34.9)	3.0 (76.2)	---

(a) Heat Treatment in Accordance with Applicable Military, ASTM or Aluminum Association Specifications.

COMPOSITION

Cu	Mg	Si	Fe	Mn	Zn	Cd	Li	Ti
A	4.5N	0.03M	0.4M	0.5N	0.25M	0.23%	1.3N	0.1M

ALUMINUM, Copper Alloy: 2021 and 2219 (Sheet 1 of 2)

Table 33

Temper	Form	Compo- sition, Heat Treat- ment	Test Orienta- tion	Temp °F (°C)	Yield Strength KSI (MPa)	Typical K <sub>IC</sub> KSI√in (MPa√m)	2.5 (K <sub>IC</sub> ) <sup>2</sup> in (mm)	Specimens					
								Type	Thickness in (mm)	Width in (mm)	Gage Length in (mm)		
2021 T6		A, —	I-S	70(294)	60(414)	23(25)	0.367 (9.3)	—	—	—	—	—	—
2021 T81	Plate: 1.0 in (25.4 mm) thick	C, 1	T-L	70(294)	61(421)	25(25)	0.355 (9.0)	Bead	1.0 (25.4)	—	—	—	—
			T-L	-100(200)	65(448)	27(29)	0.451 (10.9)	Bead	1.0 (25.4)	—	—	—	—
			T-L	-321 ( 78)	73(503)	32(35)	0.483 (12.2)	Bead	1.0 (25.4)	—	—	—	—
		A, (a)	T-L	-423(22)	80(552)	40(44)	0.625 (15.9)	CT	1.0 (25.4)	2.0 (50.8)	2.0 (50.8)	2.0 (50.8)	34
	Plate: 0.5 in (12.7 mm) thick	B, 2	L-T	70(294)	65(448)	27(29)	0.451 (10.9)	Bead	0.500 (12.7)	1.5 (38.1)	1.5 (38.1)	1.5 (38.1)	43
			T-L	70(294)	64(441)	25(25)	0.325 ( 8.2)	Bead	0.500 (12.7)	1.0 (25.4)	—	—	0.500 (12.7)
	Plate: 1.0 in (25.4 mm) thick	A, (a)	L-T	70(294)	66(455)	36(39)	0.745 (18.9)	(a)	1.0 (25.4)	2.0 (50.8)	—	—	1.0 (25.4)
			T-L	70(294)	65(448)	24(26)	0.342 ( 8.7)	(a)	1.0 (25.4)	2.0 (50.8)	—	—	1.0 (25.4)
	Plate: 10.5 in (12.7 mm) thick	A, (a)	L-T	70(294)	65(448)	26(28)	0.4 ( 10.3)	(a)	0.5 (12.7)	1.0 (25.4)	—	—	0.5 (12.7)
			T-L	70(294)	64(441)	21(23)	0.369 ( 9.4)	(a)	0.5 (12.7)	1.0 (25.4)	—	—	0.5 (12.7)
2219 T87	Plate: 1 in (25.4 mm) Thick	B, (a)	L-T	70(294)	58(400)	33(36)	0.809 (20.5)	SEB	1.0 (25.4)	3.0 (76.2)	1.0 (25.4)	1.0 (25.4)	41
		B, (a)	T-L	70(294)	55(379)	30(33)	0.743 (19.5)	SEB	1.0 (25.4)	3.0 (76.2)	1.0 (25.4)	1.0 (25.4)	41
	Plate: 2.5 in (63.5 mm) Thick	B, 3	T-S	72(296)	55(379)	37(40)	1.191 (29.7)	Bead	1.25 (31.8)	2.5 ( 63.5)	1.25 (31.8)	1.25 (31.8)	26
				-320 ( 78)	67(462)	42(44)	0.982 (24.9)	Bead	1.25 (31.8)	2.5 ( 63.5)	1.25 (31.8)	1.25 (31.8)	26
				-423 ( 21)	73(503)	47(51)	1.466 (36.3)	Bead	1.25 (31.8)	2.5 ( 63.5)	1.25 (31.8)	1.25 (31.8)	26

Table 33

ALUMINUM, Copper Alloy: 2021 and 2219 (Sheet 2 of 2)

Temper	Form	Composition, Heat Treatment	Test Orientation	Temp F (°C)	Yield Strength KSI (N/mm <sup>2</sup> )	Typical $\frac{K_{IC}}{K_{ISRT}}$ (mm <sup>3/2</sup> )	$2.5 \left( \frac{K_{IC}}{Y} \right)^2$ in (mm)	Specimens			Ref.	
								Type	Thickness in (mm)	Width in (mm)		Crack Length in (mm)
2219 T851	Plate:	B, -	--	70(294)	51(352)	33(36)	1.047(26.6)	Round	1.40 (35.6)	1.9 (76.2)	1.5 (58.1)	44
	Plate: 1 in (25.4 mm) Thick	B, (a)	L-T	70(294)	59(407)	38(41)	1.057(26.4)	SEB	1.0 (25.4)	5.0 (127.0)	1.6 (40.6)	40
		B, (a)	L-L	70(294)	59(400)	37(40)	1.017(25.6)	SEB	1.0 (25.4)	5.0 (127.0)	1.6 (40.6)	
	Plate: 1.375 in (34.9 mm) Thick	B, (a)	L-T	70(294)	51(352)	36(39)	1.246(31.6)	(b)	1.375(34.9)	2.75(70.0)	1.375(34.9)	37
		B, (a)	T-L	70(294)	57(395)	32(35)	0.788(20.0)	(b)	1.375(34.9)	2.75(70.0)	1.375(34.9)	
		B, (a)	T-L	70(294)	50(345)	29(32)	0.841(21.1)	(b)	1.375(34.9)	1.9 (76.2)	1.55 (59.4)	56

(a) Fabrication and Heat Treatment in Accordance with Applicable Military, Federal, or Aluminum Association Specifications  
 (b) Specimen in accordance with ASTM Recommendations

COMPOSITION

	Cu	Mg	Si	Fe	Mn	Zn	Ti	V	Zr	Cd	Sn
A	6.3N	0.02N	0.2M	0.3M	0.3N	0.1M	0.06N	0.1M	0.15N	0.15M	0.03M
B	6.3N	0.02M	0.2M	0.3M	0.3N	0.1M	0.06N	0.1M	0.15N	-	-
C	6.08	0.05	0.07	0.11	0.25	0.01	0.05	0.08	0.15	0.14	0.05

HEAT TREATMENT

- 985F (503K), 2 Hr, Oil Quenched, Presaged 300F (422K), 1 Hr; Stretch 1.5% Maximum, Age 325F (436K), 24 Hrs.
- 990F (506K), Water Quenched, Presaged 300F (422K), 1 Hr, Stretch 1.0% Maximum, Aged 325F (436K), 16 Hr
- Annealed 1550F (1117K) Argon Atmosphere, 8 Hr, Furnace Cool

ALUMINUM, Copper Alloy: 2024, DTD 5090 and A-U4G1 (Sheet 1 of 2) Table 34

Temper	Form	Composition, Heat Treatment	Test Orientation	Temp °F (°K)	Yield Strength KSI (N/mm <sup>2</sup> )	Typical $K_{IC}$ KSI/√in (N/mm <sup>3/2</sup> )	$2.5 \left( \frac{K_{IC}}{\sigma} \right)^2$ in (mm)	Specimen			Ref.	
								Type	Thickness in (mm)	Width in (mm)		Crack Length in (mm)
2024	Plate: 1.375 in (34.9 mm) Thick	A, (a)	T-L	70(294)	64(441)	20(22)	0.244( 6.2)	Bend 1.375(34.9)	3.0 ( 76.2)	1.51(38.4)	39	
			T-L	-112(193)	69(476)	22(24)	0.254( 6.5)	Bend 1.375(34.9)	3.0 ( 76.2)	1.51(38.4)		
			T-L	-320( 78)	79(545)	22(24)	0.209( 5.1)	Bend 1.375(34.9)	3.0 ( 76.2)	1.51(38.4)		
			L-T	70(294)	66(455)	24(26)	0.331( 8.4)	Bend 1.375(34.9)	3.0 ( 76.2)	1.51(38.4)		
			L-T	70(294)	66(455)	33(36)	0.625(15.9)	(B)	---	---	---	37
			T-L	70(294)	65(448)	32(35)	0.606(15.4)	(B)	---	---	---	
			L-T	70(294)	62(427)	32(35)	0.625(15.9)	(B)	1.0 (25.4)	2.0 ( 50.8)	1.0 (25.4)	37
			T-L	70(294)	61(420)	25(27)	0.42 (10.5)	(B)	1.0 (25.4)	2.0 ( 50.8)	1.0 (25.4)	
			L-T	70(294)	56(386)	25(27)	0.498(12.6)	Bend 0.55 (14)	1.02(26)	0.55 (14)	0.55 (14)	27
			T-L	70(294)	56(386)	22(24)	0.386( 9.8)	Bend 1.0 (25.4)	2.0 ( 50.8)	1.0 (25.4)	---	42
T8510	Extrusion: 1.45 in (36.8 mm) Thick	A, (a)	L-T	70(294)	69(476)	30(33)	0.400(10.2)	Bend 1.01 (25.7)	3.0 ( 76.2)	---		
			T-L	70(294)	66(455)	18(20)	0.165( 4.2)	Bend 0.375( 9.5)	0.937( 23.8)	---		
T852	Forging: 2.0 in (50.8 mm) Thick	B,1	L-T	70(294)	65(448)	24(26)	0.341( 8.7)	Bend 0.750(19.1)	1.5 ( 38.1)	---	41	
			T-L	70(294)	64(441)	22(24)	0.295( 7.5)	Bend 0.750(19.1)	1.5 ( 38.1)	---		
			L-T	70(294)	56(386)	30(33)	0.717(18.2)	Bend 2.0 (50.8)	4.0 (101.6)	---		
T4	Plate: 1 in (25.4 mm) thick	A, (a)	T-L	70(294)	48(331)	31(34)	0.41(10.4)	SEN 1.0 (25.4)	5.0 (127)	1.6(40.6)	40	
			S-L	70(294)	54(372)	16(17)	0.219( 5.6)	Bend 0.5 (12.7)	1.0 ( 25.4)	---		



ALUMINUM, Copper Alloy: 2024, DTD 5090 and A-U4G1 (Sheet 2 of 2) Table 34

Temper	Form	Composition, Heat Treatment	Test Orientation	Temp °F (°K)	Yield Strength KSI (N/mm <sup>2</sup> )	Typical $K_{IC}$ KSI√in (MPa√m)	$2.5 \left( \frac{K_{IC}}{\sigma_{YS}} \right)^2$ in (mm)	Specimens			Ref.
								Type	Thickness in (mm)	Width in (mm)	
<b>DTD 5090</b>											
WP	Plate: 3 in (76.2 mm) Thick	D,2	L-T	70 (294)	54 (379)	42 (45)	1.441 (36.6)	(b)	---	---	72
<b>A-U4G1</b>											
T351		D,-	T-S	70 (294)	50 (345)	24 (27)	0.576 (14.6)	Bend	0.5 (12.7)	1.0 (25.4)	60
T6S1		D,-	T-S	70 (294)	58 (400)	22 (24)	6.360 (9.1)	Bend	0.5 (12.7)	1.0 (25.4)	---
T8S1		D,-	T-S	70 (294)	61 (421)	24 (27)	0.387 (9.8)	Bend	0.5 (12.7)	1.0 (25.4)	---

(a) Fabrication and Heat Treatment in accordance with Military, Federal, ASTM or Aluminum Association Specifications  
 (b) Specimen Accordance with ASTM Recommendations

**COMPOSITION**

	Cu	Mg	Fe	Si	Mn	Zn	Ti	Cr	Ni	Pb
A	4.5N	1.5N	0.5N	0.5N	0.6N	0.25M	-	0.1M	-	-
B	4.63	1.54	0.15	0.11	0.53	0.07	0.02	-	-	-
C	4.56	1.69	0.14	0.12	0.65	0.08	0.03	-	-	-
D	4.35	1.5	0.5N	0.5N	0.6	0.2M	-	-	0.5M	0.05M

**HEAT TREATMENT:**

- Solution Heat Treated, Cold Worked and Artificially Aged in accordance with MIL Specification MIL-H-6048D or Aluminum Standards and Data, Aluminum Association, April 1968
- 922F (768K), Water Quench; Stretch 1.5-2.5%

ALUMINUM, Copper Alloy: 2618, RR58, DTD 731, CM 9031/4D, A-U2GN

Table 35

Type	Form	Composition, Heat Treatment	Test Orientation	Temp °F (°K)	Yield Strength KSI (MN/m <sup>2</sup> )	Typical $K_{IC}$ KSI√in (MN m <sup>3/2</sup> )	$2.5 \left( \frac{K_{IC}}{\sigma_{ys}} \right)^2$ in (mm)	Specimen				Ref.			
								Type	Thickness in (mm)	Width in (mm)	Crack Length in (mm)				
2618															
T651	Plate: 1 in (34.9 mm) Thick	A, (a)	T-L	70(294)	58(400)	33(37)	0.85 (22.6)	Bend	1.0(25.4)	2.0 (50.8)	1.0 (25.4)	37			
RR58															
WP	Plate: 3 in (76.2 mm) Thick	B, -	L-F	70(294)	60(414)	22(24)	0.356 (8.5)	Bend	0.75 (19.1)	3.0 (76.2)	1.0 (25.4)	62			
		B, -	T-L	70(294)	58(400)	19(21)	0.268 (6.8)	Bend	0.75 (19.1)	3.0 (76.2)	1.0 (25.4)				
		B, -	S-L	70(294)	55(379)	20(22)	0.351 (8.4)	Bend	0.75 (19.1)	3.0 (76.2)	1.0 (25.4)				
WP	Forging	S, -	R-L	70(294)	61(421)	24(26)	0.367 (9.8)	Bend	1.4 (35.6)	0.38(9.7)	0.45(12.4)				
DTD 731															
WP	Forging	B, -	L-T	70(294)	58(400)	21(23)	0.328 (8.3)	Bend	0.38 (9.7)	1.5 (38.1)	0.34 (8.6)	62			
			T-S	70(294)	58(400)	21(23)	0.328 (8.3)	Bend	0.38 (9.7)	1.5 (38.1)	0.34 (8.6)				
			S-L	70(294)	57(393)	16(17.6)	0.197 (5.0)	Bend	0.25 (6.4)	0.75(19.1)	0.30 (7.6)				
CM 903/4D															
WP	Plate: 1.5 in (38.1 mm) Thick	C, 1	L-T	70(294)	61(423)	23(25)	0.355 (9.0)	(b)	---	---	---	72			
	Plate: 3 in (76.2 mm) Thick	C, 1	L-T	70(294)	60(417)	26(22)	0.278 (7.1)	(b)	---	---	---				
			L-T	70(294)	58(399)	17(19)	0.215 (5.5)	(b)	---	---	---				
			S-L	70(294)	55(376)	16(18)	0.212 (5.4)	(b)	---	---	---				
A-U2 GN															
T 651		A, -	T-S	70(294)	57(393)	21(23)	0.339 (8.6)	Bend	0.5 (12.7)	1.0 (25.4)	---	62			
T 652		A, -	L-T	70(294)	58(400)	24(26)	0.428 (10.9)	Bend	0.5 (12.7)	1.0 (25.4)	---				
COMPOSITION															
							Cu	Mg	Si	Fe	Mn	Zn	Al	Pb	NI
							2.3%	1.5%	0.25%	1.1%	-	-	0.07%	-	1.05%
							2.5%	1.5%	0.2%	1.0%	-	-	0.1%	-	1.2%
							2.25%	1.5%	0.25%	1.15%	0.2%	0.1%	-	0.05%	1.1%
HEAT TREATMENT															
1. 985F (803K), Water Quenched; Stretch 1.5-2.5%; Aged 375F (463F)															

(a) Fabrication and Heat Treatment in accordance with Military, Federal, ASTM or Aluminum Association Specifications.  
 (b) Specimen in accordance with ASTM Recommendations.



Sheet 2 of 2 Table 36

Temper	Form	Composition, Heat Treatment	Test Orientation	Temp °F	Temp (°K)	Yield Strength KSI (MN/m <sup>2</sup> )	Typical $K_{IC}$ KSI√in (MN m <sup>3/2</sup> )	$2.5 \left( \frac{K_{IC}}{\sigma} \right)^2$ in (mm)	Specimen			Ref.	
									Type	Thickness in (mm)	Width in (mm)		Crack Length in (mm)
7049 T76	Extrusion: 20X3.3X3.5 in (508X84X89 mm)	D, (a)	L-T	70(294)	70(294)	76(524)	33(36)	0.471(12)	CT	1.0(25.4)	2.0(50.8)	1.0(25.4)	97
			T-L	70(294)	70(294)	69(476)	20(22)	0.210(5.3)	CT	1.0(25.4)	2.0(50.8)	1.0(25.4)	
			L-T	-65(219)	-65(219)	80(552)	30(33)	0.352(8.9)	CT	1.0(25.4)	2.0(50.8)	1.0(25.4)	
			T-L	-65(219)	-65(219)	72(496)	19(21)	0.174(4.4)	CT	1.0(25.4)	2.0(50.8)	1.0(25.4)	

(a) Heat Treatment in accordance with Applicable Military, Federal, ASTM or Aluminum Association Specification  
 (b) Specimen in accordance with ASTM Recommendations.

## COMPOSITION

	Cu	Mg	Fe	Si	Mn	Zn	Cr	Ti
A	2.1N	3.0N	0.4N	0.35M	0.2M	7.4N	0.28N	0.2M
B	2.26	3.03	0.16	0.12	0.04	7.61	0.21	0.02
C	1.48	2.45	0.13	0.07	0.01	7.5	0.16	-
D	1.5N	2.5N	0.35M	0.25M	0.2M	7.6N	0.15N	0.1M

ALUMINUM, Zn-Mg Alloy: 7007

Temper	Form	Composition, Heat Treatment	Test Orientation	Temp °F (°K)	Yield Strength KSI (MN/m <sup>2</sup> )	Typical K <sub>IC</sub> KSI√in (MN m <sup>3/2</sup> )	2.5 (K <sub>IC</sub> /σ <sub>ys</sub> ) <sup>2</sup> in (mm)	Specimen			Ref.	
								Type	Thickness in (mm)	Width in (mm)		Crack Length in (mm)
7007 T6	Plate: 1.0 in (25.4 mm) Thick	A, (a)	L-T	70(294)	73(503)	44(48)	0.903(23.1)	(b)	1.0 (25.4)	2.0(50.8)	1.0 (25.4)	37
			T-L	70(294)	69(476)	37(40)	0.719(18.3)	(b)	1.0 (25.4)	2.0(50.8)	1.0 (25.4)	
			T-L	70(294)	65(448)	32(35)	0.606 (15.4)	CT	1.0 (25.4)	2.0 (50.8)	1.0 (25.4)	58
			T-L	-321(77)	80(552)	23(25)	0.207 (5.2)	CT	1.0 (25.4)	2.0 (50.8)	1.0 (25.4)	
			T-L	-423(22)	85(586)	28(31)	0.271 (6.9)	CT	1.0 (25.4)	2.0 (50.8)	1.0 (25.4)	
T6E136	Plate: 1.0 in (25.4 mm) Thick	B, 1	L-T	70(294)	73(503)	46(50)	0.999(25.2)	Bend	1.0 (25.4)	2.0(50.8)	1.0 (25.4)	43
			T-L	70(294)	69(476)	37(40)	0.685(17.4)	Bend	1.0 (25.4)	2.0(50.8)	1.0 (25.4)	

(a) Fabrication and Heat Treatment in accordance with Aluminum Association Specifications.  
 (b) Specimen in accordance with ASTM Recommendations.

COMPOSITION

	Cu	Mg	Si	Fe	Mn	Zn	Ti	Cr	Zr	Ag
A	0.25M	1.8N	(0.4M Total)	0.4M	6.5N	0.04N	0.12N	0.12N	-	-
B	0.06	1.76	0.05	0.11	0.21	6.55	0.03	0.11	0.10	-

HEAT TREATMENT

1. 860F (754K). Controlled Moderate Quench; Stretched 1.5 to 3%; Aged 275F (408K), 16 Hr.

ALUMINUM, Zn-Mg Alloys: 7075, DTD 5050, DTD 5074, BS 195, AZ 74, and 7175 (Sheet 1 of 4) Table 38

Temper	Form	Composition, Heat Treatment	Test Orientation	Temp °F	Temp (°K)	Yield Strength KSI (MN/m <sup>2</sup> )	Typical $K_{Ic}$ KSI√in (MN m <sup>3/2</sup> )	$2.5 \left( \frac{K_{Ic}}{\sigma_{ys}} \right)^2$ in (mm)	Specimen			Ref.	
									Type	Thickness in (mm)	Width in (mm)		Crack Length in (mm)
7075													
T6	Plate: 3 in (76.2 mm) Thick	A, 1	T-S	70(294)		63(435)	27(29)	0.459 (11.7)	(b)	---	---	---	76
T651	Plate: 0.5 in (12.7 mm) Thick	A, (a)	T-L	70(294)		73(503)	25(27)	0.290( 7.4)	(b)	0.5 (12.7)	1.0 (25.4)	0.5 (12.7)	37
	Plate: 1.375 in (44.5 mm) Thick	A, (a)	T-L	70(294)		74(510)	19(21)	0.165( 4.2)	(b)	1.75 (44.4)	3.0 (76.2)	1.75 (44.4)	
		A, (a)	S-L	70(294)		---	15(16)	---	(b)	1.75 (44.4)	3.0 (76.2)	1.75 (44.4)	
	Plate: 1.375 in (34.9 mm) Thick	A, (a)	L-T	70(294)		75(517)	28(31)	0.350( 8.9)	Bend	1.375(34.9)	3.0 (76.2)	1.5 (38.1)	38
		A, (a)	T-L	70(294)		78(537)	23(25)	0.218( 5.5)	---	---	---	---	
	Plate: 1.375 in (34.9 mm) Thick	A, (a)	T-L	70(294)		78(537)	21(23)	0.180( 4.6)	Bend	1.390(35.3)	3.0 (76.2)	1.5 (38.1)	39
		A, (a)	T-L	-112(193)		83(572)	23(25)	0.193( 4.9)	Bend	1.390(35.3)	3.0 (76.2)	1.5 (38.1)	
		A, (a)	T-L	-320( 78)		92(633)	25(27)	0.185( 4.7)	Bend	1.390(35.3)	3.0 (76.2)	1.5 (38.1)	
	Plate: 4 in (101.6 mm) Thick	A, 2	T-S	70(294)		67(459)	22(24)	0.270 (6.8)	(b)	---	---	---	76
T6511	Extrusion: 0.688 in (17.5 mm) Thick	A, (a)	L-T	70(294)		79(544)	26(28)	0.277( 7.0)	(b)	0.625(15.9)	1.25(31.8)	0.625(15.9)	37
		A, (a)	T-L	70(294)		75(517)	25(27)	0.278( 7.1)	(b)	0.625(15.9)	1.25(31.8)	0.625(15.9)	
	Extrusion: 3.5 in (88.9 mm) Thick	A, (a)	L-T	70(294)		75(517)	31(34)	0.427(10.8)	(b)	1.5 (30.1)	3.0 (76.2)	1.5 (38.1)	
		A, (a)	T-L	70(294)		67(46?)	21(23)	0.246( 6.3)	(b)	1.5 (30.1)	3.0 (76.2)	1.5 (38.1)	
		A, (a)	S-L	70(294)		61(421)	19(21)	0.242 (6.2)	CT	1.0 (25.4)	2.0 (50.8)	1.0 (25.4)	61
T73511	Extrusion: 0.688 in (17.5 mm) Thick	A, (a)	L-T	70(294)		64(441)	34(37)	0.706(17.9)	(b)	0.625(15.9)	1.25(31.8)	0.625(15.9)	37
		A, (a)	T-L	70(294)		62(427)	30(33)	0.585(14.9)	(b)	0.625(15.9)	1.25(31.8)	0.625(15.9)	
	Extrusion: 3.5 in (88.9 mm) Thick	A, (a)	L-T	70(294)		54(441)	35(38)	0.748(19.0)	(b)	1.5 (38.1)	3.0 (76.2)	1.5 (38.1)	
		A, (a)	T-L	70(294)		58(400)	24(26)	0.428(10.9)	(b)	1.5 (38.1)	3.0 (76.2)	1.5 (38.1)	
		A, (a)	S-L	70(294)		54(372)	20(22)	0.343 (8.7)	CT	1.0 (25.4)	2.0 (50.8)	1.0 (25.4)	61
T76511	Extrusion: 0.688 in (17.5 mm) Thick	A, (a)	L-T	70(294)		67(462)	33(36)	0.606(15.4)	(b)	0.625(15.9)	1.25(31.8)	0.625(15.9)	
		A, (a)	T-L	70(294)		64(441)	30(33)	0.549(13.9)	(b)	0.625(15.9)	1.25(31.8)	0.625(15.9)	

ALUMINUM, Zn-Mg Alloys: 7075, DTD 5050, DTD S074, BS L95, AZ 74, and 7175 (Sheet 2 of 4) Table 38

Temper	Form	Composition, Heat Treatment	Test Orientation	Temp °F (°K)	Yield Strength KSI (MPa/m <sup>2</sup> )	Typical $K_{IC}$ KSI√in (MN m <sup>-3/2</sup> )	$2.5 \left( \frac{K_{IC}}{\sigma_{ys}} \right)^2$ in (mm)	Specimen			Ref.																																													
								Type	Thickness in (mm)	Width in (mm)		Crack Length in (mm)																																												
T7351	Plate: 1.375 in (34.9 mm) Thick	A, (a)	T-L	70(294)	57(393)	28(31)	0.603(15.3)	Bend	1.375(34.9)	3.0( 76.2)	1.5(38.1)	39																																												
													A, (a)	T-L	-112(193)	59(407)	28(31)	0.563(16.6)	Bend	1.375(34.9)	3.0( 76.2)	1.5(38.1)	39																																	
																								A, (a)	T-L	-320( 78)	66(455)	29(32)	0.483(12.3)	SEN	1.0( 25.4)	5.0(127.0)	1.6(40.6)	40																						
																																			A, (a)	L-T	70(294)	67(462)	33(36)	0.606(15.4)	SEN	1.0( 25.4)	5.0(127.0)	1.6(40.6)	40											
																																														A, (a)	T-L	70(294)	65(448)	27(29)	0.431(10.9)	Bend	0.55( 14)	1.02( 26)	0.55( 14)	27
---	T-L	70(294)	57(393)	28(31)	0.603(15.3)	Bend	0.55( 14)	1.02( 26)	0.55( 14)	27																																														
											A, 3	T-S	70(294)	66(452)	27(30)	0.418( 10.6)	Bend	0.55( 14)	1.02( 26)	0.55( 14)	27																																			
																						---	L-T	70(294)	58(400)	33(36)	0.809(20.5)	Bend	1.0( 25.4)	2.0( 50.8)	1.0(25.4)	60																								
																																	---	T-L	70(294)	58(400)	22(24)	0.359( 9.1)	Bend	0.5( 12.7)	1.0( 25.4)	1.0(25.4)	60													
																																												B, 1	T-S	70(294)	54(370)	27(30)	0.625(15.9)	Bend	0.5( 12.7)	1.0( 25.4)	1.0(25.4)	60		
																																																							---	L-T
---	T-L	70(294)	65(448)	24(26)	0.341( 8.7)	Bend	0.75(19.0)	1.5( 38.1)	1.5(38.1)	41																																														
											C, 1	L-T	70(294)	55(379)	40(44)	1.322(33.6)	Bend	2.0( 50.4)	4.0(101.6)	4.0(101.6)	60																																			
																						---	T-L	70(294)	50(345)	28(31)	0.784(19.9)	Bend	2.0( 50.4)	4.0(101.6)	4.0(101.6)	60																								
																																	A, (a)	S-L	70(294)	49(338)	26(28)	0.703(17.9)	Bend	2.0( 50.4)	4.0(101.6)	4.0(101.6)	60													
																																												---	T-S	70(294)	57(393)	30(33)	0.692( 17.6)	Bend	0.5( 12.7)	1.0( 25.4)	1.0(25.4)	60		
																																																							F, 2	L-T
---	L-S	70(294)	76(522)	28(31)	0.339( 8.6)	Bend	0.5( 12.7)	1.0( 25.4)	1.0(25.4)	62																																														
											F, -	T-L	70(294)	70(482)	21(23)	0.225( 5.7)	Bend	0.5( 12.7)	1.0( 25.4)	1.0(25.4)	62																																			
																						---	T-S	70(294)	70(482)	22(24)	0.247( 6.3)	Bend	0.5( 12.7)	1.0( 25.4)	1.0(25.4)	62																								
																																	F, -	S-L	70(294)	65(445)	20(22)	0.237( 6.0)	Bend	0.5( 12.7)	1.0( 25.4)	1.0(25.4)	62													

ALUMINUM, Zn-Mg Alloy:: 7075, DTD 5050, DTD 5074, BS L95, AZ 74, and 7175 (Sheet 3 of 4) Table 38

Temper	Form	Compo- sition, Heat Treat- ment	Test Orienta- tion	Temp °F (°K)	Yield Strength KSI (MN/m <sup>2</sup> )	Typical K <sub>IC</sub> (KSI√in) (MN m <sup>-3/2</sup> )	2.5 (K <sub>IC</sub> <sup>2</sup> / σ <sub>y</sub> <sup>2</sup> ) in (mm)	Specimen			Ref.	
								Type	Thickness in (mm)	Width in (mm)		Crack Length in (mm)
<b>DTD 5074</b>												
MP	Plate	D <sub>1</sub> -	---	70(294)	70(483)	27(29)	0.372 (9.4)	Bend	0.38 (9.7)	0.75(19.1)	0.34 (8.6)	57
MP	Extrusion	D <sub>1</sub> -	L-	70(294)	83(572)	33(36)	0.395 (10.0)	Bend	0.32 (8.1)	1.5 (38.1)	0.45 (11.4)	62
<b>BSL-95</b>												
MP	Plate: 3 in (76.2 mm) Thick	E <sub>2</sub>	T-S	70(294)	74(510)	24(26)	0.263 (6.7)	Bend	0.25 (6.4)	0.75(19.1)	0.23 (5.8)	76
<b>AZ 74</b>												
	Plate: 4.5 in (114.3 mm) Thick	G <sub>1</sub> -	L-T	70(294)	60(411)	25(27.5)	0.431 (10.8)	(b)	---	---	---	76
	Hand forging: 1.1 in (28.4 mm) Thick	---	L-S	70(294)	---	22(24)	---	(b)	---	---	---	27
T61		---	L-T	70(294)	71(490)	26(29)	0.335 (8.5)	(b)	---	---	---	60
T73		---	L-S	70(294)	67(462)	25(27)	0.347 (8.8)	(b)	---	---	---	37
7175		---	T-S	70(294)	69(476)	29(32)	0.442 (11.2)	Bend	0.5 (12.7)	1.0 (25.4)	---	99
T66		---	T-S	70(294)	66(455)	18(20)	0.19 (4.7)	Bend	0.5 (12.7)	1.0 (25.4)	---	99
<b>Die Forging: 3 in (76.2 mm) H,4 Max. Thickness</b>												
		H,4	L-T	70(294)	80(552)	34(37)	0.452(11.5)	(b)	---	---	---	37
			T-L	70(294)	70(483)	25(27)	0.319(8.1)	(b)	---	---	---	37
			S-T	70(294)	---	21(23)	---	(b)	---	---	---	37
<b>Die Forging: 3 in (76.2 mm) H,4 Max. Thickness</b>												
		H,4	L-T	70(294)	72(496)	35(38)	0.591(15)	(b)	---	---	---	37
			T-L	70(294)	67(462)	26(28)	0.376(9.6)	(b)	---	---	---	37
			S-L	70(294)	---	27(29)	---	(b)	---	---	---	37
<b>Forging: 2.5 in (63.5 mm) H,4 Square</b>												
		H,4	T-L	70(294)	66(455)	23(25)	0.304(7.7)	CT	1.0(25.4)	2.0(50.8)	1.0(25.4)	99
			S-T	70(294)	65(448)	32(35)	0.606(15.4)	CT	1.0(25.4)	2.0(50.8)	1.0(25.4)	99
			S-T	0(256)	66(455)	27(29)	0.419(10.6)	CT	1.0(25.4)	2.0(50.8)	1.0(25.4)	99
			S-T	-65(219)	67(462)	26(28)	0.376(9.6)	CT	1.0(25.4)	2.0(50.8)	1.0(25.4)	99



Table 38

ALUMINUM, Zn-Mg Alloys: 7075, DTD 5050, DTD 5074, B5 195, AZ 74, and 7175 (Sheet & of 4)

Temper	Form	Composition, Heat Treatment	Test Orientation	Temp °F	Yield Strength KSI (N/m <sup>2</sup> )	Typical $K_{IC}$ KSI√in (MPa√m)	2.5 $\left(\frac{K_{IC}}{Y_s}\right)^2$ in (mm)	Specimen			Ref.
								Type	Thickness in (mm)	Width in (mm)	

(a) Fabrication and Heat Treatment in accordance with Aluminum Association Specifications.  
 (b) Specimen in accordance with ASTM Recommendations.

COMPOSITION

	Cu	Mg	Si	Fe	Mn	Zn	Ce	Ti	Pb	Az
A	1.68	2.58	0.58	0.78	0.38	5.68	0.38	0.28	-	-
B	1.6	2.50	0.10	0.15	0.02	5.65	0.19	0.02	-	-
C	1.4	2.50	0.10	0.14	0.02	5.68	0.19	0.02	-	-
D	1.48	2.58	-	-	0.158	5.88	0.28	-	-	-
E	1.68	2.58	0.68	0.58	0.38	5.88	-	-	0.028	0.028
F	0.98	2.78	0.58	0.58	0.18	5.858	0.148	0.38	2.18	0.028
G	0.92	2.5	0.09	0.15	<.01	5.85	-	-	-	0.39
H	1.68	2.58	0.158	0.28	0.318	5.68	0.248	0.18	-	-

HEAT TREATMENT

1. Stress Relieved and Aged to meet requirements of paragraph 4.10 of Federal Spec. QQ-367g, Paragraph 4.6.5.1 MIL Spec. MILA-22771C
2. 859F (733K), Water Quenched, Stretch 1.5-2.5%; Aged 275F (408K)
3. 870F (739K), Water Quench, Stretch 1.5-3%; 225F (380K), 6-8 Hr, + 525F (436K), 9 Hr.
4. Proprietary Heat Treatment

Table 39

Temper	Form	Composition, Heat Treatment	Test Orientation	Temp of (°F)	Yield Strength KSI (98N/m <sup>2</sup> )	Typical $K_{IC}$ KSI√in (YS <sup>1/2</sup> )	$2.5 \left( \frac{K_{IC}}{\sigma_{YS}} \right)^2$ in (mm)	Specimen			Ref.											
								Type	Thickness in (mm)	Width in (mm)		Crack Length in (mm)										
7178 T651	Plate: 1.375 in (34.9 mm) Thick	A, (a)	L-T	70(294)	63(572)	21(23)	0.192(4.9)	(b)	1.0 (25.4)	2.0 (50.8)	1.0 (25.4)	37										
													L-T	70(294)	78(538)	20(138)	0.164(4.2)	CT	1.0 (25.4)	2.0 (50.8)	1.0 (25.4)	41
76510	Extrusion: 0.18 to 2.2 in (4.6 to 55.9 mm) Thick	A, (a)	L-T	70(294)	86(585)	21(23)	0.150(3.8)	S2S	0.18 min (4.6)	0.9 min (22.8)	0.4 min (10.2)	42										
													L-T	70(294)	81(558)	23(25)	0.202(5.1)	(b)	1.0 (25.4)	2.0 (50.8)	1.0 (25.4)	42
76511	Plate: 1.375 in (34.9 mm) Thick	A, (a)	L-T	70(294)	73(503)	26(28)	0.317(8.1)	(b)	1.0 (25.4)	2.0 (50.8)	1.0 (25.4)	37										
													L-T	70(294)	71(490)	21(23)	0.239(5.6)	(b)	1.0 (25.4)	2.0 (50.8)	1.0 (25.4)	37
76511	Extrusion: 3.5 in (88.9 mm) Thick	A, (a)	L-T	70(294)	71(490)	28(30)	0.391(9.9)	(b)	2.0 (50.8)	4.0 (101.6)	2.0 (50.8)	37										
													L-T	70(294)	78(538)	23(25)	0.217(5.5)	(b)	1.5 (38.1)	3.0 (76.2)	1.5 (38.1)	37
76511	Extrusion: 0.688 in (17.5 mm) Thick	A, (a)	L-T	70(294)	83(572)	22(24)	0.175(4.4)	(b)	0.625(15.9)	1.25(31.8)	0.625(15.9)	61										
													L-T	70(294)	83(572)	20(22)	0.145(3.7)	(b)	0.625(15.9)	1.25(31.8)	0.625(15.9)	61
762	Extrusion: 0.4 in (10.2 mm) Thick	A, (a)	L-T	70(294)	90(620)	23(25)	0.155(4.1)	(b)	0.404(10.3)	1.5(38.1)	---	42										
													L-T	70(294)	83(573)	23(25)	0.192(4.9)	(b)	0.312(7.9)	0.940(23.9)	---	42

(a) Composition, Fabrication and Heat Treatment in accordance with Aluminum Association Specifications (b) Specimen in accordance with ASTM Recommendations

ALUMINUM, Zn-Mg Alloys: 7178 and DTD 363 (Sheet 2 of 2) Table 39

Temper	Form	Composition, Heat Treatment	Test Orientation	Temp °F (°C)	Yield Strength KSI (N/m <sup>2</sup> )	Typical $K_{IC}$ KSI√in (MPa√m)	$2.5 \left( \frac{K_{IC}}{\sigma_{YS}} \right)^2$ in (mm)	Specimen			Ref.	
								Type	Thickness in (mm)	Width in (mm)		Crack Length in (mm)
MP	Extrusion	B, -	L-T	70 (294)	87 (600)	28 (31)	0.259 (6.6)	Round	0.8 (20.5)	2.6 (66)	0.75 (19.1)	62
COMPOSITION												
		Cu	Mg	Si	Fe	Mn	Zn	Ti	Cr			
A		2.0N	2.75N	0.5N	0.7N	0.3N	6.8N	0.2N	0.29N			
B		2.0N	2.7N	-	-	-	6.8N	-	0.3N			

ALUMINUM, Zn-Mg-Mn Alloy: 7039 and 7005

Table 40

Temper	Form	Composition, Heat Treatment	Test Orientation	Temp °F (°K)	Yield Strength KSI (MN/m <sup>2</sup> )	Typical $K_{Ic}$ KSI√in (MN <sup>3/2</sup> /m <sup>3/2</sup> )	2.5 $(\frac{K_{Ic}}{\sigma})^2$ in (mm)	Specimen			Ref.	
								Type	Thickness in (mm)	Width in (mm)		Crack Length in (mm)
7039 T6	Forging: 4.0 in (101.6 mm) Thick	A, 1	T-L	70 (294)	57 (393)	19 (21)	0.277 ( 7.0)	WOL	4.0 (101.6)	16.2 (259)	4 (101.6)	45
7005 T651	Plate: 2.0 in (50.8 mm) Thick	B, 2	MR	0 (256)	59 (407)	17 (19)	0.208 ( 5.5)	WOL	4.0 (101.6)	10.2 (259)	4 (101.6)	6
			T-L	75 (294)	49 (338)	29 (32)	0.877 (22.5)	Bend	1.75 ( 44.5)	3.5 ( 89)	1.75 ( 44.5)	4
7005 T651	Plate: 3 in (76.2 mm) Thick	C, (a)	T-L	-100 (200)	53 (365)	30 (33)	0.804 (20.4)	Bend	1.75 ( 44.5)	3.5 ( 89)	1.75 ( 44.5)	5
			T-L	-321 ( 78)	58 (400)	31 (34)	0.715 (18.2)	Bend	1.75 ( 44.5)	3.5 ( 89)	1.75 ( 44.5)	5
7005 T651	Plate: 3 in (76.2 mm) Thick	C, (a)	L-T	70 (294)	53 (365)	47 (51)	1.966 (49.9)	Bend	3.0 (76.2)	6.0 (152)	3.0 (76.2)	98
			T-L	70 (294)	52 (359)	40 (44)	1.479 (37.8)	Bend	3.0 (76.2)	6.0 (152)	3.0 (76.2)	98
			S-L	70 (294)	48 (331)	28 (31)	0.851 (21.6)	CT	1.25 (31.8)	2.5 (63.5)	1.25 (31.8)	

(a) Fabrication and Heat Treatment in accordance with Aluminum Association Specification  
 (b) Specimen in Accordance with ASTM Recommendations

COMPOSITION

	Cu	Mg	Si	Fe	Mn	Zn	Cr	Ti	Zr
A	0.1M	2.8N	0.3M	0.4M	0.25N	4.0N	0.2N	0.1M	--
B	0.04	2.5	0.3M	0.4M	0.25N	3.75	0.2N	0.1M	--
C.	0.1M	1.4N	0.55M	0.35	0.45N	4.6N	0.13N	0.03N	0.13N

HEAT TREATMENT

- 850F (728K), 4Hr, Aged 320F (433K), 18 Hr
- 850F (728K), 2.5 Hr, Water Quench, Age Room Temperature, 8 Hr, Age 320F (433K), 18 Hr

ALUMINUM, Zn-Mg-Mn Alloy: 7079

Table 41

Temper	Form	Composition, Heat Treatment	Test Orientation	Temp of F (°F)	Yield Strength KSI (MN/m <sup>2</sup> )	Typical K <sub>IC</sub> KSI√in (MN m <sup>3/2</sup> )	2.5 (K <sub>IC</sub> /σ <sub>ys</sub> ) <sup>2</sup> in (mm)	Specimen			Ref.	
								Type	Thickness in (mm)	Width in (mm)		Crack Length in (mm)
T6	Plate: 1.0 in (25.4 mm) Thick	A, (a)	T-L	70(294)	75(517)	22(24)	0.215( 5.5)	SEN	1.0 (25.4)	5.0 (127.0)	1.6 (40.6)	40
	Forging: 3.0 in (76.1 mm) Thick	A, 1	L-T	75(297)	64(441)	32(35)	0.625(15.9)	MOL	2.0 (50.8)	2.25( 57.3)	1.0 (25.4)	11
			T-L	75(297)	64(441)	28(31)	0.503(12.7)	MOL	2.0 (50.8)	2.25( 57.3)	1.0 (25.4)	
			L-T	-75(214)	69(476)	33(36)	0.570(14.5)	MOL	2.0 (50.8)	2.25( 57.3)	1.0 (25.4)	
T651	Plate: 1.375 in (34.9 mm) Thick	A, (a)	L-T	70(294)	78(538)	31(34)	0.395(10.0)	Bend	1.375(34.9)	3.0 ( 76.2)	1.5 (38.1)	36
			T-L	70(294)	75(517)	25(27)	0.277( 7.0)	Bend	1.375(34.9)	3.0 ( 76.2)	1.5 (38.1)	
			T-L	-112(193)	81(558)	26(28)	0.258( 6.6)	Bend	1.380(35.1)	3.0 ( 76.2)	1.65(41.9)	39
			T-L	-320( 78)	91(627)	27(29)	0.220( 5.6)	Bend	1.380(35.1)	3.0 ( 76.2)	1.45(36.8)	
T6510	Extrusion: 0.5 in (12.7 mm) Thick	A, (a)	L-T	70(294)	74(510)	31(34)	0.439(11.1)	SEN	0.5 (12.7)	1.5 ( 38.1)	0.5 (12.7)	42
			T-L	70(294)	71(490)	29(32)	0.417(10.6)	SEN	0.5 (12.7)	1.5 ( 38.1)	0.5 (12.7)	
T652	Forging: 2.0 in (50.8 mm) Thick	B, (b)	L-T	70(294)	71(490)	28(31)	0.389( 9.9)	Bend	0.75 (19.1)	1.5 ( 38.1)	---	41
		B, (b)	T-L	70(294)	65(448)	25(27)	0.370( 9.4)	Bend	0.75 (19.1)	1.5 ( 38.1)	---	
		C, (b)	L-T	70(294)	64(441)	30(33)	0.549(13.9)	Bend	2.0 (50.8)	4.0 (101.6)	---	
			T-L	70(294)	58(400)	24(26)	0.428(10.9)	Bend	2.0 (50.8)	4.0 (101.6)	---	
			S-L	70(294)	58(400)	18(20)	0.241( 6.1)	Bend	6.5 (12.7)	1.0 ( 25.4)	---	

(a) Fabrication and Heat Treatment in accordance with Military, Federal, ASTM or Aluminum Assoc. Specifications  
 (b) Fabrication and Heat Treatment in accordance with Military, Federal, ASTM or Aluminum Assoc. Specifications

COMPOSITION

	Cu	Zn	Mg	Si	Fe	Mn	Cr	Ti
A	0.06	4.36	3.36	0.34	0.46	0.26	0.18	0.16
B	0.76	4.57	3.48	0.11	0.18	0.18	0.14	0.03
C	0.72	4.60	3.55	0.10	0.16	0.17	0.15	0.02

HEAT TREATMENT

1. Solution Treated 830F (717K); Aged 5 Days at Room Temp.; 240F (389K), 48 Hr

ALUMINUM, Zn-Mg-Mn Alloys: DTD 5024 and DTD 5094

Table 42

Temper	Form	Composition, Heat Treatment	Test Orientation	Temp °F (°K)	Yield Strength KSI (MN/m <sup>2</sup> )	Typical $K_{IC}$ KSI√in (MN m <sup>3/2</sup> )	$2.5 \left( \frac{K_{IC}}{\sigma_{ys}} \right)^2$ in (mm)	Specimen			Ref.	
								Type	Thickness in (mm)	Width in (mm)		Crack Length in (mm)
<b>DTD 5024</b>												
WP	Forging: 6 x 6 x 11 in (152 x 152 x 279 mm)	A, 1	T-S	70(294)	68(471)	19(21)	0.195 (5.0)	(a)	---	---	---	74
WP	Forging: 6 x 6 x 4 in (152 x 152 x 102 mm)	A, 1	T-L	70(294)	63(435)	18(20)	0.204 (5.2)	(a)	---	---	---	
<b>DTD 5094</b>												
WP	Forging:	B, -	L-	70(294)	61(421)	24(26)	0.39 (9.9)	Bend	0.32 (8.0)	1.5 (38.1)	0.32 (8.1)	62
			T-	70(294)	60(414)	22(24)	0.35 (8.4)	Bend	0.32 (8.0)	1.5 (38.1)	0.35 (8.9)	
			S-	70(294)	50(400)	14(15)	0.15 (3.8)	Bend	0.32 (8.0)	1.5 (38.1)	0.32 (8.1)	

(a) Specimen in accordance with ASTM Recommendations.

**COMPOSITION**

	Cu	Mg	Si	Fe	Mn	Zn	Cr	Ni	Pb
A	0.5N	2.7N	0.5M	0.5M	0.5N	5.7M	-	0.1M	0.05M
B	0.5N	2.5N	-	-	0.5N	5.5M	0.2M	-	-

**HEAT TREATMENT**

1. 859F (733K), Water Quenched at 211F (373K); Aged 275F (403K)

ALUMINUM, Zn-Mg-Mn Alloys: 7080 and M-75S

Table 43

Temper	Form	Composition, Heat Treatment	Test Orientation	Temp. °F (°K)	Yield Strength KSI (MN/m <sup>2</sup> )	Typical $K_{IC}$ KSI√in (MN m <sup>-3/2</sup> )	$2.5 \left( \frac{K_{IC}}{\sigma_{ys}} \right)^2$ in (mm)	Specimen			Ref.	
								Type	Thickness in (mm)	Width in (mm)		Crack Length in (mm)
<b>7080</b>												
T751	Plate: 1.375 in (34.9 mm) Thick	A, (a)	L-T	70 (294)	60 (414)	36 (40)	0.9 (22.9)	CT	1.0 (25.4)	2.0 (50.8)	1.0 (25.4)	61
T751X	Extrusion: 3.5 in (88.9 mm) Thick	B, (a)	T-L	70 (294)	60 (414)	29 (200)	0.58 (14.7)	CT	2.0 (50.8)	2.0 (50.8)	1.0 (25.4)	39
			L-T	70 (294)	64 (441)	38 (42)	0.88 (22.4)	Bend	1.0 (25.4)	2.0 (50.8)	1.0 (25.4)	
			T-L	70 (294)	59 (407)	26 (29)	0.49 (12.4)	Bend	2.7 (68.6)	1.0 (25.4)	0.5 (12.7)	
			S-L	70 (294)	56 (386)	23 (25)	0.42 (10.7)	CT	2.0 (50.8)	2.0 (50.8)	1.0 (25.4)	
<b>M-75S</b>												
MP		C, -	T-L	70 (294)	74 (510)	25 (28)	0.29 (7.4)	Bend	0.38 (9.7)	1.4 (35.6)	0.48 (12.2)	62

COMPOSITION							
	Cu	Mg	Si	Fe	Mn	Zn	Ti
A	0.92	2.01	0.014	0.19	0.32	6.25	0.03
B	1.12	2.04	0.04	0.14	0.39	6.08	0.03
C	1.5N	2.5N	-	-	0.25N	6.0N	0.15N

(a) Fabrication and Heat Treatment in accordance with Aluminum Association Specifications.

Table 44

Temper	Form	Composition, Heat Treatment	Test Orientation	Temp °F (°K)	Yield Strength KSI (MN/m <sup>2</sup> )	Typical $K_{IC}$ KSI√in (MN m <sup>-3/2</sup> )	$2.5 \left( \frac{K_{IC}}{\sigma_{ys}} \right)^2$ in (mm)	Specimen			Ref.	
								Type	Thickness in (mm)	Width in (mm)		Crack Length in (mm)
T651	Plate: 1.5 in (38.1 mm) Thick	A, (a)	T-L	70 (294)	43 (296)	26 (28)	0.914 (23.2)	Bend	1.5 (38.1)	3.0 (76.2)	1.5 (38.1)	39
			T-L	-112 (193)	45 (310)	30 (33)	1.111 (28.2)	Bend	1.5 (38.1)	3.0 (76.2)	1.5 (38.1)	
	Plate: 3 in (76.2 mm) Thick	A, (a)	L-T	70 (294)	42 (290)	30 (33)	1.276 (32.4)	Bend	3.0 (76.2)	6.0 (152)	3.0 (76.2)	98
			T-L	70 (294)	41 (283)	27 (30)	1.084 (27.5)	Bend	3.0 (76.2)	6.0 (152)	3.0 (76.2)	
			S-L	70 (294)	40 (276)	21 (23)	0.689 (17.5)	Bend	3.0 (76.2)	6.0 (152)	3.0 (76.2)	

(a) Fabrication and Heat Treatment in Accordance with Aluminum Association Standards

COMPOSITION

Cu	Mg	Si	Fe	Mn	Zn	Ti	Cr
A	0.28N	1.0N	0.6N	0.7M	0.15M	0.25M	0.15M 0.2N



Table 45

Form	Composition, Heat Treatment	Test Orientation	Temp °F (°K)	Yield Strength KSI (MN/m <sup>2</sup> )	Typical $K_{IC}$ KSI/√in (MN m <sup>-3/2</sup> )	$2.5 \left( \frac{K_{IC}}{\sigma_{ys}} \right)^2$ in (mm)	Specimen			Ref.	
							Type	Thickness in (mm)	Width in (mm)		Crack Length in (mm)
Hot Pressed: 30 in (762 mm) Dia x 32 in (813 mm) Long Forged: 16 in (406 mm) Dia x 1 in (25.4 mm) Thick	A, -	---	70(294)	37(255)	10(11)	0.183 (4.6)	Bend	0.5 (12.7)	1.0 (25.4)	0.25 (6.4)	86
	B, -	---	70(294)	61(421)	11(12.1)	0.81 (2.1)	Bend	0.5 (12.7)	1.0 (25.4)	0.25 (6.4)	

COMPOSITION (ppm)						
Be	Fe	C	Al	Mg	Si	Be
A	16,500	1180	1000	700	40	300
B	17,100	1280	1300	400	110	260

K<sub>C</sub> Results (Figure 1)

Table 46

Form	Composition, Heat Treatment	Test Orientation	Temp		Yield Strength KSI (MN/m <sup>2</sup> )	Typical K <sub>C</sub> KSI/√in (MN m <sup>-3/2</sup> )	2.5 (K <sub>C</sub> <sup>2</sup> / σ <sub>ys</sub> ) in (mm)	Specimen			Ref.	
			°F	(°K)				Type	Thickness in (mm)	Width in (mm)		Crack Length in (mm)
<b>Maraging Steel 300 Grade</b>												
A,1	A,1	T-L	70(294)		318(2193)	109(120)	0.294 (7.5)	CC	0.030(0.76)	2 (50.8)	---	88
					323(2227)	123(135)	0.362 (9.2)	CC	0.038(0.97)	2 (50.8)	---	
					322(2220)	119(131)	0.341 (8.7)	CC	0.058(1.47)	2 (50.8)	---	
					315(2172)	126(139)	0.400 (10.2)	CC	0.077(1.96)	2 (50.8)	---	
					310(2144)	148(163)	0.570 (14.5)	CC	0.121(3.07)	2 (50.8)	---	
					307(2117)	62(68)	0.102 (2.6)	CC	0.200(5.08)	2 (50.8)	---	
<b>Ti-4Al-3Mo-1V</b>												
B,2	B,2	T-L	70(294)		162(1117)	50(55)	0.238 (6.0)	CC	0.42 (1.07)	12 (305)	---	89
					153(1055)	55(61)	0.323 (8.2)	CC	0.58 (1.47)	12 (305)	---	
					153(1055)	63(69)	0.424 (10.8)	CC	0.87 (2.2)	12 (305)	---	
					160(1103)	35(39)	0.120 (3.0)	CC	0.124(3.15)	12 (305)	---	
<b>7025-17351</b>												
C,(a)	C,(a)	L-T	70(294)		58(399)	74(81)	4.07 (103)	CC	0.62 (1.37)	8 (203)	---	87
					60(413)	95(105)	6.27 (159)	CC	0.25 (6.35)	16 (406)	---	
					62(427)	70(77)	3.18 (8.09)	CC	0.50 (12.7)	6 (203)	---	
					61(421)	41(45)	2.38 (60.5)	CC	1.0 (25.4)	8 (203)	---	
					61(421)	52(57)		CC	1.0 (25.4)	16 (400)	---	

(a) Fabrication and Heat Treatment in accordance with ASTM Recommendations.

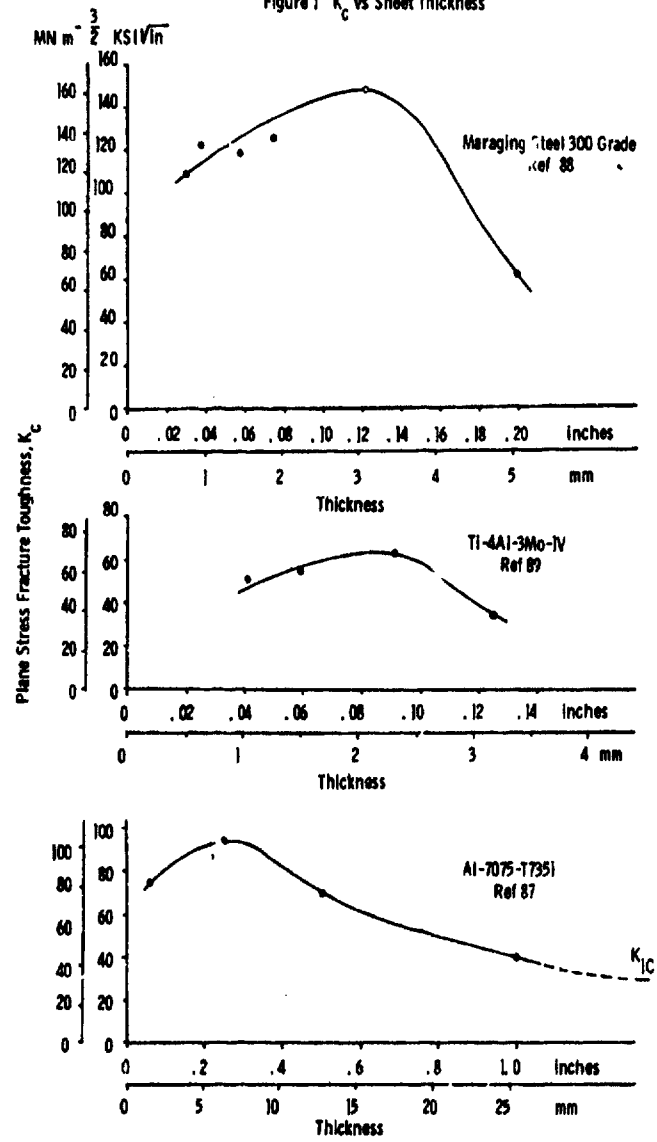
HEAT TREATMENT

1. 1650F (1172K), 1 Hr, Water Quenched; Aged 900F (756K), 3 Hr

2. 1650F (1172K), 15 Minutes, Water Spray Quench; Age 925F (770K), 14 Hr, Air Cool

COMPOSITION

	C	Mn	P	S	Si	Ni	Co	Mo	Ti	Al	N	H	B	Cu	Fe	Mg	Zr	Ce	V
A	0.015	0.021	0.001	0.010	0.080	17.2	8.26	4.76	0.99	0.095	0.003	-	0.003	-	Bal	-	-	-	-
B	0.817	-	-	-	-	0.05	-	3.0N	Bal	4.25N	-	0.015	-	0.25M	-	-	-	-	1.0N
C	-	0.3M	-	-	0.5M	-	-	-	0.2M	Bal	-	-	1.6N	0.7M	2.5N	5.6N	0.3N	-	-

Figure 1  $K_{IC}$  vs Sheet Thickness

## APPENDIX 2

## FRACTURE TOUGHNESS TEST RESULTS

W. T. Kirkby

## INTRODUCTION

This list gives valid fracture toughness test results from tests which conform to the recommendations of the American Society for Testing Materials (STP 410 - 1967) and the corresponding British Standards Institution recommendations (BSI Draft for Development No 3 - 1971).

Data for titanium alloys, steels and aluminium alloys have been collated. The composition of the alloys, their form, their treatments and the fracture plane orientation of the fracture toughness test pieces are given. Tensile test results for the various heat treatments are included. The results have been obtained from room temperature tests.

## PRESENTATION OF DATA

Tensile and fracture toughness test results for titanium alloys are given in Table 1, together with the alloy form, the heat treatment and the crack plane orientation of the fracture toughness test piece. Tensile test results and related  $K_{1C}$  values are from the same batch of material. In general, the tensile test results are average figures from a number of tests. The  $K_{1C}$  figures are actual values obtained on testing and thus an indication of the degree of scatter in  $K_{1C}$  is provided. Insufficient data is available to allow meaningful standard deviations or coefficients of variation to be derived.

The designation of the plane strain fracture plane, which is coincident with the notch orientation, follows the practice recommended in British Standard Draft for Development No 3, Appendix D which uses three reference axes for non-cylindrical sections as follows:

- L = longitudinal, ie parallel to the grain flow
- T = transverse, ie in the direction of minimum movement
- S = short transverse, ie across the plane of maximum material deformation.

"Using a two letter code the first letter will indicate the direction perpendicular to the crack plane and the second the direction of the crack front movement."

For cylindrical sections the axes are designated:

- L = the long axis of the cylinder
- C = a circumferential axis
- R = radial axis.

The tensile test direction is such that the long axis of the test piece is perpendicular to the fracture plane orientation of the fracture toughness test piece.

The heat treatments are, in general, those actually used. Where the actual heat treatment was not available, that recommended in the appropriate specification is given.

The compositions of titanium alloys are listed in Table 2. Actual analyses are given where available and specification composition ranges are given in other cases. The index number in the first column of Tables 1 and 2 relates the material test results to its composition in the two tables.

A similar presentation has been made of the data for steels in Table 3 for results etc., and in Table 4 for steel compositions. Actual analyses are listed for the majority of the steels.

Again, a similar presentation has been made for Aluminium alloy data in Table 5 and aluminium alloy compositions in Table 6. The heat treatments listed are, in the main, the heat treatments recommended in the appropriate specifications. In Table 5 the alloys have been listed in order of their numerical designation and therefore alloys of similar composition are not necessarily adjacent to one another in the table. Specification compositions rather than actual analyses are given in Table 6.

## ACKNOWLEDGMENTS

The references list the sources of data used in the tables and thanks are due to the following for permission to use the data:

Imperial Metal Industries Ltd., Index Nos 3-6, 9-18, 21 and 22  
 British Aircraft Corporation Ltd., Index Nos 8, 10, 20, 29, 35 and 47  
 Iron and Steel Institute, Index No 19  
 British Steel Corporation, Index Nos 23, 24, and 27  
 Firth Brown Ltd., Index Nos 31-34  
 Publishers of Welding and Metal Fabrication, Index No 39

Acknowledgment is made to Hawker Siddeley Aviation Ltd, to Fulmer Research Institute and to High Duty Alloys Ltd for results determined during work sponsored by the UK Ministry of Defence (Procurement Executive.) Thanks also due to Materials Department, RAE for the provision of unpublished test results.

## REFERENCES

1. A. A. Braithwaite Unpublished work Procurement Executive, Ministry of Defence.
2. M. Broadway Private Communication, Imperial Metals Industries Ltd, New Metals Division.
3. M. J. Rea Research into the improvement of fracture toughness of high strength titanium alloys and the reduction of cracking susceptibility in aqueous environment  
 High Duty Alloys Ltd Research Div Rep No 1 SX 5663/1  
 March 1971
4. M. R. Armitage Private communication. British Aircraft Corporation, Preston.
5. K. T. Lee Relationship between fracture toughness plain tensile  
 R. J. Hubbard properties and metallurgical structure of a titanium alloy.  
 Iron and Steel Inst Publication 120, 1970. Fracture Toughness  
 of High Strength Materials.
6. J. I. Norwood A comparison of the strength and tensile properties of several  
 high strength steels.  
 British Steel Corporation Report 88D 33/70 P 25/PD Oct 1970.
7. D. S. McDermid Unpublished work Procurement Executive, Ministry of Defence.
8. J. Bayliss The effect of microstructure on the crack propagation resis-  
 T. J. Baker tance of high strength steels for aircraft applications.  
 M. A. Dewey Fulmer Research Inst Rep R 30/2/Dec 1970.
9. Maraging Steels  
 Firth Brown Ltd Publication November 1971.
10. C. Roberts Fractography and Fracture Mechanics  
 Ministry of Defence NVEE Report No 70505 May 1970.
11. M. S. Binning Unpublished work Procurement Executive, Ministry of Defence
12. T. Chisholm Plane strain fracture toughness of electron beam welds in HD  
 P. Reuter 66, 54, and 48 aluminium alloy plate.  
 Weld and Met Fab, June 1971 39 6 235-241.
13. C. J. Peel The fracture toughness of Al Zn Mg Cu Mn alloys to DTD 5024.  
 P. J. E. Forsyth Royal Aircraft Establishment Tech Rep 70162 Sept 1970.
14. C. J. Peel Unpublished work Procurement Executive, Ministry of Defence.  
 P. J. E. Forsyth
15. A. R. Simpson Aluminium alloy plates - an evaluation of the scatter in  
 J. Fielding  $K_{Ic}$  values.  
 Hawker-Siddeley Aviation Ltd.  
 Report ER/MISC/MAN/1050. July 1971.
16. R.A. Wood "Titanium Alloys Handbook," MCIC-HB-02, Metals and Ceramic  
 Information Center, Battelle, December 1972

Table 1. TENSILE PROPERTIES AND FRACTURE TOUGHNESS

Index No.	Alloy designation	Size and form	Treatment	0.2% proof stress		Tensile strength		Elongation	Reduction of area	K <sub>IC</sub>		Reference
				ksi	MPa	ksi	MPa			ksi√in	MPa√m	
1	Ti-6Al-4V (IMI 310)	57.5mm x 25.5mm rectangular bar	811 annealed (700°C AC) 76 850°C AC - 76 875°C AC	882.5 872.2	607.5 607.5	728 728	503.5 503.5	15 15	28 28	57.0 57.0	57.0 57.0	2
2	Ti-6Al-4V (IMI 310)	50.8mm diameter bar	200°C AC	882.5	607.5	728	503.5	17	37	57.0	57.0	2
3	Ti-6Al-4V (IMI 310)	7mm bar	oil tempered - 100°C AC • • • 570°C AC - 700°C AC	872	607	727.3	503	15 21	44 52	56.7 56.7	56.5 56.5	•
4	Ti-6Al-4V (IMI 310)	50mm bar	tempered during 8 → 6 → 8 - 700°C AC • • • 570°C AC - 700°C AC	1059	740	755.0	522	12 21	44 47	61.7 61.7	61.7 61.7	•
5	Ti-6Al-4V (IMI 310)	20mm square bar	8 tempered - 100°C AC	872	607	727.7	503	11	22	52.5	52.5	•
6	Ti-6Al-4V (IMI 310)	7mm x 50mm bar	oil tempered - 700°C AC • • • 570°C AC - 700°C AC • • • 570°C AC - 700°C AC • • • 1070°C AC - 700°C AC	872 882 882	607 607 607	727.7 727.7 727.7	503 503 503	15 21 12	44 44 44	61.7 61.7 61.7	61.7 61.7 61.7	•
7	Ti-6Al-4V -25% -0.5% (IMI 550)	65.2mm x 15.5mm bar	76 800°C AC 76 800°C AC 200 800°C • • • 810°C AC 200 800°C	846.7 822	589.7 589.7	737.3 734.5	512 512	11 11 11	27 27 27	57.4 57.4	57.4 57.4	•
8	Ti-6Al-4V -25% -0.5% (IMI 550)	50.8mm x 68.5mm bar	800°C AC 200 800°C	822	589.7	734.5	512	11 11	27 27	57.4 57.4	57.4 57.4	•
9	Ti-6Al-4V -25% -0.5% (IMI 550)	21.75mm plate	40 800°C AC 200 800°C 76 800°C AC 200 800°C 76 800°C AC 40 800°C AC 200 800°C	845 822	589 589	740 738.2	512 512	10 10 10	37 38 40	55.4 55.4	55.4 55.4	•
10	Ti-6Al-4V -25% -0.5% (IMI 550)	21.75mm thick plate	40 800°C AC 200 800°C 76 800°C AC 200 800°C 76 800°C AC 40 800°C AC 200 800°C	822 822	589 589	740 737	512 512	10 10 10	40 40 40	55.4 55.4	55.4 55.4	•
11	Ti-6Al-4V -25% -0.5% (IMI 550)	5mm thick plate	26 800°C AC 200 800°C • • • 26 800°C AC 200 800°C	774 774	553 553	770.3 770.3	522 522	11 11	37 37	61.7 61.7	61.7 61.7	•

Table 1 (continued)

Index No.	Alloy designation	Size and form	Treatment	U. S. steel strength		Tensile strength		Elongation %	Reduction of area %	$R_{10}$		Fracture zone orientation	Reference
				ksi	MPa	ksi	MPa			ksi	MPa		
12	Ti-6Al-4V -Zr-0.5Si (IM 550)	40L Ann x 5mm sheet plate	anneal	1740	1225	177.7	1225	18	37	48.5	38.8	45°	A
				1720	1225	177.7	1225	16	35	48.9	41.5	45°	
13	Ti-6Al-4V -Zr-0.5Si (IM 550)	12mm x 2.5mm forging	anneal	1870	1343	181.3	1343	15	24	30.2	33.6	45°	A
				1850	1336	181.3	1336	12	25	30.7	34.3	45°	
				1820	1322	181.3	1322	14	21	45.2	41.1	45°	
				1810	1314	181.3	1314	12	21	45.2	41.1	45°	
14	Ti-6Al-4V -Zr-0.5Si (IM 550)	Forging	anneal	1850	1336	182.3	1336	12	42	34.6	40.7	45°	A
				1840	1328	182.3	1328	17	47	35.1	41.0	45°	
				1830	1319	182.3	1319	15	35	45.3	41.2	45°	
				1820	1311	182.3	1311	16	35	45.3	41.2	45°	
15	Ti-6Al-4V -Zr-0.5Si (IM 550)	Extrusion	anneal	1840	1328	182.6	1328	17	28	36.4	34.0	45°	A
				1830	1319	182.6	1319	17	30	36.5	34.2	45°	
				1820	1311	182.6	1311	17	30	36.5	34.2	45°	
				1810	1303	182.6	1303	17	30	36.5	34.2	45°	
16	Ti-6Al-4V -Zr-0.5Si (IM 550)	Extrusion	anneal	1840	1328	182.6	1328	17	30	36.4	34.0	45°	A
				1830	1319	182.6	1319	17	30	36.5	34.2	45°	
				1820	1311	182.6	1311	17	30	36.5	34.2	45°	
				1810	1303	182.6	1303	17	30	36.5	34.2	45°	
17	Ti-6Al-4V -Zr-0.5Si (IM 550)	Rolling square bar	anneal	1820	1311	182.6	1311	17	30	36.4	34.0	45°	A
				1810	1303	182.6	1303	17	30	36.5	34.2	45°	
				1800	1295	182.6	1295	17	30	36.5	34.2	45°	
				1790	1287	182.6	1287	17	30	36.5	34.2	45°	
18	Ti-6Al-4V -Zr-0.5Si (IM 550)	25.4mm bar	anneal	1840	1328	182.6	1328	15	40	34.6	31.5	45°	A
				1830	1319	182.6	1319	15	40	34.6	31.5	45°	
				1820	1311	182.6	1311	15	40	34.6	31.5	45°	
				1810	1303	182.6	1303	15	40	34.6	31.5	45°	
19	Ti-6Al-4V -Zr-0.5Si (IM 550)	Thin sheet temped 6hr	temped 6hr	1810	1303	182.6	1303	4	8	38.9	38.0	45°	B
				1800	1295	182.6	1295	4	8	38.9	38.0	45°	
				1790	1287	182.6	1287	4	8	38.9	38.0	45°	
				1780	1279	182.6	1279	4	8	38.9	38.0	45°	





Table 2  
COMPOSITION OF TITANIUM ALLOYS

Index No.	Alloy designation	Weight %																		
		Al	Mo	V	Sn	Fe	Si	O	N	H	Zr									
1	IMI 318 (1)	6.18		3.91		0.07														
2	IMI 318 (1)	6.56		4.24		0.7					0.16			0.007						
3, 4 & 5	IMI 318 (1)	6.03		3.93		0.15						0.2								
6	IMI 318 (2)	5.5-6.75		3.5-4.5		0.3 max														
7	IMI 550 (1)	4.0	3.95		2.19	0.12					0.54									
8	IMI 550 (2)	3.0-5.0	3.0-5.0		1.5-2.5	0.2 max					0.3-0.7									
9	IMI 550 (1)	4.10	3.97		2.00						0.67	0.185								
10	IMI 550 (1)	4.125	4.08		2.04						0.48	0.19								
11	IMI 550 (1)	4.00	3.99		2.10						0.48	0.24								
12	IMI 550 (1)	4.00	3.95		2.04						0.41	0.19								
13 & 14	IMI 550 (1)	4.02	4.03		2.10						0.46	0.14								
15	IMI 550 (1)	4.11	3.95		2.00						0.53	0.2								
16 & 17	IMI 551 (1)	4.08	3.89		3.97						0.55	0.2								
18	IMI 551 (1)	3.93	4.02		4.10						0.48	0.19								
19 & 20	IMI 600 (2)	2.0-2.5	3.5-4.5		10.5-11.5	0.2 max					0.1-0.3									
21 & 22	IMI 605 (1)	6.06	0.5								0.18	0.15								4.57

(1) Actual analysis  
(2) Specification composition.

Table 2

STEELS - TENSILE PROPERTIES AND FRACTURE CHARACTERISTICS

Index No.	Alloy designation	Size and form	Treatment	0.2% proof stress ksi / MPa	Tensile strength ksi / MPa	Elongation %	Reduction of area %	$\sigma_y / \sigma_u$	Fracture surface orientation	Reference
21	A5 (A533)	25.4mm diameter bar, etc. normalized	800°C AC 200°C 2h 200°C 2h 200°C	1469	772.9	22.8	29.8	27.8	45.7	L-H
				1636	244.9	228	29.3	25.7	45	
26	302 B	72.9mm diameter bar, etc. normalized	800°C AC 200°C 2h 200°C 2h 200°C	1482	775.9	24.9	29.3	27.5	45.5	L-H
				1636	244.9	228	29.3	25.7	45	
25	A533 B	25.4mm diameter bar, etc. normalized	800°C AC 200°C 2h 200°C 2h 200°C	1467	772.7	22.8	29.3	27.5	45.5	L-H
				1636	244.9	228	29.3	25.7	45	
26	A533 B	72.9mm diameter bar, etc. normalized	800°C AC 200°C 2h 200°C 2h 200°C	1467	772.7	22.8	29.3	27.5	45.5	L-H
				1636	244.9	228	29.3	25.7	45	
25	A533 B	25.4mm diameter bar, etc. normalized	800°C AC 200°C 2h 200°C 2h 200°C	1467	772.7	22.8	29.3	27.5	45.5	L-H
				1636	244.9	228	29.3	25.7	45	
26	A533 B	72.9mm diameter bar, etc. normalized	800°C AC 200°C 2h 200°C 2h 200°C	1467	772.7	22.8	29.3	27.5	45.5	L-H
				1636	244.9	228	29.3	25.7	45	
27	A533 B	25.4mm diameter bar, etc. normalized	800°C AC 200°C 2h 200°C 2h 200°C	1467	772.7	22.8	29.3	27.5	45.5	L-H
				1636	244.9	228	29.3	25.7	45	
28	A533 B	72.9mm diameter bar, etc. normalized	800°C AC 200°C 2h 200°C 2h 200°C	1467	772.7	22.8	29.3	27.5	45.5	L-H
				1636	244.9	228	29.3	25.7	45	
29	A533 B	25.4mm diameter bar, etc. normalized	800°C AC 200°C 2h 200°C 2h 200°C	1467	772.7	22.8	29.3	27.5	45.5	L-H
				1636	244.9	228	29.3	25.7	45	
30	A533 B	72.9mm diameter bar, etc. normalized	800°C AC 200°C 2h 200°C 2h 200°C	1467	772.7	22.8	29.3	27.5	45.5	L-H
				1636	244.9	228	29.3	25.7	45	

Table 2 (continued)

Index No.	Alley description	Size and type	Treatment	0.2% roof slope		Tensile strength		Dispersion %	Reaction of area %	$\epsilon_{1c}$		Fracture of the reinforcement	Reference
				MPa <sup>2</sup>	ksi	MPa <sup>2</sup>	ksi			MPa $\sqrt{ft}$	ksi $\sqrt{ft}$		
21	105 ft sampling steel (S 170)	72mm square for double wt. method	cast in concrete	1000	292					81.5 79.2 82.5	88.7 86.5 89.9	2	11
22	105 ft sampling steel (S 170)	20mm square for double wt. method	cast in concrete	1790	290					88.7 88.3 88.7	87.5 84.9 88.9	2	11
23	105 ft sampling steel (S 170)	25mm square for double wt. method	cast in concrete	1000	290					88.3 91.4 88.7	88.7 92.2 85.3	2	11
24	105 ft sampling steel (S 173)	150mm x 150mm double wt. method	cast in concrete	2000	290	2000	290			86.9 88.8 71.4 86.2 88.8	88.1 92.5 85.8 88.2 88.5	2	11
25	105 ft sampling steel	100mm round casting	cast in concrete	1627	235	1751	254	7		71.1	84.7		6
26	105 ft sampling steel	50.8mm thick plate	cast in concrete	1200	192	1460	204	12.5	44.2	100.5 102.5 97.5	100.5 102.7 97.8	2	12
				1226	192	1381	213.5	12.5	46.3	102.3 117 105.3	102.9 97.8 101.5	2	12
27	105 ft sampling steel	50.8mm thick plate	cast in concrete	1330	193.5	1460	204	12.5	38.5	87.8 85.3 85.4	90.2 87.8 87.7	2	12
				1517	193.3	1460	204	12.5	35.7	105.3 87.8 85.3	101.5 97.8 101.5	2	12
28	105 ft sampling steel	50.8mm thick plate	cast in concrete	1322	198.8	1377	205.8	2.8	2.7	81.8 81.2 81.2	84.9 81.5 81.2	2	12
				1266	198.8	1467	204.8	1.5	4.5	81.8 81.2 81.2	84.9 81.5 81.2	2	12
				1385	198.8	1428	203.5	1.5	4.5	81.8 81.2 81.2	84.9 81.5 81.2	2	12

Table 4  
COMPOSITION OF STEELS

Index No.	Alloy designation	Weight %											
		C	Mn	P	S	Si	Ni	Cr	Mo	V	Co	Al	Ti
23	D6 AC (1) (AMS 6431A)	0.47	0.90	0.01	0.007	0.3	0.55	0.10	0.92	0.10		0.026	
24	300 M (1)	0.42	0.73	0.009	0.006	1.45	1.82	0.98	0.4	0.11	-	0.029	
25	Rex 685 (1) (300 M)	0.44	0.81	0.005	0.006	1.69	1.34	0.85	0.38	0.90			
26	AISI 4337 (1)	0.43	0.63	0.013	0.004	0.24	1.56	1.03	0.3				
27	35 WCD 16 (1) S(012)	0.35	0.33	0.009	0.009	0.27	3.99	1.69	0.44	0.05	-	0.026	
28	FV 520 B (2)	0.07 max	1.0 max	0.035 max	0.025 max	0.6 max	5.0-5.6	13.2-14.7 + Cu 1.2-2.0, Mo 0.2-0.5					
29	18% Ni maraging steel (DID 5212) (2)	0.015 max	0.1 max	0.01 max	0.01 max	0.01 max	17.0-19.0	0.25 max	4.6-5.2		7.0-8.5	0.05-0.15	0.3-0.6
30	18% Ni maraging steel (G 110) (1)	0.003	0.05	0.005	0.004	0.05	18.3	0.05	4.72		7.64	0.119	0.8
31, 32 & 33	G 110 (2)	0.01	0.05	0.005	0.005	0.05	17.5		4.85	0.10	8.0	0.50	
34	G 125 (2)	0.01	0.05	0.005	0.005	0.05	18.5		4.85	0.10	9.0	0.75	
35	18% Ni maraging steel (2)	0.03 max	0.1 max	0.01 max	0.01 max	0.1 max	16.0-17.5	0.25 max	4.4-4.9	-	9.6-11.0	0.07-0.15	0.15-0.60
36	18% Ni maraging steel (2)	0.03 max	0.12 max	0.01 max	0.01 max	0.12 max	17.0-19.0	0.50 max	3.0-3.5	-	8.0-9.0	0.05-0.15	0.20-0.35

(1) Actual analysis

(2) Specification composition

Table 5  
ALUMINUM ALLOYS - TENSILE PROPERTIES AND FRACTURE TOUGHNESS

Index No.	Alloy designation	Size and form	Treatment	0.2% proof stress		Tensile strength		Elongation %	Reduction of area %	$K_{Ic}$ $ksi \sqrt{in}$	Fracture plane orientation	Reference
				MPa	ksi	MPa	ksi					
37	6061 S20	76.2mm thick plate	W (305°C 90 stretch 1.5-2.9% - 100-100°C)	438.8	63.8	577.8	83.3 (average of 12 tests)	14		28.1 28.2 27.3	L-1	13
38	6061 S20	25.4mm thick plate	W (305°C 90 stretch 1.5-2.9% - 100-100°C)	404.0	58.6	474.4	68.8	12		25.7 26.0 26.2	L-1	13
39	6061 S5	12.7mm thick plate	W (300°C 90 135-185°C)	425.4	61.7	472.3	66.5	10.5		23.4 24.7 24.5	L-5	14
40	6061 S20	27mm x 152mm x 152mm forging	W (400°C 90 at 100°C - 135°C)	429.0	62.2	482.6	70.0	8.7		22.1 21.6 20.9	L-5	13
41	6061 S20	152mm x 152mm x 102mm forging	W (400°C 90 at 100°C - 135°C)	435	63.1	534.4	77.5 (average of 3 tests)	10.5		21.3 15.4 17.1	L-4	16
42	6061 S20	76.2mm thick plate	W (400°C 90 stretch 1.5-2.9% - 135°C)	527.8	75.7	576.2	82.7 (average of 12 tests)	15.4		19.0 21.2 20.6 20.5 20.3 21.3 21.3 21.9	L-1	13
				487.8	69.9	550.9	80.2	12		20.7 21.0 21.1 20.8	L-5	
										22.6 23.3 23.0 22.7 22.8	L-1	
										20.6 21.2 20.9 20.7 20.6	L-1	
										22.8 22.7 23.1	L-1	
										21.7 21.8 21.0	L-5	
										24.3 24.6 24.3 24.7	L-5	



**Table 6**  
**SPECIFICATION COMPOSITION OF ALUMINIUM ALLOYS**

Index No.	Alloy designation	Weight %									
		Cu	Mg	Si	Fe	Mn	Ni	Zn	Pb	Cr	
37 & 38	DTD 5020A	3.8-4.8	0.4-0.85	0.6-0.9	1.0 max	0.4-1.2	0.2 max	0.2 max			
39	HID 66	as for DTD 5020									
40 & 41	DTD 5024	0.3-0.7	2.2-3.2	0.5 max	0.5 max	0.3-0.7	0.1 max	5.2-6.2	0.05 max		
42	DTD 5050	0.3-1.5	2.2-3.2	0.5 max	0.5 max	0.1 max	0.05 max	5.2-6.5	0.08-0.25	(Cr + Mn 0.18-0.5)	
43	DTD 5090	3.8-4.9	1.2-1.8	0.5 max	0.5 max	0.3-0.9	0.05 max	0.2 max	0.05 max		
44 & 45	CH 0030	1.8-2.7	1.2-1.8	0.25 max	0.9-1.4	0.2 max	0.8-1.4	0.1 max	0.05 max		
46	L77	3.9-5.0	0.2-0.8	0.5-0.9	0.5 max	0.4-1.2	0.2 max	0.2 max	0.05 max		
47	L93	3.9-5.0	0.2-0.8	0.5-0.9	0.5 max	0.4-1.2	0.2 max	0.2 max	0.05 max		
48	L95	1.2-2.0	2.1-2.9	0.4 max	0.5 max	0.3 max	0.05 max	5.1-6.4	0.05 max		

APPENDIX 3  
STRESS INTENSITY FACTOR SOLUTIONS  
D. P. Rooke and D. J. Cartwright

Introduction

This appendix contains the titles and references of approximately 140 configurations for which stress intensity factors have been determined. Section 1 gives the titles of the various configurations together with reference numbers, which are detailed in section 2. The solutions are given in graphical form together with relevant formulae in:

"A compendium of stress intensity factors"  
by D.P. Rooke and D.J. Cartwright

published in the United Kingdom by Her Majesty's Stationery Office.

SECTION 1

FLAT SHEETS

Stress boundary conditions

1	Slant crack in an infinite sheet: biaxial tension.	[1]
2	Central slant crack in a rectangular sheet: uniaxial tension.	[2]
3	Central slant crack in a rectangular sheet: uniaxial tension (parabolic distribution).	[2]
4	Circular arc crack in an infinite sheet: uniaxial or biaxial tension.	[3]
5	Crack in a semi-infinite sheet: uniaxial tension.	[4,5]
6	Semi-infinite crack in half-plane: constant load or constant moment.	[6]
7	Two collinear semi-infinite cracks in an infinite sheet: constant load or constant moment.	[6]
8	Central crack in a finite width sheet: uniaxial tension.	[5,7,8,9,10,11,12]
9	Central crack in a rectangular sheet: uniaxial tension.	[11,13]
10	Eccentric crack in a finite width sheet: uniaxial tension.	[14]
11	Crack in infinite sheet: bending.	[3]
12	Central crack in a finite width sheet: bending.	[5,15]
13	Single edge crack in a finite width sheet: uniaxial tension with or without bending constraints.	[16,17,18]
14	Single edge crack in a rectangular sheet: uniaxial tension with or without constrained ends.	[19,20]
15	Single edge crack in a finite width sheet: bending.	[18,21]
16	Long single edge crack in a finite height sheet: bending	[22]
17	Single edge crack in a finite width sheet: 3 point bending.	[18,23]
18	Slant edge crack in finite width sheet: uniaxial tension.	[24]
19	Double edge cracks in a rectangular sheet: uniaxial tension with or without constrained ends.	[7,25,26]
20	Edge crack in a cantilever beam: end loading.	[24]
21	Slant edge crack in a rectangular sheet: bending.	[24]
22	One or two cracks at the edge of a circular hole in an infinite sheet: uniaxial or biaxial tension.	[27]
23	Two cracks at the edge of a circular hole in a rectangular sheet: uniaxial tension.	[28]
24	Two cracks at the edge of an elliptical hole in an infinite sheet: uniaxial tension.	[28]
25	Two cracks at the edge of a rectangular hole in an infinite sheet: uniaxial tension.	[29]



26	Crack near a circular hole in an infinite sheet: uniaxial tension.	[30]
27	Crack near a circular hole in an infinite sheet: bending.	[30]
28	Crack near a circular elastic inclusion in an infinite sheet: uniaxial tension.	[31,32]
29	Crack between two circular holes, on the crack line, in an infinite sheet: uniaxial tension.	[28]
30	Crack between two circular holes, not on the crack line, in an infinite sheet: uniaxial tension.	[28]
31	Two equal length collinear cracks in an infinite sheet: uniaxial tension or shear.	[33,34]
32	Two equal length collinear cracks in a finite height sheet: uniaxial tension.	[35,36]
33	Two unequal collinear cracks in an infinite sheet: uniaxial tension or shear.	[37,38]
34	Two parallel overlapping cracks in an infinite sheet: uniaxial tension.	[38,39]
35	Two parallel overlapping cracks in an infinite sheet: shear.	[38]
36	Two equally inclined cracks in an infinite sheet: uniaxial tension.	[38]
37	Odd number of periodic collinear cracks in an infinite sheet: uniaxial tension or shear.	[38]
38	Infinite array of periodic collinear cracks in an infinite sheet: uniaxial tension or shear.	[38,40,41,42,43]
39	Odd number of periodic parallel cracks in an infinite sheet: uniaxial tension or shear.	[38]
40	Infinite array of periodic parallel cracks in an infinite sheet: uniaxial tension or shear.	[38,44,45]
41	Radial crack in a hollow cylinder: internal pressure.	[46]
42	Radial crack in a hollow cylinder: external radial tension.	[47]
43	Internal radial crack in a rotating disc.	[48]
44	Radial edge crack in a rotating disc.	[49]
Displacement boundary conditions		
45	Edge crack in a rectangular sheet: uniform displacement.	[50]
46	Single edge crack in a rectangular sheet: linearly varying end displacement.	[50,51,52]
47	Edge crack in a rectangular sheet: rotation of ends.	[53]
48	Two collinear cracks in a finite height sheet: uniform displacement.	[35,36]
49	Long edge crack in a finite height sheet: uniform displacement.	[22,54]
Point loading		
50	Crack in an infinite sheet: point force.	[55]
51	Crack in an infinite sheet: point moment.	[55]
52	Periodic array of collinear cracks in an infinite sheet: periodic array of point forces on crack centreline.	[56]
53	Periodic array of collinear cracks in an infinite sheet: periodic array of point forces on lines of symmetry between cracks.	[56]
54	Crack at the centre of a disc: diametral compressive forces collinear with crack.	[57,58]
55	Crack at the centre of a disc: symmetrical radial forces in disc perpendicular to crack.	[57,58]
56	Radial crack in disc: tensile forces perpendicular to crack at edge of disc.	[57,58]
Crack line boundary conditions		
57	Crack in an infinite sheet: point force.	[1,55]
58	Crack in an infinite sheet: distribution of tensile or shear forces.	[1]

59	Long edge crack in an infinite sheet: wedge opening displacement.	[59]
60	Long edge crack in an infinite sheet: point forces.	[55]
61	Long double edge cracks in an infinite sheet: point forces.	[55]
62	Crack in a finite height sheet: point force.	[60]
63	Crack in a finite height sheet: uniform pressure.	[35,60,61]
64	Central slant crack in a rectangular sheet: uniform pressure.	[24]
65	Crack in a finite height sheet: uniform shear.	[60]
66	Central slant crack in a rectangular sheet: uniform shear.	[24]
67	Long edge crack in a slender beam: uniform moment.	[22]
68	Crack in a finite height sheet: uniform moment.	[60]
69	Crack in an infinite sheet: wedge opening displacement and uniform pressure.	[62]
70	Crack in a finite height sheet: wedge opening displacement.	[35]
71	Long edge crack in a rectangular sheet: splitting forces.	[63]
72	Single edge crack in a tapered sheet: splitting forces.	[63]
73	Long edge crack in a slender beam: splitting force or wedge opening.	[59]
74	Crack at edge of a circular hole in an infinite sheet: uniform pressure.	[28]
75	Symmetrical star shaped crack in an infinite sheet: uniform pressure.	[64]
76	Internal radial crack in a circular disc: uniform pressure.	[65,66]
77	Edge crack in a circular disc: uniform pressure.	[67]
78	Central crack in an elliptical disc: uniform pressure.	[66]
79	Two equal length collinear cracks in an infinite sheet: point force on one crack.	[55]
80	Periodic array of cracks in pairs: symmetrical point forces.	[68]
<b>Plates and shells</b>		
81	Slant crack in an infinite plate: bending.	[1]
82	Crack in a finite width plate: bending.	[69]
83	Crack in an infinite plate: biaxial twisting.	[1]
84	Slant crack in an infinite plate: shear couple.	[1]
85	Crack in an infinite plate: point moment on crack surface.	[68]
86	Crack in an infinite plate on an elastic foundation: uniformly distributed plate load.	[70]
87	One or two cracks at the edge of a circular hole in an infinite plate: bending.	[71]
88	Spherical shell with a meridional crack: internal pressure.	[72,73]
89	Cylindrical shell with an axial crack: internal pressure.	[72,74,75,74]
90	Cylindrical shell with a circumferential crack: internal pressure and axial tension.	[77,78,79]
91	Cylindrical shell with an axial crack: torsion.	[80]
92	Cylindrical shell with a circumferential crack: torsion.	[81]
<b>Stiffened Sheets</b>		
93	Infinite sheet with a crack symmetrical about a single integral stiffener: uniform tension, stiffener intact.	[82]
94	Infinite sheet with a crack symmetrical about a single integral stiffener: uniform tension, stiffener broken or intact.	[83]

- 95 Infinite sheet with a crack near to a single integral stiffener: uniform tension, stiffener intact. (82)
- 96 Finite width sheet with a crack located centrally between integrally stiffened sheet edges: uniform tension with stiffener having zero or infinite in-plane bending stiffness. (5,84)
- 97 Infinite sheet with periodic cracks in alternate bays of a multi-bay integrally stiffened panel: uniform tension. (5)
- 98 Infinite sheet with a crack symmetrical about a single riveted stiffener: uniform tension, broken or intact stiffener. (85,86)
- 99 Infinite sheet with a crack asymmetrical to a single riveted stiffener: uniform tension. (85)
- 100 Infinite sheet with a crack located centrally between two riveted stiffeners: uniform tension. (86)
- 101 Infinite sheet with a crack symmetrical about the central unbroken stiffener of an array of riveted stiffeners: uniform tension. (87,88)
- 102 Crack symmetrical between two riveted stiffeners in an array: uniform tension. (87)
- 103 Crack in an infinite sheet reinforced with patches: uniform tension. (89)
- 104 Cylindrical shell with an axial crack in the vicinity of a circumferential stiffener: internal pressure. (76)
- Bars in shear and torsion
- 105 Internal crack along a diameter in a circular bar: torsion. (90)
- 106 One or two radial edge cracks in a circular bar: torsion and shear. (90,91)
- 107 Arbitrary number of equally spaced, equal length radial cracks in a circular bar: torsion. (91)
- 108 Single edge crack along the major diameter to the near focus in an elliptical bar: torsion. (90)
- 109 External circumferential crack in a solid circular bar: torsion. (16)
- 110 External circumferential crack in a hollow bar: torsion. (16)
- 111 Double edge cracks in a square bar: torsion. (92)
- 112 Single edge crack in a square bar: torsion, longitudinal and transverse shear. (92,93)
- 113 External radial crack in a hollow bar: torsion and transverse shear. (94)
- Solids under longitudinal shear
- 114 Crack in an infinite sheet: longitudinal shear at an arbitrary angle to the crack line. (95)
- 115 Right angled crack in an infinite sheet: longitudinal shear at an arbitrary angle to the crack. (95)
- 116 Symmetrical star crack (3 tips) in an infinite sheet: longitudinal shear at an arbitrary angle to the crack. (95)
- 117 Symmetrical star crack (4 tips) in an infinite sheet: longitudinal shear at an arbitrary angle to the crack. (95)
- 118 Circular arc crack in an infinite sheet: longitudinal shear at an arbitrary angle to the crack. (95)
- 119 Two equal cracks at the edge of a circular hole in an infinite sheet: longitudinal shear at an arbitrary angle to the crack. (95)
- 120 Three collinear cracks in an infinite sheet with outer cracks the same length: longitudinal shear parallel to the cracks. (96)
- Three-dimensional configurations
- 121 Half plane crack in an infinite solid: symmetrical point forces on the crack. (97,98)
- 122 Penny shaped crack in an infinite solid: pair of point forces perpendicular to the crack on the axis of symmetry. (55)

123	Penny shaped crack perpendicular to surface of a semi-infinite solid; uniform and linearly varying stress.	(99)
124	Penny shaped crack parallel to the surface of a semi-infinite solid; internal pressure, surface of solid rigidly clamped or stress free.	(100)
125	Penny shaped crack in a large beam; bending.	(101)
126	Penny shaped crack in a thick plate; uniform pressure or displacement.	(102, 103)
127	Circular annulus crack in an infinite solid; uniform pressure.	(104, 105, 106)
128	Penny shaped crack in a sphere; uniform internal pressure, spherical surface rigidly fixed, stress free, or zero radial displacement and shear stress.	(107)
129	Penny shaped crack in a circular cylinder; uniform and parabolic pressure, cylindrical surface stress free or zero radial displacement and shear stress.	(108, 109)
130	External circumferential crack in a hollow circular cylinder; uniform tension.	(2, 16, 68)
131	External circumferential crack in a hollow circular cylinder; bending.	(16)
132	External circumferential crack in a hollow circular cylinder; transverse shear.	(16)
133	Semi-circular penny shaped surface crack in a semi-infinite solid; uniform and linearly varying stress.	(110)
134	Incomplete penny shaped surface crack in a semi-infinite solid; uniform and linearly varying stress.	(111)
135	Incomplete penny shaped surface crack in a finite thickness plate; uniform tension.	(112)
136	Elliptical crack in an infinite solid; uniform tension and internal pressure.	(113, 114, 115)
137	Elliptical crack in an infinite solid; arbitrarily inclined shear stress.	(116)
138	Elliptical junction between two semi-infinite solids; uniform tension perpendicular to the junction plane or uniform shear along major axis of junction.	(117)
139	Elliptical junction between two semi-infinite solids; uniform displacement along major axis of junction.	(118)
140	Elliptical crack in a semi-infinite solid; uniform tension and bending.	(119)
141	Elliptical crack in a finite thickness plate; uniform tension.	(120)
142	Semi-elliptical surface crack in a semi-infinite solid; uniform tension.	(121)
143	Semi-elliptical surface crack in a finite thickness plate; uniform tension.	(122, 123, 124)
144	Quarter-circular crack in a quarter infinite solid; uniform tension.	(125)

The respective stress intensity values for the above cases will be of particular interest to research engineers, designers and materials scientists needing a source of stress intensity factors for the application of fracture mechanics principles to fatigue, stress corrosion cracking, mechanical testing and the analysis of structural failure.

The solutions in the Rooke and Cartwright book have been obtained from an exhaustive survey of published reports and papers, of which approximately 150 are cited; the results have been analysed and most are presented in graphical form.

The following is an example of the stress intensity solutions given by Rooke and Cartwright. Figures and other references will be found in their book.

#### CRACK IN AN INFINITE SHEET: POINT FORCE

An infinite sheet contains a crack situated along the line  $y = 0$  with tips at  $x = \pm a$ . A force, with horizontal component  $Q$  (force/unit thickness) and a vertical component  $P$ , acts in the plane of the sheet at a point  $(x, y)$  (see figures (102) to (113)). This configuration has been studied by Erdogan [55] using complex stress functions; both opening and sliding modes have been considered.

The stress intensity factors for the tip at  $x = a$  can be written in terms of the real and imaginary parts of the two complex functions  $G(z)$  and  $H(z)$ , which are defined as

$$G(z) = \frac{a + z}{\sqrt{z^2 - a^2}} \quad \text{and} \quad H(z) = \frac{a(\bar{z} - z)}{(\bar{z} - z)\sqrt{z^2 - a^2}} \quad (1)$$

where  $z = x + iy$  and  $\bar{z} = x - iy$  ( $i = \sqrt{-1}$ ). Four auxiliary functions are required

$$\begin{aligned} u_1 &= 1 = \operatorname{Re}(G(z)), & H_1 &= \operatorname{Re}(H(z)) \\ u_2 &= -\operatorname{Im}(G(z)), & H_2 &= -\operatorname{Im}(H(z)), \end{aligned} \quad (2)$$

where  $\operatorname{Re}$  and  $\operatorname{Im}$  respectively denote real and imaginary parts.

Curves of these functions vs.  $x/a$  are shown for various values of  $y/a$ . Each function is plotted separately for the three regions  $x/a \leq 0.5$ ,  $0.5 < x/a \leq 1.5$  and  $x/a \geq 1.5$ .

For the horizontal force the stress intensity factors are given by

$$\frac{K_I}{K_0} = G_1 + \frac{H_1}{(\nu + 1)} \quad \text{with } K_0 = \frac{Q}{2\sqrt{\pi a}} \left( \frac{\nu - 1}{\nu + 1} \right) \quad (3)$$

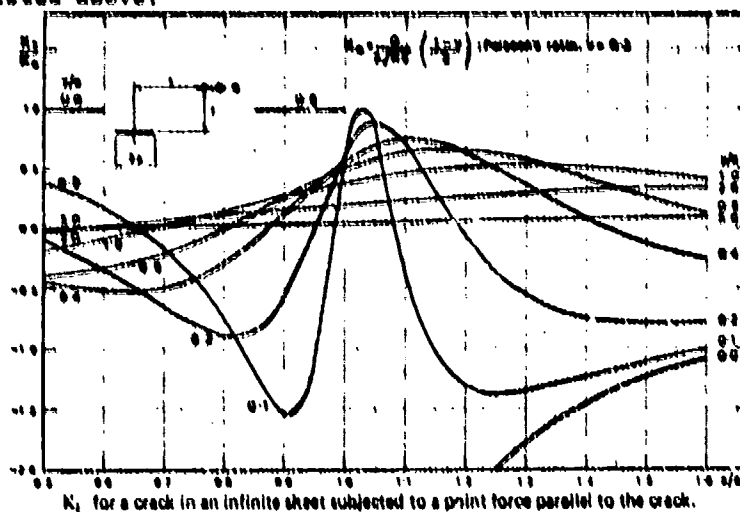
$$\text{and } \frac{K_{II}}{K_0} = G_2 + \frac{H_2}{(\nu + 1)} \quad \text{with } K_0 = \frac{Q}{2\sqrt{\pi a}} \quad (4)$$

for the vertical force

$$\frac{K_I}{K_0} = G_2 - \frac{H_2}{(\nu + 1)} \quad \text{with } K_0 = \frac{P}{2\sqrt{\pi a}} \quad (5)$$

$$\text{and } \frac{K_{II}}{K_0} = G_1 - \frac{H_1}{(\nu - 1)} \quad \text{with } K_0 = -\frac{P}{2\sqrt{\pi a}} \left( \frac{\nu - 1}{\nu + 1} \right) \quad (6)$$

The  $K_0$ 's defined above are the stress intensity factors if the appropriate forces were acting at the midpoint of the crack;  $\nu$  is a function of Poisson's ratio ( $\nu$ ) given, for plane strain, by  $3 - 4\nu$  and, for plane stress, by  $(3 - \nu)/(1 + \nu)$ . Plane stress curves of  $K_I/K_0$  and  $K_{II}/K_0$  vs.  $x/a$ , for various values of  $y/a$ , are shown in figures (114) to (125) for both horizontal and vertical forces ( $\nu = 0.3$ ). The curves are plotted separately in the three regions listed above.



$K_0$  for a crack in an infinite sheet subjected to a point force parallel to the crack.

Ref.

#### SECTION 2

- 1 G.G. Sih, P.C. Paris, F. Erdogan. J. appl. Mech., 29, 306 (1962)
- 2 W.K. Wilson. J. bas. Engng., 93, 685 (1971)
- 3 G.N. Savin. "Stress distribution around holes" (translation), NASA TT F-607, Ch.VIII (1970)
- 4 M. Isida. Japan Soc. Mech. Engrs., 22, 803 (1956)
- 5 M. Isida, Y. Itagaki. Proc. 4th U.S. Nat. Congr. on Applied Mechanics, p.955 (1962)
- 6 H. Neuber. Kerbspannungslehre, Springer, Berlin (1958)
- 7 W.T. Koiter. Report No.314 (1963), Dept. of Mech. Engng., Technological University, Delft
- 8 M. Isida. Japan Soc. Mech. Engrs., 21, 507 (1955)
- 9 R.G. Forman, A.S. Kobayashi. J. bas. Engng., 86, 693 (1964)
- 10 I.N. Sneddon. Int. J. Engng. Sci., 9, 479 (1971)
- 11 O.L. Bowie, D.M. Neal. Engng. fracture Mech., 2, 181 (1970)

## Ref.

- 12 N. Tada. *Engng. fracture Mech.*, 2, 345 (1971)
- 13 N. Tada. *Int. J. fracture Mech.*, 2, 301 (1971)
- 14 N. Tada. *J. appl. Mech.*, 33, 674 (1966)
- 15 N. Tada. *Japan Soc. Mech. Engrs.*, 22, 809 (1956)
- 16 D.O. Harris. *J. bas. Engrg.*, 89, 49 (1967)
- 17 B. Gross, J.R. Srawley, W.P. Brown. NASA TN D-1395 (1964)
- 18 W.P. Brown, J.R. Srawley. STP 410, ASTM (1966)
- 19 O.L. Bowie, D.M. Neal. *J. appl. Mech.*, 32, 708 (1965)
- 20 O.L. Bowie, D.M. Neal. US Army Materials Research Agency Technical Report, AMRA TR 65-20 (1965)
- 21 B. Gross, J.R. Srawley. NASA TN D-2603 (1965)
- 22 J.O. Rice. *J. appl. Mech.*, 34, 248 (1967)
- 23 B. Gross, J.R. Srawley. NASA TN D-3902 (1965)
- 24 W.K. Wilson. Research Report 69-127-VNROH-R1, Westinghouse Research Laboratories, Pittsburg (1969)
- 25 O.L. Bowie. *J. appl. Mech.*, 31, 208 (1964)
- 26 O.L. Bowie. *J. appl. Mech.*, 31, 736 (1964)
- 27 O.L. Bowie. *J. Math. Phys.*, 35, 60 (1956)
- 28 J.C. Newman. NASA TN D-6376 (1971)
- 29 D.M. Neal. *Int. J. fracture Mech.*, 6, 393 (1970)
- 30 N. Tada. *Engng. fracture Mech.*, 2, 61 (1970)
- 31 O. Tamate. *Int. J. fracture Mech.*, 1, 257 (1968)
- 32 C. Atkinson. *Int. J. Engrg. Sci.*, 10, 127 (1972)
- 33 C.J. Tranter. *Q.J. Mech. appl. Math.*, 14, 283 (1961)
- 34 T.J. Willmore. *Q.J. Mech. appl. Math.*, 2, 53 (1949)
- 35 B.I. Swamin. *Appl. Math. Mech.*, 34, 348 (1970)
- 36 N. Lowengrub, K.N. Srivastava. *Int. J. Engrg. Sci.*, 6, 425 (1968)
- 37 G.N. Savin. "Stress distribution around holes" (translation), NASA TT F-607, p.626 (1970)
- 38 N. Tada. *Bull. JSME*, 13, 635 (1970)
- 39 T. Yokobori, M. Uozumi, M. Ichikawa. *Rep. Res. Inst. Strength and Fracture of Materials, Tohoku Univ.*, 2, 23 (1971)
- 40 H.M. Westergaard. *J. appl. Mech.*, 6, A-49 (1939)
- 41 G.R. Irwin. *J. appl. Mech.*, 24, 361 (1957)
- 42 I.N. Sneddon, R.P. Srivastav. *Proc. Roy. Soc. Edin., A*, 67, 39 (1965)
- 43 W.T. Koiter. *Ingen Arch.*, 28, 168 (1959)
- 44 W.T. Koiter. *Problems of continuum mechanics*, (Ed. J.R.M. Radok), Society for Industrial and Applied Mathematics (Publishers), pp.246-259 (1961)
- 45 A.H. England, A.E. Green. *Proc. Camb. phil. Soc.*, 59, 489 (1963)
- 46 A.F. Emery, C.M. Segedin. *J. bas. Engrg.*, 94, 387 (1972)
- 47 O.L. Bowie, C.E. Freese. *Army Materials and Mechanics Research Centre Report AMMRC MS 70-3* (1970)
- 48 D.P. Rooke, J. Tweed. *Int. J. Engrg. Sci.*, 10, 709 (1972)
- 49 D.P. Rooke, J. Tweed. *Int. J. Engrg. Sci.* (to be published) (1972)
- 50 A.S. Kobayashi, D.E. Maiden, B.J. Simon, S. Iida. Paper 69-WA/PVP-12, ASME Annual Meeting, Nov. 1969

## Ref.

- 51 J.N. Bloom. Int. J. fracture Mech., 3, 597 (1966)
- 52 J.N. Bloom. Int. J. fracture Mech., 3, 335 (1967)
- 53 J.N. Bloom. J. appl. Mech., 33, 689 (1966)
- 54 W.O. Krauss. J. appl. Mech., 33, 356 (1966)
- 55 F. Erdogan. Proc. 4th US Nat. Congr. of Applied Mechanics, p.947 (1962)
- 56 H. Tada. Engng. fracture Mech., 2, 177 (1970)
- 57 D.P. Rooke, J. Tweed. Int. J. Engng. Sci. (to be published) (1972)
- 58 L.L. Lihachik, N.K. Kovchik. Soviet Mater. Sci., 3, 334 (1967)
- 59 G.I. Barenblatt. Advances in Appl. Mech., VII, 55 (1962)
- 60 W.A. Pichter. NASA TR R-265 (1967)
- 61 N. Lowengrub. Int. J. Engng. Sci., 4, 289 (1966)
- 62 J. Tweed. J. of Elasticity, 1, 29 (1971)
- 63 J.E. Srawley, N. Gross. Mater. Res. Stands., 7, 153 (1967)
- 64 K.A. Westmann. J. Math. Phys., 43, 191 (1965)
- 65 J. Tweed, D.P. Rooke, S.G. Das. Int. J. Engng. Sci., 10, 323 (1972)
- 66 O.L. Bowie, D.M. Neal. Int. J. fracture Mech., 6, 199 (1970)
- 67 J. Tweed, D.P. Rooke. Int. J. Engng. Sci. (to be published) (1972)
- 68 P.C. Paris, G.C. Sih. STP. 381, p.30, ASTM (1965)
- 69 W.K. Wilson, D.G. Thompson. Engng. fracture Mech., 3, 97 (1971)
- 70 E.S. Folias. Int. J. fracture Mech., 6, 257 (1970)
- 71 R. Roberts, T. Rich. J. appl. Mech., 34, 777 (1967)
- 72 F. Erdogan, J.J. Kibler. Int. J. fracture Mech., 3, 229 (1969)
- 73 E.S. Folias. Int. J. fracture Mech., 1, 20 (1965)
- 74 E.S. Folias. Int. J. fracture Mech., 1, 104 (1965)
- 75 L.G. Copley, J.L. Sanders. Int. J. fracture Mech., 3, 117 (1969)
- 76 M.E. Duncan, J.L. Sanders. Int. J. fracture Mech., 3, 133 (1969)
- 77 E.S. Folias. Int. J. fracture Mech., 3, 1 (1967)
- 78 V.V. Murthy, M.N. Bapu Rao. J. appl. Mech., 37, 539 (1970)
- 79 M.E. Duncan-Fama, J.L. Sanders. Int. J. fracture Mech., 8, 15 (1972)
- 80 S.I. Chou. J. appl. Mech., 38, 535 (1971)
- 81 F.E. Erdogan, M. Rawani. Int. J. fracture Mech., 8, 87 (1972)
- 82 R. Greif, J.L. Sanders. J. appl. Mech., 32, 59 (1965)
- 83 J.L. Sanders. NASA Tech. Report R-13 (1959)
- 84 M. Isida, S. Tagami, Y. Itagaki. J. Japan Soc. aeronaut. Space Sci., 10, 141 (1962)
- 85 J.M. Bloom, J.L. Sanders. J. appl. Mech., 33, 561 (1966)
- 86 J.P. Romualdi, J.T. Frazier, G.R. Irwin. NRL Report 4956, Washington DC (1957)
- 87 C.C. Poe. NASA TR R-358 (1971)
- 88 A.S. Kobayashi, D.E. Maiden. Office of Naval Research, NR 064 478, Tech. Rep. No.10 (1969)
- 89 T.A. Terry. Ph.D. Thesis, Lehigh University (1963)
- 90 G.C. Sih. J. appl. Mech., 30, 419 (1963)

## Ref.

- 91 J. Tweed, D.P. Rocks. *Int. J. Engng. Sci.* (to be published)
- 92 A.F. Emery. Sandia Corp. Report, SCL-DC-67-130 (1968)
- 93 R.A. Westmann, W.H. Yang. *J. appl. Mech.*, 34, 693 (1967)
- 94 A.F. Emery. Sandia Corp. Report, SCL-DR-69-39 (1969)
- 95 G.G. Sih. *J. appl. Mech.*, 32, 51 (1965)
- 96 G.G. Sih. *Proc. 2nd Conf. Theor. and Appl. Mech.* (1964)
- 97 Y.S. Uflyand. Internal report, University of North Carolina, Raleigh, N.C. (1965)
- 98 G.G. Sih, H. Liebowitz. *Fracture* 2, Chapter 2 (1968)
- 99 F.W. Smith, M.J. Alavi. *Engng. fracture Mech.*, 3, p.241 (1971)
- 100 K.N. Srivastava, Kripal Singh. *Int. J. Engng. Sci.*, 7, 469 (1969)
- 101 F.W. Smith, A.S. Kobayashi, A.F. Emery. *J. appl. Mech.*, 34, 947 (1967)
- 102 N. Lovengrub. *Q. appl. Math.*, 19, 119 (1961)
- 103 Y.N. Tsai. *Engng. fracture Mech.*, 4, 155 (1972)
- 104 L.W. Moss, A.S. Kobayashi. *Int. J. fracture Mech.*, 7, 89 (1971)
- 105 B.I. Smetanin. *Appl. Math. Mech.*, 32, 458 (1968)
- 106 D.L. Clements. Ph.D. thesis, University of Melbourne (1969)
- 107 K.N. Srivastava, J.P. Dwivedi. *Int. J. Engng. Sci.*, 9, 399 (1971)
- 108 I.N. Sneddon, R.J. Tait. *Int. J. Engng. Sci.*, 1, 391 (1963)
- 109 I.N. Sneddon, J.T. Welch. *Int. J. Engng. Sci.*, 1, 411 (1963)
- 110 F.W. Smith, A.F. Emery. *J. appl. Mech.*, 34, 953 (1967)
- 111 F.W. Smith, M.J. Alavi. *Proc. 1st Int. Conf. Pressure Vessel Technology, Delft* (1969)
- 112 R.W. Thresher, F.W. Smith. *J. appl. Mech.* (to be published)
- 113 A.E. Green, I.N. Sneddon. *Proc. Camb. phil. Soc.*, 46, 159 (1950)
- 114 M.K. Kassir, G.C. Sih. *J. Math. Mech.*, 16, 927 (1967)
- 115 M.K. Kassir, G.C. Sih. *Int. J. Engng. Sci.*, 5, 890 (1967)
- 116 M.K. Kassir, G.C. Sih. *J. appl. Mech.*, 33, 601 (1966)
- 117 M.K. Kassir, G.C. Sih. *J. appl. Mech.*, 35, 531 (1968)
- 118 M.K. Kassir. *J. appl. Mech.*, 35, 422 (1968)
- 119 R.C. Shah, A.S. Kobayashi. *Proc. 5th Nat. Symposium on Fracture Mechanics, Urbana* (1971)
- 120 A.S. Kobayashi, M. Ziv, L.R. Hall. *Int. J. fracture Mech.*, 1, 81 (1965)
- 121 G.R. Irwin. *J. appl. Mech.*, 29, 651 (1962)
- 122 W.L. Moss, A.S. Kobayashi. *Proc. 2nd Int. Conf. on Fracture, pp.31-45, Brighton* (1969)
- 123 R.C. Shah, A.S. Kobayashi. *Int. J. fracture Mech.* (to be published)
- 124 H. Miyamoto, T. Miyoshi. Presented at the colloquium of IUTAM high speed computing of elastic structures, Liege (1970)
- 125 F.W. Smith. Structural Development Research Memorandum No.17, Boeing, Seattle (1966)



APPENDIX 4  
INTERNATIONAL SYSTEM OF UNITS (SI)\*

THE THREE CLASSES OF SI UNITS

The International System of Units was adopted by the Eleventh General Conference on Weights and Measures, Paris, October 1960.

SI units are divided into three classes:  
base units,  
derived units,  
supplementary units.

From the scientific point of view division of SI units into these three classes is to a certain extent arbitrary, because it is not essential to the physics of the subject.

Nevertheless the General Conference, considering the advantages of a single, practical, worldwide system for international relations, for teaching and for scientific work, decided to base the International system on a choice of seven well-defined units which by convention are regarded as dimensionally independent: the metre, the kilogram, the second, the ampere, the kelvin, the mole, and the candela. These SI units are called base units.

The second class of SI units contains derived units, i.e., units that can be formed by combining base units according to the algebraic relations linking the corresponding quantities. Several of these algebraic expressions in terms of base units can be replaced by special names and symbols which can themselves be used to form other derived units.

Although it might be thought that SI units can only be base units or derived units, the General Conference admitted a third class of SI units, called supplementary units, for which it declined to state whether they were base units or derived units.

The SI units of these three classes form a coherent set in the sense normally attributed to the expression "coherent system of units".

The decimal multiples and sub-multiples of SI units formed by means of SI prefixes must be given their full name multiples and sub-multiples of SI units when it is desired to make a distinction between them and the coherent set of SI units.

SYMBOLS

The base units of the International System are collected in table 1 with their names and their symbols.

TABLE 1

<i>SI base units</i>		
Quantity	Name	Symbol
length.....	metre	m
mass.....	kilogram	kg
time.....	second	s
electric current.....	ampere	A
thermodynamic temperature*.....	kelvin	K
amount of substance.....	mole	mol
luminous intensity.....	candela	cd

\* Celsius temperature is in general expressed in degrees Celsius (symbol °C)

DERIVED UNITS

**Expressions.** Derived units are expressed algebraically in terms of base units by means of the mathematical symbols of multiplication and division. Several derived units have been given special names and symbols which may themselves be used to express other derived units in a simpler way than in terms of the base units.

Derived units may therefore be classified under three headings. Some of them are given in tables 2, 3, and 4.

\* Adapted from the International System of Units (SI), NBS Special Publication 330, 1972 Edition

TABLE 2

*Examples of SI derived units  
expressed in terms of base units*

Quantity	SI unit	
	Name	Symbol
area	square metre	m <sup>2</sup>
volume	cubic metre	m <sup>3</sup>
speed, velocity	metre per second	m/s
acceleration	metre per second squared	m/s <sup>2</sup>
wave number	1 per metre	m <sup>-1</sup>
density, mass density	kilogram per cubic metre	kg/m <sup>3</sup>
concentration (of amount of substance)	mole per cubic metre	mol/m <sup>3</sup>
activity (radioactive)	1 per second	s <sup>-1</sup>
specific volume	cubic metre per kilogram	m <sup>3</sup> /kg
luminance	candela per square metre	cd/m <sup>2</sup>

TABLE 3

*SI derived units with special names*

Quantity	SI unit			
	Name	Sym- bol	Expression in terms of other units	Expression in terms of SI base units
frequency	hertz	Hz		s <sup>-1</sup>
force	newton	N		m·kg·s <sup>-2</sup>
pressure	pascal	Pa	N/m <sup>2</sup>	m <sup>-1</sup> ·kg·s <sup>-2</sup>
energy, work, quantity of heat	joule	J	N·m	m <sup>2</sup> ·kg·s <sup>-2</sup>
power, radiant flux	watt	W	J/s	m <sup>2</sup> ·kg·s <sup>-3</sup>
quantity of electricity, electric charge	coulomb	C	A·s	s·A
electric potential, potential difference, electromotive force	volt	V	W/A	m <sup>2</sup> ·kg·s <sup>-3</sup> ·A <sup>-1</sup>
capacitance	farad	F	C/V	m <sup>-2</sup> ·kg <sup>-1</sup> ·s <sup>4</sup> ·A <sup>2</sup>
electric resistance	ohm	Ω	V/A	m <sup>2</sup> ·kg·s <sup>-3</sup> ·A <sup>-2</sup>
conductance	siemens	S	A/V	m <sup>-2</sup> ·kg <sup>-1</sup> ·s <sup>3</sup> ·A <sup>2</sup>
magnetic flux	weber	Wb	V·s	m <sup>2</sup> ·kg·s <sup>-2</sup> ·A <sup>-1</sup>
magnetic flux density	tesla	T	Wb/m <sup>2</sup>	kg·s <sup>-2</sup> ·A <sup>-1</sup>
inductance	henry	H	Wb/A	m <sup>2</sup> ·kg·s <sup>-2</sup> ·A <sup>-2</sup>
luminous flux	lumen	lm		cd·sr (*)
illuminance	lux	lx		m <sup>-2</sup> ·cd·sr (*)

(\*) In this expression the steradian (sr) is treated as a base unit.

TABLE 4

Examples of SI derived units  
expressed by means of special names

Quantity	SI unit		
	Name	Symbol	Expression in terms of SI base units
dynamic viscosity	pascal second	Pa·s	$m^{-1} \cdot kg \cdot s^{-1}$
moment of force	metre newton	N·m	$m^2 \cdot kg \cdot s^{-2}$
surface tension	newton per metre	N/m	$kg \cdot s^{-2}$
heat flux density, irradiance	watt per square metre	W/m <sup>2</sup>	$kg \cdot s^{-3}$
heat capacity, entropy	joule per kelvin	J/K	$m^2 \cdot kg \cdot s^{-2} \cdot K^{-1}$
specific heat capacity, specific entropy	joule per kilogram kelvin	J/(kg·K)	$m^2 \cdot s^{-2} \cdot K^{-1}$
specific energy	joule per kilogram	J/kg	$m^2 \cdot s^{-2}$
thermal conductivity	watt per metre kelvin	W/(m·K)	$m \cdot kg \cdot s^{-3} \cdot K^{-1}$
energy density	joule per cubic metre	J/m <sup>3</sup>	$m^{-1} \cdot kg \cdot s^{-2}$
electric field strength	volt per metre	V/m	$m \cdot kg \cdot s^{-3} \cdot A^{-1}$
electric charge density	coulomb per cubic metre	C/m <sup>3</sup>	$m^{-3} \cdot s \cdot A$
electric flux density	coulomb per square metre	C/m <sup>2</sup>	$m^{-2} \cdot s \cdot A$
permittivity	farad per metre	F/m	$m^{-2} \cdot kg^{-1} \cdot s^4 \cdot A^2$
current density	ampere per square metre	A/m <sup>2</sup>	
magnetic field strength	ampere per metre	A/m	
permeability	henry per metre	H/m	$m \cdot kg \cdot s^{-2} \cdot A^{-2}$
molar energy	joule per mole	J/mol	$m^2 \cdot kg \cdot s^{-2} \cdot mol^{-1}$
molar entropy, molar heat capacity	joule per mole kelvin	J/(mol·K)	$m^2 \cdot kg \cdot s^{-2} \cdot K^{-1} \cdot mol^{-1}$

## SUPPLEMENTARY UNITS

The General Conference has not yet classified certain units of the International System under either base units or derived units. These SI units are assigned to the third class called "supplementary units", and may be regarded either as base units or as derived units.

For the time being this class contains only two, purely geometrical units: the SI unit of plane angle, the radian, and the SI unit of solid angle, the steradian.

TABLE 5  
SI supplementary units

Quantity	SI unit	
	Name	Symbol
plane angle	radian	rad
solid angle	steradian	sr

The radian is the plane angle between two radii of a circle which cut off on the circumference an arc equal in length to the radius.

The steradian is the solid angle which, having its vertex in the center of a sphere, cuts off an area of the surface of the sphere equal to that of a square with sides of length equal to the radius of the sphere.

Supplementary units may be used to form derived units. Examples are given in table 6.

TABLE 6

*Examples of SI derived units formed by using supplementary units*

Quantity	SI unit	
	Name	Symbol
angular velocity	radian per second	rad/s
angular acceleration	radian per second squared	rad/s <sup>2</sup>
radiant intensity	watt per steradian	W/sr
radiance	watt per square metre steradian	W·m <sup>-2</sup> ·sr <sup>-1</sup>

## SUBJECT INDEX

## A

Accuracy of  $K_{IC}$  values, 511  
 Acidity at crack tips, 117  
 Acoustic emission, 417, 419, 420  
 Acoustic emission as a nondestructive inspection method, 425  
 Acoustic emission as a precursor of fracture, 453  
 Acoustic emission bursts, 420  
 Acoustic emission during and immediately after welding, 442  
 Acoustic emission from welded aluminum, 451  
 Acoustic emission system, 436  
 Acoustic emission with size of crack and crack growth rate, 465  
 Aerospace pressure vessels, 294  
 Aircraft failure, 8  
 Aluminum alloys - tensile properties and fracture toughness, 590  
 Analysis of cracked stiffened panels, 233  
 Anodic dissolution, 112  
 Apollo propellants and fluids, 313  
 Applicability of penetrant process, 480  
 Applications of fracture mechanics concepts, 58  
 Applied stress, 22  
 Assurance index of NDT measurements, 400  
 ASTM standard method of test, 371, 372, 373  
 ASTM standard methods of tests for determining fracture toughness, 391  
 Atmospheric turbulence, 3  
 Available energy curve, 77  
 Axial skin stress, 240

## B

Basic fracture toughness data, 125  
 Bend specimen, 372  
 Blue brittleness, 333  
 Bond delamination, 248, 249  
 British Standards Institution, 580  
 Brittle-ductile transition, 333  
 Brittle-ductile transition temperature, 328, 333  
 Brittle fracture, 35  
 Brittle fracture appearance, 328  
 Buckling, 147, 148  
 Buffeting turbulence, 3  
 Built-up sheet structures, 181  
 Built-up sheet structures: wings, 195

## C

Cadmium plating, 338  
 Center cracked and double or single edge cracked plate, 377  
 Center cracked plate, 378  
 Centrally cracked configuration, 217  
 Characteristics of selected  $K_{IC}$  materials, 511  
 Charpy specimens, 326  
 Chromium plating, 338  
 Circumferential crack, 235, 254, 282  
 Circumferentially cracked round bar, 379  
 Coalescence (microgrowth), 104  
 Combined cyclic and sustained stress flaw growth, 297  
 Combined cyclic and sustained loading, 6  
 Combined mode fracture in AL-alloys, 146  
 Combined mode fracture of plexiglass, 146  
 Comparison of welded and unwelded, unnotched specimens, 452  
 Compliance, 78, 79  
 Compliance test results, 378  
 Compact tension data, 29  
 Compact tension specimen, 372  
 Composition of steels, 589  
 Composition of titanium alloys, 586  
 Compound specimen, 374  
 Condensed water, 340  
 Confirmatory testing, 145  
 Confirmatory testing, 179  
 Constant amplitude fatigue loading, 62  
 Constant amplitude loadings, 349  
 Continuous emission, 420  
 Corner cracks at holes, 129, 130  
 Correlation between specimens and pressure vessels, 297

## C

Correlation between various specimen types, 297  
 Correlation of acoustic emission and extent of cracking, 444  
 Corrosion cells, 340  
 Corrosion fatigue, 432, 433  
 Corrosion process, 337  
 Crack, 38  
 Crack arrest, 30, 87, 191, 205  
 Crack arrest temperature (CAT), 58  
 Crack at a hole, 288  
 Crack buckling and antibuckling guides, 146  
 Crack-critical points in sheet material, 405  
 Crack detection, 403  
 Crack extending across a stiffener, 221  
 Crack extension, 173  
 Crack growth, 28, 184, 188, 190, 250, 288  
 Crack growth laws, 62, 97  
 Crack growth rate, 23, 63, 97, 99, 105, 114, 115, 149, 150, 151, 152, 157,  
 176, 265, 266, 208, 435  
 Crack growth resistance curves (R-curves), 54  
 Crack growth retardation, 265  
 Crack in an infinite sheet: point force, 581  
 Crack instability, 54, 57  
 Crack length, 8, 21, 197, 289, 398  
 Crack length parameter, 21  
 Crack opening displacement (COD), 52, 54, 118  
 Crack opening displacement models, 216  
 Crack propagation, 96, 167, 169, 170, 171, 172, 178, 183, 187, 197,  
 250, 279, 281, 332  
 Crack propagation data, 29  
 Crack propagation experiments, 111  
 Crack propagation laws, 95, 119  
 Crack propagation life, 315  
 Crack propagation rate, 96, 98, 153, 154, 158, 159, 160, 161  
 Crack propagation relationships, 101  
 Crack running, 208  
 Crack size, 23  
 Cracked stiffened panel, 195  
 Crack stopper straps, 231  
 Crack tip, 175  
 Crack velocity-stress intensity relation, 116  
 Cracks, 338  
 Cracks emanating from cutouts and holes, 143  
 Crevices corrosion, 342  
 Criteria for validity of typical  $K_{IC}$  values, 511  
 Critical crack length, 92, 127, 383, 384, 386, 390  
 Critical crack size, 58, 61  
 Critical flaw size, 423  
 Critical fracture toughness values, 44  
 Critical stress intensities, 384, 423, 424, 429  
 Critical stress intensity factor, 383  
 C-shaped specimen, 379  
 Cumulative damage concepts, 173  
 Cumulative stress wave count, 442, 445, 448  
 Current flow magnetic particle testing method, 485  
 Current induction method, 488  
 Curved panels, 252, 268  
 Cyclic and sustained stress flaw growth, 295  
 Cyclic life, 308

## D

Damage by concentrated sharp contact, 338  
 Damage tolerance, 19, 228  
 Damage tolerance requirements, 27  
 Damage tolerant aircraft, 27  
 Damage tolerant structures, 58  
 Dangers of slow rates of pressurization and depressurization, 300  
 Defects, 463  
 Delayed crack detection, 444  
 Delayed weld cracking, 440  
 Delay of crack propagation, 155  
 De-magnetization, 489  
 Depressurization, 310  
 Detection and determination of flaw size by acoustic emission, 419  
 Determination of crack size at free accessible surfaces, 410  
 Determination of flaw size, 396, 410

## D

Difference between red and fluorescent penetrants, 483  
 Differential aeration, 340  
 Double cantilever beam specimen, 381  
 Double edged cracked plate, 378  
 Drop weight tear test, 88  
 Drying, 477  
 Ductile fracture, 34  
 Dugdale's strip-yield model, 52  
 Dye penetrant, 411  
 Dynamic tear test, 382, 383

## E

Eddy current, 411, 416  
 Eddy current testing of bolt holes, 401  
 Effect of attachment stiffness, 244  
 Effect of cyclic ratio, 152  
 Effect of long hold times, 298  
 Effect of strain rate on  $K_{IC}$  values, 390  
 Effect of thickness, 300  
 Effect of trigger level, 457, 458  
 Effect of wall thickness, 298  
 Elastic strain energy release rate, 41, 43  
 Elastic stress-strain relations, 44  
 Electrical disturbances, 468  
 Electrochemical reactions, 337  
 Embrittlement due to temperature cycling, 390  
 Emission amplitude, 420  
 Emission count, 420  
 Emission rate, 420  
 Energy release, 386  
 Energy release method, 224  
 Energy release rate, 201, 218, 225  
 Energy release rate curves, 83  
 Engineering classification of fracture, 34  
 Environmental cracking, 110, 113  
 Environmental effects in fracture, 110  
 Environmental effects on fracture toughness, 388  
 Environmental testing, 437  
 Equivalent notch factor, 349, 351  
 Examples of SI derived units expressed in terms of base units, 602  
 Examples of SI derived units expressed by special names, 603  
 Examples of SI derived units formed by using supplementary units, 604  
 Experimental techniques, 371  
 Extension of dominant crack, 104  
 Extraneous noise from metallurgical sources, 468  
 Elastic energy release rate G, 78, 79, 85

## F

Fail-safe, 30  
 Fail-safe design, 161, 122, 367  
 Fail-safe design and structural integrity, 368  
 Fail-safe design concepts, 121, 167  
 Fail-safe design procedures, 121  
 Fail-safe development tests, 251  
 Fail-safe methods, 124  
 Fail safety, 122, 123  
 Failure, 8  
 Fastener failure criterion, 207  
 Fastener forces, 219, 220  
 Fatigue center crack and machined sharp edge-notch specimen, 376  
 Fatigue crack, 340, 396, 397, 401  
 Fatigue crack growth, 62, 108, 314  
 Fatigue crack growth data, 23  
 Fatigue crack growth rate, 105, 108  
 Fatigue crack growth rate extrapolation, 503  
 Fatigue crack initiation and propagation, 374  
 Fatigue crack propagation, 149, 167, 317, 348  
 Fatigue crack propagation curve, 319  
 Fatigue damage, 330, 334, 355  
 Fatigue life assessment, 346, 505  
 Fatigue limit, 315  
 Fatigue loadings, 351  
 Fatigue pre-treatment, 328  
 Fatigue quality index, 350, 351

## F

Fatigue stress analysis, 505  
 Fatigue test acceleration, 359  
 Fatigue test results, 364  
 Filter level, 453  
 Films, 112  
 Final static fracture, 348  
 Finite element analysis of cracked panels, 222  
 Flat panel versus curved panel testing, 279  
 Flat panels with circumferential cracks, 253, 257  
 Flat panels with longitudinal cracks, 252, 255  
 Flaw detection, 396  
 Flaw detection in sheet material, 409  
 Flaw detection in solid metallic parts, 409  
 Flaw growth, 302, 304, 306  
 Flaw growth data, 303, 305, 306, 307, 308, 309  
 Flaw growth rate curves, 303  
 Flaw opening, 304  
 Flaw parameter, 126  
 Flight profile, 6  
 Flight load profile, 167  
 Flight load spectra, 356  
 Flight simulation tests, 156  
 Flight simulation test basis, 179  
 FMM, 287  
 Force matrix method, 283  
 Format, 285, 286  
 Fractographic examination, 503  
 Fractography, 503  
 Fracture analysis diagram (FAD), 58  
 Fracture behavior, 195  
 Fracture control, 24, 25  
 Fracture control procedures, 19  
 Fracture initiation, 330  
 Fracture mechanics, 35, 111  
 Fracture mechanics concepts in proof testing, 423  
 Fracture models, 14  
 Fracture on the atomic scale, 34  
 Fracture process, 85  
 Fracture safe design (FSD), 58  
 Fracture surface of a wing attachment, 334  
 Fracture toughness, 20, 23, 84, 86, 126, 127, 132, 372, 380  
 Fracture toughness in corrosive environments, 389  
 Fracture toughness in semibrittle fracture, 51  
 Fracture toughness of thick walled tubes, 379  
 Fracture toughness of weldments, 386  
 Fracture toughness test results, 580  
 Fracture toughness tests at high or low temperatures, 388  
 Fracture toughness values, 59, 371, 375  
 Frame criteria, 277  
 Frequency of occurrence and significance of airframe loadings, 4  
 Full scale fatigue tests, 347, 348  
 Full scale testing, 180  
 Fundamentals of magnetic particle testing, 485  
 Fuselage fatigue, 251

## G

Gamma rays, 416  
 Gasket materials, 340  
 Griffith and Irwin approaches, 41  
 Griffith's formula, 37  
 Griffith's theory, 43  
 Ground induced loadings, 3  
 Gust loads, 4  
 Gusts and atmospheric turbulence, 4

## H

Hand filing, 340  
 Heat treatments, 337  
 Heavy sections, 288  
 High dye penetrant, 482  
 History of loading of aircraft, 3  
 Holographic flaw detection measurements, 499  
 Holographic interferometry, 496  
 Holography, 495  
 Hot gas corrosion, 390



## H

Hydrogen, 112  
 Hydrogen cracking, 330  
 Hydrogen induced embrittlement, 330  
 Hydrophilic emulsifier, 402

## I

Impact damage, 145  
 Indoor full scale fatigue tests, 347  
 Initial stress intensity factors in service, 299  
 Ink concentration versus current intensity, 489  
 Inspection of flat surfaces using ultrasonics, x-ray, dye penetrants, magnetic particles, and eddy currents, 396  
 Instrumentation for in-field flaw detection, 462  
 Instrumentation system for fracture testing, 459  
 Intensifying the sensitivity of penetrants, 480  
 Internal airframe environment, J  
 International system of units (SI), 601  
 Interrupted slow crack growth, 141  
 Isolation of an acoustic emission source from extraneous noise, 459

## J

J-integral, 55, 118

## K

K-calibration of specimen, 377  
 Kuhn-Hardrath method, 89, 119

## L

Laboratory tests, 325  
 Life prediction model, 100  
 Limit design, 14  
 Linear elastic fracture mechanics, 14, 38  
 Liquid oxygen containers, 482  
 Liquid penetrant, 415  
 Loading rate effect, 332  
 Loading types, 351  
 Loads, 6  
 Load sequence and block size, 6  
 Load spectrum, 167, 346  
 Load-time history, 167  
 Longeron criteria, 277  
 Longeron geometric shape, 232  
 Longitudinal cracks, 253, 281  
 Longitudinal skin cracks, 228  
 Low cycle high stress intensity fatigue, 425  
 Low temperature brittleness, 326, 330  
 Low temperature brittleness of steels, 326

## M

Macroscopic, 34  
 Macroscopic classification of fracture, 34  
 Magnetic particle, 411, 416  
 Magnetic particle testing procedure, 485  
 Magnetization, 489  
 Magnetization using coils, 489  
 Magnetizing methods, 485  
 Maneuver loads, 3  
 Material properties, 20  
 Materials and welding procedure, 440  
 Materials utilization, 19  
 Maximum principal stress, 322  
 Maximum shear strain energy, 322  
 Maximum shear stress, 322  
 Mean probability of crack detection, 403, 404  
 Mechanistic considerations, 112  
 Microgrowth, 104  
 Miner's rule, 100, 170  
 Modes of crack surface displacements, 38  
 Monitoring a known crack, 460  
 Motor case failure, 301  
 Multiple proof tests, 300

## N

Natural cracks, 129, 130  
 NDT measurements, 399  
 NDT methods, 415  
 NDT techniques, 414  
 Neutron radiography, 416  
 Nil ductility transition temperature, 80  
 Nominal critical stress intensity, 22  
 Nondestructive inspection, 312  
 Nondestructive testing method, 396, 397  
 Nondestructive testing (NDT), 413  
 Nonlinear correction factor, 306  
 Nonlinear energy characteristics of fracture toughness, 85  
 Nonlinear fracture toughness measure, 87  
 Non-service test temperature, 299  
 Nonstandard methods with various specimen geometries, 377  
 Normal fracture appearance, 32  
 Notch strengths, 333  
 Nucleation of microcracks, 104

## O

One load parameter laws, 95  
 Opening mode crack surface displacements, 41  
 Opening mode displacements, 38  
 Operational environment, 3  
 Optical inspection, 411  
 Optical interferometry, 494  
 Optimum attachment stiffness, 247  
 Overcraft load spectra, 168

## P

Palmgren-Miner rule, 63, 64, 170, 351  
 Parameters influencing  $K_{IC}$ , 511  
 Penetration, 477  
 Fitting, 338, 340  
 Plane strain fracture mechanics, 383  
 Plane strain fracture toughness, 382  
 Plane strain problems, 135  
 Plane strain size requirements, 45  
 Plane strain toughness, 20  
 Plane stress, 133  
 Plane stress and transitional modes; sheets, 133  
 Plane stress fracture, 138  
 Plane stress fracture toughness, 136  
 Plane stress fracture toughness testing, 137  
 Plane stress of mixed mode  $K_Q$  data, 511  
 Passivation, 338  
 Plasticity correction, 43  
 Plastic energy consumed, 139  
 Plastic zone, 175  
 Plastic zone size, 43, 44, 80, 87  
 Poisonous elements, 338  
 Pole magnetizing, 488  
 Pop-in instability, 75  
 Predicting failure, 314  
 Prediction methods, 170  
 Pressure and other service loadings combined, 300  
 Pressure vessel monitoring, 462  
 Pressure vessels, 294  
 Preventing failures, 295  
 Probability and zones of confidence, 407  
 Programmed and random loading, 99  
 Programmed loading spectrum, 109  
 Proof test, 310  
 Proof testing concepts, 421  
 Proof tests on actual vessels, 299  
 Pulsar generated signal, 461

## Q

Qualification of penetrant inspector, 483  
 Qualification of penetrant inspection materials, 483  
 Quasi-linear rule of cumulative damage, 64  
 Quenching flaws, 338

n

Radius of plastic zone, 22  
 Randomized ordering, 6  
 Random loading, 99, 349, 363  
 Random load spectrum, 351  
 Rate of crack propagation, 106, 107  
 Rate of growth of crack, 4  
 Real-time computer based systems, 463  
 Released elastic energy, 139  
 Reliability of the detection of flaws, 396  
 Removal of penetrant, 477  
 Repeated loads, 4  
 Required energy curve, 77  
 Research fatigue tests, 340  
 Residual static strength, 334  
 Residual strength, 0, 92, 94, 128, 132, 134, 136, 138, 140, 141, 142, 198, 196, 212, 216, 217, 241, 244, 247, 279, 288, 291, 300  
 Residual strength diagram, 197  
 Residual strength of stiffened panels and wings, 209, 228  
 Residual strength of unreinforced panels, 141  
 Residual strength test data, 198  
 Residual strength under combined tension and shear, 144  
 Residual stress, 34, 191, 200  
 Residual stress curves, 74, 76, 84  
 Residual stress method, 74, 110, 110  
 Retardation effect, 157  
 Retardation factor, 129, 172  
 Rivet shear deflection, 234, 271  
 Rivet shear load, 275, 276, 277  
 Rivet shear load test, 274  
 Rupture of the paint film, 338

n

Safe crack growth life, 23  
 Salt water corrosion, 309  
 Sampling the test media, 490  
 Sandwich panels, 185, 217  
 Scratches, 340  
 Semibrittle fracture, 34, 37  
 Sensitivity of eddy current method, 402  
 Sensitivity of NDT methods, 398, 399  
 Service behavior and laboratory tests, 338  
 Service failures, 325  
 Service life, 6  
 Severe loadings, 5  
 Short transverse cracking, 340  
 Single edged cracked plate, 378  
 SI supplementary units, 603  
 Skin crack criterion, 207  
 Skin criteria, 277  
 Skin fracture criterion, 240  
 Skin material, 231  
 Skin thickness, 231  
 Slow crack growth, 30, 139, 148  
 Slow, stable crack growth, 249  
 Slow stable crack propagation, 305  
 Sludge deposits, 340  
 Specification composition of aluminum alloys, 592  
 Specimen geometries, 372  
 Spectrum of loading of aircraft, 3  
 Stable crack growth, 138  
 Standard method of sharp notch tension testing of high strength sheet materials, 375  
 Stationary crack, 35  
 Statistical evaluation of  $K_{IC}$  values, 375, 376  
 Steels-tensile properties and fracture toughness, 587  
 Stiffened panels, 181, 271  
 Stiffening elements, 202  
 Stiffener failure criterion, 205  
 Stiffener strength criteria, 242  
 Stop holes and other crack stoppers, 143  
 Strain aging embrittlement, 333, 438  
 Strain energy of the cracked body, 35  
 Strain energy release rate, 381  
 Strain-rate effects on plane strain fracture toughness, 49  
 Stress concentrations, 8, 33, 35  
 Stress concentration factor,  $K_N$ , 89

## H

Stress corrosion, 326, 334, 337, 342, 343  
 Stress corrosion cracking and hydrogen embrittlement, 434  
 Stresses and displacements, 38  
 Stresses at crack tip, 142  
 Stress factors under biaxial loading, 106  
 Stress intensity, 108, 131, 467  
 Stress intensity factor, 40, 61, 131, 144, 149, 151, 181, 182, 195,  
 201, 245, 251, 266, 306, 309, 314, 392  
 Stress intensity factor and fracture toughness, 32  
 Stress intensity reduction factor, 182  
 Stress severity factor, 350, 351  
 Stress wave count rate, 443  
 Stress wave data, 431  
 Stress wave emission, 449  
 Structural efficiency, 21  
 Structural environment, 3  
 Structural integrity, 6  
 Subcritical cracking, 438  
 Surface condition, 337  
 Surface corrosion initiation, 337  
 Surface damage, 340  
 Surface dye penetrant, 474  
 Surface energy, 43  
 Surface flaw data, 29  
 Surface flawed specimen, 115, 126, 303  
 Surface flaws, 129, 130, 161  
 Sustained loading-environmental spectra, 5  
 Systematic fatigue tests, 348

## T

Temperature and fracture mode transition, 47  
 Temper embrittlement, 333  
 Tensile properties and fracture toughness, titanium alloys, 383  
 Test factor, 289  
 Testing methodology, 110  
 Theoretical stress concentration factor,  $K_T$ , 89, 90  
 Thermal methods, 416  
 Thickness and fracture mode transition, 45  
 Threading bar method, 408  
 Threshold stress intensities, 111, 114, 116  
 Titanium alloy, 300  
 Tolerable flaw size, 127  
 Total strain energy, 57  
 Toughness, 135  
 Transition approaches, 16  
 Transverse skin cracks, 229  
 Turbulence, 5  
 Two-load parameter laws, 97  
 Typical fracture toughness of aircraft metallic materials, 511  
 Typical plane strain fracture toughness of aircraft materials, 509

## U

Ultimate strength factor, 91  
 Ultrasonics, 416  
 Ultrasonic carousel method, 406  
 Ultrasonic methods, 411  
 Ultrasonic testing, 404, 405  
 Undesirable flaw growth during proof test, 299  
 Unstiffened cylinders, 268  
 Usefulness of magnetizing process, 490

## V

Valuation of NDI-methods, 408  
 Variable amplitude fatigue loading, 63  
 Variable-amplitude service loading, 157  
 Very low dynamic frequencies, 349

## W

Wake turbulence, 3  
 Weakening by adsorption, 112  
 Welded fitting, 288  
 White noise, 468

X

X-radiography, 416

Y

Yield criteria, 319, 322

Yoke magnetizing, 468

## AUTHOR INDEX

- Achter, M.R., 168  
 Alburger, R., 484  
 Allen, F.C., 104, 163, 282, 394  
 Allen, N.D., 344  
 Anderson, W.H., 7, 345  
 Anderson, W.F., 7  
 Argarwal, A.B.L., 472  
 Armiento, D.F., 71  
 Atkinson, C., 598  
 Austin, D.A., 323
- Baker, C.S., 471  
 Bapu Rao, M.N., 599  
 Baratta, F., 103  
 Barenblatt, G.I., 599  
 Barress, R.A., 471  
 Barrois, W., 93, 102, 163, 344, 365, 366  
 Barsom, J.M., 71, 96, 103, 311  
 Bartelds, G., 187, 192, 225  
 Barth, C.F., 113  
 Bates, R.C., 164, 472, 508  
 Beachem, C.D., 69, 113, 311, 344  
 Beuwwkes, R., 97, 103  
 Bevers, C.J., 73  
 Begley, J.A., 72, 118  
 Bernstein, H., 394  
 Beta, C.R., 484  
 Biggs, W.B., 69  
 Bill, R.C., 472  
 Bloom, J.M., 599  
 Bluhm, J.I., 75, 77, 79, 80, 81, 87, 88, 89, 92, 93, 98, 103, 104, 163  
 Borchers, H., 337, 345  
 Bowie, D.L., 163  
 Bowie, O.L., 93, 104, 162, 597, 598, 599  
 Bowles, C.Q., 164, 165  
 Boyle, R.W., 70, 81  
 Bradshaw, F.J., 69, 164  
 Branger, J., 365  
 Broek, D., 73, 91, 92, 93, 94, 97, 98, 103, 104, 143, 162, 163, 164, 165, 166, 192, 283, 285, 332, 344, 393  
 Brown, B.F., 113, 311  
 Brown, S.J., 471  
 Brown, W.F., Jr., 70, 71, 393, 473, 508, 598  
 Brummer, S.B., 344  
 Bryan, D., 7  
 Bucci, R.J., 72, 103  
 Bueckner, H.F., 70  
 Bunting, P.M., 73  
 Burckhard, C.B., 501  
 Burdekin, F.M., 72, 163  
 Bussa, S.L., 103  
 Butler, J.P., 7  
 Buxbaum, D., 192  
 Buxbaum, O., 366
- Campbell, M.D., 145, 163  
 Carlson, E.L., 164  
 Carman, C.M., 71  
 Cartwright, D.J., 293  
 Chambers, R.H., 472  
 Chan, S.K., 225  
 Chou, S.I., 599  
 Christensen, R.H., 95, 102, 139, 162, 163, 425, 473  
 Clark, A.W., 71  
 Clark, W.G., Jr., 103, 393, 394, 508  
 Clausing, D.P., 75, 76, 77, 79, 81, 84  
 Clements, D.L., 600  
 Clevenson, S.A., 366  
 Climent, F.J., 472  
 Cocks, F.H., 345  
 Coleman, T.L., 192
- Collier, R.J., 496, 501  
 Conner, L.P., 473  
 Cooke, R.J., 73  
 Copley, L.G., 599  
 Corten, H.J., 73  
 Cowan, A., 72  
 Creager, H., 225  
 Creager, N., 163  
 Crews, J.H., 192  
 Crichlow, W.J., 139, 163, 217, 225, 365  
 Crimmins, P.P., 471, 472, 473  
 Crockett, C.D., 472
- Dahlberg, E.P., 164  
 Dai, P.K., 72  
 Danek, G.J., 343, 345  
 Davis, J.A., 345  
 Day, C.K., 472  
 DeJonge, J.B., 192  
 Deneff, G.V., 365  
 Denke, P.H., 139, 292  
 Denton, K., 104, 317, 318  
 DeRijk, P., 157, 165, 189, 193  
 Dixon, J.R., 93, 97, 103, 164, 225  
 Doherty, E.T., 496, 501  
 Dolan, T.J., 73, 102  
 Donaldson, D.R., 7, 165  
 Downey, F.K., 113  
 Driscoll, G.W., 103  
 Dugdale, D.S., 52, 72, 96, 102  
 Duncan, M.E., 599  
 Duncan-Fama, M.E., 599  
 Dunagan, H.L., 419, 465, 472, 473  
 Dwivedi, J.P., 600
- Eftis, J., 55, 72, 386, 394  
 Eggwirts, S., 193  
 Egle, D.M., 472  
 Eichenberger, T.W., 163  
 Eide, G.R., 282  
 Ekvall, J.C., 7, 217  
 Elber, W., 164  
 Emery, A.F., 598, 600  
 England, A.H., 598  
 Engle, R.B., 472  
 Engle, R.M., 73, 103, 283  
 Ennos, A.E., 502  
 Erard, M., 330, 344  
 Erdogan, F., 73, 96, 102, 145, 152, 163, 164, 283, 314, 323, 508, 597, 599  
 Erisman, T.H., 104  
 Esgar, J.B., 311, 472, 473
- Feddern, G., 393  
 Feddersen, C.E., 139, 162, 163, 386, 394  
 Felbeck, D.K., 472  
 Fichter, W.B., 599  
 Field, F.A., 72  
 Figge, I.E., 93, 104, 139, 153, 164  
 Finger, R.W., 344  
 Flugge, W., 283  
 Folias, E.S., 599  
 Ford, G., 332, 344  
 Forman, R.G., 73, 97, 103, 164, 192, 283, 597  
 Foster, L.R., 192  
 Francis, P.H., 161, 165  
 Freche, J.C., 412  
 Frederick, J. R., 472  
 Freed, C.N., 70, 71, 72, 393  
 Freese, C.E., 598  
 Freudenthal, A.M., 73, 124, 162  
 Friesen, A. A., 502  
 Frost, N.E., 96, 97, 102, 103, 104, 165, 317, 318, 323

- Fryer, P.A., 501  
 Gabor, D., 501  
 Gallagher, J.P., 7  
 Gassmann, H., 466  
 Gassner, K., 162, 365  
 Gentilicore, V.J., 394  
 Gerberich, W.W., 71, 471, 473  
 Goode, R.J., 58, 73, 77, 81, 393  
 Goodier, J.N., 69, 72  
 Gordon, B.E., Jr., 73, 81  
 Gran, R.J., 7  
 Green, A.E., 129, 162, 598, 600  
 Green, A.T., 471, 472  
 Greenan, A.F., 323  
 Greenberg, H.D., 472  
 Grewal, K., 81  
 Grief, R., 192, 599  
 Griffith, A.A., 14, 16, 35, 37, 33, 41, 43, 69, 89, 92  
 Groover, R.E., 113  
 Gross, B., 70, 81, 598, 599  
 Gross, J.H., 473  
 Grosskreutz, J.C., 102  
 Grossman, N., 343  
 Grover, H.J., 102  
 Grünewald, K., 502  
 Habibie, B.J., 173, 175, 179, 192  
 Haese, W.P., 311  
 Hagiwara, Y., 119  
 Hahn, G.T., 23, 69, 70, 72, 164  
 Hall, L.R., 161, 165, 311, 344  
 Halsey, N., 363, 366  
 Hanna, G. L., 473  
 Hardrath, H., 7, 89, 93, 102, 119, 162, 165, 179, 192  
 Harpur, N.F., 163  
 Harris, D.O., 472, 473, 598  
 Harris, H.G., 365  
 Hartbower, C.E., 344, 440, 471, 472, 473  
 Hartman, A., 164, 165  
 Haslam, G.H., 323  
 Hayes, J.E., 365  
 Head, A.K., 96, 102  
 Heller, A.S., 162  
 Heller, R.A., 73, 162  
 Henthorne, M., 345  
 Hertzberg, R.W., 103, 165, 508  
 Meyer, R.H., 72, 75, 79, 81, 394  
 Hillberry, B.M., 73  
 Hinders, U.A., 31, 344  
 Hoagland, R.G., 393  
 Hodge, P.G., Jr., 16  
 Holden, J., 330, 344  
 Hopkins, B.E., 344  
 Hoskin, B.C., 163  
 Hudson, C.H., 164  
 Hudson, C.M., 103, 163, 165  
 Hunt, R.T., 282  
 Hussain, M.A., 393  
 Iida, S., 165  
 Iinno, N., 164  
 Illg, W., 90, 93  
 Impellizzeri, L.F., 102  
 Impellizzeri, L.P., 192  
 Inglis, C.E., 16, 69  
 Irwin, G.R., 14, 16, 41, 69, 70, 71, 72, 73, 76, 77, 81, 87, 89, 96, 102, 119, 162, 163, 219, 225, 282, 311, 386, 393, 598, 600  
 Isida, M., 164, 597, 598, 599  
 Jacobs, F.A., 163  
 Jacoby, G.H., 102, 363, 366  
 Jacques, H.E., 330, 343  
 James, C.A., 166  
 Jarfall, L., 350, 365  
 Jensen, J.K., 149, 163  
 Johnson, H.A., 312  
 Johnson, H.H., 73, 113, 311  
 Johnson, R.K., 103  
 Jelly, W.D., 440, 473  
 Jones, D.L., 73  
 Jones, J.W., 7, 192  
 Jones, M.H., 163  
 Joshi, S.R., 103  
 Judy, H.W., Jr., 98, 73, 77, 81, 393  
 Kaiser, J., 471  
 Kaletsch, D., 502  
 Kassir, M.K., 600  
 Kaufmann, J.G., 393  
 Kearney, N.E., 73  
 Kearney, V.E., 164  
 Kendall, D.P., 303  
 Kerawalla, J.N., 472  
 Kershaw, J., 508  
 Kiemle, H., 501  
 Kies, J.A., 70, 81, 394  
 Kies, J.E., 393  
 King, T.T., 7  
 Kirby, N., 72  
 Kirkby, W.T., 334, 344  
 Klausnitzer, E., 393  
 Klima, S.J., 412  
 Knauss, W.G., 599  
 Knott, J.F., 70  
 Kobayashi, A.S., 73, 129, 162, 163, 165, 311, 312, 597, 598, 599, 600  
 Koetje, E.L., 311  
 Koiter, W.T., 597, 598  
 Konazawa, T., 119  
 Kovchik, S.E., 599  
 Krafft, J.M., 70, 71, 72  
 Kraft, J.M., 77, 81, 163  
 Kuhn, P., 89, 90, 93, 119, 139, 163, 283  
 Kyrola, A.A., 471  
 Lachenaud, R., 165  
 Laird, C., 102  
 Lakshimikantham, C., 104  
 Lambert, J.A.B., 162  
 Landis, J.D., 72, 118  
 Langer, B.F., 73  
 Lehmann, V., 502  
 Lehmann, W., 345  
 Lois, H., 393  
 Lesso, D.J., 412  
 Lessells, J.M., 330, 343  
 Libatskii, L.L., 599  
 Liebowitz, H., 55, 69, 70, 71, 72, 73, 386, 394, 471, 600  
 Lin, L.H., 197, 215, 501  
 Liptai, R.G., 472  
 Little, C.D., 73  
 Liu, A.F., 163, 225, 283  
 Liu, H.W., 104, 164, 508  
 Lockman, C.S., 471  
 Lorenz, P.M., 311  
 Loss, F.J., 71  
 Love, A.E.H., 219, 225  
 Low, J.R., 69  
 Lowengrub, M., 598, 599, 600  
 MacGregor, C.W., 343  
 Maiden, D.E., 163  
 Manford, B.T., 365  
 Mann, J.Y., 192  
 Manson, S.S., 102  
 Mardirosian, M.M., 104  
 Marin, J., 71  
 Marschall, C.W., 344  
 Martienssen, W., 501  
 Mason, W.R., 472  
 Masters, J.N., 113, 311

- May, M.J., 393  
 Maynor, H.W., Jr., 343  
 McCabe, F.B., 72, 76, 79, 81, 394  
 McClintock, F.A., 70, 184  
 McCulloch, A.J., 363, 366  
 McEvily, A.J., Jr., 90, 93  
 McMaster, R.C., 417  
 McMillan, J.C., 73, 103, 165, 508  
 Makague, E.L., 502  
 Melcon, N.A., 366  
 Mertens, D., 394  
 Meyn, D.A., 165  
 Michida, S., 119  
 Miner, M.A., 63, 64, 73, 100, 170, 192  
 Mitchell, L.D., 472  
 Miyamoto, H., 600  
 Miyoshi, T., 600  
 Momota, S., 119  
 Morais, C.F., 472, 473  
 Nordfin, L., 363, 366  
 Morris, R.C., 282  
 Morrison, J.L.M., 317, 323  
 Morrissey, R.J., 75, 81  
 Morrow, J.D., 192  
 Moss, L.W., 600  
 Mukherjee, A.K., 69, 70, 99  
 Mukherjee, B., 103  
 Müller, E.A.W., 484, 490  
 Murthy, V.V., 599  
 Mylonas, C., 332, 344
- Neal, D.M., 597, 598, 599  
 Nederveen, A., 162, 165, 344  
 Nelson, F.G., 393, 513, 514  
 Neuher, H., 90, 93, 597  
 Newbegin, R.L., 113  
 Newman, J.C., Jr., 104, 153, 598  
 Niemi, R.M., 514  
 Nolan, M.J., 473  
 Norwood, J.I., 514, 581  
 Notvest, K., 440, 473  
 Novak, S.R., 514
- Oberparleiter, W., 393, 394  
 Orner, G.M., 344  
 Orowan, E., 14, 16, 69, 92, 93, 473  
 Owen, W.S., 344  
 Owens, J.S., 412
- Packman, P.L., 31  
 Packmann, P.F., 412  
 Palmgren, A., 63, 64, 73, 170, 192  
 Paris, P.C., 70, 72, 73, 96, 97, 98,  
 102, 103, 104, 113, 149, 162, 163,  
 164, 283, 311, 314, 323, 508, 597,  
 599  
 Parish, H.E., 192  
 Parker, E.R., 69, 71  
 Parry, J.S.C., 317, 323  
 Paxton, H.W., 113  
 Payne, A.E., 103  
 Payne, A.O., 365  
 Payne, W.F., 162  
 Pearson, H.S., 412  
 Pearson, S., 103, 508  
 Peel, C.J., 162, 508, 514, 581  
 Pellini, W.F., 71  
 Pellini, W.S., 73, 81  
 Pelloux, R.M.N., 73, 97, 99, 102, 164  
 Pendleberry, S.L., 513  
 Pennington, K.S., 496, 501  
 Pense, A.W., 394  
 Petch, N.J., 69  
 Peters, R.W., 93  
 Petersen, V.C., 513  
 Peterson, M.H., 311, 113  
 Petrak, G.J., 393  
 Pian, T.H.H., 225  
 Picard, J., 282
- Pierce, W.B., 166  
 Piper, D.E., 113, 311  
 Poe, C.C., Jr., 104, 185, 192, 197,  
 225, 599  
 Pook, L.P., 163, 317, 318, 323  
 Poterat, L.E., 473  
 Powell, R.L., 496, 501  
 Prager, W., 16  
 Proctor, R.P.M., 113
- Radon, J.C., 332, 344, 514  
 Raithby, R.D., 165  
 Raju, K.N., 163  
 Randall, P.N., 162  
 Randon, J.C., 72  
 Rathbone, A.M., 473  
 Rea, M.J., 514, 581  
 Rees, W.P., 344  
 Repho, A.J., 514  
 Reuter, P., 514, 581  
 Reuter, W.G., 471, 472, 473  
 Rice, J.C., 598  
 Rice, J.R., 72  
 Rich, T., 599  
 Roberts, C., 514, 581  
 Roberts, R., 599  
 Rockey, K.C., 344  
 Rolfe, S.T., 71, 394, 512, 514  
 Romine, H.E., 394  
 Romualdi, J.P., 219, 225, 599  
 Rooke, D.P., 69, 293, 598, 599, 600  
 Rosenfeld, S.J., 365  
 Rosenfield, A.R., 69, 70, 72  
 Röss, D., 501  
 Rossow, E., 393  
 Rotvel, F., 102
- Saito, H., 502  
 Salkin, R.V., 330, 344  
 Sanders, J.L., 599  
 Sankar, N.G., 472  
 Savin, G.N., 69, 597, 598  
 Scardina, J.T., 98, 103  
 Schijve, J., 7, 73, 97, 98, 102, 103,  
 157, 159, 162, 164, 165, 170, 173,  
 179, 191, 193, 225, 366  
 Schilling, P.E., 393, 513, 514  
 Schofield, B.H., 419, 465, 471, 473  
 Schra, L., 165  
 Schutz, D., 365  
 Schütz, W., 162, 365, 393, 394, 513  
 Schwartzberg, F.R., 514  
 Seagle, S.R., 514  
 Segedin, C.M., 598  
 Sertour, G., 514  
 Server, W.L., 394  
 Shah, R.C., 311, 312, 600  
 Shannon, J.L., Jr., 513  
 Shaw, R.C., 73  
 Shewchuck, J., 103  
 Shoemaker, A.K., 71, 394, 512  
 Sih, G.C., 69, 70, 101, 104, 145, 162,  
 163, 323, 597, 599, 600  
 Simpson, A.R., 514, 581  
 Smetanin, B.I., 598, 600  
 Smith, C.R., 192  
 Smith, F.W., 293, 311, 600  
 Smith, G.C., 102  
 Smith, H.L., 70, 394  
 Smith, H.M., 501  
 Smith, H.R., 113, 311  
 Smith, J.H., 514  
 Smith, S.H., 162, 165, 192, 225  
 Sneddon, I.N., 129, 597, 598, 600  
 Sokolnikoff, I., 70  
 Sollid, J.E., 502  
 Spalder, G.J., 514  
 Spanner, J.C., 472  
 Sprowls, D.O., 393, 514



Spurr, W.F., 513  
 Srawley, J.E., 70, 71, 72, 81, 163,  
 192, 311, 332, 344, 393, 473, 508,  
 512, 513, 598, 599  
 Srivastava, K.N., 600  
 Stavros, A.J., 113  
 Steel, R.K., 471  
 Steigerwald, E.A., 71, 113, 311, 343,  
 473, 512, 514  
 Steiner, R., 366  
 Stetson, K.A., 496, 501  
 Stone, D.E., 72  
 Stone, M., 282  
 Stoop, J., 70, 71, 514  
 Stout, R.D., 394  
 Sullivan, A.M., 70, 71, 72, 81, 514  
 Sullivan, T.L., 166  
 Swanson, S.R., 99, 103, 363, 366, 394  
 Swift, T., 225, 283  
  
 Tada, H., 598, 599  
 Tagami, S., 599  
 Tamate, O., 598  
 Tatro, C.A., 419, 465, 472  
 Taylor, J., 7  
 Tetelman, A.S., 394, 473  
 Thompson, D.G., 599  
 Thresher, R.W., 600  
 Tiffany, C.F., 113, 162, 311, 312, 472  
 Timoshenko, S.P., 69  
 Tipper, C.F., 69  
 Tonkins, B., 103  
 Tracey, D., 225  
 Tranter, C.J., 598  
 Troiano, A.R., 113, 473  
 Trotman, C.K., 164  
 Troughton, A.J., 162, 225  
 Tsai, Y.M., 600  
 Tuba, L.S., 163  
 Tupper, N.G., 514  
 Turner, C.E., 72, 332, 344  
 Tweed, J., 598, 599, 600  
  
 Valluri, S.R., 102  
 Van der Veer, I., 187, 217, 225  
 Van Dijk, G.M., 192  
 Van Leeuwen, H.P., 161, 165, 181, 188,  
 189, 190, 192, 193  
 Vest, C.M., 502  
 Vialatte, M., 343  
 Vishnevsky, C., 333, 343, 512  
 Vlieger, H., 143, 163, 192, 201, 225,  
 283  
 Vogt, F., 365  
 Von Euw, E.F.J., 192  
  
 Wachutka, H., 502  
 Walker, E.F., 393, 514  
 Walker, E.K., 162, 164  
 Walsh, P.F., 225  
 Wang, D.Y., 201, 203, 209, 225, 282  
 Wanhill, R.J.H., 127, 162  
 Warner, W.L., 473  
 Watwood, V.B., 225  
 Webster, D., 514  
 Weertman, J., 164  
 Wei, R.P., 165, 311  
 Weibull, W., 425, 473  
 Weiss, V., 69, 81  
 Weiss, W., 103  
 Weisz, M., 344  
 Wells, A.A., 71, 72, 119, 163  
 Wells, M.G.H., 514  
 Wernimont, G., 412  
 Wessel, E.T., 70, 71, 103, 343, 394,  
 513, 514  
 Westergaard, H.M., 225, 238, 283, 598  
 Westerlund, D.J., 514  
 Westmann, R.A., 599, 600  
  
 Wheeler, O.E., 175, 177, 179, 193  
 Wilhem, D.P., 67, 70, 103, 164, 293  
 Willenborg, J., 173, 177, 193, 283  
 Williams, M.L., 70  
 Willmore, T.J., 598  
 Willner, A.M., 311  
 Wilson, W.K., 163, 597, 598, 599  
 Wilson, W.R., 514  
 Winterton, K., 473  
 Wood, H.A., 31, 103, 394, 412  
 Wood, W.A., 102  
  
 Yamaguchi, J., 502  
 Yang, W.H., 600  
 Yokobori, T., 69, 598  
 Young, G., 97, 152, 216, 374, 412  
 Yukawa, S., 69  
  
 Eackay, V.F., 71  
 Zinkham, R.E., 73  
 Ziv, M., 312